ELECTE
APR 27 1995
F

Physical Metallurgy and Materials Science

METALLURGICAL AND MATERIALS TRANSACTIONS

Volume 25A–No. 12 December 1994 Pages 2549-2844 plus Index

N00014-93-1-0026

This document has been approved for public release and sale; its distribution is unlimited.

19950426 047

ASM INTERNATIONAL The Materials Information Society

TMS Minerals • Metals • Materials

INSTRUCTIONS FOR AUTHORS

METALLURGICAL AND MATERIALS TRANSACTIONS publishes contributions on all aspects of research and significant engineering advances in materials science and metallurgy. Approved manuscripts will be published according to subject matter in Section A or B. Assignment will be made in the Editor's Office, but author guidance will be appreciated concerning appearance in Section A or B and the classification of the manuscript according to current nomenclature used in the Table of Contents.

Metallurgical and Materials Transactions A publishes contributions on all aspects of physical metallurgy and materials science, with a special emphasis on relationships among the processing, structure, and properties of materials.

Metallurgical and Materials Transactions B publishes contributions on the theoretical and engineering aspects of the processing of metals and other materials, including studies of electro- and physical chemistry, mass transport, modeling, and related computer applications.

All manuscripts, including symposia, will be judged by qualified reviewers according to established criteria for technical merit. The review procedure begins in the editorial office as a Key Reader is assigned by the Editor or Associate Editor. The Key Reader chooses one or two reviewers for the manuscript and submits his recommendation, based on his own and the reviewers' judgments, to the editorial office. The Editor or Associate Editor then makes a final decision on the paper.

Submission of a manuscript is representation that it has neither been copyrighted, published, nor submitted for publication elsewhere. Prior publication is a basis for rejection. Appearance in a conference proceedings or similar special presentation with limited distribution is not necessarily prior publication. In such cases the article should be so referenced. There are two classes of papers:

Technical Publication: Manuscripts should represent completed original work embodying the results of extensive field, plant, laboratory, or theoretical investigation, or new interpretations of existing problems. Material must be considered to have significant permanent value. In addition to technical acceptability, material should be presented clearly and concisely.

Communication: This class provides more rapid publication of short items. Abstracts and divisional headings are not used. The length for a Communication should be about 1000 words of text, accompanied by whatever figures and tables may be required to support this text. These fall in the following categories:

(a) theoretical or experimental work of immediate current interest;
(b) discussion of Technical Papers and Communications. These should contribute to the original article by providing confirmation or additional interpretation. They will be referred to authors for reply. Discussion and authors' reply will be published concurrently;
(c) announcements and summaries of computations and computer programs or other compilations which are available on request from the author or a specified agency.

MANUSCRIPT

1. Send to: *Metallurgical and Materials Transactions*
   Carnegie Mellon University
   Schenley Park
   Pittsburgh, PA 15213
2. **Submit three copies, each complete with abstract, tables, and figures.** All copy (abstract, text, footnotes, references, figure captions) should be typed double-spaced on one side of 22 × 28 cm (8½ × 11 in.) paper, with a margin of at least 2.5 cm (1 in.) all around. **Three sets of high quality micrographs** are required for review purposes; Xerox-type copies are not acceptable. *Printer's copy of all figures (drawings and halftones) should be retained by the author until requested by the editor (see items 3a and 3b).*
   a. Copyright transfer must accompany the manuscript. See section entitled **COPYRIGHT POLICY** which follows.
   b. A separate list of figure captions should be included (double-spaced) in addition to the caption appearing with each figure.
   c. All tabulated data identified as tables should be given a table number and a descriptive caption. Tables should be numbered consecutively, using Roman numerals.
3. **Figures (halftones and line drawings) should be designed for final printing in single column 8.5 cm (3¼ in.) width.** Double column 18 cm (7 in.) treatment will be used only when required by the complexity of the material.
   a. **Line drawings.** These should be no larger than 22 × 28 cm (8½ × 11 in.). Lettering should be large enough to be 2 mm (1/16 in.) after reduction. Glossy photocopies of larger drawings are preferred.
   b. **Photographic material.** One mounted set of glossy prints with captions should be furnished for the printer's use. These should be protected by cardboard to avoid creases and markings. Staples, tape or clips should not be used. If necessary, indicate suitable framing, position, and proportion on a working copy.
   c. **Color printing** of photographic material can be arranged. This will involve an additional charge. Authors should correspond with the editor regarding specific papers.
   d. Original drawings and photographic material will be returned to the author by the printer after publication.
4. **The abstract is the author's summary of a scientific paper and is included in the review procedure.** It should indicate newly observed facts, conclusions, and the essential parts of any new theory, treatment, apparatus, technique, *etc.* It should be concise and informative and only in exceptional cases exceed 200 words.
5. **References** should be double-spaced and listed on a separate sheet. The required format is shown in the section entitled **STYLING OF REFERENCES.**
6. If the paper depends on unpublished work, three copies of the unpublished material should be included to assist the referees in their evaluation.
7. On the printer's copy, symbols should be clearly identified, *i.e.*, "Greek omicron," "One and ell" and "oh and zero" should be differentiated by a marginal note to avoid ambiguity.
8. Extensive revision at the author's option of text or figures in proof is costly and will be charged to the authors. Typographical errors may be corrected and references updated without charge.
9. There are no facilities for translating or making editorial revisions of foreign contributions. All publication is in English, and papers must be submitted in proper form. Canadian and British spelling should be changed to Americanized version.
10. The policy of *Metallurgical and Materials Transactions* is to use the International System of Units (SI). For guidelines, see National Bureau of Standards Special Publication 003-003-02380-9 (for sale by the Superintendent of Documents, U.S. Government Printing Office, Washington, DC 20402). If other units are required for special situations, a conversion to SI must be provided in parentheses or in a table.
11. Avoid the use of trade names and proprietary information whenever possible. Such use can occasionally be justified if this is the best way to specify a particular material or process.
12. A series of papers dealing with separate aspects of a subject should be cross referenced. Divisions, such as Part I, Part II, *etc.*, are not recommended as they complicate the review procedure and abstract listings. If such divisions are considered essential, they should be justified by the author at the time of submission and are subject to approval in review.
13. A **Table of Symbols** should be included when symbols are used extensively throughout a paper.

(continued on cover 3)

METALLURGICAL AND MATERIALS TRANSACTIONS A

Physical Metallurgy and Materials Science

VOLUME 25A, NUMBER 12 **DECEMBER 1994**

Metallurgical and Materials Transactions A publishes contributions on all aspects of physical metallurgy and materials science, with a special emphasis on relationships among the processing, structure, and properties of materials. All papers, including symposia contributions, are reviewed by a committee consisting of one member of the Board of Review and one or two other reviewers. See inside covers for detailed instructions for authors.

EDITORIAL STAFF

Editor: David E. Laughlin
Editor Emeritus: Gerhard Derge†
Associate Editors: Alan W. Cramb
R.J. Fruehan
S. Mahajan
Thaddeus B. Massalski
Production Editor: Dora Moscatello
Carnegie Mellon University
Pittsburgh, Pennsylvania 15213
FAX: (412) 268-7169
E-mail: mettrans@andrew.cmu.edu

JOINT COMMISSION FOR METALLURGICAL AND MATERIALS TRANSACTIONS

C. Parker, *Chair*
B. Attwood
D. Granger
M. Ozgu
A. Romig
J. Salsgiver

Alexander R. Scott
Edward L. Langer

JOINT MANAGERS

Edward L. Langer
ASM INTERNATIONAL

Alexander R. Scott
The Minerals, Metals & Materials Society

SOCIETY PRESIDENTS

ASM INTERNATIONAL
John G. Simon

The Minerals, Metals & Materials Society
Lionel C. Kimerling

Iron & Steel Society
Harry E. Follwell

BUSINESS STAFF

TMS Subscriptions and Advertising:
Linda L. Gibb, *TMS*

ASM Subscriptions:
Faye D. Balser, *ASM INTERNATIONAL*

Published jointly by

The Minerals, Metals & Materials Society
420 Commonwealth Drive
Warrendale, PA 15086

ASM INTERNATIONAL
Materials Park, OH 44073

Metallurgical and Materials Transactions "A" is published monthly by THE MINERALS, METALS & MATERIALS SOCIETY (TMS), 420 Commonwealth Drive, Warrendale, PA 15086, telephone (412) 776-9000, and ASM INTERNATIONAL, Materials Park, OH 44073, telephone (216) 338-5151. TMS and ASM are not responsible for any statements made or opinions expressed in their publications.

Subscription rates per year—Metallurgical and Materials Transactions "A": Individual non-members and multi-user facilities (libraries, corporate information centers, documentation services, military installations, government and private laboratories, etc.) $696.00 U.S., $696.00 other countries; individual members of TMS or ASM $50.00 U.S., $50.00 other countries. Metallurgical and Materials Transactions "B": Individual non-members and multi-user facilities $498.00 U.S., $498.00 other countries; individual members of TMS or ASM $36.00 U.S., $36.00 other countries. Combined Metallurgical and Materials Transactions "A" and "B": Individual non-members and multi-user facilities $1134.00 U.S., $1134.00 other countries; individual members of TMS or ASM $82.00 U.S., $82.00 other countries. Back issues of Metallurgical and Materials Transactions "A" and "B" are available by contacting TMS or ASM. Bound volumes of Metallurgical and Materials Transactions are available through TMS. Claims to either ASM or TMS for issues not received must be made within 120 days of expected delivery date.

Copyright 1994 by THE MINERALS, METALS & MATERIALS SOCIETY and ASM INTERNATIONAL . . . indexed by major abstracting services . . . second class postage paid at Warrendale, PA 15086, and at additional entry offices. Send all 3579 forms to Metallurgical and Materials Transactions, TMS, 420 Commonwealth Drive, Warrendale, PA 15086.

Authorization to photocopy items for internal and/or personal use of specific clients is granted upon request to TMS or ASM. Libraries and other users registered with the Copyright Clearance Center (CCC) Transactional Reporting Service, may photocopy items provided that the base fee of $00.75 per copy is paid directly to CCC, 21 Congress St., Salem, MA 01970.

Metallurgical and Materials Transactions "A" prior to 1972 is available from University Microfilms International, 300 North Zeeb Rd., Ann Arbor, MI 48106.

ISSN: 1073-5623/83

CODEN: MTTABN 25A(12) 2549-2844 (1994)

BOARD OF REVIEW

H.I. Aaronson
J. Ainsworth
S. Ankem
S.D. Antolovich
S.A. Argyropoulos
M.J. Aziz
A.S. Ballantyne
R.G. Bautista
C. Beckermann
W.D. Bennon
J.T. Berry
R. Berryman
C.P. Blankenship, Jr.
C.L. Briant
C.R. Brinkman
A. Bronson
W.E. Brower, Jr.
V. Brusic
A. Bustos
M. Byrne
R.W. Carpenter
K.S. Chan
K.-M. Chang
P. Chaubal
P.K. Chaudhury
H. Chen
N.S. Cheruvu
H. Cialone
M.J. Cieslak
J.A. Clum
T.H. Courtney
J.A. Dantzig
D.L. Davidson
G.P. Demopoulos
P. Desclaux
M. Dollar
F.M. Doyle
S. Dregia
D. Dreisinger
T.W. Eagar
G.R. Edwards
N. El-Kaddah
J.W. Elmer
W.H. Emling
M. Enomoto
B. Farouk
S.G. Fishman
R.A. Fournelle
D. Frear
P.D. Funkenbusch
A. Garg
W.M. Garrison
D.R. Gaskell
W.W. Gerberich
P.C. Glaws
J. Goldak
T. Gross
J. Grubb
D. Gupta
J.E. Hack
K.N. Han
R.L. Harris
M.J. Haun
J.B. Hiskey
J.M. Howe
Hsun Hu
S.-C. Huang
G. Irons
A.F. Jankowski
K.V. Jata
W.C. Johnson
R.H. Jones
J.S. Kallend
S.L. Kampe
M.E. Kassner
T.Z. Kattamis
A.H. King
C.C. Koch
B. Lally
C. Landefeld
J.D. Landes
T.G. Langdon
J. Lankford
E.J. Lavernia
H.M. Ledbetter
C.G. Levi
J.J. Lewandowski
P.K. Liaw
B. Lichter
K. Liddell
J.C. Liu
H. Margolin
S. Marsh
M. Mataya
R. Matway
J. Mazumder
A. McLean
T.R. McNelley
S.K. Menon
P.J. Meschter
M. Meshii
M.A. Meyers
G.M. Michal
B. Mishra
F. Mohamed
N.R. Moody
M.B. Mooiman
J.J. Moore
J.E. Morral
A.E. Morris
D.R. Morris
W.C. Moshier
K. Mukherjee
K.L. Murty
R.H. Nafziger
S. Nourbakhsh
D.L. Olson
M. Ozgu
B. Ozturk
R.A. Page
U. Pal
C. Pande
J.M. Papazian
H.G. Paris
C.A. Parker
R.D. Pehlke
T. Piwonka
M.R. Plichta
J.H. Poveromo
M. Przystupa
V.A. Ravi
D. Rego
W.T. Reynolds, Jr.
C.G. Rhodes
G. Richards
R.E. Ricker
J.M. Robertson
P. Rohatgi
A.K. Sachdev
I.V. Samarasekera
M. Sarikaya
A. Saxena
H. Schade
J.H. Schneibel
S.K. Sharma
G.J. Shiflet
G.K. Sigworth
J.E. Smugeresky
G. Spanos
S.K. Srivastava
G.R. Stafford
K.P. Staudhammer
D.M. Stefanescu
R. Stevenson
C. Suryanarayana
J.M. Tartaglia
B.G. Thomas
J.A. Todd
J.M. Toguri
A.K. Vasudevan
J.M. Vitek
V. Voller
P.W. Voorhees
G.W. Warren
G.S. Was
C.M. Wayman
C.A. Wert
J.A. Wert
S.H. Whang
J.E. Wittig
M. Wuttig

DTIC QUALITY INSPECTED 5

Contents

Pacific Rim Symposium—Part II

T.Y. Hsu (Xu Zuyao) and X.W. Zhou	2555	Thermodynamic Consideration of Formation Mechanism of α_1 Plate in βCu-Base Alloys
J.B. Cohen	2565	Long-Range Ordering in the Early Stages of Precipitation—A Brief Review
T. Tadaki and K. Shimizu	2569	High-Resolution Analytical Electron Microscopy Study of Isothermal Plate-Shaped Products in Some β-Phase Alloys
M.H. Wu, Y. Hamada, and C.M. Wayman	2581	Transformation Characteristics of α_1 Plates in Cu-Zn-Al Alloys
X.K. Meng, M.K. Kang, Y.Q. Yang, and D.H. Liu	2601	The Formation Mechanism of Plate in Beta Cu-Zn and Cu-Zn-Al Alloys
Y.Q. Yang, D.H. Liu, X.K. Meng, and M.K. Kang	2609	Growth Kinetics and High-Temperature TEM *in situ* Observation of Bainite in a Cu-Zn Alloy
Hong-Sheng Fang and Chun-Ming Li	2615	Study on the Transformation Mechanism of α_1 Plates in a Cu-Zn-Al Alloy
K. Takezawa, S. Maruyama, K. Marukawa, and S. Sato	2621	A Discussion on the Formation of Bainite and Other Precipitates in Cu-Zn and Ag-Zn Alloys
N. Ravishankar, H.I. Aaronson, and K. Chattopadhyay	2631	Mechanism of the Early Stages of α_1 Plate Formation in a Cu-39 Pct Zn Alloy
J.K. Chen, T.W. Ross III, G. Chen, M. Kikuchi, and W.T. Reynolds, Jr.	2639	The Selection of Precipitate Habit Planes in Cr-32 Wt Pct Ni
N. Nakanishi, T. Shigematsu, T. Furukawa, and N. Machida	2647	Bainitelike Transformations in Some Oxide Ceramics
H.I. Aaronson, J.P. Hirth, B.B. Rath, and C.M. Wayman	2655	General Discussion Sessions of the "Pacific Rim Conference on the Roles of Shear and Diffusion in the Formation of Plate-Shaped Transformation Products"

Alloy Phases

V. Raghavan and Dara P. Antia	2675	The Chromium Equivalents of Selected Elements in Austenitic Stainless Steels
V. Raghavan and Dara P. Antia	2827	Communication: The Chromium Equivalents of Ferrite Stabilizers in Commercial Stainless Steels

Transformations

J.P. Bourne, C. Atkinson, and R.C. Reed	2683	Diffusion-Controlled Growth in Ternary Systems
Werner Hort and William C. Johnson	2695	Diffusional Boundary Conditions during Coarsening of Elastically Interacting Precipitates
Joon-Woong Noh, Moon-Hee Hong, Geun-Hong Kim, Suk-Joong L. Kang, and Duk Yong Yoon	2828	Communication: The Cause of Matrix Penetration of W/W Grain Boundaries During Heat Treatment of W-Ni-Fe Heavy Alloy

Transport Phenomena

V. Sabathier, G.R. Edwards, and C.E. Cross	2705	Kinetic Study of Low-Temperature Transient Liquid Phase Joining of an Aluminum-SiC Composite

Mechanical Behavior

J.L. Freer Goldstein and J.W. Morris, Jr.	2715	The Effect of Substrate on the Microstructure and Creep of Eutectic In-Sn
Xiaoyu Hu, Robert H. Wagoner, Glenn S. Daehn, and Somnath Ghosh	2723	The Effect of Inertia on Tensile Ductility
M.C. Mataya and V.E. Sackschewsky	2737	Effect of Internal Heating During Hot Compression on the Stress-Strain Behavior of Alloy 304L
S.L. Semiatin, V. Seetharaman, and V.K. Jain	2753	Microstructure Development during Conventional and Isothermal Hot Forging of a Near-Gamma Titanium Aluminide
P.R. Subramanian, M.G. Mendiratta, and D.B. Miracle	2769	Microstructures and Mechanical Behavior of NiAl-Mo and NiAl-Mo-Ti Two-Phase Alloys
Xiao-Hu Zeng and Frédéric Barlat	2783	Effects of Texture Gradients on Yield Loci and Forming Limit Diagrams in Various Aluminum-Lithium Sheet Alloys
Ming Lei and Hassel Ledbetter	2832	Communication: Elastic Constants of SiC_p/Al: Measurements and Modeling
Chi-Sing Man	2835	Communication: Elastic Compliance and Hill's Quadratic Yield Function for Weakly Orthotropic Sheets of Cubic Metals

Physical Chemistry

Bart J. Kooi, Marcel A.J. Somers, and Eric J. Mittemeijer	2797	Thermodynamics and Long-Range Order of Interstitials in a Hexagonal Close-Packed Lattice

Surface Treatment

T.C. Totemeier, W.F. Gale, and J.E. King	2837	Communication: Microstructural Evolution of an Overlay Coating on a Single-Crystal Nickel-Base Superalloy

Solidification

Seong-Gyoon Kim, Sung-Ho Shin, Toshio Suzuki, and Takateru Umeda	2815	Numerical Analysis of the Rapid Solidification of Gas-Atomized Al-8 Wt Pct Fe Droplets
	2841	Contents, *Metallurgical and Materials Transactions B*, Volume 25A, December 1994

Combined Index to Volumes 25A and 25B follows page 2842

Accesion For
NTIS CRA&I ☑
DTIC TAB ☐
Unannounced ☐
Justification .....
By .....
Distribution /
Availability Codes
Dist | Avail and / or Special
A-1

DISCLAIMER. The acceptance and publication of manuscripts in METALLURGICAL AND MATERIALS TRANSACTIONS does not imply that the reviewers, key readers, editors, or the sponsoring Societies (ASM INTERNATIONAL, The Minerals, Metals & Materials Society, and The Iron and Steel Society) accept, approve, or endorse the data, opinions, and conclusions of authors. While manuscripts published in METALLURGICAL AND MATERIALS TRANSACTIONS are intended to have archival significance, authors' data and interpretations are frequently insufficient to be directly translatable to specific design, production, testing, or performance applications without independent examination and verification of their applicability and suitability by professionally qualified personnel.

Part II

Proceedings of the Pacific Rim Conference on The Roles of Shear and Diffusion in the Formation of Plate-Shaped Transformation Products

(Part I appeared in September A, 1994)

Foreword

The question as to whether the atomic movements involved in the formation of plates during phase transformations in crystalline solids taking place at temperatures above the martensite range occur by closely coordinated glide-type motions, *i.e.*, shear, or by biased random walk diffusion has been a controversial issue since it was raised by J.M. Robertson (1929), E.S. Davenport, and E.C. Bain (1930) and R.F. Mehl and C.S. Barrett (1931). Contrary to reasonable expectation, the increasing availability of sharper experimental tools (particularly visual and analytical transmission electron microscopy) and improved theoretical analyses has made this controversy more intense, albeit also more precisely defined. Since it has become clear that at least part of the difficulty being encountered in resolving this basic issue is one of communication between the two schools of thought, the Phase Transformations Committee of ASM International (Chaired by Professor Hayden Chen during the organization of this conference and then by Professor James M. Howe) decided to hold a conference focused as tightly as practicable solely upon this question. All speakers at this conference were invited, as were those additional conferees who have maintained an active interest in the subject. Approximately equal numbers of papers were commissioned from the two schools, as well as several from leading authorities in related phase transformation research areas who were not identified with either school. In addition to time for discussion scheduled after the presentation of each paper, most of the last day of the conference was devoted to two General Discussions sessions in which the main issues which arose during the Conference were publically discussed at length. Recordings were made of these Discussions. After some editing by the organizers, the individual discussions were returned to those who had given them for modification into final form. The compilation of these discussions, together with the large set of papers obtained on the formation of α_1 plates in Cu-Zn, Cu-Zn-Al, and Ag-Zn alloys, will appear soon in Part II of these proceedings, also to be published in this journal.

Because interest in this controversy has increasingly shifted in recent years to Japan and China, it was decided the conference would be held in the Hawaiian Islands—in particular on the "big island" of Hawaii—because these islands have won wide acceptance and the vote of preference as a meeting place for persons from the Pacific Rim countries. The Kona Hilton Hotel provided an outstanding milieu for the conference in the form of a relaxed and informal but very comfortable environment in which private discussions flourished as vigorously as did those held in public. (Indeed, considerable correspondence and research has already resulted from this conference.)

The organizers would like to express their gratitude to the Office of Naval Research (Dr. Robert C. Pohanka, Dr. George Yoder, and Dr. A.K. Vasudevan) and the National Science Foundation (Dr. Bruce A. MacDonald) for financial support which made possible the participation of a number of the conferees. Ms. Althena Franklin of the Kona Hilton Hotel staff and Mrs. Melody Guthrie, whose services as conference manager were provided by the Naval Research Laboratory, handled

the operation of the conference so smoothly and efficiently that the organizers were able to devote their full attention to the technical business of the conference itself. We are grateful to the members of the Phase Transformations Committee of ASM International for their support and constructive suggestions during the formulation of the conference program. Thanks are also due to Professors Tsun Ko (University of Science and Technology Beijing), Makato Kikuchi (Tokyo Institute of Technology), Gregory Olson (Northwestern University), Ken'ichi Shimizu (Kanazawa University), George Weatherly (McMaster University), Hayden Chen (University of Illinois at Urbana–Champaign), Barry Muddle (Monash University), Yasuya Ohmori (Ehime University), George Krauss (Colorado School of Mines), Mats Hillert (Royal Institute of Technology), T.Y. Hsu (Xu Zuyao) (Shanghai Jiao Tong University), James Howe (University of Virginia), and William Reynolds, Jr. (Virginia Polytechnic Institute and State University) for their service as session chairmen. Finally we thank Professor David E. Laughlin, Editor, and Ms. Dora Moscatello, Production Editor, Metallurgical and Materials Transactions, for supervising the review procedures for the conference papers.

C.M. Wayman, General Chairman
University of Illinois at Urbana–Champaign

H.I. Aaronson, Administrative Chairman
Geo-Centers, Inc., stationed at the Naval Research Laboratory

J.P. Hirth, Advisory and General Discussions Chairman
Washington State University

B.B. Rath, Government Relations Chairman
Naval Research Laboratory

Symposium Organizers

Thermodynamic Consideration of Formation Mechanism of α_1 Plate in βCu-Base Alloys

T.Y. HSU (XU ZUYAO) and X.W. ZHOU

For the possible ordering structures of the parent phase β'—*i.e.*, B2 in Cu-Zn alloys, DO_3 in Cu-Al alloys, and B2 and $L2_1$ in Cu-Zn-Al alloys—the driving forces for the α_1 plate formation have been calculated for the three βCu-base alloys. The driving force, ΔG, is larger than zero for the $\beta' \rightarrow \alpha_1$ shear mechanism and less than zero for the $\beta' \rightarrow \beta_1' + \alpha_1$ diffusional mechanism. Furthermore, the equilibrium temperature, T_0, between the parent β' phase and the α_1 plate has been evaluated to be much less than the experimental start temperature, B_s, of the α_1 plate formation. Therefore, the α_1 plate formation cannot be initiated by a diffusionless $\beta' \rightarrow \alpha_1$ shear reaction without other causative factors such as stress field, defects, *etc*. However, the α_1 plate can be formed through a diffusional $\beta' \rightarrow \beta_1' + \alpha_1$ reaction. Results in Cu-Al alloys also show that the composition of the α_1 plate produced in the diffusional reaction has to deviate from that of the parent phase to a certain extent. For some compositions of Cu-Zn-Al alloys, $\Delta G^{\alpha_1(\text{dis.})\rightarrow\alpha_1(\text{ord.})} < 0$ within a temperature range. Thus, the fresh α_1 plate produced after the diffusional reaction may further transform into the ordered α_1 plate within this temperature range. Calculated driving forces for the disordered parent phase reveal that the ordering of the parent phase resists the α_1 formation in Cu-Zn and Cu-Zn-Al alloys and enhances it in Cu-Al alloys.

I. INTRODUCTION

GARWOOD[1] first found the surface relief phenomenon accompanying the α_1 formation in a Cu-Zn alloy, and later, Garwood[2] and Cornelis and Wayman[3] revealed that the crystallography of $\beta' \rightarrow \alpha_1$ exhibited all the characteristics generally ascribed to a martensitic transformation. In addition, they found in Cu-Zn-Al[4] and Cu-Zn-Au[5] alloys that the α_1 phase even inherits the ordering of the parent phase. However, the interface and inner structure of α_1 in a Cu-Zn alloy are different from those of the martensite.[6] Recent measurements show that at an earlier stage of the α_1 formation in Cu-Zn-Al[7,8] and Cu-Zn-Au[5] alloys, the composition of α_1 is markedly different from that of the matrix. Thus, some authors thought that the partitioning of Cu and solute atoms only influences the characteristics of the α_1 plate after its formation in a diffusionless manner,[4] while others believed that the composition change by a long-range diffusion of solute atoms takes place before the α_1 nucleation by shear[8,9] or that the directional diffusion of solute atoms stimulates the nucleation and growth of α_1 plate.[10] Recently, it was reported that in Cu-Zn-Al alloys, the antiphase domain structures of the parent phase are inherited by the α_1 plate, the composition of the α_1 plate is different from that of the parent phase, and some local solute depletions occur at the dislocation in the parent phase.[11] Thus, the authors suggested that some solute-depleted defects act as nucleation sites for the formation of the α_1 plate, which lengthens through a shear mechanism but thickens by a diffusional process.[11] The role of dislocation in an elastic anisotropy medium in promoting both solute diffusion and shear for the α_1 plate formation has been emphasized.[12] Internal friction study of Cu-Zn-Al alloys revealed that the damping peaks appear within the incubation period of the α_1 formation, and the maximum damping values are inversely proportional to the incubation period; *i.e.*, directly proportional to the nucleation rate of the α_1 plate. Consequently, it is concluded that the pretransformation of α_1 formation involves the nucleation process.[13,14] Kinetic characteristics of the α_1 formation in Cu-Zn-Al alloys under stress[15] through upquenching from the martensitic state[16,17] or cooling from high-temperature B2 parent phase[17] obey the Austin-Rickett equation[18] for diffusional transformation. The activation energy is in good agreement with that of the diffusion of the solute atoms. X-ray diffractometry indicated that in a Cu-Zn-Al alloy, ordering of the α_1 is totally different from that of the martensite, which implies that the α_1 cannot inherit the ordering of the parent phase.[19,20] The composition change during the α_1 formation involves long-range diffusion of atoms, which may destroy the ordering structure. Thus, Aaronson *et al.*[21] concluded that the α_1 freshly formed cannot even partially inherit the ordering of the parent phase. This article summarizes the results of the thermodynamic studies of the α_1 formation in Cu-Zn,[22] Cu-Al,[23] and Cu-Zn-Al[24] alloys, based upon the thermodynamic surveys of these alloy systems,[25–28] and attempts to give a clear view of the formation mechanism of the α_1 plates.

II. THERMODYNAMIC APPROACH

In βCu-base alloys, the α_1 is produced from an ordered parent β' phase possessing the B2 ordering structure, as in Cu-Zn and Cu-Zn-Al alloys, or DO_3 ordering

T.Y. HSU (XU ZUYAO), Professor, is with the Department of Materials Science, Shanghai Jiao Tong University, Shanghai 200030, People's Republic of China. X.W. ZHOU, Ph.D. student, is with the Department of Mechanical Engineering, Clemson University, Clemson, SC 29634-0921.

This article is based on a presentation made at the Pacific Rim Conference on the "Roles of Shear and Diffusion in the Formation of Plate-Shaped Transformation Products," held December 18–22, 1992, in Kona, Hawaii, under the auspices of ASM INTERNATIONAL's Phase Transformations Committee.

structure, as in Cu-Al alloys, or $L2_1$ ordering structure, as in Cu-Zn-Al alloys. Any diffusionless transformation forming the α_1 can be expressed as $\beta' \rightarrow \alpha_1$ reaction, where the α_1 inherits the composition and ordering of the β' phase. Any diffusional transformation of the α_1 can be viewed as $\beta' \rightarrow \beta_1' + \alpha_1$ reaction, where the composition of the disordered α_1 is somewhat different from that of the β', which in turn, causes some composition change in the ordered matrix. This resulting matrix with changed composition is notated here as β_1'. In order to determine the possibility of these two reactions occurring, their driving forces have to be evaluated. In addition, the disordered α_1 formed from the diffusional reaction may undergo ordering upon aging or cooling from its formation temperature to ambient temperature. This process also can be determined by calculating the driving force for α_1 (disorder) $\rightarrow$ α_1 (order) ordering transition.

1. *Calculation of* $\Delta G^{\beta' \rightarrow \alpha_1}$

The change in free energy attending the shearing can be written as

$$\Delta G^{\beta' \rightarrow \alpha_1} = \Delta G^{\beta' \rightarrow \beta} + \Delta G^{\beta \rightarrow \alpha} + \Delta G^{\alpha \rightarrow \alpha_1} \qquad [1]$$

where $\Delta G^{\beta \rightarrow \alpha}$ is the change of free energy between the disordered α and β phases and $\Delta G^{\beta \rightarrow \beta'}$ $(= -\Delta G^{\beta' \rightarrow \beta})$ the change of free energy associated with the ordering $\beta \rightarrow \beta'$ (B2, DO_3, or $L2_1$). Because the α and α_1 phases have a similar structure [such as face-centered cubic (FCC)], except that the latter is ordered, $\Delta G^{\alpha \rightarrow \alpha_1}$ simply can be regarded as the change of free energy for the $\alpha \rightarrow \alpha_1$ ordering, where α_1 inherits the ordering of the β'.

If the disordered α and β phases are regarded as regular solutions, the general formula for the driving force $\Delta G^{\beta \rightarrow \alpha}$ of phase transformation is expressed as follows:

$$\Delta G^{\beta \rightarrow \alpha} = \sum_i X_i \Delta G_i^{\beta \rightarrow \alpha} + \sum_{i \neq j} \Delta E_{ij}^{\beta \rightarrow \alpha} X_i X_j \qquad i, j = \text{Cu}, \ldots \qquad [2]$$

Here, $\Delta G_i^{\beta \rightarrow \alpha}$ stands for the lattice stability parameter of the i element, $\Delta E_{ij}^{\beta \rightarrow \alpha} = E_{ij}^{\alpha} - E_{ij}^{\beta}$, with E_{ij}^{α} and E_{ij}^{β} representing, respectively, the interaction energy parameters between i and j components in the α and β phases. X_i is the atomic fraction of i element. According to the regular solution model for the binary system, the activity coefficient of component i in solution ϕ, γ_i^{ϕ}, should be

$$RT \ln \gamma_i^{\phi} = E_{ij}^{\phi} (1 - X_i)^2 \qquad [3]$$

In addition, it can also be derived[27] for the regular solution that

$$E_{ij} = -0.5 N_0 \sum_k (Z_k W_{ij}^{(k)}) \qquad [4]$$

where N_0 is Avogadro's constant, Z_k represents the number of the kth nearest neighbors, and $W_{ij}^{(k)} = e_{ii}^{(k)} + e_{jj}^{(k)} - 2e_{ij}^{(k)}$ stands for the chemical interchange energy between i and j elements, with the superscript (k) denoting the kth nearest neighbor interactions and e denoting the various pair energies. The interaction parameters, E_{ij}^{ϕ}, can therefore be determined either from the experimental activity data[29] through Eq. [3] or from the known chemical interchange parameters[30,31,32] through Eq. [4].

In an i-j binary system, if the α and β phases are in equilibrium, the chemical potentials of components in the α and β phases are equal, and the following equations hold

$$\Delta G_i^{\beta \rightarrow \alpha} = -RT \ln (X_i^{\alpha/\beta} / X_i^{\beta/\alpha}) - E_{ij}^{\alpha} (X_j^{\alpha/\beta})^2 + E_{ij}^{\beta} (X_j^{\beta/\alpha})^2 \qquad [5]$$

and

$$\Delta G_j^{\beta \rightarrow \alpha} = -RT \ln (X_j^{\alpha/\beta} / X_j^{\beta/\alpha}) - E_{ij}^{\alpha} (X_i^{\alpha/\beta})^2 + E_{ij}^{\beta} (X_i^{\beta/\alpha})^2 \qquad [6]$$

where $X_i^{\alpha/\beta}$, $X_i^{\beta/\alpha}$, $X_j^{\alpha/\beta}$, and $X_j^{\beta/\alpha}$ are equilibrium phase boundaries of the binary system. By fitting Eqs. [5] and [6] to the experimental binary phase diagram,[29] we can get the lattice stability parameters of i and j as functions of temperature. It should be noted here that $\Delta G_{\text{Cu}}^{\beta \rightarrow \alpha}$ determined from different Cu-i (i = Zn, Al) binary phase diagrams differs in value. In the calculation of the ternary Cu-Zn-Al alloys, the weighted average of the $\Delta G_{\text{Cu}}^{\beta \rightarrow \alpha}$ (Cu-i) (i = Zn, Al) obtained from the Cu-i binary system is used as $\Delta G_{\text{Cu}}^{\beta \rightarrow \alpha}$, *i.e.*:

$$\Delta G_{\text{Cu}}^{\beta \rightarrow \alpha} = \frac{X_{\text{Zn}} \Delta G_{\text{Cu}}^{\beta \rightarrow \alpha}(\text{Cu-Zn}) + X_{\text{Al}} \Delta G_{\text{Cu}}^{\beta \rightarrow \alpha}(\text{Cu-Al})}{1 - \text{Cu}}$$

With the various E_{ij} and $\Delta G_i^{\beta \rightarrow \alpha}$, determined as described above, we can calculate the driving force $\Delta G^{\beta \rightarrow \alpha}$ for $\beta \rightarrow \alpha$ transformation through Eq. [2].

$\Delta G^{\beta \rightarrow \beta'}$ $(= -\Delta G^{\beta' \rightarrow \beta})$ and $\Delta G^{\alpha \rightarrow \alpha_1}$ in Eq. [1] were treated using the GBW model,[30] which is a counterpart of the regular solution model. In (TBW model, the energy of the system is approximated as the total pair energies, while the entropy of the system is derived on the basis that the atoms are distributed on the lattice (or sublattice) sites as independent points (i.e., the tendency for the system to form different pairs, triangles, etc., is neglected). Since both the solid solutions α and β are substitutional, the number of lattice sites which Cu, . . . may occupy should be identical in the two phases; *i.e.*, the configurational entropy of the β equals that of the α: $S^{\beta} = S^{\alpha}$. In addition, because no change in the relative positions of atoms takes place in the diffusionless reaction, the configurational entropies are such that $S^{\beta'} = S^{\alpha_1}$. Considering only the configurational alteration, we give $\Delta S^{\beta \rightarrow \beta'} = \Delta S^{\alpha \rightarrow \alpha_1}$ for the entropy change in the ordering transition. As the volume change in the ordering transition is small enough, then it is straightforward to write

$$\Delta G^{\beta' \rightarrow \beta} + \Delta G^{\alpha \rightarrow \alpha_1} = -\Delta U^{\beta \rightarrow \beta'} + \Delta U^{\alpha \rightarrow \alpha_1} \qquad [7]$$

where U refers to the internal energy.

In order to derive the driving force for the $\beta \rightarrow \beta'$ and $\alpha \rightarrow \alpha_1$ ordering transitions, the body-centered cubic lattice of the parent phase is divided into four sublattices

named a, b, c, and d.[28] Letting the probability of i atoms on the L sublattice be shown by $P_{i\mathrm{L}}$, L = a, b, c, and d, the various ordering structures in the parent βCu-base alloys can be defined:

$$\text{Disordered: } P_{\mathrm{Cu}a} = P_{\mathrm{Cu}b} = P_{\mathrm{Cu}c} = P_{\mathrm{Cu}d} = X_{\mathrm{Cu}} \quad [8]$$

$$\text{B2: } P_{\mathrm{Cu}a} = P_{\mathrm{Cu}b} > P_{\mathrm{Cu}c} = P_{\mathrm{Cu}d} \quad [9]$$

$$\text{DO}_3\text{: } P_{\mathrm{Cu}a} = P_{\mathrm{Cu}b} = P_{\mathrm{Cu}c} > P_{\mathrm{Cu}d} \quad [10]$$

$$\text{L2}_1\text{: } P_{\mathrm{Cu}a} = P_{\mathrm{Cu}b} > P_{\mathrm{Cu}c} > P_{\mathrm{Cu}d} \quad [11]$$

From the relationship among these four sublattices, it is easy to derive the number of the various bonds for the nearest and next nearest neighbors for the β phase. The change in internal energy of the β phase during its ordering transition is approximated by the total change in bonding energy of the nearest and next nearest atoms, *i.e.*:

$$\Delta U^{\beta\to\beta'} = \sum_{i,j} (\Delta A_{ij}^{(1)} e_{ij}^{(1)} + \Delta A_{ij}^{(2)} e_{ij}^{(2)}) \qquad i, j = \mathrm{Cu}, \ldots \quad [12]$$

where $\Delta A_{ij}^{(1)}$ and $\Delta A_{ij}^{(2)}$ represent, respectively, the change of the number of the nearest and next nearest i-j bonds during the ordering transition. Subject to certain constraining conditions imposed on all the variables $P_{i\mathrm{L}}$, we have for the Cu-i-j ternary system.[28]

B2 β' structure:

$$\Delta U^{\beta\to\beta'} = 0.5\mathrm{N}_0\eta^2 \left[\frac{X_i}{1 - X_{\mathrm{Cu}}} (Z_2 W_{\mathrm{Cu}i}^{(2)} - Z_1 W_{\mathrm{Cu}i}^{(1)}) + \frac{X_j}{1 - X_{\mathrm{Cu}}} (Z_2 W_{\mathrm{Cu}j}^{(2)} - Z_1 W_{\mathrm{Cu}j}^{(1)}) - \frac{X_i X_j}{(1 - X_{\mathrm{Cu}})^2} (Z_2 W_{ij}^{(2)} - Z_1 W_{ij}^{(1)}) \right] \quad [13]$$

DO_3 β' structure:

$$\Delta U^{\beta\to\beta'} = -0.5\mathrm{N}_0\eta^2 \left[\frac{X_i}{1 - X_{\mathrm{Cu}}} (Z_2 W_{\mathrm{Cu}i}^{(2)} + Z_1 W_{\mathrm{Cu}i}^{(1)}) + \frac{X_j}{1 - X_{\mathrm{Cu}}} (Z_2 W_{\mathrm{Cu}j}^{(2)} + Z_1 W_{\mathrm{Cu}j}^{(1)}) - \frac{X_i X_j}{(1 - X_{\mathrm{Cu}})^2} (Z_2 W_{ij}^{(2)} + Z_1 W_{ij}^{(1)}) \right] \quad [14]$$

and $\mathrm{L2}_1$ β' structure:

$$\Delta U^{\beta\to\beta'} = 0.25\mathrm{N}_0 \left\{ \frac{X_i}{1 - X_{\mathrm{Cu}}} [(\eta_1^2 - 2\eta_1\eta_2 - \eta_2^2) Z_2 W_{\mathrm{Cu}i}^{(2)} - 2\eta_1^2 Z_1 W_{\mathrm{Cu}i}^{(1)}] + \frac{X_j}{(1 - X_{\mathrm{Cu}})} [(\eta_1^2 - 2\eta_1\eta_2 - \eta_2^2) Z_2 W_{\mathrm{Cu}j}^{(2)} - 2\eta_1^2 Z_1 W_{\mathrm{Cu}j}^{(1)}] - \frac{X_i X_j}{(1 - X_{\mathrm{Cu}})^2} [(\eta_1^2 - 2\eta_1\eta_2 - \eta_2^2) Z_2 W_{ij}^{(2)} - 2\eta_1^2 Z_1 W_{ij}^{(1)}] \right\} \quad [15]$$

where the ordering degrees are defined as $\eta = \eta_1 = P_{\mathrm{Cu}a} - X_{\mathrm{Cu}}$, and $\eta_2 = P_{\mathrm{Cu}c} - X_{\mathrm{Cu}}$. Because in the $\mathrm{L2}_1$ ordered structure, the $P_{i\mathrm{L}}$'s are less dependent than those in B2 or DO_3 ordered structure, two ordering degree parameters, η_1 and η_2, are introduced for the $\mathrm{L2}_1$ structure. η, η_1, and η_2 are confined to the following conditions:

$$\text{B2: } \begin{cases} 0 \le \eta \le X_{\mathrm{Cu}} & X_{\mathrm{Cu}} \le 0.5 \\ 0 < \eta \le 1 - X_{\mathrm{Cu}} & X_{\mathrm{Cu}} > 0.5 \end{cases} \quad [16]$$

$$\mathrm{DO}_3\text{: } \begin{cases} 0 \le \eta \le X_{\mathrm{Cu}}/3 & X_{\mathrm{Cu}} \le 0.75 \\ 0 < \eta \le 1 - X_{\mathrm{Cu}} & X_{\mathrm{Cu}} > 0.75 \end{cases} \quad [17]$$

and

$$\mathrm{L2}_1\text{: } \begin{cases} \begin{cases} 0 < \eta_1 \le X_{\mathrm{Cu}} \\ -\eta_1 < \eta_2 \le \min(\eta_1, X_{\mathrm{Cu}} - 2\eta_1) \end{cases} & X_{\mathrm{Cu}} \le 0.5 \\ \begin{cases} 0 < \eta_1 \le 1 - X_{\mathrm{Cu}} \\ -\eta_1 < \eta_2 \le \min(\eta_1, X_{\mathrm{Cu}} - 2\eta_1) \end{cases} & X_{\mathrm{Cu}} > 0.5 \end{cases} \quad [18]$$

The configurational entropy changes in ordering transition are given by

B2 β' structure:

$$\begin{aligned} \Delta S^{\beta\to\beta'} = 0.5\mathrm{R}/\lambda[&2X_{\mathrm{Cu}} \ln X_{\mathrm{Cu}} + 2(1 - X_{\mathrm{Cu}}) \ln (1 - X_{\mathrm{Cu}}) \\ &- (\eta + X_{\mathrm{Cu}}) \ln (\eta + X_{\mathrm{Cu}}) \\ &- (1 - X_{\mathrm{Cu}} - \eta) \ln (1 - X_{\mathrm{Cu}} - \eta) \\ &- (\eta + 1 - X_{\mathrm{Cu}}) \ln (\eta + 1 - X_{\mathrm{Cu}}) \\ &- (X_{\mathrm{Cu}} - \eta) \ln (X_{\mathrm{Cu}} - \eta)] \end{aligned} \quad [19]$$

DO_3 β' structure:

$$\begin{aligned} \Delta S^{\beta\to\beta'} = 0.25\mathrm{R}/\lambda[&4X_{\mathrm{Cu}} \ln X_{\mathrm{Cu}} + 4(1 - X_{\mathrm{Cu}}) \ln (1 - X_{\mathrm{Cu}}) \\ &- 3(\eta + X_{\mathrm{Cu}}) \ln (\eta + X_{\mathrm{Cu}}) \\ &- 3(1 - X_{\mathrm{Cu}} - \eta) \ln (1 - X_{\mathrm{Cu}} - \eta) \\ &- (X_{\mathrm{Cu}} - 3\eta) \ln (X_{\mathrm{Cu}} - 3\eta) \\ &- (1 - X_{\mathrm{Cu}} + 3\eta) \ln (1 - X_{\mathrm{Cu}} + 3\eta)] \end{aligned} \quad [20]$$

and $\mathrm{L2}_1$ β' structure:

$$\begin{aligned} \Delta S^{\beta\to\beta'} = 0.25\mathrm{R}/\lambda[&4X_{\mathrm{Cu}} \ln X_{\mathrm{Cu}} + 4(1 - X_{\mathrm{Cu}}) \ln (1 - X_{\mathrm{Cu}}) \\ &- 2(\eta_1 + X_{\mathrm{Cu}}) \ln (\eta_1 + X_{\mathrm{Cu}}) \\ &- 2(1 - X_{\mathrm{Cu}} - \eta_1) \ln (1 - X_{\mathrm{Cu}} - \eta_1) \\ &- (\eta_2 + X_{\mathrm{Cu}}) \ln (\eta_2 + X_{\mathrm{Cu}}) \\ &- (1 - X_{\mathrm{Cu}} - \eta_2) \ln (1 - X_{\mathrm{Cu}} - \eta_2) \\ &- (X_{\mathrm{Cu}} - 2\eta_1 - \eta_2) \ln (X_{\mathrm{Cu}} - 2\eta_1 - \eta_2) \\ &- (1 - X_{\mathrm{Cu}} + 2\eta_1 + \eta_2) \ln (1 - X_{\mathrm{Cu}} + 2\eta_1 + \eta_2)] \end{aligned} \quad [21]$$

where R is the universal gas constant and λ is the correction factor for short-range order.[30] By comparison of the calculated results of the critical temperature of ordering obtained using the cluster variation method and the GBW model, respectively, λ was determined as 0.67 for Cu-Zn alloys.[30] In addition, λ was chosen to be $\lambda = 0.78$ in Cu-Al alloys,[24] so as to minimize the deviation of the critical temperature of ordering calculated using the GBW model from the experimental critical temperature. In the ternary Cu-Zn-Al alloys, λ is evaluated as the weighted average of its binary counterparts, *i.e.*

$$\lambda = \frac{0.67X_{Zn} + 0.78X_{Al}}{1 - X_{Cu}}$$

where X_{Cu} is the atomic fraction of Cu in the ternary alloys. As long as ΔU and ΔS are known, the Gibbs energy change associated with any process $\delta_1 \rightarrow \delta_2$ can be expressed as

$$\Delta G^{\delta_1 \rightarrow \delta_2} = \Delta U^{\delta_1 \rightarrow \delta_2} - T\Delta S^{\delta_1 \rightarrow \delta_2} \qquad [22]$$

The ordering structure of the parent β' phase is B2 in Cu-Zn alloys and DO_3 in Cu-Al alloys, with both structures formed during the $\beta \rightarrow \beta'$ transition. In Cu-Zn-Al alloys, the parent β' phase has two types of ordering structures; that is, B2 and $L2_1$, where B2 formed during the $\beta \rightarrow \beta'$ transition and $L2_1$ formed during the $\beta'(B2) \rightarrow \beta'(L2_1)$ transition.

Since the $\beta \rightarrow \beta'$(B2 or DO_3) ordering transition is a second-order transition, the ordering degree should be a function of temperature. By fitting to the phase diagram of the Cu-Zn system, we found that η can be described simply as $\eta = \eta_{max}[1 - (T/T_c)^5]^{1/2}$,[25] where η_{max} represents the maximum ordering degree the β' phase can actually obtain and T_c the critical ordering transition temperature. η_{max} was determined as $\eta_{max} = 0.32$ for B2 ordering[25] and $\eta_{max} = 0.16$ for DO_3 ordering,[27] and T_c can be obtained from the phase diagram.[29,33,34] In Cu-Zn-Al alloys, however, the $\beta'(B2) \rightarrow \beta'(L2_1)$ transition is a first-order transition, and the ordering degree parameters of the $L2_1\beta'$ phase should be treated differently. Here the ordering degree parameters η_1 and η_2 are chosen as values which renders a quasi-equilibrium $L2_1$ ordered phase at a given temperature. For a Cu-24.77Zn-9.00Al at. pct alloy, we get $\eta_1 = 0.31$ and $\eta_2 = 0.04$ at 150 °C for the extreme point of $\Delta G^{\beta \rightarrow \beta'(L2_1)}$ described in Eqs. [15], [21], and [22], respectively.

In the $\beta' \rightarrow \alpha_1$ shear reaction, we may suppose that the low-temperature α_1 phase inherits the ordering of the parent β' phase; *i.e.*, the Bain correspondence between the atoms of the α_1 and β' phases is assumed to hold. The numbers of all the different bonds of the α_1 then can be expressed as functions of the P_{iL} variables defined above. If only the nearest interactions among atoms are considered for the α_1 phase, the changes in internal energy during the ordering transitions can be approximated as

$$\Delta U^{\alpha \rightarrow \alpha_1} = \sum_{i,j} \Delta A_{ij} e_{ij} \qquad i, j = Cu, \ldots \qquad [23]$$

For the ternary system, our derivation gives[28]

B2 β' structure:

$$\Delta U^{\alpha \rightarrow \alpha_1} = 2N_0\eta^2 \left(-\frac{X_i}{1 - X_{Cu}} W^{\alpha}_{Cui} - \frac{X_j}{1 - X_{Cu}} W^{\alpha}_{Cuj} + \frac{X_iX_j}{(1 - X_{Cu})^2} W^{\alpha}_{ij} \right) \qquad [24]$$

DO_3 β' structure:

$$\Delta U^{\alpha \rightarrow \alpha_1} = 6N_0\eta^2 \left(-\frac{X_i}{1 - X_{Cu}} W^{\alpha}_{Cui} - \frac{X_j}{1 - X_{Cu}} W^{\alpha}_{Cuj} + \frac{X_iX_j}{(1 - X_{Cu})^2} W^{\alpha}_{ij} \right) \qquad [25]$$

and $L2_1$ β' structure:

$$\Delta U^{\alpha \rightarrow \alpha_1} = N_0(-3\eta_1^2 - 2\eta_1\eta_2 - \eta_2^2) \cdot \left(\frac{X_i}{1 - X_{Cu}} W^{\alpha}_{Cui} + \frac{X_j}{1 - X_{Cu}} W^{\alpha}_{Cuj} - \frac{X_iX_j}{(1 - X_{Cu})^2} W^{\alpha}_{ij} \right) \qquad [26]$$

where the symbol W^{α}_{ij} is used for the α phase referring to the nearest chemical interchange energy. Because $\Delta S^{\alpha \rightarrow \alpha_1} = \Delta S^{\beta \rightarrow \beta'}$, the Gibbs energy change, $\Delta G^{\alpha \rightarrow \alpha_1}$, associated with $\alpha \rightarrow \alpha_1$ reaction can then be calculated through Eqs. [19] through [21] and [22] through [26].

Using the procedures described above, we can determine all the driving forces, such as $\Delta G^{\beta \rightarrow \alpha}$, $\Delta G^{\beta \rightarrow \beta'}$, and $\Delta G^{\alpha \rightarrow \alpha_1}$ as functions of temperature for a given alloy. $\Delta G^{\beta' \rightarrow \alpha_1}$ can then be calculated using Eq. [1].

2. *Calculation of* $\Delta G^{\beta' \rightarrow \beta_1' + \alpha_1}$

Supposing that the β' phase with composition $X^{\beta'}_{Cu}$ decomposes into the β_1' phase with composition $X^{\beta_1'}_{Cu}$ and the α_1 plate with composition X^{α}_{Cu}, the driving force for the phase transformation should be

$$\Delta G^{\beta' \rightarrow \beta_1' + \alpha_1} = G^{\alpha} + \frac{X^{\beta'}_{Cu} - X^{\alpha}_{Cu}}{X^{\beta_1'}_{Cu} - X^{\alpha}_{Cu}} (G^{\beta_1'} - G^{\alpha}) - G^{\beta'} \qquad [27]$$

Here, the α_1 is treated as the α phase so that the known thermodynamic properties of the α phase can be fully utilized. This treatment should be correct, at least to a certain extent, because: (1) analogous to the α_1 phase, the α phase also is a nonequilibrium phase at the given composition; and (2) the structure of the α_1 is close to that of the disordered α (FCC), especially as α_1 loses the ordering of the parent phase. Also, we can list

$$G^{\beta'} = G^{\beta} + \Delta G^{\beta \rightarrow \beta'} = G^{\beta} + \Delta U^{\beta \rightarrow \beta'} - T\Delta S^{\beta \rightarrow \beta'} \qquad [28]$$

$$G^{\beta_1'} = G^{\beta_1} + \Delta G^{\beta_1 \rightarrow \beta_1'} = G^{\beta_1} + \Delta U^{\beta_1 \rightarrow \beta_1'} - T\Delta S^{\beta_1 \rightarrow \beta_1'} \qquad [29]$$

and

$$G^{\phi}(\phi = \alpha, \beta, \beta_1) = \sum_i X_i^{\phi} G_i^{\phi} + RT \sum_i X_i^{\phi} \ln X_i^{\phi} + \sum_{i \neq j} E_{ij}^{\phi} X_i^{\phi} X_j^{\phi} \qquad i, j = Cu, \ldots \qquad [30]$$

Using Eq. [27] and the parameters derived in Eqs. [28] through [30], driving force $\Delta G^{\beta' \rightarrow \beta_1' + \alpha_1}$ can be calculated as a function of X_{Cu}^{α} composition (if the amount of the α_1 decomposed from the β' is fixed, $X_{Cu}^{\beta_1'}$ will be dependent upon the X_{Cu}^{α}) at a given temperature. If X_{Cu}^{α} and $X_{Cu}^{\beta_1'}$ are known, $\Delta G^{\beta' \rightarrow \beta_1' + \alpha_1}$ then can be determined as a function of temperature. It should be pointed out here that although Eqs. [13], [14], [24], and [25] are derived for a ternary system, they also can be used for a binary system as long as the composition of one of the components is equal to 0.

3. *Calculation of the Driving Force for Ordering of Fresh α_1 in a Cu-24.77Zn-9.00Al at. pct Alloy*

The disordered α_1 plate formed during the diffusional reaction $\beta' \rightarrow \beta_1' + \alpha_1$ may further transform to the ordered plate upon aging or subsequent cooling to the ambient temperature. The driving force accompanying this transition is expressed as $\Delta G^{\alpha_1(\text{dis.}) \rightarrow \alpha_1(\text{ord.})}$. In order to judge the possibility of such a transition, the value of $\Delta G^{\alpha_1(\text{dis.}) \rightarrow \alpha_1(\text{ord.})}$ is calculated for a Cu-24.77Zn-9.00Al at. pct alloy. Following the calculation of the driving force of ordering,[25] we assume arbitrarily a rather small value of η_{max}—*i.e.*—$\eta_{max} = 0.20$, and substitute it into $\eta = \eta_{max}[1 - (T/T_c)^5]^{1/2}$. $\Delta G^{\alpha_1(\text{dis.}) \rightarrow \alpha_1(\text{ord.})}$ then can be calculated using Eqs. [19], [22], and [24]. The $\Delta D^{\alpha_1(\text{dis.}) \rightarrow \alpha_1(\text{ord.})}$ thus calculated refers to an ordered α_1 inherited from the β' phase. For a real $\alpha_1(\text{dis.}) \rightarrow \alpha_1(\text{ord.})$ reaction where the constraints on the ordering types and ordering degree are removed, $\Delta G^{\alpha_1(\text{dis.}) \rightarrow \alpha_1(\text{ord.})}$ should be smaller.

III. RESULTS OF CALCULATION

The parent phase of the Cu-40.00 at. pct Zn alloy is the β' phase with the B2 structure. Letting the composition of the alloy be $X_{Zn} = 0.4000$, the driving forces for various phase transformations are calculated in terms of Eqs. [1], [2], [7], [13], [19], [22], [24], and [27] through [30]. When calculating the driving forces $\Delta G^{\beta' \rightarrow \beta_1' + \alpha_1}$ for diffusional transformations, it is assumed that $X_{Zn}^{\alpha} = 0.3380$ and $X_{Zn}^{\beta_1'} = 0.4010$, according to the experimental results of Lorimer *et al.*[35] Within the temperature range from 473 to 673 K of the α_1 plate formation, regression and simplification by computer yield

$$\Delta G^{\beta' \rightarrow \alpha_1} = -222.6 + 1.5672T - 3.27 \times 10^{-4}T^2 - 5.324 \times 10^{-12}T^5 \qquad T = 473 \text{ to } 673 \text{ K} \qquad [31]$$

$$\Delta G^{\beta' \rightarrow \beta_1' + \alpha_1} = -9.8 + 8.17 \times 10^{-2}T - 2.603 \times 10^{-4}T^2 + 2.141 \times 10^{-7}T^3 \qquad T = 473 \text{ to } 673 \text{ K} \qquad [32]$$

and if the ordering degree parameter $\eta = 0$, we get the driving forces for the transformation between disordered phases

$$\Delta G^{\beta \rightarrow \alpha_1} = -1117.4 + 1.5672T - 3.27 \times 10^{-4}T^2 \qquad [33]$$

$$\Delta G^{\beta \rightarrow \beta_1 + \alpha_1} = -25.5 + 0.0288T - 4.4 \times 10^{-6}T^2 \qquad [34]$$

The results of Eqs. [31] through [34] are shown in Figures 1 and 2, respectively.

The β phase of the Cu-24.00Al at. pct alloy will transform into the β' phase with DO_3 structure, so Eqs. [14], [20], and [25] are used instead of Eqs. [13], [19], and [24] in calculating the driving forces for shear reaction. Regression simplification yields

$$\Delta G^{\beta' \rightarrow \alpha_1} = -333.2 - 0.3692T + 1.3246 \times 10^{-3}T^2 \qquad T = 300 \text{ to } 750 \text{ K} \qquad [35]$$

and

$$\Delta G^{\beta \rightarrow \alpha_1} = -365.1 + 0.6824T \qquad \text{T} = 750 \text{ to } 800 \text{ K} \qquad [36]$$

The results of Eqs. [35] and [36] are plotted in Figure 3.

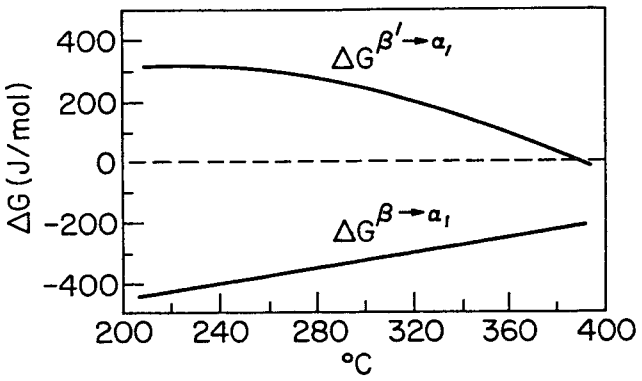


Fig. 1—Driving forces $\Delta G^{\beta \rightarrow \alpha 1}$ and $\Delta G^{\beta' \rightarrow \alpha 1}$ in a Cu-40.00Zn at. pct alloy. ----: $\Delta G = 0$.

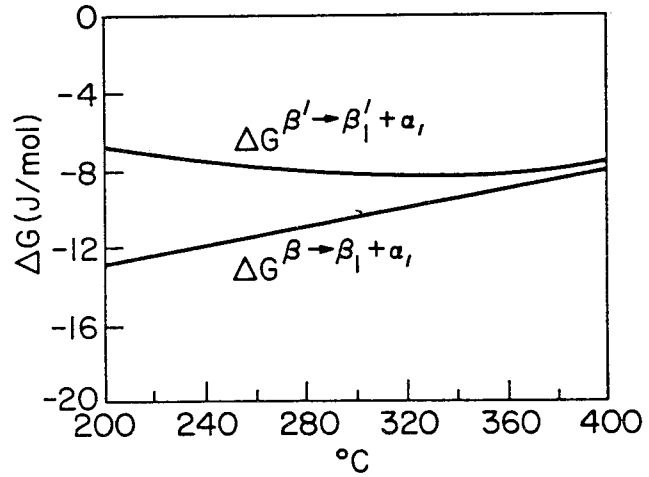


Fig. 2—Driving forces $\Delta G^{\beta' \rightarrow \beta_1' + \alpha 1}$ and $\Delta G^{\beta \rightarrow \beta_1 + \alpha 1}$ in a Cu-40.00Zn at. pct alloy.

If the α_1 formation produces 5 pct of the α_1 at its initial stage through the diffusional reaction, the Lever principle is used to calculate the driving force for precipitating the α_1 as a function of its composition at a given temperature. The calculated results for the 700 and 750 K temperatures are shown in Figure 4. The minimum $\Delta G^{\beta' \rightarrow \beta_1' + \alpha_1}$ values to precipitate the equilibrium α also are calculated, and the results are plotted in Figure 5 as a function of temperature.

The α_1 in the Cu-Zn-Al alloys forms from the B2 β' or the $L2_1$ β' matrix in the elevated temperature range from 523 to 623 K. For the Cu-24.77Zn-9.00Al at. pct alloy, calculation from Eq. [22] gives

$$\Delta G^{\beta' \rightarrow \alpha_1} = 19.6 - 1.4940T + 8.1215 \times 10^{-3}T^2 - 8.1925 \times 10^{-6}T^3$$
$$T = 300 \text{ to } 750 \text{ K} \quad B2, \beta' \qquad [37]$$

$$\Delta G^{\beta' \rightarrow \alpha_1} = 2549.6 - 3.4348T - 1.868 \times 10^{-4}T^2$$
$$T = 300 \text{ to } 600 \text{ K} \quad L2_1, \beta' \qquad [38]$$

and

$$\Delta G^{\beta \rightarrow \alpha_1} = -1098.8 + 1.3516T \qquad T = 300 \text{ to } 800 \text{ K} \qquad [39]$$

the results of Eqs. [37] through [39] are shown in Figures 6 through 8.

Wu and Wayman[7] indicated a 3 wt. pct difference in

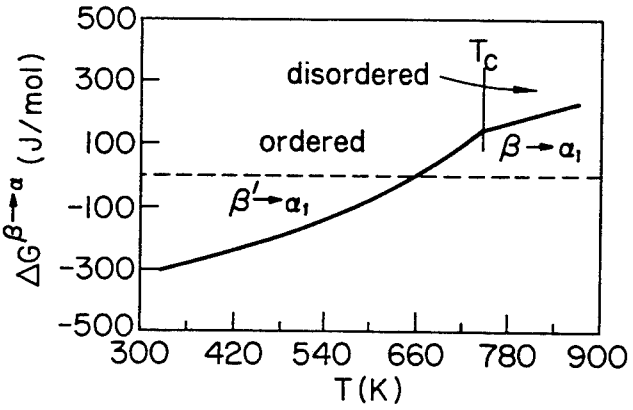


Fig. 3—Driving forces $\Delta G^{\beta' \rightarrow \alpha_1}$ and $\Delta G^{\beta \rightarrow \alpha_1}$ in a Cu-24.00Al at. pct alloy. ----: $\Delta G = 0$.

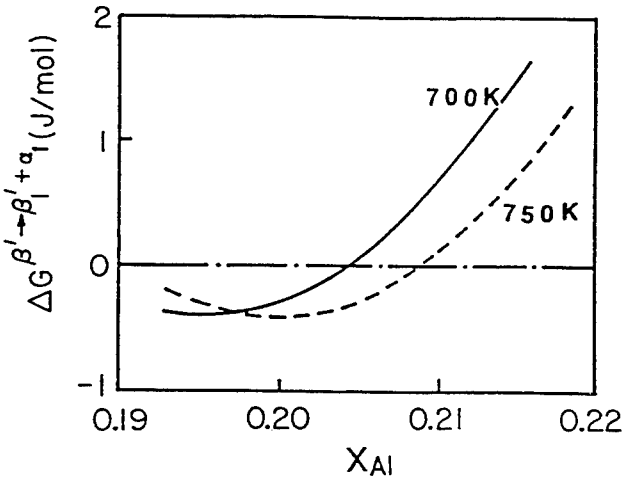


Fig. 4—Driving force $\Delta G^{\beta' \rightarrow \beta_1' + \alpha_1}$ as a function of α_1 composition in a Cu-24.00Al at. pct alloy. ———: 700 K; ----: 750 K; — — —: $\Delta G = 0$.

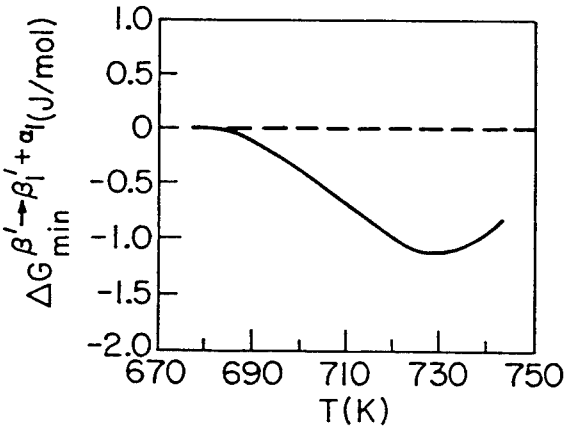


Fig. 5—Minimum $\Delta G^{\beta' \rightarrow \beta_1' + \alpha_1}$ values as a function of temperature for a Cu-24.00Al at. pct alloy. ----: $\Delta G = 0$.

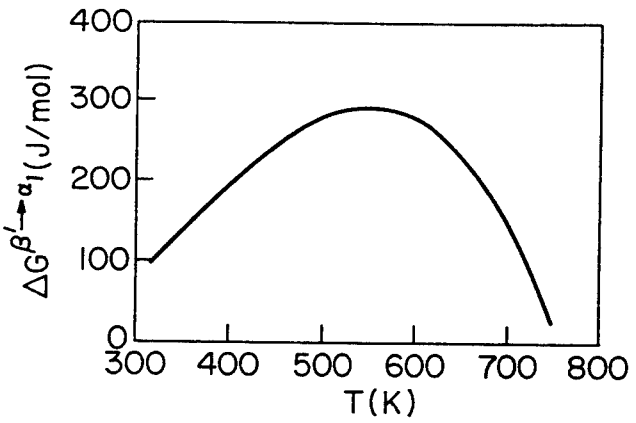


Fig. 6—Driving force $\Delta G^{\beta' \rightarrow \alpha_1}$ in a Cu-24.77Zn-9.00Al at. pct alloy. (β' is with B2 structure.)

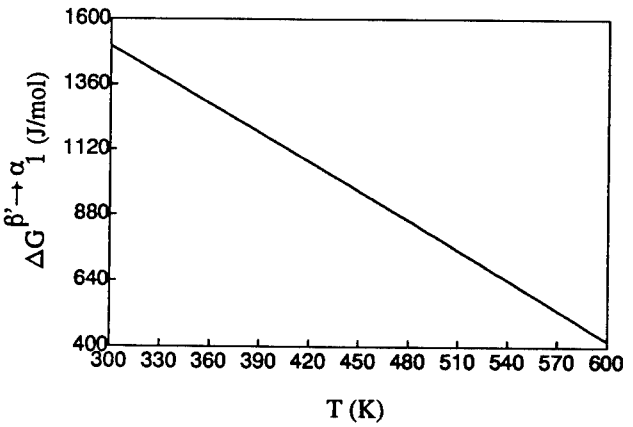


Fig. 7—Driving force $\Delta G^{\beta' \rightarrow \alpha_1}$ in a Cu-24.77Zn-9.00Al at. pct alloy. (β' is with $L2_1$ structure.)

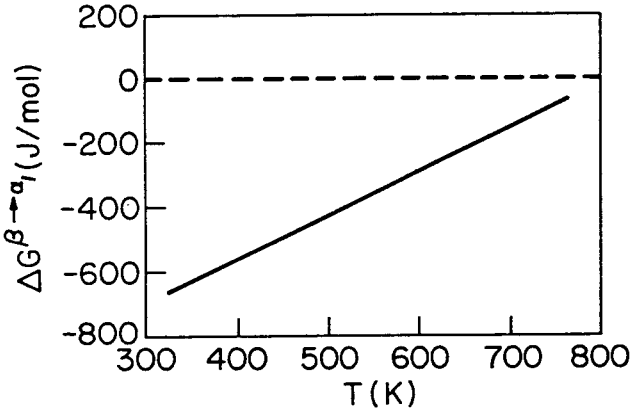


Fig. 8—Driving force $\Delta G^{\beta \rightarrow \alpha_1}$ in a Cu-24.77Zn-9.00Al at. pct alloy. ----: $\Delta G = 0$.

Zn and about a 0.5 to 1 wt. pct difference in Al between the α_1 plate and the β' matrix in the Cu-24.77Zn-9.00Al at. pct alloy, even at the earliest accessible stage of the α_1 plate formation. Accordingly, the values $X_{Zn}^{\beta_1'} = 0.2480$, $X_{Al}^{\beta_1'} = 0.0902$, $X_{Zn}^{\alpha_1} = 0.2218$, and $X_{Al}^{\alpha_1} = 0.0738$ are adopted. The calculated driving forces are as follows

$$\Delta G^{\beta' \rightarrow \beta_1' + \alpha_1} = 6.3 - 1.71 \times 10^{-2}T - 3.99 \times 10^{-5}T^2 + 5.71 \times 10^{-8}T^3$$

$$T = 300 \text{ to } 750 \text{ K} \quad B2, \beta' \qquad [40]$$

$$\Delta G^{\beta' \rightarrow \beta_1' + \alpha_1} = 15.5 - 0.0375T - 1.9 \times 10^{-6}T^2$$

$$T = 300 \text{ to } 600 \text{ K} \quad L2_1, \beta' \qquad [41]$$

and

$$\Delta G^{\beta \rightarrow \beta_1 + \alpha_1} = -17.7 + 1.73 \times 10^{-2}T$$

$$T = 300 \text{ to } 750 \text{ K} \qquad [42]$$

Results of Eqs. [40] through [42] are plotted in Figure 9.

In order to determine the possibility of the disordered α_1 undergoing ordering once it is formed after a diffusional reaction, $\Delta G^{\alpha_1(\text{dis.}) \rightarrow \alpha_1(\text{ord.})}$ also is calculated according to the procedure described in Eqs. [19], [22], and [24], and the results are

$$\Delta G^{\alpha_1(\text{dis.}) \rightarrow \alpha_1(\text{ord.})} = -520.4 + 1.1931T$$

$$T = 300 \text{ to } 450 \text{ K} \qquad [43]$$

which are shown in Figure 10.

Letting $\Delta G^{\beta' \rightarrow \alpha_1}$ be equal to zero, the equilibrium temperature, T_0, between the β' and α_1 phases can be calculated. Figure 11 shows the results of the calculated T_0 and the experimental B_s[3,36] in Cu-Zn alloys. In addition, the equilibrium temperatures between the DO_3 β' parent phase and α_1 phase and between $L2_1$ β' parent phase and α_1 phase are calculated for the Cu-24.00Al at. pct and Cu-24.77Zn-9.00Al at. pct alloys, respectively, and the corresponding results are approximately 660 and 240 K.

IV. DISCUSSION

This work focuses on the possible mechanisms for the initiation of the α_1 plate formation through the calculation of the driving force for the shear $\beta' \rightarrow \alpha_1$ and the diffusional $\beta' \rightarrow \beta_1' + \alpha_1$ processes. In the former case,

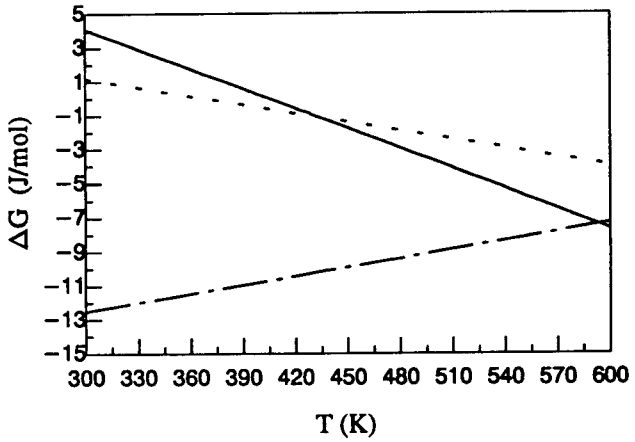


Fig. 9—Driving forces $\Delta G^{\beta' \rightarrow \beta_1' + \alpha_1}$ and $\Delta G^{\beta \rightarrow \beta_1 + \alpha_1}$ in a Cu-24.77Zn-9.00Al at. pct alloy. -----: $\Delta G^{\beta' \rightarrow \beta_1' + \alpha_1}$ (β' is with B2 structure); ———: $\Delta G^{\beta' \rightarrow \beta_1' + \alpha_1}$ (β' is with $L2_1$ structure); — - —: $\Delta G^{\beta \rightarrow \beta_1 + \alpha_1}$.

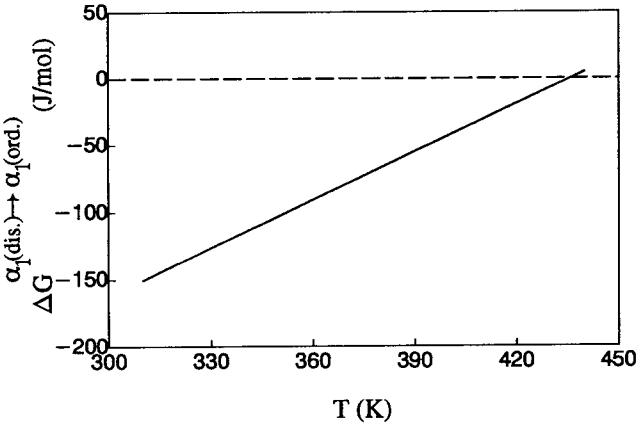


Fig. 10—Driving force $\Delta G^{\alpha_1(\text{dis.}) \rightarrow \alpha_1(\text{ord.})}$ for a Cu-24.77Zn-9.00Al at. pct alloy. -----: $\Delta G = 0$.

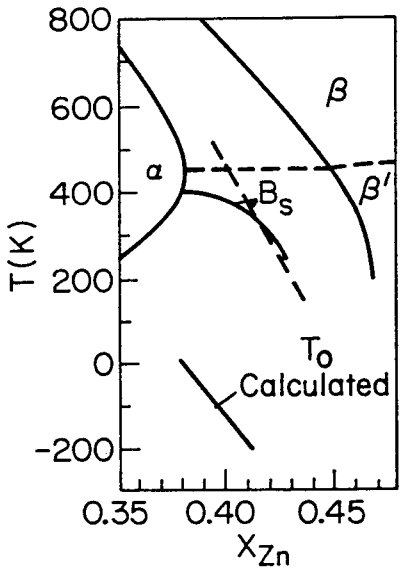


Fig. 11—T_0 and B_s as a function of X_{Zn} in Cu-Zn alloys.

the α_1 is the shear product which inherits the ordering and composition of the parent phase, while in the latter case, the α_1 is by definition a disordered FCC phase. From this point of view, the fault structures of 9R and 18R of the α_1 plate do not need to be considered. An experiment in Cu-Zn-Al also has given evidence that at a very early stage of transformation, small α_1 plate forms with narrow fault-free edges.[10]

The start temperature at which α_1 plate is formed is about 400 to 500 K (*i.e.*, $B_s \doteq 450$ K[3,36] in Figure 11) for the Cu-40.00 Zn at. pct alloy. The α_1 plate formation temperatures for Cu-Al alloys and Cu-Zn-Al alloys are over 660 and 300 K, respectively. As revealed in Eqs. [1], [5], [7], and [8] and Figures 1, 3, 6, and 7, the values of the $\beta' \rightarrow \alpha_1$ shear driving force $\Delta G^{\beta' \rightarrow \alpha_1}$ are all positive within these temperature ranges of the α_1 plate formation. Therefore, the α_1 plate formation from the parent phase with the same composition through a shear mechanism is thermodynamically impossible without the influence of other factors. In some cases, however, α_1 may be formed through a shear mechanism. For example, if there is a stress field in the alloy, α_1 may be induced. In addition, some defects, such as dislocations, may change the local compositions of the alloy and cause α_1 to nucleate. This requires the defect density to be high enough to be consistent with the nucleation density, which rarely happens. Conversely, as can be seen from Eqs. [32], [40], and [41] and Figures 2 and 9, the values of the $\beta' \rightarrow \beta'_1 + \alpha_1$ diffusional driving force, $\Delta G^{\beta' \rightarrow \beta'_1 + \alpha_1}$, are negative within the corresponding α_1 plate formation temperature range for Cu-Zn and Cu-Zn-Al alloys, respectively. This indicates that α_1 plate can be formed in a diffusional reaction, $\beta' \rightarrow \beta'_1 + \alpha_1$, in the Cu-Zn and Cu-Zn-Al alloys. The same results can be obtained for Cu-Al alloys from Figures 4 and 5. Because the experimental information about the composition of α_1 plate is not available for Cu-Al alloys, we calculate the driving force, $\Delta G^{\beta' \rightarrow \beta'_1 + \alpha_1}$, for Cu-Al alloys as a function of the composition of α_1 plate at given temperatures. Figure 4 shows that in order for the driving force $\Delta G^{\beta' \rightarrow \beta'_1 + \alpha_1}$ to be negative, the composition of the α_1 plate has to be less than $X_{Al} = 0.209$ at 750 K and $X_{Al} = 0.204$ at 700 K, which greatly deviates from the composition of the parent β' phase ($X_{Al} = 0.240$). Figure 5 verifies that the diffusional driving force, $\Delta G^{\beta' \rightarrow \beta'_1 + \alpha_1}$, achieves a negative value within the temperature range from 680 to 750 K, as long as the requirement of the abrupt alteration in the composition of the α_1 plate is satisfied. Therefore, the α_1 plate formation can be initiated through a reaction, $\beta' \rightarrow \beta'_1 + \alpha_1$, by a diffusional mechanism.

It can be seen from Figure 11 that the equilibrium temperature, T_0, between β' and α_1 is about 700 K lower than the B_s[3,36] temperature of Cu-Zn alloys. Also, T_0 is calculated to be much lower than B_s in Cu-24.00Al at. pct alloy and Cu-24.77Zn-9.00Al at. pct alloy. As one of the characteristics of the thermoelastic martensitic transformation, M_s is close to T_0–*i.e.*, $T_0 \doteq M_s \ll B_s$—which also explains why it is impossible for shearing transformation to take place near the temperature of B_s.

The possibilities which would allow the shear reaction to take place above the temperature T_0 should be the alteration of the composition of the parent β' phase or nucleation at solute-depleted sites near dislocations or at stress field.[9–12] Composition change in the parent phase within the incubation period will cause the increase of the free energy unless an α_1 plate with different composition is nucleated. Thus, we would emphasize here that diffusion for the formation of solute-depleted zone before the formation of the α_1 is thermodynamically impossible. Diffusion may occur for the nucleation of α_1 as indicated in our previous experiment, which shows that nucleation has already started in the incubation period.[13,14] It seems possible that α_1 forms by shear at solute-depleted zone near dislocations or at stress field above M_s.[10,11,12] However, problems may arise if the nucleation density and the dislocation or stress field density in the parent phase do not match. In addition, it is well known that stress-induced martensite will form above M_s.

Experiments show that the α_1 plate inherits the ordering[4] and the antiphase domain structures[11] of the parent phase in Cu-Zn-Al alloys and partially inherits the ordering of the parent phase in Cu-Zn-Au alloys.[5] However, these transmission electron microscopy experiments are unable to measure the ordering degree in the α_1 plate. In Eq. [43] and Figure 10, $\Delta G^{\alpha_1(\text{dis.}) \rightarrow \alpha_1(\text{ord.})}$ is negative within the temperature range from 300 to 430 K for a Cu-24.77Zn-9.00Al at. pct alloy. This suggests that the disordered α_1 phase produced after the diffusional $\beta' \rightarrow \beta'_1 + \alpha_1$ reaction may further transform into the ordered α_1 phase during the isothermal holding or the subsequent cooling process in this alloy. That the ordering degree of the α_1 phase is much less than that of the parent phase (or martensite), as predicted in the present work, is in agreement with the experiments.[17] Calculation of $\Delta G^{\alpha_1(\text{dis.}) \rightarrow \alpha_1(\text{ord.})}$ for other temperatures and other compositions of the α_1 plate shows that $\Delta G^{\alpha_1(\text{dis.}) \rightarrow \alpha_1(\text{ord.})}$ might be positive unless the ordering degree, $\eta_{\max}$, is changed to lower values. This implies that there is a range of temperature associated with a given composition of the α_1 in which the α_1 plate either keeps the disordered state or has an ordering degree too low to be detected by experiments.

The parent phases of α_1 plate formation are all ordered. In order to investigate the effects of ordering on the α_1 plate formation, the corresponding driving forces for the disordered parent phase are calculated and the results shown in Eqs. [33], [34], [36], [39], and [42] and Figures 1, 2, 3, 8, and 9. Compared with those for the ordered parent β' phase, the values of various driving forces are much less in Cu-Zn and Cu-Zn-Al alloys and larger in Cu-Al alloys. Therefore, the B2 (in Cu-Zn and Cu-Zn-Al alloys) and $L2_1$ (in Cu-Zn-Al alloys) ordering of the parent phase resists the α_1 plate formation in Cu-Zn and Cu-Zn-Al alloys, while the DO_3 ordering of the parent phase enhances the α_1 plate formation in Cu-Al alloys.

The results of the thermodynamic consideration of the formation mechanism of α_1 plate for βCu-base alloys obtained in this paper are in agreement with the results of the thermodynamic treatment for Fe-C,[37] and Fe-X-C[38] alloys and the experimental results of internal friction for

Fe-Ni-C[39] alloys; that is, the mechanism of the α_1 plate formation at intermediate temperature is diffusional.

V. CONCLUSIONS

Calculations on the thermodynamics of the α_1 plate formation in βCu-base alloys in this article give the following conclusions:

1. For all the ordered structures of the parent phase—*i.e.*, B2 structure in Cu-Zn alloys, DO_3 structure in Cu-Al alloys, and B2 and $L2_1$ structures in Cu-Zn-Al alloys, the driving forces for the shear reaction $\beta' \rightarrow \alpha_1$ are positive for all three Cu-base alloys within their α_1 plate formation temperature range. Conversely, the corresponding driving forces for the diffusional reaction $\beta' \rightarrow \beta'_1 + \alpha_1$ are negative. Therefore, the α_1 plate formation can be initiated by a diffusional reaction $\beta' \rightarrow \beta'_1 + \alpha_1$.
2. Results in Cu-Al alloys show that a composition difference between the α_1 plate produced in the diffusional reaction $\beta' \rightarrow \beta'_1 + \alpha_1$ and the parent β' phase is required in order for the diffusional reaction to take place.
3. The calculated equilibrium temperature, T_0, between the α_1 plate and the parent β' phase is much lower than the start temperature for the α_1 plate formation, which further proves that it is impossible for the α_1 plate formation to be initiated through a shear reaction without other preferential conditions.
4. Since $\Delta G^{\alpha_1(\text{dis.})\rightarrow\alpha_1(\text{ord.})} < 0$ in the temperature range between 300 and 430 K, the fresh α_1 plate produced after the diffusional $\beta' \rightarrow \beta'_1 + \alpha_1$ reaction may further transform into the ordered α_1 plate for a Cu-24.77Zn-9.00Al at. pct alloy.
5. Calculation on the various driving forces for the disordered parent phase shows that the ordering of the parent phase resists the α_1 plate formation in Cu-Zn and Cu-Zn-Al alloys and enhances it in Cu-Al alloys.

REFERENCES

1. R.D. Garwood: *J. Inst. Met.*, 1954–1955, vol. 83, pp. 64-68.
2. R.D. Garwood and D. Hull: *Acta Metall.*, 1958, vol. 6, pp. 98-102.
3. I. Cornelis and C.M. Wayman: *Acta Metall.*, 1974, vol. 22, pp. 301-11.
4. M.H. Wu, J. Perkins, and C.M. Wayman: *Acta Metall.*, 1989, vol. 37, pp. 1821-37.
5. T. Tadaki, J.Q. Cai, and K. Shimizu: *Mater. Trans. Jpn. Inst. Met.*, 1991, vol. 32, pp. 757-65.
6. K. Chattopadhyay and H.I. Aaronson: *Acta Metall.*, 1986, vol. 34, pp. 695-711 and 713-20.
7. M.H. Wu and C.M. Wayman: *Proc. Int. Conf. on Martensitic Transformations—1986*, Japan Institute of Metals, Sendai, 1987, p. 619.
8. Y. Nakata, T. Tadaki, and K. Shimizu: *Mater. Trans. Jpn. Inst. Met.*, 1989, vol. 30, pp. 107-16.
9. K. Takezawa and S. Sato: *Proc. Int. Conf. on Martensitic Transformations—1986*, Japan Institute of Metals, Sendai, 1987, p. 625.
10. K. Takezawa and S. Sato: *Metall. Trans. A*, 1990, vol. 21A, pp. 1541-45.
11. Y. Hamada, M.H. Wu, and C.M. Wayman: *Mater. Trans. Jpn. Inst. Met.*, 1991, vol. 32, p. 747.
12. A. Schmit, M. Chandrasekaran, G. Ghosh, and L. Delaey: *Acta Metall.*, 1989, vol. 37, pp. 3151-55.
13. J. Zhang, S. Chen, and T.Y. Hsu (Xu Zuyao): *Acta Metall.*, 1989, vol. 37, pp. 241-46.
14. T.Y. Hsu (Xu Zuyao): *Metall. Trans. A*, 1990, vol. 21A, pp. 811-16.
15. K. Takezawa and S. Sato: *Trans. Jpn. Inst. Met.*, 1988, vol. 29, pp. 894-902.
16. Eon-sike Lee and Y.G. Kim: *Acta Metall. Mater.*, 1990, vol. 38, pp. 1669-76.
17. L. Jiang, W. Lu, B. Jiang, and T.Y. Hsu (Xu Zuyao): *Trans. Non-Ferrous Metals Soc. China*, 1991, vol. 1, p. 57 (English edition).
18. J.B. Austin and R.L. Rickett: *Trans. Am. Inst. Min. Eng.*, 1939, vol. 135, pp. 396-415.
19. W. Lu, B. Jiang, and T.Y. Hsu (Xu Zuyao): *Trans. Non-Ferrous Metals Soc. China*, 1992, vol. 2, p. 51 (English edition).
20. W. Lu, B. Jiang, and T.Y. Hsu (Xu Zuyao): *Scripta Metall. Mater.*, 1992, vol. 27, pp. 861-64.
21. H.I. Aaronson, W.T. Reynolds, Jr., G.J. Shiflet, and G. Spanos: *Metall. Trans. A*, 1990, vol. 21A, pp. 1343-80.
22. T.Y. Hsu (Xu Zuyao) and X.W. Zhou: *Acta Metall.*, 1989, vol. 37, pp. 3095-98.
23. T.Y. Hsu (Xu Zuyao) and X.W. Zhou: *Acta Metall. Sinica*, 1992, ser. A, vol. 5, pp. 465-67 (English edition).
24. T.Y. Hsu (Xu Zuyao) and X.W. Zhou: *Acta Metall. Mater.*, 1991, vol. 39, pp. 2615-19.
25. X.W. Zhou and T.Y. Hsu (Xu Zuyao): *Acta Metall.*, 1989, vol. 37, pp. 3085-90.
26. T.Y. Hsu (Xu Zuyao) and X.W. Zhou: *Acta Metall.*, 1989, vol. 37, pp. 3091-94.
27. X.W. Zhou and T.Y. Hsu (Xu Zuyao): *Acta Metall. Mater.*, 1991, vol. 39, pp. 1041-44.
28. X.W. Zhou and T.Y. Hsu (Xu Zuyao): *Acta Metall. Mater.*, 1991, vol. 39, pp. 1045-51.
29. *Selected Values of the Thermodynamic Properties of Binary Alloys*, ASM, Metals Park, OH, 1973, pp. 1-1435.
30. G. Inden: *Z. Metallkd.*, 1975, vol. 66, pp. 577-82 and 648-53.
31. R. Rapacioli and M. Ahlers: *Scripta Metall.*, 1977, vol. 11, pp. 1147-50.
32. A.A. Arab and M. Ahlers: *Acta Metall.*, 1988, vol. 36, pp. 2627-38.
33. P.R. Swann and H. Warlimont: *Acta Metall.*, 1963, vol. 11, pp. 511-27.
34. S.C. Singh, Y. Murakami, and L. Deleay: *Scripta Metall.*, 1978, vol. 12, pp. 435-38.
35. G.W. Lorimer, G. Cliff, H.I. Aaronson, and K.R. Kinsman: *Scripta Metall.*, 1975, vol. 9, pp. 271-80.
36. P.E.J. Flewitt and J.M. Towner: *J. Inst. Met.*, 1967, vol. 95, pp. 273-80.
37. T.Y. Hsu (Xu Zuyao) and Mou Yiwen: *Acta Metall.*, 1984, vol. 32, pp. 1469-81.
38. Yiwen Mou and T.Y. Hsu (Xu Zuyao): *Metall. Trans. A*, 1988, vol. 19A, pp. 1695-1701.
39. Weizhong Chen, T.Y. Hsu (Xu Zuyao), Shuchuan Chen, and Jihua Zhang: *Acta Metall. Mater.*, 1990, vol. 38, pp. 2337-42.

Long-Range Ordering in the Early Stages of Precipitation—A Brief Review

J.B. COHEN

Local order adjusts more rapidly than long-range order for several reasons, and this local order need not mimic the low-temperature precipitate (although it does in many cases). This may drastically alter the activation energy for nucleation. Strain energy can play a key role in determining whether precipitation, ordering, or a displacive transformation occurs and in determining not only the shape but also the compositions of the phases. Long-range ordering in the matrix may develop prior to precipitation of an ordered phase. A plate-like morphology for ordered precipitates can occur for several reasons, *e.g.* strain, anisotropic interfacial energy, or planar antiphase boundaries in an ordered matrix.

I. INTRODUCTION

IT is the purpose of this article to briefly review what is currently known about the initial stage of precipitation in solid solutions, with particular emphasis on ordering phenomena. We will first explore the local atomic arrangements above a phase boundary, then the changes with temperature, and finally, what is expected on quenching below a phase boundary (in terms of what is feasible from a thermodynamic and kinetic point of view), as well as the evidence for these phenomena.

II. ABOVE A PHASE BOUNDARY

In many solid solutions that precipitate below a solvus, there are local atomic arrangements forming and breaking that resemble the phase that develops below the solvus. This occurs in Al-2 pct Cu, Au 40 at. pct Ni (see Reference 1 for a review), and Ni-12.7 at. pct Al,[2] for example. This is also true in many cases of ordering as well, the classic case being Cu_3Au,[1] but this is not yet proven to be the general case. In fact, there are already clear exceptions.[3]

Nevertheless, in such cases where this is true, the concept of nucleation below a phase boundary needs careful consideration because embryonic regions are present already. These regions should considerably decrease or even eliminate the activation energy for nucleation, and this has recently been reported by Haubold and coworkers in dilute Cu-Fe alloys.[4] When these regions are *not* like the low-temperature phase, the energy should be increased over that for a random alloy.

These arrangements can be described by the well-known concept of concentration fluctuations. On changing the temperature (still above a phase boundary), these regions relax to a new form, with a relaxation time $\tau(\mathbf{k})$, where $\mathbf{k}$ is the wave vector:

$$\tau^{-1}(\mathbf{k}) = \frac{2D}{f''} B^2(\mathbf{k})\, F(\mathbf{k}) \qquad [1]$$

Here, D is the diffusivily, f'' the second derivative of the Helmholtz free energy with respect to composition, B a geometric factor depending on the structure, and $F(\mathbf{k})$ the kth Fourier component of this free energy, including chemical and elastic terms. This relaxation time depends both on wavelength and crystallographic direction, as shown in Figure 1 for a Cu-Au alloy.[5]

III. CROSSING A PHASE BOUNDARY

Strain energy can play an important role not only in controlling the shape of a precipitate or zone, but also in deciding whether a system can form a precipitate or order or even undergo a displacive transformation. (Of course, chemical interactions are important as well and dominate if the atoms are close in size.)

To examine this, we consider the formation of a solid solution and focus on the strain energy. We can write the following equation for the Fourier coefficients of this term, $E(1/\lambda)$:[6]

$$E\left(\frac{1}{\lambda}\right) = E_0 + E_1\left(\frac{1}{\lambda}\right) + E_2\left(\frac{1}{\lambda}\right) \qquad [2]$$

initial strain energy for a random alloy: atoms at average lattice points—a constant term

composition fluctuations $f\left[\dfrac{d^2(\omega)^2}{d\left(\frac{1}{\lambda}\right)^2}\right]$

relaxation: $f\left(\frac{1}{\lambda}\right) - 0$ at superlattice points

We can think of this strain energy as developing in three stages represented in Eq. [2] by three terms. First, randomly arranged atoms are strained to conform to the average lattice from their own lattice, which costs energy represented by the constant term E_0. Then fluctuations form, whose elastic energy coefficient, E_1, is a function of the second derivative of the square of the phonon dispersion curve (whose shape depends on the strengths of interatomic forces and hence on electron

J.B. COHEN, Dean, is with the Department of Materials Science and Engineering, Robert R. McCormick School of Engineering and Applied Science, Northwestern University, Evanston, IL 60208.

This article is based on a presentation made at the Pacific Rim Conference on the "Roles of Shear and Diffusion in the Formation of Plate-Shaped Transformation Products," held December 18–22, 1992, in Kona, Hawaii, under the auspices of ASM INTERNATIONAL's Phase Transformations Committee.

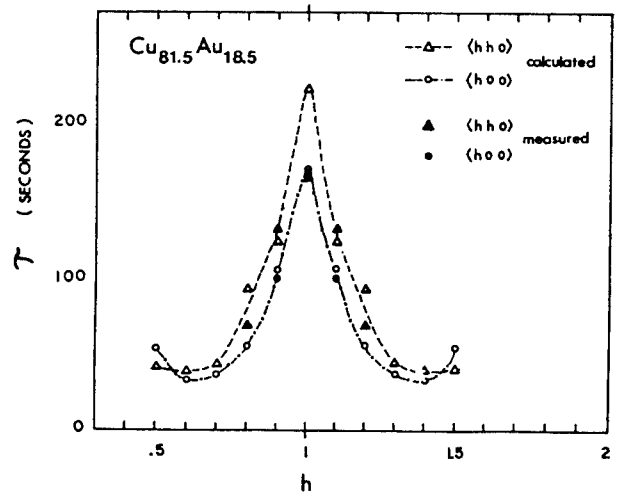


Fig. 1—The relaxation time estimated with the measured Fourier representation of total free energy, $F(\mathbf{k})$. Experimental results are also shown.[5]

shielding). Finally, the atoms relax from the average lattice points to more comfortable positions, the term E_2, and the total elastic energy coefficient is thereby decreased. This last term is a function of the reciprocal of the wavelength of decomposition, and it turns out that this term is zero (makes no contribution) at superlattice positions in reciprocal space. Thus, the shape of phonon dispersion is critical. If the phonon dispersion is "normal" (the solid lines in Figure 2), the second term is lowest at superlattice points and, therefore, the total elastic energy favors ordering. If there is a dip or softening in this curve (due to electron shielding effects, the dotted lines in Figure 2), E_1 is negative at the wavelength of the maximum, favoring clustering. Such softening has been detected in the Au-Ni system[7] (and the spacing of the fine coherent regions below the miscibility gap is that predicted from the maximum in the phonon dispersion).

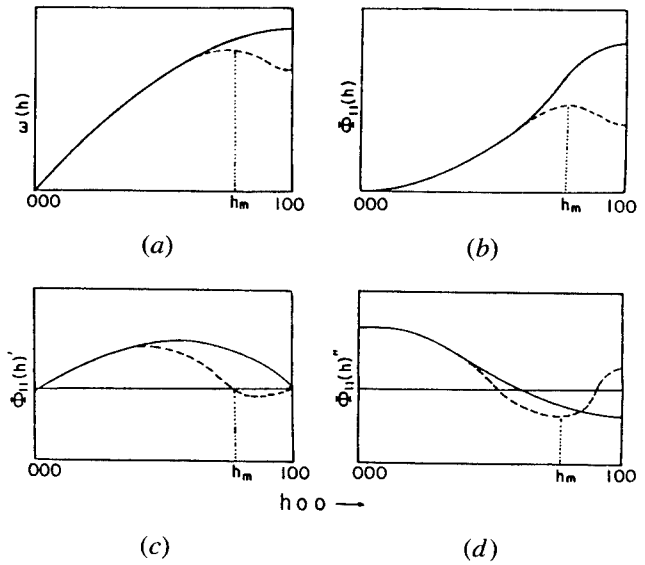


Fig. 2—(*a*) Phonon dispersion curves: solid line—normal; dotted line—softened. (*b*) the elastic energy coefficient, (*c*) its first derivative, and (*d*) its second derivative.[6]

We have detected softening in the Cu-Be system as well.[8] (In dilute Al-Cu alloys, bound states appear in the dispersion but there is no theory yet as to this contribution.) Of course, it is already well known that the shape of the phonon dispersion curve can stimulate a displacive transformation. Soft regions in the dispersion lead to long-lived fluctuations in displacement (usually referred to as the tweed structure to describe its appearance in transmission electron microscopy (TEM)) which can start the low-temperature phase. This is particularly well known in body-centered cubic lattices, whose phonon dispersions usually show a "dip" near wavelengths that are known to set up precursor hexagonal close-packed (hcp) or omega-like distortions in the solid solution.[9]

Indeed, even displacements around individual atoms may initiate precipitation and/or displacive transformations—by trapping a phonon and/or lowering the free energy barrier. Here again, there may be no real homogeneous nucleation. For example, in NiAl, for Al-rich alloys, there are Ni vacancies, whereas in excess Ni alloys, Ni is on the Al sublattice. In both cases, omega-like regions form around the point defect.[10] Heiming *et al.*[11] have recently reported similar displacements in Zr-Nb alloys at high temperature, those akin to the hcp phase that can occur in this system, as well as those for the omega phase. Thus, displacements around individual point defects can assist decomposition, ordering, or displacive transformations. Only when atoms are the same size (and there is no electron transfer) will this effect vanish.

If strain effects can assist the initiation of both replacive and displacive transformations, we can certainly expect that there will be situations where these two transformations interact, competing with or assisting each other, as Tanner has suggested.[12] Furthermore, it is well established that some (if not all) of these systems exhibit enhanced diffusion near a critical temperature due to the phonon softening, which could aid the formation of clustering.[13] In this new picture, displacive transformations might start just because diffusion is too slow for the other reactions.

During decomposition, basic thermodynamics predicts a variety of paths, recently nicely reviewed by Soffa and Laughlin.[14] Decomposition can precede ordering, the entire solid solution can order first followed by decomposition into ordered and disordered phases, the precipitation can occur fully ordered, or the matrix can order after precipitation. This depends on the relative free energies of the phases.

There are many examples of decomposition followed by ordering—in the development of GP zones in Al-Cu, Cu-Be, and Al-Ag systems, for example, where the GP zones are initially disordered but eventually an ordered phase appears (Reference 1). What about ordering preceding precipitation? Chen and co-workers[15] sampled the small-angle scattering for signs of precipitation and a superstructure reflection for signs of ordering in an Al-Li alloy. Ordering clearly preceded precipitation. (However a recent TEM and field-ion microscopy study of the same alloy[16] disagrees, claiming the matrix is disordered.) Thermodynamics predicts the possible, so kinetic considerations can be important. Based on Monte

Carlo simulations of the kinetics with the pair approximation, Khachaturyan and co-workers[17,18,19] indicate that if a nonstoichiometric ordered matrix appears first, a plate-like disordered phase then forms at the antiphase boundaries and the matrix adjusts its composition toward the stoichiometric ordered phase. A periodic array of precipitates results. The authors point out that this has been actually observed by Matsumara *et al.* in Fe-13.8 at. pct Si[20] and in the Fe-Al system[21] prior to precipitation. While the final phases in the Al-Cu, Al-Ag, and Cu-Be systems are ordered, ordering of the matrix is not observed in these systems. Clearly, different sequences are already observed.

Fultz[22] has pointed out that thermodynamic arguments may not be correct far from equilibrium, because a system may be changing its microstates rapidly. As a result, the statistical argument of sampling all of these may not be met. Fultz shows that if a system approaches a saddle point between local order and long-range order (which it always does at least in the pair approximation), kinetics can slow drastically. This is so because if S is a state variable, at a saddle point following Fultz,

$$\frac{\partial F}{\partial S} = 0 \qquad [3]$$

and

$$\frac{\partial S}{\partial t} = f\left(\frac{\partial F}{\partial S}\right) = 0 \qquad [4]$$

It is often observed that local order adjusts rapidly below an ordering transition, but long-range order develops more slowly. While it has been thought that this might be due to nucleation of ordered regions or domain boundary impingement, the only thing necessary is the saddle point. Fultz calls such a nearly stalled state "pseudostable." This pseudostability can occur in another way, as pointed out by Kikuchi *et al.*[23] and illustrated in Figure 3, from their work. The free energy curve may change with time. Immediately after a quench, an alloy has configurations like those at the higher temperature, and even a rigorous mathematical treatment shows subsidiary minima in the free energy. An alloy of composition 0.1 or so is in a local minimum which evolves to the flat bottomed curve with time—hence, pseudostability. What is the evidence for these predictions? We've already alluded to the well-known rapid evolution of local order below T_c followed by a slow development of long-range order.

Fultz has also been studying kinetic factors, particularly in the case of the development of any long-range ordered phase below an ordus. In binary (or higher) systems, unusual phases can appear.[24,25] For example, if there are four (interpenetrating) sublattices in a cubic structure, there are three order parameters which can describe order for B2, DO_3, or B32 phases. Second neighbor interactions as well as first are important for stabilizing DO_3 and B32. At low temperatures, the B32 structure is not favored when first neighbor interactions favor unlike neighbors. However, strong repulsion of like second neighbors can lead to the transient appearance of B32. This is not a metastable state, as the free

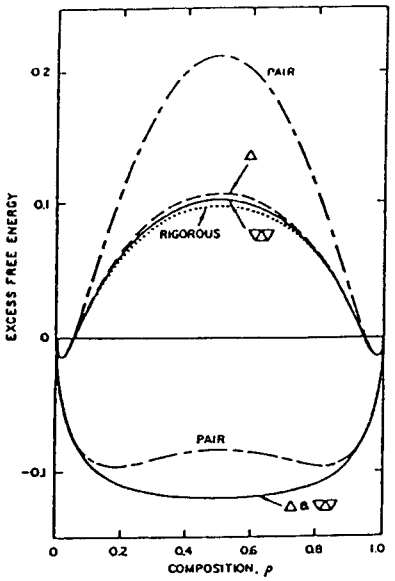


Fig. 3—Free energy F_q after quench, reprinted with permission from Ref. 23. Horizontal lines are compositions of phases, which vary with alloy composition.

energy is decreasing continuously. Fultz has also pointed out that the diffusion of species to favor strong bonds can force vacancies onto a particular sublattice, making it likely for another species to jump there, even though there is no energy preference to do so and this atom type can find itself in the wrong sublattice temporarily.

Distortions may also affect the compositions of the phases and even whether the lever rule is followed.[26,27,28] This is illustrated with calculations for the Ni-V system following the theory in Reference 28 (Figure 4). Despite the fact that the strain is quite small (0.3 pct or less), the predicted effect is significant and there are clearly regions where the lever rule is not followed; these regions are larger the larger the strain. This has not yet been confirmed experimentally, but it is obviously quite important to do so soon. Certainly, most previous measurements of the coherent regions of existence have assumed the lever rule, which is why current

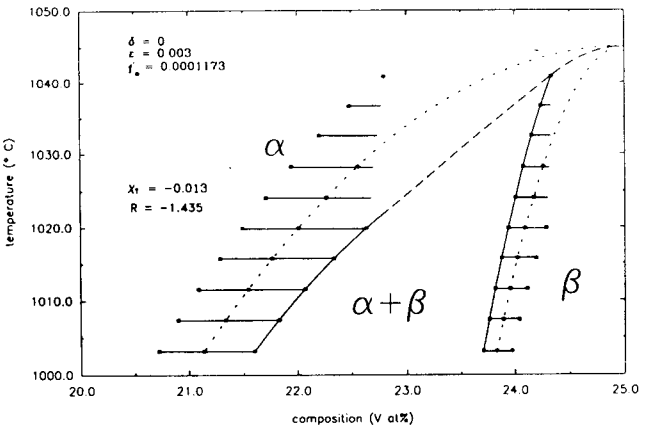


Fig. 4—The Ni-V phased diagram in the vicinity of Ni_3V, calculated by D.K., Na. The term ε is the coherency strain between the matrix and precipitate. Horizontal lines are compositions of phases, which vary with alloy composition.

coherent phase diagrams are probably only approximate regions of coexistence.

IV. PLATE-LIKE FORMATION

Plates form due to the faceted antiphase domains in Fe-Si, as mentioned in Section III. They also occur in the Al-Cu and Cu-Be systems. However, in the former, there are plate-like regions in the solid solution before precipitation starts, whereas in the Cu-Be system, the initial zones are ellipsoidal and then flatten during aging (Reference 1) while retaining their initial regularity in the ⟨110⟩ directions. Apparently, interfacial energy is more important in the Cu-Be system than in Al-Cu alloys.

V. CONCLUSIONS

Regions exist in a solid solution that may drastically increase or decrease the activation energy for nucleation. Coherency strains may affect whether ordering or precipitation or a displacive transformation will occur and the compositions of the phases as well as their shapes. Ordering of the matrix may precede precipitation of an ordered phase.

Plate-like morphologies can arise if the matrix is ordered and the antiphase boundary energy is anisotropic or due to elastic effects. Finally, local atomic arrangements (local order or clustering and the attendant distortions) may impede or assist the growth of plates. This area has yet to be explored.

ACKNOWLEDGMENTS

This article and our prior research in this area was supported by NSF under Grant No. DMR 18920567 (Dr. Bruce MacDonald, Program Director).

REFERENCES

1. J.B. Cohen: *Metall. Trans. A*, 1992, vol. 23A, pp. 2685-97.
2. J.E. Epperson and P. Fürnrohr: *Acta Cryst.*, 1983, vol. A39, pp. 740-46.
3. L. Reinhard, J.L. Robertson, S.C. Moss, G.E. Ice, P. Zschack, and C.J. Sparks: *Phys. Rev. B*, 1992, vol. 45, pp. 2662-2760.
4. P. Fratzi, Y. Yoshida, G. Vogland, and H.G. Haubold: *Phys. Rev. B*, 1992, vol. 46, pp. 11323-331.
5. H. Chen and J.B. Cohen: *J. Phys.*, 1977, vol. c7, pp. 324-27.
6. T.B. Wu: *MRS Symp. Proc.*, North-Holland, New York, NY, 1984, vol. 32, pp. 19-25.
7. T.B. Wu, J.B. Cohen, and W. Yelon: *Acta Metall.*, 1982, vol. 30, pp. 2065-70.
8. Y.M. Koo, J.B. Cohen, S.M. Shapiro, and L.E. Tanner: *Acta Metall.*, 1988, vol. 36, pp. 591-604.
9. G.M. Michal, P. Moine, and R. Sinclair: *Acta Metall.*, 1982, vol. 30, pp. 125-38.
10. P. Georgopoulos and J.B. Cohen: *Acta Metall.*, 1981, vol. 29, pp. 1535-51.
11. A. Heiming, W. Petrg, G. Vogel, J. Trampenau, B.R. Schober, J. Chevrier, and O.S. Scharpf: *Condensed Matter*, 1991, vol. 85, pp. 239-48.
12. L.E. Tanner: *Competing Interactions and Microstructures: States and Dynamics*, Springer-Verlag, New York, NY, 1988, pp. 74-83.
13. H.I. Aaronson and P.G. Shewmon: *Acta Metall.*, 1967, vol. 15, pp. 385-87.
14. W.A. Soffa and D.E. Laughlin: *Acta Metall.*, 1989, vol. 37, pp. 3014-28.
15. M.S. Xu, H. Chen, G.B. Stephenson, and B. Park: *MRS Proc.*, in press.
16. K. Hono, S.S. Babu, K. Hiraga, R.O. Kano, and T. Sakurai: *Acta Metall.*, 1992, vol. 40, pp. 3027-34.
17. L.Q. Chen, Y. Wang, and A.G. Khachaturyan: *Phil. Mag. Lett.*, 1991, vol. 64, pp. 241-51.
18. L.Q. Chen and A.G. Khachaturyan: *Scripta. Metall. Mater.*, 1991, vol. 25, pp. 61-66.
19. L.Q. Chen and A.G. Khachaturyan: *Scripta. Metall. Mater.*, 1991, vol. 25, pp. 67-72.
20. S. Matsumara, H. Oyama, and K. Oki: *Mater. Trans. JIM*, 1989, vol. 30, p. 695.
21. S.M. Allen and J.W. Cahn: *Acta Metall.*, 1976, vol. 24, pp. 425-37.
22. B. Fultz: "*NonEquilibrium States*", submitted for publication.
23. R. Kikuchi, T. Mohri, and B. Fultz: *Mater. Res. Soc. Symp. Proc.*, 1992, vol. 205, pp. 387-92.
24. B. Fultz: *J. Mater. Res.*, 1991, vol. 168, pp. 145-57.
25. B. Fultz: *J. Mater. Res.*, 1992, vol. 7, pp. 946-54.
26. R.O. Williams: *Metall. Trans. A*, 1980, vol. 11A, pp. 247-53.
27. J.W. Cahn and F. Larché: *Acta Metall.*, 1984, vol. 33, pp. 1915-23.
28. M.J. Pfeifer and P.W. Voorhees: *Metall. Trans. A*, 1991, vol. 22A, pp. 1921-34.

High-Resolution Analytical Electron Microscopy Study of Isothermal Plate-Shaped Products in Some β-Phase Alloys

T. TADAKI and K. SHIMIZU

The isothermal plate-shaped products in β-phase Cu-Zn-Al, Cu-Zn-Au, and Ag-Cd alloys have been studied from the viewpoints of morphology, crystal structure, and composition using a high-resolution analytical electron microscope equipped with a field-emission electron gun. It is shown that thin plate-shaped products, at early stages of the isothermal formation, exhibit crystallographic properties characteristic of martensites formed at subzero temperatures but that their compositions were definitely different from those of the surrounding matrices. Therefore, atom diffusion is conceivable to be involved in the plate formation from the nucleation stage and to occur across the coherent plate/matrix interfaces. In order for nucleation of the isothermal transformation to occur, two kinds of reactions should be thermally activated at intermediate temperatures above T_0 for the martensitic transformation: (1) atom diffusion to achieve the observed composition differences between plates and matrices and (2) martensitic transformation in hypothetical alloys with compositions less than those of the original ones by the observed composition differences. The incubation periods experimentally observed should be associated with these two thermal activation processes.

I. INTRODUCTION

THE isothermal plate-shaped products in β-phase noble metal-base alloys such as Cu-Zn are widely known[1,2,3] to exhibit a dual nature as though they are formed by both a crystallographic-shear mechanism and a diffusion-controlled reaction. But, the questions of when and how atom diffusion is involved in plate formation are not clearly understood yet. Recently, analytical electron microscopy studies on these topics have been made for several β-phase alloys.[4–15] As a result, it is being established that the plate-shaped products possess certain solute concentrations definitely different from those in the surrounding matrices.[5,7–15] This fact strongly suggests that atom diffusion is involved in plate formation from the nucleation stage.

However, Doig and Flewitt[6] formerly reported that no composition difference between the plate-shaped product and its matrix in a Cu-Zn alloy was found in the vicinity of the growth edge. They also reported that the solute concentration was uneven inside the plate-shaped products of Cu-Zn-Au alloys, *i.e.*, appreciably higher in the central regions than at both sides, and was also higher in matrix regions close to the matrix/plate interfaces than in those far from them. On the other hand, Wu *et al.*[16] reported that very thin plate-shaped products in a Cu-Zn-Al alloy had an even antiphase domain (APD) structure throughout, which inherited the next nearest neighbor (nnn) type APDs in the aged $L2_1$ matrix, while thicker plates were observed to have a composite substructure with respect to the APD structure, *i.e.*, the central region consisted of the APD structure inheriting the nnn type, with both sides inheriting the nearest neighbor (nn) type in the matrix. They thus inferred that plate lengthening takes place due to the crystallographic-shear mechanism but that plate thickening occurs due to atom diffusion. These results appear to suggest that the isothermal formation of plate-shaped isothermal products in substitutional alloys proceeds in two steps: (1) lengthwise growth by a crystallographic-shear mechanism and (2) sidewise growth by a diffusion-controlled reaction.

Taking those previous studies into consideration, the present authors and their group have extensively investigated the isothermal plate-shaped products in β-phase Cu-Zn-Al, Cu-Zn-Au, and Ag-Cd alloys to clarify the dual nature, *i.e.*, diffusionless and diffusional, of the reaction from the viewpoint of morphology, crystal structure, and composition using a high-resolution analytical electron microscope equipped with a field-emission electron gun. This analytical electron microscope[17] makes it possible to produce a narrow electron beam 1 to 2 nm in diameter with extremely high brightness, good coherency, and parallelism and thus enables us to take electron diffraction (ED) patterns and energy dispersive X-ray (EDX) spectra from very small areas of thin plate-shaped products just after nucleation. The results obtained are described, and nucleation of the plate-shaped products in the substitutional β-phase noble metal-base alloys is discussed.

II. EXPERIMENTAL PROCEDURES

The methods of specimen preparation of Cu-29.1Zn-6.7Al (at. pct), Ag-45 at. pct Cd, and $Cu_{60-x}Zn_{40}Au_x$ (x = 4, 9, and 15) alloys have been described in detail elsewhere.[9,10,14] For simplicity, the $Cu_{60-x}Zn_{40}Au_x$ alloys with x = 4, 9, and 15 are called the 4, 9, and 15 pct Au alloys, respectively, in the present article.

T. TADAKI, Associate Professor, is with The Institute of Scientific and Industrial Research, Osaka University, Osaka 567, Japan. K. SHIMIZU, Professor, is with the Department of Mechanical Engineering, Kanazawa Institute of Technology, Kanazawa-South, Ishikawa 921, Japan.

This article is based on a presentation made at the Pacific Rim Conference on the "Roles of Shear and Diffusion in the Formation of Plate-Shaped Transformation Products," held December 18–22, 1992, in Kona, Hawaii, under the auspices of ASM INTERNATIONAL's Phase Transformations Committee.

After solution treatments, disk-shaped specimens of these alloys were quenched into iced water and heat-treated to form the plate-shaped products at 473 or 573 K for various periods ranging from 1.5 hours to 28 days for the Cu-29.1Zn-6.7Al (at. pct) alloy, at 433 K for up to 17 days for the Ag-45 at. pct Cd alloy, and at temperatures between 373 and 623 K for up to 60 hours for the $Cu_{60-x}Zn_{40}Au_x$ (x = 4, 9, and 15) alloys.

Thin foils of these specimens were examined by a Hitachi H-600FE analytical electron microscope equipped with a field-emission electron gun, operating at 100 kV. The spatial resolution in the present experiment was estimated to be about 20 nm by using the formula proposed by Goldstein *et al.*,[18] because the foil thickness was less than 100 nm. The compositions of the plate-shaped product and its adjacent matrix were quantitatively analyzed using the formula presented by Cliff and Lorimer.[18] The factor K in this formula is reported to vary under various experimental conditions.[19] In the present study, however, it is of interest to know whether or not the composition of plate-shaped products is different from that of the matrices just after transformation; in fact, the difference in solvent content between the products and matrices rather than their absolute contents was determined. It was thus assumed that a slight variation in the K factor does not affect the results seriously, because composition analyses of plate-shaped products and matrices were carried out under almost the same conditions.

The EDX spectroscopy of nanometer-size areas was partly performed in the transmission electron microscopy (TEM) mode. The probe size in the TEM mode was less than 20 nm in diameter, and they were larger than that in the scanning transmission electron microscopy (STEM) mode which was 1 to 2 nm in diameter. The TEM mode was used because very small regions could be observed during the acquisition of the characteristic X-ray spectra from those areas.

The EDX spectra were taken under diffraction conditions where low-order reflections were not strongly excited, because it is well known that EDX spectra are significantly affected by the crystal orientation near the exact Bragg conditions. However, TEM images of isothermal plate-shaped products were recorded under diffraction conditions where some reflections were properly excited so that good contrast images of them were obtained.

Characteristic X-ray quanta emitted from constituent atoms were counted up to the order of 10^4 except Al and Au atoms, for which the X-ray intensities were on the order of 10^3 under the same condition. The overall error involved in the experimentally determined solvent content of each phase was thus estimated to be about ±10 pct. The measurement for the solvent content of the plate-shaped product and matrix was repeated several times for each region. The solvent content of the matrix obtained by using defocused electron beams approximately 500 nm in diameter was regarded as the average one of the matrix. The difference in the solvent content between the two phases was obtained by subtracting the average value of the matrix from each measured value of plate-shaped product. The range of variation in the difference in solvent content was roughly less than ±20 pct.

In order to examine how the isothermal formation of plate-shaped products and the martensitic transformation are interrelated, M_s temperatures of the present alloys were measured through electrical resistivity *vs* temperature curves or differential scanning calorimetry. As a result, they were about 225, 218, 223, 123, and <80 K for the Cu-Zn-Al, Ag-Cd, 15 pct Au, 9 pct Au, and 4 pct Au alloys, respectively.

III. RESULTS

A. *Morphology of Isothermal Plate-Shaped Products*

Figure 1 shows examples of TEM images of isothermal plate-shaped products formed in Cu-Zn-Al alloy specimens heat-treated at 473 K for (a) 2 hours and (b) 8 hours. No such plates were observed in specimens heat-treated at the same temperature for 1.5 hours or less. These plates are thus considered to be at early stages of their growth and are seen to have such characteristic features of martensitic products as parallel straight interfaces and internal faults. But, it is to be noted that the size of the plates is on the order of two times smaller than that of martensite plates formed during subzero cooling of the same alloy.[20] Such a large difference in size between the two kinds of products

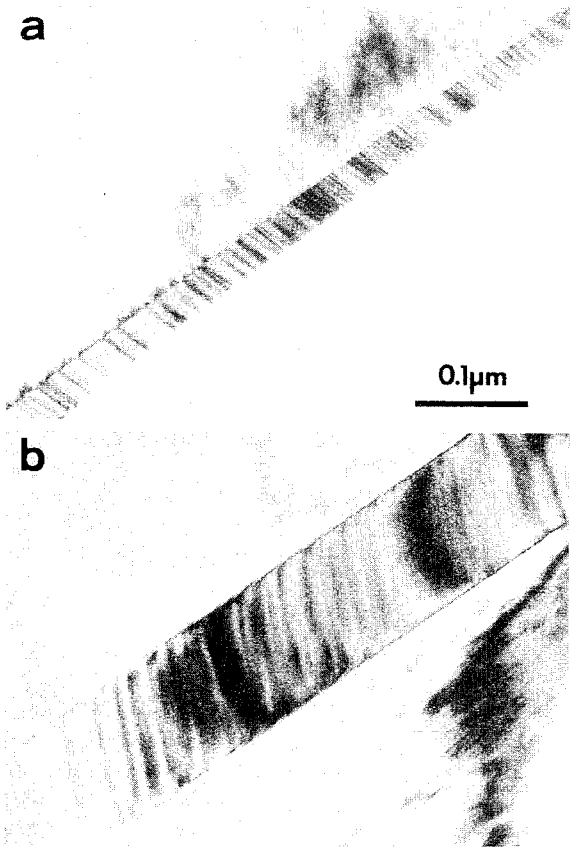


Fig. 1—TEM images of isothermal plate-shaped products in a Cu-Zn-Al alloy specimen heat-treated at 473 K for (*a*) 2 h and (*b*) 8 h.

seems to be a common feature in β-phase alloys, although their morphology is quite similar.

The thickness of the plate-shaped products was in general different from plate to plate even in an identical specimen; *e.g.*, in a Cu-Zn-Al alloy specimen heat-treated at 473 K for 2 hours, it varied roughly in a range of 15 to 50 nm. However, at this stage of aging, the individual plates were observed to be separated far from one another so that they were assumed not to impede the growth by interaction. Thus, it is possible that the difference in thickness from plate to plate reflects the differences in the elapsing times after the formation of individual plates; although, this may not always be true.

It is interesting to note that in the Ag-45 at. pct Cd alloy, the morphologies of the plate-shaped isothermal and martensitic products were observed to be entirely different from each other, as shown in Figure 2. Figure 2(a) is an optical micrograph of the β_2 matrix, which was taken from a polished surface of an as-quenched specimen at room temperature. No specific structure is observed there. When aged at 433 K for 1 hour, plate-shaped products appeared in the etched specimen (Figure 2(b)). Also shown are massive products without any specific habit plane (indicated by an arrow). Figure 2(c) shows the martensite plates, which were formed upon subzero cooling to 183 K below the M_s. It should be noted in this case that the plate-shaped products are entirely different from the martensite both in size and morphology. Moreover, while the spearlike-shaped martensite possesses a 2H-type structure, as verified by the present authors,[21] the plate-shaped products is of a 9R type, as described later.

Figure 3 reveals the composition dependence of the morphology of isothermal products in the $Cu_{60-x}Zn_{40}Au_x$ alloys. Figures 3(a), (b), and (c) show optical micrographs of the plate-shaped products formed in the 4, 9, and 15 pct Au alloys upon aging at 473 K for 60 hours, 2 hours, and 30 minutes, respectively. It is seen that the amount of plate-shaped products increases, while the size decreases remarkably with increasing Au content. This observation suggests that as the Au content increases, the incubation period for the isothermal formation of plate-shaped products becomes shorter, or simply the degree of supersaturation becomes higher. A very recent study,[22] however, shows that the former is the case. Hence, it is to be noted that since the M_s temperatures of these alloys were about 223, 123, and below 80 K for the 15, 9, and 4 pct Au alloys, respectively, there exists a strong correlation between the M_s temperature and the incubation period.

A lattice-fringe TEM image of an interface between the plate-shaped product and matrix is shown in Figure 4, which was taken from a plate about 50-nm thick and formed in a Cu-Zn-Al alloy specimen aged at 473 K for 3 hours. The lattice fringes corresponding to the $(\bar{1}\bar{1}4)$ planes of the plate-shaped product with an ordered 9R structure are continuous with the $(0\bar{1}1)$ planes of the matrix with a *B2*-type structure at the interface. This observation suggests that the plate-shaped product is largely coherent with the matrix at least until this growth stage, although whether or not the product phase is fully coherent should be closely examined by observing other lattice-fringe images.

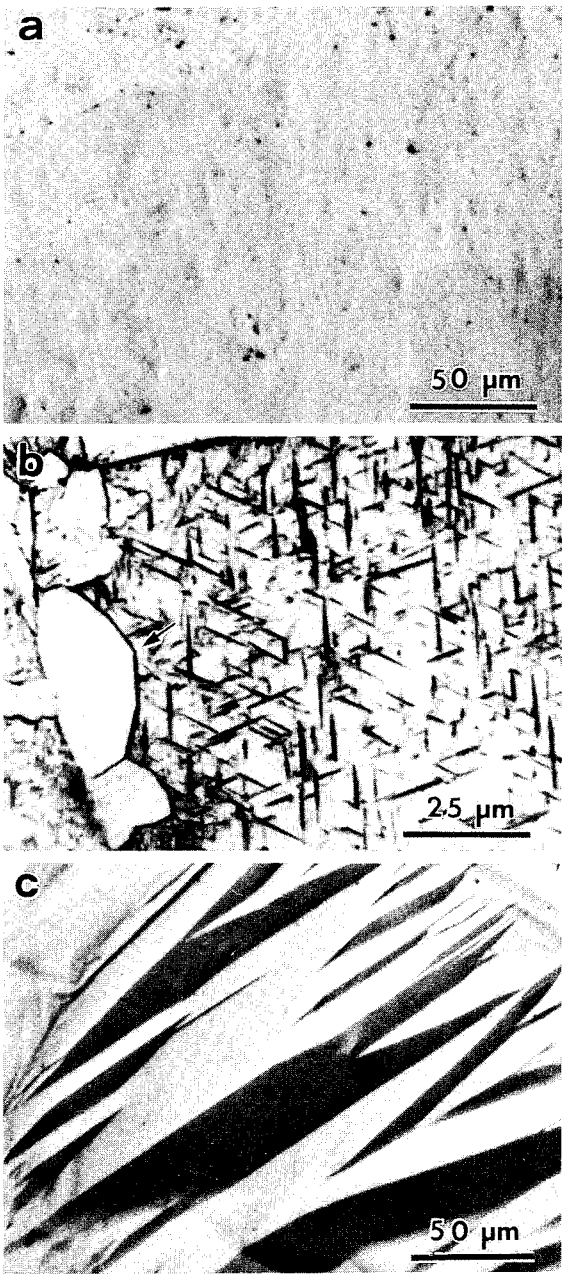


Fig. 2—Optical micrographs of a Ag-45 at. pct Cd alloy: (*a*) as-quenched; (*b*) isothermal plate-shaped products formed in the alloy subsequently heat-treated at 433 K for 1 h; and (*c*) martensites produced in the as-quenched alloy upon subzero cooling to 183 K.

B. *Crystal Structure of Isothermal Plate-Shaped Products*

Figure 5 shows (a) a TEM image of the plate-shaped products observed in a Cu-Zn-Al alloy specimen aged at 473 K for 8 hours and (b) an ED pattern taken from the central plate and (c) from the adjacent matrix. The thickness of the central plate is approximately 100 nm. Figure 5(b) is indexed as an ordered 9R structure like that of the martensite formed at subzero temperatures. The angle between the a^*-axis and c^*-axis, β^*, is about 91 deg, showing that the plate-shaped product possesses a monoclinic 9R structure. The present authors previously measured the β angle of the martensite with an

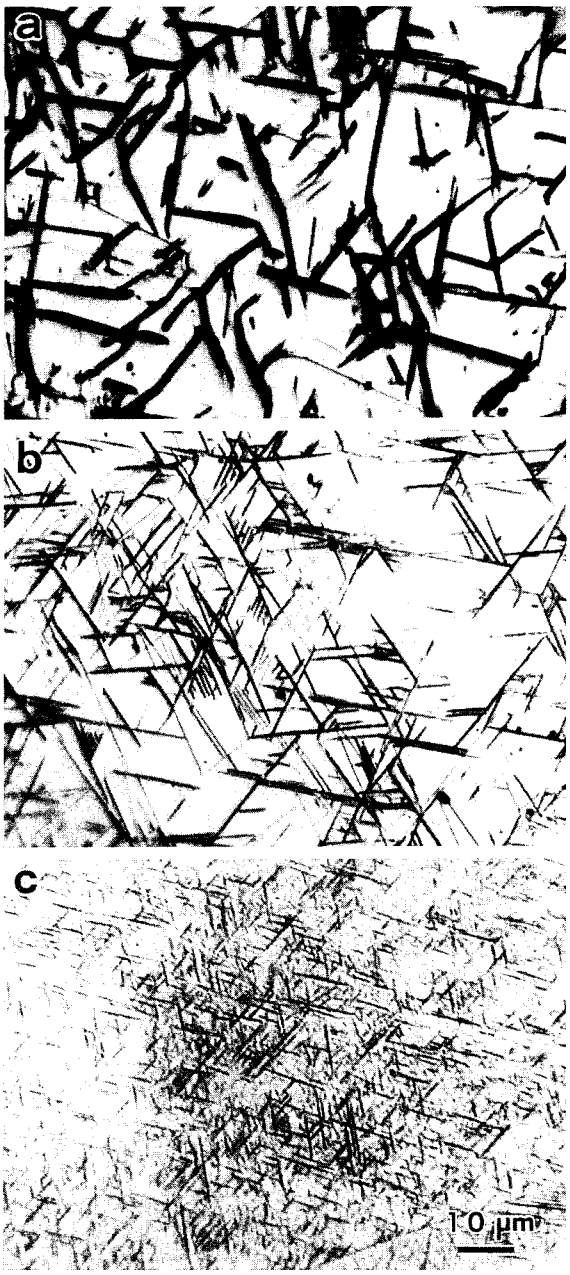


Fig. 3—Optical micrographs of isothermal plate-shaped products in (*a*) 4 pct, (*b*) 9 pct, and (*c*) 15 pct Au alloys heat-treated at 473 K for 60 h, 2 h, and 30 min, respectively.

ordered 9R structure of the same alloy below M_s by means of X-ray diffraction.[23] The β angle was 88.5 deg, or nearly equal to 89 deg in the present case. Superlattice reflections are hardly seen in the ED patterns of both the plate-shaped product and the adjacent matrix because of their extreme weakness. However, weak but sharp 100-type superlattice reflections exhibiting *B*2 order in the matrix are in fact recognized in the original film corresponding to Figure 5(c). Such weak superlattice reflections become visible also in the ED patterns from the plate-shaped products when observing under systematic reflection conditions, as shown for example, in the inserted pattern in Figure 5(b). The similarity in crystal structure between the plate-shaped

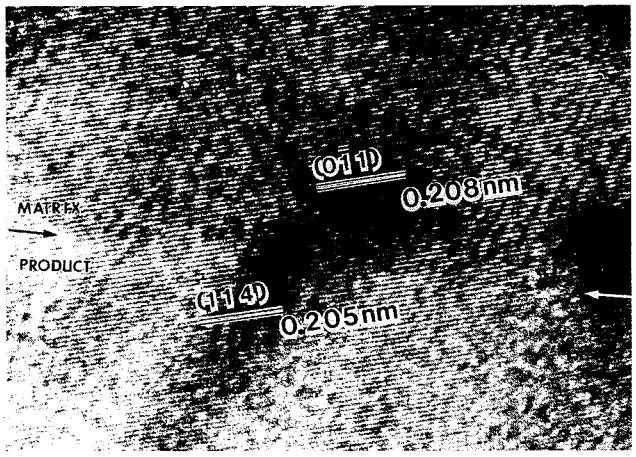


Fig. 4—Lattice-fringe TEM image around an interface between the matrix and isothermal plate-shaped product in a Cu-Zn-Al alloy specimen heat-treated at 473 K for 3 h.

product and the martensite indicates that the former has an ordered 9R structure inheriting the *B*2-type order of the matrix. This suggests that the plate-shaped product formed by a crystallographic shear mechanism rather than by diffusion-controlled reaction. Similar suggestions have been made by Wu *et al.*[7,16] and Takezawa *et al.*[24] for Cu-Zn-Al alloys with different compositions.

Although the isothermal plate-shaped product exhibits some characteristics of the martensitic product in terms of the crystallographic and morphological aspects, as described earlier, this does not necessarily mean that the crystal structure is entirely the same. Figure 6(a) is a TEM image of a plate-shaped product in a Cu-Zn-Al alloy aged at 473 K for 2 hours, and Figure 6(b) shows the corresponding ED pattern taken from the encircled area. Weak 003 and 006 reflections are still observed along the c^*-axis, although other reflections parallel to the c^*-axis are not visible. This indicates that these reflections are not due to double diffraction and are intrinsic to the plate-shaped product. As suggested by Hornbogen and Warlimont,[25] these reflections may be due to segregation of solute atoms on every third layer parallel to the basal plane.

Figure 7(a) is a TEM image of the isothermal plate-shaped product observed in a Cu-Zn-Al alloy specimen aged at 473 K for 28 days. Interfaces of the product are no longer as straight as seen in Figures 1, 4, 5, and 6. Then it appears that the coherence of the interface between the product and matrix becomes worse in this stage of growth. Figures 7(b) and (c) show ED patterns taken from the product and the adjacent matrix marked with black spots, respectively. In Figure 7(b), the β^* angle in the ED pattern from the product is exactly 90 deg, and no ordered reflections are observed, although the matrix still has the *B*2 structure (Figure 7(c)). This result indicates that the crystal structure of the isothermal product has changed from the ordered 9R to a disordered one during the isothermal growth. Prolonged aging at the same temperature or for shorter times at higher temperatures is supposed to bring about further change of the disordered 9R structure to a disordered

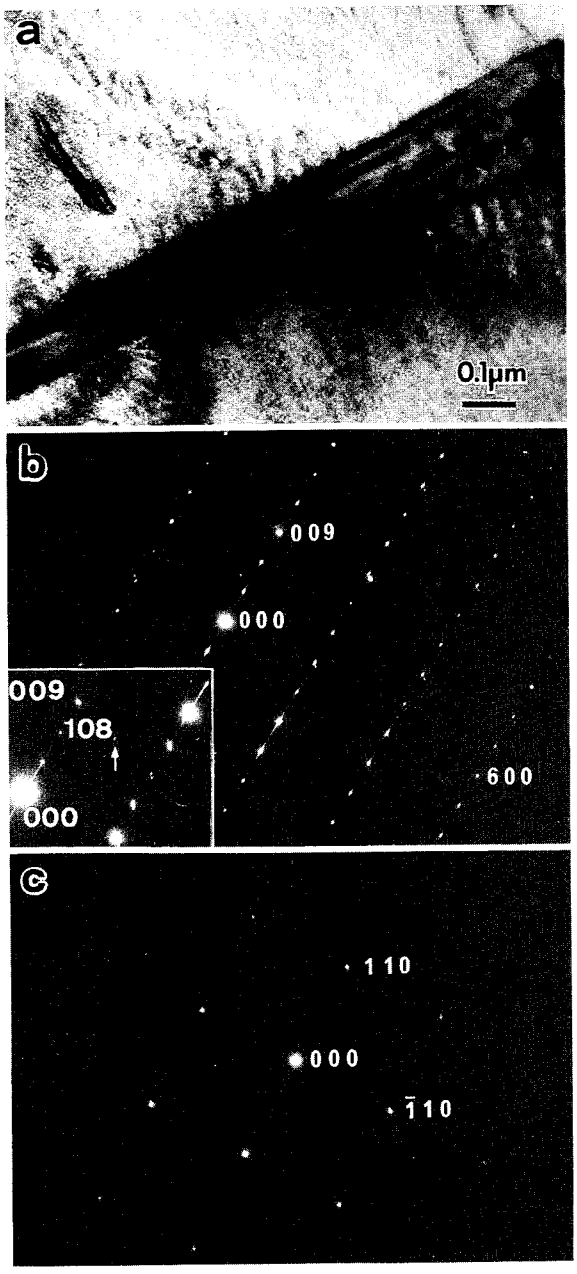


Fig. 5—(*a*) TEM image of plate-shaped products in a Cu-Zn-Al alloy specimen heat-treated at 473 K for 8 h; (*b*) ED pattern taken from the central plate; and (*c*) its adjacent matrix.

face-centered cubic (fcc) one, which is the thermal equilibrium α phase. In fact, by aging at 573 K for 7 days, the disordered fcc phase was obtained (Figure 8). Figure 8(a) shows the fcc phase with a low density of stacking faults, although it is not of the completely equilibrium α phase yet. The interfaces of the fcc phase are no longer flat and are considerably bowed. Figures 8(b) and (c) show the corresponding ED patterns taken from the product and the matrix in Figure 8(a), respectively, showing these regions to be of the fcc and the $B2$ structure, respectively.

The crystal structures of plate-shaped products in the $Cu_{60-x}Zn_{40}Au_x$ alloys were observed to depend on the Au

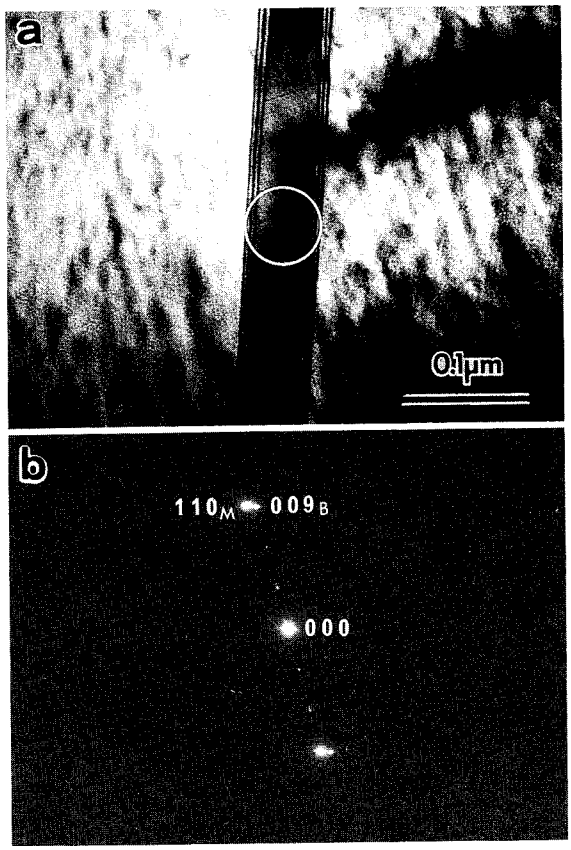


Fig. 6—(*a*) TEM image of a plate-shaped product in a Cu-Zn-Al alloy specimen heat-treated at 473 K for 2 h. (*b*) An ED pattern taken from the encircled area.

content. The plate-shaped product in the 4 pct Au alloy aged at 473 K possessed an ordered 9R structure, as in the Cu-Zn-Al alloy mentioned earlier, while the products in the 9 and 15 pct Au alloys had an 18R structure, corresponding to a change in the ordered structure of the matrix phase from $B2$ to $L2_1$ with increasing Au content. On the other hand, the plate-shaped product in the Ag-45 at. pct Cd alloy was observed to be a disordered 9R structure even at very early stages of formation. A similar result was also reported by Wu *et al.*[8]

C. *Composition of Isothermal Plate-Shaped Products*

The existence of composition differences between isothermal plate-shaped products and their matrices was examined by EDX spectroscopy. The EDX spectra were taken from plate-shaped products whose thickness was greater than about 20 nm (the spatial resolution) and whose interfaces were set to be as parallel to the incident electron beam as possible, especially for thin products. Figure 9 shows an example of a series of TEM images and EDX spectra obtained for a plate-shaped product about 30-nm thick in a Cu-Zn-Al alloy specimen aged at 473 K for 2 hours. Figures 9(b) and (c) are the EDX spectra taken from the product and the matrix in Figure 9(a), respectively. It is apparent in Figures 9(b) and (c) that the concentration of Cu and Zn atoms are different between the product and the adjacent matrix. The results of the EDX spectroscopy for plate-shaped

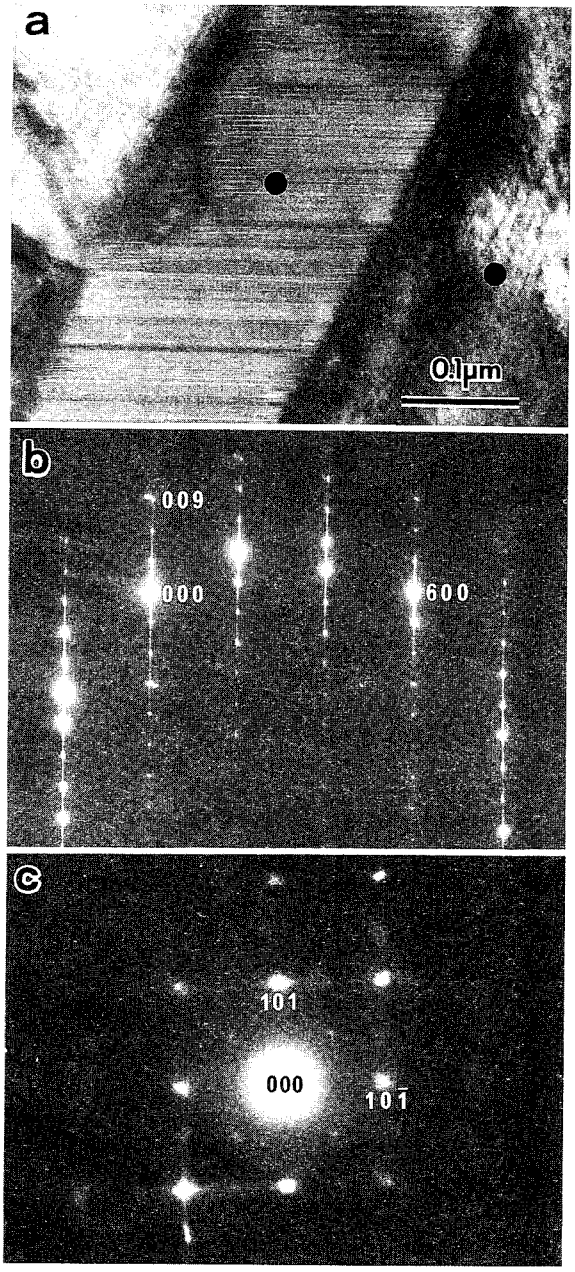


Fig. 7—(*a*) TEM image of a plate-shaped product in a Cu-Zn-Al alloy specimen heat-treated at 473 K for 28 days; (*b*) ED patterns taken from the plate; and (*c*) matrix regions marked with black spots.

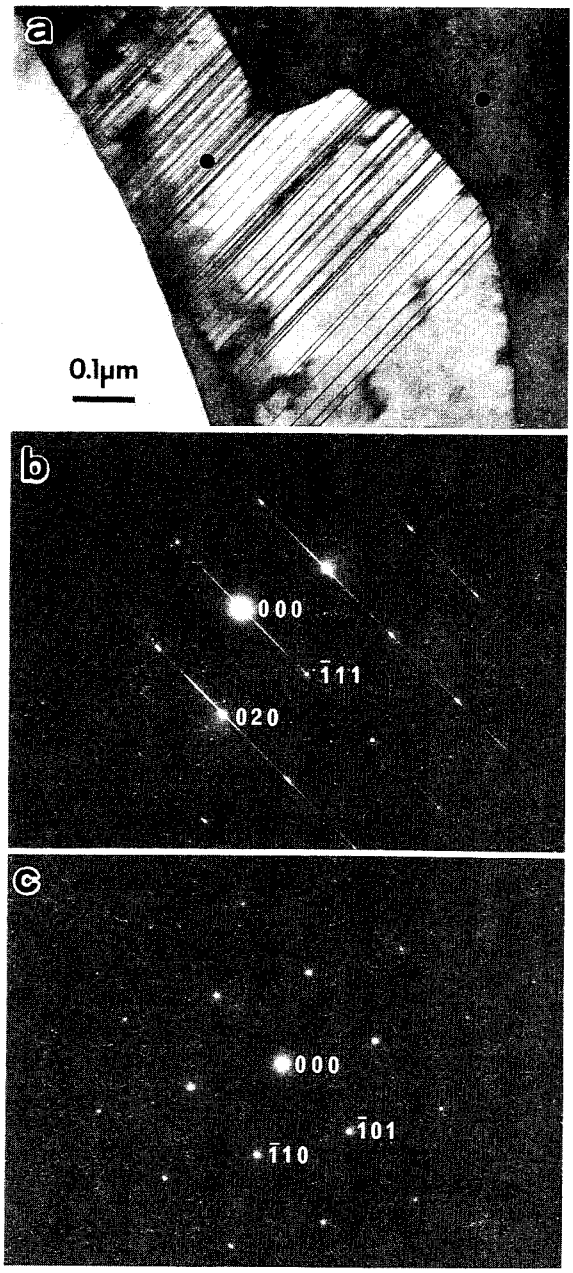


Fig. 8—(*a*) TEM image of an isothermal product in a Cu-Zn-Al alloy specimen heat-treated at 573 K for 7 days; (*b*) ED patterns taken from the plate; and (*c*) the matrix regions marked with black circles.

products in the Cu-Zn-Al alloy are summarized in Figure 10. For simplicity, the difference in composition between the product and matrix is expressed by that in the solvent content as a function of plate thickness of the product. The thickness of product may be considered to be a measure of reaction periods which have elapsed after the formation of plate-shaped products, although this may not always be true.

When the amount of the products was small, the composition of the matrices was nearly the same as that of the as-quenched specimens. But the solute content in the matrix increased markedly as the amount of the products increased. Then, the two data points on the right-hand side in Figure 10 were obtained by subtracting the Cu content of the as-quenched specimen from those of the isothermal products.

It is clear in Figure 10 that the isothermal plate-shaped products form with a certain composition that is definitely different from their matrices and that they grow keeping the composition almost constant. The farthest point on the right-hand side in Figure 10 is from the equilibrium fcc α phase shown in Figure 8. Since the fcc product was formed at 573 K, it might have had a little higher Cu content than this value if formed at 473 K. But, such a difference is probably less than the EDX experimental measurement error. Roughly speaking then, the isothermal plate-shaped product appears to form with nearly the same composition as the equilibrium fcc α phase from the very beginning of formation.

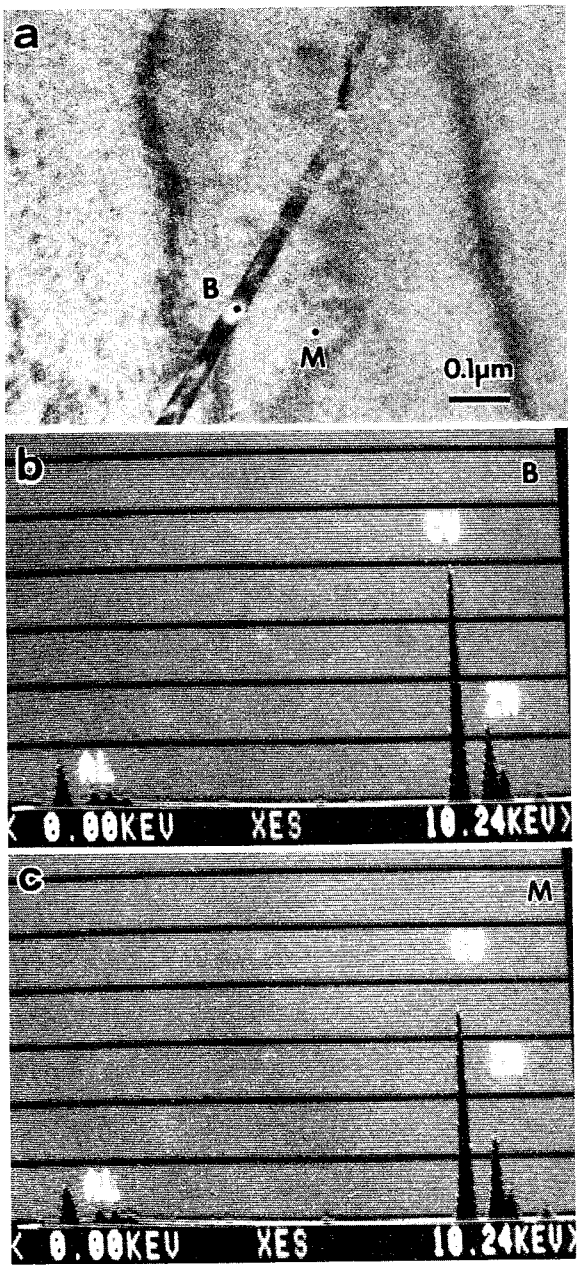


Fig. 9—(*a*) TEM image of a plate-shaped product in a Cu-Zn-Al alloy specimen heat-treated at 473 K for 2 h; (*b*) EDX spectrum taken from the plate; and (*c*) the matrix regions marked with black spots.

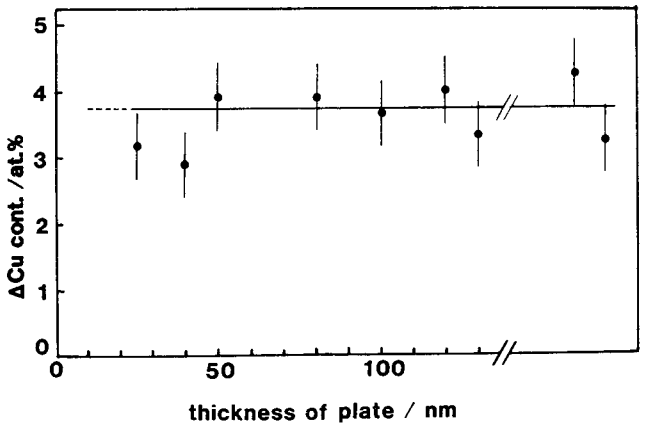


Fig. 10—Difference in Cu content between plate-shaped products and matrices.

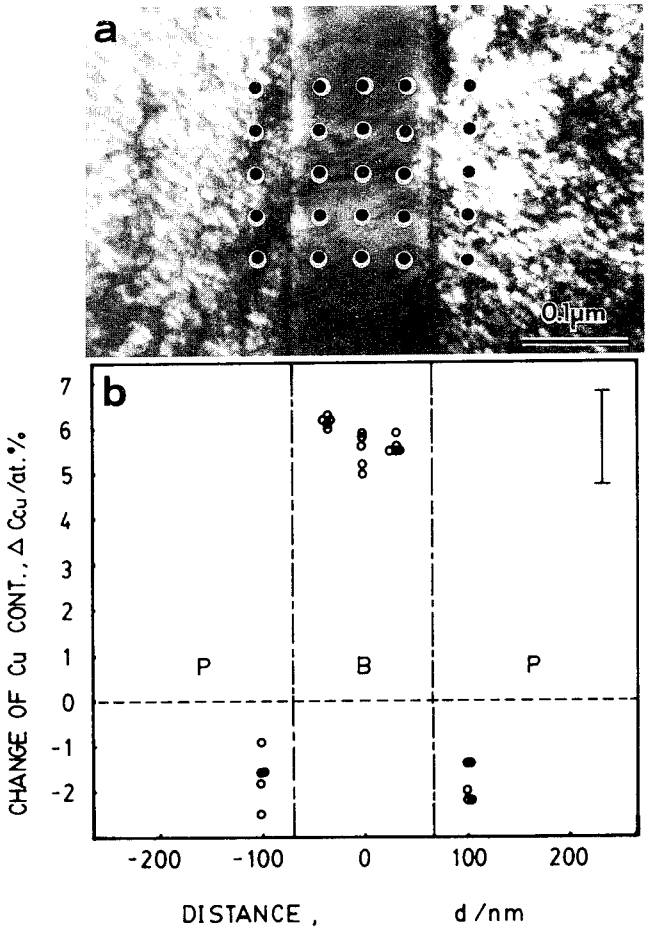


Fig. 11—(*a*) TEM image of a plate-shaped product about 100-nm thick formed in the 4 pct Au alloy heat-treated at 473 K for 5 h. (*b*) Results of EDX analyses on the interior of the plate and the adjacent matrix.

Whether or not there is a difference in solute concentration between the central regions and both sides close to the matrix/product interfaces inside the plate-shaped products was examined for products with thicknesses from 100 to 200 nm. Two examples of such examinations are shown in Figures 11 and 12, which are for a 4 pct Au alloy specimen aged at 473 K for 5 hours. The result of EDX analyses on the plate-shaped product about 100-nm thick in Figure 11(a) is shown in Figure 11(b). Here, the difference in solvent content, ΔC_{Cu}, is measured on the basis of the average obtained by irradiating the matrix regions with a defocused electron beam approximately 500 nm in diameter. The base line is thus drawn at $\Delta C_{Cu} = 0$ with a dashed line in the figure. It appears that ΔC_{Cu} is substantially the same between the central region and both sides. It is to be noted, however, that ΔC_{Cu} in the matrix regions adjacent to the interfaces is somewhat lower than the average of the matrix. Although the difference is small, it is believed to be real, because such a tendency was reproduced

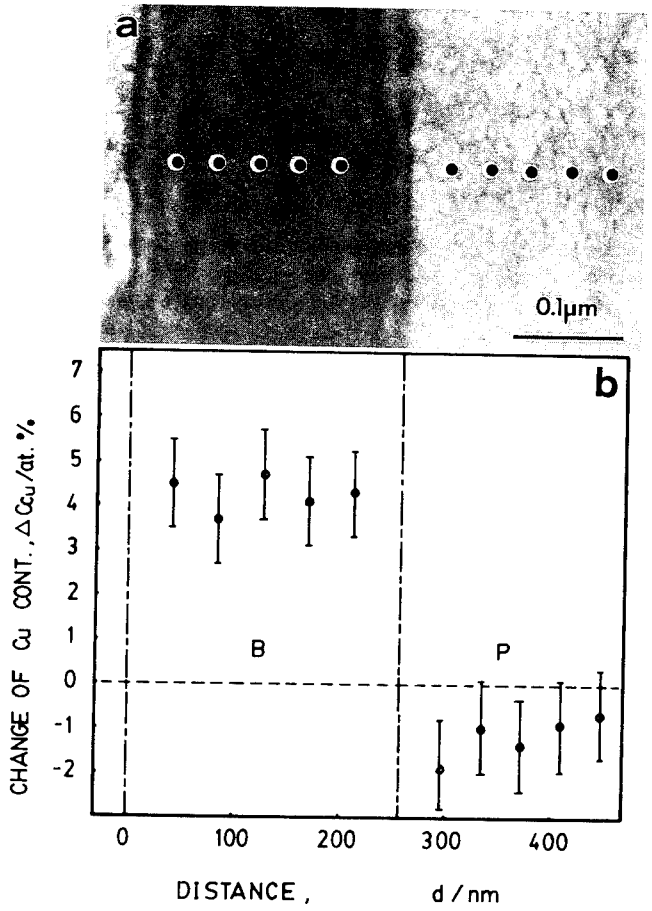


Fig. 12—(*a*) TEM image of a plate-shaped product about 200-nm thick formed in the 4 pct Au alloy heat-treated at 473 K for 5 h. (*b*) Results of EDX analyses on the interior of the plate and the adjacent matrix.

along a number of plate-shaped products. Another example of the EDX analyses is shown in Figure 12, which is for a plate-shaped product about 200-nm thick, as seen in Figure 12(a). Figure 12(b) shows the result of EDX analyses on the product. There are no statistically significant composition differences between the central region and both sides of the plate. However, the tendency for solute enrichment in the matrix regions near the interfaces is again seen.

Figures 13(a), (b), and (c) show the results of EDX analyses on plate-shaped products in the 4, 9, and 15 pct Au alloys aged at 473 K for 5 hours, 4 hours, and 15 minutes, respectively. The analyses were made on isolated products where the diffusion fields around individual plates did not overlap. The average differences measured for the plate-shaped products about 100-nm thick in the 4, 9, and 15 pct Au alloys were 5.8, 4.4, and 1.5 at. pct, respectively. It thus turned out that there is a tendency for ΔC_{Cu} to decrease with increasing Au content.

Although the values of ΔC_{Cu} for the 15 pct Au alloy was small and comparable to the error involved in the EDX spectroscopy, a similar result was also obtained for a thin product 25-nm thick, as shown in Figure 13(d), which was observed in the 15 pct Au alloy aged at 373 K for 84 hours and appeared to be at an early stage of growth. Each measured value of ΔC_{Cu} is seen to lie around 1.5 at. pct.

IV. DISCUSSION

A. *Composition of Isothermal Plate-Shaped Products*

In Figure 10, the thickness of isothermal plate-shaped products is regarded as a measure representing their growth stage. This may be a reasonable assumption unless the individual plates are arrested during growth by impinging upon one another or grain boundaries. As described in the previous section, isolated products were carefully selected for the EDX spectroscopy. Hence, the ΔC_{Cu} *vs* the plate-thickness line may be extrapolated to zero thickness. The figure thus indicates that atom diffusion is involved in the isothermal formation of plate-shaped products from the nucleation stage, and moreover, that the composition of the products is almost the same as that of the thermal equilibrium α phase from the very beginning of formation. If this is the case, the role of diffusion is essential for the isothermal formation of plate-shaped product.

Strictly speaking, however, a question arises if the plate-shaped products examined by the EDX spectroscopy have not been affected at all by aging after their formation even though their thicknesses were on the order of 10 nm. Such a possibility cannot be denied completely at present, but it is unlikely. One way to examine this possibility experimentally may be to perform *in situ* EDX spectroscopy on growing plate-shaped products at a certain temperature. Although such an attempt was not tried in the present study, a plate-shaped product was examined by EDX spectroscopy immediately after it was confirmed to form in a thin foil under observation by TEM and thus was considered not to be held for prolonged periods after its formation. As a result, it was found that even such a product possesses a composition definitely different from that of the surrounding matrix. Therefore, the observed composition differences between the plate-shaped product and matrix are not considered to be entirely "postformation" effect. Furthermore, according to a thermodynamic consideration of the isothermal formation of plate-shaped products in Cu-Zn alloys by Hsu and Zhou,[26] the formation due to the crystallographic-shear mechanism is impossible at the intermediate temperature regions examined. These results seem to strongly suggest that the formation of plate-shaped products and atom diffusion take place simultaneously.

Wu *et al.*[18] have extensively examined the isothermal formation of plate-shaped products in a Cu-Zn-Al alloy by means of TEM. Observing that the products have a composite substructure with respect to the APD structure, as mentioned in Section I, they concluded that lengthening of the plate-shaped product takes place due to the crystallographic-shear mechanism, whereas the thickening occurs by atom diffusion.

Additionally, in the 15 pct Au alloy aged at 373 K for 108 hours, the $L2_1$-type order in the matrix was observed to develop about 30-nm nnn APDs on the average, as shown in Figure 14. Then, the thickness of the plate-shaped products examined by the EDX spectroscopy, as

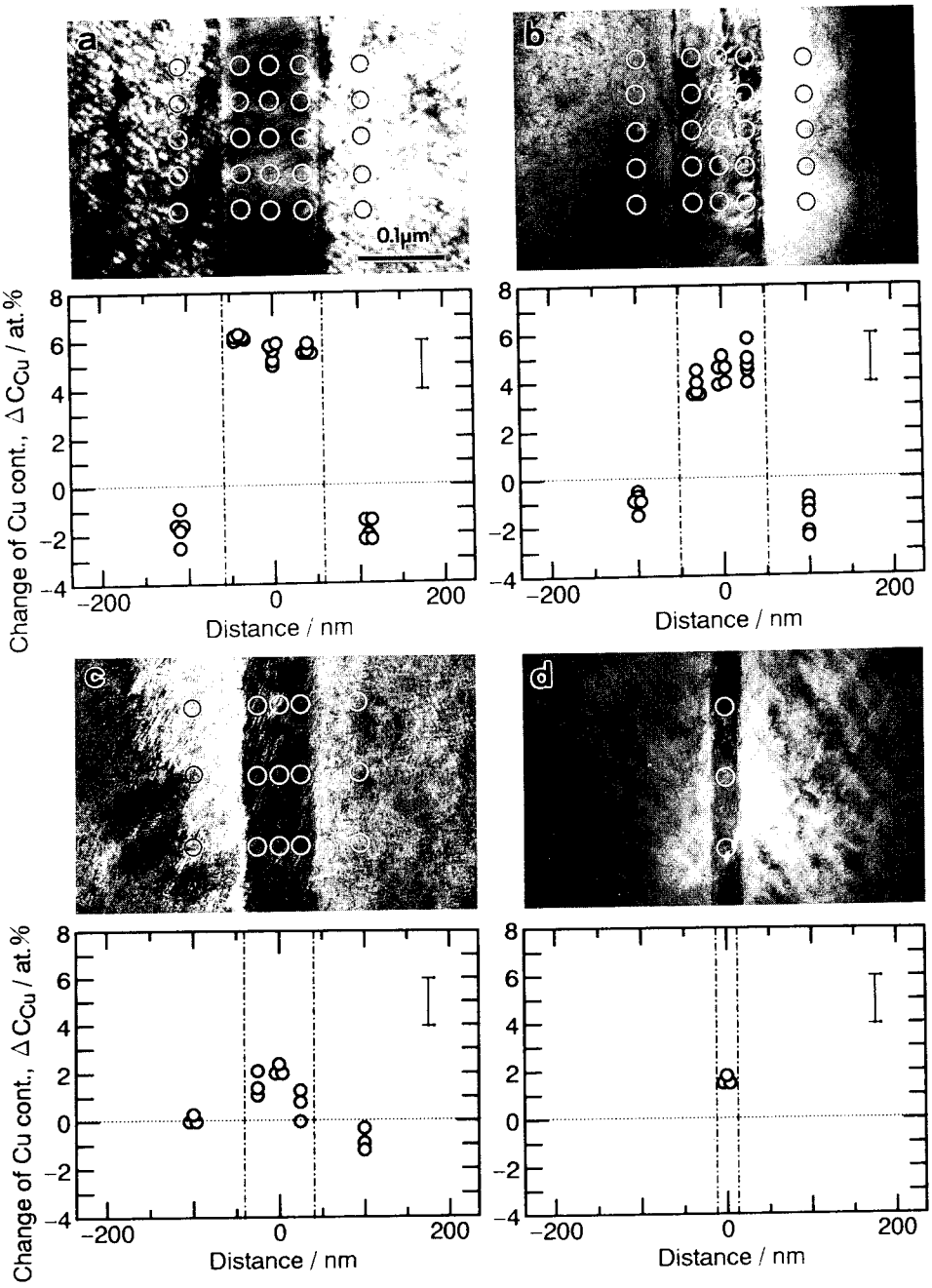


Fig. 13—TEM images of plate-shaped products about 100-nm thick and the EDX analyses on them formed in the (*a*) 4 pct, (*b*) 9 pct, and (*c*) 15 pct Au alloys, heat-treated at 473 K for 5 h, 4 h, and 15 min, respectively. (*d*) is for a very thin plate-shaped product about 25-nm thick in the 15 pct Au alloy heat-treated at 373 K for 84 h.

shown in Figure 13(d), is comparable to the size of the nnn-type APDs. Nevertheless, the EDX spectroscopy has revealed that even at such a very early stage of formation, a certain composition difference exists between the matrix and the plate-shaped product. A similar result was also reported by Hamada *et al.*[13] on a Cu-Zn-Al alloy. These observations indicate that the inheritance of the APD structure from the matrix to the plate-shaped product does not necessarily mean the crystallographic-shear mechanism operates for the isothermal formation of plate-shaped products.

B. *Significance of Dependence of ΔC_{Cu} upon Alloy Composition in the Cu-Zn-Au Alloys*

In Table I, the data obtained for the $Cu_{60-x}Zn_{40}Au_x$ alloys are summarized. Here, T_f means the formation temperature of plate-shaped products, at which aging was performed. It is interesting to note that when the temperature difference, $\Delta T = (T_f - M_s)$, becomes smaller, the composition difference, ΔC_{Cu}, does also. On the other hand, Figure 3 indicates that nucleation of the plate-shaped products becomes much easier as the Au content increases. In other words, it does so as the ΔT

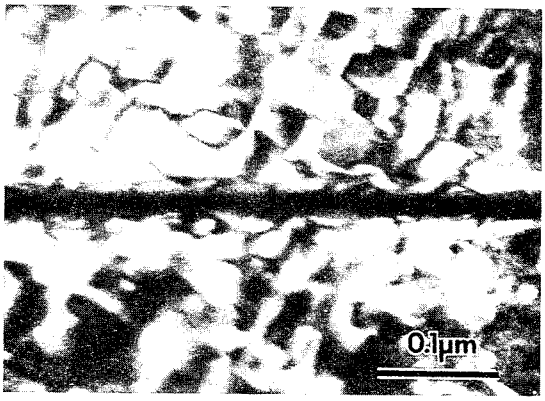


Fig. 14—Dark-field TEM image of a plate-shaped product formed in the 15 pct Au alloy heat-treated at 373 K for 108 h taken with a 111-type superlattice reflection of the $L2_1$-type matrix.

Table I. Dependence of M_s Temperature, Temperature Difference, $\Delta T = (T_f - M_s)$, and Composition Difference, ΔC_{Cu}, upon Alloy Composition in the $Cu_{60-x}Zn_{40}Au_x$ Alloys

x (At. Pct)	4	9	15
M_s (K)	<80	123	223
$T_f - M_s$ (K)	>393	350	250
ΔC_{Cu} (at. pct)	5.8	4.4	1.5

becomes smaller, because the M_s temperature increases with increasing Au content. This is reasonably understood by the fact that ΔC_{Cu} decreases with decreasing ΔT. Then, if the Au content could further be increased so that ΔT becomes less than zero, ΔC_{Cu} would be expected to become zero, and then the transformation could be diffusionless, *i.e.*, martensitic. Therefore, as long as ΔT is positive, the transformation cannot be purely martensitic, because a change in composition is inevitably involved.

C. *Isothermal Formation of Plate-Shaped Products in the Ag-Cd Alloy*

From the previous argument, if it is supposed that the plate-shaped product is a martensitic one formed in the matrix depleted in solute by the composition difference actually observed, its crystal structure may be different from that of the martensites formed at subzero temperatures. As is well known for Cu-Al alloys, the crystal structure of the martensite depends on alloy composition; Cu-Al alloys with a higher Al content (26 to 28 at. pct) exhibit a 2H-type martensite, while those with a lower Al content (22 to 26 at. pct) have an 18R type.[27] The fact that the crystal structures of the isothermal plate-shaped product and the martensite formed at subzero temperatures are entirely different from one another in the Ag-Cd alloy may correspond to such a composition dependence of crystal structure of the martensite. Although the martensite in the Ag-45 at. pct Cd alloy is of a 2H structure, another martensite with a 9R structure was verified[28] to be stress-induced in the same alloy. Therefore, it may be plausible that 2H- and 9R-type martensites are produced in the Ag-Cd alloys with higher and lower Cd contents, respectively. If so, there may be a possibility that the plate-shaped product with a 9R structure in the aged Ag-45 at. pct Cd alloy is a martensite in a Ag-Cd alloy with a composition less than 45 at. pct Cd by the observed composition differences. It thus appears that the structural difference between plate-shaped product and martensite in the Ag-Cd alloy exhibits a strong correlation between the isothermal and martensitic transformations, as in the $Cu_{60-x}Zn_{40}Au_x$ alloys.

D. *Nucleation of Isothermal Plate-Shaped Products*

Our experimental results have indicated that the plate-shaped product is just like a martensitic one formed in a matrix with a solute concentration less than that of the original alloy. Therefore, the plate-shaped product is not the martensite of a diffusionless reaction, because its composition is entirely different from that of the original matrix. It is not likely that diffusion takes place during aging after the plate-shaped product is formed due to a crystallographic-shear mechanism, because the driving force for the martensitic transformation at temperatures where the plate-shaped product is actually formed is negative.[26] There may then be a possibility that diffusion alone occurs first in the matrix, followed by martensitic transformation to the plate-shaped product.[12] But this is not plausible either, because if it were true, the solute concentration in the matrix regions close to the interfaces should not be higher than the average of the matrix for not fully grown plate-shaped products, this being in contrast to our experimental data that the matrix regions in the vicinity of the interfaces are always somewhat enriched with solute atoms for very thin and even fairly thick products. Therefore, it is reasonable to assume that for nucleation of the plate-shaped products the crystallographic shear and atom diffusion occur simultaneously, the latter of which takes place across largely coherent interfaces. The atomistic mechanism for the diffusion of atoms across the coherent interfaces, which are structurally not much different from those of martensites, is unclear at present, but our experimental results suggest that diffusion to achieve the observed composition difference should occur across the coherent interfaces. In fact, a transformation dislocation motion coupled with solute redistribution has been proposed for the formation of isothermal plate-shaped products by Aaronson and his co-workers.[29,30]

The simultaneous occurrence of crystallographic shear and atom diffusion should be thermally activated for the isothermal transformation of plate-shaped products to nucleate. The transformation kinetics would thus be governed by the thermal activation process not only for atom diffusion but also for the nucleation of the martensitic transformation. In fact, it was recently shown[31,32] that the nucleation of the martensitic transformation is thermally activated, even at temperatures above M_s in some ferrous alloys. Therefore, it is considered that in a temperature region, $M_s < T < T_0$, a purely martensitic transformation can be thermally activated, but in a temperature region, $T_0 < T$, the formation of plate-shaped products accompanied by atom diffusion is thermally activated. In this sense, the isothermal formation

of plate-shaped products is a more general case of a shear-type phase transformation which allows atom diffusion.

ACKNOWLEDGMENT

The authors are indebted to Dr. Y. Nakata, Messrs. T. Uyeda, J.Q. Cai, F.X. Yin, and Professor N.J. Gu for fruitful discussion and experiment. The present study was partly supported by grants from the Research Projects on "Creation of New Materials through Intelligent Design" and on "Creation of Functional Materials by Nano Synthetic Processing" of ISIR, Osaka University, and by the Grant-in-Aid for Fundamental Scientific Reasearch (Sōgo: 1989–1990 and 1992–1993; Ippan C: 1989; Ippan B: 1990–1991) of Ministry of Education, Science, and Culture, Japan. The support is greatly appreciated.

REFERENCES

1. Z. Nishiyama: *Martensitic Transformations (Application)*, Maruzen, Tokyo, 1974, pp. 71-85 (in Japanese).
2. H.I. Aaronson, W.T. Reynolds, Jr., G.J. Shiflet, and G. Spanos: *Metall. Trans. A*, 1990, vol. 21A, pp. 1343-80.
3. H.I. Aaronson, T. Furuhara, J.M. Rigsbee, W.T. Reynolds, Jr., and M.J. Howe: *Metall. Trans. A*, 1990, vol. 21A, pp. 2369-2409.
4. I. Cornelis and C.M. Wayman: *Scripta Metall.*, 1973, vol. 7, pp. 579-90.
5. G.W. Lorimer, G. Cliff, H.I. Aaronson, and K.R. Kinsman: *Scripta Metall.*, 1975, vol. 9, pp. 271-79.
6. P. Doig and P.E. Flewitt: *Met. Sci.*, 1983, vol. 17, pp. 601-08.
7. M.H. Wu and C.M. Wayman: *Proc. Int. Conf. on Martensitic Transformations*, August 26–30, Nara, Japan, Japan Institute of Metals, Sendai, 1986, pp. 619-24.
8. M.H. Wu, B.C. Muddle, and C.M. Wayman: *Acta Metall.*, 1988, vol. 36, pp. 2095-2106.
9. Y. Nakata, T. Tadaki, and K. Shimizu: *Mater. Trans. Jpn. Inst. Met.*, 1989, vol. 30, pp. 107-16.
10. T. Tadaki, T. Uyeda, and K. Shimizu: *Mater. Trans. Jpn. Inst. Met.*, 1989, vol. 30, pp. 117-26.
11. G. Cliff, F. Hasan, G.W. Lorimer, and M. Kikuchi: *Metall. Trans. A*, 1990, vol. 21A, pp. 831-35.
12. K. Takezawa and S. Sato: *Metall. Trans. A*, 1990, vol. 21A, pp. 1541-45.
13. Y. Hamada, M.H. Wu, and C.M. Wayman: *Mater. Trans. Jpn. Inst. Met.*, 1991, vol. 32, pp. 747-56.
14. T. Tadaki, J.Q. Cai, and K. Shimizu: *Mater. Trans. Jpn. Inst. Met.*, 1991, vol. 32, pp. 757-65.
15. T. Tadaki, J.Q. Cai, K. Shimizu, F.X. Yin, and N.J. Gu: *Proc. Int. Conf. on Martensitic Transformations*, July 20–24, Monterey, CA, 1992, in press.
16. A. Kore'eda, T. Ishibashi, K. Shimizu, M. Tomita, C. Kimura, and H. Okano: *Mater. Characterizations*, 1990, vol. 25, pp. 375-95.
17. J.J. Hren, J.I. Goldstein, and D.C. Joy: *Introduction to Analytical Electron Microscopy*, Plenum Press, New York, NY, 1979, pp. 83-120.
18. M.H. Wu, J. Perkins, and C.M. Wayman: *Acta Metall.*, 1989, vol. 37, pp. 1821-37.
19. Z. Horita, T. Sano, and M. Nemoto: *Bull. Jpn. Inst. Met.*, 1989, vol. 9, pp. 742-52 (in Japanese).
20. T. Tadaki, M. Takamori, and K. Shimizu: *Proc. Int. Conf. on Martensitic Transformations*, August 26–30, Nara, Japan, Japan Institute of Metals, Sendai, 1986, pp. 806-11.
21. T. Tadaki, S. Hamada, and K. Shimizu: *Trans. Jpn. Inst. Met.*, 1977, vol. 18, pp. 135-43.
22. T. Tadaki, N. Kondo, T. Kakeshita, and K. Shimizu: Osaka University, Osaka, Japan, unpublished research, 1993.
23. T. Tadaki, M. Takamori, and K. Shimizu: *Trans. Jpn. Inst. Met.*, 1987, vol. 28, pp. 120-28.
24. K. Takezawa, H. Watanabe, and S. Sato: *Proc. Int. Symp. on Shape Memory Alloys*, SMA-86, September 6–9, Guilin, China, Academic Publisher, Beijing, China, 1986, pp. 344-49.
25. E. Hornbogen and H. Warlimont: *Acta Metall.*, 1967, vol. 15, pp. 943-51.
26. T.Y. Hsu and X.W. Zhou: *Acta Metall.*, 1989, vol. 37, pp. 3095-98.
27. Z. Nishiyama: *Martensitic Transformation*, Academic Press, New York, NY, 1978, pp. 74-106.
28. T. Tadaki, T. Nagaura, and K. Shimizu: *Scripta Metall.*, 1978, vol. 12, pp. 453-56.
29. H.I. Aaronson, J.K. Lee, and K.C. Russell: *Precipitation Processes in Solids*, TMS-AIME, Warrendale, PA, 1977, pp. 31-85.
30. J.M. Howe and N. Prabhu: *Acta Metall. Mater.*, 1990, vol. 38, pp. 881-87.
31. M. Lin, G.B. Olson, and M. Cohen: *Metall. Trans. A*, 1992, vol. 23A, pp. 2987-98.
32. T. Kakeshita, K. Kuroiwa, K. Shimizu, T. Ikeda, A. Yamagishi, and M. Date: *Mater. Trans. JIM*, 1993, vol. 34, pp. 423-28.

Transformation Characteristics of α_1 Plates in Cu-Zn-Al Alloys

M.H. WU, Y. HAMADA, and C.M. WAYMAN

The formation of α_1 plates during isothermal aging of a Cu-26.7 wt pct Zn-4.0 wt pct Al alloy at 150 °C to 350 °C follows thermally activated incubation kinetics. Early stage α_1 plates possess an ordered 18R or 9R long-period stacking order (LPSO) crystal structure, with antiphase domain boundaries running continuously across the interface. The plates also exhibit invariant plane strain (IPS) crystallography consistent with calculations of the phenomenological theory of martensite crystallography (PTMC). The ordered LPSO structure and IPS crystallography are gradually annealed out only after extended aging as the structure changes to the equilibrium disordered face-centered cubic (fcc) one. High-resolution transmission electron microscopy (TEM) analyses reveal that early stage α_1 plates have straight coherent interfaces. Prolonged aging induces misfit dislocations at the interface and causes the interface to protrude into the parent phase. Although microanalytical analyses indicate that a composition difference exists between the α_1 plates and the parent matrix, solute depletion was observed at neighboring defects. These observations support the proposed transformation mechanism that the α_1 plates nucleate at solute depleted defects through a shear mechanism and that subsequent plate growth is then controlled by a diffusional process.

I. INTRODUCTION

A. $\beta_2 \rightarrow \alpha_1$ *Transformations in Cu-Zn and Ag-Cd Alloys*

THE plate-shaped α_1 phase that forms during isothermal aging of B2 (CsCl) ordered β_2 phase* Cu-Zn and Ag-Cd alloys represents a transitional, metastable transformation product that eventually changes to the equilibrium disordered face-centered cubic (fcc) α phase after prolonged annealing. Early stage α_1 plates exhibit crystallography consistent with the phenomenological theory of martensite crystallography (PTMC) and other characteristics of a diffusional transformation. The common features of the $\beta_2 \rightarrow \alpha_1$ transformation are summarized in the following paragraphs.

(1) An incubation time, following C-curve kinetics, is required for the transformation,[2,3] typical of a thermally activated process. The incubation C-curve shifts toward shorter times when the transformation takes place under external stress.[4]

(2) The growth of the α_1 plate proceeds first by fast lengthening beyond that permitted by volume diffusion. Plate thickening occurs only after the lengthening is more or less complete[5,6,7] and follows the kinetics consistent with Frank-Zener model of volume diffusion-controlled growth of a plate-shaped precipitate.[6]

(3) Early stage α_1 plates possess a disordered 9R long period stacking order (LPSO) structure with the presence of random faults parallel to the $(009)_{9R}$ periodic faults. The structure conforms to that of low-temperature martensite where random faults are the fine structure generated by lattice invariant shear.[8] Other crystallographic features and the surface relief effect also resemble those of martensite and are in agreement with the calculations of PTMC.[9,10,11]

(4) Although early microanalytical studies[3,12] on Cu-Zn alloys observed no composition difference between the α_1 plate and the β_2 matrix at early stages of transformation, recent analyses on Cu-Zn,[13,14,15] Cu-Au-Zn,[14,16] and Ag-Cd[17,18] with improved resolution have repeatedly confirmed the presence of a composition difference between α_1 plates and parent β_2 matrix. The α_1 plate tip, however, appears to inherit the parent composition.[14]

B. *Transformation of α_1 Plate in Cu-Zn-Al Alloys*

The formation of α_1 plates in Cu-Zn-Al alloys shares close similarity with the transformation in Cu-Zn and Ag-Cd alloys. Here, the formation of an α_1 plate gives rise to a reverse-shape memory effect where external stress assists the incubation and limits the variant selection of the plate, thus creating a macroscopic shape change.[19,20] The incubation kinetics also follow a C-curve.[21] The LPSO crystal structure and crystallographic characteristics are again similar to those of low-temperature martensite and are in agreement with the PTMC calculations.[21,22] Earlier study[20] reported disordered 9R Cu-Zn-Al α_1 plates. More detailed transmission electron microscopy (TEM) analyses[21,22] suggested that early stage α_1 plates possess an ordered 18R structure when they transform in an $L2_1$, β_3 parent phase or

*Present notations for various types of β phase superlattices and martensites follow those proposed by Delaey *et al.*[1]

M.H. WU, Chief Metallurgist, is with Memry Technologies, Inc., Brookfield, CT 06804. Y. HAMADA, Formerly Visiting Scientist, with the Department of Materials Science and Engineering, University of Illinois, is Engineer, Sumitomo Metal Mining Co., Tokyo, Japan. C.M. WAYMAN, Professor, is with the Department of Materials Science and Engineering, University of Illinois, Urbana, IL 61801.

This article is based on a presentation made at the Pacific Rim Conference on the "Roles of Shear and Diffusion in the Formation of Plate-Shaped Transformation Products," held December 18–22, 1992, in Kona, Hawaii, under the auspices of ASM INTERNATIONAL's Phase Transformations Committee.

an ordered 9R structure when the transformation takes place in a B2 ordered β_2 matrix at temperatures above the second nearest neighbor ordering transition temperature. Both the nearest neighbor (NN) and the next nearest neighbor (NNN) antiphase domain (APD) structures of the β_3 parent phase are inherited by the α_1 plate during the early stage of transformation. The ordered α_1 crystal structure and the inheritance of APD structures have been further confirmed by Nakata *et al.*[23] and Hamada *et al.*[24] The α_1 crystal structure becomes disordered at high temperatures, *e.g.*, 350 °C or after prolonged aging.

Several microanalytical analyses[23,24,25] have been carried out to study the α_1 composition in Cu-Zn-Al alloys. Again, the chemistry difference between the two phases is distinct even at the earliest accessible stage of transformation. Takezawa and Sato,[25] in particular, have noticed an asymmetric composition profile in the parent matrix adjacent to the α_1 plate.

C. *Proposed Transformation Mechanisms for α_1 Plate*

The implication of experimental results on the transformation mechanism remains controversial. Based on the observed composition profile of an α_1 plate, Doig and Flewitt[14] proposed that α_1 plates lengthen by a shear mechanism and that subsequent plate thickening is controlled by diffusion. Lorimer *et al.*[13] suggested that a diffusional ledge mechanism operates during α_1 plate thickening. Recent study by Chattopadhyay and Aaronson[26] reported an interfacial structure for α_1 plates, in support of ledge thickening. They also claimed the observation of a ledge structure at α_1 plate edges, although they presented with no crystallographic evidence, and inferred that α_1 plates lengthen by a ledge mechanism as well. Takezawa and Sato,[25] on the other hand, argued that α_1 plates nucleate by a shear mechanism at pre-existing sites of solute depletion in the parent matrix. They suggested that solute depletion at these sites is created by stress-induced diffusion around defects. The presence of solute depletion at defects in the parent matrix was confirmed by Hamada *et al.*[24] However, the validity of this nucleation concept was questioned by Russell[27] as to whether the geometrical significance of such chemistry precursors can provide sufficient driving force for the nucleation to occur above the nominal T_0 temperature.[28]

D. *Background*

Based on a presentation at "The Pacific Rim Conference on the Role of Shear and Diffusion in the Formation of Plate-Shaped Transformation Products," this article reviews our results on the crystal structure, crystallography, and microchemistry of α_1 plates in a Cu-26.7 wt pct Zn-4.0 wt pct Al alloy. The implications of the present results and other viewpoints regarding the transformation mechanism will be discussed.

1. *Long-range order of the parent β phase*

High-temperature β Cu-Zn-Al alloys possess an A2, disordered body-centered cubic (bcc) structure that goes through two ordering transitions upon cooling. The first NN ordering transition results in a B2, CsCl superlattice, designated as β_2. Further cooling induces NNN ordering, and the ordered structure has been identified to be an $L2_1$, Cu_2MnAl superlattice, designated as β_3.[29] For the present alloy, the A2 → B2 transition temperature has been calculated using a modified Bragg-William-Gorski approximation to be 500 °C.[30] The B2 → $L2_1$ ordering transition occurs at approximately 250 °C.[29]

2. *Crystallographic equivalency between different ordered structures*

Because long-range order changes the translation symmetry, the relationship between equivalent lattice vectors and plane normals for B2 and $L2_1$ parent structures and for 9R and 18R α_1 structures are described in Table I.

II. EXPERIMENTAL

Specimens of Cu-26.7 wt pct Zn-4.0 wt pct Al alloy were solution treated at 900 °C for 3 minutes and then quenched into a 10 pct brine bath at room temperature. They were subsequently aged isothermally in a nitrite/nitrate bath maintained at temperatures of 150 °C to 350 °C to induce α_1 plates.

Foil specimens for transmission electron microscopy (TEM) and analytical electron microscopy (AEM) were initially profiled using a twin-jet method and a 50 pct H_3PO_4 water solution. Final perforation was carried out in a static microwindow electropolishing bath of H_3PO_4 saturated with CrO_3. Diffraction contrast and phase contrast TEM analyses were performed in a JEOL JEM-100 CX and a JEOL JEM-2000 EX transmission electron microscope, respectively. Analytical electron microscopy analyses were carried out using a VG HB5 scanning transmission electron microscope (STEM) equipped with a KEVEX* energy dispersive X-ray (EDX) detector, operating at 100 kV with a nominal probe size of 1 nm. The quantification of the EDX spectrum and the absorption correction for the Al Kα line are described in References 17 and 24, respectively.

*KEVEX is a trademark of the Kevex Corporation, Foster City, CA.

The PTMC crystallographic calculations follow the Suzuki method formulated for the bcc → 9R transformation.[31] The input data of lattice constants for B2 and 9R structures for the PTMC calculation were determined by the X-ray powder diffraction method. Habit planes were measured using a TEM trace analysis technique. By first measuring the line direction of interfacial dislocations and that of the intersection between habit plane and foil surface, the habit plane normal was determined by taking the cross product of these two directions.

III. EXPERIMENTAL RESULTS

A. *Incubation C-Curve*

The incubation C-curve in the temperature range of 150 °C to 350 °C, determined using electrical resistivity measurements and optical metallography, is presented in Figure 1. The incubation period ranges from 10 seconds at 350 °C to 48 hours at 150 °C.

Table I. Equivalent Lattice Vectors and Plane Normals between B2 and $L2_1$ Parent-Ordered Structures and between 9R and 18R Ordered α_1 Structures

	Parent Phase		α_1 Plate	
	B2	$L2_1$	9R	18R
Lattice constants	a	2a	a	a
			b	2b
			c	2c
Lattice vectors	$[h, k, l]$	$1/2[h, k, l]$	$[h, k, l]$	$1/2[2h, k, l]$
Plane normals	(h, k, l)	$2(h, k, l)$	(h, k, l)	$(h, 2k, 2l)$

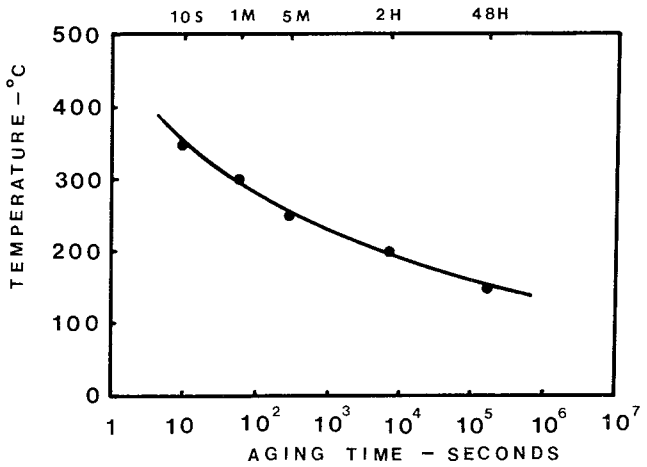


Fig. 1—Incubation curve for α_1 plates in a Cu-26.7 wt pct Zn-4.0 wt pct Al alloy in a temperature range of 150 °C to 350 °C.

B. *Morphology and Fine Structures of α_1 Plates*

Bright-field and dark-field electron micrographs of an α_1 plate after aging at 350 °C for 10 seconds are shown in Figure 2. The dark-field micrograph was imaged using the $\bar{1}1\bar{8}$ reflection of the α_1 plate, the diffraction condition of which is shown in Figure 2(d). The plate, 0.015 μm in thickness, exhibits a thin plate morphology with sharp plate edges and a small aspect ratio, c/r, around 0.01, where c is the semithickness and r is the plate radius. Striations inside the plate are visible in both micrographs. A $[\bar{1}10]_{9R}/[1\bar{1}1]_{B2}$ composite zone pattern (Figure 2(c)) taken from the plate and the adjacent matrix indicates that the α_1 plate possesses a 9R LPSO structure with the striations corresponding to random faults along the $(009)_{9R}$ basal plane.

Midribs are often present in early stage α_1 plates. Figure 3 shows (a) a bright-field and (b) a dark-field TEM micrograph of an α_1 plate after aging at 150 °C for 48 hours. Contrast of a planar trace is clearly present at the center of the plate.

With extended aging, α_1 plates thicken, and both periodic and random faults are gradually annealed out. The crystal structure eventually becomes equilibrium fcc with residual stacking faults. An example of this structural evolution during aging at 250 °C is shown in Figure 4. Note that the equilibrium γ phase precipitates after prolonged aging (Figure 4(e)). These equilibrium phases are consistent with the quasibinary phase diagram of Cu-Zn-Al system at 4 wt pct Al.[32] The annihilation

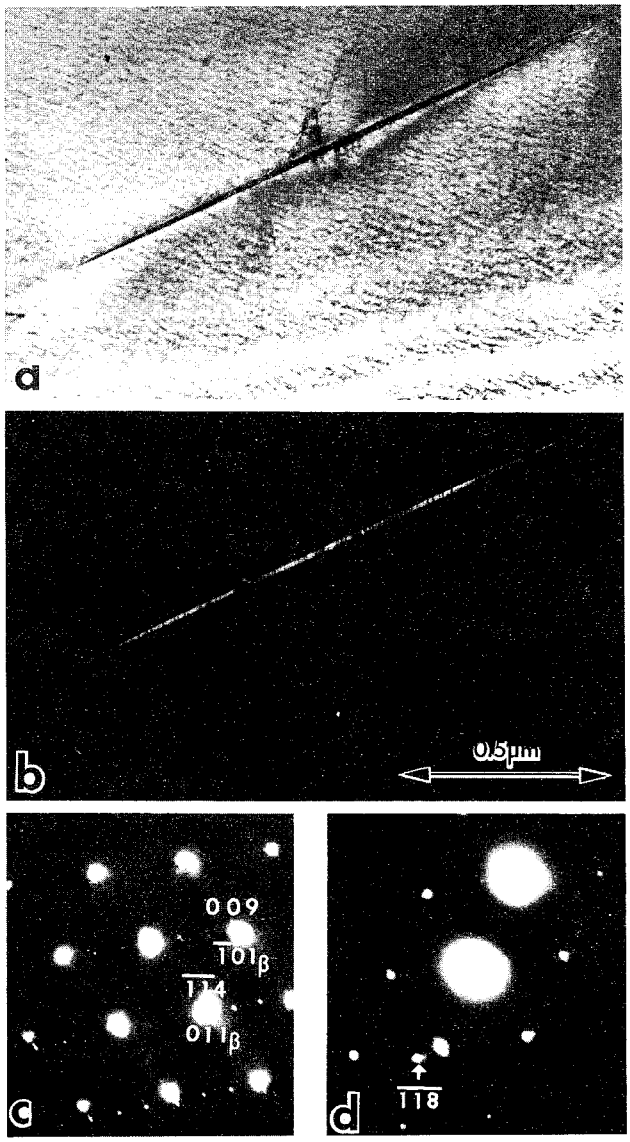


Fig. 2—(*a*) Bright-field micrograph and (*b*) dark-field micrograph imaged using the $\bar{1}1\bar{8}$ α_1 reflection together with the corresponding diffraction conditions (*c*) and (*d*) of an α_1 plate after aging at 350 °C for 10 s.

of the faulting structure is also demonstrated in a change in the intensity distribution of reflections along the 009 reciprocal direction. As shown in Figure 5, the $11\bar{4}$ and 115 9R reflections gradually shift toward the positions for 111 and 002 fcc reflections, respectively, and the $11\bar{1}$

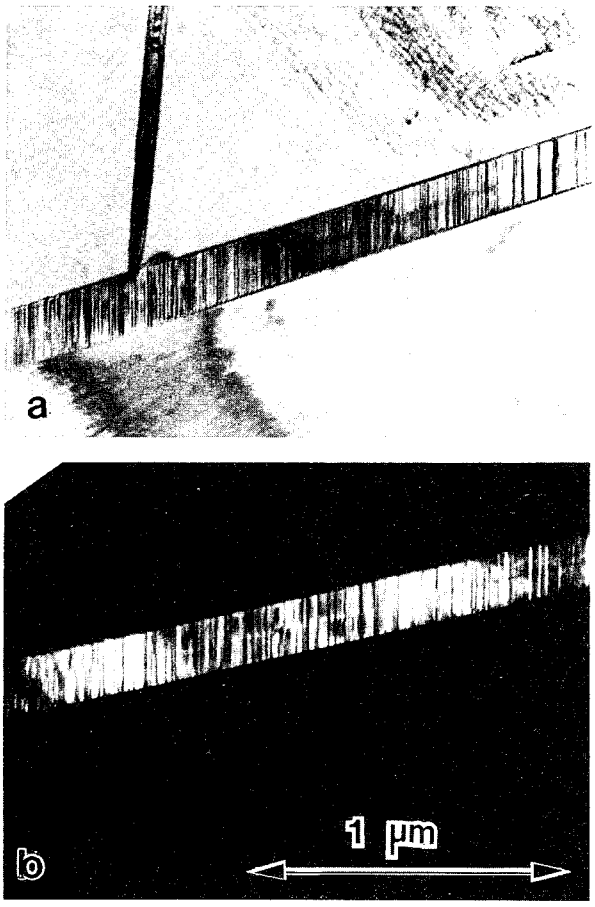


Fig. 3—(*a*) Bright-field and (*b*) dark-field micrographs of an α_1 plate after aging at 150 °C for 48 h showing the presence of a midrib contrast.

and 112 9R reflections, together with streaking along the 009 reciprocal axis, gradually disappear during aging.

C. *Crystal Structure and Long-Range Order of α_1 Plates*

Further details of the α_1 crystal structure and long-range order have been studied by systematic tilting of the plate along the faulting plane normal. Figure 6 includes a series of electron diffraction patterns taken from an α_1 plate and the adjacent parent matrix after aging at 150 °C for 96 hours. These patterns are in agreement with (a) $[\bar{2}10]_{18R}/[1\bar{1}1]_{\beta 3}$, (b) $[\bar{1}10]_{18R}/\sim[1\bar{2}1]_{\beta 3}$, (c) $[\bar{2}30]_{18R}/\sim[1\bar{3}1]_{\beta 3}$, and (d) $[010]_{18R}/\sim[0\bar{1}0]_{\beta 3}$ zone patterns, suggesting that the α_1 plate has an 18R crystal structure. In the $[\bar{1}10]_{18R}$ zone pattern (Figure 6(b)), two types of superlattice reflections have been identified according to calculation of the structural factor for 18R reflections.[33] The 33*l* and 11*l* reflections are derived from the NNN order of the $L2_1$ ordered parent β_3 phase and will be referred to as NNNSR. The 22*l* reflections, together with the 30*l* reflection in the $[010]_{18R}$ zone pattern (Figure 6(d)), are derived from the NN order of the parent β_3 phase and will be referred to as NNSR. The angle between 0 0 18 and 300 g vectors, measured from the $[010]_{18R}$ pattern (Figure 6(d)) is 89 deg, suggesting the presence of a monoclinic distortion. Supportive of this, reflections such as $32\bar{6}$ and $3\ 2\ \bar{1}\bar{2}$, are present in the $[\bar{2}30]_{18R}$ zone pattern (Figure 6(c)).[33] The α_1 plates after aging at 150 °C for 96 hours thus possess an M18R structure, the same as that of low-temperature martensite.[33]

Among the four zone patterns in Figure 6, only the $[\bar{1}10]_{18R}$ zone pattern contains both NNSR and NNNSR. This zone axis was therefore selected for the study of temperature effect on the long-range order of α_1 plates. Early stage plates after aging at 150 °C to 350 °C were tilted to the $[\bar{1}10]_{18R}$ axis, or the equivalent $[\bar{1}20]_{9R}$ axis when NNNSR is extinct. The patterns recorded are shown in Figure 7. Figure 7(a) shows the same pattern as Figure 6(b) for comparison. The pattern of Figure 7(b) was taken from an α_1 plate after aging at 200 °C for 3 hours and again shows the presence of 22*l* NNSRs and 33*l* NNNSRs, suggesting an 18R crystal structure of the α_1 plates that form at 200 °C. A pattern taken from an α_1 plate after aging at 250 °C for 10 minutes (Figure 7(c)) conforms to a $[\bar{1}20]_{9R}$ pattern with only 21*l* NNSRs present, suggesting an ordered 9R structure of the plates that form at 250 °C. The pattern of Figure 7(d) was taken from a plate after aging at 350 °C for 10 seconds and reveals no detectable superlattice reflections. The α_1 plates that transform at 350 °C therefore possess a disordered 9R structure.

D. *APD Structures*

Figure 8(a) shows a bright-field electron micrograph of α_1 plates after aging at 150 °C for 48 hours. The area micrograph of Figure 8(b) is a superimposed dark-field electron micrograph of β_3 NN APD imaged using the $\bar{2}\bar{2}\bar{2}$ NNSR of the β_3 matrix, and α_1 NN APD imaged using the 228 18R α_1 NNSR; the diffraction conditions are shown in the diffraction patterns of Figures 8(c) and 8(d), respectively. It is evident that NN APD structures are present in both α_1 plate and β_3 matrix, and the NN APD boundaries are continuous across the interface.

The dark-field micrograph of NNN APD of the area is shown in Figure 9(a), which was imaged using the superimposed 111 NNNSR of the 18R α_1 plate and $\bar{1}\bar{1}\bar{1}$ NNNSR of the $L2_1$ β_3 matrix under the diffraction condition shown in Figure 9(b). Again, NNN APD contrast is present in both phases and the APD boundary extends continuously across the interface.

The continuity of both NN and NNN APD boundaries at the interface suggests that both APD structures are inherited by the α_1 plates upon the $\beta_3 \rightarrow \alpha_1$ transformation and persist during initial plate growth during aging at 150 °C.

The progressive evolution of APD structures in both α_1 plate and β_3 matrix during aging at 150 °C for 96 to 720 hours is shown in Figure 10 where Figures 10(a) through (c) (1) show the bright-field micrographs of α_1 plates studied and Figures 10(a) through (c) (2) and 10(a) through (c) (3) reveal the NN and the NNN APD structures, respectively. As seen in Figures 10(a) (2) and 10(a) (3), both NN and NNN APD boundaries maintain their continuity across the interface after 96 hours of aging at 150 °C. After 240 hours of aging, most NN

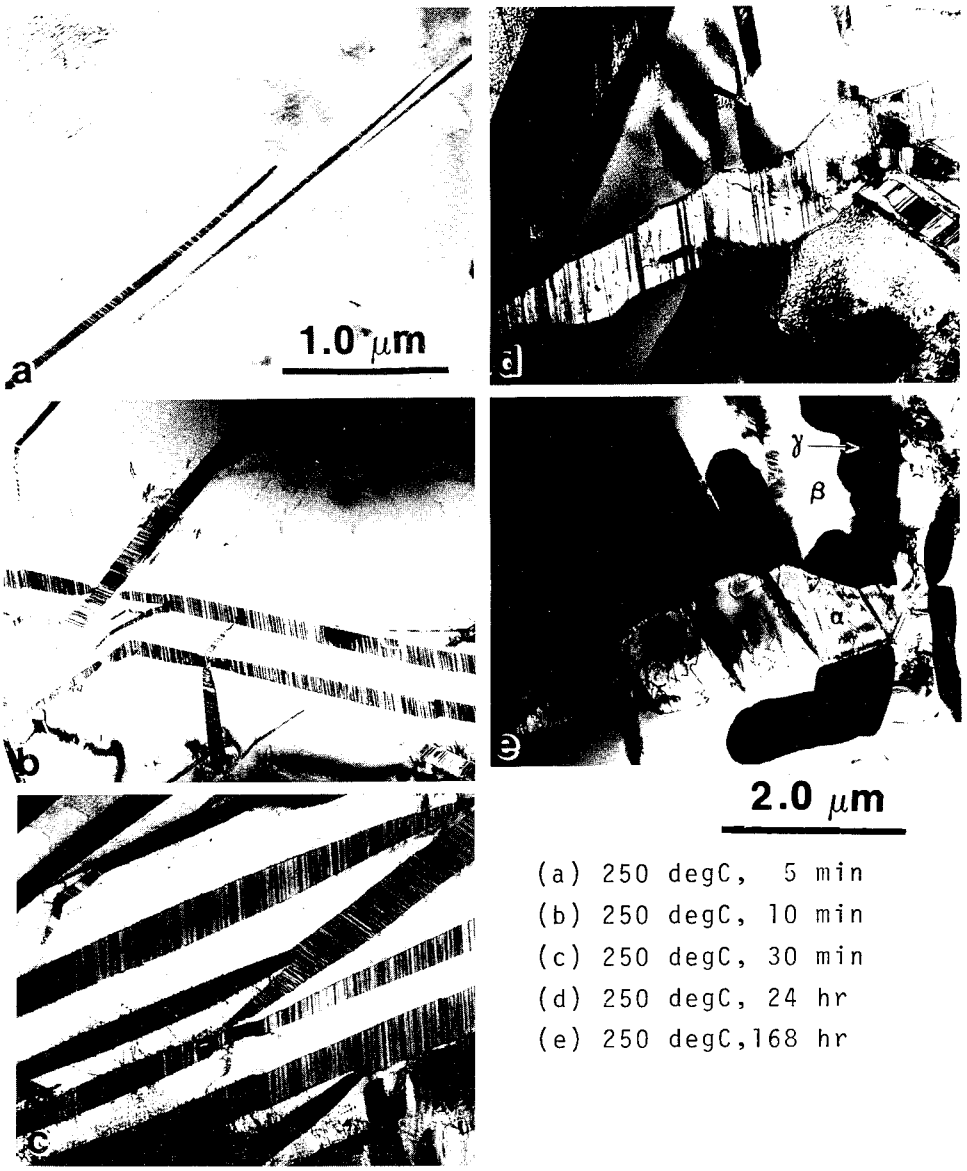


Fig. 4—Electron micrographs of α_1 plates in specimens aged at 250 °C for 5 min to 168 h.

APD boundaries remain continuous across the interface (Figure 10(b) (2)). However, some NN APD boundaries that terminate at the interface are also present.

In contrast to the well-preserved NN APD structure, the outer layer of an α_1 plate after aging at 150 °C for 240 hours is out of NNN reflection contrast (Figure 10(b) (3)), suggesting the absence of NNN order. NNN APD structure in the α_1 plate is present only in the central region, about 0.05 μm thick, which corresponds to an earlier stage α_1 structure. The inheritance of NNN order and its APD structure is thus limited to early stage plate growth. The NNN order is lost during later stage plate thickening.

Further aging, *e.g.*, 720 hours at 150 °C, anneals out most NN APD boundaries in the β_3 matrix as they are not observed in the β_3 matrix, Figure 10(c) (2). Residual NN APD boundaries are present only in the α_1 plates. Note that the entire α_1 plate exhibits bright reflecting contrast, indicating that the NN order in the α_1 plate is preserved after aging for 720 hours at 150 °C.

The NNN APD in α_1 plates after such prolonged aging is shown in Figure 10(c) (3), which exhibits the same general characteristics as shown in Figure 10(b) (3). NNN APDs are present only in the central layer of 0.05 μm thickness. The rest of the α_1 plate is not in NNNSR reflection contrast.

The evolution of APD structures in α_1 plate during aging at 200 °C is similar to that observed during aging at 150 °C, as seen in Figure 11 for specimens aged at 200 °C for 3 to 24 hours. However, the thickness of the NNN-ordered central layer is only 0.025 μm thick, much smaller than that after aging at 150 °C. The lifetime of NNN order in the α_1 plates is also much shorter owing to more rapid diffusion at 200 °C. The NNN order and APD are annealed out after aging for 24 hours; no NNNSR are observed in the $[\bar{1}20]_{9R}$ zone pattern (Figure 11(c) (3)).

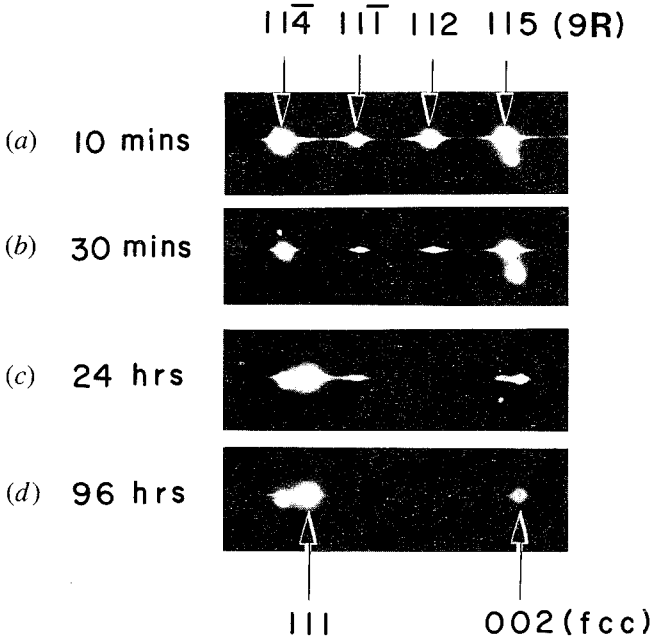


Fig. 5—Change in reflection intensity distribution along the $(009)_{9R}$ plane normal during aging at 250 °C.

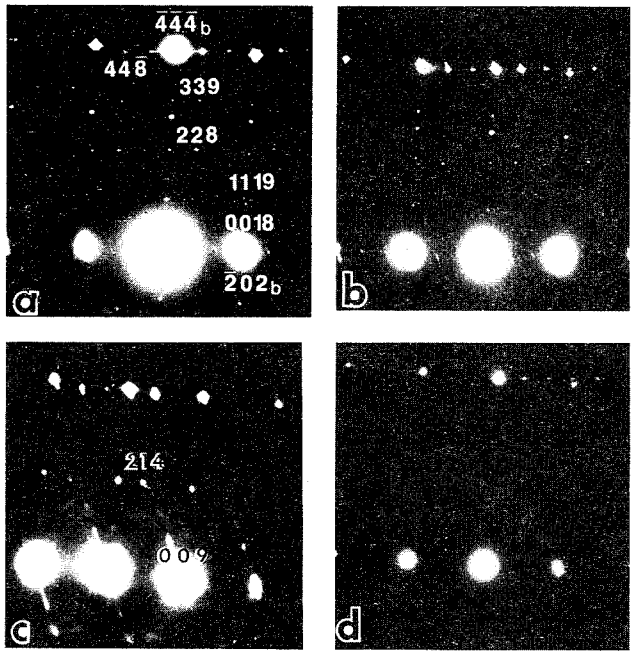


Fig. 7—$[\bar{1}10]_{18R}/[\bar{1}20]_{9R}$ zone patterns from α_1 plates in conjunction with $[1\bar{2}1]_{\beta 3}$ patterns of adjacent β_3 matrix in specimens after aging: (*a*) 150 °C, 96 h; (*b*) 200 °C, 3 h; (*c*) 250 °C, 10 min; and (*d*) 350 °C for 10 s.

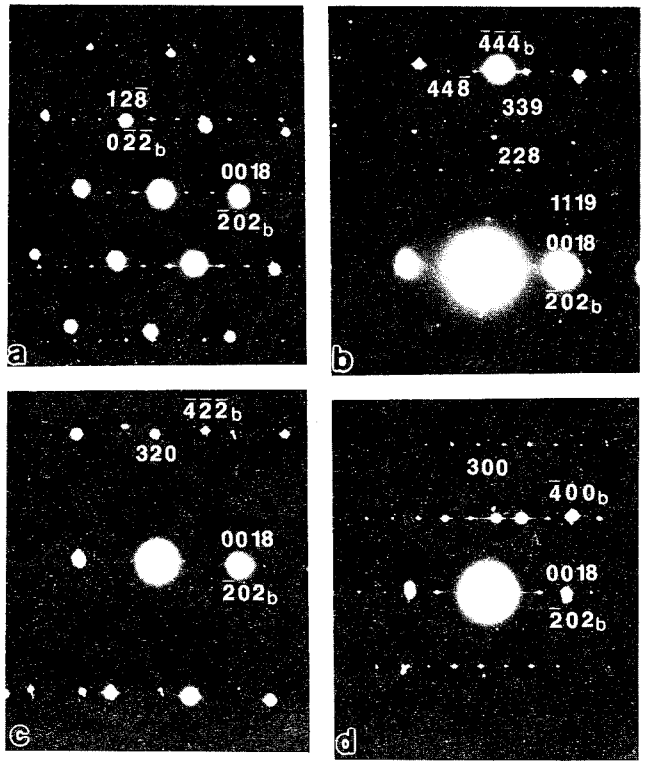


Fig. 6—Selected area diffraction patterns from an α_1 plate after aging at 150 °C for 96 h: (*a*) $[\bar{2}10]_{18R}//[1\bar{1}1]_{\beta 3}$, (*b*) $[\bar{1}10]_{18R}/\sim[1\bar{2}1]_{\beta 3}$, (*c*) $[\bar{2}30]_{18R}/\sim[1\bar{3}1]_{\beta 3}$, and (*d*) $[010]_{18R}/\sim[0\bar{1}0]_{\beta 3}$. Reflections *hkl* are from α_1 plates, and reflections hkl_b are from the parent β_3 phase.

At 250 °C, despite the absence of NNN order, the α_1 plates exhibit NNSR reflection contrast as shown in Figure 12, where the micrograph was imaged using the 214 NNSR of the 9R α_1 plate. Again, continuous NN APD boundaries across the interface are observed.

The $[\bar{1}20]_{9R}$ diffraction pattern of Figure 7(d) indicates that the α_1 plates formed at 350 °C are not ordered. The NN order is either lost during the transformation or is annealed out immediately after the plate formation and before experimental accessibility.

E. *Crystallography*

1. *PTMC calculations*

For simplicity, NNN order will be ignored in the PTMC calculations, and the transformation will be treated as a B2 → 9R transformation. Since B2 and bcc lattices have identical lattice constants, Kajiwara's formulation[31] can be applied directly to the B2 → 9R transformation. Equivalent $L2_1$ and 18R lattice vectors and plane normals can be converted following the relationship listed in Table I.

The input data for the calculation is listed as follows:

Lattice constants (Å):
B2: $a = 2.94$
9R: $a = 4.41$, $b = 2.67$, $c = 19.18$, $\beta = 89$ deg
Lattice correspondence:
$[101]_{B2} \rightarrow [100]_{9R}$
$[0\bar{1}0]_{B2} \rightarrow [010]_{9R}$
$[50\bar{4}]_{B2} \rightarrow [001]_{9R}$
Lattice invariant shear:
$1/3[100]_{9R}/(009)_{9R}$

Note that the lattice correspondence has already included

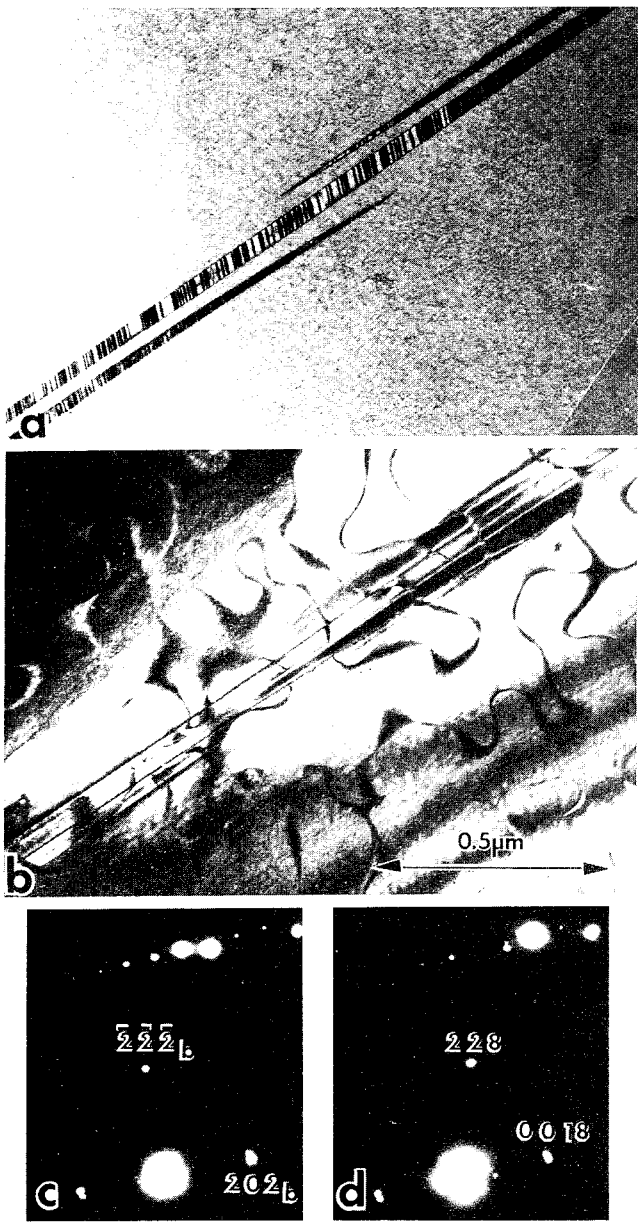


Fig. 8—(*a*) Bright-field micrograph and (*b*) dark-field micrograph with the accompanying diffraction patterns in (*c*) and (*d*) showing the imaging condition for β_3 NNAPD and α_1 NNAPD, respectively, after aging at 150 °C for 48 h.

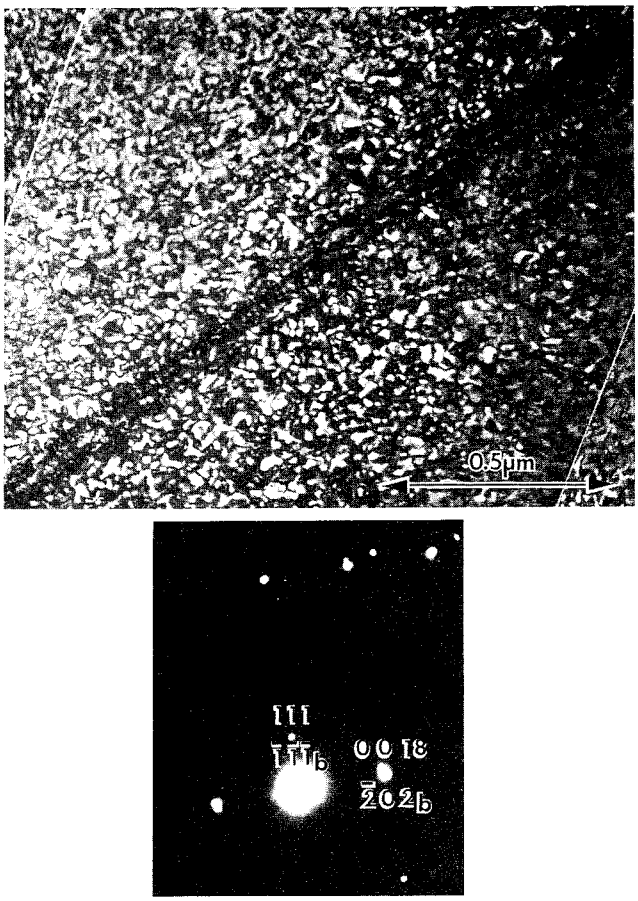


Fig. 9—Dark-field micrograph, with the corresponding diffraction condition, showing NNN APD of α_1 plates and β_3 matrix of the same specimen region as in Figure 8; specimen aged at 150 °C for 48 h.

9R periodic faults, and that the lattice invariant shear will account for only the random faults.

2. *Numerical results of PTMC calculations and experimental verification*

a. *Lattice invariant shear*

According to the calculation, the magnitude of lattice invariant shear, $g' = +0.0185$. A positive g' suggests that random faults are of 2H hexagonal close-packed (hcp) type.[31] This magnitude of g' will produce 2H faults averaging 80 Å in spacing. Experimental evidence confirming the calculation is presented in Figure 13, a phase contrast electron micrograph of a $[\bar{1}10]_{9R}$ projection of an α_1 plate after aging at 250 °C for 5 minutes. Two types of fringes are present in the plate. The 6.4 Å fringes correspond to the 9R periodic faults while the 4.3 Å fringes conform to the 2H random faults. Experimental results in quantitative agreement with the present prediction on the random fault spacing were also reported by Kang *et al.*[34] who, in their study of α_1 interfacial structure in a Cu-26.84 wt pct Zn-4.22 wt pct Al alloy, showed that the average spacing between interface dislocations associated with random faults is 72.7 Å in early stage α_1 plates.

b. *Habit plane*

Present calculations yield a theoretical invariant plane strain (IPS) habit plane of $(1, 5.181, 5.252)_{B2}$. The experimentally determined habit planes of α_1 plates are plotted in a stereographic triangle in Figure 14. Good agreement within 2 deg between theoretical and experimental values was observed for plates transformed at 150 °C to 200 °C. Deviations become more significant with increasing aging temperature as the habit plane gradually shifts toward $(278)_{B2}$.

c. *Orientation relationship*

According to the calculation, the $[\bar{1}10]_{9R}$ (equivalent to $[\bar{2}10]_{18R}$) and $[1\bar{1}1]_{B2}$ axes are 0.38 deg apart; and $(\bar{1}\bar{1}4)_{9R}$ (equivalent to $(\bar{1}\bar{2}8)_{18R}$) is 0.54 deg away from the $(011)_{B2}$ plane normal. This is consistent with the $[\bar{2}10]_{18R}/[1\bar{1}\bar{1}]_{\beta 3}$ composite zone pattern presented in Figure 6(a). The orientation relationship is plotted in a stereographic projection in Figure 15.

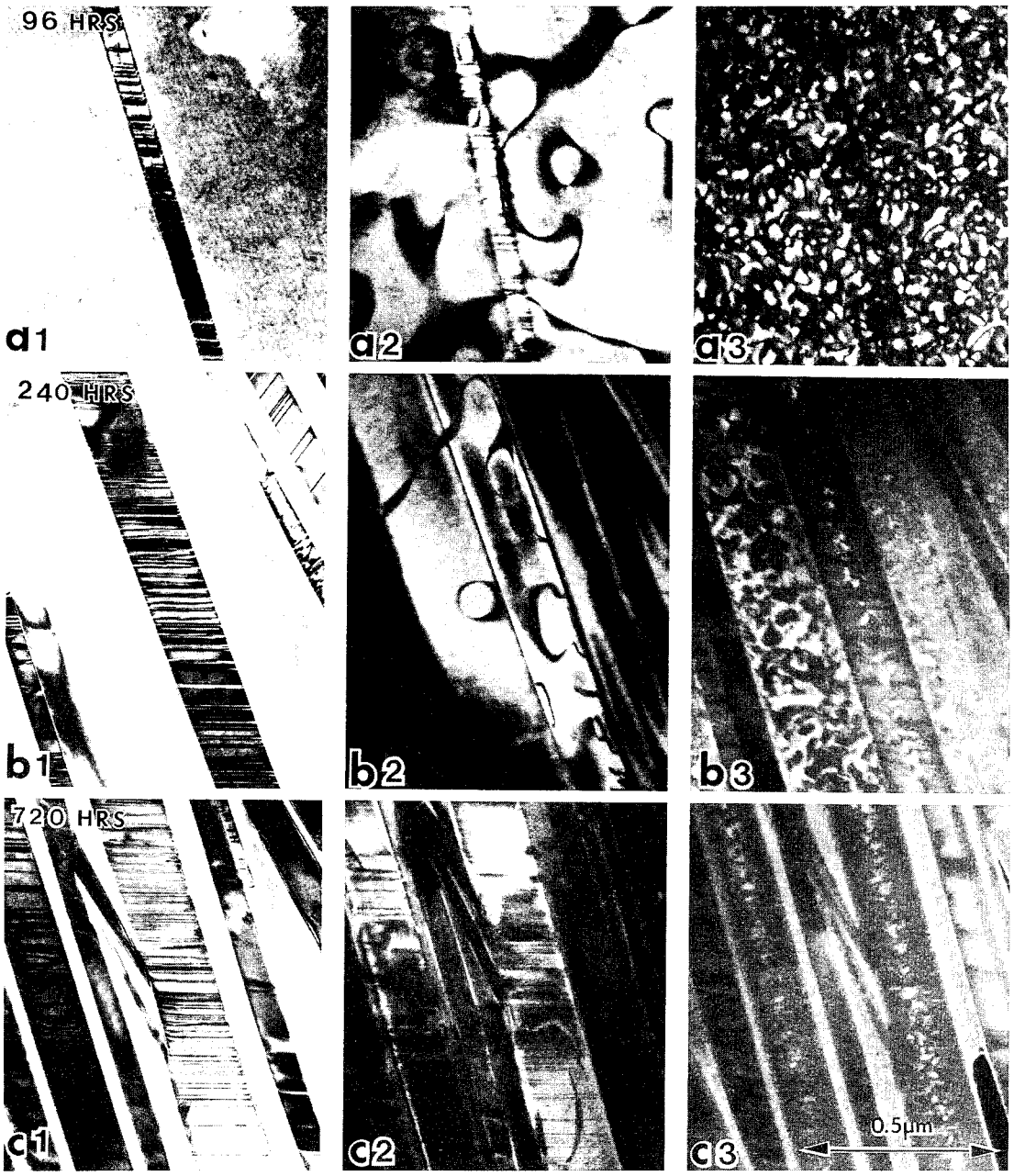


Fig. 10—(1) Bright-field micrographs and (2) and (3) dark-field micrographs showing NN and NNN APDs, respectively, of α_1 plates and the adjacent β_3 matrix after aging at 150 °C for (*a*) 96 h, (*b*) 240 h, and (*c*) 720 h.

d. *Shape deformation*

The calculated shape-deformation vector is $0.187[0.160, -0.732, 0.662]_{B2}$, which should produce a surface relief of 10.6 deg. Quantitative measurement of the shape change is difficult because of the small plate width. However, an optical micrograph taken under oblique illumination and the corresponding interference micrograph in Figure 16, where three α_1 plates are labeled *a*, *b*, and *c*, respectively, do confirm the presence of a shear type of surface relief associated with the α_1 plates.

e. *Intervariant relationship between paired variants*

According to the PTMC calculations, there are 12 possible lattice correspondences, each yielding two IPS habit plane variants. Lattice correspondences, habit planes, and shape-change vectors of the total 24 variants have been calculated and are listed in Table II. The designation for each variant follows that used by Adachi *et al.*[35] The variant discussed in the PTMC calculation corresponds to A_1. The calculation based on the same lattice correspondence yields another variant, D_2, which has a habit plane of $(1, -5.185, 5.252)_{B2}$ and a shape-change vector of $0.187[0.160, 0.732, 0.662]_{B2}$.

It is well known that α_1 plates often form in pairs with obtuse angles.[5,10] The intervariant relationship between the paired variants is to be described with reference to A_1 variant.

The most frequently found α_1 pair has an A_1/D_1 combination. A micrograph of an A_1/D_1 pair in a specimen after aging at 350 °C for 5 seconds is shown in

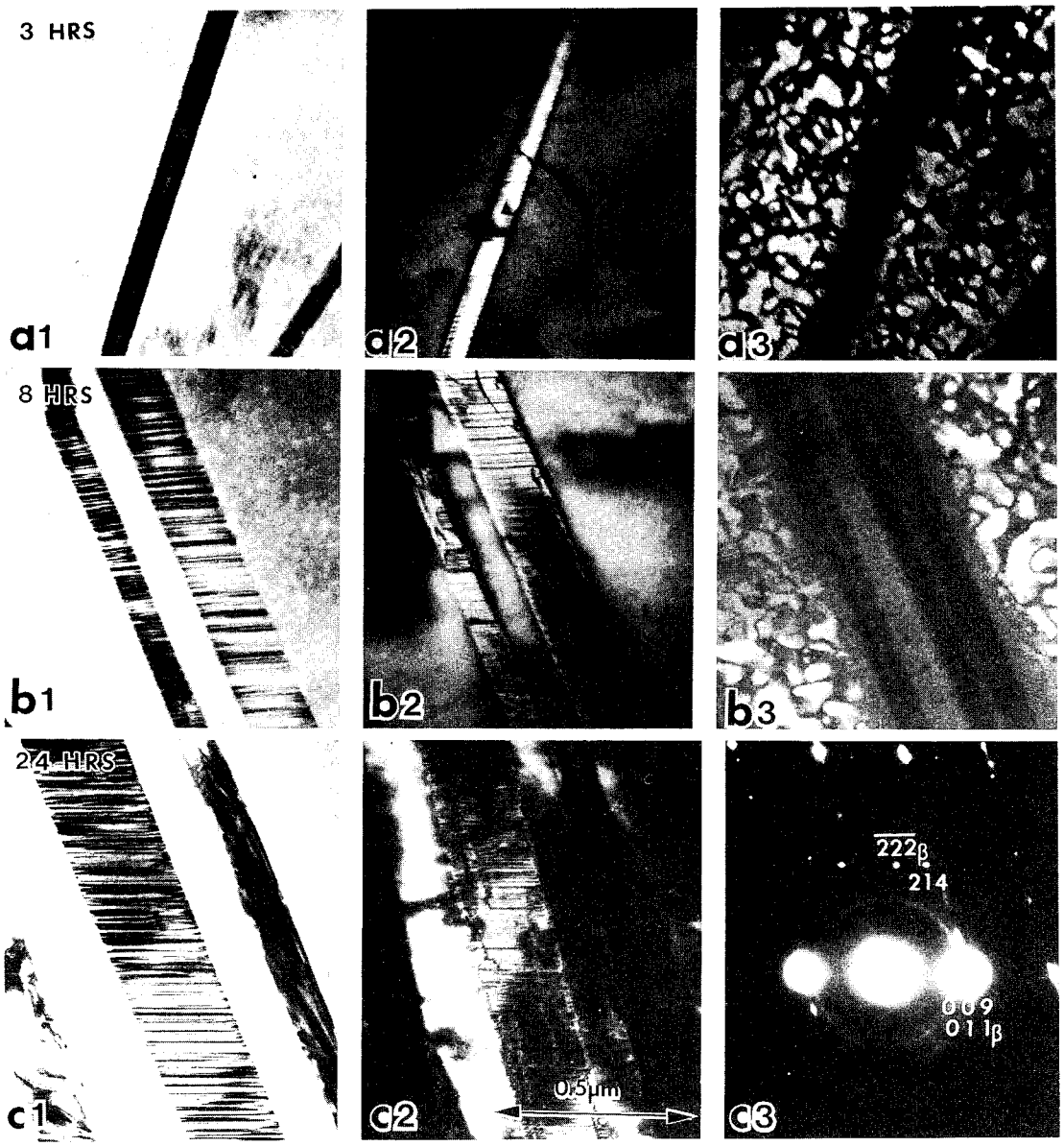


Fig. 11—(1) Bright-field micrographs and (2) and (3) dark-field micrographs showing NN and NNN APDs, respectively, of α_1 plates and the adjacent β_1 matrix after aging at 200 °C for (*a*) 3 h, (*b*) 8 h, and (*c*) 24 h. A $[\bar{1}20]_{9R}$ zone pattern in (c3) demonstrates the absence of NNN order in the α_1 plates after 24 h at 200 °C.

Figure 17. According to the calculation, the pair forms an angle of 164.6 deg between the habit planes and is twin-related with respect to the $(100)_{B2}$ atomic plane. The measured angle between the habit plane from the micrograph is deviated from the calculated value, because the micrograph was not viewed under the edge-on orientation of the habit plane. The measured angle between the streaking from the diffraction pattern is 87.0 deg in agreement with the calculated angle of 85.5 deg between the basal $(009)_{9R}$ plane normals of A_1 and D_1 α_1 variants.

Another type of pair observed in a specimen aged at 350 °C for 10 seconds is shown in Figure 18, which has a combination of A_1/D_5. The two variants are twin-related with respect to the $(\bar{1}01)$ atomic plane of the parent phase, and the calculated angle between the two habit planes is 132.4 deg. The measured angle between the diffraction streaking is 172.5 deg in agreement with the calculated angle of 172.8 deg between the basal $(009)_{9R}$ plane normals of A_1 and D_5 α_1 variants.

The most common martensite variant combination of A_1/C_1 is also observed for α_1 plates, as shown in Figure 19. The micrograph was taken from a specimen aged at 200 °C for 4 hours. The habit planes of the pair form an angle of 164.5 deg and the measured angle between the two streaking directions is 128.0 deg, in good agreement with the calculated 127.1 deg. The pair is twin-related with respect to the $(011)_{B2}$ atomic plane. However, A_1 and C_1 variants do not share an obvious interface, as do the other two types of α_1 pairs. It is likely that the two variants nucleated separately, and the pair is simply created by the impingement of the two variants during growth.

According to Adachi *et al.*,[35] there is a total of 16

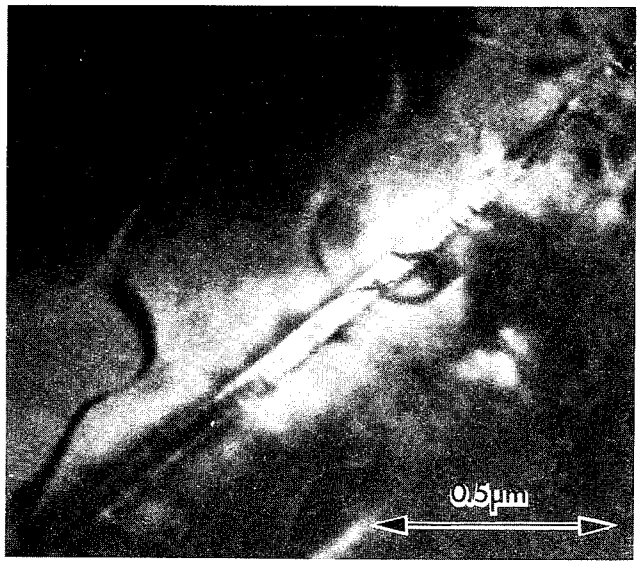


Fig. 12—A dark-field micrograph of NNAPD in an α_1 plate and the β_2 matrix after aging at 250 °C for 10 min.

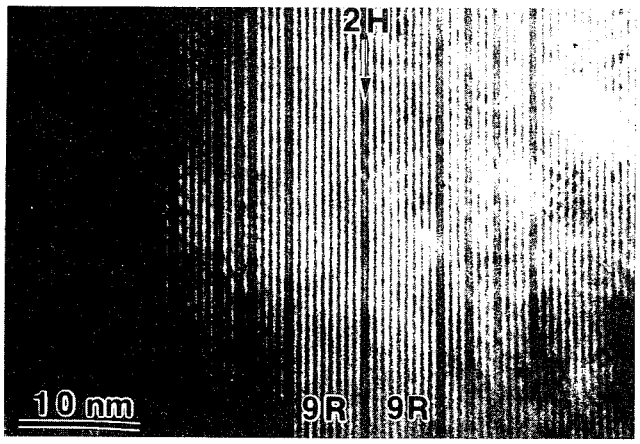


Fig. 13—Phase contrast electron micrograph of a $[\bar{1}10]_{9R}$ projected α_1 plate showing 9R periodic faults and 2H random faults after aging at 250 °C for 5 min.

unique variant combinations for 18R martensites. The combined shape-change vectors of these 16 combinations for α_1 plates are listed in Table III. The results suggest that both A_1/D_1 and A_1/C_1 pairs are very effective in shape-change accommodation; the A_1/D_5 combination, however, is the least effective. Strain energy is clearly not the only deciding factor in the choice of these pair formations. This can be understood, since strain energy is not significant when early stage α_1 plates adopt a small aspect ratio. In comparison to martensite, α_1 plates thicken at a much slower rate. When the aspect ratio becomes significant at a later thickening stage, the transformation shape change is perhaps relieved by diffusion.

F. *Composition of α_1 Plates*

An α_1 plate formed after aging at 150 °C for 48 hours is shown in Figure 20. Regions labeled x and y were

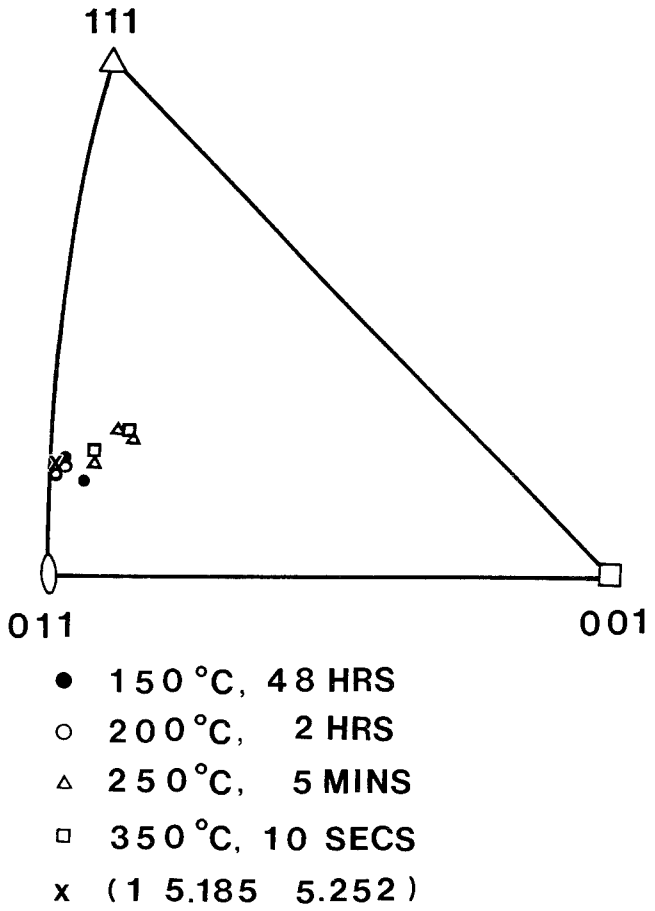
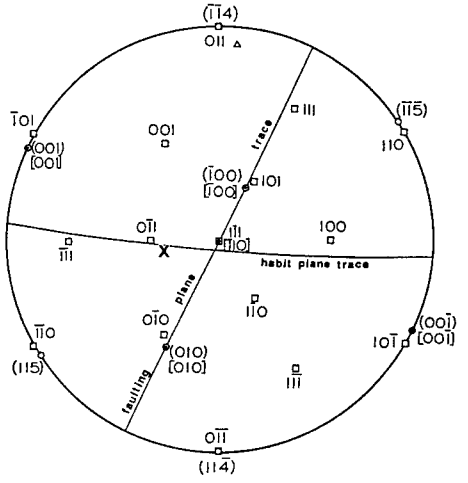


Fig. 14—Distribution of habit plane normals of α_1 plates that transform at temperatures from 150 °C to 350 °C.



○ (hkl): 9R plane normals
● [hkl]: 9R lattice directions
□ hkl : B2 plane normals and lattice direction
△ : α_1 habit plane normal, (1,5.185,5.252)
X : α_1 shape change direction, [0.160,-0.732,0.662]

Fig. 15—Stereographic projection of α_1 crystallography and its orientation relationship with the parent β_2 phase.

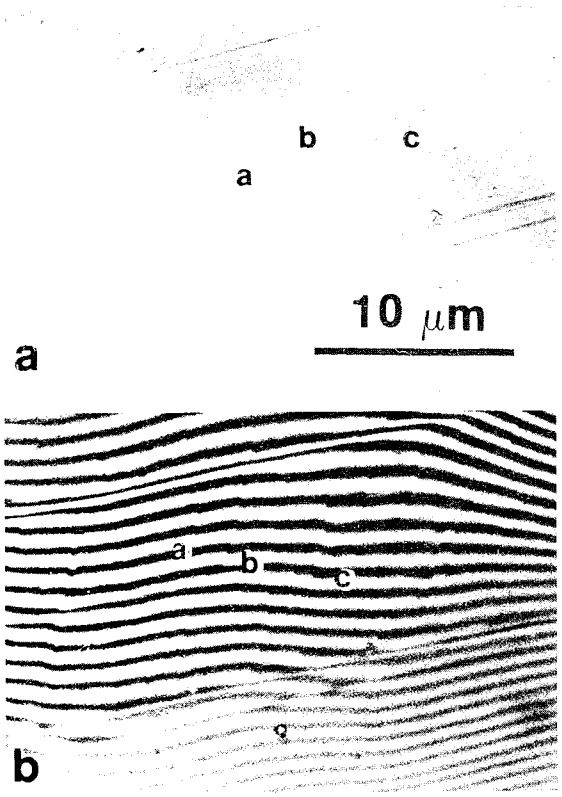


Fig. 16—(*a*) Surface relief micrograph and (*b*) the corresponding interference micrograph of α_1 plates after aging at 150 °C for 48 h.

subjected to microanalytical EDX analyses. The Zn and Al concentration profiles were traced along line segments of *a-b* and *c-d*. Both traces run across the α_1 plate and the adjacent parent matrix including a dislocation line indicated by an arrow. The results are plotted in Figure 21.

Along these traces, both Zn and Al concentrations in the α_1 plate are consistently lower than those in the parent matrix. The solute concentration appears to vary from point to point of analysis inside the α_1 plate. The composition of the plate at the point of the lowest solute content along the *a-b* trace line is Cu-24.7 wt pct Zn-3.6 wt pct Al, while the α_1 composition at the lowest solute content along the *c-d* trace line is Cu-25.5 wt pct Zn-4.0 wt pct Al. Asymmetric concentration profiles are also observed in the Al concentration along the *a-b* trace in both the α_1 plate and the parent matrix, confirming the observation by Takezawa and Sato.[25]

Depletion of Zn is observed at dislocation lines in both Figures 21(a) and (b). The Zn concentration at the dislocation segment in region *x* is 25.3 wt pct, in agreement with that in the α_1 plate. The Zn depletion at the dislocation segment in region *y* and the Al depletion in both dislocation segments are less significant but yet detectable.

The composition profiles after aging at 150 °C for 96 and 240 hours are plotted in Figures 22(a) and (b), respectively. The Zn concentration in the α_1 plate after 96 hours is in the range of 23.7 to 25.7 wt pct, while the Al concentration is around 3.5 wt pct, as shown in Figure 22(a). After 240 hours, the Zn concentration of the α_1 plate ranges from 24.3 to 26.0 wt pct and the Al concentration falls into a range of 3.5 to 4.2 wt pct (Figure 22(b)). At this stage, significant diffusional composition profiles, with Zn concentration up to 29.0 wt pct after 96 hours of aging (Figure 22(a)) and 31.1 wt pct after 240 hours of aging (Figure 22(b)) and

Table II. Lattice Correspondences, Habit Planes, and Shape-Change Vectors of the 24 α_1 Variants (Indices in B2 Coordinates)

Variant	Lattice Correspondence $[100]_{9R}$	Lattice Correspondence $[010]_{9R}$	Lattice Correspondence $[001]_{9R}$	Habit Plane	Shape-Change Vector		
B_6	[011]	[$\bar{1}$00]	[0$\bar{4}$5]	(−5.185 5.252 1)	[0.137	0.124	0.030]
C_5	[011]	[$\bar{1}$00]	[0$\bar{4}$5]	(5.185 5.252 1)	[−0.137	0.124	0.030]
D_3	[011]	[100]	[05$\bar{4}$]	(5.185 1 5.252)	[−0.137	0.030	0.124]
A_4	[011]	[100]	[05$\bar{4}$]	(−5.185 1 5.252)	[0.137	0.030	0.124]
D_4	[0$\bar{1}$1]	[$\bar{1}$00]	[0$\bar{5}\bar{4}$]	(−5.185 −1 5.252)	[0.137	−0.030	0.124]
A_3	[0$\bar{1}$1]	[$\bar{1}$00]	[0$\bar{5}\bar{4}$]	(5.185 −1 5.252)	[−0.137	−0.030	0.124]
B_5	[0$\bar{1}$1]	[100]	[045]	(−5.185 −5.252 1)	[0.137	−0.124	0.030]
C_6	[0$\bar{1}$1]	[100]	[045]	(5.185 −5.252 1)	[−0.137	−0.124	0.030]
D_2	[101]	[0$\bar{1}$0]	[50$\bar{4}$]	(1 −5.185 5.252)	[0.030	0.137	0.124]
A_1	[101]	[0$\bar{1}$0]	[50$\bar{4}$]	(1 5.185 5.252)	[0.030	−0.137	0.124]
D_5	[101]	[010]	[$\bar{4}$05]	(5.252 5.185 1)	[0.124	−0.137	0.030]
D_6	[101]	[010]	[$\bar{4}$05]	(5.252 −5.185 1)	[0.124	0.137	0.030]
A_6	[10$\bar{1}$]	[0$\bar{1}$0]	[$\bar{4}$0$\bar{5}$]	(5.252 −5.185 −1)	[0.124	0.137	−0.030]
A_5	[10$\bar{1}$]	[0$\bar{1}$0]	[$\bar{4}$0$\bar{5}$]	(5.252 5.185 −1)	[0.124	−0.137	−0.030]
D_1	[10$\bar{1}$]	[010]	[504]	(1 −5.185 −5.252)	[0.030	0.137	−0.124]
A_2	[10$\bar{1}$]	[010]	[504]	(1 5.185 −5.252)	[0.030	−0.137	−0.124]
C_4	[110]	[00$\bar{1}$]	[$\bar{4}$50]	(5.252 1 −5.185)	[0.124	0.030	0.137]
C_3	[110]	[00$\bar{1}$]	[$\bar{4}$50]	(5.252 1 5.185)	[0.124	0.030	−0.137]
B_1	[110]	[001]	[5$\bar{4}$0]	(1 5.252 5.185)	[0.030	0.124	−0.137]
B_2	[110]	[001]	[5$\bar{4}$0]	(1 5.252 −5.185)	[0.030	0.124	0.137]
C_2	[$\bar{1}$10]	[00$\bar{1}$]	[5$\bar{4}$0]	(−1 5.252 −5.185)	[−0.030	0.124	0.137]
C_1	[$\bar{1}$10]	[00$\bar{1}$]	[5$\bar{4}$0]	(−1 5.252 5.185)	[−0.030	0.124	0.137]
B_3	[$\bar{1}$10]	[001]	[450]	(−5.252 1 −5.185)	[−0.124	0.030	0.137]
B_4	[$\bar{1}$10]	[001]	[450]	(−5.252 1 5.185)	[−0.124	0.030	−0.137]

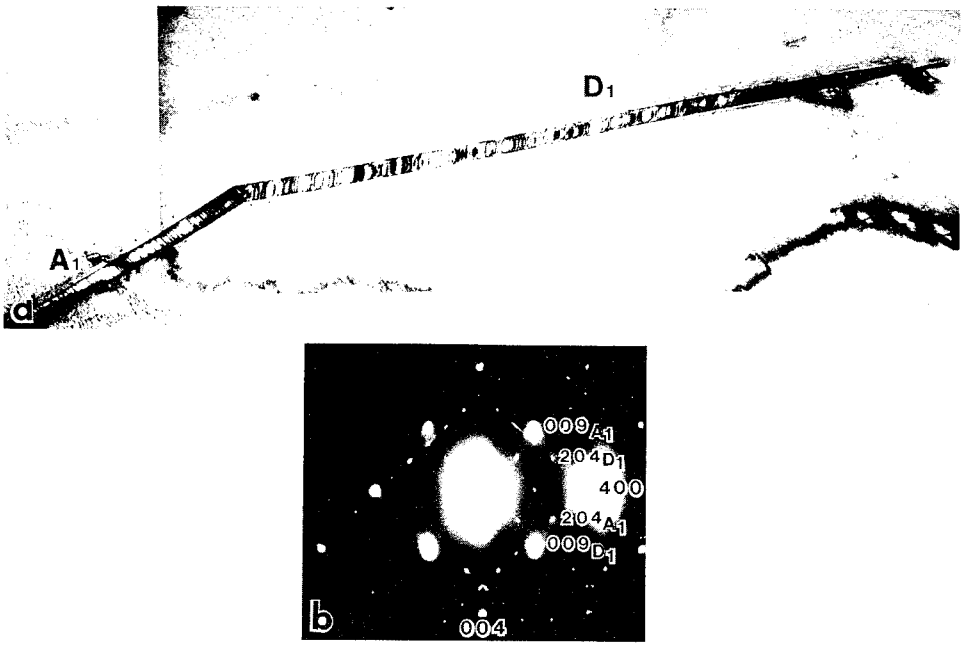


Fig. 17—(*a*) Bright-field micrograph and (*b*) the corresponding diffraction pattern of an A_1/D_1 α_1 pair in a specimen aged at 350 °C for 5 s.

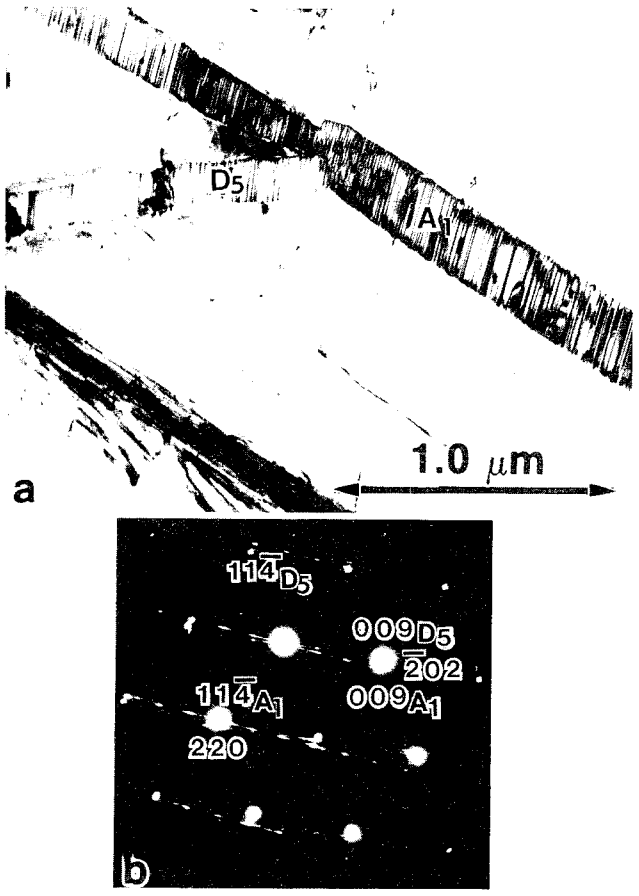


Fig. 18—(*a*) Bright-field micrograph and (*b*) the corresponding diffraction pattern of an A_1/D_5 α_1 pair in a specimen aged at 350 °C for 10 s.

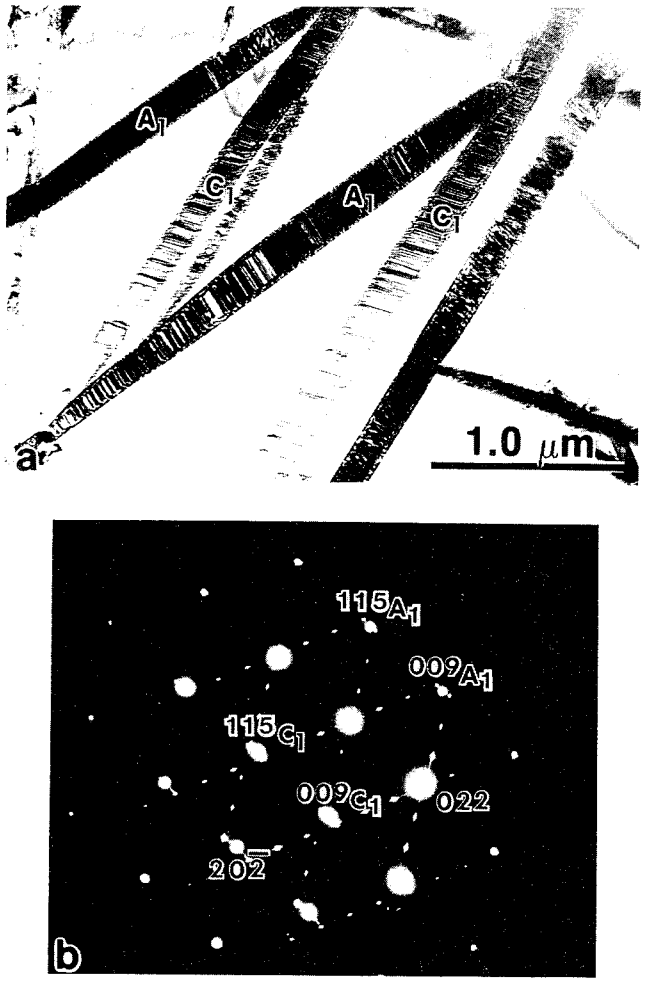


Fig. 19—(*a*) Bright-field micrograph and (*b*) the corresponding diffraction pattern of A_1/C_1 α_1 pairs in a specimen aged at 200 °C for 4 h.

Table III. Comparison between the Intervariant Relationships of the Observed α_1 Pairs and the 16 Unique Variant Combination of Martensite[35]

Variant *vs* A_1	Intervariant Relationship	Combined Shape Change of the Pair				Theoretical Angle between Basal Planes (deg)	Measured Angle between Basal Planes (deg)
B_1	T - $[011]_{B2}$	0.063	[0.956,	−0.207,	−0.207]	61.68	
C_1*	T - $(011)_{B2}$	0.018	[0.000,	−0.707,	−0.707]	127.11	128.0
D_1*	T - $(100)_{B2}$	0.060	[1.000,	0.000,	0.000]	85.53	87.0
A_2	T - $(001)_{B2}$	0.280	[0.214,	−0.977,	0.000]	85.27	
B_2	—	0.268	[0.224,	−0.048,	0.973]	57.39	
D_2	I - $(010)_{B2}$	0.255	[0.235,	0.000,	0.972]	5.51	
A_3	—	0.318	[−0.337,	−0.526,	0.781]	62.69	
B_3	—	0.297	[−0.316,	−0.360,	0.878]	55.64	
C_3	—	0.188	[0.819,	−0.569,	−0.069]	119.64	
D_3	T - $(110)_{B2}$	0.291	[−0.368,	−0.368,	0.852]	58.12	
B_4	—	0.143	[−0.657,	−0.748,	−0.091]	60.01	
C_4	—	0.321	[0.479,	−0.333,	0.812]	115.47	
D_4	T - $(110)_{B2}$	0.342	[0.488,	−0.488,	0.724]	67.12	
A_5	—	0.328	[0.469,	−0.835,	0.287]	89.87	
D_5*	T - $(101)_{B2}$	0.350	[0.440,	−0.783,	0.440]	172.81	172.5
D_6	T - $(101)_{B2}$	0.218	[0.707,	0.000,	0.707]	175.33	

*Observed α_1 pairs, (I) = Identical, (T) = Twin-related.

Al concentration up to 4.8 wt pct in both cases (Figures 22(a) and (b)), are present in the parent phase immediately adjacent to the interface. Asymmetric composition profiles of both Zn and Al contents, again, are observed in both the α_1 plates and the parent matrix.

G. *High Resolution TEM of α_1 Interface*

A phase contrast TEM micrograph of an α_1 interface after aging at 150 °C for 48 hours is shown in Figure 23(a). The projection axis is parallel to the common zone axis of $[1\bar{1}1]_{\beta 3}/[\bar{2}10]_{18R}$. Periodic faults at every third $(0\,0\,18)_{18R}$ basal plane of the α_1 plate appear as bright dots. It can be seen from the micrograph that all three close-packed planes, $(1\ 2\ 10)_{18R}$, $(0\ 0\ 18)_{18R}$, and $(12\bar{8})_{18R}$, of the α_1 plate maintain full coherency with the $\{220\}_{\beta 3}$ atomic planes. The presence of a strain field near the interface is also obvious as $(0\ 0\ 18)_{18R}$ and $(202)_{\beta 3}$ lattice planes are bent near the interface.

Another micrograph of an α_1 interface, taken under the same imaging condition from a sample aged at 150 °C for 240 hours, is shown in Figure 23(b). The annihilation of basal stacking faults after extended aging causes the faulting periodicity to become less regular. A stepped interface protruding into the parent β_3 matrix is also present. Although the coherency between the $(202)_{\beta 3}$ and the $(0\ 0\ 18)_{18R}$ lattice planes is maintained along the broad interface where the 18R stacking sequence is preserved, misfits are present, as indicated by arrows, at both the stepped interface and the local interface where the 18R stacking periodicity is interrupted.

H. *Isothermal Thickening of Martensite during Aging*

Despite the fact that the martensitic-transformation-temperature start temperature of the present alloy is around −10 °C after aging at 150 °C, isothermal thickening of quench-induced and stabilized martensite has been observed to be similar to that of α_1 plates formed during aging at 150 °C. Figure 24 shows (a) a bright-field micrograph and (b) and (c) dark-field micrographs showing NN and NNN APDs, respectively, of a martensite plate after aging at 150 °C for 96 hours. The plate consists layers divided by planar traces parallel to the interfaces (Figure 24(a)). These layers contain different APD structures. The central layer features NNAPD of 0.07 μm in size but does not show NNN order. Such order and APD structures are consistent with those of the parent phase in the as-quenched state,[29] indicating that the central layer corresponds to a quench-induced martensite plate. The outer layer contains both NN and NNN APDs with domain sizes of 0.1 and 0.02 μm, respectively. Comparing this to the growth pattern of APDs in β_3 parent phase,[29] this particular martensite plate obviously has thickened considerably after approximately 1 hour of aging at 150 °C. Similar to the α_1 plates, isothermally thickened layers of the martensite plate inherit both NN and NNN order and the associated APD structures of the parent β_3 phase.

IV. DISCUSSION

A. *Morphology and Internal Fine Structure*

As seen in Figure 2, early stage α_1 plates in Cu-Zn-Al alloys clearly adopt a thin plate morphology with sharp plate edges and a small aspect ratio. The plates contain LPSO periodic faults as well as 2H random faults consistent with the fine structure of a lattice invariant shear. The faulting fine structure is annealed out only after prolonged aging when the structure changes

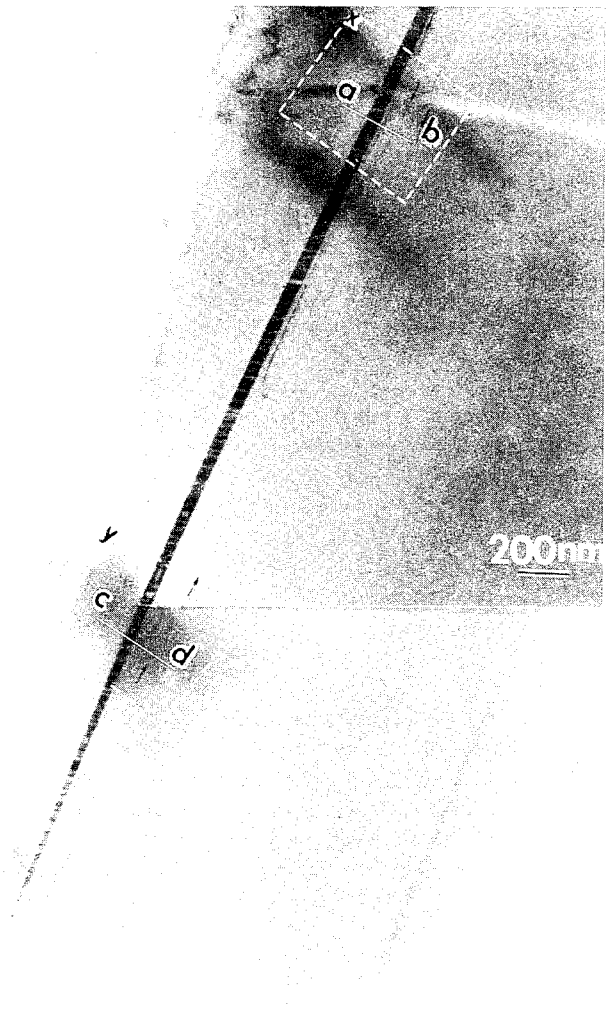


Fig. 20—An α_1 plate in a specimen after aging at 150 °C for 48 h that was subjected to microanalytical analyses along *a-b* and *c-d* traces.

from LPSO structure to equilibrium fcc. Such morphology and fine structure are in agreement with earlier studies on the α_1 plates in Cu-Zn,[5,10] Ag-Cd,[11,17] and Cu-Zn-Al[23] but do not support an observation reported by Chattopadhyay and Aaronson[26] that initial α_1 plates appear in the form of coherent precipitates with no faulting fine structure and that internal faults develop during secondary growth in association with the generation of misfit dislocations. Without detailed diffraction information supporting their interpretation, we have to question whether the fault-free structure described as an initial α_1 plate in Figure 4 of Reference 26 truly represents early stage α_1 plates. In fact, the only α_1 diffraction pattern presented, Figure 2 of Reference 26, is consistent with a 9R α_1 structure with random faults.

B. *Crystal Structure and Long-Range Order*

Clearly demonstrated in this study is that at temperatures below the $\beta_2 \rightarrow \beta_3$ ordering transition temperature, both NN and NNN order components and associated APD structures are preserved in early stage α_1 plates, which possess an ordered M18R structure. Both NN and NNN APD boundaries are continuous across the interface. The NNN order is lost during later stage plate thickening, and the structure of the α_1 plates becomes ordered 9R, creating a composite α_1 plate with an ordered 18R inner layer and ordered 9R outer layers. The NN APD boundaries remain continuous at the interface at this stage. The loss of continuity of NN APD boundaries at the interface is observed only after extended aging, *i.e.*, 240 hours at 150 °C. This is probably caused by the faster diffusion, and therefore the higher growth rate of NN APD, in the parent β_3 phase than that in the α_1 plate such that the APD boundaries break away from continuity at the interface.

At temperatures above the $\beta_2 \rightarrow \beta_3$ transition temperature, the NN order and APD structure are preserved in early stage α_1 plates during aging at 250 °C. The NN APD boundaries again run continuously across the interface. It is only at 350 °C that the early stage α_1 plates possess a disordered 9R structure.

As compared in Table IV, the long-range order of early stage α_1 plates is consistent with that of the martensite, the product of a shear transformation. The evolution of α_1 long-range order during aging is also in agreement with that of tempered martensite.[36] These results suggest that the NNN order component of the 18R structure of both α_1 plates and martensite is metastable at temperatures below the $\beta_2 \rightarrow \beta_3$ transition temperature. One would expect that the ordered 9R structure is also metastable in nature, since the structure will eventually become disordered fcc during extended aging. As shown in this study and Reference 36, both NN order and 9R stacking structure are annealed out during prolonged aging of α_1 plates and tempering of martensite, and the structure changes to the ground state, disordered fcc, in agreement with the equilibrium phase of the phase diagram.[32] The absence of long-range order in the α_1 plates at 350 °C is therefore most likely due to the fast diffusion inside the plate at such a high temperature such that, even though the plate may form with long-range order, it is annealed out well before experimental observation.

The continuity of APD boundaries across the interface suggests that long-range order in α_1 plates is an inherited feature, a result of a shear transformation, rather than a consequence of secondary reordering inside the plate after the plate formation, as suggested by Hsu,[28] for the following reasons. As discussed in this section, long-range order in the α_1 is not a stable configuration. If the plates form with a disordered structure, there is no driving force for the reordering to occur. In addition, even if the reordering occurs, the probability of the APD boundaries to match perfectly at the interface is remotely small. These factors suggest that the thermodynamic calculation carried out by Hsu[28] is in contradiction with both the experimental evidence and the phase diagram[32] and needs to be reexamined.

Increasing 18R layer thickness with decreasing temperature suggests that the ability of the α_1 plates to inherit the parent long-range order during plate growth increases as the transformation temperature approaches the martensitic transformation temperature. This suggests that the volume free energy change in the formation of α_1 plate is related to that of martensitic

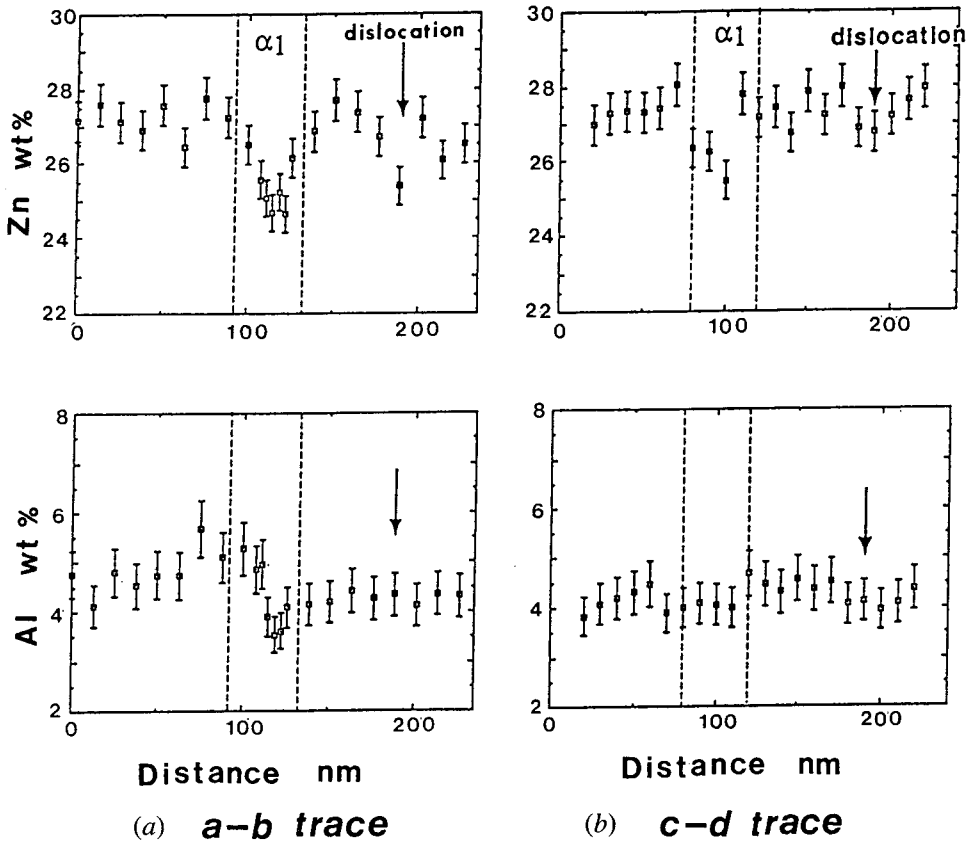


Fig. 21—Zinc and Al concentration profiles along (*a*) *a-b* and (*b*) *c-d* traces of an α_1 plate shown in Fig. 20.

transformation, which is well expected due to their structural similarity. Previous studies concluding disordered α_1 plates in binary Cu-Zn[5,26] and Ag-Cd[11,17] were carried out using compositions with M_s temperatures below −100 °C. Compared to the transformation in the present Cu-Zn-Al alloy with M_s temperature around −10 °C, the formation of α_1 plates in the former binary alloys proceeds at a much higher temperature above the M_s temperature. It is therefore not surprising that the inheritance of long-range order in binary Cu-Zn and Ag-Cd alloys is less readily detectable than that in Cu-Zn-Al alloys. Studies of α_1 long-range order in binary alloys or other ternary derivatives with higher M_s temperature are worthwhile to validate this argument. However, care must be taken with binary Cu-Zn and Ag-Cd alloys with higher M_s temperatures, as it is difficult to completely retain the β phase without partial decomposition during quenching.

C. *Crystallography*

The crystallography of the α_1 plates in present Cu-Zn-Al alloy is in good agreement with PTMC calculations in all aspects and is consistent with that of low-temperature martensite.[33] Quantitative agreements are demonstrated in the orientation relationship, habit plane, and the magnitude of lattice invariant shear. The observed surface relief again indicates the presence of a shear type of transformation shape change that is essential for the observed reverse-shape memory effect.[19] Although α_1 pairs do not always adopt a configuration of the optimum shape-change accommodation, this can be understood as the α_1 plates thicken at a much slower rate than does martensite, and the aspect ratio becomes significant only after considerable plate thickening at which time diffusion may have somewhat relieved the transformation shape change.

These results are in agreement with earlier studies on the crystallography of α_1 plates in Cu-Zn[9,10] and Ag-Cd[11] alloys. Aaronson and Lorimer[37] argued that a diffusional transformation may equally likely adopt a habit plane and orientation relationship conforming to the PTMC in order to minimize interfacial energy. However, their argument does not explain the presence of a transformation shape change and the observed reverse-shape memory effect. Neither does it provide any implication on the presence of 2H random faults and the inheritance of highly metastable long-range order and APD structures. We suggest that these pieces of evidence constitute solid support for the direct presence of a shear process during initial α_1 plate formation and which is difficult to rationalize by a diffusion-controlled transformation *per se*.

D. *Composition*

Consistent with earlier microanalytical studies, a composition difference exists between early stage α_1 plates and parent matrix, even at a stage when both NN and NNN order and APD structures are fully inherited. Solute distributions inside α_1 plates and the adjacent parent matrix are characterized by asymmetric profiles,

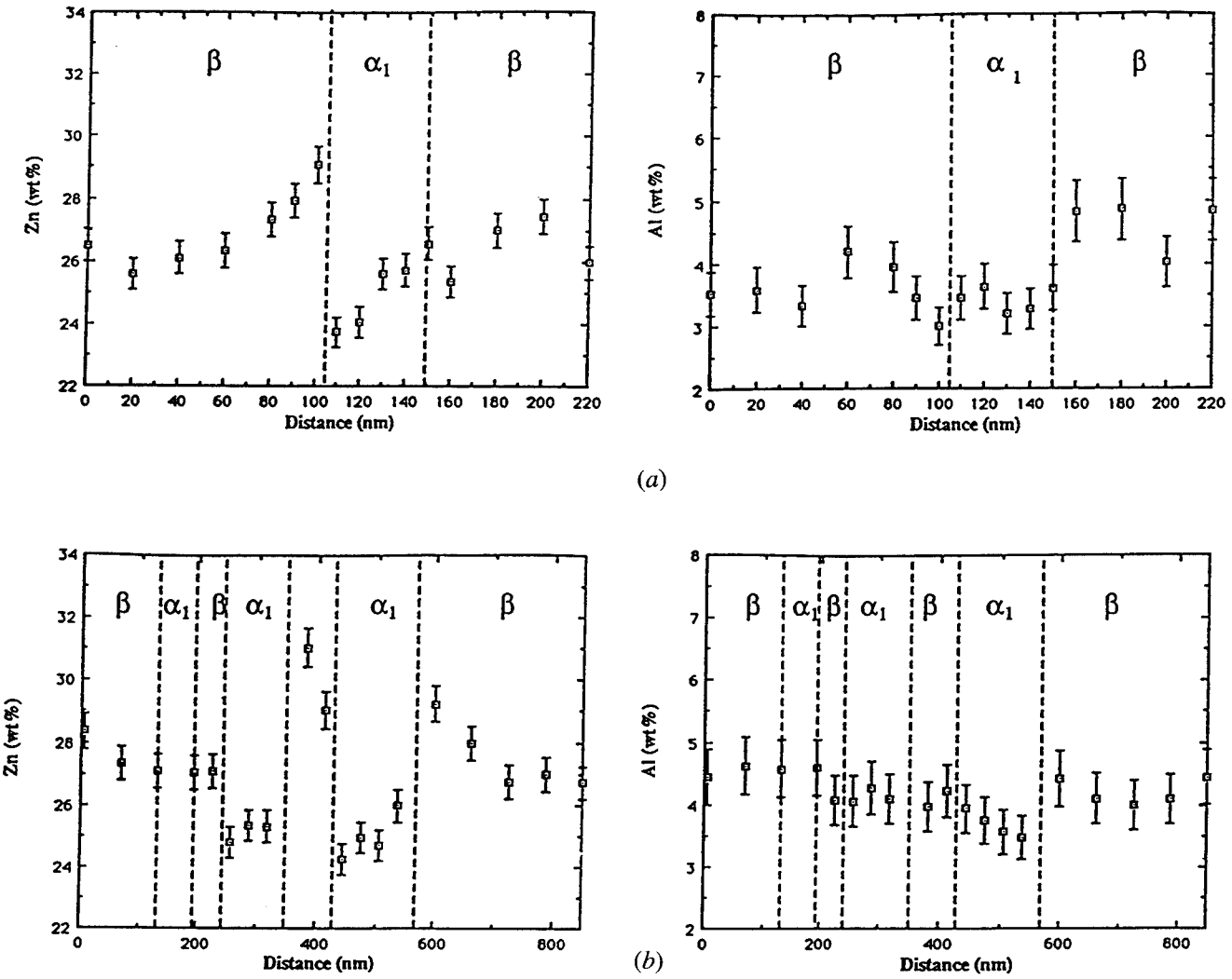


Fig. 22—Zinc and Al concentration profiles of α_1 plates and adjacent matrix after aging at 150 °C for (*a*) 96 h and (*b*) 240 h.

supporting the result reported by Takezawa and Sato,[25] who implied that local composition perturbation exists in the parent matrix due to directional diffusion caused by the stress field around pre-existing defects. This implication was supported by Schmitz *et al.*,[38] who suggested that elastic anisotropy may play an important role in promoting solute depletion at defects. Present microanalysis detects evident solute depletion at dislocation lines in the parent matrix adjacent to the α_1 plate, thus providing direct experimental confirmation to both studies. It is possible that a combined effect of solute depletion and increasing elastic anisotropy leads to a sufficient driving force for a shear process to commence at these defects.

Whether the combined effect of solute depletion and high anisotropy is geometrically significant enough to permit a martensitic transformation to occur at these defects needs to be examined in more detail. However, as suggested by Schmitz *et al.*,[38] further solute depletion may continue to occur ahead of the lengthening α_1 plate tip, as the stress field ahead of the plate tip would provide similar driving force for solute depletion and increasing elastic anisotropy for the lengthening to continue.

E. *Transformation Kinetics*

The study by Weisner and Hornbogen[4] indicated that the nucleation C-curve of α_1 plates in Cu-Zn alloys shifts toward shorter incubation periods when the transformation takes place under uniaxial tensile stress. This result supports a shear transformation mechanism operating in the nucleation stage of the α_1 plates.

Similar to martensite growth, initial α_1 plates lengthen rapidly. Significant plate thickening follows only after the lengthening more or less is complete.[5,6] The lengthening kinetics of α_1 plates in Cu-Zn Alloys during aging at 250 °C to 350 °C, reported by Simonen and Trivedi,[7] indicate that the rapid lengthening kinetics are incompatible with volume diffusion. The rapid lengthening can be rationalized only with the assumptions of semicoherent interfaces and supersaturation of Zn concentration; the latter increases significantly with decreasing temperature. Kostic *et al.*[6] also pointed out that the lengthening kinetics of α_1 plates in a Ag-45 at. pct Cd alloy at 160 °C is clearly beyond that which can be dictated by volume diffusion. The evidence suggests that the similarity in the lengthening kinetics between α_1 plates and low-temperature martensite also becomes more evident with decreasing temperature.

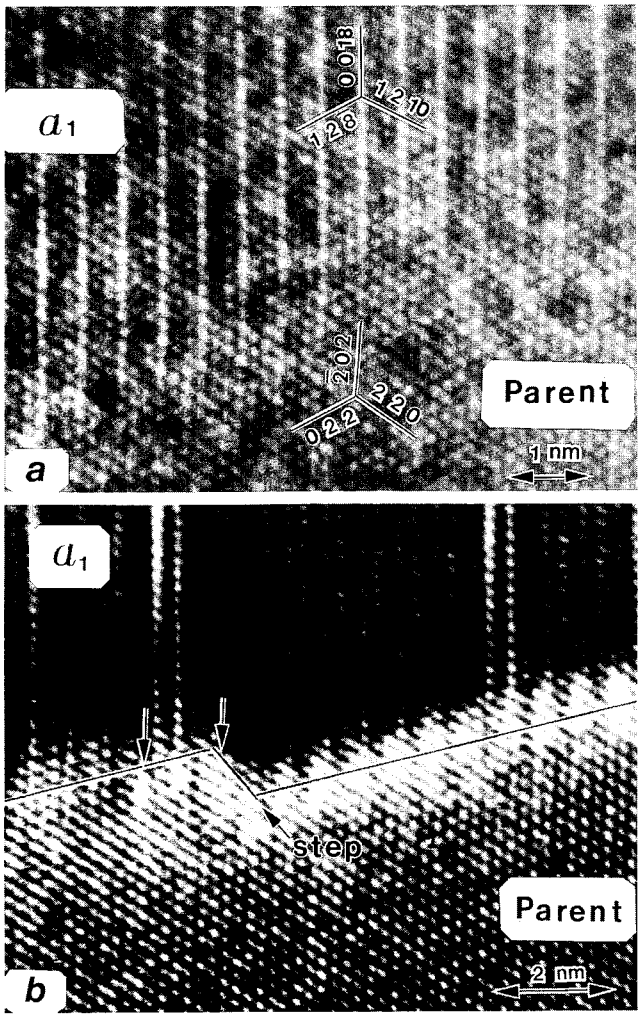


Fig. 23—High-resolution micrographs of α_1 plates and the adjacent parent matrix after aging at 150 °C for (*a*) 48 h and (*b*) 240 h. Projection axis is $[\bar{2}10]_{18R}//[1\bar{1}1]_{\beta 3}$.

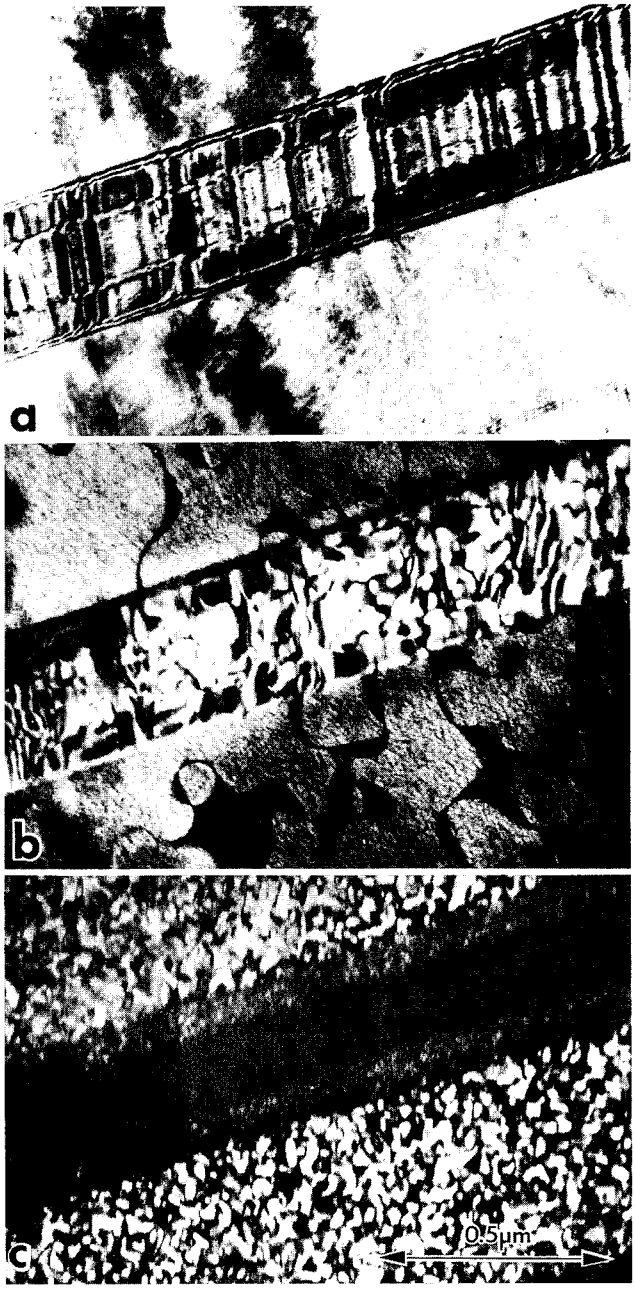


Fig. 24—(*a*) Bright-field micrograph, (*b*) dark-field micrograph showing NN APD, and (*c*) dark-field micrograph showing NNN APD of a quench-induced martensite plate after isothermal thickening in a specimen aged at 150 °C for 96 h.

The thickening kinetics of α_1 plates in a Ag-45 at. pct Cd alloy reported by Kostic *et al.*[6] are consistent with the Frank-Zener model for the growth of planar precipitates. However, the smallest plate thickness at 160 °C studied by Kostic *et al.* was approximately 0.5 μm, an order of magnitude greater than the 18R layer of the present α_1 plate at 150 °C. If the plate formation is initiated by a shear process with the later growth controlled by diffusion, a plate of 0.5 μm thickness may have surpassed this transitional stage. It is therefore not surprising that the thickening kinetics follow the Frank-Zener model.

F. *Interfacial Structure*

Interfacial structure may bear direct evidence related to the transformation mechanism as a shear mechanism produces glissile interfacial dislocations with the combined Burgers vector of the dislocation network consistent with the shape change of the transformation. A diffusional mechanism, on the other hand, would generate sessile interfacial dislocations with their nature dictated by the lattice misfit between the two phases.

A TEM study of the interfacial structure carried out by Chattopadhyay and Aaronson[26] implied that the interfacial dislocations of α_1 plates in Cu-Zn alloys consist of growth ledges and misfit dislocations. However, their analysis was based solely on the invisibility criteria, the accuracy of which may be affected by the extremely high anisotropy of the parent matrix, which causes residual contrast and makes any accurate determination of Burgers vectors very difficult. They also claimed to observe ledge structures along plate tips, on which they base their argument that the lengthening of the plate is also controlled by a ledge mechanism. Again, such argument lacks supportive evidence, since

Table IV. Evolution of Crystal Structure and Long-Range Order of α_1 Plates during Aging and that of Martensite during Tempering[36]

Temperature (°C)	β Phase	Martensite*	α_1 Plate
150	$L2_1$	18R → (O)9R	18R → (O)9R
200	$L2_1$	—	18R → (O)9R
250	B2	(O)9R → (DO)9R → fcc	(O)9R → (DO)9R → fcc
350	B2	—	(DO)9R → fcc

*(O) = Ordered, (DO) = Disordered.

the nature of the defects they interpreted as ledges has not been quantitatively characterized.

Early stage α_1 plates possess interfacial dislocations associated with random faults of a lattice invariant shear and must be glissile in nature. At this stage, coherency of close-packed planes is maintained across the straight interface of the IPS habit plane, as shown in the present high-resolution TEM analysis. Stepped interfaces and the loss of coherency are developed only after significant plate thickening, at which point misfit dislocations are generated at the interface where stacking faults are annealed out.

The Burgers vector of these interfacial dislocations has not been studied conclusively. Modeling based on the PTMC and more detailed TEM studies with the assistance of computer image analysis on the α_1 interfacial structure are necessary. Such in-depth analyses will add more direct evidence for the clarification of the actual transformation mechanism.

G. *Transformation Mechanism*

Based on the evidence discussed, we support the proposed mechanism that the formation of α_1 plates in Cu-Zn-Al alloys is initiated by a shear mechanism that controls initial plate lengthening. A combined effect of elastic anisotropy and solute depletion at parent phase defects provide the driving force for the shear transformation to take place at these defects as nucleation sites, which would otherwise be thermodynamically infeasible. The shear process explains the rapid-lengthening kinetics of the α_1 plates and allows the plates to adopt IPS crystallography and to inherit parent long-range order and the associated APD structures. The mechanism also gives rise to the observed reverse-shape memory effect and is consistent with the reported effect of uniaxial tensile stress that promotes the incubation of α_1 plates in Cu-Zn alloys.

Volume diffusion inevitably becomes necessary in order to provide additional driving force for further growth of α_1 plates. Diffusion in the parent β phase ahead of plate tip may be induced by the stress field around the plate tip, which permits the shear lengthening to continue. Diffusion at the interface eventually controls the plate thickening, which maintains a lower solute concentration in the α_1 plates and explains the Frank-Zener plate-thickening kinetics.

Whether the shear-diffusion transition is an abrupt process or the two mechanisms are compatible and cooperate during a gradual transition process remains to be answered. However, early stage diffusion evidently does not immediately destroy the IPS crystallography, faulting fine structure, and long-range order as these features are slowly annealed out during extended aging.

The proposed transformation mechanism is supported by the observation that a quench-induced martensite plate can thicken isothermally during aging at a temperature above M_s and inherit the long-range order and APD structures of the parent phase. The evidence suggests a structurally glissile martensite interface that, although possibly immobile due to various stabilization effects,[39] can migrate during isothermal aging at the α_1 transformation temperatures. The presence of planar traces of original martensite interfaces suggests that reconstruction of the interface may have occurred before aging-induced plate thickening. It is possible that the observed midrib in α_1 plates and the planar traces in the isothermally thickened martensite plate share similar features. The nature of these planar defects may provide further insight into the transformation mechanism that remains to be characterized.

ACKNOWLEDGMENTS

The authors gratefully acknowledge support from the following organizations: International Copper Research Association (INCRA), Naval Postgraduate School, Sumitomo Metal Mining Co., and Memry Technologies, Inc.

REFERENCES

1. L. Delaey, M. Chandrasekaran, M. Andrade, and J. Van Humbeeck: in *Proc. Int. Conf. on Solid–Solid Phase Transformations*, TMS-AIME, Pittsburgh, PA, 1981, pp. 1429-53.
2. R.D. Gardwood: Special Report No. 93, Iron and Steel Institute, London, 1965, pp. 90-99.
3. P.E.J. Flewitt and J.W. Towner: *J. Inst. Met.*, 1967, vol. 95, pp. 273-80.
4. E.L.F. Weinser and E. Hornbogen: *Scripta Metall.*, 1969, vol. 3, pp. 243-46.
5. E. Hornbogen and H. Warlimont: *Acta Metall.*, 1967, vol. 15, pp. 943-51.
6. M.M. Kostic, E.B. Howbolt, and L.C. Brown: *Metall. Trans. A*, 1976, vol. 7A, pp. 1643-53.
7. E.P. Simonen and R. Trivedi: *Acta Metall.*, 1977, vol. 25, pp. 945-50.
8. S. Kajiwara: *Trans. Jpn. Inst. Met.*, 1976, vol. 17, pp. 447-56.
9. G.R. Srinivasan and M.T. Hepworth: *Acta Metall.*, 1971, vol. 19, pp. 1121-31.
10. I. Cornelis and C.M. Wayman: *Acta Metall.*, 1974, vol. 22, pp. 301-11.
11. M.M. Kostic and E.B. Howbolt: *Metall. Trans. A*, 1979, vol. 10A, pp. 165-76.

12. I. Cornelis and C.M. Wayman: *Scripta Metall.*, 1973, vol. 7, pp. 579-90.
13. G.W. Lorimer, G. Cliff, H.I. Aaronson, and K.R. Kinsman: *Scripta Metall.*, 1975, vol. 9, pp. 271-79.
14. P. Doig and P.E.J. Flewitt: in *Proc. Int. Conf. on Solid–Solid Phase Transformations*, TMS-AIME, Pittsburgh, PA, 1981, pp. 983-92.
15. G. Cliff, F. Hasan, G.W. Lorimer, and M. Kikuchi: *Metall. Trans. A*, 1990, vol. 21A, pp. 831-35.
16. T. Tadaki, C.J. Qiang, and K. Shimizu: *Mater. Trans. JIM*, 1991, vol. 32, pp. 757-65.
17. M.H. Wu, B.C. Muddle, and C.M. Wayman: *Acta Metall.*, 1988, vol. 36, pp. 2095-2106.
18. T. Tadaki, T. Uyeda, and K. Shimizu: *Mater. Trans. JIM*, 1989, vol. 30, pp. 117-26.
19. M.M. Reyhani and P.G. McCormick: *Scripta Metall.*, 1986, vol. 20, pp. 571-74.
20. K. Takezawa, H. Imamura, K. Tanizaki, and S. Sato: *J. Phys. Colloq.*, 1982, vol. C4, pp. 741-46.
21. M.H. Wu, J. Perkins, and C.M. Wayman: *Acta Metall.*, 1989, vol. 37, pp. 1821-1989.
22. M.H. Wu and C.M. Wayman: in *Proc. Int. Conf. on Martensitic Transformations*, Nara, Japan, 1986, The Japan Institute of Metals, Sendai, Japan, pp. 619-24.
23. Y. Nakata, T. Tadaki, and K. Shimizu: *Mater. Trans. JIM*, 1989, vol. 30, pp. 107-16.
24. Y. Hamada, M.H. Wu, and C.M. Wayman: *Mater. Trans. JIM*, 1991, vol. 32, pp. 747-56.
25. K. Takezawa and S. Sato: *Metall. Trans. A*, 1990, vol. 21A, pp. 1541-45.
26. K. Chattopadhyay and H.I. Aaronson: *Acta Metall.*, 1986, vol. 34, pp. 695-711.
27. K.C. Russell: *Metall. Mater. Trans. A*, 1994, vol. 25A, pp. 1933-39.
28. T.Y. Hsu: *Metall. Mater. Trans. A*, 1994, vol. 25A, pp. 2555-63.
29. M.H. Wu and C.M. Wayman: *Scripta Metall. Mater.*, 1991, vol. 25, pp. 1635-40.
30. S.C. Singh, Y. Murakami, and L. Delaey: *Scripta Metall.*, 1978, vol. 12, pp. 435-38.
31. S. Kajiwara: *Trans. Jpn. Inst. Met.*, 1976, vol. 17, pp. 435-46.
32. L. Delaey, A. Deruyttere, E. Aernoudt, and J.R. Roos: Research Project No. 238, Report No. 78R1, International Copper Research Association, Inc., New York, NY, 1978.
33. S. Chakravorty and C.M. Wayman: *Acta Metall.*, 1977, vol. 25, pp. 989-1000.
34. Y.Q. Yang, M.K. Kang, D. Han, Z.G. Zhou, and J.E. Wang: *Metall. Mater. Trans. A*, 1994, vol. 25A, pp. 2609-14.
35. K. Adachi, J. Perkins, and C.M. Wayman: *Acta Metall.*, 1988, vol. 36, pp. 1343-64.
36. M.H. Wu and C.M. Wayman: in *Proc. Int. Conf. on Martensitic Transformations*, Sydney, Australia, 1989, Trans Tech Publications, Brookfield, VT, pp. 553-58.
37. H.I. Aaronson and G.W. Lorimer: *Scripta Metall.*, 1972, vol. 6, pp. 1091-94.
38. A. Schmitz, M. Chandrasekaran, G. Ghosh, and L. Delaey: *Acta Metall.*, 1989, vol. 37, pp. 3151-55.
39. M. Ahlers: in *Proc. Int. Conf. on Martensitic Transformations*, Nara, Japan, 1986, The Japan Institute of Metals, Sendai, Japan, pp. 786-93.

The Formation Mechanism of Plate in Beta Cu-Zn and Cu-Zn-Al Alloys

X.K. MENG, M.K. KANG, Y.Q. YANG, and D.H. LIU

The initial formation and the subsequent early and late stage growth of the α_1 plates in Cu-Zn and Cu-Zn-Al alloys are studied by optical microscopy, transmission electron microscopy (TEM), and high-temperature TEM *in situ*. Single-phase α_1 plates (initial α_1 plates) can be obtained only at the early stage of isothermal transformation. Striations corresponding to stacking faults are observed during the nucleation of initial α_1 plates. A strong and discontinuous strain-stress field exists in front of the tips of initial α_1 plates and causes inducing nucleation and crossing growth. The displacement between stacking fault faces and the thickening along the direction of streaking contrast show that the growth of initial α_1 plate has the nature of shear transformation, and the shear direction along the streaking contrast corresponds to stacking faults. The superledges at the broad faces of the α_1 plates are also observed, but they move only along the direction of streaking contrast during plates thickening. The "overannealing" of initial α_1 plates during longer transformation time results in the disappearing of stacking faults, and corresponding initial α_1 plates are partially or completely "degenerated" into equilibrium α phase (here designated as late α_1 (α) plates). The thickening kinetics of late α_1 (α) plates seems to be compatible with the diffusional ledge mechanism, but the lateral movement of superledges along the broad faces of late α_1 (α) plates is not observed. According to the facts mentioned previously, a possible atomic mechanism for the formation of the α_1 plates is suggested.

I. INTRODUCTION

AS a branch of the solid state transformation, the bainitic reaction is still a heated controversial topic as to its formation mechanism. Much research on the crystallography, morphology, thermodynamics, and kinetics of bainite plates has so far been carried out to clarify which mechanism (displacive shear or diffusional ledge) operates the bainitic transformation. In Fe-C-X alloys, however, the awkward ranking of bainite between the obviously diffusionless martensitic reaction and pearlitic reaction, which is a clear example of a reconstructive transformation, has in the past led to difficulties.[1]

It is well known that the precipitating process of the β' (β_1, β_2, β_3 matrix phase) $\rightarrow$ α_1 (bainite plate) reaction in some nonferrous alloys, such as Cu-Zn and Cu-Zn-Al, is not only undisturbed by diffusion of institial atoms but also simple and hence helpful to the analyses of crystallography and kinetics. Therefore, the $\beta' \rightarrow \alpha_1$ transformation has recently become an important model reaction.[2]

The composition analytical results of bainitic α_1 plates in a Cu-39.3 wt pct Zn alloy and γ_1 plates in a Cr-33 wt pct Ni alloy given by Cliff *et al.*[3] showed that even at the early stages of plate formation, and near the tips of the growing plates, the composition of the plates is different from that of the matrix and near the equilibrium composition of the second phase. Thus, Cliff *et al.* denied the initial formation of these bainitic plates by a mechanism solely involving crystallographic shear. Hsu and Zhou's thermodynamics calculations[4] also showed that the bainitic transformation in a Cu-26.77 wt pct Zn-4.00 wt pct Al alloy could only proceed with a diffusional mechanism. In a Cu-24.3 wt pct Zn-4.7 wt pct Al-0.8 wt pct Mn alloy and a Cu-19.51 wt pct Zn-5.88 wt pct Al alloy, however, Liu and co-workers[5,6] observed the midribs in initial α_1 plates, the slabby stress field in front of the tips of the plates, and the twisting of the intersected plates. These phenomena provided evidence for the shear mechanism of bainitic transformation. Wu *et al.*[7] concluded that the formation and early growth of α_1 plates formed in a Cu-26.67 wt pct Zn-4 wt pct Al alloy involved a shear process and the classical diffusion dominated the growth of late α_1 (α) plates, because both NN and NNN antiphase domains (APDs) are inherited by the product α_1 plates and the long-range order in initial α_1 plates annealed out at the late stage of transformation. The initial shear and late diffusion mechanism, which depend upon the time frame of observation during the course of total transformation, should be further proved and a clear atomic process for the formation of the α_1 plates should be described.

II. EXPERIMENTAL PROCEDURE

A Cu-42.85 wt pct Zn and a Cu-26.84 wt pct Zn-4.22 wt pct Al alloy were prepared by melting high-purity (99.99 pct) Cu, Zn and Cu, Zn, Al, respectively, in

X.K. MENG, Ph.D., and M.K. KANG, Professor, are with the Department of Materials Science and Engineering, Northwestern Polytechnical University, Xi'an, 710072, People's Republic of China. Y.Q. YANG, formerly with Northwestern Polytechnical University, Ph.D. Candidate, is Postdoctoral Researcher, Laboratory of Solid State Microstructures, Nanjing University, Nanjing, 210008, People's Republic of China. D.H. LIU, formerly with Northwestern Polytechnical University, Postgraduate, is Lecturer, Pingyuan University, Xinxiang, 453000, People's Republic of China.

This article is based on a presentation made at the Pacific Rim Conference on the "Roles of Shear and Diffusion in the Formation of Plate-Shaped Transformation Products," held December 18–22, 1992, in Kona, Hawaii, under the auspices of ASM INTERNATIONAL's Phase Transformations Committee.

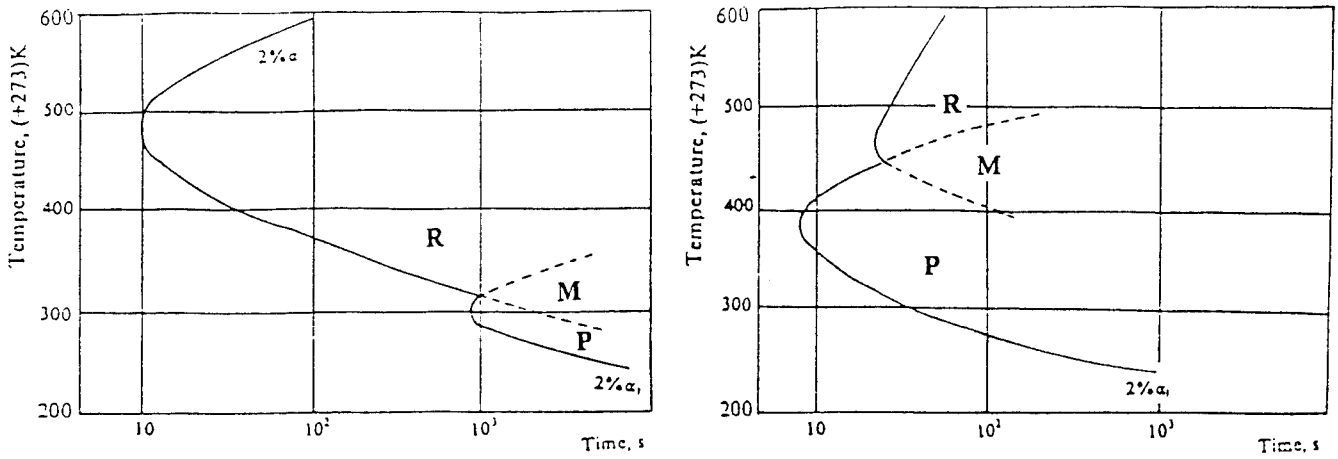


Fig. 1—The TTT diagrams of (*a*) Cu-Zn and (*b*) Cu-Zn-Al alloys.

graphite crucibles and then homogenizing. The Cu-Zn and Cu-Zn-Al specimens were betanized in a molten salt bath at 1063 K for 180 seconds, water quenching to room temperature. The thin foils made from the quenched specimens, after final thinning, were held at 523 and 543 K in high-temperature TEM, respectively, and observed *in situ* when the α_1 plates nucleated and grew. On the other hand, some betanized specimens were held in another molten salt bath at the medium temperature range and quenched into water to obtain initial α_1 plates statically. The time-temperature-transformation (TTT) diagrams were detected with a quantitative metallographical method. Optical microscopy observation was carried out with the Neophot-I-type photomicroscope, and TEM studies were made with the JEM-200CX and PHILIPS*EM 400 and H800 type equipment.

*PHILIPS is a trademark of Philips Electronic Instruments Corp., Mahwah, NJ.

III. EXPERIMENTAL RESULTS

The TTT diagrams (Figure 1) within the medium temperature range for the Cu-Zn and Cu-Zn-Al alloys have been found to consist of two separate C-curves representing the start of transformation, the upper curve being associated with the rod-like α product and the lower with the plate-like α_1. At temperatures below the intersection of the two C-curves, to be referred to as bay temperatures, plates are formed initially (Figure 2(a)) but subsequently rods ($\uparrow$) occur (Figure 2(b)). The α_1 plates appear as V-shaped plates separated by an obtuse angle. Some plates are annealed out to equilibrium α phase (late α_1 (α) plates, $\uparrow$) more rapidly than others during longer transformation time, as can be seen in Figure 3. Late α_1 (α) plate is resoluble under optical microscopy, because it is much coarser than initial α_1 plate. At temperatures above the bay, rods (Figure 4(a)) occur prior to plates ($\uparrow$, Figure 4(b)) although the plates are difficult to find.

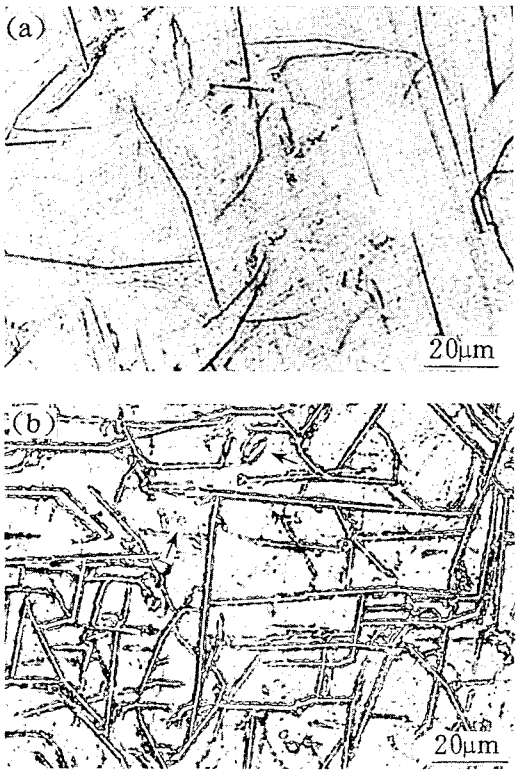


Fig. 2—Optical microscopy images of (*a*) single product (initial α_1 plates) and (*b*) mixed product (initial α_1 plates + α rods ($\uparrow$)) formed in Cu-Zn-Al alloy at 653 K for 10 and 600 s, respectively.

When the foil of Cu-Zn alloy is held at 543 K in high-temperature TEM, the $\beta' \rightarrow \alpha_1$ transformation can be observed *in situ* and it is found that each α_1 plate has a clear striation contrast ($\uparrow$) corresponding to stacking faults the moment it nucleates, and the initial plate ($\Uparrow$) also keeps this contrast, as shown in Figure 5. A new nucleus (point B) breaks out in front of the tip of an old nucleus or plate (point A) when the original nucleus grows to a degree, then the two nuclei combinate and continue to grow ($\Updownarrow$), as also shown in Figure 5.

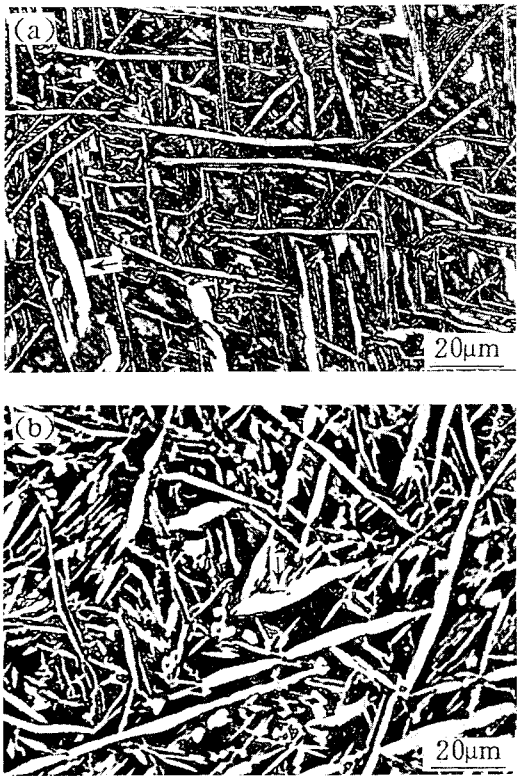


Fig. 3—Optical microscopy images of mixed product (initial α_1 plates + equilibrium α phase or late α_1 (α) plates ($\uparrow$)) formed in (*a*) Cu-Zn alloy at 523 K for 9000 s and (*b*) Cu-Zn-Al alloy at 653 K for 960 s.

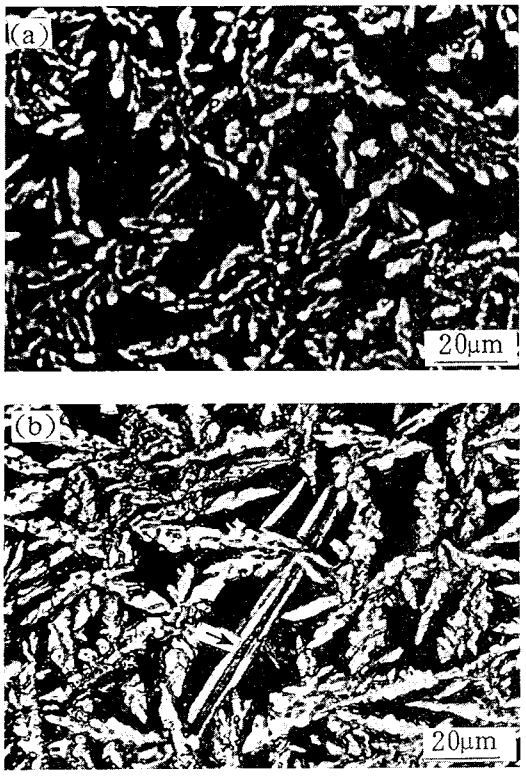


Fig. 4—Optical microscopy images of (*a*) single product (α rods) and (*b*) mixed product (α rods + initial α_1 plates ($\uparrow$)) formed in Cu-Zn-Al alloy at 743 K for 30 and 160 s, respectively.

Figure 6 is another example of this phenomenon; the new nucleus ($\uparrow$) in Figure 6(b) is induced near the tip ($\Uparrow$) of the α_1 plate. Figure 7 is a TEM photograph obtained statically. When the growing tip ($\uparrow$) of an α_1 plate formed in Cu-Zn-Al alloy meets the side of another plate, a new α_1 nucleus ($\Uparrow$) is also induced on the other side.

The detailed thickening process of an initial α_1 plate (A-A) formed in Cu-Zn alloy is observed *in situ* by high-temperature TEM, as shown in Figure 8. Similar to the result obtained in Cu-Zn-Al-Mn alloy by Han *et al.*,[5] the ledge (X, Y, Z, Figure 8) at the broad faces of the α_1 plate is observed. In fact, this ledge is similar to the superledge found in a hypereutectoid steel by Jin *et al.*[8] From the "macroscale," the superledge just moves along the direction of streaking contrast corresponding to stacking faults during the early stages (B-B and C-C) of thickening. The α_1 plate in Figure 9 is formed statically in Cu-Zn alloy. The double ledges ($\uparrow$) located at two

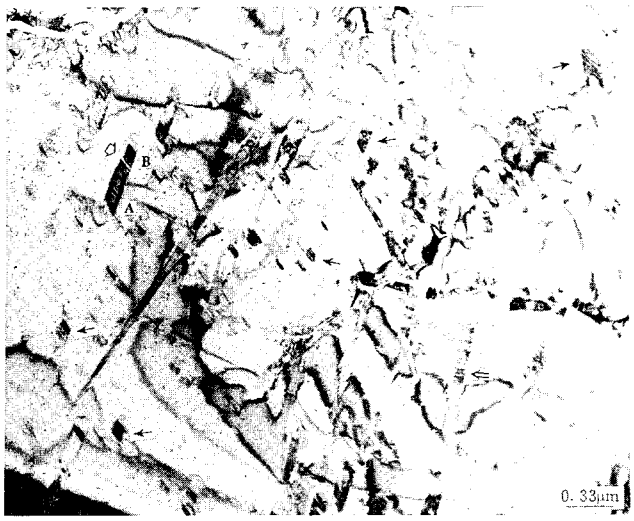


Fig. 5—High-temperature TEM image of the nucleation and growth of initial α_1 plates formed in Cu-Zn alloy at 543 K for 4800 s.

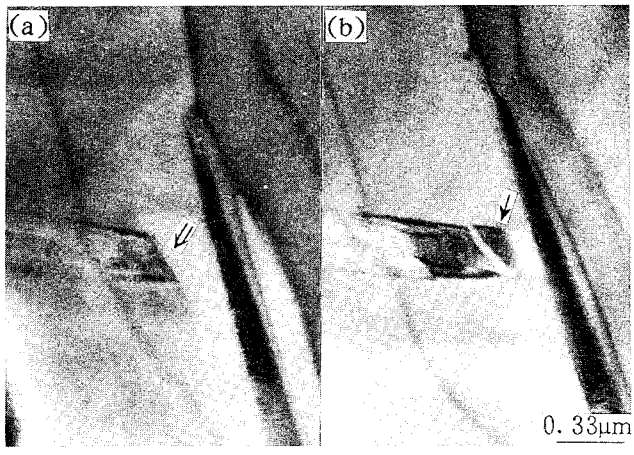


Fig. 6—High-temperature TEM image of a new nucleus ($\uparrow$, (*b*)) induced in front of the tip of an initial α_1 plate ($\Uparrow$, (*a*)) formed in Cu-Zn alloy. The heating temperature is 523 K.



Fig. 7—TEM image of two initial α_1 plates formed in Cu-Zn-Al alloy at 543 K for 1980 s.

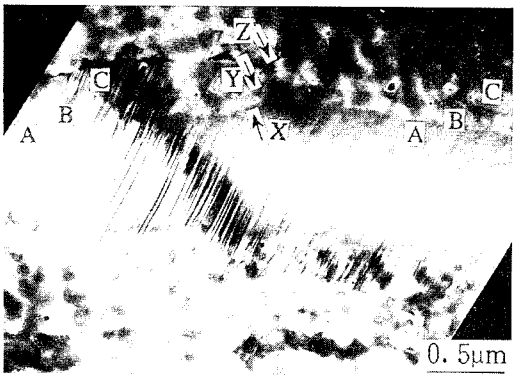


Fig. 8—Three stages of thickening (A-A, B-B, and C-C) of an initial α_1 plate formed in Cu-Zn alloy. The plate is first formed in a molten salt bath at 543 K for 2400 s (A-A) and then in a high-temperature TEM at 543 K (B-B and C-C).

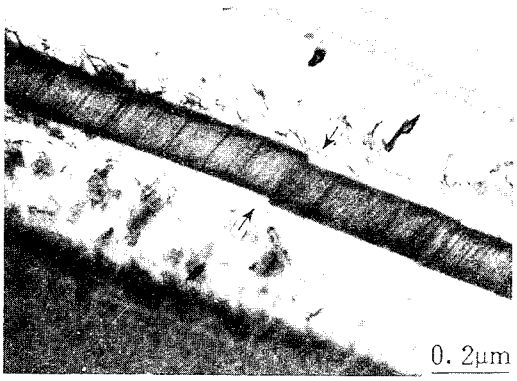


Fig. 9—TEM image of an initial α_1 plate formed in Cu-Zn alloy at 543 K for 3240 s.

broad faces along the direction of streaking contrast (corresponding to stacking fault faces) show clearly the feature of displacement between stacking faults. For another α_1 plate formed in Cu-Zn-Al alloy, the direction of streaking contrast can be resolved at point A and the displacement along the streaking contrast is also observed, as shown in Figure 10.

Figure 11 shows the subsequent thickening of a late α_1 (α) plate formed statically in Cu-Zn alloy at 543 K

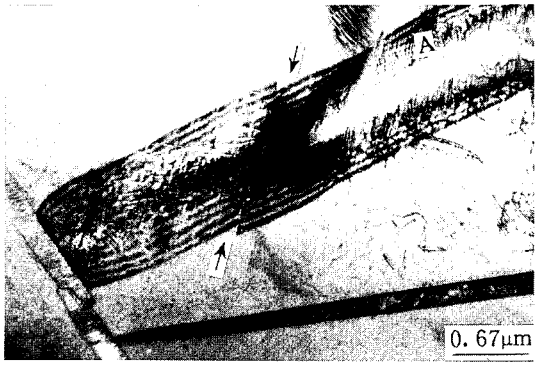


Fig. 10—TEM image of an initial α_1 plate formed in Cu-Zn-Al alloy at 563 K for 540 s.

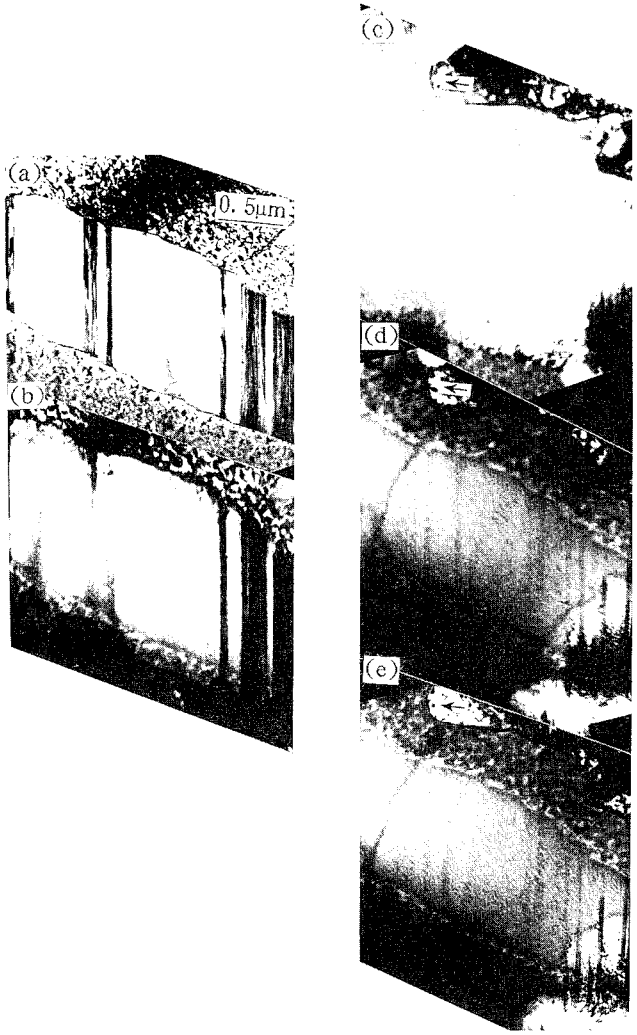


Fig. 11—The subsequent thickening process of a late α_1 (α) plate in the TEM specimen heating holder at 543 K for (*a*) 0 s, (*b*) 660 s, (*c*) 3000 s, (*d*) 3600 s, and (*e*) 4080 s. The late α_1 (α) plate is first formed in a molten bath at 543 K for 14400 s.

for 14,400 seconds. Superledge ($\uparrow$) clearly appears during thickening from Figures 11(c) through (e). One can find that the superledge moves only along the direction of original streaking contrast (A-A, Figure 11(a)).

This should indicate that the weak streaking contrast in Figures 6, 7, and 10 is possibly due to the value of $\mathbf{R} \cdot \mathbf{g}$ near zero or integer, where $\mathbf{R}$ and $\mathbf{g}$ are the vectors of fault and reflection, respectively.

IV. ANALYSIS AND DISCUSSION

A. *Mixed Product and Single Product*

Flewitt and Towner[9] designated the bay temperature in the TTT diagram as B_s, the α_1 plates start temperature, because they found that the plate-like α_1 product was formed only below the bay temperature. Nevertheless, the present results show that the α_1 plates, although accompanied by the α rods, may also be obtained at temperatures above the bay. Moreover, initial α_1 plates formed below the bay temperature will "degenerate" themselves into equilibrium α phase when the isothermal holding is prolonged. Therefore, only during shorter transformation time can the single-phase α (α rods, Figure 4(a)) or α_1 (initial α_1 plates, Figure 2(a)) product be obtained (corresponding to region R or P, respectively, in Figure 1). In general, a mixed α and α_1 product (Figures 2(b), 3, and 4(b)) occurs (corresponding to region M in Figure 1).

B. *Substructure of Initial α_1 Plates*

A TEM study made by Chattopadhyay and Aaronson[2] showed that no stacking faults were observed within an initial α_1 plate formed in a Cu-43.4 at pct (43.8 wt pct) Zn alloy, and no misfit dislocations were seen on the faces of this plate. Therefore, they concluded that the growth of the α_1 plate was different from that of martensite but consistent with the diffusion-controlled ledge growth mechanism. However, the plate observed in Figure 4 of their article was formed at 523 K enough to 9000 seconds. In fact, the composition of the present Cu-Zn alloy is quite near that of their alloy, but it is found that some of the α_1 plates formed at the same temperature for the same time described by them have been annealed out and transformed into equilibrium α phase (Figure 3(a)); hence, the mixed product ($\alpha_1 + \alpha$) occurs. It is well accepted that equilibrium α phase has no internal substructure. Moreover, the α_1 plate shown in Figure 4 of their article exhibits an aspect ratio, c/r, around 0.12, which is significantly larger than the usual value, approximately, 0.01, as well as a blunt plate tip and a wavy interface.[7] These features are possessed generally by equilibrium α phase. Therefore, it is doubtful whether the structure described as initial α_1 plates by Chattopadhyay and Aaronson truly represents initial α_1 plates. Han *et al.*'s TEM observation[5] showed that initial α_1 plates formed in a Cu-Zn-Al-Mn alloy have internal stacking faults. It proved to be true by the present high-temperature TEM *in situ* observation of the nucleation and growth of the α_1 plates (Figure 5). Therefore, so far as the faults substructure is concerned, there is no difference between initial α_1 plate and martensite.

C. *The Strain-Stress Field*

Takezawa and Sato[10] supposed that the nucleus of an α_1 plate is formed with shear, and hence, a special stress field may be reasonably produced at the tip of the nucleus. The present *in situ* observation of the formation of a new nucleus (or plate) in front of the tip of a plate ($\curvearrowright$ Figure 5 and $\uparrow$ Figure 6(b)) has proven directly the existence of the inducing effect of a strain-stress field. Moreover, the separated nuclei (or plates) imply that the strain-stress field is discontinuous. In Figure 7, the strain-stress field at the tip of the first plate may be transported across the second plate, which is met by the tip of the first plate on one side, and induce a new nucleus (or plate) on the other side; *i.e.*, the first plate "crosses over" the second and continues to grow. The discontinuous strain field at the tip of the initial bainitic plate formed in a Si alloyed steel is also observed by Gong *et al.*[11] It is the strong strain-stress field existing at the tip of the bainitic plate that makes the nucleation by "inducing" and the growth by crossing over possible, because this field can be transported by means of elastic wave and hence causes the induced strain. It is unimaginable that the growth by diffusion mechanism can produce so much strong strain-stress field at the tip of a plate.

D. *The Shear between Stacking Fault Faces*

The thickening kinetics of initial α_1 plates have been analyzed with Zener-Hillert's model by Yang *et al.*[12] recently. They found that the thickening process is only macroscopically controlled by volume diffusion, but the nature is a shear process. The present *in situ* observation (shown in Figure 8) further reveals that the atomic shear takes place between stacking fault faces, because the straight propagation trace of streaking contrast can be observed clearly during the plate thickening from A-A to B-B or C-C. Therefore, the shear direction is inconsistent with that reported formerly, *i.e.*, it is only along the trace of the β'/α_1 interface.[10] The present shear is also in conformity with that of ε-martensite nucleated by propagation of faults.[13] The double ledges at the broad faces of initial α_1 plates shown in Figures 9 and 10 are also convincible evidence for the shear between stacking fault faces. With the shear growth of an initial α_1 plate (Figure 10), the concentrated strain-stress field is produced. When the plate meets another, the "strong impact" causes a large magnitude of slip between the weak fault faces to release the strain energy.

Though the atomic movement during initial α_1 plates growing cannot be directly observed at present, it can still be proven that the superledge in Figure 8 displaces just along the streaking contrast during plate thickening. According to diffusional ledge mechanism, the ledge should displace laterally along the trace of the β'/α_1 interface to make the broad faces thickened. Therefore, the growth of an initial α_1 plate does not fit into the framework provided by diffusional ledge thickening. As for the formation of ledges, it is possibly due to the slipping of interfacial dislocation along stacking fault faces.

E. *Growth of Late α_l (α) Plates by Volume Diffusion*

The thickening kinetics of a late α_1 (α) plate shown in Figure 11 is modeled using a diffusional ledge model.[14] The calculated and measured values of maximum thickness are shown in Figure 12. By way of calculation, the thickening of the late α_1 (α) plate seems to be compatible with the ledge mechanism. However, the moving direction of the superledge ($\uparrow$, Figures 11(c) through (e)) formed during the thickening process is not along the lateral of the plate. Accordingly, it can be concluded by direct observation that the growth of the late α_1 (α) plate is dominated by volume diffusion rather than by diffusional ledge mechanism.

F. *A Possible Atomic Mechanism*

The shear behavior, characterized by shear between stacking fault faces, of initial α_1 plates and the volume diffusion nature of late α_1 (α) plates have been revealed in several aspects as discussed earlier. Referring to the shear model for martensitic transformation in Cu-Zn alloys[15] and the model of one-dimensional domain of multilayer structure,[16] the atomic process of the α_1 plate formation can be suggested as follows.

1. *Bain distortion for a bcc → fct transition*

The adjacent four original body-centered cubic (bcc) cells are defined as a unit, and a possible direction, for example, [001] is chosen as the Bain axis; then the parent bcc lattice can be transmitted to the face-centered tetragonal (fct) lattice, as schematically shown in Figure 13. The principal distortions for such a case are

$$\eta_1 = \eta_2 = \frac{a}{\sqrt{2a_a'}} (<1) \text{ and } \eta_3 = \frac{c}{a_\beta'} (>1)$$

2. *The generation of stacking faults and the formation of initial plates*

In the fct lattice obtained after the Bain distortion, the magnitude of slip by displacement of $a/6$ $[\bar{1}\bar{1}2]$ on every third (111) plane causes the 9R structure. Thus, the regularly spaced stacking faults are generated (ABCBCACABA, Figure 14(a)). Followed by an invariant lattice deformation (the secondary shear) between the stacking fault faces, the lattice structure of an initial α_1 plate is formed (Figure 14(b)). The lengthening and thickening of initial α_1 plates depend on the continuous generation of stacking faults and displacement between stacking fault faces, respectively.

3. *Initial α_l plates to late α_l (α) plates*

During the growth of the α_1 plates from initial stage to late one, the "overannealing" results in diffusion of solute or even solvent atoms' internal plates. As verified by many authors,[7,17] the diffusion brings about a structural change from the 9R structure into the face-centered cubic one. The present article shows that the thickening of late α_1 (α) plates is in contradiction to the diffusional ledge mechanism. Therefore, the growth process of late α_1 (α) plates may be a volume diffusion process. The lattice structure of a late α_1 (α) plate is schematically shown in Figure 15.

V. REMARKS

The experiment of Cliff *et al.* showed that the composition of an initial α_1 (or γ_1) plate was different from

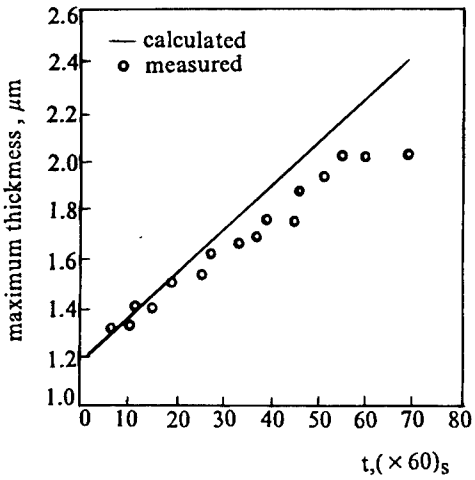


Fig. 12—The calculated and measured maximum thickness of a late α_1 (α) plate shown in Fig. 11.

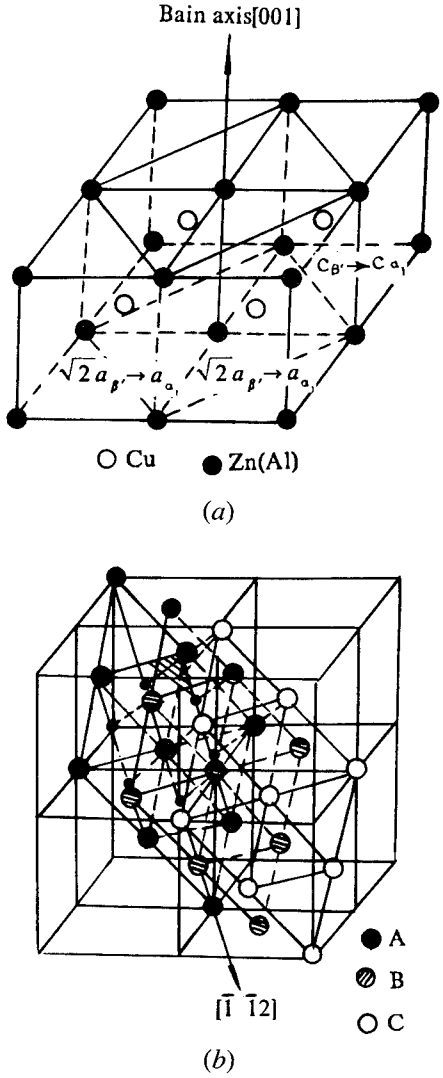
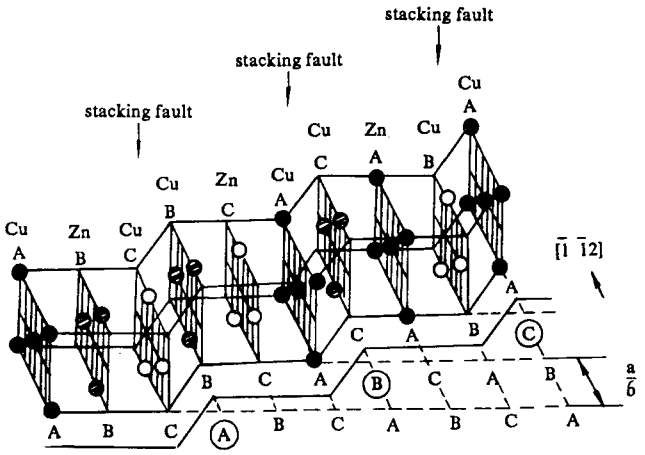
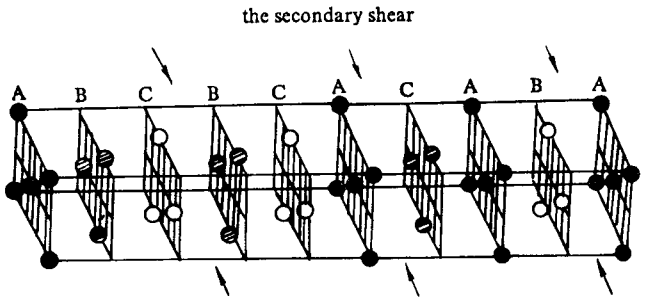


Fig. 13—Bain distortion for a bcc → fct transition: (*a*) bcc and fct lattice and (*b*) three adjacent (111) planes (A, B, C).



(*a*)



(*b*)

Fig. 14—The formation of initial α_1 plates: (*a*) atoms slipping on every third (111) plane and hence causing the deformed 9R multilayer structure (the atom plane corresponding to the shadow plane shown in Figure 13(b)); and (*b*) the secondary shear (invariant lattice deformation) causing the lattice structure.

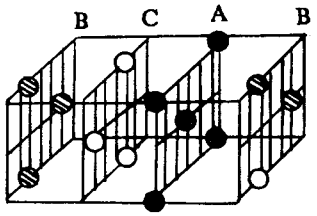


Fig. 15—The lattice structure of a late α_1 (α) plate.

that of the surrounding matrix.[3] The latest work conducted by Yang[18] also found that there was little composition difference between the growing tip of an initial α_1 plate and its adjacent matrix, while the composition at the two sides of the plate is obviously inconsistent with that at the matrix. It gives us the impression that the formation of initial α_1 plates is inconsistent with shear mechanism. However, this inconsistency is resolved by the assumption of the solute-depleted region formed within the incubation period.[17] According to the assumption, diffusion has already occurred in the matrix prior to transformation. As a result, the M_s temperature increases and a shear transformation becomes thermodynamically possible. On the other hand, the strain-stress field in front of the tip of an initial α_1 plate increases the driving force of transformation remarkably. Thus, the condition for thermodynamical shear may be met and the plate therefore formed by self-strain triggering.[19] Because of shear formation, the compression and tension stresses are produced in two sides of the plate, respectively.[10] The effective atomic radius of Cu was reported to be 0.128 nm and that of Zn to be 0.137 nm. Accordingly, the solute atoms with bigger radius at the tip of the plate would move from the compression region to the tension one. As a result, the new solute-depleted region is formed and hence the bainite plate keeps growing by shear. Moreover, at the growing tip, the driving force for the shear formation may be obtained by removing only a few solute atoms because of the small radius of curvature. But to the broad face of the plate, due to its planar boundary, much more solute atoms must be shifted to get enough driving force for the shear transformation. This is why the composition difference between the growing tip and the adjacent matrix is not obvious but between the side of the broad face and the matrix is quite evident. Nevertheless, Hsu inferred that the effect of the bainite incubation period was far from the process of the formation of solute-depleted region by their internal friction measurement[20] and denied the shear mechanism of bainite formation in terms of their thermodynamics analyses.[4] No matter what controversy may arise, the present results by means of optical microscopy, TEM, and high-temperature TEM support convincingly the conclusion of the shear formation of initial α_1 plate. The volume diffusion only dominates the growth of late α_1 (α) plates, *i.e.*, equilibrium α phase.

REFERENCES

1. H.K.D.H. Bhadeshia: *Mater. Sci. Forum*, 1990, vol. 56–58, pp. 263-74.
2. K. Chattopadhyay and H.I. Aaronson: *Acta Metall.*, 1986, vol. 34, pp. 695-711.
3. G. Cliff, F. Hasan, G.W. Lorimer, and M. Kikuchi: *Metall. Trans. A*, 1990, vol. 21A, pp. 831-35.
4. T.Y. Hsu and X.W. Zhou: *Acta Metall. Mater.*, 1991, vol. 39, pp. 2615-19.
5. M. Han, F.M. Chen, J.M. Chen, Y.R. Chen, and W.X. Liu: *Acta Metall. Sinica*, 1990, vol. 26, pp. A81-A85.
6. J.X. Dong, F.M. Chen, J.M. Chen, and W.X. Liu: *Acta Metall. Sinica*, 1990, vol. 26, pp. A467-A469.
7. M.H. Wu, J. Perkins, and C.M. Wayman: *Acta Metall.*, 1989, vol. 37, pp. 1821-37.
8. Q. Jin, H.S. Fang, J.J. Cao, Y.K. Zheng, and X.Y. Chen: *Acta Metall. Sinica*, 1990, vol. 26, pp. A391-A395.
9. P.E.J. Flewitt and J.M. Towner: *J. Inst. Met.*, 1967, vol. 95, pp. 273-80.
10. K. Takezawa and S. Sato: *Metall. Trans. A*, 1990, vol. 21A, pp. 1541-45.
11. F.Y. Gong, Y.R. Chen, J.M. Chen, Q.S. Liu, and L.B. Yang: Chinese Society of Metals, Beijing, *Proc. 2nd Nat. Conf. on Bainitic Reaction*, Emei, China, 1990, pp. 77-79.
12. Y.Q. Yang, D.H. Liu, M.K. Kang, and Y. Sun: *Acta Metall. Sinica*, 1992, vol. 28, pp. A95-A99.
13. H. Fujita and S. Ueda: *Acta Metall.*, 1972, vol. 20, pp. 759-67.
14. X.K. Meng, M.K. Kang, Y.Q. Yang, X.N. Zhao, and J.M. Hong: *J. Chin. Elec. Micro.*, 1993, vol. 12, No. 4.
15. I. Cornelis and C.M. Wayman: *Acta Metall.*, 1974, vol. 22, pp. 291-300.
16. W.X. Liu, X.Y. Huang, and Y.R. Chen: *The Microstructure Analyses by Electric Microscopy*, Tianjin University Press, Tianjin, 1989, pp. 328-39 (in Chinese).

17. Y. Nakata, T. Tadaki, and K. Shimizu: *Mater. Trans. JIM*, 1989, vol. 30, pp. 107-16.
18. Y.Q. Yang: Ph.D. Thesis, Northwestern Polytechnical University, Xi'an, People's Republic of China, 1991, pp. 70-80.
19. Q.M. Wei: Ph.D. Thesis, Northwestern Polytechnical University, Xi'an, People's Republic of China, 1991, pp. 30-54.
20. T.Y. Hsu: *J. Shanghai Met.*, 1991, vol. 13, pp. 7-12 (in Chinese).

Growth Kinetics and High-Temperature TEM *in situ* Observation of Bainite in a Cu-Zn Alloy

Y.Q. YANG, D.H. LIU, X.K. MENG, and M.K. KANG

A kinetics study with *in situ* observation of the growth process of bainitic plates in a Cu-Zn alloy was conducted by means of high-temperature transmission electron microscopy (TEM). The lengthening and thickening rates of bainitic plate were measured and analyzed, respectively. It was pointed out that the measured lengthening rate of bainitic plate is not consistent with Trivedi's model and that the thickening process is only macroscopically controlled by volume diffusion, although its thickening kinetics is inconsistent with diffusional ledge mechanism. It was found that the stacking-fault substructure exists just in the growing tip of fresh bainitic plate and so does the shear stress field in the matrix around the tip. Superledges in the interphase boundaries of bainite were found but their moving direction is not the same as that predicted by ledge mechanism. The degeneration of bainite to equilibrium α phase was also observed. The shear mechanism of bainitic transformation in Cu-Zn alloy is supported by this investigation.

I. INTRODUCTION

A bainitic transformation in β brasses has been widely studied since the 1950s. Nevertheless, its mechanism is not yet clear. Studies of crystallography[1,2,3] showed that surface relief, habit plane, and orientation relationship of bainite are the same as those of martensite, respectively. Bainite in its early growth stage inherits the ordered structure of the matrix.[4] Therefore, bainite forms by shear. But, thermodynamic calculations[5] indicated that bainite can only form by volume diffusion. It was found by transmission electron microscopy (TEM) at room temperature that the fresh bainite is fully coherent with the matrix and free of internal substructure.[6] So, it is inconsistent with the phenomenological theory of martensite. Growth kinetics studies by optical microscopy or by TEM at room temperature also showed that bainite grows by volume diffusion.[6,7] However, it should be pointed out that the optical microscopy used in kinetics studies does not seem accurate enough to measure the growth rates of very fine bainitic plates and that it is not clear whether or not the bainite plates observed statically by TEM at room temperature can really represent their different growth stages. On the other hand, some features which may be important in understanding the mechanism of bainite formation cannot be found at room temperature after quenching because these features may appear only during the growth of bainite. Therefore, in this article, high-temperature TEM was used to study the growth kinetics and to observe *in situ* the growth process of bainite in a Cu-Zn alloy.

Y.Q. YANG, formerly with Northwestern Polytechnical University, is Postdoctoral Researcher, National Laboratory of Solid States Microstructure, Nanjing University, Nanjing, People's Republic of China. D.H. LIU, formerly with Northwestern Polytechnical University, is Lecturer, Pingyuau University, Xingxiang, People's Republic of China. X.K. MENG, Ph.D. Candidate, and M.K. KANG, Professor, are with the Department of Materials Science and Engineering, Northwestern Polytechnical University, Xian, People's Republic of China.

This article is based on a presentation made at the Pacific Rim Conference on the "Roles of Shear and Diffusion in the Formation of Plate-Shaped Transformation Products," held December 18–22, 1992, in Kona, Hawaii, under the auspices of ASM INTERNATIONAL's Phase Transformations Committee.

II. EXPERIMENTAL PROCESSES

A Cu-42.85Zn (wt pct) alloy was prepared by melting high-purity (99.99 pct) Cu and Zn in a graphite crucible. The ingot, with a dimension of 80-mm diameter, was homogenized at 800 °C for 48 hours and a 10-mm outer layer of the ingot was machined off so that the entire layer of Zn sublimation was eliminated. The machined bar was forged into rods of 20 mm in diameter. Specimens 1 mm in thickness were cut from the rods and betanized in a molten salt bath at 790 °C for 3 minutes before water quenching to room temperature. The thin foils made from the quenched specimens, after final thinning, were held at 230 °C, 250 °C, and 270 °C, respectively, in a Phillips EM400 TEM and observed as bainite formed. No reversible martensitic transformation occurred during heating in the TEM, because the Ms temperature of this alloy is below room temperature.[2]

III. RESULTS AND DISCUSSION

A. *Growth Rates of Bainitic Plate*

The growth process of a bainite plate in the foil holding at 270 °C in TEM is shown in Figure 1. After holding for 78 minutes, the plate forms and lengthens rapidly but thickens slowly. When the holding time is 91 minutes, the plate grows in a direction which makes an obtuse angle with its initial growth direction. At 96 minutes of holding time, due to impingement with another plate, the bainite plate stops lengthening but continues to thicken slowly. The maximum length is 23.6 μm, and the measured value of lengthening rate is 2.23×10^{-8} m/s, as shown in Figure 2(a). A parabolic curve of the half-thickness *vs* holding time is seen in Figure 2(b).

If the lengthening of bainitic plate is controlled by



Fig. 1—The growth process of a bainitic plate in the sample held at 270 °C in TEM: (*a*) 80 min; (*b*) 81 min; (*c*) 89 min; (*d*) 96 min.

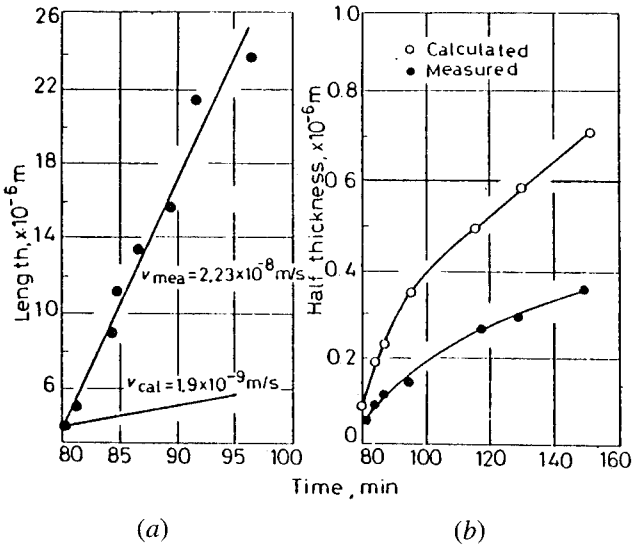


Fig. 2—The measured and calculated values of (*a*) lengthening rate and (*b*) half-thickness of bainitic plate in CuZn alloy.

volume diffusion, the diffusivity and the molar volume of solute are independent of concentration and the interface migrates at a constant rate. If the effects of the anisotropy of strain energy and interfacial energy are neglected, Trivedi's model of lengthening kinetics yields:[7,8]

$$\Omega_0 = \sqrt{\pi P}\, e^P[1 - \mathrm{erfc}(\sqrt{P})]\left[1 + \frac{V}{V_c}\Omega_0 S_1\{P\} + \frac{\rho_c}{\rho}\Omega_0 S_2\{P\}\right] \quad [1]$$

According to Zener's maximum growth rate hypothesis,[7]

$$\frac{\partial \Omega_0}{\partial \rho} = 0 = \frac{\Omega_0}{2P}(2P+1) - \frac{\Omega_0}{\sqrt{\pi P}e^P[1 - \mathrm{erfc}(\sqrt{P})]} + \sqrt{\pi P}e^P[1 - \mathrm{erfc}(\sqrt{P})]\left[\frac{V}{V_c}S_1'\{P\} + \frac{\rho_c}{\rho}S_2'\{P\} - \frac{\rho_c}{\rho}S_2\{P\}\right] \quad [2]$$

When interface kinetics are neglected, Eq. [1] becomes:

$$\Omega_0 = \sqrt{\pi P}e^P \mathrm{erfc}(\sqrt{P})\left[1 + \frac{\rho_c}{\rho}\Omega_0 S_2\{P\}\right] \quad [3]$$

where Ω_0 is dimensionless supersaturation defined as $(C_0 - C_\infty)/(C_0 - C_P)$ in which C_0 and C_P are respectively the concentration in bainite and in the matrix at the bainite/matrix interface, and C_∞ is the initial concentration in the matrix; V is the lengthening rate of the bainitic plate; V_c is the migration rate of a flat interface when controlled only by the interfacial kinetics; ρ is the radius of curvature at the tip of the plate; ρ_c is the critical equilibrium radius equal to $[C_0(1 - C_0)/(C_\infty - C_0)(C_P - C_0)]\ (\sigma V_{\alpha 1}/\mathrm{R}Te_{1\beta'})$ in which σ is the interfacial free energy, $V_{\alpha 1}$ is the molar volume of bainite, R is the gas constant, T is the absolute temperature, and $e_{1\beta'}$ is a thermodynamical parameter; P is the dimensionless Peclet number equal to $V_\rho/2D$ in which D is the diffusivity of solute; and $S_1\{P\}$ and $S_2\{P\}$ are mathematically complicated functions.

Equations [2] and [3] are used for calculation. The numerical values of the parameters used in calculation are as follows: C_P = 42.85 pct, C_0 = 36 pct, and C_∞ = 46.5 pct according to the CuZn equilibrium phase diagram,[9] σ = 0.25 J/m^2 for semicoherent interface,[7] $e_{Zn\beta'}$ = 13,[10] $V_{\alpha 1} = 7.8 \times 10^{-6}$ m^3/mol[7] and $D = 4.65 \times 10^{-16}$ m^2/s.[9]

The result calculated with the computer is $V_{cal} = 1.9 \times 10^{-9}$ m/s which is one order of magnitude smaller than the measured one, as shown in Figure 2(a). So large of a discrepancy between the measured and the calculated values indicates that the lengthening of bainitic plate is not consistent with Trivedi's volume diffusion model.

Because the measured curve of half-thickness *vs* holding time is a parabolic one which is consistent with Hornbogen's result,[3] the thickening is not consistent with a diffusion-controlled ledge mechanism in which the thickening kinetic curve is linear because of a ledge spacing of 0.5 to 1 $\times 10^{-7}$ m in a Cu-Zn alloy held at 250 °C to 270 °C, as indicated by Chattopadhyay and

Aaronson,[6] and this is also confirmed later. Therefore, the Zener's volume diffusion-thickening model which is consistent with the parabolic feature is used. The model is shown in the following:[11]

$$X = L\sqrt{Dt} \qquad [4]$$

$$\Omega_0 = \frac{\sqrt{\pi}}{2} L \exp\left(\frac{L^2}{4}\right) \operatorname{erfc}\left(\frac{L}{2}\right) \qquad [5]$$

where L is a dimensionless growth coefficient which depends only on Ω_0, t is the growth time and the meanings of the other parameters are the same as those mentioned earlier. The measured and calculated curves of half-thickness *vs* time are shown in Figure 2(b). Because the thickening kinetics of bainite in so-treated specimen is smaller than that in the specimen quenched directly to and held in the temperature range of bainite formation,[6] from Figure 2(b), one may conclude that the thickening of the bainite plate is identical with Zener's volume diffusion model. The thickening is macroscopically controlled by volume diffusion.

B. *Growth Activation Energy of Bainite*

Activation energy is the increased energy of the atoms' migration from one equilibrium position to another. If the controlling factor of phase transformations is different, then the activation energy is not the same. So the calculation of activation energy is helpful for understanding the mechanism of bainitic transformation.

The Arrhenius equation was used to calculate the growth activation energy:[12]

$$V = V_0 \exp\left(-\frac{Q}{RT}\right) \qquad [6]$$

where V is the growth rate which can be determined from the experiment, V_0 is the pre-exponential term, and Q is the growth activation energy. Then the activation energy may be written as

$$Q = -R\frac{\partial(\ln V)}{\partial(1/T)} \qquad [7]$$

The curves of (ln V) *vs* ($1/T$) is drawn according to experimental data, as shown in Figure 3. Then the activation energy can be determined from Figure 3 in terms of Eq. [7]. The calculated lengthening activation energy is 25.15 KJ/mol which is much smaller than the diffusion activation energy of Zn atoms in the ordered matrix β' (which is 135 or 150 KJ/mol[13]) but very close to the growth activation energy of martensite in a Cu-Al-Ni alloy (which is 21.08 KJ/mol[12]). Therefore, from the point of view of energy, the lengthening of bainite is a shear process similar to martensite transformation, which is also supported by comparing its measured lengthening rate with a calculated one according to Trivedi's volume diffusion model.

However, previous results only exhibit the macroscopical features of bainite growth. Perhaps it is not enough to explain the mechanism of bainite formation only with these macroscopical results. Therefore, in the rest of this article, we show the details of bainitic plates in their growing process observed *in situ* by high-temperature TEM.

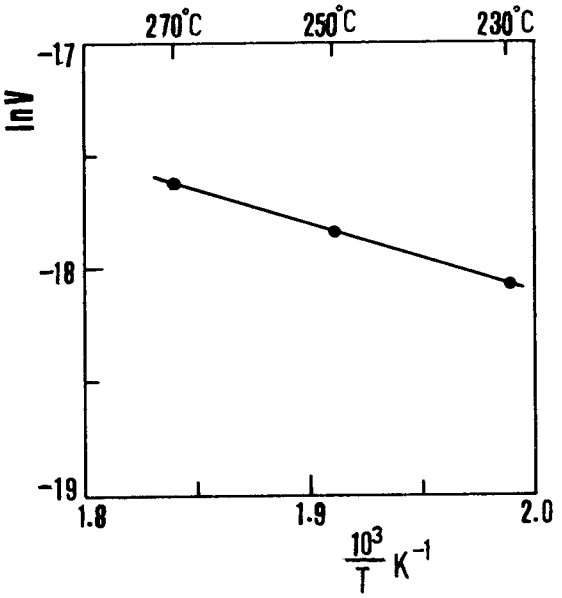


Fig. 3—The ln V *vs* $1/T$ relationships for lengthening of bainite plates.

C. *Stacking-Fault Substructure*

In terms of the crystallographic theory of martensitic transformation, there are two kinds of deformation, *i.e*, lattice deformation which changes the lattice of matrix into that of martensite and lattice invariant deformation which keeps the habit plane as an invariant plane and produces internal substructure. Therefore, if bainite forms by shear as in a martensite transformation, the internal substructure must exist in a fresh bainite plate. The stacking-fault substructure of bainite in Cu-Zn and Cu-Zn-Al alloys can be seen everywhere.[1–4] Cornelis and Wayman[2] have further pointed out that there exist regularly distributed stacking faults and extra disordered stacking faults in bainite according to their TEM observation and crystallographic analysis. But, as described in Section I, Chattopadhyay and Aaronson[6] observed a small bainite plate which formed at 250 °C holding for 150 minutes and found that no internal substructure exists in the plate. However, according to its wavy interface with matrix β', Wu *et al.*[4] thought that this plate may not be a really fresh bainite plate. They found that the stacking-fault substructure indeed exists in fresh bainite. Although many authors have reported the existence of the stacking-fault substructure in fresh bainite, in those static observations, what really is the fresh bainite may be easily questioned.

However, in this *in situ* observation, it was found that the stacking-fault substructure indeed exists in fresh-formed bainite plates in the specimens held at all three experimental temperatures. As shown in Figure 4(a), the stacking-fault substructure can be clearly seen in growing bainite plates, especially in their growing tips which are no doubt the fresh-formed ones. A more clear

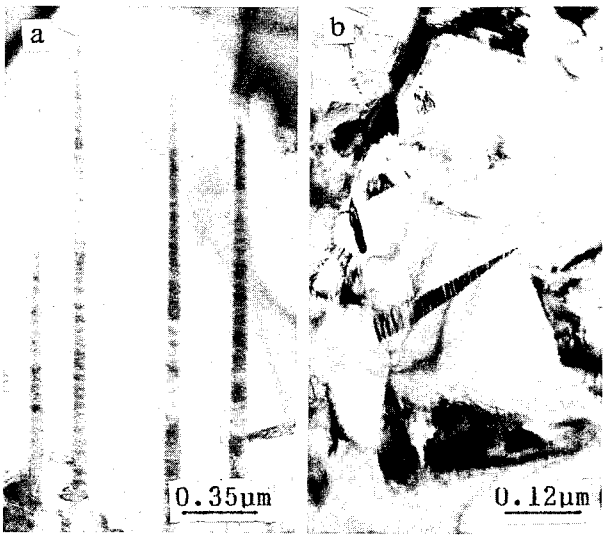


Fig. 4—The stacking-fault substructure in fresh-formed bainitic plates. (*a*) High temperature *in situ* observation in the sample holding at 250 °C. (*b*) The sample which was held at 250 °C in TEM and cooled rapidly to room temperature when bainitic plate just formed.

stacking-fault substructure can be observed in the specimen which was held at 250 °C in TEM and cooled rapidly to room temperature when bainite just formed, as shown in Figure 4(b). This bainitic plate is 266 nm in length and its maximum thickness is only 36 nm. It should be emphasized that the growing tip of this plate is very thin (at least, thinner than that observed by Chattopadhyay and Aaronson[6]) and there also exist the stacking-fault substructure.

D. *The Observation of Shear Stress Field*

It is known that, because of the curvature of the TEM thin-foil specimen which is bent a little, strong electron diffraction occurs at some atomic planes which are consistent with Bragg's condition, and so, the bend-extinction contours appear. Takezawa and Sato[14] have proposed a shear stress field around the tip of a bainite plate in order to explain the composition difference at opposite sides of a bainite plate, but they did not confirm the existence of the shear stress field experimentally. However, if bainite growth is accompanied with the shear stress field, when the bainite grows through the bend-extinction contour, it is predicted that the curvature of the thin foil will locally change under the action of the shear stress field. Therefore, the bend-extinction contour will be sharply twisted at opposite sides of the bainite plate, and this phenomenon can only be seen during the growing process of a bainite plate observed *in situ* by TEM. Figures 5 and 1(a) show us the sharply twisted bend-extinction contour by single arrows, which indicate the shear feature of bainite formation. In Figure 5, one can find that there is an identical change of the bend-extinction contour at the tips of the bainite plates which are parallel to each other. Therefore, the stress in the matrix between two parallel bainite plates can partly counteract, and it is favorable to relax the

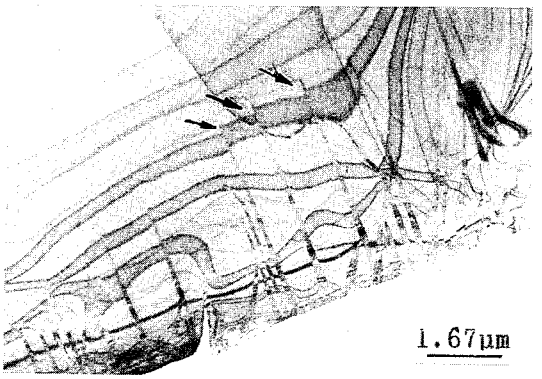


Fig. 5—The change of bend-extinction contour when bainitic plates grow through it.

stress in the matrix. However, the bend-extinction contour becomes continuous at the medial part of the bainitic plates shown in Figure 5. This means that the shear stress field is gradually relaxed as the bainitic plates continue growing. Meanwhile, it also implies that the twisted bend-extinction contour is not induced by the surface relief.

In fact, the shear feature of bainite formation can also be shown by other phenomena. For example, as shown in Figure 6, the intersecting and the branching of bainite plates were observed very often in copper-base alloys. A simple crystallographic analysis[15] eliminates the possibility of sympathetic nucleation.[16] In fact, when a bainite plate encounters a second plate during its growing, another plate can be induced at the other side of the second one by the shear stress field which can spread over the obstacle as an elastic wave, which is very similar to that of martensitic transformation.[17]

Examining Figure 6(a) in detail, one can find that, under the action of the stress field, the contrast change appears within the bainitic plate just in front of the tip of another plate which encounters the first one, as shown by single arrows. It is also believed that the contrast is produced by the shear stress accompanying bainite formation. Some contrast change also appears at the two sides of the bainite plate indicated by the double arrow in Figure 6(a). Therefore, the shear stress field exists not only in lengthening but also in thickening of a bainite plate. According to the study of interfacial structure of bainite in β brasses, the interfacial dislocation can move conservatively on the stacking-fault plane in the normal direction to the interface.[18] Therefore, although the thickening of bainite shows macroscopically the feature of volume diffusion control as mentioned previously, its atomic mechanism may still be a shear process.

E. *The Movement of Growth Ledges*

Many articles concerned the growth ledges of bainite, and some superledges have been published.[19] We also find superledges during the process of bainite thickening. However, the TEM *in situ* observation clearly shows that, as a bainite plate thickens, the superledges do not move laterally as predicted by diffusional ledge

mechanism,[20] but they move in the direction of stacking-fault propagation on the stacking-fault plane. Figure 7 shows the successive movement of a superledge from 1 to 3 as the whole plate thickens. This observation is in disagreement with the theoretical prediction of diffusional ledge mechanism.

F. *Degeneration of Bainite Plates*

After a bainite plate stops growing, if the holding time is extended or the holding temperature is increased, the stacking-fault substructure of bainite anneals out gradually, *i.e.*, the bainite degenerates gradually to equilibrium α phase with a face-centered cubic (fcc) crystal structure and grows again.[3,14] Finally, the whole plate degenerates into an equilibrium α phase. As shown in Figure 8, after stopping growth at 250 °C, a bainitic plate becomes an equilibrium α phase at 310 °C which is still in the temperature range of bainite formation. Because bainite with 9R structure is thermodynamically metastable, it tends to transform into stable α phase. In this process, the extra solute atoms[14] in bainite would diffuse into the surrounding matrix. As a result, the stacking substructure is gradually eliminated, and the interfacial structure is changed.[18] Bhadeshia[19] has reported the degeneration of bainite in ferrous alloys held in the bainite-formation temperature range for a long time and pointed out that the degeneration process is not the same as the mechanism of bainite formation. However, the degeneration of bainite in copper-base alloys

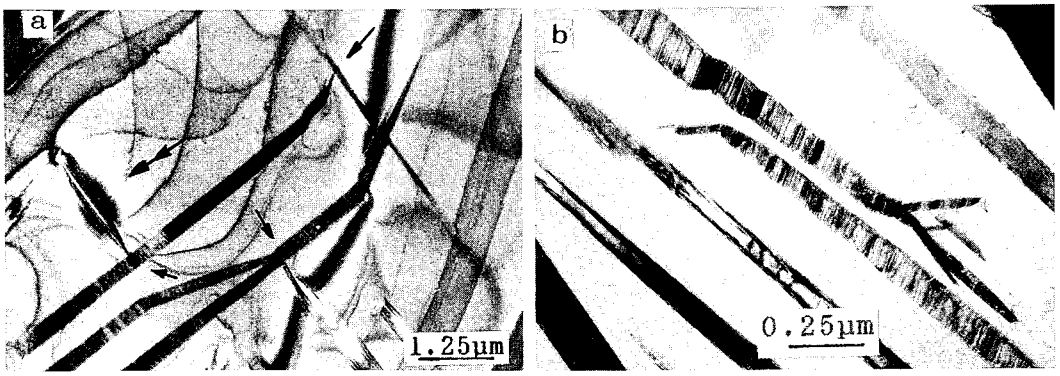


Fig. 6—Stress-induced growth of bainite plates showing with intersecting (*a*), branching and kink (*b*) morphology.



Fig. 7—Three growth stages of a bainitic plate showing the movement of super ledge with arrows; the sample was first held in a molten salt bath at 270 °C for 40 min, then in TEM at the same temperature for 40 min.

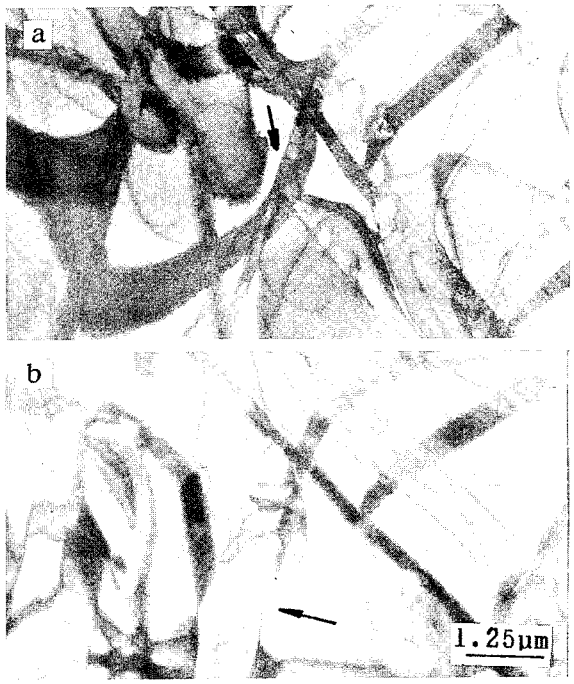


Fig. 8—Degenerating of bainitic plate to equilibrium α phase holding at (*a*) 250 °C and (*b*) 310 °C after the plate stops its growth at 250 °C.

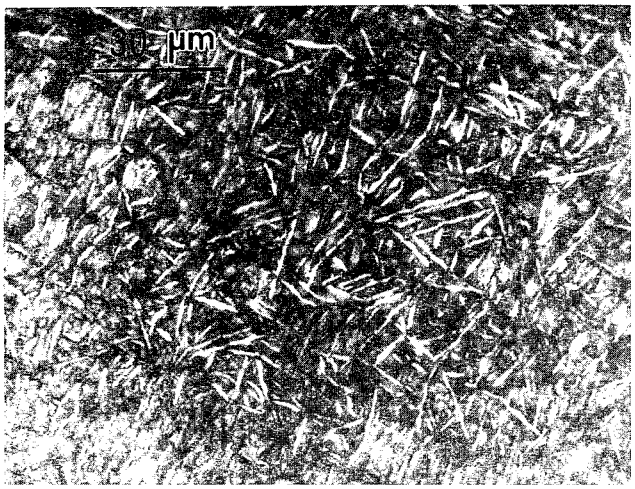


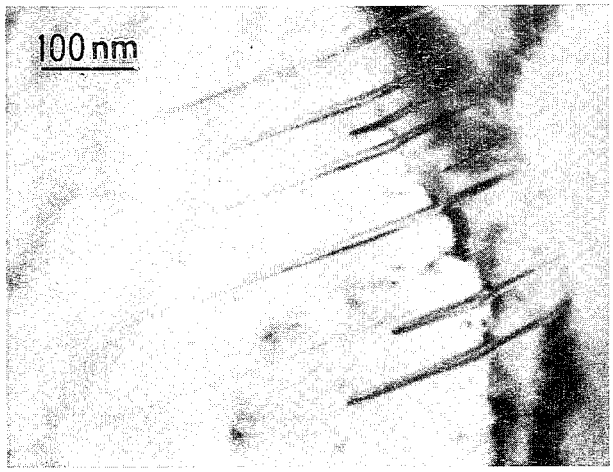
Fig. 1—Microstructure of the specimen (623 K, 1 min).

fcc/dhcp transformations). The present experimental observation shows no such internal inhomogeneity in the α_1 plates, so the bainitic transformation in Cu-Zn-Al alloys is considered inconsistent with the shear mechanism.

Chattopadhyay and Aaronson[5] studied the bainitic transformation in brass and found a similar result. They found that α_1 plates are coherent with the matrix during their initial growth stage, free of stacking faults, and possess misfit dislocations after they reach a size of 200 to 300 nm. On the contrary, the martensite α_1' plates exhibit the previously mentioned defects, which means that they produce the LID. So Chattopadhyay and Aaronson proved that α_1 plate cannot be formed by a shear mechanism.

But Wu *et al.*[3] disagreed with Chattopadhyay and Aaronson's conclusions. They argued that the coherent α_1 plates shown in Figure 4 of Chattopadhyay and Aaronson's article[5] exhibit a significantly large aspect ratio, c/r, around 0.12, as well as a blunt plate tip and a wavy interface, which is inconsistent with the reported α_1 plate morphologies for aspect ratios around 0.01, which have a sharp plate tip, a 9R long-period stacking order structure, and a randomly faulted fine structure. Wu *et al.* questioned whether the structure described as initial α_1 plates by Chattopadhyay and Aaronson truly represents initial α_1 plates, as Chattopadhyay and Aaronson provided no detailed diffraction information to support their interpretation.

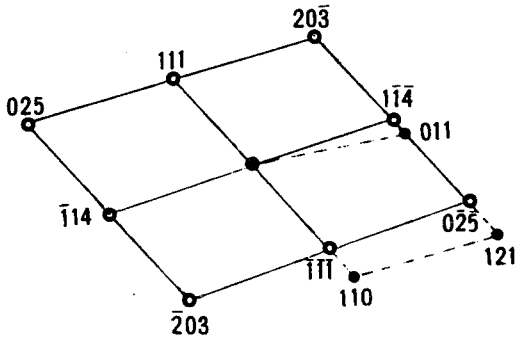
In fact, the conditions of the experiment described in the present article are almost the same as those of Wu *et al.* (Table I). It has been shown that there are no stacking faults or other internal substructures inside the initially formed bainites. This indicates that α_1 plates are free of substructures during their initial stage, confirming the observation of Chattopadhyay and Aaronson[5] and contrary to the requirements of the shear mechanism of formation. As time progresses, stacking faults appear inside the α_1 plates, as shown in Figure 3. The appearance of the stacking faults might result from the difference in the specific volume between the bainite and the matrix phases (according to a rough calculation, the specific volume difference amounts to 8 pct). At the initial transformation stage, the transformation product is so small that there is no obvious change inside the bainites. The difference of the total volume between these two phases increases gradually as the transformation continues. When the resulting elastic strain energy reaches a certain level, the strain has increased to such an extent that stacking faults form inside the bainites, as the stacking fault energy of this alloy is very low.



(*a*)



(*b*)



(*c*)

Fig. 2—Initial α_1 plates: (*a*) TEM micrograph after holding at 623 K for 10 s; (*b*) small-angle diffractometer pattern, consistent with $[1\bar{1}1]_{B2}//[3\bar{5}2]_{\alpha_1}$; and (*c*) indexing result.

Table I. Comparison between the Specimen Conditions of Wu et al.[3] and the Present Study

Conditions	Wu *et al.*	Present Study
Composition (wt pct)	Cu-26.67Zn-4Al	Cu-25.9Zn-3.75Al
Isothermal temperature (K)	623	623
Time (s)	10	10
Aspect ratio (c/r)	0.01	0.01 to 0.02

B. *Three-Dimensional Superledges on α_1 Plates*

So far, ledges on platelike precipitates have been found in both ferrous alloys and nonferrous alloys.[9–12] Also, using the results of a large number of experimental observations, this article will provide a detailed description of superledges and discuss their mobility.

Figure 4(a) shows the morphology of the interphase boundary between an α_1 plate and the matrix. It is a dark-field micrograph imaged using the $2\bar{1}\bar{5}$ reflection in Figure 4(b). From the thickness fringes, the three-dimensional ledges on the broad face of the plate can be judged without any doubt. The ledge indicated by arrow A is about 80-nm high, while the array of small ledges indicated by arrows have a height of approximately 2 nm.

Christian and Edmonds have suggested that superledges cannot exist because the Burgers vector associated with the riser of a superledge is too large.[13] The experimental observation of the three-dimensional ledges shown in Figure 4(a) (also Figure 5) conflicts with this viewpoint. Considering previous studies,[9–12] we conclude that superledges do exist on the broad faces of bainites in both ferrous and nonferrous alloys.

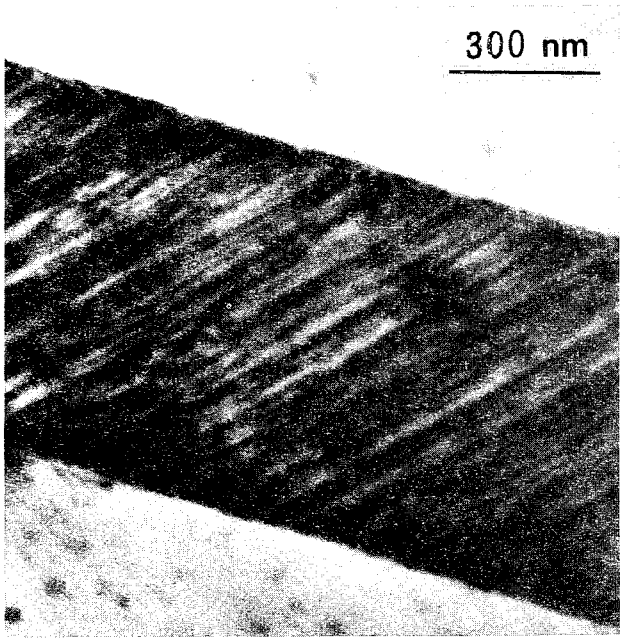
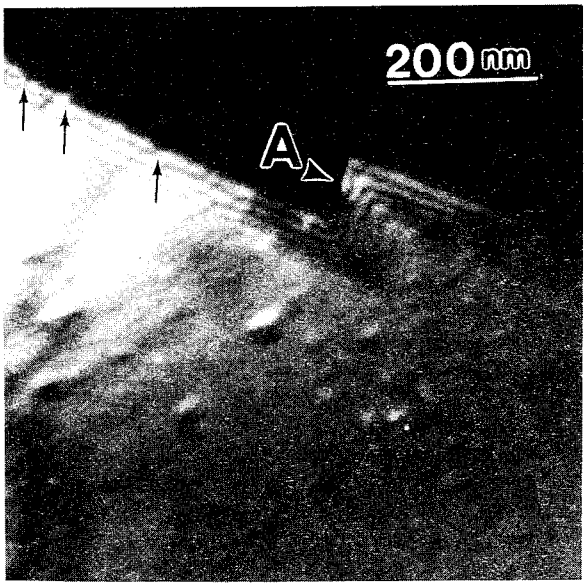


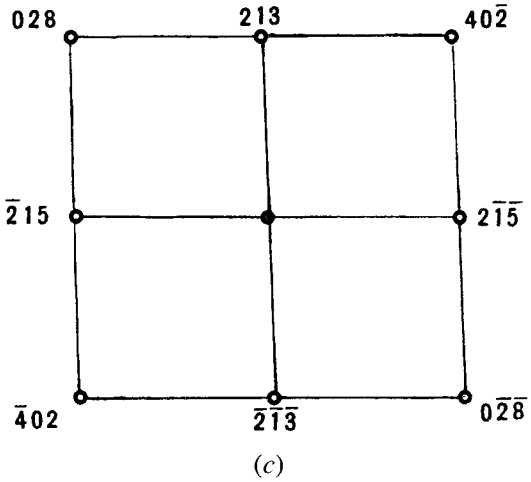
Fig. 3—Stacking fault substructure of an α_1 plate (623 K, 1 min).



(*a*)

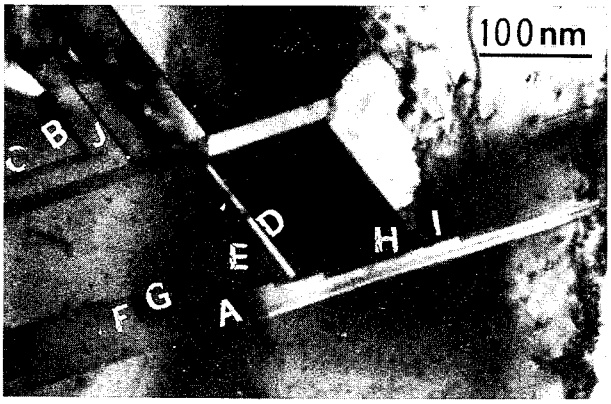


(*b*)

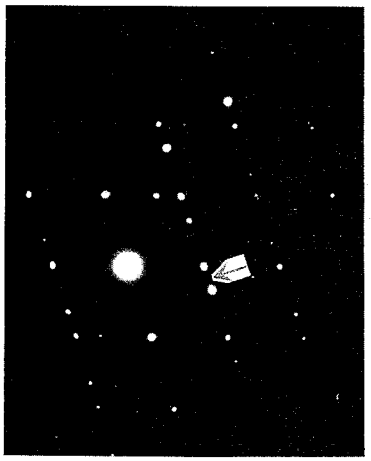


(*c*)

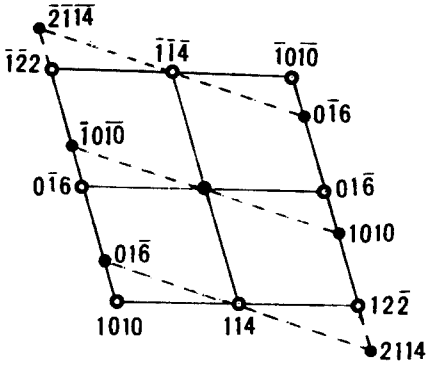
Fig. 4—Three-dimensional superledges of a bainite (623 K, 3 min): (*a*) dark-field micrograph imaged using the $2\bar{1}\bar{5}$ reflection of (b); (*b*) diffraction pattern, the zone axis is $[1\bar{8}2]_{\alpha_1}$; and (*c*) indexing result.



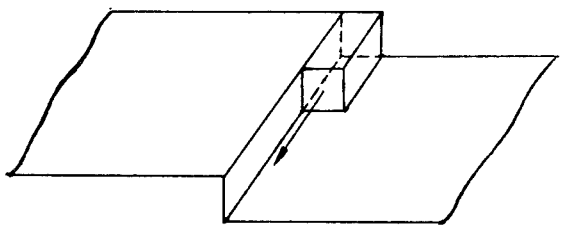
(*a*)



(*b*)



(*c*)



(*d*)

Fig. 5—Superledges of bainites (623 K, 5 min): (*a*) bright-field micrograph; (*b*) small-angle diffractometer pattern with the zone axis $[\bar{1}061]_{\alpha_1}$; ○—bainite, ●—twin; (*c*) indexing result; and (*d*) schematic illustration of the ledge-on-ledge mechanism.[14]

C. *Mobility of the Superledges*

The observation of superledges provides direct proof that superledges exist at the broad face of α_1 plates, but this is not enough to establish the ledgewise growth mechanism of bainite plate formation. According to the ledgewise theory of growth,[14] a plate can thicken only by the migration of ledges.

As mentioned in Section A, Wu *et al.* questioned the behavior of initial α_1 plates studied by Aaronson and Chattopadhyay. Also, they disagreed with the argument raised by Aaronson and Chattopadhyay, *i.e.*, that the thickening of α_1 plates is controlled by a ledge mechanism, as this argument lacked complete supportive evidence, such as a description of the nature of the ledges, and quantitative analysis.[3]

Figure 5(a) shows a micrograph of α_1 plates aged at 623 K for 5 minutes, and Figure 5(b) shows the corresponding selected area electron diffraction pattern taken from the area which involves part of α_1 plates A and D. The streaks between diffraction spots (indicated by the arrow) indicate that there are stacking faults inside the plates. It is apparent that one side of the α_1 plate A is very smooth, while the opposite side is relatively rough; *i.e.*, there are superledges on it. The spacing of the ledges is 50 to 230 nm, and the height is 10 to 40 nm. Close inspection shows that the terraces are parallel to the smooth side (the habit plane of the bainite). The habit plane of the α_1 plate was measured as $(114)_{\alpha_1}$ by means of the trace analysis method.[15] All the diffraction spots in Figure 5(b) were indexed as shown in Figure 5(c). The diffraction pattern implies that α_1 plates A and D have a twin relationship; the twin plane is also $(114)_{\alpha_1}$.

It should be noted that there is evidence that the superledges on the bainite plates are mobile. In Figure 5(a), bainite plates I, D, and B lie in front of the ledges H, E, and J, respectively, and hinder their movement along the longitudinal direction of the α_1 plates. Considering the fact that plate A takes on a gradually tapering morphology from the left to the right, it is possible to conclude that the α_1 plate thickens by the movement of ledges, which cease moving when they meet barriers. Following the hypothesis of previous ledge mechanisms, the terraces should have a partially or fully coherent structure, while the risers have a disordered or incoherent structure.[16] But many experimental studies have indicated that risers also have a partially or fully coherent structure.[14] Therefore, they must be replaced by a ledge-on-ledge or kink-on-ledge variant in order to provide the disordered areas of interface boundary required in order that atomic attachment and detachment may proceed with viable kinetics,[14,17,18] as illustrated in Figure 5(d). There is now abundant experimental evidence for this.[17,19,20] Observing the bright-field micrograph shown in Figure 5(a), it could be considered that the movement of the small ledge G on the riser of ledge F results in the lengthening of ledge F, as indicated by the arrow in Figure 5(d). In this way, plate A thickens continuously.

IV. CONCLUSIONS

Based upon the experiments described in this article, the following conclusions can be obtained.

1. Initially formed α_1 plates in Cu-25.9 pct Zn-3.75 pct Al alloy aged at 623 K are free of stacking faults and thus cannot have been formed by a shear mechanism.
2. There exist three-dimensional superledges on the broad faces of α_1 plates. The typical height of the ledges is approximately 10 to 40 nm, and their spacing is 50 to 230 nm. The terraces of these ledges are parallel to the habit plane, which is $(114)_{\alpha_1}$.
3. It has been found that barriers in front of superledges hinder their movement and that small ledges exist on the risers of superledges.
4. Superledges are considered to be mobile; they move forward along the plate, allowing the bainite plate to thicken. These results indicate that growth of α_1 plates occurs by a diffusion-controlled ledgewise mechanism.

ACKNOWLEDGMENTS

This work was partially supported by the Zhongguancun Measurement and Analysis Fund of the People's Republic of China. Appreciation is also expressed to Professor H.I. Aaronson for his careful review and valuable suggestions.

REFERENCES

1. R. Rapacioli and M. Ahlers: *Scripta Metall.*, 1977, vol. 11, p. 1147.
2. S.C. Singh, Y. Murakami, and L. Delaey: *Scripta Metall.*, 1978, vol. 12, p. 435.
3. M.H. Wu, J. Perkins, and C.M. Wayman: *Acta Metall.*, 1989, vol. 37, pp. 1821-37.
4. K. Takezawa and S. Sato: *Metall. Trans. A*, 1990, vol. 21A, pp. 1541-45.
5. K. Chattopadhyay and H.I. Aaronson: *Acta Metall.*, 1986, vol. 34, pp. 695-711.
6. C.M. Wayman: *Phase Transformations*, ASM, Metals Park, OH, 1970, p. 59.
7. D.S. Lieberman: *Phase Transformations*, ASM, Metals Park, OH, 1970, p. 1.
8. J.W. Christian: *Physical Properties of Martensite and Bainite*, Iron and Steel Institute, London, 1965, p. 1.
9. T. Furuhara, H.J. Lee, E.S.K. Menon, and H.I. Aaronson: *Metall. Trans. A*, 1990, vol. 21A, pp. 1627-43.
10. Qiang Jin and Hong-Sheng Fang: *Metall. Trans. A*, 1990, vol. 21A, pp. 2637-43.
11. Jin Qiang, Fang Hong-sheng, Cao Jianjun, Zheng Yankang, and Chen Xiuyun: *Acta Metall. Sin.*, 1990, vol. 26A, pp. 391-95.
12. H.J. Lee and H.I. Aaronson: *J. Mater. Sci.*, 1988, vol. 23, pp. 150-60.
13. J.W. Christian and D.V. Edmonds: *Phase Transformation in Ferrous Alloy*, TMS, Warrendale, PA, 1984, pp. 293-325.
14. H.I. Aaronson, C. Laird, and K.R. Kinsman: in *Phase Transformation*, ASM, Metals Park, OH, 1970, p. 313.
15. Peter Hirsch, A. Howie, R.B. Nicholson, D.W. Pashley, and M.J. Whelan: *Electron Microscopy of Thin Crystals*, Huntington, New York, NY, 1976, pp. 311-13.
16. H.I. Aaronson: *Decomposition of Austenite by Diffusional Processes*, Interscience, New York, NY, 1962, p. 387.
17. C. Laird and H.I. Aaronson: *Acta Metall.*, 1969, vol. 17, pp. 505-19.
18. J.M. Howe, U. Dahmen, and R. Gronsky: *Phil. Mag. A*, 1987, vol. 56, pp. 31-61.
19. T. Furuhara, A.M. Dalley, and H.I. Aaronson: *Scripta Metall.*, 1988, vol. 22, p. 1509.
20. N. Prabhu and J.M. Howe: *Acta Metall.*, 1990, vol. 38, p. 881.

A Discussion on the Formation of Bainite and Other Precipitates in Cu-Zn and Ag-Zn Alloys

K. TAKEZAWA, S. MARUYAMA, K. MARUKAWA, and S. SATO

Various transformation products appearing in Cu-Zn and Ag-Zn alloys upon aging at temperatures in the $\alpha + \beta$ and single α-phase range were examined by optical and electron microscopy. Upon aging at relatively low temperature, bainite plates with the 9R structure are first formed and then retransformed to face-centered cubic (fcc). At higher temperature, other transformation products with the fcc structure, such as rod-shaped α and massive α, are concurrently observed with the bainite. Measurements of solute concentration in bainite were performed by using analytical electron microscopy. Bainite plates were found to have lower solute concentration than that of stable α, not only in Cu-Zn but also in Ag-Zn alloys. These results were discussed in terms of the free-energy change in the transformation. The first appearance of the 9R bainite in place of the stable fcc phase in low-temperature aging should be attributed to the "shear" process which lowers the nonchemical energy and diminishes the necessary driving force for the transformation. The measured solute concentration of the bainite is well reproduced theoretically on the view that the bainite is a product of shear transformation combined with the concentration change.

I. INTRODUCTION

THE martensite of 9R (or 18R) structure with the stacking sequence ABCBCACAB is known to appear upon cooling in noble metal-based β-phase alloys having B2 (or $L2_1$) ordered structure.[1] In addition, plate-shaped precipitates with the 9R structure and crystallographic characteristics similar to martensite are formed during aging at moderately high temperatures in Cu-Zn,[2–5] Cu-Zn-Al,[6,7] Ag-Cd,[8,9] and Ag-Zn[10] alloys. These plates are thought to correspond to the aging products forming the "bainite morphology" in steels, and so we also call these plates bainite,[2,3] α_b, hereafter. The plate initially has 9R structure and is again transformed to face-centered cubic (fcc) on further aging.[5,7] Therefore, the product α_b is thought to be an intermediate phase which forms prior to the equilibrium α phase. On the origin or mechanism of α_b formation, many studies have been done, but still a general agreement among researchers has not been attained. Moreover, the other products such as the rod-shaped precipitate, α_w,[3,11,12] and massive alpha phase, α_m,[13,14] with fcc structure are often formed concurrently with α_b under the same aging treatment in these alloys. As for these precipitates, details of formation mechanisms are not clear. Therefore, it is important to study the mutual relationship of these precipitates with α_b in order to explore the origin of α_b formation.

Figure 1 shows portions of equilibrium phase diagrams of Cu-Zn and Ag-Zn alloys. The matrix crystal β_1 has B2 ordered structure below the transition temperature T_c, about 450 °C, in Cu-Zn alloys. But in Ag-Zn alloys, T_c for B2 order is about 200 °C[15] and the matrix crystal, β, has the disordered body-centered cubic (bcc) structure at ordinary aging temperature. Therefore, by making use of these differences between Cu-Zn and Ag-Zn alloys, the information associated with the effect of ordering on the transformation of α_b as well as of martensite can be obtained. Moreover, we notice in Figure 1 that the α phase is more stable in Ag-Zn alloys in the range of a higher solute concentration and lower temperature. Therefore, we can study α_b formed in the single α-phase range[10] in Ag-Zn alloys, for example, in Ag-38 at. pct Zn alloys aged at 300 °C, where any change in the solute concentration should not be required during the phase change.

In the present study, therefore, morphological examinations are performed using optical and electron microscopy on β_1 Cu-Zn alloys aged in the $\alpha + \beta$ range as well as on β Ag-Zn alloys aged in the α single-phase range. In addition, the solute concentration in α_b is measured by analytical electron microscopy for Cu-Zn and Ag-Zn alloys. Based on these results, the functions of the "shear" and "diffusion" mechanisms in bainitic and related transformations are studied through thermodynamical calculations.

II. EXPERIMENTAL PROCEDURE

Ingots of Cu-Zn and Ag-Zn alloys containing between 38 and 42 at. pct Zn were prepared by melting high-purity metals in capsules filled with argon gas under 1/3 atmosphere. These ingots were hot-rolled to 0.2 mm in thickness after homogenizing at a temperature in the β range. The thin-plate specimens were again homogenized at 850 °C and 670 °C for Cu-Zn and Ag-Zn alloys, respectively, followed by quenching into water at room temperature. The aging was performed in a silicone or salt bath at temperatures between 200 °C and 450 °C for

K. TAKEZAWA, Research Associate, K. MARUKAWA, Professor, Department of Applied Physics, Faculty of Engineering, and S. SATO, Professor Emeritus, are with Hokkaido University, Sapporo 060, Japan. S. MARUYAMA, formerly Graduate Student, Hokkaido University, is with Olympus Optical Co. Ltd., Hachioji 192, Japan.

This article is based on a presentation made at the Pacific Rim Conference on the "Roles of Shear and Diffusion in the Formation of Plate-Shaped Transformation Products," held December 18–22, 1992, in Kona, Hawaii, under the auspices of ASM INTERNATIONAL's Phase Transformations Committee.

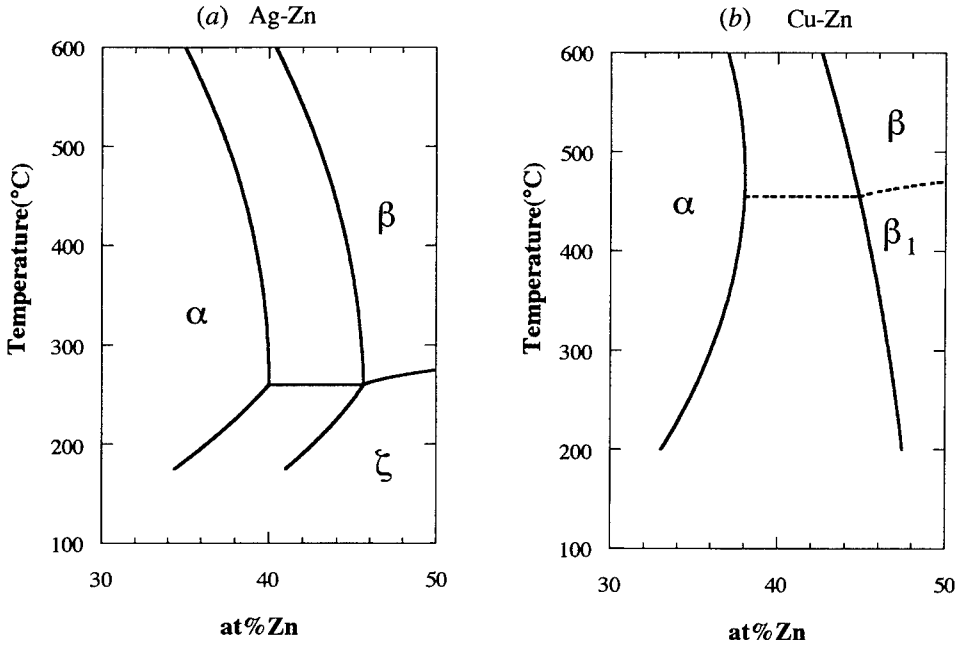


Fig. 1 — Portions of equilibrium phase diagrams. (*a*) Ag-Zn alloy and (*b*) Cu-Zn alloy.

a prescribed period.* The Cu-Zn specimens were electropolished in a CrO_3-H_3PO_4 solution and then etched in a solution of $FeCl_3$-HCl-H_2O. For Ag-Zn alloys, the electropolishing was made in a H_3PO_4-H_2O solution at 2 volt, followed by etching in the same solution at 1 volt. After making observations on the etched surface of aged specimens under an optical microscope, thin specimens were prepared by jet-polishing for transmission electron microscopy.

Measurements of solute concentration inside the α_b plate were performed using energy-dispersive X-rays (EDX) attachments of Hitachi H-700 and JEOL 2000EX electron microscopes. In order to get accurate values of solute concentration, the following procedures were taken to determine the correction factor, *k*-factor,[16] in advance.

Step 1: Four specimens of metastable β crystals with nominal compositions of 38.5, 39, 40, and 42 at. pct Zn were prepared by quenching from 850 °C.
Step 2: The previous specimens were thinned by an electropolishing for transmission electron microscopy, and the solute concentration was measured by an electron probe microanalyzer (EPMA).*
Step 3: The concentration measurement was performed for the same specimen using EDX of electron microscopes.
Step 4: The *k*-values were determined by taking the least-squares fit between the obtained values of the EPMA and EDX.

The solid circles in Figure 2 represent the relation between the values of solute concentration measured by EDX and EPMA.**

*Denoted aging times in later sections are actually the time of immersing in a bath. It has been found that it takes 0.5 to 1.0 s for a specimen to attain the temperature of the bath after immersion. Therefore, the results of observations for short-period aging should be taken as qualitative rather than quantitative.

*The measurement was made at the Central Research Laboratory, Sumitomo Metal Mining Co., Ltd., Ichikawa 272, Japan.

**The EPMA values were smaller than the nominal ones by 1 pct, at most, possibly due to the evaporation of Zn during the specimen preparation. The nominal values are used to label the alloys.

III. RESULTS

A. *Transformation Products in α + β Range*

In agreement with previous reports,[7,12] the α_b plates with the disordered 9R structure were observed in the form of Chevron pairs consisting of variant crystals having $\{551\}_\beta$ and $\{55\bar{1}\}_\beta$ habit planes. The rod-shaped α_w with the fcc structure was observed to have an axial direction parallel to $\langle 111\rangle_\beta$ with a diamond-shaped cross section.

As the aging is prolonged, the α_b plate grows with the second structural change from 9R to fcc and with different morphology depending on the aging temperature. Especially at the aging temperature where both α_b and α_w appear,[3] the local difference in morphology inside the plate was remarkable. Figure 3(a) shows an electron micrograph taken of a specimen of Cu-40 at. pct Zn alloys aged for 120 seconds at 300 °C, showing α_b plates. Most of the plates are of the 9R structure, but some regions with bright contrast give fcc spots in the diffraction pattern. Figure 3(b) shows a bainite plate consisting of 9R α_b and fcc α_w in the same alloy aged for 5 seconds in a bath at 400 °C. The region marked by the arrow has grown extraordinarily wide. Figure 3(c) shows a region where the transformation proceeds further in the alloy aged for 1.8 ks at 350 °C. A plate seems to decompose to several α_w rods, as marked by the

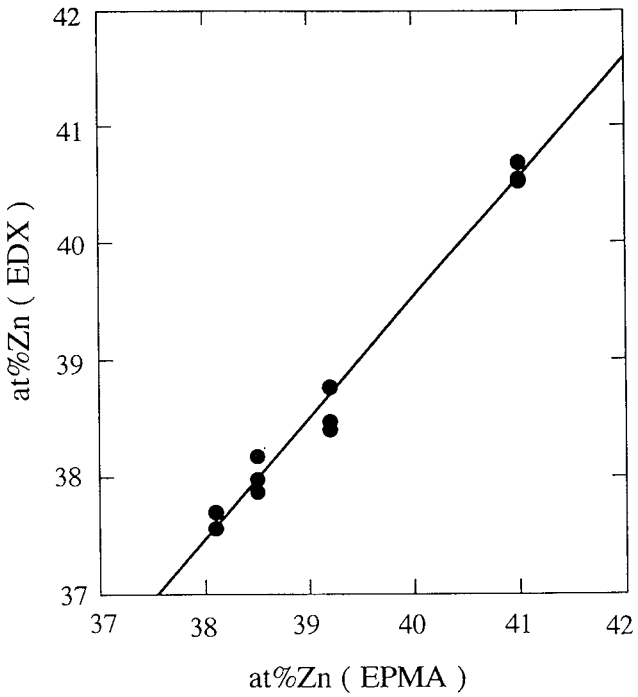


Fig. 2—Relation between measured EPMA and EDX values of solute concentration in quenched β Cu-Zn alloys.

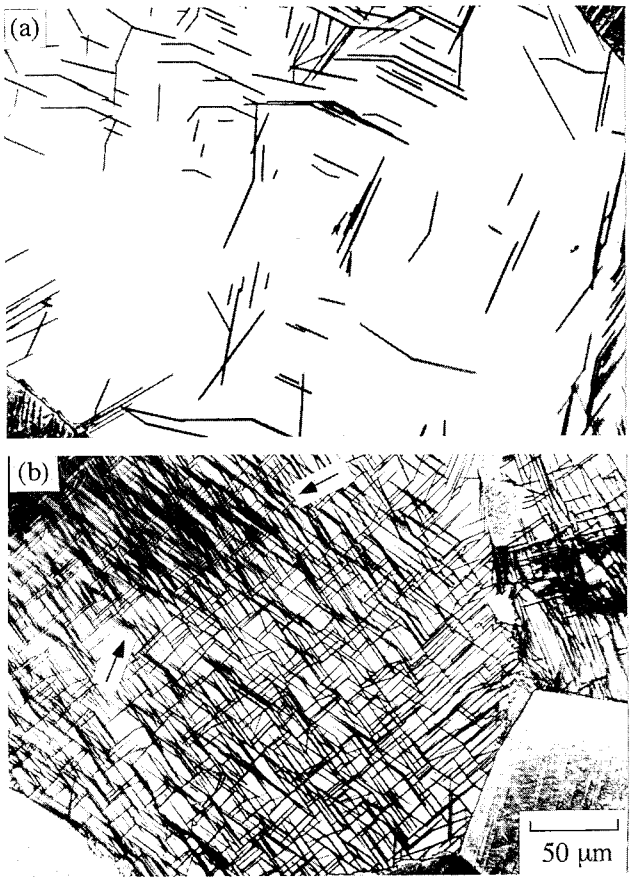


Fig. 4—Optical micrographs of α_b plates in Ag-38 at. pct Zn alloy aged for 1 s at 250 °C. →: Self-accommodation morphology.

arrows. In optical micrographs, a pattern consisting of α_b plates and linearly arranged dots of α_w rods is often observed for the specimen treated with an aging procedure similar to that in Figure 3(c).

B. *Transformation Products in the α Single-Phase Range*

Figures 4(a) and (b) represent optical micrographs showing α_b plates in Ag-38 at. pct Zn alloys aged for 1 second at 250 °C. The behavior of α_b formation is quite different from grain to grain. The plates sometimes occupy the whole area in some grains but are almost absent in other grains. The same tendency has been reported by Kostic and Hawbolt[17] in an Ag-45 at. pct Cd alloy. Figure 4(a) shows an example of grains in which only a small number of Chevron pairs appear with a few different orientations. On the other hand in Figure 4(b),

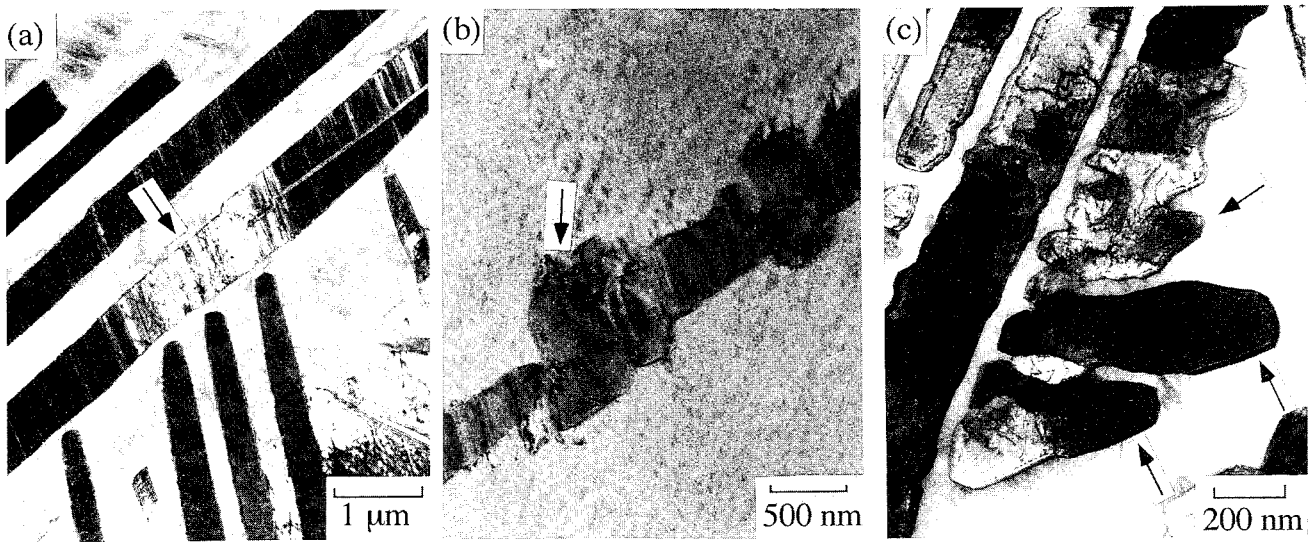


Fig. 3—Electron micrographs showing α_b bainite plate and α_w rod in Cu-40 at. pct Zn alloy aged (*a*) for 120 s at 300 °C, (*b*) for 5 s at 400 °C, and (*c*) for 1.8 ks at 350 °C.

numbers of pairs are observed in parallel with the same orientation and in some region, one sees a pattern similar to the self-accommodation pattern of the martensitic transformation.[18,19] Moreover, we observed relief patterns on the polished surface after aging, which was almost the same as that observed in the case of martensite.

Electron micrographs from specimens of Ag-39 at. pct Zn aged for 1 to 5 seconds at 250 °C show parallel α_b plates, consisting of 9R only, of a mixture of 9R and fcc, or of fcc only. Figure 5 shows an electron micrograph and its associated diffraction pattern from a specimen aged for 3 seconds. Two α_b plates of different variant crystals, A and B, are observed adjacent to each other in Figure 5(a). They have the orientation relationship of $(101)_{bcc}//(\bar{1}14)_{9R}$ and $[\bar{1}11]_{bcc}//[110]_{9R}$ with the matrix. The diffraction pattern in Figure 5(b) is composed of three patterns, *i.e.*, one with $[\bar{1}11]_{bcc}$ zone axis and two of twin-related $[110]_{9R}$ patterns. The second transformation from 9R to fcc takes place homogeneously in the overall region of an α_b plate. This is in contrast to the inhomogeneous growth of plates in the Cu-Zn alloy (Figure 3).

Figure 6 shows optical micrographs taken of specimens aged at temperatures higher than 300 °C

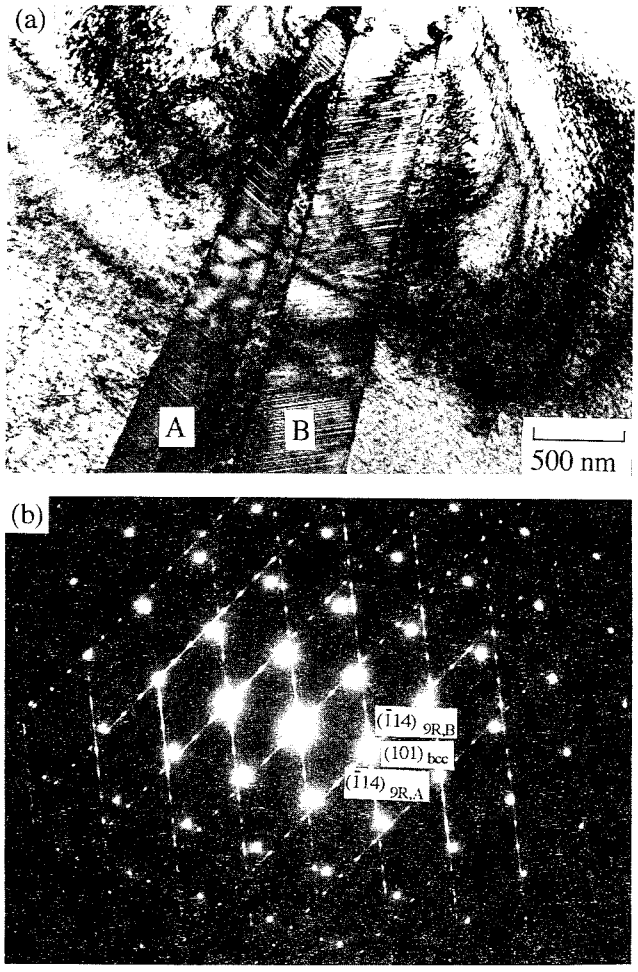


Fig. 5—Electron micrograph and diffraction pattern of a twin-related α_b pair in Ag-39 at. pct Zn alloy aged for 3 s at 250 °C.

Figure 6(a) is taken of Ag-38 at. pct Zn alloy aged for 2 seconds at 300 °C. Figure 6(a) shows three types, A, B, and C, of transformation products. Most of the α_b plates appear densely in the form of bundles as noted by A. The Chevron pairs are hardly seen in this case. An electron diffraction study revealed that the second transformation to fcc has taken place in all of the plates. Plate B is very large compared with α_b and this type of plate usually traverses a matrix grain. These plates have been found by Ayers and reported as "thermally activated martensites."[20] The present authors have recently revealed that these plates are athermally produced upon heating as a burst phenomenon.[10] These plates are confirmed by electron microscopy to have the fcc structure with numerous fine twins inside and are thought to be formed by shear with the lattice invariant shear of $\{111\}_{fcc}$ twinning as Ayers has reported. We call this type of large plate α' martensite. A similar martensite with fcc structure has been reported to appear at a high temperature in Cu-Al alloys.[21] A massive α_m precipitate is observed inside the grain at C in Figure 6(a).

Figure 6(b) shows a micrograph of Ag-39 at. pct Zn alloy aged for 2 seconds at 300 °C. The α_b plates are sparsely formed in the matrix grain similarly as in Figure 4(a). However, the plates grow thicker in comparison with those in Figure 4(a). These plates have been confirmed to have the fcc structure. Besides the plates, α_w rods are observed with a shape of dots in the surrounding matrix. Figure 6(c) is a micrograph of Ag-39 at. pct Zn alloy aged for 2 seconds at 350 °C. The precipitation of α_w rods predominates over α_b plates. One sees at the center of the photograph that a large massive α_m precipitate grows surrounding a few thin α_b plates. The massive α_m seems to grow faster than the bainite.

C. *Solute Concentration in α_b Plate*

The solid circles in Figure 7 show the measured values of solute concentration in α_b plates in Cu-Zn alloys, which have been transformed by various aging treatments and verified to have the 9R structure by electron diffraction. The measurements were made on three Cu-Zn alloys containing 39, 40, and 42 at. pct Zn. Since the obtained values were independent of the initial alloy composition, no indication is applied on the composition of specimens. All of the measured values were slightly lower than the equilibrium concentrations of α. The same experimental result that the solute concentration in the bainite is less than that in the equilibrium α has been obtained by Lorimer *et al.*[16] and Doig and Flewitt.[22] The empty circles indicate measured values for α_b plates having the fcc structure. The tendency that the empty circles situate between the solid circles and the solubility limit of the α phase can be observed.

A preliminary measurement of solute concentration has been performed for 9R α_b in Ag-39 at. pct Zn alloy. Lower values of Zn concentration by about 2 at. pct Zn than those in the matrix have been obtained in α_b plates transformed in the α single-phase range.

IV. DISCUSSION

A. *Morphological Features*

Transformation products with the 9R structure principally take the shape of plates. These are α_b plates and

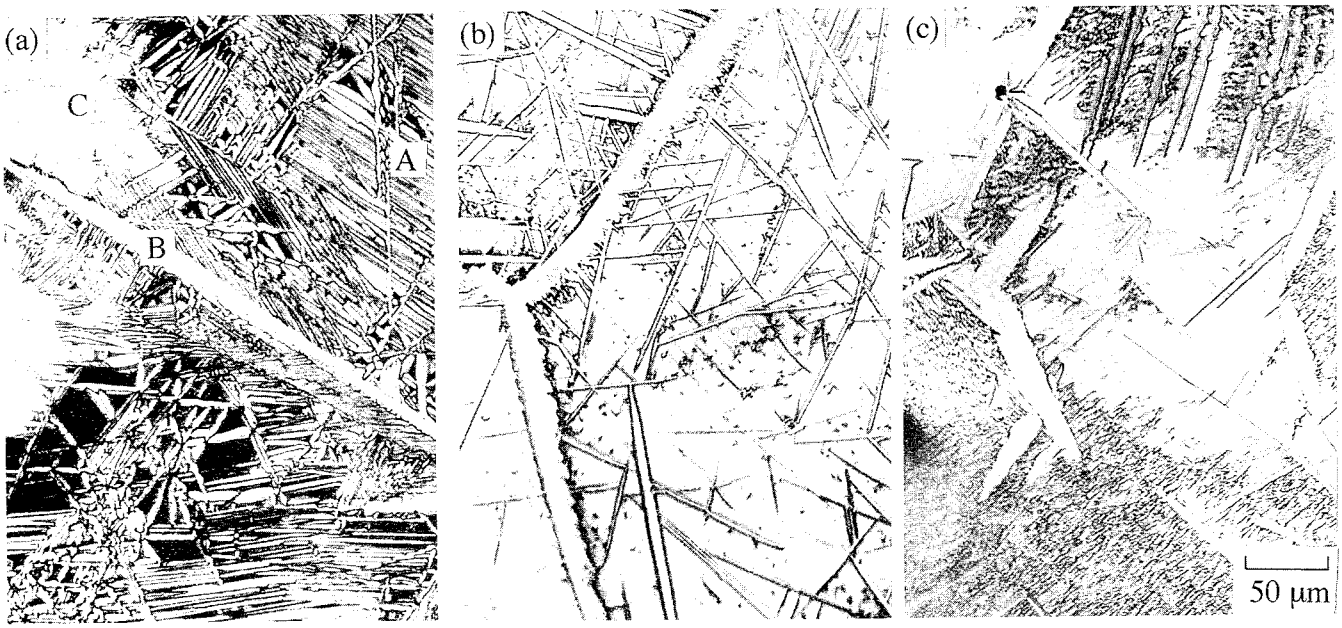


Fig. 6—Optical micrographs showing various transformation products in Ag-Zn alloys. (*a*) Ag-38 at. pct Zn alloy aged for 2 s at 300 °C, A: α_b bainite, B: α' martensite, C: α_m massive-α. (*b*) Ag-39 at. pct Zn alloy aged for 2 s at 300 °C. (*c*) Ag-39 at. pct Zn alloy aged for 2 s at 350 °C.

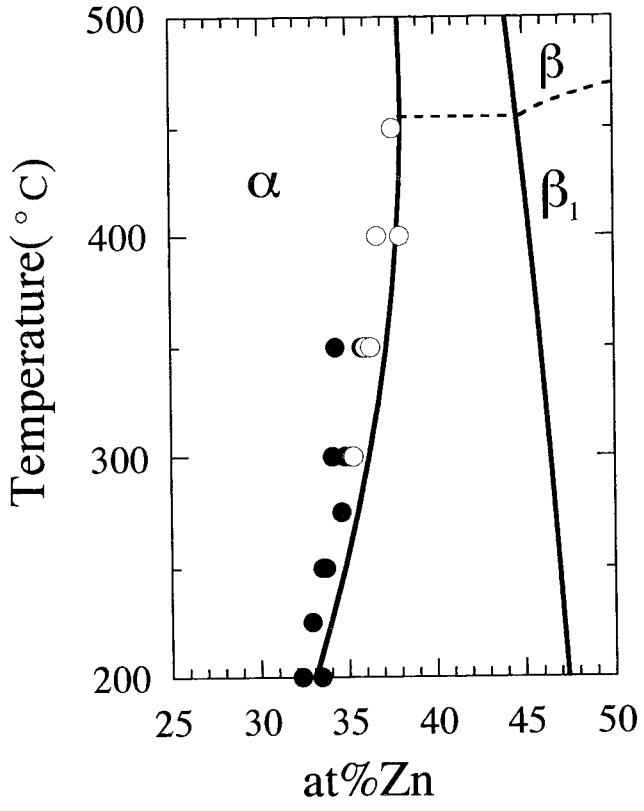


Fig. 7—Measured values of solute concentration in α_b plotted in the equilibrium phase diagram of Cu-Zn alloy. Solid circle: in α_b plate of 9R. Empty circle: in α_b plate of fcc.

ordinary martensites, denoted by β'_1 hereafter, induced upon cooling. The shape of plates would be a reflection of their origin of "lattice shear." The shape may be changed by a subsequent transformation. Figure 3 shows a typical example of the morphological change in Cu-Zn alloys aged in the $\alpha + \beta$ range. As the second structural change takes place locally in a part of a 9R α_b plate, the growth in the thickness direction is promoted in that part and the phase boundary bows out into the matrix. Therefore, the growth velocity in the thickness direction in the fcc region must be larger than that in the 9R region.

The situation is a little different in the case of the aging in the α single-phase region of Ag-Zn alloys. In this case, α_b plates with the 9R structure are quickly retransformed to fcc without changing their shape. As the aging proceeds, the plates grow thicker homogeneously and finally occupy the whole area of matrix grain. This is because the fcc structure is stable in the single α-phase range. It should be noted, however, that the phase change from β to α takes place *via* the transformation to 9R plates, in spite of the fact that the fcc could be directly formed on the aging in the α range.

In the case of Ag-Zn alloy, especially in an area with dense α_b plates, these plates seem to be arranged in a morphology similar to the self-accommodation morphology in the martensitic transformation. Since the bainitic transformation has been known to be accompanied by the surface relief[23] as well as macroscopic shape changes,[24] it is reasonable that we observe the self-accommodation morphology in bainite plates. It

should be noted that self-accommodation of transformation shears between neighboring plates becomes more evident in the case of the α single-phase range, because the α_b plates are produced in a higher density in comparison with the case of the two-phase range.

Two fcc phases, α' and α_m, are concurrently formed with α_b bainite plates through a certain aging treatment in Ag-Zn alloys (Figure 6(a)). The plate morphology of α', together with its internal structure of dense twins, indicates that the phase is produced by shear. It is to be noted that the fcc structure can directly be induced by shear from the bcc. The massive alpha α_m takes a rather indefinite shape. This phase is known to form by diffusion over short distances.[13]

B. *Thermodynamics of Phase Transformations*

As previously shown, we have obtained a number of phases as transformation products. In Cu-Zn alloy of which the matrix phase is the ordered bcc, the product phases are α_b bainite and β_1' martensite, and in Ag-Zn alloy whose matrix has the disordered bcc structure, there are α' and α_m in addition to α_b and β_1'.[10] All of these have close-packed structures, fcc or 9R. Therefore, the next question to be answered is how these are related with each other, or how these are to be coordinated in terms of thermodynamics. In the following, we try to answer this question. First, the free energy of each phase is calculated for Cu-Zn alloys. The calculation procedure of Hsu and Xiaowang[25,26] is closely followed, but the energy difference between the fcc phase and the 9R phase is explicitly evaluated on the basis of the experimental results.

The free energy of disordered fcc (α) and bcc (β) phases is, assuming the regular solution model, given by

$$\begin{aligned} G_{\text{dis}}(c,T) = {} & (1-c)G_{\text{Cu}} + cG_{\text{Zn}} \\ & + RT\{(1-c)\ln(1-c) + c\ln c\} \\ & - Ec(1-c) \end{aligned} \quad [1]$$

where G_{Cu} and G_{Zn} are the free energies of pure Cu and Zn metals, c, T, and R being the concentration of Zn, absolute temperature, and gas constant, respectively. The E's are the interaction parameters in α and β phases and

$$E_\alpha = -29{,}047, \quad E_\beta = -43{,}014 \text{ (J/mol)} \quad [2]$$

are assumed.[26] The free-energy change for Cu and Zn at the transformation from disordered β to α can be determined from the concentrations of phase boundaries in the phase diagram. The results are approximated by linear functions of

$$\begin{aligned} \Delta G_{\text{Cu}}^{\text{bcc}\rightarrow\text{fcc}} &= -6440 + 2.16T, \\ \Delta G_{\text{Zn}}^{\text{bcc}\rightarrow\text{fcc}} &= -5310 - 1.12T \text{ (J/mol)} \end{aligned} \quad [3]$$

The ordering energy is calculated from the Inden's equation.[15] The order parameter η is defined as

$$\eta = P_{\text{Cu}} - (1-c) \quad [4]$$

where P_{Cu} is the probability of having Cu atoms in the Cu site of the B2 structure. Then, the ordering energy in the transition from bcc to B2 is given by

$$\begin{aligned} \Delta G_{\text{ord}}(c,T,\eta) = {} & \Delta H_{\text{ord}} - RT\{2(1-c)\ln(1-c) \\ & + 2c\ln c - (1-c+\eta)\ln(1-c+\eta) \\ & - (1-c-\eta)\ln(1-c-\eta) \\ & - (c+\eta)\ln(c+\eta) - (c-\eta)\ln(c-\eta)\}/1.34 \end{aligned} \quad [5]$$

where ΔH_{ord} represents the change in enthalpy due to the ordering and is given by[26]

$$\Delta H_{\text{ord}}^{\text{bcc}\rightarrow\text{B2}} = -18{,}415.5\,\eta^2 \text{ (J/mol)} \quad [6]$$

Assuming that the lattice transformation from bcc to fcc is described by the Bain distortion, Eq. [5] will be directly used for the $L1_0$ ordering with the replacement of the enthalpy term by

$$\Delta H_{\text{ord}}^{\text{fcc}\rightarrow\text{L1}_0} = -9677.5\,\eta^2 \text{ (J/mol)} \quad [7]$$

The total energy of the ordered bcc or fcc phase is expressed as

$$G(c,T,\eta) = G_{\text{dis}}(c,T) + \Delta G_{\text{ord}}(c,T,\eta) \quad [8]$$

The equilibrium order parameter at any temperature can be calculated by solving $\partial G/\partial\eta = 0$. The transition temperature T_c, at which $\eta = 0$, is obtained to be 440 °C for bcc and 100 °C for fcc, at the concentration of $c = 0.4$.

Thermodynamic data for the 9R structure are not available at present. Nevertheless, the change in free energy associated with the structural change from fcc to 9R can be estimated from the critical shear stress τ of stress-induced martensitic transformation from β_1' to α_1', as follows:[1]

$$\Delta G^{\text{fcc}\rightarrow\text{9R}} = -V_m\gamma\tau \quad [9]$$

where V_m is the molar volume and γ is the shear strain of the transformation. The critical shear stress has been measured for binary Cu-Zn alloys,[27] but the number of measurements is not sufficient for the present purpose. Therefore, the values previously obtained by the present authors for Cu-Zn-Al ternary alloys[28] are used here. We use average values of the forward and reverse transformations as

$$\begin{aligned} \tau &= \{\tau(\beta_1' \rightarrow \alpha_1') + \tau(\alpha_1' \rightarrow \beta_1')\}/2 \\ &= 1744(z-1) - 0.156T - 733 \text{ (MPa)} \end{aligned} \quad [10]$$

where z is electron concentration, e/a. Since the obtained values of τ were independent of Al content,* we apply Eq. [10] also for binary Cu-Zn alloy with the substitution $z - 1 = c$. Using $\gamma = 0.215$,[30] $\Delta G^{\text{fcc}\rightarrow\text{9R}}$ is obtained as

*Values of τ which depend on Al content have been reported for Cu-Zn-Al alloys with high e/a values.[29]

$$\Delta G^{fcc \rightarrow 9R}(c, T) = -2920c + 0.262T + 1230 \text{ (J/mol)} \quad [11]^{**}$$

**No marked difference is observed in Eq. [11] when we use the values of τ reported by Ahlers.[1]

Then, the free energy of the 9R phase is given by

$$\Delta G^{9R}(c, T, \eta) = \Delta G^{fcc}(c, T, \eta) + \Delta G^{fcc \rightarrow 9R}(c, T) \quad [12]$$

C. *Mutual Relation between the Products*

The energy change, ΔG, due to the phase transformation may be given by the sum of two terms,

$$\Delta G = -|\Delta G_C| + \Delta G_{NC} \quad [13]$$

where the first term of the right-hand side represents the decrease in chemical-free energy due to the phase change (*i.e.*, "driving force" as is called sometimes) and the second or nonchemical term means the additional energy necessary for the process of the transformation, such as the interfacial energy or the elastic energy. The transformation will take place only when $\Delta G < 0$. The existence of a variety of transformation products, as shown in the present observations, obviously indicates a variety of nonchemical terms for different phases. Since the nonchemical term depends upon details of the transformation, such as the size and shape of phase nuclei, its precise evaluation is a difficult task. In the following, a rough estimation is given.

Figure 8 represents a schematic diagram of free-energy curves. The solute concentration of equilibrium phases are given by c_α and c_β. The initial concentration of the matrix phase is denoted by c_0. According to Ayers and Massalski,[14] the upper-most temperatures for the massive transformation are situated along the solubility line of the α phase and slightly higher. Therefore, if we neglect the slight deviation from the line, an estimate of the nonchemical energy ΔG_m for the massive transformation may be given by the free-energy difference between α (disordered fcc) and β (disordered bcc) phases at c_α. By using Eqs. [1] and [2], we obtain the value $\Delta G_m = 200$ J/mol,* which is shown to be almost independent of temperature. The nonchemical energy for fcc α' martensite may be fairly different from this value, because the structures of its interface and internal defects are quite different from those of the massive phase. Although the estimation for this has not been performed, the value is thought to be less than that of the massive phase, judged from the fact of the better coherence with the matrix at its interface. More detailed knowledge will be necessary for differentiating this phase from the massive phase.

*Subramanian *et al.*[31] have obtained 410 J/mol in their calculation.

The nonchemical energy ΔG_s for the transformation to β'_1 martensite phase with the 9R structure has been obtained as $\Delta G_s = 10.4$ J/mol from the calorimetric measurement and hysteresis curve of transformation.[32] Obviously, this value is much lower than the value obtained earlier for the fcc massive phase. Therefore, for a given temperature, the martensitic transformation takes place at a concentration quite close to the intersecting point between the free-energy curves, as sketched in Figure 8. The nonchemical energy for the bainitic transformation may not be much different from this value, for the structure of interface is similar between α_b bainites and β'_1 martensites. The smallness of this nonchemical term explains the reason why the 9R phase is first produced on low-temperature aging, in spite of the fact that the most stable phase is the fcc phase.

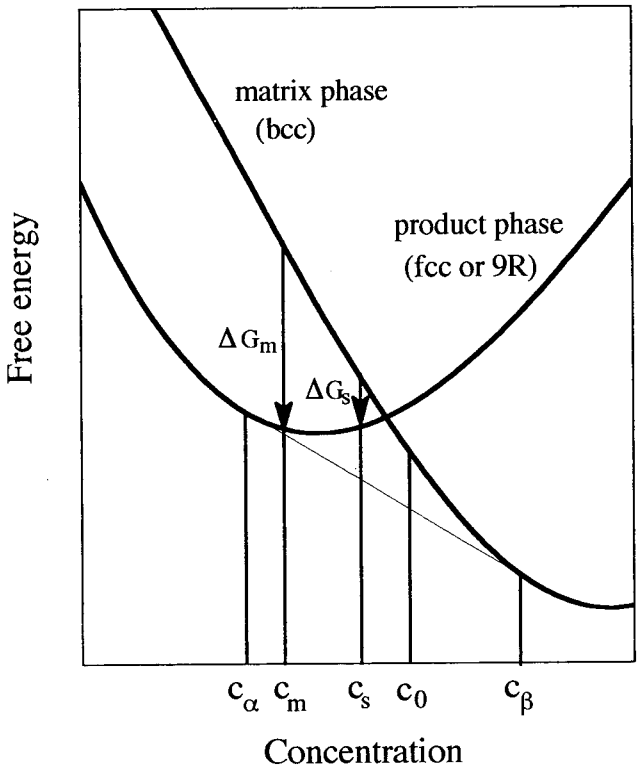


Fig. 8—Schematic diagram showing free-energy curves of matrix and product phases. The initial concentration and the concentrations of final decomposition products are denoted by c_0, c_α, and c_β, respectively. c_m and c_s are concentrations of the massive α phase and the 9R phase.

Next, we discuss the distinction between bainite and martensite, both of which have the 9R structure and are products of shear transformation. The obvious difference between them is the concentration change in the transformation. In the martensitic transformation, the concentration of the product is the same as the matrix. On the other hand, the concentration of the bainite is different from that of the matrix, as shown in Figure 7. This fact is explained only by assuming a diffusion process involved in the latter transformation. Although both transformations occur at a concentration near the intersecting point of free-energy curves, as discussed earlier, the concentration change from c_0 to c_s (Figure 8) by diffusion is necessary for the bainitic transformation to take place. We now estimate the concentration of the bainite and compare with the experimental results.

According to the previous discussion, the first approximation to the concentration of the bainite may be the concentration at the intersecting point of free-energy curves. This is calculated by equating the free energy of the matrix (Eq. [8]) to that of the 9R phase (Eq. [12]).

An important difference between the bainite and the martensite is the one in the order parameter. If we assume that the order parameter takes a constant value, *e.g.*, the value at 100 °C, the calculation gives rise to the concentration and the temperature (M_s) corresponding to the martensitic transformation,[33] which is supposed to occur at a temperature lower than 100 °C. For the bainitic transformation, we use the order parameter evaluated at the aging temperature in the matrix. We assume that the value remains the same even after the transformation to the bainite. The results can be expressed as the relation between the temperature (T_0) and the concentration. This is shown as the curve $T_0(\alpha_\beta)$ in Figure 9. In the figure, the extrapolated line from the curve for the M_s temperature $T_0(\beta_1')$ is also included. Another temperature curve $T_0(\alpha)$ in the figure corresponds to the intersection between free-energy curves of the disordered fcc and the matrix phases.

The curve $T_0(\alpha_b)$ should be compared with the experimental values shown in Figure 7. This curve is rather close to the $\alpha/\alpha + \beta$ phase boundary but is located in a lower concentration region. The location and the temperature variation of the curve seem to correspond well to the measured values. It is to be noted that the difference in the order parameter gives rise to the large difference of the location between the $T_0(\beta_1')$ curve (martensite) and the $T_0(\alpha_b)$ curve (bainite). This also gives an explanation for the reason why the 9R phase appears at rather high temperatures (bainite) as well as at lower temperatures (martensite). In order to confirm the present view further, the measurement of the order parameter in the bainite would be necessary. As for the concurrent occurrence of the concentration change and the lattice shear in the bainitic transformation, we speculate that the concentration fluctuation is essential. At the growing tip of α_b plate, a favorable concentration fluctuation may immediately be followed up by shear deformation which is attributed to the dislocation motion. This point has been discussed in more detail elsewhere.[34]

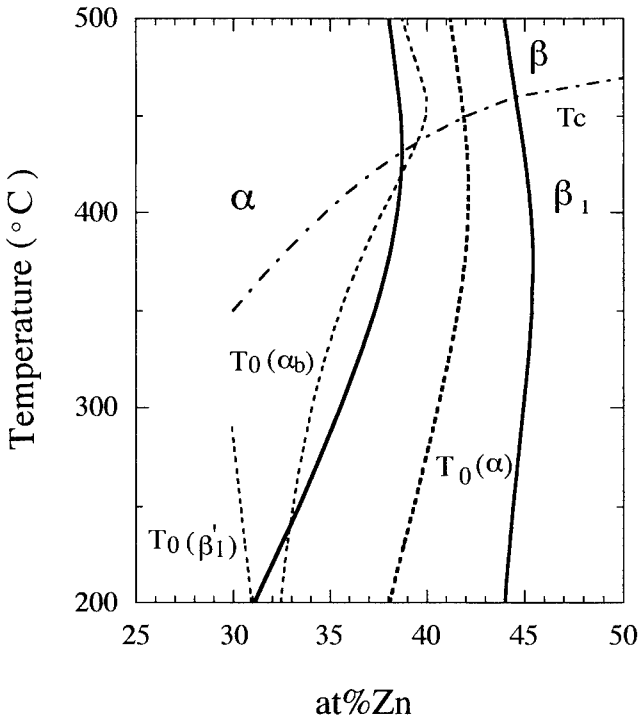


Fig. 9—Calculated equilibrium phase diagram of Cu-Zn alloy and T_0 lines of β_1', α_b, and α. The line T_c denotes the order-disorder transition temperature in equilibrium or nonequilibrium bcc phase.

V. CONCLUSIONS

1. Upon aging β-phase alloys at relatively low (200 °C to 250 °C) temperature, α_b plates with the 9R structure are first formed and then retransformed to fcc. In the case of aging in the $\alpha + \beta$ range of Cu-Zn alloys, the second transformation takes place at local areas and the transformed parts grow faster. As a result, the plate morphology is disintegrated. In the case of aging in the α single-phase range of Ag-Zn alloys, the second transformation proceeds homogeneously in a plate, and the plate shape remains unchanged.
2. A self-accommodation morphology of α_b plates, similar to the case of the martensitic transformation, is observed in the bainitic transformation in the α single-phase range.
3. At higher temperature, the massive α fcc martensite, and rod-shaped α are formed concurrently with α_b bainite in Ag-Zn alloys.
4. The solute concentration in 9R bainites has been measured and found to be lower than that in the matrix in both Cu-Zn and Ag-Zn alloys. Bainite plates have a solute concentration less than that of the solubility limit of the α phase.
5. The nonchemical energy to be overcome at the transformation has been estimated on the basis of thermodynamics. The results show that the energy for the phase with the 9R structure is much lower than that for the fcc phase. This explains why the 9R bainite appears in advance of the stable fcc phase in low-temperature aging.
6. With the view that the bainite is a product of shear transformation combined with the concentration change through concentration fluctuations, the relation between the transformation temperature and the solute concentration has been deduced. The results are in good agreement with the measured solute concentration in bainite.
7. The change in order parameter gives rise to the difference between the transformation temperatures of the martensite and bainite.

ACKNOWLEDGMENTS

The authors are greatly indebted to Dr. Kenji Adachi of the Central Research Laboratory, Sumitomo Metal Mining Co. Ltd., for allowing them to use the EPMA and analytical electron microscope of JEOL 2000CX in the Laboratory. They would like to thank Mr. T. Kawanaka for his assistance in the experiment.

REFERENCES

1. M. Ahlers: *Progress in Materials Science*, Pergamon Press, Oxford, 1986, vol. 30, pp. 135-86.

2. R.D. Garwood: *J. Inst. Met.*, 1954, vol. 83, pp. 64-68.
3. P.E.J. Flewitt and J.M. Towner: *J. Inst. Met.*, 1967, vol. 95, pp. 273-80.
4. E. Hornbogen and H. Warlimont: *Acta Metall.*, 1967, vol. 15, pp. 943-51.
5. I. Cornelis and C.M. Wayman: *Acta Metall.*, 1974, vol. 22, pp. 301-11.
6. M.H. Wu and C.M. Wayman: *Proc. Int. Conf. on Martensitic Transformation*, ICOMAT-86, Nara, Japan, 1986, pp. 619-24.
7. K. Takezawa and S. Sato: *Metall. Trans. A*, 1990, vol. 21A, pp. 1541-45.
8. M.M. Kostic, E.B. Hawbolt, and L.C. Brown: *Metall. Trans. A*, 1976, vol. 9A, pp. 1643-53.
9. T. Tadaki, T. Uyeda, and K. Shimizu: *Mater. Trans. JIM*, 1989, vol. 30, pp. 117-26.
10. K. Takezawa, S. Sato, K. Minato, S. Maruyama, and K. Marukawa: *Mater. Trans. JIM*, 1992, vol. 33, pp. 294-301.
11. A. Crosky, P.G. McDougall, and J.S. Bowles: *Acta Metall.*, 1980, vol. 28, pp. 1495-1504.
12. K. Takezawa and S. Sato: *Mater. Trans. JIM*, 1991, vol. 32, pp. 766-73.
13. T.B. Massalski: *Phase Transformation*, ASM, Metals Park, OH, 1970, pp. 433-86.
14. J.D. Ayers and T.B. Massalski: *Metall. Trans.*, 1972, vol. 3, pp. 261-71.
15. G. Inden: *Z. Metallkd.*, 1975, vol. 66, pp. 648-53.
16. G.W. Lorimer, G. Cliff, H.I. Aaronson, and K.R. Kinsman: *Scripta Metall.*, 1975, vol. 9, pp. 271-79.
17. M.M. Kostic and E.B. Hawbolt: *Metall. Trans. A*, 1979, vol. 10A, pp. 165-76.
18. K. Takezawa, T. Shindo, and S. Sato: *Scripta Metall.*, 1976, vol. 10, pp. 13-18.
19. T. Saburi and C.M. Wayman: *Acta Metall.*, 1979, vol. 27, pp. 979-95.
20. J.D. Ayers: *Acta Metall.*, 1974, vol. 22, pp. 611-18.
21. P.R. Swann and H. Warlimont: *Acta Metall.*, 1963, vol. 11, pp. 511-26.
22. P. Doig and P.E.J. Flewitt: *Mater. Sci.*, 1983, vol. 17, pp. 601-08.
23. H.M. Clark and C.M. Wayman: *Phase Transformation*, ASM, Metals Park, OH, 1970, pp. 59-114.
24. K. Takezawa and S. Sato: *Trans. JIM*, 1988, vol. 29, pp. 894-902.
25. T.Y. Hsu (X. Zuyao) and Z. Xiaowang: *Acta Metall.*, 1989, vol. 37, pp. 3091-98.
26. Z. Xiaowang and T.Y. Hsu (X. Zuyao): *Acta Metall.*, 1989, vol. 37, pp. 3085-90.
27. W. Arneodo and M. Ahlers: *Acta Metall.*, 1974, vol. 22, pp. 1475-80.
28. H. Sato, K. Takezawa, and S. Sato: *Sci. Rep. RITU*, 1981, vol. A29, Suppl. 1, pp. 85-90.
29. G. Barcelo, M. Ahlers, and R. Rapacioli: *Z. Metallkd.*, 1979, vol. 70, pp. 732-38.
30. K. Takezawa and S. Sato: *Proc. Int. Conf. on Martensitic Transformations*, ICOMAT-1979, Cambridge, MA, 1979, pp. 655-60.
31. P.R. Subramanian, T.B. Massalski, and D.E. Laughlin: *Acta Metall.*, 1988, vol. 36, pp. 937-43.
32. T.Y. Hsu (X. Zuyao), X.W. Zhou, J.V. Humbeeck, and L. Delaey: *Scripta Metall.*, 1991, vol. 25, pp. 165-66.
33. K. Takezawa and S. Sato: *Mater. Trans. JIM*, 1992, vol. 33, pp. 102-09.
34. K. Marukawa: *Proc. Int. Conf. on Martensitic Transformation*, ICOMAT-92, Monterey, CA, 1993, in press.

Mechanism of the Early Stages of α_1 Plate Formation in a Cu-39 Pct Zn Alloy

N. RAVISHANKAR, H.I. AARONSON, and K. CHATTOPADHYAY

The early stages in the formation of α_1 plates in the ordered β' matrix of a Cu-39 pct Zn alloy have been studied with transmission electron microscopy (TEM). The early stage plates were found to be free of stacking faults. Their contrast features are indeed those normally expected from small coherent plates. Electron microdiffraction confirms that these plates have the 9*R* structure characteristic of α_1 with the same lattice parameters and orientation relationships reported by previous investigators at much later stages of growth. Similarly, the 9*R* structure was disordered, even though it was formed in an ordered matrix, again repeating previous results obtained at a later stage of growth. These results further support the view that the α_1 Cu-Zn plates form by a diffusion-controlled mechanism.

I. INTRODUCTION

THERE is considerable controversy in the literature regarding the mechanism of formation of α_1 plates from the β' matrix in Cu-Zn and Cu-Zn-Al alloys. It has been shown that the morphology, surface relief, and crystallography of α_1 plates conform to the phenomenological theory of martensite crystallography.[1] It was, therefore, concluded that the transformation occurs by shear, as had been deduced by a number of earlier investigators beginning with Garwood[2] in 1954. This view was contested by Lorimer *et al.*[3] who established that the change in composition occurs during the growth of these plates. Their finding is inconsistent with shear-controlled growth, supporting instead a diffusion mechanism. The initial questions as to the accuracy of composition microanalysis[3–6] have been resolved only recently, with the earlier conclusion of a change in composition even in the early stages of growth having been confirmed with high-resolution analytical microscopes.[7–10] The earlier uncertainty in composition analysis, however, prompted Chattopadhyay and Aaronson[11] to carry out a detailed study on the crystallography and interfacial structure of α_1 plates. Three major conclusions were reached during this study: (1) at early stages of isothermal transformation, coherent α_1 plates with no internal structure are formed; (2) the α_1 plates that form from an ordered β' matrix have a disordered structure, confirming an earlier observation by Hornbogen and Warlimont;[12] and (3) the thickening of α_1 plates during at least the later stages of growth occurs by a ledge-controlled mechanism characteristic of diffusional growth. It is now widely accepted that the later stages of growth of α_1 plates involve diffusion;[7,8,13,14] hence, agreement appears to be fairly general on the third conclusion. However, disagreement has developed about the first two conclusions concerning the early stages of growth. The conclusion that α_1 is initially coherent and fault free has been disputed by stating that no diffraction evidence for this transformation product had been presented.[14,15] The circumstance that the α_1 plates observed by Chattopadhyay and Aaronson[11] had a perceptibly smaller aspect ratio than those previously seen at earlier reaction times also aroused doubt as to the identity of these plates.[15] Finally, α_1 plates have been reported to be initially ordered.[14] It has, therefore, become imperative to take a fresh look at the early stage of α_1 plate growth. The present article reports the results of an investigation undertaken to fulfill this task.

II. EXPERIMENTAL PROCEDURE

The alloy used was prepared by Brush Wellman Company (Cleveland, OH) through the courtesy of Dr. Amitava Guha in the form of hot-rolled plates. The chemical analysis revealed a composition of 61.36 at. pct Cu and 38.64 at. pct Zn. This is part of the same plate used in Reference 11 as alloy 2. In the balance of the text, we denote this material as a Cu-39 pct Zn alloy. Thin strips of the Zn alloy were held in the single-phase β region at 1143 K for 3 minutes and then quenched into saturated brine at room temperature (300 K). These samples were then aged in an oil or salt bath maintained at 523 or 423 K for 15 to 900 seconds at the former and from 420 to 43,200 seconds at the latter temperature. This heat-treatment sequence was used by most of the earlier investigators and, in particular, those suggesting a shear-controlled mechanism of growth.[1,3,14] Examination of a few samples quenched directly into the aging bath from the betatising temperature did not indicate any significant difference in results. Samples for transmission electron microscopy (TEM) investigation were prepared with the twin-jet polishing technique, using Struers D2 electrolyte at room temperature. The TEM investigation was carried out using a JEOL* 2000 FX-II microscope operated at 200 kV.

N. RAVISHANKAR, Graduate Student, and K. CHATTOPADHYAY, Professor, are with the Department of Metallurgy, Centre for Advanced Study, Indian Institute of Science, Bangalore 560 012, India. H.I. AARONSON is with Geo-Centers, Inc., stationed in the Physical Metallurgy Branch, Code 6320, Naval Research Laboratory, Washington, DC 20375-5313.

This article is based on a presentation made at the Pacific Rim Conference on the "Roles of Shear and Diffusion in the Formation of Plate-Shaped Transformation Products," held December 18–22, 1992, in Kona, Hawaii, under the auspices of ASM INTERNATIONAL's Phase Transformations Committee.

*JEOL is a trademark of Japan Electron Optics Ltd, Tokyo, Japan.

III. RESULTS AND DISCUSSION

A. *Distinction between α_1 Plates and Superdislocation Pairs at Early Stages of Growth*

Some typical morphologies of α_1 plates at early stages of development can be seen in Figure 1. Representative α_1 plates are marked by arrows. This micrograph, which also contains a significant number of dislocations, was also chosen to highlight the fact that resolvable superdislocation pairs could not be seen in the alloy used, which is consistent with earlier work on dislocations in ordered β' Cu-Zn alloys.[16]

B. *On the Identity of α_1 Plates during Early Stages of Growth*

Microdiffraction experiments were carried out to obtain unambiguous identification of early stage α_1 plates. Figure 2(a) shows a typical microdiffraction pattern obtained from the small plate indicated by the filled circle in Figure 2(b). Analysis of Kikuchi lines indicates that the pattern belongs to a zone tilted about 8 deg from $[100]_{\beta'}$ toward the $[0\bar{1}0]$ direction. This zone is nearly parallel to the $[\bar{1}60]_{\alpha_1}$ zone and also nearly parallel to $[7\bar{1}0]_{\beta'}$. The matrix superlattice reflections can be seen as faint spots. Figure 2(c) is a computer-calculated microdiffraction pattern for the α_1 and β' ($B2$) lattices under the above-mentioned condition. The orthorhombic unit cell proposed by Hornbogen and Warlimont, [12] termed $9R$,[17] was adopted. Their lattice parameters, *i.e.*, $a = 0.446$ nm, $b = 0.267$ nm, and $c = 1.93$ nm, were utilized. Figure 3(a) shows another plate at an early stage of growth. The selected area pattern from the plate is shown in Figure 3(b) and is near $[1\bar{1}0]_{\alpha_1}$ zone. Under strong matrix operating reflection $(01\bar{1})_{\beta'}$, the plate shows a dislocation-like contrast similar to Figure 2(b). The dark field $(115)_{\alpha_1}$ reflection clearly illuminates the plate. The good agreement seen to be obtained between the experimental patterns of Figure 2(a) and the calculated pattern of Figure 2(c) and the bright and dark field

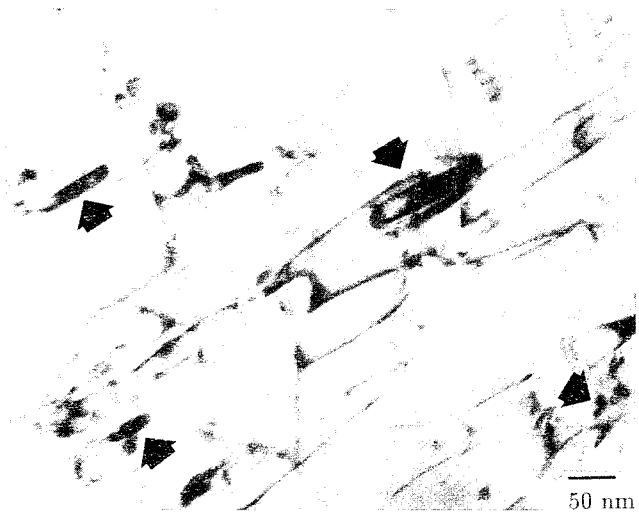


Fig. 1—Bright-field micrograph from a region containing α_1 plates during early stages of growth (400 s at 423 K, upquenched from room temperature (UQRT)). The early stage plates are indicated by arrows.

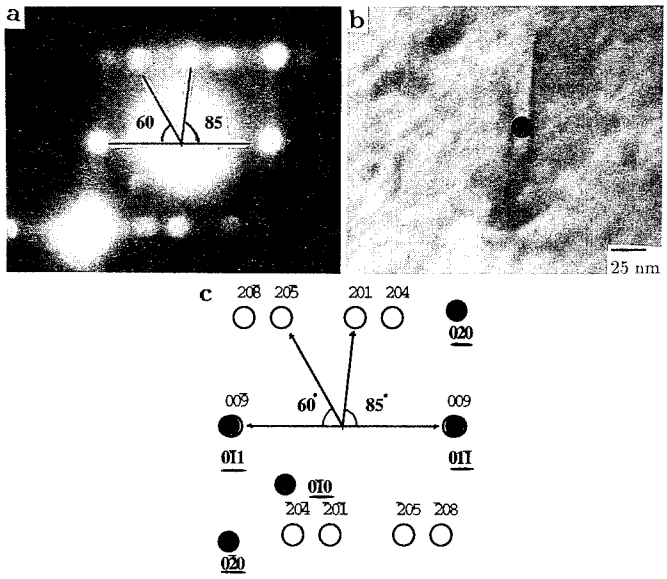


Fig. 2—(*a*) Microdiffraction pattern from an early stage plate near $[010]_{\alpha_1}$ pattern (15 s at 523 K, UQRT). Kikuchi line analysis indicates the zone to be $[\bar{1}60]_{\alpha_1}$ which is about 8 away from the $[100]_{\beta'}$ zone. The very faint diffuse intensity passing through β' reflections in two orthonormal directions are characteristic of the β' phase and verified by shifting the spot to β' matrix; (*b*) small plate from which the pattern was taken. The location of the beam is marked by the filled circle; and (*c*) a calculated microdiffraction pattern corresponding to the experimentally observed zone indicating the expected α_1 (open circle) and β' (filled circle) spots. The spots in the $[100]_{\beta'}$ direction are stronger, revealing the $(010)_{\beta'}$ superlattice reflection of the β' matrix.

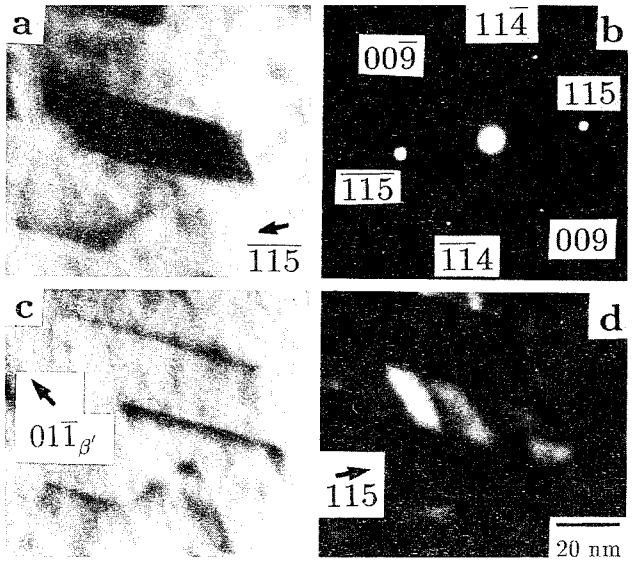


Fig. 3—(*a*) A bright-field image of a very early stage α_1 plate (15 s at 523 K, UQRT); (*b*) SAD pattern from the α_1 plate, which is near $[1\bar{1}0]_{\alpha_1}$ zone; (*c*) shows a dislocation pair contrast from the same plate when imaged with the matrix reflection $(01\bar{1})_{\beta'}$ strongly diffracting, indicating the presence of coherency strains at the interface; and (*d*) precipitate dark field of the same α_1 plate using $(115)_{\alpha_1}$ reflection. The nonuniform intensity is probably due to local bending of the plate.

pair from precipitate reflection in Figure 3 lead to the conclusion that early stage α_1 plates indeed have the 9*R* crystal structure and lattice parameters characteristic of α_1 plates determined by Hornbogen and Warlimont[11] at much later stages of growth.

Further support for this conclusion is obtained from the orientation relationship determined between small α_1 plates and their β' matrix. Figure 4(b) is the selected area diffraction (SAD) pattern from which the orientation relationship was determined, and Figure 4(c) is its calculated counterpart. The α_1 plates from which the SAD pattern was obtained is shown in Figure 4(a). The orientation relationship can be represented as

$$[401]_{9R} \parallel [010]_{\beta'}$$

$$(\bar{1}\bar{1}4)_{9R} \parallel (\bar{1}01)_{\beta'}$$

$$(\bar{2}08)_{9R} \text{ about 5 deg from } (001)_{\beta'}$$

$$(0\bar{1}0)_{9R} \text{ about 5 deg from } (\bar{1}00)_{\beta'}$$

$$(001)_{9R} \text{ about 5 deg from } (0\bar{1}1)_{\beta'}$$

This relationship thus described is identical to that deduced by Kubo *et al.*[18] for α_1 plates at later stages of growth.

C. *On the Question of Long-Range Order in α_1 Plates*

Figures 5(b) and (c) show the $[010]_{\alpha_1}$ and $[1\bar{1}0]_{\alpha_1}$ zone SAD patterns, respectively, from the α_1 plate in Figure 5(a). Figures 5(d) and (e) are the computed patterns for a disordered unit cell of α_1, assuming $[010]_{\alpha_1}$ and $[1\bar{1}0]_{\alpha_1}$ zone axes, respectively. (These calculated patterns do not include the effects of stacking faults.)

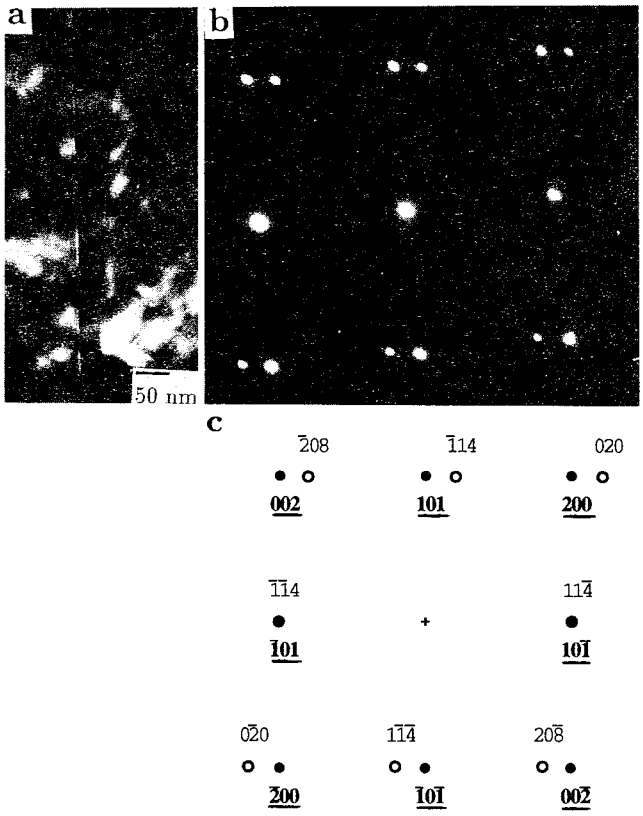


Fig. 4—A composite selected area electron diffraction pattern (*b*) taken from α_1 plate (*a*). The zones of β' and α_1 are, respectively, $[010]_{\beta'}$ and $[401]_{\alpha_1}$. The schematic is given in (*c*).

To establish the presence or absence of long-range order, one needs to look at a zone axis that is expected to show superlattice reflections if the structure were ordered. In the present case, the $[010]_{\alpha_1}$ serves this purpose. Figure 5(b) shows a SAD pattern corresponding to the $[010]_{\alpha_1}$ zone axis. This zone contains rows of spots parallel to the *c*-axis. The calculated pattern for this zone is shown in Figure 5(d). It can be seen that this zone contains only *h*01 rows, equivalent to c^* rows for which *h* is even. In the case of the ordered α_1 structure, the *h*01 rows for which *h* is odd also appear as superlattice rows. Since this is absent in the present case, it can be concluded that the α_1 structure is disordered.

There are two problems associated with this analysis. The first problem is that the structure factors of Cu and Zn are very similar, and therefore, the superlattice spot intensity is expected to be very low. To prove that we do observe superlattice spots despite this limitation, we have included a $[010]_{\alpha_1'}$ zone pattern (Figure 5(f) from an α_1' martensite plate formed by subzero quenching of the present alloy. This zone shows faintly but definitely the presence of a 101 superlattice row. The 301 row that is present in the computed pattern is not visible due to additional reduction in intensity at further removal from the transmitted spot.

Further, the second problem is that the $[1\bar{1}0]_{\alpha_1}$ bears a considerable and potentially confusing resemblance to the $[010]_{\alpha_1}$ zone. The $[1\bar{1}0]_{\alpha_1}$ zone from the same plate is presented in Figure 5(c) along with its computed pattern (Figure 5(e)). The main difference that can be observed experimentally between these patterns is the difference between their c^* rows. Since they differ by a very small, yet measurable, amount, comparison of the patterns is a more definitive approach than an absolute measurement of interlayer spacings. This enables the unambiguous identification of the zone axis. The interlayer spacing of the $(200)_{\alpha_1}$ planes is 0.223 nm, which corresponds to about a 1.97-nm interlayer spacing (for a camera length of about 175 cm) in the $[010]_{\alpha_1}$ pattern, while the interplanar spacing of $(110)_{\alpha_1}$ planes is 0.229 nm, equivalent to an interlayer spacing of 1.91 cm. The calculated difference of about 0.6 mm (for a 175-cm camera length) is in good agreement with that measured on Figures 5(b) and (c).

The aging time for the specimen of Figure 5(a) at 523 K was 15 minutes, while that for Figure 2(a) was only 20 seconds. Since the $[010]_{\alpha_1}$ patterns are the same, the absence of long-range order in this time range at 523 K appears certain. Hsu *et al.*,[14] on the other hand, aged a specimen of a Cu-39 pct Zn alloy for 15 minutes at this temperature. They reported the presence of long-range order in this specimen. The reason for the difference of these results from the two investigations remains uncertain.

D. *On the Question of Stacking Faults in α_1 Plates at an Early Stage of Growth*

The early stage α_1 plates in Figure 2(b) do not exhibit any internal contrast due to stacking faults. This is confirmed by tilting the foil. The diffraction discs in the

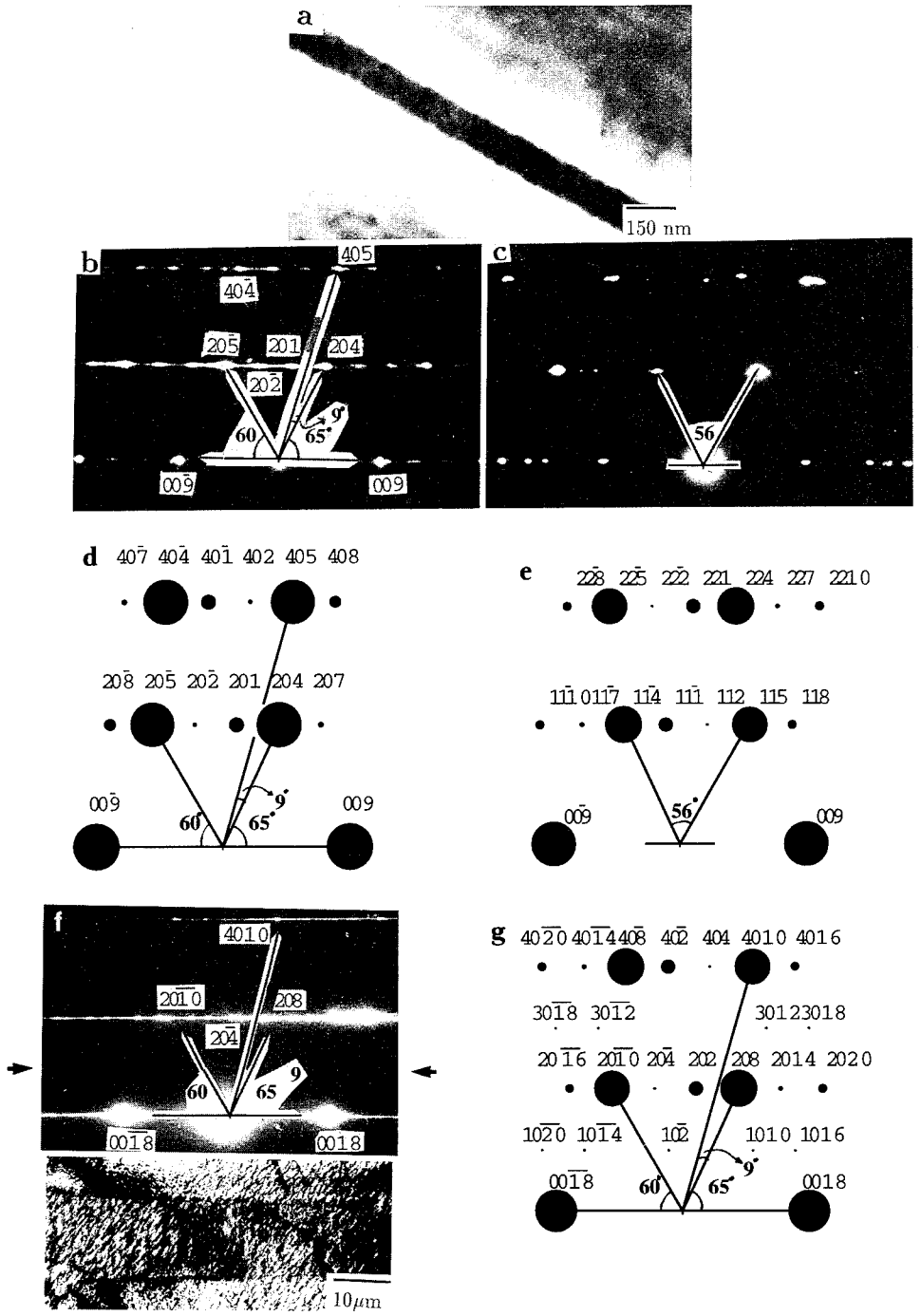


Fig. 5—(*a*) A bright-field micrograph of α_1 plate; (*b*) $[010]_{\alpha_1}$ pattern (15 min at 523 K, UQRT); (*c*) $[1\bar{1}0]_{\alpha_1}$ pattern (same heat treatment as (b)); (*d*) computed $[010]_{\alpha_1}$ pattern; (*e*) computed $[1\bar{1}0]_{\alpha_1}$ pattern for disordered α_1; (*f*) [010] pattern from a martensite plate shown in the bottom inset; and (*g*) computed [010] pattern for ordered α_1.

microdiffraction pattern obtained from such a plate (Figure 2(a)) are undistorted. In the pattern of Figure 2(a), the $B2$ superlattice spots can be seen as faint discs. The $B2$ spots are labeled in bold-face type and underlined in the computed pattern in Figure 2(c). A distribution of diffuse intensity passing through orthogonal $(110)_{\beta'}$ type reflections can also be seen. Diffraction from the $[100]_{\beta'}$ zone axis orientation is often associated with such diffuse intensity, consistent with earlier observations.[19] The diffuse intensity remains unaltered when the specimen is moved such that the beam is on the matrix. The result suggests growth of fault-free plates at an early stage of growth. For comparison, we also present a microdiffraction pattern using the same zone axis (Figure 6(b)) obtained from a bigger plate containing faults in Figure 6(a)). This pattern shows distortion of discs and pronounced streaking in one direction due to the presence of stacking faults. On the other hand, even at a later stage of growth, the stacking fault density can still be quite low. We must first note, though, that at this stage of growth, a pronounced tendency for edge-to-edge sympathetic nucleation appears.[20] As illustrated

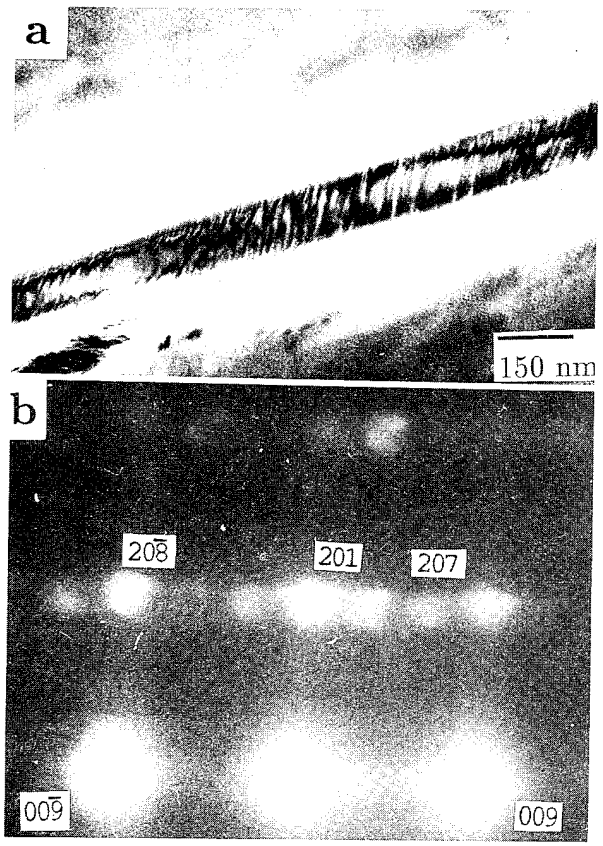


Fig. 6—(*a*) A bright-field micrograph of a faulted plate; (*b*) microdiffraction corresponding to $[010]_{\alpha_1}$ from the large plate shown in (a), showing distortion of α_1 disc and streaking along c^*-axis due to the presence of faults (20 s at 523 K, UQRT).

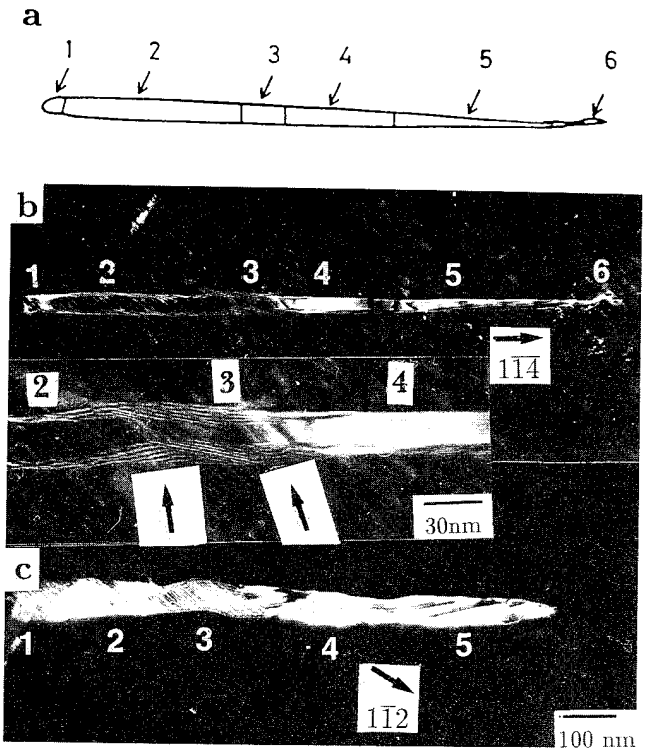


Fig. 7—Intermediate stage of plate growth (15 s at 523 K), (*b*) and (*c*) Dark field using different reflections, (*a*) showing the schematic of the plate in (b), indicating various segments. The inset shows an enlargement of a portion of the plate showing the interface between the segments.

in Figure 7, a single plate often consists of a number of segments. Figure 7(a) is a sympathetic of the plate shown in Figure 7(b) under dark-field illumination with the $(1\bar{1}4)_{\alpha_1}$ operating reflection. The plate consists of at least six segments. An enlargement of segments 2 through 4 is shown in the inset. Imaging with a large number of α_1 reflections revealed that segments 2 through 5 differ in orientations by the small angles characteristic of sympathetic nucleation.[20] Note that some of these segments still do not show the densely packed stacking faults usually observed in large plates. Only a few faults can be seen in segments 4 and 5, as revealed in Figure 7(c), when imaged with the $(1\bar{1}2)_{\alpha_1}$ reflection, though many are present in segments 2 and 3. We emphasize that the tilts employed to change to the various images are very large, and in no case have we observed any additional faults. Figure 8(c) shows that the fault density in another plate decreases significantly near the tip of the plate, though their density is rather high in the interior of the plate. Figure 8(a) shows the $[1\bar{1}0]_{\alpha_1}$ microdiffraction pattern near the tip of the plate, in the area indicated by the filled circle. The schematic of this pattern is shown in Figure 8(b). Undistorted discs and the absence of streaking in the c^* direction further support the view that faults develop only at later stages of growth, presumably in order to reduce the accumulated elastic transformation strain energy.[11]

E. *On the Question of Coherency of Small α_1 Plates*

Chattopadhyay and Aaronson[11] described early reaction time α_1 plates as coherent with their β' matrix. It is difficult to establish unambiguously complete coherency without high-resolution imaging. Weatherly *et al.*[21] have earlier shown that coherency strains that develop in the early stage precipitation process often show a dislocation-like displacement field contrast having a dipole character.[22] The early stage α_1 plates often show dislocation contrast with a pair of dislocation-like images bounding the precipitate. Since the matrix is ordered, the possibility of these being superdislocations exists. A $+g/-g$ experiment carried out with the $(200)_{\beta'}$ operating reflection is shown in Figure 9. The apparent width of this plate is seen to change, thus establishing its dipole character.[22] If these plates were actually superdislocations, their width would have remained constant during this experiment.

In order to further evaluate this feature, systematic tilting experiments were carried out on an α_1 plate. Figure 10(a) shows a bright-field image of the plate. The dark contrast is due to some of the precipitate planes satisfying the near-Bragg condition. Tilting away reveals the interface (Figure 10(b)). No defectlike feature is apparent at the interface. Figure 10(c) shows the strain in the matrix associated with the plate. Figure 10(d) shows a dislocation pair contrast. Using conditions for complete extinction obtained from a detailed contrast experiment with a large number of operating reflections, the

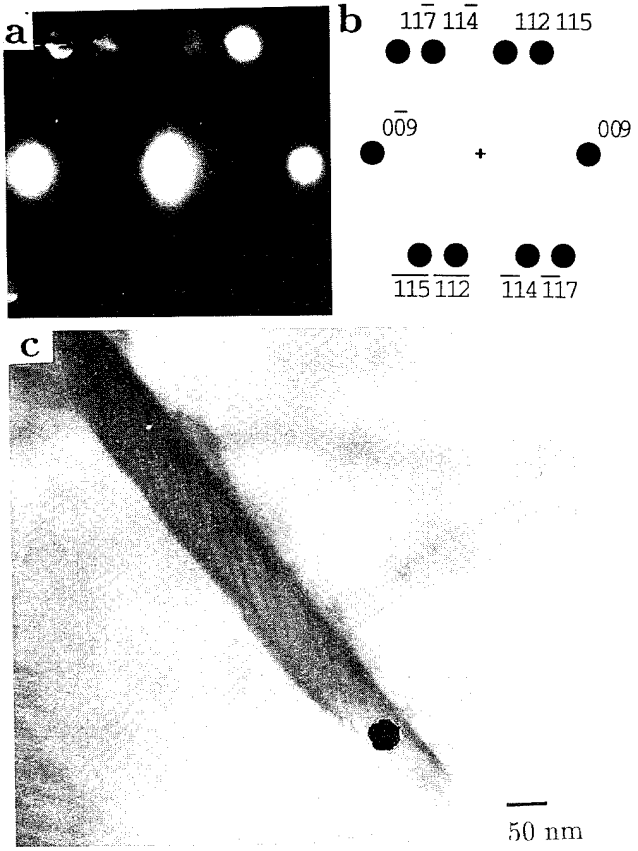


Fig. 8—(*a*) Microdiffraction pattern obtained from a region near the tip (indicated by black dot) of the plate in (c). The spots appear undistorted and do not contain streaks due to the low density of faults in the plate. (*b*) Schematic of the pattern shown in (a) corresponding to $[1\bar{1}0]_{\alpha_1}$ zone. (*c*) Bright-field micrograph of the α_1 plate with fault density decreasing toward the tip (15 s at 523 K, UQRT).

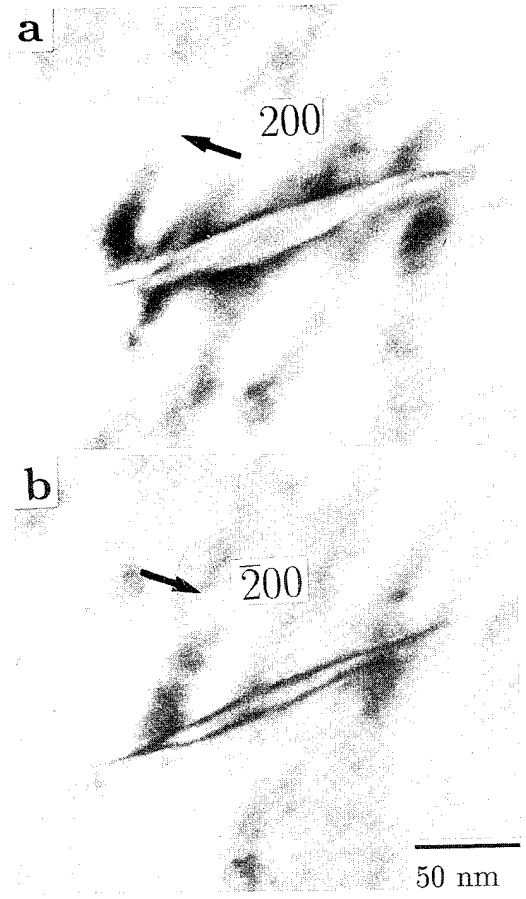


Fig. 9—(*a*) and (*b*) $+g/-g$ pair revealing dipole character of early stage α_1 plate (15 s at 523 K, UQRT).

displacement vector associated with the strain field was determined to be $[131]_{\beta'}$. These features are consistent with the presence of coherency strain at the interface, suggesting the presence of a coherent or a semicoherent interface.

F. *On the Question of the Aspect Ratio of α_1 Plates*

Wu *et al.*[15] remarked that the aspect ratio of α_1 plates observed at early reaction times by Chattopadhyay and Aaronson[11] is considerably larger than that estimated from observations made during previous investigations. This consideration added further doubt that the plates Chattopadhyay and Aaronson studied were actually α_1. What Wu *et al.* failed to note, however, was that these plates were photographed at a much earlier stage in their growth than those examined by previous investigators. The resulting difference in aspect ratio can then be explained on the basis of the ledgewise diffusional growth mechanism.[23] On this mechanism, plates form when the intergrowth ledge spacing at one boundary orientation is considerably greater than at any other boundary orientation. Experimental observations on this spacing[24,25] indicate that it tends to be very large at early growth times, to pass through a minimum at an intermediate time, and then to become increasingly large at still longer times. Evidently, the intergrowth ledge spacing at the broad face of α_1 plates is close to its minimum at the earliest stages that we have usually observed. The larger aspect ratio at later times is then consistent with the anticipated increase in the interledge spacing under these circumstances.

G. *Atomic Mechanism of α_1 Plate Formation*

We would conclude by re-emphasizing the importance of recent results obtained with high-resolution analytical electron microscopy, particularly those of Hamada *et al.*[10] These studies established a distinct difference in composition between α_1 plates only 3-nm thick and their surrounding β' matrix. It is also important to note that the α_1 plate composition was not observed to change during subsequent growth. Thermodynamic calculations[26] have established that there is no driving force for the β'-to-α_1 transformation without a change in composition in the aging temperatures customarily used in Cu-Zn alloys capable of producing α_1 plates, since T_0 and M_s are hundreds of degrees Kelvin lower than these temperatures. Although there have been suggestions that local fluctuations can significantly decrease the Zn content and thus increase the M_s temperature of these regions,[13] there is no physical basis for the presence of fluctuations of the magnitude required for the nucleation

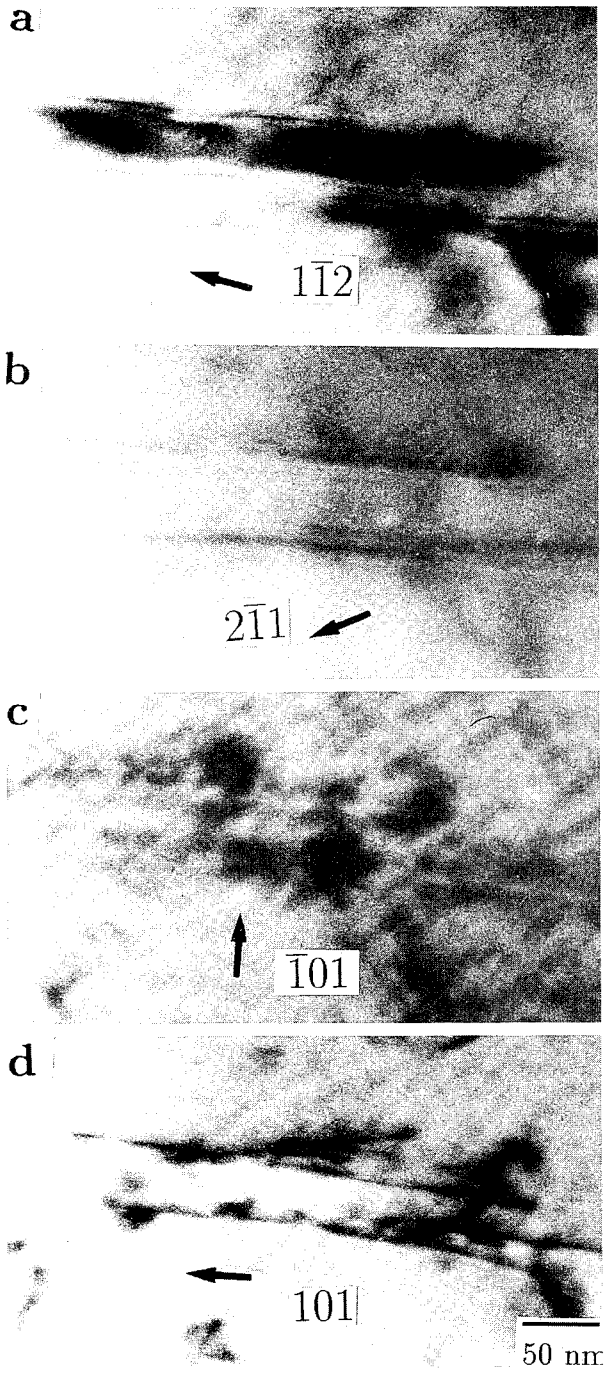


Fig. 10—(*a*) Shows the plate under precipitate diffraction contrast (zone near $[131]_{\beta'}$). The interface obtained by slightly tilting away from (a) can be seen in (*b*). (*c*) Shows strain field in the matrix near the plate matrix interface, indicating the presence of coherency strains at the interface; (*d*) shows the dislocation pair contrast from the α_1 plate. Both (c) and (d) are near $[010]_{\beta'}$ zone.

of martensite.[27] As an alternative mechanism for evading the T_0 stricture on transformation by shear, the suggestion has recently been made that the stress field around the edge of an α_1 plate provides the driving force for diffusion that will increase M_s locally to the aging temperature.[13] As also pointed out by Russell,[27] however, stress fields of this type cannot change the driving force for nucleation and growth. On the basis of the results presently available, therefore, the conclusion that α_1 plates form by diffusional nucleation and growth[3,11] remains valid.

ACKNOWLEDGMENTS

Much appreciation is expressed to Professor W.T. Reynolds, Jr. (Virginia Polytechnic Institute and State University) and Dr. George Spanos (Naval Research Laboratory) for their valuable comments upon earlier versions of this article.

REFERENCES

1. I. Cornelis and C.M. Wayman: *Acta Metall.*, 1974, vol. 22, pp. 301-11.
2. R.D. Garwood: *J. Inst. Met.*, 1954–55, vol. 83, pp. 64-68.
3. G.W. Lorimer, G. Cliff, H.I. Aaronson, and K.R. Kinsman: *Scripta Metall.*, 1976, vol. 9, pp. 271-80.
4. I. Cornelis and C.M. Wayman: *Scripta Metall.*, 1973, vol. 7, pp. 579-90.
5. P. Doig and P.E.J. Flewit: *Mater. Sci.*, 1983, vol. 17, pp. 601-08.
6. P. Doig and P.E.J. Flewitt: *Proc. Int. Conf.* on Solid-Solid Phase Transformations, TMS-AIME, Warrendale, PA, 1983, pp. 983-92.
7. Y. Nakata, T. Tadaki, and K. Shimuzu: *Mater. Trans. Jpn. Inst. Mater.*, 1989, vol. 30, pp. 107-16.
8. T. Tadaki, T. Uyeda, and K. Shimuzu: *Mater. Jpn. Inst. Mater.*, 1989, vol. 30, pp. 117-26.
9. C. Cliff, F. Hasan, G.W. Lorimer, and M. Kikuchi: *Metall. Trans. A*, 1990, vol. 21A, pp. 831-35.
10. Y. Hamada, M.H. Wu, and C.M. Wayman: *Metall. Trans. A*, 1994, vol. 25A, pp. 2581-99.
11. K. Chattopadhyay and H.I. Aaronson: *Acta Metall.*, 1986, vol. 34, pp. 695-711.
12. E. Hornbogen and H. Warlimont: *Acta Metall.*, 1971, vol. 19, pp. 943-51.
13. K. Takezawa and S. Sato: *Metall. Trans. A*, 1990, vol. 21A, pp. 1541-45.
14. Y.F. Hsu, W. Wang, and C.M. Wayman: *Scripta Metall. Mater.*, 1991, vol. 25, pp. 1059-64.
15. M.H. Wu, J. Perkins, and C.M. Wayman: *Acta Metall.*, 1989, vol. 37, pp. 1821-38.
16. M.J. Marcinkowski: *Electron Microscopy and Strength of Crystals*, G. Thomas and J. Washburn, eds., Interscience, New York, NY, 1963.
17. Z. Nishiyama: *Martensitic Transformations*, Academic Press, New York, NY, 1978, pp. 74-75.
18. H. Kubo, M. Ishii, and K. Shimuzu: *Trans. Jpn. Inst. Met.*, 1976, vol. 17, pp. 527-33.
19. K. Otsuka, C.M. Wayman, and H. Kubo: *Metall. Trans. A*, 1978, vol. 9A, pp. 1075-85.
20. E.S.K. Menon and H.I. Aaronson: *Acta Metall.*, 1987, vol. 35, pp. 549-63.
21. G.C. Weatherly, P. Humble, and D. Borland: *Acta Metall.*, 1979, vol. 27, pp. 1815-28.
22. J.W. Edington: *Practical Electron Microscopy in Materials Science*, The Macmillan Press Ltd., London, 1976, vol. 3.
23. H.I. Aaronson, T. Furuhara, J.M. Rigsbee, W.T. Reynolds, Jr., and J.M. Howe: *Metall. Trans. A*, 1990, vol. 21A, pp. 2369-2409.
24. H.I. Aaronson, C. Laird, and K.R. Kinsman: *Phase Transformations*, 1970, ASM, Materials Park, OH, 1970, p. 313.
25. R. Sankaran and C. Laird: *Acta Metall.*, 1974, vol. 22, p. 957.
26. T.Y. Hsu and Z. Xiaowing: *Acta Metall.*, 1989, vol. 37, pp. 3095-98.
27. K.C. Russell: *Metall. Trans. A*, 1994, vol. 25A, pp. 1933-39.

The Selection of Precipitate Habit Planes in Cr-32 Wt Pct Ni

J.K. CHEN, T.W. ROSS III, G. CHEN, M. KIKUCHI, and W.T. REYNOLDS, Jr.

Causes are investigated for the changes in precipitate crystal structure (fcc to 9R) and in morphology (degenerate plate to plate), which are observed to take place in Cr-Ni alloys as the reaction temperature decreases. Transmission electron microscopy (TEM) study is performed to determine the matrix/precipitate orientation relationship, habit plane, and growth ledge spacing. O-lattice modeling is used to show that it is likely that the metastable 9R phase forms as a transition phase at lower reaction temperatures because lattice matching at the bcc/9R habit plane is better than the matching at the bcc/fcc habit plane. The ability of the phenomenological theory of martensite crystallography (PTMC) to predict the habit plane of 9R plates precipitated by a diffusional mechanism is explained by the small lattice invariant deformation required to produce an invariant plane in Cr-Ni. Under this circumstance, the PTMC habit plane nearly coincides with the best-matching interface that presumably appears and is predicted by O-lattice theory.

I. INTRODUCTION

PLATE-shaped transformation products can exhibit characteristics of diffusional and martensitic transformations. This has led to debate over the mechanism of plate formation. The formation of 9R* plates from the parent B2-ordered phase in Cu-Zn alloys is one case in which the formation mechanism has been examined in detail.[1,2] The plates appear martensitic in that there are internal stacking faults that have been interpreted as evidence of a lattice invariant deformation, and their habit plane can be explained by the phenomenological theory of martensite crystallography (PTMC).[1,7] On the other hand, the interfacial structure of the plates is sessile and is incapable of migrating in a displacive fashion.[9] There are also data suggesting that the composition of the plates differs from the parent phase.[10] Although this point is controversial,[11–14] a recent work clearly demonstrates a composition difference at very early stages of plate growth.[15]

9R plates have also been observed by Emoto *et al.*[16] in chromium-rich Cr-Ni alloys. These workers showed that a high-temperature bcc phase decomposes to an irregularly shaped fcc precipitate, (hereafter, called degenerate fcc precipitate) at temperatures above about 1050 °C but to a well-defined Widmanstätten morphology, later identified as a metastable 9R phase,[17] at lower temperatures. Kikuchi *et al.* concluded the 9R plates form by a diffusional mechanism for two reasons: the plate composition is greatly different from that of the matrix even at the initial stages of growth, and the plates form at temperatures where a bcc → 9R martensitic transformation is thermodynamically impossible.[17]

The present work has two objectives. One is to explain why the metastable 9R phase rather than the more stable fcc phase forms in Cr-Ni alloys at lower temperatures. As a working hypothesis, it is assumed the 9R phase is a transition phase that nucleates more readily than the fcc phase at larger undercoolings. If this hypothesis is correct, the total energy of bcc 9R interphase boundaries must be less than the energy of bcc/fcc boundaries in order to provide a kinetic advantage for the 9R phase over the fcc phase during nucleation. Lower boundary energies for the 9R phase suggest that the 9R phase has better atomic matching with the bcc phase than does the fcc phase. To test this hypothesis, the matching across bcc/fcc and bcc/9R habit planes observed with transmission electron microscopy (TEM) in a Cr-32 wt pct Ni alloy is investigated with Bollmann's O-lattice model.[18]

The second objective is to explain why martensite crystallography is sometimes applicable to diffusional transformation. The change from a degenerate plate morphology to a plate morphology in Cr-32 wt pct Ni allows a comparison of the habit planes in two types of precipitates and facilitates investigation of why diffusionally formed precipitates select a habit plane predicted by the PTMC.

II. PROCEDURE

A. *Experimental*

A 100-g Cr-32 wt pct Ni ingot was made by arc melting appropriate amounts of (99.99 pct pure) Ni and (99.99 pct pure) Cr. The ingot was placed in a quartz capsule, evacuated to 10^{-5} torr, and sealed under an argon pressure of 1/3 atmosphere. The ingot was homogenized for 72 hours at 1300 °C and quenched to room temperature in water. Samples 10 × 10 × 1-mm

*The 9R structure (Ramsdel notation) has also been referred to as 3R[1,3–7] and, if ideal, has the Pearson symbol hR3.[8]

J.K. CHEN and G. CHEN, Graduate Students, and W.T. REYNOLDS, Jr., Associate Professor, are with the Department of Materials Science and Engineering, Virginia Polytechnic Institute and State University, Blacksburg, VA 24061-0237. T.W. ROSS III, formerly Graduate Student, Department of Materials Science and Engineering, Virginia Polytechnic Institute and State University, is Metallurgist, Beretta USA Corp., Accokeek, MD 20607. M. KIKUCHI, Professor, is with the Department of Metallurgical Engineering, Tokyo Institute of Technology, Tokyo 152, Japan.

This article is based on a presentation made at the Pacific Rim Conference on the "Roles of Shear and Diffusion in the Formation of Plate-Shaped Transformation Products," held December 18–22, 1992, in Kona, Hawaii, under the auspices of ASM INTERNATIONAL's Phase Transformations Committee.

in size were cut from this ingot, wrapped in tantalum foil, and resealed in an argon atmosphere.

Two different heat treatments were used to produce the precipitate morphologies for this study. To obtain 9R plates, encapsulated samples were solution annealed for 12 hours at 1325 °C, direct quenched to 1000 °C, held for 300 seconds, and quenched to room temperature in water. To obtain the fcc degenerate morphology, encapsulated samples were solution annealed at 1325 °C for 12 hours, direct quenched to 1100 °C, held for 900 seconds, and quenched to room temperature.

For optical microscopy, an etchant composed of 20 mL HNO_3 and 60 mL HCl was employed. The TEM specimens were jet polished at −30 °C with a potential of 220 V using a solution[19] containing (by volume): 7 pct perchloric acid, 11 pct butyl-cellosolve, 31 pct *n*-type butanol, and balance ethanol. Transmission electron microscopy was performed in a PHILIPS EM420 operated at 120 kV to determine the morphology, the matrix/precipitate orientation relationship, and the precipitate habit plane. Precipitate habit planes were determined using double-trace analysis.[20,21]

B. *O-Lattice Calculation*

The O-lattice theory developed by Bollmann[18] is employed here to evaluate the matching across the precipitate/matrix habit plane. While considering the bcc matrix as lattice 1 and either an fcc or 9R precipitate as lattice 2, the geometric transformation of lattice 2 from lattice 1 can be written as[18]

$$\mathbf{X}_{(2)} = \mathbf{R}\mathbf{S}_{(2)}\mathbf{S}_{(1)}^{-1}\mathbf{X}_{(1)} \equiv \mathbf{A}\mathbf{X}_{(1)} \qquad [1]$$

where $\mathbf{S}_{(1)}$ and $\mathbf{S}_{(2)}$ are matrices whose columns are the basis vectors for the primitive cells of lattices 1 and 2, respectively, expressed in an arbitrary Cartesian coordinate system. The matrix, $\mathbf{R}$, is the rotation needed to generate the specified orientation relationship, $\mathbf{X}_{(1)}$ is any arbitrary vector in the parent phase, and $\mathbf{X}_{(2)}$ is the vector in the product phase onto which $\mathbf{X}_{(1)}$ is mapped by the transformation.

O-points are defined as those positions with the same internal coordinates in both the matrix and precipitate. These points form a lattice defined by the condition[18]

$$\mathbf{X}_{(O)} = (\mathbf{I} - \mathbf{A}^{-1})^{-1}\mathbf{b}_{(L)} \qquad (\mathbf{I} = \text{identity matrix}) \quad [2]$$

where $\mathbf{b}_{(L)}$ is a lattice vector in lattice 1 and it is mapped to an O-point, $\mathbf{X}_{(O)}$, in the O-lattice.

The columns in the $(\mathbf{I} - \mathbf{A}^{-1})^{-1}$ matrix are the basis vectors of the O-lattice. In moving from one O-point to the next, the precipitate and matrix lattice undergo a disregistry of one basis vector with respect to lattice 1. The longer the O-lattice vectors, the larger the volume of the O-lattice unit cell and the better the precipitate and matrix crystal lattices match each other. The determinant of $(\mathbf{I} - \mathbf{A}^{-1})^{-1}$ represents the volume of the O-lattice unit cell and is thus an indicator of how well the two lattices match.

The O-lattice generated by two crystals with a given orientation relationship is not unique. The most significant one, from a physical point of view, is the one giving the best matching between the precipitate and matrix. This implies $\mathbf{S}_{(1)}$ and $\mathbf{S}_{(2)}$ should be chosen so that $\mathbf{A}$ is close to $\mathbf{I}$, or equivalently, $\mathbf{A}$ should be selected so that the distortion transforming lattice 1 to lattice 2 is as small as possible.[22,23] For an fcc/bcc transformation, this leads to the Bain correspondence and the Bain distortion.

The primitive cells for bcc and 9R structures

A convenient primitive cell for the bcc phase is described by three vectors:[18] $1/2[111]_{bcc}$, $[010]_{bcc}$, and $1/2[11\bar{1}]_{bcc}$. The 9R phase can be constructed by stacking close-packed planes in the sequence . . . *ABCBCACAB* . . .. This is equivalent to an fcc crystal with an intrinsic stacking fault every three planes. An orthorhombic unit cell of the 9R structure is shown in Figure 1. The ideal ratios of the lattice constants $a:b:c$ are $1:\sqrt{3}:3\sqrt{6}$.

To construct a primitive 9R cell (dashed in Figure 1) similar to the bcc primitive cell, two close-packed directions, $1/2[110]_{9R}$ and $[100]_{9R}$, are selected. The third basis vector must span at least three close-packed planes to produce the correct stacking sequence. The inclusion of three close-packed planes requires inclusion of two more atoms within the primitive cell, so a 9R primitive

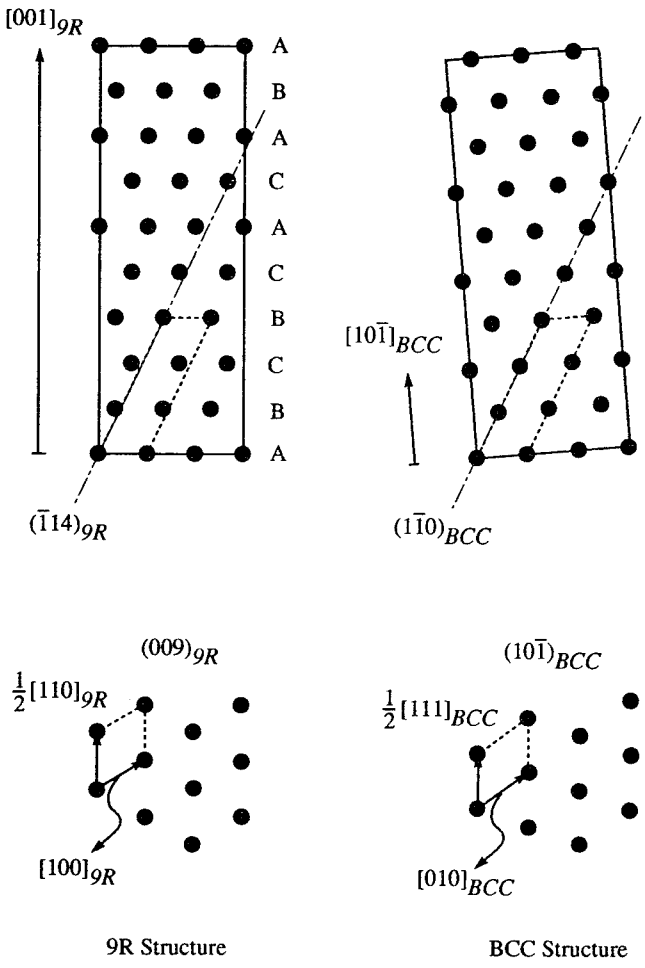


Fig. 1—The 9R structure (in orthorhombic notation) and the bcc structure. The primitive cells used in the O-lattice calculation are dashed. The bottom portion of the figure depicts the locations of atoms in the $(009)_{9R}$ and the $(10\bar{1})_{bcc}$ planes—the closest-packed planes of the two crystal structures. The upper portion of the figure represents the stacking sequence of these planes.

cell contains a total of three atoms. The bcc cell must be increased in size to include the same number of atoms as the 9R cell, and this is done by stacking three of the bcc primitive cells together (dashed in Figure 1). Increasing the size of the bcc unit cell does not affect the resulting O-lattice provided the atoms within the larger unit cell are included in the O-lattice calculation.

When the crystals can be described with only one atom per unit cell, a misfit dislocation network in the interphase boundary can be calculated in a straightforward way: Wigner–Seitz cells are constructed about the O-lattice points. The intersection of the boundary plane and the Wigner–Seitz cells represents lines of maximum misfit between the two crystals and can be interpreted as misfit dislocation.[18]

However, this now classical approach to obtaining interphase boundary structure (Eq. [2]) fails to locate all the regions of good matching if the unit cells of either crystal contain more than one atom, as is the case for the 9R and bcc lattices considered here. The effect of the two additional atoms in the bcc and 9R cells on the interfacial matching can be included by using a modified O-lattice developed by Mou.[24] In this approach, the O-points are given by

$$\mathbf{X}_{(O)} = \mathbf{X}_{(2)} + \mathbf{t} = \mathbf{X}_{(1)} + \mathbf{b}_{(L)}$$

Manipulation of this condition yields

$$\mathbf{X}_{(O)} = (\mathbf{I} - \mathbf{A}^{-1})^{-1}\,\mathbf{b}_{(L)} + (\mathbf{I} - (\mathbf{I} - \mathbf{A}^{-1})^{-1})\mathbf{t} \quad [3]$$

where $\mathbf{t} = \mathbf{R}\mathbf{t}_{(2)} - \mathbf{t}_{(1)}$ and $\mathbf{t}_{(2)}$ are the vectors describing the locations of the atoms in crystals 1 and 2, respectively. From Eq. [3], it can be seen that the O-points due to the extra atoms are shifted $(\mathbf{I} - (\mathbf{I} - \mathbf{A}^{-1})^{-1})\,\mathbf{t}$ from the original O-points. Each extra atom in a unit cell generates an additional set of O-points, because the extra atom doubles the number of atom planes in a given direction. However, the total amount of linear misfit in any direction remains unchanged.

The additional O-points from extra atoms in the unit cells can make locating the Wigner–Seitz cell walls by the conventional geometric approach difficult. In the present work, the cell walls were determined numerically by locating the points in space for which the misfit, u, is a maximum. The misfit is given by

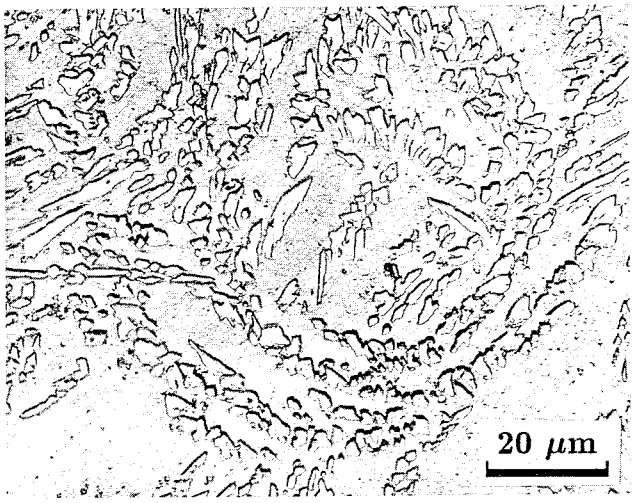
$$\text{misfit} = u(\mathbf{r}) = (\mathbf{I} - \mathbf{A}^{-1})\mathbf{r} \quad [4]$$

where $\mathbf{r}$ is the position vector from the nearest O-point to a point of interest. The loci of points around a given O-point for which $u(\mathbf{r})$ is a maximum are the Wigner–Seitz cell walls.

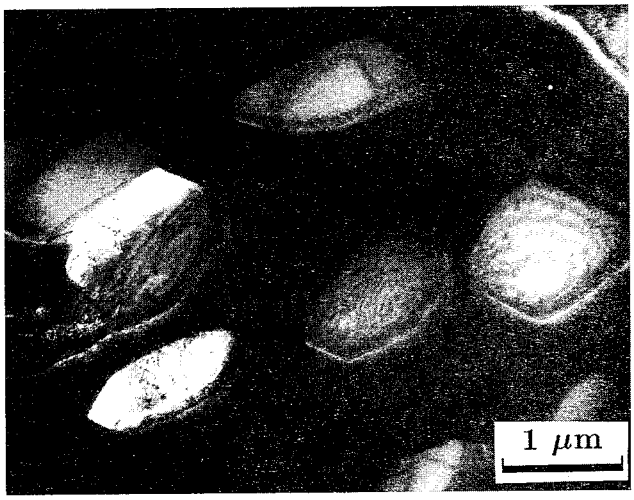
III. RESULTS

A. *Experimental*

The morphology of the degenerate fcc precipitates and the 9R plates are shown with optical microscopy in Figures 2 and 3(a) and (b). The degenerate fcc precipitates appear irregular and highly branched. With TEM, they are seen to be a collection of small, faceted crystals. The connected nature of the precipitates suggests that they form by a sympathetic nucleation process.[25,26] The



(*a*)

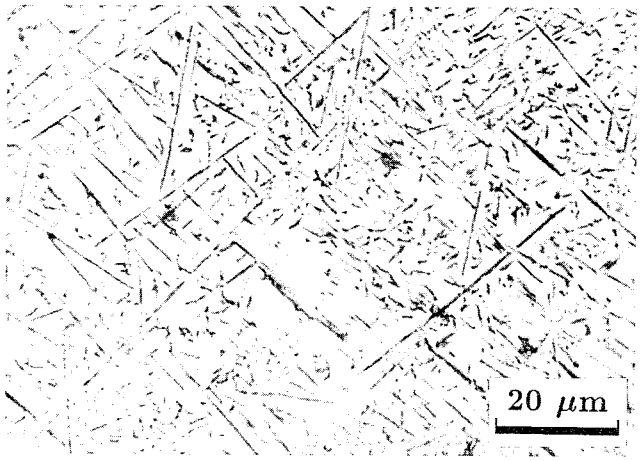


(*b*)

Fig. 2—Microstructure of degenerate fcc precipitates in Cr-32 wt pct Ni isothermally reacted for 900 s at 1100 °C: (*a*) optical micrograph and (*b*) TEM micrograph.

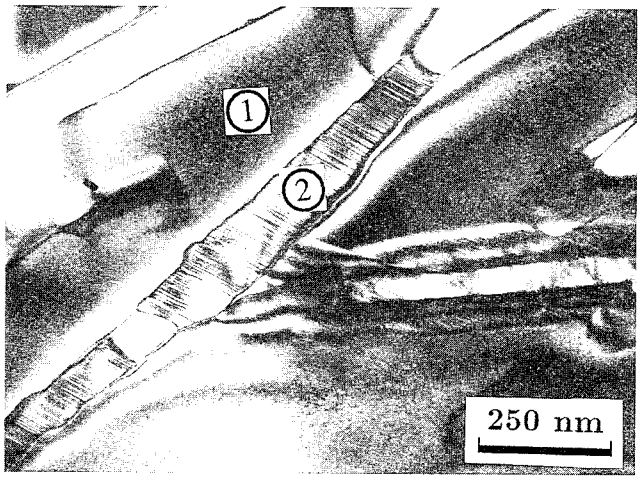
fcc precipitates exhibit a Kurdjumov–Sachs (KS) orientation relationship with the parent bcc matrix[27] in agreement with earlier reports.[16]

The 9R plates have a large aspect ratio and a well-developed habit plane, as shown in Figures 3(a) and (b). The diffraction pattern of these plates differs somewhat from that of a 9R phase (Figure 3(c)). A true 9R phase does not exhibit streaking in the diffraction pattern. The streaks in Figure 3(c) are consistent with the presence of random stacking faults on the $(009)_{9R}$ planes or the random removal of stacking faults from a periodically faulted fcc structure. The latter process occurs as the 9R phase transforms to the equilibrium fcc phase;[1] this is apparently a rapid process at 1000 °C in the Cr-Ni alloy. Operationally, the faulting of the 9R phase occurs by the passage of a Shockley partial on every third $(009)_{9R}$ plane. If each of these partials has the same Burgers vector, the 9R lattice undergoes a simple shear of 0.24 to convert it completely to the fcc structure.

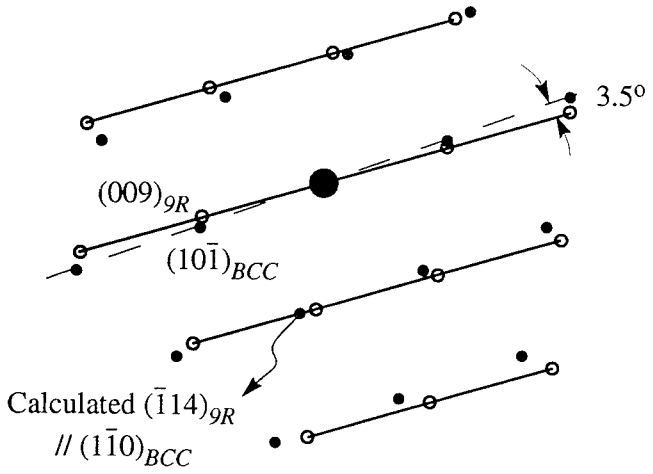


(a)

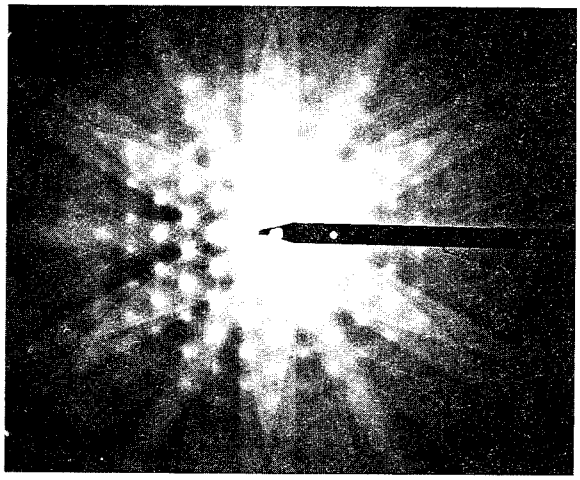




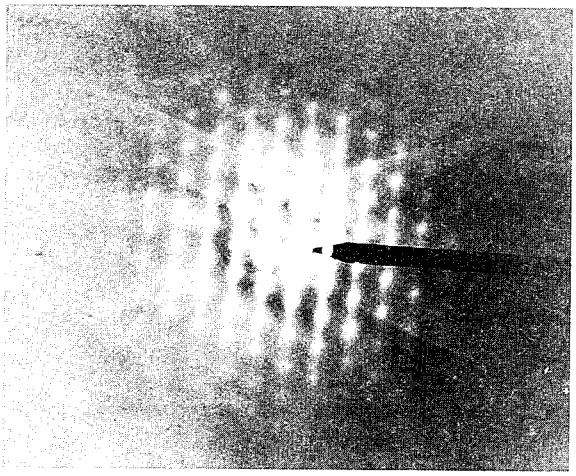
(b)



(c)



(d)



(e)

Fig. 3—Microstructure of 9R plates in Cr-32 wt pct Ni isothermally reacted for 300 s at 1000 °C: (*a*) optical micrograph; (*b*) TEM micrograph; (*c*) diffraction pattern from the bcc and 9R phases; (*d*) diffraction pattern from the bcc matrix (location 1 in (b)); (*e*) diffraction pattern from the 9R precipitate (location 2 in (b)). The locations of the Kikuchi lines in (d) and (e) indicate the bcc phase is on its zone axis while the 9R precipitate is slightly off its zone axis.

The orientation relationship between the 9R phase and the bcc phase before the 9R converts to fcc can be deduced from Figures 3(c) through (e). The streaks lie perpendicular to the $(009)_{9R}$ plane and become a $(111)_{fcc}$ plane after annealing. The open circles, which actually correspond to fcc diffraction spots, indicate that the zone axis is in a close-packed $[\bar{1}10]_{fcc}$ direction. Thus, the 9R zone must also have been in the $[110]_{9R}$ close-packed direction. The calculated location of the $(\bar{1}14)_{9R}$ diffraction spot in the $[110]_{9R}$ zone is parallel to the observed $(1\bar{1}0)_{bcc}$ plane. The bcc/9R orientation relationship is thus inferred to be $[111]_{bcc} \parallel [110]_{9R}$ (to within 1 deg) and $(1\bar{1}0)_{bcc} \parallel (\bar{1}14)_{9R}$. This orientation relationship is the same as that reported in similar Cr-Ni alloys[16,28] and in Cu-Zn alloys.[7,1,9]

It is interesting to note that the close-packed planes of the two crystal structures are *not* parallel in this orientation relationship as is often assumed to occur for precipitation reactions. The angle between the $(10\bar{1})_{bcc}$ and $(009)_{9R}$ planes is approximately 3.5 deg, or about 2 deg less than the angle reported in the previous studies. This discrepancy may be due to a different extent of conversion of the 9R phase to fcc because the *c*-axis of the 9R phase must expand slightly as it transforms,[28] and the passage of Shockley partials on the $(009)_{9R}$ plane can cause this plane to rotate slightly.

The measured orientations of three 9R habit planes are shown in Figure 4. Four different zone axes were used to determine each habit plane. The three 9R habit planes lie within 10 deg of each other, and the average index of the three planes is $(2.25\ \overline{1.96}\ 1)_{bcc}$. Kikuchi[28] determined that the habit plane in an alloy of the same concentration reacted at 1000 °C for 100 seconds to be $(4.85\ \overline{4.27}\ 1)_{bcc}$, which is approximately 10 deg from the average habit plane obtained here.

The facet planes of the fcc degenerate precipitates were also determined. The individual crystals had two predominant facets. The habit plane of the long facet is close to a $(2\bar{1}1)_{bcc}$ plane and that of the short facet of the precipitate is near a $(\bar{2}\bar{4}3)_{bcc}$ plane.

Growth ledge spacings were measured on the degenerate plate morphology. On facets exhibiting a $(2\bar{1}1)_{bcc}$ habit plane, the growth ledge spacings are regular and 22.1 nm on average. For facets exhibiting a $(\bar{2}\bar{4}3)_{bcc}$ habit plane, the average ledge spacing is 14.7 nm. The ledges on the two habit planes can be seen in Figure 5. An accurate determination of ledge spacing was not possible for the 9R plates because of difficulty in distinguishing ledges from stacking faults intersecting the precipitate/matrix interface. In addition, the ledge structure of the plates almost certainly changed as the 9R phase decomposed to the fcc phase. Arrays of parallel linear features were observed in the fcc degenerate precipitate interfaces and in the 9R plate interface, but not under enough diffracting conditions to characterize them unambiguously.

B. *Dislocation Network on Habit Planes Evaluated from O-Lattice Theory*

The basis vectors of the O-lattice are given by the columns of the matrix $(\mathbf{I} - \mathbf{A}^{-1})^{-1}$ with $\mathbf{A}$ calculated from Eq. [1]. For an fcc precipitate in a KS orientation relationship with a bcc matrix (*i.e.*, $(1\bar{1}1)_{fcc} \parallel (101)_{bcc}$ and $[\bar{1}01]_{fcc} \parallel [\bar{1}\bar{1}1]_{bcc}$) and an fcc/bcc lattice parameter ratio of 1.255,[29,30] the matrix $(\mathbf{I} - \mathbf{A}^{-1})^{-1}$ is

$$(\mathbf{I} - \mathbf{A}^{-1})^{-1} = \begin{bmatrix} 608.825 & -39.670 & 527.674 \\ 704.188 & -55.691 & 607.016 \\ -567.344 & 39.670 & -486.193 \end{bmatrix} \quad [5]$$

The determinant of this matrix is −27,564; this is a measure of the size of the O-lattice unit cell (the negative sign indicates the O-lattice unit cell is in a left-handed coordinate system). The dislocation network evaluated on the observed $(2\bar{1}1)$ facet plane is shown in Figure 6(a).

For the orientation relationship between the 9R plates

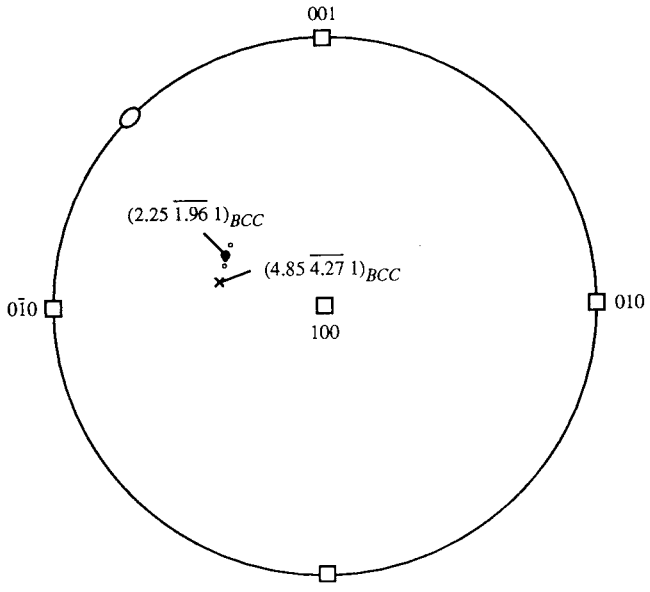


Fig. 4—Stereographic projection showing the location of the 9R plate habit planes determined using double-trace analysis.

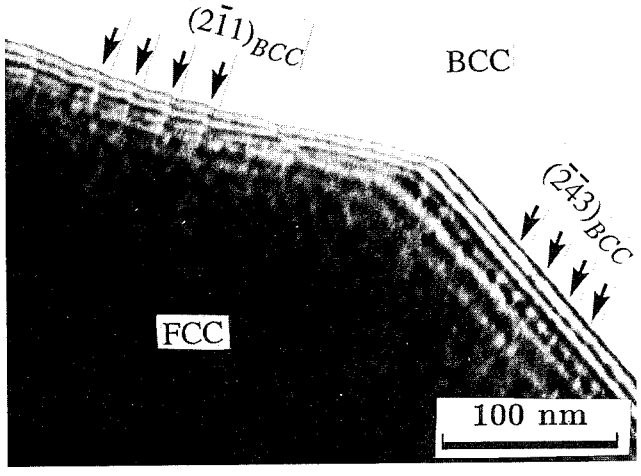


Fig. 5—Interfacial structure of the $(2\bar{1}1)_{bcc}$ and $(\bar{2}\bar{4}3)_{bcc}$ facet planes on degenerate fcc precipitates.

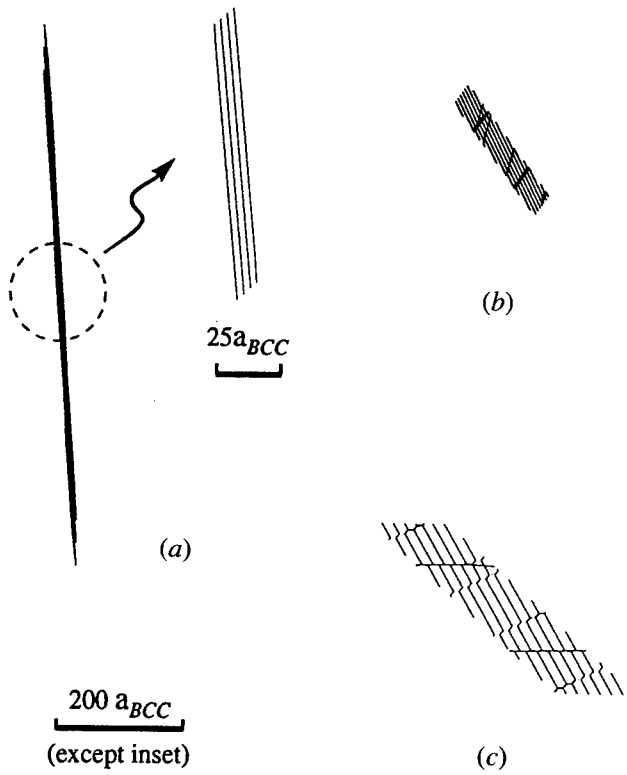


Fig. 6—Dislocation network evaluated by O-lattice theory on (*a*) $(2\bar{1}1)_{bcc}$ habit plane (bcc/fcc), (*b*) (2.25 $\overline{1.96}$ 1)$_{bcc}$ habit plane (bcc/9R), and (*c*) (4.85 $\overline{4.27}$ 1)$_{bcc}$ habit plane (bcc/9R).

and the bcc matrix, the best matched primitive cells under the above orientation relationship are shown in Figure 1. The bcc primitive cell basis vectors are $1/2[111]_{bcc}$, $[010]_{bcc}$, and $3/2[11\bar{1}]_{bcc}$. The primitive cell of the 9R structure is then constructed by $1/2[110]_{9R}$, $[100]_{9R}$, and $[3/2\ 1/6\ k/3]_{9R}$, where k is the ratio of the length of the actual c-axis to that of the ideal c-axis for closed-packed stacking of the closed-packed $(009)_{9R}$ planes. For Cr-Ni, this ratio at room temperature is approximately $7.330/3\sqrt{6}$.[28] The matrix $(\mathbf{I} - \mathbf{A}^{-1})^{-1}$ for matching of 9R and bcc phases is

$$(\mathbf{I} - \mathbf{A}^{-1})^{-1} = \begin{bmatrix} 75.052 & -66.675 & 33.103 \\ 118.174 & -112.173 & 35.480 \\ 305.803 & -261.863 & -2.459 \end{bmatrix} \quad [6]$$

and its determinant is 86,357. Figure 6(b) shows the evaluated dislocation network on the experimentally observed (2.25 $\overline{1.96}$ 1)$_{bcc}$ habit plane. Figure 6(c) shows the calculated dislocation structure on the (4.85 $\overline{4.27}$ 1)$_{bcc}$ habit plane reported by Kikuchi.[28] The results of the two types of O-lattices described above, as well as results obtained from O-lattices calculated with different precipitate/matrix lattice parameter ratios, are summarized in Table I.

IV. DISCUSSION

A. *Precipitation of a Metastable Transition Phase*

In order for a metastable phase to nucleate, the work of formation of its critical nucleus must be lower than that for the equilibrium phase. The formation energy is a sensitive function of the interphase boundary energy and the shape of the nucleus.[31] In the absence of detailed information on the shape and energy of the critical nucleus, even for the simple case of an fcc precipitate in a bcc matrix, it is reasonable to assume a large proportion of the nucleus is enclosed by a good-matching (low-energy) interphase boundary.[32]

Such a boundary can be identified by intersecting planes through the O-lattice. Good matching boundaries are those with widely spaced O-points (or widely spaced Wigner–Seitz cell walls). The presence of at least one long column vector in the matrices of Eqs. [5] and [6] indicates that the O-lattice cells for the bcc/fcc and bcc/9R cases considered here are highly elongated. Thus, the good-matching boundaries for these cases should contain the long vectors of the O-lattice. The near-parallel misfit dislocation arrays shown in Figure 6 are characteristic of such good-matching boundaries.

By comparing these dislocation arrays, it can be seen that Figure 6(c) has the largest dislocation spacing of the experimentally observed habit planes. The (4.85 $\overline{4.27}$ 1)$_{bcc}$ habit plane for 9R has slightly better interfacial matching than the (2.25 $\overline{1.96}$ 1)$_{bcc}$ habit plane, and this interface matches better than the $(2\bar{1}1)_{bcc}$ habit plane for fcc in the KS orientation relationship.

The effect of lattice parameter ratio on the interfacial matching can be seen in the last three rows of Table I. If the interatomic distances in the closed-packed directions of the matrix and precipitate phases are the same, *i.e.*, $a_{fcc}/a_{bcc} = \sqrt{3/2}$ or $\sqrt{2}\ a_{9R}/a_{bcc} = \sqrt{3/2}$, then the O-lattice cell becomes infinitely long in one direction and the determinant is infinite. This direction is an invariant line,[33] or a direction of perfect registry between the two phases.

If the closed-packed planes in the 9R phase are stacked with the ideal spacing ($k = 1$), the determinant of $(\mathbf{I} - \mathbf{A}^{-1})^{-1}$ is 125,141, 45 pct larger than the value obtained (86,355) using the experimental value of k (Table 1). This indicates that the small contraction of the Cr-Ni 9R phase along the c direction produces slightly worse matching with the bcc phase than the ideal, closed-packed 9R phase.

These comparisons indicate that 9R precipitates in the Cr-Ni system exhibit better matching with the bcc parent phase than the fcc precipitates. Thus, the 9R phase is likely to have a lower interfacial energy than the equilibrium fcc phase, and it is reasonable to expect 9R to nucleate more readily at lower reaction temperatures where there is sufficient supersaturation to overcome the reduced driving force associated with formation of the metastable phase. This deduction is consistent with the observed transformation sequence. At 1100 °C in Cr-32Ni alloy, fcc is the precipitate phase. At 1050 °C, slightly below the 9R solvus,[17] 9R forms first, but the fcc phase appears to precipitate soon after,[16] as the supersaturation for 9R formation is depleted. At 1000 °C, a large volume fraction of the 9R plates can be formed. At both 1050 °C and 1000 °C, continued holding of 9R plates at the reaction temperature causes the 9R phase to decompose to the equilibrium fcc phase.

Table I. Comparison of the Evaluated O-Lattices in Different Conditions

Structures (Matrix/Precipitate)	a_{fcc}/a_{bcc} (or $\sqrt{2}a_{9R}/a_{bcc}$)	k (c/Ideal c)	$\lvert\mathrm{Det}(\mathbf{I} - \mathbf{A}^{-1})^{-1}\rvert$ (in bcc Coordinate)
bcc/fcc	1.255	1	27,564
bcc/9R	1.255	$7.330/3\sqrt{6}$	86,355
bcc/fcc	$\sqrt{3/2}$	1	∞
bcc/9R	$\sqrt{3/2}$	1	∞
bcc/9R	1.255	1	125,141

B. *Applicability of Phenomenological Theory of Martensite Crystallography*

The PTMC has been used in other systems exhibiting a bcc → 9R precipitation sequence to predict habit planes and orientation relationships. Kajiwara *et al.*[34] employed Suzuki's version[35] of the PTMC to show that the observed habit plane and orientation relationship of 9R plates in Cu-Al alloys agree quite well with predicted values, and the OR reported by Kikuchi[28] is also in close agreement with the predictions of the PTMC. This raises an apparent dichotomy: why does a martensitic theory accurately predict the crystallography of a diffusional precipitation reaction?

For the case of a diffusional reaction, the orientation relationship is likely to be selected to minimize the work of formation of the critical nucleus.[31] The orientation relationship is thus very likely to produce at least one good-matching boundary plane, although it is not necessarily a crystallographically invariant plane.

In order to keep the parent and product phases together across the interphase plane during a martensitic transformation, on the other hand, a shear strain is generally needed in addition to the deformation that transforms the parent lattice to the product lattice. Operationally, this shear component of the PTMC (sometimes called the lattice invariant deformation) is the only difference between the PTMC theory and the O-lattice construction. Thus, for cases in which the shear component of the PTMC is small, the habit plane predicted by this theory will be close to a good-matching plane determined by the O-lattice construction.

This is the case for some 9R precipitation reactions. A lattice invariant shear of less than 2 pct relative to the length of the a-axis is required to produce an invariant plane in the Cr-Ni alloy. The lattice invariant shear in Cu-Al[34] (if chosen in the $(009)_{9R}$ plane in the $[010]_{9R}$ direction) has a magnitude of less than 1 pct relative to the length of the shortest axis.* These small shears indicate that precipitation of 9R in the Cr-Ni and Cu-Al systems can produce a near-invariant plane without a lattice invariant shear, and this plane is close to the good-matching plane predicted by the O-lattice theory. Because, in Cu-Al, the lattice parameter ratio ($\sqrt{2}a_{9R}/a_{bcc}$) ranges from 1.260 to 1.264, within 1 pct of the lattice parameter ratio in Cr-Ni (1.255), the good-matching plane is almost the same in both alloy systems.

*Kajiwara[34] uses a different orthorhombic coordinate system from that employed here; the shortest axis corresponds to the a-axis in this work.

The O-points calculated from Eq. [6] for matching between bcc and 9R are distributed in a thin slab in three dimensions. The index of the slab plane, which is the good-matching plane, can be determined analytically[36] and is approximately $(8.62\ \overline{7.72}\ 1)$. This plane is about 3.9 deg from the observed $(4.85\ \overline{4.27}\ 1)_{bcc}$[28] habit plane. The habit plane predicted by Suzuki's method is $(3.10\ \overline{3.14}\ 1)_{bcc}$, about 5.6 deg from the observed plane. Thus, both PTMC and O-lattice theories give similar agreement with the observed bcc/9R habit plane in the Cr-Ni alloy. Similar agreement is found for the Cu-Al alloy.

Although the shape of 9R precipitates in these systems is probably not the equilibrium shape, the good-matching boundary orientation set during nucleation almost certainly affects the subsequent growth of the precipitate. At least for Cr-Ni and Cu-Al 9R plates, the habit plane appears to correspond to the good-matching boundary orientation. The $(2\bar{1}1)_{bcc}$ facet plane of the fcc degenerate precipitates is a good-matching boundary, but the $(\bar{2}43)_{bcc}$ facet plane has considerably poorer matching.

It seems clear that agreement between observed and predicted habit planes by the PTMC does not necessarily indicate that the transformation mechanism is diffusionless. Precipitation reactions can also produce facet planes near the PTMC predicted habit planes if the lattice invariant deformation (shear) component of the theory is small and if the precipitate/matrix orientation relationship is close to the PTMC orientation relationship.

V. CONCLUSIONS

The O-lattice model was used to investigate the interfacial matching of fcc and 9R precipitates with a bcc matrix in Cr-Ni alloys. The following conclusions were drawn from the interfacial matching calculated using experimentally observed habit planes and orientation relationships.

1. The 9R phase in Cr-Ni alloys produces better matching with the bcc matrix than the equilibrium fcc phase. As a result, it is likely to have a lower interfacial energy with the bcc phase and will nucleate more rapidly than the equilibrium phase provided sufficient supersaturation (undercooling) is available. This is consistent with the view that the 9R phase in Cr-Ni is a metastable transition phase that forms because it has better interfacial matching with the parent bcc phase than does the equilibrium fcc phase.

2. The PTMC predicts habit planes of diffusional transformations in cases where the lattice invariant deformation is small. For these cases, the PTMC and the O-lattice theory are practically the same and both identify planes of good-matching between the precipitate phase and the product phase.

ACKNOWLEDGMENTS

The National Science Foundation is gratefully acknowledged for the support of this study through Grant No. DMR 89-21943. The authors also thank H.I. Aaronson, Y. Mou, G. Spanos, U. Dahmen, and M.H. Wu for discussions that prompted some of this analysis.

REFERENCES

1. I. Cornelis and C.M. Wayman: *Acta Metall.*, 1974, vol. 22, pp. 301-11.
2. K. Chattopadhyay and H.I. Aaronson: *Acta Metall.*, 1986, vol. 34, pp. 713-20.
3. H. Sato, R.S. Toth, and G. Honjo: *J. Phys. Chem. Solids.*, 1967, vol. 28, pp. 137-60.
4. H. Sato, R.S. Toth, and G. Honjo: *Acta Metall.*, 1967, vol. 15, pp. 1381-96.
5. R.S. Toth and H. Sato: *Acta Metall.*, 1968, vol. 16, pp. 413-33.
6. S.P. Gupta: *Mater. Sci. Eng.*, 1972, vol. 10, pp. 341-56.
7. I. Cornelis and C.M. Wayman: *Acta Metall.*, 1974, vol. 22, pp. 291-300.
8. W.B. Pearson: *The Crystal Chemistry and Physics of Metals and Alloys*, Wiley Series on the Science and Technology of Materials, Wiley-Interscience, New York, NY, 1972.
9. K. Chattopadhyay and H.I. Aaronson: *Acta Metall.*, 1986, vol. 34, pp. 695-711.
10. G.W. Lorimer, G. Cliff, H.I. Aaronson, and K.R. Kinsman: *Scripta Metall.*, 1975, vol. 9, pp. 271-80.
11. I. Cornelis and C.M. Wayman: *Scripta Metall.*, 1973, vol. 7, pp. 579-90.
12. P. Doig and P.E.J. Flewitt: in *Proc. Int. Conf. on Solid-Solid Phase Transformations*, R.F. Sekerka, H.I. Aaronson, D.E. Laughlin, and C.M. Wayman, eds., TMS-AIME, Warrendale, PA, 1982, pp. 983-87.
13. B.C. Muddle and H.L. Fraser: in *Proc. Int. Conf. on Solid-Solid Phase Transformations*, R.F. Sekerka, H.I. Aaronson, D.E. Laughlin, and C.M. Wayman, eds., TMS-AIME, Warrendale, PA, 1982, pp. 987-90.
14. K. Chattopadhyay: in *Proc. Int. Conf. on Solid-Solid Phase Transformations*, R.F. Sekerka, H.I. Aaronson, D.E. Laughlin, and C.M. Wayman, eds., TMS-AIME, Warrendale, PA, 1982, pp. 990-91.
15. M.H. Wu, Y. Hamada, and C.M. Wayman: *Metall. Mater. Trans. A*, 1994, vol. 25A, pp. 2581-99.
16. H. Emoto, R. Ni-Ikura, and M. Kikuchi: in *Phase Transformations '87*, G.W. Lorimer, ed., Institute of Metals, London, 1988, pp. 169-73.
17. M. Kikuchi, A. Fernandez Guillermet, M. Hillert, G. Cliff, and G.W. Lorimer: *Acta Metall. Mater.*, 1990, vol. 38, pp. 165-71.
18. W. Bollmann: *Crystal Defects and Crystalline Interfaces*, Springer-Verlag, New York, NY, 1970.
19. B.J. Kestel: *Ultramicroscopy*, 1984, vol. 19, pp. 213-16.
20. M.H. Loretto and R.E. Smallman: *Defect Analysis in Electron Microscopy*, Chapman and Hall, London, 1975.
21. G. Spanos and H.I. Aaronson: *Acta Metall.*, 1990, vol. 38, pp. 2721-32.
22. M.G. Hall, J.M. Rigsbee, and H.I. Aaronson: *Acta Metall.*, 1986, vol. 34, pp. 1419-31.
23. W. Bollmann: *Phys. Status Solidi*, 1974, vol. A21, pp. 543-50.
24. Y. Mou: Ph.D. Thesis, Carnegie Mellon University, Pittsburgh, PA, 1992.
25. H.I. Aaronson and C. Wells: *Trans. AIME*, 1956, vol. 206, pp. 1216-23.
26. E.S.K. Menon and H.I. Aaronson: *Acta Metall.*, 1987, vol. 35, pp. 549-63.
27. G.V. Kurdjumov and G. Sachs: *Z. Phys.*, 1933, vol. 64, p. 647.
28. M. Kikuchi: *Metall. Mater. Trans. A*, 1995, in press.
29. W.C. Wyder and M. Hoch: *Trans. TMS-AIME*, 1963, vol. 227, pp. 588-92.
30. D.W. Bare, E.D. Gibson, and O.N. Carlson: *Trans. TMS-AIME*, 1964, vol. 230, pp. 934-36.
31. K.C. Russell and H.I. Aaronson: *J. Mater. Sci.*, 1975, vol. 10, p. 1991.
32. W.F. Lange III, M. Enomoto, and H.I. Aaronson: *Metall. Trans. A*, 1988, vol. 19A, pp. 427-40.
33. U. Dahmen: *Scripta Metall.*, 1981, vol. 15, pp. 77-81.
34. S. Kajiwara: *Trans. JIM*, 1976, vol. 17, pp. 435-46.
35. H. Suzuki: in *Physical Properties of Metals*, J. Yamashita and T. Suzuki, eds., Syokabo, Tokyo, 1968, pp. 394-420 (*in Japanese*).
36. J.K. Chen and W.T. Reynolds, Jr.: Virginia Polytechnic Institute and State University, Blacksburg, VA, unpublished research, 1993.

Bainitelike Transformations in Some Oxide Ceramics

N. NAKANISHI, T. SHIGEMATSU, T. FURUKAWA, and N. MACHIDA

The authors show two examples of "bainitelike" transformations in some oxide ceramics. A bainitelike transformation means that a shear (martensitic) mechanism is controlled by, or together with, ionic diffusion in the lattice as well as the case of lower bainite in steel. The first example is a tetragonal-to-monoclinic transformation in ZrO_2-Y_2O_3 ceramics, where the bainitelike transformation must be characterized by (1) the increase in concentration of oxygen vacancies caused by the substitution of Zr^{4+} ions by Y^{3+} ions, (2) a fairly high mobility of oxygen ions through their vacancies, and (3) the formation of clusters composed of oxygen vacancies and oxygen ions. The second case is an inverse spinel to corundum structural change observed in γ Fe_2O_3 to α Fe_2O_3, in which the bainitelike transformation may be explained by cooperative movements of oxygen and ferric ions, which are sandwiched between oxygen layers.

I. INTRODUCTION

ACCORDING to Nishiyama,[1] so-called lower bainite is made by a diffusionless transformation from austenite (γ) to ferrite (α) in steels where the transformation requires not only a shear mechanism but also an individual atomic movement and accompanies small nonchemical energies. Lattice invariant deformation and interface energies are associated with the transformation. Therefore, if the temperature is lower than T_0 (the equilibrium temperature between γ and α phases), the lower-bainitic transformation can occur even at temperatures higher than the M_s temperature. Although the progress of this transformation is usually prevented by volume strains caused by an expansion of the martensitic transformation, the growth of the bainitic α phase will be able to continue when the expansion stress is released by the contraction due to the precipitation of carbide in the α region. This fact suggests that the activation energy for the growth of lower bainite is close to that for the carbon diffusion in the α region. A fairly large surface relief can usually be observed with the lower bainitic transformation. Simply said, the lower bainitic transformation requires a cooperative atomic shear movement together with the diffusion of solute atoms.[2]

The "bainitelike" transformation, which the authors are proposing here in oxides, points out the following two cases:

(1) A tetragonal-to-monoclinic transformation occurs isothermally in ZrO_2-Y_2O_3 ceramics, this being similar to the eutectoidal transformation, $\gamma \rightarrow \alpha + Fe_3C$, in steel. In other words, as shown in the phase diagram (Figure 1), the bainitelike transformation occurs during isothermal holding after a rapid cooling from high temperature into the two-phase region of monoclinic + cubic. The bainitelike transformation is associated with the following phenomena: (a) A surface relief appears in the transformation from tetragonal to monoclinic; (b) this transformation, however, occurs not athermally but isothermally; and (c) the rate of isothermal transformation, as will be shown in Section III–A–2, is considered to be controlled by rotation or short-range diffusion of oxygen ions. This means that a fairly large strain can be released by these ionic movements. From the crystallographic point of view, the herringbone tetragonal phase of ZrO_2-2.0 mol pct Y_2O_3 thin films has been observed[3] to undergo partial transformation to the monoclinic phase with an orientation relationship similar to that found in pure ZrO_2: $(100)_m$ // $\{100\}_t$, $[001]_m$ // $\langle 001\rangle_t$. The habit plane of these plates is reported to be near $(301)_m$, and each plate has a substructure of fine striations interpreted to be planar faults on the $\{101\}_m$ plane, which corresponds to the $\{101\}_t$ twin plane of the twinned tetragonal band. Hayakawa *et al.*[4] have applied the W-L-R crystallographic theory, assuming a lattice invariant shear on whichever of the planes $(110)_m$, $(101)_m$, or $(011)_m$ is parallel to the $\{101\}_t$ twin plane.

(2) The bainitelike behavior has been observed also in the γ Fe_2O_3 to α Fe_2O_3 transformation, from inverse spinel structure to the corundum one, in which the short-range diffusion of Fe^{3+} ions through their vacancies may associate with the martensitic shear movement of oxygen ions.

There are two modifications in Fe_2O_3, *i.e.*, the γ and α forms. The former has an inverse spinel structure[5] with cell dimension $a = 0.8322$ nm, and $2 \cdot 2/3$ vacancies per unit cell in the cation lattice, while the latter is determined to be a rhombohedral corundum one[6] with cell dimensions $a = 0.54271$ nm, $\alpha = 55$ deg 17 min. It can also conveniently be described as a hexagonal structure with $a = 0.50345$ nm and $c = 1.3749$ nm.

The transformation of γ Fe_2O_3 to α Fe_2O_3 is found to occur irreversibly above 673 K. Bernal *et al.*[7] and Kachi *et al.*[8,9] studied this transformation by using X-ray diffraction (XRD) and electron diffraction techniques, respectively. They pointed out that there exists an orientation relationship between these forms, such as $(111)_\gamma$ // $(0001)_\alpha$ and $[1\bar{1}0]_\gamma$ // $[01\bar{1}0]_\alpha$. Also, the habit plane has been observed as a $(111)_\gamma$ (= $(0001)_\alpha$) plane. This transformation is of the ferrimagnetic to antiferromagnetic type.

The purpose of this article is to make clear the meaning of bainitelike transformation observed both in the cases

N. NAKANISHI and T. SHIGEMATSU, Professors, T. FURUKAWA, Postdoctoral Fellow, and N. MACHIDA, Lecturer, are with the Faculty of Science, Konan University, Higashinada-Ku, Kobe 652, Japan.

This article is based on a presentation made at the Pacific Rim Conference on the "Roles of Shear and Diffusion in the Formation of Plate-Shaped Transformation Products," held December 18–22, 1992, in Kona, Hawaii, under the auspices of ASM INTERNATIONAL's Phase Transformations Committee.

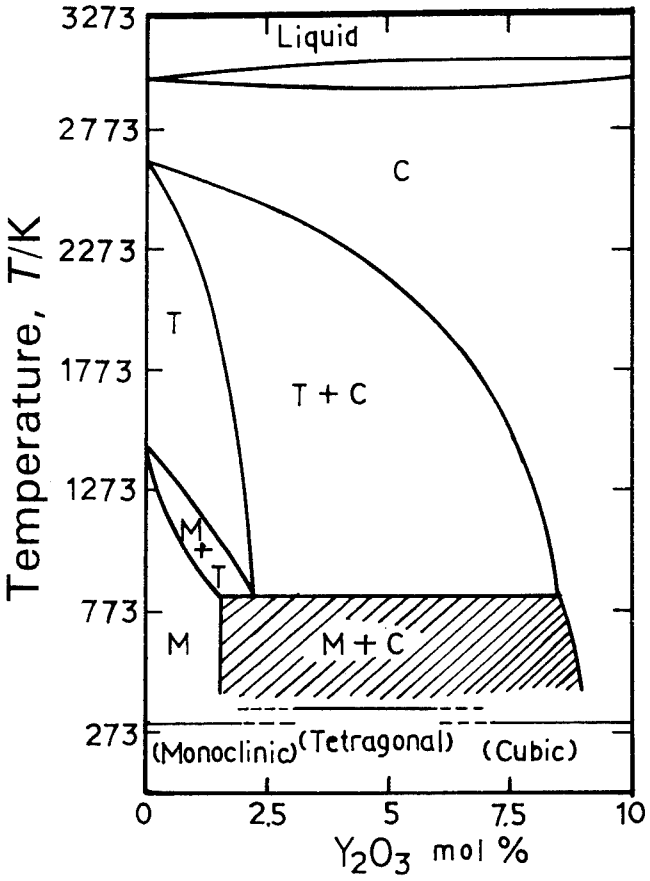


Fig. 1—Phase diagram of ZrO_2-Y_2O_3.

of the tetragonal-to-monoclinic transformation in the Y_2O_3-ZrO_2 solid solution and the $\gamma \rightarrow \alpha$ transformation in Fe_2O_3 ceramics. The mechanism of the bainitelike transformation would be that the martensitic shear was operated together with rotation or short diffusion of oxygen ions (in the former) and with synchronous rearrangement of ferric ions (in the latter).

II. EXPERIMENTAL PROCEDURES

The raw materials were 2.2 to 5.0 mol pct Y_2O_3 containing ZrO_2 powders. These powders were pressed at 100 MPa, and calcined for several hours at 1673 and 1873 K in air. Their average grain sizes after sintering were in the range of 0.3 to 5.0 μm. X-ray diffraction, Fourier-transform infrared spectroscopy (FT-IR) absorption spectra, thermogravimetric and differential scanning calorimeter (TG-DSC), bending strength, and thermal expansion measurements were made to check the monoclinic amounts transformed from the tetragonal phase during isothermal aging and upon cyclic thermal treatments.

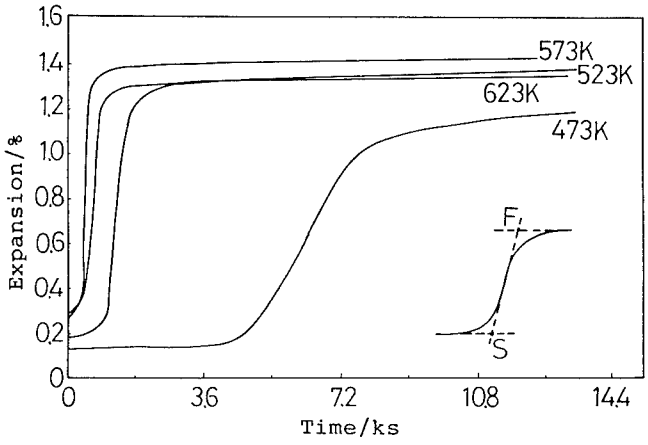
The starting material for obtaining thin plates of γ Fe_2O_3 was a lepidocrocite (γ FeOOH) precipitate with a thin-plate habit. It was approximately 5 μm in length, 1 μm in width, and a few tens of nanometers in thickness. The crystal was dehydrated and completely converted to γ Fe_2O_3 by heating at 523 K for a few hours. The authors observed these samples before and after the transformation with a JEOL* 120 electron microscope (120 kV) by using dark-field imaging and selected area diffraction as well as ordinary techniques.

*JEOL is a trademark of Japan Electron Optics Ltd., Tokyo, Japan.

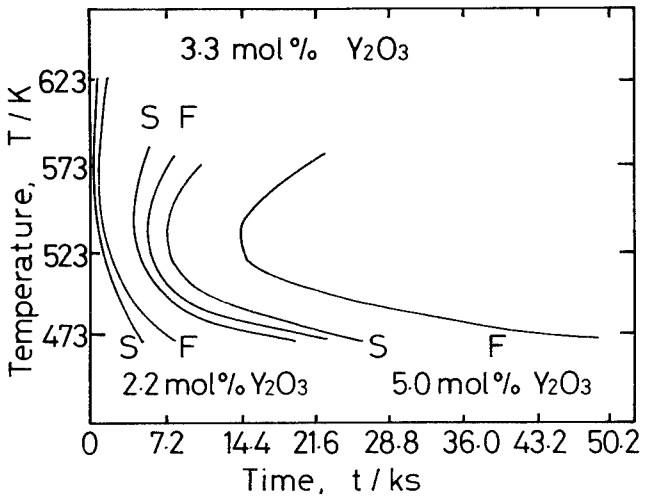
III. EXPERIMENTAL RESULTS AND DISCUSSION

A. *Isothermal Propagation of the Tetragonal-to-Monoclinic Transformation in ZrO_2-2.2 to 5.0 Mol Pct Y_2O_3 Sintered Ceramics*

ZrO_2-Y_2O_3 powder specimens were sintered for 10.8 ks (10.8×10^3 seconds) at 1673 and 1873 K and then isothermally held for several hours in the temperature range from 473 to 673 K in air. In Figure 2(a),[10] plots are shown of the isothermal growth of monoclinic phase detected by thermal expansion measurement, in which S and F note, respectively, "start and finish" of



(*a*)



(*b*)

Fig. 2—(*a*) Thermal expansion *vs* aging time in 2.2 mol pct Y_2O_3-ZrO_2. (*b*) TTT diagram obtained after isothermal holding in 2.2, 3.3, and 5.0 mol pct Y_2O_3-ZrO_2, after being sintered at 1873 K for 10.8 ks in air.[10]

the transformation, and time-temperature-transformation (TTT) diagram thus obtained is shown in Figure 2(b), where the *C*-curve behavior in the diagram was made by plotting the S and F points, and this was also confirmed by XRD. It is to be noted that the *C*-curves are much affected by their grain sizes.

As shown in Figure 3,[11] similar *C*-curves are obtained in a TTT diagram, where the shape of the *C*-curve and the nose temperature are very similar to one another, but the addition of Al_2O_3 retards the transformation, suggesting that a segregation phenomenon of Al_2O_3 occurs at grain boundaries in the specimens containing Al_2O_3 and results in the suppression of martensite propagation.

In order to study the isothermal character of the tetragonal $\rightleftharpoons$ monoclinic martensitic transformation, a cyclic thermal treatment, using 2.2 mol pct Y_2O_3-ZrO_2 Tetragonal Zirconia Polycrystals (TZP) specimens, was carried out, and the change in thermal expansion and contraction associated with the tetragonal $\rightleftharpoons$ monoclinic transformation was plotted against temperature (Figure 4). In the figure, where the grain size was 2 to 3 μm and the cycle rate was 2.1×10^{-2} ks^{-1}, an extraordinary expansion was observed in the first heating process, which was due to the appearance of the monoclinic phase. The subsequent contraction due to the reverse monoclinic-to-tetragonal transformation was followed at about 823 K. In the second and third cycles, similar expansion and contraction were also markedly observed, where the transformation temperatures M_s and A_s increased with increasing cycle number, *i.e.*, M_s = 673 K at the second, 723 K at the third, and 753 K at the fourth rising curve, whereas A_s = 723 K at the second and 823 K at the third falling curve, respectively. The following must be noted: (1) when the cycle-rate was increased to 8.4×10^{-2} ks^{-1} (four times larger), no expansion and contraction occurred both during heating and cooling, because of its isothermal (velocity dependent) character; and (2) if the athermal nature was assumed to control the rate of transformation, the expansion due to the tetragonal-to-monoclinic transformation could not occur during the first heating, but it was observed during the first cooling. Moreover, the amount of thermal expansion increased with the cycle number, suggesting a gradual increase in the monoclinic phase accompanying a small amount of cracks. A similar isothermal character of the tetragonal-to-monoclinic transformation was clearly observed in ZrO_2-2.0 mol pct Er_2O_3 ceramics.[12]

1. *Consideration of the tetragonal and monoclinic crystal structures related to oxygen-ion defects*

The crystallographic relationships between tetragonal and monoclinic phases in pure ZrO_2 have been studied.[13] Here, a dynamical behavior of oxygen ions associated with the transformation is discussed. The relative ionic positions between Zr^{4+} and O^{2-} are shown in Figures 5(a) and (b) corresponding to tetragonal and monoclinic lattices, respectively. In the case of Figure 5(a), the transformation into tetragonal from cubic is associated with the shift of oxygen ions in the direction parallel to the *c*-axis of the cubic lattice, the Zr-O_8 relation being maintained.

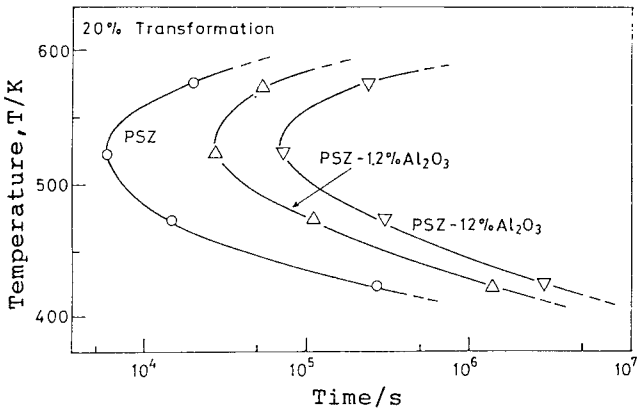


Fig. 3—TTT curves in partially stabilized zirconia (PSZ) with and without Al_2O_3.[11]

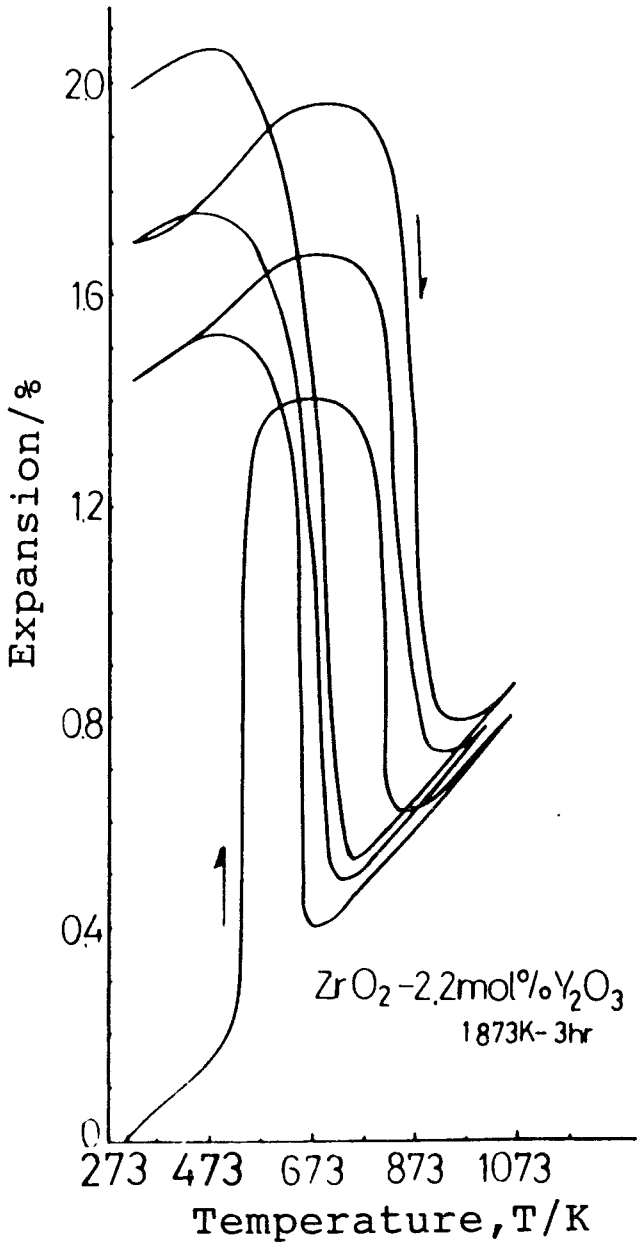


Fig. 4—Thermal expansion *vs* temperature associated with thermal cycles in 2.2 mol pct Y_2O_3-ZrO_2.

As shown in Figure 5(b), to make the monoclinic lattice, a complicated displacement of oxygen ions needs to occur, corresponding to the change in the coordination number from Zr-O_8 to Zr-O_7. Therefore, the authors suggest that this displacement of oxygen ions must be accompanied with the ionic shear from tetragonal-to-monoclinic symmetry.

As the specimens contain a small amount of Y_2O_3, and consequently, the oxygen ion vacancies are induced by holding the ionic neutralization in the lattice,

$$ZrO_2 + Y_2O_3 \rightleftharpoons ZrO_2 + 2Y_{Zr} + V_o + 3O_o$$

Here, V_0 is the oxygen vacancy. Since the vacancy concentration increases with the increase in Y_2O_3 concentration, it is expected that the tetragonal-to-monoclinic transformation character in the ZrO_2-Y_2O_3 solid solution, having a fairly large amount of oxygen vacancies, should be somewhat different from that of pure ZrO_2. More recently, it has been reported[14] that oxygen ions neighboring their vacancies tend to occupy some interstitial sites that are shifted from the equilibrium lattice positions in the CaF_2-type structure. The shifted positions are understood to be the Frenkel defect. Figure 6 illustrates that the interaction between the vacancies and oxygen ions located at the Frenkel positions can produce a kind of cluster.[15] It is probable, accordingly, to produce the same types of cluster or defect structure in the ZrO_2-Y_2O_3 lattice. It is of importance that in the tetragonal → monoclinic transformation, a more complicated displacement of oxygen ions (and related other cations) is required together with the martensitic shear to complete the transformation. This is the basis of the argument for the bainitelike nature of the tetragonal-to-monoclinic transformation in the ZrO_2-Y_2O_3 lattice.

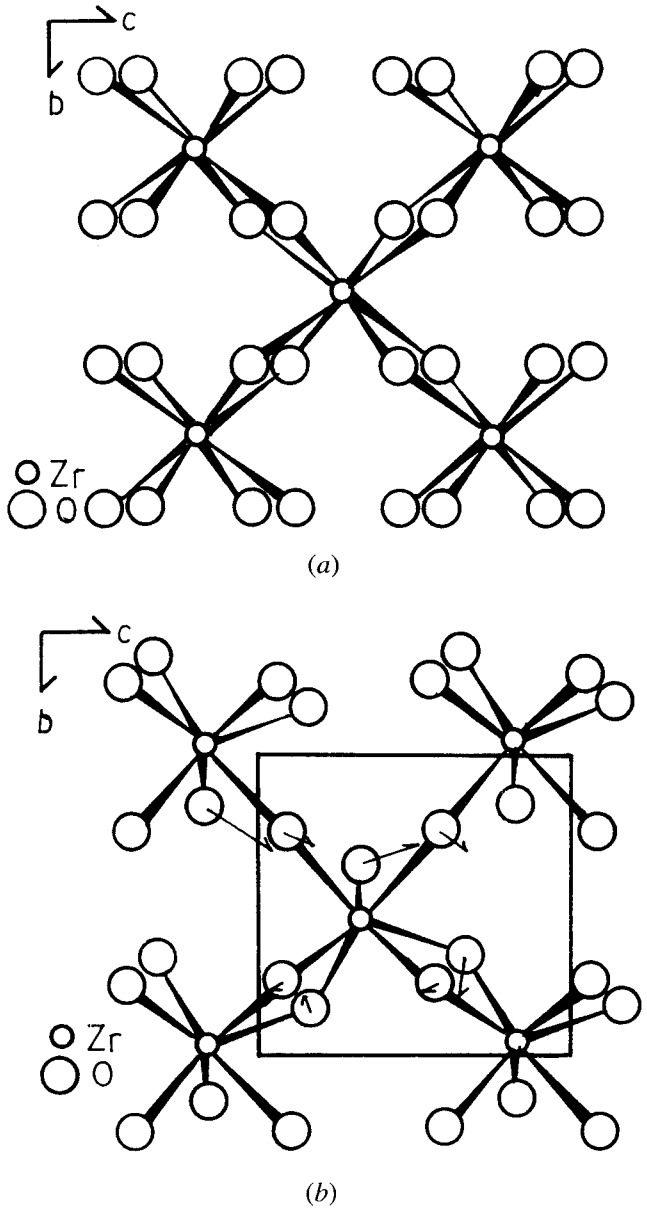


Fig. 5—Configuration of Zr-O groups: (*a*) Zr-O_8 groups on the (100) plane in the tetragonal lattice and (*b*) Zr-O_7 groups in the monoclinic lattice after being transformed.

2. *A simple description of the isothermal propagation of tetragonal-to-monoclinic transformation using "homogeneous nucleation theory"*

The growth rate of the monoclinic phase can be expressed as

$$N = K \exp\left[-(\Delta G_{n^*} + \Delta G_a)/RT\right]$$

Here, K contains the number of ions of critical radius and the frequency number of lattice vibrations. The terms ΔG_{n^*} and ΔG_a are, respectively, the activation energies for the formation of the critical nuclei and that necessary for the propagation or diffusion.

The authors assume a martensitic nucleus of disc shape having the radius of r, and the thickness c ($c \ll r$), and then the total change of the Gibb's free energy for martensitic nucleation is given by

$$\Delta G_n = \pi r^2 c \Delta G_c + 2\pi r^2 \sigma + \pi r^2 c(c/r \cdot A)$$

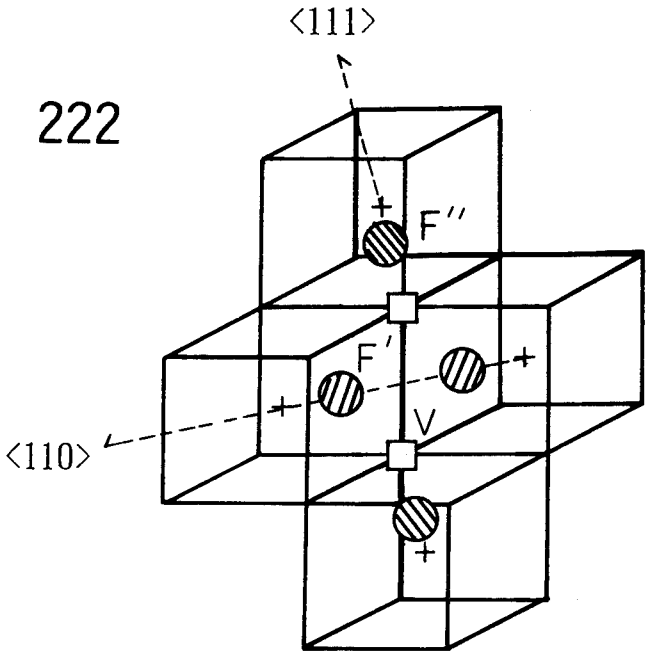


Fig. 6—The 222 cluster composed of two oxygen-ion vacancies, two interstitial F^{1-} ions along ⟨111⟩, and two interstitial F^{1-} ions along ⟨110⟩ directions.[15]

where ΔG_c is the change in the chemical free energy associated with transformation per unit volume, σ is the surface energy per unit surface area, and A is the unit strain energy.

The critical values for the stable nucleation can be obtained by the following condition:

$$\left(\frac{\partial G_n}{\partial r}\right)_c = \left(\frac{\partial G_n}{\partial c}\right)_r = 0$$

Therefore,

$$\Delta G_{n^*} = \frac{19\pi A^2\sigma^3}{\Delta G_c^4}$$

$$r_c = \frac{16A\sigma}{3\Delta G_c^2}$$

$$C_c = -\frac{r\cdot\Delta G_c}{2A}$$

where $\Delta G_c = \Delta H_c - T\cdot\Delta S_c = \Delta S_c^e\cdot\Delta T$. Here, ΔS_c^e is the entropy change at the equilibrium temperature, T_0, and $\Delta T = T_0 - T$. Since it is roughly assumed that the values σ, A, and ΔS_c^e are constant over the temperature change, ΔG_{n^*} can be expressed as

$$\Delta G_{n^*} = \frac{\Delta G_n^0}{(\Delta T)^4}$$

If one can assume that the value of ΔG_a (~95 kJ/mol) is only due to the activation energy for the oxygen-ion diffusion in the tetragonal lattice (5.0 mol pct Y_2O_3-ZrO_2), the result obtained is described in Figure 7, where (a) the *C*-type behavior of the growth rate of monoclinic phase having a maximum (nose temperature) controlled by the diffusion of oxygen ions, and (b) the change in activation energies, $\Delta W = \Delta G_{n^*} + \Delta G_a$, can both be plotted as a function of temperature.

Similar values for the activation energy, ΔG_a = 70 to 90 kJ/mol, have been obtained by Tsubakino,[16] using the *C*-curves (3.0 mol pct Y_2O_3-ZrO_2).

B. *A Shearlike Mechanism Associated with Short-Range Diffusion of Ferric Ions in the Transition from γ Fe_2O_3 (Inverse Spinel Structure) to α Fe_2O_3 (Corundum Structure)*

When the mechanism of γ to α Fe_2O_3 transformation is considered, it is convenient for us to understand the crystal structures of γ and α Fe_2O_3 in terms of the stacking sequence of atomic planes, as described by Iida[17] and Nicolls.[18]

According to Iida's descriptions, γ Fe_2O_3 is constructed in such a way that the close-packed oxygen layers have a stacking sequence of A, B, C, A, B, C, . . ., and metallic ions are present in their interstices, themselves forming two-dimensional trigonal lattices. These intervening ferric ion layers consist of two kinds of trigonal lattices. One is called a "kagome" lattice, in which all lattice points are surrounded by six oxygen ions, and the other is a "mixed trigonal" lattice, in which two-thirds of the lattice points are tetrahedral and the remaining one-third are octahedral. These two kinds of

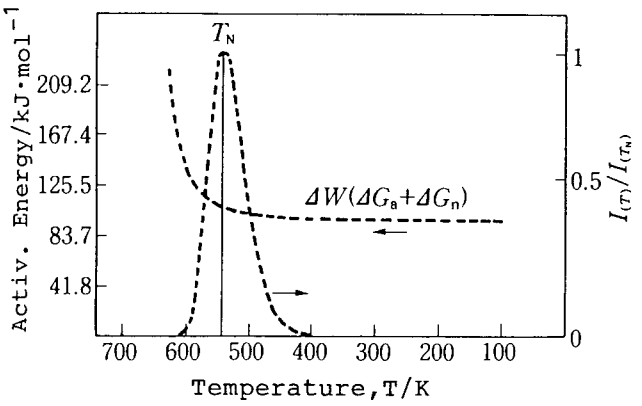


Fig. 7—The change in the growth rate $[I(T)/I(T_n)]$ and the activation energy, ΔW values, against temperature (5.0 mol pct Y_2O_3-ZrO_2).

trigonal lattices are shown in Figures 8(a) and (b). The nearest interatomic distance in the kagome lattice is a = 0.297 nm, and the mesh size of the "mixed lattice" is $2/\sqrt{3}a$ = 0.337 nm, where a is the nearest interatomic distance of oxygen in the close-packed plane. These two kinds of layers are alternately found between oxygen layers along $\langle 111\rangle_{sp}$ directions.

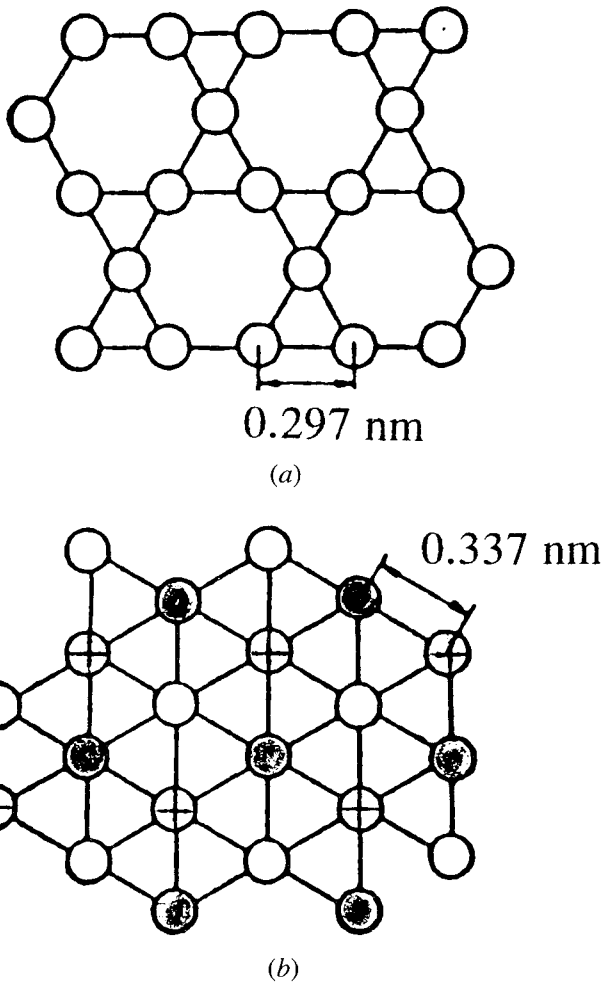


Fig. 8—Two kinds of trigonal lattices in spinel structure. (*a*) Kagome lattice and (*b*) mixed trigonal lattice.

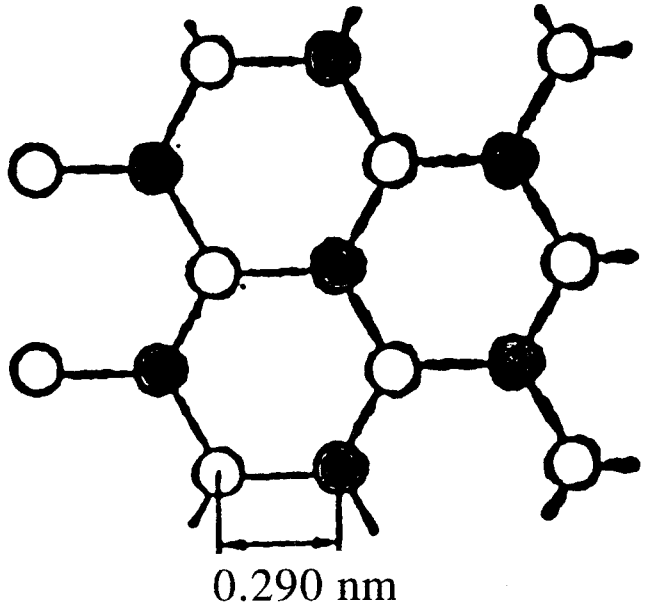


Fig. 9—Honey comb lattice in α Fe_2O_3.

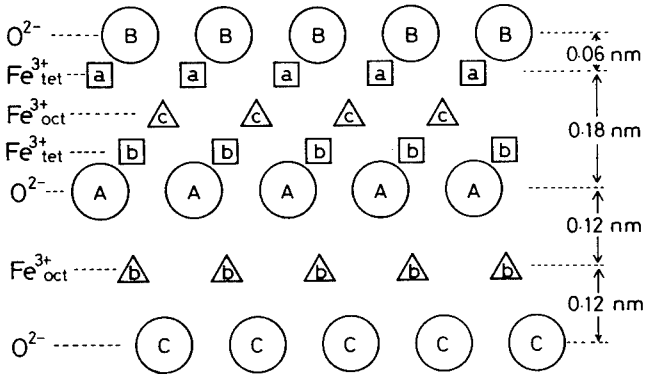


Fig. 10—The spinel structure of γ Fe_2O_3. Large circles show oxygen ions with small triangles and squares, ferric ions, sandwiched between them.

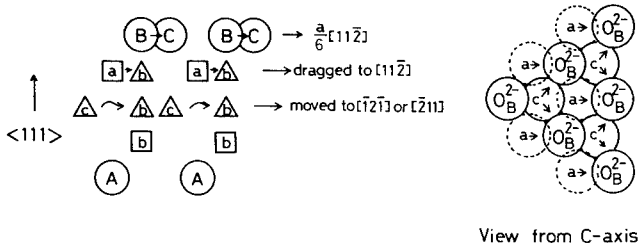


Fig. 12—Two kinds of displacement of ferric ions associated with the $(a/6)\cdot[11\bar{2}]$ shear of oxygen ions on the (111) planes.

On the other hand, the main framework of the α Fe_2O_3 structure is a hexagonal close packing of oxygen ions, in which metallic ions lie at octahedral interstices. The stacking sequence of the close-packed oxygen layer is A, C, A, C, . . ., and intervening metallic ion layers form a "honey comb" lattice, as shown in Figure 9. The mesh size of the honey comb lattice is 0.29 nm, being equal to the nearest interatomic distance of oxygen in a close-packed plane. It is noted that this value is almost equal to that of the kagome lattice in γ Fe_2O_3, *i.e.*, 0.297 nm. Between the oxygen layers are found honey comb layers in the *C* direction, in such a way that the stacking sequence of oxygen-metal-oxygen is A, B, C, A, B, C, ... The layer structure of γ Fe_2O_3 is schematically illustrated in Figure 10.

From the orientation relationship and the layer structures of γ and α Fe_2O_3, it is accordingly suggested that the transformation occurs by a restacking of close-packed oxygen layers with simultaneous movement or short-range diffusion of metallic ions: Fe^{3+}. These are described in the following:[8]

(1) The stacking sequence A, B, C, A, B, C, . . . of oxygen layers in the γ Fe_2O_3 is changed to A, C, A, C, . . . of the α Fe_2O_3 by a similar mechanism to that proposed for the transformation in metallic cobalt from face-centered cubic (fcc) to hexagonal close-packed (hcp), that is, by a shear in the $[11\bar{2}]_{sp}$ direction with every two close-packed oxygen layers locked together,[19] as shown in Figure 11. The shear of amount is 19 deg, and each set of two atomic layers moves $(1/\sqrt{3})\cdot a$ with respect to the layer above or below it, where a is the nearest interatomic distance in oxygen ion layers, *i.e.*, 0.297 nm.

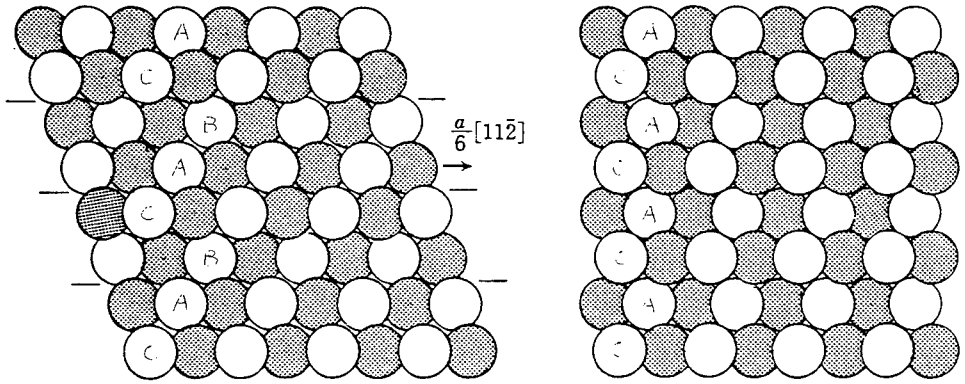


Fig. 11—Change of stacking of $(111)_{sp}$ oxygen layers from fcc to hcp.

(2) This shear occurs between oxygen layers that sandwich the "mixed trigonal" lattice, in which the tetrahedral ferric ions are lying between shearing oxygen layers and dragged to $[11\bar{2}]_{sp}$ direction together with the moving oxygen layer, while ferric ions in the octahedral sites may move in a $[\bar{1}2\bar{1}]_{sp}$ or $[\bar{2}11]_{sp}$ direction together with the $a/\sqrt{3} \cdot [11\bar{2}]$ displacement of upper-lying oxygen layer (Figure 12). Therefore, after the cooperative movements of both oxygen and ferric ions, the original "mixed trigonal" lattice of ferric ions has been changed to "kagome" lattice, that is, all of the tetrahedral configurations were changed to the octahedral ones.
(3) During the restacking of oxygen layers described earlier in this section, metallic Fe^{3+} ions of the kagome lattice that lie between the locked oxygen layers are assumed to move together with them without changing their configurations.
(4) Since, in the kagome lattice, one-ninth of the ferric lattice points must be occupied by vacancies, the ferric ions shown by ◍ may cooperatively migrate to neighboring positions shown by arrows to satisfy the electrostatic equilibrium. The honey comb configuration can then be made, if the ferric vacancies are distributed in a regular way such as shown in Figure 13.

In view of the bainitelike transformation mechanism, it is possible to assume that first, the irregular movement of ferric ions in kagome lattice having some ferric vacancies occurs at temperatures above ~673 K, and subsequently, the shear movement of oxygen layers can be induced by triggering the role of the short-range diffusion of the ferric ions. In all cases, the γ- to α-Fe_2O_3 transformation can be completed by this cooperative movement of oxygen and ferric ions, leading to the term bainitelike.

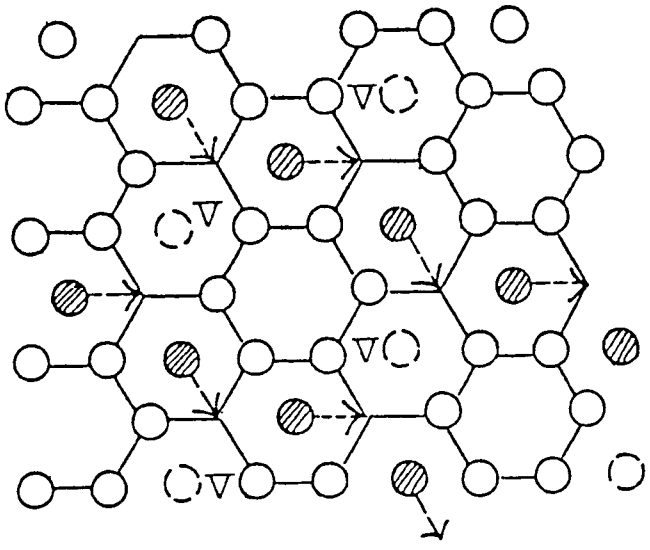


Fig. 13—The lattice points shown by ○, ◍, and ○ represent a kagome lattice, and meshes of solid lines represent honey comb lattice. Dotted arrows represent the displacement of ferric ions to the neighboring sites.

IV. CONCLUDING REMARKS

As characteristics of bainitelike transformation proposed by the authors, the following mechanisms are evident:

1. In the case of ZrO_2-Y_2O_3, the propagating rate of isothermal martensite can be controlled by a short diffusional process or by rotation of oxygen ions, because this solid solution is called "superionic conduction," which contains many oxygen vacancies and related defect clusters.
2. In the process from γ to α Fe_2O_3, the authors also proposed that it can occur in a bainitelike manner, because oxygen shear occurs in such a way that A, B, C, A, B, C, . . . → A, C, A, C, . . . similar to the case in pure cobalt, fcc → hcp type, together with some diffusional movement of ferric ions sandwiched between them. However, this transformation is irreversible and it is possible to occur in a diffusional manner. This is only speculation by the authors, since any martensite plate and even surface relief have not been reported so far. Hence, experimental evidence is required.

REFERENCES

1. Z. Nishiyama: *Martensitic Transformation: Application Series*, Maruzen, Tokyo, 1974, pp. 29-68.
2. H.I. Aaronson and G.W. Lorimer: *Scripta Metall.*, 1972, vol. 6, pp. 1091-94.
3. G.K. Bansal and A.H. Heuer: *Acta Metall.*, 1972, vol. 20, pp. 1281-89.
4. M. Hayakawa, N. Kuntani, and M. Oka: *Acta Metall.*, 1989, vol. 37, pp. 2223-28.
5. G. Hägg: *Z. Phys. Chem.*, 1935, vol. B29, pp. 95-103.
6. B.T.M. Wills and H.P. Rooksby: *Proc. Phys. Soc.*, 1952, vol. B65, pp. 950-54.
7. J.D. Bernal, D.R. Dasgupta, and A.L. Mackay: *Nature*, 1957, vol. 180, pp. 645-47.
8. S. Kachi, K. Momiyama, and S. Shimizu: *J. Phys. Soc. Jpn.*, 1963, vol. 18, pp. 106-16.
9. S. Kachi, N. Nakanishi, K. Kosuge, H. Hiramatsu, and M. Kiyama: *Proc. Int. Conf. on Ferrites*, University of Tokyo Press, Tokyo, 1970, pp. 141-43.
10. N. Nakanishi, T. Shigematsu, T. Sugimura, and H. Okinaka: *Zirconia Ceramics*, Uchidarokakuho, Tokyo, 1986, vol. 8, pp. 71-85.
11. H. Tsubakino: Himeji Institute of Technology, Himeji, Hyogo, private communication, 1992.
12. M. Yashima: Ph.D. Thesis, Tokyo Institute of Technology, Tokyo, 1991, pp. 92-117.
13. G.K. Bansal and A.H. Heuer: *Acta Metall.*, 1974, vol. 22, pp. 409-17.
14. K. Koto, H. Shulz, and R.A. Huggins: *Solid State Ionics*, 1980, vol. 1, pp. 355-65.
15. A.K. Cheetham, B.E.F. Fender, and M.J. Cooper: *J. Phys. C*, 1971, vol. 4, pp. 3107-21.
16. H. Tsubakino: Himeji Institute of Technology, Himeji, Hyogo, private communication, 1992.
17. S. Iida: *J. Phys. Soc. Jpn.*, 1957, vol. 12, pp. 222-33.
18. G.D. Nicolls: *Adv. Phys.*, 1955, vol. 4, pp. 113-90.
19. J.W. Christian: *Proc. R. Soc. London A*, 1951, vol. A206, pp. 51-64.

General Discussion Sessions of the "Pacific Rim Conference on the Roles of Shear and Diffusion in the Formation of Plate-Shaped Transformation Products"

Edited by H.I. AARONSON, J.P. HIRTH, B.B. RATH, and C.M. WAYMAN

J.P. Hirth, Washington State University, U.S.A.; General Discussions Chairman: To begin the General Discussions, Hub Aaronson would like to take a few minutes to summarize the intent of the conference in order to set the stage for these discussions. Then, we can more or less follow the sequence of the conference organization and look at different aspects of phase transformations yielding plate-shaped products.

H.I. Aaronson, Geo-Centers/Naval Research Laboratory, U.S.A.: This conference arose from discussions among the four organizers and others concerning the increasingly contentious dichotomy that has developed amongst two quite different schools of thought as to the atomic mechanism through which plate-shaped transformation products form above the M_s (or M_d) temperature. From the standpoint of the school espousing the shear or martensitic mechanism, if the shape change and the crystallography of the transformation product can be well explained by the phenomenological theory of martensite crystallography (PTMC), then the atomic mechanism of transformation is likely to be one in which the shear of parent into product phase is accomplished by the glide of transformation dislocations, supplemented, if necessary, by that of lattice-invariant deformation dislocations. The other school, advocating the ledgewise diffusional growth mechanism, views plates as the result of a strong anisotropy of the inter-*growth ledge* spacing, with the broad faces of plates forming at that boundary orientation at which this spacing (as normalized by the growth-ledge height) is a pronounced maximum. The migration of ledges, in this view, is controlled by the kinetics of (usually volume) diffusion in the matrix phase toward or away from kinks on the risers of growth ledges. Members of each school have recently been emphasizing experimental observations that the views of the other school seem unable to explain as well as theoretical constraints that the alternative view appears to violate. Progress in resolving these disagreements has long seemed discouragingly slow.

However, the emergence of the invariant line hypothesis, which was developed by Ulrich Dahmen and his colleagues at Berkeley from the PTMC, and the successes that this hypothesis has achieved in explaining the transformation crystallography of plates and rods or needles that cannot have formed by shear has opened up a realistic possibility of at least a partial reconciliation of the two contesting points of view, though not at the ultimate level of the atomic mechanism. Such progress can be considerably facilitated by open public discussions amongst the adherents of both schools. Especially because we have managed to assemble a considerable proportion of the more active participants in both schools from around the world for the present conference, as well as some senior scientists in phase transformations research who have not been involved in these disputations and who can thus provide both moderating and clarifying influences, this conference should be a particularly suitable milieu in which to seek the desired progress—perhaps aided more than a little by the mellowing influence of the very pleasant Hawaiian climate and the efficient ministrations of the Kona Hilton Hotel staff!

A. Khachaturyan, Rutgers University, U.S.A.: I would like to comment that we actually have two different sides of the problem. One is a prediction of the morphology of martensite crystals using the crystallographic analysis based on the Wechsler, Lieberman, and Read (WLR) and Bowles and Mackenzie (BM) theories. The other is a prediction of the mesoscopic morphology of the ordered alloys based on the diffusional dynamics where a coherency strain is taken into account. Although establishing the morphologies of the diffusionless martensitic transformation and diffusional ordering are very different physical processes, there is a lot in common in their microstructural morphology. This commonality can be understood because the mesoscopic microstructure in both martensitic and ordering alloys is actually determined by the same phenomenon: an accommodation of the coherency strain induced by the phase transformation. Particularly, minimizing the volume-dependent strain energy results in the crystallographic theory of the martensitic transformation. Minimizing the surface-dependent strain energy and the surface energy gives the size of orientation variants comprising the martensite plate. Diffusional transformations that are not associated with long-range diffusion, such as ordering, also generate the coherency strain caused by coupling between the long-range order parameter and the transformation strain. If this strain is high enough and has the

H.I. AARONSON, Administrative Chairman for the Conference, is associated with Geo-Centers, Inc., Ft. Washington, MD and stationed in the Physical Metallurgy Branch of the Naval Research Laboratory, Code 6320, Washington, D.C. 20375. J.P. HIRTH, who chaired the General Discussion sessions and also served as Advisory Chairman to this Conference, is Professor, Department of Mechanical and Materials Engineering, Washington State University, Pullman, WA 99164. B.B. RATH, Conference Government Relations Chairman, is Associate Director for Materials Science and Component Technology of the Naval Research Laboratory, Washington, D.C. 20375. C.M. WAYMAN, Conference General Chairman, is Professor, Department of Materials Science and Engineering, University of Illinois at Urbana–Champaign, Urbana, IL 61801.

This conference was held from Dec. 18 through Dec. 22, 1992 at the Kona Hilton Hotel, Kona, Hawaii, under the sponsorship of the Phase Transformations Committee of ASM INTERNATIONAL. The two General Discussions, which occupied most of the conference's time on Dec. 22, were tape-recorded, transcribed by Ms. Rene Wamsley, edited by the symposium organizers and then reviewed and modified by the contributors to the General Discussions prior to submittal to *Metallurgical and Materials Transactions A*. Conferees who had not contributed to the recorded General Discussions were given the opportunity to do so at that time.

same symmetry as the transformation strain in the martensitic crystal lattice rearrangement, it is natural that minimizing the strain energy, which occurs due to the microstructure self-assembling during the ordering, produces the same type of morphology as the martensitic transformation. Predictions of the crystallographic theory of the martensitic transformation applied to ordering alloys with a large transformation strain turn out to be very good (for example, in the case of the CuAu II phase). The ordered structure in the CuAu II system even shows retained (disordered) matrix phase, an effect typical of "strong" martensitic transformations, in which it is also associated with the transformation strain.

J.W. Cahn, National Institute of Science and Technology, U.S.A.: I agree with Armen Khachaturyan that including considerations of thermodynamics in energy minimizing is important, but we must put models into this minimization that specify what variations are allowed by the physical mechanisms and what their relative kinetics rates are. There are several possible models that give the geometrical and kinetic constraints on how the phases fit together, and how they grow, and what stresses develop.

Without any geometrical constraints, apart from fixing the temperature of the heat bath, applied hydrostatic pressure, and masses of the chemical components, the equilibrium is the one given in the standard phase diagram. Temperature and chemical potentials are constant throughout the system. If capillary effects are ignored, stresses are hydrostatic and constant. This is the result for fluids and for solids under conditions where the role of the lattices is not significant (*i.e.*, large grains at temperatures and times where creep has relaxed all nonhydrostatic components of the stresses). If this is not the observed equilibrium in multiphase solids, such as precipitates or martensitic morphologies, we have to look for constraints on the allowed variations.

Phase transformations generally result in a lattice deformation. If there is a composition change and if lattice parameters change with composition, these compositional-lattice-parameter changes are part of the lattice deformation. These lattice deformations are the causes of strains and an elastic energy. We recognize that the elastic energy depends on the morphology and that there are a number of mechanisms for reducing the elastic energy. The phenomenological theory of martensite is based on finding a particular morphology with a very low elastic energy; if, by adding a lattice invariant shear, the theory finds an invariant plane geometry with its nearly vanishing elastic energy, many predictions follow. Note that no sliding of one phase past the other at the interface is assumed; the lattice invariant shear is in the martensite. This assures that the locations of all atoms in the new phase are prescribed in military parade fashion by the transformation strain and the lattice invariant strains (as well as by the calculated lattice rotations). Martensite transformations generally occur at temperatures at which there is no diffusion and creep, and the absence of diffusion is an assumed constraint with important thermodynamic consequences. The lattice correspondence and the specifications of the mechanisms of the lattice invariant shears provide the geometric constraints, because they specify where the atoms go when there is an incremental amount of transformation and the elastic strains. What is at issue at this conference is whether the diffusion that is thermodynamically required for some phase transformations necessarily removes the geometric constraints that are part of the phenomenological theory, because the diffusion destroys the correspondence and can relax all stresses. Or, conversely, whether finding morphologies that are predicted by the phenomenological theory implies that the initial steps of the transformation occurred without diffusion.

It is important to realize that there still can be a lattice correspondence when there is diffusion and some types of creep. This has come up a number of times; Jim Howe mentioned it this morning. Coherent precipitates are good examples of a lattice correspondence where diffusion occurs and diffusional and other kinds of creep are not prescribed. This more general correspondence is truly a lattice rather than an atom correspondence, because it specifies where the lattice sites and atom positions go. The atom positions thus specified must be filled with atoms (or with vacancies thus defined), but which atom or vacancy is to occupy the site is left unspecified. Isolated vacancies or even groups of vacancies can move about, but they cannot condense and remove plane segments of lattice sites, bounded by dislocations. We have to assume a nucleation barrier for such condensation. Similarly, vacancy sources cannot create new plane segments of sites. Small coherent precipitates are actually in equilibrium, because the stresses cannot relax; inserting misfit dislocations by removing or inserting lattice plane segments would raise the energy.

For larger stressed precipitates, a kinetic argument, such as the nucleation barrier for dislocation loops or the long time scale of diffusional creep, must operate. In Nabbaro-Herring and Coble creep, no nucleation barrier is assumed, and lattice sites are created and removed at surfaces and interfaces by the process. Still there may be enormous differences in the time scales for the thermodynamically required diffusion and for the diffusional creep. Consider, for instance, the iron-carbon system, in which carbon can diffuse rapidly to achieve the thermodynamically required composition changes in a time short compared to that for creep by the diffusion of iron by a vacancy mechanism.

But the phenomenological theory shows that there is another way of reducing stress: with a morphology in which stresses can be avoided. For many coherent precipitates, such as misfitting cubic precipitates from a cubic matrix with a cube-cube correspondence, the phenomenological theory of martensite cannot apply, and energy minimization cannot lead to a vanishing elastic energy. When the transformation has a lattice strain with a compositional component plus a lattice invariant shear that allows an invariant plane, the phenomenological theory should still apply whenever it is reasonable to assume that there will be a correspondence of lattice sites, because diffusing atoms within a crystal and across some interfaces will not change the lattice correspondence; at the interface there should be no creation and destruction of lattice sites and no sliding of one crystal past the other. Strictly, this implies that there are no

climbing misfit dislocations, and that steps in the interface are neatly dovetailed, so that when they move they only transfer sites.

If there is an invariant plane, the system should tend toward a plate on that plane, because that would reduce the elastic energy to zero. When there are no stresses there is no driving force for creep and no reason to deviate from this morphology at large plate sizes. The result would be that the phenomenological theory of martensite applies to a situation in which diffusional creep would have been able to relax stresses that never developed.

A modified phenomenological theory may be more widely applicable to even more complicated diffusional phase transformations. Sometimes, as Jim Howe described this morning with large unit cells, the correspondence may be rather complex, with specific sites systematically removed in the transformation by diffusion or transformation dislocations. There may even be cases where there is no definable three-dimensional lattice correspondence and only a two-dimensional correspondence at the interface, motivated both by interface and elastic energy minimization.

J.W. Christian, Oxford University, U.K.: My first two points concern (1) invariant lines (ILs) and planes (IPs) in a homogeneous deformation, and (2) the importance of the scale of observation in a description of an interphase interface. The finite strains of a homogeneous deformation may be specified in various ways. Consider a homogeneously deformed continuum with embedded, discrete points that define a network (*i.e.*, a primitive space lattice). We describe the distortion of the network as a lattice deformation, **S**, if (a) each atom site in the initial and final states either corresponds to an embedded point or is displaced from an embedded point by a constant vector **t**; or (b) if some of the atom sites (a reasonably large integral fraction) conform to the description in (a). If in case (a) there is also no diffusion, the atomic displacements are completely specified by **S**, but in case (b), atomic shuffles must be added to **S**. Shuffles are relative translations of atoms on interpenetrating primitive lattices; they are required if there is more than one atom in the primitive unit cell of either structure and/or if **S** is uniform only for unit cells larger than the primitive cells. Thus, there is a lattice correspondence if **S** is homogeneous on a scale extending from an interatomic distance, or a small multiple thereof, up to a distance that may be tens, hundreds, or thousands of interatomic distances but is not necessarily without limit. A "macroscopic" or "shape" deformation **E** has embedded points with much larger separations and is an average effect, homogeneous only on this macroscale. It is measured from fiducial marks on free surfaces, from internal inert "markers," as in a Kirkendall-type experiment, or from surface tilts.

In a finite homogeneous deformation, we may have no IPs, or a single IP, or all planes invariant; there are no other possibilities. A lattice deformation cannot usually satisfy the restrictive condition for a single IP, and all planes are invariant only in the trivial case of no deformation. If there is a single IP, it is one of two undistorted planes, either of which is an IP only for a specific orientation relation. In most other cases, there will be a cone of undistorted lines, any one of which may be an IL at a specific orientation of the phases.

We often refer, without precise definitions, to fully coherent (f-c), partially coherent (p-c), and incoherent interfaces or particles. Shear strains are not transmitted across incoherent interfaces and there is no continuity of the lattice network. Small enclosed particles always can be forced into coherency, even with large lattice principal strains, but coherent particles with one or two long dimensions (needles or plates) only can form if the macrodeformation approximates to an IL or an IP, respectively. For most structural changes, this means that the local lattice deformation differs from the macrodeformation because of periodic discontinuities (interface dislocations) or twins; such an interface is said to be p-c.

I now have to disagree mildly with Hub Aaronson's remarks about "diffusionists" and "shearists"; I have never thought of myself, or indeed of anyone here, as being either one or the other. I think that many disputes in the literature have arisen from linguistic confusions and from a belief that there is some feature of the growth mechanism, in addition to the absence of diffusion, which characterizes a shear transformation. But as John Cahn emphasized, the constraint of no diffusion, applicable to martensite, can be independent of the constraint provided by a lattice correspondence, which may apply to both types of transformation. Consider a f-c diffusional change with a lattice deformation that is near to an IP. Jim Howe's beautiful pictures this morning showed clearly that the martensitic "transformation dislocation" corresponds to the diffusional "growth ledges." This carries over to p-c interfaces where the PTMC may well predict the habit plane, shape change, and orientation relations for a diffusional transformation. I think, however, that there is an alternative possibility. The "no diffusion" constraint implies, *a fortiori*, that the number of atoms lost by the parent phase in any increment of growth equals the number gained by the product phase, and hence any interface dislocations in martensite must be "glissile" (*i.e.*, able to move conservatively with the interface). But, this constraint will only apply to highly mobile atoms if they are confined to a fixed set of sites. Relaxation of this conservation constraint allows "epitaxial" interfaces with nonglissile misfit dislocations to be mobile. Such interfaces, unlike those predicted by the PTMC, are usually rational. Both martensitic and epitaxial interfaces have a macroscopic IP as the interface plane; if both are feasible, it is not obvious which will be preferred.

This conference is about the growth of plate-shaped products, so that much of our discussion concerns morphology. Armen Khachaturyan and John Cahn have already explained that one reason for plate formation is that the strain energy of a particle in a constraining matrix will usually be minimized if it adopts a plate shape. This result applies to incoherent particles and, more importantly, to coherent particles that have an IP parallel to the plane of the plate, so that the strain energy per unit volume is linear in the aspect ratio of the plate. The strain energy depends on the "stress-free strains" accompanying the transformation of an unconstrained

particle, but these are not lattice strains, as Eshelby assumed, unless they are homogeneous over the whole particle. For large strains, this restricts full coherency to very small particles (of any shape) and to large plates in a few special cases where **S** is close to an IP. In other cases, large p-c plates can form only if the local lattice deformation is modified into a macrodeformation with an IP. Figure 3 of my paper (J.W. Christian: *Metall. Mater. Trans. A*, 1994, vol. 25A, pp. 1821-40) shows a number of virtual operations added to Eshelby's original procedure. Armen's formulation allows the volume removed from the matrix in (a) to have any general shape (although an ellipsoid is still most convenient), and the operations (b) and (e) then complete the Eshelby cycle to give a self-stressed assembly of a matrix and a fully coherent particle. The extra operation (c) allows long-range diffusion and hence changes in composition or long-range order while preserving the number of atoms and available sites. The operations (d) illustrate different ways of modifying **E** so that it has an IP. The mass flow of atoms (d_1) eliminates the shape change and the strain energy completely, so that particles of any shape may form, whilst in (d_2) any atomic flux is around the particle. Operations (d_3) and (d_4) are of most interest: they allow an evenly spaced array of dislocations either to glide or to climb through the structure, thus producing a lattice invariant deformation (LID), which is, respectively, either a simple shear or a uniaxial extension or contraction. If the dislocations are in the interface, the lattice deformation and the LID are produced together as the interface migrates, and they combine to given an IP interface, which is respectively martensitic or "epitaxial." (An epitaxial interface may require a crossed double array of misfit dislocations, rather than a single array.)

I think the distinction between martensitic and epitaxial interfaces is important; recent debates on bainite have largely concentrated on the feasibility of an epitaxial interface between bainitic ferrite and austenite. Dislocation models of interfaces are obtained in two different ways. In PTMC, the slip plane and Burgers vectors of the "anticoherency" dislocations are selected, but the orientation of the phases and the habit plane are free variables to be determined by the IP condition. The other approach, familiar from grain boundary theory, preselects the habit plane and orientations and then asks what dislocations are needed to make this plane macroscopically invariant. This second procedure will not generally give entirely glissile dislocations. In both cases, however, the Frank–Bilby–Bollmann equation specifies the dislocation density needed to ensure macrocompatibility in any direction of the interface.

May I now comment very briefly on Jim Howe's coins (or two-dimensional spherical atoms)? He showed how shuffling preserved the shape change, but he did not constrain the shape change by a surrounding matrix nor consider that vacancies might condense in highly compressed regions and evaporate from extended regions, thus transferring sites from the former to the latter and reducing the strain energy. This is analogous to Herring–Nabarro creep, and I originally thought that if the atoms are mobile, this effect would remove the shape change. However, we have known now for some considerable time that, in a few examples at least, the shape change is not destroyed by diffusion. Possibly, the creation and removal of vacancies requires Bardeen–Herring (or similar) sources and sinks and is too difficult in dislocation-free regions.

I have agreed to comment on the minimum and maximum height of a ledge, but may I first make a bid for the retention of the terms "twinning dislocation" and "transformation dislocation" in any new terminology? I am very much in favor of rationalizing our varied descriptions, but these two have a long history, going back to Russian work in the late 1940s in the case of the twinning dislocation. Armen Khachaturyan thinks the concept may have come either from Vladimirsky (see my paper) or from one of his colleagues.

There is a minimum ledge height to ensure that the interfaces on each side of the step have the same (equilibrium) structure. In twinning, this is fixed by the number, q, of lattice K_1 planes traversed by a primitive lattice vector parallel to η_2; the structure repeats at every q planes for q odd, or every $(1/2)q$ planes for q even. Hence, the step height of a so-called "zonal" twinning dislocation exceeds that of an "elementary" twinning dislocation if $q > 2$. However, if the extra energies of the nonequilibrium interfaces are small, an elementary dislocation may form, either by equilibrium dissociation of a zonal step or as an isolated metastable defect. It might even be possible to have a stable partial twinning dislocation (*e.g.*, in bcc) with a step height equal to one-half of the interplanar spacing.

Similarly, slightly more complex conditions apply when the deformation is a general IP with different interplanar spacings and periodicities in the two structures. The minimum step height is now the spacing of nearly coincident lattice planes or some multiple of this spacing. For example, every atomic {111} plane of the fcc structure is a lattice plane, but only alternate {001} planes of hcp contain a lattice point, so the minimum step height in an fcc–hcp interface is the separation of two close-packed atomic planes. A minimum step height may also be defined for an irrational interface, but I do not think I should discuss it here.

The f-c step or ledge is a "coherency" dislocation in Olson's terminology and has an effective Burgers vector proportional to the step height. Hence, the maximum step height equals the minimum height because of the square dependence of the line energy on the Burgers vector. However, John Hirth has shown in his conference paper (the first issue of *Metall. Mater. Trans. A* containing the proceedings of this conference) that a dislocation may be introduced into a relatively high ledge to release most of its strain energy. The high energy of a coherent superledge comes from the discontinuities in the shear and normal strains of the IPs. If the shear component of the total Burgers vector of y elementary transformation dislocations is approximately equal to a lattice repeat vector, the shear will be largely cancelled by adding an opposite lattice dislocation every y planes, and the overall shape deformation becomes small (zero if the cancellation is exact and there is no strain normal to the interface). A p-c superledge of this type remains glissile, and the only theoretical limit on its height arises from

any discrepancy in the interplanar spacings. A misfit of $1/z$ of the interplanar spacing will be accommodated elastically for small superledges, but the increase in energy with height demands a misfit dislocation about every z planes. This type of superledge, however, is epitaxial rather than martensitic and is unlikely to be mobile.

It may seem anomalous that a p-c superledge, across which there is no shape discontinuity, can form on a particle in which all the other interfaces correspond to a large shape change. To understand this, we have to answer the question "where do the lattice dislocations originate?" They must come from somewhere, and, in principle, they could form spontaneously as dipole pairs in a region of perfect lattice. If one of the dislocations then glides into the interface, the other can either remain or glide in the opposite direction until stopped by an obstacle, a grain boundary, or a free surface. The same result is obtained from a slightly different model based on emissary slip, as discussed previously.

If we allow the height of a p-c superledge to increase without limit, it becomes a facet (*i.e.*, a second interface) and we no longer have a plate. This is self-consistent, because the total shape deformation is now close to zero (we have two approximate IPs and hence all planes are invariant). One of my assertions which did not, I think, command general agreement was that if we have an enclosed particle, either all the interfaces are coherent or they are all incoherent. Clearly some interfaces may be f-c while others are p-c, because we have just discussed such a particle. But as there is no correlation of atomic positions across an incoherent interface, I believe my assertion follows from simple lattice continuity. It is, for example, impossible to construct a closed circuit that crosses two parts of the interface, one f-c or p-c and the other incoherent. So, I believe it is misleading to describe the step growth of a f-c or p-c particle in terms of incoherent risers or kinks. If these are the preferred sites at which atoms join the growing phase, it must be because they are the places at which the binding to the new phase is strongest. The analogy with crystal growth from the vapor, which can be misleading, seems to be applicable to the final sites. A kink in a step of minimum height, for example, provides not a "gateway" but a repeatable step (the famous "wiederholbare Schritt") at which the configuration is unchanged after adding an atom.

John Hirth, Washington State University, U.S.A.: There are a few remarks that I would like to make about ledges and dislocations at interfaces. I previously talked about looking at O-lattices or dichromatic complexes to see a localized dislocation at an interface. I think I can now show this in another way. We first imagine a pure transformation dislocation at a close-packed fcc–hcp interface with matching lattice spacings. Then there are no coherency strains. However, there will be a localized strain field of the transformation, manifested by locally bent lattice planes. A twinning dislocation would provide a simple example of such a strain field, as can be explicitly seen in a "complete pattern shift lattice" or DSC lattice projection of the adjoining crystals, as shown by R.W. Balluffi and J.P. Hirth (*Acta Metall.*, 1973, vol. 21, pp. 929-942).

Now imagine that in retaining coherency, we had expanded one crystal by, say, five percent. The configuration remains the same, except that we now introduce a set of continuous, infinitesimal dislocations at the interface to represent the coherency strain field. If transformation dislocations are now placed at a regular spacing of about one per twenty sites, their strain field exactly compensates the coherency strain field at long distances from the interface. They can then correspond to structural ledges or misfit compensating ledges (for some cases) or, locally, to unit-height growth ledges. A dichromatic complex description or, in some cases, an O-lattice description would lead to the same result: undistorted, long-range strain-free crystals with local dislocation strains near the interface. Related views are presented by U. Dahmen (*Scripta Metall.*, 1987, vol. 21, pp. 1029-34) and J.M. Howe and D.A. Smith (*Acta Metall. Mater.*, 1992, vol. 40, pp. 2343-50).

The point is that even with long-range strain cancellation, the dislocation-like defects retain their local strain fields and interact with one another in the usual way. So, for example, they would tend to repel one another, though if there is a regular array, there is a balance of forces and equal spacings between the dislocations. They would also respond to a shear stress in the usual manner.

The other aspect of the interaction is that, despite the fact that they repel at large separation, if for some reason they are pushed together, there is actually an elastic attraction between them. Thus, there is a short-range interaction force that tends to snap them into a superledge if they come close enough together. Hence, transformation dislocations or structural ledges or, in principle, growth ledges can interact to form elastically stable superledges.

J.W. Christian, Oxford University, U.K.: What makes the two dislocations appear so close to each other that they become attracted?

John Hirth: Well, there might be an external stress, or one dislocation might be held up at an obstacle and the next one pushed along. There is a free energy driving force that would tend to move them, as well.

J.W. Christian: I take it that the short-range attraction you are talking about would only involve edge dislocations?

John Hirth: That is correct. Only edge dislocations would exhibit the short-range attraction. Screw dislocations would always repel one another.

J.W. Christian (written discussion): I want to show that the attraction mentioned by John Hirth is very short range. Consider $2n$ lattice edge dislocations forming an incomplete wall with spacing D. The force on a similar dislocation at (x, y), where x is the distance normal to the wall and y is the height from the center of the wall given by Eq. 71 of A.M. Kosevich (*Dislocations in Solids*, F.R.N. Nabarro, ed., North-Holland, Amsterdam, 1979, vol. 1, pp. 33-141). The maximum interaction energy is at $x^2 - y^2 + (nD)^2 = O$, and for $y > nD$, the dislocation is attracted into the wall for small values of x and otherwise repelled. Applying this to a single step of height d escaping from the top of a superledge composed of $2n$ such steps, the critical value of x for escape is $(2n + 1)^{1/2}d$ (*i.e.*, about $3d$ for a ledge of

height $9d$). This value is too small for the preceding elastic theory to be applicable, but it shows that it is unlikely that a single step can approach a superledge sufficiently closely to be captured and, conversely, that although an existing superledge is in principle metastable, it requires only a small fluctuation to enable it to dissociate into single steps.

J.P. Hirth (reply to written discussion): Subsequent to the conference, we calculated capture and escape distances for a superledge using a slightly different result (S.V. Kamat and J.P. Hirth: *Acta Metall. Mater.*, in press, including helpful suggestions from Jack Christian). The results give somewhat larger capture distances than the Kosevich approach but considerably larger escape distances if flexibility of the superledge is included in the analysis, and they predict substantial metastability for ledges containing up to 14 unit ledges. These critical distances are still in the range of a few to a few tens of nanometers, however, so I agree with Jack Christian that the likelihood of two ledges condensing spontaneously is small. Any pinning events, on the other hand, would lead to pileups of ledges that strongly favor coalescence into a superledge.

H.I. Aaronson, Naval Research Laboratory, U.S.A.: In response to one of Professor Christian's remarks, incoherent kinks are not being claimed. The view currently taken is based on the work of Howe, Dahmen, and Gronsky (*Phil. Mag. A.*, 1987, vol. 56, pp. 31-61). They show that at the riser of a biatomic ledge at an fcc:hcp interface an otherwise coherent kink contains a built-in vacancy-like defect through which an atom can jump across the interphase boundary without requiring an excessive activation energy. Thus, atomic migration across the boundary can take place at a reasonable rate.

On another aspect of Professor Christian's remarks, the reason why atoms do not attach to terraces and risers or to kinks not incorporating a Howe–Dahmen–Gronsky–like defect is exactly the opposite of that which prevents atomic attachment to terraces and risers from the vapor phase. In the case of growth from the vapor, attachment to terraces is unlikely because there are too few bonds to retain adsorbed atoms. Risers are better in this respect, but they still do not offer the largest available number of bonds. Kinks are best of all because they do provide the largest number of bonds with which to "grip" an incoming atom. In the case of fully or partially coherent solid:solid interfaces with a difference in stacking sequence across the boundary, an atom attempting to diffuse across such an interface will normally be unable to do so because the atom would have to occupy (albeit temporarily) what amount to an interstitial site in a close-packed plane. The energetics of such an atom movement make it highly improbable. This stricture applies equally to the terraces and risers of a ledged p-c boundary between two crystals differing significantly in crystal structure. Indeed, the average number of nearest-neighbor bonds to an atom penetrating the squashed-vacancy-in-the-kink is probably less than that to an atom attempting interstitialcy diffusion into a terrace.

My final remark concerns not atomic geometry but rather the approach so far taken by the theoreticians to phase transformation mechanisms in this General Discussion. They sometimes seek to minimize the interfacial energy, the elastic strain energy, or both simultaneously in a given system. Let me give you two examples (of the same type) that strongly suggest that none of these criteria is relevant to the *growth* kinetics and morphology of *diffusional* phase transformations products.

In unpublished work with Norman A. Gjostein performed at the Ford Scientific Laboratory in the 1960s, specimens of high-purity hypoeutectoid Fe-C alloys were double encapsulated in fused quartz under a reduced pressure of purified He, austenitized, and then isothermally reacted just above the eutectoid temperature in lead baths for times as long as about one month. The aspect ratio of Widmanstatten ferrite plates shrank from about 30-40-to-1 down to about 3-4-to-1 during the course of this time. Clearly, minimization of neither interfacial energy nor elastic strain energy could have played a dominant role during the growth of these plates. Had this been so, the drastic change in aspect ratio actually observed would not have occurred. Similarly, in unpublished work with Mark Plichta that was performed at Michigan Technological University a decade later, the aspect ratio of hcp proeutectoid α plates formed in the bcc β matrix of a hypoeutectoid Ti-X alloy diminished several-fold during prolonged annealing. Further reduction in aspect ratio was probably much retarded by the loss of growth ledges during later stages of coarsening.

W.T. Reynolds, Jr., Virginia Technological Institute & State University, U.S.A. (written discussion): A number of contributors have suggested that precipitate shapes and habit planes can be found by minimizing strain energy and interfacial energy. In some cases, this approach may underestimate the importance of local phenomena. The availability of growth ledges affects the mobility of precipitate boundaries, and the formation of these ledges is an intrinsically local phenomenon. For example, ledge formation can be encouraged by a favorable strain field at the corner of a precipitate, by a higher supersaturation at a stationary region of the precipitate boundary, or by the presence of a defect, such as a dislocation. These factors affect precipitate shape, yet they are not usually included in minimization approaches.

Local effects may be responsible for the fact that facet planes of individual precipitates in many systems fall within a narrow range of values rather than adopting a specific value. In ferrous alloys, the shape of proeutectoid ferrite plates changes in subtle ways with substitutional alloying elements. These differences are likely to depend upon a local growth process because strain energy is insensitive to small changes in solute concentrations. In a slightly different context, the shape of crystals grown from vapors or liquids can be altered dramatically by adding small concentrations of impurities that segregate to specific interface sites and "poison" step formation and migration. Energy minimization may predict the precipitate shape or habit plane a given system tends to adopt, but there may be substantial deviations from this ideal shape due to local details of the growth process.

K. Tsuzaki, Kyoto University, Japan: I would like to

make a comment on the possibility of the appearance of surface relief in transformations where the growth of a product phase is controlled by the long-range diffusion of substitutional atoms. I would like to note that at least two conditions must be met for the occurrence of surface relief in such transformations. The first condition is the existence of one-to-one atomic site correspondence between the product phase and the matrix, as was pointed out by Professor Howe this morning. The second condition is that the transformation dislocations have the same Burgers vector (*i.e.*, atoms jump in the identical direction at the growing interphase boundary for a lattice change). In addition to these two conditions, it is of course required that a reconstructive reaction by diffusion of substitutional atoms does not occur quickly compared with the growth of a product phase.

The first condition can be obtained when a particular crystallographic orientation relationship exists between the product phase and the matrix and the interphase boundary is at least semicoherent. The second condition must be taken into account particularly in the case of fcc–hcp transformations, because there are three crystallographically equivalent transformation dislocations for the formation of an hcp plate with a {111} fcc habit plane (Figure 1(a)). When each of these dislocations operates to the same extent, the macroscopic shear strain vanishes (J.W. Christian: *Decomposition of Austenite by Diffusional Processes*. Interscience, New York, NY, 1962, p. 371). The results is a self-accommodation to reduce the strain energy. Thus, for the occurrence of surface relief in fcc–hcp transformations, a special condition for the preferential operation of one Burgers vector of transformation dislocations must be met. In contrast, the second condition is automatically met in fcc ⇒ bcc (or bcc ⇒ fcc) transformations, as there is only one kind of transformation dislocation (M.A. Jaswon: *The Mechanism of Phase Transformations in Metals*, Institute of Metals Report and Monograph Series No. 18, 1955, p. 173), as shown in Figure 1(b). Thus, once the atomic site correspondence is satisfied, the appearance of surface relief is possible, unlike the case of fcc–hcp transformations.

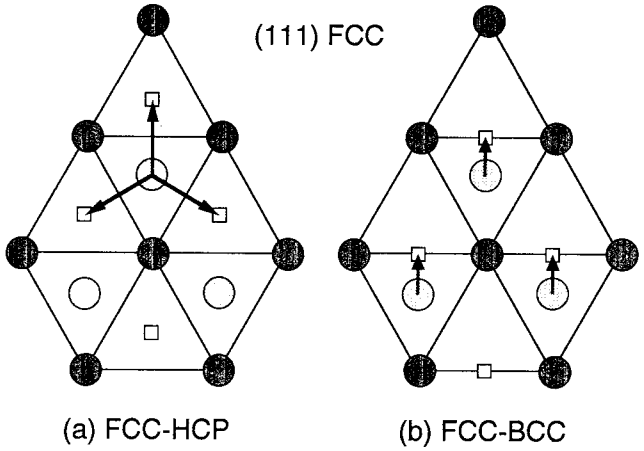


Fig. 1—Schematic drawing showing the Burgers vector of transformation dislocations for (*a*) fcc–hcp and (*b*) fcc–bcc lattice changes. There are three crystallographically equivalent transformation dislocations for fcc–hcp but only one for fcc–bcc.

However, I should say that we have to examine the structure of a growing interphase boundary, in particular that of ledges and kinks, in more detail in order to clarify the appearance of surface relief in fcc–bcc diffusional transformations.

H.I. Aaronson: You still have a choice of many different directions to jump in a diffusional transformation, whereas in a martensitic transformation you do not.

K. Tsuzaki: I think this is the point that we have to discuss. If one-to-one atomic site correspondence exists between the product phase and the matrix and the transformation dislocations for a product plate have the same Burgers vector, the directions of atom jumps at kinks are identical, regardless of the different directions of kink movement. This means that a kink does not prevent the formation of surface relief, as far as atomic site correspondence is satisfied at a kink.

G.B. Olson, Northwestern University, U.S.A.: I just have to comment: I think coherency means site correspondence.

Unidentified Discusser: But the actual operating process involves diffusional jumping through vacancies. So that means you maintain the lattice correspondence, right?

G.B. Olson: That is what he means. He doesn't mean atomic correspondence. He means just site correspondence.

J.W. Christian: With respect to your first point, John Cahn has almost convinced me that condensation or generation of vacancies might not be possible, despite the high driving force.

J.M. Howe, University of Virginia, U.S.A.: I wanted to respond to your comments of just a minute ago. I've changed my viewpoint a little bit on the role of this extra volume in the kink. I know in the original *Phil. Mag.* paper (J.M. Howe, U. Dahmen, and R. Gronsky: *Phil. Mag. A*, 1987, vol. 56, pp. 31-61), we looked at it as lowering the activation energy to get an atom across the kink. And that is a different sort of role than is played by kinks in the solid/vapor case. But, at that time, I made the analogy that it's very much similar to the solid/vapor case. And the reason for that is that if we think of this growth ledge, or this transformation dislocation, or whatever we want to call it, as having a Burgers vector, then it has some strain energy (J.M. Howe and N. Prabhu: *Acta Metall. Mater.*, 1990, vol. 38, pp. 881-887 and 889-896). If kinks are created along the ledge in order to advance the interface, we lengthen the dislocation line and add strain energy as well as create some new surface at the kinks. So that's always going to be an unfavorable event to happen randomly (unless one has a "rough" interface), just like it's going to be unfavorable for atoms to attach randomly to a terrace because of the additional strain and surface associated with the nucleating ledge.

But, once we overcome that barrier and we have a nucleation event, a double kink, then it's favorable for the rest of the atoms to go to the edge of that kink, just like it is in solid/vapor transformations, because it costs less energy both in terms of the strain field as well as the new surface. And so, I think it is very much analogous to the solid/vapor case, which is a slightly different viewpoint than we had previously on that subject.

H.I. Aaronson: I think there is still a problem here, because this is not crystal growth from the vapor phase. You still have to make the transfer across the interphase boundary. And in this case, in the situation you're outlining, the transfer would take place through a coherent region without that defect.

J.P. Hirth, Washington State University, U.S.A.: He actually had a vacancy involved.

J.M. Howe, University of Virginia, U.S.A.: I tried to do this hard sphere experiment, and there was a vacancy that assisted the process so that it wasn't just the open volume in the kink.

H.I. Aaronson: In other words, there is a temporary open volume that is assisting the transfer.

J.M. Howe: Well, the open volume is always there. And that's always assisting the transfer. But it's not big enough for an atom to hop through. You still have to have a vacancy arrive there. When the vacancy arrives there, the atom then has a place to go and it's assisted by this additional strain and it can hop into an atomic site.

H.I. Aaronson: Then the hole would still be assisting the passage of an atom through the kink.

J.M. Howe: Yes, it is still assisting.

G.B. Olson: I just want to make a couple of short comments about the theory of interfacial structure. There is a fairly well-developed theory for the classic problem we call "grain boundaries," in which the input is an arbitrary misorientation between two crystals meeting at a boundary. A rotation R is then the input into the theory. Out of the theory comes predictions of possible dislocation structures (*i.e.*, ways in which the system accommodates that rotation) and that is very sensible for a grain boundary. Extension of that kind of theory to interphase boundaries is really what I would call the problem of "interphase grain boundaries," in which, in addition to an arbitrary misorientation, you have some pure lattice deformation **B** relating the two crystals. The theory of interphase grain boundaries then uses the same machinery to predict possible dislocation structures that accommodate both of those operations. But I think really the class of problem I would call an "interphase boundary" does not involve an arbitrary orientation relationship. What we really want out of a theory of interphase boundaries is the *prediction* of orientation relations. In the case of martensitic crystallography, we have such a theory, where the input is the pure lattice deformation **B** and also possible simple modes of relaxation, which define possible dislocation structures accomplishing a lattice-invariant deformation **P**. And the output then is the orientation relation **R**. Now, the problem we have as we go on to progressively larger states of relaxation, where this process might become nonconservative and we might have several lattice invariant deformations (*e.g.*, $\mathbf{P}_2\mathbf{P}_1$), is that we lose the predictive power of this theory because we lack sufficient constraints to extract unique solutions. And so we are looking for sources of those additional physical constraints, and I think the place to look is back in the grain boundary form of the theory. Because we rationalize these operations in terms of the minimization of volume elastic energy, the martensite theory enforces only a condition of macroscopic invariant-plane matching, whereas the grain boundary theory explores conditions of local pattern matching and looks towards the principle of minimization of interfacial energy. I think that is what is missing from the interphase boundary theory right now. So, we want to bring the concept of interfacial energy minimization into the invariant-plane theory in such a way that we constrain the $\mathbf{P}_1\mathbf{P}_2$ operations sufficiently to predict habit planes and orientation relations. I think one unused piece of information throughout the discussions at this conference is that, although there has been some reconciliation of invariant plane and invariant line notions and O-lattice concepts of grain boundary theory, I don't think the next step has been taken to the concept of coincidence site lattices (CSL) and the use of complete pattern shift lattice (DSC) dislocations where we really are getting in principles of interfacial energy minimization. In a paper with Bob Balluffi (R.W. Balluffi and G.B. Olson: *Metall. Trans. A*, 1985, vol. 16A, p. 529), we looked at combining these theories and identified the principal types of dislocations that could exist. In the combined approach, we considered the concept of primary correspondences of the type that predict primary interfacial dislocations, as in grain boundary theory, as well as secondary correspondences that predict the secondary dislocations. The secondary correspondences are the ones defined by the CSL, and I think Jim Howe showed us in this conference a very good example of a phase transformation that appears to involve a CSL and secondary interfacial dislocations, known as DSC dislocations.

C.M. Wayman, University of Illinois at Urbana–Champaign, U.S.A.: Referring to Professor Olson's viewgraph, I think it would be more consistent in terminology to consider **RB** to be a lattice deformation and **R** to be a rotation and **BP** a matrix product, which produces an undistorted but, nevertheless, rotated plane. If you are going to go one-on-one with the phenomenological theory, then **RB** itself is the lattice deformation. **B** would be the pure distortion.

Unidentified Discusser: You said that there is a correspondence in the grain boundary, but I'm not sure I can see a correspondence in a small-angle grain boundary.

G.B. Olson: In a low-angle grain boundary, it is the "identity" correspondence defining the simple rotation that in turn defines the O-lattice.

Unidentified Discusser:* You didn't start with a single crystal, and I mean the **R** and the grain boundary are not the same. Free particles can rotate one another as they interact. But you know there is a difference between when you create something from a single crystal as you do in a transformation; and where we have a grain boundary, we can start from a single crystal and sort of erode material and create a new crystal. There's a lot of excess baggage that you carry with you when you start with a martensite view point. There's also a lot of excess baggage going backwards if you start with grain boundaries and try to go to phase boundaries.

J.W. Cahn: Well, I suspect that if you really are looking for those extra constraints, you will need all that baggage.

G.B. Olson: That's right. Let me make one further

*Edited by Professor G.B. Olson, Northwestern University.

comment on that point. Figure 2(a) from the previously mentioned Balluffi–Olson paper shows two lattices and defines a primary lattice correspondence relating primitive cells with minimal principal strains. The region of lattice 1 in Figure 2(b) is then transformed coherently to lattice 2 by an array of (partial) coherency dislocations in Figure 2(c) introducing dipoles of lattice dislocations inside the particle of Figure 2(c); a semicoherent particle is illustrated in Figure 2(d) now containing an additional array of primary interfacial dislocations. For the rational relation chosen between lattices 1 and 2, the lower portion of Figure 2(d) superimposes the construction of a CSL and associated DSC lattice. Referred to the primary correspondence, the interface is semicoherent. Referred to the secondary correspondence defined by the CSL, the interface is fully coherent. The CSL construction provides information on pattern matching relevant to interfacial energy minimization.

Figure 3 represents a closely related variation on the interface of Figure 2(d), but now with an irrational relation between lattices 1 and 2, so that the primary dislocations in Figure 3(a) are unevenly spaced. This introduces perturbations relative to the structure of Figure 2(d), which are represented by secondary DSC dislocations in Figure 3(b). The latter are defined by the DSC lattice superimposed in Figure 2(b), which is in turn defined by the CSL of Figure 2(d). While the primary dislocation description of Figure 3(a) relates to the strain-energy minimizing operations of the martensite-type theory (although the lattice-invariant deformation is in this case nonconservative), the CSL-based secondary dislocation description of Figure 3(b) relates to pattern matching and interfacial energy minimization.

J.W. Christian: There is a well-known difficulty here, namely an infinite number of different lattice deformations will give the same end result: the question is whether a particular description has physical significance. If we tie labels on the atoms (or lattice points) and then identify them after transformation, this will generally allow corresponding vectors, planes, and unit cells to be identified. Note that a correspondence can be defined only for an interface that has been displaced. Even with labels, ambiguities are possible; a high-angle symmetrical tilt boundary may also be regarded as a deformation twin, and the more appropriate description may depend on how it has been formed.

G.B. Olson: It will always be that for a given interface, even when you know where all the atoms are, there are choices you can make in correspondences as you view its structure. But I think there are different functions in these alternative choices, and it's really in the CSL concepts that you are going beyond just looking for strain accommodation (Figure 3(a)) and looking for pattern matching (Figure 3(b)), which relates back to the minimization of interfacial energy.

J.P. Hirth: Well, we've had somewhat over an hour on this topic. Possibly we can return to it at the end of this session. Perhaps we can now turn to issues of thermodynamics and kinetics.

M. Enomoto, Ibaraki University, Japan: My comments concerns the claim made by Tsuzaki and Maki that their bainitic ferrite is supersaturated with respect to

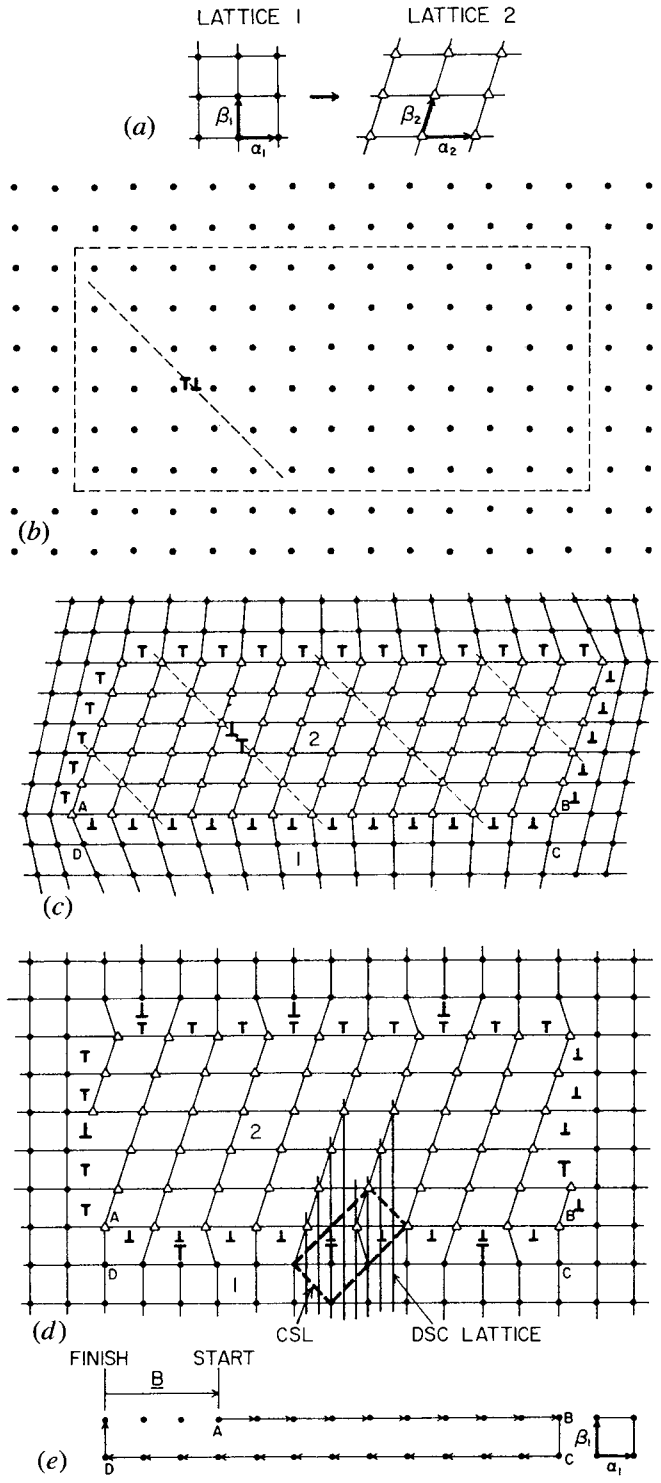


Fig. 2—Formation of occluded particle of Phase 2/Lattice 2 in a large matrix of Phase 1/Lattice 1 by a phase transformation. (*a*) Lattice transformation between Phases 1 and 2. (*b*) First step in transformation. Coherency dislocation dipoles are generated in interior of region to be transformed (dashed region) and are expanded (by combined glide and climb) on successive {110} planes (dashed) of Lattice 1. (*c*) Second step in transformation. Lattice (primary) dislocation dipoles are generated in Phase 2/Lattice 2 region and are expanded (by combined glide and climb) on dashed {110} planes. (*d*) Final configuration. Interphase boundary contains both coherency and primary dislocations. Also shown are CSL and DSC Lattice formed by Lattices 1 and 2. (*e*) Burgers circuit, A → B → C → D → A in (*d*), mapped in the reference lattice (*i.e.*, Lattice 1) to reveal primary interfacial dislocation content. (R.W. Balluffi and G.B. Olson: *Metall. Trans. A*, 1985, vol. 16A, p. 529.)

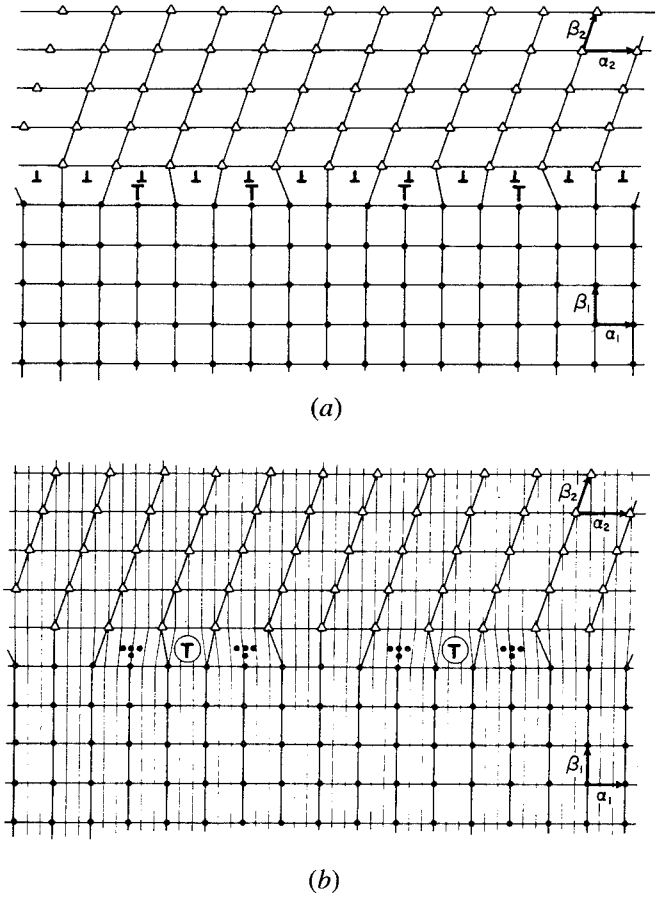


Fig. 3—(*a*) Final semicoherent interphase boundary produced when lattice parameter of Lattice 2 in Fig. 2 is increased slightly (*i.e.*, by ≅5 pct). (*b*) Same as (*a*), except that the Σ = 3:4 DSC Lattice is shown embedded in Lattices 1 and 2. Secondary edge dislocations are shown encircled. Primary dislocations are shown dotted. (R.W. Balluffi and G.B. Olson: *Metall. Trans. A*, 1985, vol. 16A, p. 529).

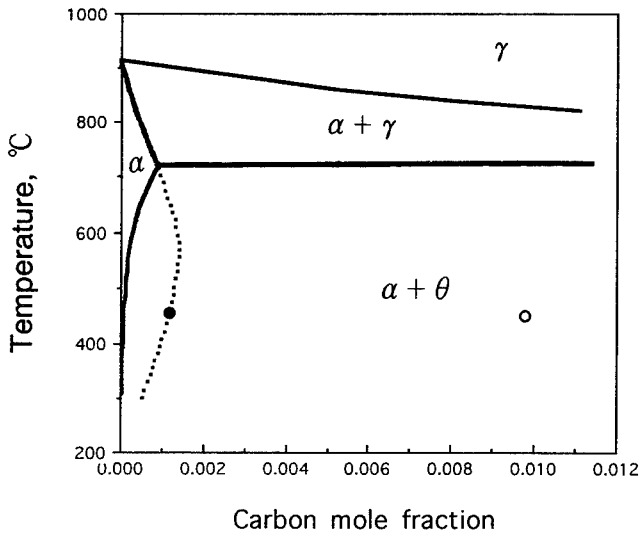


Fig. 4—Fe-Fe_3C metastable equilibrium phase diagram.

carbon. The amount of excess carbon was said to be approximately 0.2 wt pct (approximately 1 at. pct). For the sake of simplicity, I will discuss this point using the binary Fe-C phase diagram (Figure 4). The para-equilibrium phase boundaries in the Fe-C-Si and Fe-C-Si-Mn systems may be somewhat higher than and similar to their counterparts in the Fe-C system, respectively. In both alloys studied, it is very likely that at 723 K the solubility of carbon in ferrite is not far from the maximum solubility (a few hundreds weight parts per million). Obviously, the ferritic component of bainite formed at this temperature is supersaturated with respect to the precipitation of cementite, even if it is formed maintaining equilibrium with austenite (marked by the solid circle). We usually expect a large amount of carbide from ferrite containing approximately 0.2 wt. carbon (marked by the open circle). So, the fine carbides they showed (they may be cementite or ε carbide) are likely to have been formed during cooling to room temperature or by the time of transmission electron microscope (TEM) observation.

Then, the authors may argue that carbon diffused to the retained austenite before carbides were formed. They used the mass balance of carbon (equivalent to the lever rule) between the ferritic component of bainite and the retained austenite to calculate the excess amount of carbon in ferrite. (They determined the carbon concentration in austenite by measuring the lattice spacing by X-ray diffraction.) If ferrite were formed with such a high percentage of excess carbon, the amount of ferrite tends to be very large compared to that of final equilibrium in view of the lever rule. This implies that the ferrite:austenite interface has to go back as the carbon diffuses out, if the mobility of the ferrite:austenite interface is sufficiently large. At least the driving force would be for the backward motion of the interface.

The authors consider that carbon diffused out to the retained austenite in several tens of seconds. The conclusion of my comments, therefore, is that they need to acquire more experimental data using the same technique and show the time variation of carbon supersaturation in the ferritic component of bainite and/or the volume fraction of ferrite in their alloys.

K. Tsuzaki: I respond to Professor Enomoto's comments. For the first comment, I should say that I estimated the carbon content in the ferrite of a specimen quenched after 50 seconds holding at 823 K by using the average carbon content of retained austenite and the volume fractions of ferrite and austenite, but not by the amount of carbides in the ferrite. At this stage (823 K, 50 seconds), there were no carbides in ferrite and austenite in the present Fe-2 wt pct Si-0.6 wt pct C alloy. At the middle stage of transformation (823 K, 100 seconds), the ferrite laths were still surrounded by austenite where I had observed large carbide plates. (Because of the presence of Si in the alloy, these carbides were not cementite.) This means that the supersaturated carbon in the ferrite formed by 50 seconds of isothermal holding had at least 50 seconds to diffuse out from the ferrite to the austenite. This is probably the reason why in the final stage of transformation (823 K, 1.8 ks), the amount of carbides in the primary ferrite is not so large in comparison with the carbon content of the primary ferrite estimated at 823 K and 50 seconds.

I could not understand your comment on the moving back of the ferrite/austenite interphase boundary. I can

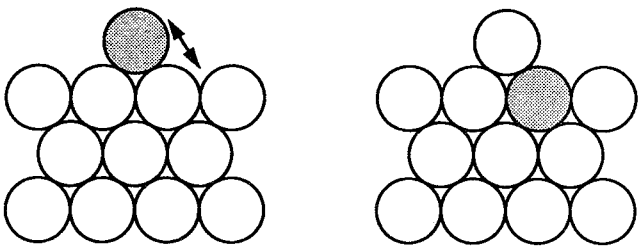
just say that at the stage of 50 seconds isothermal holding, the interphase boundaries have already lost their martensite-like mobility (*i.e.*, a glissile interface). This is consistent with the result that the width of ferrite laths did not change during the subsequent isothermal holding at 823 K after 50 seconds holding.

With respect to the final comment, I should say that the study of the time variation of carbon supersaturation in ferrite is possible but hard to do with the present alloy because the formation of carbides, which prevents use of my method to estimate the carbon content in ferrite, occurs relatively fast.

M. Enomoto: How much accuracy do you expect from your measurement? I would like to know the error limit in the determination of carbon concentration in austenite from the diffraction peaks, and then of the carbon concentration in ferrite from the mass balance.

J.K. Lee, Michigan Technological University, U.S.A.: I would like to call your attention to recent field ion microscope observations on the "direct atomic exchange" mechanism presented in Materials Research Society (MRS) meetings and also published in the literature (S. Fukatsu, K. Fujita, H. Yaguchi, Y. Shiraki, and R. Ito: *App. Phys. Lett.*, 1991, vol. 59, p. 2103; H. Jorke: *Surface Sci.* 1988, vol. 193, pp. 569-578). In a diffusion class, one learns that for a large substitutional solute atom to diffuse in a crystalline lattice, a vacancy is required. However, some recent observations indicate that the direct interchange mechanism is apparently working between a large substitutional adatom, such as Sb, and a host atom Si (Figure 5). The investigators claim that there is no indication of any particular defect that might aid solute diffusion at the surface layer of Si atoms, and yet significant atomic exchanges lead to solute segregation and intermixing. Conventional wisdom suggests that the activation energy for direct exchange is too high to be operative, but this is not so (at least not for diffusion at a surface). If direct atomic exchange is indeed an active diffusion mechanism, the implication seems very profound for our understanding of diffusion at an interphase boundary, as well as the motion of such a boundary, as there appears no reason to suspect that the activation energy should be much higher than that at a free surface.

H. Chen, University of Illinois at Urbana-Champaign, U.S.A.: I recall that Professor Gert Ehrlich of the University of Illinois did Monte Carlo simulation of adatoms on a surface. The exchange process was greatly assisted by lattice dynamics, especially at a free surface where large displacements of atoms could occur.



(*a*) (*b*)

Fig. 5 — Schematic drawing showing direct atomic interchange between a solute Sb adatom and a solvent Si atom (*a*) before and (*b*) after interchange.

T.Y. Hsu, Shanghai Jiao Tong University, China: I would like to say a few words about the kinetics and discuss some other problems concerning bainite formation according to our experimental results. K. Takezawa and S. Sato (*Trans. Jpn. Inst. Met.*, 1988, vol. 19, p. 894) showed that under stress, the kinetic characteristics of bainite formation taking place through up-quenching from the martensitic state in Cu-Zn-Al alloys obey the Austin–Rickett equation for diffusional transformations with an activation energy close to that for the diffusion of Zn. E.S. Lee and G. Kim (*Acta. Metall. Mater.*, 1990, vol. 38, p. 1669) got the same results in Cu-Zn-Al alloys up-quenched from a martensitic state. Our study (L. Jiang, W. Lu, B. Jiang, and T.Y. Hsu (Xu Zuyao): *Trans. Non-Ferrous Met. Soc. of China (English Edition)*, 1993, vol. 3, p. 66) on the time-temperature-transformation (TTT) diagram and the kinetics curves for bainite formation in Cu-Zn-Al up-quenched from the martensitic (DO_3) state, as well as cooled from the high-temperature parent phase (B2), shows that the kinetic characteristics of bainite formation obey the Austin–Rickett equation with $n = 2.25$ for up-quenched specimens and $n = 1.80$ for specimens cooled from high temperature, and an activation energy for bainite formation of about 110 kJ/mole, corresponding to that for the diffusion of solute atoms. Thus, we believe that the kinetics of bainite formation in Cu-Zn-Al alloys may conform to those for a diffusional transformation.

The second problem concerns the so-called inheritance of the ordering of the parent phase during bainite formation. Our X-ray diffractometry study in Cu-Zn-Al alloys (Jiang *et al.: Trans. Non-Ferrous Met. Soc. of China (English Edition)*, 1993) shows that in 9R or 18R martensite, the (115) diffraction peaks are separate from ($\bar{2}05$) peaks, and (1 2 10) peaks are distinguishable from ($\bar{2}$ 0 10) peaks. However, in bainite formed and cooled from various conditions, the (115) and ($\bar{2}05$) as well as the (1 2 10) and ($\bar{2}$ 0 10) peaks overlap. For example, as formed from the high temperature $L2_1$ matrix, the spacing Δd between diffraction peaks in martensite is about 0.0079 mm but less than 0.002 mm in bainite. Figure 6 shows the (1 2 10) and ($\bar{2}$ 0 10) diffraction peaks for bainite and martensite, revealing that ordering in bainite is quite different from that in martensite formed from the same ordered parent phase, with the degree of ordering in bainite being much smaller than in martensite. Continuous observations by means of high-temperature X-ray investigation completely confirmed these results. As we know, martensite must inherit the ordering of substitutional atoms in the parent phase, and experiments have revealed the change in composition associated with the formation of bainite, in conformity with the results of our thermodynamic calculations. Referring to the results of the thermodynamic study (T. Y. Hsu (Xu Zuyao) and X.W. Zhou: *Acta Metall. Mater.*, 1991, vol. 39, p. 2615), it may be conceived that the bainite is essentially formed in a disordered state and will become ordered on aging or slow cooling. After long-term isothermal holding, the formation of the stable

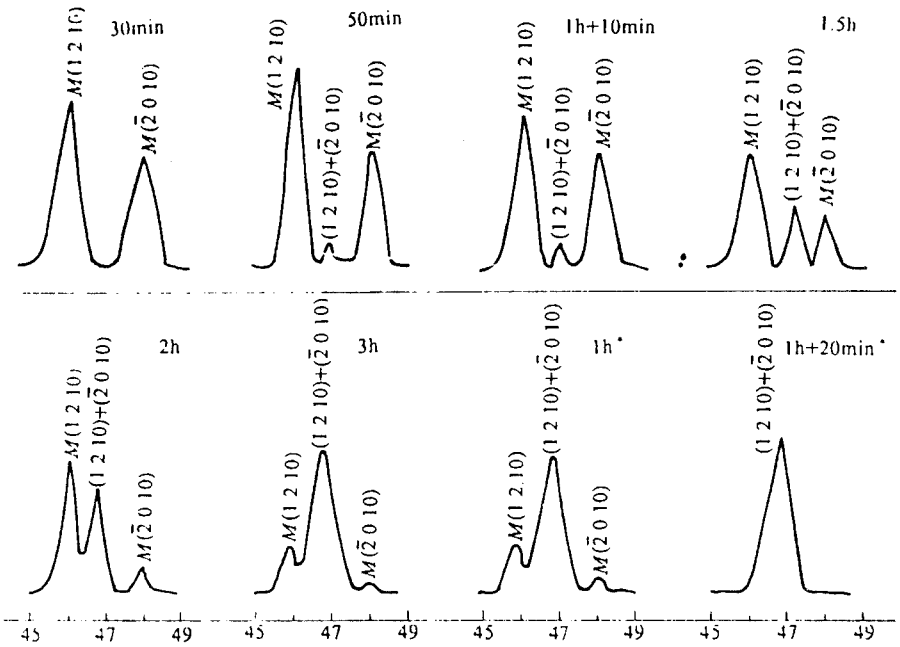


Fig. 6—The (1 2 10) and ($\bar{2}$ 0 10) diffraction peaks for bainite and martensite formed from the $L2_1$ parent phase by isothermal holding at 250 °C for different times and then slow cooled (L. Jiang, W. Lu, B. Jiang, and T.Y. Hsu (Xu Zuyao): *Trans. Non-Ferrous Metals Soc. of China: (English Edition)*, 1993, vol. 3, p. 66.)

disordered α phase will occur. Accordingly, the non-inheritance of the ordering of the parent phase during bainite formation can be deduced (W. Lu, B. Jiang and T.Y. Hsu (Xu Zuyao): *Scripta Metall. Mater.*, 1992, vol. 27, p. 861).

I would also like to point out that shape-memory alloys exhibit the crystallographic reversibility associated with the martensitic transformation and the reverse transformation (*i.e.*, shape recovery occurs in the deformed martensite upon heating to a temperature above A_s). However, in Cu-Zn-Al shape-memory alloys there is no crystallographic reversibility associated with the bainitic transformation (*i.e.*, shape recovery does not occur in the deformed bainite on heating to the parent state). Only the so-called "reverse shape-memory effect" occurs (*i.e.*, extension and compression associated with bainite formation in specimens under tensile and compressive stresses, respectively).

In this conference, someone mentioned the so-called prebainitic transformation. Our internal friction measurements on ferrous alloys, copper alloys (J. Zhang, S. Chen and T.Y. Hsu (Xu Zuyao): *Acta. Metall. Mater.*, 1991, vol. 39, p. 2615), and a Ag-Cd alloy (J. Zhang, S. Chen and T.Y. Hsu (Xu Zuyao): *Metall. Trans. A*, 1989, vol. 20A, p. 1169) all show that the damping peak appears within the incubation period, and the maximum damping values are inversely proportional to their incubation periods. That means the damping capacity value is directly proportional to the nucleation rate. Thus, we suggested that the so-called prebainitic transformation is actually the nucleation of the bainite within the incubation period (T.Y. Hsu (Xu Zuyao)): *Metall. Trans. A*, 1990, vol. 21A, p. 811). The appearance of solute-depleted zones by means of diffusion of the solute atoms during the incubation period will raise the free energy of the system and so is thermodynamically impossible unless it takes place in association with nucleation.

In addition, our experimental results on Fe-Ni-C alloys obtained with internal friction measurements revealed that the internal friction behavior of the martensitic transformation conforms with the hysteresis loss mechanism associated with stress-induced motion of the interface dislocations. The mechanism of the internal friction change associated with the pearlitic and bainitic transformations is in agreement with Postnikov's mode. Hence bainite formation is similar to the pearlitic but not to the martensitic transformation.

H.I. Aaronson: How did you determine experimentally the activation energy for transformation in Cu-Zn-Al alloys?

T.Y Hsu: We calculated the activation energy from the overall kinetics curve, using the rate of formation of 50 pct transformation product.

H.I. Aaronson: You should realize that the activation energy for overall transformation kinetics has no physical meaning because, with diffusivity rapidly falling with decreasing temperature while the driving force is rising, the overall kinetics are just a compromise and you cannot get a physically meaningful activation energy out of that information. Also, you are combining nucleation and growth. But, even if you have just growth, you cannot get a meaningful activation energy from growth kinetics as a function of temperature.

T.Y. Hsu: The activation energy we got is the activation energy for overall kinetics involving that for nucleation and growth. If, at a certain temperature range, both the nucleation and growth processes are controlled by the diffusion of solute atoms, the activation energy for overall kinetics may be close to that for the diffusion of the solute atoms, though only apparently.

H.I. Aaronson: Even so, there is no single activation energy for growth, because in growth the driving force increases with decreasing temperature and diffusivity decreases. So, above a certain temperature, you can get a negative activation energy. And you only get a single positive value if you use a narrow temperature range below the maximum growth rate where you can approximate a straight line relationship on an Arrhenius plot.

T.Y. Hsu: I agree.

C.M. Wayman: I have a question for Professor Hsu. Do you feel that the T_0 temperature can be higher in the presence of a defect or cluster of defects?

T.Y. Hsu, Shanghai, Jiao Tong University, P.R.C.: Yes. There is a fixed T_0 temperature in a homogeneous matrix. If defects are present in a matrix, there may be an interaction between the defects and solute atoms, resulting in a solute-depleted zone where the local T_0 can be higher. Thus, martensitic transformation may occur above T_0. But the problem is that the defect density must correspond to the density of nuclei; this situation seems unlikely to obtain in practice.

K.C. Russell, Massachusetts Institute of Technology U.S.A.: The question was, I believe, would defects or clusters of defects contribute to T_0, the temperature where the bulk free energies of the two phases are the same. The free energies of defects are generally extremely small compared to the bulk free energy, even in a heavily defected material. You can add up the free energy of the dislocations, the vacancies and the interstitials, and you don't get much. However, the M_s temperature, which depends on defects for nucleation sites, could very well change in a significant way.

S. Banerjee, Bhabha Atomic Research Center, India: I agree with Professor Russell that in the classical nucleation approach, defects and defect clusters have no significant influence on the T_0 temperature. It is also recognized that for a transformation to proceed to a reasonable extent above T_0, it is essential to have partitioning of alloying elements. However, in many first order martensitic and displacive transitions, lattice softening occurs to a partial extent as a precursor to the nucleation event. This is reflected in the observed phonon anomaly, which is related to the resultant structure. In such cases, defects play a very important role in localized amplification of displacement waves. I am raising this point only to emphasize the fact that incomplete lattice softening, in conjunction with defects, can cause the formation of martensitic embryos at temperatures above T_0.

From the deliberations of this conference, I gather that there is general agreement that atomic site correspondence is present across the transformation front in a large number of diffusional transformations. This correspondence can be differentiated from the lattice correspondence in displacive and martensitic transformations on the basis of the fact that one-to-one correspondence between the labelled lattice points of the parent and the product lattices is absent in a diffusional transformation.

It is also agreed upon that the interface between the parent and the product phases in diffusional transformations is generally made up of regions of good fit, these coherent regions being separated by steps. The deviation of the interface plane from the crystallographic plane of good fit is related to the spacing of these steps. Misfit along the plane is corrected by an array of misfit-compensating dislocations. However, there are some issues on which a consensus has not yet been reached. These are listed below.

(a) What is the motivating factor for establishing the atomic site correspondence and a specific crystallographic habit (sometimes irrational) in diffusional transformations? The relative importance of different criteria, namely, minimization of surface energy, minimization of strain energy, and maximization of growth rate in determining the shape of plate-shaped products of diffusional transformations, is still not clear.

(b) The strain-energy-minimization criterion and the invariant plane strain (IPS) conditions have been shown to be equivalent in several cases of martensitic products. The fulfillment of the IPS condition can, therefore, imply strain-energy minimization in a given case, irrespective of whether the transformation is martensitic or diffusional. It is not clear whether the operation of the IPS condition can be used to decide the mechanism of atom movements (diffusional or martensitic) in a given transformation.

(c) How are the irrational habit planes of martensite plates constructed at the atomic level? Are they made up of rational terraces and periodic steps?

(d) What is the role of the invariant line in diffusional transformations? Is it a necessary condition that at least one invariant line be present along the parent/product interface for all diffusional transformations?

It is worthwhile to address these specific questions and arrive at some consensus. This is especially important for teaching a course on phase transformations.

H.I. Aaronson: I would like to offer a summary of the present situation with regard to our understanding of the formation mechanism of α_1 Cu-Zn (and Cu-Zn-X) plates, as I see it. M.-H. Wu, Y. Hamada, and C.M. Wayman (in these proceedings) have now shown definitively that the composition of these plates differs from that of their ordered β matrix from the earliest stages of growth. This important result makes clear, on the basis of the rules for the applicability of the phenomenological theory of martensite crystallography, that α_1 plates cannot be formed by a shear mechanism. The earlier finding by M.-H. Wu, J. Perkins, and C.M. Wayman (*Acta Metall.*, 1989, vol. 37, p. 1821) that both first and second nearest-neighbors long-range order can be retained during α_1 plate formation does not contravene the implication of the composition-change result, because composition changes require long-range diffusion, whereas long-range ordering can be accomplished with short-range diffusion. Long-range order retention can be readily explained on the basis of ledgewise diffusional growth through epitaxial transmission of matrix long-range order across partially coherent interphase boundaries, as has been described in several articles dealing with multi-layer epitaxial growth (G.P. Srivastava, J.L. Martins, and A. Zunger: *Phys. Rev. B*, 1985, vol. 31, p. 2561; M.A. Shahid and S. Mahajan: *Phys. Rev. B*, 1988, vol. 38, p. 1344; P. Bellon, J.P. Chevalier, E. Argarde, J.P. Andre, and G.P. Martin: *J. Appl. Phys.*, 1989, vol. 66, p. 2388). The lengthening kinetics

of α_1 plates in Cu-Zn and Ag-Cd alloys have been reported to be somewhat more rapid than long-range volume diffusion can allow. However, inaccuracies in auxiliary parameters, such as the metastable equilibrium phase boundary compositions of the α_1 + ordered β region and the interdiffusivity *vs* composition in the ordered β matrix, could account for these discrepancies (H.I. Aaronson, T. Furuhara, J.M. Rigsbee, W.T. Reynolds, Jr., and J.M. Howe: *Metall. Trans. A*, 1990, vol. 21A, p. 2369). One issue remaining unresolved is whether or not stacking faults exist in α_1 plates during the earliest stages of their growth. If they do not, then what is evidently the preferred mechanism for the lattice-invariant deformation during this transformation does not appear to have been operative, thereby casting further doubt upon the role of shear in its occurrence. There remain some problems with conflicting experimental evidence on this point, though two conference papers in *Metall. Mater. Trans. A* (by Fang *et al.* pp. 2001-08, and by Ravishankar *et al.*, pp. 2631-38) support their absence during the earliest stages of growth. But, at the very least, the microanalysis data reported by Wu, Hamada, and Wayman in this issue appear to be decisive in demonstrating that the atomic mechanism of α_1 plate formation must be diffusional.

J.M. Howe: I would like to discuss the idea of irrational habit planes and ask whether there is something systematic about their structure that we find throughout. We have looked at that problem. The way we did it was to take all possible combinations of fcc, bcc, and hcp crystal structures and to look at the interfaces in the cases where they were low index, rational habit planes, and also high index ones typical of martensite, as well as various combinations of these extremes (J.M. Howe and S.A. Roseveld: unpublished research). At least in the cases we have looked at, where the close-packed planes between the two phases are parallel or very nearly parallel, at the atomic level the habit plane is made up of steps on these close-packed planes. The steps may be one atom high in the case of, say, a {252} martensite plate in a steel that we studied (G.J. Mahon, J.M. Howe, and S. Mahajan: *Phil. Mag. Lett.*, 1989, vol. 59, pp. 273-279), where each step also accomplishes the transformation. But the steps allow the habit plane to rotate. The steps may also be two atomic planes high, as in the case of Al-Ag or Ti-Al (J.M. Howe, U. Dahmen, and R. Gronsky: *Phil. Mag. A*, 1987, vol. 56, pp. 31-61; S.R. Singh and J.M. Howe: *Phil. Mag. A*, 1992, vol. 66, pp. 739-771). The height depends on the system, but the steps inevitably seem to be on the close-packed planes. You can achieve any apparent habit plane you want simply by varying the densities of these steps, much like in the example we saw this morning, where we saw that a precipitate could achieve any facet just by varying the density of kinks. And so I think there are certain parallels. They have to obey the requirements of the particular system that is undergoing the transformation, but, in essence, a precipitate plate can achieve any habit plane by adjusting the density of steps on the close-packed planes.

C.M. Wayman: I would like to ask the following question. In a first-order ordering reaction, such as the formation of CuAu II, Professor Cohen showed very nicely a short-range ordered segment of CuAu II at temperatures substantially above the actual transformation temperature. And I am wondering if in any of his similar X-ray or small-angle neutron scattering (SANS) experiments he has found equivalent evidence for the existence of microregions of martensite above the M_s temperature?

H. Chen: My name is not Jerry Cohen but I was once a student of his. I'm trying to put words into his mouth. It is clear that for ordering, disordering, or clustering, lattice distortion associated with short-range ordering above the transformation temperature has been shown by X-ray measurements as well as by other techniques. As far as the precursor phase for the martensitic transformation is concerned, I do recall that for NiAl near 50 at. pct there is clear evidence that you have extended either vacancy-complex or substitutional-atom short-range ordered regions in the form of plates, depending upon solute concentrations. I don't really know whether there is any solid X-ray evidence to show that there is pre-existing martensite above the transformation temperature. However, I would like to add that Dr. Srikumar Banerjee mentioned the phonon effect, which may have profound implications with respect to transformations that occur below the transition point. I also think that in order to understand fully the physical origin of the nucleation process, long before the ledges, the terraces, and the plates have formed, we need to understand the physical mechanism of the nucleation process. I don't think the classical nucleation model can explain martensite formation. We do have to introduce nonlinearity into the free-energy expression and to include the phonon behavior, as well as anharmonicity.

J.B. Cohen (written discussion): Professor Chen is referring to our work on NiAl, but these initial remarks concern the omega phase. Dr. Georgopoulos and I showed in the 1970s that point "defects," the vacancies in alloys with excess Al, or substitutional atoms in the presence of excess Ni both stimulate formation of the omega phase (P. Georgopoulos and J.B. Cohen: *Acta Metall.*, 1981, vol. 29, pp. 1535-1551). This work has been confirmed in Ti and Zr systems by others since then, most recently by Petry and co-workers (A. Heiming, W. Petry, G. Vogel, J. Trumpenau, B.R. Schober, J. Chevier, and O. Scharpf: *Condensed Matter*, 1991, vol. 85, pp. 239-248).

As far as martensite is concerned, the evidence of premonitory effects is less clear. In Fe-Ni alloys, Robert Comstock (R.J. Comstock, J.B. Cohen, and H.R. Harrison: *Acta Metall.*, 1985, vol. 33, pp. 423-36) found that there was no increase in the mean-squared atomic displacements as M_s was approached, though earlier Mossbauer studies had suggested this. There was softening of long wavelength (100)[100] modes, which could produce the Bain distortion. Also, Brent Butler found a density of {011} microtwins in the as-quenched tetragonal martensite in Fe-1.0 wt. pct. C-13 wt. pct. Ni (B.D. Butler and J.B. Cohen: *Metall. Trans. A*, 1992, vol. 213A, pp. 1617-26). These could form as a premonitory phase between the austenite and martensite, as has been suggested by Khachaturyan and coworkers (A.G. Khachaturyan, S.M. Shapiro, and S. Semenovskaya: *Phys. Rev. B*, 1991, vol. 43,

pp. 10832-843). To confirm this, data will have to be taken just above M_s, not just in the as-quenched materials.

G.B. Olson: I would like to make some observations about steps and the habit plane. The point is that if we have a deviation of the habit plane from a certain rational orientation, then there is a predetermined distance between steps in this case. On the other hand, if each step is a partial dislocation, it has a certain width, and therefore we have the criterion that if the width of the dislocation is much larger than the distance between two steps, then we probably cannot observe these steps in the usual way. The step still exists in principle but observation may be difficult.

K.C. Russell: This business of embryos of the phase to be formed at a considerably lower temperature existing at a higher temperature, even above the solvus, goes back a long time. Certainly, Professor J.B. Cohen showed some very impressive results, displaying clusters of copper in an aluminum-base alloy, which looked suspiciously like the GP zones, which experimentally we find only form at hundreds of degrees lower temperatures. This is an issue that I'll have to address in my paper for the proceedings of the conference. Now, on the matter of martensite embryos, you may recall many years ago Morris Cohen had a student named Marc Richman looking for martensite embryos in iron-nickel alloys, and after years and years of peering through the TEM, he saw something which he deemed a martensite embryo, and graduated. Some years later, another student, Satya Pati, who was at M.I.T. doing his doctorate just about the time I got there, did measurements on the nucleation of isothermal martensite. He concluded that the nucleation site density, the number of whatevers that create the martensite particles, is so low that the chances of finding even one in many, many TEM foils were extraordinarily small. So, I think with the conventional ferrous martensite, the nucleating defects, as Greg Olson likes to call them, whatever they are, are awfully thin on the ground.

C.M. Wayman: Actually, the probability of finding a nucleus of martensite in a thin foil is about one in 10^8, which is beyond a graduate student's lifetime, usually. But later experiments involving high magnetic fields by M. Korenko and M. Cohen (*Scripta Metall.*, 1974, vol. 8, pp. 751-756) were entirely negative. There was no evidence for anything that had any ferromagnetic nature to it at any temperature anywhere near the M_s temperature.

G.B. Olson: Concerning the first point about the sparseness of martensite nucleation sites, those low numbers refer to sites potent enough to start transformation at M_s. But, of course, we know from the small particle experiments that there is actually a distribution of site potency. So, if you are willing to look at much less potent nucleation sites, the numbers do go up. The Korenko–Cohen experiment was really looking at evidence for pre-existing embryos quite far above the M_s temperature. Currently, interest is in finding systems that have the right kind of oxide films to suppress the surface nucleation that normally gets in the way. I think certainly the best observation we have of this type is the observation by T. Saburi and S. Nenno (*Proc. ICOMAT '86, Japan Institute of Metals*, Tokyo, 1986, p. 671) in titanium-nickel-copper, where you really see a bulk-like defect. Nucleation is on an oxide particle inside the foil, not on a surface artifact. An embryo is formed there in much the way you would predict from elasticity calculations, so I think we have seen embryos. And I'm sure that was not one of the extremely high potency sites that would trigger at the M_s, but a much less potent one. They actually made numerous observations at defects with different potency that could operate. I think what was really crucial in their experiment is that the oxide film was suppressing the surface phenomena that normally get in the way. You can find them.

I want to comment on the question about Jerry Cohen's observations, because I have talked with Jerry about the precursor phenomena and his interpretation of his X-ray studies. In a number of systems, including the nickel-aluminum alloys studied by I.M. Robertson and C.M. Wayman (*Phil. Mag.*, 1983, vol. 4, p. 629), there are Huang scattering centers at which distortions occur above the transformation temperature on an extremely local scale. As far as the relation of these distortions to the martensitic transformation that ultimately starts at M_s is concerned, we are back to the same issue that Ken Russell was talking about: that the size scale of a critical nucleus is very large whether you compare that with composition fluctuations or the very-fine-scale distortions that can exist around those defects. The fine-scale defects, we believe, have a role in interfacial friction and can, in fact, have a role in isothermal martensite formation by providing the thermal obstacles that slow down interfacial motion. But the fine-scale events are certainly not going to stabilize a critical nucleus.

Haydn Chen mentioned bringing in anharmonicity and that if we see these kinds of effects taking place, particularly anomalies in phonon dispersion curves, we should be taking that into account in nucleation. We have modeled martensitic nucleation in a nonlinear, nonlocal continuum, using Landau–Ginsberg-type models (G.B. Olson: *Proc. ICOMAT '86, Japan Institute of Metals*, Tokyo, 1986, p. 25) and we get out behavior very similar to nonclassical nucleation that Cahn and Hilliard treated very close to an instability, which in this case would be a lattice instability. We find that strongly nonclassical behavior occurs only very close to an instability. Transformation at the bulk M_s temperatures is classical.

H. Chen: I think some of you may be familiar with work by Krumhansl and his concept of the weakly first-order transition with a barrier which softens, but not completely. He has been able to show that the activation energy barrier that nucleation must overcome is significantly smaller than that derived from classical theory. I must say I haven't done enough studying to understand it fully, but I do feel that in the multiple dimensions involved in transformations of the martensitic type, there are several order parameters operative. There may be several saddle points involved as a consequence, with the energy path followed by the transformation not being as simple as one would imagine based upon a single parameter approach.

The other thing that I want to add is that at this conference most of us are talking about metals and alloys.

There was one talk today discussing the martensitic transformation in ceramics. I think that is another fascinating field but one in which you have to consider the long- and short-range charge effects, as well as the transformation strain and a larger volume change than is usually found in metallic alloys. This is another field that certainly can be benefit from the understanding of phase transformations already achieved in the metals community.

G.B. Olson: I first want to respond briefly to Professor Chen's comments. The model we used (G.B. Olson: *Proc. ICOMAT '86*, Japan Institute of Metals, Tokyo, 1986, p. 25) is based on the model that G.R. Barsch and J.A. Krumhansl (*Phys. Rev. Lett.*, 1984, vol. 53, p. 1069) developed to treat nonclassical nucleation. They took it as far as just treating interfaces, and we applied it to homogeneous nucleation. I would say that our results are entirely consistent with theirs. If you really want to see nonclassical martensitic nucleation, you can find it when you have about 90 percent of the driving force for lattice instability. So, in principle, such a nucleation process exists. In practice, however, we do not get that close to an instability because heterogeneous nucleation intervenes.

Now, insofar as treating nonclassical heterogeneous nucleation is concerned, that gets difficult. Everyone who has tried has had to employ approximations. The approximations we have applied, though, are different from those that Krumhansl used. The most recent work that he has done (W. Cao, J.A. Krumhansl, and R.J. Gooding: *Phys. Rev. B* 1990, vol. 41, p. 11319), while based upon different approximations, yielded the same result. Once you have a strong enough defect to make something happen near the M_s temperature (*i.e.*, the unrestricted growth of an embryo), defect interaction results in classical embryo formation prior to the growth event. Thus, even when you put in all the anharmonicities and allow for nonclassical behavior, the actual variational solution is classical at low driving forces.

H. Chen: Thank you for the clarification. I am now going to raise another question because I'm not in this field. I've been listening to the talks all this week. There seems to be a separation between the people who believe that the thickening and lengthening of the plates is governed by diffusion-controlled ledgewise growth and that shear is impossible. On the other hand, there is also a group of shear people who believe shear is the mechanism through which the transformation operates. I wonder if it is possible to have a combined effect between the diffusion and the shear mechanisms? Perhaps they may not necessarily occur simultaneously, but instead very close to each other in terms of time. And, for instance, is it possible to have diffusion that drives the solute closer to the ledges, and to form such a favorable environment so that localized shear (rather than macroscopic shear) can take place? Thus, you can have this diffusion-assisted shear mechanism, or perhaps a shear-assisted diffusion mechanism, that make the plates thicken. I'm just asking whether you can combine both mechanisms and come to the same point.

J.P. Hirth: With the advent of work on artificially modulated structures, it would seem possible to have a modulated structure where you could grow something through varying compositions and vary the driving force. You could have something growing, and then it hits a region characterized by a different supersaturation and it may then grow by a different mechanism.

H.I. Aaronson: I would like to raise some points about surface reliefs associated with diffusional transformations. Evidence is increasing that one can have multiple planar tilts associated with a single plate or lath. The tent-shaped relief has been found repeatedly in diffusional transformations, including the proeutectoid ferrite and bainite reactions in steel (J.D. Watson and P.G. McDougall: *Acta Metall.*, 1973, vol. 21, p. 961; M.G. Hall and H.I. Aaronson: *Metall. Mater. Trans. A*, 1994, vol. 25A, pp. 1923-32; G.R. Speich: *Decomposition of Austenite by Diffusional Processes*, Interscience, New York, NY, 1962, p. 353), the precipitation of Cr-rich plates from Cu-Cr alloys (M.G. Hall, H.I. Aaronson, and G.W. Lorimer: *Scripta Metall.*, 1975, vol. 9, p. 533), the formation of proeutectoid α laths in a hypoeutectoid Ti-Cr alloy (H.J. Lee and H.I. Aaronson: *Acta Metall.*, 1988, vol. 36, p. 787), and α_1 plates in ordered β Cu-Zn (I. Cornelis and C.M. Wayman: *Acta Metall.*, 1974, vol. 22, p. 291). Dr. Malcolm Hall has presented results during this conference showing that the two sides of tent-shaped reliefs often associated with ferrite plates are identically oriented within experimental limits of error (*i.e.*, <1 deg, M.G. Hall and H.I. Aaronson: *Metall. Trans. A*, 1994, vol. 25A, pp. 1923-32). They are thus not separate plates, as has often been proposed. And Dr. K.R. Kinsman, having looked at many surface reliefs atop ferrite plates, has concluded that even tents are relatively rare, with far more complex reliefs being of general occurrence. Dr. Kinsman has also looked at the structure of the underlying plate and has found that these complex reliefs are also associated with single plates (K.R. Kinsman, E. Eichen, and H.I. Aaronson: *Metall. Trans. A*, 1975, vol. 6A, p. 303). From the viewpoint of diffusional growth, one might explain such reliefs in terms of growth ledges with the same Burgers vector oriented toward the free surface, until the accumulated shear strain energy becomes large enough to make the activation of another set of growth ledges with a crystallographically equivalent but different Burgers vector energetically preferable. (Later-formed sets of growth ledges may be directed well away from perpendicularity to the free surface, perhaps even toward the specimen interior.) Is there an explanation available for tent-shaped and more complicated reliefs atop monocrystalline plates on the basis of the shear mechanism? And is the experimental observation of such reliefs in association with single plates still being contested?

H.S. Fang, Tsinghua University, P.R.C.: Many people talk about evidence for the transformation mechanism of bainite. I want to offer evidence for superledges on bainitic ferrite plates and bainitic α_1 plates in a Cu-Zn-Al alloy, for subunits in these plates and also for bainitic carbide precipitation in austenite at austenite: bainitic ferrite boundaries. Figure 7 shows superledge A and superledge C in an Fe-C-Cr steel, with heights of about 3.4 and 22 nm, respectively. The arrowheads point out carbide precipitates at austenite: ferrite boundaries, evidently formed in the austenite phase at these

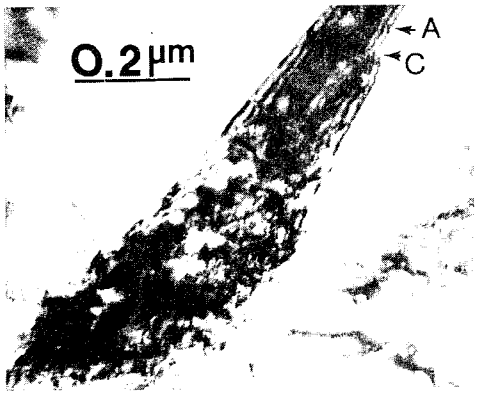


Fig. 7—Superledges on the broad face of bainitic ferrite in an Fe-2 pct C-12 pct Cr alloy reacted 22 hours at 300 °C.

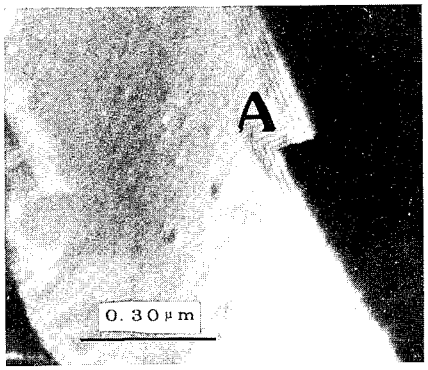


Fig. 8—A superledge ("A") on a broad face of an α_1 plate in a Cu-Zn-Al alloy.

boundaries. Figure 8 shows superledge A on an α_1 plate formed in a Cu-Zn-Al alloy with a height of about 85 nm. The arrowheads of Figure 9 point out carbide precipitates at austenite:ferrite boundaries, evidently formed in the austenite phase at these boundaries. Figure 10 shows various levels of subunits in ferrite. As can be clearly seen in Figure 10, all the subunits are of different sizes. For example, subunit D is apparently larger than subunit C. This can be fully interpreted with the theory of sympathetic nucleation of ferrite subunits.

C.M. Wayman: Well, the only thing I want to say is I think there is no dispute at all about tent-shaped reliefs. The only problem is that in a number of these transformations, you can't conveniently put scratches on a plane of polish before they happen and actually follow what has happened with respect to an optically flat surface. And that's one of the things that you can do to martensite, but you can't do with the high-temperature transformations.

B.C. Muddle, Monash University, Australia: I can't explain tent-shaped reliefs from a shearist point of view. But about ten or fifteen years ago, at the University of New South Wales, a graduate student by the name of Alan Crosky was working on Widmanstatten α rods in Cu-Zn alloys. These rods can be accounted for in terms of an invariant line-type approach. They produce surface reliefs, sometimes quite complicated reliefs. The one observation that has always stuck firmly in my mind is that often, when Alan had polished the relief away, there was no precipitate beneath it. And not until he had sectioned the sample normal to the surface did he find the Widmanstatten rod quite some distance, *e.g.*, micrometers below the surface. I'd be interested to know how a ledge approach would account for the transmission of that shape deformation to the free surface in that circumstance.

H.I. Aaronson: It's been evident and I think agreed for some time that the shape change that accompanies the movement of a partially coherent boundary by a ledge mechanism, whether the ledges glide by shear or move by individual atomic attachments to kinks on their risers, can be the same. This identity is particularly marked in fcc/hcp transformations. Therefore the transmission of the shape strain to the surface through an intervening layer of untransformed matrix in a diffusional transformation would be the same as in a shear

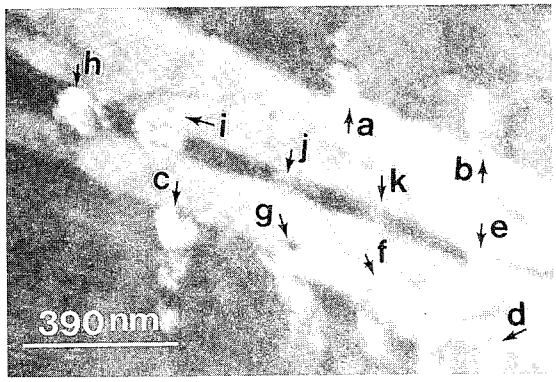


Fig. 9—Dark field image of carbides precipitating inside the austenite near the $\alpha:\gamma$ boundaries in an Fe-2 pct C-12 pct Cr alloy reacted 29 hours at 300 °C.

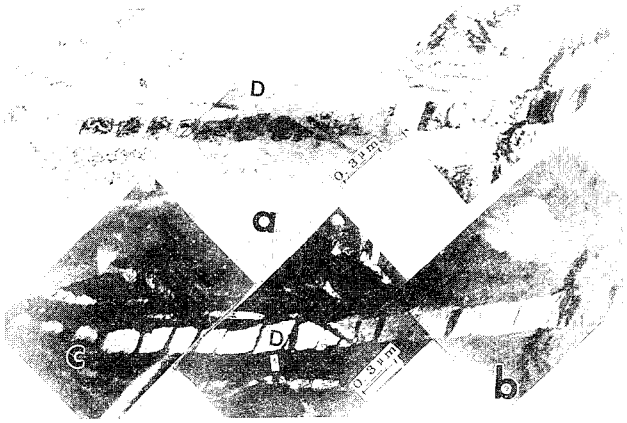


Fig. 10—A sheaf of bainitic ferrite consisting of subunits with different sizes in an Fe-2 pct C-12 pct Cr alloy reacted 22 hours at 300 °C: (*a*) bright field and (*b*) dark field.

transformation. On either mechanism, this transmission through a micron or more of matrix presumably occurs through plastic deformation, occasioned by the successive passage of many ledges in the same direction. In order to test this mechanism and explore further the process Professor Muddle has described, it would be of interest to ascertain the maximum depth below the surface

at which surface upheavals could still be produced during the formation of α Cu-Zn rods. Additionally, the ability of rods or laths produced during bcc/hcp transformations to produce a similar effect would also be of interest. (The crystallography of fcc/hcp transformations presumably restricts their Widmanstatten morphology to that of plates, which by their nature can extend to the free surface when formed near and nonparallel to the surface.) Similarly, the ability of martensite laths (evidently martensite rods form only at a free surface) to produce an invariant plane strain-type of surface relief when formed below a free surface should be examined.

J.P. Hirth: Actually, that raised something I was going to ask about, not being familiar with this field myself. I wondered if one had a plate growing with either rejection of some solute or enrichment, you might think that as the plate approached the surface it would finally deplete supersaturation of the adjacent near-surface region and change the kinetics locally? Conceivably, something like that might have come into play in what you were talking about. If there were emissary dislocations, you might expect growth to stop below the surface.

J.W. Christian: I drew a picture on the board the other day that might explain the tent shape with a single crystal. If there is a kink band or some secondary slip that accommodates the product plate on one side and so produces a tent-shape on the surface, is it not conceivable that if the plate is at an angle to the surface, an X-ray or electron beam will mainly see not the intervening matrix but the underlying plate? Thus, although the tent is actually plate + matrix, it might be wrongly identified as all plate. On the whole, I do not believe this: Dr. Hall's beautiful photographs convinced me something more elaborate is going on. But is it possible?

M.G. Hall, University of Birmingham, U.K.: In using Electron Back Scatter Patterns, we paid particular attention to estimating the spatial resolution of the technique by observing the change in the pattern as the probe was displaced across the boundary of the plate with the surrounding matrix. We were able to make orientation measurements from one side of the plate to the other without any detectable change in the pattern, but as the boundary with the matrix (of either pearlite or martensite) was passed, there would be an abrupt change in the orientation of the pattern. Our observations showed that we could approach to within 100 nm of the boundary without any interference from the matrix, and I am sure if Professor Christian's mechanism had been in operation we would not have observed such a sharp transition in moving from the matrix to the plate. In all cases, it was possible to see clearly the boundary of the plate with the matrix, but it was not possible to observe boundaries within single plates, even though the direction of surface tilt may have altered. In cases where there had been impingement of two or more plates, the boundary between them was also usually clearly seen. The resolution issue is discussed in more detail in our conference paper.

C.M. Wayman: The possibility here is one that John Bowles and his students explored some years ago, namely that of a degenerate situation where you can have two shape strains with a common habit plane. And they had a hard time finding a boundary along the common habit plane. So, in effect, they were observing tent relief in martensite, which, insofar as I can tell, is similar to what is being described here.

G.B. Olson: I can't say anything about calculations at free surfaces, but in Dennis Haezebrouk's model of the dynamics of martensite growth for both plates and laths in iron-nickel alloys (D.M. Haezebrouck, Sc.D. Thesis, Massachusetts Institute of Technology, Cambridge, MA, 1987), what comes out is the following. If you take a particle of the type that he simulated, which got arrested in its radial growth by plastic zone effects, and if we have a particle shearing in one direction, we can calculate the locus over which the critical resolved shear stress for slip in an alloy at the M_s temperature is exceeded. Figure 11 shows the results of such a calculation for Fe_3Pt in the ordered and disordered conditions (G.B. Olson and W.S. Owen: *Proc. JIM Int. Symp. on Martensite Transformations, Japan Institute of Metals*,

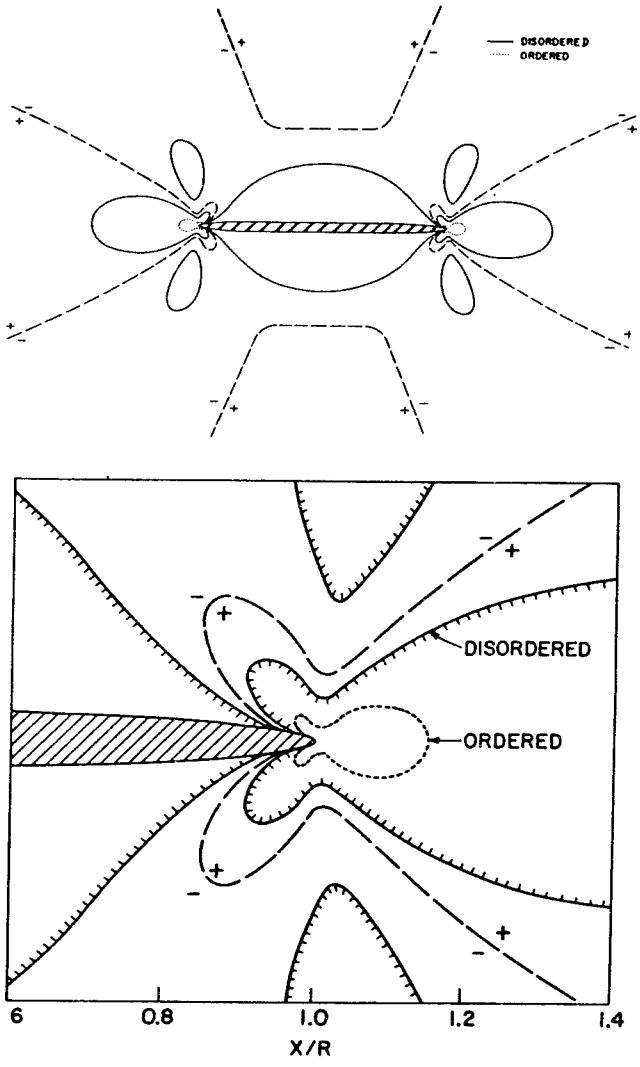


Fig. 11 — Stress-field contours of a martensitic particle lying in the xz-plane with transformation in the x-direction. Solid contours denote critical shear stress for slip in ordered and disordered Fe_3Pt. (G.B. Olson and W.S. Owen: *Proc. JIM International Symposium on Martensite Transformations*, Japan Institute of Metals, Tokyo, 1976, p. 105.)

Tokyo, (1976, p. 105). The dashed lines represent node lines across which the sign of the shear reverses. The material in the negative sign regions will tend to deform plastically in the direction opposite to that of the transformation shear. Now, out on a free surface, that would look something like a double-IPS tent. You would have a plastic zone on either side of the plate. You would also have the effect that was just alluded to with the surface observations of actually seeing surface relief (in the "positive" direction) out ahead of a unit that is forming. When you look at the size of the strains we're talking about in these transformations and look at the low flow stresses of the material outside, the real challenge is to explain how you could *not* get all this plastic deformation going on. Now, this is a very simplified calculation that so far has only been done with small-scale-yielding approximations, which become entirely invalid for the large plastic zones expected. One of the things we want to do is to take Dennis' model, include all of the same dynamics, but put it into a finite element code and do the mechanics right and then let a unit grow, go plastic, and even grow through its plastic zone, and ascertain what kind of effects we are going to see. I think if we put anisotropic crystal plasticity-type constitutive relations in the matrix, we're going to break some of the symmetry at the plate tip region (Figure 11). In some preliminary calculations, we have seen some asymmetry of this type. If you're just looking at part of a plate at a free surface, you may see more plasticity on one side than the other.

H.I. Aaronson: The situation Professor Olson has described looks very much like one of Jack Christian's drawings in his paper in *Decomposition of Austenite by Diffusional Processes*: (Interscience, N.Y., 1962, p. 371), showing deformation in the austenite on both sides of a plate-shaped martensitic transformation product (Figure 2, p. 382). There was no indication in this set of drawings of a tent-shaped relief. In our studies of tent-shaped reliefs, on the other hand, it was quite conclusively proved in steel, Ti-Cr, and Cu-Cr that what gave the relief was all precipitate, *not* the surrounding deformed zone.

G.B. Olson: Well, that's the issue I'd really like to get to with a finite-element calculation. If the plate goes plastic and then grows through its plastic zone, what is the final displacement field across the plate? It is a very complex problem, but I think it's something we can model.

H.I. Aaronson: Would not the surface relief be very messy if it had to grow through a plastic accommodation zone?

G.B. Olson: Yes, of course, the tent is very heterogeneous, in that if you invoke plastic accommodation, it is kind of one-sided plastic accommodation.

H.I. Aaronson: Yes, but the relief consists of two tilted planar surfaces.

G.B. Olson: Are you saying that there is no curvature to the tilts?

J.W. Christian, University of Oxford, U.K.: I just wondered if Dr. Hall had any comment himself. I was very impressed by his photographs, which showed no discontinuity at all along that line where the tilt changes.

M.G. Hall (written discussion): I do not feel that I can add to my colleague's comments relating to the general mechanism of formation of the tent-shaped surface relief. However, with regard to Professor Olson's remarks, it was apparent in our experiments that, within the resolution limit of the scanning electron microscope, the start of the surface relief and the edge of the precipitate (as observed by the thermal groove) were invariably coincident, and there was no evidence, on either side of the precipitate plates, that the surface upheaval might have occurred before the transformation took place—as would be expected if one side had formed as a result of plastic accommodation. The symmetry of many of the tents also tends to suggest that the surface tilts on either side of the apex had been formed by similar mechanisms, rather than one side being formed by a "martensitic tilting" and the other by plastic accommodation followed by transformation.

The Chromium Equivalents of Selected Elements in Austenitic Stainless Steels

V. RAGHAVAN and DARA P. ANTIA

Using the well-established thermodynamic description of the Fe-Cr-Ni system, we have computed the austenite-ferrite equilibrium in Fe-Cr-Ni-X quaternary systems, where X is a ferrite-stabilizing element. The results are considered reliable, especially for small additions of X. From the computed equilibria, the Cr equivalents of a number of ferrite stabilizers, Al, Mo, Nb, Si, Ti, V, and W, have been derived. They show satisfactory agreement with the known experimental range. The distinguishing feature of the thermodynamic calculations is that the Cr equivalents are established as a function of annealing temperature as well as Ni content, in contrast to the fixed values reported in the empirical diagrams obtained under variable experimental conditions.

I. INTRODUCTION

IN austenitic stainless steels, data about the combinations of Cr and Ni that will yield the fully austenitic structure with the minimum addition of Ni are important from cost considerations. For this purpose, empirically developed diagrams such as the Schaeffler[1] and the DeLong[2] diagrams on the constitution of stainless steels are used in the industry. Other intentionally added or residual alloying elements in stainless steels are usually present in smaller concentrations. The empirical diagrams take these into account by using a nickel or chromium equivalent depending on whether the alloying element stabilizes austenite or ferrite. Fixed values of the equivalents obtained from a limited number of experimental results are used. In some cases, the values given by different researchers show wide variations. Most experiments do not consider the possibility that the equivalents may vary with the basic composition of the steel (*i.e.*, with Ni and Cr contents) as well as with the annealing temperature[3] or cooling rates of a weldment or casting. Detailed determination of the effect of these variables will require an enormous experimental input.

The thermodynamic computation of phase equilibria for use in practical applications is now becoming increasingly common. For the problem at hand, a well-established thermodynamic description of the Fe-Cr-Ni phase diagram is available. The computed isothermal sections of this system are in close agreement with the experimental results. This fact enables us to compute the quaternary Fe-Cr-Ni-X phase equilibria with confidence. Updated thermodynamic interaction parameters, which are key to the calculations, are reported in recent literature. The results obtained by using these parameters are considered reliable, especially when the fourth element X is present in small concentrations. From the computed equilibria, we have derived the Cr equivalents of a number of ferrite stabilizing elements in this article. These are compared with the available experimental results.

V. RAGHAVAN, Professor, is with the Indian Institute of Technology, New Delhi, 110016, India. DARA P. ANTIA, Chairman of the APD Committee, is with the Indian Institute of Metals, Calcutta, India.

Manuscript submitted January 14, 1994.

II. THE THERMODYNAMIC MODELS AND PARAMETERS

The substitutional solid solution model of Hillert and Jarl,[4] which accounts separately for the excess free energy due to magnetic ordering, is used in this investigation. The chemical and magnetic interaction parameters for the binary combinations of the elements are described as Redich–Kister polynomials. The Appendix lists the parameters used in this study. References to the data sources are given.[2–25] Ternary interaction parameters are included, wherever these are available. No quaternary parameters for the systems under study are known.

The Ni-V system does not appear to have been assessed thermodynamically. The thermochemical data on this system reviewed by Smith *et al.*[26] show complex behavior. Here, the partial molar free energy of V in Ni-rich fcc solid solution at low V contents is used to derive the interaction parameters listed in the Appendix. In the absence of data for the V-rich bcc solid solution, the same parameter is used for the bcc phase.

The molar Gibbs energy of the α or γ phase is defined as follows. Using the Fe-Cr-Mo-Ni system as an example,

$$\begin{aligned} G_m = {} & X_{Fe}\,{}^{\circ}G_{Fe} + X_{Cr}\,{}^{\circ}G_{Cr} + X_{Mo}\,{}^{\circ}G_{Mo} + X_{Ni}\,{}^{\circ}G_{Ni} \\ & + RT(X_{Fe} \ln X_{Fe} + X_{Cr} \ln X_{Cr} + X_{Mo} \ln X_{Mo} \\ & + X_{Ni} \ln X_{Ni}) + X_{Fe}X_{Cr}L_{Fe,Cr} + X_{Fe}X_{Mo}L_{Fe,Mo} \\ & + X_{Fe}X_{Ni}L_{Fe,Ni} + X_{Cr}X_{Mo}L_{Cr,Mo} + X_{Cr}X_{Ni}L_{Cr,Ni} \\ & + X_{Mo}X_{Ni}L_{Mo,Ni} + X_{Cr}X_{Fe}X_{Ni}L_{Cr,Fe,Ni} \\ & + X_{Fe}X_{Mo}X_{Ni}L_{Fe,Mo,Ni} + {}^{mo}G \end{aligned}$$

Here, X stands for atomic fraction and L for the interaction parameter. A ternary interaction parameter is defined as follows:[21]

$$L_{Fe,Mo,Ni} = X_{Fe}L^{Fe}_{Fe,Mo,Ni} + X_{Mo}L^{Mo}_{Fe,Mo,Ni} + X_{Ni}L^{Ni}_{Fe,Mo,Ni}$$

For the definition of the magnetic free energy ${}^{mo}G$, see the Appendix. The nonlinear equations obtained by equating the chemical potentials of the components in the two phases are solved by the Newton–Raphson iterative method.

III. THE QUATERNARY PHASE EQUILIBRIA

The α/γ equilibria in the Fe-Cr-Ni-X (X = Al, Mo, Nb, Si, Ti, V, or W) quaternary systems were computed at two typical annealing temperatures: 1100 °C and 1000 °C. These X elements are the common ferrite stabilizers present in stainless steels. Except Nb, the rest form a gamma loop with iron. More than 100 tie-lines were computed for each element at each temperature. For plotting two-dimensional isothermal sections, the concentration of one of the elements is to be kept constant. The tie-lines in general do not fall on the plane of constant concentration. The points of intersection of the phase boundary surface with the isoconcentration plane were determined by interpolation between closely spaced tie-line compositions.

The phase boundary of main interest in this work is the $(\gamma/\gamma + \alpha)$ boundary. The locations of this boundary for a constant concentration of 3 wt pct Si, Mo, or W are shown in Figures 1 and 2 for 1100 °C and 1000 °C, respectively. For reference, the computed $(\gamma/\gamma + \alpha)$ phase boundary of the Fe-Cr-Ni ternary system is also shown. The effectiveness of Si, Mo, and W as ferrite stabilizers decreases in that order. Detailed comparison of Figures 1 and 2 shows that the annealing temperature has a small but significant effect on the locations of the boundary. For Al, Nb, Ti, and V, a constant concentration of 1 wt pct was chosen. Figures 3 and 4 show the boundary locations for these elements at 1100 °C and 1000 °C, respectively.

Figures 5 and 6 are drawn at 1100 °C for a constant concentration of 8 wt pct Ni. The locations of the $(\gamma/\gamma + \alpha)$ phase boundary are shown as a function of the chromium and ferrite stabilizer contents. A similar variation was found at 1000 °C (not plotted here).

IV. THE CHROMIUM EQUIVALENTS

The information in the preceding figures can be used to derive the chromium equivalents of the ferrite stabilizers. The equivalent is evaluated as the amount of chromium substituted by 1 wt pct of the ferrite stabilizer at the $(\gamma/\gamma + \alpha)$ phase boundary. Figures 7 and 8 show the equivalents for the seven elements as a function of Ni content between 6 and 22 wt pct at 1100 °C and 1000 °C, respectively. If averaging is done between 0 and 3 wt pct, it makes a small difference to the equivalent, the maximum change being in the case of Si (an increase of about 9 pct).

Several interesting trends are noted in Figures 7 and 8. A general comparison of the two figures indicates that the annealing temperature has only a minor effect on the Cr equivalents. In all cases, the equivalents decrease with increasing Ni. Titanium is the most effective ferrite stabilizer. Its Cr equivalent at 1100 °C is 4.4 at 8 wt pct Ni and decreases to 2.8 at 22 wt pct Ni. Titanium is used in the stabilized types of austenitic steels; residual Ti left after the formation of carbides and nitrides is in solution in austenite. This can increase significantly the amount of Ni required to retain the fully austenitic state.

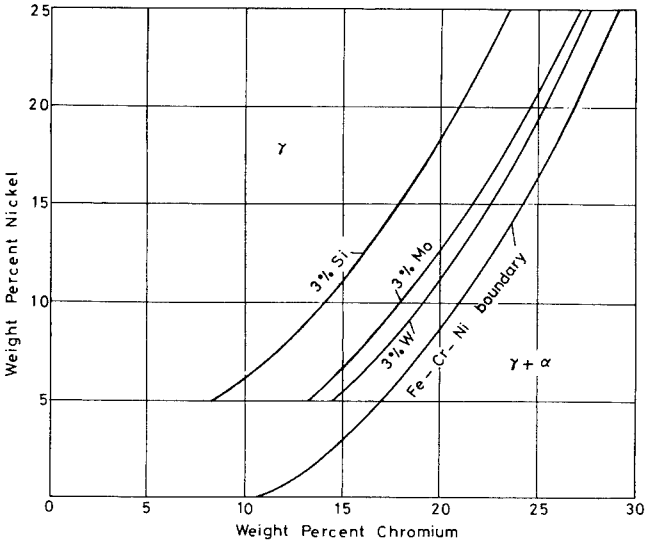


Fig. 2—The $(\gamma/\gamma + \alpha)$ phase boundary at 1000 °C for 3 wt pct addition of Mo, Si, or W to Fe-Cr-Ni alloys.

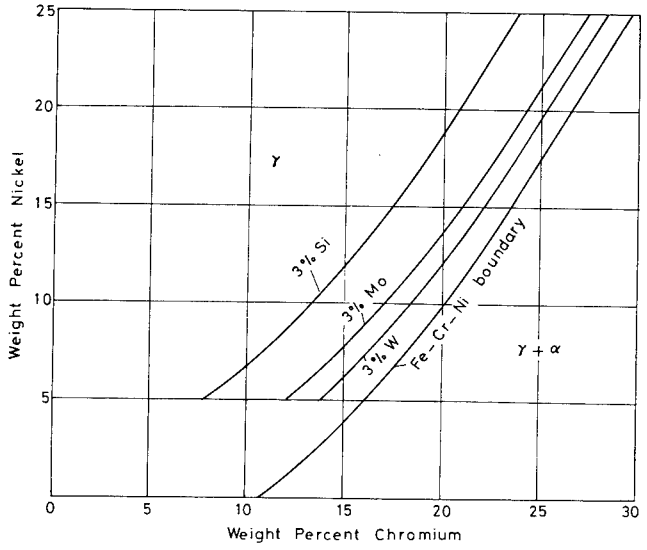


Fig. 1—The $(\gamma/\gamma + \alpha)$ phase boundary at 1100 °C for 3 wt pct addition of Mo, Si, or W to Fe-Cr-Ni alloys.

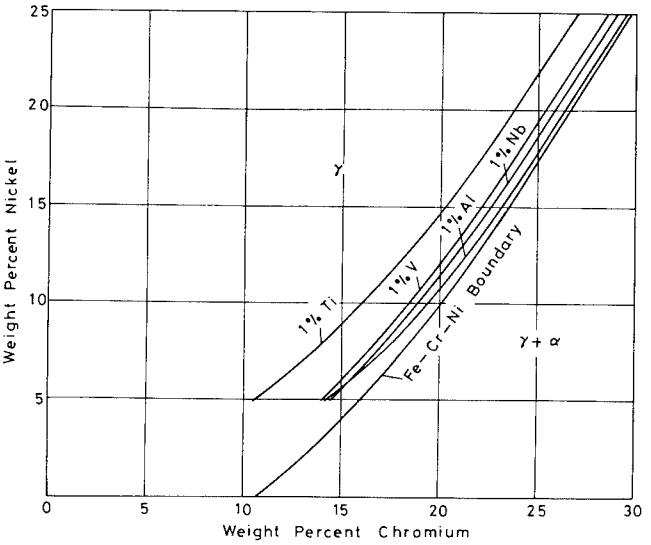


Fig. 3—The $(\gamma/\gamma + \alpha)$ phase boundary at 1100 °C for 1 wt pct addition of Al, Nb, Ti, or V to Fe-Cr-Ni alloys.

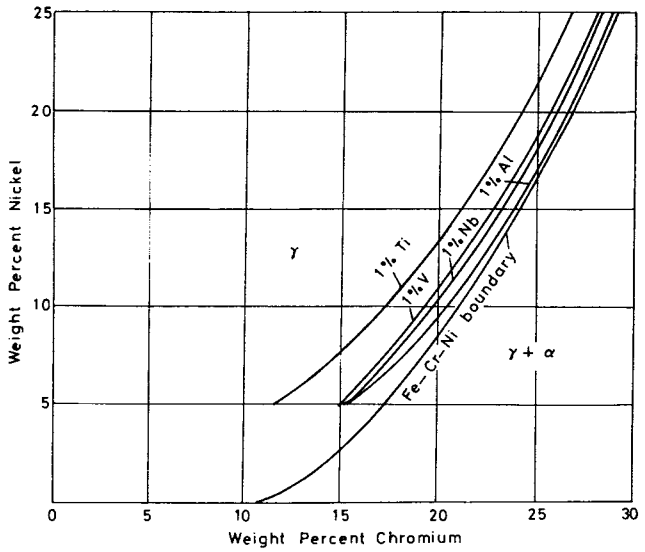


Fig. 4—The ($\gamma/\gamma + \alpha$) phase boundary at 1000 °C for 1 wt pct addition of Al, Nb, Ti, or V to Fe-Cr-Ni alloys.

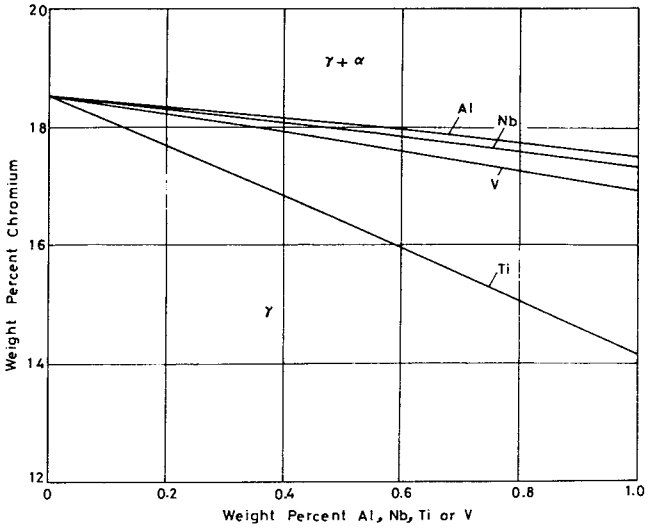


Fig. 6—The ($\gamma/\gamma + \alpha$) phase boundary at 8 wt pct Ni in Fe-Cr-Ni-X (X = Al, Nb, Ti, or V) alloys at 1100 °C.

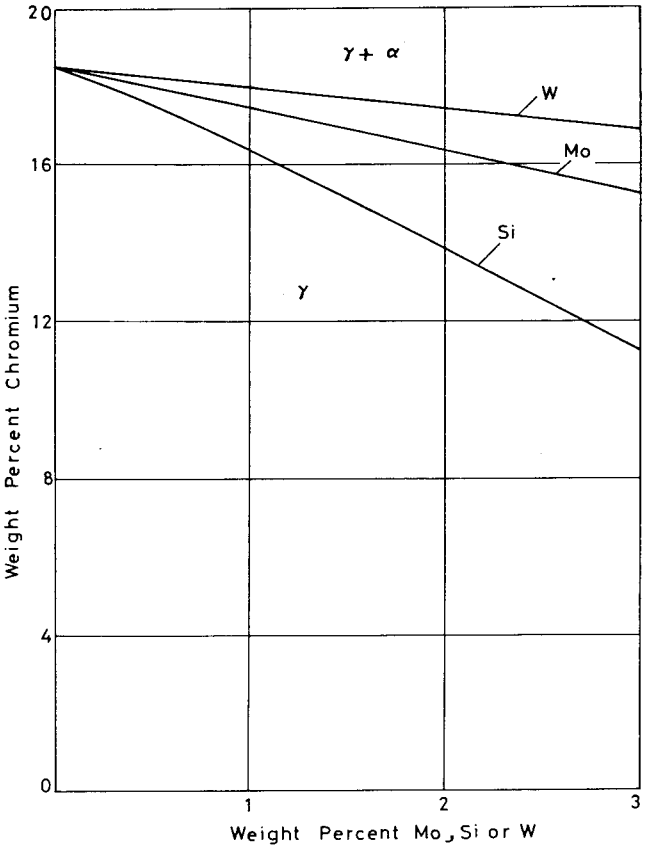


Fig. 5—The ($\gamma/\gamma + \alpha$) phase boundary at 8 wt pct Ni in Fe-Cr-Ni-X (X = Mo, Si, or W) alloys at 1100 °C.

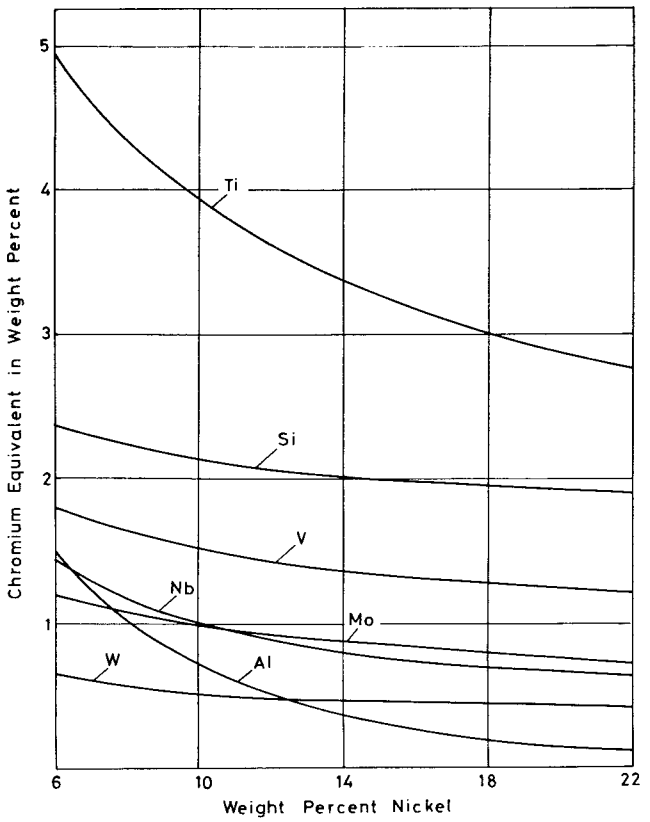


Fig. 7—Chromium equivalents of ferrite stabilizers X in Fe-Cr-Ni-X austenite annealed at 1100 °C.

Silicon is the next most effective ferrite stabilizer. Residual Si is present in many types of stainless steels. The decrease in the effectiveness with increasing Ni is not so marked here as it is with Ti. The remaining five elements, Al, Mo, Nb, V, and W, are less effective as compared to Ti and Si and have equivalents in the range of 0.6 to 1.6 at 8 wt pct Ni and 1100 °C. The order of decreasing effectiveness is V, Nb, Mo, Al, and W, both at 1100 °C and 1000 °C. This order can change at lower or higher Ni contents.

A number of articles[1,2,27–30] report on Cr equivalents from experimental results obtained under very different cooling conditions such as water quenching, air cooling, and cooling of weldments and chill castings. In most

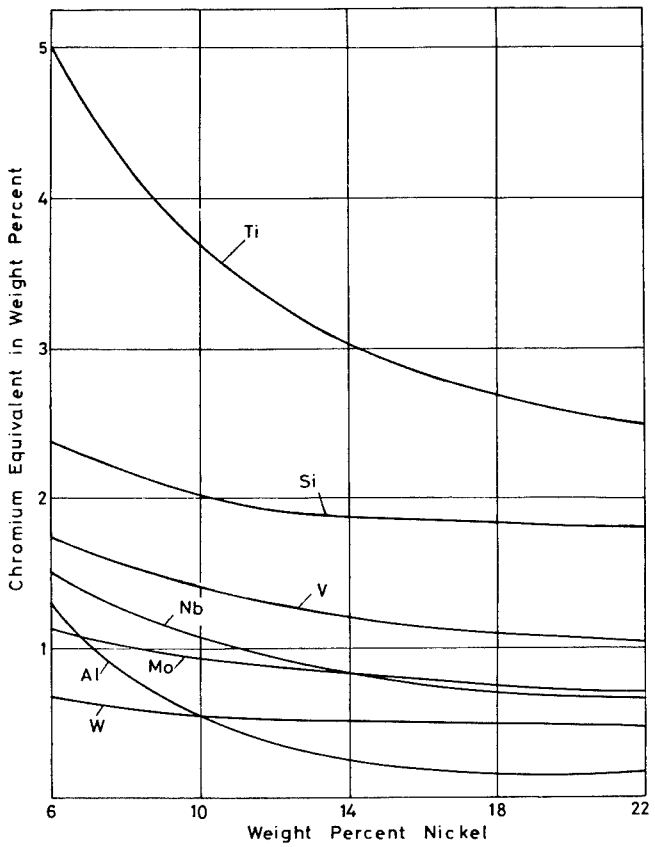


Fig. 8—Chromium equivalents of ferrite stabilizers X in Fe-Cr-Ni-X austenite annealed at 1000 °C.

cases, the effect of the basic composition of the steel (*i.e.*, of Ni and Cr contents) on the equivalents is not specifically identified. The reported values in some cases show wide variations between different researchers. The experimental ranges summarized by Solomon and Devine[31] are Al (2.48), Mo (1.0 to 1.21), Nb (0.14 to 4.0), Si (0.48 to 3.0), Ti (2.2 to 10), V (2.27), and W (0.72). In contrast to these, the computed values in this work are at specific annealing temperatures as a function of Ni content. The systematic variations of the computed equivalents with temperature and Ni content have already been illustrated.

Figure 9 compares the overall ranges of experimental and computed values of the Cr equivalents. Even though this comparison is not exactly in order, the figure shows satisfactory agreement between the two sets of data. The large variations in the experimental values of Ti and Nb point to the importance of a careful distinction between the combined and free forms of these elements, when evaluating the Cr equivalent. The experimental and computed results agree on the following conclusion. In a stabilized type of steel, the same amount of residual Nb in solution requires a smaller increase of Ni as compared to Ti to retain the fully austenitic state.

Finally, Figure 10 is a plot of the Cr equivalents in atomic percent as a function of increasing atomic number for the transition metals at a constant 8 at pct Ni (which corresponds to 8.2 to 8.5 wt pct Ni). The values for V, Nb, Mo, and W are approximately equal and are

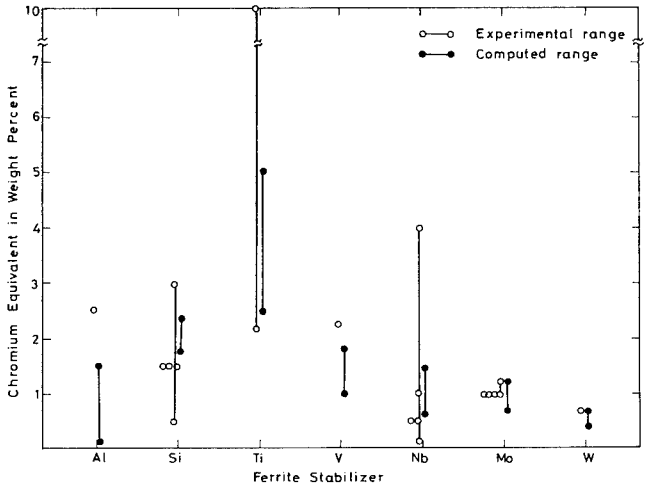


Fig. 9—Experimental and computed ranges of chromium equivalents in stainless steels.

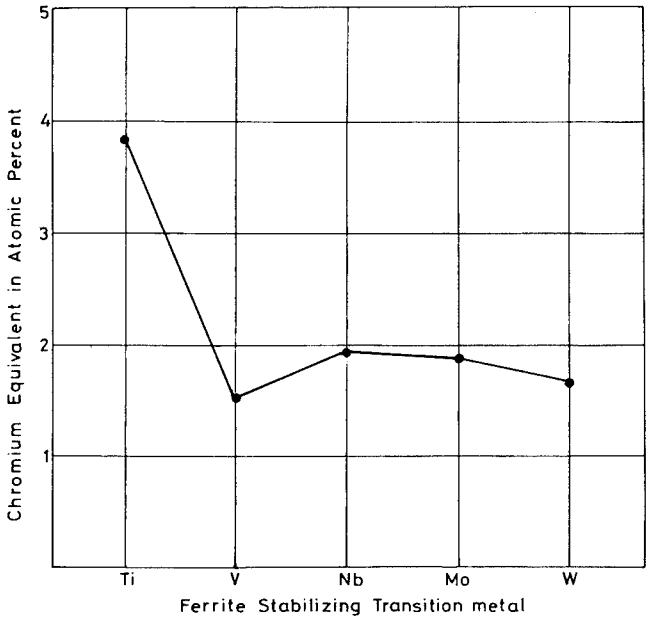


Fig. 10—The chromium equivalent in atomic percent at 1100 °C for the ferrite-stabilizing transition metals.

around 1.7. Titanium stands out in comparison, with a value of nearly 4.

No simple explanation can be given for the high effectiveness of Ti. It arises from the complex way in which the free energy functions vary with composition and temperature. One may note, however, that among the elements forming gamma loop with Fe, Ti is most effective in restricting the austenite field (or promoting ferrite formation). At 1100 °C, the maximum solubility of Ti in (γFe) is only 0.8 at. pct, whereas it is 1.2 (Al), 1.6 (Mo), 3.1 (Si), 1.3 (V), and 1.4 (W), all in at. pct.[32]

V. SUMMARY

1. Using recent thermodynamic interaction parameters, the quaternary phase equilibria in the Fe-Cr-Ni-X

systems (X = Al, Mo, Nb, Si, Ti, V, or W) have been computed at 1100 °C and 1000 °C for small additions of X.
2. From the computed results, the Cr equivalent of a ferrite stabilizer is evaluated as the amount of Cr substituted by 1 wt pct of the ferrite stabilizer at the $(\gamma/\gamma + \alpha)$ phase boundary. The Cr equivalents vary systematically with annealing temperature and Ni content. This is in contrast to the fixed values of equivalents used in the empirical diagrams on the constitution of stainless steels.
3. Titanium is the most effective ferrite stabilizer, its Cr equivalent at 1100 °C being 4.4 at 8 wt pct Ni. This decreases to 2.8 at 22 wt pct Ni. Silicon is the next most effective element.
4. The Cr equivalents of Al, Mo, Nb, V, and W are lower than those of Ti and Si and fall in the range of 0.6 to 1.6 at 8 wt pct Ni. The order of decreasing effectiveness at 8 wt pct Ni is V, Nb, Mo, Al, and W.
5. A comparison of the overall ranges of the known experimental values and those computed here shows satisfactory agreement.
6. In the stabilized types, the same amount of residual Nb present in solution in austenite requires a smaller increase of Ni as compared to Ti to retain the fully austenitic state.
7. Even if they require revision with future refinement of the thermodynamic interaction parameters, the computed Cr equivalents can be useful in applications, in the absence of detailed experimental data.

APPENDIX

Thermodynamic interaction parameters of the Fe-Cr-Ni-X systems

(All energy values in J mol^{-1})

The magnetic contribution of Gibbs energy — References

$^{mo}G = RT \ln (\beta + 1) f(\tau)$ — 4

where T_c is the Curie (or Neel) temperature in K,
β is the magnetic moment per atom in Bohr magnetons,
$\tau = T/T_c$, and $f(\tau)$ is given by,

for $\tau < 1$,

$$f(\tau) = 1 - \frac{1}{A}\left[\frac{79\,\tau^{-1}}{140\,p} + \frac{158}{497}\left(\frac{1}{p} - 1\right)\left(\frac{\tau^3}{2} + \frac{\tau^9}{45} + \frac{\tau^{15}}{200}\right)\right]$$

for $\tau > 1$:

$$f(\tau) = -\frac{1}{A}\left[\frac{\tau^{-5}}{10} + \frac{\tau^{-15}}{315} + \frac{\tau^{-25}}{1500}\right]$$

where $$A = \frac{518}{1125} + \frac{11{,}692}{15{,}975}\left(\frac{1}{p} - 1\right)$$

For bcc, $p = 0.4$, and for fcc, $p = 0.28$. Negative values of T_c and β are divided by -1 for bcc and by -3 for fcc.

Gibbs energies of pure components — 5

$^{\circ}G^{fcc} - {}^{\circ}G^{bcc}$ (Fe) $= -1462.4 + 8.282T - 1.15\,T \ln T + 6.4 \times 10^{-4}\,T^2$

$^{\circ}G^{fcc} - {}^{\circ}G^{bcc}$ (Al) $= -10{,}083 + 4.813T$

$^{\circ}G^{fcc} - {}^{\circ}G^{bcc}$ (Cr) $= 7284 + 0.163T$

$^{\circ}G^{fcc} - {}^{\circ}G^{bcc}$ (Mo) $= 15{,}200 + 0.63T$

$^{\circ}G^{fcc} - {}^{\circ}G^{bcc}$ (Nb) $= 8995.6 + 3.5564T$

$^{\circ}G^{fcc} - {}^{\circ}G^{bcc}$ (Ni) $= -8715.084 + 3.556T$

$^{\circ}G^{fcc} - {}^{\circ}G^{bcc}$ (Si) $= 4000 + 0.7T$

$^{\circ}G^{fcc} - {}^{\circ}G^{bcc}$ (Ti) $= 241.456 - 38.48985T + 7.4305\,T \ln T - 9.363565 \times 10^{-3}\,T^2 + 1.048054 \times 10^{-6}\,T^3 + 52{,}090\,T^{-1}$

$^{\circ}G^{fcc} - {}^{\circ}G^{bcc}$ (V) $= 7500 + 1.7T$

$^{\circ}G^{fcc} - {}^{\circ}G^{bcc}$ (W) $= 19{,}300 + 0.63T$

Interaction parameters for bcc (α) phase

$L_{Fe,Al} = -115{,}713 + 26.6T + (31729 - 19.42T)(X_{Fe} - X_{Al})$ — 6

$L_{Fe,Cr} = 20{,}500 - 9.68T$ — 7

$L_{Fe,Mo} = 36{,}818 - 9.14T - (362 + 5.72T)(X_{Fe} - X_{Mo})$ — 8

$L_{Fe,Nb} = -14{,}021 + 11.39T$ — 6

$L_{Fe,Ni} = -957 - 1.29T + (1789 - 1.93T)(X_{Fe} - X_{Ni})$ — 9

$L_{Fe,Si} = -155{,}636 + 35.57T - 27{,}982\,(X_{Fe} - X_{Si})$ — 6

$L_{Fe,Ti} = -38{,}242 + 8.59T - (32{,}778 - 5.95\,T)\,(X_{Fe} - X_{Ti})$ — 6

$L_{Fe,V} = -21{,}427 + 6.846T + (7345 - 1.509T)(X_{Fe} - X_{V})$ — 6

$L_{Fe,W} = 41{,}544 - 12{,}621\ (X_{Fe} - X_W)$ 10

$L_{Al,Cr} = -53{,}652 - 10T + (10{,}223 - 10T)(X_{Al} - X_{Cr})$ 6

$L_{Al,Ni} = -139{,}000$ 11

$L_{Cr,Mo} = 28{,}890 - 7.96T + (5974 - 2.43T)(X_{Cr} - X_{Mo})$ 12

$L_{Cr,Nb} = 25{,}941 + 3347\ (X_{Cr} - X_{Nb})$ 13

$L_{Cr,Ni} = 21{,}310 - 13.66T + (25{,}800 - 7.89T)(X_{Cr} - X_{Ni})$ 14

$L_{Cr,Si} = -108{,}300 + 23.43T - (48{,}447 - 8.37T)(X_{Cr} - X_{Si})$ 6

$L_{Cr,Ti} = 24{,}667 - 6.67T + 300\ (X_{Fe} - X_{Ti})$ 15

$L_{Cr,V} = -9874 - 2.6964T - (1720 + 2.5237T)(X_{Cr} - X_V)$ 16

$L_{Cr,W} = 31{,}520 - 1320\ (X_{Cr} - X_W)$ 17

$L_{Mo,Ni} = 46{,}422$ 18

$L_{Nb,Ni} = -18{,}828.09 + 21.65977T$ 19

$L_{Ni,Si} = -176{,}467 + 46.7T - (96{,}846 - 38.87T)(X_{Ni} - X_{Si})$ 6

$L_{Ni,Ti} = -119{,}717 + 43T - (44{,}536 - 12.5T)(X_{Ni} - X_{Ti})$ 6

$L_{Ni,V} = -68{,}170$

$L_{Ni,W} = 82{,}000$ 20

$L^{Cr}_{Cr,Fe,Ni} = L^{Fe}_{Cr,Fe,Ni} = L^{Ni}_{Cr,Fe,Ni} = 1390$ 21

$L_{Cr,Fe,V} = 14{,}881X_{Cr} + 17{,}968X_{Fe} - 7692X_V$ 16

$L^{Fe}_{Fe,Mo,Ni} = L^{Mo}_{Fe,Mo,Ni} = L^{Ni}_{Fe,Mo,Ni} = -35{,}743$ 22

$T_c = 1043X_{Fe} - 311.5X_{Cr} + 575X_{Ni} + X_{Fe}X_{Al}[-384.8 + 1525.1(X_{Fe} - X_{Al})]$
$+ X_{Fe}X_{Cr}[1650 - 550(X_{Fe} - X_{Cr})] + X_{Fe}X_{Mo}[335 + 526(X_{Fe} - X_{Mo})]$
$+ X_{Fe}X_{Si}[91.18 - 139.8(X_{Fe} - X_{Si}) + 231.4(X_{Fe} - X_{Si})^2 - 1640X_{Fe}X_{Ti}$
$+ X_{Fe}X_V[-110 + 3075(X_{Fe} - X_V) + 808(X_{Fe} - X_V)^2 - 2169(X_{Fe} - X_V)^3]$
$+ X_{Cr}X_{Ni}[2373 + 617(X_{Cr} - X_{Ni})]$ 6–8, 14, 24, 25

$\beta = 2.22X_{Fe} - 0.008X_{Cr} + 0.85X_{Ni} - 0.85X_{Fe}X_{Cr} - 2.26X_{Fe}X_V + 4X_{Cr}X_{Ni}$ 7, 14, 25

Interaction parameters for fcc (γ) phase

$L_{Fe,Al} = -96{,}053 + 18.41T + (31{,}654 - 19.47T)(X_{Fe} - X_{Al})$ 6

$L_{Fe,Cr} = 10{,}833 - 7.48T - 1410(X_{Fe} - X_{Cr})$ 7

$L_{Fe,Mo} = 28{,}347 - 17.69T$ 8

$L_{Fe,Nb} = -5102$ 6

$L_{Fe,Ni} = -12{,}054 + 3.72T + (11{,}082 - 4.45T)\ (X_{Fe} - X_{Ni}) - 726(X_{Fe} - X_{Ni})^2$ 9

$L_{Fe,Si} = -151{,}652 + 30.93T - 27{,}982(X_{Fe} - X_{Si})$ 6

$L_{Fe,Ti} = -26{,}665 - 1.43T - 19{,}999(X_{Fe} - X_{Ti})$ 6

$L_{Fe,V} = -15{,}260 + 1.765T$ 6

$L_{Fe,W} = 25{,}977 - 3.36T - 7259(X_{Fe} - X_W)$ 10

$L_{Al,Cr} = -63{,}019 - 5T + 11{,}815(X_{Al} - X_{Cr})$ 6

$L_{Al,Ni} = -139{,}000$ 11

$L_{Cr,Mo} = 28{,}890 - 7.96T + (5974 - 2.43T)(X_{Cr} - X_{Mo})$ 12

$L_{Cr,Nb} = 25{,}941 + 3347(X_{Cr} - X_{Nb})$ 13

$L_{Cr,Ni} = 8347 - 12.1T + (29{,}895 - 16.38T)(X_{Cr} - X_{Ni})$ 14

$L_{Cr,Si} = -104{,}600 + 23.43T - (58{,}576 - 8.37T)(X_{Cr} - X_{Si})$ 6

$L_{Cr,Ti} = 40{,}403$ 15

$L_{Cr,V} = -9874 - 2.6964T - (1720 + 2.5237T)(X_{Cr} - X_V)$ 16

$L_{Cr,W} = 31{,}520 - 1320(X_{Cr} - X_W)$ 17

$L_{Mo,Ni} = 4803.7 - 5.96T + 10{,}880(X_{Mo} - X_{Ni})$ 18

$L_{Nb,Ni} = -70{,}034.36 + 16.66039T$ 19

$L_{Ni,Si} = -176{,}467 + 46.7T - (96{,}846 - 38.87T)(X_{Ni} - X_{Si})$ 6

$L_{Ni,Ti} = -128{,}785 + 43T - (47{,}048 - 12.5T)(X_{Ni} - X_{Ti})$ 6

$L_{Ni,V} = -68{,}170$

$L_{Ni,W} = 2556 + 11.6T - 52{,}900(X_{Ni} - X_W)$ 20

$L^{Cr}_{Cr,Fe,Ni} = L^{Fe}_{Cr,Fe,Ni} = L^{Ni}_{Cr,Fe,Ni} = 1618$ 21

$L_{Fe,Mo,Ni} = (-204{,}791 + 163.93T)X_{Fe} + (11{,}555 - 55.81T)X_{Mo} + 77{,}975\ X_{Ni}$ 22

$L_{Fe,Ni,W} = -35{,}044X_{Fe} + 50{,}436X_{Ni}$ 23

$T_c = -201\ X_{Fe} - 1109X_{Cr} + 633X_{Ni} + X_{Fe}X_{Ni}[2133 - 682(X_{Fe} - X_{Ni})] - 3605X_{Cr}X_{Ni} -$
$X_{Ni}X_{Si}[6363 - 2911(X_{Ni} - X_{Si})]$ 6, 9, 14

$\beta = -2.1X_{Fe} - 2.46X_{Cr} + 0.52X_{Ni} + X_{Fe}X_{Ni}[9.55 + 7.23(X_{Fe} - X_{Ni}) + 5.93(X_{Fe} - X_{Ni})^2$
$+ 6.18(X_{Fe} - X_{Ni})^3] - 1.91X_{Cr}X_{Ni}$ 9, 14

ACKNOWLEDGMENT

The computations were carried out using the MULTITM computer program, developed with the assistance of Mr. G. Khanna.

REFERENCES

1. A.L. Schaeffler: *Met. Prog.*, 1949, vol. 56, p. 680B.
2. W.T. DeLong: *Met. Prog.*, 1960, vol. 77 (2), pp. 98-101.
3. V. Raghavan: *Metall. Mater. Trans. A*, 1995, vol. 26A, in press.
4. M. Hillert and M. Jarl: *CALPHAD*, 1978, vol. 2, pp. 227-38.
5. A.T. Dinsdale: *SGTE Data for Pure Elements*, National Physical Laboratory, Teddington, United Kingdom, 1989.
6. K.C. Hari Kumar: Ph.D. Thesis, Indian Institute of Technology, Delhi, India, 1991.
7. J.O. Andersson and B. Sundman: *CALPHAD*, 1987, vol. 11, pp. 83-92.
8. A.F. Guillermet: *Bull. Alloy Phase Diagrams*, 1982, vol. 3, pp. 359-66.
9. Z.S. Xing, D.D. Gohil, A.T. Dinsdale, and T. Chart: Report No. DMA(A)103, National Physical Laboratory, Teddington, United Kingdom, 1985.
10. P. Gustafson: *Metall. Trans. A*, 1987, vol. 18A, pp. 175-88.
11. R. Hultgren, P.D. Desai, D.T. Hawkins, M. Gleiser, and K.K. Kelly: *Selected Values of Thermodynamic Properties of Binary Alloys*, ASM, Metals Park, OH, 1973, pp. 191-95.
12. J.O. Andersson and N. Lange: *Metall. Trans. A*, 1988, vol. 19A, pp. 1385-94.
13. L. Kaufman and H. Nesor: *CALPHAD*, 1978, vol. 2, pp. 55-80.
14. T. Chart: National Physical Laboratory, Teddington, United Kingdom, unpublished research, 1985.
15. J.L. Murray: *Bull. Alloy Phase Diagrams*, 1981, vol. 2, pp. 174-81.
16. B.J. Lee and D.N. Lee: *J. Phase Equilibria*, 1992, vol. 13, pp. 349-64.
17. P. Gustafson: *Metall. Trans. A*, 1988, vol. 19A, pp. 2531-46.
18. K. Frisk: *CALPHAD*, 1990, vol. 14, pp. 311-20.
19. Z. Kejun, X. Xianzhang, and J. Zhanpeng: *J. Alloys Compounds*, 1992, vol. 179, pp. 177-85.
20. P. Gustafson, A. Gabriel, and I. Ansara: *Z. Metallkd.*, 1987, vol. 78, pp. 151-56.
21. M. Hillert and C. Qiu: *Metall. Trans. A*, 1990, vol. 21A, pp. 1673-80.
22. K. Frisk: *Metall. Trans. A*, 1992, vol. 23A, pp. 639-49.
23. A.F. Guillermet and L. Ostlund: *Metall. Trans. A*, 1986, vol. 17A, pp. 1809-23.
24. B.J. Lee, S.K. Lee, and D.N. Lee: *CALPHAD*, 1987, vol. 11, pp. 253-70.
25. J.O. Andersson: *CALPHAD*, 1983, vol. 7, pp. 305-15.
26. J.F. Smith, O.N. Carlson, and P.G. Nash: *Bull. Alloy Phase Diagrams*, 1982, vol. 3, pp. 342-48.
27. L. Pryce and K.W. Andrews: *J. Iron Steel Inst.*, 1960, vol. 195, pp. 415-17.
28. F.C. Hull: *Weld. J.*, 1973, vol. 52 (5), pp. 193S-203S.
29. C.J. Long and W.T. DeLong: *Weld. J.*, 1973, vol. 52 (7), pp. 281S-297S.
30. E.A. Schoefer: *Weld. J.*, 1974, vol. 53 (1), pp. 10S-12S.
31. H.D. Solomon and T.W. Devine, Jr.: *Duplex Stainless Steels*, ASM, Metals Park, OH, 1983, pp. 693-756.
32. *Binary Alloy Phase Diagrams*, T.B. Massalski, ed., ASM INTERNATIONAL, Materials Park, OH, 1990.

Diffusion-Controlled Growth in Ternary Systems

J.P. BOURNE, C. ATKINSON, and R.C. REED

Diffusion-controlled growth of particles, dendrites, and plates in infinite media is examined for ternary systems. The growth kinetics associated with planar, cylindrical, and spherical particles are shown to be limiting cases of a more complete analysis (also presented) for shape-preserving growth. The theory is applied to the growth of allotriomorphic ferrite from austenite in ternary Fe-C-X steels, where X represents a substitutional alloying element. Numerical results are given, the analysis relying on the ability to predict multicomponent phase equilibria. The work represents an attempt at coupling together thermodynamic and kinetic models for the diffusion-controlled phase transformations that occur in steels.

I. INTRODUCTION

IN the past 30 years or so, there has been a tremendous international effort concerned with the collection and assessment of thermodynamic data particularly for metals and alloys. The spirit of the work is perhaps best captured by the CALPHAD (Calculation of Phase Diagrams) meetings and by the journal of the same name.[1] Such work is near fruition, since there are now available several software systems capable of estimating the phase diagram as a function of pressure temperature, and the combined effect of numerous alloying elements, given a starting set of possible phases.[2,3] Of course, such data banks are best regarded as convenient methods of storing and retrieving the assessed thermodynamic data. Yet at the same time, they employ rigorous thermodynamic expressions and numerical methods for the minimization of the Gibbs energy of the system so that the equilibrium state can be calculated. The data banks allow interpolation between the available thermodynamic data and extrapolation from binary systems to multicomponent systems to be achieved with more confidence than would otherwise be possible.

In the authors' view, the situation has reached the point where, for systems for which the thermodynamic properties are rather well established, one needs to ask how these data banks might be most usefully employed in the future. Of course, the data banks are now being used widely, as a research tool for the purpose of alloy design. However, many of the routes used for processing metals (*e.g.*, rolling, casting, and welding) leave the material in a highly metastable state. Moreover, unstable microstructural configurations (*e.g.*, ultrafine grains, nonequilibrium solute concentrations, *etc.*) are often deliberately utilized because of the advantageous properties that can be attained. Of course, the thermodynamic data banks cannot be used for the estimation of microstructure in such situations; there is a need to design kinetic models that make use of the thermodynamic data banks.

It is possible that, in the future, kinetic models might be developed, which enable microstructures to be estimated as a function of composition and processing history, to within useful accuracy. The theory of phase transformations in metals and alloys is likely to be at the heart of such models.[4] The role of the thermodynamic data banks will then be to define the equilibrium state and the kinetic models will describe the route between equilibrium states. With such validated models, it might be possible to search for alloys with improved and novel properties in a more fundamental and systematic fashion than has been possible in the past.

With such ideals in mind, the purpose of this article is to consider the diffusion-controlled growth of precipitates,[5] with a view to establishing kinetic models for steels that can be readily coupled to existing thermodynamic theory. For the growth of allotriomorphic ferrite from austenite, the experimental evidence[6] suggests that the shape of the growing phase is most realistically modeled as an oblate ellipsoid of revolution,[7] an aspect ratio of approximately 3 being appropriate.[6] Atkinson *et al.*[8] have reported a model for the diffusion-controlled growth of precipitates with such a shape in binary Fe-C steels, but the effect of diffusion of substitutional alloying elements has never been considered previously. This extension will be dealt with in the present work.

It should be recognized that the theory described here is applicable to all systems in which the diffusion-controlled growth of precipitates occurs and, as such, is not solely restricted to steels. The authors therefore hope that their analysis will be of particular interest to those readers who are concerned with other systems.

II. BACKGROUND

Diffusion-controlled precipitate growth of particles, dendrites, and plates has been the subject of much discussion over the past 30 years. The models for radially symmetric particle growth in binary systems were originally developed by Zener,[9] Frank,[10] and Ham.[11,12] In each case, constant diffusion coefficients were assumed. Horvay and Cahn[13] subsequently generalized the analysis to include ellipsoidal and dendritic growth using a technique proposed by Ivantsov.[14] Again, the work was based on constant diffusion coefficients. As an extension to that work, Trivedi and Pound[15] and Atkinson[16] considered the ellipsoidal and dendritic growth problems for

J.P. BOURNE, Research Assistant, and R.C. REED, Lecturer, are with the Department of Materials, and C. ATKINSON, Professor, is with the Department of Mathematics, Imperial College of Science, Technology, and Medicine, London SW7 2RH, United Kingdom.

Manuscript submitted January 12, 1994.

situations in which the diffusion coefficients were concentration dependent. In each case, a numerical procedure was formulated. In an associated article, Atkinson[17] applied perturbation theory to tackle the ellipsoidal and dendritic growth problem for a quite general class of diffusion coefficients. Both slow and fast particle growth was addressed. More recently, Enomoto and Atkinson[18] have developed a numerical scheme based on Kolodner's free boundary formulation[19] to analyze planar and spherical growth in a finite matrix.

In the present work, we intend to collate and extend the analysis of ellipsoidal and dendritic particle growth to ternary systems (the theory we outline, however, is true for N component systems). The growth kinetics associated with planar, cylindrical, and spherical particles are shown to be special limiting cases. Naturally, this adds to the complexity of the growth behavior, although it is shown that many of the patterns observed in binary systems carry over for the ternary analysis. In this respect, we believe that the current work will complement the numerical approach of multicomponent diffusion described by Kirkaldy and co-workers[20–23] and Coates.[24,25,26]

The outline of this article is as follows. Section III summarizes the conditions and assumptions of precipitate particle growth. In Section IV, the ellipsoidal growth problem is solved based on an eigenvalue analysis. The problem of dendritic growth is then addressed. Section VI outlines the theory used in the phase diagram calculations. A selection of numerical results is given in Section VII. An appendix is also included in which asymptotic expressions are noted for limiting cases of the above analysis. These are seen to be direct analogues of the binary analysis.

III. ANALYSIS

Our analysis begins with a brief summary of the usual assumptions made in precipitate particle growth problems. Later, these conditions will be applied in turn to ellipsoidal and dendritic particle growth.

Consider then a particle of initial zero size, growing *via* diffusion in a matrix that is assumed to be of infinite extent. Thus, within the matrix phase of the alloy, the composition of each component C_i will be governed by solutions to the diffusion equation

$$\frac{\partial C_i}{\partial t} = \nabla \cdot (D_{ij} \nabla C_j) \quad (i, j = 1, 2; \text{ sum over } j) \qquad [1]$$

where the variables D_{ij} denote the diffusion coefficients. Also, it will be assumed that each component of the alloy will have constant composition C_i^P within the particle. Similarly, just outside the particle-matrix interface each component will have constant composition denoted by C_i^M. Furthermore, the initial concentration of each component and at large distances in the matrix phase will be of constant composition C_i^∞. A typical concentration profile is shown schematically in Figure 1. Flux of matter at the particle-matrix boundary will determine the growth rate of the particle, and for shape-preserving growth, the appropriate condition will take the form

$$(C_i^M - C_i^P) N \cdot \frac{dN}{dt} = J_i N \quad (i = 1, 2) \qquad [2]$$

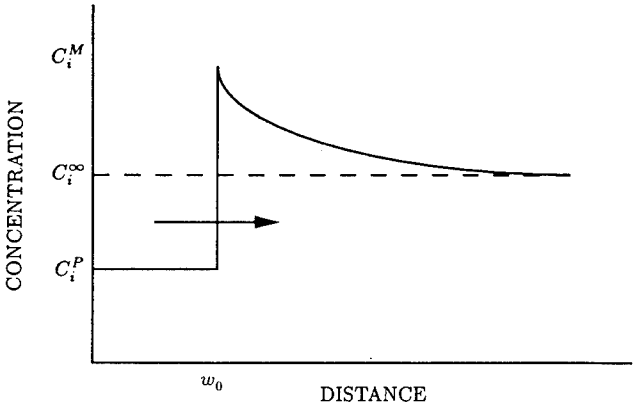


Fig. 1 — Schematic illustration of an advancing interface showing concentration profiles and interfacial concentrations associated with the growing particle and matrix.

at the surface. Here $N = (N_1, N_2, N_3)$ defines the outward normal to the surface and $J_i = -\sum_{j=1}^{2} D_{ij} \nabla C_j$. The reader should also note that throughout the analysis, it is assumed implicitly that the densities of the matrix and particle are equal, *i.e.*, that the molar volumes of the two phases are identical.

IV. ELLIPSOIDAL GROWTH

We begin with the growth kinetics associated with an expanding ellipse, initially of zero size, and introduce the variable w defined implicitly *via*

$$\frac{x^2}{w + a_1} + \frac{y^2}{w + a_2} + \frac{z^2}{w + a_3} = 4t \qquad [3]$$

The surface parameters a_i ($i = 1, 2, 3$) are constants, different combinations of which can be associated with limiting cases of the ellipsoidal growth, *i.e.*, planar, cylindrical, and spherical particle growth (Table I).

The boundary of the particle is designated by the expanding ellipsoidal shape specified by Eq. [3] with $w = w_0$, where w_0 is to be determined. Substituting Eq. [3] into Eq. [1] leads to the following pair of coupled ordinary differential equations:

$$\frac{dC_i}{dw} + \frac{d}{dw}\left(D_{ij}\frac{dC_j}{dw}\right) + \frac{1}{2}\left(\sum_{p=1}^{3}\frac{1}{w + a_p}\right) D_{ij}\frac{dC_j}{dw} = 0 \quad (i, j = 1, 2; \text{ sum over } j) \qquad [4]$$

Here, it has been assumed that each component C_i is a function of w alone and that w_0 defines the location of the expanding ellipse. The ellipsoidal growth problem

Table I. Surface Parameters

	a_1	a_2	a_3
Planar	0	∞	∞
Cylindrical	0	0	∞
Spherical	0	0	0

thus amounts to solving Eq. [4] subject to the following boundary conditions:

$$C_i = C_i^M \quad \text{when } w = w_0$$
$$C_i = C_i^\infty \quad \text{as } w \to \infty \qquad [5]$$

In addition, one can show that the flux Eq. [2] at the particle-matrix interface reduces to

$$D_{ij}\left(\frac{dC_j}{dw}\right)_{w=w_0} = C_i^P - C_i^M, \quad (i, j = 1, 2; \text{ sum over } j) \qquad [6]$$

The value of $w = w_0$ that specifies the boundary of the growing ellipsoidal particle is thus to be determined by solving Eqs. [4] through [6] simultaneously. In seeking exact solutions to the above problem, it will be necessary to assume constant diffusion coefficients. With this assumption and regarding Eq. [4] as an eigenvalue problem, define

$$P_i = D_{ij}\frac{dC_j}{dw} \quad (i, j = 1, 2; \text{ sum over } j) \qquad [7]$$

and seek solutions to Eq. [4] in the form

$$P_i = \frac{A_i \exp(-\lambda w)}{\sqrt{(w + a_1)(w + a_2)(w + a_3)}} \qquad [8]$$

The coefficients A_i and eigenvalues λ are determined from

$$(D_{ij}^{-1} - \lambda\delta_{ij})A_j = 0 \qquad [9]$$

with $D_{ik}^{-1}D_{kj} = \delta_{ij}$, where δ_{ij} is the Kronecker delta $\delta_{ij} = 1$, $i = j$; $\delta_{ij} = 0$, $i \neq j$. Nontrivial solutions exist provided

$$|D_{ij}^{-1} - \lambda\delta_{ij}| = 0 \qquad [10]$$

(These and subsequent procedures are equally applicable to multicomponent systems $i, j = 1, \ldots, N$. However, the details are carried through only or the ternary case.) Expanding the determinant and solving Eq. [10] establishes the eigenvalues as

$$\lambda_1, \lambda_2 = \frac{(D_{11} + D_{22}) \mp \sqrt{(D_{11} - D_{22})^2 + 4D_{12}D_{21}}}{2(D_{11}D_{22} - D_{12}D_{21})} \qquad [11]$$

where the plus and minus signs preceeding the radical are associated with λ_2 and λ_1, respectively. (This is also consistent with solutions to Eq. [4] for situations when $D_{12} = 0 = D_{21}$.) It should also be noted that implicit in the statement is that $D_{11} > D_{22}$. This convention will be assumed throughout the analysis. A suitable choice for the associated eigenvectors is $A^{(1)} = (A_1^{(1)}, A_2^{(1)})^T$ and $A^{(2)} = (A_1^{(2)}, A_2^{(2)})^T$, where

$$A_1^{(1)} = A$$
$$A_2^{(1)} = \frac{2D_{21}A}{(D_{11} - D_{22}) + \sqrt{(D_{11} - D_{22})^2 + 4D_{12}D_{21}}}$$
$$A_1^{(2)} = \frac{2D_{12}B}{(D_{22} - D_{11}) - \sqrt{(D_{11} - D_{22})^2 + 4D_{12}D_{21}}}$$
$$A_2^{(2)} = B \qquad [12]$$

and where A and B are arbitrary constants to be determined. Accordingly,

$$P_i = A_i^{(j)}Q_j(w) \quad (\text{summing over } j) \qquad [13]$$

where

$$Q_j(w) = \frac{\exp(-\lambda_j w)}{\sqrt{(w + a_1)(w + a_2)(w + a_3)}} \qquad [14]$$

Inverting Eq. [7] and applying the boundary conditions in Eq. [5] determines the constants A and B and establishes the concentration profiles within the matrix as

$$C_1(w) = \frac{B_{11}[B_{22}(C_1^\infty - C_1^M) - B_{12}(C_2^\infty - C_2^M)]}{(B_{11}B_{22} - B_{12}B_{21})}\frac{\int_{w_0}^{w} Q_1(s)ds}{\int_{w_0}^{\infty} Q_1(s)ds}$$
$$+ \frac{B_{12}[-B_{21}(C_1^\infty - C_1^M) + B_{11}(C_2^\infty - C_2^M)]}{(B_{11}B_{22} - B_{12}B_{21})}\frac{\int_{w_0}^{w} Q_2(s)ds}{\int_{w_0}^{\infty} Q_2(s)ds} + C_1^M$$
$$C_2(w) = \frac{B_{21}[B_{22}(C_1^\infty - C_1^M) - B_{12}(C_2^\infty - C_2^M)]}{(B_{11}B_{22} - B_{12}B_{21})}\frac{\int_{w_0}^{w} Q_1(s)ds}{\int_{w_0}^{\infty} Q_1(s)ds}$$
$$+ \frac{B_{22}[-B_{21}(C_1^\infty - C_1^M) + B_{11}(C_2^\infty - C_2^M)]}{(B_{11}B_{22} - B_{12}B_{21})}\frac{\int_{w_0}^{w} Q_2(s)ds}{\int_{w_0}^{\infty} Q_2(s)ds} + C_2^M \qquad [15]$$

Here,

$$B_{11} = D_{22} - \frac{2D_{12}D_{21}}{(D_{11} - D_{22}) + \sqrt{(D_{11} - D_{22})^2 + 4D_{12}D_{21}}}$$
$$B_{12} = \frac{2D_{22}D_{12}}{(D_{22} - D_{11}) - \sqrt{(D_{11} - D_{22})^2 + 4D_{12}D_{21}}} - D_{12}$$
$$B_{21} = \frac{2D_{11}D_{21}}{(D_{11} - D_{22}) + \sqrt{(D_{11} - D_{22})^2 + 4D_{12}D_{21}}} - D_{21}$$
$$B_{22} = D_{11} - \frac{2D_{12}D_{21}}{(D_{22} - D_{11}) - \sqrt{(D_{11} - D_{22})^2 + 4D_{12}D_{21}}} \qquad [16]$$

Finally, it remains to determine the position of the moving boundary w_0. Applying the transformed flux Eq. [6], one can show that

$$(D_{11}B_{11} + D_{12}B_{21})E_1Q_1(w_0) + (D_{11}B_{12} + D_{12}B_{22})E_2Q_2(w_0) = C_1^P - C_1^M$$
$$(D_{21}B_{11} + D_{22}B_{21})E_1Q_1(w_0) + (D_{21}B_{12} + D_{22}B_{22})E_2Q_2(w_0) = C_2^P - C_2^M \qquad [17]$$

where

$$E_1 = \frac{[B_{22}(C_1^\infty - C_1^M) - B_{12}(C_2^\infty - C_2^M)]}{(B_{11}B_{22} - B_{12}B_{21})} \frac{1}{\int_{w_0}^{\infty} Q_1(s)ds}$$

$$E_2 = \frac{[-B_{21}(C_1^\infty - C_1^M) + B_{11}(C_2^\infty - C_2^M)]}{(B_{11}B_{22} - B_{12}B_{21})} \frac{1}{\int_{w_0}^{\infty} Q_2(s)ds} \quad [18]$$

Recall that B_{11}, B_{12}, B_{21}, and B_{22} were defined in Eq. [16]. For Q_1 and Q_2, see Eq. [14]. Of the four interface parameters C_1^P, C_2^P, C_1^M, and C_2^M, only one is independent, *e. g.*, C_1^P. The remaining three compositions are determined from the phase diagram boundaries and endpoints of the tie-lines. The system of Eq. [17] can thus be regarded as two equations in two unknowns, the solution to which will establish values for w_0 and C_1^P, the growth rate parameter and particle composition, respectively. A selection of numerical examples outlining this procedure will be given in Section VII. Typical experimental data will be used.

V. DENDRITIC GROWTH

The analysis for dendritic growth, in which the particles are either rodlike (ellipsoidal paraboloids) or platelike (parabolic cylinders), will be described here. It is assumed that the particles translate with uniform speed V in their lengthwise direction Z and that diffusion of each component in the matrix phase is governed by

$$\frac{\partial C_i}{\partial t} = \nabla \cdot (D_{ij} \nabla C_j) \quad (i, j = 1, 2; \text{ sum over } j) \quad [19]$$

In the above (X, Y, Z) refers to a fixed cartesian coordinate system. Consider now a moving coordinate system (x, y, z) translating with the body, where

$$x = \frac{pX}{R}, \qquad y = \frac{pY}{R},$$

$$z = \frac{p}{R}(Z - Vt), \qquad \text{and } p = \frac{VR}{2} \quad [20]$$

Here, R denotes the radius of curvature at the tip of the dendrite. Note that the model here will suffer from the usual drawbacks of the classical models of a growing dendrite in that only the product of the velocity and the tip radius of curvature will be determined in the solution. For the growth of an ellipsoidal paraboloid, we write

$$\frac{x^2}{w} + \frac{y^2}{w + a_4} = w - 2z \quad [21]$$

in which $w = w_0 = p$ defines the moving interface and where the surface parameter a_4 is assumed to be positive. (The limits $a_4 = 0$ and $a_4 \to \infty$ correspond to a circular paraboloid and a parabolic platelet, respectively.) With this change of variable, Eq. [19] becomes

$$\frac{dC_i}{dw} + \frac{d}{dw}\left(D_{ij}\frac{dC_i}{dw}\right) + \frac{1}{2}\left(\frac{1}{w} + \frac{1}{w + a_4}\right)D_{ij}\frac{dC_j}{dw} = 0$$

$$(i, j = 1, 2; \text{ sum over } j) \quad [22]$$

and where, again, it has been assumed that each component C_i is a function of w alone. The following boundary conditions also obtain:

$$C_i = C_i^M \quad \text{when } w = w_0$$

$$C_i = C_i^\infty \quad \text{as } w \to \infty \quad [23]$$

In addition, C_i^P will denote the constant composition of each component within the particle. The flux condition at the interface as similarly treated, and as before, it is found that

$$D_{ij}\left(\frac{dC_j}{dw}\right)_{w=w_0} = C_i^P - C_i^M$$

$$(i, j = 1, 2; \text{ sum over } j) \quad [24]$$

determines w_0. The analysis for the growing dendrite is identical to that for the ellipsoidal growth. Indeed, the form of the concentration profiles [15] is the same, except here, Eq. [14] should be replaced by

$$Q_j(w) = \frac{\exp(-\lambda_j w)}{\sqrt{w(w + a_4)}} \quad (j = 1, 2) \quad [25]$$

(λ_1 and λ_2 are again defined by Eq. [11]). Likewise, the position of the moving boundary w_0 is to be determined from Eq. [17], provided the above forms for Q_1 and Q_2 are used.

VI. PHASE DIAGRAM CALCULATION

The results that are presented in Section VII depend crucially upon the ability to calculate multicomponent, multiphase equilibria. As was discussed in Section I, there exists currently a desire to couple together thermodynamic and kinetic calculations so that microstructures can be estimated as a function of processing history. There is evidence that this is being addressed by a number of researchers,[27,28,29] but the task is immense and there remains much to do.

In the present work, the authors have employed Sundman and Ågren's regular solution model for phases with several components and sublattices.[30] This represents a generalization of the Hillert–Staffansson subregular solution model.[11] The Gibbs energy per mole of structural units is given by[30]

$$G_m = G_m^{\text{ref}} - TS_m^{\text{ideal}} + {}^E G_m$$

$$= \sum_{I0} P_{I0}(Y) \cdot {}^\circ G_{I0} + \text{RT} \sum_s a^s \sum_i y_i^s \ln(y_i^s) + \sum_{Z>0} \sum_{IZ} P_{IZ}(Y) \cdot L_{IZ} \quad [26]$$

where G_m^{ref} represents the reference for the molar Gibbs energy, S_m^{ideal} represents the ideal entropy of mixing, T is the temperature, and ${}^E G_m$ represents a molar excess Gibbs energy. The term y_i^s represents the site fraction of

component i on site s, and a^s represents the number of sites on the lattice s per mole of formula units of the phase ϕ. The term G_{I0} represents the Gibbs energy of compound defined by I, L_{IZ} is an interaction parameter, and the terms $P_{I0}(Y)$ and $P_{IZ}(Y)$ represent products of site fractions. For an exact definition of the terms in equation [26], and for details of how to calculate G_m from the composition matrix n_i^ϕ, readers are directed toward Sundman and Ågren's article,[30] which the present authors have found particularly useful. Assessed thermodynamic data for this model can be found readily in the literature.[32–36] The minimization of the integral molar Gibbs energy, subject to the linear constraints imposed by the condition of conservation of mass in the system, represents an optimization problem, which can be solved with standard algorithms that are available in the Numerical Algorithms Group (NAG) library.[37] This enables the phase diagram to be constructed. An example is given in Figure 2; this represents an isopleth for the ternary Fe-C-Mn system at 750 °C, with the ferrite, ferrite + austenite, and austenite phase fields labeled. This particular phase diagram is used throughout the work, in order to make the theory appear less abstract and to emphasize that the analysis described here is capable of being applied to real systems. However, since much of the theory is couched in terms of dimensionless parameters (such as the Ω's of Eq. [35]), it should be recognized that the theory described here is applicable to any ternary phase diagram.

VII. RESULTS

Illustrations to the theory developed in the previous sections will be described here. We focus attention on the growth of ferrite in the Fe-C-X system at 750 °C with manganese taken to be the substitutional alloying element X. Note that the subscripts 1 and 2 appearing in the earlier sections will now correspond to carbon and manganese, respectively. In particular, we consider the diffusional growth of ferrite in two alloys, of mean composition (C_1^∞, C_2^∞) = (0.015, 0.02) (Alloy 1) and (0.0025, 0.01) (Alloy 2), respectively. From an examination of Figure 2 and recognizing Coates geometrical construction[24,25,26] for the regimes in which the partitioning local equilibrium (PLE) on the nonpartitioning local equilibrium (NPLE) modes of growth are expected to be operative growth of ferrite in alloys 1 and 2 are expected by the PLE and NPLE modes, respectively.

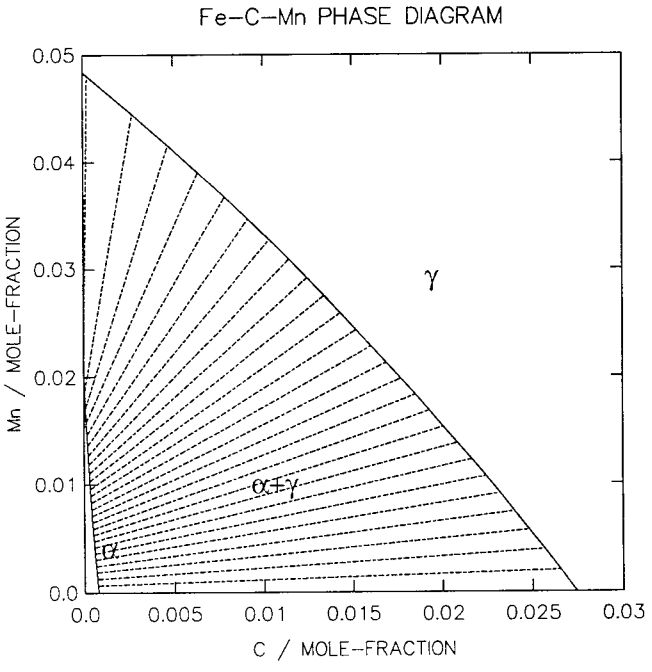


Fig. 2—Ternary isopleth for the Fe-C-Mn system at 750 °C, showing the positions of the ferrite (α), austenite (γ), and ferrite + austenite ($\alpha + \gamma$) phase fields.

Limiting cases of the fuller analysis presented will now be addressed in turn.

A. $D_{12} = D_{21} = 0$

In an attempt to make the solution of the flux equations tractable, we first address situations in which ternary diffusion interaction can be ignored, in effect deleting the off-diagonal diffusion coefficients. The flux equations become uncoupled, and the ternary analysis for different geometries is a straightforward extension of the binary analysis, as detailed by Coates.[24,25,26] For reference purposes, the concentration distributions of each component in the matrix phase of the alloy together with the corresponding interface mass conservation conditions are noted below. Each set of results has been obtained using appropriate modifications of Eqs. [15] through [18].

1. *Planar growth*

The concentration profiles within the matrix phase are found is

$$C_i(w) = C_i^\infty + (C_i^M - C_i^\infty)\frac{\text{erfc}\,(\sqrt{w/D_{ii}})}{\text{erfc}\,(\sqrt{w_0/D_{ii}})} \quad (i = 1, 2; \text{ no summation}) \qquad [27]$$

Here, $x^2 = 4\omega t$. Accompanying Eq. [27] are the flux equations

$$\sqrt{\pi}\,\mu_1 \exp(\mu_1^2)\,\text{erfc}\,(\mu_1) = \frac{C_1^M - C_1^\infty}{C_1^M - C_1^P}$$

and

$$\sqrt{\pi}\,\mu_2 \exp(\mu_2^2)\,\text{erfc}\,(\mu_2) = \frac{C_2^M - C_2^\infty}{C_2^M - C_2^P} \qquad [28]$$

where $\mu_1 = \sqrt{w_0/D_{11}}$ and $\mu_2 = \sqrt{w_0/D_{22}}$. Note that

$$\text{erfc}\,(x) = \frac{2}{\sqrt{\pi}}\int_x^\infty \exp(-t^2)dt \qquad [29]$$

denotes the complementary error function and that w_0 refers to the particle interface position and is to be determined.

2. *Cylindrical growth*

The analogue of Eq. [27] for cylindrical growth is

$$C_i(w) = C_i^M + (C_i^\infty - C_i^M)\frac{\int_{w_0}^{w} s^{-1}\exp(-s/D_{ii})ds}{\int_{w_0}^{\infty} s^{-1}\exp(-s/D_{ii})ds}$$

($i = 1, 2$; no summation) [30]

where $x^2 + y^2 = 4\omega t$. The flux equations are similarly obtained as

$$\mu_1 \exp(\mu_1)E_1(\mu_1) = \frac{C_1^M - C_1^\infty}{C_1^M - C_1^P} \quad [31a]$$

and

$$\mu_2 \exp(\mu_2)E_1(\mu_2) = \frac{C_2^M - C_2^\infty}{C_2^M - C_2^P} \quad [31b]$$

where $\mu_1 = w_0/D_{11}$ and $\mu_2 = w_0/D_{22}$. Note that

$$E_1(x) = \int_x^\infty \frac{\exp(-t)}{t}dt, \quad x > 0 \quad [32]$$

defines the exponential integral.

3. *Spherical growth*

Here, the concentration profiles are

$$C_i(w) = C_i^\infty + (C_i^M - C_i^\infty)\cdot\left[\frac{\sqrt{D_{ii}/w}\exp(-w/D_{ii}) - \sqrt{\pi}\,\mathrm{erfc}\,(\sqrt{w/D_{ii}})}{\sqrt{D_{ii}/w_0}\exp(-w_0/D_{ii}) - \sqrt{\pi}\,\mathrm{erfc}\,(\sqrt{w_0/D_{ii}})}\right] \quad [33]$$

Again, $i = 1, 2$, and note that no summation is assumed in Eq. [33]. Also, $x^2 + y^2 + z^2 = 4\omega t$, erfc (x) denotes the complementary error function (Eq. [29]), and w_0 defines the interface position of the particle to be determined *via* the simultaneous solution of the flux equations

$$2\mu_1^3\exp(\mu_1^2)\left[\frac{\exp(-\mu_1^2)}{\mu_1} - \sqrt{\pi}\,\mathrm{erfc}\,(\mu_1)\right] = \frac{C_1^M - C_1^\infty}{C_1^M - C_1^P} \quad [34a]$$

and

$$2\mu_2^3\exp(\mu_2^2)\left[\frac{\exp(-\mu_2^2)}{\mu_2} - \sqrt{\pi}\,\mathrm{erfc}\,(\mu_2)\right] = \frac{C_2^M - C_2^\infty}{C_2^M - C_2^P} \quad [34b]$$

in which $\mu_1 = \sqrt{w_0/D_{11}}$ and $\mu_2 = \sqrt{w_0/D_{22}}$

A numerical scheme for solving the flux equations will now be outlined. A geometric construction employing interpolation is used to partition the phase diagram into regions in which the fractional supersaturations Ω_1 and Ω_2 vary between zero and one. Figures 3 and 4 illustrate this. Note that

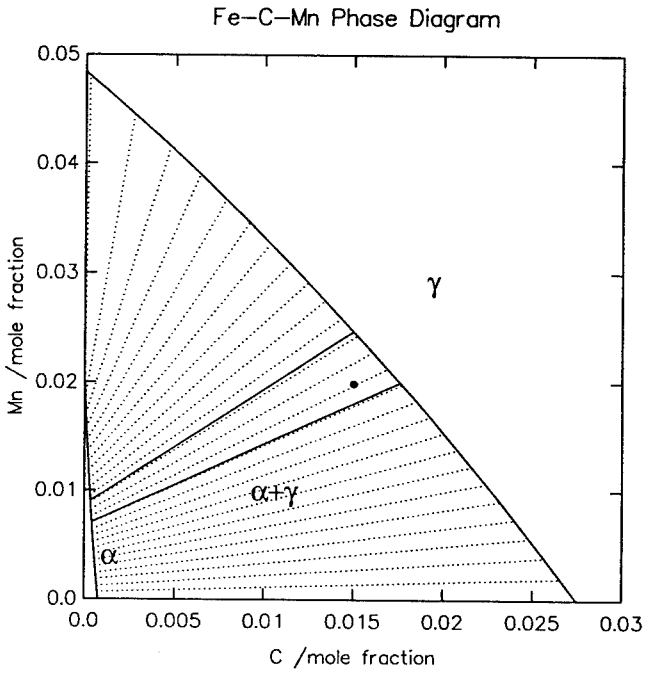


Fig. 3—Ternary isopleth for the Fe-C-Mn system at 750 °C. Marked is the mean composition of alloy 1 (0.015, 0.02), as well as the regime within the two-phase field for which $0 \leq \Omega_i \leq 1$, for $i = 1, 2$. Alloy 1 lies within the PLE regime.[24,25,26]

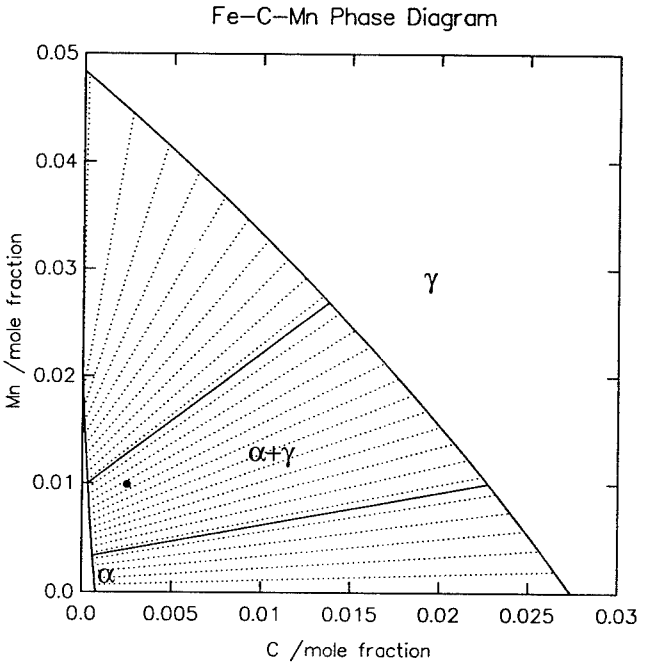


Fig. 4—Ternary isopleth for the Fe-C-Mn system at 750 °C. Marked is the mean composition of alloy 2 (0.0025, 0.01), as well as the regime within the two-phase field for which $0 \leq \Omega_i \leq 1$, for $i = 1, 2$. Alloy 2 lies within the NPLE regime.[24,25,26]

$$\Omega_1 = (C_1^M - C_1^\infty)/(C_1^M - C_1^P)$$
$$\Omega_2 = (C_2^M - C_2^\infty)/(C_2^M - C_2^P) \quad [35]$$

(This notation will be used henceforth.) This, of course, assumes that the mean composition (C_1^∞, C_2^∞) of the alloy

has been prescribed. That each of the line within this region is characterized by its endpoints (C_1^P, C_2^P) and (C_1^M, C_2^M) permits values for the supersaturations to be computed. The flux equations can then be solved numerically for μ_1, μ_2, and the interface tie-line determined. It would appear that the two flux equations can be solved independently of one another. This, however, is not the case as they are in fact constrained in that the interface position of each component must be the same. The parameters μ_1 and μ_2 are, therefore, related. For example, in the case of planar and spherical particle growth, $\mu_2 = \mu_1 \sqrt{D_{11}/D_{22}}$, whereas for cylindrical behavior, $\mu_2 = \mu_1 D_{11}/D_{22}$. This said, the solution procedure is as follows. Solve the first flux equation for μ_1. Relate μ_2 to μ_1 in terms of the appropriate diffusivity ratio D_{11}/D_{22}. Solve the second flux equation for D_{11}/D_{22} and construct a graph of D_{11}/D_{22} *vs* C_1^P for each tie-line in the partitioned region. Recall that the parameter C_1^P characterizes each tie-line.) Figures 5 and 6 serve as illustrations to this and correspond to planar and spherical particle growth, respectively. Typical mean alloy compositions have been used in each case. Note the vertical asymptotes to each of the curves. In the case of curve (1), the asymptotes with D_{11}/D_{22} tending to infinity correspond to the supersaturation Ω_1 tending to zero; hence, the solution μ_1 to Eq. [28a] or [34a] tends to zero. (Recall $D_{11}/D_{22} = (\mu_2/\mu_1)^2$.) Likewise, the asymptotes with D_{11}/D_{22} tending to zero corresponds to the supersaturation Ω_2 tending to zero. Hence, the solution μ_2 to Eq. [28b] or [34b] tends to zero. Curve (2) may be interpreted in a similar manner except here the asymptotes with D_{11}/D_{22} tending to infinity occurs because Ω_2 tends to unity. Hence, the solution μ_2 to Eq. [28b] or [34b]; tends to infinity. The asymptote with D_{11}/D_{22} tending to zero is associated with Ω_2 tending to zero. Accordingly, the solution μ_2 to Eq. [28b] or [34b] tends to zero. The interface position of the particle for planar or spherical particle growth is determined *via* either of the relations $w_0 = \mu_1^2 D_{22}$ or $w_0 = \mu_2^2 D_{22}$, provided that values for the diffusion coefficients D_{11} and D_{22} have been specified. (Similar relations hold for other geometries.) It is then straightforward to compute the concentration profiles of each component within the matrix phase of the alloy—simply insert the appropriate values in Eq. [27] or [33].

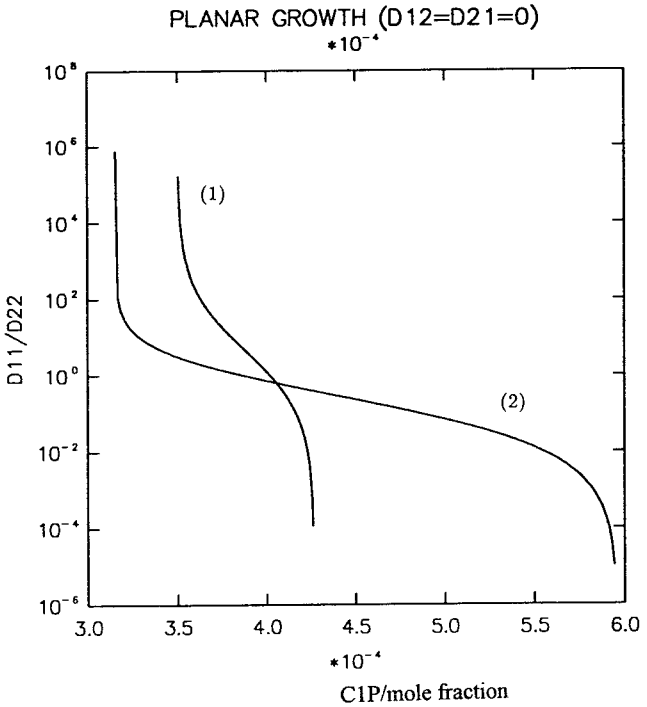


Fig. 5—Graph of D_{22}/D_{11} *vs* C_1^P for planar particle growth assuming $D_{12} = D_{21} = 0$. Data for a Fe-C-Mn system at 750 °C. The suffices 1 and 2 denote carbon and manganese, respectively. The mean alloy compositions for curves (1) and (2) are (0.015, 0.02) and (0.0025, 0.01), respectively.

4. *Oblate ellipsoidal growth*

The analysis already described will now be extended to cover the growth of an oblate ellipsoid, with the following equation:

$$\frac{x^2 + y^2}{w + a} + \frac{z^2}{w} = 4t \qquad [36]$$

The notation of Section IV has been used here (Eq. [3]) with $x = y$, $a_3 = 0$, and $a_1 = a_2 = a$, where $a = w_0(1 - K^2)/K^2$. Here, K defines the aspect ratio of the particle and must be determined experimentally (Similar results also obtain for prolate spheroids.) Making appropriate modifications to the full analysis, the flux equations can be written as

$$\sqrt{w_0}/D_{11} \exp(w_0/D_{11})(w_0 + a) \int_{w_0}^{\infty} \frac{\exp(-s/D_{11})}{(s + a)\sqrt{s}}\, ds = \Omega_1 \qquad [37a]$$

$$\sqrt{w_0}/D_{22} \exp(w_0/D_{22})(w_0 + a) \int_{w_0}^{\infty} \frac{\exp(-s/D_{22})}{(s + a)\sqrt{s}}\, ds = \Omega_2 \qquad [37b]$$

It proves convenient to introduce the scaled variables $w_0' = w_0/D_{11}$ and $a' = a/D_{11}$ and to make an obvious change of variables within the integrands to give

$$\exp(w_0')(w_0' + a')\sqrt{w_0'} \int_{w_0'}^{\infty} \frac{\exp(-s)}{(s + a')\sqrt{s}}\, ds = \Omega_1 \qquad [38a]$$

$$\exp(w_0'')(w_0'' + a'')\sqrt{w_0''} \int_{w_0''}^{\infty} \frac{\exp(-s)}{(s + a'')\sqrt{s}}\, ds = \Omega_2 \qquad [38b]$$

where $w_0'' = w_0' D_{11}/D_{22}$ and $a'' = a' D_{11}/D_{22}$. Here, the oblate parameter a and the diffusion coefficient D_{11} must be prescribed. For each tie-line (again characterized by the parameter C_1^P), Eq. [37a] is solved for w_0'. This is then used in Eq. [38b], which in turn is solved for the ratio D_{11}/D_{22}. This ensures that the interface position for each component is the same. A graph of D_{11}/D_{22} *vs* C_1^P can then be constructed. Figure 7 illustrates this. Again, note the vertical asymptotes. Similar arguments to those given for Figures 5 and 6 are applicable here.

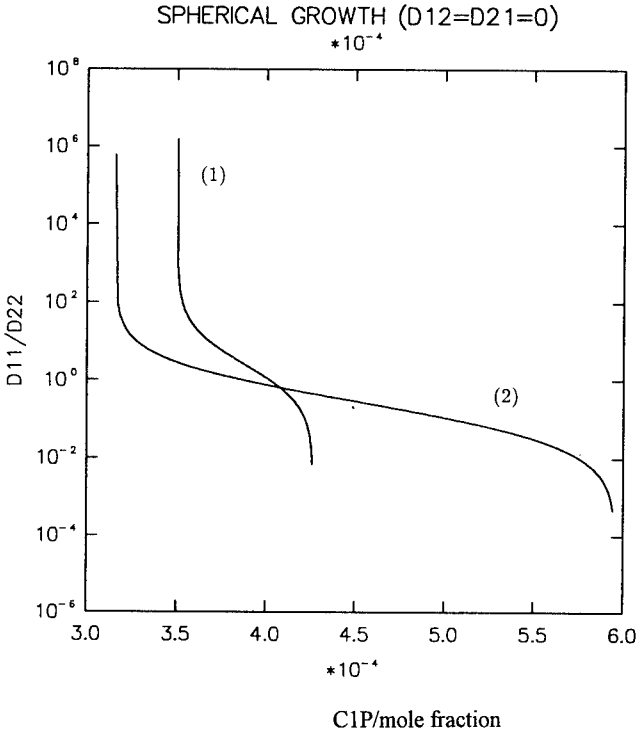


Fig. 6—Graph of D_{22}/D_{11} *vs* C_1^P for spherical particle growth assuming zero off-diagonal diffusion coefficients. Data and notation as in Fig. 5.

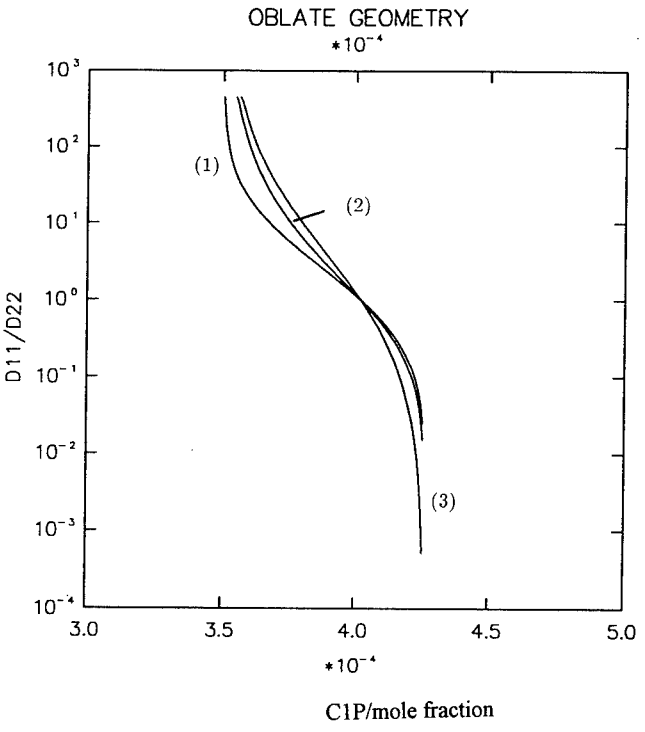


Fig. 7—Graph of D_{22}/D_{11}, *vs* C_1^P for the growth of an oblate ellipsoid with surface parameter a (Eq. [36]). Data associated with a Fe-C-Mn system at 750 °C and a mean alloy composition of (0.015, 0.02). For curve (1), $a = 10^{-6}$ and $D_{11} = 1$. In curve (2), $a = 1$ and $D_{11} = 1$, and for curve (3), $a = 10^6$ and $D_{11} = 1$.

Also, note that the asymptotic results in the appendix have also been used (Eqs. [A11] and [A12]).

B. $D_{12} \neq 0$, $D_{21} = 0$

Here, it will be assumed that the first component diffuses faster than the second, *i.e.*, that $D_{11} > D_{22} \geqslant D_{12} \gg D_{21}$. With this assumption, we set $D_{21} = 0$. The effect of this is to render the second flux equation to a binary-type relationship. Again, we shall be content to examine the growth kinetics of planar, spherical, and oblate ellipsoidal particles.

1. *Planar growth*

The concentration profiles within the matrix phase are found as

$$C_1(w) = C_1^\infty + \left[\frac{D_{12}(C_2^M - C_2^\infty)}{D_{11} - D_{22}} + (C_1^M - C_1^\infty)\right] \frac{\operatorname{erfc}(\sqrt{w/D_{11}})}{\operatorname{erfc}(\sqrt{w_0/D_{11}})} + \left[\frac{D_{12}}{D_{22} - D_{11}}(C_2^M - C_2^\infty)\right] \frac{\operatorname{erfc}(\sqrt{w/D_{22}})}{\operatorname{erfc}(\sqrt{w_0/D_{22}})} \quad [39]$$

and

$$C_2(w) = C_2^\infty + (C_2^M - C_2^\infty) \frac{\operatorname{erfc}(\sqrt{w/D_{22}})}{\operatorname{erfc}(\sqrt{w_0/D_{22}})} \quad [40]$$

where $x^2 = 4\omega t$. Following Coates,[24] the flux equations may be expressed in the form

$$F(\mu_1) - \frac{mD_{12}}{D_{11}(1 - D_{22}/D_{11})}[F(\mu_2) - F(\mu_1)] = \Omega_1$$

$$F(\mu_2) = \Omega_2 \quad [41]$$

where, again, Ω_1 and Ω_2 denote the fractional supersaturations (Eq. [35]) and m is the slope of the tie-line on the ternary phase diagram; i.e.,

$$m = \frac{C_2^M - C_2^P}{C_1^M - C_1^P} \quad [42]$$

In addition,

$$F(\mu) = \sqrt{\pi}\mu \exp(\mu_2) \operatorname{erfc}(\mu) \quad [43]$$

and $\mu_1 = \sqrt{w_0/D_{11}}$ and $\mu_2 = \sqrt{w_0/D_{22}}$

2. *Spherical growth*

The concentration profile of each component within the matrix phase of the alloy can be expressed as

$$C_1(w) = C_1^\infty + \left[(C_1^M - C_1^\infty) + \frac{D_{12}(C_2^M - C_2^\infty)}{D_{11} - D_{22}}\right] \cdot G(w, w_0, D_{11}) + \left[\frac{D_{12}}{D_{22} - D_{11}}(C_2^M - C_2^\infty)\right] \cdot G(w, w_0, D_{22}) \quad [44]$$

and

$$C_2(w) = C_2^{\infty} + (C_2^M - C_2^{\infty})\, G(w, w_0, D_{22}) \qquad [45]$$

where

$$G(w, w_0, D) = \left[\frac{\sqrt{D/w}\exp(-w/D) - \sqrt{\pi}\,\mathrm{erfc}\,(\sqrt{w/D})}{\sqrt{D/w_0}\exp(-w_0/D) - \sqrt{\pi}\,\mathrm{erfc}\,(\sqrt{w_0/D})} \right] \qquad [46]$$

Also, $x^2 + y^2 + z^2 = 4\omega t$. The flux equations may again be written in the form of Eq. [41], except here,

$$F(\mu) = 2\mu^3 \exp(\mu^2)\left[\frac{\exp(-\mu^2)}{\mu} - \sqrt{\pi}\,\mathrm{erfc}\,(\mu) \right] \qquad [47]$$

Note also that $\mu_1 = \sqrt{w_0/D_{11}}$ and $\mu_2 = \sqrt{w_0/D_{22}}$.

To illustrate the manner in which the various parameters appearing in these flux equations interact with one another, we include Figure 8. This depicts a series of results for the planar analysis and reproduces Coates results. Similar figures exists for spherical and cylindrical particle growth (see Reference 24 for a full discussion). Equations [41], however, may be interpreted slightly differently. An obvious rearrangement is

$$D_{12}/D_{11} = \frac{-(1 - D_{22}/D_{11})}{m}\left[\frac{F(\mu_1) - \Omega_1}{F(\mu_1) - \Omega_2} \right] \qquad [48]$$

Cast in this form, the solution procedure is as follows: For a specified mean alloy composition (C_1^{∞}, C_2^{∞}) and a particular tie-line (characterized by C_1^P), the fractional supersaturations Ω_1 and Ω_2 are evaluated. The second flux equation is then solved for μ_2. (Recall that for planar and spherical particle growth, $\mu_1 = \sqrt{w_0/D_{11}}$ and $\mu_2 = \sqrt{w_0/D_{22}}$.) Analogous relations exist for other geometries. That the interface position coincides for each component requires that $\mu_1 = \mu_2\sqrt{D_{22}/D_{11}}$. This is evaluated for a suitable ratio of D_{22}/D_{11} and used Eq. [48]. (Typically, D_{11} and D_{22} differ in magnitude by a factor of $\simeq 10^6$ for the case of low-alloy steels.[38]) A graph of D_{12}/D_{11} *vs* D_{22}/D_{11} for each tie-line is then constructed. One can interpret Eq. [48] as a consistency relation for the simultaneous solution of the flux equations. That is, for predetermined diffusivity ratios D_{22}/D_{11}, it determines admissable values for the off-diagonal diffusion coefficient D_{12} to ensure that the interface motion for each component is the same. Figure 9 illustrates this scheme for planar growth.

3. *Oblate ellipsoidal growth*

A similar analysis to that described in Section 2 exists for a growing oblate ellipsoid. Again, it proves convenient to introduce the scaled variables $w_0'' = w_0/D_{22}$ and $a'' = a/D_{22}$. With this notation, the second of the two flux equations takes the form

$$F(w_0'', a'') = \Omega_2 \qquad [49]$$

where

$$F(w, a) = \exp(w)\,(w + a)\sqrt{w}\int_w^{\infty} \frac{\exp(-s)}{(s + a)\sqrt{s}}\,ds \qquad [50]$$

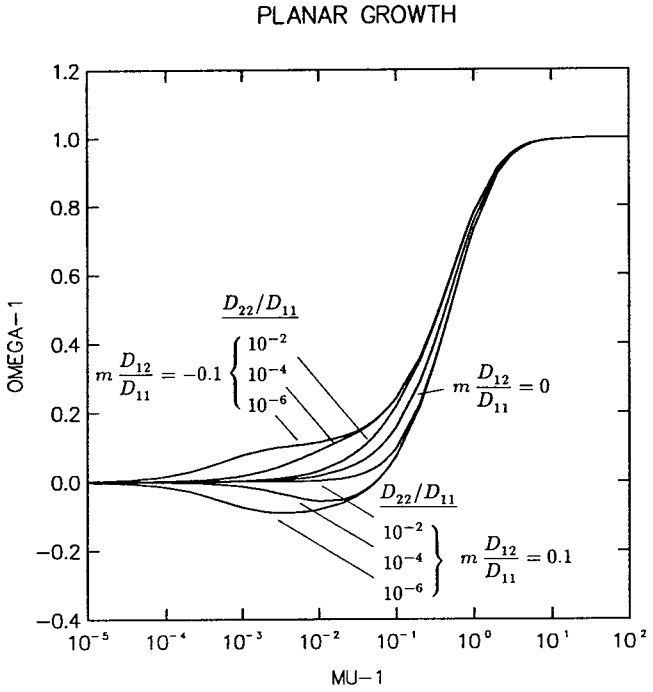


Fig. 8—Plot of Ω_1 *vs* $\mu_1 = \sqrt{w_0/D_{11}}$ for planar particle growth illustrating the effects of the parameters mD_{12}/D_{11} and D_{22}/D_{11} when $D_{21} = 0$ (Eq. [48]). Data for a Fe-C-Mn system at 750 °C with a mean alloy composition of (0.015, 0.02).

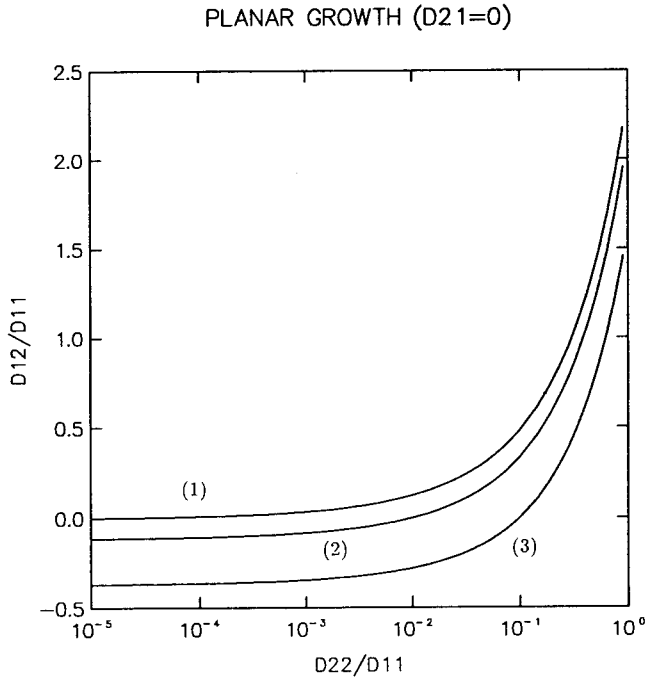


Fig. 9—Plot of D_{12}/D_{11} *vs* D_{22}/D_{11} for planar particle growth assuming $D_{21} = 0$. Data for a Fe-C-Mn system at 750 °C with a mean alloy composition (0.015, 0.02). For curve (1), $C_1^P = 3.5069 \times 10^{-4}$. In curve (2), $C_1^P = 3.632 \times 10^{-4}$ and in curve (3), $C_1^P = 3.8043 \times 10^{-4}$.

In a similar manner, the first flux equation can be rearranged as

$$D_{12}/D_{11} = \frac{-(1 - D_{22}/D_{11})}{m}\left[\frac{F(w_0', a') - \Omega_1}{F(w_0', a') - \Omega_2}\right] \quad [51]$$

where $w_0' = w_0'' D_{22}/D_{11}$ and $a' = a''\, D_{22}/D_{11}$. The solution procedure is as follows: For a prescribed oblate parameter a, diffusion coefficient D_{22}, and tie-line, Eq. [49] is solved for w_0''. The corresponding values for a' and w_0' are then computed for a suitable choice of the ratio D_{22}/D_{11}. In this way, a value for D_{12}/D_{11} can be computed *via* Eq. [51]. In turn, a graph of D_{12}/D_{11} *vs* D_{22}/D_{11} for different tie-lines can be compiled. Again, one can regard Eq. [51] as a consistency relationship for the simultaneous solution of the two flux equations. A series of curves illustrating the effects of different input parameters appears in Section VIII (Figure 10).

VIII. SUMMARY

Diffusion-controlled growth of particles, dendrites, and plates growing in infinite media has been examined for ternary systems. Part of this work established that the growth kinetics associated with planar, cylindrical, and spherical particles were limiting cases of a more complete analysis for shape preserving growth. The theory was applied to the growth of allotriomorphic ferrite from austenite in ternary Fe-C-X steels, where X represents a substitutional alloying elements. For the growth of allotriomorphic ferrite from austenite, the experimental evidence suggests that the shape of the growing phase is most realistically modeled as an oblate ellipoid of revolution the theory necessary to handle the growth of allotriomorphs of this geometry has been discussed. Numerical results were given based on work that is reliant on the ability to predict multicomponent phase equilibria.

Future work must address the growth of precipitates in finite (rather than infinite) media. This should also be extended to multicomponent systems. In this respect, we regard the work presented here as a precursor to such problems. The ultimate goal is to produce quantitative models that allow multicomponent, multiphase phase transformations to be estimated as a function of alloy composition alone.

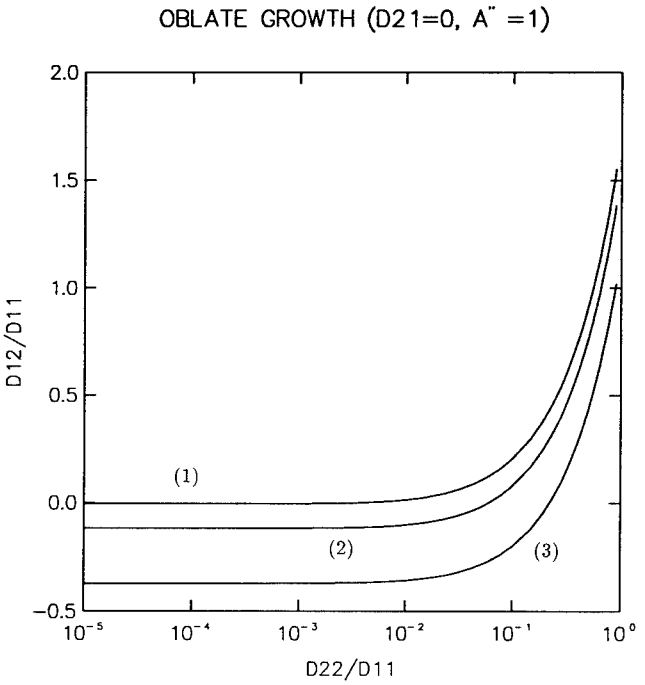


Fig. 10—Plot of D_{12}/D_{11} *vs* D_{22}/D_{11} for the growth of an oblate ellipsoid assuming $D_{21} = 0$. Data as in Fig. 9. Also $a'' = 1$. (Eqs. [49] through [51] for notations.)

APPENDIX

Asymptotic results

As both an aid to the numerical solution of the nonlinear flux equations given in Sections [III] through [VII], we include here a selection of asymptotic results. The limiting cases of the full ellipsoidal analysis described earlier will again be considered here, *i.e.*, planar, cylindrical, spherical, and oblate ellipsoidal particle growth. Each set of results are direct analogues of those obtained by Zener[9] and Frank[10] for binary systems. Note also that, where appropriate, the derivations have made use of the following standard approximations:[39]

$$\text{erfc}\,(x) \sim 1 - \frac{2}{\sqrt{\pi}}\left[x - \frac{x^3}{3} + \frac{x^5}{10} - \ldots\right], \quad x \to 0^+ \quad [A1]$$

$$\text{erfc}\,(x) \sim \frac{\exp(-x^2)}{\sqrt{\pi}}\left[\frac{1}{x} - \frac{1}{2x^3} + \frac{3}{4x^5} - \ldots\right], \quad x \to +\infty \quad [A2]$$

where

$$\text{erfc}\,(x) = \frac{2}{\sqrt{\pi}}\int_x^\infty \exp(-t^2)\, dt \quad [A3]$$

denotes the complimentary error function. Also,

$$E_1(x) \sim -\gamma - \ln x + x - \frac{x^2}{4} + \frac{x^4}{18} - \ldots, \quad x \to 0^+ \quad [A4]$$

where $\gamma = 0.5772 \ldots$ denotes Euler's constant.

$$E_1(x) \sim \frac{\exp(-x)}{x}\left[1 - \frac{1}{x} + \frac{2}{x^2} - \ldots\right], \quad x \to +\infty \quad [A5]$$

Here,

$$E_1(x) = \int_x^\infty \frac{\exp(-t)}{t}\, dt, \quad x > 0 \quad [A6]$$

defines the exponential integral. The reader is reminded that the notation of Section VI will be used, *i.e.*, Ω_1 and Ω_2 denote the fractional supersaturations.[35]

1. *Planar growth*

To leading order, the flux equations as defined by Eq. [28], can be approximated as

$$\mu_i \sim \begin{cases} \Omega_i/\sqrt{\pi}, & \Omega_i \to 0 \\ 1/\sqrt{2(1-\Omega_i)}, & \Omega_i \to 1 \end{cases} \quad [A7]$$

2. *Cylindrical growth*

Recall that for cylindrical particle growth, Eq. [31] obtains. An explicit representation of μ_i in terms of the fractional supersaturations is not available when $\Omega_i \to 0$. Instead, the following nonlinear equations must be solved in this limit.

$$-\mu_i \exp(\mu_i)\left[\gamma + \ln \mu_i - \mu_i + \frac{\mu_i^2}{4} - \frac{\mu_i^3}{18} + \ldots\right] \sim \Omega_i, \quad \Omega_i \to 0 \quad [A8]$$

The leading order approximation can, however, be found when $\Omega \to 1$. Direct application of Eq. [A5] establishes

$$\mu_i \sim 1/(1-\Omega_i) \quad \text{as } \Omega_i \to 1 \quad [A9]$$

3. *Spherical growth*

The following approximations to Eq. [34] obtain here:

$$\mu_i \sim \begin{cases} \sqrt{\Omega_i/2}, & \Omega_i \to 0 \\ \sqrt{3/2(1-\Omega)}, & \Omega_i \to 1 \end{cases} \quad [A10]$$

4. *Oblate ellipsoidal growth*

In the case of a growing oblate ellipsoid, the following results may be used. For details, see Reference 40. For a/w_0 small ($K \to 1$),

$$\int_{w_0}^{\infty} \frac{\exp(-s)}{(s+a)\sqrt{s}}\,ds \sim \frac{2\exp(-w_0)}{\sqrt{w_0}}\left[1 + \frac{2a}{3}\left(1 - \frac{1}{2w_0}\right) + \frac{4a^2}{15}\left(1 - \frac{1}{2w_0} + \frac{3}{4w_0}\right)\right] - 2\sqrt{\pi}\,\mathrm{erfc}(\sqrt{w_0})\left(1 + \frac{2a}{3} + \frac{4a^2}{15}\right) \quad [A11]$$

while for a/w_0 large ($K < \sim 1/3$),

$$\int_{w_0}^{\infty} \frac{\exp(-s)}{(s+a)\sqrt{s}}\,ds \sim \frac{\pi}{\sqrt{a}}\,e^a\,\mathrm{erfc}(\sqrt{a}) - \frac{\sqrt{\pi}}{a}\,\mathrm{erf}(\sqrt{w_0})\left[1 - \frac{1}{2a} + \frac{3}{4a^2}\right] + \frac{\sqrt{w_0}\exp(-w_0)}{a^2}\left[1 - \frac{(3/2) + w_0}{a}\right] \quad [A12]$$

The notation of Sections III and IV applied here (see Eqs. [3] and [36]). A direct substitution of either Eq. [A11] or Eq. [A12] into Eq. [37] results in a pair of nonlinear equations for the interface position w_0, the limiting solutions to which must be obtained numerically.

ACKNOWLEDGMENTS

One of the author's (JPB) contribution was carried out under SERC Grant No. CR/H6903S, "Modelling of the High Temperature Deformation in Materials Subject to Phase Transformations." The contribution of (RCR) was carried out under SERC Grant No. GR/H 69069 "Modelling of the Evolution of Steel Microstructures." The authors are grateful to Professor M. McLean for the provision of research facilities at Imperial College.

REFERENCES

1. *CALPHAD Journal*, Pergamon Press, Oxford.
2. B. Sundman: Report D53, The Royal Institute of Technology Stockholm, 1984.
3. NPL Metallurgical and Thermochemical Databank (MTDATA) National Physical Laboratory, Teddington, Middlesex, United Kingdom.
4. J.W. Christian: *The Theory of Transformations in Metals and Alloys*. 2nd ed., Pergamon Press, Oxford, 1975. Part 1.
5. J.S. Kirkaldy and D.J. Young: *Diffusion in the Condensed State*. The Institute of Metals, London, 1987.
6. J.R. Bradley, J.M. Rigsbee, and H.I. Aaronson: *Metall. Trans. A*, 1977, vol. 8A, pp. 323-33.
7. H.K.D.H. Bhadeshia: *Prog. Mater. Sci.*, 1985, vol. 29, pp. 321-86.
8. C. Atkinson, H.B. Aaron, K.R. Kinsman, and H.I. Aaronson: *Metall. Trans.*, 1973, vol. 4, pp. 783-92.
9. C. Zener, *J. Appl. Phys.*, 1949, vol. 20, pp. 950-53.
10. F.C. Frank: *Proc. R. Soc.*, 1950, vol. A201, pp. 586-99.
11. F.S. Ham: *J. Phys. Chem. Solids*, 1958, vol. 6, pp. 335-51.
12. F.S. Ham: *Q. Appl. Math.*, 1959, vol. 17, pp. 137-45.
13. G. Horvay and J.W. Cahn: *Acta Metall.*, 1961, vol. 9, pp. 695-705.
14. G.P. Ivantsov: *Dokl. Akad. Nauk SSSR*, 1947, vol. 58, pp. 567-70.
15. R. Trivedi and G.M. Pound: *J. Appl. Phys.*, 1967, vol. 38, pp. 3569-76.
16. C. Atkinson: *J. Appl. Phys.*, 1969, vol. 40, pp. 4859-65.
17. C. Atkinson: *Q.J. Mech. Appl. Math.*, 1974, pp. 299-316.
18. M. Enomoto and C. Atkinson: *Acta Metall. Mater.*, 1993, vol. 41, pp. 3237-3244.
19. I.I. Kolodner: *Comm. Pure Appl. Math.*, 1956, vol. 6, pp. 1-31.
20. J.S. Kirkaldy: *Can. J. Phys.*, 1958, vol. 36, pp. 899-925.
21. J.S. Kirkaldy: *Can. J. Phys.*, 1959, vol. 37, pp. 30-34.
22. J.S. Kirkaldy, D. Weichert, and Zia Ul-Haq: *Can. J. Phys.*, 1963, vol. 41, pp. 2166-73.
23. J.S. Kirkaldy: *Adv. Mater. Res.*, 1970, vol. 4, pp. 55-100.
24. D.E. Coates: *Metall. Trans.*, 1973, vol. 4, pp. 1077-86.
25. D.E. Coates: *Metall. Trans.*, 1973, vol. 4, pp. 2313-25.
26. D.E. Coates: *Metall. Trans.*, 1973, vol. 4, pp. 395-96.
27. *Computer Simulation of Microstructural Evolution*, D.J. Srolovitz, ed., TMS-AIME. Warrendale, PA, 1986.
28. *Phase Transformations*, G.W. Lorimer, ed., The Institute of Metals, London, 1987.
29. J. Ågren: *Dictra Program*, The Royal Institute of Technology, Stockholm, 1993.
30. B. Sundman and J. Ågren: *J. Phys. Chem. Solids*, 1981, vol. 42, pp. 297-301.
31. M. Hillert and L.-I. Staffansson: *Acta Chem. Scand.*, 1970, vol. 24, pp. 3618-26.
32. P. Gustafson: *Scand. J. Metall.*, 1985, vol. 14, pp. 259-67.
33. J.-O. Andersson: *CALPHAD*, 1988, vol. 12, pp. 9-23.
34. J. Lacaze and B. Sundman: *Metall. Trans. A*, 1991, vol. 22A, pp. 2211-23.
35. W. Huang: *Metall. Trans. A*, 1991, vol. 22A, pp. 1911-20.

36. M. Hillert and C. Qiu: *Metall. Trans. A*, 1991, vol. 22A, pp. 2187-98.
37. *The NAG Fortran Library Manual*, NAG Ltd., Wilkinson House, Oxford, 1991.
38. J. Fridberg, L. Torndahl, and M. Hillert: *Jernkontorets Ann.*, 1969, vol. 153, pp. 263-76.
39. M. Abramowitz and I.A. Stegun: *Handbook of Mathematical Functions*, Dover, London, 1955.
40. G. Horvay and J.W. Cahn: G.E. Research Report No. 60-RL-2561M, General Electric Research and Development Center, Schenectady, NY, 1960.

Diffusional Boundary Conditions during Coarsening of Elastically Interacting Precipitates

WERNER HORT and WILLIAM C. JOHNSON

The elastic fields associated with a dispersion of spherical particles in an isotropic matrix are determined using the equivalent inclusion approach of Moschovidis and Mura. The coherent particles possess a misfit strain and have elastic constants different from those of the matrix phase. A spatially nonuniform stress field can be applied to the system. The stress fields are used to calculate the equilibrium compositions at the precipitate-matrix interface for use as diffusional boundary conditions in computer simulations of multiparticle coarsening in elastically stressed systems.

I. INTRODUCTION

PRECIPITATION-hardened materials are used in structural high-temperature applications because of their superior deformation properties. A typical example is the use of nickel-based superalloys in the construction of turbine blades for aircraft engines. The microstructure of these materials consists of a dispersion of $Ni_3Al(\gamma')$ precipitates in a nickel-rich matrix that is often highly resistant to coarsening. Strong spatial correlations between precipitates are often observed with the γ' particles aligned along the elastically soft $\langle 100 \rangle$ directions of the matrix phase. Particle shape and alignment in these alloys have been correlated with misfit strain[1,2,3,4,5] and contribute to the high creep resistance of these materials.

Several theoretical investigations and computer simulations have been performed recently in order to explore the influence of misfit strain on microstructural evolution in two-phase coherent alloys.[6,7,8,9,10,11,12,13,14] The long-range goal of this effort has been to identify how misfit strains can be used to control microstructure and thereby, material properties. Of particular interest have been elastically induced particle shape changes, particle migrations, inverse coarsening, and the development of spatial correlations between particles during precipitation and coarsening. The simulations have been conducted in both two and three dimensions using several different methods, but all approaches, excluding that of Kawasaki and Enomoto,[7,8] require determination of the elastic fields associated with a dispersion of second-phase particles. Both particle growth and migration rates depend strongly on the local elastic fields.

In this work, we determine the elastic fields associated with a dispersion of many misfitting spherical particles. The particles possess elastic constants different from those of the matrix phase (elastically heterogeneous), and a nonhomogeneous external field can be applied to the system. The determination of the elastic fields is based on a method outlined by Eshelby[15] and employed by Moschovidis and Mura[16] and Mura[17] for calculating elastic fields around two interacting cavities in an external field. This method is presented in Section II. Since our motivation is to calculate equilibrium compositions near a coherent interface for use as a diffusional boundary condition for understanding the effect of stress on coarsening, we examine the dependence of both the elastic fields and equilibrium interfacial compositions on the number of nearest-neighbor particles in Section III.

WERNER HORT, Graduate Student, and WILLIAM C. JOHNSON, Professor, are with the Department of Materials Science and Engineering, University of Virginia, Charlottesville, VA 22903-2442.

Manuscript submitted September 10, 1993.

II. GOVERNING EQUATIONS

In section II, we present the equations and methods used to determine the diffusional boundary conditions for the coarsening of elastically interacting precipitates.

A. *Elastic Fields*

The elastic fields are determined using an equivalent inclusion method.[16,17] The actual system is represented by an equivalent system in which the particles have the same spatial distribution as in the actual system, but the elastic constants of the particles are identical to those of the matrix phase. The misfit of each particle in the equivalent system is chosen such that the linear superposition of the elastic fields of the individual particles in the equivalent system is identical to that of the actual system. The challenge in using the equivalency method is to determine the equivalent transformation strain of each particle.

In the following, the unstressed matrix phase serves as the reference state for the measurement of strain, ε_{kl}. Stresses, σ_{ij}, are thus obtained from Hooke's law as

$$\sigma_{ij} = C_{ijkl}\varepsilon_{kl} \quad [1]$$

for the matrix phase and

$$\sigma_{ij} = C^p_{ijkl}\,(\varepsilon_{kl} - \varepsilon^{T,p}_{kl}) \quad [2]$$

for the precipitate phase. (Repeated indices appearing as a subscript are summed from 1 to 3, while a comma appearing in a subscript denotes differentiation.) C_{ijkl} and C^p_{ijkl} are the stiffness tensors of the matrix and precipitate phases, respectively, and $\varepsilon^{T,p}_{kl}$ is the stress-free transformation strain of precipitate p. The partial molar volumes of the component species in the matrix phase are assumed equal, so that compositional heterogeneity in the matrix phase does not engender stress. (Even if the partial molar volumes are not equal, it is reasonable to neglect the elastic strains induced by compositional

heterogeneity, since any supersaturation is vanishingly small in the coarsening regime.)

The strain field of the actual system with N particles must satisfy the integrodifferential equation in the displacement gradients, $u_{m,n}$[18,19]

$$u_{m,n}(\mathbf{x}) = u^a_{m,n}(\mathbf{x}) - \sum_{p=1}^{N} \int_{V_p} [C^p_{ijkl}\varepsilon^{T,p}_{ij}(\mathbf{x}') - \Delta C^p_{ijkl} u_{i,j}(\mathbf{x}')] \cdot G_{ml,kn}(\mathbf{x} - \mathbf{x}')\, d\mathbf{x}' \quad [3]$$

where $\Delta C^p_{ijkl} = C^p_{ijkl} - C_{ijkl}$, $\mathbf{u}^a$ is the displacement field arising from the externally applied load, and G_{ml} is the elastic Green's function.

If $\beta^p_{ij}(\mathbf{x})$ is the position-dependent, equivalent transformation strain of particle p, the displacement field in the elastically homogeneous equivalent system is given through superposition as

$$u_{m,n}(\mathbf{x}) = u^a_{m,n}(\mathbf{x}) - \sum_{p=1}^{N} C_{ijkl} \int_{V_p} G_{ml,kn}(\mathbf{x} - \mathbf{x}')\, \beta^p_{ij}(\mathbf{x}')\, d\mathbf{x}' \quad [4]$$

Equating Eqs. [3] and [4], the equivalent system will engender the same strain field as the actual system when

$$\Delta C^p_{ijkl}\varepsilon_{kl}(\mathbf{x}) - C^p_{ijkl}\varepsilon^{T,p}_{kl}(\mathbf{x}) + C_{ijkl}\beta^p_{kl}(\mathbf{x}) = 0 \quad p = 1, 2, \ldots, N \quad [5]$$

Equation [5] must be satisfied within the volume of each particle p and is valid for anisotropic systems and particles of arbitrary shape.

In the following development, we assume the particles to be spheres and the elastic constants of both phases to be isotropic. Furthermore, we simplify Eq. [5] substantially by assuming identical Poisson's ratios in each phase and by assuming that the elastic constants of all precipitates are identical. The elastic heterogeneity of the system is then described by one parameter, $\delta = \mu^p/\mu$, the ratio of the shear moduli of the precipitate and matrix phases. Multiplying Eq. [5] with the compliance tensor, S_{mnij}, leads then to the simplified equivalency condition

$$(\delta - 1)\varepsilon_{mn}(\mathbf{x}) - \delta\varepsilon^{T,p}_{mn} + \beta^p_{mn}(\mathbf{x}) = 0 \quad p = 1, 2, \ldots, N \quad [6]$$

We have assumed position independence for $\varepsilon^{T,p}_{mn}$, but in order to account for precipitate variants, we allow the misfit strain, $\varepsilon^{T,p}_{mn}$, to be different for different particles. In order to solve Eq. [6] for the β^p_{ij}, the equivalent misfit strain of each precipitate is expanded as a polynomial about its center, $\mathbf{d}^p$

$$\beta^p_{ij}(\mathbf{x}) = B^p_{ij} + B^p_{ijk}(x_k - d^p_k) + B^p_{ijkl}(x_k - d^p_k)(x_l - d^p_l) + \ldots \quad [7]$$

where B^p_{ij}, B^p_{ijk}, B^p_{ijkl}, *etc.* are the Taylor coefficients. If Eq. [7] is substituted into Eq. [4], the strain field induced by the equivalent misfit strain of particle p, β^p_{ij}, can be written as

$$\varepsilon^p_{ij}(\mathbf{x}) = D^p_{ijkl}(\mathbf{x} - \mathbf{d}^p) B^p_{kl} + D^p_{ijklm}(\mathbf{x} - \mathbf{d}^p) B^p_{klm} + \ldots \quad [8]$$

where the functions $D_{ijkl}(\mathbf{x})$, $D_{ijklm}(\mathbf{x})$, *etc.*, can be calculated analytically for ellipsoidal precipitates in an isotropic matrix and have been compiled by Mura.[17] If $\mathbf{x}$ is a point within the strain-inducing particle, the functions $D^p_{ijkl}(\mathbf{x})$, $D^p_{ijklm}(\mathbf{x})$, $D^p_{ijklmn}(\mathbf{x})$ ... are polynomials of degree 0, 1, 2, ..., respectively. The polynomials of degree n contain terms of degree n, $n - 2$, $n - 4$, *etc.* Therefore, for $\mathbf{x}$ within precipitate p, the strain, $\varepsilon_{ij} = \varepsilon^{p,in}_{ij}$, induced by the equivalent misfit strain of this particle p, can be written as

$$\varepsilon^{p,in}_{ij}(\mathbf{x}) = D^0_{ijkl}B^p_{kl} + D^0_{ijklm,s}B^p_{klm}(x_s - d^p_s) + D^0_{ijklmn}B^p_{klmn} + \frac{1}{2}D^0_{ijklmn,st}B^p_{klmn}(x_s - d^p_s) \cdot (x_t - d^p_t) + \ldots \quad [9]$$

where the coefficients $D^0_{ijk\ldots m}$ are independent of position and the precipitate under consideration. Thus, with $\varepsilon^a_{ij}(\mathbf{x})$ being the applied strain field, we can write for the overall strain within precipitate p

$$\varepsilon_{ij}(\mathbf{x}) = \varepsilon^a_{ij}(\mathbf{x}) + \sum_{p'=1}^{N} \varepsilon^{p'}_{ij}(\mathbf{x}) = \boldsymbol{\varepsilon}^a_{ij}(\boldsymbol{x}) + \boldsymbol{\varepsilon}^{p,in}_{ij}(\boldsymbol{x}) + \sum_{\substack{p'=1 \\ p' \neq p}}^{N} \boldsymbol{\varepsilon}^{p'}_{ij}(\boldsymbol{x}),\ \mathbf{x} \in \mathbf{V_p} \quad [10]$$

For each p in Eq. [6], we expand the functions $D^{p'}_{ijkl}(\mathbf{x})$, $D^{p'}_{ijklm}(\mathbf{x})$, ... around the center of precipitate p, $\mathbf{d}^p$, within which Eq. [6] has to be satisfied

$$D^{p'}_{ijkl}(\mathbf{x}) = D^{p'}_{ijkl}\big|_{(\mathbf{d}^p - \mathbf{d}^{p'})} + D^{p'}_{ijkl,s}\big|_{(\mathbf{d}^p - \mathbf{d}^{p'})}(x_s - d^p_s) + \ldots \quad [11]$$

and

$$D^{p'}_{ijklm}(\mathbf{x}) = D^{p'}_{ijklm}\big|_{(\mathbf{d}^p - \mathbf{d}^{p'})} + D^{p'}_{ijklm,s}\big|_{(\mathbf{d}^p - \mathbf{d}^{p'})} (x_s - d^p_s) + \ldots, \textit{etc.} \quad [12]$$

Expanding the applied strain field in a polynomial about the center of the system

$$\varepsilon^a_{ij}(\mathbf{x}) = \varepsilon^a_{ij} + \varepsilon^a_{ijs}x_s + \ldots \quad [13]$$

substituting for the polynomial expressions in Eq. [6], and sorting the terms according to the powers of the spatial coordinates, we obtain a system of linear equations for the Taylor coefficients of the $\beta^p_{ij}(\mathbf{x})$; *e.g.*, for $p = 1, 2, \ldots, N$

$$(\delta - 1)\left[D^0_{ijkl}B^p_{kl} + \sum_{\substack{p'=1 \\ p' \neq p}}^{N} (D^{p'}_{ijkl}(\mathbf{d}^p - \mathbf{d}^{p'})\, B^{p'}_{kl} + D^{p'}_{ijklm}(\mathbf{d}^p - \mathbf{d}^{p'})\, B^{p'}_{klm} + \ldots)\right] + B^p_{kl}\delta_{ik}\delta_{jl} = -(\delta - 1)[\varepsilon^a_{ij} + \varepsilon^a_{ijs}d^p_s + \ldots] + \delta\varepsilon^{T,p}_{ij}, \quad [14]$$

$$(\delta - 1)\left[D^0_{ijklm,s}B^p_{klm} + \sum_{\substack{p'=1 \\ p'\neq p}}^{N}(D^{p'}_{ijkl,s}(\mathbf{d}^p - \mathbf{d}^{p'})B^{p'}_{kl} + D^{p'}_{ijklm,s}(\mathbf{d}^p - \mathbf{d}^{p'})B^{p'}_{klm} + \ldots)\right]$$

$$+ B^p_{klm}\delta_{ik}\delta_{ij}\delta_{ms} = -(\delta - 1)\varepsilon^a_{ijs} \quad [15]$$

etc. Equations [14] and [15] obtain from terms independent and linear in the spatial coordinates, respectively. Higher-order terms are obtained in like manner.

B. *Interfacial Compositions*

The intent of our research is the computer simulation of multiparticle coarsening in elastically stressed systems. During these simulations, we use the elastic fields to determine compositional boundary conditions, which are then used to solve the diffusion equation. Particle growth and migration rates are obtained from the diffusional fluxes and are time-integrated to give the microstructural evolution of the system.

The diffusional boundary conditions are derived from the assumption of local thermodynamic equilibrium at the precipitate-matrix interface. If c_e^α and c_e^β are the equilibrium compositions of the matrix and precipitate phase in contact along a planar, unstressed interface—*i.e.*, those compositions obtained from the unstressed phase diagram—the composition in the matrix phase evaluated at the coherent precipitate-matrix interface, c^α, is given to first order in $(c^\alpha - c_e^\alpha)$ by the following equation:[20]

$$c^\alpha(\mathbf{x}) = c_e^\alpha + \frac{[g(\mathbf{x}) + 2\sigma/r]}{\chi(c_e^\beta - c_e^\alpha)} \quad [16]$$

The function $g(\mathbf{x})$ determines the contribution of the elastic fields to the interfacial composition and is given by

$$g(\mathbf{x}) = (\varepsilon_{ij}^\alpha - \varepsilon_{ij}^\beta)\,\sigma_{ij}^\alpha + \frac{1}{2}(\varepsilon_{ij}^\beta - \varepsilon_{ij}^T)\,\sigma_{ij}^\beta - \frac{1}{2}\sigma_{ij}^\alpha\varepsilon_{ij}^\alpha \quad [17]$$

whereas the interfacial energy, σ, together with the particle radius, r, gives the capillary contribution. χ is a thermodynamic factor representing the curvature of the stress-free, free energy of the matrix phase with respect to composition and evaluated at c_e^α

$$\chi = \frac{\rho_0 \mathrm{k}\theta}{c_e^\alpha(1 - c_e^\alpha)}\left[1 + \frac{\partial \ln \gamma}{\partial \ln c}\right] \quad [18]$$

where ρ_0 is the density of lattice sites in the reference state, θ is the absolute temperature, k is Boltzmann's constant, and γ is the activity coefficient of the component in solution.

The introduction of nondimensional quantities greatly reduces the number of physical parameters which have to be specified to determine the elastodiffusion problem. We employ a scaled composition, C, defined as

$$C = \frac{c^\alpha - c_e^\alpha}{c_e^\beta - c_e^\alpha} \quad [19]$$

A scaled strain is defined by

$$E_{ij} = \frac{\varepsilon_{ij}}{\varepsilon} \quad [20]$$

where ε is a characteristic strain for the system. We shall associate ε with the misfit strain, ε_{ij}^T. Nondimensional stresses are introduced as

$$T_{ij} = \frac{\sigma_{ij}\varepsilon}{\chi(c_e^\beta - c_e^\alpha)^2} \quad [21]$$

and the length scale of the system is given by the capillary length, l_c

$$l_c = \frac{2\sigma}{\chi(c_e^\beta - c_e^\alpha)^2} \quad [22]$$

With these nondimensional quantities, the equilibrium composition of the matrix evaluated at the precipitate-matrix interface is

$$C(\mathbf{x}) = \frac{1}{R} + G(\mathbf{x}) \quad [23]$$

where $R = \tau/l_c$ and

$$G(\mathbf{x}) = (E_{ij}^\alpha - E_{ij}^\beta)T_{ij}^\alpha + \frac{1}{2}(E_{ij}^\beta - E_{ij}^T)T_{ij}^\beta - \frac{1}{2}E_{ij}^\alpha T_{ij}^\alpha \quad [24]$$

Thus, the time when the variations of $G(\mathbf{x})$ along the particle-matrix interface become important depends on the nondimensional particles size, R. The actual particle size at which this happens depends on the material parameters.

III. CALCULATIONS

In Section III, we calculate the diffusional boundary conditions or equilibrium matrix compositions evaluated at the precipitate-matrix interface associated with a system of elastically and diffusionally interacting precipitates. These calculations form the basis for simulating coarsening behavior in elastically stressed systems. We here are primarily concerned with the effect of the various approximations that can be employed in determination of the elastic fields (or equivalent transformation strains) and their influence on the interfacial compositions. Results of the computer simulations of coarsening behavior will follow.

In order to solve the system of linear equations (Eqs. [14], [15], and higher-order equations), it is necessary to truncate the Taylor expansion of the equivalent misfit strains, β_{ij}^p, at a finite number of terms. We assume the equivalent misfit strains are adequately represented by a linear spatial dependence. This corresponds to setting all Taylor coefficients of order B_{klmn} and higher equal to zero. This approximation should be valid so long as the externally applied elastic field can be represented as a polynomial of order one and the second- and higher-order derivatives of $D_{ijkl}^{p'}$ and $D_{ijklm}^{p'}$ are sufficiently small when evaluated at $(\mathbf{d}^p - \mathbf{d}^{p'})$.[16,17] Under these conditions, Eqs. [14] and [15] are sufficient to determine the $24N$ independent Taylor coefficients.

Solving the system of linear equations requires an algorithm of order three, and computing time increases

as the cube of the number of particles, N^3. When N is large, a second truncation must be employed, and only a certain number of nearest neighbors, n, are assumed to influence the equivalent transformation strain of a given particle. Of course, each particle has a different set of nearest neighbors, and a linear system of equations for $24n$ unknowns must be solved N times to determine the equivalent misfit strains. This approximation must be applied with care and in accordance with the convergence behavior of the Taylor coefficients and the interfacial compositions; *i.e.*, both should not change by more than some specified amount when more neighbors are included in the calculation. The application of this method to coarsening simulations in which periodic boundary conditions are employed must be done judiciously, as the strain field obtained through the summation of the individual strain fields of a periodic arrangement of precipitates is conditionally convergent.[17]

In order to evaluate the various approximations to the elastic field, a dispersion of 1000 nonoverlapping particles was created and placed in a cubic region of an infinite matrix. The size distribution of the particles employed was typical of that for a coarsening system. The density of particles is characterized by an effective precipitate volume fraction within the imaginary cube. For calculation purposes, we used a Poisson's ratio of $\nu = 1/3$ and a nondimensional shear modulus of $\mu = 10^{-4}$ for the matrix phase. The shear modulus of the precipitate phase was chosen as either $\mu^p = 1.25\ \mu$ (the particle is 25 pct harder than the matrix) or $\mu^p = 0.75\ \mu$ (the particle is 25 pct softer than the matrix). The misfit strain of the precipitates was assumed isotropic with $\varepsilon_{ij}^{T,p} = \varepsilon\delta_{ij}$, and the strains have been scaled by the misfit strain ε.

Figure 1 shows the variation of two representative Taylor coefficients, B_{11} and B_{113}, as a function of the number of interacting neighbors for two different approximations. (The difference between the B_{11} and its value for an isolated precipitate, $B_{11}(0)$ is plotted.) The precipitates are elastically harder than the matrix, and the effective volume fraction of the system is 5 pct. For an isolated particle, $n = 0$, the equivalent transformation strain is a constant given by $\beta_{ij} = \beta_{ij}(0) = 1.0714\delta_{ij}$. The solid lines represent the first-order approximation for which all particles have equivalent misfit strains with linear spatial dependence. The broken lines are calculated using a limited first-order approximation for which the equivalent misfit strain of all *neighboring* particles is assumed spatially constant. (The equivalent misfit strain of the particle of interest still retains its linear dependence.) The two approximations yield Taylor coefficients that differ by significantly less than 5 pct and show the same dependence on the number n of interacting nearest neighbors. This dependence of the equivalent misfit strain on n is typical for particles of various size and systems of different effective volume fraction, so long as the particles are not too close to the edge of the precipitate cluster.

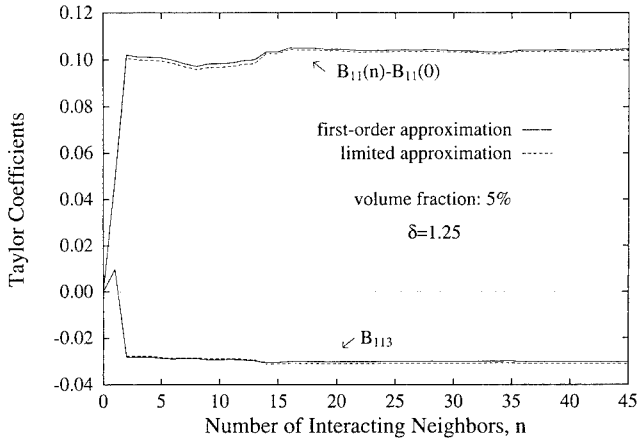


Fig. 1—Two Taylor coefficients for the equivalent misfit strain, B_{11} and B_{113}, are plotted as a function of the number of elastically interacting neighboring particles, n. B_{11} is given in units of scaled strain and B_{113} in units of scaled strain per average radius. The solid lines are approximations for which the linear terms of the equivalent misfit strain of each particle are retained. The broken lines refer to the approximation for which the equivalent misfit strain is assumed constant in all particles except the one of interest.

Figure 2 illustrates how elastic stresses affect the spatial dependence of the equilibrium matrix composition evaluated at the interface for the particle considered in Figure 1. Capillary effects are not included, and the fifty nearest neighbors ($n = 50$) were used in determining the equivalent misfit strains. The interfacial position is chosen by first making a planar cut in an arbitrary direction through the center of the particle and then parametering by an angle, ϕ, with $0 \le \phi \le 2\pi$. Solid and broken lines refer to the first-order and limited first-order approximations, respectively, as in Figure 1. The dotted line represents a quasi-limited approximation, for which only the q nearest particles ($q < n$ in general and $q = 1$ in Figure 2) are allowed to have misfit strains with linear spatial dependence. For comparison, the shift in the equilibrium matrix composition of an isolated particle owing to the misfit strain is 4.2857×10^{-4} and independent of interfacial position. Thus, the shifts in matrix composition at the interface resulting from particle interactions are about 20 pct of the shift due to the misfit strain alone in this example.

The first-order and limited first-order approximations

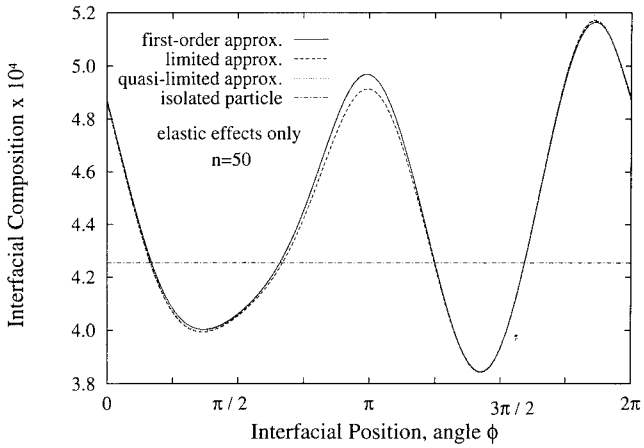


Fig. 2—The spatial dependence of the interfacial compositions for the precipitate considered in Fig. 1. The error associated with the limited first-order approximation is typical of that encountered for many different systems and materials parameters.

predict approximately the same compositional shifts along the interface. Only at the peak position, $\phi \approx \pi$, does the first-order approximation give more than a 1 pct higher value in the composition. The quasi-limited approximation in Figure 2, calculated with $q = 1$, is barely distinguishable from the first-order approximation. This also is true for higher values of q. Again, this behavior is typical of many different effective volume fractions, particle distributions, and degrees of elastic heterogeneity. In much of what follows, we therefore employ the limited first-order approximation to investigate the influence of elastic inhomogeneity, effective volume fraction, and the number of nearest-neighbor particles on the equivalent misfit coefficients and interfacial compositions.

Figures 3(a) and (b) show the influence of the effective volume fraction and the number of interacting particles, n, on the magnitudes of the Taylor coefficients of the equivalent misfit strain, B_{12} and B_{123}, respectively. (Both of these coefficients vanish for the isolated particle.) A random dispersion of hard particles with an effective volume fraction of 10 pct was first generated. Systems possessing lower volume fractions of particles were obtained from this distribution by increasing the interparticle distances while keeping the distribution geometrically similar. The particles are elastically harder than the matrix, and the Taylor coefficients are calculated for a particle located near the center of the system, using the limited first-order approximation.

In Figure 3(c), the scaled difference between the Taylor coefficient, $B_{12}(n)$, for n interacting neighbors and its value for 200 interacting neighbors, $B_{12}(200)$, is plotted as a function of n for the four volume fractions considered in Figure 3(a). There is a clear convergence of the Taylor coefficient and a scaling behavior, as the curves from all four effective volume fractions overlap. The zeroth-order coefficients ($B_{ij} - B_{ij}(0)$) scale proportional to the volume fraction, whereas the first-order coefficients, B_{ijk}, scale proportional to the 4/3 power of the volume fraction. The other zeroth-order coefficients converge at about the same rate as B_{12}, while the first-order terms converge much more rapidly; *i.e.*, the relative error associated with a first-order coefficient is much less for a given number of interacting particles than the error associated with a zeroth-order term. For example, if we define the point of acceptable convergence as that value of n for which a Taylor coefficient deviates by less than 5 pct of its value at $n = 200$, then B_{12} converges by $n \approx 75$, whereas B_{123} converges by $n < 20$.

A more important criterion for the intended coarsening

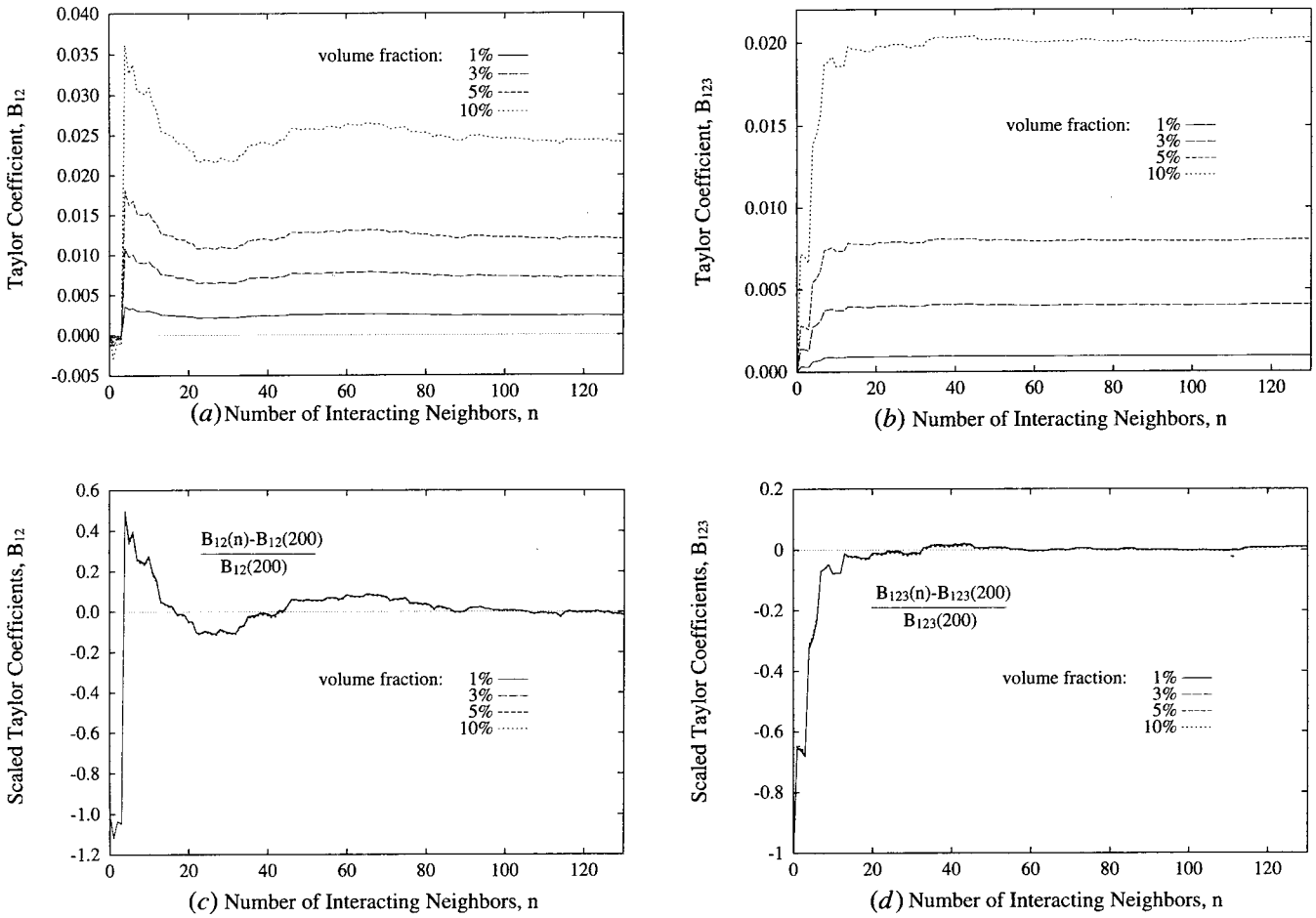


Fig. 3—The dependence of the Taylor coefficients, B_{12} and B_{123}, on the number of elastically interacting neighboring particles is depicted for four effective volume fractions in (*a*) and (*b*), respectively, while their relative error with respect to 200 interacting particles is shown in (*c*) and (*d*). The units of the Taylor coefficients are as in Fig. 1.

simulations is the convergence of the interfacial compositions. This convergence is illustrated in Figures 4(a) through (d) for the same system of particles and four effective volume fractions treated in Figure 3. The nondimensional matrix composition evaluated at the interface is plotted as a function of interfacial position. The interfacial compositions were obtained using the limited first-order approximation with $n = 0$, 3, 10, 50, and 200 interacting neighbors. The nondimensional interfacial composition for an isolated particle ($n = 0$) is given by the horizontal line. The spatial dependence of the interfacial compositions already is strongly determined by the particle's closest neighbors ($n = 3$).

In the present example, the second and third nearest neighbors to the particle considered possess a radius about half that of the nearest neighbor. Since the elastic field of a particle is proportional to a^3/r^3, where a is the radius of the strain-inducing particle and r is the distance to the point at which the strain is to be calculated, the influence of the second and third nearest neighbors on the strain state of the particle of interest is only about one-tenth that of the contribution of the nearest neighbor. The curve for $n = 3$ therefore also is representative of the composition field calculated by considering only one interacting neighbor in the determination of the equivalent transformation strain. In this example, the nearest particle induces a large maximum in the interfacial composition at the point ($\phi \approx 3\pi/2$) which is closest to the interacting particle and a smaller double maximum at the opposite side of the particle ($\phi \approx \pi/2$). Thus, the large maximum is located where the induced strain is the largest, and the smaller double maximum is located where the induced strain is the lowest.

Accounting for additional nearest-neighbor interactions in the determination of the equivalent misfit strains results in minor shifts in the positions as well as the heights and depths of the maxima and minima in the interfacial compositions from the approximation $n = 3$. The convergence behavior is not significantly affected by the effective volume fraction of particles. However, an increase in the volume fraction enhances the compositional variations along the interface arising from particle interactions. When the volume fraction is increased by a factor of 10, from 1 pct to 10 pct, the deviation in interfacial composition from that of the isolated particle increases by a factor of about 35. Furthermore, the relative heights of different maxima are increased, and the angular positions of the extrema are shifted slightly.

These changes in the relative heights and positions of the extrema in the interfacial compositions arise from the nonscaling of particle center-interface distances in the

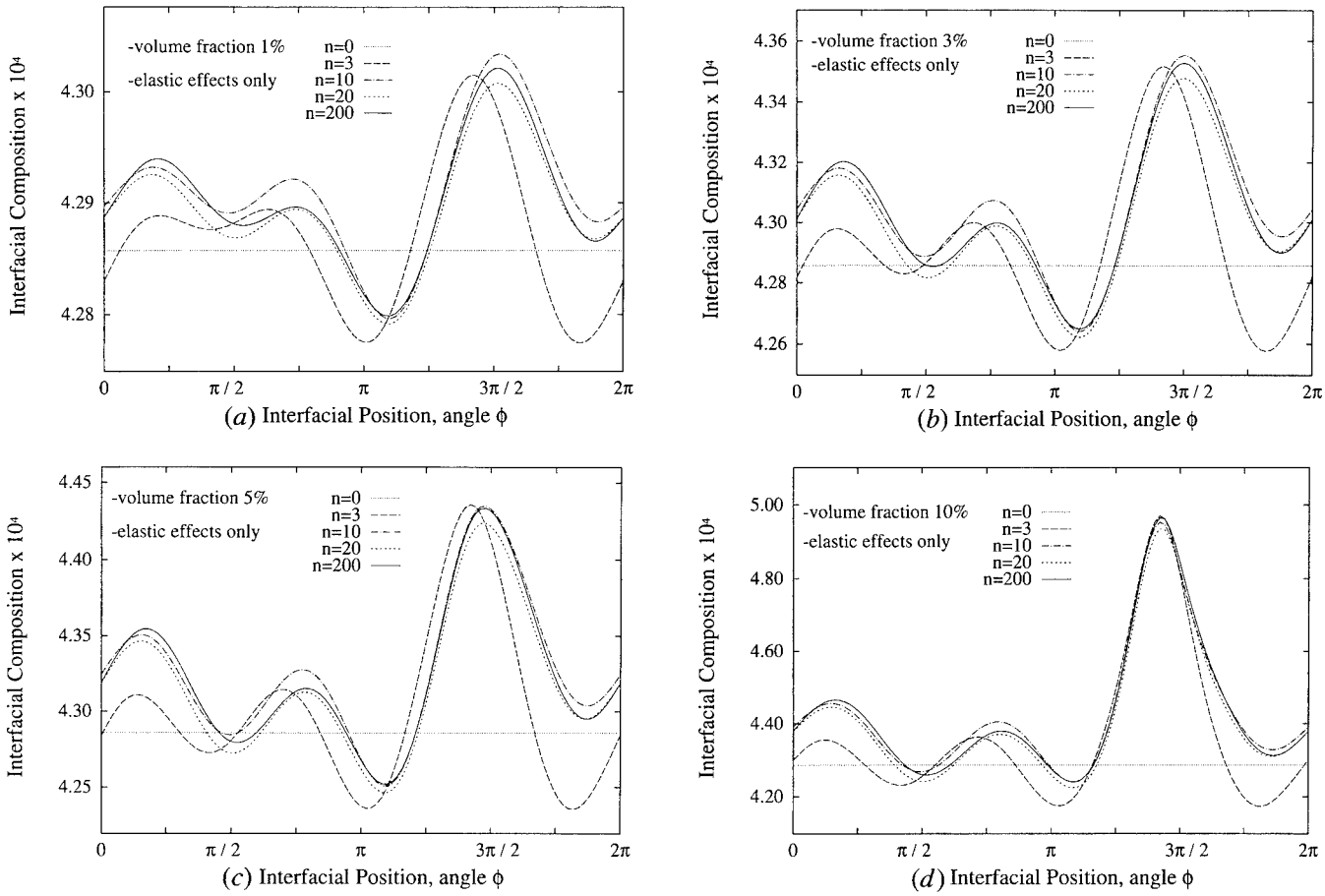


Fig. 4—The spatial variations of the nondimensional interfacial composition due to elasticity are plotted for the particle and the volume fractions of Fig. 3 for several nearest-neighbor approximations. Interfacial positions are chosen and parameterized as in Fig. 2. The position-independent shift in the interfacial composition of an isolated particle, $n = 0$, is given by the horizontal line. Note the changing scale with increasing effective volume fraction.

system. Increasing the volume fraction reduces interparticle distances (measured from center to center) by a constant factor. However, the factor describing the change in interface-particle center separation of two neighboring particles depends on the interfacial position. For increasing volume fraction, it is smallest for the point closest (position of the large maximum) and largest for the point farthest away (position of the smaller double maximum) from the strain-inducing particle. Since the leading term of the induced strain field is proportional to $1/r^3$, the primary maximum increases faster with volume fraction than the secondary, thus changing their relative heights. This effect is most pronounced for the closest particles. The overall composition already is dominated by the closest particles. Decreasing the interparticle distances (increasing the volume fraction) further enhances the influence of the closest neighbors on the position of the major maximum. Including more neighboring particles in the determination of the interfacial composition leads to smaller shifts in the position of the primary maximum. Thus the final ($n = 200$) position of the primary maximum in Figure 4(d), coincides with that for $n = 3$.

The convergence behavior of the Taylor coefficients and interfacial compositions is similar for both elastically soft and hard precipitates. This is illustrated in Figure 5, where the nondimensional interfacial composition has been plotted as a function of interfacial position for several values of n. The same system of particles and particle of interest have been used as in Figure 4(c), except that the elastically hard particles of Figure 4(c) have been replaced by soft particles. The interfacial composition for an isolated particle ($n = 0$) in the absence of capillarity is 3.6×10^{-4}. The variations of the interfacial composition due to the influence of neighboring precipitates are highly correlated to those of Figure 4(c). The relationship between the two is approximately given by

$$\Delta G^s(\mathbf{x}) \approx -\frac{G^s(n=0)}{G^h(n=0)}\Delta G^h(\mathbf{x}) \qquad [25]$$

where $\Delta G(\mathbf{x})$ is the deviation of $G(\mathbf{x})$ from its value, $G(n = 0)$, without neighbor interaction, and the superscripts "s" and "h" refer to elastically soft and hard particles, respectively.

The influence of an applied elastic field on the nondimensional matrix composition evaluated at the interface is shown in Figure 6. Both the particle examined and the system of particles employed are identical to those used in Figure 4(c). In addition to the misfit strain, a nondimensional, uniaxial tensile stress of $T = 10^{-5}$ has been applied to the system. The direction of the applied stress intersects the particle at $\phi = \pi/2$ and $\phi = 3\pi/2$. The interfacial composition owing to the misfit strain and applied stress for an isolated particle ($n = 0$) is given by the line of small dots and possesses minima at points coinciding with the direction of the applied stress and maxima along directions perpendicular to it. The nondimensional composition is represented by a cosine of period π with an amplitude of approximately 2.4×10^{-6} and median value 4.171×10^{-4}. Thus, the median composition has been shifted to a smaller value by the applied stress and no longer is spatially constant. The inclusion of nearest-neighbor interactions in the determination of the equivalent transformation strain results in an interfacial composition profile that is qualitatively similar to that depicted in Figure 4(c). However, the positions and magnitudes of the maxima and minima in the interfacial compositions are shifted in comparison to Figure 4(c), where no applied stress is present. The convergence behavior of the Taylor coefficients and interfacial composition are not affected by the presence of an applied field.

IV. DISCUSSION

We tested the numerical code by calculating the stress concentration due to two spherical cavities subject to a uniform applied stress field ($\sigma^a_{11} = \sigma^a_{22} = \sigma^a_{33}$) and compared our results to the exact values of Sternberg and Sadowsky.[21] The stress values we calculated with the first-order equivalent inclusion method deviated by less

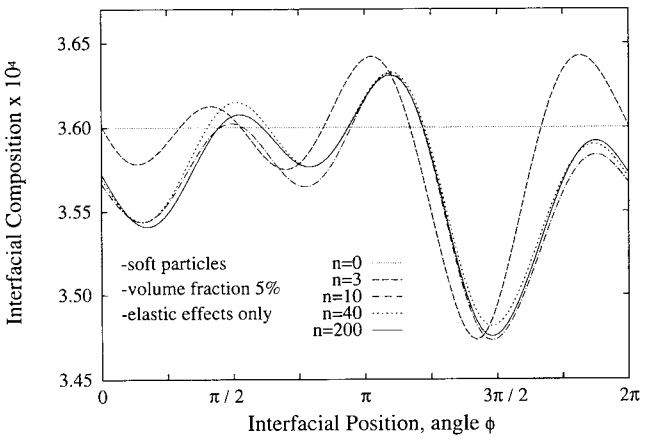


Fig. 5—The spatial dependence of the interfacial composition owing to elasticity is depicted for a distribution of soft particles. The particle examined and the distribution of particles used are identical to those employed in Fig. 4(c).

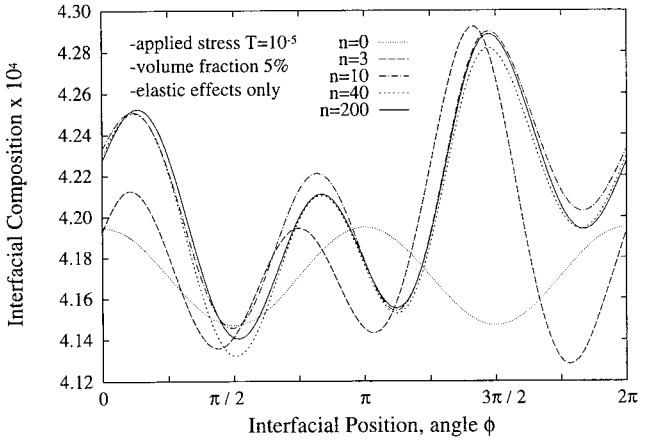


Fig. 6—The spatial variations of the nondimensional interfacial composition due to both misfit strain and an applied, uniaxial tensile stress are depicted. The distribution of hard particles is identical to that used in Fig. 4(c).

than 1 pct of the applied stress from the exact values. Moschovidis and Mura[16] used the same problem to check their implementation of the equivalent inclusion method. Our values deviate slightly from theirs and are sometimes, but not always, closer to the exact values of Sternberg and Sadowsky. We therefore also checked our code against an analytical formula for the equivalent misfit strain.[22] The formula applies to two misfitting spherical particles which possess slightly different elastic constants than the matrix and is correct up to second order in the differences in the elastic constants. Our result always were identical to those following from this formula up to the predicted accuracy. This meant coincidence up to six significant digits in the case of small differences in the elastic constants. We therefore believe that our implementation of the equivalent inclusion method is correct.

The first-order approximation to the equivalent inclusion method assumes that the actual strain field is adequately represented by the strain field due to precipitates with a linear spatial dependence of the equivalent misfit strains. This is a reasonable approximation for ellipsoidal particles, so long as the applied strain field can be represented as a polynomial of order one and the higher-order derivatives of $D^{p'}_{ijkl}$ and $D^{p'}_{ijklm}$ evaluated at $(\mathbf{d}^{p} - \mathbf{d}^{p'})$ are sufficiently small. The second criterion is more difficult to satisfy as the effective volume fraction increases, but the higher-order derivatives of $D^{p'}_{ijkl}$ and $D^{p'}_{ijklm}$ do not diverge since $|\mathbf{d}^{p} - \mathbf{d}^{p'}|$ has a lower bound due to the nonoverlapping of the particles. The equivalent inclusion method also has been applied to isolated cuboidal heterogeneities.[23] Unlike isolated ellipsoidal particles, the equivalent misfit strain is a function of position for the cuboids even when the applied stress and misfit strain are constant. In the case of an isolated cuboid with constant dilatational misfit strain, the strain field calculated using the second-order terms was in good agreement with the strain field calculated using a second-order Taylor expansion of Eq. [3].[23] The equivalent inclusion method was found to give the better results near the cube edges and in the case of large differences in the shear moduli.

The strain fields calculated using the limited first-order approximation, for which the equivalent misfit strain of each neighboring particle is assumed to be spatially constant while that of the particle of interest possesses a linear dependence, have been shown to differ only slightly from the fields calculated using the first-order approximation. In systems with many particles, the limited first-order approximation offers a significant computation advantage, since it reduces the number of unknowns to be determined from $24N$ to $6N + 18$.

The differences between the first-order and limited first-order approximations are reduced when, in addition to the particle of interest, its q nearest neighbors also are assumed to possess equivalent misfit strains with a linear spatial dependence. The number of nearest neighbors required for the quasi-limited approximation, q, depends on the local configuration and relative sizes of the particles but is generally small.

We have shown that the number of neighbors to be included in the calculation of the equivalent misfit strain of a particle is independent of volume fraction, sign of the elastic inhomogeneity, and applied fields. The number of neighbors needed for the determination of the zeroth-order Taylor coefficients of the equivalent misfit strains ($n \approx 75$) is significantly larger than for the first-order coefficients ($n < 20$). This also is consistent with the small number of neighbors, q, needed in the quasi-limited approximation.

The interfacial compositions presented obtain for systems in which capillary effects are negligible; *i.e.*, the particles are very large compared to the capillary length used to nondimensionalize the variables. For effectively smaller particles, the spatial dependence of the interfacial compositions will be correspondingly smaller in comparison to the (uniform) interfacial composition shift resulting from capillarity. This means that the elastic effects become progressively more important as the absolute size of the particles increases. The actual particle size at which the elastic effects become important depends upon the material parameters.

V. SUMMARY

An equivalent inclusion method was used to calculate the stress field engendered by a distribution of misfitting, spherical particles in an infinite matrix subjected to an externally applied elastic field. Particles and matrix can possess different elastic constants. The stress field then was used to calculate the diffusional boundary conditions necessary to perform coarsening simulations in elastically stressed systems. We conclude that:

1. The Taylor coefficients for the equivalent misfit strain converge with increasing number of nearest-neighbor interactions for a random distribution of particles. The zeroth-order coefficients are the slowest to converge, and the convergence is independent of the effective volume fraction of the system.
2. The primary topological features and magnitude of the interfacial composition are determined by a relatively small number of nearest neighbors.
3. The zeroth-order Taylor coefficients scale proportional to the volume fraction, while the first-order coefficients scale proportional to the 4/3 power of the volume fraction.
4. The equivalent inclusion method should be computationally viable for determining elastic fields and diffusional boundary conditions for the coarsening simulations.
5. Particle interactions are expected to influence strongly the local coarsening behavior.

ACKNOWLEDGMENT

We are indebted to the Division of Materials Science at the Department of Energy through Grant DE-FG05-93ER45507 for their support of this work.

REFERENCES

1. A.J. Ardell, R.B. Nicholson, and J.D. Eshelby: *Acta Metall.*, 1966, vol. 14, pp. 1295-1309.
2. D.M. Barnett, J.K. Lee, H.I. Aaronson, and K.C. Russell: *Scripta Metall.*, 1974, vol. 8, pp. 1447-50.

3. A.G. Khachaturyan and V.M. Airapetyan: *Phys. Status Solidi A*, 1974, vol. 26, pp. 61-70.
4. W.C. Johnson and J.W. Cahn: *Acta Metall.*, 1984, vol. 32, pp. 1925-33.
5. H. Nishimori and A. Onuki: *Phys. Rev. B*, 1990, vol. 42, pp. 980-83.
6. W.C. Johnson: *Acta Metall.*, 1984, vol. 32, pp. 465-75.
7. K. Kawasaki and Y. Enomoto: *Physica A*, 1988, vol. 150, pp. 463-98.
8. Y. Enomoto and K. Kawasaki: *Acta Metall.*, 1989, vol. 37, pp. 1399-1406.
9. W.C. Johnson, T.A. Abinandanan, and P.W. Voorhees: *Acta Metall.*, 1990, vol. 38, pp. 1349-67.
10. P. Leo, W.W. Mullins, R.F. Sekerka, and J. Viñals: *Acta Metall. Mater.*, 1990, vol. 38, pp. 1573-80.
11. A. Onuki and H. Nishimori: *Phys. Rev. B*, 1991, vol. 43, pp. 13649-652.
12. Y. Wang, L.-Q. Chen, and A.G. Khachaturyan: *Phys. Rev. B*, 1992, vol. 46, pp. 11194-97.
13. T.A. Abinandanan and W.C. Johnson: *Acta Metall. Mater.*, 1993, vol. 41, pp. 17-25.
14. T.A. Abinandanan and W.C. Johnson: *Acta Metall. Mater.*, 1993, vol. 41, pp. 27-39.
15. J.D. Eshelby: *Proc. R. Soc. London A*, 1957, vol. 241, pp. 376-96.
16. Z.A. Moschovidis and T.A. Mura: *J. Appl. Mech.*, 1975, vol. 42, pp. 847-52.
17. T. Mura: *Micromechanics of Defects in Solids*, 2nd ed., Martinus Nijhoff Publishers, Dordrecht, The Netherlands, 1987.
18. F.C. Chen and K. Young: *J. Math. Phys.*, 1977, vol. 18, pp. 1412-16.
19. W.C. Johnson, Y.Y. Earmme, and J.K. Lee: *J. Appl. Mech.*, 1980, vol. 47, pp. 775-80.
20. P.W. Voorhees and W.C. Johnson: *J. Chem. Phys.*, 1986, vol. 84, pp. 5108-21.
21. E. Sternberg and M.A. Sadowsky: *J. Appl. Mech.*, 1952, vol. 19, pp. 19-27.
22. W.C. Johnson, P.W. Voorhees, and D. Zupon: *Metall. Trans. A*, 1989, vol. 20A, pp. 1175-89.
23. W.C. Johnson, Y.Y. Earmme, and J.K. Lee: *J. Appl. Mech.*, 1980, vol. 47, pp. 781-88.

Kinetic Study of Low-Temperature Transient Liquid Phase Joining of an Aluminum-SiC Composite

V. SABATHIER, G.R. EDWARDS, and C.E. CROSS

The transient liquid phase (TLP) joining of an aluminum 6061-SiC composite using a gallium interface has been investigated. The observed kinetics of this process suggest that diffusion occurs along interphase and subgrain boundaries at low temperatures (<723 K). An existing TLP model has been modified to account for this behavior.

I. INTRODUCTION

ALUMINUM matrix composites are advanced materials that present unique mechanical, thermal, and electrical properties. These materials can now be tailored to satisfy specific requirements.[1–8] Their high specific strength and modulus, arising from both the reinforcement and an age-hardened matrix, make them especially attractive to aerospace structural applications.[3–8] Discontinuously reinforced aluminum matrix materials are cheaper, nearly isotropic, and readily formable.[1,2,6] However, the joining of aluminum matrix composites remains a key issue limiting the use of these advanced materials.

Joining techniques such as conventional arc-welding methods deteriorate the matrix, the reinforcement particles, and the metal/ceramic interfacial bonds. Similarly, commercially available aluminum brazing materials involve temperatures above 673 K, which degrade the age-hardened matrix. Moreover, liquid brazing alloys infiltrate composites *via* the ceramic/metal interface, resulting in reduced strength.[9] Solid-state bonding (diffusion bonding) requires temperatures and pressures too high to preserve the age-hardening treatment of the matrix and the quality of the ceramic/metal interface.[10,11,12] Furthermore, adhesive bonding produces joints of modest strength and poor thermal and electrical conductivities.[13,14]

The transient liquid phase (TLP) joining technique is considered here for joining aluminum MMCs because it offers potential for higher strength joints than is obtainable with other joining methods. Gallium was selected as a filler metal to take advantage of both the low-temperature melting point eutectic it forms with aluminum and the large solubility of this element in aluminum,[15–20] as shown in the phase diagram of Figure 1. High solid-state solubility of gallium in aluminum is important to the engineering integrity of the TLP joints; excess gallium at interphase boundaries would be expected to embrittle the composite. The nature of composites, with numerous high-diffusivity paths such as ceramic/matrix interfaces and dislocation networks, should enhance the kinetics of liquid infiltration. While monolithic alloys can be conditioned to contain high-diffusivity paths for rapid liquid infiltration, the degree of microstructural refinement possible is significantly less than that for metal matrix composites. Thus, the joining of MMCs by liquid infiltration should be accomplished at shorter times and lower temperatures than would be expected for conventional aluminum alloys. In this study, the kinetics of the transient liquid phase joining of an aluminum matrix composite, reinforced with particulate silicon carbide (SiC_p), is characterized and modeled.

V. SABATHIER, Director of Research, is with the Centre National D'Etudes Spatiales, Evry, France. G.R. EDWARDS, Director, and C.E. CROSS, Assistant Professor, are with the Center for Welding and Joining Research, Colorado School of Mines, Golden, CO 80401.

Manuscript submitted August 6, 1993.

II. BACKGROUND

Transient liquid phase joining has been used to produce acceptable bonds in a variety of different materials, including Ni/B/Ni[21] and Ag/Cu/Ag.[22] This technique is a joining process that combines the ease of brazing and the diffusional characteristics of solid-state bonding. As in brazing, the melting of an interlayer or filler metal generates a liquid phase at the joint interface. Unlike brazing, however, the solidification of the liquid filler occurs isothermally under a slight clamping pressure.[23]

At the joining temperature, the interlayer material melts nearly instantaneously. If good wetting occurs, the capillarity force drives liquid into the voids between the two substrates. Then, depending upon the temperature, substrate, and liquid filler material, atomic diffusion of the filler material into the substrate will initiate and control isothermal solidification. The bond ultimately reaches a composition and structure close to that of the base material, thus ensuring continuity at the interface.

Several models have been developed to describe the kinetics of the process. Among them, a model proposed by Sekerka[21,24,25] involves a four-stage mechanism, as depicted in Figure 2.

Stage 1 represents dissolution of the interlayer. This stage is equivalent to homogenization of a film of thickness $2h_0$ and of concentration C_β, where B (interlayer) atoms diffuse into a finite medium of A (matrix) atoms. In effect, the diffusion of B atoms into the matrix induces the formation of a liquid phase at the concentration $C_{l\alpha}$, as shown on the hypothetical binary eutectic phase diagram in Figure 3. It should be noted that this stage usually occurs very fast, since the interlayer is normally very thin. Obviously, this stage is not necessary for an interlayer that melts below the joining temperature.

Stage 2 represents homogenization of the liquid phase. Once the interlayer is completely melted, its composition lies within the concentrations $C_{l\beta}$ and $C_{l\alpha}$, as shown

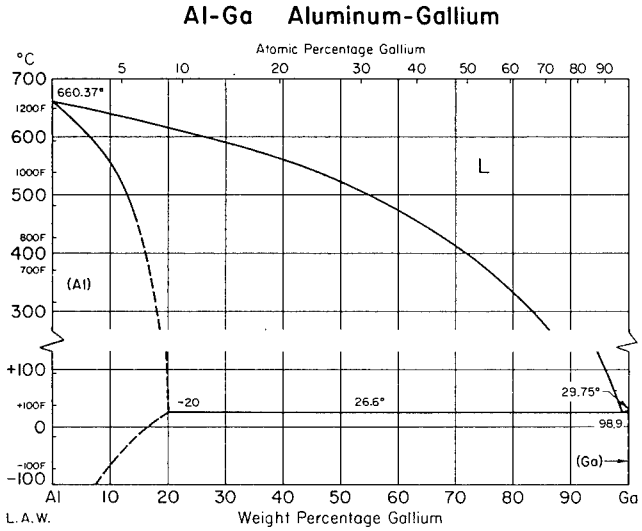


Fig. 1—Aluminum-gallium binary phase diagram.[191]

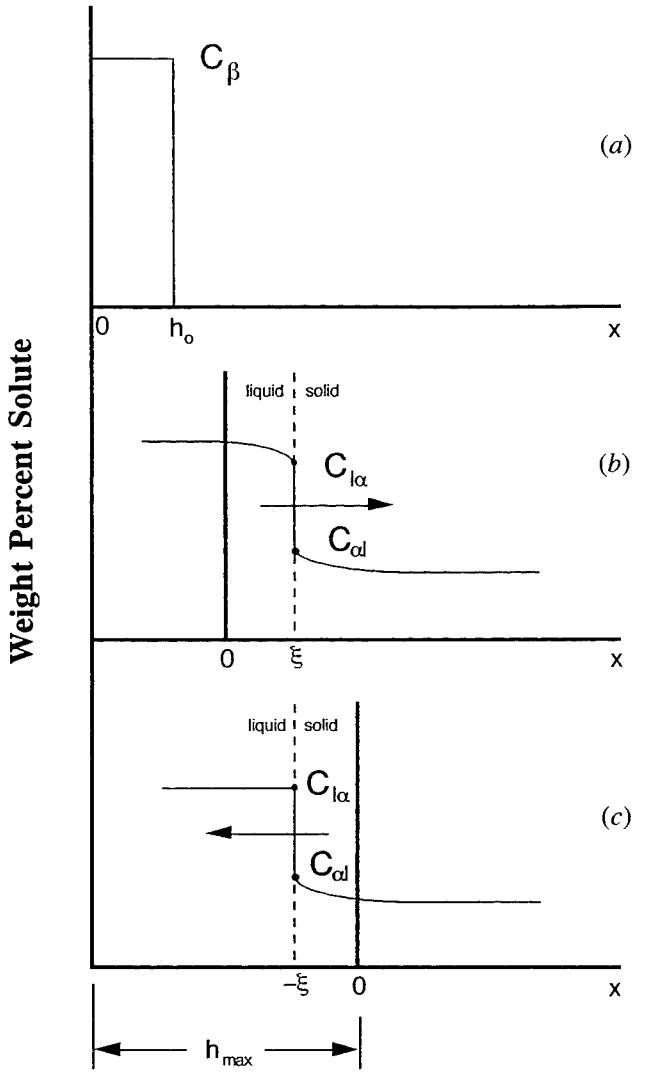


Fig. 2—Schematic representation of original TLP model showing solute concentration profiles for (*a*) initial boundary condition in stage 1, (*b*) interface boundary conditions in stage 2, and (*c*) interface boundary conditions in stage 3.

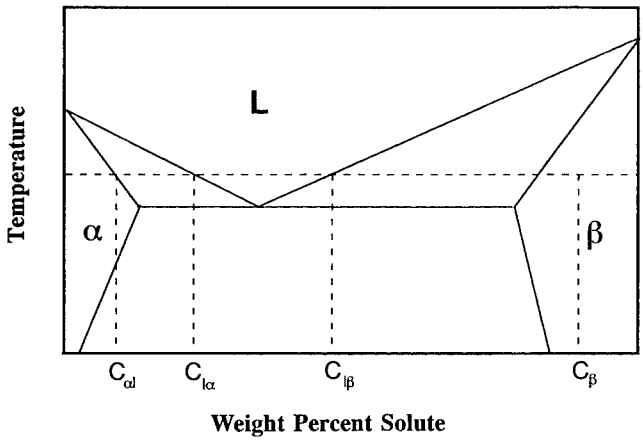


Fig. 3—Phase equilibrium in hypothetical binary eutectic system during isothermal TLP joining.

in Figure 3. Considering the fact that liquid diffusion is very rapid (a typical liquid metal diffusion coefficient is approximately 10^{-3} mm^2/s), it is reasonable to expect that liquid homogenization will occur.

Stage 3 represents isothermal solidification. As *B* atoms continue diffusing into the substrate, solidification occurs as the concentration of the liquid drops below the liquid/solid equilibrium concentration $C_{l\alpha}$ shown in Figure 3. However, stage 3 will take longer than stage 2 because it is controlled by diffusion in the solid phase.

Stage 4 involves classical homogenization and deals with diffusion in the solid only. The solution to this final stage assumes a layer of a given thickness at a concentration $C_{\alpha l}$, present at the interface at the end of the isothermal solidification (stage 3). Hence, this problem can be considered as the homogenization of a thin film with an exponential solution similar to stage 1. A more thorough description of all four stages is given in the Appendix.

III. EXPERIMENTAL PROCEDURE AND DATA ANALYSIS

A. *Experimental Procedure*

The composite material evaluated in this investigation was 6061 aluminum reinforced with 20 vol pct SiC particulates. The average length and aspect ratio of the particulates were found to be 2.6 μm and 1.4, respectively. Specimens measuring 1.0 × 6.3 × 25.4 mm were cut from sheet material. Each specimen was annealed at 673 K for 20 hours, solution treated at 838 K for 1 hour, and water quenched. The lap joint specimen geometry is shown in Figure 4.

Each specimen half was mechanically polished on one side with 240-grit SiC grinding paper and rinsed in acetone for 5 minutes. A liquid, 99.9 wt pct pure gallium interlayer was brushed onto the surfaces to be bonded. Faying surfaces were rubbed against each other to decrease the initial thickness of the interlayer and to achieve a more uniform coating.

Following assembly, specimens were stored on ice to preserve the initial boundary conditions: the gallium interlayer concentration was 100 pct (C_β = 100 pct) and

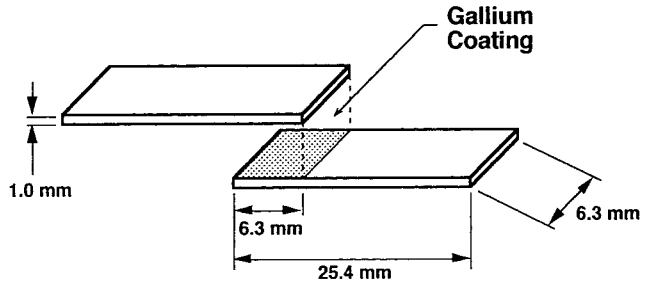


Fig. 4—Geometry of composite substrate and TLP joint.

the substrate contained no gallium (C_α = 0 pct). They were then placed in a furnace preheated to a calibrated joining temperature. The following temperatures were investigated: 423, 473, 523, 573, 623, 673, 773, and 873 K with holding times of 24 and 48 hours.

Following TLP joining, specimens were sectioned perpendicular to the bond interface and polished. Polishing included grinding from a sequence of 240- to 600-grit silicon carbide paper. Final surface preparation involved polishing with an aqueous 2.0-μm aluminum-oxide suspension, followed with 0.05-μm colloidal silica. Using scanning electron microscopy, X-ray measurements were taken across the bonded interface to obtain gallium concentration profiles for each of the joining temperatures and times.

B. *Data Analysis*

Knowing the initial interlayer concentration C_β allows concentration profiles to be used to determine the initial interlayer thickness. Conservation of matter yields

$$C_\beta h_0 = \int_0^{+\infty} C(x, t)dx \qquad [1]$$

where the integrand of this equation represents the area below the concentration profile. Concentration profiles for bonding temperatures ranging from 873 to 423 K were used to determine h_0 values given in Table I.

Applying the Sekerka[24] model to this study leaves the system with boundary conditions equivalent to a thin film of width $2h_1$ and concentration $C_{l\alpha}$, because the first two stages of the Sekerka model (interlayer dissolution and liquid homogenization) require very little time for completion. The final two stages are controlled by solid-state interdiffusion; consequently, the concentration profile can be described by a thin film solution similar to Eq. [A2]. Hence, the logarithm of concentration at constant time should be a linear function of the distance squared:

$$\ln C(x) = B - \frac{x^2}{4 D_{app} t} \qquad [2]$$

If the concentration profiles are plotted on a semilog plot, for a given time, the slope of the resulting line should yield the apparent diffusion coefficient (D_{app}). Such results are plotted in Figures 5 through 12.

For temperatures above 673 K, a single line can be drawn as predicted by the Sekerka[24] model and a lattice

Table I. Experimentally Determined Values for Apparent Diffusivity and Critical Half-Thicknesses

T (K)	t (h)	D_{app} (mm^2/s $\times$ 10^{-2})	h_0 (μm)	h_{exp} (μm)
873	24	3.10^{-8}	—	—
773	24	5.10^{-9}	—	—
673	24	3.10^{-10}	—	—
623	48	7.10^{-10}	21	264
623	24	8.10^{-10}	13.5	190
573	48	2.10^{-10}	13	164
573	24	4.10^{-10}	16.8	216
573	24	2.10^{-10}	16.2	228
573	48	4.10^{-10}	17.5	245
523	24	1.10^{-9}	17	187
523	24	2.10^{-11}	1.7	—
523	48	2.10^{-11}	4.5	51
523	52	4.10^{-10}	15	184
473	48	4.10^{-11}	5.9	63
473	24	9.10^{-11}	8	81
423	48	7.10^{-10}	25	291
423	24	2.10^{-11}	3.1	40
423	24	5.10^{-11}	9.6	96

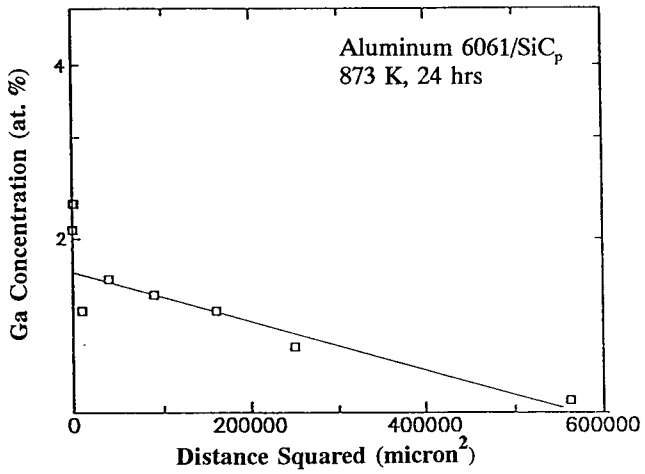


Fig. 5—Penetration of gallium into a 6061 Al/10 (vol pct) SiC$_p$ composite in 24 h at 873 K.

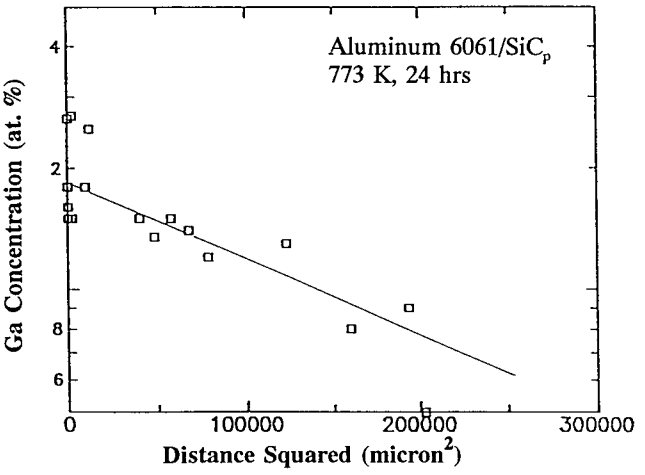


Fig. 6—Penetration of gallium into a 6061 Al/20 (vol pct) SiC$_p$ composite in 24 h at 773 K.

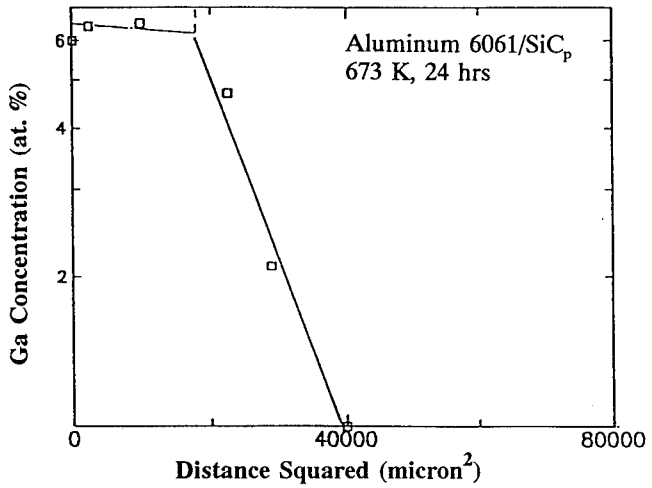


Fig. 7—Penetration of gallium into a 6061 Al/20 (vol pct) SiC_p composite in 24 h at 673 K.

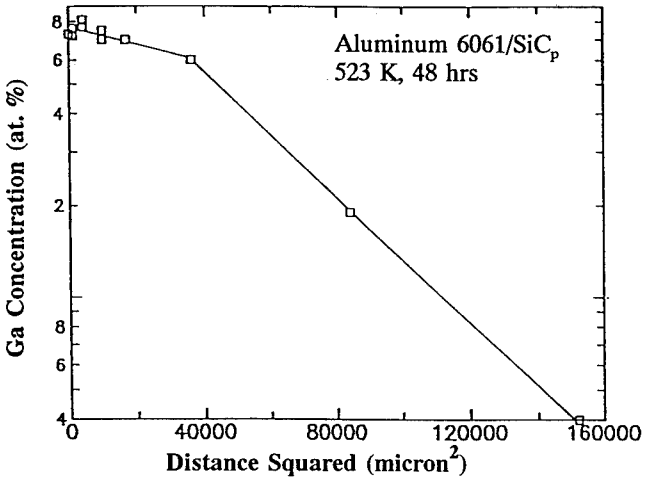


Fig. 10—Penetration of gallium into a 6061 Al/20 (vol pct) SiC_p composite in 24 h at 523 K.

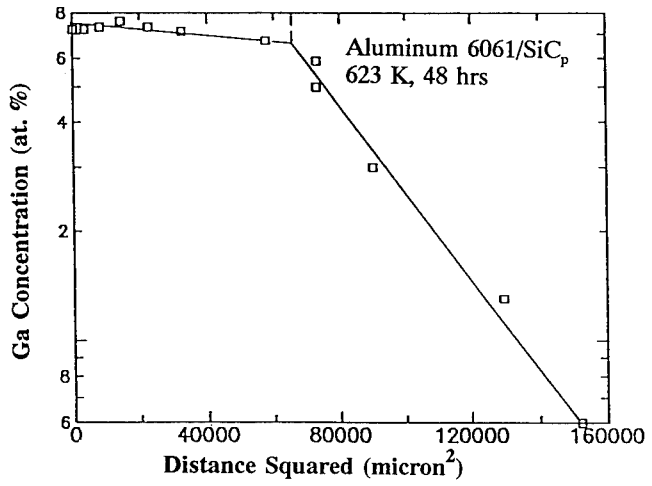


Fig. 8—Penetration of gallium into a 6061 Al/20 (vol pct) SiC_p composite in 48 h at 623 K.

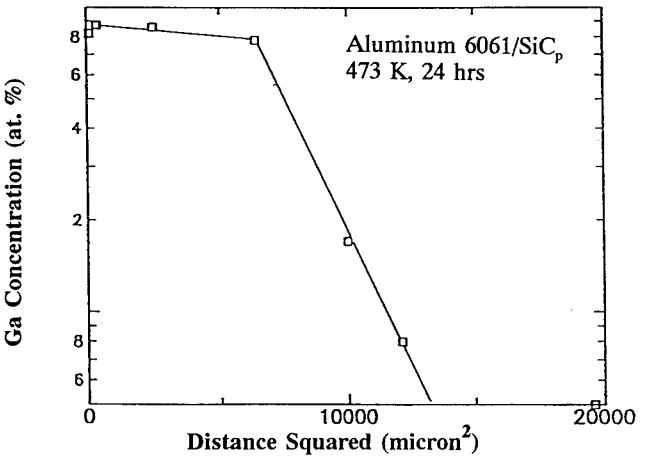


Fig. 11—Penetration of gallium into a 6061 Al/20 (vol pct) SiC_p composite in 24 h at 473 K.

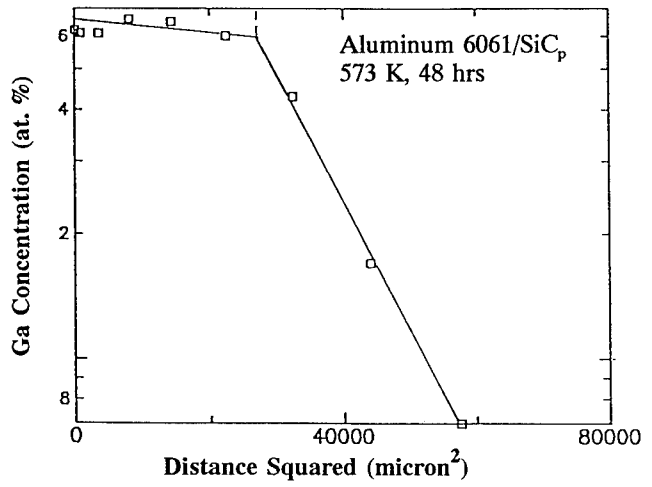


Fig. 9—Penetration of gallium into a 6061 Al/20 (vol pct) SiC_p composite in 24 h at 573 K.

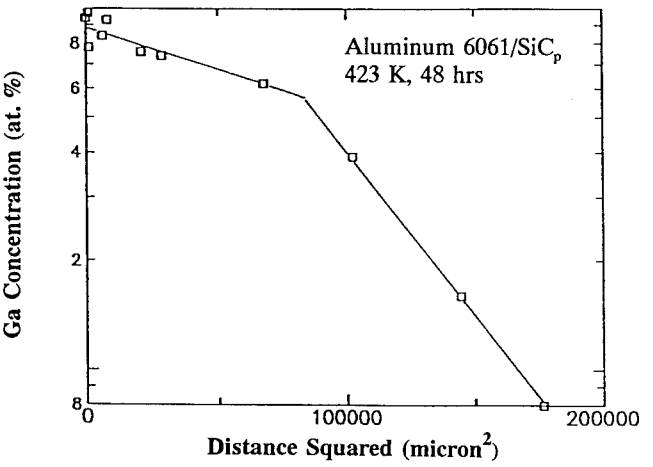


Fig. 12—Penetration of gallium into a 6061 Al/20 (vol pct) SiC_p composite in 48 h at 423 K.

diffusion coefficient can be determined. For temperatures below 673 K, a transition occurs at a characteristic distance h_{exp} from the interface where two distinct lines intersect. Apparent diffusion coefficients were determined by considering only the linear part of the semilog plots at distances above h_{exp}, as will be discussed later. Table I shows, for each time and temperature, the calculated apparent diffusion coefficients.

Once a diffusion coefficient is known for a wide range of temperatures, it is possible to present the data using an Arrhenius plot, as shown in Figure 13. For all temperatures (except 523 K, where a large variance existed and the average was considered), the maximum experimental values of diffusion coefficient were used to generate this plot. The bilinearity of the Arrhenius plot is apparent with a marked change of slope around 723 K. For the lowest temperatures, an activation energy of 35 kJ/mol was calculated. This low value cannot be indicative of lattice diffusion, but must be related to short-circuit diffusion. The high-diffusivity path transport is the dominant mechanism up to relatively high temperatures (723 K), which reveals that the density of short-circuit paths for diffusion is high. The pre-exponential term (D_0) has been measured and determined to be 5.10^{-5} mm^2/s.

For the highest temperatures, an activation energy of 120 kJ/mol and a pre-exponential term of 250 mm^2/s have been measured. This activation energy is close to the 122 kJ/mol value reported for impurity diffusion of gallium in aluminum.[26] It should be noted that the apparent activation energy for low temperatures is less than one third of the value of lattice diffusion.

IV. REVISED TLP MODEL

The transition in slope in the semilog plots (Figures 7 through 12) reveals the existence of a change in kinetic mechanism for TLP joining. The effect of liquid diffusion and the special nature of the composite material must be considered to understand this unexpected behavior. Numerous researchers have reported accelerated aging kinetics for Al-SiC composites,[27–30] citing high dislocation density as being responsible for enhanced atomic transport during precipitation. These dislocations were observed to form around particulates upon quenching from solution treatment, presumably due to an order of magnitude difference in thermal expansion between matrix and reinforcement. Dislocation networks have also been found to decorate the spaces between particles, forming submicron subgrains.[26] Because it is well established that gallium will rapidly penetrate the grain boundaries of aluminum,[23,31–34] it is reasonable to assume that interphase and subgrain boundaries in composites will behave in a similar manner. The revised three-stage TLP model described below incorporates short-circuit boundary infiltration.

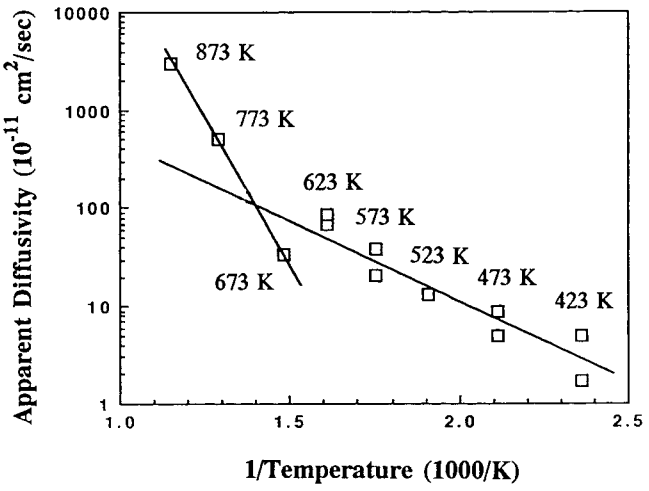


Fig. 13—An Arrhenius analysis showing the relationship between apparent diffusion coefficient (D_{app}) and TLP joining temperature. The change in slope indicates a change in transport mechanisms below 723 K.

A. *Stage 1: Liquid Infiltration*

Stage 1 of the original model does not exist in the revised model, since gallium melts at 302 K and is thus liquid at the joining temperature. Stage 1 of the revised model involves the infiltration of liquid gallium into the composite. This liquid phase is assumed to diffuse along all short circuit paths (*i.e.*, subgrain boundaries) and infiltrate the substrate over a distance h_1. Infiltration stops when the liquid source located at the interface is depleted. Because these subgrains are small and surrounded by the gallium-rich liquid phase, they are assumed to be homogenized at the equilibrium concentration $C_{\alpha l}$ during this first stage.

1. *Liquid flux*

Penetration distance (ξ) of liquid into the subgrain boundaries is expected to vary as a function of time:

$$\xi(t) = 2\gamma\sqrt{D_l t} \qquad [3]$$

where the origin of time is chosen to be that moment when the interlayer is completely melted. The term γ is a growth constant given in Table II for the aluminum-gallium system at temperatures ranging from 423 to 623 K.

The derivative of Eq. [3] gives

$$\frac{\partial \xi}{\partial t} = \gamma\sqrt{D_l/t} \qquad [4]$$

where

$$t = \frac{\xi^2}{4\gamma^2 D_l} \qquad [5]$$

As liquid advances along the boundary, a small amount of aluminum is dissolved at the penetration front and is assumed to be homogenized within the liquid very quickly. Liquid penetration at an arbitrary time t is shown schematically in Figure 14.

If it is assumed that the width of the liquid film (δ) at the boundary is constant, it is possible to estimate the flux of liquid in the boundary:

$$J_x(\xi) = \frac{\partial \xi}{\partial t} C_{l\alpha} \qquad [6]$$

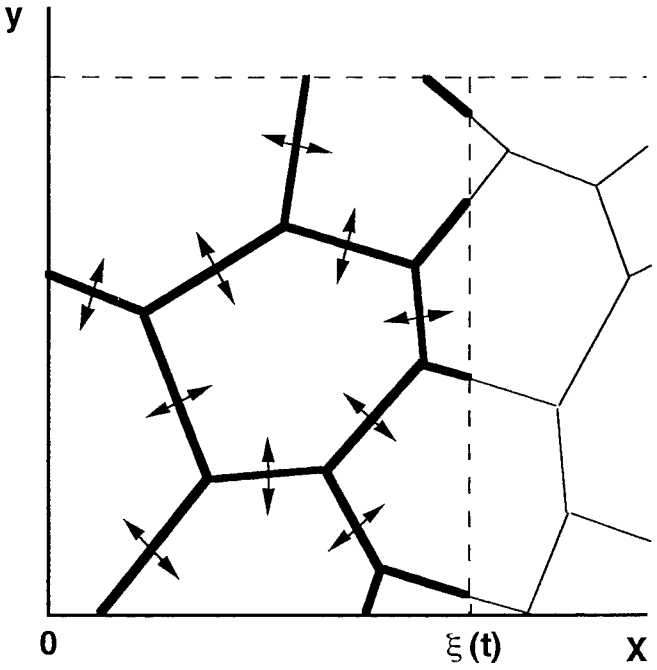


Fig. 14—Schematic diagram illustrating gallium penetration into the composite *via* subgrain boundaries during stage 1.

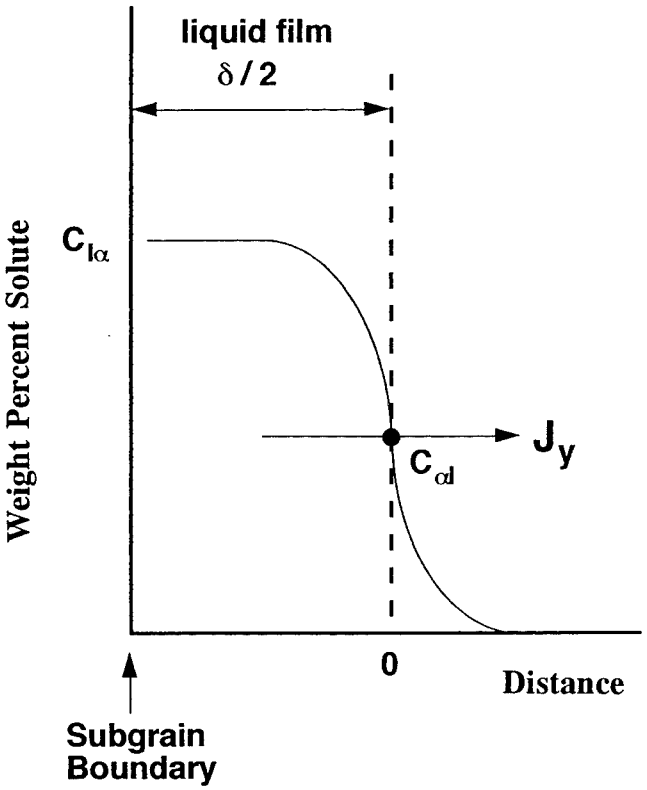


Fig. 15—Schematic showing the gallium concentration profile at a subgrain boundary.

2. *Subgrain diffusion*

At this point, every subgrain at a position $x < \xi(t)$ is completely surrounded by a liquid film. A one-dimensional diffusion model can be used to describe diffusion into the subgrains (y direction) with the following boundary conditions:

$$C(y, 0) = 0 \qquad [7a]$$

$$C(0, t) = C_{\alpha l} \qquad [7b]$$

$$C(\infty, t) = 0 \qquad [7c]$$

An error function can be used to describe the concentration profile through a subgrain as shown in Figure 15. At the liquid/matrix interface, the concentration will remain equal to $C_{\alpha l}$, if equilibrium is assumed. Hence, the concentration profile is

$$C(y, \tau) = C_{\alpha l} \operatorname{erfc}\left(\frac{y}{2\sqrt{D_s \tau}}\right) \qquad [8]$$

where τ is the time a subgrain spends in equilibrium with the liquid. This residence time is, of course, a function of the distance x from the interface, so that the concentration profile becomes a function of both x and y. For Eq. [8] to be valid, the diffusion distance must be a small fraction of the subgrain size.

3. *Correction for liquid residence time*

The relationship between x and τ must be found. The conservation of matter in a portion dx of liquid film of width δ can be written[135]

$$\frac{\partial C}{\partial t} = \frac{\partial J_x}{\partial x} + \frac{2}{\delta} J_y \qquad [9]$$

If the maximum infiltration distance in the boundary is h_1, then the time $\tau(x)$ spent in equilibrium with the matrix for $x < h_1$ can be determined using Eq. [5],

$$\tau(x) = \tau(h_1) - t(x) = \frac{h_1^2 - x^2}{4\gamma^2 D_l} \qquad [10]$$

This expression for residence time can be substituted into Eqs. [4] and [6] to obtain an expression for flux, which is also described using Fick's first law:

$$J_y = -D_s \frac{\partial C}{\partial y}(y = 0) = \gamma^2 \delta \frac{D_l C_{l\alpha}}{h_1^2 - x^2} \qquad [11]$$

where $y = 0$ defines the matrix/liquid interface. From Eq. [11], it follows that:

$$\frac{\partial C}{\partial y}(y = 0) = -\frac{D_l}{D_s} \gamma^2 \frac{\partial C_{l\alpha}}{h_1^2 - x^2} \qquad [12]$$

but from Eq. [8], it also follows that:

$$\frac{\partial C}{\partial y}(y = 0) = -\frac{C_{\alpha l}}{2\sqrt{D_s \tau}} \qquad [13]$$

Solving for $\sqrt{D_s \tau}$ in Eq. [13] and substituting this back into Eq. [8] yields:

$$C(x, y) = C_{\alpha l} \operatorname{erfc}\left[\gamma^2 \frac{D_l}{D_s} \frac{C_{l\alpha}}{C_{\alpha l}} \frac{\delta y}{h_1^2 - x^2}\right] \qquad [14]$$

Clearly, the use of this equation requires knowledge of the maximum infiltration distance h_1. Section 4 provides a method for determining this parameter.

4. *Maximum infiltration distance*

If the matrix and the liquid phase are homogenized at the equilibrium concentrations $C_{\alpha l}$ and $C_{l\alpha}$, respectively, a solute balance provides a solution for the maximum infiltration distance. If X_l is the volume fraction of the liquid phase, the conservation of matter can be written as

$$C_\beta h_0 = [X_l C_{l\alpha} + (1 - X_l) C_{\alpha l}] h_1 \qquad [15]$$

As a first approximation, assume $X_l \ll 1$, so that the maximum penetration distance can be evaluated from Eq. [15]:

$$h_1 = h_0 \frac{C_\beta}{X_l(C_{l\alpha} - C_{\alpha l}) + C_{\alpha l}} \approx h_0 \frac{C_\beta}{C_{\alpha l}} \qquad [16]$$

The maximum infiltration distance is thus related to the initial concentration and thickness of the interlayer. The time necessary to complete stage 1 can be found using Eqs. [5] and [16]:

$$t(h_1) = \frac{\left(\frac{C_\beta}{C_{\alpha l}}\right)^2 h_0^2}{4\,\gamma^2\, D_l} \qquad [17]$$

Because this stage is controlled by the diffusion in the liquid phase, it is very rapid. If the conditions $D_l = 10^{-3}$ mm^2/s and $h_0 = 10$ μm are assumed, and the equilibrium concentrations (from the equilibrium phase diagram shown in Figure 1) and the dissolution constants (shown in Table II) are used, then t_1 (423 K) = 150 s and t_1 (773 K) = 23.7 s.

B. *Stage 2: Depletion of Solute in the Liquid Phase*

When stage 1 is completed, the substrate on each side of the original interface has the following characteristics:

(a) liquid and solid phase coexist and are in equilibrium over a distance h_1;
(b) the lattice is homogenized at the equilibrium concentration $C_{\alpha l}$;
(c) the liquid is present in subgrain boundaries and interfaces at the equilibrium concentration $C_{l\alpha}$ at vol fraction X_l; and
(d) for distances x greater than h_1, the matrix is gallium free.

Therefore, a large concentration gradient exists at $x = h_1$, which drives gallium atoms into the gallium-free matrix at the beginning of stage 2. This results in a subsequent decrease in gallium concentration in the homogenized lattice for $x < h_1$. Meanwhile, gallium atoms will continue to diffuse from liquid films into adjacent subgrains to make up for the loss of solute atoms diffusing into the gallium-free lattice, thus preserving equilibrium.

Appropriate boundary conditions for the solid state are as follows:

$$C(x > h_1, 0) = 0 \qquad [18a]$$

$$C(h_1, t) = C_{\alpha l} \qquad [18b]$$

$$C(\infty, t) = 0 \qquad [18c]$$

and the appropriate solution to Fick's second law can be written as:

$$C(x, t) = C_{\alpha l} \operatorname{erfc}\left[\frac{x - h_1}{2\sqrt{D_{app} t}}\right], \quad x > h_1 \qquad [19]$$

Stage 2 will end when the concentration in the liquid films drops to $C_{\alpha l}$ over the distance h_1. In other words, when the amount of gallium diffused into the gallium-free matrix ($x > h_1$) is equal to the excess amount of gallium contained in the liquid boundaries (I). This condition can be written as:

$$I = h_1 X_l (C_{l\alpha} - C_{\alpha l}) = h_0 C_\beta X_l \frac{(C_{l\alpha} - C_{\alpha l})}{C_{\alpha l}} \qquad [20]$$

If gallium penetrates the lattice a distance h_2 in stage 2, the excess gallium from stage 1 will raise the concentration in this region to approximately $C_{\alpha l}$. It thus follows that:

$$I \cong h_2 C_{\alpha l} \qquad [21]$$

An expression for h_2 can be found by combining Eqs. [20] and [21]. Furthermore, the gallium concentration at this location ($x = h_1 + h_2$) must be $C_{\alpha l}/2$, as shown in Figure 16. When this value for concentration is substituted into Eq. [19], the time required for stage 2 (t_2) can be calculated. If it is assumed that the original insert of 100 pct gallium is 20 μm thick, and that the

Table II. Dissolution Growth Constants Computed from Equation [A6] (Appendix)

Temperature (K)	423	473	523	573	623	673	773
Dissolution Constant γ	0.14	0.21	0.24	0.34	0.37	0.47	0.60

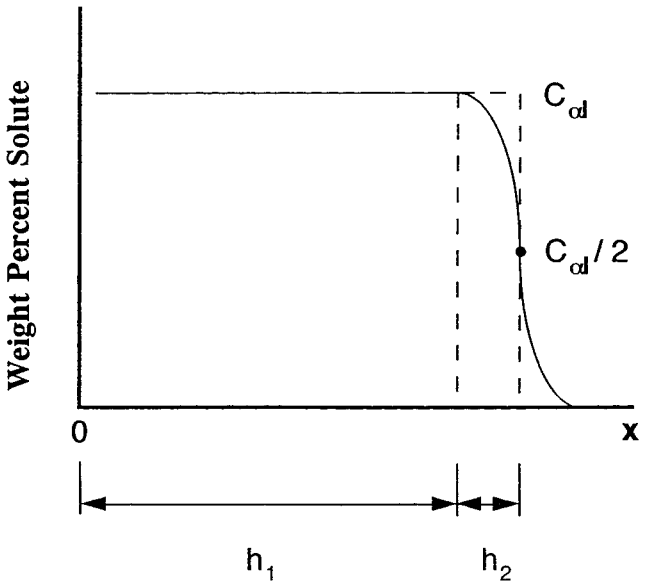


Fig. 16—Schematic diagram illustrating the gallium concentration profile in the lattice at the end of stage 2.

volume fraction of liquid is 10^{-2}, then the calculated time to complete stage 2 will vary from 12 hours (423 K) to 40 seconds (773 K), as shown in Table III. Calculated values for h_2 within this temperature range do not vary significantly from 10 μm.

C. *Stage 3: Solid-State Homogenization*

Stage 3 involves solid-state homogenization of a film of concentration $C_{\alpha l}$ and half-width h_1 (the distance penetrated in stage 2 is neglected). If a long time (t_3) is needed for homogenization, a thin film solution can be used to describe stage 3 as:

$$C(x, t) = \frac{C_{\alpha l}\, h_1}{\sqrt{D_{\text{app}} \pi t}}\, e^{-x^2/4D_{\text{app}}t} \qquad [22]$$

V. MODEL VERIFICATION

A. *Slope Change in Semilog Plots*

One of the least expected features of the experimental data was the occurrence of a change in slope on every semilog plot for temperatures below 723 K. This change in slope occurred at a distance h_{exp} measured from the original interface. This section attempts to correlate the three-stage model described previously with this observed phenomenon.

The semilog plots (Figures 5 through 12) take into account the total experimental time t (24 and 48 hours), which can now be written as follows:

$$t = t_1 + t_2 + t_3 \qquad [23]$$

where t_1, t_2, and t_3 are the times needed to achieve the three respective stages. Furthermore, since t_1 is much smaller than t_2 or t_3, it can be neglected (recall that t_1 was calculated to be on the order of 20 to 200 seconds in duration). Thus, the slope of the semilog plots, which should be represented by $[4D_{\text{app}}t_3]^{-1}$ according to Eq. [22], is actually represented by a slope $[4D_{\text{app}}(t_2 + t_3)]^{-1}$ in the region $x < h_1$. At low temperatures, t_2 may be very large (Table III), and a long stage 2 will delay the moment when stage 3 is initiated. Thus, the difference in time required for stage 2 is believed responsible for the change in slope of the semilog plots. This change in slope did not take place at higher temperatures (Figures 5 and 6) because the time interval t_2 is negligible compared to the overall experiment time at these temperatures.

B. *Infiltration Distance*

One simple and efficient way to check the model is to compare experimental and theoretical infiltration distances for stage 1. The theoretical distance h_{theo} was computed assuming that the volume fraction of the liquid phase at the boundaries X_l is zero. The initial thickness (h_0) was determined from the concentration profiles (Table I). The equilibrium concentrations were taken from the phase diagram (Figure 1). Experimental diffusivity values were read directly from each semilog plot (Figures 5 through 12). When plotted, as shown in Figure 17, a correlation coefficient of 0.95 is observed, indicating good agreement between experiment and theory.

It is now possible, using the correlation coefficient measured previously, to find the real liquid fraction in stage 1. Correcting the theoretical infiltration distance by the correlation factor, Eq. [16] becomes:

$$h_1 = \frac{h_0 C_\beta}{X_l(C_{l\alpha} - C_{\alpha l}) + C_{\alpha l}} = 0.95\, h_0 \frac{C_\beta}{C_{\alpha l}} \qquad [24]$$

and solving for X_l provides:

$$X_l = \left(\frac{0.05}{0.95}\right) \frac{C_{\alpha l}}{(C_{l\alpha} - C_{\alpha l})} \qquad [25]$$

Values for liquid fraction calculated using Eq. [25] are shown in Table IV.

VI. CONCLUSIONS

The concept of using a liquid phase to accelerate atomic transport and facilitate joining of an Al-SiC composite has been demonstrated. However, the transport mechanism was found to be quite different from earlier ones formulated for TLP joining of homogeneous material. This difference appears to arise from the nature

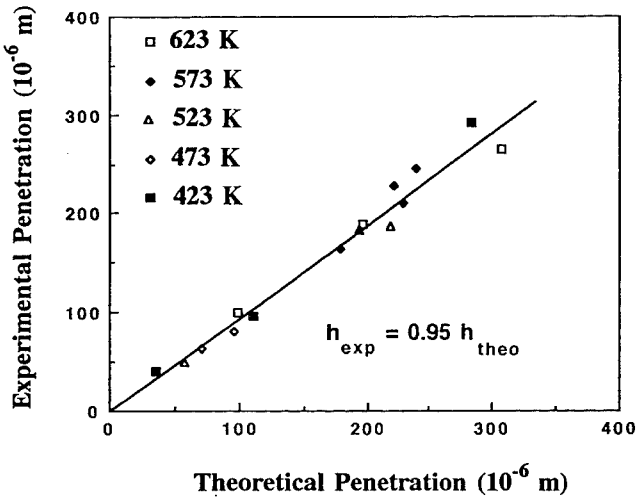


Fig. 17—Comparison between computed and measured stage 1 gallium infiltration distance (h_1).

Table III. Time t_2 Needed to Complete Stage 2

Temperature (K)	423	473	300	673	773
Time t_2	12 hours	4.5 hours	1 hour	20 minutes	40 seconds

Table IV. Calculated Volume Fraction of Liquid Phase as a Function of Temperature

Temperature (K)	423	473	573	673	773
$X_l \cdot 10^{-2}$	0.62	0.67	0.75	0.87	1

of the composite. The following conclusions were drawn:

1. The presence of short-circuit paths for diffusion such as grain boundaries, subgrain boundaries, dislocations, and ceramic/matrix interfaces enhanced diffusion.
2. Short-circuit diffusion dominated atomic transport up to 723 K, with an activation energy as low as 35 kJ/mol (8.35 kcal/mol).
3. The activation energy for the interdiffusion coefficient of gallium in aluminum was measured to be 120 kJ/mol (28.8 kcal/mol), consistent with the value of 122 kJ/mol (29.24 kcal/mol) reported in the literature.[26]
4. The joining mechanism appeared to occur in three successive stages:

   Stage 1—Rapid (seconds) infiltration of the liquid phase until the original interlayer is depleted, and simultaneous homogenization of the solid matrix. Penetration distance is dependent upon temperature and initial interlayer thickness.

   Stage 2—Depletion of the liquid phase from grain boundaries and interfaces. The duration of this second stage is dependent upon the temperature and interlayer thickness. Completion of this stage is crucial in reducing the potential for liquid metal embrittlement.

   Stage 3—Homogenization in the solid state.
5. This study has a direct and practical application. The presence of a liquid phase and numerous high-diffusivity paths enables the joining of aluminum-SiC composites at temperatures as low as 423 K (below the aging temperature of the matrix), and in times less than typical aging times. Conceivably, the aging treatment and joining process could be performed simultaneously.
6. This transport mechanism for composites should apply equally well to more common aluminum brazing alloys such as Al-Ge, Al-Zn, and Al-Si eutectic liquids.

NOMENCLATURE

C	binary solute concentration
C_β	solute concentration in original predeposited film
t	time coordinate
D_l, D_s	solute diffusivity in liquid and solid
h_0	half-thickness of original predeposited solute film
ξ	position of solid/liquid interface (x direction)
γ	growth constant
$C_{l\alpha}$	solute concentration at α liquidus
$C_{\alpha l}$	solute concentration at α solidus
D_{app}	apparent solute diffusivity
h_{exp}	location of experimentally observed slope change on semilog plots
h_{theo}	location of theoretically predicted slope change on semilog plots
τ	liquid residence time
δ	thickness of liquid film at grain boundaries
x, y	Cartesian coordinates
h_1, h_2, h_3	maximum penetration distance (x direction) for stages 1 through 3
t_1, t_2, t_3	time required to complete stages 1 through 3
X_l	volume fraction of liquid phase
I	excess solute content
J_x, J_y	flux of solute in x and y directions
D	interdiffusion coefficient

APPENDIX

Four-stage model for transient liquid phase joining[21,24,25]

Stage 1. Initial and boundary conditions are shown in Figure 2(a). Assuming unidimensional diffusion and using the interdiffusion coefficient D, Fick's second law can be written as:

$$\frac{\partial C}{\partial t} = D\frac{\partial^2 C}{\partial^2 x} \qquad [A1]$$

where C represents the concentration of B atoms, and the distance normal to the interface, x, is measured from the initial median line of the interlayer. The solution associated with these boundary conditions is:

$$C(x, t) = \frac{C_\beta h_0}{\sqrt{D\pi t}} e^{-x^2/4Dt} \qquad [A2]$$

Stage 2. This second stage involves analysis of diffusion in a system with moving boundaries[36] and is a derivative of Stefan's problem.[37] The following assumptions apply: (1) unidimensional diffusion, (2) static liquid with no convection, (3) constant diffusion coefficient, (4) equilibrium at the solid/liquid interface, and (5) semi-infinite medium. The concentration profile during this stage must account for both solid and liquid diffusion and, hence, two variants of Fick's second law are needed. If ξ is defined as the position of the interface at a time t during the second stage (Figure 2(b)) and is measured from the position of the original interface, it can be written as:

$$\text{liquid: } \frac{\partial C}{\partial t} = D_l\frac{\partial^2 C}{\partial x^2} \quad (x < \xi) \qquad [A3a]$$

$$\text{solid: } \frac{\partial C}{\partial t} = D_s\frac{\partial^2 C}{\partial x^2} \quad (x > \xi) \qquad [A3b]$$

where D_l and D_s are diffusion coefficients in the liquid and solid state, respectively. Conservation of matter must also be satisfied:

$$(C_{l\alpha} - C_{\alpha l})\frac{d\xi}{dt} = -D_l\left(\frac{\partial C}{\partial x}\right)_\xi = +D_s\left(\frac{\partial C}{\partial x}\right)_\xi \qquad [A4]$$

The general solution obeys a regular diffusion law;

$$\xi = 2\gamma_2\sqrt{D_l t} \qquad [A5]$$

where γ_2 is a growth constant and can be determined independently:

$$\gamma_2 \cong \left(\frac{C_\beta - C_{l\alpha}}{C_{l\alpha} - C_{\alpha l}}\right)\frac{e^{-\gamma_2^2}}{1 + \text{erf}(\gamma_2)}\frac{1}{\sqrt{\pi}} \qquad [A6]$$

for a large D_l/D_s ratio.

It is now easy to get the time required for homogenization of the liquid phase by rewriting Eq. [A5]:

$$t_2 = \frac{h_{max}^2}{4\,\gamma_2^2\,D_l} \qquad [A7]$$

where $2h_{max}$ is the maximum width attained by the liquid film.

Stage 3. Boundary conditions are given in Figure 2(c). Fick's second law for the solid and the liquid, respectively, yields the following equations:

$$\text{solid: } \frac{\partial C}{\partial t} = D_s \frac{\partial^2 C}{\partial x^2} \quad (x > -\xi) \qquad [A8a]$$

$$\text{liquid: } \frac{\partial C}{\partial x} = 0 \quad (x < -\xi) \qquad [A8b]$$

The solute balance provides:

$$(C_{l\alpha} - C_{\alpha l}) \frac{d\xi}{dt} = -D_s \frac{\partial C}{dx} \qquad [A9]$$

The general solution, if equilibrium is assumed, can be written as:

$$\xi = 2\gamma_3 \sqrt{D_s t} \qquad [A10]$$

and γ_3 is found as before;

$$\gamma_3 \cong \frac{C_{l\alpha} - C_l}{C_{l\alpha} - C_{\alpha l}} \frac{e^{-\gamma_3^2}}{1 + \text{erf}\,(\gamma_3)} \frac{1}{\sqrt{\pi}} \qquad [A11]$$

The time for stage 3 takes a form similar to that for stage 2, except that the kinetics of the process are now controlled by diffusion in the solid:

$$t_3 = \frac{h_{max}^2}{4\gamma_3^2 D_s} \qquad [A12]$$

Stage 4. This stage involves solid state homogenization and is described by a thin film solution similar to stage 1:

$$C(x, t) = \frac{C_{\alpha l}\, h_{eff}}{2\sqrt{D\pi t}}\, e^{-x^2/4Dt} \qquad [A13]$$

where h_{eff} is the effective film thickness at the beginning of stage 4.

ACKNOWLEDGMENTS

The authors appreciate the donation of composite material and funding support given by Martin Marietta Astronautics Group in Denver, CO. The studies conducted by the Office of Naval Research on metal matrix composites, monitored by Dr. Steve Fishman, and on metal-ceramic brazing, monitored by Dr. George Yoder, also contributed to this research by providing us with a community of peers. Jose Ramirez, Ph.D. Candidate, CSM, provided a critical review of the manuscript.

REFERENCES

1. K.K. Chawla: *Composite Materials*, Springer-Verlag, New York, NY, 1987.
2. J.E. Schoutens and K. Tempo: *Introduction to Metal Matrix Composites*, DoD Metal Matrix Composites Information Center, Santa Barbara, CA, 1982.
3. T. Minoru and R.J. Arsenault: *Metal Matrix Composites—Thermomechanical Behavior*, Pergamon Press, New York, NY, 1989.
4. A.L. Geiger and M. Jackson: *Adv. Mater. Process.*, 1989, vol. 136, pp. 23-30.
5. C.A. Updike, R.G. Bhagat, M.J. Pechersky, and M.F. Amateau: *J. Met.*, 1990, vol. 42, pp. 42-46.
6. S.J. Harris: in *Aluminum Alloys—Contemporary Research and Applications*, A.K. Vasudevan and R.D. Doherty, eds., Academic Press, New York, NY, 1989, pp. 255-94.
7. J.M. Papazian and P.N. Adler: *Metall. Trans. A*, 1990, vol. 21A, pp. 401-10.
8. X. Dumant, E. Beaumont, and G. Regazzoni: *J. Met.*, 1989, vol. 41, pp. 46-51.
9. W.C. Moshier, J.S. Ahearn, and D.C. Cooke: *J. Mater. Sci.*, 1987, vol. 22, pp. 115-22.
10. M.J. Salkind: *Metall. Trans.*, 1968, vol. 242, pp. 2518-20.
11. T. Enjo, K. Ikeuchi, Y. Murakami, and N. Suzuki: *Trans. Jpn. Weld. Res. Inst.*, 1987, vol. 16, pp. 285-92.
12. N.F. Kazakov: *Diffusion Bonding of Materials*, Pergamon Press, New York, NY, 1985.
13. J.C. Prucz, C.C. Spyrakos, and B. Hendrson: *Proc. of 4th Japan–U.S. Conf. on Composite Materials*, Technomic Pub. Co., Lancaster, PA, 1989, pp. 815-24.
14. N. Albee: *Adv. Compos.*, 1989, vol. 4, pp. 42-50.
15. J.W.H. Clare: *J. Inst. Met.*, 1957-58, vol. E6, pp. 431-32.
16. V.E. Jenckel: *Metallkunde*, 1934, vol. 11, pp. 249-51.
17. H. Zoller: *Metall*, 1957, vol. 5, pp. 378-81.
18. L.F. Mondolfo: *Aluminum Alloys: Structure and Properties*, Butterworth Publishers, Stoneham, MA 1976, pp. 289-91.
19. *Metals Handbook*, 8th ed., ASM INTERNATIONAL, Metals Park, OH, 1973, vol. 8, p. 260.
20. M. Hansen: *Constitution of Binary Alloys*, McGraw-Hill, New York, NY, 1958, pp. 95-96.
21. J.E. Ramirez: Master's Thesis T-3751, Colorado School of Mines, Golden, CO, 1989.
22. I. Tuah-Poku, M. Dollar, and T.B. Massalski: *Metall. Trans. A*, 1988, vol. 19A, pp. 675-86.
23. D.F. Paulonis, D.S. Suvall, and W.A. Owczarski: U.S. Patent No. 3,678,570, 1972.
24. R.F. Sekerka: *Physical Metallurgy of Metal Joining*, TMS-AIME, Warrendale, PA, 1980, pp. 1-3.
25. A. Lasalmonie: *Ann. Chim. Fr.*, 1987, vol. 12, pp. 247-57.
26. N.L. Peterson and S.J. Rothman: *Phys. Rev. B*, 1970, vol. 1, pp. 3264-73.
27. I. Dutta and D.L. Bourell: *Mater. Sci. Eng.*, 1989, vol. A112, pp. 67-77.
28. I. Dutta, D.L. Bourell, and D. Latimer: *J. Compos. Mater.*, 1988, vol. 22, pp. 829-49.
29. J.M. Papazian: *Metall. Trans. A*, 1988, vol. 19A, pp. 2945-53.
30. M. Vogelslang, R.J. Arsenault, and R.M. Fisher: *Metall. Trans. A*, 1986, vol. 17A, pp. 379-89.
31. L. Peters, C. Roques-Carmes, M. Aucouturier, and G. Wyon: *Mem. Sci. Rev. Metall.*, 1972, vol. 69, pp. 81-95.
32. C. Roques-Carmes, M. Aucouturier, and P. Lacombe: *Met. Sci. J.*, 1973, vol. 7, pp. 128-32.
33. C. Elbaum: *Metall. Trans.*, 1959, vol. 215, pp. 476-77.
34. C. Roques-Carmes, M. Aucouturier, and P. Lacombe: *Mem. Sci. Rev. Metall.*, 1973, vol. 70, pp. 207-17.
35. A.D. LeClaire: *Br. J. App. Phys.*, 1963, vol. 14, pp. 351-56.
36. R.F. Sekerka, C.L. Jeanfils, and R.W. Heckel: *Lecturers on the Theory of Phase Transformations*, TMS-AIME, Warrendale, PA, 1975.
37. R. Ghez: *A Primer of Diffusion Problems*, Wiley Interscience, New York, NY, 1988.

The Effect of Substrate on the Microstructure and Creep of Eutectic In-Sn

J.L. FREER GOLDSTEIN and J.W. MORRIS, Jr.

This study was conducted in order to determine and understand the effect of substrate on the behavior of eutectic In-Sn. Samples for mechanical testing were produced with either bare Cu or Ni on Cu substrates. Both the microstructure and the mechanical behavior are strongly dependent on substrate. When eutectic In-Sn is joined to bare Cu, Cu diffusion into the joint causes the alloy to become off-eutectic, giving a nonuniform and irregular microstructure. The addition of a layer of Ni acts as a diffusion barrier, preventing Cu diffusion sufficiently such that a uniform, normal colony-based eutectic forms. Deformation is more uniform in the In-Sn on Ni, while it is concentrated along the length of the joint in the In-Sn on Cu. This distinction is reflected in the different shapes of shear stress-strain curves between In-Sn on Cu and In-Sn on Ni. The stress exponents and activation energies for creep also vary with substrate. Creep deformation is governed by the In-rich β phase for In-Sn on Cu and by the Sn-rich γ phase for In-Sn on Ni. If In-Sn on Ni samples are aged, the microstructure coarsens and the mechanical behavior changes to resemble that of the as-cast In-Sn on Cu.

I. INTRODUCTION

EUTECTIC In-Sn is often used as a solder for applications in which a low-melting-point alloy is required. It has been observed[1] that poor-quality solder joints result when soldering In-Sn directly to a copper substrate, due to rapid diffusion of Cu into the In-rich alloy. For this reason, a layer of Ni is generally used as a diffusion barrier. However, no detailed studies have been conducted to understand exactly what effect the Ni layer has on the microstructure and mechanical behavior of the In-Sn alloy. The purpose of this study is to determine and understand the effect of substrate on eutectic In-Sn by examining In-Sn on Cu and In-Sn on Ni.

In-Sn alloys have low strength, high ductility, and correspondingly low creep resistance as compared to standard soft solders, such as Sn-Pb. Relatively little research has been done on In-Sn. In particular, mechanistic studies of the mechanical behavior and its correlation with the microstructure are absent.

The In-Sn binary phase diagram is shown in Figure 1. The eutectic, with a melting point of 120 °C, is composed of two intermediate phases. The primitive hexagonal γ phase is a Sn-rich random solid solution. The β phase has a tetragonal crystal structure, but there is some question as to the arrangement of In and Sn atoms in the structure. There is probably partial ordering, but the phase is not a true ordered intermetallic compound.[2] Both the γ and β phases are relatively soft and ductile and have wide solubility ranges, in contrast to the behavior expected for ordered intermetallics. The composition of the γ phase of the eutectic does not change much as the alloy is cooled. The composition of the β phase, however, varies from 44 at. pct at the eutectic temperature to 30 at. pct at 25 °C.

J.L. FREER GOLDSTEIN, formerly with the Department of Materials Science and Mineral Engineering, University of California at Berkeley, is Process Development Engineer, nCHIP, Inc., San Jose, CA 95132. J.W. MORRIS, Jr., Professor, is with the Department of Materials Science and Mineral Engineering, University of California at Berkeley, and also Faculty Senior Scientist, Lawrence Berkeley Laboratory, Berkeley, CA 94720.

Manuscript submitted September 28, 1993.

II. EXPERIMENTAL PROCEDURE

The samples used for mechanical testing and microstructural analysis are modified double-lap shear samples (Figure 2). The design of the samples is such that when the entire sample is pulled in tension, the central gage region is deformed in shear. The effective shear stress (τ) and shear strain (γ) on the In-Sn in the gage region are expressed by the following equations:

$$\tau = P/(x * h) \quad [1]$$

$$\gamma = \Delta x/w \quad [2]$$

where P is the load on the sample, x is the length of the joint (central gage section length), h is the sample thickness, Δx is the displacement along the joint length, and w is the width of the joint. The values of x and h varied from sample to sample, with x between 5.8 and 8.4 mm and h between 1.1 and 1.9 mm. For all samples, the value of w was fixed at 0.5 mm. For simplicity, further references to deformation in a sample or a joint will always imply deformation within the central gage region. The shear stress and shear strain are uniform throughout most of the gage region. Concentrations of both stress and strain exist at the corners marked "x" in Figure 3(a).[3] Extensive deformation results in a shearing of the sample in the manner shown schematically in Figure 3(b).

All samples were made using Cu blocks, which were immersed into molten solder, solidified and machined to produce samples (Figure 2). For the In-Sn on Ni samples, the Cu was plated with about 8 μm of Ni before immersion into the solder. Details of the method used to manufacture the samples have been published elsewhere.[4,5] One major difference between the current method and that described in Reference 4 is in the metallographic preparation. The current method involves

U.S. GOVERNMENT WORK
NOT PROTECTED BY U.S. COPYRIGHT

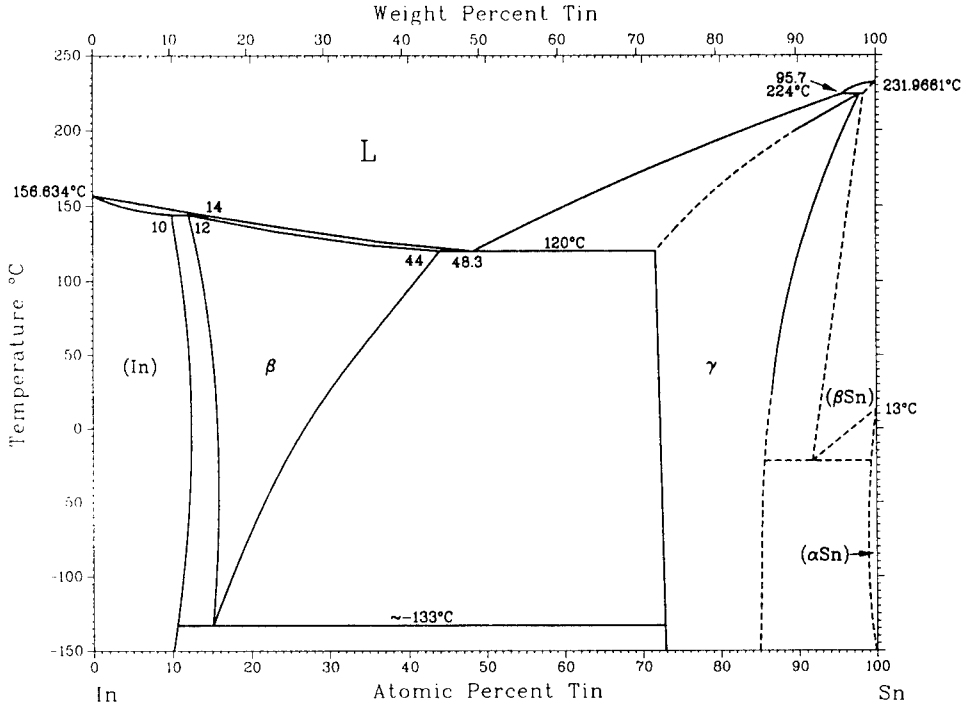


Fig. 1—In-Sn phase diagram.[115]

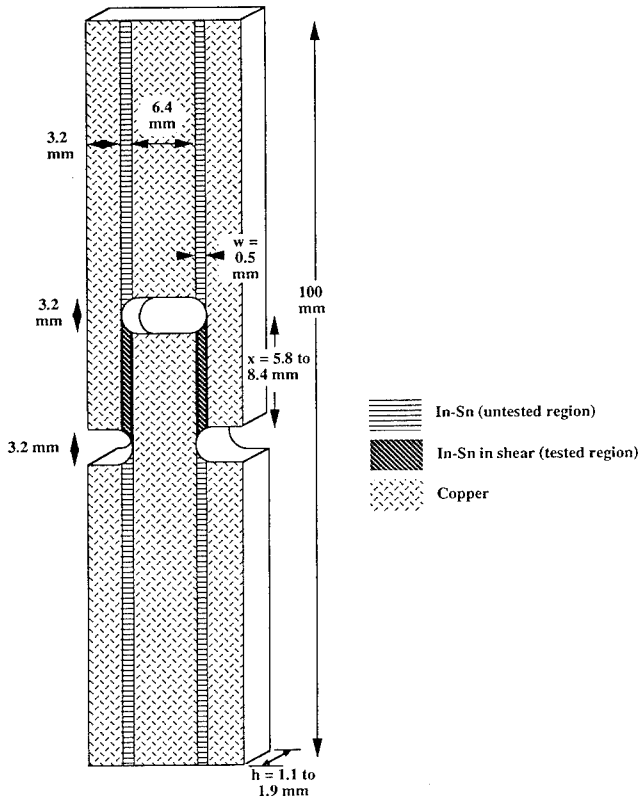


Fig. 2—Drawing of the modified double-lap shear sample.

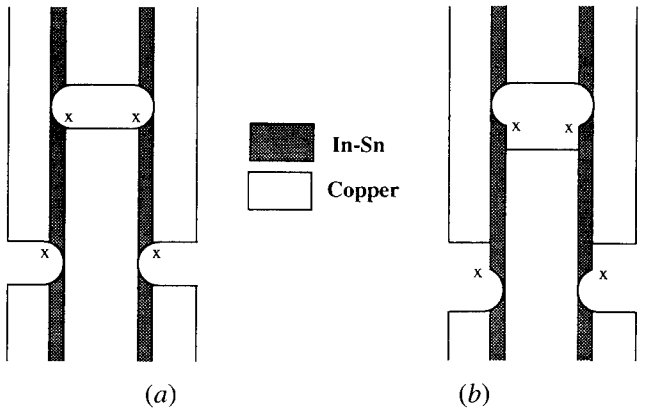


Fig. 3—Drawing of the central region of the modified double-lap shear sample, showing concentrations of stress and strain, marked by "x" (*a*) before testing and (*b*) schematic of deformation due to shear strains.

first mounting the samples in an acrylic mount before polishing, using a silicon mold release on the mounting holder and the sample. Mounting is required because the extreme softness of the In-Sn alloy causes it to be worked into a depression between the copper plates if mechanical polishing is done on an unmounted sample. Acrylic was chosen as the mounting material because it cures relatively quickly (in 30 to 40 minutes) at room temperature without significant temperature increase and can be separated from the sample after polishing. Separation requires machining the acrylic from the sides of the mounted sample and then prying the sample away from the remaining acrylic. The advantage of this method over the previous one, in which sections were cut and mounted from tested samples, is that the microstructure in the same region of a single sample can be examined before and after testing. Also, polishing the sample before testing allows for examination of the surface relief developed in an as-tested sample, showing where deformation is concentrated.

Samples were tested under both creep (constant load)

and constant-strain-rate conditions. Test temperatures were between 0 °C and 75 °C for creep tests, with applied stresses ranging from 1 to 12 MPa. Constant-strain-rate tests were run at 40 °C at applied strain rates between 2×10^{-4} and 8×10^{-4} mm/mm/s.

Creep data are presented in the form of log-log plots of steady-state strain rate *vs* applied stress and are analyzed in terms of the power-law creep equation, shown below, which describes the effect of stress and temperature on the steady-state creep rate.

$$d\gamma/dt = A\tau^n \exp(-Q/kT) \quad [3]$$

The pre-exponential factor, A, is a microstructural parameter roughly independent of stress and temperature, n is the stress exponent, and Q is the apparent activation energy for creep. Evaluation of n and Q can often help identify the dominant mechanism of creep deformation for a given system and range of experimental conditions. The activation energy for creep of each type of sample was determined by using multivariable linear regression to fit all stress, temperature, and strain-rate data to a single equation of the form

$$Y = m_1x_1 + m_2x_2 + b \quad [4]$$

In this case, $Y = \ln(d\gamma/dt)$, $x_1 = \ln(\tau)$, $x_2 = 1/T$, $m_1 = n$, $m_2 = -Q/k$, and $b = \ln(A)$.

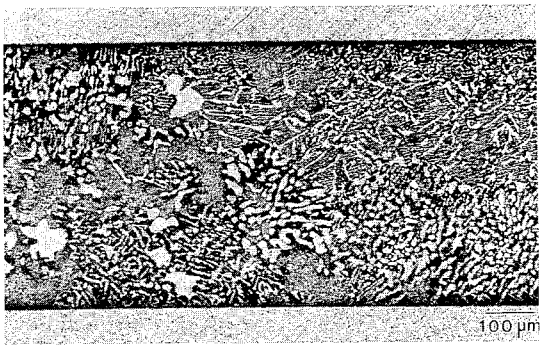
Some samples were aged at 81 °C (0.9 T_m) to investigate the effect of aging on the microstructure and to observe better the intermetallic compounds formed at the interface between the In-Sn alloy and the substrate.

III. RESULTS

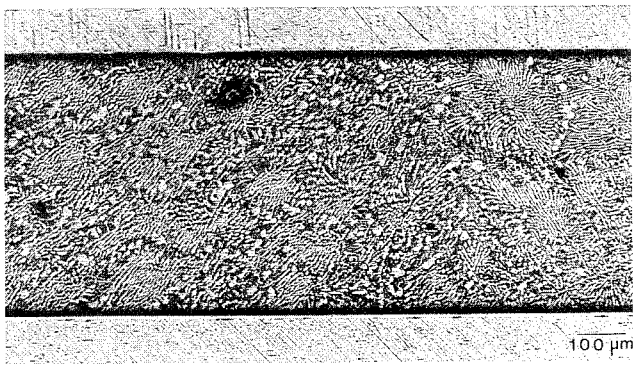
A. *Microstructure*

The microstructure of eutectic In-Sn depends strongly on the substrate. In-Sn on Cu (Figure 4(a)) has an irregular microstructure, the scale and morphology of which varies throughout the joint. No well-developed lamellar structure exists, although lamellae form in isolated regions. Many large dendrites of the Sn-rich γ phase are also observed. The γ phase is discontinuous, implying that the γ-phase regions are imbedded in a matrix of the β phase. The microstructure of In-Sn on Ni is quite different (Figure 4(b)). The eutectic phases are arranged in lamellar colonies, in a microstructure which is much more uniform. No large regions of either phase are present, and neither phase seems to form a continuous matrix.

The intermetallic layer at the solder-substrate interface naturally varies with substrate. In-Sn on Cu forms ternary intermetallics. These have been discussed elsewhere.[4,5] The intermetallic region is actually composed of two layers, with a layer of Cu_2In_3Sn on the solder side and a layer of $Cu_2(Sn,In)$ on the Cu side of the interface. A scanning electron microscope (SEM) micrograph and accompanying X-ray images of the intermetallic region of an In-Sn on Cu sample are shown in Figure 5. In-Sn on Ni samples develop a ternary In-Sn-Ni-intermetallic layer, though its stoichiometry has not been determined. It is possible that this intermetallic is composed of two layers, as well. The intermetallic region is too thin to be seen clearly in the SEM.



(*a*)



(*b*)

Fig. 4—Optical micrographs of untested In-Sn samples on (*a*) bare Cu and (*b*) Ni substrates. The Sn-rich γ phase appears light and the In-rich β phase appears dark.

Deformation in all samples begins at the corners where stress and strain are concentrated, but the manner in which it spreads can vary. In-Sn on Ni samples show surface relief throughout the width and length of the sample, though the most severe deformation is often within particular colonies. The deformation pattern for In-Sn on Cu is much more concentrated, following in a band along the length of the joint. These differences are illustrated in Figures 6 and 7. For all samples, some minimum amount of strain is required to induce visible surface relief.

Aging has no visible effect on the microstructure of In-Sn on Cu. In-Sn on Ni samples aged for two months at 81 °C show remarkable microstructural changes. No trace of the as-cast colony microstructure remains. Instead, the microstructure throughout the joint has evolved into what appear to be islands of γ phase in a matrix of the β phase, similar to the situation in In-Sn on Cu. The micrograph in Figure 8 is that of an In-Sn on Ni sample after aging, which illustrates the dramatic effect of aging on the microstructure.

B. *Creep Data*

Log-log plots of steady-state strain rate *vs* applied shear stress for In-Sn on Cu and In-Sn on Ni appear in Figures 9(a) and (b). The data fit very well to straight lines for all temperatures tested. Stress exponents are near 3 for samples on Cu and close to 5 for samples on

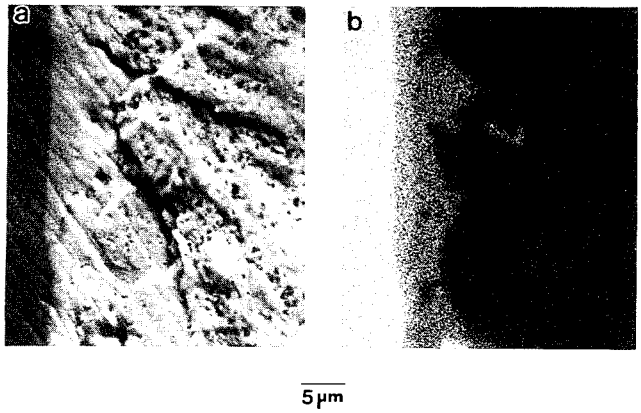
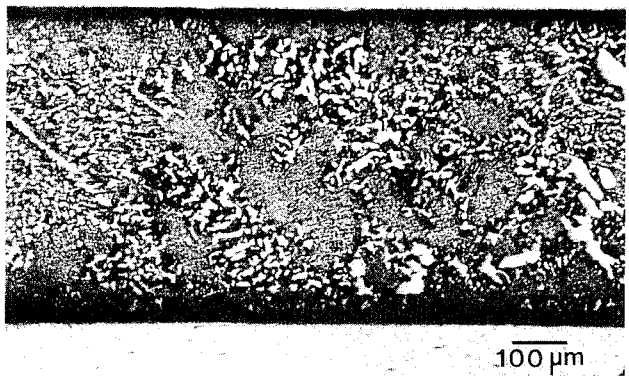
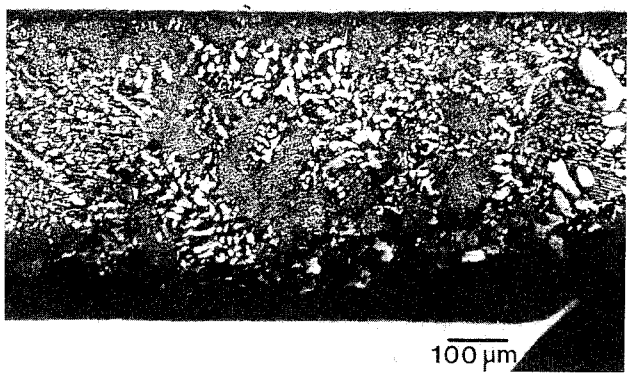


Fig. 5—(*a*) SEM micrograph of In-Sn on Cu and corresponding X-ray images of (*b*) Cu, (*c*) Sn, and (*d*) In.



(*a*)



(*b*)

Fig. 6—Optical micrographs of In-Sn on Cu sample (*a*) before and (*b*) after testing. The dark region along the bottom of the joint shows concentrated deformation.

Ni and are relatively constant with temperature. Due to the difference in stress exponents, the Cu and Ni data lines at a given temperature will cross. Therefore, at high stresses, the creep rate of Ni samples is generally higher than the creep rate for Cu samples at the same stress, whereas at lower stresses the opposite is true. Activation energies for creep of the two systems calculated using Eq. [4] resulted in $Q = 0.73$ eV for In-Sn on Cu and $Q = 1.04$ eV for In-Sn on Ni.

Creep testing of an aged In-Sn on Ni sample at 65 °C gave a stress exponent of 3.4. The strain rate *vs* stress data follow the same curve as the data for In-Sn on Cu samples at the same test temperature (Figure 10) The creep behavior of In-Sn on Cu does not change with aging.

C. *Stress-Strain Data*

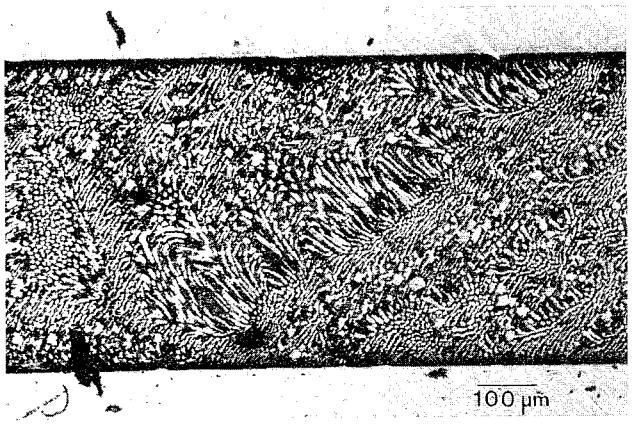
The stress *vs* strain plots for In-Sn on Cu and In-Sn on Ni are qualitatively different. The stress rises quickly to a maximum in both cases, but In-Sn on Cu samples subsequently experience an approximately logarithmic decay in the stress, while for In-Sn on Ni the stress remains fairly constant. Figure 11 shows stress-strain curves for both types of samples at several applied strain rates. There are significant differences in the maximum stresses. For example, an In-Sn on Ni sample with an applied strain rate of 5.4×10^{-4}/s had a peak stress of 5.4 MPa, whereas the peak stress for a Cu sample tested at a similar strain rate was 10.6 MPa.

There is a definite correlation between creep and constant-strain-rate tests, as shown in Figure 12. The creep data are steady-state strain rate *vs* applied stress, as before, and the stress-strain data are presented as applied strain rate *vs* peak stress. Data from both types of tests lie on the same line for samples on both substrates.

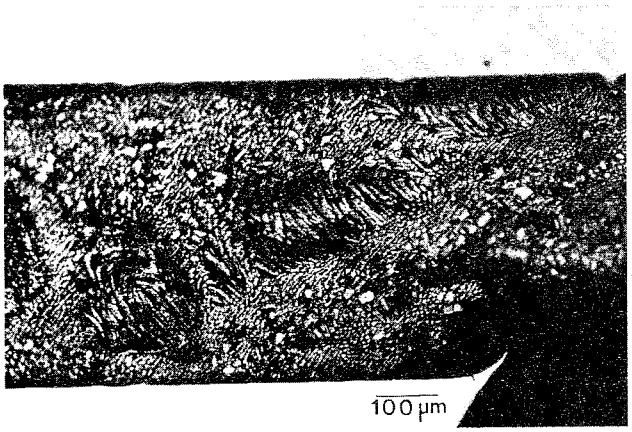
IV. IMPLICATIONS

A. *Microstructure*

The microstructure of In-Sn is severely affected by the substrate. It appears that the diffusion of Cu into the samples without a Ni diffusion barrier is significant enough to disturb the formation of the eutectic structure. Cu diffuses into the In-Sn while it is still liquid. Due to the relatively slow cooling rate used, the alloy remains in the liquid state for several minutes. If the solder is now an off-eutectic ternary alloy, that would explain the observed microstructure. Unfortunately, no ternary-phase diagrams are available for In-Sn-Cu in the low-Cu region. Therefore, differential scanning calorimetry (DSC) tests were run on In-Sn pieces taken from both In-Sn on Cu and In-Sn on Ni samples to determine the effect of the substrate on solidification. Results showed a large peak at the eutectic temperature for both samples,



(*a*)



(*b*)

Fig. 7—Optical micrographs of In-Sn on Ni sample (*a*) before and (*b*) after testing. The dark regions show concentrated deformation within two colonies.

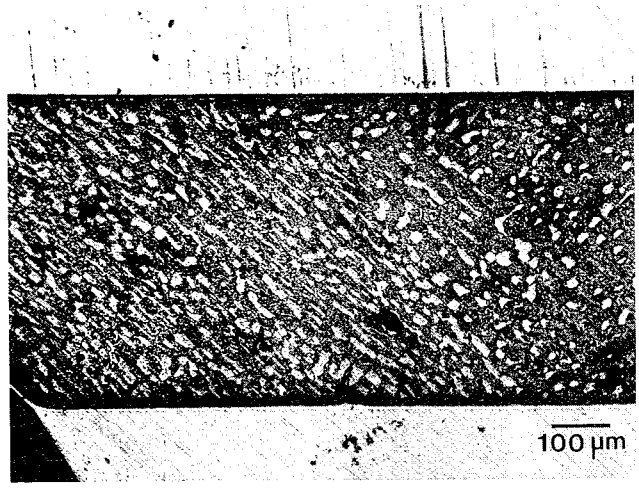
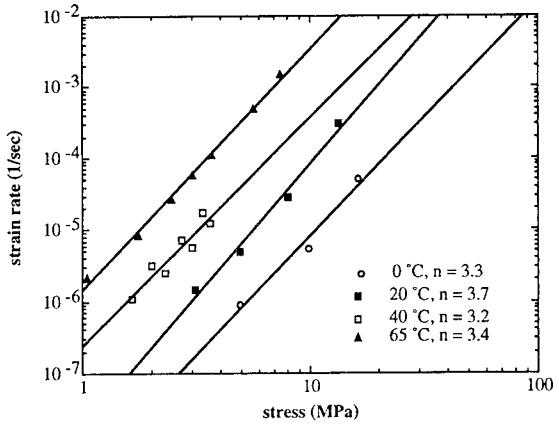
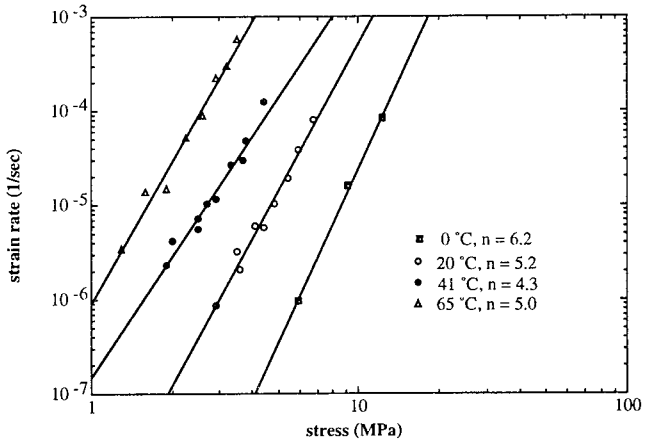


Fig. 8—Optical micrograph of In-Sn on Ni sample aged for 2 months at 81 °C. The Sn-rich γ phase appears light and the In-rich β phase appears dark.



(*a*)



(*b*)

Fig. 9—Log-log plots of creep data (steady-state strain rate *vs* applied stress) for (*a*) In-Sn on Cu and (*b*) In-Sn on Ni, tested at a variety of temperatures.

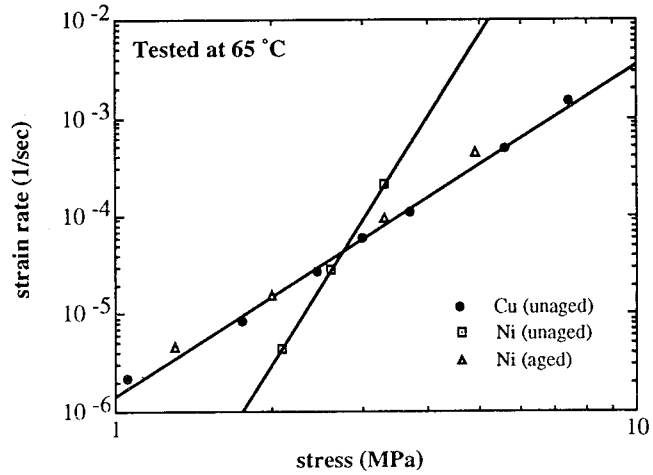


Fig. 10—Log-log plots of creep data for unaged In-Sn on Cu, unaged In-Sn on Ni, and aged In-Sn on Ni.

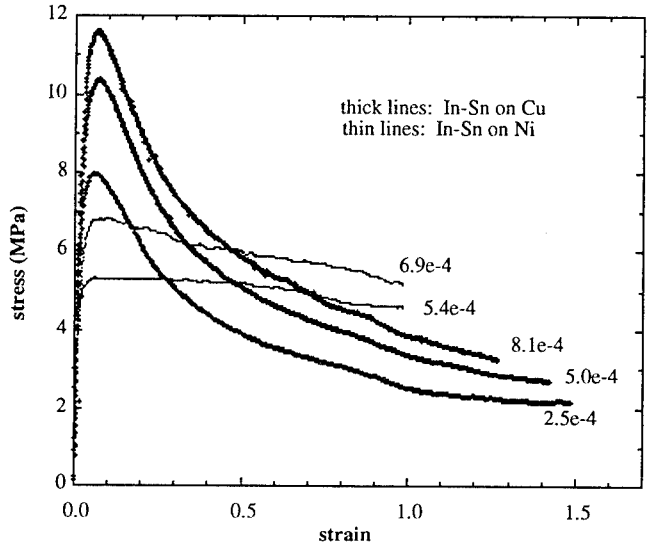


Fig. 11—Engineering stress-strain curves for In-Sn on Cu and In-Sn on Ni. Applied strain rates are given on the plot for each curve. All samples were tested at 40 °C.

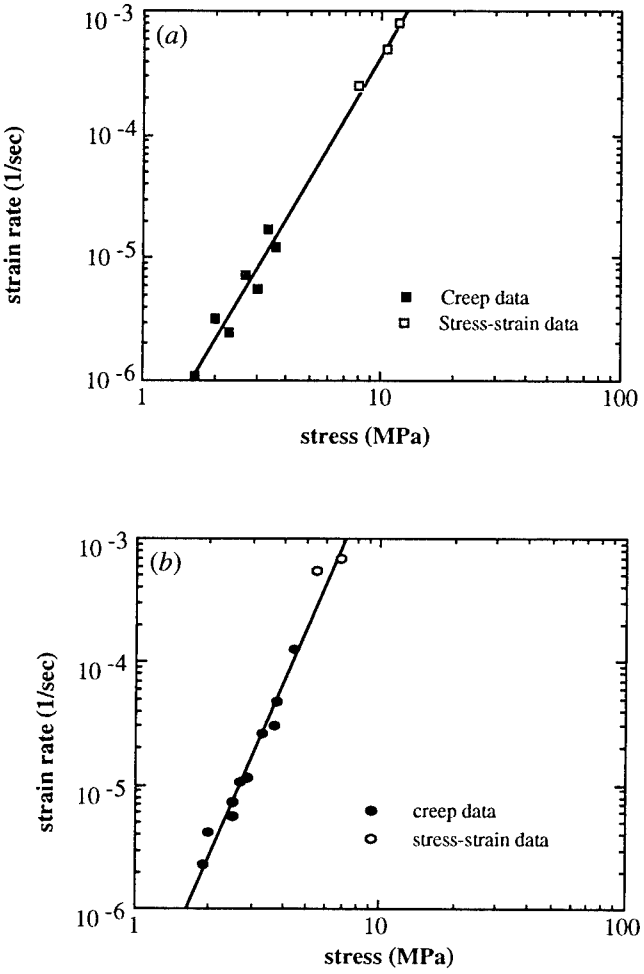


Fig. 12—Correlation between creep and constant-strain-rate data for (*a*) In-Sn on Cu and (*b*) In-Sn on Ni. Creep data is presented as steady-state strain rate *vs* applied stress, and constant-strain-rate data are presented as applied strain rate *vs* peak stress.

with an additional smaller peak at higher temperature for the In-Sn on Cu. These results confirm the hypothesis that the In-Sn on Cu is off-eutectic. Dendrites of the Sn-rich γ phase solidify first, and subsequent nucleation of the eutectic near the γ dendrites is coarse and irregular. Regions of the In-Sn far removed from γ dendrites solidify in a fairly normal manner, thus producing some lamellar regions in the joint. The regions of very fine eutectic structure are large β-phase regions in which lamellae of the γ phase have precipitated during cooling. This is a result of the variation in composition of the β phase with temperature, as mentioned earlier.

The 8-μm layer of Ni in the Ni-plated samples is sufficient to prevent diffusion of Cu into the joint. This effect is expected, because a previous study showed that a 2-μm layer of Ni deposited on a Cu substrate underneath a coating of a Sn-bearing alloy was sufficient to prevent formation of Cu-Sn intermetallics.[6] Ni diffuses much more slowly than does Cu into liquid In-Sn, so only trace quantities of Ni reach the In-Sn. Therefore, no obstacles exist to prevent the formation of a normal, colony-based eutectic microstructure.

The effect of aging on the microstructure can be explained as a result of simple coarsening. The fine, lamellar eutectic of the In-Sn on Ni samples is inherently unstable, due to the high interfacial energy of the many interphase boundaries between the lamellae. When exposed to a high temperature, the phases will rearrange to lower their interfacial energy by reducing the number of interphase boundaries. This reduction is done not merely by coarsening the lamellar structure but also by spheroidization of the γ-phase regions, toward a geometry with the lowest possible surface-to-volume ratio. The microstructure of the In-Sn on Cu does not coarsen in this manner because it is fairly coarse in the as-cast condition and, therefore, has a much lower interfacial energy and insufficient driving force to cause noticeable rearrangement of the phases under the aging conditions of this study.

B. *Mechanical Behavior*

The creep data can be interpreted in terms of possible mechanisms for creep deformation in the two systems. The power law creep equation (Eq. [3]) is used to explain several creep mechanisms, among them dislocation creep controlled by diffusion. When diffusion in the lattice dominates, as opposed to diffusion in dislocation cores or along grain boundaries, the stress exponent is generally between 3 and 7. The activation energy for creep is equal to the activation energy for bulk self-diffusion in the case of a pure metal. For creep of two-phase alloys, the activation energy is often equal to the activation energy for creep/self-diffusion of the dominant phase, assuming that one phase dominates the creep deformation. In fine-grained materials, grain-boundary sliding can dominate over dislocation motion. In this case, the stress exponent drops to between 2 and 3 and the activation energy becomes equal to the activation energy for grain-boundary diffusion.

The data obtained in this study point strongly to diffusion-controlled dislocation creep as a likely creep mechanism. The stress exponents for In-Sn on Ni have

a mean value near 5 and those for In-Sn on Cu are all near 3, as mentioned previously. Studies on creep of the pure elements gave stress exponents near 7 for both tin[7] and indium.[8] While the stress exponent for In-Sn on Ni is below these values, it is still within the range for dislocation climb-controlled creep. An explanation for the lower stress exponent of In-Sn on Cu can be found by examining research on aluminum. Bradley[9] tested Al alloys at constant strain rate and found the strain-rate sensitivity to be near 0.15 for pure Al and near 0.3 for Al-2.9Mg. The strain-rate sensitivity is the inverse of the stress exponents, so the corresponding stress exponent would be near 7 for Al and 3 for Al-Mg. The Al-Mg alloy is a solid solution, similar to the β and γ phases in eutectic In-Sn. Reasons for the difference in behavior between In-Sn on Cu and on Ni will be made clearer in the discussion of activation energies.

Literature values for bulk self-diffusion activation energies of In and Sn are 0.78[10] and 1.08 eV,[11,12] respectively. The result of 0.73 eV for creep of In-Sn on Cu compares favorably to the value for pure In, and the result of 1.04 eV for creep of In-Sn on Ni is remarkably similar to that for self-diffusion of pure Sn. Kaur *et al.*[13] have surveyed the available data on grain-boundary diffusion in Sn and found reliable activation energies ranging from 0.41 to 0.464 eV. These values are significantly below the activation energies calculated for creep of In-Sn, implying that grain-boundary sliding is not dominant in either system. One factor complicating the determination of creep mechanisms for eutectic In-Sn is the fact that the alloy is composed of intermediate phases rather than terminal solid solutions, as mentioned earlier. Therefore, it is likely that the diffusivity within these phases will not be equal to the diffusivities of either of the pure elements. Diffusion data for In-Sn alloys are scarce. One reference reports diffusion of indium within a Sn-rich (1 to 8 at. pct In) γ' phase, located between the eutectic γ phase and pure Sn on the phase diagram.[14] Their data indicate an activation energy of 0.75 eV for diffusion along twist boundaries.

The calculated activation energy for creep of In-Sn on Cu is similar to activation energies for both self-diffusion of In and diffusion of In through the γ phase. Consequently, it is impossible to determine from these data alone which phase is controlling the creep. However, because the microstructure appears to consist of γ-phase regions in a β-phase matrix, it is reasonable to presume that the β phase dominates the creep deformation. The islands of γ phase are discontinuous and do not control the deformation but are swept along in the flow of the β phase. For In-Sn on Ni, the data strongly suggest that the Sn-rich γ phase is controlling the creep behavior. In the lamellar eutectic microstructure, the two phases are strongly coupled and the deformation is dominated by the harder phase. Creep controlled by the Sn-rich phase is also supported by creep data on pure Sn,[7] in which the authors found an activation energy for creep of 1.0 eV, similar to the activation energy for creep of In-Sn on Ni.

The correlation between creep and constant-strain-rate data is important but not surprising. The In-Sn alloy is tested at a high homologous temperature and will naturally creep (*i.e.*, undergo time-dependent plastic deformation) under any type of testing conditions above 200 K. Creep deformation is generally tested under constant-load conditions, both to allow unconstrained motion and to give a wider range of possible test conditions (minimum strain rates can range over many orders of magnitude). The continuity between the data from the two types of tests indicates that the same deformation mechanisms are operating regardless of whether stress or strain is the independent variable. It also shows that the shear strength at a given applied strain rate can be inferred from creep data.

The rapid decay in flow stress of the In-Sn on Cu can be explained in two different ways. The nonuniform deformation mentioned earlier has the consequence that the entire sample is not experiencing the strain measured by the strain gage, which registers overall displacement. Therefore, the local strain rate is actually higher than that measured by differentiating "bulk" strain with respect to time. The stress is also distributed over a smaller area than assumed, so that the stress calculated using Eq. [1] is too low, implying that the stress drop is not really as steep as the plots in Figure 8 indicate. However, this probably does not account for all of the stress drop. A second reason for a decrease in flow stress is microstructural softening, because recovery is expected to be significant at the testing temperatures used. Because the concentration of deformation cannot be quantified, it is difficult to tell how much of the apparent stress drop is due to this concentration and how much is due to microstructural softening.

The In-Sn on Ni samples exhibit neither severe deformation concentrations nor dramatic drops in the flow stress during stress-strain tests. It appears that with the geometrical factors eliminated, the slight decrease in stress during testing is due only to microstructural softening. This strengthens the idea that stress and strain concentrations are responsible for much of the stress decay observed in In-Sn on Cu.

V. CONCLUSIONS

The observed differences in mechanical behavior between In-Sn on Cu and on Ni are caused by the variation in the microstructure. The addition of a Ni diffusion barrier produces a more uniform microstructure, which in turn causes deformation to be more uniform; hence, the effect on the shape of the stress-strain curves. The microstructural effect also influences the operant mechanisms of creep deformation. The creep of In-Sn on Cu samples is dominated by bulk diffusion of In, most likely in the matrix β phase. In the colony microstructure of In-Sn on Ni, the two phases are interconnected, and, in this case, the creep deformation is governed by Sn diffusion through the harder γ phase. This explains the observed differences in activation energies for creep in the two systems. The equivalence of activation energies for creep and activation energies for self-diffusion of In or Sn is consistent with a diffusion-controlled dislocation climb mechanism. It is reasonable for stress exponents to be different for the deformation of each phase, as observed, while still being within range for dislocation

creep. When In-Sn on Ni samples are aged, they coarsen into a microstructure that is qualitatively similar to the In-Sn on Cu microstructure in that the soft β forms a matrix phase. The creep is now dominated by the β phase and, therefore, the behavior matches that of the In-Sn on Cu. This demonstrates the well-known fact that it is the nature of the microstructure, and not how it was formed, that determines mechanical behavior such as creep.

ACKNOWLEDGMENTS

The authors would like to thank Dr. C. Kim for conducting the DSC tests and for helpful discussions. The solder alloy used in this study, Indalloy lE, was provided by the Indium Corporation of America. This work was supported by the Director, Office of Energy Research, Office of Basic Energy Sciences, United States Department of Energy, under Contract No. DE-AC03-76SF00098.

REFERENCES

1. C.E.T. White and G.P. Evans: *Res. Dev.*, 1986, vol. 28, pp. 88-90.
2. R. Kubiak, M. Wolcyrz, and W. Zacharko: *J. Less-Common Met.*, 1979, vol. 65, pp. 263-69.
3. Fuh-Kuo Chen: Ph.D. Dissertation, University of California, Berkeley, CA, 1989.
4. J.L. Freer and J.W. Morris, Jr.: *J. Electron. Mater.*, 1992, vol. 21, pp. 647-52.
5. J.L. Freer Goldstein: Ph.D. Dissertation, University of California, Berkeley, CA, 1993.
6. V.V. Slepushkin and G.S. Mukovnina: *Zashch. Met.*, 1985, vol. 21, pp. 280-82.
7. F.A. Mohamed, K.L. Murty, and J.W. Morris, Jr.: *Metall. Trans.*, 1973, vol. 4, pp. 935-40.
8. R. Darveaux, E. Yung, I. Turlik, and K.L. Murty: *Mater. Res. Soc. Symp. Proc.*, 1991, vol. 203, pp. 443-48.
9. E.L. Bradley III: Ph.D. Dissertation, University of California, Berkeley, CA, 1993.
10. R.E. Eckert and H.J. Drickamer: *J. Chem. Phys.*, 1952, vol. 20, pp. 13-17.
11. J.D. Meakin and E. Klokholm: *Trans. TMS-AIME*, 1960, vol. 218, pp. 463-66.
12. C. Coston and N.H. Nachtreib: *J. Phys. Chem.*, 1964, vol. 68, pp. 2219-29.
13. I. Kaur, W. Gust, and L. Kozma: *Handbook of Grain and Interface Boundary Diffusion*, Ziegler Press, Stuttgart, Germany, 1989, pp. 1277-85.
14. E.I. Rabkin, L.S. Shvindlerman, and B.B. Straumal: *J. Less-Common Met.*, 1990, vol. 158, pp. 23-33.
15. C.E.T. White and H. Okamoto: *Phase Diagrams of Indium Alloys and Their Engineering Applications*, Indium Corporation of America, Utica, NY, and ASM INTERNATIONAL, Metals Park, OH, 1992, p. 255.

The Effect of Inertia on Tensile Ductility

XIAOYU HU, ROBERT H. WAGONER, GLENN S. DAEHN, and SOMNATH GHOSH

One-dimensional numerical simulations of dynamic tensile tests have been carried out over a wide range of test velocities for materials having a *Hollomon*-type constitutive law with power-law strain-rate sensitivity. A variety of values of the strain-hardening exponent and strain-rate-sensitivity index have been used to analyze the effect of inertia on tensile ductility. Results show that the total elongation of the specimen is enhanced by inertia at high test velocities. This inertial effect varies with the strain-hardening exponent and strain-rate-sensitivity index and can be scaled with the normalized material density and the test velocity. Based on these results, the critical test velocity for the onset of the inertial effect as a function of material parameters has been numerically determined. To account for the effect of inertia on the enhancement of tensile ductility, a simple phenomenological explanation has been proposed.

I. INTRODUCTION

THE estimation of tensile ductility has been studied from a variety of theoretical perspectives, including those involving plastic-instability and flow-localization (necking) concepts. The earliest analysis describing the onset of instability in uniaxial tension was conducted by Considére,[1] according to whom instability occurs at the load maximum, where the load increment caused by strain hardening is equal to the load decrement caused by geometrical softening. However, Considére's criterion is only valid for a rate-independent material. For this material, necking and failure follow rapidly after the maximum load is attained.

For materials that exhibit rate-dependent behavior, on the other hand, the extensive analytical and experimental investigations of Hart[2] and others[3–26] indicate that strain-rate sensitivity delays the onset of instability pertaining to rate-independent materials and induces post-uniform elongation, leading to an enhancement of tensile ductility. For such materials, several criteria for predicting the onset of instability have been proposed, and relationships between the failure strain, e_T, and material parameters (the strain-hardening exponent, n, and strain-rate-sensitivity index, m) have been established. Although it has been commonly accepted that m is unimportant prior to the maximum load and n is unimportant after the maximum load,[27] a detailed, two-dimensional finite element analysis of the sheet tensile test[22] has revealed that the total elongation, e_T, is strongly affected by both n and m. Furthermore, it has been of interest to note that for the given n and m values, the strain distribution and necking behavior of rate-dependent materials, which obey power-law strain-rate sensitivity, are independent of the strain rate under quasi-static and isothermal conditions.[21,28,29]

Although the influence of strain rate on tensile instability and necking has been extensively studied, the strain rates employed in these investigations were typically limited to low values. When materials deform at low rates, the variation of the material velocity with time is small. In these cases, the material acceleration and the propagation of plastic waves are negligible, so that quasi-static equilibrium can be assumed. The development of strain gradients during such tests relies only on the static axial-force equilibrium at any cross section of the gage length. A tensile test at high strain rates must be distinguished from a test at low strain rates by the fact that inertia becomes significant. In this case, a dynamic-equilibrium condition should be satisfied.

Experimentally, an improvement of tensile ductility at high strain rates has been observed in high-strength steel,[30] stainless steel,[31] oxygen-free, high-conductivity copper (OFHC copper),[32,33] tantalum,[34] and Ti alloys.[35] Compared with the results obtained at rates ranging from 10^{-4} to 10^{-2} s^{-1}, the total elongation of the specimen for these materials increases by 20 to 50 pct at a strain rate around 3×10^3 s^{-1}. Recently, it also has been shown that the plane-strain formability of interstitial-free iron sheet can be dramatically enhanced (to about three times the quasi-static, plane-strain forming limit) at a strain rate of 10^3 s^{-1}. These experiments were performed with an electrohydraulic forming technique.[36]

In spite of these interesting observations, however, it is difficult to distinguish the effect of inertia on tensile ductility from strain-rate sensitivity experimentally, because rate sensitivity can change with strain rates.[18] This difficulty motivates the theoretical modeling of tensile ductility at high strain rates.

Taylor *et al.*[37] presented a one-dimensional hydrodynamic formulation to analyze the effect of inertia on the growth rate of an assumed perturbation in a thin, stainless steel sheet stretching dynamically. They found that many perturbations will be harmless at strain rates of 10^4 s^{-1} or greater. Within the framework of a one-dimensional theoretical model for uniaxial tension, Fressengeas and Molinari[38,39] have examined the influence of inertia and thermal softening together on the ductility of materials with both the linear perturbation and nonlinear analyses. The calculations revealed a more than 40 pct increase of the total elongation at 500 °C and around 10^3 s^{-1} for tantalum, which was consistent with

XIAOYU HU, Postdoctoral Researcher, ROBERT H. WAGONER, Professor, and GLENN S. DAEHN, Associate Professor, Department of Materials Science and Engineering, and SOMNATH GHOSH, Assistant Professor, Department of Engineering Mechanics, are with The Ohio State University, Columbus, OH 43210.

Manuscript submitted June 21, 1993.

experimental results.[34] In the work of Regazzoni *et al.*,[40] a one-dimensional numerical simulation of the dynamic tensile test was carried out using the finite-difference method for copper. In their study, two different material laws were considered simultaneously. At low strain rates, a power-law was used simply to describe the stress-strain relationship, while another material law, having a linear relation between the stress and strain rate,[41–44] was introduced when the strain rate was high. The emphasis of this investigation was on the effect of inertia on the unloading of the nonperturbed region. Simulated results indicated that when the strain rate is around 10^3 s^{-1}, inertia can induce an additional postuniform elongation of 5 pct for rate-insensitive materials and 10 pct for rate-sensitive materials. These results were in reasonable agreement with the experimental observations.[32] Following the work done by Regazzoni *et al.*, a similar simulation of the dynamic tensile test also has been carried out using the finite element method by Dumont *et al.*[45] In this study, the inertial effect was investigated for various locations of the geometric defect in the specimen and different rheological parameters. The results showed that the inertial effect is independent of the location of the geometric defect, except that this defect is at the mobile end. In addition, they also found that for a given high rate, the increment of postuniform elongation can be promoted by increasing the material density, ρ, or decreasing the strength coefficient, k.

The present work was undertaken as a follow-up to the studies cited previously for high rate deformation. In this study, a simple one-dimensional dynamic numerical treatment has been proposed to simulate the uniaxial sheet-tensile test over a wide range of test velocities for materials having a *Hollomon*-type[46] material law with power-law strain-rate sensitivity. On this basis, the effects of inertia on tensile ductility for a range of strain-hardening exponents, n, and strain-rate-sensitivity indices, m, have been examined. Additionally, the scaling of the inertial effect with the normalized material density, ρ_n, and the test velocity, V, also has been studied. To isolate the inertial effect in this work, elastic strains, thermal softening, and other effects (such as the change of deformation micromechanisms and the microstructure) have been ignored.

II. ANALYSIS

A. *Problem Formulation*

Consider one-half of a tapered sheet-tensile specimen with the tensile axis defined as x (Figure 1). When the specimen is dynamically subjected to an uniaxial tensile force, for materials being assumed to be incompressible, the momentum equation governing the one-dimensional dynamic deformation is simply expressed as

$$\frac{\partial}{\partial x} f(t, x) = \rho A(x) \frac{\partial v(t, x)}{\partial t} \qquad [1]$$

where $v(t, x)$ is the material velocity at time t, $A(x)$ is an original cross section area of the specimen, and ρ is the material density.

In Eq. [1], $f(t, x)$ is called the axial internal force and is equal to the product of the axial true stress, $\sigma(t, x)$, and the specimen cross section area at time t, $a(t, x)$.

$$f(t, x) = \sigma(t, x)\, a(t, x) \qquad [2]$$

In Eq. [2], $\sigma(t, x)$ is generally a function of the true axial strain, ε, and true axial strain rate, $\dot{\varepsilon}$. Although various forms for $\sigma = \sigma(\varepsilon, \dot{\varepsilon})$ are available,[46–49,18,19] in the present study, a *Hollomon*-type material law[46] with power-law strain-rate sensitivity is assumed and $\sigma(t, x)$ is thus given by

$$\sigma(t, x) = k\varepsilon(t, x)^n \dot{\varepsilon}(t, x)^m \qquad [3]$$

where k, n, and m refer to the strength coefficient, strain-hardening exponent, and strain-rate sensitivity index, respectively.

By imposing the invariance of the plastic volume, $a(t, x)$ then can be determined from the following relation:

$$a(t, x) = A(x) \exp\left[-\varepsilon(t, x)\right] \qquad [4]$$

To simulate a displacement-controlled uniaxial tensile test at a uniform crosshead speed (the test velocity), the initial and boundary conditions, which are the same as those used by earlier investigators,[37–40,45] are specified.

At $t = 0$,

$$v(0, x) = \frac{V}{l_0} x \quad \text{and} \quad \varepsilon(0, x) = 0 \qquad [5]$$

At $t = t$,

$$v(t, 0) = 0 \quad \text{and} \quad v(t, l_0) = V \qquad [6]$$

where V is the test velocity and l_0 is the specimen gage length. In Eqs. [5] and [6], an initial linear material velocity distribution in the specimen is defined and a transit period for establishing this velocity distribution is ignored. The influence of the transit period on ductility will be reported in a forthcoming article,[50] in which the calculations have been carried out by imposing the boundary velocity

$$V(t) = V_m[1 - \exp(-t/t_c)][51]$$

where V_m is the crosshead speed the machine can reach finally and t_c is a critical time that characterizes the acceleration of the transit period.

The nonlinear partial differential equation, Eq. [1], along with the material law, Eq. [3], sets the problem of dynamic plastic flow during tension. However, a solution that satisfies the initial and boundary conditions, Eqs. [5] and [6], cannot be given in a closed form.

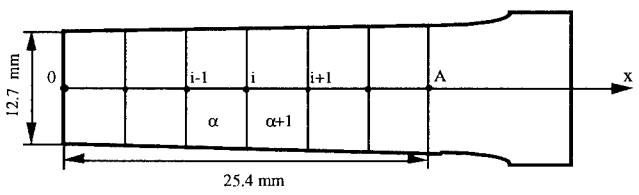


Fig. 1—Schematic illustration of the spatial discretization of a sheet tensile specimen.

Therefore, a numerical treatment in which the problem is discretized spatially and temporally, is used.

B. *Problem Discretization*

Figure 1 schematically shows the spatial discretization of the specimen performed by dividing it into a finite number of elements of equal length L along the x-axis. Each element is assumed to have a constant true axial stress, true axial strain, true axial strain rate, and cross section area. In Figure 1, Greek and English letters are used to represent the element and element node, respectively. For this system of finite elements, the variational form of momentum equation, Eq. [1], consists of maintaining an equilibrium between a resultant internal force, F_i, and an inertial force, $M_i\ddot{u}_i$, in the x-direction on each node.

$$M_i\ddot{u}_i + F_i = 0 \qquad [7]$$

where $\ddot{u}_i$ and M_i are designated as the nodal acceleration and mass, respectively.

The nodal resultant internal force, F_i, is obtained by summing the internal forces of two adjacent elements associated with this node, α and $\alpha + 1$ (Figure 1). Following the assumption previously described, the internal force of each element is simply equal to the product of the element true stress, σ_α, and the element current cross section area, a_α. Thereby, F_i is expressed as

$$F_i = \sigma_\alpha a_\alpha - \sigma_{\alpha+1}a_{\alpha+1} \qquad [8]$$

Using Eqs. [3] and [4], Eq. [8] can be written easily as an alternative form.

$$F_i = k[\varepsilon_\alpha^n \dot{\varepsilon}_\alpha^m A_\alpha \exp(-\varepsilon_\alpha) - \varepsilon_{\alpha+1}^n \dot{\varepsilon}_{\alpha+1}^m A_{\alpha+1} \exp(-\varepsilon_{\alpha+1})] \qquad [9]$$

Equation [9], although it is derived for the nodal-resultant internal force under dynamic response, also can be applied in the quai-static case. If F_i is set to zero to meet the static equilibrium, Eq. [9] provides a direct calculation for the strain and strain-rate distributions along the x-axis in the specimen. This method has been employed successfully to predict plastic instability and necking development in the quasi-static tensile test simulation.[52,53]

The nodal mass, M_i, is obtained by lumping the mass of all connecting elements at associated nodes.[54–57] For the element mesh presented in Figure 1, M_i is readily calculated by

$$M_i = \frac{\rho L}{2}(A_\alpha + A_{\alpha+1}) \qquad [10]$$

By introducing the natural logarithm relation between the element true strain ε_α and the nodal displacement u_i, and assuming $\dot{\varepsilon} = \Delta\varepsilon/\Delta t$ during each time step Δt, a substitution of Eqs. [9] and [10] into Eq. [7] yields

$$\rho_n\ddot{u}_i - \frac{1}{\Delta t^m}\sum_{\kappa=\alpha}^{\kappa=\alpha+1}\xi_\kappa\left[\ln\left(1+\frac{u_\kappa}{L}\right)\right]^n \cdot\left[\Delta\ln\left(1+\frac{u_\kappa}{L}\right)\right]^m \frac{\partial\ln(1+u_\kappa/L)}{\partial u_i} = 0 \qquad [11]$$

Equation [11] is a system of nonlinear equations with respect to u_i at time t with the following definitions:

$$\rho_n = \frac{\rho}{k} \qquad [12]$$

$$u_\alpha = u_i - u_{i-1} \qquad [13]$$

$$u_{\alpha+1} = u_{i+1} - u_i \qquad [14]$$

$$\xi_\alpha = \frac{2A_\alpha}{L(A_\alpha + A_{\alpha+1})} \qquad [15]$$

$$\xi_{\alpha+1} = \frac{2A_{\alpha+1}}{L(A_\alpha + A_{\alpha+1})} \qquad [16]$$

where ρ_n is called the normalized material density.

The solution of Eq. [11] can be solved with the progression of time by numerical time integration. As a solver, the average acceleration method[58] in the most widely used *Newmark* family of numerical-time-integration algorithms[59,60,61] is employed.

$$\ddot{u}_i^t = \frac{4(u_i^t - u_i^{t-\Delta t})}{\Delta t^2} - \frac{4\dot{u}_i^{t-\Delta t}}{\Delta t} - \ddot{u}_i^{t-\Delta t} \qquad [17]$$

where the superscripts t and $t - \Delta t$ present the current and last times, respectively. The average acceleration method provides an unconditional stability and establishes an implicit implementation for the solution, in which u is solved iteratively according to the equilibrium condition at time t.

The time-step, Δt, shown in Eqs. [11] and [17], is usually determined by the prescribed boundary condition for the simple tension test. From Eq. [6], one can obtain

$$\Delta t = \frac{\Delta U}{V} \qquad [18]$$

where ΔU is the displacement increment at the mobile end of the specimen.

When Eqs. [17] and [18] are applied to Eq. [11]. Eq. [11] is rearranged into

$$\frac{4\rho_n V^{2-m}}{\Delta U^{2-m}}(u_i^t - \psi_i^{t-\Delta t}) - \sum_{\kappa=\alpha}^{\kappa=\alpha+1}\xi_\kappa\left[\ln\left(1+\frac{u_\kappa^t}{L}\right)\right]^n \cdot\left[\Delta\ln\left(1+\frac{u_\kappa^t}{L}\right)\right]^m \frac{\partial\ln(1+u_\kappa^t/L)}{\partial u_i^t} = 0 \qquad [19]$$

where $\psi_i^{t-\Delta t}$ is a constant with respect to time t and is given by

$$\psi_i^{t-\Delta t} = u_i^{t-\Delta t} + \Delta t\dot{u}_i^{t-\Delta t} + \frac{\Delta t^2\ddot{u}_i^{t-\Delta t}}{4} \qquad [20]$$

Equation [19] is the final form of the one-dimensional dynamic governing equation employed in the present work, which allows one to study numerically the effect of inertia on tensile ductility over a wide range of test velocities.

C. *Calculation Procedures*

The simulation was performed on a half-gage length of the tensile specimen with 1-mm thickness. The dimensions of the gage length are given in the region 0*A* of Figure 1. Within the gage length, the geometry of the specimen has a linear 1 pct taper.

A program was developed to implement the problem formulation. At every time t, the nodal accelerations, velocities, displacements, element strains, and strain rates were calculated. Based on these calculated values, engineering stress-strain curves were determined.

In an actual tensile test, physical failure can be characterized by a degree of strain localization defined by $\dot{\varepsilon}_c/\dot{\varepsilon}_{Av}$, where $\dot{\varepsilon}_c$ is the rate of deformation at the center of the specimen and $\dot{\varepsilon}_{Av}$ is the average rate of deformation of the entire tensile test sample. This ratio increases after the maximum load has been reached and continues to increase until fracture. Thus, by choosing a value for this ratio, which reasonably corresponds to physical failure, the failure criterion is set. In this simulation, $\dot{\varepsilon}_c/\dot{\varepsilon}_{Av}$ was numerically set to 5, as was employed in earlier investigations,[22,53] for all of the calculations proceeded at different test velocities. This value has no direct physical meaning.

To explore the inertial effect for a range of material parameters, six cases of n values have been simulated (n = 0.0, 0.0625, 0.125, 0.25, 0.375, and 0.5), each having seven cases of m values (m = 0.0, 0.01, 0.02, 0.05, 0.1, 0.2, and 0.3). These simulations were carried out using a material density of 7870 kg/m^3 and a strength coefficient of 622 MPa (the corresponding normalized material density was ρ_n = 12.65 kg/(m^3 MPa)). The value of the strength coefficient, k, was obtained from experimental data of interstitial free steel.[62]

The test velocity, V, was considered from 2.54×10^{-6} to 127.0 m/s. Note that the transition time for the test velocity to reach during testing is generally around 5 to 20 μs.[51,63,40] Thus, in the calculations, the test velocity was selected in such a way that this transit occupies only a small part of the deformation. Under this circumstance, the use of the initial and boundary conditions, Eqs. [5] and [6], appears justified.

III. RESULTS

A. *Numerical Accuracy Analysis*

In order to converge to the correct strain distribution in the specimen using the smallest number of elements and the largest end-displacement increment, ΔU, possible with the least error, a measure of the relative error of the strain distribution, S, was introduced:

$$S = \frac{\sqrt{\dfrac{\sum_{i=1}^{N} (\varepsilon_i - \varepsilon_i^{\text{base}})^2}{N}}}{(\varepsilon_i^{\text{base}})_{\min}} \qquad [21]$$

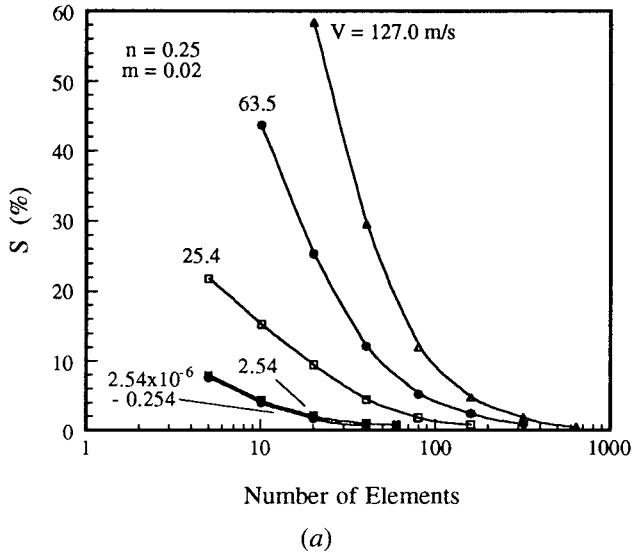
where $\varepsilon_i^{\text{base}}$ is the accurate strain distribution, which in principle could be obtained by analytically solving Eq. [1] at the failure time, and ε_i is the strain distribution calculated numerically at the same time. The term N is the number of data points used in comparison of ε_i with $\varepsilon_i^{\text{base}}$. In effect, however, for the calculation of S, $\varepsilon_i^{\text{base}}$ in Eq. [21] was replaced by a strain distribution calculated numerically with a very large element number and a very small ΔU, because, as indicated previously, Eq. [1] cannot be solved analytically in general. As such, the systematic error of the numerical procedure unrelated to the element size or step size will be built into $\varepsilon_i^{\text{base}}$.

Optimization was first performed for the spatial discretization. Then, using the selected number of elements, the temporal discretization was subsequently examined. The criterion employed to optimize the number of elements and ΔU is that S must be less than or equal to 1 pct.

With n = 0.25, the typical variation of S with the number of elements at different test velocities is plotted in Figures 2(a) and (b) for m = 0.02 and 0.2, respectively. The numbers of elements and ΔU used to calculate $\varepsilon_i^{\text{base}}$ for these two cases were 1280 and 2.54×10^{-7} m. Figure 2(a) shows a strong influence of the velocity on the S variation at m = 0.02. The higher the velocity is, the larger the variation of S with the number of elements. This behavior arises from the fact that the error produced in the inertial force calculation is velocity-dependent. For a given number of elements, the spatial discretization error of the inertial force increases with an increase in the test velocity because of an increase of the material acceleration in the specimen. When m = 0.2 is employed, however, the effect of the velocity on the S curve is considerably reduced (Figure 2(b)). This reduction is primarily ascribed to a rise in $(\varepsilon_i^{\text{base}})_{\min}$ due to increases of strains at high m values (*i.e.*, the effect of strain-rate sensitivity), leading to a drop in S.

From the results of Figure 2, one would anticipate that the number of elements optimized by an estimation of S would increase with an increase of the velocity, especially at small m values. The numbers of elements required at different test velocities for various m values are listed in Table I for n = 0.25. As expected, Table I indicates that the number of elements is increased by increasing the velocity at m = 0.0 to 0.2 and remains nearly the same when m is equal to 0.3. These numbers are also adequate for other n values, with the exception of when a small n is associated with a small m. When materials have both small n and m values, more elements are needed in order to satisfy the error criterion.

As an example, Figure 3 shows S as a function ΔU at different test velocities for the case n = 0.25 and m = 0.02. In this case, ΔU used to calculate $\varepsilon_i^{\text{base}}$ was still 2.54×10^{-7} m, but the numbers of elements used here were those shown in Table I. As shown in Figure 3, all of the errors are located in a band for the entire velocities considered in this simulation. The behavior demonstrated in Figure 3 does not change significantly by changing n and m. As a result, in this study, a ΔU of 2.54×10^{-4} m was adopted for all calculations, thereby satisfying the error condition. The time step, Δt, used for different velocities then can be readily determined by Eq. [18].



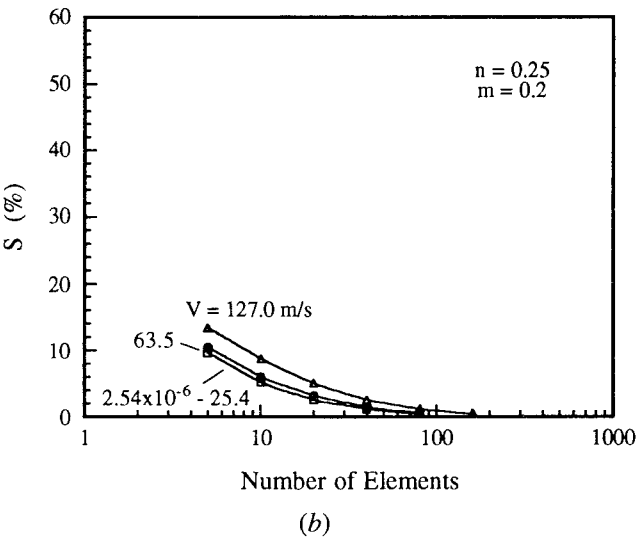


Fig. 2—The relative error, S, as a function of the number of elements at different test velocities for (*a*) $n = 0.25$ and $m = 0.02$ and (*b*) $n = 0.25$ and $m = 0.2$.

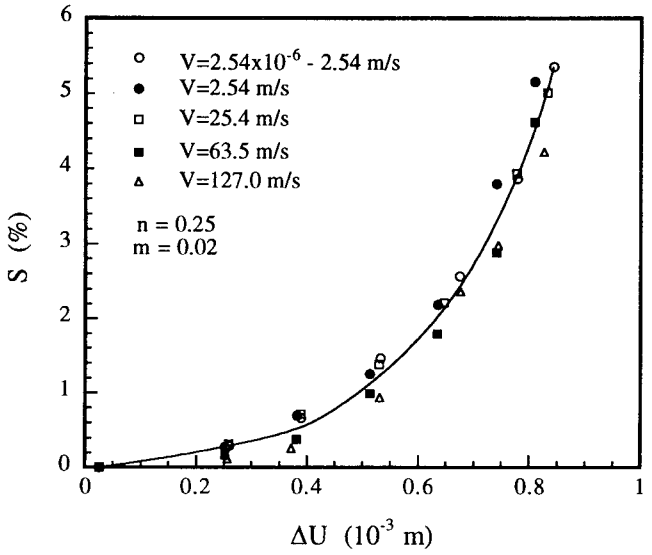


Fig. 3—The relative error, S, as a function of the displacement increment step, ΔU, at different test velocities for $n = 0.25$ and $m = 0.02$.

B. *Engineering Stress-Strain Relations at Different Test Velocities*

The simulated engineering stress-strain curves over a range of the test velocities are plotted in Figure 4 for various values of n and m. The engineering stress, Σ, which is normalized by k, is obtained from the tensile force at the mobile end divided by the original cross-sectional area, while the engineering strain (elongation), e, is calculated by the total end displacement divided by the gage length l_0.

Figure 4(a) demonstrates engineering stress-strain curves for the case $n = 0.25$ and $m = 0.02$. From these curves, it can be seen that the total elongation of the specimen, e_T, defined at the failure, remains the same when the specimen deforms at low test velocities from 2.54×10^{-6} to 2.54 m/s. When this range of velocities is exceeded, however, an increasing test velocity increases e_T. As was noted previously, quasi-static simulations yield results independent of test velocities, corresponding to the low test velocities computed here. Therefore, the results shown in Figure 4(a) indicate that the increase of the total elongation at high test velocities must be attributed to the inertia term in Eq. [7], $M_i \ddot{u}_i^t$. Accordingly, it can be concluded that the presence of inertia can enhance tensile ductility and that this inertial effect must appear beyond a critical test velocity.

It can also be noted in Figure 4(a) that the maximum load elongation (uniform elongation), e_u, marked by the cross sign on these curves, does not change significantly by changing the test velocity. This observation implies that the contribution of inertia to e_T is primarily through a stabilization of nonuniform strain distribution.

Engineering stress-strain curves for different material

Table I. Number of Elements Required for 1 Pct Error ($n = 0.25$)

m	2.54×10^{-6}-0.254 m/s	2.54 m/s	12.7 m/s	25.4 m/s	63.5 m/s	127.0 m/s
0.0	40	80	160	320	640	1280
0.01	40	60	80	160	320	640
0.02	40	60	80	160	320	640
0.05	40	60	80	160	320	640
0.10	60	60	60	80	160	320
0.20	60	60	60	60	80	160
0.30	60	60	60	60	60	80

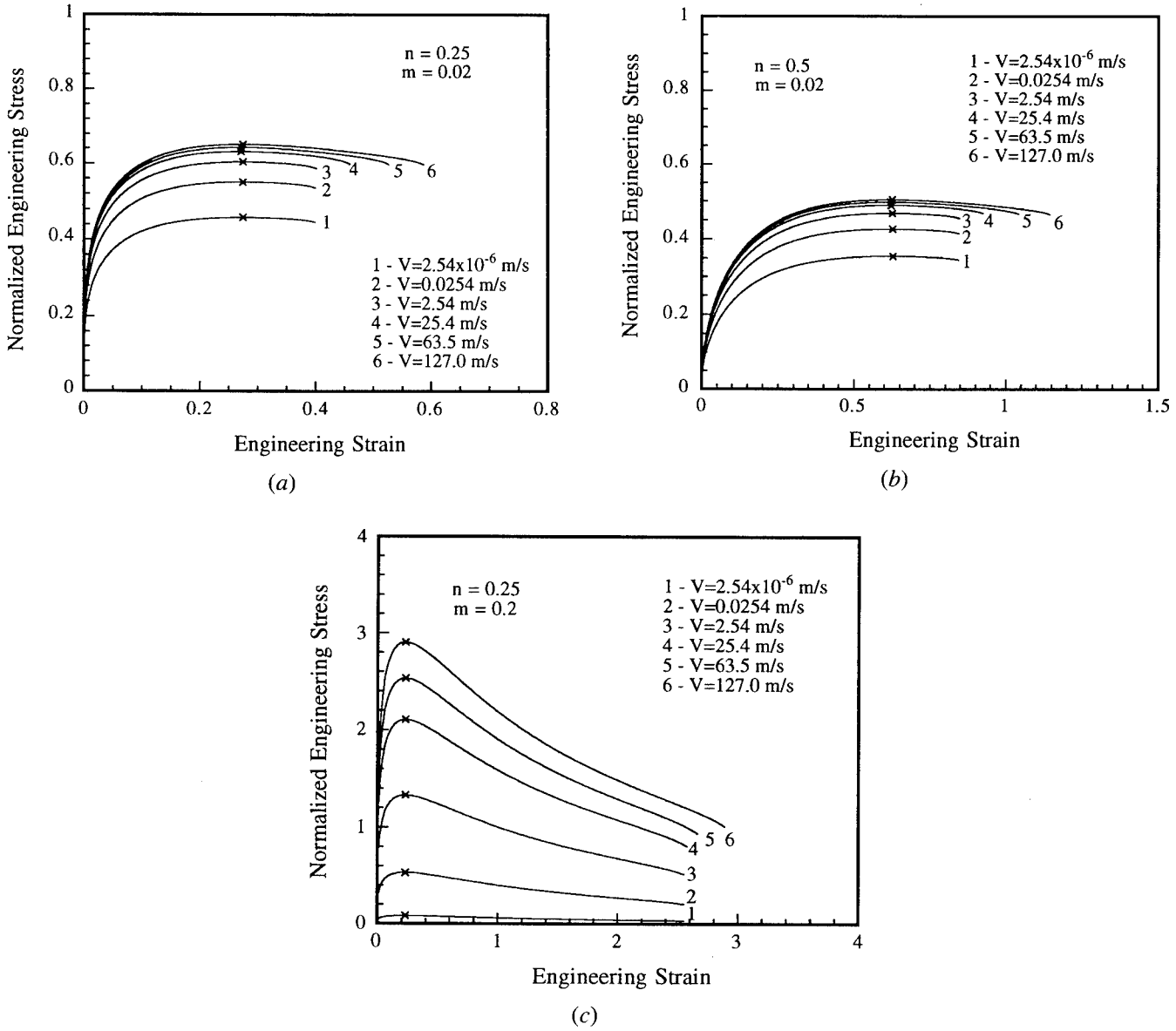


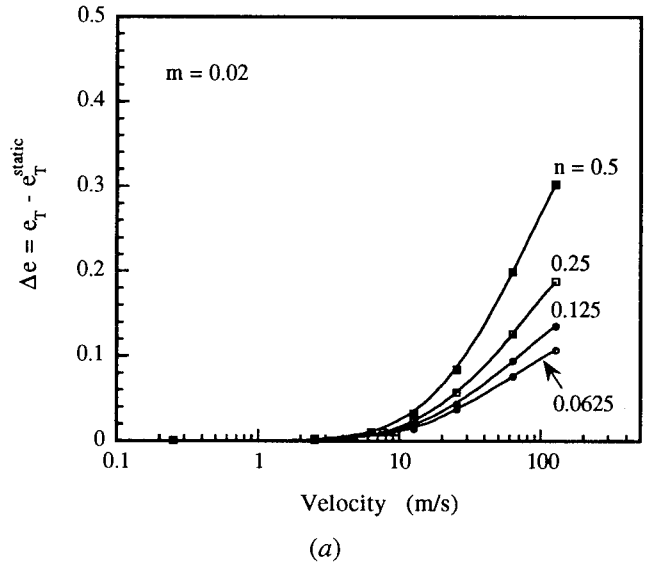
Fig. 4—Engineering stress-strain curves at different test velocities for various values of n and m: (*a*) $n = 0.25$ and $m = 0.02$, (*b*) $n = 0.5$ and $m = 0.02$, and (*c*) $n = 0.25$ and $m = 0.2$.

constants are represented in Figures 4(b) and (c), respectively. Velocity-dependent stress-strain behavior similar to that indicated in Figure 4(a) is also shown in these two figures. Within the test velocity regime studied, in each combination of n and m, e_T rises at high velocities but e_u does not vary. However, a comparison between these figures and Figure 4(a) reveals that the extent of the total elongation increment caused by inertia changes for different cases. This change is examined in Section C.

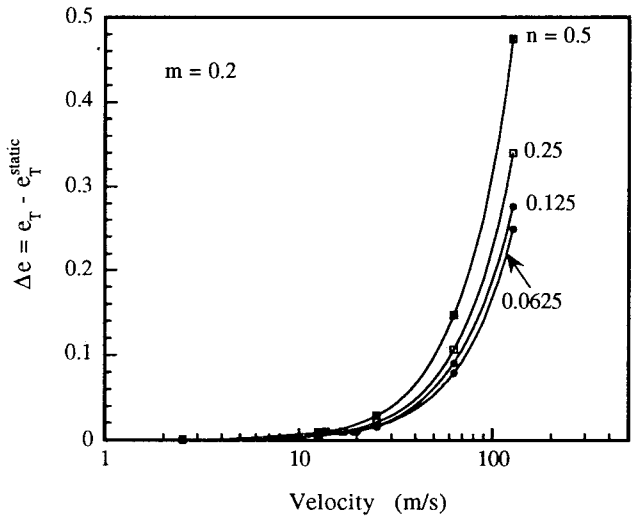
C. *The Effect of n and m on Inertia-Enhanced Ductility*

If the total elongation of the specimen, e_T, obtained using the dynamic formulation (Eq. [19]) is subtracted from that obtained by using the quasi-static one (Eq. [9] with a zero F_i), the difference, $\Delta e = e_T - e_T^{\text{static}}$, denotes the additional elongation induced by inertia. By this definition, the influence of inertia on tensile ductility and the critical test velocity for the onset of the inertial effect, V_{crit}, can be studied for different material parameters. In this simulation, V_{crit} was designated when Δe was equal to $0.01\ e_T^{\text{static}}$.

The variation of Δe with the test velocity for different n is illustrated in Figures 5(a) and (b) for $m = 0.02$ and 0.2, respectively. It shows that increasing n increases Δe for a given test velocity. The value of Δe as a function of the test velocity for different m is represented in Figures 6(a) and (b) for $n = 0.25$ and 0.5, respectively. Unlike the results shown in Figure 5, a simple relationship between Δe and m does not exist. The Δe curves in Figure 6 overlap. The critical velocity, V_{crit}, as a function of material parameters, n and m, is summarized in Figure 7, which indicates that V_{crit} increases with either an increase of n or m.

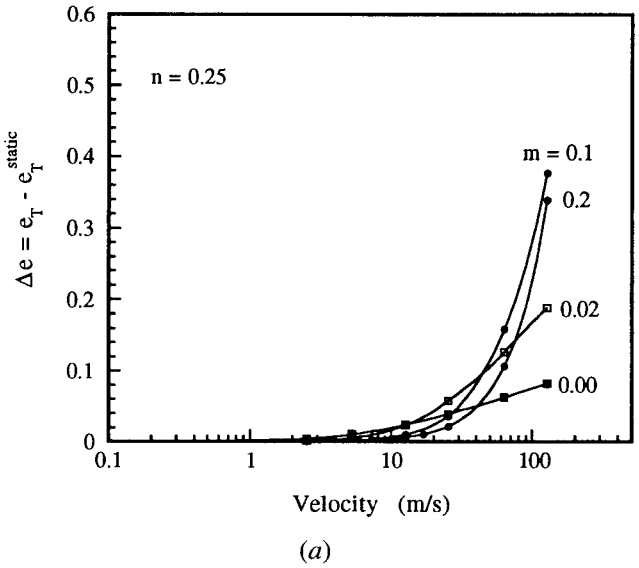


(a)

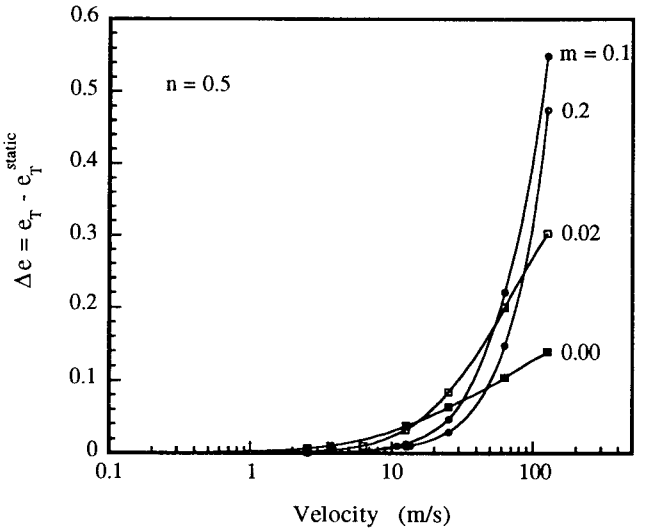


(b)

Fig. 5—The influence of n on the inertia-induced additional elongation, Δe, for (*a*) $m = 0.02$ and (*b*) $m = 0.2$.



(a)



(b)

Fig. 6—The influence of m on the inertia-induced additional elongation, Δe, for (*a*) $n = 0.25$ and (*b*) $n = 0.5$.

The previous results have already shown that the inertial effect introduces an additional elongation to the specimen at high test velocities and that the magnitude of this inertia-induced additional elongation is dependent upon n and m. However, it is well known that an increase of n and m increases static tensile ductility. Thus, a question arises as to how important the inertia-induced additional elongation is relative to the total elongation when n and m are varied. Answering this question can facilitate an understanding of the relative contribution of inertia to tensile ductility. Toward this end, $\Delta e/e_T$ was examined as a function of n and m, with the results presented in Figures 8 and 9 for four test velocities, V = 12.7, 25.4, 63.5, and 127.0 m/s.

Figures 8(a) and (b) demonstrate an influence of n on $\Delta e/e_T$ for $m = 0.02$ and 0.2, respectively. These figures show that the inertial effect is most important in materials of limited ductility (*i.e.*, those with low n and m values). However, a closer look at m *vs* $\Delta e/e_T$ (Figure 9) reveals that small values of m originally promote a greater relative contribution of inertia to tensile ductility.

D. *The Scaling of the Inertial Effect*

Equation [19] shows that the product of $\rho_n V^{2-m}$ appears in the first term. As a result, for given n and m, the inertial effect by using the normalized material density, ρ_n, can be regarded as equivalent to varying V. This scaling is followed by the following relation.

$$\rho_n V^{2-m} = C \qquad [22]$$

where C is a constant. This relation states that the inertial effect produced by a change in the normalized material density (by factor of 10) is equivalent to that produced by a change in the test velocity (by $10^{1/(2-m)}$).

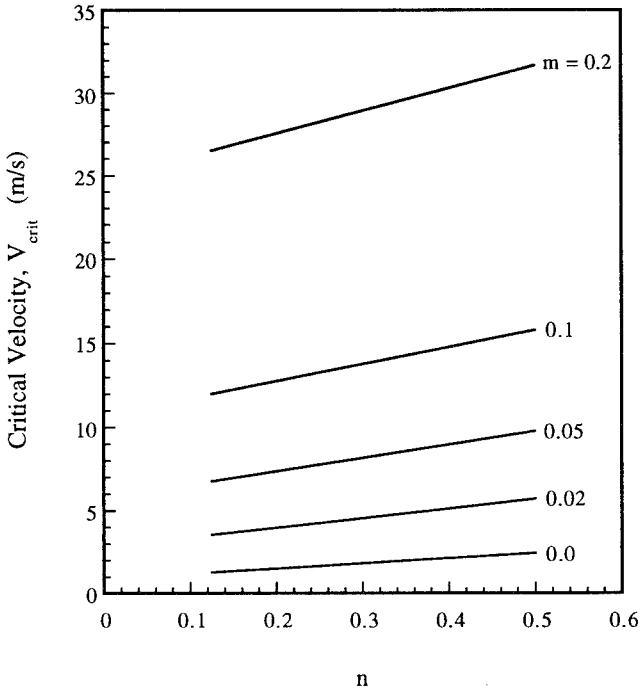


Fig. 7—The critical velocity for the onset of the inertial effect, V_{crit}, as a function of material parameters, n and m.

As an example, Figure 10 plots Δe as a function of ρ_n/ρ_n^{base} and V/V_{crit} simultaneously, where V_{crit} is defined as before and ρ_n^{base} is the normalized material density that corresponds to V_{crit}. As shown in Figure 10, when the relation $V/V_{crit} = (\rho_n/\rho_n^{base})^{1/(2-m)}$ is employed, an identical increase of Δe occurs with those two different scales, thus verifying the inertial scaling. To calculate Δe, the values $V_{crit} = 4.26$ and 28.24 m/s, determined previously, were used for Figures 10(a) and (b), respectively, and a normalized material density of 12.65 kg/(m^3 MPa) was used as ρ_n^{base} for both figures.

Note that increasing ρ_n increases Δe (Figure 10). Since ρ_n is defined by ρ/k (Eq. [12]), the results in Figure 10 indicate that the inertial effect can be enhanced either by increasing ρ or decreasing k. This is in agreement with the earlier observations.[45]

A direct implication of this scaling is to calculate V_{crit} for a group of materials that have the same n and m but different ρ_n. A typical calculation is shown in Figure 11. In this figure, with $m = 0$, solid lines represent V_{crit} calculated using Eq. [22] for $n = 0.25$ and 0.375, respectively, and the marked signs represent those determined numerically for two groups of selected materials having the same n and m. From Figure 11, it can be seen that the V_{crit} determined numerically coincides with those obtained by the scaling calculation, showing a decrease of V_{crit} with an increase of ρ_n. This behavior is also true when $m \neq 0$, which is not represented here.

Figure 12 summarizes V_{crit} for 22 metals and alloys. The parameters of these materials, n, m, k, ρ, and ρ_n, are listed in Table II together with V_{crit}. In this table, for materials for which n and k are not available, n and k were approximately calculated by

$$n = \ln (1 + e_u) \quad [23]$$

$$k = \frac{\Sigma_u(1 + e_u)}{[\ln (1 + e_u)]^n} \quad [24]$$

where Σ_u and e_u are designated as the tensile strength and uniform elongation, respectively, and can be found in the literature. Note that all real materials have $m \neq 0$, but there are little data available. Hence, most of V_{crit} presented in Figure 12 (also in Table II) were calculated by assuming $m = 0$. The open circles in Figure 12 stand for materials having real m and the solid ones for those with $m_{assumed} = 0$. From the fact that increasing m increases V_{crit} Figure 7, the calculated V_{crit} for materials having $m_{assumed} = 0$ can provide a reasonable estimate of minimum critical velocities for the onset of the inertial effect. The results of Figure 12 qualitatively demonstrate the degree of the inertial effect for different materials.

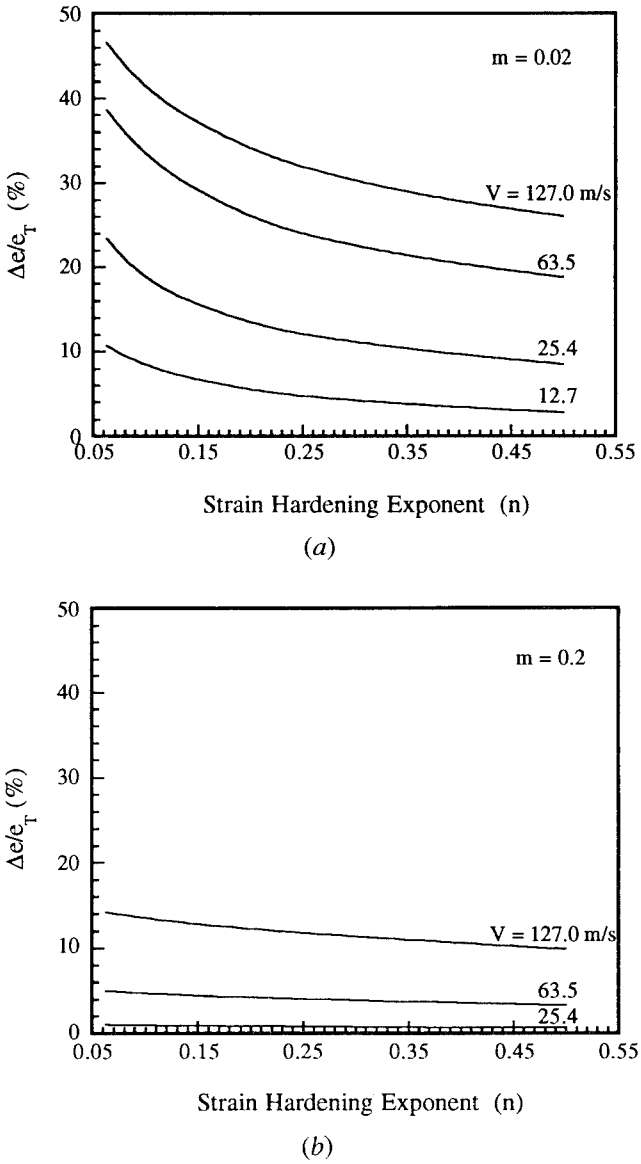
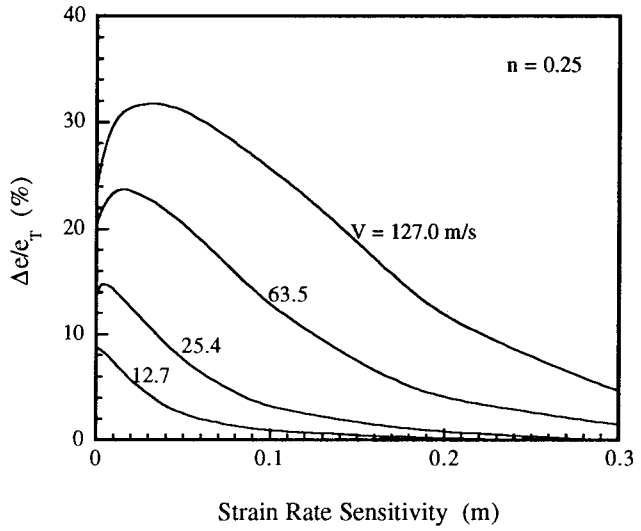
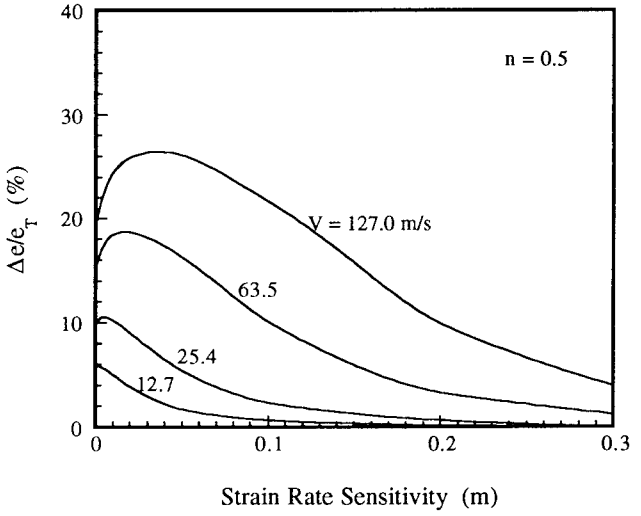


Fig. 8—$\Delta e/e_T$ as a function of n at different test velocities for (*a*) $m = 0.02$ and (*b*) $m = 0.2$.

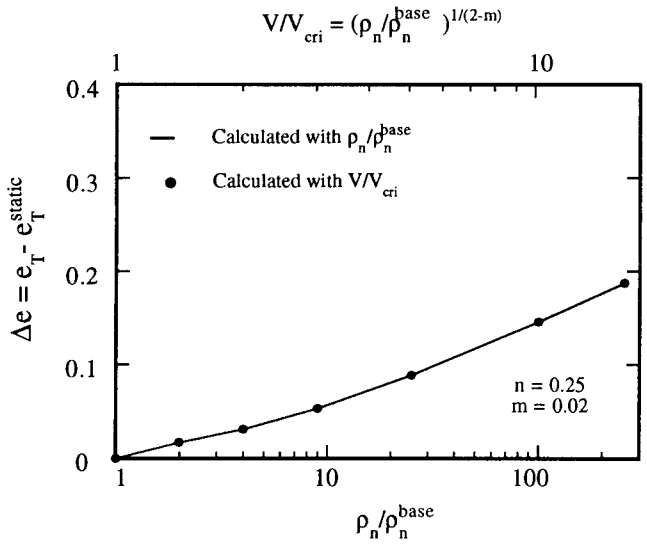


(*a*)

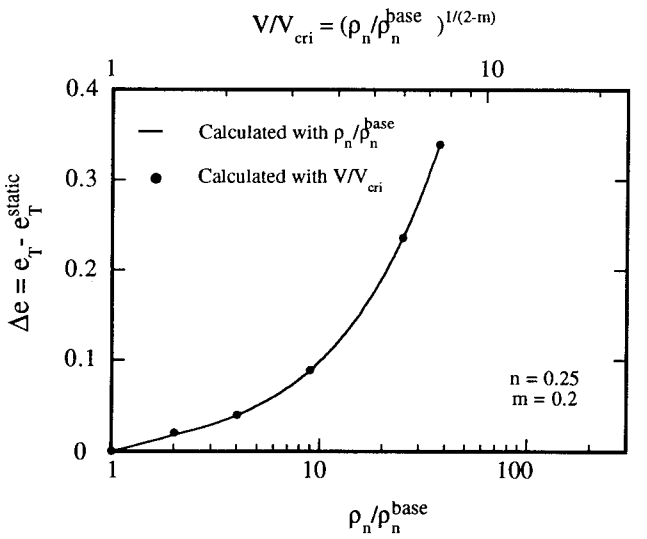


(*b*)

Fig. 9—$\Delta e/e_T$ as a function of m at different test velocities for (*a*) $n = 25$ and (*b*) $n = 0.5$.



(*a*)



(*b*)

Fig. 10—The scaling of the inertial effect with the normalized material density, ρ_n, and the test velocity, V, at (*a*) $m = 0.02$ and $n = 0.25$ and (*b*) $m = 0.2$ and $n = 0.25$.

IV. DISCUSSION

A. *The Origin of Tensile Ductility Enhancement at High Test Velocities*

During high-velocity deformation, the primary role of inertia in enhancement of tensile ductility is in stabilizing necking. This can be demonstrated in a semi-qualitative and intuitive way as follows.

Figure 13(a) is a schematic illustration of the velocity distributions in one-half of the tapered tensile specimen. The velocities are specified at the two boundaries. During stable or uniform deformation, the velocity of the material varies linearly with position. This is approximately true with or without inertial forces. Strain localization requires a sharp curvature to be developed in the velocity-distance relationship. With boundary conditions defined, the velocity in the localizing specimen is everywhere greater than in the stably deforming specimen.

When the specimen deforms at low test velocities, as indicated previously, $\Delta v/\Delta t$ is small and inertia due to $\Delta v/\Delta t$ can be justifiably ignored. In this case, the momentum equation (Eq. [1]) indicates that $f(t,x)$ is constant through the whole specimen. Increasing the test velocity raises $\Delta v/\Delta t$ and signifies inertial forces. Following the variation of $\Delta v/\Delta t$ with x (Figure 13(a)), one expects from Eq. [1] that the existence of inertial forces will increase the tensile force in the gripped end of the specimen; that is, inertial forces present load the "uniform" part of the gage length with a tensile force that is not present in quasi-static deformation. Thus, there is an extra strain increment that develops in this region. This is the reason why high velocity deformation promotes a smaller strain gradient, consequently stabilizing necking.

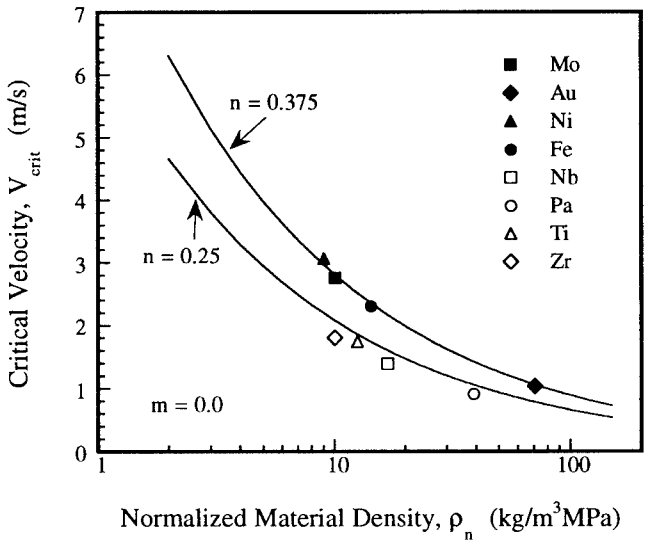


Fig. 11—The critical velocity for the onset of the inertial effect, V_{crit}, as a function of the normalized material density, ρ_n, for rate-insensitive materials.

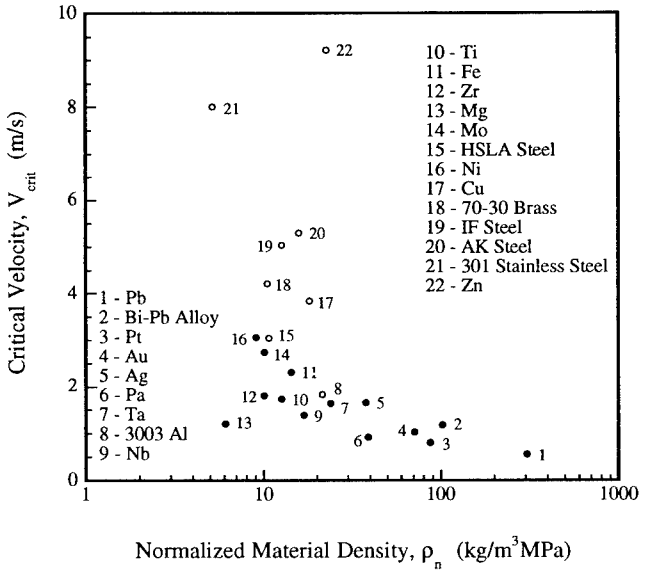
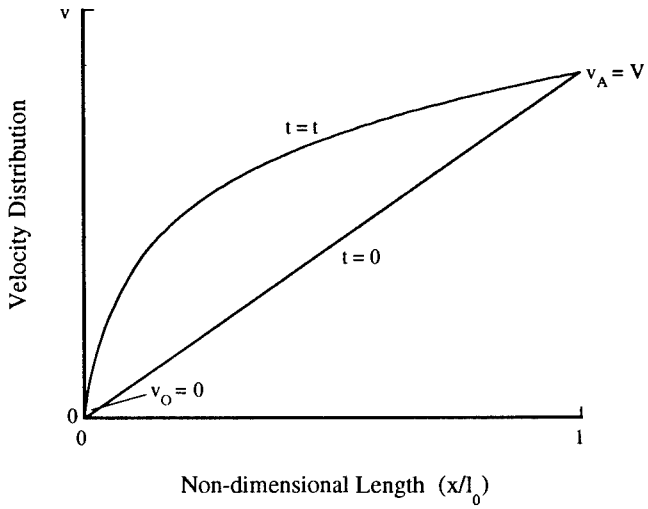


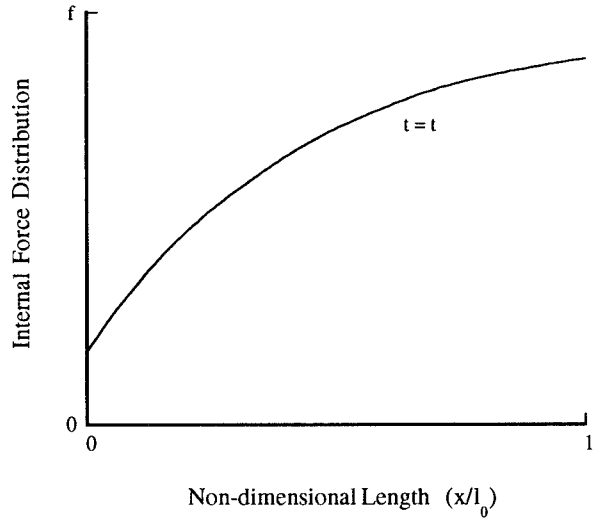
Fig. 12—The critical velocity for the onset of the inertial effect, V_{crit}, for some metals and alloys.

From the model previously proposed, the suppression of the strain gradient by inertia would be expected to take place primarily in postuniform deformation, because the significant acceleration is only developed after necking commences. This is supported by the fact that when the test velocity is changed, there is no significant change of the maximum load elongation, e_u, while postuniform elongation varies considerably (Figure 4).

Also, this suppression can be verified by examining the true strain distributions in the specimen at different engineering strain levels for low and high test velocities (Figure 14). The left-hand side of Figure 14 corresponds to the strain distributions obtained for the specimen deformed at $V = 0.0254$ m/s, and the right-hand side of this figure corresponds to the strain distributions obtained for the specimen deformed at $V = 127.0$ m/s.



(*a*)



(*b*)

Fig. 13—(*a*) Schematic illustration of the velocity distribution (*b*) Schematic illustration of the internal-force distribution at high-velocity deformation.

When $e \leq 0.2$, it can be seen that both strain distributions at two test velocities are almost the same. However, when the elongation exceeds this value, the strain distribution starts to concentrate in the center for the low velocity specimen (Figure 14), whereas for the high velocity, the concentration of the central strain is obviously retarded, and a relatively uniform strain distribution through the whole specimen can retain at a higher engineering strain level.

The interpretation of the source of enhancement of tensile ductility at high test velocities is different from the view of Regazzoni *et al.*,[40] who proposed that the extra amount of strains received by the specimen result from an unloading front propagation.

B. *The Inertial Effect Studied under the Global Strain Rate*

In this study, the inertial effect was investigated as a function of the test velocity, V, instead of being the

Table II. Material Parameters and V_{crit} for Some Metals and Alloys*

Material	n	m	k (MPa)	ρ (kg/m^3)	ρ_n (kg/(m^3 MPa))	V_{crit} (m/s)
3003 aluminum[64]	0.24	0.005	129	2,770	21.47	1.835
Bismuth-lead alloy[65]	0.50	—	103	10,540	102.32	1.185
70-30 brass[64]	0.56	0.001	816	8,540	10.47	4.209
Copper[66]	0.37	0.014[40]	492	8,930	18.15	3.835
Gold[67]	0.37	—	272	19,360	71.17	1.035
Iron[65]	0.37	—	549	7,870	14.32	2.308
Lead[65]	0.41	—	37	11,370	304.56	0.556
Magnesium[68]	0.12	—	284	1,740	6.11	1.206
Molybdenum[65]	0.37	—	1,012	10,230	10.11	2.748
Nickel[65]	0.39	—	982	8,900	9.07	3.062
Niobium[69]	0.24	—	508	8,570	16.88	1.393
Platinum[65]	0.32	—	247	21,490	87.22	0.809
Palladium[65]	0.24	—	309	12,040	39.00	0.914
Silver[65]	0.43	—	278	10,510	37.81	1.659
AK steel[70]	0.19	0.027	497	7,870	15.84	5.300
IF steel[62]	0.26	0.017	622	7,870	12.65	5.040
HSLA steel[64]	0.18	0.007	733	7,870	10.73	3.052
301 stainless steel[64]	0.48	0.012	1,559	8,040	5.16	8.000
Tantalum[65]	0.34	—	697	16,640	23.87	1.643
Titanium[65]	0.26	—	359	4,520	12.59	1.741
Zinc[65]	0.50	0.06[71]	314	7,150	22.78	9.223
Zirconium[65]	0.24	—	647	6,500	10.05	1.805

*The parameters are obtained at the annealed condition for most of the materials in this table, except bismuth-lead alloy, tantalum, and lead and zinc. For these materials, the condition is cast, recrystallized, and rolled, respectively.

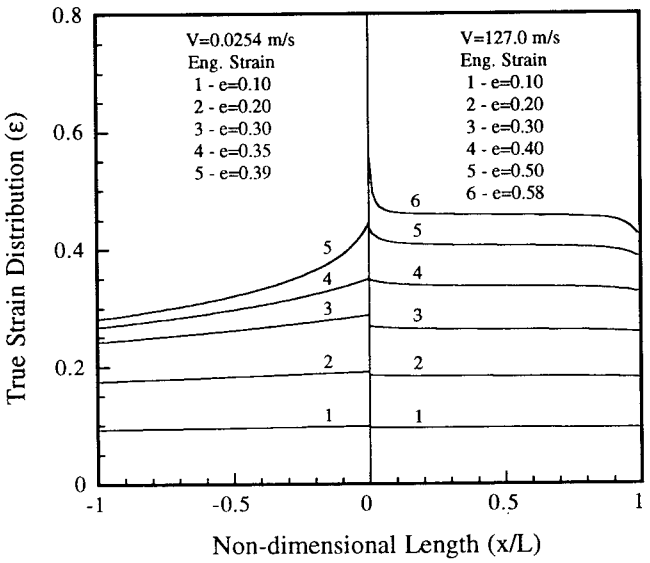


Fig. 14—A comparison of the true-strain distributions for specimens deformed at low and high test velocities with $n = 0.25$ and $m = 0.02$.

global strain rate, ε_o ($= V/l_0$). As shown in Figure 15, it can be noted that for a given V, the total elongation of the specimen, e_T, is nearly independent of the specimen gage length. However, for a given ε_o, invariance of e_T to changes of the gage length holds only in a low rate (so long as the end point velocity remains less than V_{crit}). At high rates, e_T increases with an increase of the gage length. These results indicate that the test velocity is the proper characterizing parameter for the inertial effect.

Several investigations have shown that material formability can be enhanced at high strain rates or test velocities.[30–40] It is not often clear if this enhanced formability is due to the inertial effect analyzed here or constitutive parameters changing (*e.g.*, m increasing) with increasing strain rates. The concept presented in Figure 15 can be used to provide an elegant experimental test. Constitutive-based effects should yield improved formability based on strain rates, regardless of the sample size, while the inertial effect will scale properly with test velocities.

V. SUMMARY

A simple one-dimensional dynamic numerical simulation of the sheet tensile test (1 pct linear tapered specimen) for rate-sensitive materials has been carried out over a wide range of test velocities. The *Hollomon*-type constitutive law has been applied for materials, and a variety of values of strain-hardening exponent, n, and strain-rate-sensitivity index, m, have been used to analyze the effect of inertia on tensile ductility. The results are summarized as follows.

1. The total elongation of the specimen, e_T, is enhanced by inertia at high test velocities. Since no significant change of the maximum-load elongation (uniform elongation), e_u, was noted by changing test velocities, enhancement of the total elongation is due primarily to an increase of postuniform elongation.
2. There exists a critical test velocity for the onset of the inertial effect, V_{crit}. Both increasing the strain-rate-sensitivity index, m, and decreasing the strain-hardening exponent, n, increases this critical

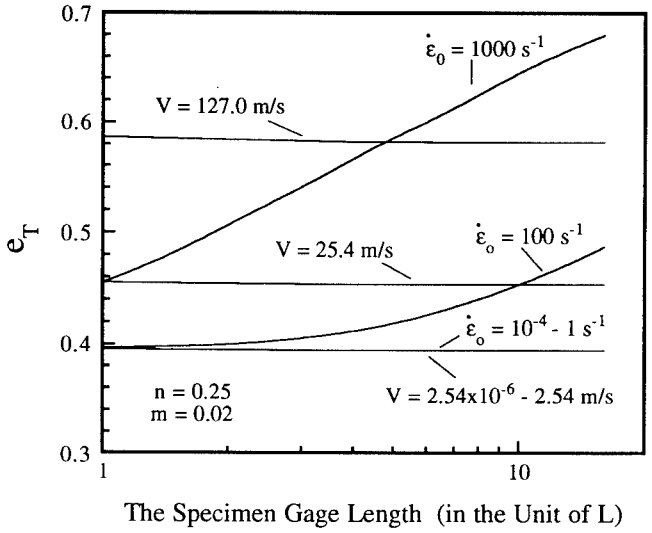


Fig. 15—The variation of e_T with the specimen gage length at different test velocities and global strain rates.

velocity. Beyond V_{crit}, increasing the test velocity increases the inertia-induced additional elongation, Δe.

3. The inertia-induced additional elongation, Δe, increases monotonically with an increase of n for a given test velocity. However, the relationship between m and Δe is complicated. The m value at which the maximum inertia-induced additional elongation occurs varies with the velocity.
4. When the percentage of the total elongation increment produced by inertia with respect to the total elongation was considered, the results indicated that the inertial effect is the most important in materials of limited ductility. (*i.e.*, those with relatively low n and m values).
5. A scaling between the normalized material density, ρ_n, and the test velocity, V, was noted and is given by

$$\rho_n V^{2-m} = C$$

where C is the constant. Based on this scaling, for a group of materials with the same n and m but different ρ_n, the inertia-induced additional elongation and critical test velocity can be readily studied.
6. In addition to the quantitative model, an intuitive explanation for the inertial effect is proposed. It shows that the inertial effect suppresses strain gradients in the specimen during necking for high-velocity deformation. The suppression of the strain gradients leads to increases in strains to failure.

ACKNOWLEDGMENTS

This work was supported by the Center for Materials Research at The Ohio State University, by The National Science Foundation through a National Young Investigation Award (G.S. Daehn, DMR 9258172), and by The Ohio Supercomputer Center (PAS 647-3).

REFERENCES

1. A. Considére: *Ann. Ponts Chaussees*, 1885, vol. 9, pp. 574-75.
2. E.W. Hart: *Acta Metall.*, 1967, vol. 15, pp. 351-55.
3. J. Campbell: *J. Mech. Phys. Solids*, 1967, vol. 15, pp. 359-70.
4. E. Dunconbe: *Int. J. Mech. Sci.*, 1972, vol. 14, pp. 325-37.
5. J.J. Jonas, R.A. Holt, and C.E. Coleman: *Acta Metall.*, 1976, vol. 24, pp. 911-18.
6. A. Argon, J. Im, and A. Needleman: *Metall. Trans. A*, 1975, vol. 6A, pp. 815-24.
7. A.K. Ghosh and R.A. Ayres: *Metall. Trans. A*, 1976, vol. 7A, pp. 1589-91.
8. A.K. Ghosh: *Acta Metall.*, 1977, vol. 25, pp. 1413-24.
9. A.K. Ghosh: *Metall. Trans. A*, 1977, vol. 8A, pp. 1221-32.
10. J.W. Hutchinson and K.W. Neale: *Acta Metall.*, 1977, vol. 25, pp. 839-46.
11. J.J. Jonas and B. Baudelet: *Acta Metall.*, 1977, vol. 25, pp. 43-50.
12. J.J. Jonas and N. Christadoulou: *Scripta Metall.*, 1978, vol. 12, pp. 393-97.
13. M.Y. Demeri and H. Conrad: *Scripta Metall.*, 1978, vol. 12, pp. 389-92.
14. U.F. Kocks, J.J. Jonas, and H. Mecking: *Acta Metall.*, 1979, vol. 27, pp. 419-32.
15. F.A. Nichols: *Acta Metall.*, 1980, vol. 28, pp. 633-73.
16. I.H. Lin, J.P. Hirth, and E.W. Hart: *Acta Metall.*, 1981, vol. 29, pp. 819-27.
17. N. Christadoulou and J.J. Jonas: *Res. Mech.*, 1982, vol. 5, p. 49.
18. R.H. Wagoner: *Scripta Metall.*, 1981, vol. 15, pp. 1135-37.
19. R.H. Wagoner and N.M. Wang: *Metall. Trans. A*, 1983, vol. 14A, pp. 2395-406.
20. S.L. Semiatin, A.K. Ghosh, and J.J. Jonas: *Metall. Trans. A*, 1985, vol. 16A, pp. 2291-98.
21. K. Chung and R.H. Wagoner: *Metall. Trans. A*, 1986, vol. 17A, pp. 1632-33.
22. K. Chung and R.H. Wagoner: *Metall. Trans. A*, 1988, vol. 19A, pp. 293-300.
23. D. Lee and W.A. Backofen: *Trans. AIME*, 1967, vol. 239, pp. 1034-37.
24. D.A. Woodford: *Trans. Am. Soc. Met.*, 1969, vol. 62, pp. 291-93.
25. G. Rai and N.J. Grant: *Metall. Trans. A*, 1975, vol. 6A, pp. 385-90.
26. A.K. Ghosh: *J. Eng. Mater. Technol.*, 1977, vol. 99, pp. 264-74.
27. S.L. Semiatin and J.J. Jonas: *Formability and Workability of Metals*, ASM, Metals Park, OH, 1984.
28. Y. Tomita, A. Shindo, S. Asada, and H. Gotoh: *Trans. JSME.*, 1988, vol. 54, p. 1124.
29. K. Chung and R.H. Wagoner: unpublished research, The Ohio State University, Columbus, OH, 1993.
30. L.W. Meyer, H.D. Kunze, and S. Scifert: *Shock Waves and High Strain Rate Phenomena in Metals*, M.A. Meyers and L.E. Murr, eds., Plenum Press, New York, NY, 1980, pp. 51-64.
31. J.M. Stuchen: *J. Eng. Mater. Technol.*, 1973, vol. 95, pp. 182-85.
32. G. Regazzoni and F. Montheillet: *3rd Int. Conf. on the Mechanical Properties of Materials at High Rate of Strain*, J. Harding, ed., The Institute of Physics, Conf. Ser. No. 70, London, 1984, pp. 63-70.
33. S. Clyens and J.D. Campbell: *Mechanical Properties at High Rates of Strain*, J. Harding, ed., The Institute of Physics, Conf. Ser. No. 21, London, 1974, pp. 62-71.
34. J.C. Gianotta, G. Regazzoni, F. Montheillet, J.P. Ansart, and R. Dormeval: Rapport *CETAM/ARMINES*, 1983, No. 6b.
35. N. Takeda and A. Kobayshi: *Shock Wave and High Strain Rate Phenomena in Materials*, M.A. Mayer, L.E. Murr, and K.P. Staudhammer, eds., Marcel Dekker Inc., New York, NY, 1990, pp. 97-106.
36. V.S. Balanethiram and G.S. Daehn: *Scripta Metall.*, 1992, vol. 27, pp. 1783-88.
37. J.W. Taylor, F.H. Harlow, and A.A. Amselen: *J. Appl. Mech.*, 1978, vol. 45, pp. 105-10.
38. C. Fressengeas and A. Molinari: *Acta Metall.*, 1985, vol. 33, pp. 387-96.
39. C. Fressengeas and A. Molinari: *J. Mech. Phys. Solids*, 1987, vol. 35, pp. 185-211.
40. G. Regazzoni, J.N. Johnson, and P.S. Follansbee: *J. Appl. Mech.*, 1986, vol. 53, pp. 519-28.
41. C.K.H. Dharan and F.E. Hauser: *Exp. Mech.*, 1970, vol. 10, pp. 370-76.

42. R.J. Clifton, A. Gilat, and C.H. Li: *Material Behavior under High Stress and Ultrahigh Loading Rates*, J. Mescall and V. Weiss, eds., Plenum Press, New York, NY, pp. 1-19.
43. P.S. Follansbee, G. Regazzoni, and U.F. Kocks: *The Mechanics of Dislocations*, E.C. Aifantis and J.P. Hirth, eds., ASM, Metals Park, OH, pp. 237-45.
44. P.S. Follansbee, U.F. Kocks, and G. Regazzoni: *Mechanical and Physical Behavior of Materials under Dynamic Loading*, DYMAT 85, *J. Phys.*, 1985, Tome 46, pp. C525-C534.
45. C. Dumont, C. Levaillant, M. Ariminjon, and J.L. Chenot: *Mechanical and Physical Behavior of Materials under Dynamic Loading*, DYMAT 88, *J. Phys.*, 1988, Tome 49, pp. C3-505-512.
46. J.H. Hollomon: *Trans. AIME*, 1945, vol. 162, pp. 268-89.
47. E. Voce: *J. Inst. Met.*, 1948, vol. 74, pp. 537, 562, and 760.
48. H.W. Swift: *J. Mech. Phys. Solids*, 1952, vol. 1, p. 1.
49. R.H. Wagoner: *Metall. Trans. A*, 1981, vol. 12A, pp. 71-75.
50. X. Hu, V.S. Balanethiram, M. Altynova, and G.S. Daehn: The Ohio State University, Cleveland, OH, unpublished research.
51. L.E. Malvern: *J. Appl. Mech.*, 1951, vol. 18, pp. 203-08.
52. K.S. Raghavan and R.H. Wagoner: *Metall. Trans. A*, 1987, vol. 18A, pp. 2143-50.
53. M.A. Harper: "A Non-Linear, One-Dimensional Computer Simulation for Tensile Tests," TMS Student Paper Contest, The Ohio State University, Cleveland, OH, 1988.
54. R.D. Cook: *Concepts and Applications of Finite Element Analysis*, John Wiley & Sons, New York, NY, 1981.
55. D.R.J. Owen: *Finite Element in Plasticity*, United Kingdom, Prineridge Press Limited, Swansea, United Kingdom, 1980.
56. W. Weaver, Jr and P.R. Johnston: *Finite Elements for Structural Analysis*. Prentice-Hall Inc., Englewood Cliffs, NJ, 1984.
57. ABAQUS/Explicit User's Manual, Hibbitt, Karlsson & Sorensen, Inc., Pawtucket, RI, 1992.
58. T.J.R. Hughes: *The Finite Element Method—Linear Static and Dynamic Finite Element Analysis*, Prentice-Hall Inc., Englewood Cliffs, NJ, 1987.
59. O.C. Zienkiewicz: *The Finite Element Method*, 3rd ed., McGraw-Hill, New York, NY, 1977.
60. K. Bathe: *Finite Element Procedures in Engineering Analysis*, Prentice-Hall Inc., Englewood Cliffs, NJ, 1982.
61. N.M. Newmark: *J. Eng. Mech. Div.*, 1959, vol. 85, pp. 67-94.
62. M.P. Miles, J.S. Siles, R.H. Wagoner, and K. Narashimhan: *Metall. Trans. A*, 1993, vol. 24A, pp. 1143-49.
63. K. Kawata, S. Hashimoto, and K. Kurokawa: *High Velocity Deformation of Solid*, K. Kawata and J. Shiori, eds., Springer-Verlag, New York, NY, 1978, pp. 1-15.
64. *Metals Handbook*, 9th ed., ASM, Metals Park, OH, 1988, vol. 14, p. 885.
65. *Properties of Some Metals and Alloys*, 3rd ed., The International Nickel Company, Inc., 1968.
66. *Metals Handbook*, 9th ed. ASM, Metals Park, OH, 1979, vol. 2, p. 276.
67. *Metals Handbook*, 9th ed. ASM, Metals Park, OH, 1979, vol. 2, p. 680.
68. *Metals Handbook*, 9th ed. ASM, Metals Park, OH, 1979, vol. 2, p. 764.
69. *Metals Handbook*, 9th ed. ASM, Metals Park, OH, 1979, vol. 2, p. 779.
70. H.E. Boyer: *Atlas of Stress-Strain Curves*, ASM, Metals Park, OH, 1987.
71. R.H. Wagoner: *Metall. Trans. A*, 1984, vol. 15A, pp. 1265-71.

Effect of Internal Heating During Hot Compression on the Stress-Strain Behavior of Alloy 304L

M.C. MATAYA and V.E. SACKSCHEWSKY

The temperature change due to the conversion of mechanical deformation to internal heat and its effect on the as-measured stress-strain behavior of alloy 304L was investigated by means of initially isothermal (compression specimen, dies, and environment at same temperature at initiation of test), constant strain rate, uniaxial compression of laboratory-sized cylindrical specimens. Strain rate was varied in the range 0.01 to 1 s^{-1}, where the thermal state of the test specimen varied from nearly isothermal to nearly adiabatic, respectively. Specimens were deformed in the temperature range of 750 °C to 1150 °C to a strain of 1. The change in specimen temperature with applied strain was calculated *via* finite-element analysis (FEA) from the as-measured stress-strain data. Selected predictions were confirmed with embedded thermocouples to verify the model employed. Temperature was found to increase monotonically with strain at a strain rate of 1 s^{-1}, consistent with what is theoretically expected for the adiabatic case. At the 0.1 and 0.01 s^{-1} rates, the sample temperature initially increased, peaked, and then decreased as the sample thinned and the contact area between the sample and the cooler dies increased. As-measured stress was corrected for softening associated with deformational heating by interpolation between the various instantaneous stress-temperature behaviors. The resulting isothermal flow data are compared to those predicted by a conventional method that employs an empirical estimate of the heat retention efficiency of the test specimen, assumed dependent on strain rate but independent of strain, to reduce the increase in temperature calculated for the adiabatic case. Differences between the calculated isothermal stress-strain data from the two methods are discussed. Values for the apparent activation energy of deformation and the strain to the peak in the flow curve, which is associated with the onset of dynamic recrystallization, determined from isothermal stress-strain data differed significantly from those obtained from the as-measured compression test data.

I. INTRODUCTION

UNIAXIAL compression of cylindrical specimens is often used to determine a material's stress-strain (σ-ε) response to plastic deformation at temperatures, strain rates, and to strains typically encountered during conventional hot-working processes such as forging. The σ-ε response yields information about a material's strain-rate sensitivity; work-hardening rate; activation energy for deformation, Q_{DEF}; and equipment loading during forming operations, and it allows upper-bound analysis of metal-working operations. These data are also useful in finite-element analysis (FEA) of metal-forming operations.[1–8]

The accuracy of measured σ-ε data from compression testing is typically degraded by friction between sample and die, causing barreling and nonuniform stress and strain in the sample, and by internal heating of the sample, which typically reduces the flow stress of materials that exhibit thermally activated plastic deformation.[9] Lubrication techniques have been developed to minimize frictional effects. However, as-measured σ-ε curves and associated analysis reported in the literature have often been presented without correction for deformational heating.[10–24]

At high strain rate, $\dot{\varepsilon}$, the heat generated in a test sample is essentially retained during the short duration of the test, and the instantaneous temperature of the test sample, T_i, can be calculated by conventional techniques, without consideration of heat loss to the environment. From sets of σ-ε-T_i data, generated by compression testing at different temperatures, isothermal σ-ε curves can be obtained by interpolation of the σ-T_i data at each increment in ε. Semiatin *et al.*[7] employed this technique to correct as-measured σ-ε curves of Ti-6242 for use in finite-element simulation of metal flow during forging of a turbine disc. Laasraoui and Jonas,[25,26] using a similar technique, showed that correction of the as-measured σ-ε data for internal heating during hot compression testing provided a significantly more precise determination of the static recrystallization kinetics for various low carbon steels.

At low $\dot{\varepsilon}$, the heat of deformation is dissipated, as it is generated, to the surrounding environment, and the test progresses isothermally. In this case, the as-measured σ-ε behavior is also the isothermal behavior. Thus, in the two $\dot{\varepsilon}$ extremes, the bounds of which are determined by test sample geometry and other test conditions that govern heat transfer to the environment, isothermal σ-ε behavior can be obtained rather easily.

In the intermediate $\dot{\varepsilon}$ realm, the process is neither adiabatic nor isothermal, and the calculation of T_i, which is a function of heat transfer from the superheated specimen to the cooler environment (*i.e.*, heat conduction to the dies), is not simple and has not been characterized in detail. Sample temperature can be measured with embedded thermocouples, but testing is complex and

M.C. MATAYA, Associate Scientist, is with EG&G Rocky Flats, Inc., Golden, CO 80402-0464. V.E. SACKSCHEWSKY, formerly Senior Systems Engineer with EG&G Rocky Flats, Inc., is retired.

Manuscript submitted April 19, 1993.

costly, and embedded thermocouples may perturb the σ-ε response of the specimens. To facilitate calculation of isothermal σ-ε curves in this intermediate $\dot{\varepsilon}$ regime, Dadras and Thomas[27] introduced an empirical term, referred to as heat retention efficiency, η, which is used to reduce the temperature rise calculated for the adiabatic case to obtain T_i. The value of η is assumed to vary linearly with log $\dot{\varepsilon}$, $\eta = \eta(\dot{\varepsilon})$, independent of ε.[27,28,29] However, because heat loss from a superheated compression specimen to the dies depends in part on the instantaneous sample geometry (*e.g.*, specimen height and specimen-die contact area), it appears that η must also vary with strain, $\eta = \eta(\dot{\varepsilon}, \varepsilon)$.

Type 304 austenitic stainless steel is a widely used material due to a combination of good corrosion resistance and strength that can be significantly enhanced during forging at elevated temperatures.[30] The flow behavior of 304 and 304L at elevated temperature from a number of investigations has been reviewed by Dadras[31] and Semiatin and Holbrook,[32] and it is apparent that a detailed systematic study of the isothermal flow behavior in the intermediate $\dot{\varepsilon}$ regime at elevated temperatures has not been performed. This type of characterization is needed in order to model processes such as radial forging and press forging, which are characteristically applied during primary and secondary breakdown of commercial ingot material.[33]

The purpose of this investigation was to develop a method to obtain an accurate isothermal σ-ε behavior for 304L at elevated temperature in the intermediate $\dot{\varepsilon}$ realm, where the thermal state of laboratory-sized test specimens is neither isothermal nor adiabatic. Deformational heating of test specimens was studied by performing a thermal-mechanically coupled FEA of the compression test in which the heat of deformation was allowed to dissipate through conduction to the dies. Interpolation of the instantaneous σ-ε-T_i behavior, where T_i is calculated by FEA, was used to determine the isothermal σ-ε behavior. The results are compared to the as-measured test data and to those obtained with the conventional method that employs $\eta(\dot{\varepsilon})$. Values and behaviors of the strain to initiate dynamic recrystallization, ε_p, and apparent activation energy for deformation, Q_{DEF}, obtained from both as-measured and isothermal data are compared and discussed.

II. EXPERIMENTAL PROCEDURE

A. *Material*

The chemical composition of the 304L alloy used in this investigation is given in Table I. The alloy was arc-melted in air and then argon-oxygen decarburized prior to casting a 356-mm-diameter electrode. The electrode was vacuum arc-remelted into a 406-mm-diameter ingot. The ingot was bloomed to a 127-mm, round-cornered square bar on a continuous mill at 1150 °C and hot-rolled to a 38.1-mm-diameter bar. Rolling started at 1100 °C and finished at approximately 900 °C. The bar was swaged at room temperature to a 15.2-mm-diameter rod. The rod was solution heat-treated at 1000 °C for 1 hour and water-quenched, providing the starting material for the investigation. Prior study of this heat of 304L showed that this particular solution heat treatment produces a well-annealed, relatively dislocation-free matrix with equiaxed grains having an average grain diameter of 0.038 mm.[30]

Table I. Chemical Analysis of 304L Alloy

Element	Analysis (Mass Pct)
Cr	18.6
Mn	1.9
Ni	10.0
P	0.011
Si	0.57
Mo	0.055
Co	0.077
C	0.022
S	0.0003
N	0.015
Fe	balance

B. *Elevated Temperature Compression Testing*

The test setup is shown schematically in Figure 1. Compression testing was accomplished in a 250 KN servohydraulic testing machine (manufactured by M.T.S. Corp., Minneapolis, MN) outfitted with an electric resistance clam-shell furnace. The vertical load column was composed of two opposing ASTROLOY* rams, which were hollowed to facilitate heating, and flat smooth (lapped to 8 rms surface finish with opposite faces parallel to within 0.0127 mm over a 69.85-mm diameter) SiN compression dies, fitted to the end of the rams. Cylindrical compression samples, 12.7-mm diameter by 19.05-mm high, were machined from the heat-treated 15.1-mm-diameter rod, with specimen axis parallel to rod axis. The end faces were recessed to form a lubricant well, an effective technique for constraining lubricant to the sliding face during compression.[34] Weis[35] verified the effectiveness of this technique compared to others and determined an optimum well geometry for the specimen used in this investigation (lower right in Figure 1). Various glass lubricants were employed to accommodate the wide range of testing temperatures: Delta Glazes No. 13 for 750 °C, No. 93 for 850 °C, No. 349M for 950 °C, and No. 347M for 1050 °C and 1150 °C (products of Atcheson Chemical Co., Port Huron, MI). The combination of hard smooth dies, lubricant well geometry, and glass lubricant provided excellent lubrication for the duration of the compression test, demonstrated by the absence of barreling of the free surface on the compressed test sample (Figure 2). Test specimens were loaded onto the bottom die in the furnace in air, held for 10 minutes at the test temperature (specimens required approximately 5 minutes to equilibrate), compressed uniaxially to a strain of 1, and quenched in water immediately after deformation. The time to quench was between 1 and 2 seconds. Test temperatures varied between 750 °C and 1150 °C. The initial grain size was found to be stable

*ASTROLOY is a trademark of Geneva Electric Company, Sun Valley, CA.

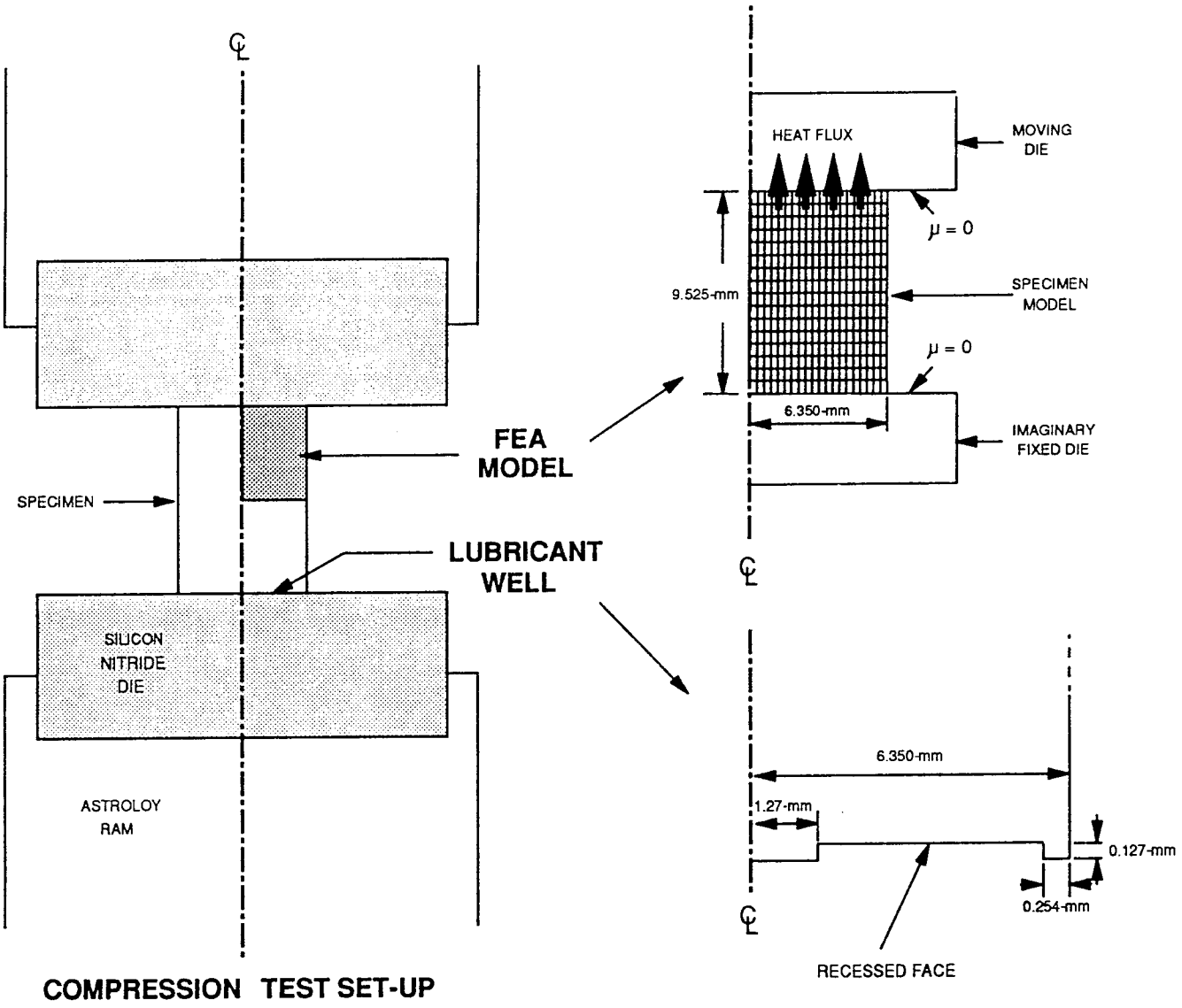


Fig. 1—Schematic of compression test setup, FEA model, and lubricant well on compression test specimen.

during preheating in the 750 °C to 1050 °C range. The average grain diameter increased from 0.040 to 0.120 mm during the 1150 °C preheat cycle. The effect of this increase on the results is considered. The velocity of the moving die was varied by computer control in order to apply deformation at a constant $\dot{\varepsilon}$ of 0.01, 0.1, or 1 s^{-1}. Compliance in the load train resulted in deviations in ε and $\dot{\varepsilon}$ up to about −5 pct with the maximum occurring at the lowest temperature, at which the greatest loads were encountered.

The true flow stress σ can be assumed equal to the true average pressure because the coefficient of friction between sample and die is near zero (Figure 2).[36] In addition, the strain distribution can be assumed uniform throughout the specimen, and true strain ε can be calculated from the change in test specimen height.[37] Note for uniform uniaxial compression, the effective or significant stress and strain reduce to the axial normal component of stress and strain, as is the case for tensile testing in the uniform elongation realm.[37] Values for σ and ε were calculated from the as-measured load and

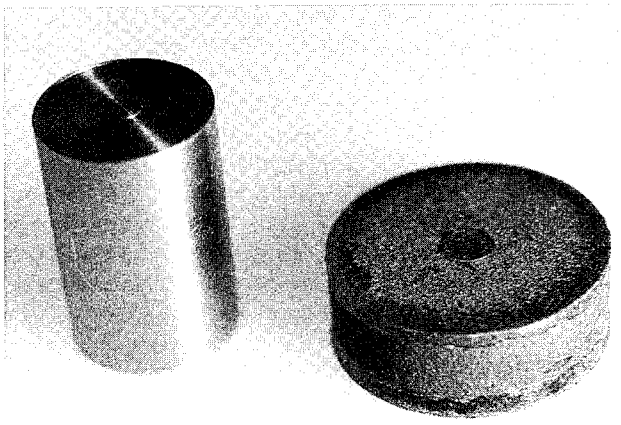


Fig. 2—Compression test specimen prior to deformation (left) and a typical deformed specimen (right).

corrected displacement data using conventional relationships.[37] Sample dimensions, measured at ambient temperature, were corrected for thermal expansion that occurs on heating to the test temperature T_0. The measured displacement of the sample, obtained with a linear-variable-differential transformer (LVDT) mounted at the lower end of the moving ram, was corrected for test system compliance. Calculated values of final ε, obtained from the LVDT displacement and corrected for compliance and for cooling to ambient temperature, were typically within 1 to 2 pct of the measured plastic strain, calculated from the actual initial and final height of the test sample.

Sample heating during deformation was measured on selected samples with an embedded thermocouple located at the specimen center (midheight and mid-diameter). The thermocouple was a sheathed type K with an exposed, beaded junction. Sheath material was type 304 stainless steel. Sheath, bead, and wire diameters were 1.57, 0.7, and 0.25 mm, respectively. The time constant to reach 62.3 pct of a stepped increase in temperature was approximately 0.45 seconds. In this study, embedded thermocouples were found to have a negligible effect on the flow curves, determined by comparing the results from samples with and without thermocouples.

C. *Determination of Isothermal Stress-Strain Behavior*

1. *An empirical analysis*

The as-measured σ-ε data were corrected for deformational heating by two different techniques. The first, discussed in this section, employs the empirical term η[27] to estimate T_i, the instantaneous temperature at the midheight position of the compression specimen, and is hereafter referred to as the empirical analysis (EA) method. It consists of calculating the change in sample temperature, ΔT, with applied ε by the following conventional relationship:

$$\Delta T = (\eta k/\rho C_p) \int_0^{\varepsilon_f} \sigma \, d\varepsilon \qquad [1]$$

where ρ is density, C_p is heat capacity per unit mass (where $C_p = C_p(T)$), ε_f is the final true plastic strain, k is a mechanical energy-to-heat conversion factor, and η is the fraction of deformational energy that appears as a temperature rise. Based on the measured value of T_i at an applied ε of 0.7, determined from an embedded thermocouple located at the midheight-midradius location, in cylindrical compression samples of aluminum alloy 2024 compression samples strained at various rates,[28] it has been suggested that η varies linearly with the logarithm of $\dot{\varepsilon}$, equaling 0 at 0.001 s^{-1} or less and 0.95 at 1.0 s^{-1} or greater.[29] Following this suggestion, the value of η is expressed as follows:

$$\eta = (0.316) \log_{10} \dot{\varepsilon} + 0.95 \qquad [2]$$

Values for ΔT were calculated, *via* Eqs. [1] and [2], for each measured increment of ε, approximately 0.005. The trapezoid rule was used for the integration in Eq. [1]. For adiabatic conditions, η is usually assumed to be between 0.9 and 0.95. The latter value is assumed in the EA method.

Next, $(\sigma, T_i)|_{\dot{\varepsilon}}$ relationships were constructed from the as-measured σ-ε data for different T_0, where $T_i = T_0 + \Delta T(\varepsilon)$, and at regular increments of ε. Finally, at a given value of ε and T_0, the softening, $\Delta\sigma$, due to ΔT was calculated, assuming a linear variation of log σ with $1/T_i$, and added to the as-measured value of σ to obtain the isothermal value.[29]

2. *A method using FEA*

An alternative method for estimating T_i from as-measured σ-ε data was developed in this study. It uses FEA to calculate the T_i in the compression sample with increasing ε. Isothermal σ-ε data are then determined by interpolation to T_0, similar to the EA method. The FEA model employs the as-measured σ-ε curve and the relevant physical properties analogous to Eq. [1]. However, as the FEA calculation progresses incrementally with ε, effects of the changes in sample geometry on heat flow to the dies are automatically included in the transient temperature calculations. Thus, FEA essentially replaces Eq. [1], adding effects of geometry changes (*i.e.*, ε), which are absent in the η term in that equation. The method is summarized briefly here and discussed in detail below.

Step 1. Frictionless compression test gives $\sigma = \sigma(\varepsilon)|_{\dot{\varepsilon}}$ for each test $\dot{\varepsilon}$ and each initial test temperature T_0.[36]

Step 2. Input the as-measured $\sigma = \sigma(\varepsilon)|_{\dot{\varepsilon}}$ from a single test as the material behavior into the FEA model and calculate instantaneous sample temperature, T_i, at specimen center for that test. Repeat for each compression test. This yields $\sigma = \sigma(\varepsilon, T_i)|_{\dot{\varepsilon}}$ for each initial test condition. Note, this step is analogous to the EA calculation in Eq. [1] with η replaced by FEA calculation of the heat flow to the die.

Step 3. Obtain $\sigma = \sigma(\varepsilon)|_{T_0,\dot{\varepsilon}}$ for each T_0 and $\dot{\varepsilon}$ by interpolation between appropriate sets of $\sigma(\varepsilon, T_i)|_{\dot{\varepsilon}}$ at regular increments of ε.

Figure 1 shows a schematic of the finite-element model used to simulate the compression tests. The MARC* finite-element code was used for the simulation. The analysis was elastic-plastic and thermal-mechanically coupled. Values of σ, ε, and T_i were calculated for each time increment during the simulation, where T_i is taken at the specimen center. The analysis assumes symmetry about the center axis, oriented in the vertical direction in Figure 1 and in the test setup, and about a perpendicular plane through the midheight of the cylinder. Axial symmetry implies that the system can be represented by a two-dimensional model. Vertical symmetry implies that only one-half of the cylinder must actually be modeled. Thus, the model consists of one quadrant of a vertical cross section through the cylinder, as shown in Figure 1. The quadrant of the 12.7-mm diameter by 19.05-mm high (0.5 × 0.75 in.) cylindrical test sample is represented by a mesh of 20 four-node

*MARC is a trademark of MARC Analysis Research Corp., Inc., Palo Alto, CA.

quadrilateral elements in the radial direction and 16 elements for the half-height. The conversion of mechanical energy to heat was assumed to have an efficiency of 0.95, consistent with the value assumed in the EA method.

The upper die of the compression test setup is represented by the upper rigid die in Figure 1. Simulated movement of this die was controlled by a subroutine within the FEA code to provide a specified constant $\dot{\varepsilon}$.

A friction coefficient of zero was used between the die and the cylindrical test specimen, based on the observed lack of barreling (Figure 2) on the free surface of compressed samples. For frictionless compression, the as-measured σ-ε behavior, which is an average for the sample, can be assumed, according to Rowe,[36] to be equal to the true material behavior, because ε and $\dot{\varepsilon}$ are uniform throughout the compression sample. Thus, the as-measured behavior was used to approximate the true material behavior throughout the test sample in the FEA model (Step 2). In both EA (conventional) and FEA, the sample temperature reference is located at the midheight of the sample. In the EA technique, temperature is measured *via* thermocouple at the midheight, at a strain of 0.7. In the FEA technique, the sample temperature at the midheight is calculated, considering heat flow to the dies, as strain increases. The temperature in the sample may vary from center to die surface, due to heat conduction from the sample, heated by deformation, to the slightly cooler die. Because the as-measured stress-strain behavior, which is an average behavior for the sample, is matched with the temperature at the sample midheight, which may be greater than the average temperature in the test sample, an associated error may be introduced during interpolation to isothermal conditions. For example, the temperature in a test sample 1 mm from the compression surface during the 850 °C, $\dot{\varepsilon} = 0.1\ s^{-1}$ test was measured to be 868 °C at a strain of approximately 0.8 compared to 874 °C at the midplane. This difference is relatively small, 6 °C, and apparently had little effect on sample geometry (barreling should be observed if significant die chill is coupled with an inverse temperature dependence of the flow stress). If an average temperature is assumed, T_i for this test is approximately 871 °C, rather than 874 °C (value at midheight), and the estimated isothermal flow stress would be reduced slightly from the value calculated assuming T_i at the sample midheight (approximately 265 *vs* 268 MPa from the data subsequently provided in Table IV).

Heat transfer due to conduction between the test specimen and die is included in the analysis to allow the heat generated in the specimen by deformation to be dissipated into the die, which acts as a constant temperature heat sink. For this analysis, T of the moving rigid die is set equal to the initial temperature of the test specimen, T_0. The lower rigid die shown in the model is an imaginary die through the specimen midplane (Figure 1), and its function in the model will be discussed. Temperature-dependent values of elastic modulus, thermal expansion coefficient, thermal conductivity, and specific heat used in the FEA model are listed in Table II.

The coefficient of heat transfer between the specimen and die was determined by matching FEA-predicted variations of ΔT with ε for various assumed values of the heat-transfer coefficient to a measured variation (*via* embedded thermocouple) obtained at 950 °C and a $\dot{\varepsilon}$ of $0.1\ s^{-1}$, as shown in Figure 3. Preliminary FEA analyses, not shown here, revealed that the temperature profile was most sensitive to the film coefficient for this particular combination of deformation parameters. Based on this figure, the coefficient was assumed to be $6.54 \times 10^3\ J/s/m^2/K$ (curve C). This value is lower, by a factor of approximately 2, than what is typically experienced in conventional forging of steel with graphite-based lubricants.[38] The lower value encountered in this study could be due to greater insulating qualities of the glass lubricants used in this study, compared to the graphite-based and other lubricants that are typically used in forging, and/or due to the use of a lubricant well on the ends of the specimens, which serves to maintain a relatively thick and continuous film of lubricant between the specimen and the dies for the duration of the test. A higher value for the coefficient might have been assumed considering that a variable die temperature in the FEA model should produce predicted curves (for Figure 3) which show less effect of die chilling at high strain. In this case, it appears that the value of the coefficient selected from Figure 3 may be greater than was assumed in this study.

Figure 4 shows the variation of as-measured ΔT, $T_i - T_0$, with ε, acquired from thermocouples embedded in test specimens, and the corresponding EA and FEA predicted curves. The FEA curves closely approximate the measured behavior, giving validity to the FEA model. The as-measured and FEA results show some difference because of a number of assumptions made in the FEA method and for the as-measured data. For example, some of the heat of deformation conducted from the specimen to the dies as the test proceeds will result in a slight heating of the dies; and therefore, slightly less heat will be transferred to the dies than predicted by FEA because of the assumption of a constant temperature for the moving rigid die. In this case, the as-measured sample T_i would be expected to lie slightly above the FEA T_i (the opposite is observed in Figure 4) and should increase with strain at a greater rate (observed in Figure 4). A number of other assumptions may have caused the FEA T_i to exceed the as-measured T_i. First, the effects of radiative and convective cooling were neglected in the FEA model, because calculations indicated that their effects on T_i would be relatively small compared to conduction effects (for example, the ratio for rate of heat dissipation by radiation to the rate of heat generation within the sample was less than 0.05). If incorporated in the FEA model, however, T_i would certainly be reduced a finite amount, and the FEA curves in Figure 4 would be lowered. Second, the lag in the as-measured temperature due to the thermocouple time constant (0.45 seconds for a 63.2 pct response) was neglected in the analysis. If a correction were applied, estimated to be on the order of 0.05 ε, the as-measured curve would shift to the left, effectively raising the as-measured curve relative to the FEA curve in Figure 4. Finally, it was assumed that mechanical work was converted to heat with a 95 pct efficiency, consistent with the EA method. The efficiency is generally assumed to

Table II. Variation of Young's Modulus, Thermal Expansion Coefficient, Thermal Conductivity, and Specific Heat with Temperature and Other Constants Used in the FEA Model*

T (°C)	Young's Modulus (MPa) ($\times 10^5$)	Thermal Expansion Coefficient (cm/cm °C) ($\times 10^{-5}$)	Thermal Conductivity (cal/s cm °C) ($\times 10^2$)	Specific Heat (cal/g °C)
−17.8	1.994	1.507	3.52	0.089
93.3	1.912	1.613	4.02	0.090
204.4	1.830	1.699	4.34	0.091
315.6	1.749	1.768	4.68	0.093
426.7	1.667	1.823	4.96	0.095
537.8	1.585	1.868	5.29	0.098
648.9	1.504	1.908	5.66	0.104
760.0	1.422	1.946	6.00	0.109
871.1	1.340	1.980	6.32	0.113
982.2	1.258	2.011	6.66	0.115
1093.3	1.177	2.034	6.98	0.117

Other constants:

Density:	7.999 g/cm^3
Poisson's ratio:	0.300
Mechanical energy to heat:	
Conversion:	0.238978 cal/MPa cm^3
95 pct efficiency:	0.227029 cal/MPa cm^3

*Sources: Department of Defense specification MIL-HDBK-5D, 2-192; Aerospace Structural Metals Handbook, AFML-tr-68-115, 1974, code 303, p. 27.

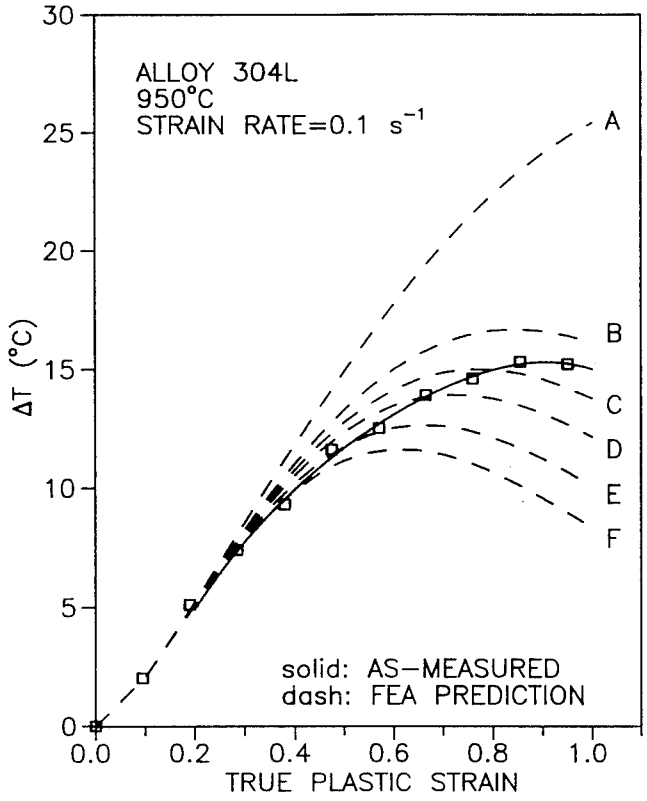


Fig. 3—The change in specimen temperature with true plastic strain for alloy 304L compressed at 950 °C and a $\dot{\varepsilon}$ of 0.1 s^{-1}. Both the as-measured (solid) and FEA (dashed) curves are shown. Curves A through F were generated with heat transfer (film) coefficients of 1.635, 4.905, 6.540, 8.175, 11.44, and 16.35 × 10^3 J/s/m^2/K, respectively. As-measured temperature data were obtained from an embedded thermocouple located at the center of the specimen.

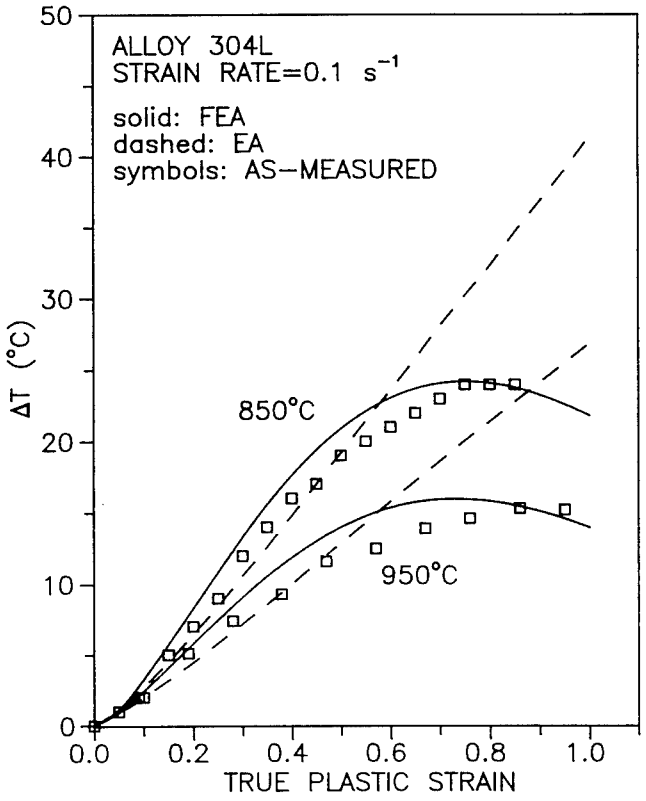


Fig. 4—The change in specimen temperature with true plastic strain for alloy 304L compressed at a $\dot{\varepsilon}$ of 0.1 s^{-1}, at temperatures of 850 °C and 950 °C. Dashed curves were calculated by the EA method and solid curves by FEA. The open symbols (squares) were measured with an embedded thermocouple located at the center of the test specimen.

be in the 90 to 95 pct range. Assuming a lower value in the analysis, *e.g.*, 90 pct, would reduce deformational heating and lower the FEA curves in Figure 4 relative to the as-measured curves. Although some errors are introduced in both FEA and as-measured data, the approximate equivalency, in magnitude and behavior with ε, between the two sets of data demonstrates that FEA provides a better approximation for T_i than does EA.

The heat-transfer coefficient between the sample and die was assumed to be constant; however, as the test proceeds, the lubricant barrier thins and microscopic contact areas may increase, causing the actual coefficient to increase. Assumption of a constant average coefficient will cause some underestimation of ΔT at low ε and overestimation at high ε.

Separate FEA analyses were run to simulate each combination of T_0 and $\dot{\varepsilon}$ employed experimentally. For each case, the corresponding as-measured σ-ε data was used as the specimen flow stress behavior for FEA, and the evolution of the T_i profile within the specimen was calculated. In essence, the FEA method is the same as that implied by Eq. [1], except that a better estimate of the effect of the η term is made by including a model of the cylinder and die, which considers effects of the film coefficient, geometry change (ε), and $\dot{\varepsilon}$ on the heat flow across the cylinder-die interface.

Initial FEA analyses showed a slightly nonuniform distribution of σ within the deformed cylinder due to nonuniform T within the cylinder and the associated thermal stresses from the temperature-dependent coefficient of thermal expansion (Table II). Thus, the desired σ-ε-T_i data could not be simply extracted from any one arbitrary FEA element in the cylinder, as would be the case for a perfectly uniform distribution of stress. The lower, stationary rigid die, shown in the model (Figure 1), was introduced to provide an independent calculation of σ. Values of σ are obtained by dividing the load on the lower rigid die (a standard quantity calculated by the FEA code) by the area at midheight, obtained by tracking the position of the outer node on this plane. For the lower imaginary die, the friction and film coefficients were assumed to be zero, because material located at the positions of these nodes in the test specimen was not actually subjected to frictional forces nor was there heat flow across the midplane of the test specimen. Strain was taken as the average of the minimum and maximum equivalent plastic ε calculated in the cylinder (a commonly supplied result of the FEA code). Typically, the two extremes of equivalent plastic strain were within 1 to 2 pct of each other. Temperature, T_i, was taken from the node located at the specimen center. As would be expected from the model, the temperature was found to be constant in the radial direction.

The FEA output gives a set of σ-ε-T_i for each test at values of ε, which are nonuniformly spaced. New sets were determined at 0.01 increments of ε by linear interpolation. For constant $\dot{\varepsilon}$, isothermal σ-ε curves for each T_0 were then obtained by linear interpolation at regular increments of ε between the five sets of σ-ε-T_i data corresponding to the five T_0 (750 °C to 1150 °C) used in testing. For interpolation, σ was assumed to vary in a piecewise linear manner with T_i at constant ε, rather than log σ with $1/T_i$, because plots (not shown) demonstrated this to be the better method for a majority of the corrections, particularly for T_0 = 750 °C, where ΔT is large and extrapolation below successive temperatures used to generate the isotherms, rather than interpolation between successive temperatures, was required. Based on a study of the data, the log σ-$1/T$ method was judged to overstate the correction because of the nearly linear behavior of σ with T_i in this temperature regime. This process, repeated for each $\dot{\varepsilon}$, gives $\sigma = \sigma(\varepsilon)|_{T_0,\dot{\varepsilon}}$.

III. RESULTS

A. *Test Specimen Temperature Behavior*

Figures 5, 6, and 7 show the calculated ΔT, $T_i - T_0$, with applied ε for compression samples deformed at a $\dot{\varepsilon}$ of 1, 0.1, and 0.01 s^{-1}, respectively. Both predictions, EA (dashed curves) and FEA (solid curves), are shown. In general, ΔT increases as deformation temperature, T, decreases, because in Eq. [1], σ varies inversely with T. For example, Figure 5 shows that ΔT is approximately 80 °C and 20 °C for the 750 °C and 1150 °C tests conducted at a $\dot{\varepsilon}$ of 1 s^{-1}. In this figure, the FEA curves lie below the corresponding EA curves, because FEA predicts a finite amount of heat conduction to the SiN dies, whereas at this $\dot{\varepsilon}$, the EA analysis assumes η to be equal to its maximum value, 0.95, which defines the thermal state of the compression sample to be purely adiabatic.

Figures 6 and 7 show that as ε increases, ΔT from FEA rises rapidly, peaks, and then decreases. The drop

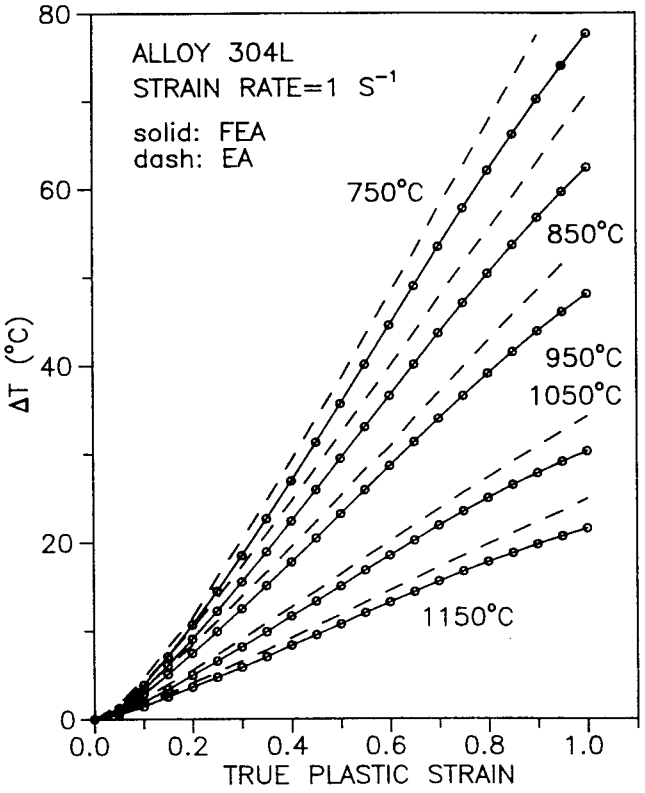


Fig. 5—The change in specimen temperature with true plastic strain for alloy 304L compressed at a $\dot{\varepsilon}$ of 1 s^{-1}. The initial test temperatures, between 750 °C and 1150 °C, are shown. Dashed curves were calculated by the EA method and the solid curves by FEA.

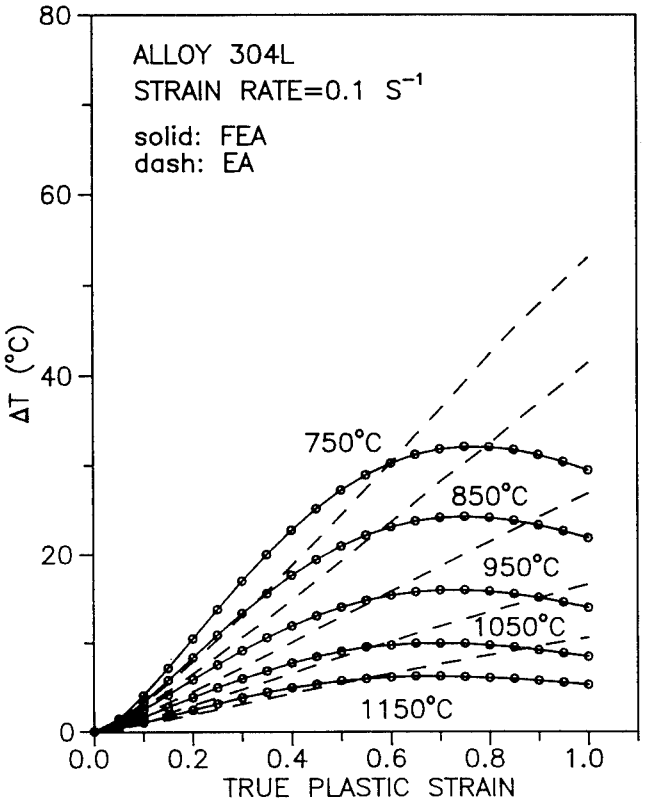


Fig. 6—The change in specimen temperature with true plastic strain for alloy 304L compressed at a $\dot{\varepsilon}$ of 0.1 s^{-1}. The initial test temperatures, between 750 °C and 1150 °C, are shown. Dashed curves were calculated by the EA method and solid curves by FEA.

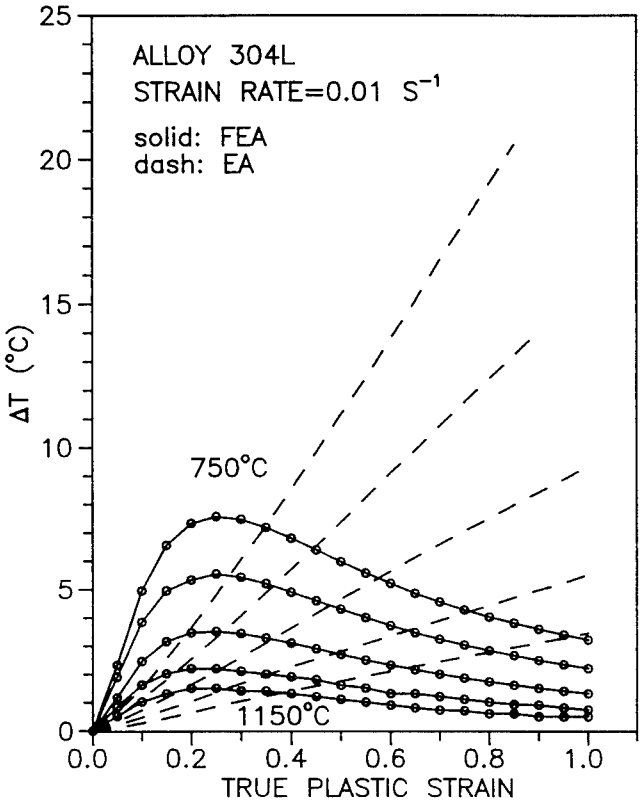


Fig. 7—The change in specimen temperature with true plastic strain for alloy 304L compressed at a $\dot{\varepsilon}$ of 0.01 s^{-1}. The initial test temperatures, between 750 °C and 1150 °C, are shown. Dashed curves were calculated by the EA method and solid curves by FEA.

in ΔT is attributed to the changing sample geometry as the test progresses. The reduction in sample height (or thickness) decreases the distance from the center of the sample to the die face. This, in turn, increases the T_i gradient and hence the heat flow. Secondly, the sample increases in diameter. The contact area between the specimen and die increases causing an increase in heat flow as deformation proceeds. Equation [1], used in the EA method, predicts monotonic increases in temperature, as shown in the figures.

Figures 6 and 7 also show that at low ε, the magnitude of ΔT from FEA is greater than from EA, and at high ε, it is less. The increase in EA ΔT with ε from Eq. [1] is moderated only by η, which is assumed independent of ε. Actually, η varies significantly with ε, as will be demonstrated. Because η was approximated from measurements of ΔT after the application of a relatively high ε, 0.7,[28,29] η represents the average heat retention behavior of a changing sample geometry for the ε range from 0 to 0.7. Thus, the calculated value of η is actually too low at low ε, resulting in anomolously low ΔT, and too high at high ε, resulting in anomolously high ΔT, as shown in Figures 4, 6, and 7.

B. *As-Measured and Isothermal Stress-Strain Behavior*

Figures 8, 9, and 10 show the as-measured and the calculated (FEA) isothermal σ-ε curves for temperatures between 750 °C and 1150 °C and strain rates of 1, 0.1, and 0.01 s^{-1}, respectively. Values for σ at regular increments of $\varepsilon = 0.1$ are provided in Tables III through V. In each case, the as-measured curves lie below the predicted isothermal curves because of the flow softening associated with deformational heating in the test sample. Comparison of the figures and tables shows that the difference between the as-measured and isothermal curves increases with increasing $\dot{\varepsilon}$ and decreasing T. For example, at the greatest $\dot{\varepsilon}$ (1 s^{-1}) and the lowest T_0 (750 °C), the corresponding values of σ at $\varepsilon = 1$ are 358 (as-measured), 430 (FEA isothermal), and 486 MPa (EA isothermal). An increase in $\dot{\varepsilon}$ allows less time for heat transfer from the superheated specimen to the dies, and the greater resulting ΔT induces relatively more softening in the measured behavior. Decreasing T gives greater σ and then a larger ΔT from Eq. [1]. At the lowest $\dot{\varepsilon}$ and highest T_0, very little correction is needed, and the as-measured curves are equal to the calculated isothermal behavior.

The as-measured behavior for 304L in this study is in excellent agreement with the as-measured flow curves for 304L reported by Semiatin and Holbrook[32] for testing conditions of $\dot{\varepsilon} = 0.01$ s^{-1} and T_0 values of 800 °C and 1000 °C and those of Barraclough and Sellars[39] for 304 at $\dot{\varepsilon} = 1$ s^{-1} and 950 °C, 1050 °C, and 1150 °C. However, as-measured 304 flow curves from Suzuki *et al.*[40] for $\dot{\varepsilon} = 0.2$ and 0.8 are relatively low at $T_0 =$ 800 °C and high at 1200 °C compared to the results presented here.

Softening due to deformational heating changes the

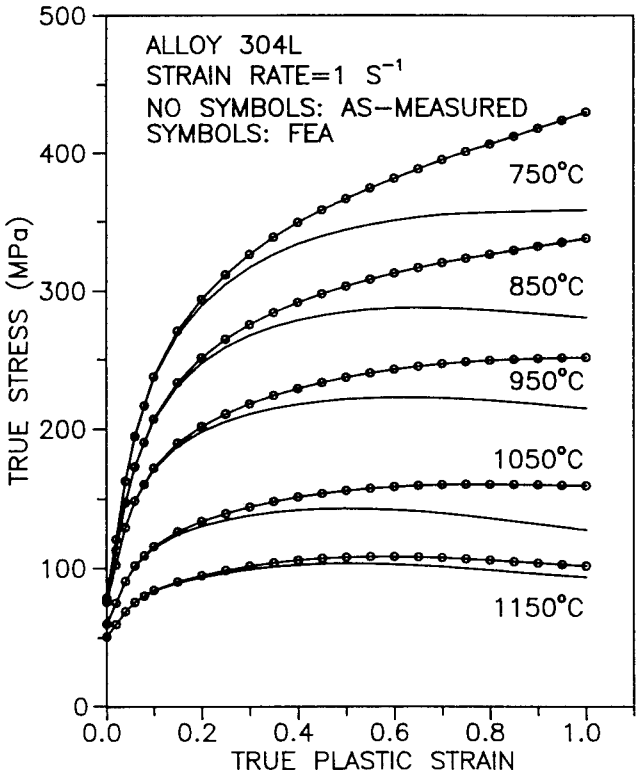


Fig. 8—True stress *vs* true plastic strain for alloy 304L compressed at a $\dot{\varepsilon}$ of 1 s^{-1}. The initial temperature of the tests ranged between 750 °C and 1150 °C. Curves without symbols are the as-measured behaviors. Curves with symbols (circles) are the predicted isothermal behaviors from the FEA method.

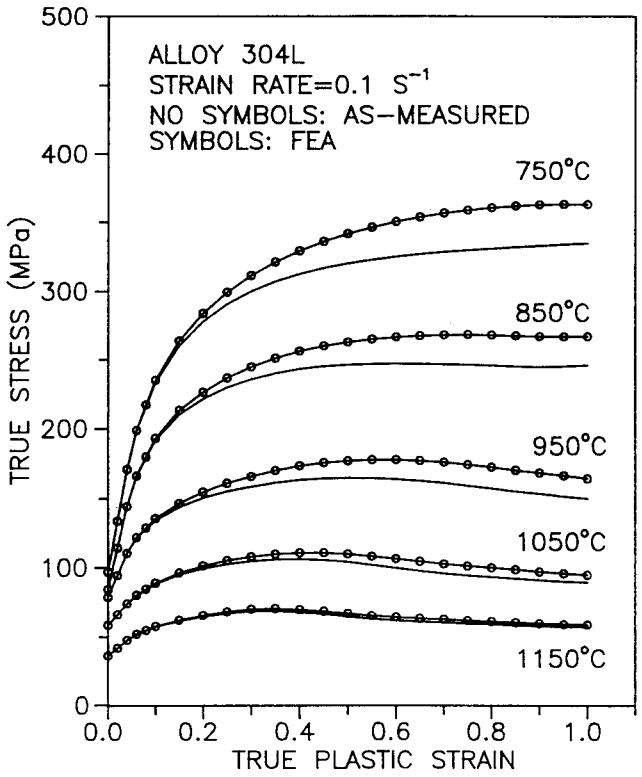


Fig. 9—True stress *vs* true plastic strain for alloy 304L compressed at a $\dot{\varepsilon}$ of 0.1 s^{-1}. The initial temperature of the tests ranged between 750 °C and 1150 °C. Curves without symbols are the as-measured behaviors. Curves with symbols (circles) are the predicted isothermal behaviors from the FEA method.

shape of the flow curves. Many of the as-measured curves exhibit initial hardening followed by softening. The softening behavior apparent in the as-measured 950 °C and 1050 °C curves in Figure 8 is consistent with that observed from the as-measured curves of Barraclough and Sellars.[39] The position of the transition or peak in the flow curve is often associated with the onset of dynamic recrystallization, which was observed for this particular 304L material[30] (Figures 23 and 24 in Reference 30), and has been related to the apparent activation energy for deformation.[41,42] Correcting the as-measured curves shifts the value of ε at the peak, ε_p, to significantly higher values, as shown in Table VII. For example, for $\dot{\varepsilon} = 1\ s^{-1}$ and $T_0 = 950$ °C, the as-measured $\varepsilon_p = 0.6$, whereas the FEA $\varepsilon_p > 1$.

The observed differences between the FEA and EA values of σ in Tables III and IV are due primarily to the difference in calculated ΔT. The EA method generally gives greater values of ΔT (Figures 5 through 7) and thus greater values of σ correction. An exception occurs at the lower strain rates and at relatively low ε, *e.g.*, $\varepsilon = 0.2$. Here, the EA ΔT is slightly less than the FEA ΔT, and the data in the Tables IV and V show that the EA isothermal σ values are slightly less than the corresponding FEA values. The overcorrection by the EA method at high ε also changes the shape of the flow curve, shifting the peak to higher values of ε. For example, for test conditions of $\dot{\varepsilon} = 0.01\ s^{-1}$, $T_0 = 850$ °C, and of $\varepsilon = 1$, the FEA $\varepsilon_p = 0.6$ (Table VII), whereas EA $\varepsilon_p > 1$ (from the behavior in Table V).

In addition to differences in ΔT from the two correction methods, the magnitude of $\Delta\sigma$ correction is also affected by the assumed relationship between σ and T, a linear σ-T relationship in FEA and a linear log σ-$1/T$ relationship in EA. Because the data does obey a near linear relationship between σ and T, especially at low T, the EA method results in a larger correction for $T_0 = 750$ °C than would be anticipated for the calculated ΔT, because the correction is obtained by extrapolation of the log σ-$1/T$ relationship to a temperature (750 °C) significantly outside the range (774 °C to 865 °C) used to define the relationship. A modified EA method, EA-MOD, employing a linear σ-T relationship is introduced here to further examine the σ correction calculated by the EA method. For $\dot{\varepsilon} = 0.01\ s^{-1}$, $T_0 = 750$ °C, and $\varepsilon = 1$, Table V shows that the corresponding values of $\Delta\sigma$ from the three methods are 3 (FEA), 47 (EA), and 30 MPa (EA-MOD). Comparing the two methods employing a linear σ-T relationship, a 10-fold difference in ΔT, 2.3 °C (FEA) compared to 24 °C (EA, EA-MOD) shown in Figure 7, results in a 10-fold difference in $\Delta\sigma$, 3 (FEA) *vs* 30 MPa (EA-MOD). In the EA method, extrapolation (log σ-$1/T$ relationship) over 24 °C results in an additional 17 MPa of σ correction compared to EA-MOD (σ-T relationship). For interpolation to $T_0 > 750$ °C, *i.e.*, 850 °C and above, where extrapolation is not required, the EA method gives lower $\Delta\sigma$ compared to EA-MOD as a result of the nonlinear relationship between σ and T in the former. For example, in Table V, for $\dot{\varepsilon} = 0.01\ s^{-1}$, $T_0 = 850$ °C, and $\varepsilon = 1$, the corresponding values of $\Delta\sigma$ are 2 (FEA), 14 (EA), and

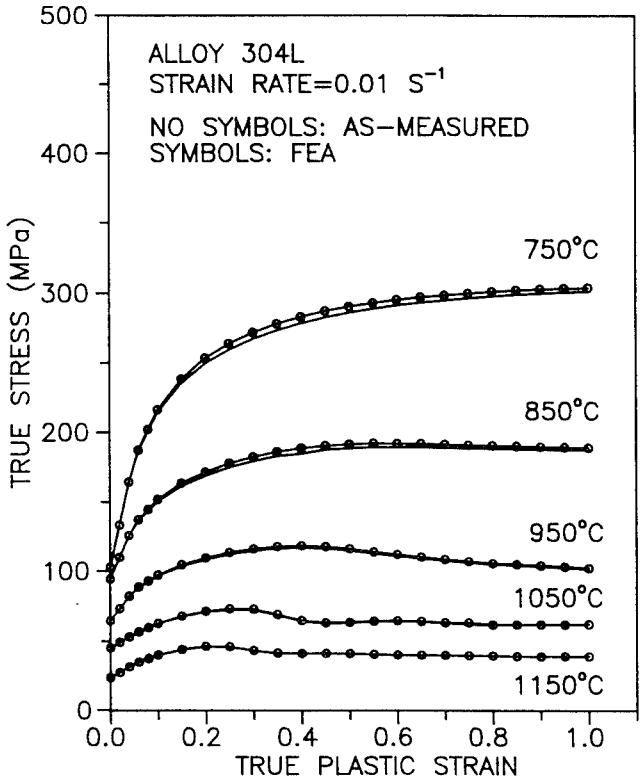


Fig. 10—True stress *vs* true plastic strain for alloy 304L compressed at a $\dot{\varepsilon}$ of 0.01 s^{-1}. The initial temperature of the tests ranged between 750 °C and 1150 °C. Curves without symbols are the as-measured behaviors. Curves with symbols (circles) are the predicted isothermal behaviors from the FEA method.

19 MPa (EA-MOD), where ΔT was 1.4 °C (FEA) and 15 °C (EA, EA-MOD). Again, a near 10-fold difference in ΔT results in a 10-fold difference in $\Delta\sigma$, comparing FEA to EA-MOD. The nonlinear correction in EA provides a smaller correction than might be expected from the differences in magnitude of ΔT calculated by the FEA and EA methods.

The close correspondence between the as-measured and FEA values of ΔT (Figure 4) demonstrates that the FEA method for obtaining $\sigma = \sigma(\varepsilon)|_{T_0,\dot{\varepsilon}}$ probably provides a better estimate of the true state of the isothermal behavior of alloy 304L compared to the EA method. The values and behavior of Q_{DEF}, calculated from both the as-measured and FEA-isothermal data, will be discussed. Although strain-rate sensitivity (m) is not discussed, it can be observed that values for an average m, calculated for a specific $\dot{\varepsilon}$ range from the data in Tables III through V, show that m is generally underestimated from the as-measured data. For example at T_0 = 950 °C and ε = 1, the average m value in the low strain-rate range, from 0.01 to 0.1 s^{-1}, is 0.17 from the as-measured data compared to 0.21 for the isothermal data. This undervaluation is due to relatively greater sample heating and associated flow softening at the higher $\dot{\varepsilon}$, of the $\dot{\varepsilon}$ pair, used to determine m.

IV. DISCUSSION

A. *Heat Retention Efficiency Term, η*

The heat retention efficiency η is assumed to vary linearly with log $\dot{\varepsilon}$ equaling 0 at $\dot{\varepsilon}$ = 0.001 s^{-1} and 0.95 at $\dot{\varepsilon}$ = 1 s^{-1},[29] as shown by Eq. [2] and graphically by the dashed line in Figure 11. For comparison, η was also calculated from the FEA data (Figures 5 through 7) by dividing the calculated ΔT by the maximum ΔT obtained for an adiabatic case. The latter value was obtained from Eq. [1], where η = 0.95, and the as-measured σ-ε data. The variation of η derived from FEA data is shown in Figure 11 for two levels of ε: 0.2 and 0.7. From the FEA data, it appears that η can be assumed to be equal to zero at 0.001 s^{-1} and 0.95 at 10 s^{-1} (rather than at 1 s^{-1}). The experimental data on aluminum,[28] shown in Figure 11, also supports this conclusion. The FEA data for 304L demonstrates that the variation of η with log $\dot{\varepsilon}$ is distinctly nonlinear. Also, it is shown that η depends distinctly on ε. Comparison of η from the two methods (Figure 11) shows that the linear approximation of η in the EA method gives significantly underestimated values of η at low ε, *e.g.*, for ε = 0.2, in the $\dot{\varepsilon}$ range from 0.01 to 0.5 s^{-1} and overestimated values at high ε, *e.g.*, for ε = 0.7, from 0.005 to 0.1 s^{-1}. The decrease in FEA η from 0.2 to 0.7 ε at constant $\dot{\varepsilon}$, observed in Figure 11, is due to changes in sample geometry, reducing thickness and increasing diameter, with increasing ε. Both

Table III. The As-Measured (MEAS), FEA Isothermal (ISO), and EA Isothermal (EA) Values of σ (MPa) for Various T_0, at 0.1 Increments of ε, and a $\dot{\varepsilon}$ of 1 s^{-1}*

	750 °C				850 °C				950 °C				1050 °C		1150 °C	
ε	MEAS	FEA	EA	EA-MOD	MEAS	FEA	EA	EA-MOD	MEAS	FEA	EA	EA-MOD	MEAS	FEA	MEAS	FEA
0.0	78.4	78.4	—	—	8.1	78.1	—	—	75.5	75.5	—	—	59.7	59.7	50.4	50.4
0.1	236	238	—	—	206	207	—	—	171	172	—	—	114	115	83.5	83.9
0.2	289	294	295	294	247	251	251	252	198	202	201	202	130	134	93.1	94.5
0.3	317	326	—	—	267	276	—	—	210	218	—	—	138	144	99.0	101
0.4	334	349	356	351	278	291	291	293	217	229	228	230	142	151	102	106
0.5	344	366	—	—	285	303	—	—	221	237	—	—	143	156	103	108
0.6	351	381	397	384	287	313	312	315	222	243	242	245	142	159	102	108
0.7	355	395	—	—	288	320	—	—	222	247	—	—	140	160	101	107
0.8	357	406	438	411	286	326	324	330	220	249	249	252	136	160	98.3	105
0.9	358	418	—	—	283	332	—	—	218	251	—	—	132	160	95.7	103
1.0	358	430	486	438	280	338	343	346	214	252	254	257	127	159	93.2	101

*Isothermal σ was also calculated with a modified EA method (EA-MOD), assuming that stress varies linearly with T_i, for interpolation of σ to T_0, rather than the assumed linear variation of log σ to $1/T_i$.

Table IV. The As-Measured (MEAS), FEA Isothermal (ISO), and EA Isothermal (EA) Values of Stress for Various Deformation Temperatures, at 0.1 Increments of ε, and a $\dot{\varepsilon}$ of 0.1 s^{-1}*

	750 °C				850 °C				950 °C				1050 °C		1150 °C	
ε	MEAS	FEA	EA	EA-MOD	MEAS	FEA	EA	EA-MOD	MEAS	FEA	EA	EA-MOD	MEAS	FEA	MEAS	FEA
0.0	96.6	96.6	—	—	84.0	84.0	—	—	78.4	78.4	—	—	58.0	58.0	35.7	35.7
0.1	233	235	—	—	192	193	—	—	134	135	—	—	87.9	88.7	57.1	57.4
0.2	278	284	284	282	222	226	222	225	150	155	150	154	99.0	101	64.4	65.3
0.3	300	311	—	—	236	245	—	—	158	166	—	—	104	108	68.3	69.7
0.4	313	329	334	326	243	256	253	254	163	174	170	172	106	110	67.6	69.5
0.5	320	342	—	—	246	263	—	—	165	177	—	—	104	110	64.3	66.6
0.6	325	350	360	350	247	266	263	267	164	178	175	178	99.3	106	61.5	63.9
0.7	328	356	—	—	247	268	—	—	161	176	—	—	95.4	102	60.0	62.3
0.8	331	360	390	371	246	268	271	276	157	172	174	178	92.8	99.5	58.7	60.8
0.9	333	363	—	—	244	267	—	—	153	168	—	—	90.6	96.7	57.4	59.4
1.0	335	363	418	388	246	267	282	288	150	164	173	180	89.0	94.4	56.7	58.4

*Isothermal σ was also calculated with a modified EA method (EA-MOD), assuming that stress varies linearly with T_i, for interpolation of σ to T_0, rather than the assumed linear variation of log σ to $1/T_i$.

Table V. The As-Measured (MEAS) and FEA Isothermal (ISO), Values of Stress for Various Deformation Temperatures, at 0.1 Increments of ε, and a $\dot{\varepsilon}$ of 0.01 s^{-1}*

	750 °C				850 °C				950 °C				1050 °C		1150 °C	
ε	MEAS	FEA	EA	EA-MOD	MEAS	FEA	EA	EA-MOD	MEAS	FEA	EA	EA-MOD	MEAS	FEA	MEAS	FEA
0.0	102	102	—	—	93.9	93.9	—	—	64.2	64.2	—	—	44.8	44.8	23.2	23.2
0.1	214	216	—	—	150	152	—	—	96.1	96.8	—	—	62.0	62.3	39.6	39.7
0.2	250	253	254	252	169	171	170	171	108	109	109	109	70.6	71.1	45.8	46.0
0.3	267	272	—	—	179	182	—	—	114	116	—	—	72.0	72.6	42.7	42.9
0.4	278	283	290	287	186	188	190	191	117	118	118	119	63.7	64.3	40.6	40.8
0.5	286	290	—	—	188	191	—	—	114	116	—	—	62.5	63.0	40.6	40.7
0.6	291	295	313	306	189	192	196	199	110	112	114	115	63.7	64.1	39.5	39.6
0.7	295	298	—	—	189	191	—	—	107	108	—	—	62.4	62.7	39.3	39.4
0.8	298	301	332	320	188	190	199	203	104	105	109	111	61.0	61.2	39.0	39.0
0.9	300	303	—	—	188	189	—	—	103	104	—	—	61.3	61.5	38.6	38.6
1.0	301	304	348	331	187	189	201	206	101	102	107	110	61.5	61.7	38.7	38.7

*Isothermal σ was also calculated with a modified EA method (EA-MOD), assuming that stress varies linearly with T_i, for interpolation of σ to T_0, rather than the assumed linear variation of log σ to $1/T_i$.

Table VI. Activation energy, Q_{DEF}, at Constant Stress and for Two Strain Levels, 0.2 and 0.6*

		Activation Energy (kJ/mole)							
		Variable							
		1 s^{-1}		0.1 s^{-1}		0.01 s^{-1}		Invariable	
Stress	(MPa)	MEAS	ISO	MEAS	ISO	MEAS	ISO	MEAS	ISO
100									
	Strain = 0.2	441	450	422	417	402	381	—	—
	Strain = 0.6	340	400	373	363	402	321	372	358
150									
	Strain = 0.2	470	469	399	394	312	302	—	—
	Strain = 0.6	408	389	386	347	364	300	386	346
200									
	Strain = 0.2	534	544	418	418	254	233	—	—
	Strain = 0.6	446	414	403	352	356	277	404	348
250									
	Strain = 0.2	609	658	471	488	271	204	—	—
	Strain = 0.6	478	457	423	366	361	245	422	358
300									
	Strain = 0.2	—	—	—	—	—	—	—	—
	Strain = 0.6	449	485	449	381	449	234	450	370
							Average =	407	356

*Values are shown for two assumptions: Q_{DEF} varies with $\dot{\varepsilon}$ or is constant over the entire $\dot{\varepsilon}$ range.

Table VII. Values for Peak Strain (ε_p) for Fine Grain 304L Tested at Various T_0-$\dot{\varepsilon}$ Pairs*

$\dot{\varepsilon}$	750 °C	850 °C	950 °C	1050 °C	1150 °C
0.01 s^{-1}					
As-measured	>1.0	0.60	0.40	0.26	0.23
Isothermal	>1.0	0.55	0.40	0.25	0.20
0.1 s^{-1}					
As-measured	>0.85	0.61	0.51	0.38	0.34
Isothermal	>1.0	0.75	0.56	0.44	0.35
1.0 s^{-1}					
As-measured	>0.86	0.65	0.61	0.51	0.50
Isothermal	>1.0	>1.0	>1.0	0.76	0.57

*Values from both as-measured and isothermal σ-ε data are given.

changes in geometry increase heat flow from the specimen to the dies, and as a result, the heat retention efficiency, η, is reduced with increasing ε. The effect of underestimation of η at low ε and overestimation at high ε in this $\dot{\varepsilon}$ range is that the EA calculated ΔT for the specimen is likewise under- and overestimated compared to the FEA values, as observed in Figures 6 and 7. Because calculated ΔT is used to correct the as-measured σ for deformational heating, the EA isothermal σ is likewise under- and overestimated for low and high ε, as shown in Tables IV and V.

B. *Observations Regarding Activation Energy for Deformation, Q_{DEF}*

The apparent activation energy for deformation, Q_{DEF}, appears in the equation attributed to Zener–Hollomon:[43]

$$Z = \dot{\varepsilon} \exp (Q_{DEF}/RT) \quad [3]$$

where T is the absolute temperature (in Kelvin), R is the universal gas constant, and Z is the Zener–Hollomon parameter. Zener and Hollomon suggest that flow stress is a function of Z and ε. For the calculation of Q_{DEF}, the following general expression for σ is assumed:

$$\sigma = f(\varepsilon)Z^u \quad [4]$$

where $f(\varepsilon)$ is some function of ε and u is a constant. The value of Q_{DEF} was calculated as a function of $\dot{\varepsilon}$ and T, for applied strains of 0.2 and 0.6, from both the as-measured and isothermal σ-ε data in Tables III through V. Figures 12 and 13 show the variation in σ, after an applied ε of either 0.2 or 0.6, respectively, with $1/T_0$ for the three strain rates studied. Each set of data was fitted to a third-order polynomial, and values of $1/T_0$ at constant σ were calculated for each $\dot{\varepsilon}$. Figures 14 and 15 show the variation of ln $\dot{\varepsilon}$ with $1/T_0$ for different σ levels. The slope of each curve corresponds to Q_{DEF}/R, from Eq. [3].

Because the 1150 °C test preheat resulted in a larger average grain diameter in the test specimen before deformation (0.12 *vs* 0.038 mm for the starting material), additional tests at 1150 °C were conducted to investigate the dependency of σ on grain size. Specimens were preheated at 1150 °C at either 1 or 8 hours, giving starting average grain diameters of 0.29 and 0.85 mm, respectively. Compression tests were then conducted at 0.01 and 1 s^{-1} at T_0 = 1150 °C. Grain size was found to have

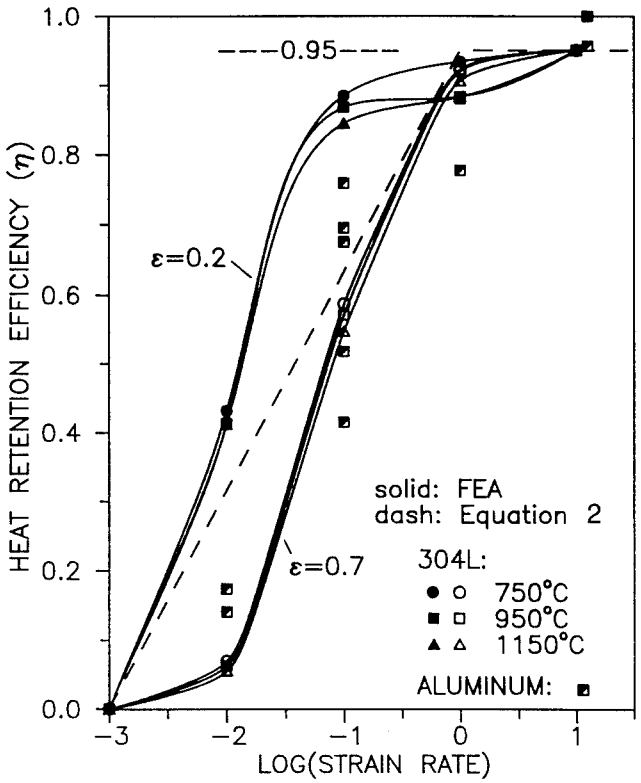


Fig. 11—Heat retention efficiency, η, *vs* log $\dot{\varepsilon}$ in the $\dot{\varepsilon}$ realm, where conventional-sized compression test samples of alloy 304L exhibit neither an isothermal nor an adiabatic state. The η from both methods, FEA and EA, are shown. Note, η calculated from FEA is dependent on strain. Data for aluminum is from Charpentier *et al.*[28]

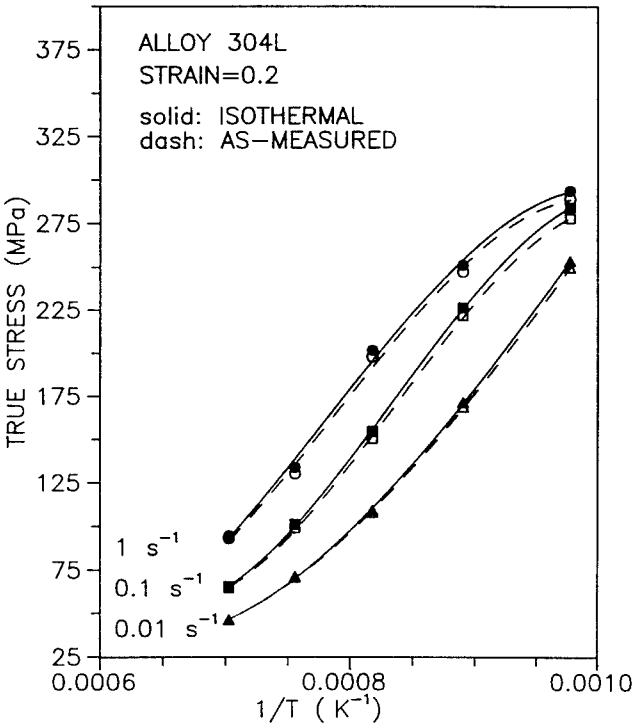


Fig. 12—The variation of true stress with inverse temperature (K^{-1}) for alloy 304L compressed at three different strain rates to a true strain of 0.2. Dashed curves are from the as-measured σ-ε data. The solid curves are from FEA isothermal data. Values of inverse temperature at various constant stress levels from this figure are used in Fig. 14.

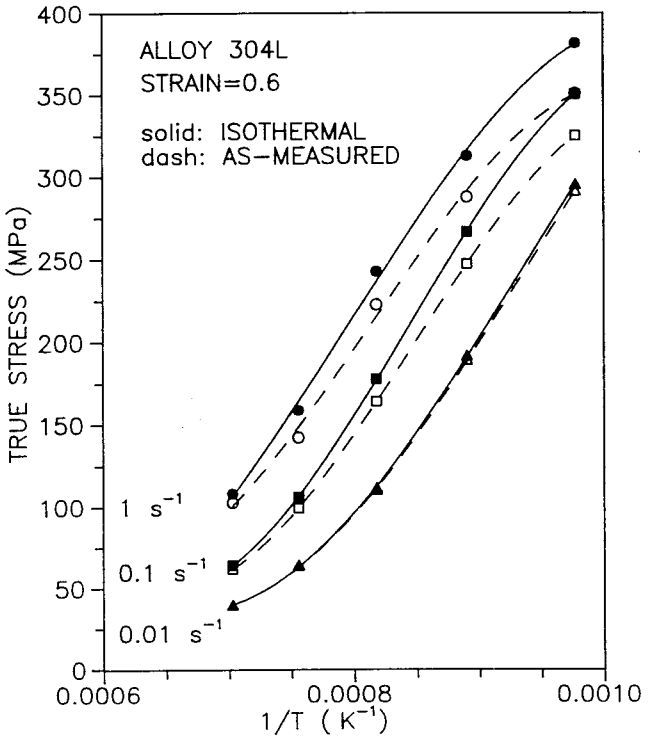


Fig. 13—The variation of true stress with inverse temperature (K^{-1}) for alloy 304L compressed at three different strain rates to a true strain of 0.6. Dashed curves are from the as-measured σ-ε data. The solid curves are from FEA isothermal data. Values of inverse temperature at various constant stress levels from this figure are used in Fig. 15.

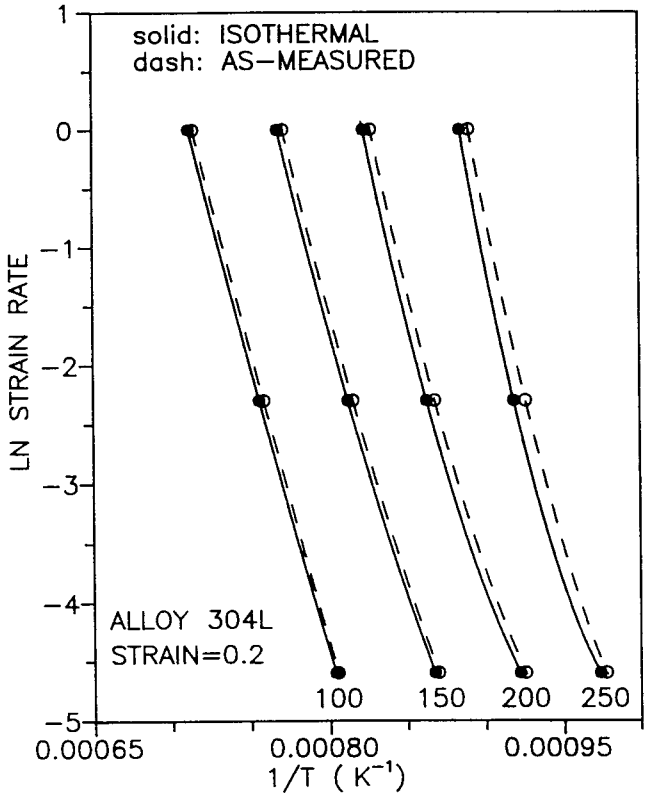


Fig. 14—The variation in natural logarithm of strain rate with inverse temperature (K^{-1}) at various constant stress levels (MPa) for alloy 304L compressed to a strain of 0.2. Dashed curves are from the as-measured σ-ε data. The solid curves are from FEA isothermal data.

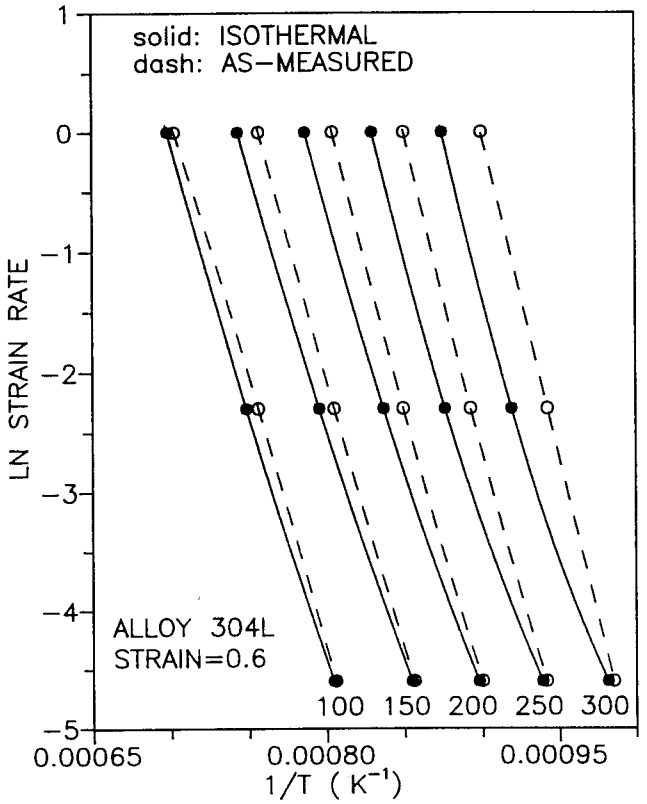


Fig. 15—The variation in natural logarithm of strain rate with inverse temperature (K^{-1}) at various constant stress levels (MPa) for alloy 304L compressed to a strain of 0.6. Dashed curves are from the as-measured σ-ε data. The solid curves are from FEA isothermal data.

little effect on the as-measured flow stress. For example, at $\dot{\varepsilon} = 1\ s^{-1}$ and $\varepsilon = 0.6$, σ was equal to 102, 99.4, and 103 MPa for average grain diameters of 0.12, 0.29, and 0.85 mm, respectively. At $\dot{\varepsilon} = 0.01\ s^{-1}$, the corresponding values of σ are 39.5, 39.8, and 42.6 MPa. Similar behavior is observed at $\varepsilon = 0.2$. Because of a lack of significant dependency of σ on grain size, the σ values from the 1150 °C tests are used in the calculation of Q_{DEF} that follows.

It has been common practice in the literature to calculate Q_{DEF} in the hot-working range from as-measured σ-ε data, probably because plots of ln $\dot{\varepsilon}$ with inverse T_0 generally exhibit a nearly linear behavior. Thus, Q_{DEF} is often assumed to be constant over the $\dot{\varepsilon}$ range studied. In fact, the as-measured data for 304L presented here and that presented for Cu[11] and Ni,[13] studied over a similar $\dot{\varepsilon}$ range, does indicate a constant Q_{DEF}. The assumption of constant Q_{DEF}, independent of T, $\dot{\varepsilon}$, and ε, is an attractive assumption, because it facilitates utilization of Z in the prediction of flow stress. However, the isothermal data in Figures 14 and 15 exhibits a distinct curvature that shows that Q_{DEF} decreases with decreasing $\dot{\varepsilon}$. Likewise, if the as-measured σ-ε data for Cu[11] and Ni[13] were corrected for adiabatic heating, Q_{DEF} would be shown to vary. A decreasing Q_{DEF} with decreasing $\dot{\varepsilon}$, in this $\dot{\varepsilon}$ range, is consistent with the general observation that Q_{DEF} in the creep realm has a lower value than in the hot-working realm. Evidence for a continuous variation of Q_{DEF} between these two realms is suggested here.

The data sets in Figures 14 and 15 were fitted with a second-order polynomial, and Q_{DEF} was calculated by differentiating the polynomial for the various deformation conditions (Table VI). At low ε, 0.2, values for Q_{DEF} from the as-measured and isothermal data are similar because of the limited amount of sample heating at low ε. The average Q_{DEF} obtained from the two sets of data is 417 and 413 kJ/mole, respectively. At a ε of 0.6, however, values of Q_{DEF} from as-measured and isothermal data are significantly different, 407 and 356 kJ/mole, respectively. In this case, significant heating of the sample occurs as a result of the greater applied ε. Samples deformed at the high $\dot{\varepsilon}$ retain most of the deformational heat, causing significant rise in T_i and decrease in σ as deformation proceeds. Thus, $1/T_i$ varies less with $\dot{\varepsilon}$ at constant σ (Figures 12 and 13) for the as-measured data compared to the isothermal data, yielding a reduced dependency of σ on T_i. This, in turn, results in a greater slope (Q_{DEF}/R) and higher values of Q_{DEF} from as-measured data in Figures 14 and 15. Thus, Q_{DEF} is overestimated from the as-measured data.

Figures 16 and 17 show the variation in Q_{DEF} with T (obtained from Table VI and Figures 14 and 15) for the three strain rates studied, at an applied ε of 0.2 and 0.6, respectively. At the lower ε (Figure 16), values for Q_{DEF} from the two sets of data, as-measured and isothermal, are very similar, as expected from the similarity of the σ-ε data. More importantly, Figure 16 shows that Q_{DEF} varies significantly with T and in a much different fashion, depending on $\dot{\varepsilon}$. For a $\dot{\varepsilon}$ of 1 s^{-1}, Q_{DEF} decreases with T. Conversely, at 0.01 s^{-1}, it increases. At 1100 K, Q_{DEF} for high and low $\dot{\varepsilon}$ have corresponding high and low values, 700 and 250 kJ/mole, respectively. At the intermediate $\dot{\varepsilon}$, 0.1 s^{-1}, Q_{DEF} first decreases and then increases with increase in T. The three curves appear to converge near a value of 400 kJ/mole as T approaches 1400 K.

Figure 17 shows that at a ε of 0.6, the variation in Q_{DEF} with T from the isothermal σ-ε data is well behaved, similar to the behavior shown in Figure 16 for lower ε. At 1100 K, Q_{DEF} increases significantly with $\dot{\varepsilon}$, having a value of 270 kJ/mole at the lowest rate and 525 kJ/mole at the highest. As T increases, Q_{DEF} for the three strain rates converges to a value of approximately 375 to 400 kJ/mole at 1400 K. In contrast, the variation in Q_{DEF} calculated from the as-measured σ-ε data (dashed curves in Figure 17) shows no consistent behavior.

Variations in the value of Q_{DEF} with $\dot{\varepsilon}$ could be attributed to a changing activity of the various dislocation mechanisms contributing to flow. For example, work-hardening moderated by cross slip is the dominant mechanism at high $\dot{\varepsilon}$ and low T. Dislocation climb and polygonization contribute to dynamic recovery at low $\dot{\varepsilon}$ and high T, similar to creep. A decrease in Q_{DEF} with an increase in T, similar to that observed in Figures 16 and 17 for a $\dot{\varepsilon}$ of 1 s^{-1}, is consistent with an increase in thermal activation for dislocations to overcome short-range barriers that obstruct their motion as T is raised. The increase in Q_{DEF} with T observed at the lowest $\dot{\varepsilon}$, 0.01 s^{-1}, indicates a decreasing dislocation mobility. For example, dislocation pinning by individual solute atoms

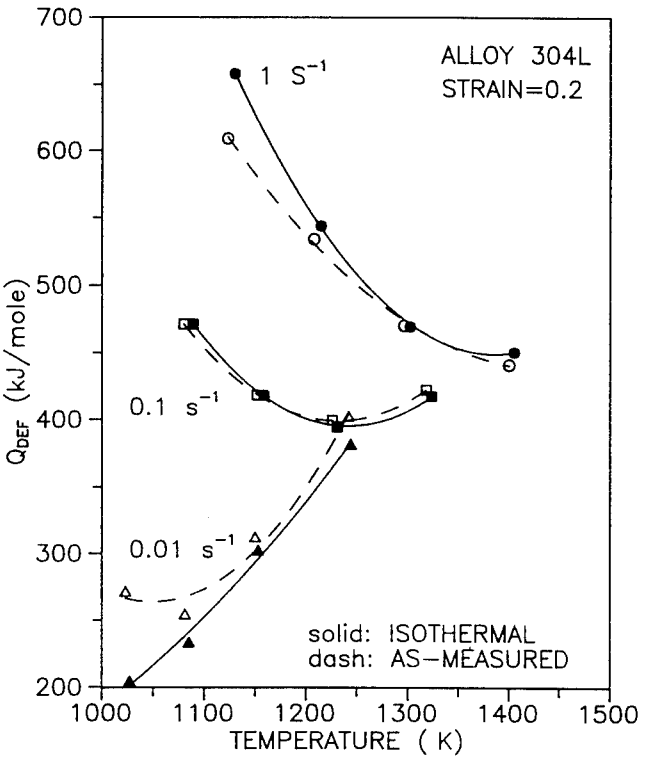


Fig. 16—The variation of activator energy, Q_{DEF}, with initial deformation temperature for alloy 304L compressed at three different strain rates to a strain of 0.2. Dashed curves are from the as-measured σ-ε data. The solid curves are from FEA isothermal data.

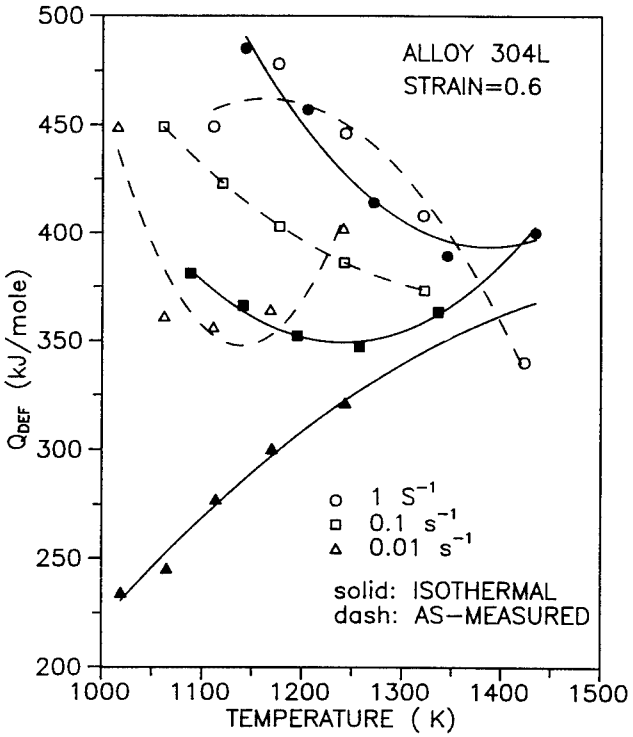


Fig. 17—The variation of activation energy, Q_{DEF}, with initial deformation temperature for alloy 304L compressed at three different strain rates to a strain of 0.6. Dashed curves are from the as-measured σ-ε data. The solid curves are from FEA isothermal data.

or atom complexes may become important at high T and low $\dot{\varepsilon}$. A similar increase in Q_{DEF} with T has been observed for creep of aluminum below $T/T_m = 0.5$, where T_m is the melting temperature (K), and at a $\dot{\varepsilon}$ of 3×10^{-11} s^{-1}.[44,45] The increase has been related to the transition from one deformation mechanism to another. At low T/T_m, creep in aluminum is controlled by dislocation intersection processes; at intermediate values by cross slip of screw dislocations; and at higher values, approaching 0.5, by dislocation climb and the nonconservative motion of jogs in screw dislocations. Above 0.5 T/T_m, creep is entirely diffusion controlled, and Q_{DEF} is relatively constant, increasing only slightly with T. However, as $\dot{\varepsilon}$ is increased to a value of 0.03 s^{-1}, a rate similar to the slowest used in this investigation, Q_{DEF} is shown to increase rapidly with T up to about 0.75 T/T_m. At the higher $\dot{\varepsilon}$, comparatively little time is available for diffusion-controlled processes, and the sensitivity of Q_{DEF} to T exhibited at low T/T_m is extended to higher T/T_m. The increase in Q_{DEF} with T for aluminum is similar to that observed here for 304L, both alloys deformed at equivalent $\dot{\varepsilon}$ and T/T_m.

The value of Q_{DEF} for $\dot{\varepsilon} = 0.01$ s^{-1} and $T = 1100$ K is 270 kJ/mole (Figure 17), which is significantly less than any of the values obtained by assuming an average linear behavior for the variation of Q_{DEF}/R for any σ level (Table VI) and is in fair agreement with the value of 314 kJ/mole reported for creep of alloy 304.[46] Similarly, Afonja[47] measured Q_{DEF} in a 23.6 Cr-5.12 Ni duplex stainless steel at a $\dot{\varepsilon} = 0.01$ s^{-1} and found the value, 242 kJ/mole, to agree with the activation energy reported for self-diffusion in similar Fe-Cr-Ni alloys. The Q_{DEF} for creep is generally equal to the activation energy for self-diffusion.[46] This suggests that Q_{DEF} for the creep realm may apply up to a $\dot{\varepsilon}$ of 0.01 s^{-1}, a few orders of magnitude above that considered to be the upper bound of the creep realm.

If the data in Figure 15 is assumed to behave in a linear fashion, Q_{DEF} from the isothermal data is relatively constant, varying little from the average value of 356 kJ/mole for different isostress levels. Conversely, Q_{DEF} from the as-measured data increases in a linear fashion from 372 kJ/mole at 100 MPa to 450 kJ/mole at 300 MPa. The assumption that Q_{DEF} can be obtained from as-measured σ-ε data probably accounts, in part, for the wide range of values of Q_{DEF} that have been reported for this alloy system (ranging from 393 to 600 kJ/mole).[30]

V. CONCLUSIONS

1. Deformational heating of laboratory-sized compression samples during testing in a $\dot{\varepsilon}$ range from 0.01 to 1 s^{-1}, at temperatures from 750 °C to 1150 °C, and to a ε of 1 can lead to significant stress softening and discrepancy between as-measured and isothermal σ-ε behaviors.
2. The FEA method presented provides an effective technique to calculate the instantaneous temperature of the compression sample, which coupled with the as-measured σ-ε values obtained from tests at different starting temperatures allows the determination of isothermal σ-ε. The FEA model predictions closely approximate measured temperature variations in the test sample during compression testing.
3. A conventional technique used to calculate instantaneous sample temperature (*via* Eqs. [1] and [2]) relies on η, a heat retention efficiency term that varies only with $\dot{\varepsilon}$, $\eta = \eta(\dot{\varepsilon})$, to reduce the heating calculated for an adiabatic condition. The FEA results show that η is also a function of ε, $\eta = \eta(\dot{\varepsilon}, \varepsilon)$, and the use of η in the simple sense can lead to significant errors in the calculated instantaneous sample temperature and resulting isothermal σ-ε behavior.
4. The apparent activation energy for deformation, Q_{DEF}, for 304L, calculated from the isothermal σ-ε data, decreases with decreasing $\dot{\varepsilon}$ in the range 0.01 to 1 s^{-1}. This behavior is consistent with the general observation that Q_{DEF} has a lower value in the creep range than in the hot-working range and suggests a smooth transition in the value of Q_{DEF} from one range to the other. Utilization of the as-measured σ-ε data, without correction for deformational heating, indicates that Q_{DEF} is constant in this $\dot{\varepsilon}$ regime. Values for Q_{DEF} from isothermal data are generally lower than those calculated from as-measured data.

ACKNOWLEDGMENTS

This work was performed under contract with the United States Department of Energy. The authors would like to acknowledge the technical support received from Michael Riendeau and Gary Coubrough, during mechanical testing. The authors would also like to acknowledge Michael Weis, Graduate Student, Advanced Steel Processing and Products Research Center, Colorado School of Mines, Golden, CO, for help in constructing the compression testing system.

REFERENCES

1. S. Kobayashi, S.I. Oh, and T. Altan: *Metal Forming and the Finite-Element-Method*, Oxford University Press, New York, NY, 1989.
2. C.R. Boer, N. Rebelo, H. Rydstad, and G. Schroder: *Process Modelling of Metal Forming and Thermomechanical Treatment*, Springer-Verlag, Heidelberg, 1986.
3. I. Haque, J.E. Jackson, Jr., T. Gangjee, and A. Raikar: *J. Mater. Shaping Technol.*, 1987, vol. 5 (1), pp. 23-33.
4. K.J. Meltsner: in *Simulation and Theory of Evolving Microstructures and Textures*, M.P. Anderson and A. Rollet, eds., TMS, Warrendale, PA, 1990.
5. A.J.M. Shih and H.T.Y. Yang: *Int. J. Numei*, 1991, vol. 31, pp. 345-67.
6. S.I. Oh, G.D. Lahoti, and T. Altan: in *Process Modeling Tools*, Proc. Soc. for Metals Process Modeling Sessions, Materials and Processes Congress, 1980, ASM, Metals Park, OH, 1981, pp. 195-216.
7. S.L. Semiatin, G.D. Lahoti, and T. Altan: in *Process Modeling: Fundamentals and Applications to Metals*, T. Altan, ed., ASM, Metals Park, OH, 1980, p. 387.
8. D.W. Livesey and C.M. Sellars: *Mater. Sci. Technol.*, 1985, vol. 1, pp. 136-44.
9. J.R. Douglas and T. Altan: *ASME Trans. J. Eng. Industry*, 1975, Feb., p. 66.
10. K.P. Rao, S.M. Doraivelu, and V. Gopinathan: *J. Mech. Work. Technol.*, 1982, No. 6, pp. 63-88.
11. V.M. Sample, G.L. Fitzsimons, and A.J. DeArdo: *Acta Metall.*, 1987, vol. 35 (2), pp. 367-79.

12. J.J. Jonas and T. Sakai: in *Deformation Processing and Structure*, G. Krauss, ed., ASM, Metals Park, OH, 1982, pp. 185-230.
13. J.J. Luton and C.M. Sellars: *Acta Metall.*, 1969, vol. 17, pp. 1033-43.
14. M.R. Staker and N.J. Grant: *Mater. Sci. Eng.*, 1985, No. 75, pp. 137-50.
15. V.M. Sample and L.A. Lalli: *Mater. Sci. Technol.*, 1987, vol. 3, pp. 28-35.
16. R. Raj: *Metall. Trans. A*, 1981, vol. 12A, pp. 1089-97.
17. C. Gandhi: *Metall. Trans. A*, 1982, vol. 13A, pp. 1233-38.
18. W. Roberts, H. Boden, and B. Ahlblom: *Met. Sci.*, 1979, Mar.-Apr., pp. 195-205.
19. M.J. White and W.S. Owen: *Metall. Trans. A*, 1980, vol. 11A, pp. 597-604.
20. J.J. McQueen, G. Gurewitz, and S. Fulop: *High Temp. Technol.*, 1983, Feb., pp. 131-38.
21. L.A. Norstrom: *Scand. J. Metall.*, 1977, vol. 6, pp. 269-276.
22. N. Cederblad and N.J. Grant: *Metall. Trans. A*, 1975, vol. 6A, pp. 1547-52.
23. W. Roberts and B. Ahlblom: *Acta Metall.*, 1978, vol. 26, pp. 801-13.
24. H.J. McQueen: *Metall. Trans. A*, 1977, vol. 8A, pp. 807-24.
25. A. Laasraoui and J.J. Jonas: *Metall. Trans. A*, 1991, vol. 22A, pp. 151-60.
26. A. Laasraoui and J.J. Jonas: *Metall. Trans. A*, 1991, vol. 22A, pp. 1545-58.
27. P. Dadras and J.F. Thomas, Jr.: *Metall. Trans. A*, 1981, vol. 12A, pp. 1867-73.
28. P.L. Charpentier, B.C. Stone, S.C. Ernst, and J.F. Thomas, Jr.: *Metall. Trans. A*, 1986, vol. 17A, pp. 2227-37.
29. J.F. Thomas, Jr. and R. Srinivasan: in *Computer Simulation in Materials Science*, R.J. Arsenault, J.R. Beeler, Jr., and D.M. Esterling, eds., ASM INTERNATIONAL, Metals Park, OH, 1988, pp. 269-90.
30. M.C. Mataya, E.L. Brown, and M.P. Riendeau: *Metall. Trans. A*, 1990, vol. 21A, pp. 1969-87.
31. P. Dadras: *J. Eng. Mater. Technol.*, 1985, vol. 107, pp. 97-100.
32. S.L. Semiatin and J.H. Holbrook: *Metall. Trans. A*, 1983, vol. 14A, pp. 1681-95.
33. M.C. Mataya and D.K. Matlock: in *Superalloy 718-Metallurgy and Applications*, E. Loria, ed., TMS, Warrendale, PA, 1989, pp. 155-78.
34. W. Reiss and K. Pohlandt: *Exp. Tech.*, 1986, Jan., pp. 20-24.
35. M.J. Weis: Master's Thesis, Colorado School of Mines, Golden, CO, 1987.
36. G.W. Rowe: *An Introduction to the Principles of Metalworking*, Edward Arnold, London, 1965, p. 245.
37. G.E. Dieter: *Mechanical Metallurgy*, 2nd ed., McGraw-Hill, Inc., New York, NY, 1976, pp. 72-102.
38. K.F. Kennedy and G.D. Lahoti: Battelle Columbus Laboratories, Columbus, OH, private communication, June 1981.
39. D.R. Barraclough and C.M. Sellars: *Met. Sci.*, 1979, Mar.–Apr., pp. 257-67.
40. H. Suzuki, Y. Hashizume, Y. Yabuki, Y. Ichihara, S. Nakajima, and K. Kenmochi: *Report of the Institute of Industrial Science of the University of Tokyo*, 1968, vol. 18 (3), pp. 1-102.
41. C.M. Sellars: *Proc. Conf. on Hot Working and Forming Processes*, Sheffield, July 1979, Metals Society, London, 1980, pp. 3-15.
42. J.J. Jonas and H.J. Mcqueen: *Treatise on Materials Science and Technology: Plastic Deformation of Materials*, R.J. Arsenault, ed., Academic Press, New York, NY, 1975, vol. 6, pp. 394-490.
43. C. Zener and J.H. Hollomon: *J. Appl. Phys.*, 1944, vol. 15, pp. 22-31.
44. O.D. Sherby and P.M. Burke: in *Progress in Materials Science*, B. Chalmers and W. Hume-Rothery, eds., Pergamon Press, London, 1968, vol. 13, pp. 325-53.
45. H. Luthy, A.K. Miller, and O.D. Sherby: *Acta Metall.*, 1980, vol. 28, pp. 169-78.
46. H.J. McQueen: *J. Met.*, 1968, Apr., pp. 31-38.
47. A.A. Afonja: *Mater. Sci. Eng.*, 1982, No. 54, pp. 257-63.

Microstructure Development during Conventional and Isothermal Hot Forging of a Near-Gamma Titanium Aluminide

S.L. SEMIATIN, V. SEETHARAMAN, and V.K. JAIN

The breakdown of the lamellar preform microstructure in the ingot metallurgy near-gamma titanium aluminide, Ti-45.5Al-2Cr-2Nb (atomic percent), was investigated. Microstructures developed during canned, conventional hot forging were compared to those from isothermal hot forging. The higher rate of deformation in conventional forging led to considerably finer and almost completely broken-down structures in the as-forged condition. Several nontraditional approaches, including the isothermal forging of a metastable microstructure (so-called "alpha forging") and the inclusion of a short static recrystallization anneal during forging, were found to produce a more fully broken-down structure in as-isothermally forged conditions. Despite the noticeable microstructure differences after forging, conventionally and isothermally forged material responded similarly during heat treatment. In both cases, almost totally recrystallized structures of either equiaxed gamma or transformed alpha grains surrounded by fine gamma grains were produced depending on the heat-treatment temperature. Metallography on forged and heat-treated pancake macroslices was useful in delineating small differences in composition not easily detected by analytical methods.

I. INTRODUCTION

THE expanding interest in intermetallic alloys has generated an acute appreciation of the relationship between processing and microstructure. Although these materials possess attractive high-temperature strength and creep properties, ambient-temperature ductility and toughness are often quite low and typically very sensitive to microstructure.[1,2] Prime examples of such behavior are found for alloys based on the face-centered tetragonal gamma phase of the titanium-aluminum system. So-called near-gamma titanium aluminides, which contain small to moderate amounts of the ordered hexagonal close-packed alpha-two phase, may exhibit a variety of microstructures, depending on the specific synthesis, deformation, and heat-treatment methods used in their manufacture. These structures range from those composed of a majority of equiaxed gamma grains to those consisting of fully transformed morphologies of lamellar alpha-two plus gamma phases. The former structure is usually more attractive from a processing standpoint in view of the fact that the latter structure, as well as various duplex (gamma grain-lamellar colony) structures, can be obtained from it *via* rather simple heat treatments.

Uniform, fine gamma grain microstructures in near-gamma titanium aluminides can be obtained *via* ingot metallurgy processing through a series of deformation and heat-treatment steps on cast or cast plus hot isostatic pressed ("hipped") material with a lamellar-starting microstructure. Typical deformation modes for breakdown of ingots include isothermal forging or canned, conventional hot extrusion.[3–6] Limited work has also been conducted to determine the feasibility of uncanned and canned conventional hot pancake forging.[3,7–9] Uncanned hot forging (with die temperatures around 260 °C) has been generally unsuccessful, resulting in gross fracture at low reductions.[3] More success has been achieved through canned hot pancake forging of cylindrical ingot mults.[7,8,9] For example, Wurzwallner and his co-workers[7,8,9] forged Ti-48Al-2Cr (atomic percent) ingots to approximately 70 pct reduction in a hydraulic press. After decanning, the pancakes revealed "flaky" and sporadically cracked plan surfaces, noticeable dead-metal zones at the center of the pancakes, and very nonuniform cross sections due to flow differences between the can and the titanium aluminide workpiece.

Deformation processes often produce partially recrystallized microstructures in cast or cast plus hipped near-gamma titanium aluminide ingot materials with lamellar starting structures. Stored work from such processes is often sufficient to effect more extensive *static* recrystallization and globularization. However, the uniformity of microstructure in wrought and recrystallization-annealed materials is strongly influenced by the presence of prior-interdendritic, single-phase gamma grain regions produced during ingot solidification. Such regions result from the double-cascading peritectic reactions that characterize the titanium-aluminum-phase diagram[10] and are often found in binary and multicomponent near-gamma alloys containing more than approximately 46 at. pct aluminum. Semiatin, and co-workers[11–14] have established the kinetics of homogenization heat treatments to eliminate such nonuniformities that result in banded microstructures in wrought products.

The objective of the present investigation was to establish the development of microstructure during

S.L. SEMIATIN, Senior Scientist, is with the Metals and Ceramics Division, WL/MLLN, Wright Laboratory Materials Directorate, Wright-Patterson Air Force Base, OH 45433. V. SEETHARAMAN, Senior Scientist, is with UES, Inc., Dayton, OH 45432. V.K. JAIN, Professor, is with the Mechanical and Aerospace Engineering Department, University of Dayton, Dayton, OH 45469.

Manuscript submitted September 16, 1993.

breakdown processing of a typical ingot metallurgy, near-gamma titanium aluminide, Ti-45.5Al-2Cr-2Nb. To this end, various isothermal and conventional hot-forging processes were designed and conducted. Microstructures developed in conventional hot forging were interpreted in terms of a simple, one-dimensional heat-transfer analysis that incorporates temperature transient effects during transfer of the canned workpiece from the furnace to the dies as well as during forging. The effects of processing method, process variables, and macrosegregation on microstructure and microstructure uniformity were determined.

II. MATERIALS AND PROCEDURES

A. *Materials*

The material used in the present investigation was the near-gamma titanium aluminide, Ti-45.5Al-2Cr-2Nb. The measured composition of the major alloying elements in this material was 45.45 aluminum, 2.20 chromium, and 2.08 niobium (atomic percent). Interstitial levels (in parts per million by weight (ppmw)) were 590 oxygen, 160 carbon, 118 nitrogen, and 15 hydrogen. The material was received from Duriron Company (Dayton, OH) as induction skull melted ingots measuring 70-mm diameter × 860-mm length. After casting, the ingots were hipped at 1260 °C/175 MPa for 4 hours to seal residual casting porosity. The cast plus hipped microstructure was nearly fully lamellar (alpha-two and gamma plates) with a prior-alpha grain size of approximately 200 μm (Figure 1). In addition, there was a very small percentage of equiaxed gamma phase ($\leq$5 pct), which probably evolved from small interdendritic gamma regions. This small amount of single-phase gamma was expected for a near-gamma titanium aluminide of the aforementioned aluminum content.[11]

The alpha transus temperature (temperature at which alpha + gamma → alpha) of the program material was determined to be 1300 °C through a series of heat treatments followed by optical metallography.

B. *Isothermal Forging Procedures*

Isothermal forge processing was conducted at Cameron Forge Division of Cooper Industries (Houston, TX). Cylindrical preforms measuring 66 mm in diameter × 76 mm in length were electric-discharge machined from the as-received ingots. After breaking the corners on both ends of each preform, the samples were spray coated with boron nitride, air dried, and then preheated in an indirect electric resistance furnace at 1150 °C for 2 hours. After preheating, the samples were transferred to a 22 MN Bliss hydraulic press and placed onto TZM molybdenum dies heated to the same temperature. This temperature is as high as the TZM molybdenum die material can withstand without suffering excessive die wear or creep deformation. After equilibration of the sample and die stack temperatures, pancake forging to a final reduction of 6:1 (effective height strain of 1.8) was conducted under constant crosshead velocity conditions, which yielded a nominal (initial) strain rate of 0.0015 s^{-1}. Following forging, the samples were removed from the dies and cooled slowly in vermiculite.



Fig. 1—Polarized light, optical microstructure of the as-received, cast + hipped Ti-45.5Al-2Cr-2Nb (atomic percent) program alloy. Ingot axis is vertical.

Selected additional isothermal forging trials were conducted using somewhat modified practices. The first of these comprised an identical preheat and deformation sequence as mentioned earlier, except for the incorporation of a 15-minute static dwell (at the prescribed forging temperature) after an initial reduction of 2:1 (effective height strain of 0.69). The purpose of this procedure was to determine whether a short intermediate static heat treatment could be used to enhance the breakdown and recrystallization of the lamellar microstructure. The second set of modified trials had a similar objective. In this case, the ability to obtain a refined as-forged microstructure through an "alpha-forge" type of approach was utilized. This method is analogous to ausforming of steels in which fine microstructures are obtained by deformation of a metastable austenite phase.[15] For the near-gamma titanium aluminide, alpha-forging consisted of a furnace preheat at T = 1260 °C (a temperature high in the alpha plus gamma phase field), followed by cooling to a forging temperature of 1150 °C, and forging to a 6:1 reduction. The time required to cool the billet and commence forging was approximately 60 seconds. The press speed was the same as for the other isothermal forging trials, except for the initial 2:1 reduction, which was conducted at a ram speed approximately one hundred times faster.

The forged pancakes were sectioned diametrically, ground, and polished for optical metallographic examination under polarized light and for backscattered electron imaging in a Leica 360 scanning electron

microscope (SEM). In addition, metallographic examination of isothermally forged pancakes, which were given a subsequent heat treatment for 2 or 8 hours at 1200 °C or 1260 °C, was conducted. Selected forged and heat-treated samples were also subjected to wavelength dispersive spectroscopy (WDS) in a JEOL* 733 electron microprobe to determine the composition of the various microconstituents and thus establish a portion of the Ti-Al pseudobinary phase diagram for near-gamma titanium aluminides containing 2 at. pct Cr and 2 at. pct Nb.

*JEOL is a trademark of Japan Electron Optics Ltd., Tokyo, Japan.

C. *Conventional Forging Procedures*

Conventional, hot forging was conducted in the Experimental Materials Processing Laboratory of the Wright Laboratory Materials Directorate (Wright Patterson AFB, OH). The objective of these trials was to determine the feasibility of using near-conventional techniques to produce sound material during ingot breakdown and to compare microstructures developed *via* such processing to those produced during isothermal forging. For this purpose, cylindrical preforms measuring 60 mm in diameter × 86 mm in length were electric-discharge machined from the as-received Duriron ingots and encapsulated in AISI type 304 stainless steel cans consisting of a welded assembly of a lateral tubular component and two end caps. Various types of proprietary methods were used to insulate the near-gamma type aluminide billets from the stainless steel cans to minimize heat losses during forging. Moreover, using information obtained from finite element method simulations of the conventional forging process, several different can geometries were utilized. The can geometry was found to strongly affect the uniformity of flow of the near-gamma preform relative to that of the stainless steel, with rather subtle changes in geometry (and process variables) leading to noticeable differences in metal flow. This aspect of the forging process design is discussed at length in Reference 16. Suffice it to say, however, that much improved forging performance with respect to pancake cross-section shape, microstructure uniformity, and the avoidance of defects was obtained using optimized can design.

The canned Ti-45.5Al-2Cr-2Nb preforms were coated with Deltaglaze 69 glass (manufactured by Acheson Colloids Corporation, Port Huron, MI) and preheated in an electric resistance furnace using a cycle consisting of 925 °C for 30 minutes followed by a 1-hour heating in a furnace operating at the nominal forging temperature. The nominal forging temperatures were 1150 °C, 1200 °C, and 1250 °C. The lower temperature was identical to that used in the isothermal forging trials; the two higher temperatures corresponded to the middle and high end, respectively, of the alpha plus gamma phase field. Following preheating, the "controlled-dwell" technique[17] was used to develop a temperature difference between the stainless steel can and the near-gamma titanium aluminide preform within it just prior to forging. By this means, the flow stresses of the two materials were almost matched, and deformation uniformity was enhanced. In the present trials, the dwell period between the removal of the billet from the furnace and the commencement of forging was approximately 40 seconds.

The samples were pancake forged in a 9 MN Erie hydraulic press between unheated, flat tool steel dies lubricated with molybdenum disulfide (Fel-Pro C-300, manufactured by Fel-Pro Chemical Corporation, Skokie, IL). The ram speed was 25 mm/s, corresponding to effective strain rates of approximately 0.25 s^{-1} at the beginning of the stroke and slightly greater than 1 s^{-1} at the end of the imposed reduction of 6:1. An attempt to forge an *uncanned* preform, preheated at 1250 °C and forged without a dwell period under identical conditions of ram speed and total reduction, led to severe cracking.

Following the deformation, the forgings were immediately removed from the dies and slow cooled to room temperature by immersing them in silicel. Metallography was conducted on the as-forged samples as well as after a 2-hour treatment at 1200 °C or 1260 °C following decanning; decanning was greatly simplified through the use of the insulation/parting agent between the preform and the can. The volume fraction and size of gamma and prior-alpha grains in selected samples heat-treated at 1260 °C were determined *via* point counting and linear intercept methods, respectively.

D. *Temperature Transient Model for Conventional Forging*

Because of the non-steady-state nature of the temperature fields characterizing the canned, conventional forging process used here, a one-dimensional finite difference model was developed and applied to predict the axial temperature transients and their possible impact on microstructure development during this operation. The temperature transients during the transfer stage/dwell period and during the forging stroke were treated separately. In each case, the temperature field was assumed to be symmetric about the midheight. The approach used here was very similar to that described by Semiatin and his co-workers for conventional pack rolling[18] and bare rolling[19] of plate and sheet and, thus, will be only briefly summarized.

For the workpiece transfer/dwell stage, the one-dimensional heat-transfer equation was solved to obtain the temperature T as a function of time t and axial position z:

$$dT/dt = k_d(d^2T/dz^2) \qquad [1]$$

where k_d denotes the thermal diffusivity. At time $t = 0$, the temperature was assumed to be uniform throughout the can and preform and equal to the furnace temperature. Boundary conditions consisted of the rate of heat loss per unit area, q_r, from the free surface of the can and the rate of conduction heat transfer per unit area, q_c, across the preform-can interface. Because of the high furnace temperatures, the former flux was assumed to be controlled solely by radiation effects:

$$q_r = eB(T_s^4 - T_a^4) \qquad [2]$$

where $e \equiv$ emissivity of the stainless steel can, $B \equiv$ Stefan-Boltzmann constant, and T_s and $T_a \equiv$ can surface temperature and ambient temperature, respectively, both

on the absolute scale. The interface heat transfer was described using the following expression:

$$q_c = h(T_{g_i} - T_{ss_i}) \quad [3]$$

where $h \equiv$ interface heat-transfer coefficient and T_{g_i} and T_{ss_i} denote the temperatures of the near-gamma titanium aluminide preform and the stainless steel can, respectively, on either side of the interface. The finite difference formulation and solution of Eq. [1] and the accompanying boundary conditions, Eqs. [2] and [3], are discussed in References 18 through 20.

An alternate approach to the one-dimensional heat-transfer solution was also investigated for the transfer/dwell stage. This involved a so-called "lumped-parameter" method and was used to estimate the effects of axial and radial heat losses from the cylindrical billet on the temperature transients. The inclusion of radial heat losses gives temperature predictions that are lower than those from the simple one-dimensional analysis. In the lumped-parameter technique, the temperatures within the stainless steel can and the near-gamma titanium aluminide preform are each assumed to be uniform. Relations analogous to Eqs. [2] and [3], in which the total heat flux from the entire surface of the can periphery (Q_r) or from the entire interface area between the can and preform (Q_c), were used in conjunction with the following expressions:

$$\Delta T_{ss}/\Delta t = -(Q_r - Q_c)/m_s c_s \quad [4a]$$

and

$$\Delta T_g/\Delta t = -Q_c/m_g c_g \quad [4b]$$

Here, m and c denote the mass and specific heat, respectively, of the stainless steel (subscript ss) and gamma (subscript g) components.

The one-dimensional heat conduction equation (in finite difference form) was used to analyze the temperature transients during the forging stroke; because of the high strain rate and short duration of this stage, the majority of the heat flow is axial. A term to account for deformation heating was included in Eq. [1] to yield the following:

$$dT/dt = k_d(d^2T/dz^2) + \bar{\sigma}\dot{\bar{\varepsilon}}/\rho c \quad [5]$$

where $\bar{\sigma} \equiv$ effective flow stress, $\dot{\bar{\varepsilon}} \equiv$ effective strain rate, and $\rho \equiv$ density. As an approximation, the deformation (axial strain rate) was assumed to be uniform throughout the can and the preform, and thus, $\dot{\bar{\varepsilon}}$ was estimated from $\dot{\bar{\varepsilon}} = V/H$, where V and H denote the ram speed and instantaneous billet height, respectively.*

*More detailed finite element method simulations of the conventional forging process[21] reveal that the effective strain and strain rate within the titanium aluminide preform vary by approximately ±15 pct from the average values during forging. Such variations give rise to approximately ±15 °C variations in the magnitude of the deformation heating-induced temperature rise. Such variations are very small compared to the temperature transients due to heat conduction, which are discussed in Section III.

Flow stress values [$\bar{\sigma} = \bar{\sigma}(\bar{\varepsilon}, \dot{\bar{\varepsilon}}, T)$] for the can and workpiece materials were obtained from References 22 and 23. Initial conditions for the simulation of the temperature transients during forging consisted of the final temperature field calculated from the transfer/dwell stage. The boundary conditions were specified using Eq. [3] for the can-preform interface and a similar expression for the can-die interface.

The myriad of thermophysical property data required for the simulations (Table I) was obtained by either direct measurements conducted by the Thermophysical Properties Research Laboratory of Purdue University (for the near-gamma titanium aluminide) or from the literature[24–27] (data for stainless steel, tool steel, and the heat-transfer coefficients). In particular, values for the interface heat-transfer coefficients in Table I were selected to correspond to the specific interface layers and pressure conditions that pertain to the present work. In addition, a limited number of experiments involving heating and cooling of thermocoupled samples were also conducted to estimate the emissivity values for glass-coated 304 stainless steel.

III. RESULTS AND DISCUSSIONS

A. *As-Forged Visual Observations and Macrostructures*

Both isothermal and canned conventional forging experiments were successful in producing sound products. The only defects found in the isothermal forgings were shallow cracks on the lateral free surfaces, which presumably resulted from workpiece barreling and the generation of secondary tensile stresses. Similar lateral free surface cracks were found in the decanned conventionally forged samples (Figures 2(a) through (c)). The severity of these cracks decreased with increasing preheat temperature. Examination of the top and bottom surfaces of the decanned samples revealed material that was smooth and essentially defect-free, except for a small circular ridge corresponding to the original preform

Table I. Thermophysical Property Data Used to Model Temperature Transients during Conventional Forging*

Ti-45.5Al-2Cr-2Nb (preform)
Thermal diffusivity, k_d (mm²/s) = −0.00489 T (°C) + 11.25
Thermal conductivity, K (W/m °C) = 0.0108 T (°C) + 34.12
Density, ρ (g/cm³) = 3.90
304 stainless steel (can)
Thermal diffusivity, k_d (mm²/s) = −0.00163 T (°C) + 3.75
Thermal conductivity, K (W/m °C) = 0.0157 T (°C) + 14.11
Density, ρ (g/cm³) = 7.43
Emissivity, e = 0.65
H13 tool steel (dies)
Thermal diffusivity, k_d (mm²/s) = 6.0
Thermal conductivity, K (W/m °C) = 24.49
Heat-Transfer coefficients, h
Preform—can during transfer stage, h (kW/m² °C) = 0.50
Preform—can during forging, h (kW/m² °C) = 5.00
Can—die during forging, h (kW/m² °C) = 20.0

*Note that $c = K/\rho k_d$

corner, at which edge folding had occurred within the can. The high localized strains here gave rise to cracking, but these flaws were also essentially superficial. Unlike previous attempts to conventionally forge near-gamma titanium aluminides,[8,9] no major fractures or flaky surfaces were generated with the present canning and forging techniques.

Macrostructures for both the isothermally and conventionally forged pancakes were also relatively uniform. Relatively small "dead-metal" zones were noted in the isothermally forged samples (Figure 3). The sample that was given an intermediate 15-minute recrystallization dwell (Figure 3(b)) showed essentially uniform deformation. Judging by the slight asymmetry in the pancake cross-section shape, the isothermal forging done without the intermediate dwell (Figure 3(a)) developed a small region of lower deformation against the lower die due to a die temperature that was probably slightly lower on the bottom *vs* that of the top die. The alpa-forged sample (Figure 3(c)) also showed a small dead-metal zone; in this case, it was on the top of the forging.

The macrostructures of the conventionally forged samples also tended to show small dead-metal zones (Figure 4) with otherwise relatively uniform flow. In most cases, the dead-metal zones were noticed on the bottom surface of the preform, which most likely resulted from small axial temperature nonuniformities arising from chilling of the bottom when the canned preform was placed on the bottom die just prior to the forging operation. Such a top-to-bottom temperature nonuniformity is also suggested by the slightly greater amount of edge folding on the bottom of the preforms as compared to that of the top surfaces. (The degree of edge folding is ascertained in Figure 4 by noting the position of the pointed "ridges" on each surface, which, as mentioned earlier in this section correspond to the material elements originally located at the preform corners.) As will be discussed in Section III–B, axial temperature nonuniformities generated within the preform during forging were concluded to play an important role, in addition to die-workpiece friction, in controlling the overall amount of edge folding.

In view of the fact that the titanium aluminide was forged within a stainless steel can of significantly different flow properties, the degree of pancake thickness and macrostructure uniformity in Figure 4 is quite pleasing, despite the axial temperature nonuniformities generated during forging. The use of process modeling techniques to design the can and select forging parameters (*e.g.*, dwell time after removing the billet from the furnace prior to forging) is thus justified. Other trials with nonoptimal can designs[16] led to nonuniform flow of the preform relative to the can and resulted in very nonuniform thickness of the pancakes, an effect that can be noted in the observations of Wurzwallner *et al.*[8]

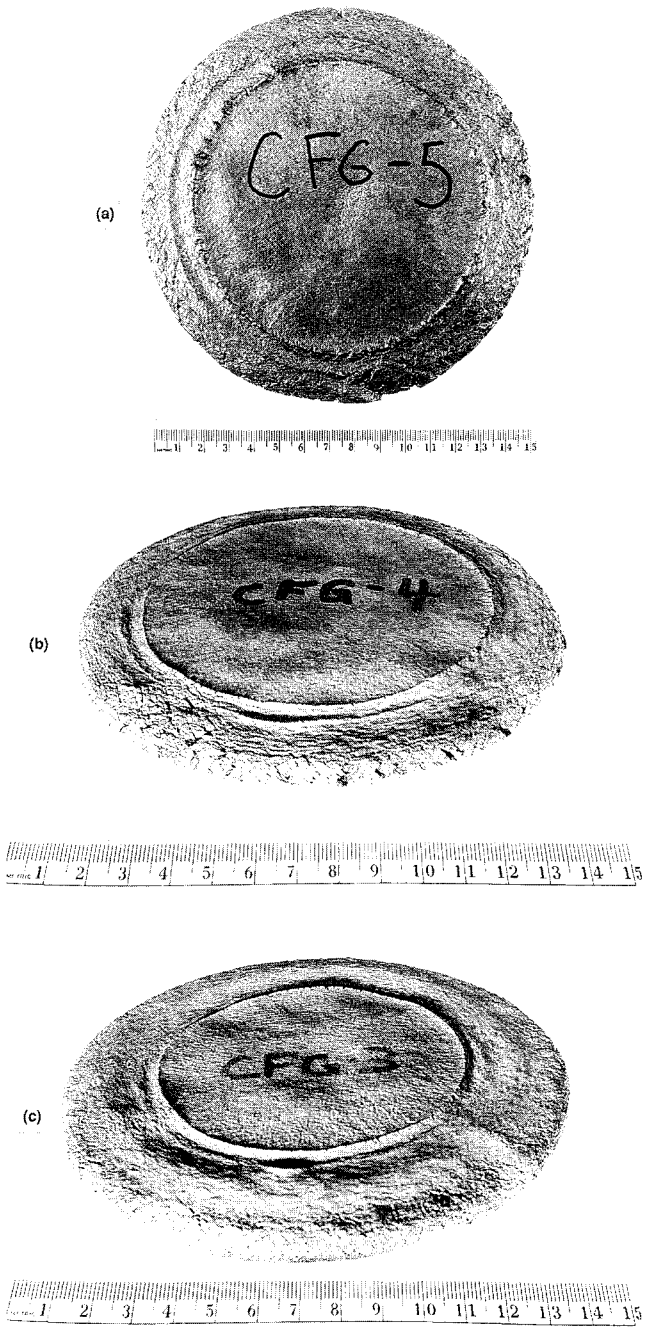


Fig. 2—Macrographs of conventionally forged and decanned pancakes. Nominal (furnace) temperatures were as follows: (*a*) 1150 °C, (*b*) 1200 °C, and (*c*) 1250 °C.

B. *As-Forged Microstructures*

The Ti-45.5Al-2Cr-2Nb alloy exhibited a wide range of as-forged microstructures depending principally on ram velocity and forging temperature. Figure 5 summarizes the microstructures from a pancake isothermally forged at 1150 °C in a single stroke. Micrographs from midplane regions at both the center ($r = 0$) and edge ($r = R$) of the pancake show a structure comprising approximately one-half dynamically recrystallized grains and one-half deformed lamellar constituent. The recrystallized grains are located at the prior-alpha grain boundaries[14] or regions of locally higher strain for this strain-rate regime. In the dead-metal zone near the axis at the bottom of the pancake, the percentage of recrystallized microstructure is substantially less (Figure 5(c)), although the remnant lamellae appeared to have suffered noticeable deformation even here.

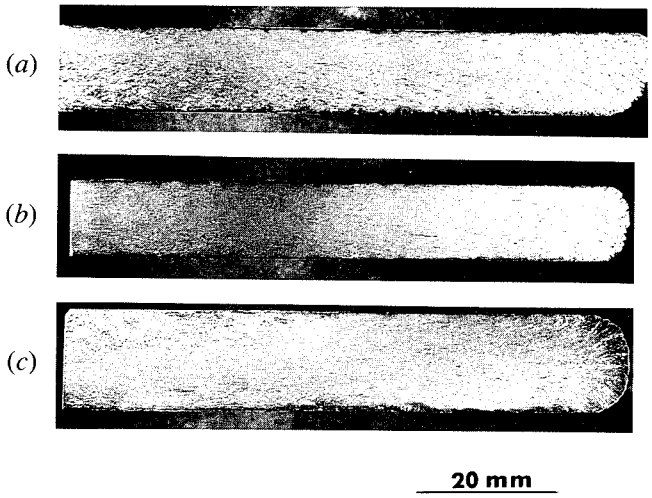


Fig. 3—Macrographs of cross sections of as-isothermally forged pancakes. Forging temperature was 1150 °C, and reduction was 6:1 in all cases. Forging practices comprised the following: (*a*) standard (uninterrupted) isothermal forging, (*b*) forged with a 15-min dwell at temperature after the initial 2:1 reduction, and (*c*) processed using an alpha-forge approach.

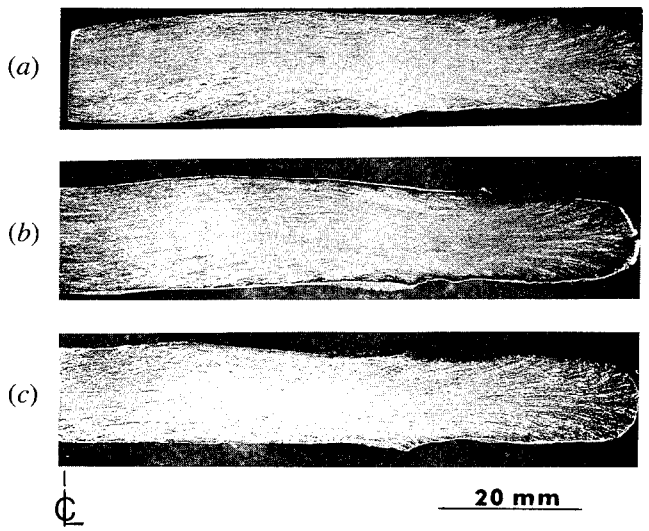


Fig. 4—Macrographs of cross sections of as-conventionally forgec pancakes. Nominal (furnace) temperatures were (*a*) 1150 °C, (*b*) 1200 °C, and (*c*) 1250 °C.

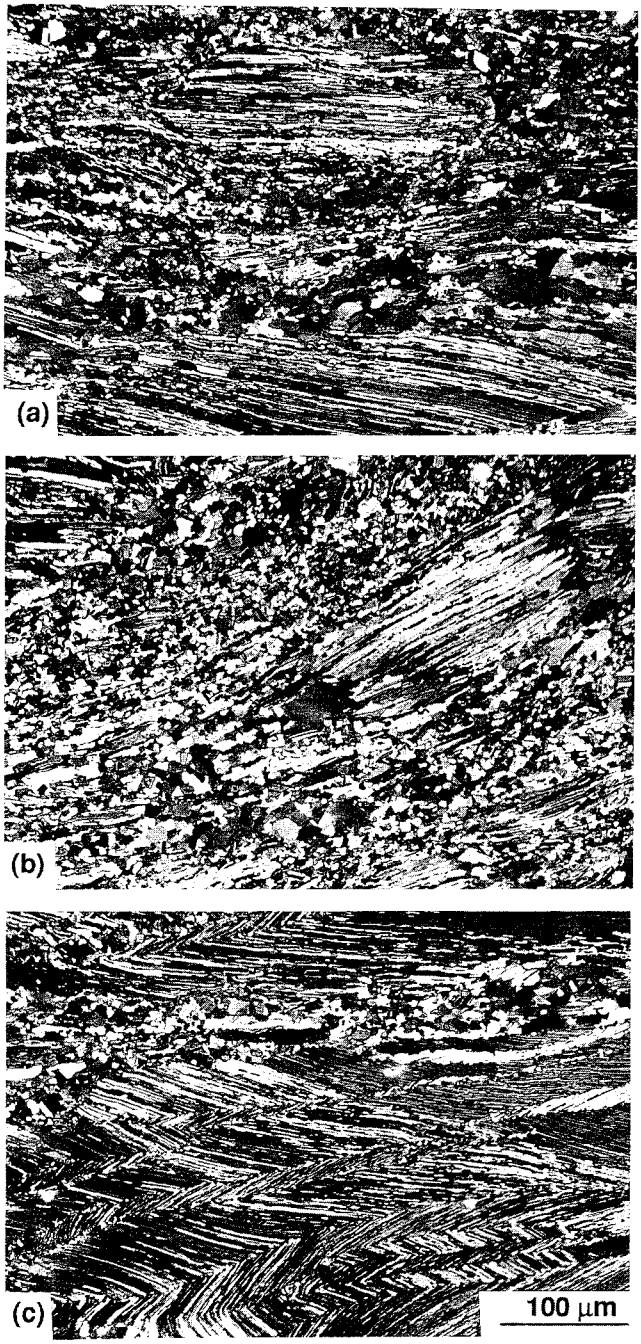


Fig. 5—Polarized light, optical microstructures developed during isothermal pancake forging at 1150 °C using standard practices. Micrographs were shot at the following locations in the pancake: (*a*) center (r = 0), midplane; (*b*) outer diameter, midplane; and (*c*) center (r = 0), bottom. The forging direction is vertical, and the radial direction is horizontal in all micrographs.

Pancakes that were isothermally forged using nonstandard practices exhibit somewhat different microstructures, typical examples of which are shown in Figure 6. The pancake isothermally forged to a 6:1 reduction with a 15-minute recrystallization dwell period after the first 2:1 reduction (Figure 6(a)) had a noticeably larger volume percent of recrystallized material and, hence, a smaller amount of deformed lamellar structure than the pancake forged in a continuous stroke (Figure 5). Similarly, the pancake that was subjected to the alpha-forge approach has a microstructure that is almost totally dynamically recrystallized (Figure 6(b)). The more complete dynamic recrystallization obtained *via* the nonstandard processes is further highlighted in backscattered micrographs (Figure 7) that reveal the various phases through atomic number contrast. In these and subsequent backscattered micrographs, the dark phase is gamma (lowest atomic number), the gray phase is alpha-two, and the small amount of white phase is beta (highest atomic number, being enriched in chromium and niobium). Both micrographs in Figure 7 show a very high percentage of gamma phase, as expected since the forging temperature was close to the eutectoid temperature at which the equilibrium volume fraction of gamma is greatest. The large amounts of the gamma phase that are in the form of recrystallized equiaxed

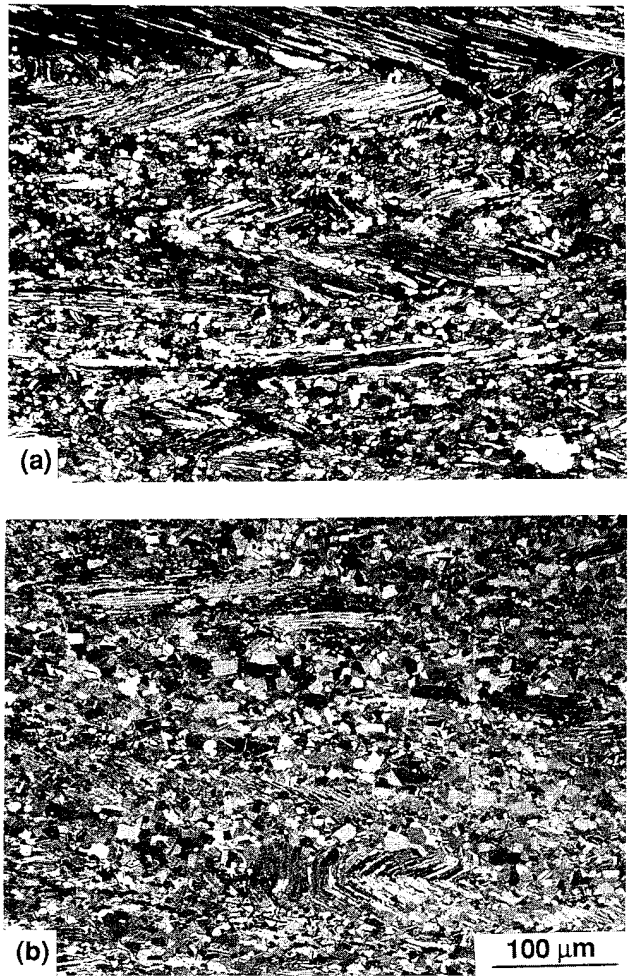


Fig. 6—Polarized light, optical microstructures developed during isothermal pancake forging at 1150 °C using modified practices: (*a*) forged with a 15-min dwell at temperature after the initial 2:1 reduction and (*b*) processed using an alpha-forge approach. Both micrographs were shot at the center ($r = 0$), midplane location of the respective pancakes. The forging direction is vertical, and the radial direction is horizontal in both micrographs.

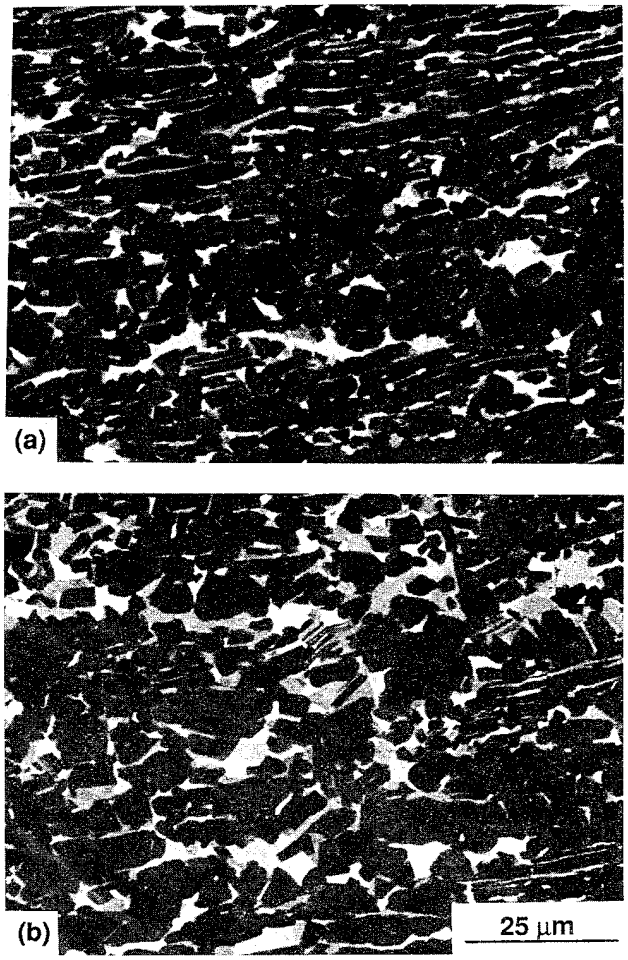


Fig. 7—Backscattered (SEM) micrographs of the structure developed during isothermal pancake forging at 1150 °C using modified practices: (*a*) forged with a 15-min dwell at temperature after the initial 2:1 reduction and (*b*) processed using an alpha-forge approach. Both micrographs were shot at the center ($r = 0$), midplane location of the respective pancakes. The forging direction is vertical, and the radial direction is horizontal in both micrographs.

grains are also evident in both cases. Furthermore, the remnant lamellar microstructure in the isothermal forging conducted with the intermediate 15-minute dwell (Figure 7(a)) appears to consist of short lengths that have started to pinch off. Thus, the modified practices have yielded microstructures that are more fully wrought than those in pancakes that were isothermally forged using standard practices.

The microstructures of the Ti-45.5Al-2Cr-2Nb alloy, which was conventionally forged, contrast to those from the isothermal forging trials. In general, these structures were much finer, were relatively uniform across the entire pancake, and revealed almost no evidence of large regions of unbroken-down lamellar structure. Typical micrographs at various locations in the pancake conventionally forged at a nominal temperature of 1150 °C are shown in Figure 8. Micrographs from the midplane, center ($r = 0$) region of pancakes forged at 1200 °C and 1250 °C are shown in Figure 9. Some of the details of these fine structures are more readily seen in higher magnification backscattered micrographs (Figure 10). The pancake forged at a furnace temperature of 1150 °C, or a temperature near the eutectoid temperature, has a structure in which gamma is the predominant phase; residual alpha-two plus gamma lamellae are either very fine and highly deformed or somewhat broken up (Figures 8 and 10 (a)). In the pancake forged at a nominal temperature of 1200 °C (Figures 9(a) and 10(b)), there are some small packets of unrecrystallized lamellar structure, but their extent and volume fraction is much smaller than those in the isothermally forged pancakes. Finally, the pancake forged at 1250 °C reveals a structure (Figures 9(b) and 10(c)) that is the most highly recrystallized and free of deformed lamellae. As the backscattered micrograph shows, there are some areas with a lamellar alpha-two plus gamma morphology, but the lack of deformation in these regions suggests that they were a transformation product of high-temperature alpha phase formed during the cooldown period after forging.

The higher degree of refinement and reduced amount of remnant lamellar microstructure in the conventionally

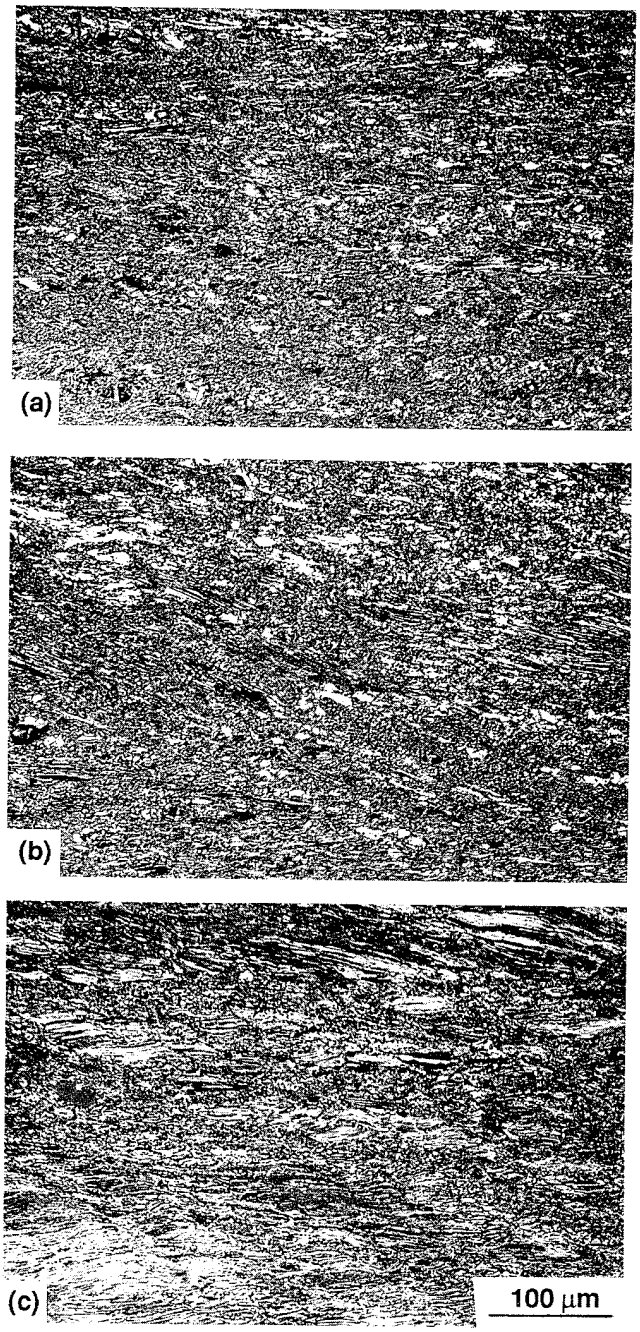


Fig. 8—Polarized light, optical microstructures developed during conventional pancake forging at a nominal (furnace) temperature of 1150 °C. Micrographs were shot at the following locations in the pancake: (*a*) center (r = 0), midplane; (*b*) outer diameter, midplane; and (*c*) center (r = 0), top. The forging direction is vertical, and the radial direction is horizontal in all micrographs.

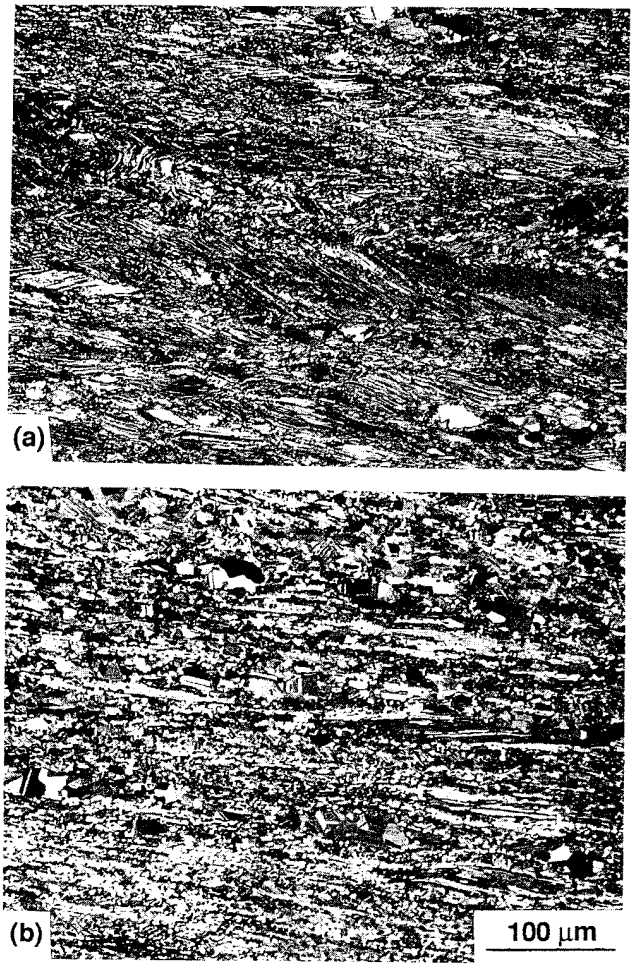


Fig. 9—Polarized light, optical microstructures developed in the center (r = 0), midplane region of pancakes conventionally forged at nominal (furnace) temperatures of (*a*) 1200 °C and (*b*) 1250 °C. The forging direction is vertical, and the radial direction is horizontal in both micrographs.

forged pancakes (particularly for conventional *vs* isothermal forgings done at the same temperature of 1150 °C) can be ascribed to the higher strain rates. Higher strain rates provide higher flow stresses and larger amounts of hot work. In addition, the amount of deformation taken up by grain boundary sliding (*vs* matrix flow) is lower at higher strain rates.[28] Thus, more work is put into the interior of the prior-alpha grains and is thus useful in breaking up the lamellar microstructure on a broader scale.

The microstructures in the conventionally forged pancakes can also be interpreted in terms of the temperature transients that pertain to the process. The predicted axial temperature fields just prior to forging (*i.e.*, after the transfer stage) and at the end of the forging stroke for a furnace temperature of 1150 °C are summarized in Figure 11. In these and other plots, temperature is plotted *vs* normalized axial position; positions of 0 and 1.0 correspond to the center of the preform and the top/bottom surface of the can, respectively. The results are for the two cases in which heat transfer prior to forging is assumed to be strictly axial (Figure 11(a)) or two dimensional (lumped-parameter solution, Figure 11(b)). The former solution shows that a rather small axial temperature nonuniformity is developed within the near-gamma titanium aluminide preform at the end of the billet transfer stage. Because of the one-dimensional nature of the solution, the average temperature in the preform is somewhat higher (1145 °C) than the temperature estimated from the lumped-parameter approach

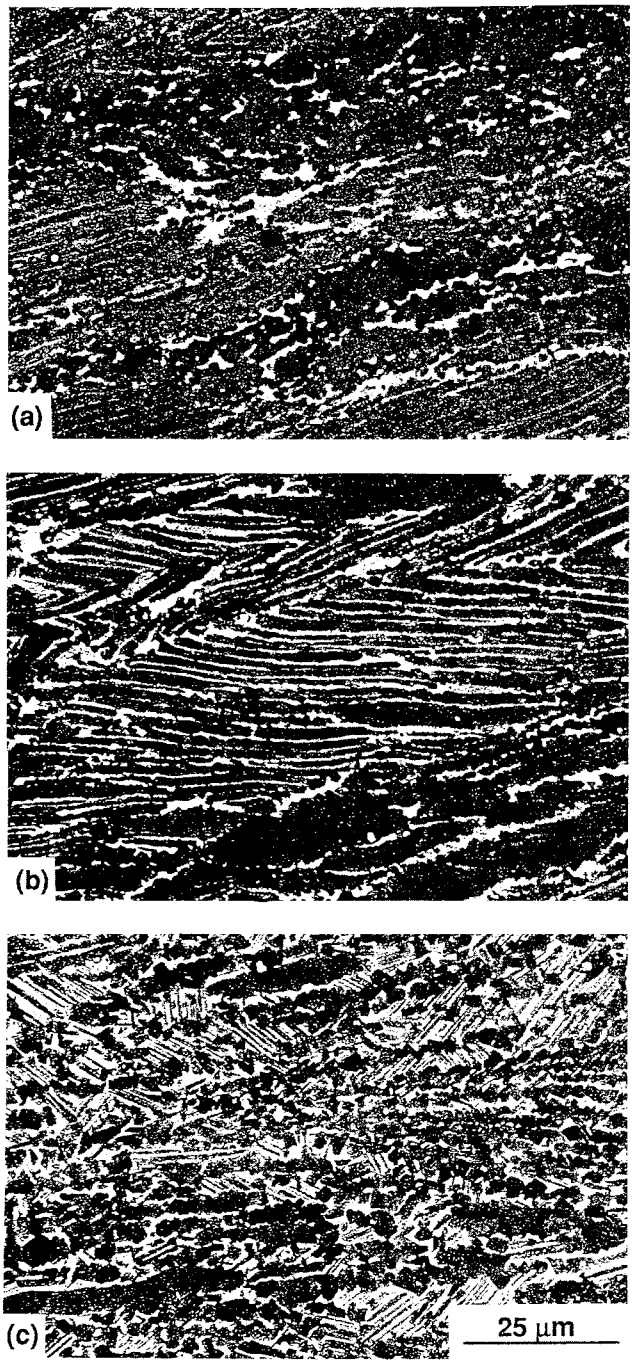


Fig. 10—Backscattered (SEM) micrographs of the structure developed in the center (r = 0), midplane region of pancakes conventionally forged at nominal (furnace) temperatures of (*a*) 1150 °C, (*b*) 1200 °C, and (*c*) 1250 °C. The forging direction is vertical, and the radial direction is horizontal in all micrographs.

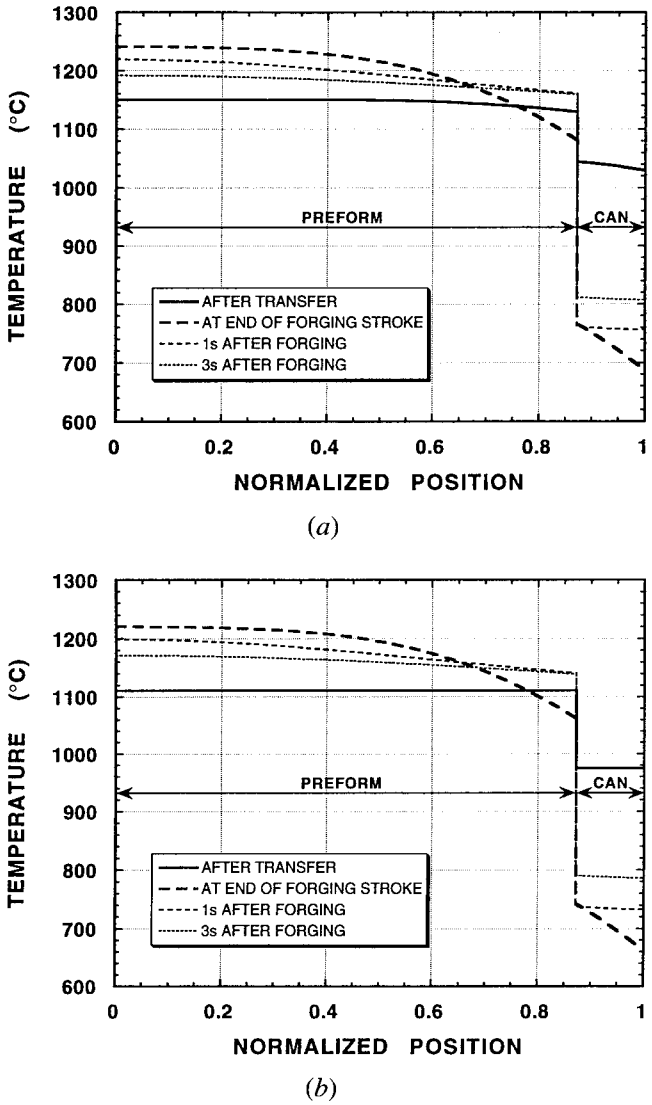


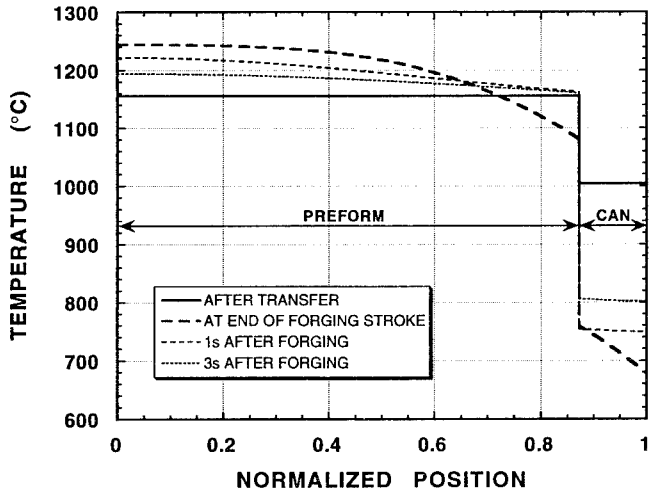
Fig. 11—Predicted axial temperature distribution developed after billet transfer, after conventional forging, and at several time increments after forging, assuming a nominal (furnace) temperature of 1150 °C. The temperature transient during the transfer period was estimated from (*a*) a one-dimensional finite difference approach or (*b*) a lumped-parameter approach.

(1110 °C). The relatively small temperature loss in the preform prior to forging predicted by both approaches contrasts to the much larger predicted temperature loss in the can (1150 °C → 980 °C to 1040 °C). At the conclusion of the forging stroke, both simulations predict noticeable temperature gradients in the preform, particularly near the preform-can interface. Moreover, in both cases, the predicted temperatures are almost identical despite the differences just prior to forging. This similarity can be ascribed to the higher flow stresses and hence levels of deformation heating encountered in the lumped-parameter solution, which had a lower initial preform temperature just prior to forging.

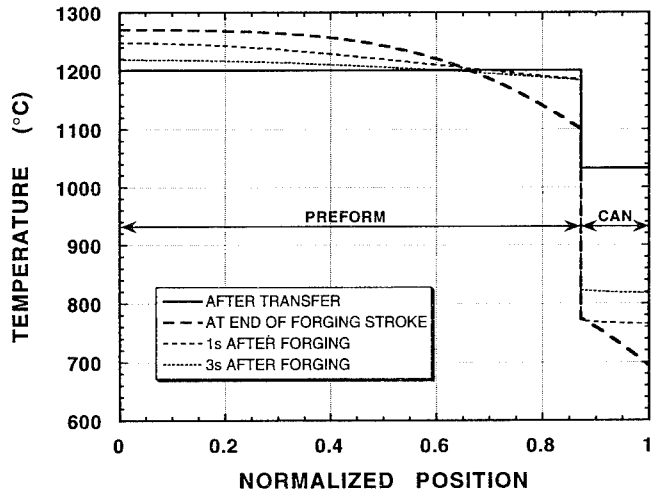
The temperature gradient developed in the preform during forging can be surmised to be one of the major causes for the observed edge folding and development of dead-metal zones shown in Figure 4. However, the simulations also reveal that the center two-thirds of the preform does maintain a relatively uniform temperature of approximately 1200 °C to 1220 °C, a temperature much below the transus temperature. This fact, coupled with the short duration of the temperature transient (simulation results such as those in Figure 11 reveal that the preform temperature gradient dampens out within several seconds after the end of the forging stroke), explains the observation of a relatively uniform microstructure,

which is predominantly gamma phase (Figures 8 and 10(a)).

Predicted temperature transients for conventional forging trials corresponding to furnace temperatures of 1200 °C and 1250 °C are summarized in Figure 12; in both cases, only the results based on the lumped-parameter solution for the billet transfer stage are given. The temperature predictions for the two higher furnace temperatures are similar to those for the 1150 °C case. Temperature losses in the preform at the end of the billet transfer stage are approximately 40 °C to 50 °C. Substantial temperature gradients are predicted to be developed in the preform during the forging stroke, but these are principally located at the preform-can interface, and their duration is small. The simulation results also demonstrate that the maximum preform temperature increase, relative to the nominal (furnace) temperature, is relatively small. The center of the preform preheated at 1200 °C experiences a temperature increase to 1240 °C (Figure 12(a)). Likewise, the preform preheated at 1250 °C experiences a short time transient at 1270 °C. This latter temperature is approximately 30 °C below the alpha transus, and it provides a plausible explanation for the small amount of undeformed lamellar microstructure but not for the complete transformation of the alpha phase during processing, as observed in the as-forged microstructure (Figure 10(c)).



(*a*)



(*b*)

Fig. 12—Predicted axial temperature distributions developed after billet transfer, after conventional forging, and at several time increments after forging, assuming a nominal (furnace) temperature of (*a*) 1200 °C or (*b*) 1250 °C. The temperature transient during the transfer period was estimated from a lumped-parameter approach.

C. *Forged and Heat-Treated Macrostructures*

Post forging heat treatment resulted in macrostructures that were more uniform than those observed in the as-forged conditions. The most noticeable effect was the reduction or almost total elimination of the dead-metal zones seen in the as-forged macrostructures. For example, the macrostructures of isothermally forged pancakes heat-treated for 2 hours at 1200 °C (Figure 13) were more uniform than their as-forged counterparts (Figure 3) for each of the three different isothermal forging approaches. A similar improvement was observed in the pancakes that were conventionally forged and then heat-treated for 2 hours at either 1200 °C or 1260 °C (Figure 14 *vs* Figure 4). From these results, it may be concluded that at least a modicum of deformation was imposed on the preform ends during both isothermal and conventional forging and that these regions really should not be considered dead-metal zones.

D. *Forged and Heat-Treated Microstructures*

Microstructures from forged and heat-treated pancakes revealed partial to full recrystallization, depending on forging method (isothermal vs conventional hot forging), heat-treatment time, and heat-treatment temperature. Microstructures developed in a pancake isothermally forged to a 6:1 reduction in a continuous stroke at 1150 °C and then heat-treated are summarized in Figures 15 (optical photographs) and 16 (backscattered photographs); in all cases, the microstructures were

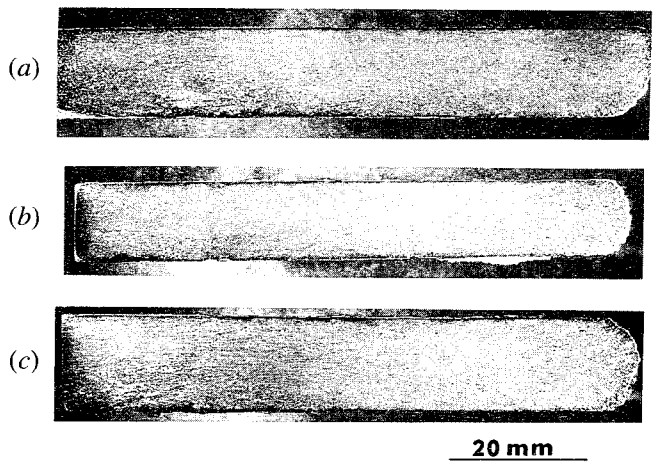


Fig. 13—Macrographs of cross sections of isothermally forged and heat-treated (1200 °C/2 h) pancakes. Forging temperature was 1150 °C, and reduction was 6:1 in all cases. Forging practices comprised the following: (*a*) standard (uninterrupted) isothermal forging, (*b*) forged with a 15-min dwell at temperature after the initial 2:1 reduction, and (*c*) processed using an alpha-forge approach.

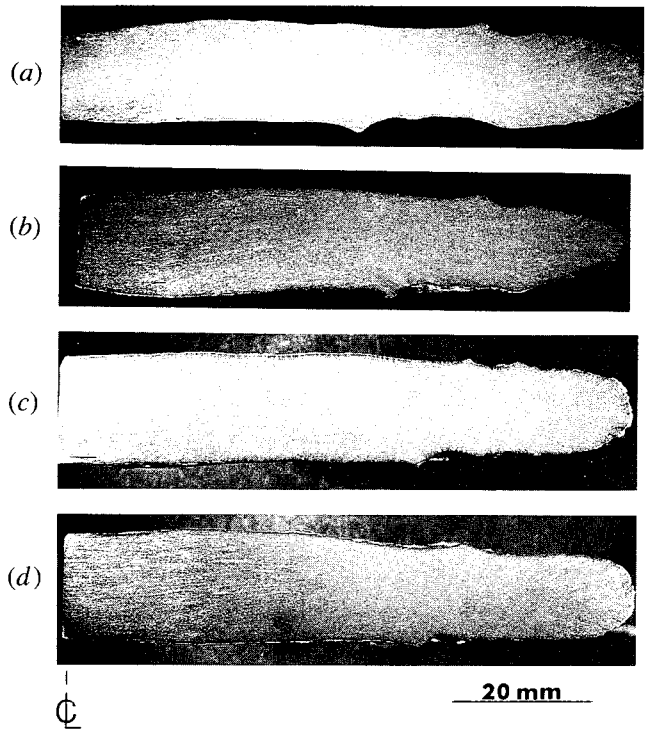


Fig. 14—Macrographs of cross sections of conventionally forged and heat-treated pancakes. Nominal (furnace) temperatures for forging and subsequent heat-treatment conditions were as follows: (*a*) 1150 °C, 1200 °C/2 h; (*b*) 1150 °C, 1260 °C/2 h; (*c*) 1200 °C, 1200 °C/2 h; and (*d*) 1200 °C, 1260 °C/2 h.

taken from the midheight location (*i.e.*, away from the dead-metal zone). After a 2 hour heat treatment at 1200 °C (Figures 15(a) and 16(a)), the structure is more than 80-pct recrystallized gamma grains (in a matrix of alpha-two and beta) or a level somewhat greater than in the as-forged condition (Figure 5). As seen in the back-scattered micrograph, the remnant lamellar structure actually consists of a number of short segments, which have started to breakup and globularize. After 8 hours at 1200 °C, the microstructure has not undergone much change. There is still a nonnegligible amount of unrecrystallized lamellar microstructure (Figures 15(b) and 16(b)). A similar resistance of the remnant lamellar structure to recrystallization during high-temperature heat treatment at 1260 °C was also noted (Figures 15(c) and 16(c)). The bulk of the recrystallized structure in this case, however, was found to be grains of partial-to-fully transformed alpha surrounded by globular gamma grains (Figure 16(c)) with no evidence of the beta phase. This reversal of the roles of the gamma and alpha-two/transformed alpha phases in going from 1200 °C to 1260 °C is as expected in view of the fact that the alpha transus temperature for this alloy is 1300 °C.

Microstructures developed in isothermally forged and heat-treated pancakes processed using the nonstandard isothermal forging approaches were similar to those just described, except for the limited extent of the remnant lamellar structure that was retained. Comparison photographs to those shown in Figures 15 and 16 for pancakes given the same heat treatments are given in Figure 17

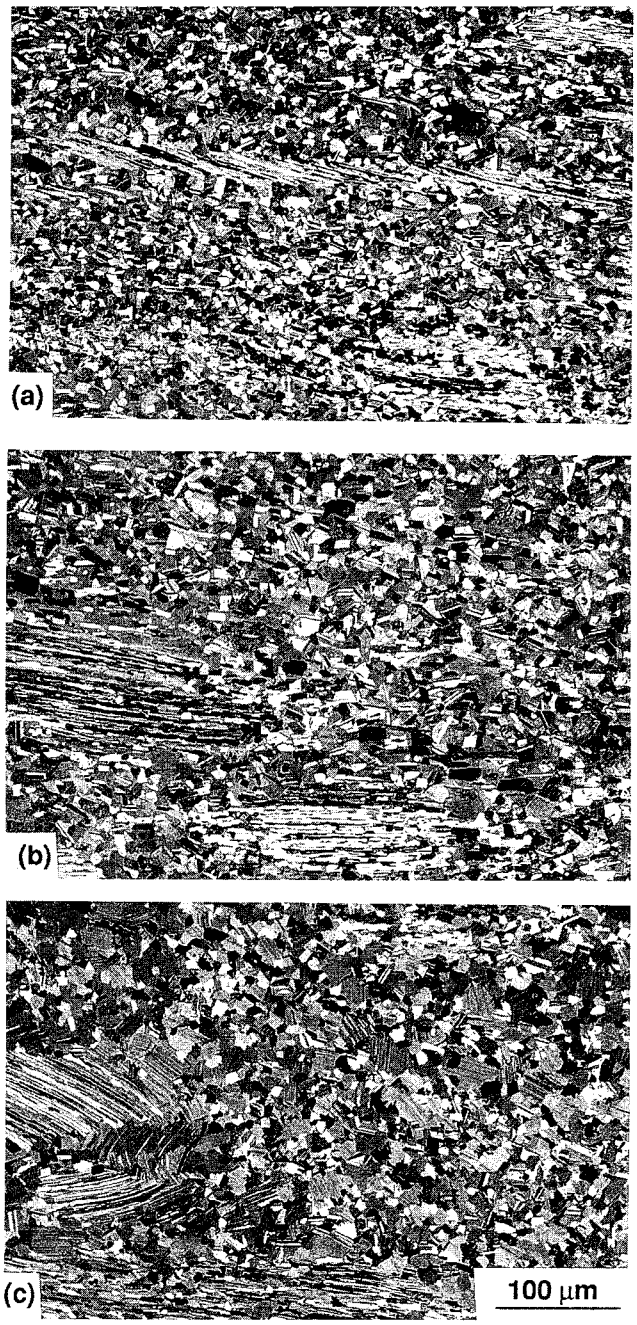


Fig. 15—Polarized light, optical microstructures developed after isothermal pancake forging at 1150 °C using standard practices and subsequent heat treatments of (*a*) 1200 °C/2 h, (*b*) 1200 °C/8 h, and (*c*) 1260 °C/2 h. All micrographs were shot at the center (r = 0), midplane location of the respective pancakes. The forging direction is vertical, and the radial direction is horizontal in all micrographs.

(isothermally forged at 1150 °C with a 15-minute intermediate recrystallization anneal) and Figure 18 (alpha-forge approach). The almost total recrystallization after 2 hours at 1200 °C and 1260 °C for both forging approaches (Figures 17(a) and (c) and 18(a) and (c)) contrasts to the microstructures in Figures 15(a), and (c). This is not surprising in view of the as-forged structures (Figures 6(a) and (b)), which were more fully recrystallized in the nonstandard approaches. It should also be noted that the 8-hour heat treatment at 1200 °C

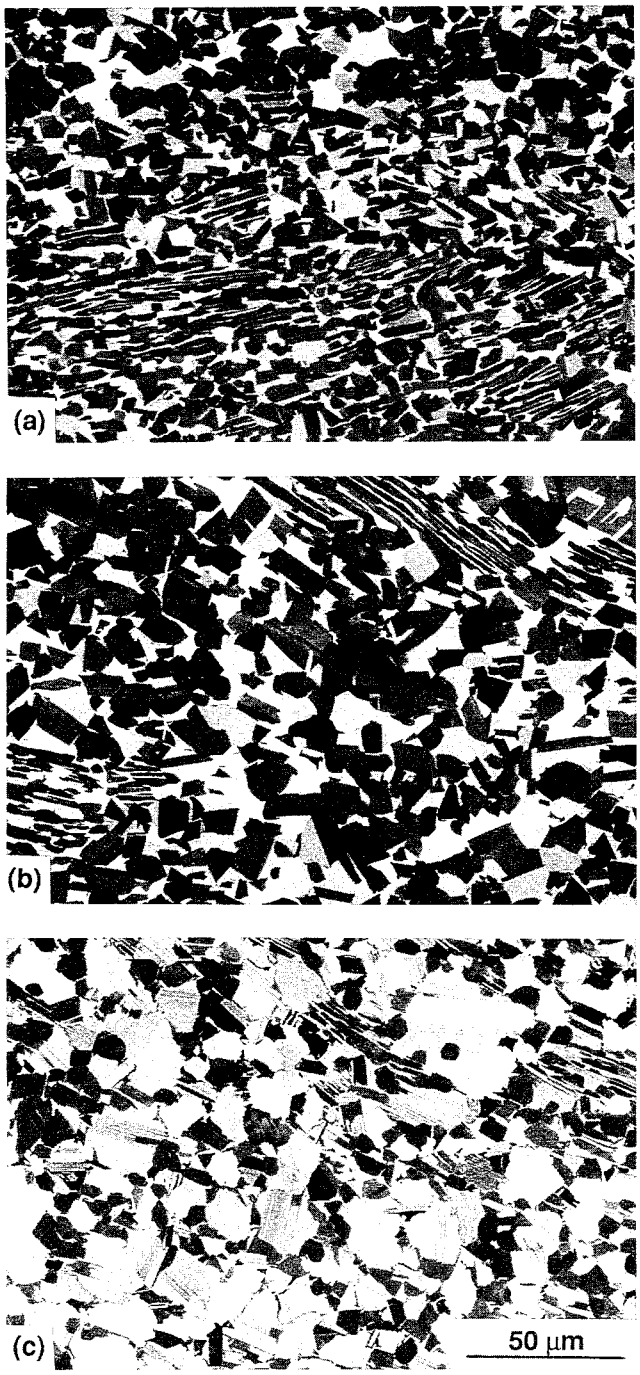


Fig. 16—Backscattered (SEM) micrographs of the structure developed in the center (r = 0), midplane region of pancakes isothermally forged at 1150 °C using standard practices and subsequently heat-treated at (*a*) 1200 °C for 2 h, (*b*) 1200 °C for 8 h, and (*c*) 1260 °C for 2 h. The forging direction is vertical, and the radial direction is horizontal in all micrographs.

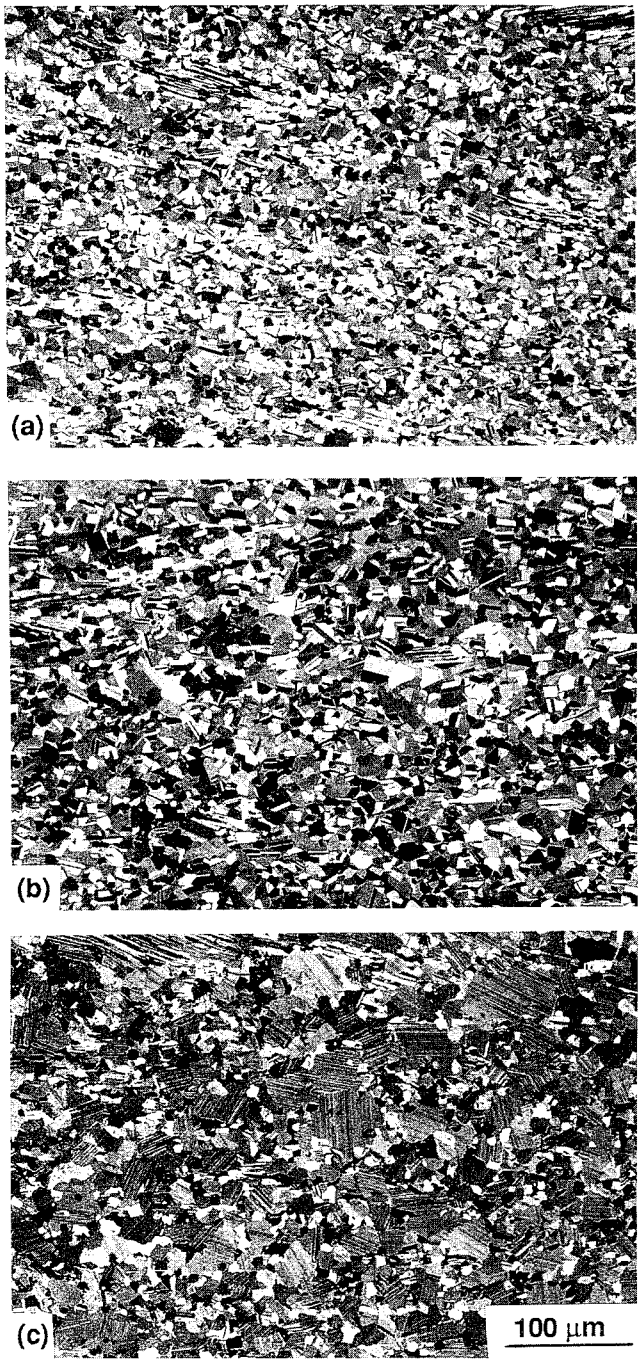


Fig. 17—Polarized light, optical microstructures developed in the center (r = 0), midplane region of pancakes isothermally forged at 1150 °C with an intermediate 15-min dwell at temperature after the initial 2:1 reduction and then heat-treated after forging at (*a*) 1200 °C for 2 h , (*b*) 1200 °C for 8 h, and (*c*) 1260 °C for 2 h. The forging direction is vertical, and the radial direction is horizontal in all micrographs.

yielded microstructures that were essentially 100 pct recrystallized, except for very small, sporadic patches of lamellar structure whose size was of the same order of magnitude as the gamma grain size. However, this longer-time heat treatment gave rise to a somewhat larger gamma grain size (~12 μm) compared to that after the 2-hour heat treatment at 1200 °C (~8 μm).

Microstructures developed in conventionally forged and heat-treated pancakes were similar to those in heat-treated pancakes that were isothermally forged using nonstandard practices. The pancake conventionally forged at a nominal (furnace) temperature of 1150 °C, or the same temperature used in isothermal forging, and heat-treated for 2 hours at 1200 °C revealed a fine, uniform recrystallized microstructure in all locations of the

cross-section (Figure 19). Only a small amount of unrecrystallized microstructure was found in the region of the dead-metal zones at the ends of the pancake (Figure 19(c)). Nevertheless, even in these regions, the recrystallized grain size was similar to that found elsewhere.

After conventional forging at 1150 °C and a 2-hour heat treatment at 1260 °C, fully recrystallized, equiaxed microstructures were obtained in all locations, even in the dead-metal zones (Figure 20). As for the isothermal forgings heat-treated at this temperature, the microstructure consisted of grains of transformed alpha-phase pinned by gamma grains.

E. *Interpretation of Microstructure Nonuniformities*

Inspection of the microstructures in Figure 20, as well as in several other pancakes heat-treated near the alpha transus, reveals a variation in the percentage of gamma grains and the size of the transformed alpha grains. In particular, the structures along the axis ($r = 0$ location) exhibit an alpha grain size of about 30 μm and approximately 15 vol pct gamma grains. On the other hand, the alpha grain size is about 15 μm, and there is approximately 25 vol pct gamma grains at the outer diameter ($r = R$) of the heat-treated pancake. The gamma particle sizes are 6 and 4 μm in diameter at $r = 0$ and $r = R$ locations, respectively.

The alpha grain size measurements can be interpreted in terms of various theories of grain boundary pinning by second-phase particles. These measurements also give insight into the magnitude of alloying macrosegregation in the present material. With regard to the former aspect, a number of theoretical treatments are available to predict the ratio of the pinned grain diameter D to the diameter of the pinning particles d as a function of the volume fraction f of particles.[29,30,31] The earliest theory, due to Zener,[29,31] gives the relation $D/d = 1/3f$ but is usually applicable only for small volume fractions, *i.e.*, $f \leq 0.01$. The theories of Hellman and Hillert[30] and Hazzledine and Oldershaw[31] treat the case involving larger volume fractions of particles; both yield D/d dependences on volume fraction of the form $(1/f)^{1/3}$. The Hellman and Hillert theory gives the expression $D/d = (6/f)^{1/3}$. The Hazzledine and Oldershaw results were obtained from computer simulations and give a different fit despite the overall dependence on $f^{-1/3}$. The observed alpha grain size measurements are compared to the various models in Table II. Although the Zener relation correctly predicts the observed inverse relationship between D/d and volume fraction of gamma particles, the predicted values of grain size are substantially less than the measurements. Similarly, the Hellman and Hillert theory underestimates the grain sizes. Only the Hazzledine and Oldershaw model gives values of the right magnitude.

The extent of possible macrosegregation in the Ti-45.5Al-2Cr-2Nb alloy was interpreted with the aid of WDS (electron microprobe) measurements on the globular phases in forged and heat-treated samples. The data are presented in the form of a high-temperature pseudobinary-phase diagram, representing the equilibria between the alpha and gamma phases (Figure 21). An approximation has been introduced due to the neglect of the occurrence of the small amount of beta phase after heat treatment at 1200 °C. The beta phase was not observed at 1260 °C or at the temperature regime of interest here; hence, the phase boundaries delineated in Figure 21 are thought to be of sufficient accuracy. Although the alpha transus phase boundary in Figure 21 is

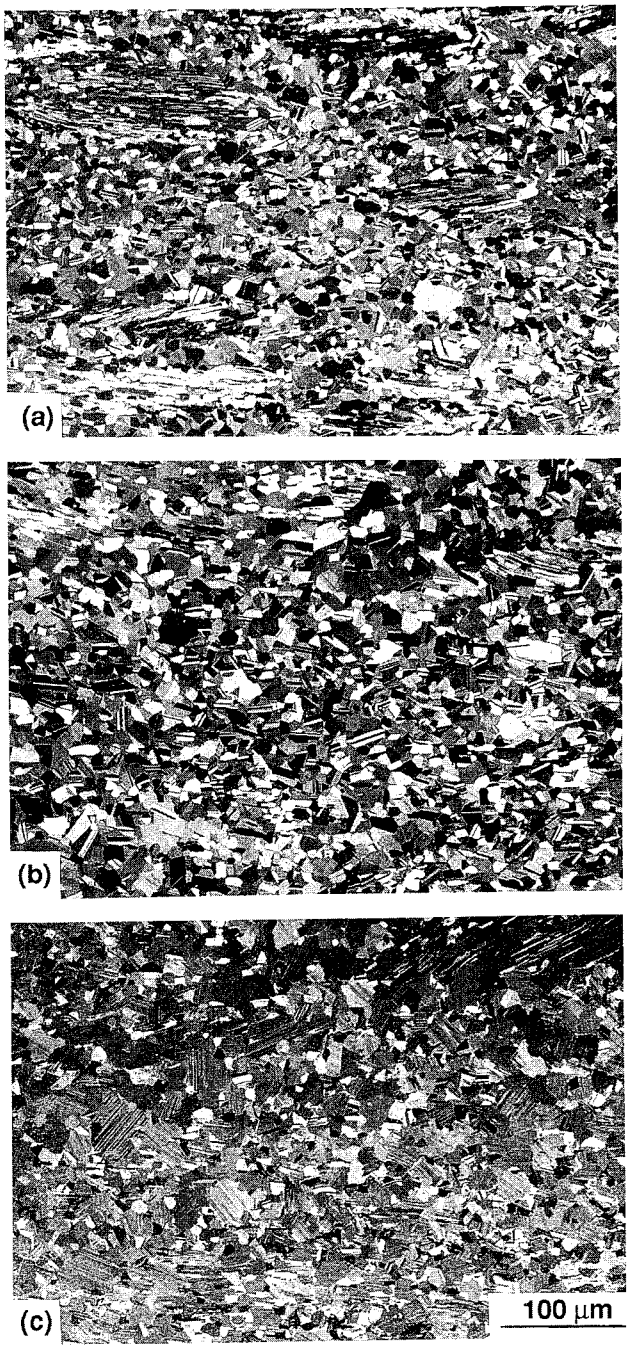


Fig. 18—Polarized light, optical microstructures developed in the center ($r = 0$), midplane region of pancakes isothermally forged at 1150 °C using an alpha-forge approach and then heat-treated after forging at (*a*) 1200 °C for 2 h, (*b*) 1200 °C for 8 h, and (*c*) 1260 °C for 2 h . The forging direction is vertical, and the radial direction is horizontal in all micrographs.

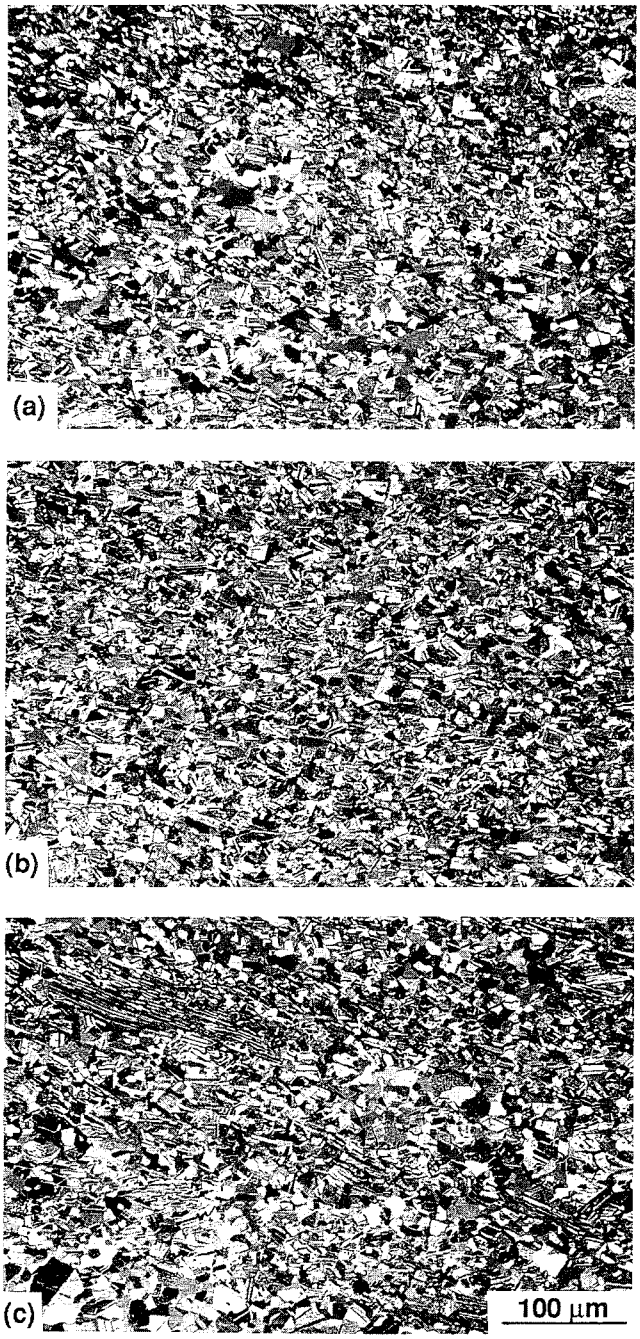


Fig. 19—Polarized light, optical microstructures developed in pancakes conventional forged at a nominal (furnace) temperature of 1150 °C and subsequently heat-treated at 1200 °C for 2 h. Micrographs were shot at the following locations in the pancake: (*a*) center (r = 0), midplane; (*b*) outer diameter, midplane; and (*c*) center (r = 0), top. The forging direction is vertical, and the radial direction is horizontal in all micrographs.

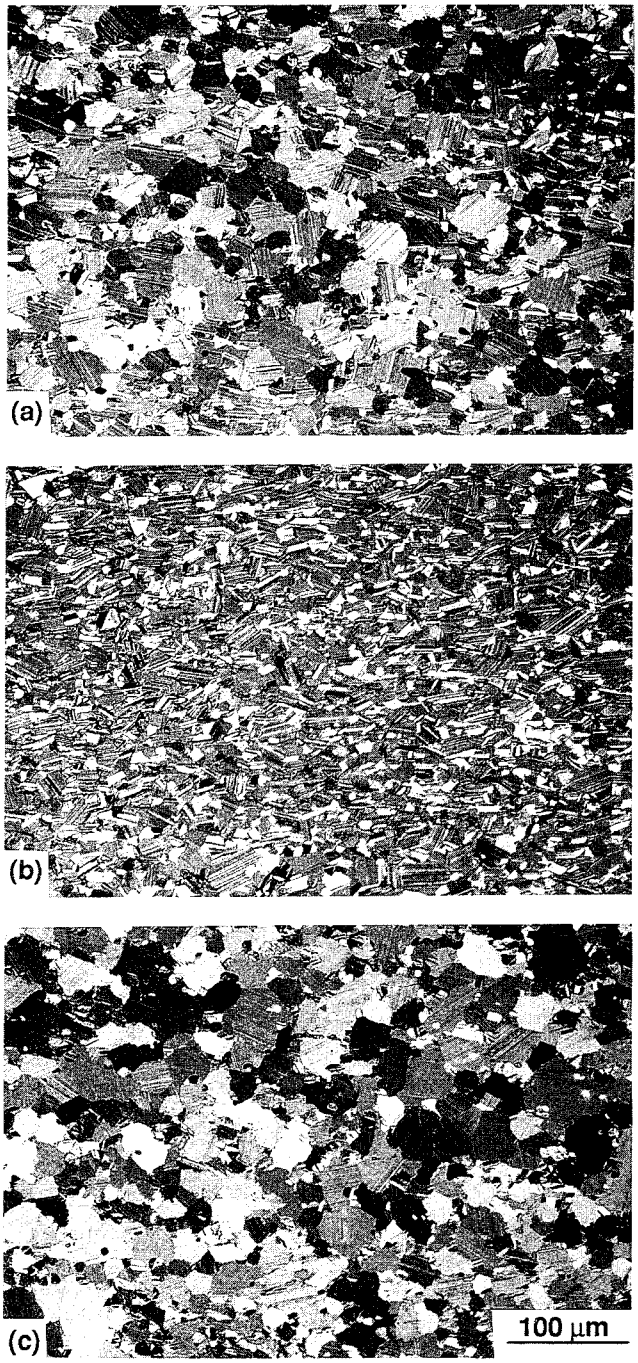


Fig. 20—Polarized light, optical microstructures developed in pancakes conventional forged at a nominal (furnace) temperature of 1150 °C and subsequently heat-treated at 1260 °C for 2 h. Micrographs were shot at the following locations in the pancake: (*a*) center (r = 0), midplane; (*b*) outer diameter, midplane; and (*c*) center (r = 0), top. The forging direction is vertical, and the radial direction is horizontal in all micrographs.

based on only two data points, the straight-line fit through these points, when extrapolated to higher aluminum contents, does yield a value very close to the measured alpha transus for Ti-48Al-2Cr-2Nb, *i.e.*, 1380 °C,[32] thereby lending credibility to the data.

For the 45.5 at. pct aluminum alloy, the pseudobinary-phase diagram suggests an alpha transus of 1310 °C, rather than the measured transus of 1300 °C. Thus, to avoid skewing of the interpretation of the experimental observations and because of the high degree of sensitivity of microstructure to temperature, attention will focus on a temperature of 1270 °C. This temperature corresponds to $T = T_\alpha - 40$ °C, or an identical decrement in temperature relative to the alpha transus to that used in the experimental heat treatments in Figure 20: T = 1260 °C = 1300 °C − 40 °C. With this proviso,

Table II. Comparison of Measured and Predicted Alpha Grain Sizes for Forged and Heat-Treated Ti-45.5Al-2Cr-2Nb Pancakes*

Pancake Location	Gamma Particle Size, d (μm)	Volume Fraction Gamma Particles, f	Measured Alpha Grain Size, D (μm)	Predicted Alpha Grain Size (μm)		
				Zener	Hellman & Hillert	Hazzledine & Oldershaw
Center	6	0.14	30	14.3	21.0	31.9
Outer diameter	4	0.23	15	5.8	11.9	18.9

*Pancake conventionally forged at 1150 °C and heat-treated at 1260 °C for 2 h.

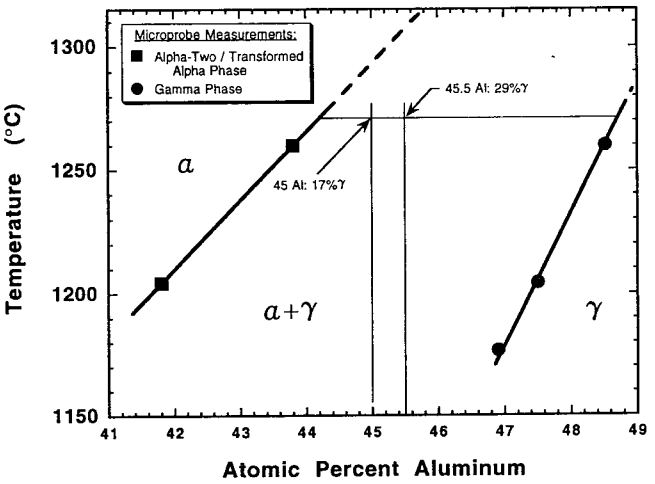


Fig. 21—Pseudobinary-phase diagram based on electron microprobe measurements and representing approximate equilibria for the alpha and gamma phases in wrought and recrystallized Ti-45.5Al-2Cr-2Nb.

the inverse lever rule can be used to estimate the equilibrium volume percentages of the gamma and alpha phases. For a 45.5 at. pct aluminum alloy, one would expect 29 vol pct of gamma grains, or a quantity similar to that observed in the outer diameter ($r = R$) region of the conventionally forged pancake heat-treated at $T = T_\alpha - 40$ °C (Figure 20(b)). By contrast, in an alloy with 45.0 at. pct aluminum, the lever-rule quantity of gamma phase at the same temperature is only approximately 17 pct, also in broad agreement with the amount observed at the center ($r = 0$) of this pancake (Figures 20(a) and (c)). Thus, from these observations and calculations, macrosegregation of the order of 0.5 at. pct aluminum can be concluded to be found in the induction skull melted ingots used in this investigation. Such variations in the aluminum level are difficult to determine by conventional wet chemistry methods on near-gamma titanium aluminides. Therefore, the heat-treatment and microstructural observation method used here appears to offer a sensitive alternative to detect macrosegregation.

IV. SUMMARY AND CONCLUSIONS

Microstructures and macrostructures developed in the cast and hipped lamellar near-gamma titanium aluminide Ti-45.5Al-2Cr-2Nb during isothermal and conventional, hot forging as well as after forging and various subtransus heat treatments were determined. The effect of forging rate, forging temperature, and various nonstandard practices (in isothermal forging) on microstructure were elucidated. The following conclusions are drawn from this work:

1. Conventional hot forging yields a finer, more completely broken-down microstructure than isothermal forging. Because of this, conventionally broken-down near-gamma titanium aluminide ingots may not need an intermediate heat treatment or a second breakdown forging step prior to finish processing via closed-die forging, sheet rolling, *etc.*
2. Nonstandard isothermal forging processes such as those incorporating a short intermediate recrystallization anneal or the application of an alpha-forge approach (*i.e.*, the forging of a metastable alpha microstructure) yield microstructures that are more uniformly wrought than the standard, constant ram speed approach.
3. Recrystallization/globularization of the as-conventionally forged microstructure during subsequent heat treatments occurs more quickly and competely than during heat treatment of isothermally forged material, presumably because of the higher strain rates and higher levels of deformation introduced during conventional hot forging.
4. Temperature nonuniformities developed during canned, conventional forging play a role in the formation of limited-deformation (dead-metal) zones but do not appear to impact overall microstructure uniformity in the forged and heat-treated condition.
5. Macrosegregation of aluminum is manifested through the development of nonuniform microstructures in forged and heat-treated pancake forgings, especially when heat treatment is conducted just below the alpha transus temperature. The 70-mm-diameter induction skull melted ingots used in the present investigation appeared to have had a variation in aluminum content of approximately 0.5 at. pct from the center-to-outer diameter.
6. The evolution of microstructure reported here applies solely to lamellar near-gamma titanium aluminides with starting alpha-grain sizes of approximately 200 μm or less. Ingots that have substantially larger alpha grain sizes may not respond as readily to forging and heat treatment[33] due to differences in the partitioning of hot work between the grain boundaries and grain interiors as well as to other workability-related considerations.

ACKNOWLEDGMENTS

This work was conducted as part of the in-house research activities of the Processing Science Group,

Metals and Ceramics Division, Air Force Wright Laboratory Materials Directorate. Two of the authors gratefully acknowledge support through Contract No. F33615-92-C-5900 (VS) and the Air Force Visiting Scientist program, Contract No. F33615-90-C-5944 (VKJ). The assistance of W. Konkel, J.D. Byrd, and the laboratory staff at Cameron Forged Products; J. Brown, T. Brown, T. Jones, and P. Fagin of the Air Force Experimental Materials Processing Laboratory; and Linda Osterloh in preparation of the manuscript is much appreciated. Technical discussions with Dr. P. Hazzledine, UES, Inc., and Dr. P. Martin, Rockwell International, are also graciously acknowledged.

REFERENCES

1. S.C. Huang and D.S. Shih: in *Microstructure/Property Relationships in Titanium Aluminides and Alloys*, Y.-W. Kim and R.R. Boyer, eds., TMS, Warrendale, PA, 1991, pp. 105-22.
2. Y.-W. Kim and D.M. Dimiduk: *JOM*, 191, vol. 43 (8), pp. 40-47.
3. T.L. Wardlaw: Timet Corporation, Henderson, NV, unpublished research, 1989.
4. S.L. Semiatin, S.I. Oh, R.J. Fiorentio, V. Seetharaman, and J.C. Malas: in *Heat Resistant Materials*, K. Natesan and D.J. Tillack, eds., ASM INTERNATIONAl, Materials Park, OH, 1991, pp. 175-86.
5. V. Seetharaman, J.C. Malas, and C.M. Lombard: in *High-Temperature Ordered Intermetallic Alloys IV*, L.A. Johnson, D.P. Pope, and J.O. Stiegler, eds., Materials Research Society, Pittsburgh, PA, 1991, pp. 889-94.
6. R.L. Goetz, V.K. Jain, and C.M. Lombard: *J. Mater. Proc. Technol.*, 1992, vol. 35, pp. 37-60.
7. K. Wurzwallner, H. Clemens, P.S. Schretter, A. Bartels, and C. Koeppe: in *High-Temperature Ordered Intermetallic Alloys V*, I. Baker, R. Darolia, J.D. Whittenberger, and M.H. Yoo, eds., Materials Research Society, Pittsburgh, PA, 1993, pp. 867-72.
8. K. Wurzwallner, H. Puschnik, H. Clemens, P. Schretter, and G. Korb: Böhler Edelstahl GmbH, Kapfenberg, Austria, unpublished research, 1992.
9. K. Wurzwallner, P. Schretter, and H. Clemens: in *Proc. 13th Int. Plansee Seminar*, H. Bildstein and R. Eck, eds., Metallwerk Plansee, Reutte, Austria, 1993, pp. 537-51.
10. C. McCullough, J.J. Valencia, C.G. Levi, and R. Mehrabian: *Acta Metall.*, 1989, vol. 37, pp. 1321-36.
11. J.D. Bryant and S.L. Semiatin: *Scripta Metall. Mater.*, 1991, vol. 25, pp. 449-53.
12. S.L. Semiatin and P.A. McQuay: *Metall. Trans. A*, 1992, vol. 23A, pp. 149-61.
13. S.L. Semiatin, R. Nekkanti, M.K. Alam, and P.A. McQuay: *Metall. Trans. A*, 1993, vol. 24A, pp. 1295-1306.
14. S.L. Semiatin, P.A. McQuay, W.R. Kerr, M. Stucke, Y.-W. Kim, and S. El-Soudani: in *High-Temperature Ordered Intermetallic Alloys IV*, L.A. Johnson, D.P. Pope, and J.O. Stiegler, eds., Materials Research Society, Pittsburgh, PA, 1991, pp. 883-88.
15. S.V. Radcliffe and E.B. Kula: in *Fundamentals of Deformation Processing*, W.A. Backofen, J.J. Burke, L.F. Coffin, Jr., N.L. Reed, and V. Weiss, eds., Syracuse University Press, Syracuse, NY, 1964, pp. 321-63.
16. V.K. Jain, R.L. Goetz, and S.L. Semiatin: Air Force Materials Directorate, Wright Laboratory, Wright-Patterson Air Force Base, OH, unpublished research, 1993.
17. S.L. Semiatin, V. Seetharaman, V. Jain, and R.L. Goetz: Air Force Materials Directorate, Wright Laboratory, Wright-Patterson Air Force Base, OH, Air Force Invention No 20, 661, 1992.
18. S.L. Semiatin, M. Ohls, and W.R. Kerr: *Scripta Metall. et Materialia*, 1991, vol. 25, pp. 1851-56.
19. S.L. Semiatin, J.C. Soper, and R. Shivpuri: *Metall. Mater. Trans. A*, 1994, vol. 25A, pp. 1681-92.
20. H.S. Carslaw and J.C. Jaeger: *Conduction of Heat in Solids*, Oxford University Press, London, 1959, ch. 18.
21. R.L. Goetz and S.L. Semiatin: Air Force Materials Directorate, Wright Laboratory, Wright-Patterson Air Force Base, OH, unpublished research, 1994.
22. S.L. Semiatin and J.H. Holbrook: *Metall. Trans. A*, 1983, vol. 14A, pp. 1681-95.
23. R. Srinivasan and I. Weiss: Wright State University, Dayton, OH, unpublished research, 1993.
24. Y.S. Touloukian: *Thermophysical Properties of High Temperature Solid Materials*, Macmillan Company, New York, NY, 1967.
25. *Metals Handbook, 8th ed.*, T. Lyman, ed., ASM, Metals Park, OH, 1961, vol. 1, pp. 52-55.
26. P.R. Burte, S.L. Semiatin, and T. Altan: Report No. ERC/NSM-B-89-20, Engineering Research Center for Net Shape Manufacturing, The Ohio State University, Columbus, OH, 1989.
27. P.R. Burte, S.L. Semiatin, and T. Altan: *Proc. NAMRC XVIII*, Soc. Manuf. Eng., Dearborn, MI, 1990, pp. 59-66.
28. H.J. Frost and M.F. Ashby: *Deformation-Mechanism Maps*, Pergamon Press, Oxford, 1982, ch. 2.
29. P.G. Shewmon: *Transformations in Metals*, McGraw-Hill, New York, NY, 1969, ch. 3.
30. P. Hellman and M. Hillert: *Scand. J. Metall.*, 1975, vol. 4, p. 211.
31. P.M. Hazzledine and R.D.J. Oldershaw: *Phil. Mag.*, 1990, vol. A61, p. 579.
32. D.S. Shih and G.K. Scarr: in *High-Temperature Ordered Intermetallic Alloys IV*, L.A. Johnson, D.P. Pope, and J.O. Stiegler, eds., Material Research Society, Pittsburgh, PA, 1991, pp. 727-32.
33. S.L. Semiatin and V. Seetharaman: Air Force Materials Directorate, Wright Laboratory, Wright-Patterson Air Force Base, OH, unpublished research, 1992.

Microstructures and Mechanical Behavior of NiAl-Mo and NiAl-Mo-Ti Two-Phase Alloys

P.R. SUBRAMANIAN, M.G. MENDIRATTA, and D.B. MIRACLE

The phase relationship in the NiAl-Mo system is characterized by a eutectic equilibrium between binary NiAl and the terminal (Mo) solid solution, thereby offering the potential for development of ductile-phase–toughened composites. A study was conducted to evaluate the effect of varying volume fraction of the (Mo) phase on the microstructure, bend strength, and ambient temperature fracture behavior of selected NiAl-Mo two-phase alloys. Above room temperature, the NiAl-Mo alloys showed an increase in bend strength compared to monolithic NiAl, with reasonable strength retention up to ~800 °C. The results demonstrated moderate improvements in toughness in the NiAl-Mo alloys in comparison to monolithic NiAl. A further enhancement in toughness was realized through hot working. Fractography studies showed evidence for substantial decohesion between the (Mo) phase and the NiAl matrix, thereby suggesting the presence of a weak interface. This weak interface between the (Mo) phase and the NiAl matrix, in conjunction with modulus mismatch stresses, causes the crack to deflect from the (Mo) reinforcement and propagate preferentially along the (Mo)/NiAl interface. These attributes limit the potential for significant ductile-phase toughening in the NiAl-Mo system. An addition of 0.2 at. pct Ti resulted in a marked improvement in the room-temperature fracture toughness of NiAl-Mo. Fractography observations show some evidence for (Mo)/NiAl interface strengthening with the Ti addition.

I. INTRODUCTION

THE B2-ordered nickel aluminide NiAl exhibits an attractive combination of properties, such as high melting temperature, high stiffness, and low density, thereby offering the potential for use as a high-temperature structural material. However, these characteristics are accompanied by a lack of ductility and inadequate fracture toughness at low temperatures. Although single-crystalline NiAl exhibits some plasticity,[1] polycrystalline NiAl shows little or no room-temperature tensile ductility[2–6] and exhibits premature fracture. The room-temperature fracture toughness of coarse-grained NiAl is below 5 MPa$\sqrt{m}$,[7] and 5 to 6 MPa$\sqrt{m}$ for a 20 μm grain-size material.[8] Intergranular fracture is the primary mode of failure in polycrystalline, stoichiometric NiAl.[3,4] The inadequate toughness and damage tolerance of polycrystalline NiAl at low temperatures limits its potential, particularly in monolithic form, for aerospace applications.

A composite systems approach, such as toughening by fiber reinforcement or by ductile-phase reinforcement, may provide the solution to the intrinsically poor damage tolerance of brittle materials. In the former approach, toughness is provided to the brittle matrix through mechanisms such as fiber pullout, crack branching, and crack deflection by interface debonding, as observed in ceramic composites.[9] On the other hand, the predominant toughening mechanism in ductile-phase–reinforced systems involves energy dissipation by plastic deformation of ductile ligaments bridging the crack surfaces behind the advancing crack tip.[10] Examples of ductile-phase toughening include systems such as Co/WC,[11] Al/Al_2O_3,[10] TiNb/TiAl,[12] and Nb/Nb_5Si_3.[13,14] The need for long-term composite stability at elevated temperatures requires that the reinforcing phase in these composite systems be in thermodynamic equilibrium with the matrix material. In this context, phase relationships showing equilibrium between the matrix phase and a terminal refractory phase, such as in eutectics, can be exploited for obtaining an *in situ* composite. Such a two-phase system offers the best prospects for long-term thermodynamic stability.

Examination of the literature[2,15–21] showed a number of NiAl-X (X = Mo, Cr, W, Re, and V) quasi-binary eutectic systems, where NiAl is in equilibrium with a nominally ductile, refractory phase. Past studies[2,20,21] on the mechanical behavior of directionally solidified (DS) NiAl-Cr and NiAl-Mo eutectics have focused on the role of the fine, fibrous (Cr) or (Mo) phases in improving the high-temperature strength and creep resistance of NiAl. However, the potential for toughening NiAl by the refractory phases was not explored in these studies. Earlier work[22] on polycrystalline NiAl-Mo alloys by the present authors demonstrated that a two-phase microstructure consisting of a dispersion of the terminal (Mo) phase in a NiAl matrix can provide some increment in toughness over monolithic NiAl. Based on indentation crack studies, Sasaki *et al.*[23] proposed that a higher fracture toughness may be expected in the NiAl-Mo eutectic alloy compared to pure NiAl. Recently, the microstructural stability and mechanical behavior of DS NiAl-Mo,[24,25,26] NiAl-Cr,[25,26,27] NiAl-Cr(Mo),[26] and NiAl-V[25] alloys have been investigated. In all the cases, the *in situ* refractory reinforcements provided an increase in fracture toughness in comparison to

P.R. SUBRAMANIAN, Senior Scientist, and M.G. MENDIRATTA, Division Director, are with the Materials Research Division, UES, Inc., Dayton, OH 45432. D.B. MIRACLE, Materials Engineer, is with the Air Force Wright Laboratory, WL/MLLM, Wright-Patterson AFB, OH 45433.

Manuscript submitted October 30, 1992.

U.S. GOVERNMENT WORK NOT PROTECTED BY U.S. COPYRIGHT

monolithic NiAl. Fracture toughness data[24,25] reported for the DS NiAl-Mo eutectic alloy agreed well with our initial investigations.[22] Noebe *et al.*[28] have evaluated the room-temperature toughness and elevated-temperature strength of NiAl composites reinforced with continuous fibers of a W-rich alloy. The composites exhibited a strong fiber-matrix bond, with little or no toughening at ambient temperature, although significant high-temperature strengthening was achieved. Bowman[29] reported bend strength *vs* temperature data for NiAl composites reinforced with continuous TZM Mo fibers. These composites exhibited a strong fiber-matrix bonding, resulting in rule-of-mixtures composite strengths. The composite toughness also was reported to be enhanced by the TZM fibers, although no toughness data were presented. Fractography studies[18,30] on NiAl-Re eutectic alloys indicated extensive local plasticity of the fibrous (Re) phase, as exhibited by necking and chisel-point fracture of this phase, although no fracture toughness data were reported.

The present investigation explores the effect of varying volume fraction of the (Mo) phase on the microstructure, bend strength, and room-temperature fracture behavior of cast and heat-treated NiAl-Mo two-phase alloys with selected compositions. Further, the effect of deformation processing on the microstructure and mechanical properties of selected NiAl-Mo alloys is briefly addressed. Deformation processing has been found to produce improvements in the mechanical properties of other ductile-phase–reinforced systems.[14] An initial investigation[22] by the present authors showed evidence for a weak interface between the (Mo) phase and the NiAl matrix; it was envisioned that minor solute additions may alter the interface behavior. Therefore, another objective of this investigation was to examine the role of alloying with Ti on the room-temperature fracture behavior of a selected hypereutectic NiAl-Mo alloy.

II. EXPERIMENTAL PROCEDURE

Four compositions were selected for this investigation: the eutectic composition Ni-45.5Al-9Mo and three hypereutectic alloys with a stoichiometric Ni/Al ratio and increasing concentrations of Mo, *viz.*, Ni-44Al-12Mo, Ni-38.5Al-23Mo, and Ni-31Al-38Mo (all compositions are in atomic percent). These alloys will be denoted as NiAl-9Mo, NiAl-12Mo, NiAl-23Mo, and NiAl-38Mo, respectively, in the rest of this article. An alloy with a nominal composition of NiAl-36Mo-2Ti (hereafter labeled as NiAl-Mo-Ti) was selected for evaluating the effect of Ti on the fracture behavior of NiAl-Mo and to compare with baseline data for the NiAl-38Mo alloy. The alloys were prepared in the form of ~250 g buttons or cigar-shaped castings by arc melting the constituent elements in a water-cooled copper hearth, using a nonconsumable tungsten electrode. The arc-melted buttons and cigars were homogenized at 1200 °C/100 h. In order to evaluate the extent of coarsening of the eutectic (Mo) phase, the NiAl-9Mo alloy was annealed at temperatures between 1200 °C and 1500 °C for time periods ranging from 24 to 500 hours. All of the annealing treatments were conducted with the samples wrapped in Ta foil and were performed under an atmosphere of flowing argon, which was first gettered over Ti chips heated to 800 °C. Backscattered scanning electron microscopy (SEM) and quantitative electron probe microanalysis (EPMA) were conducted to characterize the microstructure and composition of the equilibrium phases. Six to eight individual analyses were obtained for each phase in a given alloy. Matrix intensity corrections were made with a standard ZAF iterative correction program. The identity of the phases was verified by X-ray diffraction. Finally, the volume fraction of the (Mo) phase in each of the alloys was evaluated by quantitative image analysis. The bulk compositions of the homogenized alloys were determined by gravimetric analysis, while the interstitial impurity contents were measured by inert atmosphere fusion analysis. Trace impurities were analyzed by X-ray fluorescence.

Specimens for bend testing were obtained from the arc-melted cigars after homogenization at 1200 °C/100 h, followed by hot isostatic pressing (HIP) at 1200 °C/276 MPa/6 h. Smooth bend bars (2.86-cm long × 0.64-cm wide × 0.32-cm thick) and single-edge notched bend bars (2.86-cm long × 0.76-cm wide × 0.64-cm thick; electrical-discharge machined (EDM) notch: 0.25-cm deep, 0.02-cm root radius) were obtained from the hipped specimens by EDM. The bend specimens were finally given a coarsening heat treatment at 1450 °C/24 h prior to testing. The smooth bend bars were tested in a vacuum of $\sim 10^{-4}$ Pa at selected temperatures between ambient and 1000 °C under four-point loading. The single-edge notched bend bars were tested under three- and four-point loading conditions to determine room-temperature fracture toughness, K_Q, as per ASTM specification E-399. Scanning electron microscopy fractography was conducted on the fractured bend specimens to characterize the fracture behavior and the operative toughening mechanisms.

In order to study the effect of deformation processing on microstructure and toughness, the NiAl-9Mo eutectic alloy was hot forged to 80 pct reduction at 1200 °C, while the hypereutectic alloy NiAl-12Mo was hot extruded at 1200 °C, using a reduction ratio of 4.5:1. Following annealing at 1450 °C/24 h, the notched bend bars of the forged as well as the extruded alloys were tested for room-temperature notch toughness. The toughness of the as-hot-worked alloys was not measured, as similar work on a Nb/Nb_5Si_3 ductile-phase–toughened system had shown that reasonable toughness enhancement was possible only after hot working and heat treatment.[14]

III. RESULTS

A. *Phase Compositions and Microstructures*

1. *As-cast + heat-treated alloy*

Table I summarizes the analyzed bulk compositions and the impurity analyses of the alloys. The analyzed bulk compositions were within 1 at. pct of the nominal compositions. The impurity analyses revealed the carbon concentration to vary from 64 to 81 wppm, oxygen to vary from 21 to ~350 wppm, and nitrogen to vary from 38 to 350 wppm. X-ray fluorescence analysis revealed

Table I. Analyzed Compositions and Impurity Analysis of the NiAl-Mo Alloys

	Alloy			
	NiAl-9Mo	NiAl-12Mo	NiAl-23Mo	NiAl-38Mo
Bulk elements (at. pct)				
Ni	45.3	44.0	37.6	29.9
Al	45.7	43.4	39.1	31.4
Mo	8.8	12.2	23.1	38.6
Impurities* (wt ppm)				
C	64	69	66	81
O	100	347	115	21
N	350	467	50	38

*X-ray fluorescence showed Si, Ti, Cr, Mn, Fe, and Zn to be below detectable levels (<1 wt pct).

metallic impurities to be at trace levels. Table II lists the compositions of the observed phases in the various alloys. The composition of the NiAl matrix was typically observed to be slightly Al-rich with negligible solubility (≤0.1 at. pct) for Mo. The terminal (Mo) phase showed Al solubility in excess of 5 at. pct, and Ni solubility in the range 3 to 5 at. pct. X-ray diffraction corroborated the presence of only the NiAl and (Mo) phases.

Figure 1 shows the backscattered SEM micrographs of the as-cast + heat-treated NiAl-9Mo alloy under selected annealing conditions. The microstructure typically consisted of fine eutectic colonies separated by regions of coarse (αMo) dendrites at colony boundaries; the eutectic colonies themselves were composed of a fine, fibrous (Mo) phase dispersed fairly uniformly in an NiAl matrix. As summarized in Table III, the eutectic (Mo) fibers exhibited very sluggish coarsening kinetics. The diameter of the (Mo) fibers in the eutectic ranged from ~0.3 μm after 500 hours at 1200 °C to ~0.7 μm after 100 hours at 1500 °C. In view of the uniform size of the (Mo) phase and the negligible solubility of Mo in the NiAl matrix, Ostwald-type coarsening is expected to have a small driving force in the eutectic. The observed thermal stability against coarsening in the NiAl-9Mo alloy is a desirable attribute for high-temperature applications. Figure 2 shows the SEM micrographs of the hypereutectic alloys after heat treatment at 1450 °C/24 h. The microstructure of the hypereutectic alloys after coarsening typically showed branched primary (Mo) dendrites dispersed in a eutectic matrix for NiAl-12Mo and NiAl-23Mo; the matrix in the NiAl-38Mo alloy was essentially single-phase NiAl, with a very coarse remnant of the eutectic (Mo) phase.

2. *Hot-worked + heat-treated alloys*

Figure 3 shows the SEM micrographs of the NiAl-9Mo alloy in the as-forged condition as well as after annealing at 1450 °C/24 h. As shown in Figure 3(a), the hot-forging treatment at 1200 °C caused the eutectic colonies to be elongated normal to the forging direction. Further, large grains of elongated, primary NiAl were observed, indicating that the alloy was slightly hypoeutectic in composition. Figure 4 shows the SEM micrographs of a longitudinal section of the extruded NiAl-12Mo casting in the as-extruded condition and after annealing at 1450 °C/24 h. It was clear that the extrusion at 1200 °C had resulted in some alignment of the primary as well as the eutectic (Mo) phase along the extrusion direction. The 1450 °C/24 h annealing

Table II. Electron Microprobe Data for the NiAl-Mo Alloys

Alloy	Heat Treatment	Composition (At. Pct)		
		Element	NiAl	(Mo)
NiAl-9Mo	1450 °C/24 h	Ni	48.7 ± 0.7	5.3 ± 2.5
		Al	51.2 ± 0.8	5.0 ± 0.4
		Mo	0.1 ± 0.1	89.7 ± 2.0
NiAl-12Mo	1450 °C/24 h	Ni	46.0 ± 1.0	4.6 ± 2.7
		Al	53.9 ± 1.5	8.8 ± 1.1
		Mo	0.1 ± 0.1	86.6 ± 1.3
NiAl-23Mo	1450 °C/24 h	Ni	50.6 ± 0.1	3.3 ± 0.3
		Al	49.4 ± 0.1	8.9 ± 0.9
		Mo	~0	87.8 ± 0.9
NiAl-38Mo	1450 °C/100 h	Ni	48.6 ± 0.4	2.8 ± 0.4
		Al	51.3 ± 0.2	5.6 ± 0.2
		Mo	0.1 ± 0.1	91.5 ± 1.3
NiAl-Mo-Ti	1450 °C/24 h	Ni	49.6 ± 0.3	4.6 ± 1.4
		Al	50.1 ± 0.3	8.2 ± 0.9
		Mo	0.1 ± 0.03	87.0 ± 2.2
		Ti	0.2 ± 0.01	0.2 ± 0.03

Note: Error values refer to deviations based on a 95 pct confidence level.

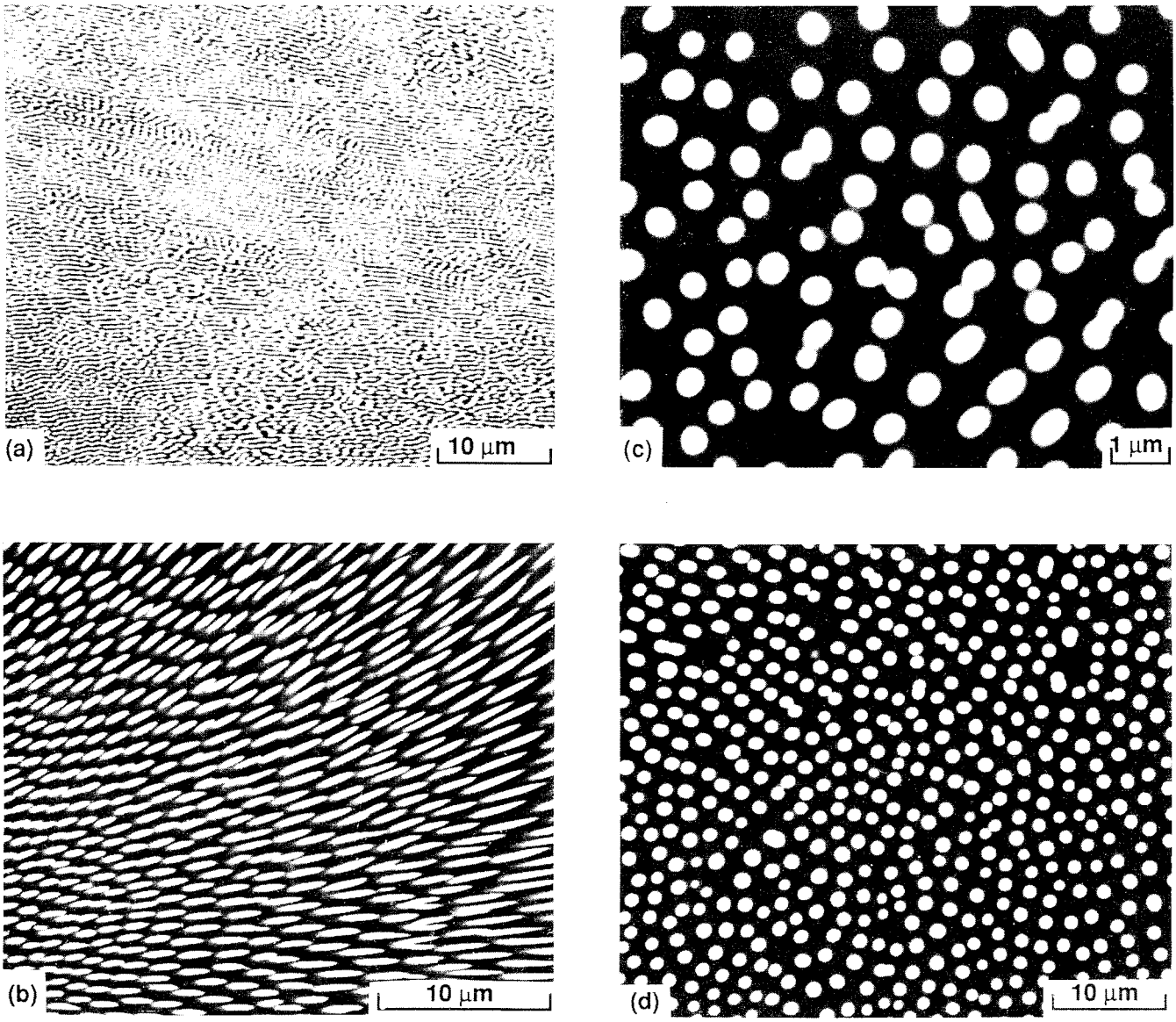


Fig. 1—Backscattered SEM micrographs of the NiAl-9Mo alloy showing the eutectic microstructure under selected conditions: (*a*) as-cast; (*b*) 1200 °C/100 h; (*c*) 1400 °C/200 h; and (*d*) 1500 °C/100 h.

treatment of the forged and the extruded alloys produced a substantial change in the microstructural size scale and morphology of the eutectic (Mo) fibers, as seen in Figures 3(b) and 4(b), respectively. Most of the eutectic (Mo) fibers were broken or spheroidized and showed considerable coarsening.

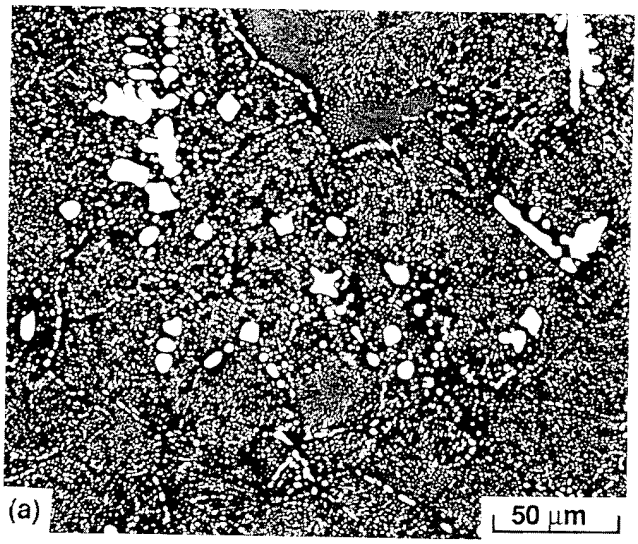
B. *Bend Properties*

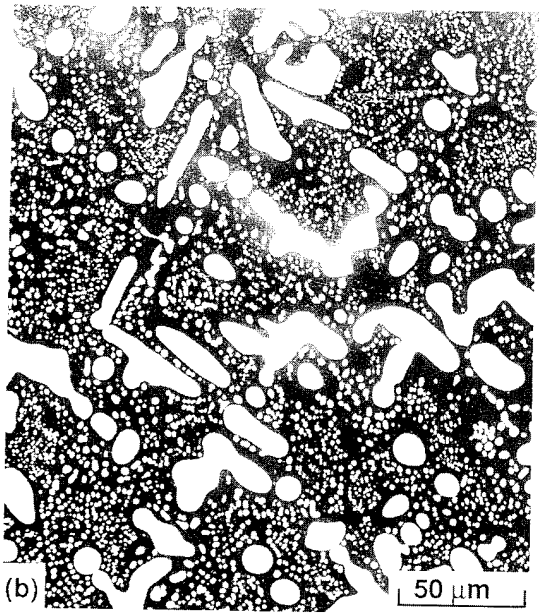
1. *Bend strength*

Figure 5 shows the variation of bending strength (elastic limit strength) with temperature for the eutectic as well as the hypereutectic alloys. The data at the lower

Table III. Cross-Sectional Size of the Eutectic (Mo) Phase in the NiAl-9Mo Alloy as a Function of Annealing Temperature and Time

Annealing Treatment	Size of Eutectic (Mo) (μm)
1200 °C/100 h	0.2
1200 °C/300 h	0.2
1200 °C/500 h	0.24 to 0.28
1300 °C/24 h	0.3
1400 °C/24 h	0.33
1400 °C/200 h	0.5
1450 °C/24 h	0.4 to 0.65
1500 °C/100 h	0.6 to 0.7





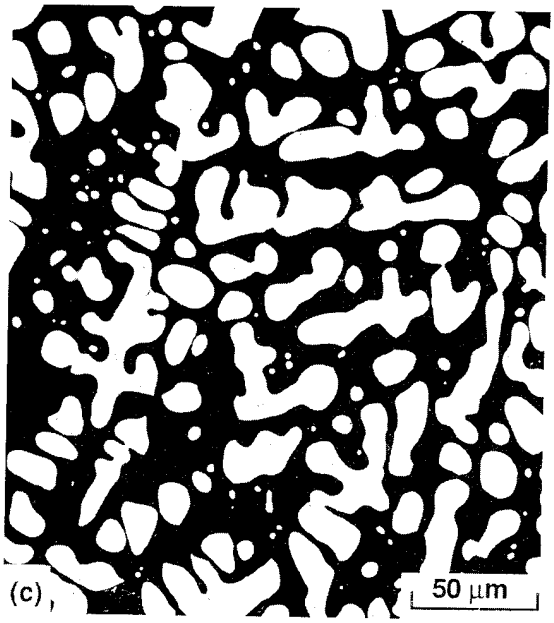


Fig. 2—Backscattered SEM micrographs of the hypereutectic NiAl-Mo alloys after annealing at 1450 °C/24 h: (*a*) NiAl-12Mo, showing the eutectic matrix and small volume fraction of the primary (Mo) phase; (*b*) NiAl-23Mo, showing a coarse eutectic matrix and large primary (Mo) dendrites; and (*c*) NiAl-38Mo, where the matrix is essentially NiAl.

temperatures represent an average of two tests. Above 600 °C, the alloys showed considerable bend ductility, as evidenced by a noticeable curvature on the bend bars. As an example, the bend bar of the NiAl-9Mo alloy bottomed out within the test fixture without fracture at 600 °C, indicating an outer fiber strain of at least 4.6 pct (as determined from the curvature of the bend bar). The load-deflection curves at ambient and 500 °C exhibited a distinct nonlinearity, implying prefailure microcracking or plasticity, with the fracture loads detectably higher than the elastic limit in most instances. The alloys showed a reasonable strength retention up to ~800 °C, with a rapid drop in strength above ~800 °C. Further, there appeared to be no clear trend in the strength level with varying volume fraction of the (Mo) phase; rather, the data for all the alloys lie within a band. Bend strength data for monolithic NiAl[2] and DS NiAl-9Mo[2] are included in Figure 5 for comparison with the alloys in this investigation. The NiAl-Mo alloys all showed an increase in bend strength above room temperature in comparison to monolithic NiAl. The DS NiAl-9Mo alloy showed a substantial strength improvement at low to intermediate temperatures, which is attributed to an aligned microstructure, consisting of fine, unidirectionally oriented (Mo) fibers in a NiAl matrix.[2] However, the bend strength data suggests that the advantage of directional alignment is lost at temperatures above ~600 °C.

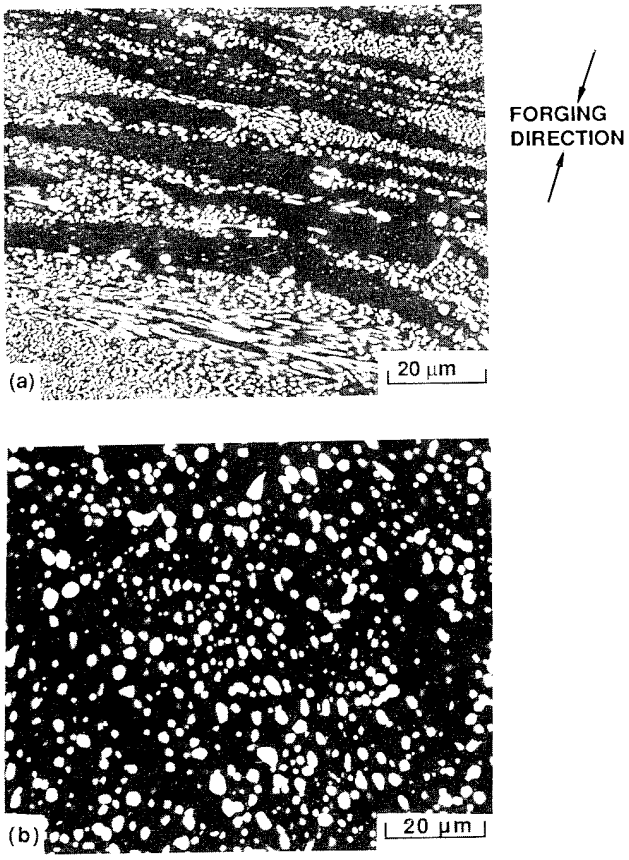


Fig. 3—Backscattered SEM micrographs of the NiAl-9Mo alloy: (*a*) after forging at 1200 °C to 80 pct reduction, some amount of primary NiAl is observed in the microstructure; and (*b*) after forging + annealing at 1450 °C/24 h, revealing extensive coarsening and spheroidization of the eutectic (Mo) phase.

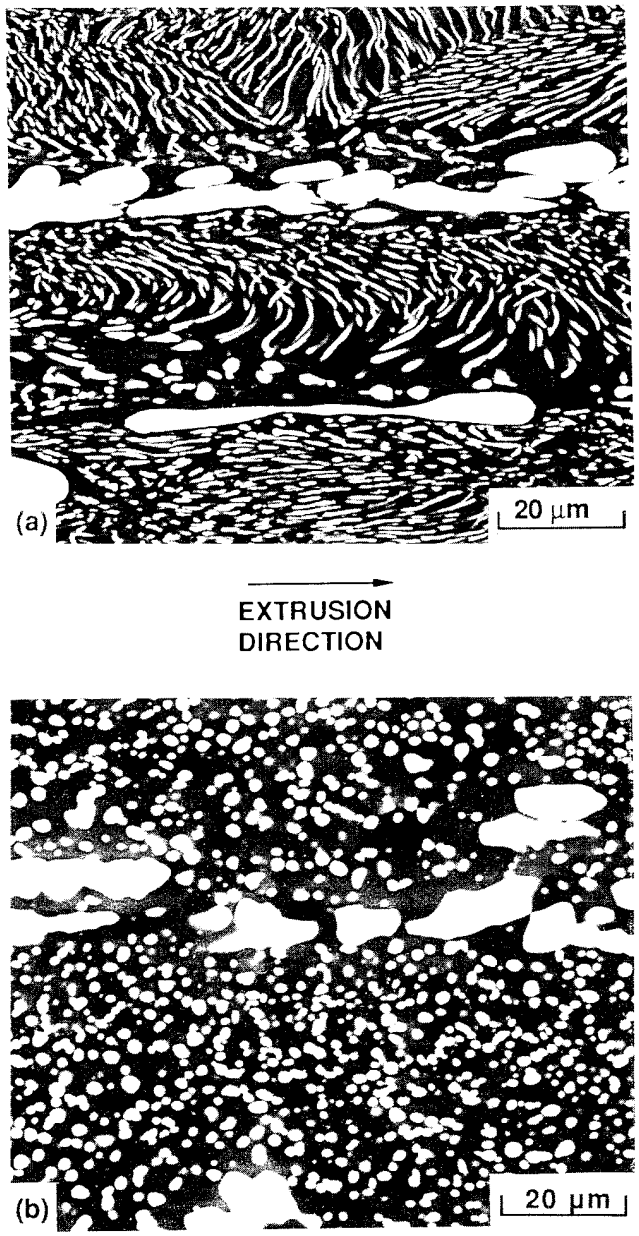


Fig. 4—Backscattered SEM micrograph of the NiAl-12Mo alloy: (*a*) after extrusion at 1200 °C using a 4.5:1 reduction ratio; and (*b*) after extrusion + annealing at 1450 °C/24 h, showing the breakdown of the eutectic (Mo) phase.

2. *Notch toughness*

Table IV lists the measured fracture toughness values as a function of the volume fraction of (Mo). Data obtained in this investigation for a monolithic NiAl alloy with composition Ni-53.2Al as well as data for stoichiometric NiAl[7] are included in Table IV for comparison. The toughness of Al-rich NiAl (Ni-53.2Al) was comparable to the data for stoichiometric, polycrystalline NiAl.[7] All of the NiAl-Mo alloys showed an improved toughness in comparison to monolithic NiAl. The increment in toughness, ΔK_Q, over that of Ni-53.2Al ranged from ~5 MPa$\sqrt{m}$ for the eutectic alloy to a maximum of ~12 MPa$\sqrt{m}$ for the extruded NiAl-12Mo alloy. As seen in Table IV, there appeared to be no significant trend in toughness enhancement with increasing volume fraction of (Mo); rather, the data suggested that there may be an optimal volume fraction beyond which there is no enhancement in toughness with increasing (Mo) concentration. The data from the hot-worked + coarsened alloys showed an additional increment in fracture toughness in comparison to the hipped alloys. The mean fracture toughness of the forged + coarsened NiAl-Mo alloy was determined to be 13.6 MPa$\sqrt{m}$ compared to a value of 9.4 MPa$\sqrt{m}$ for the as-cast + hipped alloys. In the case of the extruded NiAl-12Mo alloy, a mean fracture toughness of 16.6 MPa$\sqrt{m}$ was obtained, which is marginally higher than the value obtained for the cast + hipped alloy (13.8 MPa$\sqrt{m}$).

C. *Fractographic Observations*

1. *As-cast + heat-treated alloys*

Fractography results for the as-cast + heat-treated NiAl-9Mo and NiAl-12Mo alloys have been discussed briefly in an earlier report.[22] Scanning electron microscopy fractography of the eutectic alloy (Figure 6) indicated that a crack front had advanced in a series of steps through the microstructure, which suggests that the crack has taken a tortuous path through the bend specimen. The overall fracture morphology appeared to be

reminiscent of a fibrous fracture surface. Scanning electron microscopy fractographic analysis of the hypereutectic alloys (Figures 7, 8, and 9) indicated that the large primary (Mo) dendrites play a crucial role in the fracture process. Typically, the fractographs showed the following features: (1) regions where the crack has propagated preferentially along the NiAl/dendritic (Mo) interfaces; this is evident in the regions where one or more dendrite arms have been pulled out in the wake of the crack; (2) regions where the primary (Mo) phase exhibited some degree of plastic stretching, accompanied by interface decohesion, and (3) regions showing cleavagelike fracture within the (Mo) phase. The NiAl matrix in all cases showed brittle, cleavagelike failure.

Figures 10 and 11 represent the transverse surfaces of the notched bend samples of NiAl-23Mo and NiAl-38Mo, respectively, after the propagation of the crack. The bend bars did not fracture completely in these tests and, therefore, made it possible to observe the crack propagation through the microstructure. A significant amount of crack deflection, crack branching, or crack bifurcation was evident in the bend sample of the NiAl-23Mo alloy (Figures 10(a) and (b)). In most instances, the (Mo) dendrites exhibited only marginal stretching prior to fracture. Figure 10(b) corresponds to the edge of the bend bar away from the notch root, where it is seen that the crack has been arrested without propagating completely through the specimen. The transverse surface of the NiAl-38Mo bend sample showed distinctive features such as evidence for plastic stretching of the (Mo) phase (Figure 11(a)) and crack deflection along the Mo/NiAl interfaces (Figure 11(b)).

2. *Hot-worked + heat-treated alloys*

Scanning electron microscopy fractography of the forged + heat-treated NiAl-9Mo alloy (Figure 12) indicated that the coarse (Mo) particles have been pulled out in the wake of the advancing crack. Secondary cracking of the NiAl matrix was observed in some regions of the fracture surface. The elongated primary NiAl phase exhibited predominantly intergranular fracture, while the eutectic NiAl showed transgranular cleavage. No distinguishing features were evident in the fractographs of the extruded alloy other than interface decohesion and some secondary cracking in the matrix.

D. *Effect of Ti Addition*

Fractographic results on the NiAl-Mo alloys generally showed presence of a weak NiAl/Mo interface, leading to the deflection of the advancing crack along the interface in most instances. It was envisioned that minor alloying additions may alter the interface conditions, which in turn may have a beneficial effect on the interface strength. In the current work, the role of Ti on the hypereutectic NiAl-38Mo alloy was evaluated in terms of the overall fracture behavior. Titanium was selected as the alloying addition, as it is known to be soluble in both NiAl[31] and Mo.[32] The composition of the selected NiAl-Mo-Ti alloy was analyzed as Ni-34.5Al-36.7Mo-0.2Ti, indicating that the Ti concentration was substantially lower than the nominal composition; the Mo composition was close to the base alloy of NiAl-38Mo. Scanning electron microscopy examination of the alloy showed a two-phase microstructure, with a microstructural scale and morphology similar to that obtained in the NiAl-38Mo alloy. The equilibrium phases consisted of stoichiometric NiAl with ~0.1 at. pct Mo and ~0.2 at. pct Ti in solid solution and the terminal (Mo) phase with ~0.2 at. pct Ti in solid solution; the compositions are listed in Table II. Bend tests on this alloy in the as-cast + 1450 °C/24 h heat-treated condition showed an average fracture toughness of 17.1 MPa$\sqrt{m}$ in comparison to a value of 11.7 MPa$\sqrt{m}$ for a similar alloy with no Ti additions. It appears that with less than 0.2 at. pct Ti in solution in each phase, a 50 pct improvement in notch toughness was realized. The SEM fractographs of the fractured alloy revealed regions of cleavage failure in the (Mo) phase (Figure 13(a)) as well as regions where the crack has propagated along the interface. Regions of plastic stretching also were observed where the dendrite arms were oriented normal to the crack front (Figure 13(b)). Examination of a transverse section of one of the bend bars prior to complete fracture showed that the crack path was fairly tortuous and that there were several regions of secondary cracking parallel to the main crack.

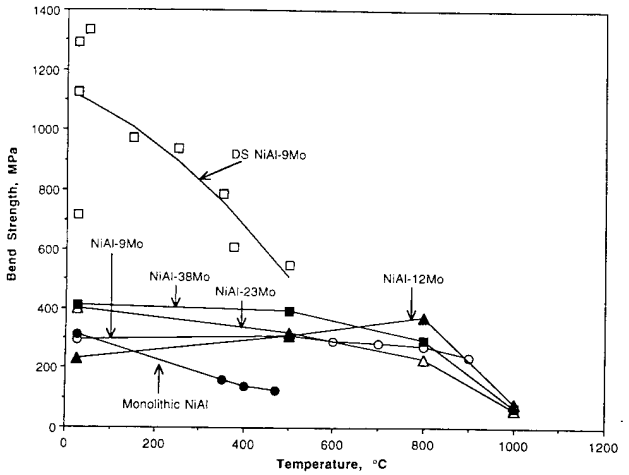


Fig. 5—Variation of bend strength with temperature for the NiAl-Mo alloys. The data for DS NiAl-Mo and monolithic NiAl are from Ref. 2.

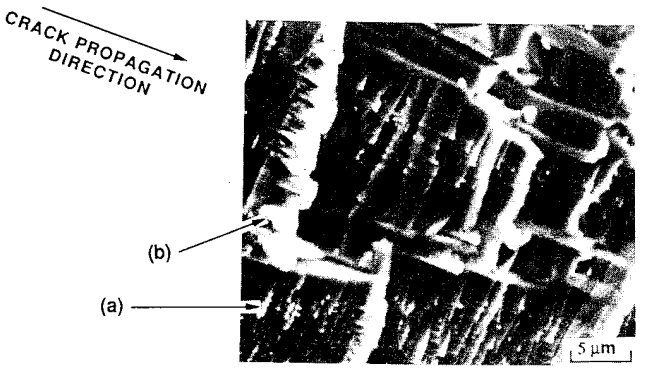
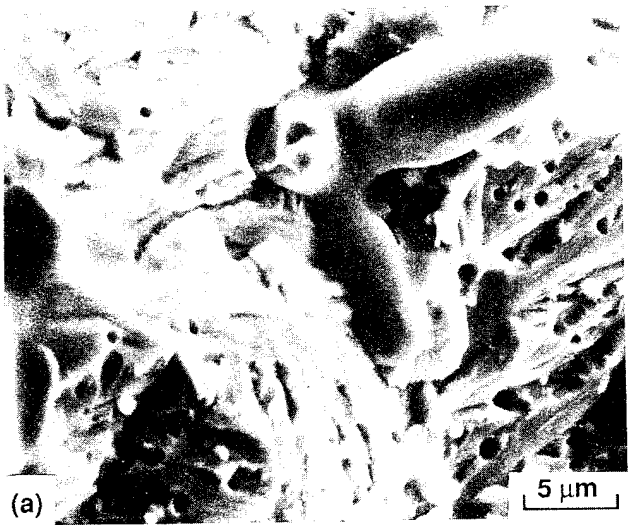


Fig. 6—SEM fractograph of the NiAl-9Mo alloy showing (*a*) a fibrous fracture morphology within the eutectic colonies and (*b*) interface decohesion.

Table IV. Room-Temperature Notch Toughness Data

Alloy	Condition	K_Q (MPa$\sqrt{m}$)	Volume Fraction of Primary (Mo)
NiAl[7]	as-cast; zone melted	<5	—
Ni-53.2 Al*	HIP + 1450 °C/24 h	4.9	—
NiAl-9Mo	HIP + 1450 °C/24 h	9.2, 9.6	0**
NiAl-9Mo	forged + 1450 °C/24 h	13.1, 14.0	0**
NiAl-12Mo	HIP + 1450 °C/24 h	12.1, 15.5	0.05
NiAl-12Mo	extruded + 1450 °C/24 h	15.5, 17.7	0.05
NiAl-23Mo	HIP + 1450 °C/24 h	10.6, 11.9	0.33
NiAl-38Mo	HIP + 1450 °C/24 h	10.7, 12.6	0.5
NiAl-Mo-Ti	HIP + 1450 °C/24 h	16.9, 17.3	~0.5

*Al-rich NiAl, from this study.
**This alloy refers to the eutectic composition and contains 0.11 volume fraction of eutectic (Mo).



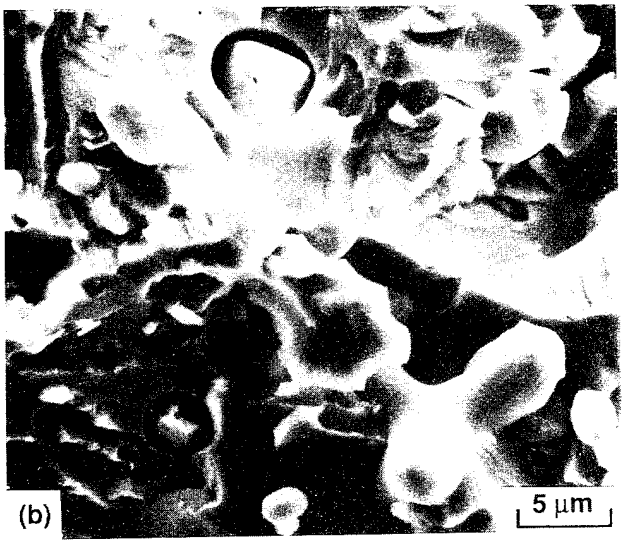


Fig. 7—SEM fractographs of the NiAl-12Mo alloy: (*a*) shows regions where the (Mo) dendrites have been pulled out in the wake of an advancing crack, indicating weak interfacial bonding; and (*b*) shows regions where the (Mo) phase exhibits some amount of plastic stretching, accompanied by interface decohesion followed by rupture.

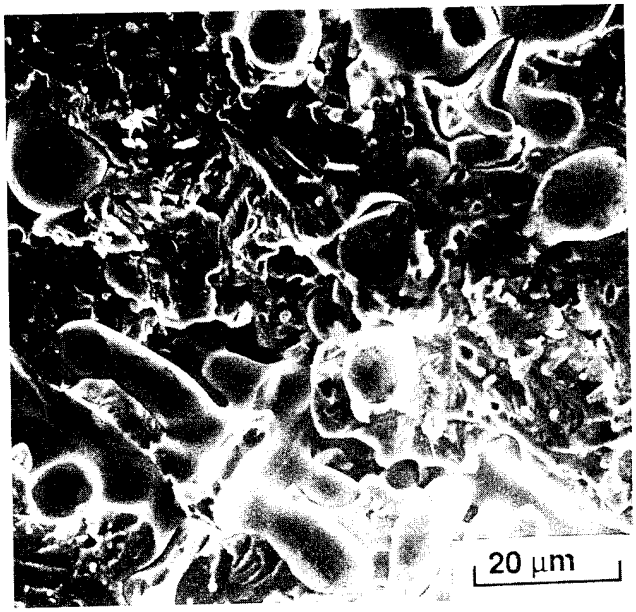
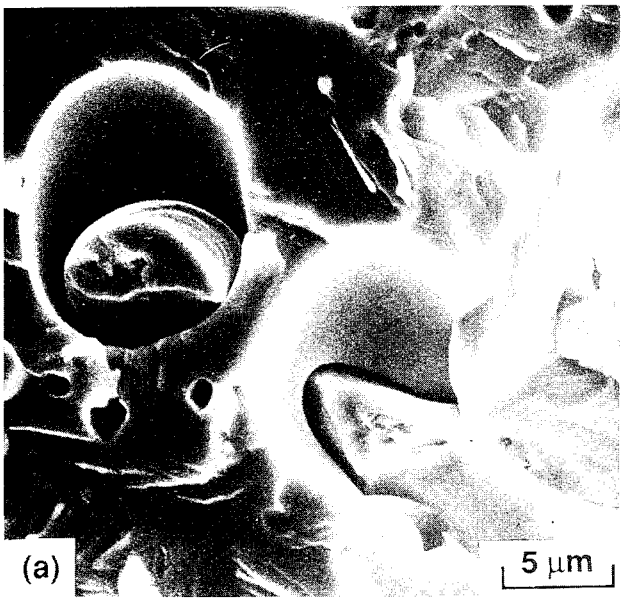


Fig. 8—SEM fractograph showing regions where the crack has propagated preferentially along the NiAl/(Mo) interfaces in NiAl-23Mo.

IV. DISCUSSION

A. *(Mo)/NiAl Interface Condition*

A major finding that emerges from the fractographic investigations is the apparently weak bonding between the (Mo) phase and the NiAl matrix, which permits the advancing crack to preferentially propagate along the interface. This precludes the possibility of extensive crack bridging, which is believed to be the primary toughening mechanism in ductile-phase–reinforced systems.[9] In most instances, the (Mo) particles appeared to have pulled free in the wake of the crack; hence, there is little contribution to the toughness by stretching of the (Mo) phase.[33] However, it is seen that, for certain orientations of the crack plane with respect to the (Mo)/NiAl interface, the crack propagates through the (Mo) dendrite. In such cases, the (Mo) phase fractures either in a cleavagelike or ductile fashion. In view of the weak interfacial bonding, the potential toughening effect



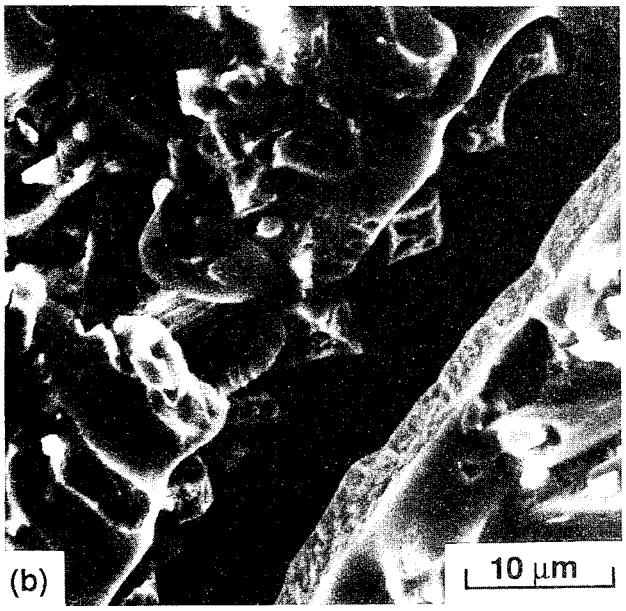


Fig. 9—SEM fractographs showing areas where the (Mo) dendrite arms show a limited amount of plastic stretching, followed by rupture: (*a*) NiAl-23Mo and (*b*) NiAl-38Mo. Note in (b) that the primary (Mo) dendrite arm has been pulled out along the interface, whereas the secondary dendrite arms oriented normal to the crack front show some plastic stretching.

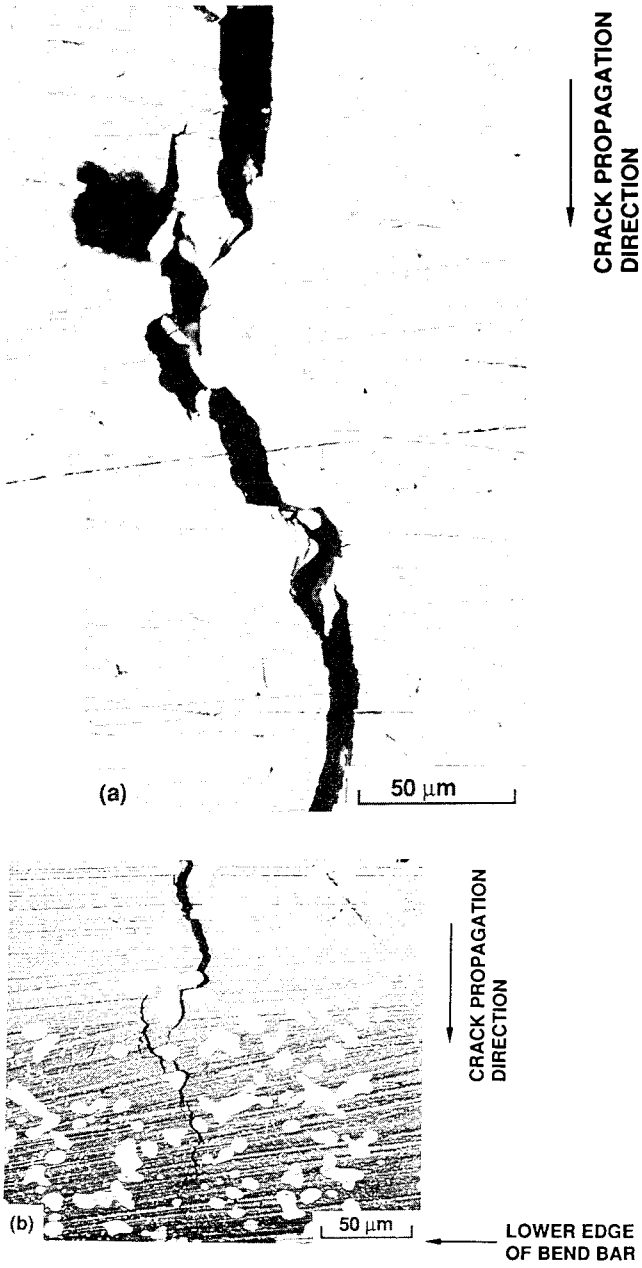


Fig. 10—Backscattered SEM micrographs from selected areas of the transverse surface of a notched bend specimen of the NiAl-23Mo alloy following crack propagation showing (*a*) crack deflection and (*b*) crack branching and crack tortuosity; this region represents the edge of the notched bend bar away from the notch root, where the crack has stopped without failing the specimen completely.

of the (Mo) phase is not fully utilized, which may explain the lack of dependence of toughness on the volume fraction of the primary (Mo) phase. Work is required on continuous Mo-wire–reinforced NiAl composites, where a crack front will be forced to advance through the (Mo) reinforcement but may permit some level of local interface debonding. This has been examined, to some extent by Bowman,[29] who reported bend strength *vs* temperature data for NiAl composites reinforced with continuous TZM Mo fibers. These composites exhibited a strong fiber-matrix bonding, resulting in rule-of-mixtures composite strengths. The composite toughness also was reported to be enhanced by the TZM fibers, although neither toughness data nor fracture morphologies were presented.

B. *Toughening Mechanisms*

The results clearly demonstrated that the enhancement of toughness in the NiAl-Mo alloys cannot be associated with any dominant toughening mechanism. Rather, the modest increase in toughness may be attributed to a number of factors, including (a) the fibrous morphology of the fine, eutectic (Mo) phase; (b) the interlocking

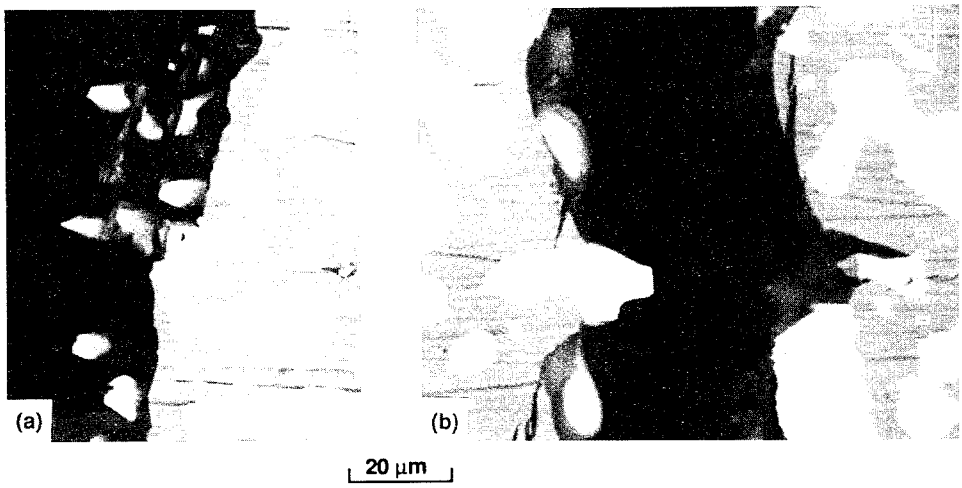


Fig. 11—Transverse section of a notched bend specimen of the NiAl-38Mo alloy taken prior to complete fracture, showing (*a*) plastic stretching of the (Mo) phase and (*b*) crack deflection along the (Mo)/NiAl interface.

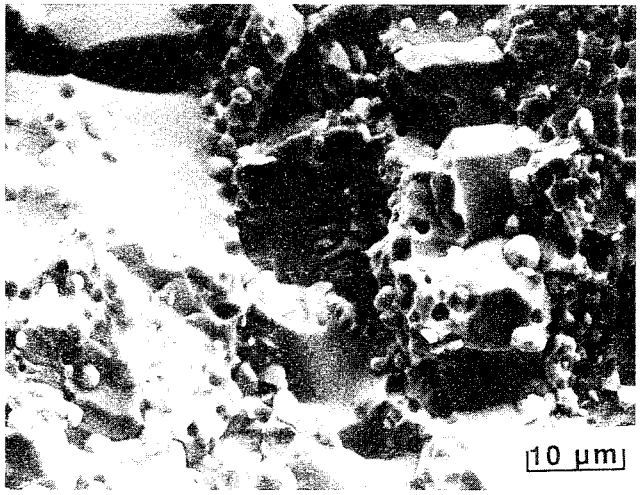


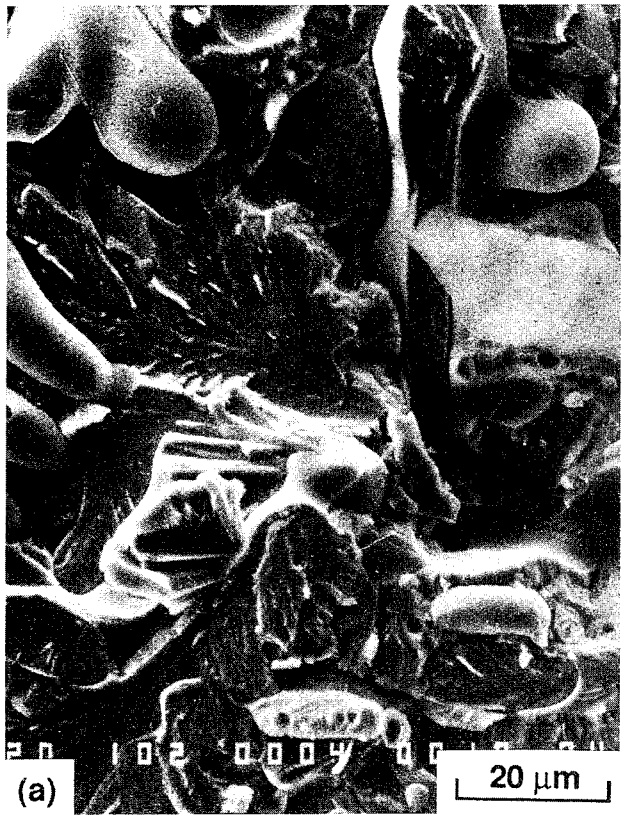
Fig. 12—SEM fractograph of forged + annealed NiAl-9Mo alloy, showing pullout of the coarse (Mo) particles and intergranular cracking of the elongated primary NiAl phase. Note that this sample was slightly hypoeutectic in composition.

morphology of the dendritic (Mo) phase in the microstructure; (c) crack deflection; and (d) small degree of crack/(Mo) phase interaction, leading to some energy dissipation by plastic stretching of the (Mo) phase. An increase in the volume fraction of the (Mo) phase did not produce a concomitant improvement in toughness as expected. In the alloys NiAl-23Mo and NiAl-38Mo, which contain 33 and 50 vol pct of primary (Mo) phase, respectively, the fraction of the (Mo) particles showing plastic stretching was roughly the same. Hence, an increase in the (Mo) volume fraction does not lead to an increase in the contribution to the toughness from the mechanism of stretching of the (Mo) phase.

In view of the complexity of the fracture behavior, it is difficult to rationalize the experimental results in terms of the analytical models[33–37] describing toughness behavior in ductile-phase composites, as these models are based on the concept of crack bridging and the work of rupture or stretching of the ductile phase. Whereas the inherent ductility of the (Mo) phase has not been independently established, indirect evidence from the fractographs in this investigation showed that, in regions where the dendrite arms are oriented normal to the crack front, the (Mo) phase showed ductile stretching prior to failure. However, only ~20 to 25 pct of the (Mo) particles showed plastic stretching in the NiAl-Mo alloys. As enumerated in the previous paragraph, other mechanisms contribute to the observed toughening; therefore, the complicated synergistic effects of these mechanisms cannot be quantified definitively as yet. Heredia and Valencia[26] reported toughness improvement in a DS NiAl/Mo fibrous eutectic alloy, the magnitude of which was similar to that observed in the present investigation. They attributed the toughness enhancement to both plastic stretching of the (Mo) fibers as well as "crack trapping," wherein the crack front circumvented the (Mo) fibers as it advanced through the eutectic microstructure, resulting in nonplanar fracture. Based on their observations, the authors concluded that ductile bridging does not fully explain the observed crack growth resistance. A quantitative analysis of these effects was not presented.

C. *Modulus Mismatch and Residual Stress Effects*

A difference in elastic properties between the reinforcement and the matrix causes stress concentration in the matrix around the reinforcement in the presence of an externally applied stress.[38] The propagation path of an advancing crack is influenced by these regions of stress magnification. In composites where the reinforcement is more compliant than the matrix, the propagating crack will be attracted toward the reinforcement. In the Mo/NiAl system, the room-temperature modulus of Mo (324 GPa)[39] is significantly higher than that of polycrystalline NiAl (188 GPa).[40] This modulus mismatch, therefore, will cause a crack to preferentially bypass the primary (Mo) reinforcement in favor of the NiAl matrix. Further, the additive effects of this elastic



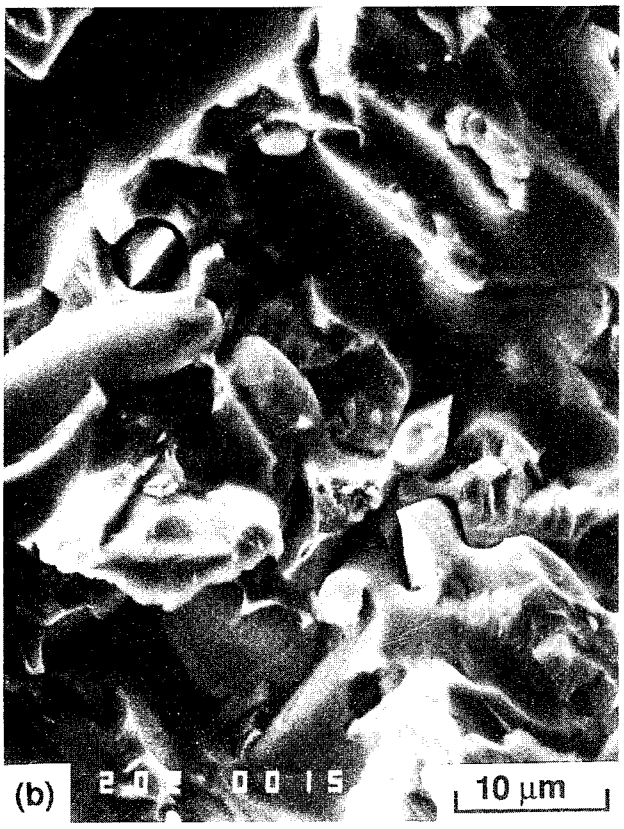


Fig. 13—SEM fractographs of the NiAl-Mo + Ti alloy: (*a*) shows regions of cleavage failure in the (Mo) phase and (*b*) shows regions of plastic stretching in the (Mo) phase.

mismatch in conjunction with the presence of a weak interface causes the advancing crack to propagate preferentially along the (Mo)/NiAl interface.[41,42]

Another consideration is the residual stresses generated due to thermal expansion mismatch between the reinforcing phase and the matrix. In the NiAl-Mo alloys, the reinforcing phase has a much lower thermal expansion coefficient than the matrix ($\alpha_{Mo} = 6.5 \times 10^{-6}/°C$;[43] $\alpha_{NiAl} = 15.1 \times 10^{-6}/°C$[44]). Consequently, the NiAl matrix next to the interface is under a residual axial tensile stress, the magnitude of which depends on the morphology of the reinforcing (Mo) phase. In most instances, this stress will influence the toughness behavior of the composite, because a residual tensile stress in the matrix will attract the advancing crack toward the reinforcement-matrix interface, as a consequence of its influence on the initial crack-opening force.[10] Since little or no bridging zone exists in the NiAl-Mo system, this residual stress will not have a direct effect on the toughness.[10] Even though this residual tensile stress aids in attracting the advancing crack toward the (Mo) phase, the experimental findings show that, in most instances, the cracks do not pass through the (Mo) reinforcement. Instead, they deviate from the (Mo) reinforcement and propagate preferentially along the interface. Hence, it appears that the overall fracture behavior is dominated by the weak interface between the (Mo) phase and the NiAl matrix, in conjunction with the elastic modulus mismatch.

D. *Addition of Ti*

Microalloying with Ti resulted in an enhancement of the fracture toughness without modifying the overall two-phase microstructure. Qualitative comparison of the fracture behavior of the NiAl-Mo-Ti alloy with the NiAl-38Mo base alloy showed more regions in the Ti-containing alloy where the crack intersected the (Mo) phase. This observation provides indirect evidence that the (Mo)/NiAl interface may be strengthened by Ti additions. The (Mo) phase in the Ti-containing alloy failed by cleavage in some locations and by ductile rupture in other locations. It is suggested that the small additions of Ti in solid solution in both (Mo) and NiAl may have resulted in subtle changes at the (Mo)/NiAl interface in order to cause the changes in the observed behavior.

E. *Effect of Hot Working*

Hot forging followed by annealing caused a noticeable change in the microstructural size scale and morphology of the NiAl-9Mo eutectic alloy. Similarly, the annealing treatment of the extruded NiAl-12Mo alloy produced a breakdown of the morphology of the eutectic (Mo) phase, resulting in spheroidization and coarsening. This is in direct contrast to the behavior in the as-cast alloys, which showed very stable microstructures even after extended annealing treatments. The hot-worked + annealed alloys showed only a moderate enhancement in toughness in comparison to the cast + annealed alloys, in spite of the much larger size of the (Mo) phase in the hot-worked alloys, thereby suggesting that it is the

(Mo)/NiAl interface that primarily controls the fracture properties.

V. SUMMARY AND CONCLUSIONS

This study has demonstrated that the terminal (Mo) phase can impart some measure of toughness to the brittle NiAl phase. The enhancement in toughness in comparison to monolithic NiAl ranged from ~5 to 11 MPa$\sqrt{m}$ in the cast + annealed NiAl-Mo alloys. Limited hot-working experiments showed that an additional increment in toughness may be possible by forging or extrusion treatments, followed by coarsening. No definite trend was observed in the toughness behavior with varying volume fraction of (Mo) in the alloys. Further, the NiAl-Mo alloys showed an increase in bend strength compared to monolithic NiAl above room temperature, with a reasonable strength retention up to ~800 °C, even though the overall strengths were very low. Fractography data showed that the fracture behavior in the NiAl-Mo alloys is very complex and not dominated by any single mechanism. Although thermal stresses attract the advancing crack toward the nominally ductile (Mo) phase, the weak interface between the (Mo) and NiAl phases, in combination with elastic modulus mismatch stresses, apparently causes an advancing crack to be deflected along the interface, thus reducing the potential for ductile-phase toughening in the NiAl-Mo system. Alloying with a small amount of Ti provided a ~40 pct improvement in fracture toughness compared to a base alloy of NiAl-38Mo. The exact mechanism responsible for this toughness enhancement remains unclear, although there is some evidence of interface strengthening with the Ti addition.

ACKNOWLEDGMENTS

This study was supported by United States Air Force Contract No. F33615-89-C-5604. The authors wish to acknowledge Dr. Dennis M. Dimiduk, Wright Laboratory, WL/MLLM, Wright-Patterson AFB, OH, for numerous technical discussions during the course of this study.

REFERENCES

1. D.F. Lahrman, R.D. Field, and R. Darolia: in *High-Temperature Ordered Intermetallic Alloys IV*, Materials Research Society Symposia Proceedings, L. Johnson, J.O. Steigler, and D.P. Pope, eds., Materials Research Society, Pittsburgh, PA, 1991, vol. 213, pp. 603-07.
2. E.R. Stover: Technical Report No. WADC-TDR-60-184, Air Force Materials Laboratory, Wright-Patterson Air Force Base, OH, 1966, vol. II (VII), pp. 1-42.
3. K.H. Hahn and K. Vedula: *Scripta Metall.*, 1989, vol. 23, pp. 7-12.
4. E.P. George and C.T. Liu: *J. Mater. Res.*, 1990, vol. 5, pp. 754-762.
5. P. Nagpal and I. Baker: *Scripta Metall.*, 1990, vol. 24, pp. 2381-84.
6. P. Nagpal and I. Baker: *Mater. Characterization*, 1991, vol. 27, pp. 167-73.
7. S. Reuss and H. Vehoff: *Scripta Metall.*, 1990, vol. 24, pp. 1021-26.
8. J.J. Lewandowski, G.M. Michal, I. Locci, and J.D. Rigney: in *Alloy Phase Stability and Design*, Materials Research Society Symposia Proceedings, G.M. Stocks, A.F. Giamei, and D.P. Pope, eds., Materials Research Society, Pittsburgh, PA, 1990, vol. 186, pp. 341-47.
9. A.G. Evans and R.M. McMeeking: *Acta Metall.*, 1986, vol. 34, pp. 2435-41.
10. L.S. Sigl, P.A. Mataga, B.J. Dalgleish, R.M. McMeeking, and A.G. Evans: *Acta Metall.*, 1988, vol. 36, pp. 945-53.
11. L.S. Sigl and H.E. Exner: *Metall. Trans. A*, 1987, vol. 18A, pp. 1299-1308.
12. G.R. Odette, B.L. Chao, J.W. Sheckherd, and G.E. Lucas: *Acta Metall. Mater.*, 1992, vol. 40, pp. 2381-89.
13. J.D. Rigney, J.J. Lewandowski, L. Matson, M.G. Mendiratta, and D.M. Dimiduk: in *High-Temperature Ordered Intermetallic Alloys IV*, Materials Research Society Symposia Proceedings, L. Johnson, J.O. Steigler, and D.P. Pope, eds., Materials Research Society, Pittsburgh PA, 1991, vol. 213, pp. 1001-06.
14. M.G. Mendiratta, J.J. Lewandowski, and D.M. Dimiduk: *Metall. Trans. A*, 1991, vol. 22A, pp. 1573-83.
15. S.B. Maslenkov and V.A. Rodimkina: *Izv. Akad. Nauk SSSR, Met.*, 1986, vol. 3, pp. 218-23.
16. I.I. Kornilov and R.S. Mints: *Izv. Sekt. Fiziko-Khim. Anal.*, 1955, vol. 26, pp. 62-66.
17. P.B. Budberg: *J. Inorg. Chem. (USSR)*, 1958, vol. 3, pp. 694-98.
18. J.G. Webber and D.C. Van Aken: *Scripta Metall.*, 1989, vol. 23, pp. 193-96.
19. P.W. Pellegrini and J.J. Hutta: *J. Crystallogr. Growth*, 1977, vol. 42, pp. 536-39.
20. J.L. Walter and H.E. Cline: *Metall. Trans.*, 1970, vol. 1, pp. 1221-29.
21. H.E. Cline, J.L. Walter, E. Lifshin, and R.R. Russell: *Metall. Trans.*, 1971, vol. 2, pp. 189-94.
22. P.R. Subramanian, M.G. Mendiratta, D.B. Miracle, and D.M. Dimiduk: in *Intermetallic Matrix Composites*, Materials Research Society Symposia Proceedings, D.L. Anton, P.L. Martin, D.B. Miracle, and R. McMeeking, eds., Materials Research Society, Pittsburgh, PA, 1990, vol. 194, pp. 147-54.
23. K. Sasaki, M. Morinaga, and N. Yukawa: in *Proc. Int. Symp. on Intermetallic Compounds-Structure and Mechanical Properties (JIMIS-6)*, O. Izumi, ed., The Japan Institute of Metals, Sendai, 1991, pp. 877-81.
24. R. Darolia, D.F. Lahrman, J. Dobbs, K.M. Chang, E.H. Goldman, and D.G. Konitzer: in *Ordered Intermetallics—Physical Metallurgy and Mechanical Behavior*, C.T. Liu, R.W. Cahn, and G. Sauthoff, eds., Kluwer Academic Publishers, The Netherlands, 1992, pp. 679-98.
25. D.R. Johnson, S.M. Joslin, B.F. Oliver, R.D. Noebe, and J.D. Whittenberger: in *Intermetallic Matrix Composites II*, Materials Research Society Symposia Proceedings, D.B. Miracle, D.L. Anton, and J.A. Graves, eds., Materials Research Society, Pittsburgh, PA, 1990, vol. 273, pp. 87-92.
26. F.E. Heredia and J.J. Valencia: in *Intermetallic Matrix Composites II*, Materials Research Society Symposia Proceedings, D.B. Miracle, D.L. Anton, and J.A. Graves, eds., Materials Research Society, Pittsburgh, PA, 1990, vol. 273, pp. 197-204.
27. K.M. Chang: in *Intermetallic Matrix Composites II*, Materials Research Society Symposia Proceedings, D.B. Miracle, D.L. Anton, and J.A. Graves, eds., Materials Research Society, Pittsburgh, PA, 1990, vol. 273, pp. 191-96.
28. R.D. Noebe, R.R. Bowman, and J.I. Eldridge: in *Intermetallic Matrix Composites*, Materials Research Society Symposia Proceedings, D.L. Anton, P. Martin, D.B. Miracle, and R. McMeeking, eds., Materials Research Society, Pittsburgh, PA, 1990, vol. 194, pp. 323-31.
29. R.R. Bowman: in *Intermetallic Matrix Composites II*, Materials Research Society Symposia Proceedings, D.B. Miracle, D.L. Anton, and J.A. Graves, eds., Materials Research Society, Pittsburgh, PA, 1990, vol. 273, pp. 145-55.
30. D.P. Mason, D.C. Van Aken, and J.G. Webber: in *Intermetallic Matrix Composites*, Materials Research Society Symposia

Proceedings, D.L. Anton, P.L. Martin, D.B. Miracle, and R. McMeeking, eds., Materials Research Society, Pittsburgh, PA, 1990, vol. 194, pp. 341-48.
31. A. Raman and K. Schubert: *Z. Metallkd.*, 1965, vol. 56, p. 99.
32. T.B. Massalski, H. Okamoto, P.R. Subramanian, and L. Kacprzak: *Binary Alloy Phase Diagrams*, 2nd ed., ASM INTERNATIONAL, Materials Park, OH, 1990, vol. 3, pp. 2675-79.
33. M.F. Ashby, F.J. Blunt, and M. Bannister: *Acta Metall.*, 1989, vol. 37, pp. 1847-57.
34. H.C. Cao, B.J. Dalgleish, H. Deve, C. Elliott, A.G. Evans, R. Mehrabian, and G.R. Odette: *Acta Metall.*, 1989, vol. 37, pp. 2969-78.
35. H.E. Deve, A.G. Evans, G.R. Odette, R. Mehrabian, M.L. Emiliani, and R.J. Hecht: *Acta Metall. Mater.*, 1990, vol. 38, pp. 1491-1502.
36. P.A. Mataga: *Acta Metall.*, 1989, vol. 37, pp. 3349-59.
37. K.S. Ravichandran: *Scripta Metall. Mater.*, 1992, vol. 26, pp. 1389-93.
38. R.W. Davidge and T.J. Green: *J. Mater. Sci.*, 1968, vol. 3, pp. 629-34.
39. *Metals Handbook*, Desk Edition, H.E. Boyer and T.L. Gall, eds., ASM INTERNATIONAL, Metals Park, OH, 1985, p. 1.47.
40. N. Rusovic and H. Warlimont: *Phys. Status Solidi A*, 1979, vol. 53, pp. 283-88.
41. M.Y. He and J.W. Hutchinson: *Int. J. Fract.*, 1976, vol. 12, pp. 187-99.
42. K.T. Venkateswara Rao, W.O. Soboyejo, and R.O. Ritchie: *Metall. Trans. A*, 1992, vol. 23A, pp. 2249-57.
43. *Smithells Reference Book*, 6th ed., E.A. Brandes, ed., Butterworth and Co., London, 1983, p. 14-1.
44. R.W. Clark and J.D. Whittenberger: in *Proc. 8th Int. Thermal Expansion Symp.*, T.A. Hahan, ed., Plenum Press, New York, NY, 1984, p. 189.

Effects of Texture Gradients on Yield Loci and Forming Limit Diagrams in Various Aluminum-Lithium Sheet Alloys

XIAO-HU ZENG and FRÉDÉRIC BARLAT

Marked through-thickness variations of preferred crystallographic orientations in aluminum-lithium (Al-Li) sheet alloys have been observed and documented. These metallurgical features could have an effect on the way in which these materials distribute strain during plastic deformation. From a theoretical or a practical point of view, it is important to investigate these texture effects on plastic-deformation properties and particularly on forming limit strains. In this work, quantitative texture data, which were determined by X-ray and neutron diffraction techniques, were used with a polycrystal model to predict the yield locus of recrystallized and unrecrystallized AA8090 and AA2090 Al-Li sheets. The conventional AA2024 alloy in the annealed condition was also investigated as a reference material. Subsequently, these yield loci were used to calculate forming limit diagrams (FLDs) in the stretching range, using the Marciniak–Kuczynski (M–K) approach with strain rate potentials to describe the constitutive properties of the sheets. A simple critical-thickness-strain criterion was used to predict the FLD in the drawing range. The predicted FLDs were found to be in fair agreement with experimental curves obtained under punch-stretching conditions. In general, experimental trends were accounted for by the results predicted using the average texture data. However, the texture gradients do not completely explain the large scatter observed in the experimental forming limits and the high average limit strain of the recrystallized AA8090.

I. INTRODUCTION

THE recently developed aluminum-lithium (Al-Li) alloys are particularly attractive to the aerospace industry because of their lower density and higher stiffness compared to conventional alloys. Usually, commercially produced Al-Li alloys have highly developed crystallographic textures, which lead to pronounced anisotropy of mechanical properties such as yield stress,[1,2] elastic modulus,[3,4] plastic flow,[4,5] and formability.[2,6,7] These pronounced directional properties are one of the main barriers that impede the replacement of conventional alloys by Al-Li alloys. Therefore, it is necessary to improve the understanding of the influence of crystallographic texture on the mechanical properties of Al-Li alloys. In addition, the prediction of mechanical properties is a useful tool for material, process, and product design. This theoretical study requires knowledge of the influence of crystallographic texture on the shape of the yield locus calculated with polycrystal models. The yield-locus shape strongly influences the plastic properties of materials. However, a strong through-thickness texture gradient has been observed in Al-Li alloys.[4,8,9] Therefore, it is important to know how this texture gradient influences the plastic properties. In previous articles the effect of a texture gradient on plastic anisotropy and yield strength for Al-Li 8090 and 2090 alloys was studied.[2,10] The purpose of the present work was to study the effects of a texture gradient on the yield-locus shape and the forming limit diagram (FLD) of Al-Li alloy sheets.

Yield loci can be assessed directly by mechanical measurements or can be predicted by phenomenological theories or polycrystal models. Experiments are expensive, time consuming, and difficult to perform and interpret. An interesting advantage of polycrystal models is that they only require simple and relatively standard experimental data as an input and the orientation distribution function (ODF) to compute the yield locus of a real material. Moreover, this theoretical approach concerning the plastic deformation of alloys can specifically address the influence of crystallographic texture on the shape of the yield locus. Finally, the yield locus can be used in conjunction with strain-hardening parameters to predict the level and shape of the FLD.

In the present work, through-thickness texture gradients have been determined systematically by X-ray texture analyses at various thickness locations in the sheets. An average texture was measured by neutron diffraction. This quantitative texture data was utilized for the prediction of yield loci. Subsequently, FLDs were calculated using these predicted yield loci as a constitutive description of the plastic behavior of the sheets[11,12] and criteria for local necking analysis.

II. THEORETICAL OUTLINE

A. *Polycrystal Model for Yield Surfaces*

The polycrystal yield surface approach used in the present article[13] is based on the Taylor[14]/Bishop–Hill[15] crystal plasticity theory (TBH). The yield locus constructed from this model is controlled by the ODF. This

XIAO-HU ZENG, Research Assistant, is with the Division of Engineering Materials, Department of Mechanical Engineering, Linköping University, S-581 83 Linköping, Sweden. FRÉDÉRIC BARLAT, Scientific Associate, is with the Alloy Technology Division, Alcoa Technical Center, Alcoa Center, PA 15069-0001.

Manuscript submitted February 14, 1994.

approach allows one to examine the effects of crystallographic texture effects on the shape of the yield locus. For anisotropic materials, the shape of the yield locus must be expressed in a material coordinate system.

In general, polycrystalline sheets are assumed to possess orthotropic symmetry, which is appropriate for a rolled sheet, and are assumed to be subjected to plane stress states, which is appropriate for many sheet-forming processes. Because the thickness of the sheets is very small compared to other dimensions, usually the stresses σ_{13}, σ_{23}, and σ_{33} are negligible. Here, 1, 2, and 3 denote the sheet rolling (RD), transverse (TD), and normal (ND) directions, respectively. If the principal stresses are superimposed on principal axes of anisotropy ($\sigma_{12} = 0$), the stress tensor can be expressed in these axes as

$$\boldsymbol{\sigma} = \begin{bmatrix} \sigma_1 & 0 & 0 \\ 0 & \sigma_2 & 0 \\ 0 & 0 & 0 \end{bmatrix} \quad [1]$$

Assuming constant volume during plastic deformation, the resulting plastic strain rate tensor is

$$\dot{\boldsymbol{\varepsilon}} = \dot{\gamma} \begin{bmatrix} 1 & 0 & 0 \\ 0 & -q & 0 \\ 0 & 0 & -(1-q) \end{bmatrix} \quad [2]$$

Because rate-independent plasticity is assumed, plastic strain rates are used in this article instead of plastic strain increments. The term $\dot{\gamma}$ is the absolute value of the strain rate and q is the ratio $-\dot{\varepsilon}_2/\dot{\varepsilon}_1$. In order for a strain to take place, a plastic work rate is necessary:

$$\dot{A} = \sigma_1\dot{\varepsilon}_1 + \sigma_2\dot{\varepsilon}_2 = \dot{\varepsilon}_1(\sigma_1 - q\sigma_2) \quad [3]$$

According to the Taylor model,[14] it is assumed that each slip system requires the same critical shear stress τ to become active and that the accumulated shear strain rate (the sum of the absolute shear strain rates on each active system) is a minimum. Therefore, the plastic work rate required to deform the polycrystal can be written as

$$\dot{A} = \tau \cdot \dot{\gamma} \quad [4]$$

The term τ is the critical resolved shear stress on the active slip systems. If the Taylor factor M is considered, $M = \sigma_1/\tau = \dot{\gamma}/\dot{\varepsilon}_1$, the mean value $\bar{M}$ over all the orientations g in a polycrystalline material can be expressed by a series of generalized spherical harmonics of the appropriate symmetry:[16]

$$\bar{M}(q) = \sum_{\lambda} \sum_{\mu} \sum_{\nu} \frac{m_\lambda^{\mu\nu}(q)\, C_\lambda^{\mu\nu}}{2\lambda + 1} \quad [5]$$

The $m_\lambda^{\mu\nu}$ values are the coefficients of the series expansion of the Taylor factor M associated with a particular deformation mode. The $C_\lambda^{\mu\nu}$ values are the coefficients describing the distribution of grain orientations of the specimens. The yield locus is defined by the principal stresses σ_1 and σ_2 at which plastic deformation initiates.[16] From the previous equations, these stresses can be expressed by

$$\sigma_1 = \tau[\bar{M} - q\bar{M}'(q)]$$
$$\sigma_2 = \tau[-\bar{M}'(q)] \quad [6]$$

Using the series expansion, the yield locus can be written as

$$\sigma_i = \tau \sum_{p=0}^{\Lambda} S_{ip} \cdot q^p \quad i = 1,2 \quad [7]$$

with

$$S_{ip} = \sum_{\lambda=0}^{L} \sum_{\mu=1}^{M} \sum_{\nu=1}^{\lambda} \frac{S_\lambda^{\mu\nu}(i,p) \cdot C_\lambda^{\mu\nu}}{2\lambda + 1}$$

B. *Phenomenological Constitutive Description of the Plasticity of Materials*

The preceding polycrystal yield loci can be approximated in the biaxial range by yield loci obtained from a strain rate potential proposed recently[11,12] for anisotropic materials, which is particularly suitable for fcc and bcc polycrystals.

$$\psi(\xi_i) = \left|\frac{2\xi_1 - \xi_2 - \xi_3}{3}\right|^m + \left|\frac{2\xi_2 - \xi_3 - \xi_1}{3}\right|^m + \left|\frac{2\xi_3 - \xi_1 - \xi_2}{3}\right|^m = 2\dot{\varepsilon}_e \quad [8]$$

where

$$\xi_1 = 2\sqrt{I_2}\cos\left(\frac{\theta}{3}\right)$$
$$\xi_2 = 2\sqrt{I_2}\cos\left(\frac{\theta - 2\pi}{3}\right)$$
$$\xi_3 = 2\sqrt{I_2}\cos\left(\frac{\theta + 2\pi}{3}\right) \quad [9]$$

$$I_2 = \frac{[c_3(\dot{\varepsilon}_{11} - \dot{\varepsilon}_{22}) - c_2(\dot{\varepsilon}_{33} - \dot{\varepsilon}_{11})]^2}{54} + \frac{[c_1(\dot{\varepsilon}_{22} - \dot{\varepsilon}_{33}) - c_3(\dot{\varepsilon}_{11} - \dot{\varepsilon}_{22})]^2}{54} + \frac{[c_2(\dot{\varepsilon}_{33} - \dot{\varepsilon}_{11}) - c_1(\dot{\varepsilon}_{22} - \dot{\varepsilon}_{33})]^2}{54} + \frac{(c_4\dot{\varepsilon}_{23})^3 + (c_5\dot{\varepsilon}_{31})^2 + (c_6\dot{\varepsilon}_{12})^2}{3} \quad [10]$$

$$I_3 = \frac{[c_3(\dot{\varepsilon}_{11} - \dot{\varepsilon}_{22}) - c_2(\dot{\varepsilon}_{33} - \dot{\varepsilon}_{11})][(c_1(\dot{\varepsilon}_{22} - \dot{\varepsilon}_{33}) - c_3(\dot{\varepsilon}_{11} - \dot{\varepsilon}_{22})][c_2(\dot{\varepsilon}_{33} - \dot{\varepsilon}_{11}) - c_1(\dot{\varepsilon}_{22} - \dot{\varepsilon}_{33})]}{54}$$
$$- \frac{[c_3(\dot{\varepsilon}_{11} - \dot{\varepsilon}_{22}) - c_2(\dot{\varepsilon}_{33} - \dot{\varepsilon}_{11})]\,(c_4\dot{\varepsilon}_{23})^2}{6} - \frac{[c_1(\dot{\varepsilon}_{22} - \dot{\varepsilon}_{33}) - c_3(\dot{\varepsilon}_{11} - \dot{\varepsilon}_{22})](c_5\dot{\varepsilon}_{31})^2}{6}$$
$$- \frac{[c_2(\dot{\varepsilon}_{33} - \dot{\varepsilon}_{11}) - c_1(\dot{\varepsilon}_{22} - \dot{\varepsilon}_{33})](c_6\dot{\varepsilon}_{12})^2}{6} + c_4c_5c_6\dot{\varepsilon}_{23}\dot{\varepsilon}_{31}\dot{\varepsilon}_{12}$$
$$\theta = \cos^{-1}\left(\frac{I_3}{I_2^{3/2}}\right) \qquad [11]$$

In the preceding set of equations, c_j are material coefficients that characterize material anisotropy. The deviatoric stress is generated by the gradient of the potential ψ with respect to the strain rate:

$$\sigma'_{ij} = \mu \frac{\partial \psi}{\partial \dot{\varepsilon}_{ij}} \qquad [12]$$

where μ is a proportionality constant. For a plane stress state, c_1, c_2, c_3, and c_6 are the only relevant coefficients. Moreover, for plastic states that do not involve shear strains, the parameter c_6 does not need to be evaluated. Equations [8] through [12], together with the assumption of isotropic work hardening, completely define the constitutive behavior of the material. In a previous work,[17] the Voce equation was identified as best fit to the flow curves of the various Al-Li alloy sheet materials. Therefore, in this work, the Voce strain-hardening relationship between effective stress and strains is used.

C. *Predicted Forming Limit Diagrams*

Formability of the Al-Li alloy sheets studied was assessed by the FLD, which represents in the plane of principal strains the limit above which localized necking occurs. In the drawing range, where the minor strain is negative, the FLD was predicted with a critical thickness criterion. This criterion has been shown to be valid for a large variety of materials, and it is consistent with different theories of plastic-flow localization,[18] in particular with Hill's classic approach.[19] However, this theory does not predict limit strains in the biaxial stretching range, where both surface strains of the sheet are positive. In this case, the FLDs were predicted using the M–K analysis.[20] In this approach, the material is assumed to contain structural heterogeneities, modeled by a linear imperfection and quantified by an imperfection parameter F. This parameter is less than one or equal to one for real and perfect materials, respectively. In the M–K approach, plastic flow of the material subjected to well-defined boundary conditions is studied. The ratio of the effective strain rate in the homogeneous part of the material to that in the imperfection is computed at each increment of the deformation. The forming limit is obtained when this ratio reaches zero, which means that the plastic deformation localizes in the imperfection. A more detailed discussion of the M–K analysis can be found in References 21 and 22.

The material description is an important parameter that has a strong influence on predicted limit strains.[23,24] In the current article, the strain rate potential described in Section B was used along with the Voce strain-hardening behavior. The coefficients of the strain rate potential were calculated so as to obtain the best fit between the associated yield locus and the yield locus computed with the polycrystal model. Because necking was observed to occur in the stretching range either in the rolling or in the transverse direction, the initial linear imperfection (necking band) was assumed to pre-exist only in these two directions. With this assumption, only plane stress states lying on the yield locus between the two-plane strain tension states, in the rolling or in the transverse direction, are relevant.[22] Therefore, the strain-rate-potential coefficients were optimized so as to get the best fit between the phenomenological and the polycrystal yield loci in this limited range of stress states only.

III. EXPERIMENTAL DETAILS

A. *Materials*

Four aluminum alloys in the form of sheet with a nominal thickness of 1.6 mm are included in the present study. The nominal chemical compositions of the alloys are listed in Table I. Two variants of AA8090 alloy sheets were supplied by Alcan (Banbury, UK). One variant, a recrystallized sheet, was in the T3 condition. The second variant, an unrecrystallized sheet, was in the T4 condition. These as-received materials were solution heat-treated at 530 °C for 20 minutes and quenched in room-temperature water. Testing was performed either in the as-quenched condition or in the as-quenched and subsequently stretched condition. The AA2090 alloy was received from ALCOA* in the T3 temper condition. This material was stretched 1-1.5 pct at Saab-Scania AB (Linköping, Sweden). The conventional aluminum-copper-magnesium alloy AA2024-O was used as a reference material. In the following discussion, the specimens are designated by letters A to F, corresponding to Table II. In this table, details of the various thermomechanical treatments are also given.

*ALCOA is a trademark of the Aluminum Company of America, Pittsburgh, PA.

Table I. Alloy Compositions in Weight Percent

Alloy	Li	Cu	Mg	Zr	Mn	Fe	Si	Al
AA8090	2.2 to 2.7	1.0 to 1.6	0.6 to 1.3	0.04 to 0.16	—	0.30 max	0.20 max	balance
AA2090	1.9 to 2.6	2.4 to 3.0	0.0 to 0.25	0.08 to 0.15	—	0.12 max	0.10 max	balance
AA2024	—	3.8 to 4.9	1.2 to 1.8	—	0.3 to 0.9	0.50 max	0.50 max	balance

Table II. Thermomechanical Treatments of Alloys

Name	Alloy	As-received Condition	Thermomechanical Treatment	Final Grain Structure
A	AA8090	T3, recrystallized	solution treated	recrystallized
B	AA8090	T3, recrystallized	solution treated + 3.5 pct stretch	recrystallized
C	AA8090	T4, unrecrystallized	solution treated	unrecrystallized
D	AA8090	T4, unrecrystallized	solution treated + 2.5 pct stretch	unrecrystallized
E	AA2090	T3, unrecrystallized	naturally aged + 1 to 1.5 pct stretch	unrecrystallized
F	AA2024	O, recrystallized	none	recrystallized

B. *Mechanical Test*

The dimensions of the tensile specimens followed ASTM standards E646. Uniaxial stress-strain tests were performed at room temperature and at a strain rate of 3×10^{-4}/s. The specimens for the determination of the FLDs were cut from the plane of the sheet at 0 deg and 90 deg to the rolling direction. The length of the specimens was 200 mm and their widths were either 20, 60, 90, 160, or 200 mm in order to achieve different strain paths. The specimens were deformed by a 100-mm-diameter hemispherical steel punch using a 0.1-mm-thick TEFLON* sheet for lubrication. A 2-mm circular grid pattern was applied by photographical printing and electrochemical etching on each of the specimens. The major and minor strains were measured from the deformed circles close to the necked region (*i.e.*, the limit strains used in this article are necking limits, not fracture limits).

*TEFLON is a trademark of E.I. Du Pont de Nemours and Co., Inc., Wilmington, DE.

C. *Texture Determination*

The dimensions of the samples used for X-ray texture measurements to examine the variation of texture through the thickness of a given sheet were about 20 × 20 × 1.6 mm. The position of the examined layer was defined by $s = 2\Delta t/t_0$, with Δt and t_0 being the distance from the sheet center of the examined layer within the sample and the initial sheet thickness (1.6 mm), respectively. The X-ray texture measurements were made at s = 1, 0.88, 0.63, 0.5, 0.16, and 0, corresponding to the surface, 0.1, 0.3, 0.4, 0.55 mm below surface and the center of the sheet, respectively. The samples used for neutron-diffraction texture measurements were cylindrical and were prepared by stacking five circular discs of 14-mm diameter on top of each other. The texture measurements were made with a Seifert (Ahrensburg, Germany) PTS goniometer using the Schulz reflection method with Cu K_α radiation. Pole figures were corrected for defocusing and background using a commercial-pure Al powder sample. The experimental setup used during the neutron texture measurements at the Risø (Roskilde, Denmark) reactor DR3 has been described by Juul Jensen and Leffers.[25] The {111}, {200}, {220}, and {311} pole figures (no. {311} measurement for the surface and center layers) were determined on different layers by X-ray diffraction to determine the through-thickness texture gradient, and the {111}, {200}, and {220} pole figures were determined over the full-sheet thickness by neutron diffraction to obtain an average texture. Using this data, the ODFs were calculated according to Bunge's series-expansion method.[26] In the present work, the series expansion was truncated at the order $l = 22$.

IV. RESULTS AND DISCUSSION

A. *Characterization of Texture*

In previous studies, the marked through-thickness variations of textures in Al-Li sheets were observed by the electron backscattering pattern (EBSP) technique[9] and X-ray diffraction.[4,9] These variations can also be found in conventional AA2024 Al alloy sheet.[10] A detailed description of the textures of the materials investigated in this article was given in Reference 10. In recrystallized Al-Li (AA8090) and common AA2024 sheets, the main texture component at the sheet surface is the classical recrystallization component: the cube texture. The Goss texture {110}⟨100⟩ is the main component at the center of these sheets. Additionally, in AA2024, a strong P orientation {011}⟨122⟩ is observed. In the unrecrystallized Al-Li (AA8090), a strong shear texture with the orientation {100}⟨110⟩ is present at the surface. In the center area of the sheet, the texture is mainly of the type {011}⟨223⟩, which is typical for cross-rolled materials. In unrecrystallized AA2090, a transition texture from the copper orientation near the surface to the brass orientation in the middle of the sheet is observed.

B. *Prediction of the Average Crystallographic Yield Loci*

Figure 1 shows the yield loci for samples A, C, E, and F in the tensile range, predicted using the bulk-average-texture data that was determined by neutron

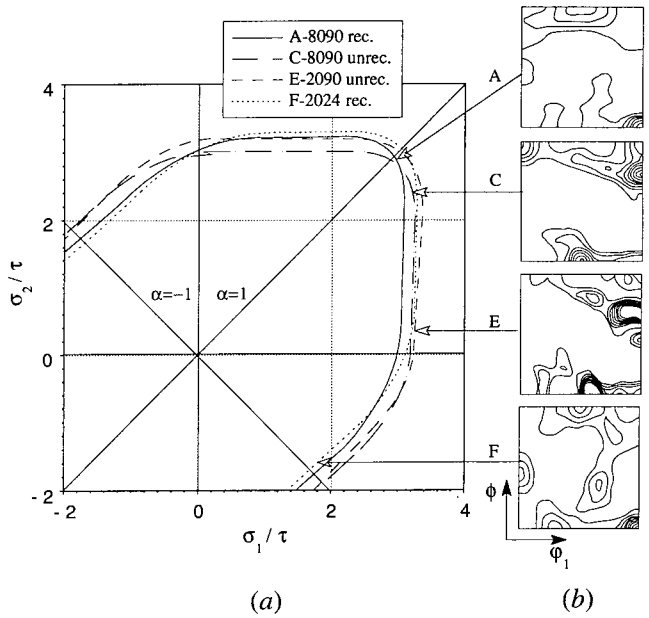


Fig. 1—(*a*) Crystallographic yield loci predicted from bulk average texture data determined by neutron diffraction, (*b*) corresponding $\varphi_2 = 45$ deg section of ODFs. The specimens are designated as sample A-recrystallized 8090, sample C-unrecrystallized 8090, sample E-unrecrystallized 2090 with stretch, and sample F-recrystallized 2024.

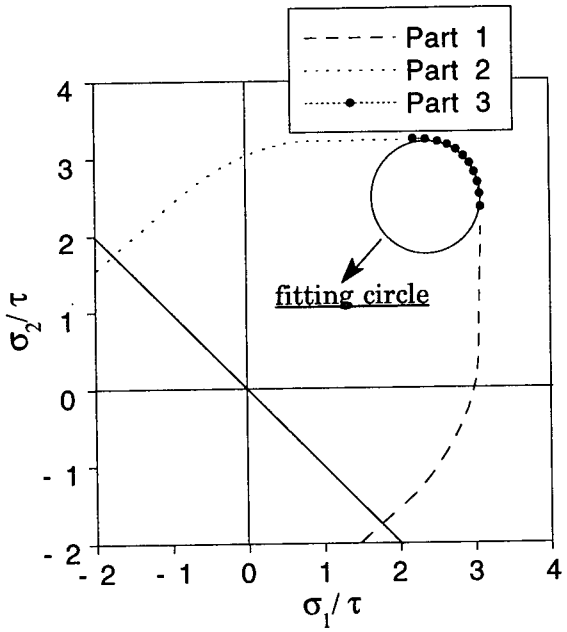


Fig. 2—Schematic description of the yield locus consisting of three parts and curvature of yield locus fitted by a circle equation.

diffraction. The curvature of the locus in the equibiaxial tension region is one important factor that affects the FLD.[27] The shape of the yield locus near this region can lead to substantial differences in the FLD. Zhou and Lian[28] used a parameter $\beta = (\sigma_{p1} - \sigma_b)\sigma_b/(\sigma_b - \sigma_{p2})\sigma_u$ to describe the characteristics of the shape of the yield loci, where σ_{p1} and σ_{p2} are the major and minor yield stresses in plane strain tension, respectively. The terms σ_b and σ_u are the yield stresses in balanced biaxial tension and in uniaxial tension, respectively. In Bunge's theory,[13] a complete yield locus in the tensile range is composed of three parts (Figure 2) with three different sets of coefficients $s_{\lambda ip}$, as appear in Eq. [7]. In this work, one of the three parts (part 3) corresponds to the stress states near equibiaxial tension ($\sigma_1 = \sigma_2$) that include the vertex of the locus. For the sake of simplicity, the equation of a circle was used to fit the yield locus in order to get the curvature of the locus in the vertex area, as shown in Figure 2. In other words, the curvature of the yield locus was obtained by a fitting program using an equation of $(\sigma_1/\tau - a)^2 + (\sigma_2/\tau - b)^2 = R^2$, where a and b are the coordinates of center of a circle and R ($= 1/\rho$) is the radius of a circle. It should be mentioned that the fit was applied on the curvature symmetry rather than the α-axis symmetry. The results of radius and curvature are given in Table III for the materials investigated in this work.

Kocks *et al.*[29] reported that flat grains due to rolling produce a region of higher curvature of the yield locus near equibiaxial tension. The grain structure of the various materials studied in the present work has been discussed in a previous article.[10] Generally, the grains are flattened and elongated in the rolling direction. This feature is less pronounced in the microstructure of the recrystallized AA8090 sheets than in the other materials. In the present study, the yield loci for unrecrystallized Al-Li alloy sheets display a slightly higher curvature near equibiaxial tension than those calculated for the recrystallized sheets. However, it is difficult to separate the influence of flat grains or texture on the curvature of the yield locus.

In the second and fourth quadrants of Figure 1 (near the line $\alpha = \sigma_2/\sigma_1 = 1$, which is related to flange deformation in deep drawing), the yield locus is larger for the unrecrystallized materials than for the recrystallized materials. The yield locus is larger in the stress states near the line $\alpha = 1$ (balanced biaxial tension), whereas it is smaller in the stress states near the line $\alpha = 1$ for the conventional AA2024 sheet compared to Al-Li sheets. An additional observation is that the yield locus exhibits higher symmetry with respect to the axis $\alpha = 1$ for recrystallized AA8090 and AA2024 than for unrecrystallized AA8090 and AA2090. The yield locus of the conventional AA2024 shows almost a mirror reflection with respect to this axis while the AA2090 sheet shows the largest distortion.

Table III. Curvature of Yield Locus

Materials	A	B	C	D	E	F
Radius (R)	0.9094	0.9022	0.8779	0.8090	0.8800	0.8976
Curvature (ρ)	1.0996	1.1084	1.1391	1.2353	1.1364	1.1141

C. *The Effect of the Texture Gradient on the Yield Locus*

The predicted crystallographic yield loci for the various layers, using texture data determined by X-ray diffraction as an input, are shown in Figure 3(a) for the recrystallized AA8090 sheet A, Figure 3(c) for the unrecrystallized AA8090 sheet without stretch C, Figure 3(e) for the unrecrystallized AA2090 sheet with stretch E, and Figure 3(g) for the recrystallized 2024 sheet F. Figures 3(b), (d), (f), and (h) give the corresponding ODFs in $\varphi_2 = 45$ deg sections for the $s = 0$, $s = 0.63$, and $s = 1$ layers, respectively. These figures show that the texture gradient through the sheet thickness is expected to result in yield locus shape changes. As mentioned previously, the main texture components on the surface are the cube and rotated-cube orientations for recrystallized and unrecrystallized AA8090 sheets, respectively. Therefore, the yield locus of the surface layers is dominated by the cube or the rotated-cube texture for materials A through D. It is possible to correlate the variation of intensity of cube texture through the sheet thickness (Figure 6 of Reference 10) with the variation of curvature of the yield loci shown in Figures 4(a) and (b) for recrystallized and unrecrystallized materials, respectively. It is important to discuss the curvature of the yield locus in the equibiaxial tension range because, as it will be shown subsequently, the balanced biaxial forming limit increases as this curvature decreases. For recrystallized materials, the yield surface curvature near equibiaxial tension ($\alpha = \sigma_2/\sigma_1 = 1$) tends to increase from the center to the surface of the sheet. In fact, for

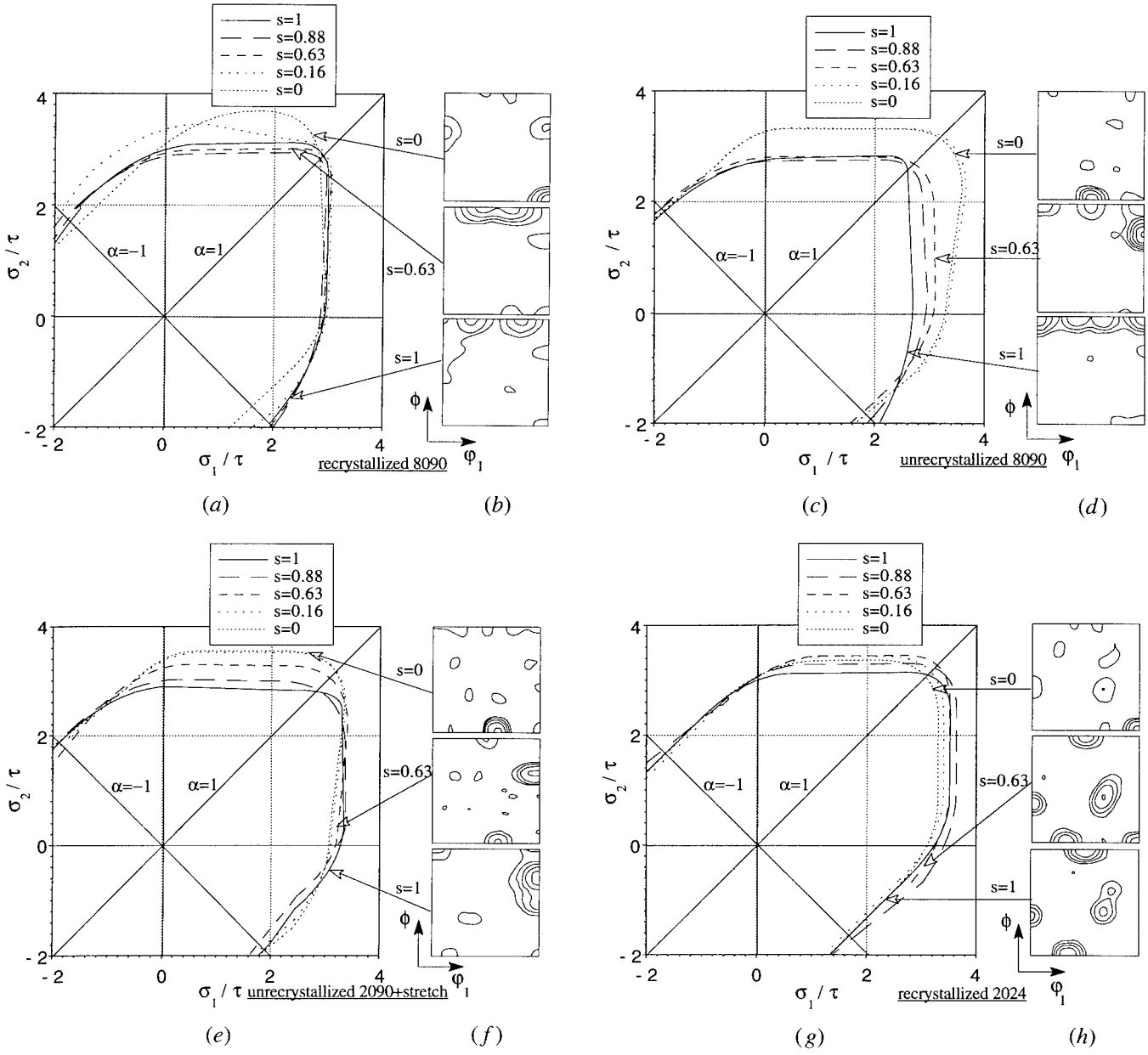
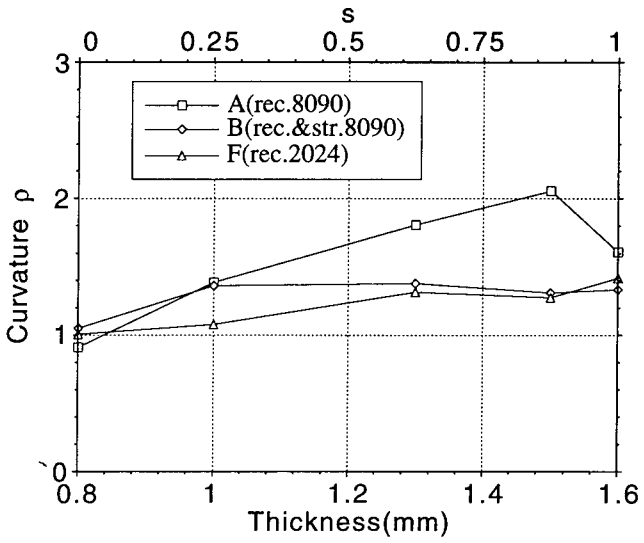
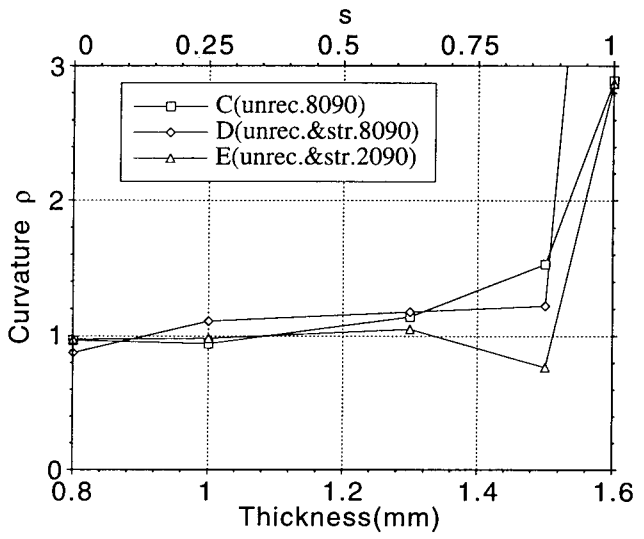


Fig. 3—Effect of texture gradient on the yield locus for (*a*) recrystallized 8090-sample A, (*c*) unrecrystallized 8090-sample C, (*e*) unrecrystallized 2090 with stretch-sample E, (*g*) recrystallized 2024-sample F. (*b*), (*d*), (*f*), and (*h*) are the corresponding ODF in $\varphi_2 = 45$ deg section for the $s = 0$, $s = 0.63$, and $s = 1$ layers, respectively.



(*a*)



(*b*)

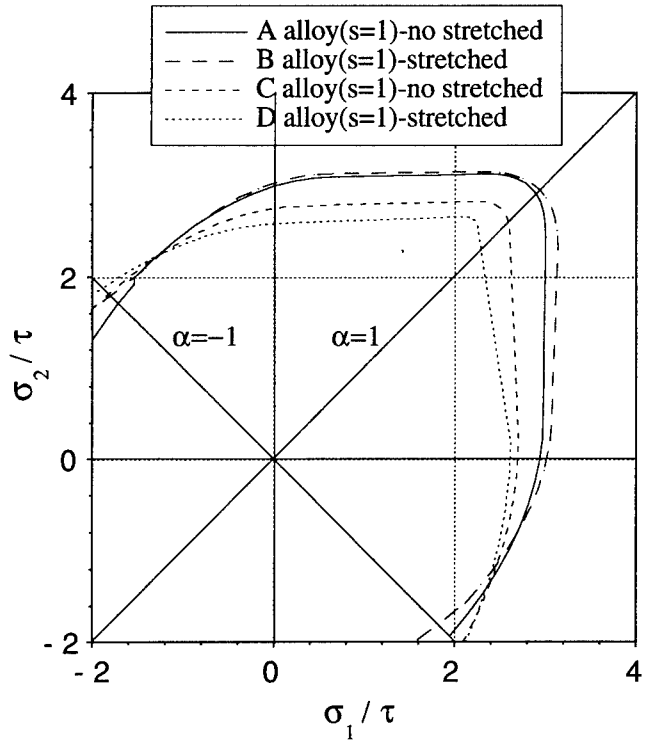
Fig. 4—The variation of curvature of yield locus across the sheet thickness (s = 0 is at center and s = 1 is at surface) for (*a*) recrystallized 8090 and recrystallized 8090 with stretch and recrystallized 2024 and (*b*) unrecrystallized 8090, unrecrystallized 8090 with stretch, and unrecrystallized 2090 with stretch.

the recrystallized AA8090 Al-Li sheets, the yield locus curvature is much smaller for the center layer than for the surface layer. This could be due to the lower amount of cube orientations in the center layer of the sheets. For unrecrystallized materials, the curvature of the yield locus is fairly constant, except at the surface of the sheet. However, in this type of material, the surface is usually covered with a thin layer of very coarse recrystallized grains. Because, in this case, the number of grain orientations measured becomes very small, the texture tends to approach that of a multicrystal. This factor can explain the very sharp yield locus at the surface of these sheets.

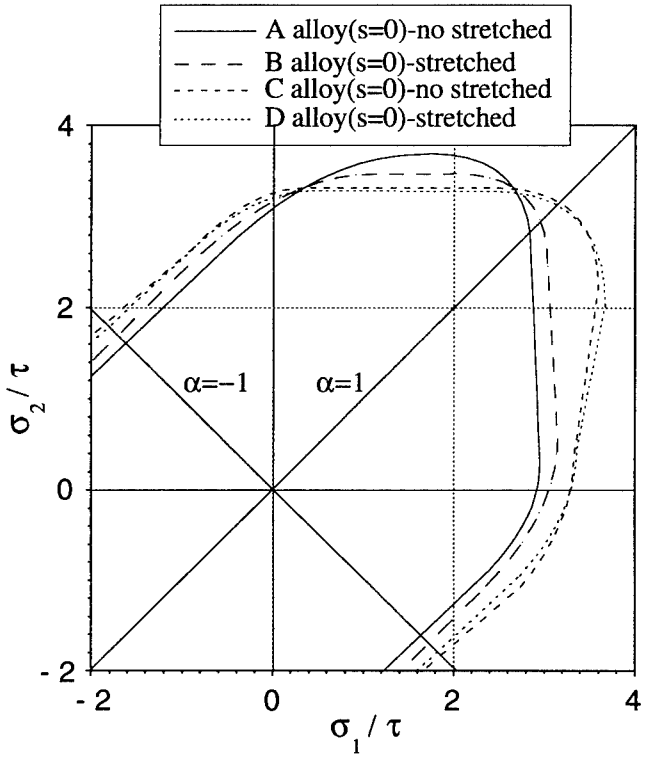
One feature of the yield locus for an isotropic texture is its high symmetry with respect to the axis $\alpha = \sigma_2/\sigma_1 = 1$. When the grain orientation distribution is not isotropic, the yield locus tends to be distorted in the σ_1 or σ_2 direction (*i.e.*, the yield locus does not display the mirror reflection with respect to the axis $\alpha = 1$). Barlat and Richmond[23] have predicted the yield loci for ideal orientations such as Cube, Goss, copper, brass, and S textures. Their results showed that Cube, copper, and S orientations give more symmetrical loci with respect to the axis $\alpha = 1$ than Brass and Goss texture components, and that the loci calculated from the ideal Brass and Goss texture are distorted on the σ_2 direction. When the parameter s decreases (nearer to the center of the sheet thickness), the size of the yield locus tends to be distorted in both σ_1 (RD) and σ_2 (TD) directions for the unrecrystallized AA8090 sheets and in the σ_2 (TD) direction only for the AA2090 sheet (Figure 3). It is also observed that as parameter s decreases, the balanced biaxial stress increases due to the variation in crystallographic texture. The distortion occurring in the σ_2 direction for unrecrystallized AA2090 can be rationalized by the fact that the Bs orientation {011}⟨211⟩ develops as the main component of the texture when s decreases. The major texture component in the center area for the unrecrystallized AA8090 sheet is the Bs-type {011}⟨322⟩, rotated about 10 deg from the Bs orientation {011}⟨211⟩. This is probably why a small distortion occurred only along the σ_1 direction. The shape of the yield locus calculated for the center layer of the recrystallized AA8090 sheet is characterized by a strong Goss texture. Therefore, the distortion consists of a pronounced flattening of the yield locus in the σ_2 direction in the entire biaxial range.

D. *The Effect of Prestretch on the Yield Locus*

The effect of prestretch on the shape of the yield locus is illustrated in Figures 5(a) and (b). In a previous article,[10] it was shown that a small amount of stretch did not influence the types of texture components, but it did change their intensity. The present study indicates that these changes of texture intensity could affect the yield locus shape and size. Figure 5 shows significant change in both the shape and size of the yield loci, particularly at the center (s = 0) of the recrystallized Al-Li sheets (A and B) and at the surface (s = 1) of the unrecrystallized sheets (C and D). However, the loci obtained at the center of the unrecrystallized Al-Li sheets (C and D) and at the surface of the recrystallized sheets (A and B) are not very different from each other in shape and size. These trends correlate well with the texture intensity (*i.e.*, a slight stretch is associated with more change in the center texture intensity than in the surface texture intensity for recrystallized Al-Li sheets). The reverse is true for unrecrystallized Al-Li alloy sheets. The very sharp corner developing near the balanced biaxial range is another feature of the yield locus at the surface for unrecrystallized Al-Li alloy sheets subjected to stretch. This sharp corner could be due to a significant increase of the intensity of the surface texture during the stretch. Finally, it is interesting to note that a slight stretch increases the shear stress (near the axis $\alpha = -1$) of the recrystallized AA8090 sheet (sample B) at midthickness, but it decreases the shear stress for the unrecrystallized



(*a*)



(*b*)

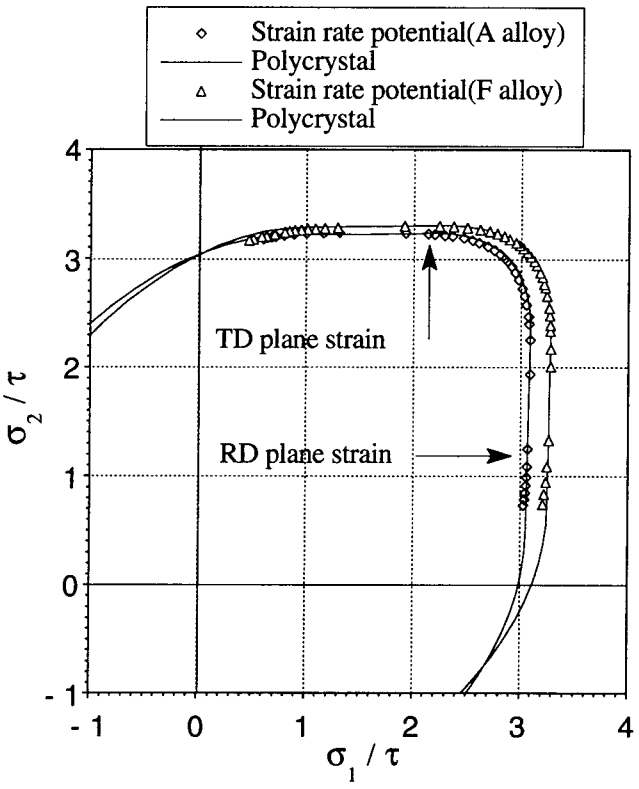
Fig. 5—Effect of stretch on the yield locus of (*a*) surface layers and (*b*) center layers for recrystallized and unrecrystallized 8090 materials.

AA8090 sheet (sample D) at midthickness. These observations indicate that the intensity of the crystallographic texture strongly influences the shape and size of yield loci.

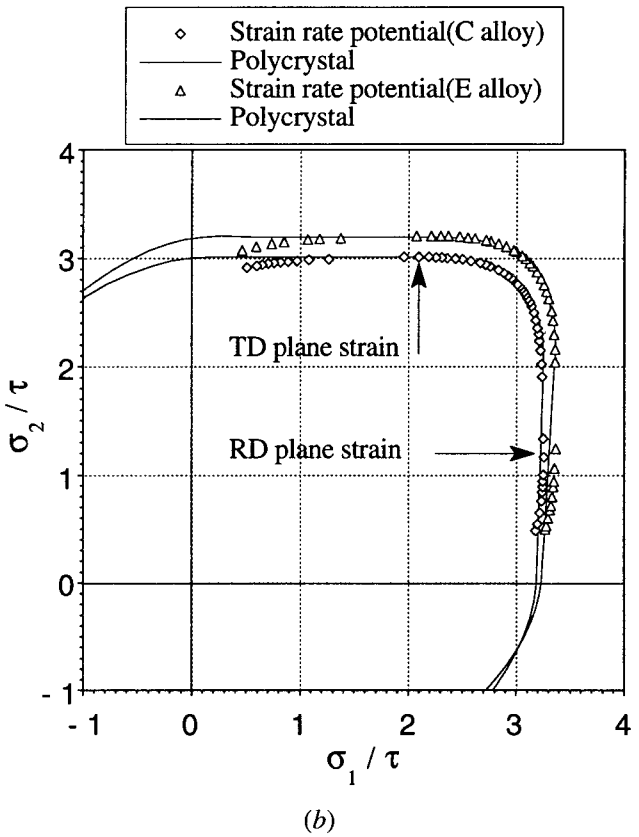
E. *Forming Limit Diagrams*

The maximum strains that can be obtained in sheet materials prior to the onset of localized necking are generally referred to as the forming limit strains. An FLD represents the relation between the major and minor principal limiting strains in the plane of the strained sheet. The FLDs were predicted in the stretching range ($\varepsilon_2 > 0$) using the M–K analysis with the strain rate potential to describe the materials' plastic behavior. Actually, because the neck was either in the rolling or in the transverse direction, only the plane stress yield locus (σ_1, σ_2) between these two stress states was necessary for the M–K analysis. That is why the coefficients of the strain rate potential were optimized so that the corresponding yield locus fits the polycrystal yield locus in this stress range. Figure 6 shows the polycrystal yield loci for the average textures of materials A, C, E, and F, together with the yield loci calculated using the strain rate potential. The stress states corresponding to plane strain tension are indicated by arrows. The crystallographic yield loci for the different materials (A, B, C, D, E, and F) and at the different thickness locations were all approximated with the strain rate potential (Eq. [8]). A larger value of the curvature of the vertex generally corresponds to a smaller exponent m. For instance, for the recrystallized AA8090 sheet, the curvature $\rho = 1.64$ is associated to an exponent $m = 1.2$ at the surface and $\rho = 0.91$ is associated to $m = 1.4$ at midthickness.

In many cases, the M–K analysis has been used as a tool to develop an understanding of the effect of material parameters, such as strain hardening,[20,30,31] strain rate sensitivity,[32,33] plastic anisotropy,[34,35,36] and yield surface shape,[21,37,38] on the FLD. In this work, the M–K approach is used in conjunction with the strain rate potential to predict FLDs. The limit strains calculated for the right-hand side ($\epsilon_2 > 0$) of the FLD are given in Figures 7(a) through (c) for samples A, C, and E, respectively. The behavior on the left-hand side of the FLD ($\varepsilon_2 < 0$) cannot be predicted with only the planar yield locus (σ_1, σ_2). Some information about the shear stress is also necessary for these predictions.[24] However, as explained in Section II–C, the left-hand side of the FLD can be approximated by a simple critical-thickness-strain criterion. The results of Figures 7(a) through (c) show that the limit strains in the biaxial stretching range predicted with the M–K model are very sensitive to the yield locus shape. For samples A, C, and E, the FLDs were computed for the surface layer, the center layer, and the average full thickness of the sheet. For each of these materials, the strain-hardening curve and the imperfection parameter $F = 0.996$ were kept constant. Only the yield locus shape was varied according to the corresponding texture. Figures 7(a) through (c) indicate that the limit strains of the center layers are obviously higher than those of the surface layers. This is a result of the higher curvature of the yield loci at the surface of the materials, as shown in Figures 3(a), (c), (e), and (g),



(*a*)



(*b*)

Fig. 6—Fitting crystallographic yield loci predicted from bulk average texture to obtain the strain rate potential: (*a*) recrystallized 8090-sample A and recrystallized 2024-sample F and (*b*) unrecrystallized 8090-sample C and unrecrystallized 2090-sample E.

implying that the center textures may be more desirable from a stretch-forming point of view.

Forming limit diagrams calculated from the bulk average texture data are closer to forming limit diagrams calculated from center layer textures than those calculated from the surface layer textures (Figure 7). This trend is more significant for unrecrystallized alloys than for recrystallized alloys. This means that, with respect to the limit strains, the center texture is more dominant than the surface texture, particularly for the unrecrystallized sheets. The results of Figures 7(a) through (c) also illustrate that forming limits in the biaxial tension range depend on both texture components (through their effect on the yield locus curvature) and the strain hardening.

For a given material, the predicted forming limits in plane strain tension ($\varepsilon_2 = 0$) for the different locations (surface, center, bulk) in the sheets are all similar (Figure 7). This can be explained in the following terms. Using the M–K theory for rate-independent plastic materials, the equation describing plastic-flow localization when the neck is perpendicular to direction 1 can be written as[22]

$$(1 - D)\frac{W(\bar{\varepsilon}^b)}{W(\bar{\varepsilon}^a)}\frac{\sigma_1^b/\bar{\sigma}}{\sigma_1^a/\bar{\sigma}} = 1 \qquad [13]$$

where $F = (1 - D)$ is the imperfection parameter, $\sigma_1/\bar{\sigma}$ is the yield stress in direction 1 normalized by the uniaxial tension yield stress, and $w(\bar{\varepsilon})$ is the strain-hardening law. Superscripts a and b denote the homogeneous and the imperfection regions of the material, respectively. For a perfect sheet, the imperfection parameter F is equal to one. In the present study, the initial value of F has been chosen to be 0.996. Different mathematical forms of the strain-hardening law $w(\bar{\varepsilon})$ can be used. As mentioned previously, the Voce strain-hardening law, which leads to the best fit with experimental stress-strain curves for the different Al-Li sheets,[17] was used in this work. $(\sigma_1^b/\bar{\sigma})/(\sigma_1^a/\bar{\sigma})$ is the ratio of the major normalized stress in the imperfection to the major normalized stress in the homogeneous sheet. The former stress tends to evolve toward the plane strain stress state because this is the stress state inside a neck. This ratio is always larger than 1 and depends on the curvature of the yield locus in the biaxial range. When a stress state corresponding to plane strain tension is imposed to the sheet, both stress states are consequently plane strain and the ratio $(\sigma_1^b/\bar{\sigma})/(\sigma_1^a/\bar{\sigma})$ is equal to 1. In this case, Eq. [13], which describes the plastic flow localization process, does not include a term related to the yield locus curvature. Therefore, this means that the FLD does not depend on the yield locus shape and, consequently, that it is independent of crystallographic texture for this strain path.

The predicted FLDs are compared to experimental FLDs in Figures 8(a) through (c) for recrystallized AA8090-T3, unrecrystallized AA8090-T4, and unrecrystallized AA2090-T3, respectively. It is interesting to note the wide spread in the experimental data. Actually, it is very difficult to define an experimental forming-limit curve. This is perhaps inherent to the nature of these materials. Nevertheless, because of these scattered experimental results, only general trends can be compared with the predictions. As mentioned previously, the right-hand sides

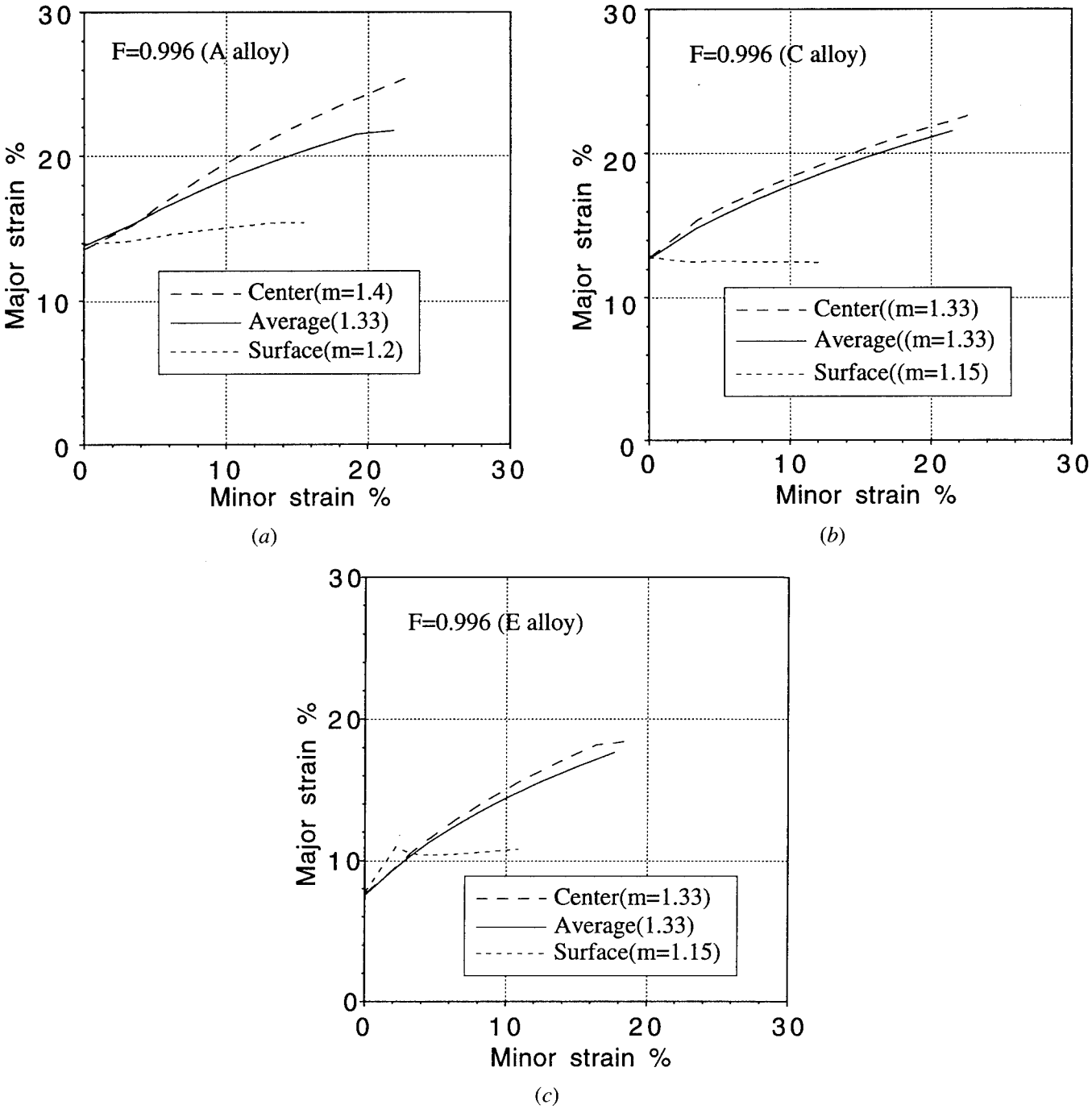


Fig. 7—Effect of the gradient of texture on the calculated FLD for (*a*) recrystallized 8090 without stretch, (*b*) unrecrystallized 8090 without stretch, and (*c*) unrecrystallized 2090 with stretch. The FLDs are computed from the gradient texture data using strain rate potential with the M–K approach.

of the predicted curves were computed using the M–K analysis, whereas the left-hand sides of the diagram were constructed using a critical-thickness criterion. The theoretical FLDs calculated using the average texture data are found to be in fair agreement with the "mean" experimental FLDs for the unrecrystallized samples, as shown in Figures 8(b) and 8(c). The predicted FLD is less satisfactory for the recrystallized AA8090 alloy (Figure 8(a)). The forming limits in the biaxial stretching range for these recrystallized sheets tend to be underestimated by about 10 pct. The samples A and C, which were not stretched, have better biaxial limits than those samples (B and D) that were stretched. This feature has been captured by the model, as indicated by Figures 8(a) and (b). Prior work hardening (stretching) obviously decreases the forming limits. Moreover, the FLD of the prestretched sheets can be considered as a FLD along nonlinear strain paths, where the prestrain is plane strain. It has been shown that the FLD of aluminum alloys determined along such nonlinear strain paths is lower than the FLD determined for linear strain paths.[39]

Three features of the experimental FLDs seem not to

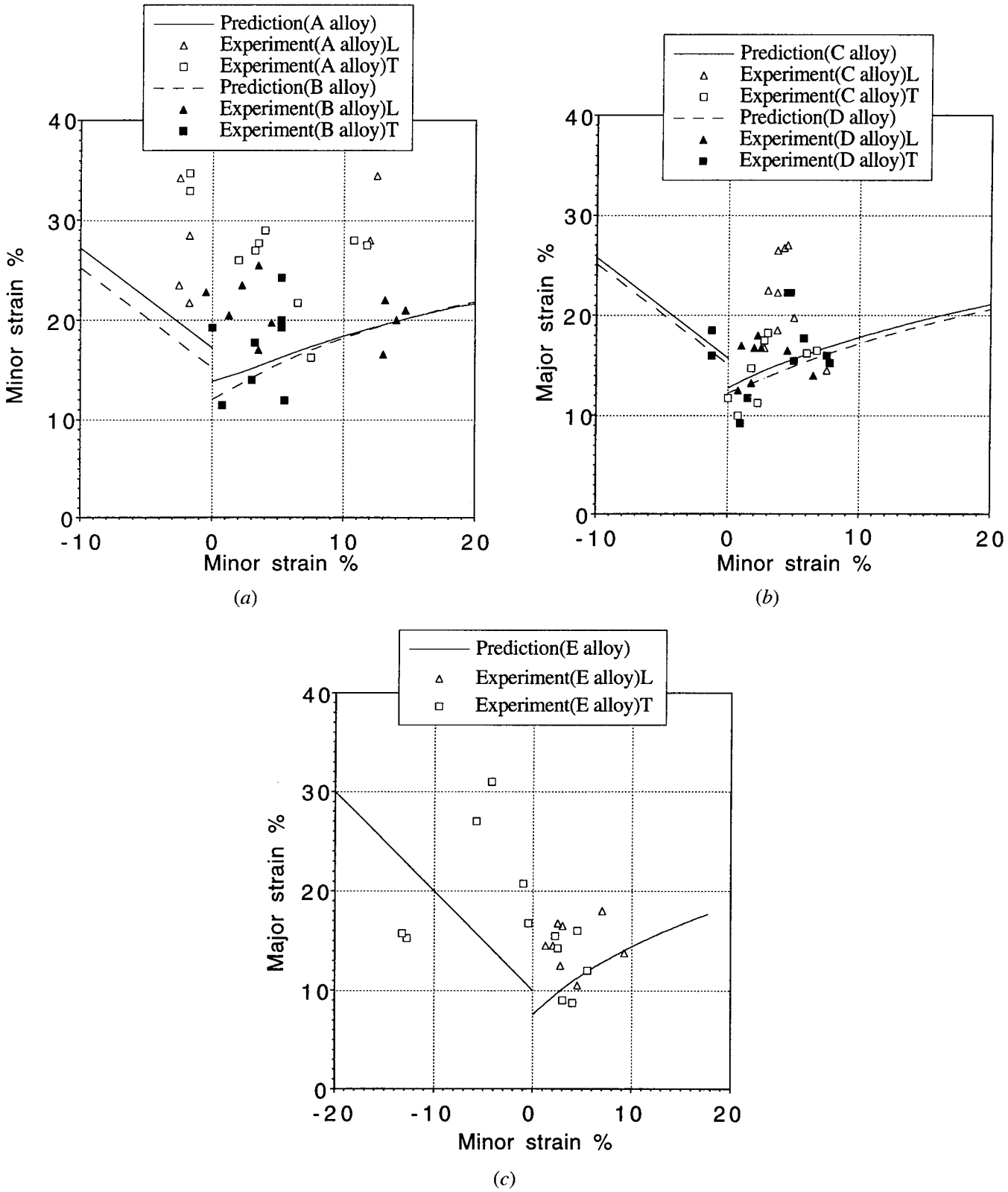


Fig. 8—Comparison of theoretical and experimental FLD for (*a*) recrystallized 8090 without stretch and recrystallized 8090 with stretch, (*b*) unrecrystallized 8090 without stretch and unrecrystallized 8090 with stretch, and (*c*) unrecrystallized 2090 with stretch. The theoretical FLD is computed from average texture data with the M–K approach.

be captured by the model: (1) the high limits strain obtained near plane strain tension (the minor strain is zero); (2) the large scatter in the limit strains for similar strain paths, particularly near plane strain tension; and (3) the high average limit strains of the recrystallized AA8090 sheets (samples A and B). It is interesting to discuss whether these effects could be due to the texture gradients. However, because these gradients are through-thickness, they should not make a difference on the behavior of the sheet from one macroscopic location to another one. Moreover, Figures 7(a) through (c) suggest that the limit strains in plane strain tension should be the same, irrespective of the crystallographic texture. Therefore, through-thickness crystallographic texture gradients do not seem to affect the experimental scatter and the average plane strain limit strain.

The scatter seems more likely to be due to some kind of in-plane heterogeneity. Much work has been conducted from a macroscopic point of view to study the effects of geometric imperfections on forming limit strains.[40,41,42] The imperfection has also been linked to the microstructure of materials such as microvoids, inclusions, and second-phase particles,[22] or grain structure and orientation heterogeneities.[43] Here, the grain structure could explain the underestimation of the predicted FLD in the recrystallized AA8090 sheets. The grain structure of the recrystallized 8090 sheets (samples A and B) differs significantly from the unrecrystallized AA8090 and AA2090 sheets, as described previously. The unrecrystallized AA8090 and AA2090 and the recrystallized AA2024 materials exhibit more elongated grains than the recrystallized AA8090. Therefore, this might lead to a smaller imperfection for the recrystallized AA8090 sheet than for the unrecrystallized AA8090 and AA2090 sheets. The scatter in the experimental FLD results could be due to a heterogeneous distribution of grain orientations in the materials (textural segregation[43]). For instance, regions of the sheet could have had clusters of orientations leading to a macroscopic imperfection. However, the initial imperfection parameter cannot be determined experimentally at the present time. Further studies on microscopic and macroscopic scales seem to be needed to understand the behavior of these Al-Li sheets.

V. SUMMARY AND CONCLUSIONS

In this work, the effects of a crystallographic texture gradient on the yield locus shape and the FLD of some Al-Li alloy sheets were discussed. Using the predictions of the polycrystal Taylor/Bishop and Hill model, a smoother yield locus near equibiaxial tension is expected at the midthickness of the sheet than at the surface. The main orientation components corresponding to the smoother loci are the Goss texture for the recrystallized AA8090 and the brass-type and the brass components for the unrecrystallized AA8090 and the unrecrystallized AA2090, respectively. The shape of the yield locus predicted from the surface layer ODF is characterized by the existence of regions of high curvature. These high-curvature regions are consistent with the cube texture for AA8090, the copper and the S components for AA2090, and the $P(110)\langle 122\rangle$ texture for the conventional AA2024 alloy.

The modeling work indicates that the forming limits in the stretching range vary with the curvature of the yield locus. An increase in curvature of the yield locus leads to a decrease in limit strains in the biaxial tension range. Therefore, the predicted limit strains of midthickness layers are higher than those of surface layers for all the materials studied. However, it seems that the textures at the midthickness of the sheet have a much larger influence on the FLD than the surface texture, particularly in the unrecrystallized alloys. The predicted FLDs were only in fair agreement with the experimental results. The large scatter in the experimental data and the high average experimental FLD for the recrystallized AA8090 sheets compared to the predicted FLD do not appear to be a consequence of the crystallographic texture gradient.

ACKNOWLEDGMENTS

The authors would like to thank Professors T. Ericsson and W.B. Hutchinson for useful suggestions and comments, Dr. M. Ahmad for fruitful discussion on various aspects and a careful reading of the manuscript, and Dr. B. Jaensson of Saab-Scania AB for providing the material and experimental FLD data. They are also grateful to Drs. C. Burman and D. Juul Jensen for their assistance in texture measurements regarding this work and Mr. D.J. Lege of Alcoa for a critical review of the manuscript.

REFERENCES

1. M.J. Bull and D.J. Lloyd: in *Proc. Conf. Aluminium-Lithium Alloys III*, C. Baker, P.J. Gregson, S.J. Harris, and C.J. Peel, eds., Institute of Metals, London, 1986, pp. 402-410.
2. F. Barlat, D.J. Lege, and C.J. Warren: in *Proc. Conf. Modelling the Deformation of Crystalline Solids*, T.C. Lowe, Anthony, D. Rollett, P.S. Follansbee, and G.S. Daehn, eds., TMS, New Orleans, LA, 1991, pp. 189-203.
3. W.D. Rooney, J.M. Papazian, E.S. Balmuth, R.C. Davis, and P.N. Adler: in *Proc. Conf. Aluminium-Lithium Alloys 5th*, T.H. Sanders, Jr., and E.A. Starke, Jr., eds., Materials and Component Engineering Publication Ltd., Williamsburg, VA, 1989, vol. II, pp. 799-808.
4. X.H. Zeng, M. Ahmad, and T. Ericsson: in *Proc. Conf. Aluminium-Lithium Alloys 6th*, M. Peters and P.-J. Winkler, eds., DGM Informationsgesellschaft, Oberursel, Germany, 1992, vol. II, pp. 1021-26.
5. O. Engler, J. Mizera, M. Delecroix, J. Driver, and K. Lücke: in *Proc. Conf. Aluminium-Lithium Alloys 6th*, M. Peters and P.-J. Winkler, eds., DGM, Oberursel, Germany, vol. I, pp. 307-14.
6. B. Jaensson and M. Ahmad: in *Proc. Conf. Aluminium-Lithium Alloys 6th*, M. Peters and P.-J. Winkler, eds., DGM, Oberursel, Germany, vol. II, pp. 1105-110.
7. I.M. Robertson: *Mater. Forum*, 1991, vol. 15, p. 102.
8. A.W. Bowen: in *Proc. Conf. ICOTOM 8, on Textures of Materials*, J.S. Kallend and G. Gottstein, eds., TMS and ASM, Santa Fe, New Mexico, 1988, pp. 971-76.
9. F. Barlat, J.C. Brem, and J. Liu: *Scripta Metall.*, 1992, vol. 27, pp. 1121-126.
10. X.H. Zeng, M. Ahmad, and O. Engler: *Mater. Sci. Technol.*, 1994, in press.
11. F. Barlat, K. Chung, and O. Richmond: *Int. J. Plas.*, 1993, vol. 9, pp. 51-63.
12. F. Barlat and K. Chung: Modelling Simul. in *Mater. Sci. Eng.*, 1993, vol. 1, pp. 403-16.

13. H.J. Bunge: in *Directional Properties of Materials*, H.J. Bunge, ed., DGM Informationsgesellschaft, Oberursel, Germany, 1988, pp. 1-64.
14. G.I. Taylor: *J. Inst. Met.*, 1938, vol. 62, pp. 307-24.
15. J.W.F. Bishop and R. Hill: *Phil. Mag.*, 1951, vol. 42, pp. 414-27.
16. H.J. Bunge: in *Quantitative Texture Analysis*, H.J. Bunge and C. Esling, eds., DGM Informationsgesellschaft, Oberursel, Germany, 1986, pp. 383-425.
17. X.H. Zeng, M. Ahmad, and T. Ericsson: in *Proc. Conf. Aluminium Alloys 3th Their Physical and Mechanical Properties*, L. Arnberg, O. Lohne, E. Nes and N. Ryum, eds., Pergamon Press Ltd., Trondheim, Norway, 1992, vol. I, pp. 303-08.
18. K.S. Chan, D.A. Koss, and A.K. Ghosh: *Metall. Trans. A*, 1984, vol. 15A, pp. 323-29.
19. R. Hill: *J. Mech. Phys. Solid*, 1952, vol. 1, pp. 19-30.
20. Z. Marciniak and K. Kuczynski: *Int. J. Mech. Sci.*, 1967, vol. 9, pp. 609-20.
21. K.S. Chan: *Forming Limit Diagrams—Concepts, Methods, and Applications*, R.H. Wagoner, K.S. Chen, and S.P. Keeler, eds., TMS, Warrendale, PA, 1989, pp. 73-110.
22. F. Barlat: *Forming Limit Diagrams—Concepts, Methods, and Applications*, R.H. Wagoner, K.S. Chen, and S.P. Keeler, eds., TMS, Warrendale, PA, 1989, pp. 275-301.
23. F. Barlat and O. Richmond: *Mater. Sci. Eng.*, 1987, vol. 95, pp. 15-29.
24. F. Barlat: *Mater. Sci. Eng.*, 1987, vol. 91, pp. 55-72.
25. D. Juul Jensen and T. Leffers: *Texture and Microstructures*, H.J. Bunge, ed., Oberursel, Germany, DGM Informationsgesellschaft, 1989, vol. 10, pp. 361-73.
26. H.J. Bunge: in *Texture Analysis in Materials Science*, Butterworth and Co., London, 1982.
27. F. Barlat and J. Lian: *Int. J. Plast.*, 1989, vol. 5, pp. 51-66.
28. D. Zhou and J. Lian: *Int. J. Mech. Sci.*, vol. 4, 1989, pp. 249-63.
29. U.F. Kocks, M.G. Stout, and G.R. Canova: *114th TMS-AIME Meeting*, New York, NY, 1985.
30. H. van Minh, R. Sowerby, and J.L. Duncan: *Int. J. Mech. Sci.*, 1975, vol. 17, pp. 339-40.
31. C.C. Chu: *J. Mech. Phys. Solid*, 1984, vol. 32, pp. 197-212.
32. V. Tvergaard: *Int. J. Mech. Sci.*, 1978, vol. 20, pp. 651-58.
33. K.W. Neale and E. Chater: *Int. J. Mech. Sci.*, 1980, vol. 22, p. 563.
34. R. Sowerby and J.L. Duncan: *Int. J. Mech. Sci.*, 1971, vol. 13, p. 217.
35. K.S. Chan: *Metall. Trans. A*, 1985, vol. 16A, pp. 629-39.
36. Z. Marciniak, K. Kuczynski, and T. Pokora: *Int. J. Mech. Sci.*, 1970, vol. 15, p. 780.
37. S.N. Rasmussen: *Int. J. Mech. Sci.*, 1982, vol. 24, pp. 729-39.
38. V. Tvergaard: *J. Mech. Phys. Solids*, 1987, vol. 25, pp. 43-60.
39. A. Graf and W.F. Hosford: *Metall. Trans. A*, 1993, vol. 24A, pp. 2503-512.
40. A.K. Ghosh and W.A. Backofen: *Metall. Trans. A*, 1973, vol. 4, pp. 1113-23.
41. R. Venter, W. Johnson, and W.C. DeMalherbe: *Int. J. Mech. Sci.*, 1971, vol. 13, pp. 299-308.
42. T.J. McCarron, K.E. Kain, G.T. Hahn, and W.F. Flanagan: *Metall. Trans. A*, 1988, vol. 19A, pp. 2067-74.
43. D.V. Wilson: *Formability and Metallurgical Structures*, TMS, Warrendale, PA, 1987, pp. 3-32.

Thermodynamics and Long-Range Order of Interstitials in a Hexagonal Close-Packed Lattice

BART J. KOOI, MARCEL A.J. SOMERS, and ERIC J. MITTEMEIJER

Statistical thermodynamics was applied to describe long-range order (LRO) of interstitial atoms in a hexagonal close-packed (hcp) host lattice. On the basis of the Gorsky–Bragg–Williams (GBW) approximation and a division of the interstitial sublattice into six interpenetrating sublattices, all the possible ordered configurations were derived for this assembly. Special attention was devoted to two of the possible ordered configurations of interstitial atoms, *viz.*, the two ground-state structures that have been indicated for ε-Fe_2N_{1-z}. A description of the order-disorder transition was obtained, and the evolution of the occupancies of the different types of interstitial sites on changing the total interstitial content was given. Composition-temperature regions of stability for the two ordered configurations were given in phase diagrams for different combinations of pairwise interaction energies. The results are compatible with observations for ε-Fe_2N_{1-z} as reported in the literature. The advantages of the present treatment were discussed relative to an earlier one, which *a priori* excluded nearest neighboring interstitial sites from simultaneous occupancy.

I. INTRODUCTION

THE present article is concerned with the thermodynamics of a binary solid solution consisting of a hexagonal close-packed (hcp) sublattice of atoms containing, in its octahedral interstices, atoms that show long-range order (LRO). Expressions for the Gibbs free energy, the interstitial-site occupancies, and the order-disorder transition are derived. The treatment can equally well be applied to a binary substitutional solid solution with a (simple) hexagonal lattice.

The energy of a given configuration of atoms can in principle be assessed according to statistical thermodynamics applying the concept of (pairwise) near-neighbor interaction. Considering such existing descriptions, the generalized Ising model has the most general validity: the partition function is obtained by summation of the energy for a given configuration of atoms over all configurations possible for a certain alloy composition.[1,2] The Ising model naturally incorporates disorder and long-range as well as short-range order. So far, exact descriptions have only been obtained for two-dimensional systems.[1] To allow a description of three-dimensional systems, approximations to the (generalized) Ising model are necessary. Such approximations comprise the zeroth or Gorsky–Bragg–Williams (GBW)[3,4] and the first approximation[5] (to the long-range-ordered solutions) and Kikuchi's cluster variation method.[6] If long-range order vanishes, the GBW and the first approximation (to long-range-ordered solutions) become the zeroth[7] and first approximation[5] to the regular solutions, respectively.

Here, the effect of long-range order on the thermodynamics of a system is accounted for by the GBW approximation to the Ising model,[3,4] considering pairwise interaction up to third nearest neighbors. Although it has been pointed out that the accuracy of the GBW approximation, if used, for example, to model the Cu-Au system, is rather poor,[1,8] it is expected to be better in the case of interstitial solid solutions, where in general pronounced strain-induced interactions occur.[9] Such interactions extend over several atomic distances and thus have a long-range character and, therefore, improve the accuracy of the GBW approximation.[9] The successful application of the present model to nitrogen absorption isotherms of ε-Fe_2N_{1-z} (*i.e.*, equilibrium nitrogen content in ε-Fe_2N_{1-z} as a function of imposed nitrogen activity) demonstrates its usefulness.[10]

Two essentially different routes are followed in the present work. The first route starts with a subdivision of the interstitial sublattice in six interpenetrating sublattices, each occupied with a certain, variable concentration of interstitial atoms. Then, equilibrium requires that the chemical potentials of the interstitial atoms on these six sublattices are equal, thus providing equilibrium conditions necessary for describing the thermodynamic properties of the system. As a result, all the possible ground-state structures for the considered assembly are derived (Section III–A). The second route begins with two of the ground-state structures found *via* route 1 and which have been proposed for ε-Fe_2N_{1-z}.[11,12] The adoption of a ground-state structure allows definition of the degree(s) of order. Then, equilibrium requires that the stable values for the degree(s) of order correspond with a minimum value for the Gibbs free energy (Section III–B).

Earlier work on interstitial ordering in an hcp lattice has been presented as a "Regular Solution Model" (RS model) in Reference 13 and presupposed a complete order of interstitials along rows of interstitial sites parallel to the *c*-axis of the hexagonal lattice, *viz.*, an alternation of permitted and excluded sites for occupancy by interstitial atoms. The present LRO model allows a variable degree of order along rows of interstitial atoms parallel to the *c*-axis, because in principle, every site is

BART J. KOOI, Ph.D. Student, MARCEL A.J. SOMERS, Assistant Professor, and ERIC J. MITTEMEIJER, Professor, are with the Laboratory for Materials Science, Delft University of Technology, NL-2628 AL Delft, The Netherlands.

Manuscript submitted November 5, 1993.

permitted for occupancy by interstitial atoms. The results obtained with the present model are compared to those of the regular solution model given in Reference 13 (Section IV–B).

II. BASIC CONSIDERATIONS

The binary solid solution M-I is considered, in which the I atoms are situated in the interstices of the crystal lattice set up by the M atoms. This assembly can be conceived as constructed from two interpenetrating sublattices: one for atoms M and one for atoms I. Both M and I atoms can only be located at sites of their own sublattices. In an hcp M sublattice, the octahedral interstices are the largest interstitial holes and the ones considered for occupation by I atoms; it is assumed that the fraction of I atoms residing at tetrahedral interstices is negligible. Hence, the sites for I atoms compose a (simple) hexagonal sublattice.

The model to be presented provides a thermodynamic description for an M-I alloy, with sublattices for M and I as given in the preceding paragraph, as a function of interstitial content. A change of the composition is realized by changing the occupancy of the I sublattice only; the M sublattice is and remains completely occupied. The I sublattice is composed of variable amounts of atoms I and empty sites V (vacancies for I atoms). The (possible) occurrence of ordering of I and V on their hexagonal sublattice is dealt with here. To arrive at a thermodynamic description for the M-I alloy, the thermodynamics of the M and the I sublattices, separately, as well as the interaction of these sublattices will be considered.

It is convenient to conceive the hexagonal I sublattice as an alternation of two types of basal planes (1 and 2), each containing three different kinds of sites (for plane 1: A1, B1, and C1; for plane 2: A2, B2, and C2; Figure 1; Reference 13). Thus, for each type of plane (denoted as (001) planes hereafter), a particular site is surrounded within the plane by sites of the other kinds (Figure 1(a)). In the direction perpendicular to the planes (denoted as the c-direction hereafter), sites A1, B1, and C1 are adjacent to sites A2, B2, and C2, respectively (Figure 1(b)). Apart from the present choice of six sublattices composing the hexagonal I lattice, other possibilities for division of the I lattice into sublattices can be considered too. If interactions up to third nearest neighbors on the I lattice are considered a subdivision of the (simple) hexagonal I lattice into 6, 8, 10, 12, and 14 sublattices (kinds of sites), analogous to the division of the hcp lattice as described in Reference 14, is appropriate. The subdivision in six kinds of sites (six sublattices) is preferred here, for it reflects the crystallography of the ground-state structures as given for ε-Fe_2N_{1-z} and the anti-CdI_2 structure type(s).[15]*

*A division into eight sublattices is appropriate for describing (dis)ordering in accordance with the ζ-Fe_2N, the Co_2C (or anti-$CaCl_2$), and the anti-CdI_2 structure types. The thermodynamic models for the subdivision into 8, 10, 12, and 14 sublattices can be obtained and dealt with in exactly the same way as the model that will be presented here for the subdivision into six sublattices.

For the case of a random distribution of I atoms over the

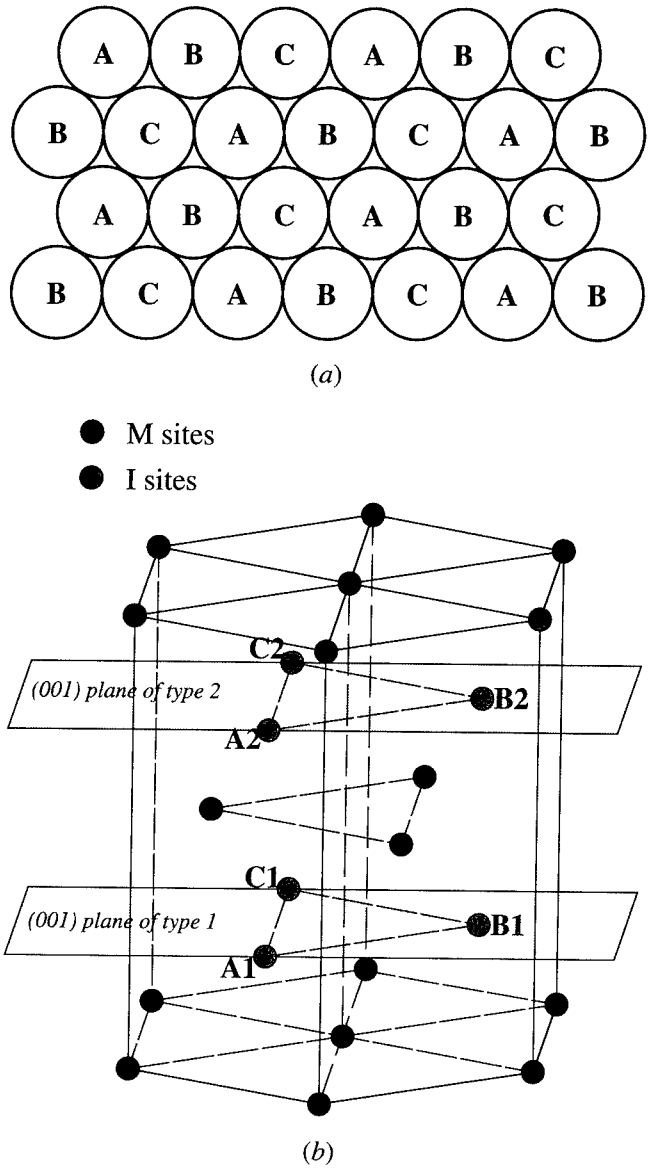


Fig. 1—(*a*) Each (001) plane of the hexagonal (interstitial) sublattice of I atoms contains three different kinds of sites: A, B, and C. (*b*) The hexagonal sublattice of I atoms, constituted by the octahedral interstices of the hcp sublattice of M atoms, is composed of planes of types 1 and 2, together having six kinds of sites (denoted by A1, B1, C1, A2, B2, and C2) that constitute a trigonal prism.

sites of the I sublattice, the six sites constituting a trigonal prism (Figure 1(b)) have the same probability to be occupied by an I atom. This probability equals the fraction of occupied sites of the I sublattice.

Ordering can occur, if it is energetically more favorable to form I-V nearest neighbors than I-I and V-V nearest neighbors, implying repulsion among I atoms. If ordering among atoms on the I sublattice occurs, in principle, each of the sites A1, ..., C2 has its own probability to be occupied by an I atom. For a hexagonal sublattice, the interaction of I atoms on neighboring sites of an (001)-plane is not equal to that of I atoms on neighboring sites in the c-direction. For an ideal hcp sublattice of M atoms, the shortest possible separation occurs for two nearest neighbors in the c-direction of the hexagonal I sublattice: it is only $\sqrt{2/3}$ of the separation between

two nearest neighbors within the (001)-plane. This suggests a larger tendency for nonoccupancy of neighboring sites in the c-direction than within the (001)-plane. If, in the c-direction, the nearest-neighbor sites to an occupied site remain vacant, then the maximum I content corresponds with the composition M_2I. This reduction of the number of sites available for occupation by I atoms is denoted by site exclusion in the present article and was presupposed for the derivation of the regular solution model in Reference 13. If all sites of the I sublattice are available for occupation by I atoms, the maximum I content corresponds with the composition MI.

III. LRO MODEL FOR INTERSTITIALS IN AN HCP LATTICE

The zeroth approximation to the Ising model due to GBW is adopted to describe LRO. This approach comprises the following:[4]

- The configurational entropy is given by the number of permutations of I (and thus V) over the types of sites. The molar vibrational entropy for each component (M, I, and V) is assumed constant, and
- The enthalpy is given by the sum of the products of each of the probabilities of I-I, V-V, I-V, M-M, M-I, and M-V pairwise interactions and their corresponding interaction energies. Interactions on the I sublattice of first nearest neighbors (A1-A2, B1-B2, C1-C2), second nearest neighbors (A1-B1, A1-C1, *etc.*) and (optionally) third nearest neighbors (A1-B2, A1-C2, *etc.*) are taken into account here.

The LRO model can be obtained *via* two essentially different routes, having different (dis)advantages. Route 1 begins with a description for the occupancy of each of the six sites Al, ..., C2 on the trigonal prism introduced and the associated six chemical potentials. Equilibrium requires that these chemical potentials are equal. Route 2 adopts a ground-state structure (*i.e.*, a completely ordered structure that generally can only be defined for a (simple) stoichiometric composition) as the starting point for distinguishing between order and disorder sites and for defining the degree(s) of order. Equilibrium requires that values for the degree(s) of order correspond to a minimum value for the Gibbs free energy. Both routes are pursued here. Obviously, route 1 needs less *a priori* information than route 2 and offers (the possibility of) a more general solution. However, if the ground-state structure of interest is known *a priori*, route 2 is useful, because it provides directly values for the order parameters, which can be related to physical properties of the assembly under consideration.

A. *Route 1*

The interpenetrating hcp M and (simple) hexagonal I sublattices are considered, the latter having six kinds of I sites: A1, B1, . . ., C2. The M sublattice is completely occupied by M atoms. Each kind of site K of the I sublattice can be occupied by a fraction of I atoms, x_K. The total number of M sites considered is $6N$, and thus, there are N sites for each kind of I site.

1. *Gibbs free energy, chemical potential, and equilibrium condition*

A full derivation of the expression for the Gibbs free energy of the M-I alloy is given in Appendix A for the example of a specific subdivision in types of interstitial sites (Section B–1). Therefore, only a brief description is given here for the case of six different sublattices composing the I lattice.

The configurational entropy corresponding to N sites of one kind, *e.g.*, A1, is given by

$$-Nk[x_{A1} \ln x_{A1} + (1 - x_{A1}) \ln (1 - x_{A1})]$$

where k is Boltzmann's constant and x_{A1} is the fraction occupied sites of kind A1. The summation of such entropy terms for all six kinds of sites yields the configurational entropy of the whole M-I alloy.

The probability for simultaneous occupancy of two adjacent sites in the c-direction (first nearest neighbors on the I sublattice), *e.g.*, A1 and A2, by I is $x_{A1}x_{A2}$, by V is $(1 - x_{A1})(1 - x_{A2})$ and by I and V is $x_{A1}(1 - x_{A2}) + x_{A2}(1 - x_{A1})$. The enthalpy (energy) associated with these interactions between sites A1 and A2 is proportional to the sum of the products of these probabilities and their corresponding interaction energies $e_{c,II}$, $e_{c,VV}$, and $e_{c,IV}$:

$$\{x_{A1}x_{A2}e_{c,II} + (1 - x_{A1})(1 - x_{A2})e_{c,VV} + [x_{A1}(1 - x_{A2}) + x_{A2}(1 - x_{A1})]e_{c,IV}\} 2N \frac{Z_c}{2}$$

with $Z_c/2$ being the number of bonds in the c-direction per atom ($Z_c/2 = 1$). This term can be rewritten as

$$(x_{A1} + x_{A2}) H^0_{I,A1A2} + [(1 - x_{A1}) + (1 - x_{A2})] H^0_{V,A1A2} + NW_c[x_{A1}(1 - x_{A2}) + x_{A2}(1 - x_{A1})]$$

where $H^0_{I,A1A2} = N Z_c/2\, e_{c,II}$ and $H^0_{V,A1A2} = N Z_c/2\, e_{c,VV}$; W_c is the "exchange energy" in the c-direction, defined as

$$W_c = \frac{Z_c}{2}(2e_{c,IV} - e_{c,II} - e_{c,VV}).$$

The term $H^0_{I,A1A2}$ is a fraction of H^0_I, the enthalpy of N atoms of the pure component I (with exactly the same lattice as the I sublattice). Accordingly, $H^0_{V,A1A2}$ is a fraction of H^0_V, the enthalpy of N atoms of the pure component V (with exactly the same lattice as the I sublattice; for the present case, where V represents vacant I sites, H^0_V of course is zero). Summation of the enthalpies associated with the interactions between atoms at sites A1 and A2, atoms at sites B1 and B2, and atoms at sites C1 and C2 yields the enthalpy corresponding to all possible pairwise interactions (between first nearest neighbors) in the c-direction. The enthalpies corresponding with pairwise interactions between second (A1-B1, A1-C1, ..., B2-C2) and third (A1-B2, A1-C2, ..., C1-B2) nearest neighbors are obtained analogously, using exchange energies W_p and W_{pc}, respectively.

To obtain the enthalpy of the whole M-I alloy, the enthalpies of N atoms of the pure component M, H^0_M, and of the interactions of M and the N atoms of I, H^0_{MI}, have to be added (H^0_{MV} of course is zero). The

Gibbs free energy $G_{M\text{-}I}$ of the M-I alloy can thus be given as follows:

$$\begin{aligned} G_{M\text{-}I} = {} & 6(H^0_M - TS^0_{vib,M}) \\ & + \sum_{K=A1}^{C2} [x_K]\,[H^0_I - TS^0_{vib,I} + H^0_{MI} + NW_c \\ & \qquad + NW_p + NW_{pc}] \\ & - 2NW_c[x_{A1}x_{A2} + x_{B1}x_{B2} + x_{C1}x_{C2}] \\ & - NW_p[x_{A1}x_{B1} + x_{A1}x_{C1} + x_{B1}x_{C1} + x_{A2}x_{B2} \\ & \qquad + x_{A2}x_{C2} + x_{B2}x_{C2}] \\ & - NW_{pc}[x_{A1}x_{B2} + x_{A1}x_{C2} + x_{B1}x_{A2} + x_{B1}x_{C2} \\ & \qquad + x_{C1}x_{A2} + x_{C1}x_{B2}] \\ & + NkT \sum_{K=A1}^{C2} [x_K \ln x_K + (1 - x_K) \ln (1 - x_K)] \end{aligned} \qquad [1]$$

where T is the temperature, H^0_Q is the enthalpy of N atoms of the pure component Q (summation of all enthalpies associated with the pairwise near-neighbor interactions considered), and $S^0_{vib,Q}$ is the vibrational entropy of N atoms of the pure component Q, which is assumed to be independent of composition and ordering. The first two terms on the right-hand side of Eq. [1] represent the standard state of the M-I alloy. It is noted that the contribution of the M sublattice and its interaction with the I sublattice only changes the standard state and consequently, does not affect ordering on the I sublattice. For brevity of notation,

$$\mu^0_I = (H^0_I - TS^0_{vib,I} + H^0_{MI} + NW_c + NW_p + NW_{pc})$$

Considering the sublattice formed by sites of kind K as an open system (V has to represent vacancies), the chemical potential for N atoms I at sites of kind K, μ^K_I, is by definition given by

$$\mu^K_I = \frac{\partial G_{M\text{-}I}}{\partial x_K} \qquad [2]$$

Using Eq. [1], one obtains

$$\begin{aligned} \mu^{A1}_I = {} & \mu^0_I - 2NW_c[x_{A2}] - NW_p[x_{B1} + x_{C1}] \\ & - NW_{pc}[x_{B2} + x_{C2}] + NkT \ln \left[\frac{x_{A1}}{1 - x_{A1}}\right] \end{aligned} \qquad [3]$$

The expressions for μ^K_I of I atoms on the other kinds of sites are similar.

Thermodynamic equilibrium for this M-I alloy involves that the chemical potentials μ^K_I of the interstitial element I are equal for all six kinds of I sites; *i.e.*,

$$\mu^{A1}_I = \mu^{B1}_I = \mu^{C1}_I = \mu^{A2}_I = \mu^{B2}_I = \mu^{C2}_I \equiv \mu_I \qquad [4]$$

Thus, a set of five relations nonlinear in $x_{A1}, \ldots, x_{C2}$ is obtained from Eqs. [3] and [4]. Equal occupancy of the six kinds of sites fulfills the equilibrium condition Eq. [4], and thus, the disordered state is always a solution of the set of relations. However, it does not necessarily yield the lowest possible Gibbs free energy.

The Gibbs free energy $G_{M\text{-}I}$ of the M-I alloy in general can be related to chemical potentials of the atoms I, μ_I, and of the atoms M, μ_M:

$$G_{M\text{-}I} = 6\mu_M + \mu_I \sum_{K=A1}^{C2} x_K \qquad [5]$$

2. *Order-disorder transition and the evolving types of ordering*

An ordered configuration of I atoms on their sublattice is only more stable than the random configuration if (a) the content of the I atoms is above some minimum value and (b) the temperature of the system is below some maximum value. The values for the I content and the temperature associated with the order-disorder transition depend on the values of the exchange energies, W_c and W_p and W_{pc}. The ordered configuration develops if, with respect to the disordered state, (one or some of) the fractions of I atoms on the different kinds of I sites are differently perturbed. To arrive at the ordered state solution(s) of the five nonlinear equations, an iterative numerical method has to be used. Root finding requires a good initial guess.[16] For a good initial guess, knowledge on the order-disorder transition is indispensable.

The equations of type Eq. [3] can each be written as $f(\underline{x}) = f(x_{A1}, x_{B1}, \ldots, x_{C2})$. If $\underline{x} + d\underline{x}$ and $\underline{x}$ are sufficiently close and if $f(\underline{x})$ is continuous for $\underline{x}$, it holds that

any difference in the occupancy of the six kinds of sites tends to nil on approaching the order-disorder transition from the ordered configuration;

the six equations that make up Eq. [3] can be replaced by their total differentials:

$$df(\underline{x}) = \frac{\partial f}{\partial x_{A1}} dx_{A1} + \frac{\partial f}{\partial x_{B1}} dx_{B1} + \ldots + \frac{\partial f}{\partial x_{C2}} dx_{C2};$$

within the range $\underline{x}$ to $\underline{x} + d\underline{x}$, the infinitesimal changes $dx_{A1}, dx_{B1}, \ldots, dx_{C2}$ can be taken proportional to each other.

Using $f = dx_{B1}/dx_{A1}$, $g = dx_{C1}/dx_{A1}$, $h = dx_{A2}/dx_{A1}$, $i = dx_{B2}/dx_{A1}$, and $j = dx_{C2}/dx_{A1}$ ($dx_{A1} \neq 0$), one thus obtains for changes of the chemical potentials at the order-disorder transition defined by T_t and x_t:

$$\begin{aligned} \frac{d\mu^{A1}_I}{Ndx_{A1}} = {} & -2W_c[h] - W_p[f + g] \\ & - W_{pc}[i + j] + kT_t \left[\frac{1}{x_t(1 - x_t)}\right] \end{aligned} \qquad [6a]$$

$$\begin{aligned} \frac{d\mu^{B1}_I}{Ndx_{A1}} = {} & -2W_c[i] - W_p[1 + g] \\ & - W_{pc}[h + j] + fkT_t \left[\frac{1}{x_t(1 - x_t)}\right] \end{aligned} \qquad [6b]$$

$$\begin{aligned} \frac{d\mu^{C1}_I}{Ndx_{A1}} = {} & -2W_c[j] - W_p[1 + f] \\ & - W_{pc}[h + i] + gkT_t \left[\frac{1}{x_t(1 - x_t)}\right] \end{aligned} \qquad [6c]$$

$$\frac{d\mu_I^{A2}}{Ndx_{A1}} = -2W_c[1] - W_p[i+j] - W_{pc}[f+g] + hkT_t\left[\frac{1}{x_t(1-x_t)}\right] \quad [6d]$$

$$\frac{d\mu_I^{B2}}{Ndx_{A1}} = -2W_c[f] - W_p[h+j] - W_{pc}[1+g] + ikT_t\left[\frac{1}{x_t(1-x_t)}\right] \quad [6e]$$

$$\frac{d\mu_I^{C2}}{Ndx_{A1}} = -2W_c[g] - W_p[h+i] - W_{pc}[1+f] + jkT_t\left[\frac{1}{x_t(1-x_t)}\right] \quad [6f]$$

Because $f(\underline{x})$ has to be continuous for $\underline{x}$ and because $f(\underline{x})$ represents first derivatives of the Gibbs free energy with respect to $x_{A1}, x_{B1}, \ldots, x_{C2}$, the order-disorder transition (in this analysis) cannot be a first-order phase transition. For equilibrium at the order-disorder transition, the six equations of Eq. [6] (linear in $f, \ldots, j$) have to give identical values for $d\mu_I/dx_{A1}$ (*cf.* Eq. [4]). The problem can be solved exactly and provides four sets of solutions.

For $d\mu_I/dx_{A1} \neq 0$, only one solution holds:

(1) $f = g = h = i = j = 1$; no ordering occurs.

For $d\mu_I/dx_{A1} = 0$ and the constraint $1 + f + g + h + i + j = 0$ (because the order-disorder transition holds for one particular total interstitial content), three solutions hold:

(2) $h = -1, f = -i, g = -j$, and $i + j = 1$; an increase of the occupancy of sites A1 is associated with a decrease of the occupancies of sites A2 and B1 + C1, and an increase of the occupancies of sites B2 + C2, *i.e.*, a tendency for not forming first and second nearest neighbors but for forming third nearest neighbors.

(3) $f = g = 1$ and $h = i = j = -1$; an increase of the occupancy of sites A1 is associated with a decrease of the occupancies of sites A2, B2, and C2 and an increase of the occupancies of sites B1 and C1, *i.e.*, a tendency for not forming first and third nearest neighbors but for forming second nearest neighbors.

(4) $h = 1, f = i, g = j$, and $i + j = -1$; an increase of the occupancy of sites A1 is associated with an increase of the occupancies of sites A2 and a decrease of the occupancies of sites B1 + C1 and B2 + C2, *i.e.*, a tendency for not forming second and third nearest neighbors but for forming first nearest neighbors.

The values of the above parameters f, g, h, i, and j can thus physically be interpreted as a prescription for the evolution of (the differences in) the occupancies of the different kinds of I sites at the onset of ordering.

From the condition $d\mu_I/dx_{A1} = 0$, necessary at the onset of ordering (to obtain the sets (2) through (4)), it immediately follows from Eq. [6] for the order-disorder transition:

$$x_t = \frac{1}{2}\left(1 \pm \sqrt{1 + \frac{4kT_t}{W_{eff}}}\right) \quad [7]$$

where W_{eff} is an effective exchange energy according to

$$W_{eff} = -2W_c[h] - W_p[f+g] - W_{pc}[i+j] \quad [8]$$

According to Eq. [7], the critical temperature for the order-disorder transition is $T_c = -W_{eff}/4k$ and occurs at $x = 1/2$.

The three possible starting points for ordering (solutions (2) through (4)) lead to five distinct cases of ordering. This is caused by a nonexplicit prescription for the values of f, g, i, and j, according to the solutions (2) and (4). Depending on the actual values for f, g, i, and j and the values for the exchange energies, two cases of ordering are found to be possible for each of the solutions (2) and (4). The two cases of ordering evolving from solution (2) will be considered in detail in Section B as configurations A and B and were reported to have been observed.[11,12,17] The case of ordering evolving from the order-disorder transition according to solution (3) can be regarded as a tendency for forming an alternation of fully occupied and completely empty (001)-planes of the I sublattice for the composition M_2I. This has been observed for many cases.[15,17]

The occurrence of disordering and of ordering according to the three discussed possibilities (2) through (4) can be presented as a function of the various exchange energies in a "phase diagram" (Figure 2). The diagrams shown represent only the type of ordering most likely to occur in the regions concerned; the actual occurrence of an ordered state requires that the total fraction of interstitial sites occupied is in between the fractions, as prescribed by Eqs. [7] and [8]. The ground-state structures of the distinct cases of ordering have also been indicated in Figure 2.

The method applied for the numerical evaluation of the cases of ordering evolving from the six nonlinear equations that make up Eq. [3] is given in Appendix B.

B. *Route 2*

The derivation of the LRO model according to route 2 starts with the two ground-state structures obtained by route 1 as solution (2), which have first been indicated for ε-Fe_2N_{1-z}.[11,12] The other possible ground-state structure types as given by route 1 will not be dealt with. For a ground-state structure, different types of sites can be discerned:

order sites for occupation by I (denoted by i);
order sites for occupation by V (denoted by v);
disorder sites (denoted by d), *i.e.*, sites that are indifferent with respect to occupation by I or V.

Assuming that the repulsion among I atoms becomes stronger on decreasing their separation is in accordance with solution (2) obtained by route 1 (see its discussion in Section A-2). This leads to the following subdivision of the sites of the trigonal prism. If A1 is an order site (i) for I, then A2 is an order site for V (v). Further, either site B1 or site C1 has to be indicated as an order site for V. Here, B1 is taken as an order site for V (v), and

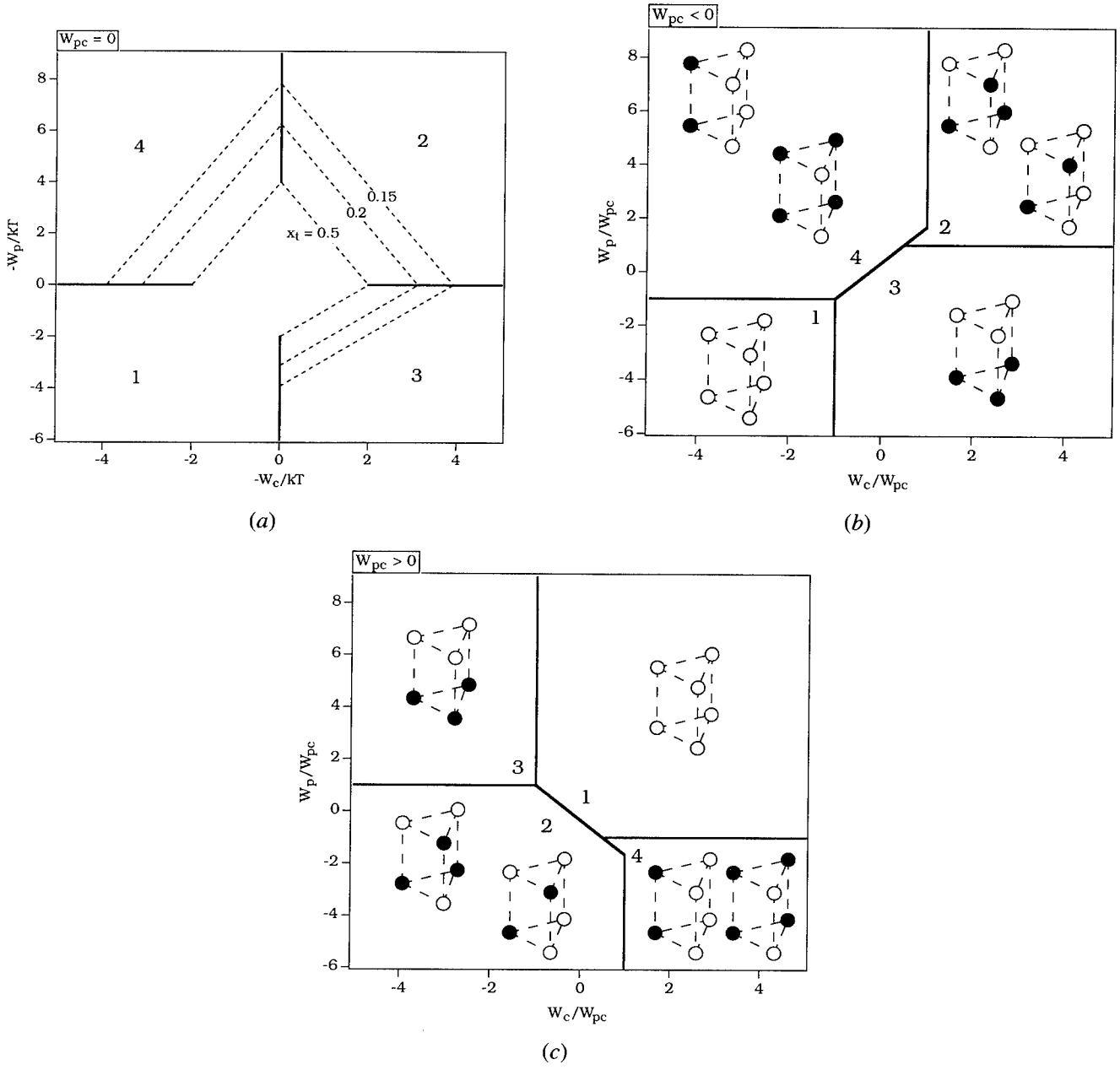


Fig. 2—Phase-stability diagram showing the region of stability for each of the four cases of interstitial configuration, cases (1) through (4) (see text), with respect to the values of W_c/kT, W_p/kT, and W_{pc}/kT: (*a*) $W_{pc} = 0$; (*b*) $W_{pc} < 0$; and (*c*) $W_{pc} > 0$. The corresponding ground-state structures on the basis of the trigonal prism of interstitial sites have also been indicated; the black, white, and shaded dots represent sites of type *i* (order sites for I atoms), *v* (order sites for V), and *d* (disorder sites), respectively. The diagrams shown represent only the type of ordering most likely to occur in the regions indicated. The actual occurrence of an ordered state requires that the total fraction of interstitial sites occupied is in between the fractions, x_t, as prescribed by Eqs. [7] and [8]. As an illustration, the dashed lines in (a) separate the ordered regions from the disordered region for various values of x_t.

consequently, B2 is an order site for I (*i*). Finally, for sites C1 and C2, two possibilities remain:

(A) one of the two sites is an order site for I (*i*), and the other is an order site for V (*v*); or
(B) both sites have the same tendency to become occupied by I or V and are disorder (*d*) sites.

Now, the possibilities for complete ordering (the ground-state structures) at the composition corresponding with M_2I are considered. Situation (A) leads to an alternation of (001) planes with unequal compositions, *viz.*, i_2v and v_2i. This is the so-called ε-Fe_2N ground-state structure (Figure 3(a)).* Possibility (B) leads to an alternation of (001) planes with equal compositions, *viz.*, *ivd* and *vid* (Figure 3(b))** and is, because of the

*This structure was proposed for the first time for the distribution of nitrogen atoms over the octahedral interstices of an hcp lattice of iron atoms in ε-Fe_2N[11] and was assessed by X-ray diffraction results.[12]

**This structure (with *i* sites completely occupied and *v* and *d* sites

completely empty) was proposed for the distribution of nitrogen atoms over the octahedral interstices in ε-Fe_2N_{1-z} ($z = 1/3$)[11] and was assessed by X-ray diffraction results.[12]

d sites, not a ground-state structure in the true sense. The specification of these two ground-state structures and the three types of sites is only meant to define the reference (ideal) structures for the LRO. In reality, the total amount of I atoms on the hexagonal sublattice and the degree of order deviate from that for the ground-state structures, which apply to absolute zero temperature.

For route 2, the degree of LRO has to be described, and to this end, the LRO parameter r is introduced. This parameter is defined with respect to the ground-state structure(s), such that $0 \le r \le 1$:

- if the fraction of the I atoms occupying v sites is equal to the fraction of the v sites relative to the total number of sites ($i + v + d$), the distribution of I atoms on its sublattice is random: $r = 0$;
- if no I atoms occupy v sites, the distribution of I atoms on its sublattice is ordered: $r = 1$.

For the case of ordering conforming to ground-state structure (A) with unequal compositions for the two types of (001)-planes, two LRO parameters are defined, one for each type of plane. The results of applying the LRO model to this ground-state structure are denoted by configuration A hereafter. For the case of ordering conforming to the ground-state structure (B) with equal compositions for the two types of (001)-planes, only one LRO parameter is defined. The results of applying the LRO model to this ground-state structure are denoted by configuration B hereafter.

1. *Configuration A*

Site occupancy

Configuration A is based on the ground-state structure with alternating (001) planes of type i_2v and v_2i. The (001) planes of composition i_2v will be denoted as planes of type 1 with order parameter r_1; the (001) planes of composition v_2i will be denoted as planes of type 2 with order parameter r_2 (Figure 3(a)). The order parameters can then be defined as follows.

For an (001) plane of composition i_2v (plane of type 1), having a total number of N sites, the numbers of I atoms on i sites ($N_{I,i1}$) and on v sites ($N_{I,v1}$) are given as follows:

$$N_{I,i1} = (2 + r_1)\, x_1 \frac{N}{3} \qquad [9a]$$

$$N_{I,v1} = x_1 N - N_{I,i1} = (1 - r_1)\, x_1 \frac{N}{3} \qquad [9b]$$

where x_1 is the fraction of the occupied N sites in a plane of type 1. Then the numbers of vacancies on i sites $N_{V,i1}$ and on v sites $N_{V,v1}$ are

$$N_{V,i1} = \frac{2}{3} N - N_{I,i1} = [2 - (2 + r_1)\, x_1] \frac{N}{3} \qquad [9c]$$

$$N_{V,v1} = \frac{1}{3} N - N_{I,v1} = [1 - (1 - r_1)\, x_1] \frac{N}{3} \qquad [9d]$$

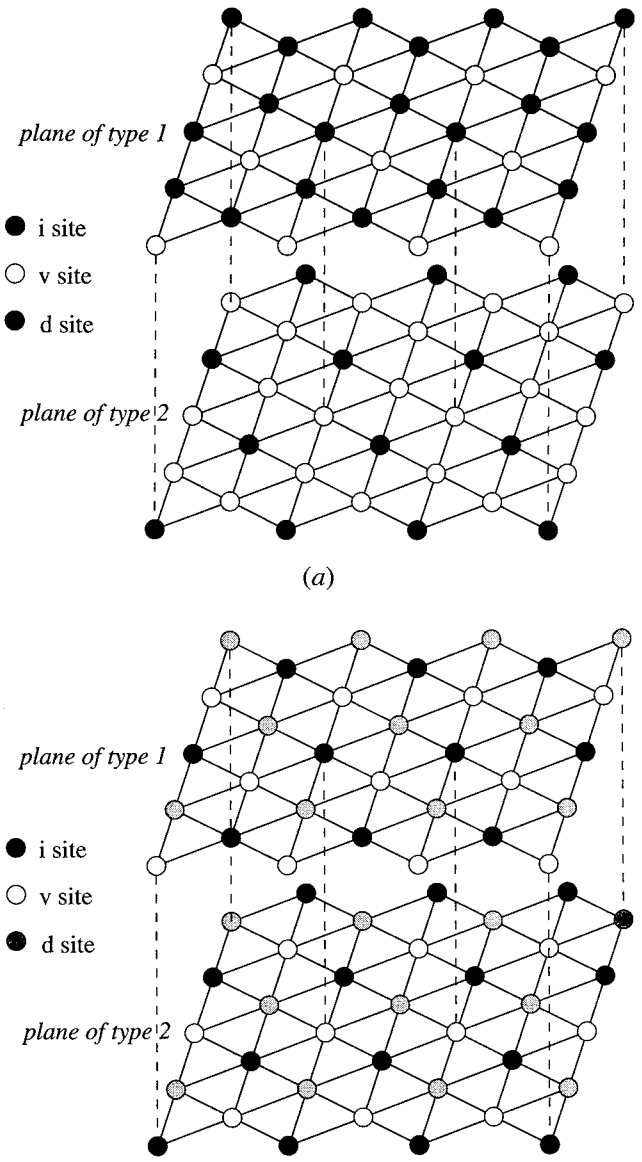


Fig. 3—(*a*) The ground-state structure consisting of an alternation of (001) planes of types 1 and 2 with compositions i_2v and v_2i, respectively, and denoted as configuration A in the text. (i = order site for interstitial atoms I; v = order site for vacancies V). (*b*) The ground-state structure consisting of an alternation of (001) planes of types 1 and 2 with compositions *ivd* and *vid*, denoted as configuration B in the text (i = order site for interstitial atoms I; v = order site for vacancies V; d = disorder site).

For an (001) plane of composition v_2i (plane of type 2), using analogously defined symbols, it is obtained that

$$N_{I,i2} = (1 + 2r_2)\, x_2 \frac{N}{3} \qquad [10a]$$

$$N_{I,v2} = (2 - 2r_2)\, x_2 \frac{N}{3} \qquad [10b]$$

$$N_{V,i2} = [1 - (1 + 2r_2)\, x_2] \frac{N}{3} \qquad [10c]$$

$$N_{V,v2} = [2 - (2 - 2r_2)\, x_2] \frac{N}{3} \qquad [10d]$$

On this basis, the expression for the Gibbs free energy according to the GBW approximation can be derived straightforwardly; see Appendix A for the description of configuration A.

2. *Configuration B*

Site occupancy

Configuration B is based on the ground-state structure with alternating (001) planes of type *ivd* and type *vid*. This ground-state structure can only be obtained if the tendency for a particular type of site to become occupied by I atoms is the same in both planes considered; *i.e.*, the degree of order is the same for both planes. This can be rationalized as follows. If the *i* site in (001)-plane 1 would have a stronger tendency to become occupied by I atoms than the *i* site in plane 2, then—because a stronger interaction occurs in the *c*-direction than within the (001) planes—also the *v* site in plane 1 would have a stronger tendency to become occupied by I atoms than the *v* site in plane 2. Thus, the planes of type 1 tend to contain more I atoms than the planes of type 2, implying that the third type of site is a *v* site in plane 1 and an *i* site in plane 2. Accordingly, the ground-state structure of configuration A results. Hence, if configuration B occurs, there is no difference in occupation of *i* sites (nor *v* or *d* sites) between planes 1 and 2. Then, for configuration B, only one LRO parameter *r* and the contents x_{iv} and x_d—representing the fractions of I on order sites (*i* and *v*) and on disorder sites (*d*), respectively—need to be considered. The LRO parameter *r* only applies to the order sites.

In contrast with configuration A, for configuration B the same description holds for all (001) planes of the I sublattice, each containing *N* sites. Thus, for a (001) plane of composition *ivd* (or *vid*), it holds for the total numbers of I atoms on *i*, *v*, and *d* sites denoted by $N_{I,i}$ $N_{I,v}$, and $N_{I,d}$, respectively:

$$N_{I,i} = (1 + r)\, x_{iv} \frac{N}{3} \qquad [11a]$$

$$N_{I,v} = (1 - r)\, x_{iv} \frac{N}{3} \qquad [11b]$$

$$N_{I,d} = x_d \frac{N}{3} \qquad [11c]$$

Then, the numbers of vacancies on *i*, *v*, and *d* sites denoted by $N_{V,i}$, $N_{V,v}$, and $N_{V,d}$, respectively, are

$$N_{V,i} = \frac{1}{3}N - N_{I,i} = [1 - (1 + r)\, x_{iv}] \frac{N}{3} \qquad [11d]$$

$$N_{V,v} = \frac{1}{3}N - N_{I,v} = [1 - (1 - r)\, x_{iv}] \frac{N}{3} \qquad [11e]$$

$$N_{V,d} = \frac{1}{3}N - N_{I,d} = [1 - x_d] \frac{N}{3} \qquad [11f]$$

On this basis, the expression for the Gibbs free energy according to the GBW approximation can be derived straightforwardly; see Appendix A for the description of configuration B.

IV. RESULTS AND DISCUSSION

A. *Results for Long-Range Order Configurations A and B*

Neglecting the effect of third nearest-neighbor interactions (*i.e.*, W_{pc}/kT is nil), the order-disorder phase boundary is depicted in Figure 4 for various combinations of values for W_c/kT and W_p/kT. Evidently, increasing the value for W_c with respect to W_p broadens the stable composition region of an ordered configuration and enlarges the stability region of an ordered configuration up to a higher temperature (Figure 4).

In the sequel of this section site occupancies of the I sublattice and the Gibbs free energy of the M-I alloy are discussed for both configuration A and B for fixed values of W_i/kT: $W_c/kT = -2$, $W_p/kT = -3$, and $W_{pc} = 0$,* except where stated otherwise. In Section B, the results of the present LRO approach will be discussed in relation to those of the Regular Solution (RS) model given in Reference 13.

*These values of W_c and W_p imply that pairwise interaction in the *c*-direction is taken twice as strong as pairwise interaction within the (001)-planes (the coordination numbers for these interactions are 2 and 6, respectively). The values chosen for W_i/kT yield representative results; the degrees of order are not very large or small and the composition regions where order and disorder occur are both of significant size. Chosing values for W_{pc} different from $W_{pc} = 0$ does not lead to major changes, and the conclusions to be drawn remain unaffected.

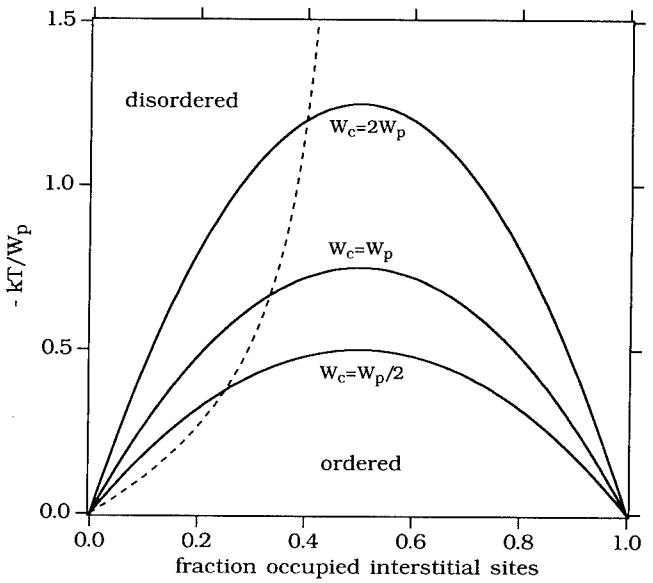
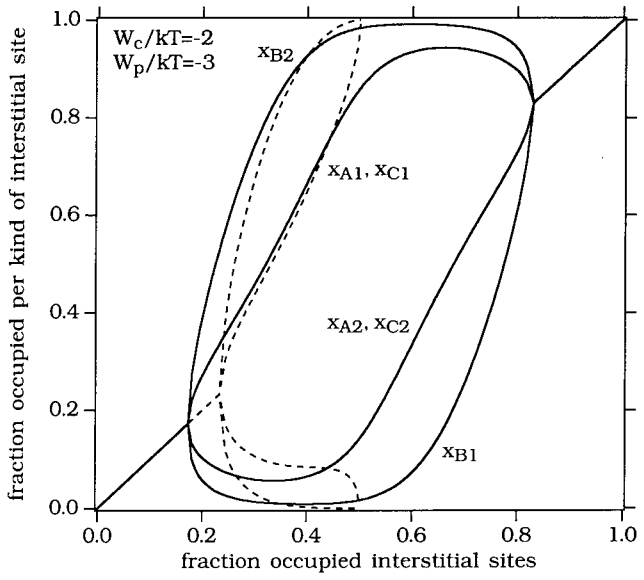
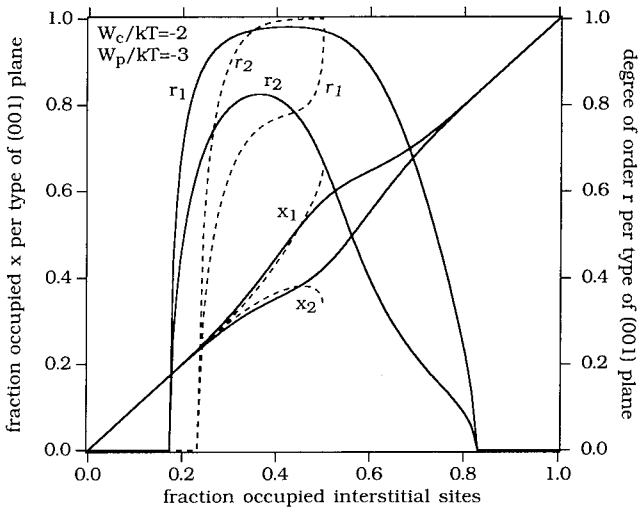


Fig. 4—Phase diagram showing order-disorder transitions according to the LRO model (solid line) and the RS model (dashed line). The composition ranges of the ordered and the disordered regions depend on the interaction energies and the temperature, *i.e.*, on the combination of W_c/kT and W_p/kT (here $W_{pc} = 0$).



(*a*)



(*b*)

Fig. 5—(*a*) Occupied fraction for each of the six kinds of I sites A1, . . ., C2 (Fig. 1(b)) as a function of the total fraction occupied of the sites of the hexagonal sublattice that is occupied by I atoms for configuration A, according to the LRO model (solid lines) and the RS model (dashed lines) for the interaction energies indicated. (*b*) Site occupancies, x_1 and x_2, and degrees of order, r_1 and r_2, as a function of the total fraction of the sites of the hexagonal sublattice that is occupied by I atoms for configuration A, according to the LRO model (solid lines) and the RS model (dashed lines; r_1 and r_2 in italics) for the interaction energies indicated.

1. *Site occupancies and degrees of order for the I sublattice*

The occupied fraction for each of the six kinds of sites (A1, B1, . . ., C2; Figure 1(b)), as obtained by route 1, is given in Figures 5(a) and 6(a) as a function of the total occupied fraction of I sites, $y(y = 1/6\ \Sigma_{K=A1}^{C2}\ x_K)$. In Figures 5(b) and 6(b), the (same) results are presented as obtained by route 2: the occupancies of the I sublattice and the degrees of order are presented as a function of the total occupied fraction of I sites, $y(y = (x_1 + x_2)/2$ for A and $y = (2x_{iv} + x_d)/3$ for B). Using Eqs. [9] and [10] for configuration A or Eq. [11] for configuration B, results obtained by route 1 can be expressed as results obtained by route 2 (and *vice versa*): it was found that, for the present case, routes 1 and 2 yield identical results.

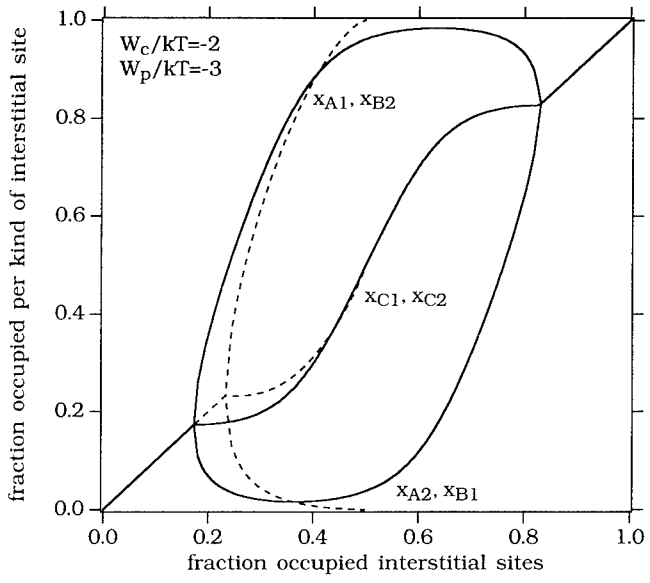
At the composition of the order-disorder transition, the degrees of order are continuous, but their derivatives, with respect to the total interstitial content, change discontinuously (Figures 5(b) and 6(b)). It is observed that the values of r are asymmetric with respect to $y = 1/2$. This can be understood from the definition of the degree of order, which is not affected in a symmetrical way by occupation by V of i sites and by I of v sites: if V "atoms" reside on i sites, r can still be equal to one, but if I atoms reside on v sites, r deviates from one (Eqs. [9] and [10]). For configuration A, the fractions x_1 and x_2 of occupied interstitial sites for the two types of (001)-planes diverge gradually at the onset of ordering and show a maximum difference at the composition M_2I (or IV on the I sublattice) (Figure 5(b)). This is accompanied with large differences in occupation of the various kinds of sites (Figure 5(a)). For configuration B, at the onset of ordering all I atoms prefer to occupy the sites involved in ordering. At the composition M_2I, the occupied fractions for the two types of sites (iv and d sites) are the same (Figure 6(b)). Of course, at the composition M_2I, a large difference occurs between the occupied fractions of the i (A1, B2) and v (A2, B1) sites (Figure 6(a)).

2. *Gibbs free energy of the M-I alloy*

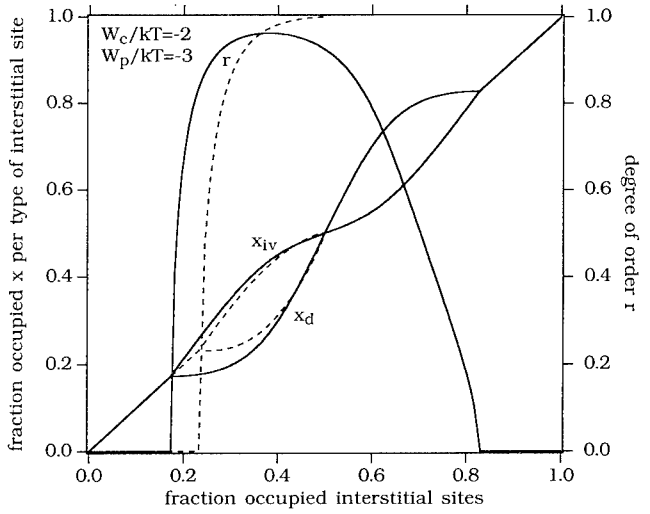
The equilibrium Gibbs free energy for the M-I alloy, $G_{M\text{-}I}$, is given as a function of the total occupied fraction of I sites, y, in Figure 7; these results were obtained by substituting the equilibrium values for $x_{A1}, x_{B1}, \ldots, x_{C2}$ in Eq. [1] (or x_1, x_2, r_1, r_2 in Eq. [A14] and x_{iv}, x_d, r in Eq. [A22]). This thermodynamic property is taken relative to a standard state, *viz.*, $G^0_{M\text{-}I} = 6(\mu^0_M + y\mu^0_I + (1 - y)\,\mu^0_V)$ (*cf.*, Eq. [1]). The bold square dots in Figure 7 indicate the order-disorder transitions; the drawn line in between these dots at less negative values for the Gibbs free energy, represents the Gibbs free energy for the disordered state.

The chemical potentials of I and M atoms on their respective sublattices can be readily obtained from $G_{M\text{-}I}$, applying Eqs. [2] and [5] for route 1 (or for route 2: Eqs. [A15] and [A16] for configuration A or Eqs. [A23] and [A24] for configuration B). The values for the Gibbs free energy are always finite. This is not the case for the chemical potentials of M and I: for $y \to 0$, $\mu_I \to -\infty$ and $\mu_M \to 0$; for $y \to 1$, $\mu_I \to +\infty$ and $\mu_M \to -\infty$. It can be easily shown that there is no discontinuity for the first derivative of the Gibbs free energy with respect to y, but the derivatives of the chemical potentials with respect to y are discontinuous at the order-disorder transition. Hence, the order-disorder transition as described by the present model is classified as second order [1], consistent with the condition that it cannot be a first-order phase transition (see Section III–A).

Obviously, for values of y in between the compositions for the order-disorder transition, ordering according to either of the configurations (A or B) leads to a



(*a*)



(*b*)

Fig. 6—(*a*) Occupied fraction for each of the six kinds of I sites A1, . . ., C2 (Fig. 1(b)) as a function of the total fraction of the sites of the hexagonal sublattice that is occupied by I atoms for configuration B, according to the LRO model (solid lines) and the RS model (dashed lines) for the interaction energies indicated. (*b*) Site occupancies, x_{iv} and x_d, and degree of order, r, as a function of the total fraction of the sites of the hexagonal sublattice that is occupied by I atoms for configuration B, according to the LRO model (solid lines) and the RS model (dashed lines) for the interaction energies indicated.

lower Gibbs free energy than that for the disordered configuration (Figures 7(a) and (b)). In view of the scale of the ordinate in Figures 7(a) and (b), the relative stabilities of configurations A and B cannot be distinguished in these figures. Therefore, the difference in Gibbs free energy between configurations B and A, $G^{B}_{M\text{-}I} - G^{A}_{M\text{-}I}$, is given as a function of the total fraction of occupied I sites, y, in Figure 7(c). Configuration B yields the more stable configuration of I atoms if $G^{B}_{M\text{-}I} - G^{A}_{M\text{-}I} < 0$ and configuration A yields the more stable configuration of I atoms if $G^{B}_{M\text{-}I} - G^{A}_{M\text{-}I} > 0$.

Phase diagrams representing the stability ranges of configurations A and B were calculated by considering thermodynamic equilibrium between these configurations for different combinations of the interaction energies W_p and W_c (*i.e.*, imposition of the conditions ${}^{A}\mu_I = {}^{B}\mu_I$ and ${}^{A}\mu_M = {}^{B}\mu_M$, where ${}^{J}\mu_K$ is the chemical potential of atoms K in configuration J). The results are given in Figure 8 for two values of W_c/W_p. If $|W_c/kT| \geq |W_p/kT|$, configuration A is the more stable type for the entire range of compositions within the ordered region, provided the value for $|W_p/kT|$ is not too large (*i.e.*, $|W_p| \leq \sim 3kT$ in Figure 8(a)). This can be understood as follows: a strong interaction in the *c*-direction (*i.e.*, a relatively large value of $|W_c/kT|$) is incompatible with the occurrence of *d* sites. If $|W_c/kT|$ becomes considerably smaller than $|W_p/kT|$, configuration A is only preferred in a narrow composition range around the composition M_2I. For example, for $W_c = 1/2\ W_p$, the homogeneity range of configuration A is confined to approximately $0.4 < y < 0.6$ (Figure 8(a)). It is noted that the transition from configuration A to configuration B is a first-order phase transition, whereas the disorder-order transition is a second-order phase transition.

The present theoretical results on the relative stabilities of configurations A and B can be compared with X-ray diffraction results for the ε-Fe_2N_{1-z} phase. This iron nitride can be conceived as an hcp sublattice of Fe-atoms containing N-atoms at the sublattice formed by the octahedral interstices. The crystal structure proposed for the composition ε-$Fe_2N_{2/3}$ ($z = 1/3$; $y = 1/3$)[11,12] is in accordance with ordering of the interstitial nitrogen atoms, according to configuration B. The crystal structure proposed for the composition ε-Fe_2N ($z = 0$; $y = 1/2$)[11,12] is in accordance with ordering of the interstitial nitrogen atoms, according to configuration A. These experimental results are thus compatible with the theoretical predictions (Figure 8).

B. *Comparison of the Long-Range Order Model with the Regular Solution Model for Ordering of Interstitials in an hcp Lattice*

Ordering on the basis of the two ground-state structures A and B (*cf.* Section III–B) was considered in Reference 13 by applying a "Regular Solution Model" (RS model). In the sequel, the present long range order approach will be indicated by LRO and the regular solution model of Reference 13 will be referred to as RS. The principal difference between the LRO and the RS models involves *a priori* exclusion of simultaneous occupation of nearest neighbor sites in the *c*-direction for the latter. This site-exclusion condition has a strong effect on the distribution possibilities of the I atoms on their sublattice and thus on the corresponding configurational entropy. Moreover, because of the site-exclusion condition, interactions in the *c*-direction do not occur, and hence, the corresponding exchange energy does not occur, and thus, the enthalpy is affected too. A further consequence of the site-exclusion condition is that the maximum occupation of the I sublattice

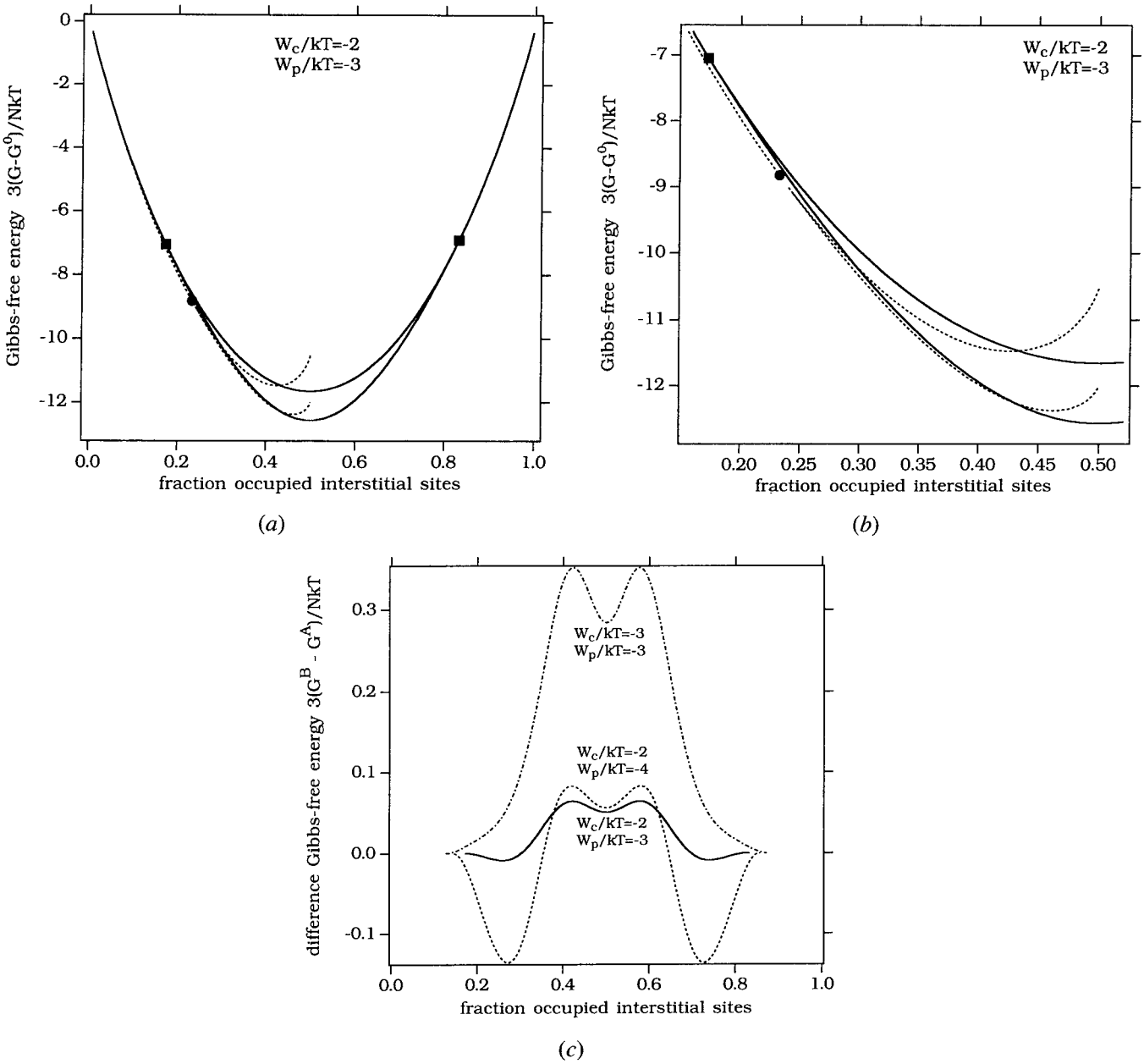


Fig. 7—(*a*) Gibbs free energy, $(G_{M\text{-}I} - G^0_{M\text{-}I})/(1/3)NkT$, as a function of the total fraction of the sites of the hexagonal sublattice that is occupied by I atoms. The drawn lines outside and in between the square dots, at the less negative values, represent the Gibbs free energy for a disordered distribution of I atoms; the drawn line in between the square dots at the more negative values represents the Gibbs free energy for the LRO configurations A and B. The dashed lines hold for the RS model that predicts ordering within the (001)-planes for I contents above that indicated by the dot (less negative values: disordered; more negative values: ordered). (*b*) Enlargement of (a). (*c*) Difference in Gibbs free energy, $G_{M\text{-}I}$, between configurations B and A. $(G^B_{M\text{-}I} - G^B_{M\text{-}I})/(1/3)NkT$, as a function of the total fraction of the sites of the hexagonal sublattice that is occupied by I atoms for different combinations of W_c/kT and W_p/kT.

is given by $y = 1/2$. Results of the RS model are presented in Figures 4 through 7(a) and (b) by use of dashed lines. These results were obtained using analogous procedures as employed in the LRO approach. Routes 1 and 2 (Section III) yielded identical results for the RS model.

For the content of interstitials at the order-disorder transition, x_t, it holds according to the RS model[13] that

$$x_t = \frac{1}{2}\left(1 - \frac{2kT_t}{W_p - W_{pc}} - \sqrt{1 + \left[\frac{2kT_t}{W_p - W_{pc}}\right]^2}\right) \quad [12]$$

In Reference 13, Eq. [12] was obtained with $W_p/k = -L/R$ (R is the gas constant) and without taking into account third nearest-neighbor interaction (represented here by W_{pc}); this effect is included here to allow comparison with the results of the present LRO model (Eqs. [7] and [A21]). A large difference occurs between the order-disorder boundaries of the LRO model and the RS model (Figure 4). In this respect, it is noted that a fully disordered state cannot exist within the RS model, since the site-exclusion condition in the *c*-direction is assumed for *all* compositions. Therefore, the dashed line

in Figure 4 in fact indicates the order-disorder transition within the (001)-planes only. For the RS model, ordering is only possible if $(W_p - W_{pc}) < 0$ (*cf.* Eq. [12]). A physically unrealistic situation arises for $y = 1/2$, because for all possible temperatures, full ordering and thus no order-disorder transition occurs (Figure 4). This result is another immediate consequence of the site-exclusion condition: for $y = 1/2$ the configurational entropy equals zero, and thus, the Gibbs free energy relative to the standard state is independent of temperature, implying that the ground-state structure occurs at all temperatures.

If $|W_c|$ is not very small (for site exclusion the virtual $|W_c| = \infty$), the content x_t for the order-disorder transition as obtained from the LRO model is smaller than that predicted by the RS model; *i.e.*, ordering according to the LRO model starts at smaller interstitial contents than according to the RS model. The partial order imposed by the site-exclusion condition in the RS model postpones ordering to a higher total occupied fraction.

1. *Site occupancy*

In order to allow a direct comparison of the results obtained with the LRO model and the RS model, the values for W_p were taken equal. The case of ordering under the constraint of the site-exclusion condition in the RS model demands the degrees of order to be equal to 1 at the composition M_2I. Equivalently, for this composition, the occupied fractions per type of (001)-plane or per type of interstitial site are strictly prescribed. This is not the case for the present LRO model. So, in principle, at least near the composition M_2I, the site occupancies according to the LRO and the RS model are different.

In contrast with the RS model, the LRO model does not prescribe a zero probability for simultaneous occupation by I atoms of neighboring sites in the *c*-direction of configurations A and B (*cf.* Eq. [A4a]). This probability is shown in Figure 9 for the values of the exchange energies indicated. As compared to the disordered situation, on ordering the probability that neighboring sites in the *c*-direction are both occupied by I atoms decreases and remains low for interstitial contents smaller than 1/2 (the composition M_2I). Obviously, the amount of nearest neighbors in the *c*-direction increases rapidly on approaching the interstitial content 1/2 and beyond. From Figure 9, it can be seen that in the LRO approach, simultaneous occupation of nearest neighboring sites in the *c*-direction tends to be excluded.

2. *Gibbs free energy*

Comparing the Gibbs free energies for configurations A and B as obtained by the RS model, it was concluded

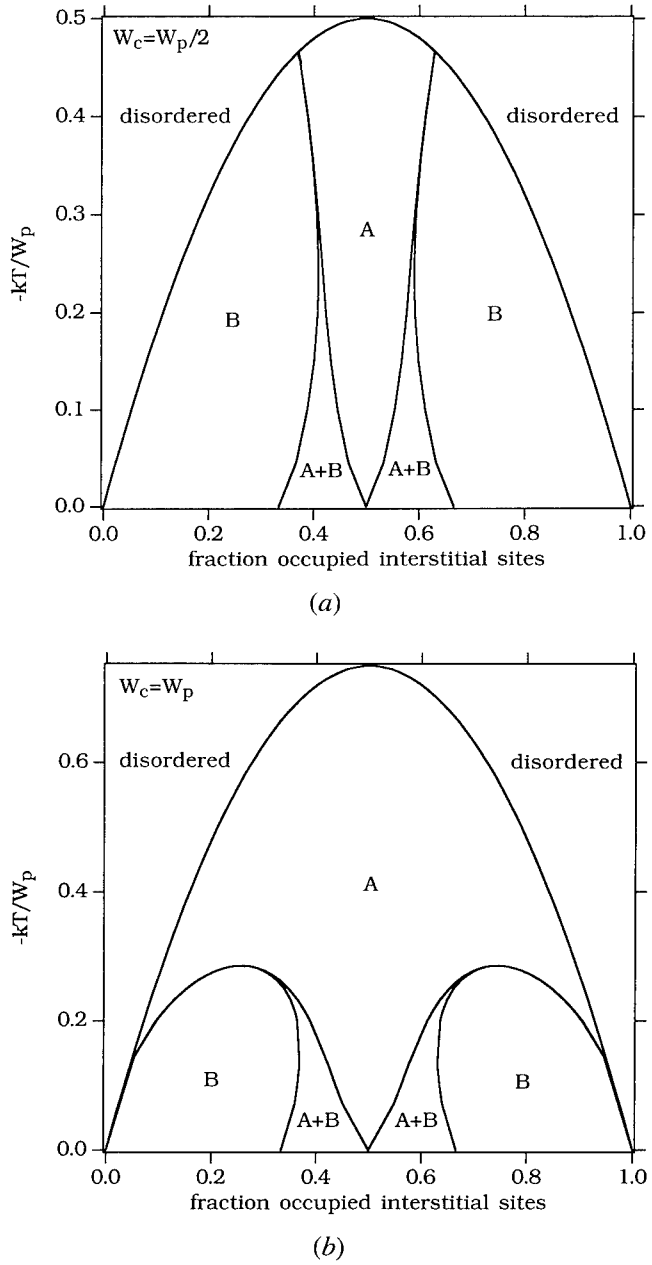


Fig. 8—Phase diagram showing single- and dual-phase regions for the ordered configurations (phases) A and B: (*a*) $W_c = W_p/2$ and (*b*) $W_c = W_p$.

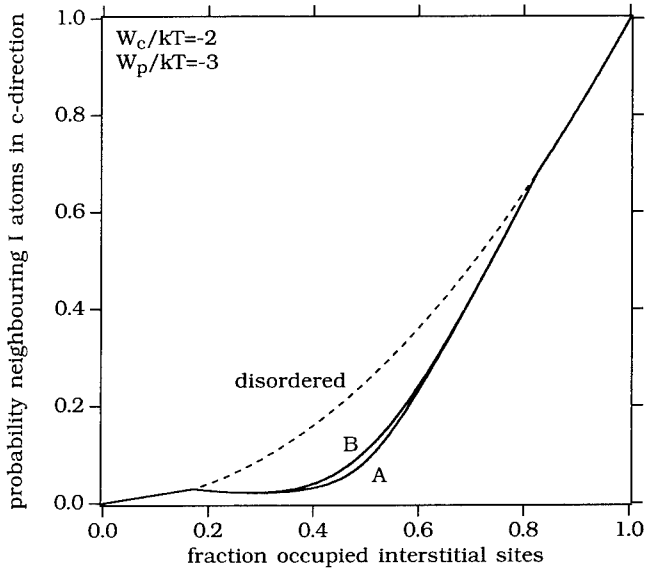


Fig. 9—Probability according to the LRO model for the occurrence of simultaneous occupancy by I atoms of neighboring sites in the *c*-direction as a function of the total fraction occupied of the sites of the I sublattice.

in Reference 13 that configuration B yields a more negative value for the Gibbs free energy than configuration A for all compositions within the ordered region according to the RS model. This finding is opposite to the results obtained with the LRO approach, where configuration A (1) is always stable near the stoichiometric composition M_2I and (2) for $|W_c/kT| \gg |W_p/kT|$ it becomes stable in the entire ordered region (Figures 7(c) and 8 and the discussion in Section A-2).

The stabilities of a configuration (A or B) according to the LRO model and the RS model can be compared on the basis of the corresponding Gibbs free energies. Such a comparison of the LRO and the RS model is only justified (1) if equal values for the exchange energies are used and (2) if the reference states, *i.e.*, $G^0_{M\text{-}I} = 6\,(\mu^0_M + y\mu^0_I + (1-y)\mu^0_V)$, are identical. Adopting the treatment of section III and taking into account interactions among I atoms up to the third nearest neighbors, it holds

LRO model: $H^0_I = N(Z_c/2\, e_{c,II} + Z_p/2\, e_{p,II} + Z_{pc}/2\, e_{pc,II})$;
RS model: $H^0_I = N(Z_p/2\, e_{p,II} + Z_{pc}/2\, e_{pc,II})$;*

*The reference state as described in Reference 13 was not explicitly defined, but expressed in the present terminology, it holds that $\mu^0_I = H^0_I - TS^0_{vib,I} + H^0_{M\text{-}I} + W_p$, with H^0_I of the RS model given above. The regular solution parameter L of Reference 13 is identical to $-NW_p$ in this article.

where $Z_{pc}/2$ is the number of bonds among third nearest neighbors. Thus, the reference states for the LRO and the RS model are not identical because of omittance of interstitial interactions in the c-direction by the RS model. Then, if the interaction energies $e_{c,IV}$ and $e_{c,VV}$ are small as compared to $e_{c,II}$, which is likely to be the case if V represents vacancies, the exchange energy W_c, as given by Eq. [A7], reads $-Z_c/2\, e_{c,II}$. Then, the reference state for the RS model can be made compatible with that for the LRO model by subtracting the value of NW_c from the value of H^0_I for the RS model, as indicated in this section. The Gibbs free energies for the RS model adapted in this way, *i.e.*, to all values for the Gibbs free energy the value of NW_c is added, are presented in Figures 7(a) and (b).

For small fractions of occupied interstitial sites, the RS model yields more negative values for the Gibbs free energy than the LRO model, but the differences are relatively small (Figure 7(b)). However, if the interstitial content approaches the composition M_2I, a substantial difference of opposite sign occurs: ordering as considered in the LRO model corresponds to the most stable state. The less stable interstitial configuration predicted by the RS model near the composition M_2I is caused by the rigid demand of the site-exclusion condition. Apparently, even if the repulsion between I atoms in the c-direction is strong, the presence of a small fraction of I atoms on nearest neighboring sites in the c-direction is favorable. Then, the small negative effect on the enthalpy is compensated by the strong positive effect on the configurational entropy.

V. CONCLUSIONS

1. Long-range ordering of atoms I and vacancies V on the sublattice constituted by the octahedral interstices of an hcp sublattice of atoms M can be described by applying the Gorsky–Bragg–Williams (GBW) approximation (or zeroth approximation to the Ising model) to a trigonal prism constituted by six kinds of sites for atoms I and vacancies V, considering pairwise interaction up to third nearest neighbors. Two routes can be followed:
   - Route 1 starts with a description for the occupancy of each of the six sites on the trigonal prism and the associated chemical potentials.
   - Route 2 starts with a ground-state structure for distinguishing between order and disorder sites. Relative to the ground-state structure, LRO parameters can be defined.
2. The possible ground-state structures on sites of the trigonal prism have been derived as a function of the pairwise interaction energies following route 1. Two of these ground-state structures form the basis for two configurations, denoted as configurations A and B, to which the GBW approximation is applied following route 2. The ground-state structure forming the basis for configuration A is characterized by an alternation of (001)-planes having average compositions I_2V and IV_2; the ground-state structure forming the basis for configuration B is characterized by (001)-planes having equal compositions.
3. The stabilities of the ordered configurations A and B with respect to one another and with respect to the disordered configuration as a function of the overall occupancy of the interstitial sublattice can be represented by phase diagrams showing monophase (A and B and disorder) and dual-phase (A + B) regions. Configuration B is the more stable configuration for interstitial contents lower than the one for the stoichiometric composition M_3I and higher than the one for the stoichiometric composition M_3I_2; configuration A is generally preferred near the stoichiometric composition M_2I. This agrees with reported data for ε-Fe_2N_{1-z}. It was found that the stronger the repulsive interaction in the c-direction, relative to the repulsive interaction within the (001)-planes, the broader is the homogeneity range of configuration A. Further, the results showed that ordering itself is a second-order phase transition, while the transition from one ordered configuration to the other is a first-order phase transition.
4. The results were compared to those of a regular solution model for interstitials in an hcp lattice that excludes simultaneous occupancy of neighboring sites in the c-direction for all compositions. The present LRO model provides a physically more realistic description and leads to thermodynamically more stable configurations in the ordered region.

APPENDIX A

The thermodynamic description of configuration A, based on the prescription of the site occupancies according to Eqs. [9] and [10], and the thermodynamic description of configuration B, based on the prescription of the site occupancies according to Eq. [11], will be given here.

Configuration A

Configurational entropy

For the (001) planes of type 1, the number of distribution possibilities D_{i1} of I and V on the $i1$ sites follows from the total number of $i1$ sites ($2/3N$), the number of I atoms on $i1$ sites ($N_{I,i1}$, Eq. [9a]), and the number of V on il sites ($N_{V,i1}$, Eq. [9c]):

$$D_{i1} = \frac{\frac{2}{3}N!}{N_{I,i1}!\,N_{V,i1}!} = \frac{\frac{2}{3}N!}{\left[(2+r_1)\,x_1\frac{N}{3}\right]!\left[(2-(2+r_1)x_1)\frac{N}{3}\right]!} \quad [A1]$$

The numbers of distribution possibilities D_{v1}, D_{i2}, and D_{v2} of I and V on the $v1$, $i2$, and $v2$ sites, respectively, are obtained in a similar way (using Eqs. [9] and [10]).

The total configurational entropy S of the pseudo-binary alloy I-V (entropy of mixing I and V) for one (001) plane of type I and one (001) plane of type 2 (each plane containing a total of N sites) is given by

$$S = k\,[\ln(D_{i1}) + \ln(D_{v1}) + \ln(D_{i2}) + \ln(D_{v2})] \quad [A2]$$

where k is Boltzmann's constant. Substituting the numbers of distribution possibilities (*cf.* Eq. [A1]) in Eq. [A2] and using Stirling's approximation ($\ln(n!) = n\ln(n) - n$ for large n) the total configurational entropy S_{conf} is readily obtained as

$$\begin{aligned} S_{conf} = \frac{1}{3}Nk\{&4\ln(2) - [(2+r_1)\,x_1]\ln[(2+r_1)\,x_1] \\ &- [2-(2+r_1)\,x_1]\ln[2-(2+r_1)\,x_1] \\ &- [(1-r_1)\,x_1]\ln[(1-r_1)\,x_1] \\ &- [1-(1-r_1)\,x_1]\ln[1-(1-r_1)\,x_1] \\ &- [(1+2r_2)\,x_2]\ln[(1+2r_2)\,x_2] \\ &- [1-(1+2r_2)\,x_2]\ln[1-(1+2r_2)\,x_2] \\ &- [(2-2r_2)\,x_2]\ln[(2-2r_2)\,x_2] \\ &- [2-(2-2r_2)\,x_2]\ln[2-(2-2r_2)\,x_2]\} \end{aligned} \quad [A3]$$

Since the occupation of the M sublattice is complete and M and I atoms do not reside on each other's sublattices, M does not contribute to the configurational entropy and Eq. [A3] pertains to the whole M-I alloy as well.

Pairwise nearest neighbor interaction in the c-direction of the I sublattice

The probability P_{II} that two neighboring sites in the c-direction are both occupied by I atoms is given by the chance for simultaneous occupancy of $i1$ and $v2$ and of $v1$ and $i2$ sites. Hence, recognizing that the probability of occupancy of, *e.g.*, an $i1$ site by an I atom is $N_{I,i1}/(2/3N)$, it follows that

$${}^cP_{II} = \frac{2}{3}\frac{N_{I,i1}}{\frac{2}{3}N}\frac{N_{I,v2}}{\frac{2}{3}N} + \frac{1}{3}\frac{N_{I,v1}}{\frac{1}{3}N}\frac{N_{I,i2}}{\frac{1}{3}N} \quad [A4a]$$

The number of $i1$-$v2$ neighbors is twice as high as the number of $v1$-$i2$ neighbors due to the respective composition of the type 1 (i_2v) and type 2 (v_2i) planes. Further, ${}^cP_{II}$ can maximally equal 1. Both constraints are expressed in Eq. [A4a] by the factors 2/3 and 1/3. The probabilities ${}^cP_{VV}$ and ${}^cP_{IV}$ for V-V and I-V nearest neighbors, respectively (in the c-direction), are obtained likewise:

$${}^cP_{VV} = \frac{2}{3}\frac{N_{V,i1}}{\frac{2}{3}N}\frac{N_{V,v2}}{\frac{2}{3}N} + \frac{1}{3}\frac{N_{V,v1}}{\frac{1}{3}N}\frac{N_{V,i2}}{\frac{1}{3}N} \quad [A4b]$$

$${}^cP_{IV} = \frac{2}{3}\left[\frac{N_{I,i1}}{\frac{2}{3}N}\frac{N_{V,v2}}{\frac{2}{3}N} + \frac{N_{V,i1}}{\frac{2}{3}N}\frac{N_{I,v2}}{\frac{2}{3}N}\right] + \frac{1}{3}\left[\frac{N_{V,v1}}{\frac{1}{3}N}\frac{N_{V,i2}}{\frac{1}{3}N} + \frac{N_{V,v1}}{\frac{1}{3}N}\frac{N_{I,i2}}{\frac{1}{3}N}\right] \quad [A4c]$$

The sum ${}^cP_{II} + {}^cP_{VV} + {}^cP_{IV}$ of course, equals 1.

The energy E_c resulting from the pairwise nearest neighbor interactions in the c-direction is proportional to the sum of the products of the probabilities ${}^cP_{II}$, ${}^cP_{VV}$, and ${}^cP_{IV}$ and their corresponding interaction energies $e_{c,II}$, $e_{c,VV}$, and $e_{c,IV}$. Neglecting pressure and volume (pV) effects of mixing I and V, the enthalpy H_c is equal to the energy E_c. Hence, recognizing that the total number of c interactions for a pair of type 1 and type 2 planes is $2N$, it follows for such a pair

$$H_c = [{}^cP_{II}\,e_{c,II} + {}^cP_{VV}\,e_{c,VV} + {}^cP_{IV}\,e_{c,IV}]\,2N \quad [A5]$$

Using Eqs. [9] and [10], substitution of the probabilities given by Eq. [A4] in Eq. [A5] yields

$$H_c = [x_1 + x_2]\,H^0_{I,c} + [(1-x_1) + (1-x_2)]\,H^0_{V,c} + NW_c[x_1(1-x_2) + x_2(1-x_1)] + 2NW_c r_1 r_2 x_1 x_2 \quad [A6]$$

where $H^0_{I,c} = N\,Z_c/2\,e_{c,II}$ and $H^0_{V,c} = N\,Z_c/2\,e_{c,VV}$ with $Z_c/2$ being the number of bonds in the c-direction per atom ($Z_c/2 = 1$). W_c is the "exchange energy" in the c-direction:

$$W_c = \frac{Z_c}{2}[2e_{c,IV} - e_{c,II} - e_{c,VV}] \quad [A7]$$

The term $H^0_{I,c}$ is a fraction of H^0_I, the enthalpy of N atoms of the pure component I (with exactly the same lattice as the I sublattice). Accordingly, $H^0_{V,c}$ is a fraction of H^0_V, the enthalpy of N atoms of the pure component V (with exactly the same lattice as the I sublattice; for the

present case, where V of the hypothetical IV alloy represents vacant I sites, H^0_V of course is zero). The first two terms on the right-hand side of Eq. [A6] represent the "ideal mixing" enthalpy of the hypothetical I-V alloy. The third term on the right-hand side of Eq. [A6] represents the change in enthalpy due to random mixing, but taking into account the difference in interaction energy of I-I, V-V, and I-V, nearest neighbors. This is the same enthalpy change as emerging in the "zeroth approximation to the *regular* solutions" for an I-V alloy. The last term on the right-hand side of Eq. [A6] represents the change in enthalpy due to ordering.

Pairwise nearest neighbor interaction within the (001) planes of the I sublattice

The probability ${}^1P_{II}$ that two neighboring sites within a plane of type 1 (i_2v) are both occupied by I atoms is given by the chance for simultaneous occupancy by I atoms of two $i1$ sites and of $i1$ and $v1$ sites:

$$ {}^1P_{II} = \frac{1}{3}\frac{N_{I,i1}}{\frac{2}{3}N}\frac{N_{I,i1}}{\frac{2}{3}N} + \frac{2}{3}\frac{N_{I,i1}}{\frac{2}{3}N}\frac{N_{I,v1}}{\frac{1}{3}N} \qquad [A8a] $$

In a plane of type 1, the number of $i1$-$i1$ interactions is half of the number of $i1$-$v1$ interactions (Figure 3(a)), which is expressed in Eq. [A8a] by the factors 1/3 and 2/3, respectively. The other probabilities in a plane of type 1, ${}^1P_{VV}$ and ${}^1P_{IV}$, are obtained analogously:

$$ {}^1P_{VV} = \frac{1}{3}\frac{N_{V,i1}}{\frac{2}{3}N}\frac{N_{V,i1}}{\frac{2}{3}N} + \frac{2}{3}\frac{N_{V,i1}}{\frac{2}{3}N}\frac{N_{V,v1}}{\frac{1}{3}N} \qquad [A8b] $$

$$ {}^1P_{IV} = \frac{1}{3}\left[\frac{N_{I,i1}}{\frac{2}{3}N}\frac{N_{V,i1}}{\frac{2}{3}N} + \frac{N_{V,i1}}{\frac{2}{3}N}\frac{N_{I,i1}}{\frac{2}{3}N}\right] + \frac{2}{3}\left[\frac{N_{I,i1}}{\frac{2}{3}N}\frac{N_{V,v1}}{\frac{1}{3}N} + \frac{N_{V,i1}}{\frac{2}{3}N}\frac{N_{I,v1}}{\frac{1}{3}N}\right] \qquad [A8c] $$

The probabilities ${}^2P_{II}$, ${}^2P_{VV}$, and ${}^2P_{IV}$ for a plane of type 2 (v_2i) can be obtained directly from Eq. [A8], by replacing $i1$ by $v2$ and $v1$ by $i2$.

The enthalpy H_p for a pair of planes of types 1 and 2 due to nearest neighbor interaction within the planes is

$$ H_p = [({}^1P_{II} + {}^2P_{II})\, e_{p,II} + ({}^1P_{VV} + {}^2P_{VV})\, e_{p,VV} + ({}^1P_{IV} + {}^2P_{IV})\, e_{p,IV}]\, 3N \qquad [A9] $$

where $e_{p,II}$, $e_{p,VV}$, and $e_{p,IV}$ are the interaction energies between I-I, V-V, and I-V nearest neighbors within the (001) planes, respectively, and the factor $3N$ accounts for the total number of nearest neighbor interactions within one plane. Using Eqs. [9] and [10], substitution of the probabilities given by Eq. [A8] in Eq. [A9] yields

$$ H_p = [x_1 + x_2]\, H^0_{I,p} + [(1 - x_1) + (1 - x_2)]\, H^0_{V,p} + NW_p[x_1(1 - x_1) + x_2(1 - x_2)] + NW_p\left[\frac{1}{4}(x_1r_1)^2 + (x_2r_2)^2\right] \qquad [A10] $$

where $H^0_{I,p} = N\, Z_p/2\; e_{p,II}$ and $H^0_{V,p} = N\, Z_p/2\; e_{p,VV}$ with $Z_p/2$ being the number of bonds within one (001) plane per atom ($Z_p/2 = 3$). The term W_p is the "exchange energy" for the (001) planes:

$$ W_p = \frac{Z_p}{2}[2e_{p,IV} - e_{p,II} - e_{p,VV}] \qquad [A11] $$

Interpretation of the terms on the right-hand side of Eq. [A10] corresponds to that given for Eq. [A6].

Interaction of the M and I sublattices

Since the occupation of the M sublattice is complete and every site of the I sublattice is surrounded by atoms M in a similar way, the probability P_{MI} of finding a pair M-I for a pair of planes of type 1 and type 2 is determined only by the occupancy of the I sublattice by I atoms:

$$ P_{MI} = \frac{1}{2}\left\{\frac{2}{3}\left(\frac{N_{I,i1}}{\frac{2}{3}N} + \frac{N_{I,v2}}{\frac{2}{3}N}\right) + \frac{1}{3}\left(\frac{N_{I,v1}}{\frac{1}{3}N} + \frac{N_{I,i2}}{\frac{1}{3}N}\right)\right\} = \frac{1}{2}(x_1 + x_2) \qquad [A12a] $$

The probability P_{MV} of finding V adjacent to M is obtained likewise:

$$ P_{MV} = 1 - P_{MI} = \frac{1}{2}(1 - x_1 + 1 - x_2) \qquad [A12b] $$

The enthalpy H_{MI} due to interaction of I atoms and their surrounding M atoms, per pair of type 1 and type 2 planes, can thus be described by

$$ H_{MI} = (x_1 + x_2)\, H^0_{MI} \qquad [A13a] $$

where H^0_{MI} represents the interaction of N atoms I with their surrounding M atoms (Note that there are $2N$ sites for I atoms per pair of type 1 and type 2 planes). For the enthalpy H_{MV} associated with interaction of M and V, it is obtained

$$ H_{MV} = (1 - x_1 + 1 - x_2)\, H^0_{MV} \qquad [A13b] $$

where H^0_{MV} represents the interaction energy of N atoms V with their surrounding M atoms. If V represents vacant I sites with no interaction of M and V, $H^0_{M\text{-}V}$ is zero.

Gibbs free energy, chemical potential, and equilibrium condition

Using Eqs. [A3], [A6], [A10], and [A13] and superimposing the Gibbs free energy of the M sublattice (*i.e.*, the Gibbs free energy of the pure component M, which is given by $H^0_M - TS^0_{vib,M}$ for N atoms M) the total Gibbs free energy $G_{M\text{-}I}$ of the M-I(-V) alloy, for the considered pair of type 1 and type 2 planes of the I sublattice and the associated pair of planes of the M sublattice (each containing N atoms M), becomes

$$G_{\text{M-I}} = 2(H^0_{\text{M}} - TS^0_{\text{vib,M}}) + [x_1 + x_2]\,(H^0_{\text{I}} - TS^0_{\text{vib,I}} + H^0_{\text{MI}}) + [(1 - x_1) + (1 - x_2)]\,(H^0_{\text{V}} - TS^0_{\text{vib,V}} + H^0_{\text{MV}}) + NW_c\,[x_1(1 - x_2) + x_2(1 - x_1)] + NW_c[2r_1r_2x_1x_2] + NW_p\,[x_1(1 - x_1) + x_2(1 - x_2)] + NW_p\left[\frac{1}{4}(x_1r_1)^2 + (x_2r_2)^2\right] - TS_{\text{conf}} \qquad [A14]$$

where S_{conf} is given by Eq. [A3] and H^0_Q is the enthalpy of N atoms of the pure component Q (Q = M, I, V; $H^0_{\text{I}} = H^0_{\text{I},p} + H^0_{\text{I},c}$, $H^0_{\text{V}} = H^0_{\text{V},p} + H^0_{\text{V},c}$) and $S^0_{\text{vib},Q}$ denotes the vibrational entropy of N atoms of the pure component Q, which is assumed to be independent of composition and ordering. The first three terms on the right-hand side of Eq. [A14] represent the standard state of the M-I alloy. It is noted that the contribution of the M sublattice and its interaction with the I sublattice only change the standard state and, consequently, do not affect ordering on the I sublattice. Recognizing that V represents empty sites on the I sublattice: $e_{\text{VV}} = 0$ and $H^0_{\text{V}} = 0$.

In $G_{\text{M-I}}$, as given by Eq. [A14], pairwise interactions on the I sublattice up to second nearest neighbors (*i.e.*, first nearest neighbors within the (001) planes: interactions A1-B1, A1-C1, *etc.*) are taken into account. Accounting for the effect of at least second nearest neighbors is necessary to attain a useful thermodynamic description. In general, the exchange energies associated with the interactions are unknown and should, therefore, be considered as parameters to be fitted to experimental data. Adding more nearest-neighbor-interaction terms to the thermodynamic description increases the number of such fit parameters. This number should be kept as small as possible.

The Gibbs free energy $G_{\text{M-I}}$ of the M-I alloy in general can be related to chemical potentials ${}^1\mu_{\text{I}}$ and ${}^1\mu_{\text{V}}$ of I and V, respectively, in (001) planes of type 1 and to chemical potentials ${}^2\mu_{\text{I}}$ and ${}^2\mu_{\text{V}}$ of I and V, respectively, in (001) planes of type 2 and to the chemical potential μ_{M} of M:

$$G_{\text{M-I}} \equiv 2\mu_{\text{M}} + x_1\,{}^1\mu_{\text{I}} + (1 - x_1)\,{}^1\mu_{\text{V}} + x_2\,{}^2\mu_{\text{I}} + (1 - x_2)\,{}^2\mu_{\text{V}} \qquad [A15]$$

where the chemical potentials pertain to N atoms (M, I, V), while the Gibbs free energy pertains to $2N$ atoms of M and $(x_1 + x_2)N$ atoms of I. If V represents vacant I sites, it holds that ${}^1\mu_{\text{V}} = {}^2\mu_{\text{V}} \equiv 0$. Then, the chemical potentials ${}^1\mu_{\text{I}}$ and ${}^2\mu_{\text{I}}$ each for N atoms I in the corresponding planes are defined as for an open system (*cf.* Eq. [2]):

$${}^1\mu_{\text{I}} = \frac{\partial G_{\text{M-I}}}{\partial x_1}, \qquad {}^2\mu_{\text{I}} = \frac{\partial G_{\text{M-I}}}{\partial x_2} \qquad [A16]$$

For equilibrium between I atoms in the two types of planes, it holds that

$${}^1\mu_{\text{I}} = {}^2\mu_{\text{I}} \equiv \mu_{\text{I}} \Rightarrow \frac{\partial G_{\text{M-I}}}{\partial x_1} - \frac{\partial G_{\text{M-I}}}{\partial x_2} = 0 \qquad [A17]$$

The occurrence of ordering originates from a Gibbs free energy for an ordered configuration of the I atoms lower than that for the disordered configuration. The degrees of order in the planes of type 1 and type 2, r_1 and r_2, respectively, will take values corresponding with a minimum value for the Gibbs free energy, according to Eq. [A14]. Hence, for equilibrium,

$$\frac{\partial G_{\text{M-I}}}{\partial r_1} = 0 \quad \text{and} \quad \frac{\partial G_{\text{M-I}}}{\partial r_2} = 0 \qquad [A18]$$

Thermodynamical equilibrium of the M-I alloy is described by the Gibbs free energy given by Eq. [A14] subject to the equilibrium conditions, according to Eqs. [A17] and [A18]. The equations for the equilibrium conditions obtained in this way are nonlinear with respect to the variables x_1, x_2, r_1, and r_2. The numerical evaluation method for solving these equations is given in Appendix B.

Order-disorder transition

The three equilibrium conditions (Eqs. [A17] and [A18]) can each be written as $f(\underline{x}) = f(r_1, r_2, x_1, x_2) = 0$. If $\underline{x} + d\underline{x}$ and $\underline{x}$ are sufficiently close, it holds for all $\underline{x}$ that

$$f(\underline{x} + d\underline{x}) = f(\underline{x}) + \frac{\partial f}{\partial r_1}dr_1 + \frac{\partial f}{\partial r_2}dr_2 + \frac{\partial f}{\partial x_1}dx_1 + \frac{\partial f}{\partial x_2}dx_2$$

provided that $f(\underline{x})$ is continuous for $\underline{x}$. If equilibrium holds for both $\underline{x}$ and $\underline{x} + d\underline{x}$ it thus follows that

$$\frac{\partial f}{\partial r_1}dr_1 + \frac{\partial f}{\partial r_2}dr_2 + \frac{\partial f}{\partial x_1}dx_1 + \frac{\partial f}{\partial x_2}dx_2 = 0$$

Moreover, the infinitesimal changes dr_1, dr_2, dx_1, and dx_2 within the range $\underline{x}$ to $\underline{x} + d\underline{x}$ can be taken proportional to one another. The ratios of dr_1, dr_2, dx_1, and dx_2 are defined as follows: $dr_2 = g \cdot dr_1$, $dx_1 = h \cdot dr_1$, and $dx_2 = i \cdot dr_1$ (g, h, and i are yet unknown real values), provided that $dr_1 \neq 0$ (this holds within the ordered region at least at the order-disorder transition). Explicit substitution of $f(\underline{x})$ by the three equilibrium conditions (Eqs. [A17] and [A18] and dropping the subscript M-I) thus yields

$$\frac{\partial}{\partial r_1}\left(\frac{\partial G}{\partial r_1}\right) + g\frac{\partial}{\partial r_2}\left(\frac{\partial G}{\partial r_1}\right) + h\frac{\partial}{\partial x_1}\left(\frac{\partial G}{\partial r_1}\right) + i\frac{\partial}{\partial x_2}\left(\frac{\partial G}{\partial r_1}\right) = 0 \qquad [A19a]$$

$$\frac{\partial}{\partial r_1}\left(\frac{\partial G}{\partial r_2}\right) + g\frac{\partial}{\partial r_2}\left(\frac{\partial G}{\partial r_2}\right) + h\frac{\partial}{\partial x_1}\left(\frac{\partial G}{\partial r_2}\right) + i\frac{\partial}{\partial x_2}\left(\frac{\partial G}{\partial r_2}\right) = 0 \qquad [A19b]$$

$$\frac{\partial}{\partial r_1}\left(\frac{\partial G}{\partial x_1} - \frac{\partial G}{\partial x_2}\right) + g\frac{\partial}{\partial r_2}\left(\frac{\partial G}{\partial x_1} - \frac{\partial G}{\partial x_2}\right) + h\frac{\partial}{\partial x_1}\left(\frac{\partial G}{\partial x_1} - \frac{\partial G}{\partial x_2}\right) + i\frac{\partial}{\partial x_2}\left(\frac{\partial G}{\partial x_1} - \frac{\partial G}{\partial x_2}\right) = 0 \qquad [A19c]$$

Since $f(\underline{x})$ has to be continuous for $\underline{x}$, and since $f(\underline{x})$ represents first derivatives of the Gibbs free energy with respect to r_1, r_2, x_1, and x_2, the order-disorder transition cannot be a first-order phase transition. At the order-disorder transition, equilibrium requires that

$$r_1 = r_2 = 0, \qquad x_1 = x_2 \qquad [A20]$$

Substitution of G according to Eq. [A14] and of Eq. [A20] in Eqs. [A19] yields a description of the order-disorder transition. It is obtained that

$$g = 0.5, \qquad h = i,$$

$$x_{1,t} = x_{2,t} = \frac{1}{2}\left(1 \pm \sqrt{1 + \frac{4kT}{2W_c + W_p - W_{pc}}}\right) \qquad [A21]$$

where $x_{1,t}$ and $x_{2,t}$ are x_1 and, x_2 respectively, at the order-disorder transition. Hence, ordering occurs for $(1 - \alpha) < x_1 + x_2 < (1 + \alpha)$ with $\alpha = \sqrt{1 + 4kT/(2W_c + W_p - W_{pc})}$. In Eq. [A21] (and in α), the influence of the third nearest-neighbor exchange energy W_{pc} (due to interactions A1-B2, A1-C2, *etc.*) on the order-disorder transition is also taken into account (Section III–A). At the onset of ordering, the evolution of the r_1 and r_2 are coupled through g, and the evolution of the interstitial contents x_1 and x_2 are coupled through h and i. The results of Eq. [A21] are identical to the results of Eq. [7] for case (2) as expected.

Configuration B

Gibbs free energy, chemical potential, and equilibrium condition

Proceeding analogously, as for configuration A, expressions are obtained for the configurational entropy of the I atoms on their sublattice and for the enthalpies associated with pairwise interactions of I atoms in the c-direction as well as within the (001) planes of the I sublattice. Then, including the interaction between the M and I sublattices, the Gibbs free energy $G_{\text{M-I}}$ for a pair of (001) planes and the associated pair of planes of M atoms is obtained as (*cf.* Eq. [A14])

$$\begin{aligned}\frac{1}{2}G_{\text{M-I}} = {} & (H^0_{\text{M}} - TS^0_{\text{vib,M}}) + \left[\frac{2}{3}x_{iv} + \frac{1}{3}x_d\right](H^0_{\text{I}} - TS^0_{\text{vib,I}} + H^0_{\text{MI}}) \\ & + \left[\left(\frac{2}{3} - \frac{2}{3}x_{iv}\right) + \left(\frac{1}{3} - \frac{1}{3}x_d\right)\right](H^0_{\text{V}} - TS^0_{\text{vib,V}} + H^0_{\text{MV}}) \\ & + NW_c\left[\frac{2}{3}x_{iv}(1 - x_{iv}) + \frac{1}{3}x_d(1 - x_d)\right] + NW_c\frac{2}{3}(x_{iv}r)^2 \\ & + NW_p\left[\frac{1}{3}x_{iv}(1 - x_{iv}) + \frac{1}{3}x_{iv}(1 - x_d) + \frac{1}{3}x_d(1 - x_{iv})\right] \\ & + NW_p\frac{1}{3}(x_{iv}r)^2 + \frac{1}{3}NkT\{[(1 + r)x_{iv}]\ln[(1 + r)x_{iv}] \\ & + [1 - (1 + r)x_{iv}]\ln[1 - (1 + r)x_{iv}] \\ & + [(1 - r)x_{iv}]\ln[(1 - r)x_{iv}] \\ & + [1 - (1 - r)x_{iv}]\ln[1 - (1 - r)x_{iv}] \\ & + [x_d]\ln[x_d] + [1 - x_d]\ln[1 - x_d]\} \qquad [A22]\end{aligned}$$

The Gibbs free energy $G_{\text{M-I}}$ of the M-I alloy in general can be related to chemical potentials μ_{M}, μ^{iv}_{I}, μ^{iv}_{V}, μ^{d}_{I}, and μ^{d}_{V} of M and I and V for *iv* and *d* sites, respectively:

$$\begin{aligned}G_{\text{M-I}} = 2\Bigg\{ & \mu_{\text{M}} + \frac{2}{3}x_{iv}\mu^{iv}_{\text{I}} + \left(\frac{2}{3} - \frac{2}{3}x_{iv}\right)\mu^{iv}_{\text{V}} \\ & + \frac{1}{3}x_d\mu^{d}_{\text{I}} + \left(\frac{1}{3} - \frac{1}{3}x_d\right)\mu^{d}_{\text{V}}\Bigg\} \qquad [A23]\end{aligned}$$

where the chemical potentials pertain to N atoms (M, I, V), while the Gibbs free energy pertains to $2N$ atoms of M and $[(4/3)x_{iv} + (2/3)x_d]N$ atoms of I. If V represents vacant I sites, it holds that $\mu^{iv}_{\text{V}} = \mu^{d}_{\text{V}} \equiv 0$. For equilibrium, the chemical potentials of I on the order (*i* and *v*) and disorder (*d*) sites, where the two contents x_{iv} and x_d refer to, have to be identical. It thus holds that (*cf.* Eqs. [A16] and [A17])

$$\mu^{iv}_{\text{I}} = \mu^{d}_{\text{I}} \equiv \mu_{\text{I}} \Rightarrow \frac{\partial G_{\text{M-I}}}{\frac{2}{3}\partial x_{iv}} - \frac{\partial G_{\text{M-I}}}{\frac{1}{3}\partial x_d} = 0 \qquad [A24]$$

The degree of order r will take a value corresponding with the minimum value (stable state) for the Gibbs free energy according to Eq. [A22]. Hence,

$$\frac{\partial G_{\text{M-I}}}{\partial r} = 0 \qquad [A25]$$

Thermodynamical equilibrium of the M-I alloy is described by the Gibbs free energy given by Eq. [A22] subject to the equilibrium conditions according to Eqs. [A24] and [A25]. The equations for the equilibrium conditions obtained in this way are nonlinear with respect to the variables x_{iv}, x_d, and r. The numerical evaluation method for solving these equations is given in Appendix B.

Order-disorder transition

A description of the order-disorder transition for configuration B can be obtained in a similar way as for configuration A. Now, instead of three equilibrium conditions with four parameters, there are only two conditions with three parameters. Of course, the same order-disorder transition is found, as expressed by Eq. [7] for case (2) (Section III–A) and by Eq. [A21]. No fixed interdependence exists for the evolutions of x_{iv}, x_d, and r at the onset of ordering in contrast with the evolutions of x_1, x_2, r_1, and r_2 at the onset of ordering, according to Eq. [A21] for configuration A.

APPENDIX B

Numerical evaluation method for route 1

For the numerical evaluation of the cases of ordering evolving from the six nonlinear equations that make up Eq. [3], the following route can be conveniently followed. For a particular combination of the values for W_c/kT, W_p/kT, and W_{pc}/kT, Figure 2 indicates the most stable configuration and the values for $f \ldots j$ to be considered. From Eqs. [7] and [8], x_t is obtained. Using

one of the six equations of Eq. [3], the value for $(\mu_I - \mu_I^0)/kT$ for the order disorder transition can now be calculated. By a small variation of this value for $(\mu_I - \mu_I^0)/kT$, the region where ordering occurs is entered. Next, a guess is made for the corresponding change of one of the x_K's with respect to x_t. The values for $f \ldots j$ now provide (estimates for) the change of the occupancies of the other kinds of I sites with respect to x_t. Then, at equilibrium and for the chosen value of $(\mu_I - \mu_I^0)/kT$, the real values for $x_{A1}, \ldots, x_{C2}$ can be obtained from the six equations that make up Eq. [3] by an iterative numerical method (*e.g.*, Newton–Raphson[16]). Subsequent stepwise variation of the value for $(\mu_I - \mu_I^0)/kT$ allows investigation over the whole composition range of the M-I alloy, where the values of $x_{A1}, \ldots, x_{C2}$ obtained in the preceding step are used as initial guesses for the step considered.

Numerical evaluation method for route 2

For a particular combination of values for W_c/kT, W_p/kT and W_{pc}/kT, the minimum content for ordering x_t is obtained from Eq. [A21]. Then, one of the interstitial content variables, x_1 for configuration A and x_{iv} for configuration B, is raised to a value just above x_t. Next, for configuration A, the three nonlinear equilibrium conditions (Eqs. [A17] and [A18]) are used to calculate the values of x_2, r_1, and r_2 pertaining to the chosen value of x_1 in an iterative manner applying the Newton–Raphson method, where initial guesses for x_2, r_1, and r_2 were taken such that $x_2 = x_1$ and $r_1 = 2r_2$ (*cf.* Eq. [A21]). For configuration B, the two nonlinear equilibrium conditions (Eqs. [A24] and [A25]) are used to calculate the values of x_d and r pertaining to the chosen value of x_{iv} in a similar manner. Investigation of the entire composition range of the M-I(V) alloy is realized by a stepwise increase (by a small amount) of the value of x_1 for configuration A and the value of x_{iv} for configuration B; for a particular step, the values of x_2, r_1, and r_2 for configuration A and of x_d and r for configuration B obtained in the preceding step are used as initial guesses for application of the Newton–Raphson procedure.

ACKNOWLEDGMENT

The authors are indebted to Ir. W.G. Sloof for stimulating discussions and valuable suggestions during the course of the present work. We are grateful to Dr. F.W. Schapink for critically reading the manuscript and for useful comments. These investigations in the program of the Foundation for Fundamental Research of Matter (FOM) have been supported (in part) by the Netherlands Technology Foundation (STW).

REFERENCES

1. F. Ducastelle: *Order and Phase Stability in Alloys*. North-Holland, Amsterdam, 1991.
2. E. Ising: *Z. Phys.*, 1925, vol. 31, p. 253.
3. W.S. Gorsky: *Z. Phys.*, 1928, vol. 50, p. 64; W.L. Bragg and E.J. Williams: *Proc. R. Soc. London*, 1934, vol. A145, p. 699; 1935, vol. A151, p. 540; 1935, vol. A152, p. 231.
4. N.A. Gokcen: *Statistical Thermodynamics of Alloys*, Plenum Press, New York, NY, 1986.
5. R.H. Fowler and E.A. Guggenheim: *Statistical Thermodynamics*, Cambridge University Press, Cambridge, 1952; H.A. Bethe: *Proc. R. Soc. London*, 1935, vol. A150, p. 552; N.A. Gokcen and E.T. Chang: *J. Chem. Phys.*, 1971, vol. 55, p. 2279.
6. R. Kikuchi: *Phys. Rev.*, 1951, vol. 81, pp. 988-1003; *J. Chem. Phys.*, 1974, vol. 60, pp. 1071-80.
7. J.H. Hildebrand: *J. Am. Chem. Soc.*, 1929, vol. 51, p. 66; E.A. Guggenheim: *Mixtures*, Oxford University Press, Oxford, 1952.
8. D. de Fontaine and R. Kikuchi: NBS Special Publications, SP-496, Gaithersburg, MD, 1977, pp. 999-1025.
9. D. de Fontaine: *Solid State Phys*, 1979, vol. 34, pp. 73-294.
10. B.J. Kooi, M.A.J. Somers, and E.J. Mittemeijer: Delft University of Technology, unpublished Research, 1993; B.J. Kooi, M.A.J. Somers, L. Maldzinski, A.M. van der Kraan, A.A. van der Horst, and E.J. Mittemeijer: Delft University of Technology, unpublished research, 1993.
11. S.B. Hendricks and P.B. Kosting: *Z. Krystallogr.*, 1930, vol. 74, pp. 511-33.
12. K.H. Jack: *Acta Crystallogr.*, 1952, vol. 5, pp. 404-11.
13. M. Hillert and M. Jarl: *Acta Metall.*, 1977, vol. 25, pp. 1-9.
14. A.K. Singh and S. Lele: *Phil. Mag. B*, 1991, vol. 64, pp. 275-97.
15. K. Hiraga and M. Hirabayashi: *J. Appl. Crystallogr.*, 1980, vol. 13, pp. 17-23; J. Dubois, T. Epicier, C. Esnouf, G. Fantozzi, and P. Convert: *Acta Metall.*, 1988, vol. 36, pp. 1891-1921.
16. W.H. Press, B.P. Flannery, S.A. Teukolsky, and W.T. Vetterling: *Numerical Recipes*, Cambridge University Press, Cambridge, 1986.
17. E. Parthé and K. Yvon: *Acta Crystallogr.*, 1970, vol. B26, 149-63; S. Yamaguchi, K. Hiraga, and M. Hirabayashi: *J. Phys. Soc. Jpn.*, 1970, vol. 28, p. 1014.

Numerical Analysis of the Rapid Solidification of Gas-Atomized Al-8 Wt Pct Fe Droplets

SEONG-GYOON KIM, SUNG-HO SHIN, TOSHIO SUZUKI, and TAKATERU UMEDA

A numerical analysis of the microstructural evolution of microcellular and cellular α-Al phase in gas-atomized Al-8 wt pct Fe droplets was represented. The two-dimensional (2-D) non-Newtonian heat transfer and the dendritic growth theory in the undercooled melt were combined, assuming a point nucleation on the droplet surface and the macroscopically smooth solid-liquid interface enveloping the cell tips. It reproduced the main characteristic features of the reported microstructures quite well and predicted a considerable volume fraction of thermal dendritic growth region in a droplet smaller than 10 μm if an initial undercooling was larger than 100 K. The volume fractions of the microcellular region, g_A, and the sum of the microcellular and cellular region, g_α, were predicted as functions of the heat-transfer coefficient, h, and the initial undercooling, ΔT. It was shown that g_A and g_α, in the typical atomization processes with h = 0.1 to 1.0 W/cm^{2}K, are dominated by ΔT and h, respectively, but for h larger than 4.0 W/cm^2 K, a fully microcellular structure can be obtained irrespective of the initial undercooling.

I. INTRODUCTION

PHYSICAL properties of materials are strongly dependent on their microstructures, and there have been many efforts to improve them. Rapid solidification is a typical method of developing new materials by controlling the microstructures. With this technology, the very fine solidification microstructures can be obtained with desirable phases through large undercooling and rapid heat removal. Rapidly solidified Al-8 wt pct Fe alloy and some ternary or quaternary alloys based on this have attracted attention as very promising high-temperature alloys, and the last decade has seen much experimental and theoretical research on microstructural evolution in the melt-spun ribbons and atomized powders of Al-8 wt pct Fe alloy.[1–8]

The most pronounced characteristic feature in the microstructures of the rapidly solidified Al-8 wt pct Fe ribbons or powder is that there are two distinct regions: zones A and B.[1] Zone A, showing a slight response to the chemical etching, has been identified as a microcellular structure of α-Al by transmission electron microscopy and believed to be formed during the recalescence stage with a large initial undercooling.[5] Zone B, highly sensitive to chemical etching, has the microstructure formed after recalescence, which is mainly cellular α-Al if the dimensions of ribbon or powder are small and a primary Al_3Fe or a eutectic of α-Al and Al_6Fe, otherwise.[5] Besides these main phases, various kinds of intermetallic compounds have been found in the intercellular region.[9,10,11] Thus, in a rapidly solidified Al-8 wt pct Fe alloy, various types of microstructures and phases can appear, depending on the specimen's dimensions and thermal conditions of the processes, and these play a critical role in the mechanical properties.[2] The prediction of the microstructural evolution in this alloy, especially the relative volume fractions of zones A and B, has thus been the subject of several works.[5,6,11,12]

Boettinger *et al.*[5] proposed a simplified one-dimensional (1-D) model for the atomized droplet solidification using the Newtonian heat transfer and the dendritic growth model proposed by Lipton *et al.*[13] They discussed the phase selection conditions and the origin of two-zone microstructure. Chu and Granger[6] calculated the volume fraction of zone A in the melt-spun ribbon by a 1-D Newtonian model with the dendritic growth model of Lipton *et al.*[14] Recently, Gremaud *et al.*[11] and Carrard *et al.*[12] performed extensive theoretical and experimental work on rapid directional solidification by laser treatment. Their main interests have been the solidification behavior at the vicinity of absolute stability limit rather than the zone A microstructure.

Gas atomization is a powerful method for the mass production of the rapidly solidified materials. During atomization of Al-8 wt pct Fe, a point nucleation of solid at the droplet surface commonly occurs and the solid phase grows into the undercooled melt.[5] In this geometry, the ratio of the solid-liquid interface area, where the latent heat is released, to the droplet's surface area, where the enthalpy of droplet is removed by a cooling gas, changes very rapidly at the early stage of solidification. This geometric effect has significant influence on the overall solidification history.[15,16] At the same time, the early stage of solidification can show a strong non-Newtonian behavior if a large undercooling is given before the onset of nucleation.[17] A two-dimensional (2-D) non-Newtonian heat-transfer analysis is needed, which includes these two important phenomena in a theoretical construction. In fact, this kind of numerical

SEONG-GYOON KIM, Associate Professor, is with the Rapidly Solidified Materials Research Center in CNU and the Department of Materials Science and Engineering, Kunsan National University, Kunsan, 573-360 Korea. SUNG-HO SHIN, Senior Researcher, is with the Central Research Institute, Sammi Steel Corp. Changwon, 641-370 Korea. TOSHIO SUZUKI, Associate Professor, and TAKATERU UMEDA, Professor, are with the Department of Metallurgy, University of Tokyo, Tokyo, 113 Japan.

Manuscript submitted October 28, 1993.

analysis on the droplet solidification was described rather early by Levi and Mehrabian,[17] but their model is restricted to the solidification of pure materials because it used linear attachment kinetics for the growth model.

In this article we present a numerical analysis of the rapid solidification of gas-atomized Al-8 wt pct Fe alloy droplets, which is based on 2-D non-Newtonian heat transfer and the dendritic growth model for an alloy melt. Our main interests are the relative roles of initial undercooling given before the onset of nucleation, droplet size, and heat removal rate from a droplet by the external coolant on the microstructural evolution of α-Al, which is the most desirable phase. In the following sections, undercooling refers to the temperature difference from the liquidus temperature of the metastable α-Al, not the stable Al_3Fe.

II. MATHEMATICAL MODEL

A. *Growth Kinetics of α-Al Phase*

In dendritic growth of an alloy, a fundamental relationship between the tip temperature, T^*, the tip velocity, v, and the dendrite scale (tip radius), r, is necessary. Including the Gibbs–Thomson effect and the attachment kinetics effect, this is given by[18]

$$T^* = T_f + mC_l^* - \frac{2\Gamma}{r} - \frac{v}{\mu} \qquad [1]$$

where T_f is the melting temperature of pure Al, C_l^* is the liquid composition at the dendrite tip, Γ is the Gibbs–Thomson coefficient, μ is the interface kinetics coefficient, and m is the nonequilibrium liquidus slope. If the dendritic growth is in a steady state and the thermal and diffusion fields around a dendrite are not disturbed by neighboring dendrites, T^* and C_l^* are given by Ivanstov solutions.[19] In a system as small as an atomized droplet, on the other hand, a steady-state thermal field and the nonoverlapping of thermal fields between neighboring dendrites are seldom anticipated, because the thermal boundary layer thickness of the released latent heat may be so large that it is comparable to the droplet size. Therefore, T^* must be calculated by a numerical analysis of heat transfer, instead of by the Ivantsov solution. As shown later, however, the solutal diffusion field is strongly restricted near the tip of each dendrite. This means that for C_l^*, we can use a simple Ivantsov solution[19]

$$C_l^* = \frac{C_0}{1 - (1 - k(v))I_v(P)} \qquad [2]$$

where C_0 is the bulk composition and P is the solutal Peclet number equal to $v_r/2D$, in which D is the solute diffusion coefficient in the liquid, $I_v(P)$ is the Ivantsov function (equal to $Pe^P E_1(P)$, in which $E_1(P)$ is the first exponential integral function), and $k(v)$ is the growth-rate-dependent partition coefficient. By combining Eqs. [1] and [2] with the Aziz model[20] for $k(v)$ and a thermodynamically consistent model by Boettinger and Coriell[21] for m, and adapting the marginal stability condition,[19] the following two equations can be obtained.

$$T^* = T_f + \frac{m_E C_0}{1 - (1 - k(v))I_v(P)}\left[1 + \frac{1}{1 - k_0}\cdot\left[k_0 - k(v)\left(1 - \ln\frac{k(v)}{k_0}\right)\right]\right] - \frac{2\Gamma}{r} - \frac{v}{\mu} \qquad [3]$$

$$r = \frac{4\pi^2\Gamma}{-\frac{2C_0P(1 - k(v))\xi_c}{1 - (1 - k(v))I_v(P)}m_E\left[1 + \frac{1}{1 - k_0}\left[k_0 - k(v)\left(1 - \ln\frac{k(v)}{k_0}\right)\right]\right] + P_{th}\Delta H\frac{\xi_t}{C_L}} \qquad [4]$$

where

$$k(v) = \frac{k_0 + \alpha_0 v/D}{1 + \alpha_0 v/D} \qquad [5]$$

$$\xi_c = 1 - \frac{2k(v)}{\sqrt{1 + (2\pi/P)^2} - 1 + 2k(v)} \qquad [6]$$

$$\xi_t = 1 - \frac{1}{\sqrt{1 + (2\pi/P_t)^2}} \qquad [7]$$

where m_E and k_0 are the equilibrium liquidus slope and the partition coefficient in the Al-Fe phase diagram,[22] assuming a straight liquidus line of α-Al, P_{th} is the thermal Peclet number (equal to $v_r/2D_{th}$, in which D_{th} is the thermal diffusivity of the melt), C_p is the specific heat of the undercooled melt, ΔH is the latent heat of fusion, and α_0 is a solute trapping parameter, which is related to the interatomic parameter. In Eqs. [3] through [7], there are two parameters, α_0 and μ, for which the accurate values are still unclear. But, α_0 has been believed to be the same order of magnitude as the interatomic distance,[23,24,25] and most of the estimations[24,25,26] of μ for various metals suggest the order of magnitude, 1 m/sK. In this article, we use $\alpha_0 = 6$ Å and $\mu = 1.0$ m/sK. Other thermophysical data are given in the Appendix. By solving Eqs. [3] and [4] with an iterative method, solutions for T^* and r as the functions of v are obtained, and this v-T^* relationship can be coupled with the heat-transfer analysis of the solidification system to give information on the overall solidification history. Though the morphologies of α-Al phase in the atomized Al-8 wt pct Fe alloy are microcellular or cellular[5] there is no easily tractable simple model on cellular growth.[27] Therefore, we assume that the foregoing dendritic growth kinetics can be applied equally to the cellular growth.

Figure 1 shows the changes of the solutal Peclet number, P, and thermal Peclet number, P_{th}, with the tip velocity, v, which are obtained from Eqs. [1] through [7]. The abrupt changes of the Peclet numbers at $v \simeq 1$ m/s are due to the transition between the solutal and the thermal dendrites. There is no second abrupt increase[14] of Peclet numbers in Figure 1, because the absolute stability of the thermal dendrite occurs at a velocity far above 100 m/s. In the range of $v = 0.001$ to 100 m/s, regarded as the typical range of the interface velocity in rapid solidification, P_{th} changes from 10^{-5} to

10^{-1} and P from 10^{-1} to 10^4 with increasing v. Considering that the Peclet number is the relative length of the tip radius to the boundary layer thickness of the diffusion field, these results imply that the thermal field of the latent heat is fairly insensitive to the microscopic interface morphology, while the solutal diffusion field, on the contrary, is strongly confined to being around each dendrite tip. The latter is a basis for using Eq. [2] for C_l^*. Taking into account the former, the solid-liquid interface in heat-transfer analysis can be approximated to the macroscopically smooth one by neglecting the detailed dendrite geometry. This greatly simplifies the heat-transfer analysis.

As pointed out by Boettinger *et al.*[5] and Rappaz,[28] one nevertheless needs information on the solidification range, *i.e.*, mushy zone length, which depends on the lateral growth procedure of the cell and on the nucleation and growth mechanism of the precipitates (mainly the icosahedral phase in Al-8 wt pct Fe alloy[11]) in the intercellular region. There is not yet a good estimation method based on the firm physical ground for rapid solidification in spite of the existence of some sophisticated models.[29,30] In the heat-transfer analysis, therefore, we will assume that all latent heat is released only at an imaginary interface enveloping the cell tips. This may result in an overestimation of the local recalescence effect by the released latent heat if the mushy zone length is much longer than the mesh spacing in the numerical analysis on heat transfer. Considering that in the atomized Al-8 wt pct Fe droplets α-Al phase crystallizes into an arrayed microcellular or cellular structure,[5] where the liquid fraction behind the tip is relatively small, however, the degree of the overestimation cannot be too severe.

Figure 2 shows a plot of the interface temperature, T^*, as a function of tip velocity, v, where we see an inversion of the slope in the transition region between the solutal dendrite with low velocity and the thermal dendrite with high velocity. Similar curves[11,12] have been obtained for dendritic growth in a directional solidification. If an isotherm velocity in a directional solidification is in the range of the inversed slope (between C and D in Figure 2), the temperature and velocity of the interface oscillate along the cycle $\cdots C \rightarrow A \rightarrow D \rightarrow B \rightarrow C \rightarrow \cdots$ in Figure 2 to result in a banded structure.[12] This has been observed experimentally in laser-scanned Al-Fe (<6 wt pct) alloys.[12] The discontinuous transition between the solutal and the thermal dendrites in *undercooled* solidification, however, results in a strong nonoscillatory instability and a highly branched structure formation instead of a banded structure.[31] This kind of structure has been found in the small (<20 μm) Al-4 wt pct Fe powders.[31] However, no banded or branched structure has been found in the rapid directional[12] or undercooled solidification[5] of Al-8 wt pct Fe alloy. This means that the high interface velocity (>1 m/s) microstructure of Al-8 wt pct Fe alloy is abnormal. The reason for the abnormality is not understood. Moreover, the nonoscillatory instability during the transition poses a significant difficulty in the tracking of the interface shape by our numerical simulation. We therefore simply assumed a continuous transition between the solutal dendritic growth and the thermal dendritic growth, as shown by line AB in Figure 2.

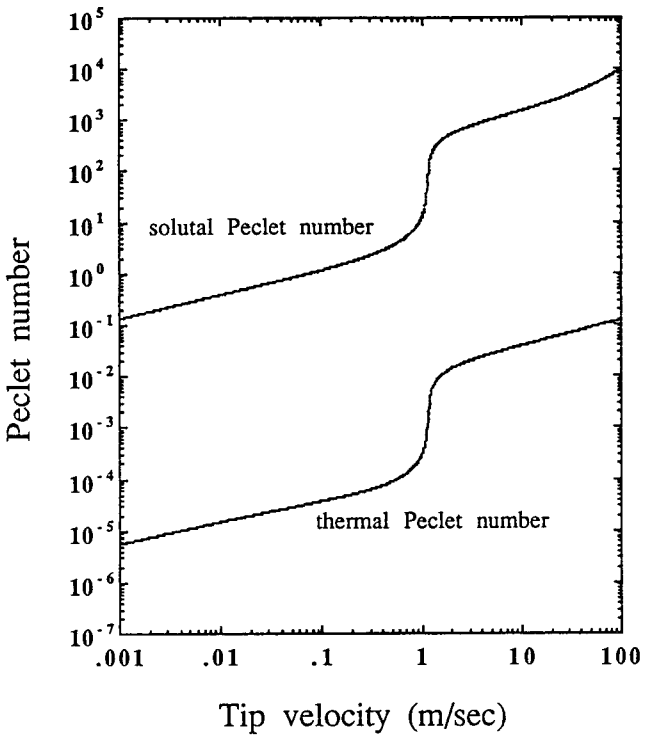


Fig. 1—Calculated solutal and thermal Peclet numbers (P and P_{th}) with the tip velocity.

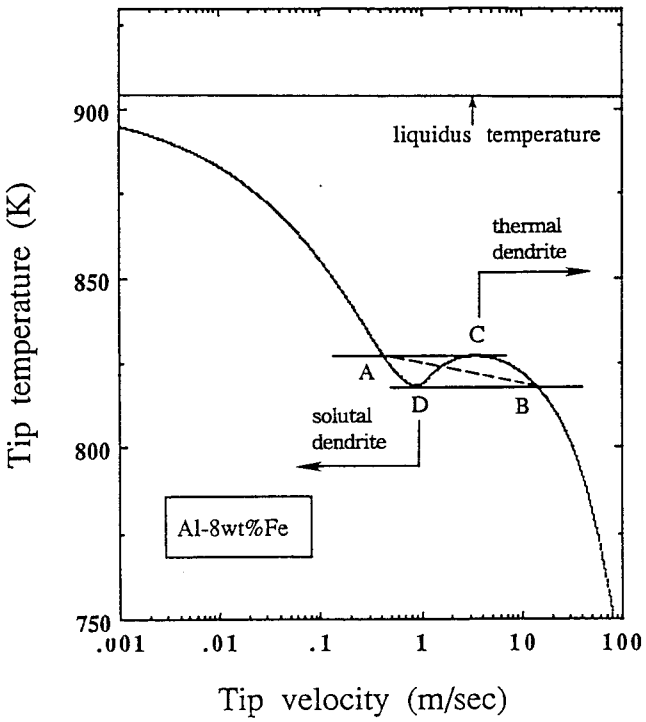


Fig. 2—Tip temperature (T^*) change with the tip velocity (v). A straight line AB is the approximate T^*-v relationship used in this calculation.

B. *Numerical Analysis of Heat Transfer*

In the numerical heat-transfer analysis on the solidification of gas-atomized Al-8 wt pct Fe droplets, the main assumptions are as follows.

(1) All latent heat is released only at an imaginary interface enveloping the cell tips, as discussed in Section A.
(2) A single nucleation occurs on a droplet surface and the solid phase grows axisymmetrically; these are consistent with the experimental observations for powders smaller than 30 μm.[5]
(3) The heat-transfer coefficient, h, for a droplet is constant during solidification; although in the atomization process, the h value for a droplet changes with the flying time on its trajectory. A constant h during the solidification of a droplet was used for easy interpretation of the physical meanings from the calculation results, as well as for numerical convenience.
(4) Before the onset of nucleation, the temperature gradient in a droplet is negligible; in the ranges of D (droplet diameter) = 1 to 100 μm and h = 0.01 to 5.0 W/cm^2 K, which our analysis is concerned with, the Biot number ($hD/2K_L$, where K_L is the thermal conductivity of melt) is less than 0.025. Because this means a uniform temperature in a droplet before the onset of nucleation, all our calculations will start just after the nucleation.

After a nucleation on the droplet surface, the heat transfer in the droplet is governed by the latent heat release at solid-liquid interface and the heat removal by the surrounding gas at the droplet surface. In this case, because there is no geometric similarity between the macroscopic solid-liquid interface shape and the droplet surface shape, the heat-transfer analysis should be 2-D. To do this, we follow an algorithm proposed by Levi and Mehrabian[17] with some modifications.

A droplet of radius R_0 is divided into axisymmetric ($n \times m$) volume elements by a rotational bipolar coordinate system (U, V), as shown in Figure 3. In this figure, the longitude and latitude are represented by the constant U and constant V surfaces, respectively. A crystal nucleates at the south pole and grows axisymmetrically. The energy balance for an element i,j is given by

$$\frac{d}{dt}\int_{\Omega_{i,j}} H\, d\Omega = \int_{A_{i,j}} K\, \nabla T \cdot d\mathbf{A} \qquad [8]$$

and

$$H = H_S + \Delta H(1 - g) + (T - T_S)(C_S g + C_L(1 - g)) \qquad [9]$$

where t is time, $\Omega_{i,j}$ is the volume of element i,j, H is the enthalpy per unit volume of the element, $A_{i,j}$ is the area of the interface by which the i,j element is separated from neighboring elements, K is the thermal conductivity, $\mathbf{A}$ is the surface area vector, T_S is the equilibrium solidus temperature, H_S is the enthalpy of solid at T_S, C_S and C_L are the specific heats of solid and liquid, respectively, and g is the fraction of solid.

An implicit finite difference equation corresponding to Eqs. [8] and [9] can be represented by

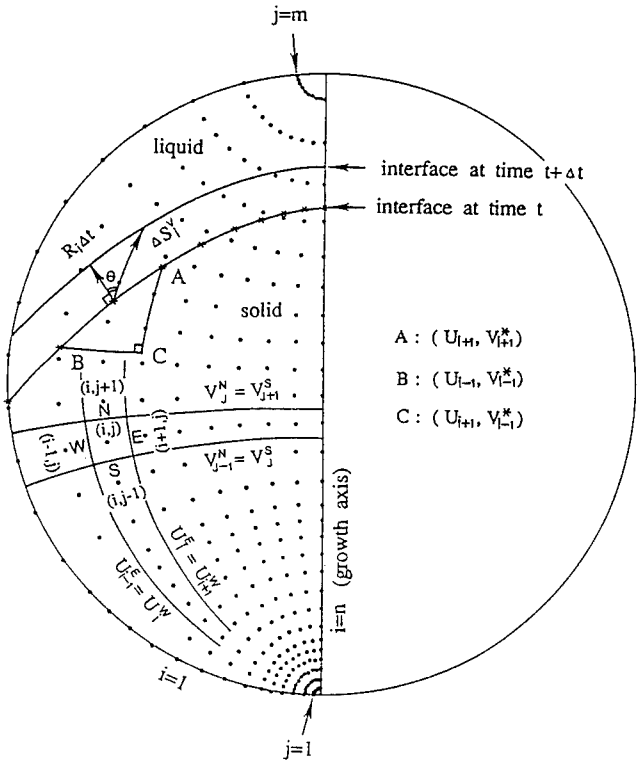


Fig. 3—Mesh system generated by a rotational bipolar coordinate system, (U,V), inside a droplet. Dots are the nodes of each element. The longitude and latitude are represented by the constant U and the constant V surfaces, respectively. A crystal nucleates at the south pole and grows axisymmetrically.

$$\begin{aligned}(H_{i,j,k+1} - H_{i,j,k})/\Delta t = {} & \alpha^N_{i,j,k\cdot 1}(T_{i,j+1,k+1} - T_{i,j,k+1}) \\ & - \alpha^N_{i,j-1,k+1}(T_{i,j,k+1} - T_{i,j-1,k+1}) \\ & - \alpha^E_{i-1,j,k+1}(T_{i,j,k+1} - T_{i-1,j,k+1}) \\ & + \alpha^E_{i,j,k+1}(T_{i+1j,k+1} - T_{i,j,k+1})\end{aligned} \qquad [10]$$

where

$$\alpha^N_{i,j,k+1} = \frac{2\pi R_0 K^N_{i,j,k+1}}{V_{j+1} - V_j} \cdot \ln\left[\frac{\cosh V^N_j - \cos U^E_i}{\cosh V^N_j - \cos U^E_{i-1}}\right] \qquad [11]$$

$$\begin{aligned}\alpha^E_{i,j,k+1} = {} & \frac{4\pi R_0 K^E_{i,j,k+1}}{U_{i+1} - U_i}\left[\tan^{-1}\left(\frac{e^{V^N_j} - \cos U^E_i}{\sin U^E_i}\right)\right. \\ & \left. - \tan^{-1}\left(\frac{e^{V^N_{j-1}} - \cos U^E_i}{\sin U^E_i}\right)\right]\end{aligned}$$

$$(\text{for } i \neq 0,\ i \neq n,\ j \neq 0, \text{ and } j \neq m) \qquad [12]$$

$$\alpha^N_{i,0,k+1} = \alpha^N_{i,m,k+1} = 0 \qquad [13]$$

$$\alpha^E_{0,j,k+1} = 2\pi R_0^2 h(\tanh V^N_j - \tanh V^N_{j-1}) \qquad [14]$$

$$T_{0,j,k+1} = T_g \qquad [15]$$

$$\alpha^{E}_{n,j,k+1} = 0 \qquad [16]$$

and

$$H_{i,j,k+1} = \Delta H(1 - g_{i,j,k+1}) + C_L(T_{i,j,k+1} - T_S)(1 - g_{i,j,k+1}) + C_S(T_{i,j,k+1} - T_S)g_{i,j,k+1} \qquad [17]$$

where the subscripts k and $k + 1$ indicate the current and next time steps, respectively, separated by an interval Δt, and the superscripts N and E are the north and the east boundaries, respectively, enclosing an element (Figure 3). $K^N_{i,j,k+1}$ (or $K^E_{i,j,k+1}$) is the weighted average between $K_{i,j,k+1}$ and $K_{i,j+1,k+1}$ (or $K_{i+1,j,k+1}$). The thermal conductivity of the i,j element, $K_{i,j,k+1}$, is given by $K_S g_{i,j,k+1} + K_L(1 - g_{i,j,k+1})$, where K_S and K_L are the thermal conductivities of solid and liquid, respectively.

When $T_{i,j,k}$, $g_{i,j,k}$, and the interface velocity in the ith column, $v_{i,k}$, are given in current time step, the physical values in the next step are calculated by the following sequence.

(1) By the method explained later, the interface migration distance in the ith column, ΔS_i, along the constant U direction during Δt is calculated.
(2) The fraction of solid at the next time step, $g_{i,j,k+1}$ is calculated from ΔS_i. From $g_{i,j,k+1}$, $K^N_{i,j,k+1}$ and $K^E_{i,j,k+1}$ can be obtained.
(3) Inserting $T_{i,j,k}$, $g_{i,j,k+1}$, $K^N_{i,j,k+1}$, and $K^E_{i,j,k+1}$ into Eq. [10], $T_{i,j,k+1}$ is calculated by the Gauss–Seidel iterative method.
(4) The temperature of the element including the interface in the ith column, T_{i,j^*}, is assigned the local interface temperature, T^*_i.
(5) Using the $T^* - v$ and $v - r$ relationships obtained in Section A, the interface velocity, $v_{i,k+1}$, and tip radius, $r_{i,k+1}$, corresponding to T^*_i are obtained.

At the first step of the preceding sequence, the calculation of ΔS_i requires some careful consideration. If one takes $\Delta S_i = v_{i,k}\Delta t$, as done by Levi and Mehrabian,[17] the growth direction is restricted to the direction of the constant U coordinate. This means that the growth procedure of the solid is fundamentally 1-D in spite of 2-D heat-transfer analysis. This results in the interface shape pointing into the growth axis even when the solidifying system is very close to the Newtonian condition, where the interface shape should be concentric to the nucleation site. The correct tracking of the interface advance requires permission of the growth into the constant V direction also. This problem can be solved by a simple geometric correction. That is, as shown in Figure 3, it is more reasonable in the physical situation to regard $v_{i,k}\Delta t$ as the migration distance during Δt along the direction normal to the interface rather than the constant U direction. In that case, $v_{i,k}\Delta t$ divided by cos θ (where θ is an angle between the interface normal and constant U directions) may be taken as the resultant migration distance along the constant U direction, ΔS_i, if the time spacing Δt is sufficiently small (where θ can be approximated by $\tan^{-1}$ (AC/BC) in the triangle of ABC of Figure 3 if the interface is smooth without any macroscopic large undulation). With these approximations, ΔS_i can be represented by

$$\Delta S_i \simeq v_{i,k}\Delta t/\cos\theta \qquad [18]$$

$$\theta \simeq \tan^{-1}(\mathrm{AC/BC}) \qquad [19]$$

where

$$\mathrm{AC} = \left[\frac{2}{\sin U_{i+1}}\left(\frac{e^V - \cos U_i}{\sin U_{i+1}}\right)\right]_{V=V^*_{i-1}}^{V=V^*_{i+1}} \qquad [20]$$

$$\mathrm{BC} = \left[\frac{2}{\sinh V^*_{i-1}}\tan^{-1}\left(\frac{\tanh(V^*_{i-1}/2)}{\tan(U/2)}\right)\right]_{U=U_{i-1}}^{U=U_{i+1}} \qquad [21]$$

where V_i is the V value of the interface position in the ith column.

In the Gauss–Seidel iteration for Eq. [10], the convergence criterion was

$$|1 - T^{v+1}_{i,j,k+1}/T^{v}_{i,j,k+1}|_{\max} \le 10^{-8} \qquad [22]$$

where v is the number of iteration.

Because the growth velocity of α-Al has a stronger dependence on the interface undercooling than the case of linear kinetics used by Levi and Mehrabian,[17] numerical instabiiity is more probable, especially at early stages of the solidification with a large initial undercooling. The instability can be avoided by using the mesh spacing smaller than the boundary layer thickness of the thermal field. Hence, as shown in Figure 3, we used a mesh system with nonuniform spacing, where nodes are concentrated in the vicinity of the south pole (nucleation point). The number of nodes was (10 × 27), but if the droplet diameter and the initial undercooling were larger than 30 μm and 80 K, respectively, (40 × 41) nodes were used to decrease the numerical fluctuation just after the interface crossed a boundary between the elements. The time spacing, Δt, was determined to be that which allowed the interface to move about a 20th of a mesh spacing in one time step.

All thermophysical data for the preceding numerical calculations are given in the Appendix.

III. RESULTS AND DISCUSSION

A. *Solidification Behavior Near the Newtonian Condition*

When a small initial undercooling, ΔT, and a low heat-transfer coefficient, h, are given for a small droplet, the droplet's overall thermal history during solidification should show the Newtonian behavior. This can be a criterion of the soundness of the non-Newtonian heat-transfer analysis. For example, under given conditions of ΔT = 10 K, h = 0.1 W/cm^2 K, and D (droplet diameter) = 10 μm, our calculation showed that the difference between the maximum and minimum temperatures inside the droplet at any moment, ΔT_d, never exceeded 0.3 K; with an increasing fraction of solid, g, ΔT_d reached a maximum value of 0.3 K at g = 0.02 (g is the solid volume fraction). Thereafter, ΔT_d decreased rapidly to become 0.1 K at g = 0.1, 0.06 K at g = 0.2, and 0.006 K at g = 0.6. Hence, the overall solidification procedure must be very close to the Newtonian condition in which the temperature difference

inside the droplet is negligible compared with the temperature difference between the droplet and the atomizing gas, with slight deviation around $g = 0.02$. Under the same conditions, Figure 4 shows the interface temperature and interface velocity changes along the growth axis as a function of the fraction of solid. The results from non-Newtonian analysis are indicated as solid curves. Filled circles are the results from the Newtonian model, combined with the T^*-v relationship of the aforementioned growth kinetics, which can be derived as

$$\frac{dT^*}{dt} R_0^3 \left[C_L + (C_S - C_L)\left(\frac{1}{2}\left(\frac{R}{R_0}\right)^3 - \frac{3}{16}\left(\frac{R}{R_0}\right)^4\right)\right] = 3v\,\Delta H\,R^2\left(\frac{1}{2} - \frac{R}{4R_0}\right) - 3R_0^2 h(T^* - T_g) \qquad [23]$$

where

$$R = \int_0^t v\,dt \qquad [24]$$

The consistencies are very good except around $g = 0.02$, where a small non-Newtonian effect plays a role. Figure 5 compares the interface positions (filled circles) predicted under the same conditions with those of the Newtonian case (solid curves). Without a geometric correction on the interface migration distance (Eq. [18]), the interface shapes are pointed toward the growth axis direction at the late stage of solidification, as shown in Figure 5(a) and in Levi and Mehrabian's results.[17] But the interface shapes in Figure 5(b) calculated with a correction given by Eq. [18] show good agreement with the Newtonian interface shapes. The fact that the interface temperature, velocity, and interface shape near the Newtonian condition are satisfactorily reproduced can be regarded as evidence of the soundness of our numerical calculations.

B. *Effects of Initial Undercooling*

Figure 6 shows the effects of the initial undercooling, ΔT, on the interface temperature during solidification for $D = 30\ \mu$m and $h = 0.5$ W/cm^2 K, which are the typical values in atomization processes.[5,32] When the initial uncercooling is 5 K (curve A), the interface temperature decreases rapidly to about 866 K (38 K undercooling) at the early stage of solidification. The maximum interface undercooling is fairly independent of ΔT in the range of $\Delta T = 0$ to 40 K, but strongly dependent on the heat-transfer coefficient. Note that even if ΔT is negligible, there is a recalescence after reaching the maximum undercooling. With $\Delta T = 50$ K (curve B), the interface temperature increases monotonously according to recalescence. When ΔT is larger than 100 K (curve C or D), on the other hand, there is a rapid increase of interface temperature from the nucleation temperature (803.4 or 783.4 K) to about 825 K. In this temperature range, the thermal dendrite can grow, as shown in Figure 2, and it grows so rapidly that its recalescence procedure cannot be resolved in Figure 6. After the interface temperature reaches about 825 K, the partitioned solutal dendrite/cell

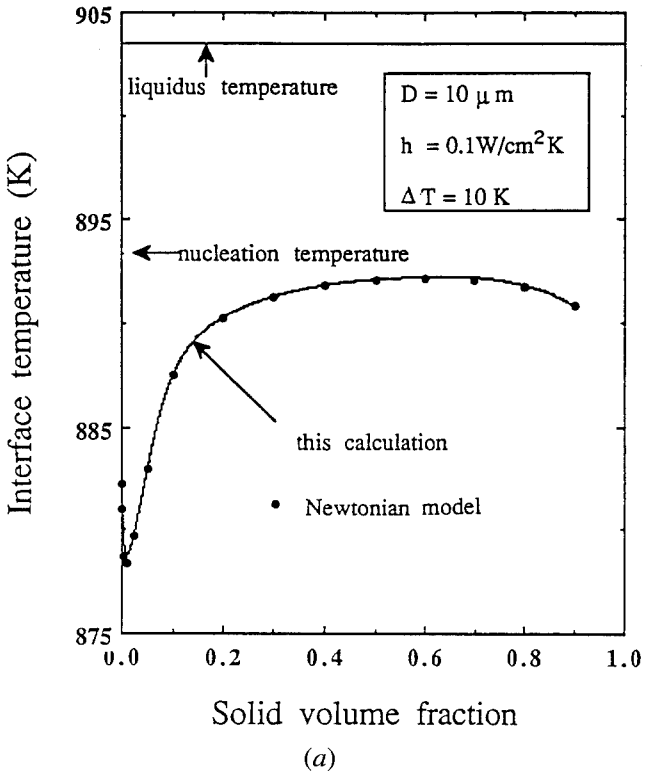
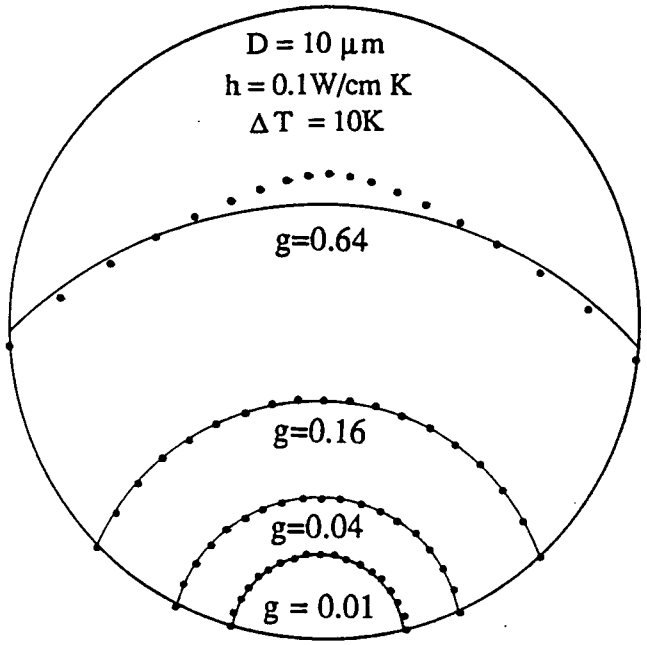
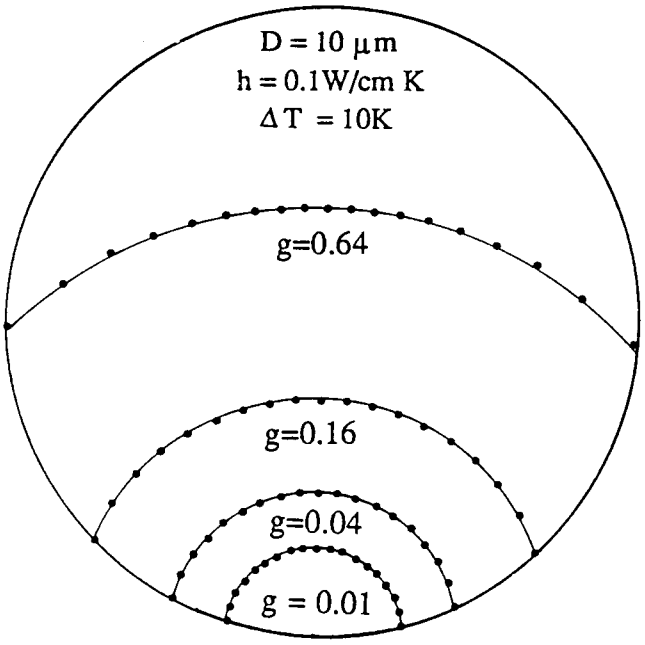


Fig. 4—(*a*) Interface temperature and (*b*) interface velocity at the growth axis with the fraction of solid for $\Delta T = 10$ K, $h = 0.1$ W/cm^2 K, and $D = 10\ \mu$m. Filled circles and solid curves represent the results from the Newtonian model (Eq. [23]) and non-Newtonian numerical model, respectively.



(*a*)



(*b*)

Fig. 5—Comparison of the calculated interface profiles (filled circles) with the Newtonian ones (solid curves) for ΔT = 10 K, h = 0.1 W/cm^2 K, and D = 10 μm (*a*) without (*b*) with a correction (Eq. [18]).

grows with relatively slow recalescence. When the fraction of solid becomes larger than a certain value (*e.g.*, g = 0.4 for ΔT = 120 K), the interface temperatures approach the same level, irrespective of ΔT. In this stage, the solidification system is very close to the Newtonian condition.

Figure 7 shows the effects of the initial undercooling, ΔT, on the microstructural scale (tip radius) for the same conditions as Figure 6. As the solidification progresses,

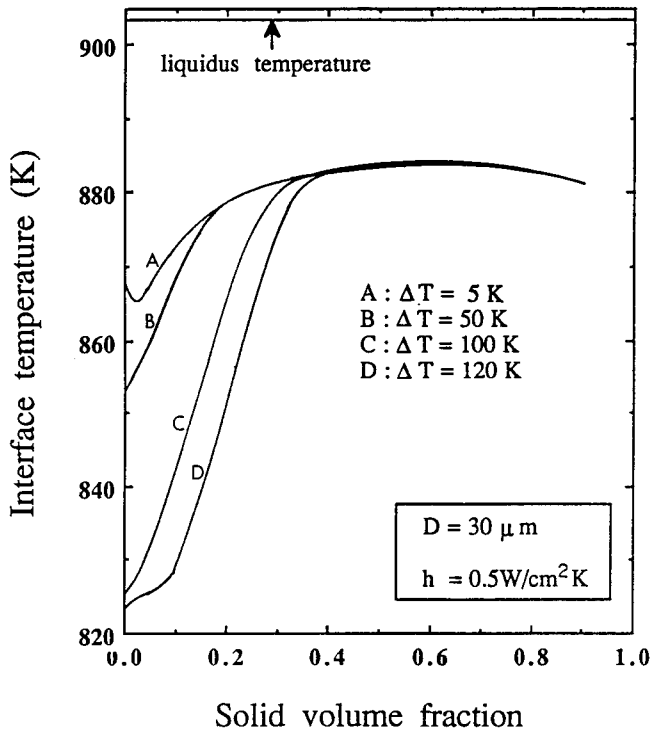


Fig. 6—The effects of initial undercooling on the interface temperature changes along the growth axis for D = 30 μm and h = 0.5 W/cm^2 K.

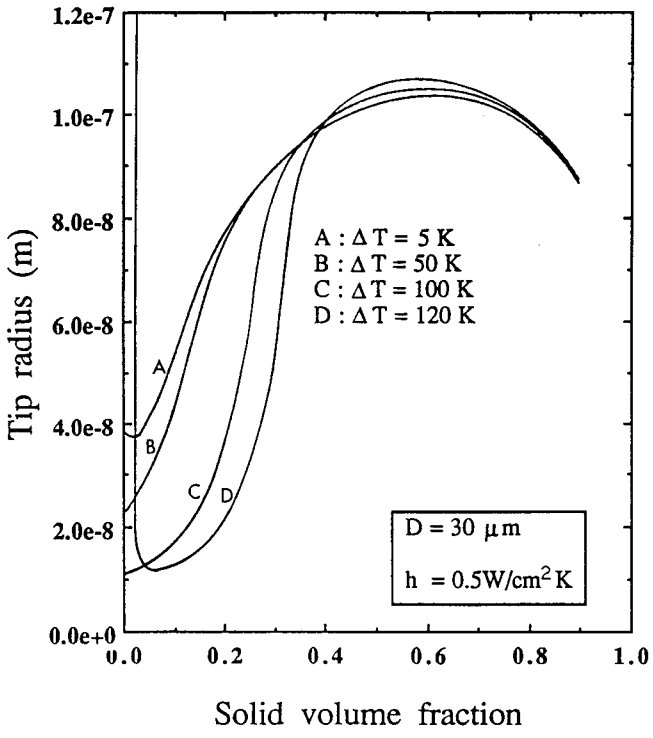


Fig. 7—The effects of initial undercooling on the tip radius changes along the growth axis for D = 30 μm and h = 0.5 W/cm^2 K.

the tip radius undergoes a transition from fine to coarse one, even if ΔT is negligible. A large ΔT gives rise to the steeper transition in a narrow range of the fraction of solid and the finer tip radius at the recalescence stage. But the minimum tip radius is limited to about $1 \cdot 10^{-8}$ m. Numerous experimental results on the microstructures of Al-8 wt pct Fe powders[1-5] have shown the transitions in the microstructural scale of α-Al. For the small powders in which ΔT is believed to be large, nearly discontinuous transitions from zone A to zone B have been observed, where zone A is the microcellular structure with a typical spacing of $2 \cdot 10^{-8}$ m and zone B is the cellular structure with the spacing between $1 \cdot 10^{-7}$ and $1 \cdot 10^{-6}$ m. Though the quantitative comparisons are very difficult because we do not have a well-established model of the relationship between the tip radius and the spacing in rapid solidification, these observed microstructural characteristics are qualitatively quite consistent with our calculated results, considering that the tip radius predicted by assuming the marginal stability is smaller than the measured spacing by a factor of 2 or 3.[27]

There are some other features to be pointed out in Figure 7. In the range of $\Delta T = 0$ to 50 K, the tip radius changes with the fraction of solid are rather insensitive to ΔT, just as the interface temperatures in Figure 6 behaved. This means that even if there was no initial undercooling (*e.g.*, nucleation at liquidus temperature), the resultant solidification microstructure may be close to that with $\Delta T = 50$ K. When $\Delta T = 120$ K, there is a region solidified with the tip radius, which is so large (about $5 \cdot 10^{-7}$ m) that it cannot be depicted in Figure 7. It is the region where the partitionless thermal dendrite grew. Its volume fraction in this case may be too small to be observed experimentally, but it can occupy a considerable volume fraction in a smaller droplet, as shown in the Section C.

Finally, in the region ($g > 0.4$) showing the Newtonian behavior of Figure 7, there is an increase of tip radius for ΔT larger than 100 K. This phenomenon is due to the slight deformation of interface profile, as depicted by filled circles in Figure 8. At the early stage of solidification, the interface velocity is retarded at the region in contact with the droplet surface where the released latent heat cannot diffuse effectively into the undercooled melt. The resultant deformed interface profile leaves its trace even at the late stage of solidification. Because the interface velocity under a Newtonian condition with constant h depends only on the area ratio of interface and droplet surface, the deviation of the interface profile from a Newtonian one (spherical configuration) in Figure 8 leads to a lower interface velocity, higher interface temperature, and a larger tip radius at the late stage of solidification.

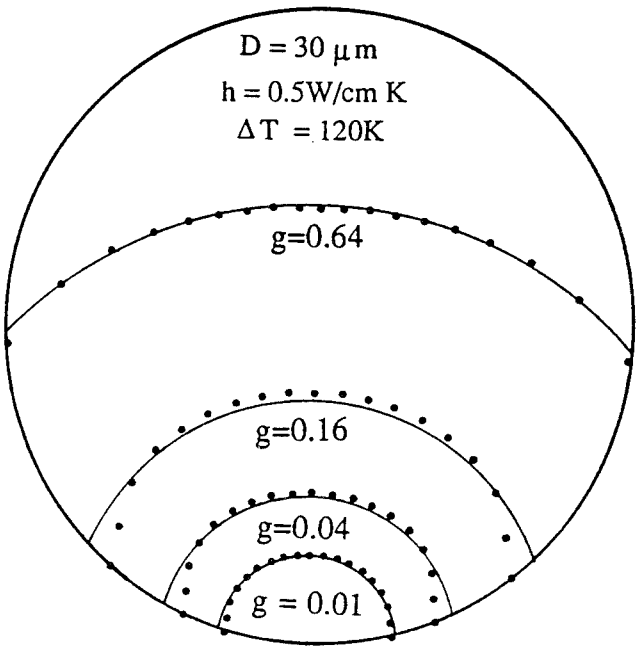


Fig. 8—Calculated interface profiles (filled circles) for $D = 30$ μm, $h = 0.5$ W/cm^2 K, and $\Delta T = 120$ K as solidification progresses. The Newtonian profiles (solid curves), which are concentric to the nucleation point, are overlapped for comparison.

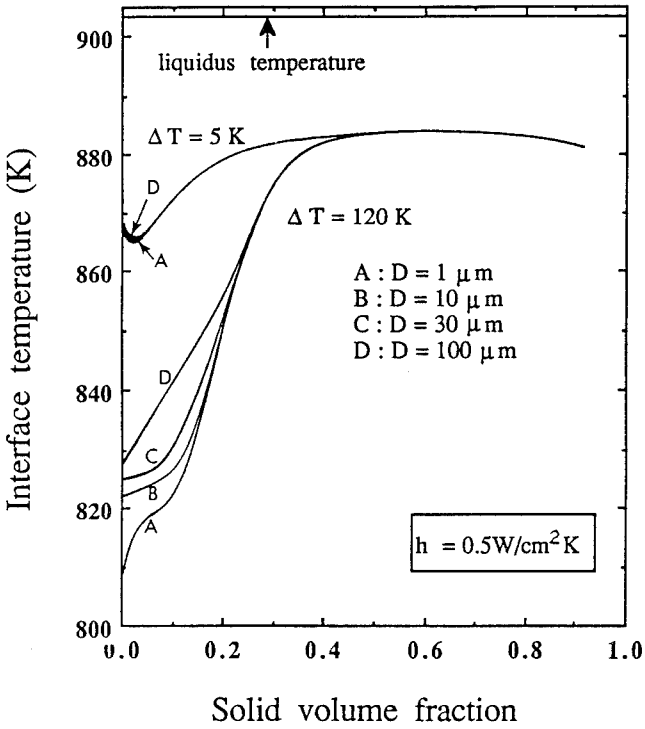


Fig. 9—The effects of droplet size on the interface temperature changes along the growth axis for $\Delta T = 5$ K and 120 K and $h = 0.5$ W/cm^2 K.

C. *Effects of Droplet Size*

The effects of droplet size on the interface temperature are shown in Figure 9. For $\Delta T = 5$ K, the size effect is negligible in the range of $D = 1$ to 100 μm because the overall interface temperature history is very close to the Newtonian one. For $\Delta T = 120$ K, however, non-Newtonian behavior due to the rapid release of latent heat at the recalescence stage makes the history dependent on the droplet size, especially in $g < 0.2$. Figure 10 shows the corresponding results on the tip radius for $\Delta T = 120$ K. In a droplet smaller than 30 μm, one can see three different scales of tip radii, which are related

to the segregation-free region, zones A and B, respectively. Droplet size has important influence only on the volume fraction of the thermal dendritic growth region, which may consist of the supersaturated dendrite arms and the partitioned interdendritic structure. In a droplet smaller than 10 μm, the thermal dendritic growth region can occupy a volume fraction larger than 0.1, which is large enough to be observed experimentally. (The aforementioned assumption that all latent heat release only at an imaginary interface enveloping the cell or dendrite tip can result in a significant overestimation on the recalescence effect during the thermal dendritic growth, considering the large portion of interdendritic region. Therefore, the predicted volume fraction of the thermal dendritic region may be regarded as a low estimate.)

These predictions regarding droplet size effects are in disagreement with the experimentally observed results. First, the microstructures and relative volume fraction of zones A and B found experimentally are strongly dependent on the droplet size.[5] Second, there has been no clear experimental evidence of the appearance of the thermal dendrite in the gas-atomized Al-8 wt pct Fe powders, though a fully microcellular structure has been observed in powders smaller than 5 μm.[5] The first inconsistency is due to the use of constant h and ΔT for the calculation of Figure 10. The size effect on the microstructures of an atomized powder is due mainly to the dependencies of h and ΔT on the droplet size. If some measured data on them becomes available, the size effect on the microstructural evolutions will be clearer. The second inconsistency is hard to understand. Boettinger *et al.*[5] tried to explain the nonappearance of the thermal dendrite by its extremely rapid recalescence rate. Our results, however, showed that there can be a considerable volume fraction of the thermal dendritic growth region in a droplet of $D < 10$ μm with $\Delta T >$ 100 K, in spite of the high initial recalescence rate. There are two possibilities for the origin of that inconsistency. One is that the current theory on dendritic growth may not correctly operate on the thermal dendrite in the undercooled Al-8 wt pct Fe alloy melt. A similar inconsistency between the theory and the experimental results has been found in the directionally solidified Al-8 wt pct Fe alloy.[11] The other possibility is that during atomization of this alloy, ΔT may not be so large as to produce an observable volume fraction of the thermal dendritic growth region. Though the observed fully microcellular structures have been discussed as evidence of the very high initial undercooling,[5] a similar structure can result from a high h with a moderate or small initial undercooling, as shown in Section D.

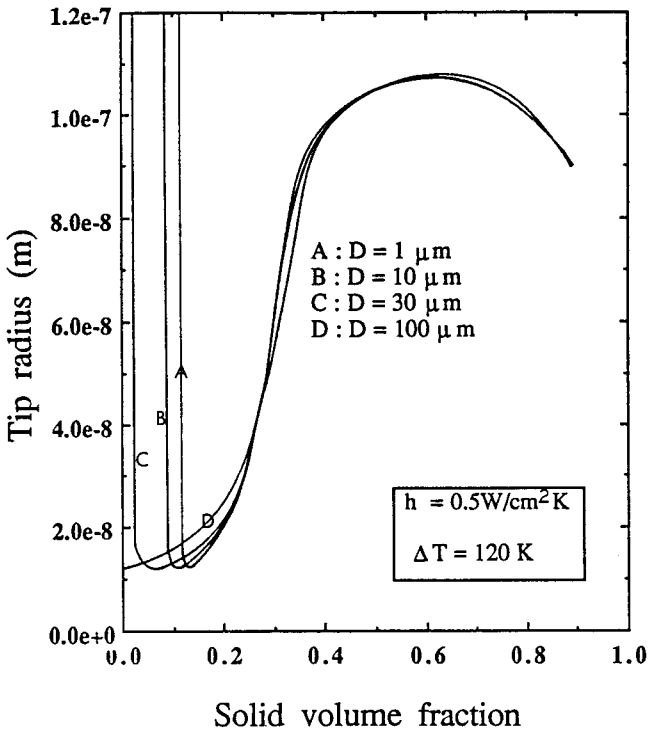


Fig. 10—The effects of droplet size on the tip radius changes along the growth axis for ΔT = 120 K and h = 0.5 W/cm^2 K.

D. *Effects of the Heat-Transfer Coefficient*

In foregoing sections, we have assumed a constant heat-transfer coefficient, h = 0.5 W/cm^2 K, which may be a typical value in the gas-atomization process. For a lower h value, the thermal histories and microstructural evolutions are similar to the foregoing results in their trends. For an h value larger than 0.5 W/cm^2 K, however, very different behavior occurs.

Figure 11 shows the interface temperature with the volume fraction of solid for D = 30 μm and h = 5.0 W/cm^2 K. Even for a negligible ΔT, the interface temperature decreases rapidly just after nucleation to reach a minimum, 835 K, in which the interface undercooling amounts to about 70 K. On the contrary, a high ΔT (100 or 120 K) gives rise to extremely rapid recalescence, with which the interface temperature increases to 825 K (interface undercooling of 80 K) just after nucleation. After these rapid interface temperature changes, the relatively slow recalescences occur until g = 0.4. The most interesting feature in Figure 11 is that the actual differences in interface undercoolings at the early stage of solidification lie in a narrow range of 10 K, although ΔT is given differently in the range of 5 to 120 K. This means that the overall temperature history is governed mainly by h value, not by ΔT, if h is near 5.0 W/cm^2 K. Figure 12 shows the tip radius changes as solidification progresses, corresponding to Figure 11. As for the interface temperature, ΔT has a negligible effect on the tip radius except in a small thermal dendritic growth region for ΔT = 120 K. Moreover, the tip radii vary in a limited range of 1.1 to $2.8 \cdot 10^{-8}$ m throughout the entire solidification procedure. Hence, h of 5.0 W/cm^2 K may result in a fully microcellular structure irrespective of ΔT, although the critical tip radius of the microcell-cell transition in Al-8 wt pct Fe alloy is still unclear.

The rapidly decreasing procedure of the interface temperature at the very early stage of solidification could not be depicted in Figure 11. In order to show it clearly, the temperature profiles along the growth axis as solidification progresses are represented for ΔT = 5 K in Figure 13. The horizontal axis is the ratio of the distance along the growth axis z, to the droplet radius, R_o. Just after nucleation at the droplet surface, the total enthalpy

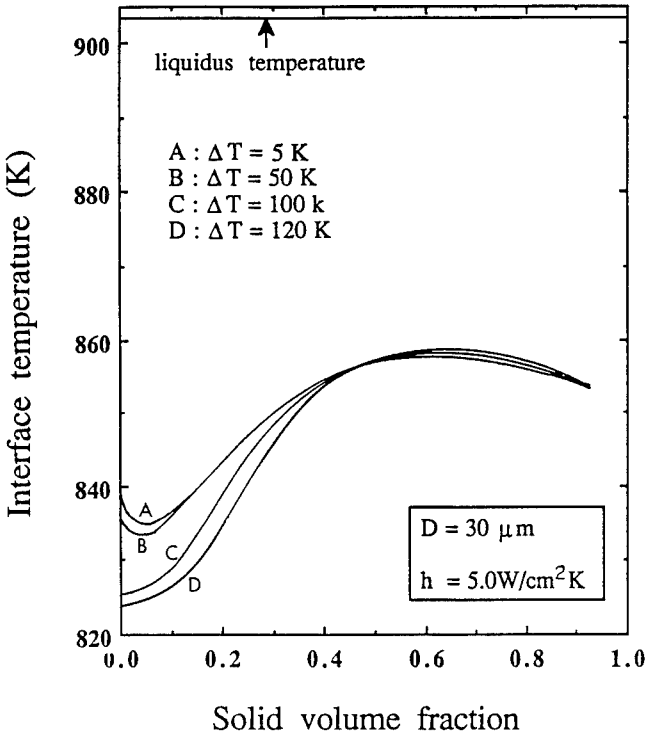


Fig. 11—The effects of initial undercooling on the interface temperature changes along the growth axis for D = 30 μm and h = 5.0 W/cm^2 K.

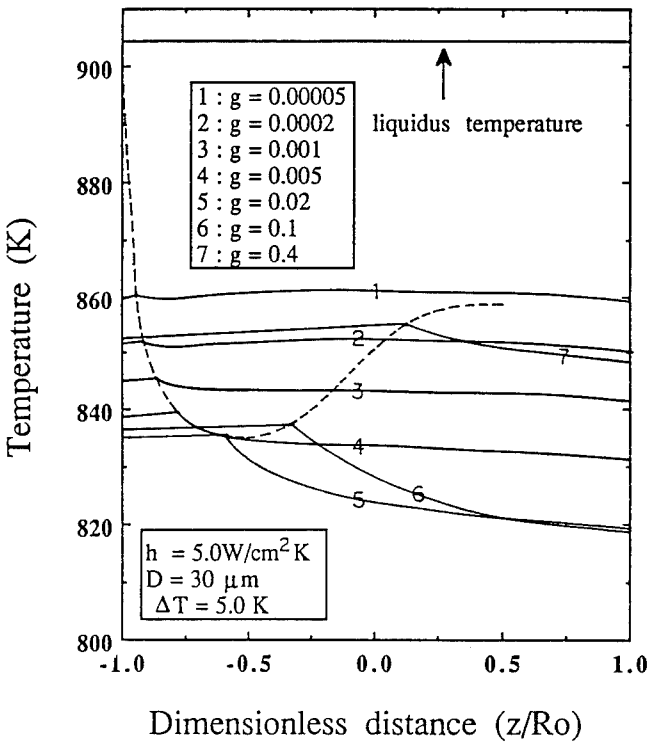


Fig. 13—Temperature profile changes inside a droplet of 30 μm diameter as solidification progresses for h = 5.0 W/cm^2 K and ΔT = 5.0 K. The dotted curve is the trace of the interface temperature change along the growth axis. The horizontal axis is the ratio of the distance between the nucleation point and interface position on growth axis, z, to the droplet radius, R_0.

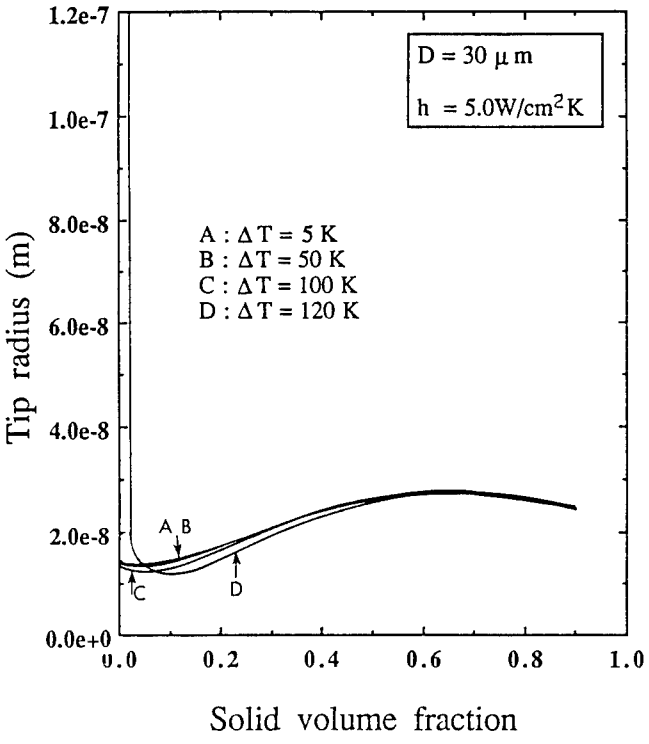


Fig. 12—The effects of initial undercooling on the tip radius changes along the growth axis for D = 30 μm and h = 5.0 W/cm^2 K.

of the droplet decreases rapidly because of the low latent heat release rate due to both the low interface velocity and small interface area. When the fraction of solid is 0.001, the interface undercooling can reach 60 K (85 pct of the maximum attainable undercooling, 70 K), but the maximum temperature difference inside the droplet is less than 3 K. That is, the major portion of the maximum undercooling is accomplished through the Newtonian cooling procedure. The maximum values of interface undercooling, interface velocity, and temperature gradient are attained at about g = 0.02, and the heat removal rate and latent heat release rate around the interface become equal at this moment. On further solidification, the high latent release rate gives rise to the recalescence phenomenon. For $g > 0.4$, the temperature gradient disappears and further solidification follows the Newtonian behavior with the ending of the recalescence.

In the thermal history described previously, a large h can play two important roles in the droplet solidification procedure. Given a small ΔT, it increases the bulk undercooling as well as the interface undercooling at the early stage of solidification to result in a microstructure similar to that with a large ΔT, and it governs directly the solidification procedure after the recalescence to produce a fine microstructure at the late stage of solidification. The initial undercooling, ΔT, which is the other important factor in rapid solidification, on the other hand, can govern the microstructure at the recalescence stage. But, unless ΔT is large enough to be hypercooled, there is a transition of the microstructural scale into a

coarse one after recalescence. Therefore, the large heat-transfer coefficient that influences the whole thermal history of a droplet is a more important factor than the large ΔT in obtaining a uniform and fine solidification microstructure in the atomization of Al-8 wt pct Fe alloy.

E. *Volume Fractions of Microcellular and Cellular α-Al*

In order to get a rapidly solidified Al-8 wt pct Fe alloy with good mechanical properties, it is very important to control or at least to predict the volume fractions of microcellular and cellular α-Al regions. In this section, we show how they depend on h and ΔT for a given droplet size (30 μm). To do this, the criteria of the appearances of the microcellular and cellular α-Al are prerequisites. In the unidirectional solidification for Al-6 wt pct Fe alloy, Hughes and Jones[33] showed that α-Al cells can grow as a primary phase at the growth velocity higher than 1 cm/s. We adopt the same condition as a criterion of the appearance of α-Al cellular structure in the undercooled Al-8 wt pct Fe alloy, as done by Boettinger *et al.*[5] The transition condition from cellular to microcellular α-Al has not been determined. We assume simply that a microcellular α-Al can grow only with the tip radius smaller than $3 \cdot 10^{-8}$ m. (Note that the tip radius begins to increase steeply around this value in Figure 7.) The corresponding critical growth velocity is 7.8 cm/s.

Figure 14 shows the calculated volume fractions of the α-Al (g_α) and microcellular regions (g_A), where the α-Al region is the sum of the microcellular and cellular regions. There are two distinct regimes which are dominated by h and ΔT, respectively; that is, g_α and g_A depend mainly on h for $h > 0.3$ W/cm^2 K and $h > 2$ W/cm^2 K, respectively, as far as ΔT is not much larger than 120 K. Especially, the whole droplet can be solidified only with α-Al cells as a primary phase for $h > 0.7$ W/cm^2 K and only with microcells for $h > 4$ W/cm^2 K. On the other hand, ΔT can play a major role in g_α and g_A only for low h. The reported values of h in the atomizing processes are very few, but they are believed to be in the range of 0.1 to 1.0 W/cm^2 K in cases aimed at rapid solidification.[5,32] In this range, h is the dominant factor on g_α while, ΔT is the dominant one on g_A. In this way, both h and ΔT have similar importance in the microstructural control of Al-8 wt pct Fe alloy through an atomizing process. As shown in Section D and Figure 14, however, the most important control factor is h if the target is a fully microcellular microstructure.

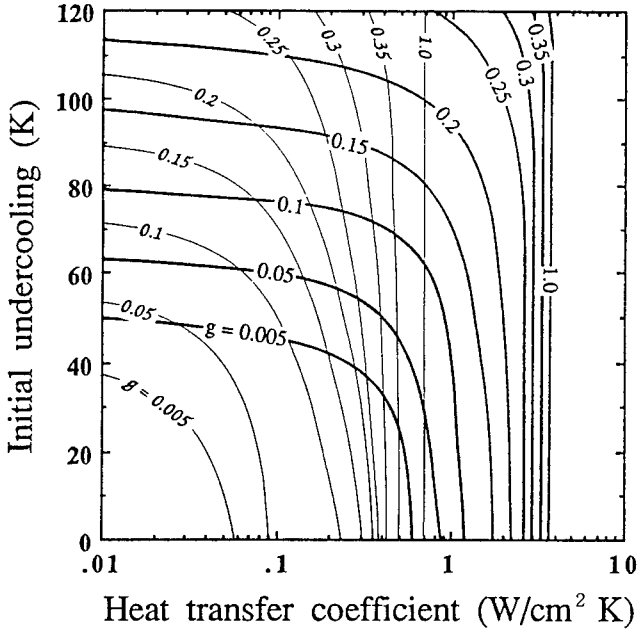


Fig. 14—Predicted volume fractions of the microcellular region (thick curves) and the sum of the microcellular and cellular regions (thin curves) as functions of the initial undercooling and the heat-transfer coefficient for a droplet (D = 30 μm).

IV. CONCLUSIONS

A numerical analysis of the growth procedures of cellular and microcellular α-Al in gas-atomized Al-8 wt pct Fe droplets, assuming a point nucleation on the droplet surface, leads to following conclusions.

1. The initial undercooling before the onset of nucleation, ΔT, in the range of 0 to 50 K has a negligible effect on the solidification microstructure for h = 0.5 W/cm^2 K, which is a typical heat-transfer coefficient in atomization processes. When the initial undercooling is larger than 100 K, there is an abrupt transition in microstructural scale. The predicted microstructural evolutions are in fairly good agreement with the reported experimental results.
2. For an initial undercooling larger than 100 K, the predicted volume fraction of the thermal dendritic growth region is large enough to be observed experimentally in a droplet smaller than 10 μm.
3. A large heat-transfer coefficient greatly increases the bulk undercooling at the early stage of solidification when the initial undercooling is small, and a fully microcellular structure can be obtained for a heat-transfer coefficient larger than 4 W/cm^2 K, irrespective of the initial undercooling.
4. The volume fractions of the microcellular region, g_A, and the sum of the microcellular and cellular region, g_α, were calculated as functions of the heat-transfer coefficient, h, and the initial undercooling, ΔT. In the range of h = 0.1 to 1.0 W/cm^2 K, which is typical in the gas-atomization processes, g_A and g_α are dominated by ΔT and h, respectively. The most important control factor for obtaining a fully microcellular structure is h.

APPENDIX

Thermophysical data used in calculations

ΔH latent heat of fusion = 1044 J/cm^3
C_L specific heat of liquid = 2.6 J/cm^3 K
C_S specific heat of solid = 3.0 J/cm^3 K
K_L thermal conductivity of liquid = 0.9 J/cm K s

K_S thermal conductivity of solid = 2.1 J/cm K s
D diffusion coefficient of Fe in liquid = $2.95 \cdot 10^{-3}$ exp $(-40{,}000/RT)$ cm^2/s
Γ capillary constant = $1.0 \cdot 10^{-5}$ K cm
T_f melting temperature of pure Al = 933.6 K
m_E liquidus slope of α-Al in Al-Fe phase diagram = −3.7 K/wt pct
k_0 equilibrium partition coefficient of Fe = 0.038
T_g atomization gas temperature = 300 K

REFERENCES

1. H. Jones: *Mater. Sci. Eng.*, 1969–1970, vol. 5, pp. 1-18.
2. D.J. Skinner, K. Okajaki, and C.M. Adam: in *Rapidly Solidified Powder Aluminum Alloys*, M.E. Fine and A.E. Starke, Jr., eds., ASTM-STM 890, ASTM, Philadelphia, PA, 1986, pp. 211-36.
3. Y.W. Kim and F.H. Froes: in *Undercooled Alloy Phases*, E.W. Collings and C.C. Koch, eds., TMS-AIME, New Orleans, LA, 1986, pp. 395-412.
4. J.H. Perepezko, S.E. LeBeau, B.A. Mueller, and G.H. Hildeman: in *Rapidly Solidified Powder Aluminum Alloys*, M.E. Fine and A.E. Starke, Jr., eds., ASTM-STM 890, ASTM, Philadelphia, PA, 1986, pp. 118-36.
5. W.J. Boettinger, L. Bendersky, and J.G. Early: *Metall. Trans. A*, 1986, vol. 17A, pp. 781-90.
6. M.G. Chu and D.A. Granger: *Metall. Trans. A*, 1990, vol. 21A, pp. 205-12.
7. D.J. Skinner, R.L. Bye, D. Raybould, and A.M. Brown: *Scripta Metall.*, 1986, vol. 21, pp. 118-36.
8. R.F. Cochrane, P.V. Evans, and A.L. Greer: *Mater. Sci. Eng.*, 1988, vol. 98, pp. 99-103.
9. C.M. Adam, V.R.V. Ramanan, and D.J. Skinner: in *Undercooled Alloy Phases*, E.W. Collings and C.C. Koch, eds., TMS-AIME, New Orleans, LA, 1986, pp. 59-70.
10. J.D. Cotton and M.J. Kaufman: *Metall Trans. A*, 1991, vol. 22A, pp. 927-34.
11. M. Gremaud, M. Carrard, and W. Kurz: *Acta Metall. Mater.*, 1990, vol. 38, pp. 2587-99.
12. M. Carrard, M. Gremaud, M. Zimmermann, and W. Kurz: *Acta Metall. Mater.*, 1992, vol. 40, pp. 983-96.
13. J. Lipton, M.E. Glickman, and W. Kurz: *Mater. Sci. Eng.*, 1984, vol. 65, pp. 57-63.
14. J. Lipton, W. Kurz, and R. Trivedi: *Acta Metall.*, 1987, vol. 35, pp. 957-64.
15. C.G. Levi and R. Mehrabian: in *Undercooled Alloy Phases*, E.W. Collings and C.C. Koch, eds., TMS-AIME, New Orleans, LA, 1986, pp. 345-74.
16. M. Rappaz and Ph. Thevoz: *Acta Metall.*, 1987, vol. 35, pp. 1487.
17. C.G. Levi and R. Mehrabian: *Metall. Trans. A*, 1982, vol. 13A, pp. 221-34.
18. W. Kurz, B. Giovanola, and R. Trivedi: *Acta Metall.*, 1986, vol. 34, pp. 823-30.
19. W. Kurz and J.D. Fisher: *Fundamentals of Solidification*, Trans. Tech. Publication, Aedermannsdorf, Switzerland, 1989, p. 73.
20. M.J. Aziz: *J. Appl. Phys.*, 1982, vol. 53, pp. 1158-68.
21. W.J. Boettinger and S.R. Coriell: in *Science and Technology of the Undercooled Melt*, P.R. Sahm, H. Jones, and C.M. Adam, eds., Martinus Nijhoff Publication, Dordrecht, The Netherlands, 1986, pp. 80-108.
22. J.L. Murray: *Mater. Res. Soc. Symp. Proc.*, 1983, vol. 19, pp. 249-62.
23. K. Eckler, R.F. Cochrane, D.M. Herlach, and B. Feuerbacher: *Mater. Sci. Eng.*, 1991. vol. A133, pp. 702-05.
24. R. Willnecker, D.M. Herlach, and B. Feuerbacher: *Appl. Phys. Lett.*, 1990, vol. 56, pp. 324-26.
25. M. Suzuki, T.J. Piccone, M.C. Flemings, and H.D. Brody: *Metall. Trans. A*, 1991, vol. 23A, pp. 2761-67.
26. S.R. Coriell and D. Turnbull: *Acta Metall.*, 1982, vol. 30, pp. 2135-39.
27. S.Z. Lu and J.D. Hunt: *J. Cryst. Growth*, 1992, vol. 123, pp. 2135-39.
28. M. Rappaz: *Int. Mater. Rev.*, 1989, vol. 34, pp. 93-123.
29. B. Giovanola and W. Kurz: *Metall. Trans. A*, 1990, vol. 21A, pp. 260-63.
30. B. Giovanola and W. Kurz: *Z. Metallkd.*, 1991, vol. 82, pp. 83-88.
31. S.G. Kim, S.H. Shin, T. Suzuki, and T. Umeda: *Mater. Sci. Eng.*, 1994, vol. A181/A182, pp. 1156-60.
32. P.S. Grant, B. Cantor, and L. Katgerman: *Acta Metall. Mater.*, 1993, vol. 41, pp. 3097-108.
33. I.R. Hughes and H. Jones: *J. Mater. Sci.*, 1976, vol. 11, pp. 1781-93.

Communications

The Chromium Equivalents of Ferrite Stabilizers in Commercial Stainless Steels

V. RAGHAVAN and DARA P. ANTIA

In a recent article,[1] the chromium equivalents of X (X = Al, Mo, Nb, Si, Ti, V, or W) were reported, as derived from the computed quaternary phase equilibria in Fe-Cr-Ni-X systems. Commercial stainless steels usually contain some residual alloying elements other than the ferrite stabilizer X. In order to take into account their effect on the derived chromium equivalents, it is necessary to compute the phase equilibria in multicomponent systems containing up to six components. We have carried out these calculations for four types of stainless steels. The newly derived Cr equivalents are compared with those obtained earlier from quaternary phase equilibria.[1]

Four types of commercial austenitic stainless steels were selected for study. The mean values of the composition ranges as per specification[2] are listed in Table I for 304, 316, 321, and 347 types. In all cases, the residual carbon was ignored for the purpose of computation. In 321 and 347 types, the residual Nb or Ti in solution in austenite was assumed arbitrarily to be 0.2 wt pct. Taking a smaller or larger residual value (0.1 or 0.3 wt pct) makes little difference to the results reported.

A single-lattice magnetic solution model is used. The molar Gibbs energy G_m of α (ferrite) or γ (austenite) phase is defined as follows:

$$G_m = \sum_i X_i^0 G_i + RT \sum_i X_i \ln X_i + \sum_{i=1}^{c-1} \sum_{j=i+1}^{c} X_i X_j L_{ij} + \sum_{i=1}^{c-2} \sum_{j=i+1}^{c-1} \sum_{k=j+1}^{c} X_i X_j X_k L_{ijk} + {}^{mo}G$$

where i, j, and k stand for components and c is the total number of components in the system. The term X is atomic fraction, and L is the thermodynamic interaction parameter. The term ${}^{mo}G$ is the magnetic contribution to the Gibbs energy.[1] The binary and ternary thermodynamic and magnetic interaction parameters given in Reference 1 were used as required. Additional binary interaction parameters[3–9] listed in Table II were also used. The nonlinear equations obtained by equating the chemical potentials of the components in the two phases were solved by the Newton–Raphson iterative method.

The simulated compositions listed in Table I were obtained as follows. The concentrations of all other alloying elements (except chromium in austenite) were fixed at the values given in the specification. The chromium concentration in austenite and the concentration of all alloying elements, including Cr in ferrite, were treated as unknowns and provided guess values to set up the chemical potential equalities. In this way, the number of unknowns to be determined was automatically set equal to the number of simultaneous equations to be solved by iteration in any multicomponent system. As the computation was to be done in atomic fractions, some trial and error calculations were necessary to match exactly the weight percents of elements (except Cr) in the specified and simulated compositions listed in Table I. The weight percents of Cr for simulated compositions in Table I are computed values corresponding to an annealing temperature of 1100 °C.

As before,[1] the Cr equivalent at 1100 °C is evaluated as the amount of Cr substituted by 1 wt pct of the ferrite stabilizer at the $(\gamma/\gamma + \alpha)$ phase boundary. To derive this value, the ferrite stabilizing element in the simulated compositions was set to zero and the computation was repeated for a system with one component less. From the difference in Cr concentrations in austenite between the two results, the equivalent was derived as an average over that concentration of the ferrite stabilizer. Where more than one ferrite stabilizer was present, this procedure was repeated separately for each ferrite stabilizer.

Table III lists the chromium equivalents for 304, 316, 321, and 347 types for the simulated compositions in Table I. These are compared with the equivalents derived from quaternary phase equilibria.[1] To rule out any effect of averaging over different concentrations, the equivalents from the quaternary phase equilibria were recomputed for the concentrations given in Table I. However, there was a negligible difference between these and the equivalents reported earlier.[1]

As seen in Table III, the equivalents obtained from

V. RAGHAVAN, Professor, is with the Indian Institute of Technology, New Delhi, 110016, India. DARA P. ANTIA, Chairman of the APD Committee, is with the Indian Institute of Metals, Calcutta.

Manuscript submitted March 22, 1994.

Table I. Specified and Simulated Compositions of Stainless Steels

Type	Composition, Wt Pct	Fe	Cr	Mn	Mo	Nb	Ni	Si	Ti
304	specification (mean)	bal	19.0	2.0	—	—	9.25	1.0	—
	simulated	bal	17.3	2.0	—	—	9.25	1.0	—
316	specification (mean)	bal	17.0	2.0	2.5	—	12.0	1.0	—
	simulated	bal	16.8	2.0	2.5	—	12.0	1.0	—
321	specification (mean)	bal	18.0	2.0	—	—	10.5	1.0	0.2*
	simulated	bal	17.4	2.0	—	—	10.5	1.0	0.2
347	specification (mean)	bal	18.0	2.0	—	0.2*	11.0	1.0	—
	simulated	bal	18.3	2.0	—	0.2	11.0	1.0	—

*Assumed amount in solution in austenite.

Table II. Additional Thermodynamic Interaction Parameters

1.	Interaction parameters for bcc (α) phase	Reference
	$L_{Cr,Mn} = -20{,}328 + 18.734\,T - (9162 - 4.418\,T)(X_{Cr} - X_{Mn})$	3
	$L_{Mn,Mo} = -7500$	4
	$L_{Mn,Ni} = -51{,}785 + 3.5\,T + 6270(X_{Mn} - X_{Ni})$	5
	$L_{Mn,Si} = -137{,}000 + 80\,T$	6
	$L_{Mo,Si} = -70{,}900$	8
	$L_{Nb,Si} = -41{,}907$	9
	$L_{Si,Ti} = -248{,}596 + 45.07\,T$	8
2.	Interaction parameters for fcc (γ) phase	
	$L_{Cr,Mn} = -19{,}088 + 17.542\,T$	3
	$L_{Mn,Ni} = -58{,}173 + 10.5\,T + 6300(X_{Mn} - X_{Ni})$	5
	$L_{Mn,Si} = -100{,}000 + 51\,T$	6
	$L_{Mn,Ti} = -2917$	7
	$L_{Mo,Si} = -70{,}900$	8
	$L_{Nb,Si} = -41{,}907$	9
	$L_{Si,Ti} = -248{,}596 + 45.07\,T$	8
3.	Other interaction parameters for bcc and fcc phases[1]	
4.	${}^{ex}T_c^{\alpha}$ (Cr, Mn) $= -X_{Cr}X_{Mn}\,[1325 + 1133\,(X_{Cr} - X_{Mn})^2]$	3
	${}^{ex}\beta^{\alpha}$ (Cr, Mn) $= X_{Cr}X_{Mn}\,[0.486 - 0.720\,(X_{Cr} - X_{Mn})^2]$	3

Table III. Chromium Equivalents in Austenitic Stainless Steels Annealed at 1100 °C

	Chromium Equivalent in Weight Percent	
Type	from Quaternary Phase Equilibria	from Specification-Simulated Composition
304	Si: 2.16	Si: 2.10
316	Mo: 0.93	Mo: 0.98
	Si: 2.05	Si: 2.11
321	Ti: 3.78	Ti: 3.95
	Si: 2.10	Si: 2.09
347	Nb: 0.95	Nb: 0.97
	Si: 2.09	Si: 2.05

the specification-simulated compositions are only slightly different from those derived from quaternary phase equilibria. The slight shift is in both directions, depending on the composition the alloy. The maximum shift is about 5 pct. We can then conclude that the Cr equivalents derived from quaternary phase equilibria are by and large valid for commercial stainless steels.

REFERENCES

1. V. Raghavan and D.P. Antia: *Metall. Mater. Trans. A*, 1994, vol. 25A, pp. 2675-81.
2. *Metals Handbook*, ASM, Materials Park, OH, 1980, vol. 3, pp. 3-40.
3. B.-J. Lee: *Metall. Trans. A*, 1993, vol. 24A, pp. 1919-33.
4. M. Hillert and M. Waldenstrom: *Scand. J. Metall.*, 1977, vol. 6, pp. 211-18.
5. K.C. Hari Kumar and V. Raghavan: *J. Alloy Phase Diagrams*, 1989, vol. 5, pp. 201-20.
6. N. Chakraborti and H.L. Lukas: *CALPHAD*, 1989, vol. 13, pp. 293-300.
7. L. Kaufman: *CALPHAD*, 1978, vol. 2, pp. 117-46.
8. C. Vahlas, P.Y. Chevalier, and E. Blanquet: *CALPHAD*, 1989, vol. 13, pp. 273-92.
9. K.C. Hari Kumar: Ph.D. Thesis, Indian Institute of Technology, Delhi, India, 1991.

The Cause of Matrix Penetration of W/W Grain Boundaries During Heat Treatment of W-Ni-Fe Heavy Alloy

JOON-WOONG NOH, MOON-HEE HONG, GEUN-HONG KIM, SUK-JOONG L. KANG, and DUK YONG YOON

Recently, it has been observed that Ni-Fe-W matrix phase penetrated into W/W grain boundaries during a cyclic heat treatment of W-Ni-Fe heavy alloy and that the amount of penetrated matrix increased with the number of cycles at the heat-treatment temperature for a total of 1 hour.[1] The result of the matrix penetration was a remarkable increase in impact energy up to three times; however, the cause of the microstructure change with the heat treatment was not clear. For this communication, the cause of matrix penetration has been studied by observing the microstructures of bulk and penetrated matrices after various heat treatments and by measuring chemical compositions.

The experimental procedure was similar to that in the previous investigation.[1] The blended powder mixture of 93W-5.6Ni-1.4Fe (wt pct) was compacted under 100 MPa into rectangular bars and sintered at 1485 °C for 1 hour in flowing H_2. Some sintered specimens were cyclically heat-treated at 1150 °C for a total period of 1 hour at 1150 °C under flowing N_2, as in the previous investigation.[1] Other specimens were heat-treated at 1150 °C for 1 to 48 hours and water-quenched. In order to observe the effect of additional heat treatment, the

JOON-WOONG NOH, formerly with the Korea Advanced Institute of Science and Technology, MOON-HEE HONG, and GEUN-HONG KIM, Senior Researchers, are with the Agency for Defense Development, Taejon, 305-600, Korea. SUK-JOONG L. KANG and DUK YONG YOON, Professors, are with the Korea Advanced Institute of Science and Technology, Taejon, 305-701, Korea.

Manuscript submitted October 13, 1993.

specimen cyclically heat-treated for 20 times was heat-treated again at 1150 °C for 48 hours, and the specimen heat-treated for 48 hours was reheat-treated at 1150 °C for 1 hour. The fracture surfaces of heat-treated specimens were observed under a scanning electron microscope (SEM) after impact tests. The chemical compositions at fresh interfaces were determined by Auger electron spectroscopy (AES) with a primary electron beam size of 0.8 μm. A transmission electron microscope (TEM) observation was made on thin foils, prepared by the jet-polishing technique, in a solution of 1 HCl-4 H_2SO_4-10 glycerol-85 ethanol (vol pct).

Figure 1 shows the impact fracture surfaces of various specimens. The fractographs of the as-sintered and the heat-treated specimens reveal that the conventional heat treatment of one cycle already induces the formation of the matrix phase at W/W grain boundaries, in agreement with the previous results.[2,3] Such a formation of matrix at W/W grain boundaries after the heat treatment of one cycle was attributed to the precipitation of a matrix phase from supersaturated W grains during an isothermal holding at the heat-treatment temperature.[3] With increasing the number of heat-treatment cycles, however, the amount of matrix at W/W grain boundaries increases, and the W/W grain boundaries are almost completely covered with the matrix phase after 20 cycles (Figure 1(d)), as shown in Reference 1. Because the dihedral angle of the alloy is greater than 0 deg (about 50 deg),[4] the formation of such a considerable amount of matrix phase at the boundaries could not be expected previously. The increase in the matrix volume at W/W grain boundaries thus implies the penetration of matrix into the boundaries rather than the matrix precipitation. When the volume of the penetrated matrix is not sufficient to completely cover the grain boundaries (Figures 1(b) and 1(c)), however, the matrix forms many droplets, possibly because of the dihedral angle being greater than 0 deg. At some boundaries, the shape of the droplets is elongated, as shown, for example, in Figures 1(b) and 1(c), possibly because of an effect of W/W grain-boundaries orientation. With increasing the volume of the penetrated matrix, the penetrated matrix forms a continuous phase.

The chemical compositions of plane W/W grain boundary, the penetrated matrix at W/W grain boundary, and the bulk matrix were measured by AES and are listed in Table I. The chemical composition at a W/W grain boundary shows considerable segregations of Ni and Fe but is essentially not changed by the heat treatment, except by an overall reduction of the impurity contents. The Ni and Fe contents in the penetrated matrix are much higher than those segregated at W/W grain boundaries. The penetrated matrix, however, contains more W than the bulk matrix. It seems that the chemical composition of the penetrated matrix is closer to an equilibrium composition with W at the heat-treatment temperature than the bulk matrix composition, which may be in equilibrium with W at low liquidus temperature. In this respect, the difference in the chemical composition between bulk and penetrated matrices may imply that the penetration occurs by the diffusion of atoms.

The observed matrix penetration with the cyclic heat treatment may be related to the thermal stresses introduced during quenching of the specimens. The thermal-expansion coefficient of a matrix of 93W-5.6Ni-1.4Fe alloy is known to be about $20 \times 10^{-6}/K$[5] and that of

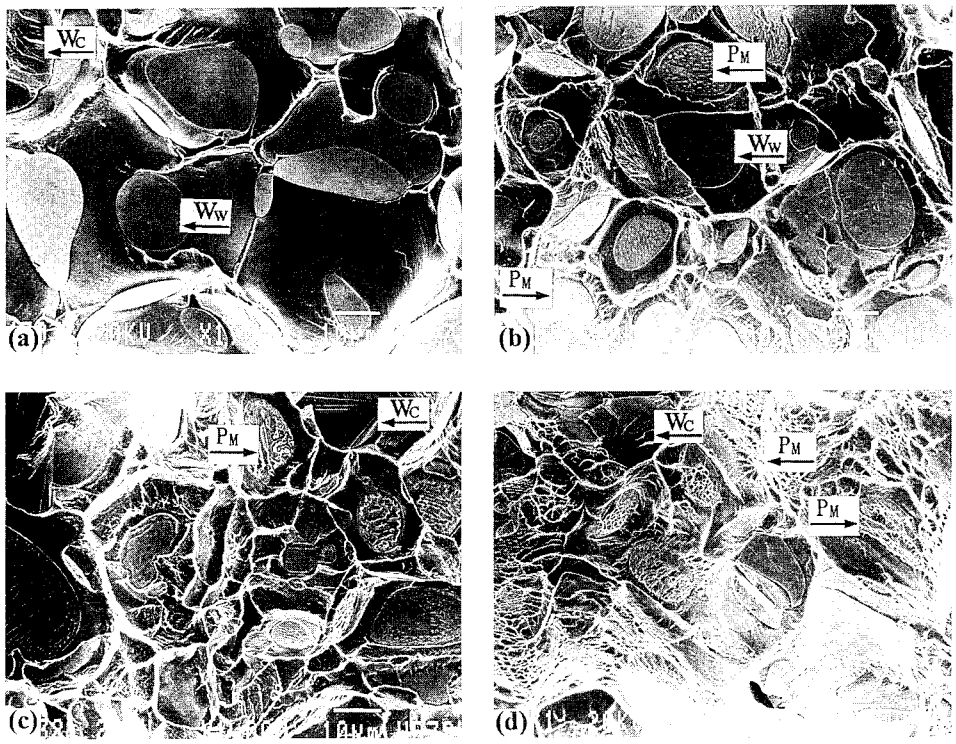


Fig. 1—The impact-fractured surfaces of the specimens with different heat-treatment cycles: (*a*) as-sintered, (*b*) 1 cycle, (*c*) 10 cycles, and (*d*) 20 cycles. The W_W, W_C, and P_M indicate W/W grain boundary, W cleavage, and penetrated matrix, respectively.

Table I. Measured Chemical Compositions of W/W Grain Boundary, Penetrated Matrix, and Bulk Matrix Atomic Percent

		W	Ni	Fe	P	O	C
As-sintered	W_W	60.0	21.9	6.8	3.9	5.0	2.0
Heat-treated for 1 cycle	W_W	63.8	20.4	7.2	1.6	3.9	2.8
Heat-treated for 20 cycles	P_M	28.9	45.6	12.5	1.4	7.5	3.7
	B_M	10.4	65.3	17.9	0.8	3.4	2.2

W_W: W/W grain boundary; B_M: bulk matrix; and P_M: penetrated matrix at W/W boundary.

pure W to be 4.6×10^{-6}/K.[6] Therefore, by cooling the specimen, tensile and compressive stresses must be built in at W/matrix interface and W/W grain boundary, respectively.[7,8,9] The penetration of matrix into W/W grain boundaries may also be understood as a result of the reduction of the stored strain energy. The stored energy can be much relieved at the heat-treated temperature; however, the cyclic heat treatment would provide it in repetition, resulting in the successive penetration of matrix with the cycles.

Because of the thermal mismatch at W/bulk matrix interface, many dislocations are observed to be generated at the interface, as shown in Figure 2(a). With increasing the number of the heat-treatment cycles, more dislocations are generated and the dislocations tend to align in a specific direction (Figure 2(b)). After 20 cycles (Figure 2(c)), the bulk matrix is recrystallized into many grains of an order of 1 μm in size. These changes in matrix microstructure are obviously the result of the cyclic heat treatment—repetitive heatings, annealings, and water quenchings. The dislocation alignment and the grain recrystallization must be a result of the reduction of the strain energy stored in matrix by the cyclic heat treatment.

The matrix penetration resulting from thermal stresses can further be confirmed by heat treating the sintered specimens for various times and also by reheat treating the cyclically heat-treated specimens. Figure 3 shows the fractographs of specimens heat-treated for various times. Compared with Figure 1(b), the size of matrix droplets at W/W grain boundaries is increased, and the number of the droplets decreased with the heat-treatment time (Figures 3(a) and (b)). It appears, however, that the matrix droplets are depleted at edge regions of grain boundaries and remains at center regions. This result suggests that the matrix droplets coarsened with the heat-treatment time and that the droplets near the edge regions diffused out. The diffusion-out of penetrated matrix during prolonged heat treatment can clearly be observed when reheat treating the cyclically heat-treated specimens at 1150 °C for 48 hours, as shown in Figure 4. The matrix films at W/W grain boundaries (Figure 1(d)) are almost completely eliminated after the long reheat treatment, and only some matrix droplets remain at some grain boundaries. In contrast, when the specimen heat-treated for 48 hours (Figure 3(b)) is reheat-treated for 1 hour at 1150 °C (Figure 3(c)), the amount of matrix at the boundaries increases considerably, indicating again that the matrix has penetrated into the boundaries during the reheat treatment. The size of the newly formed matrix

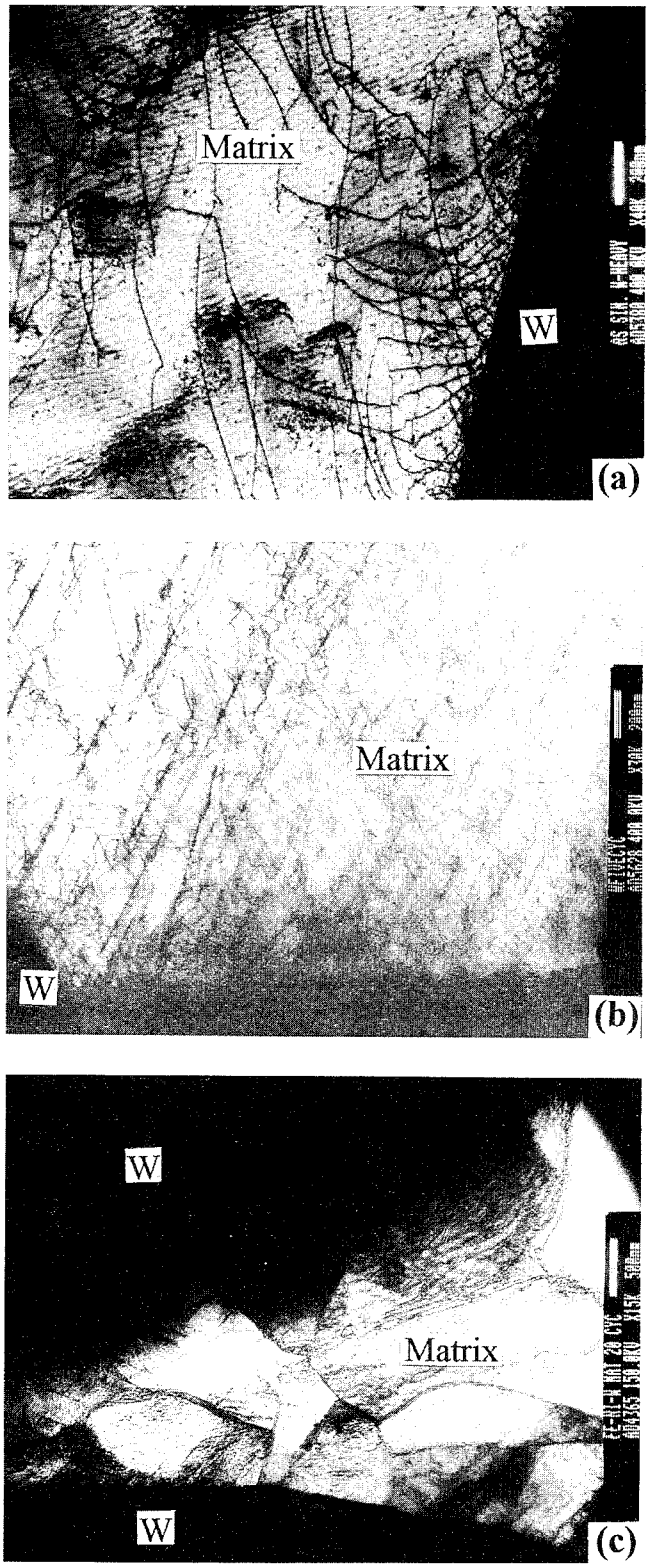
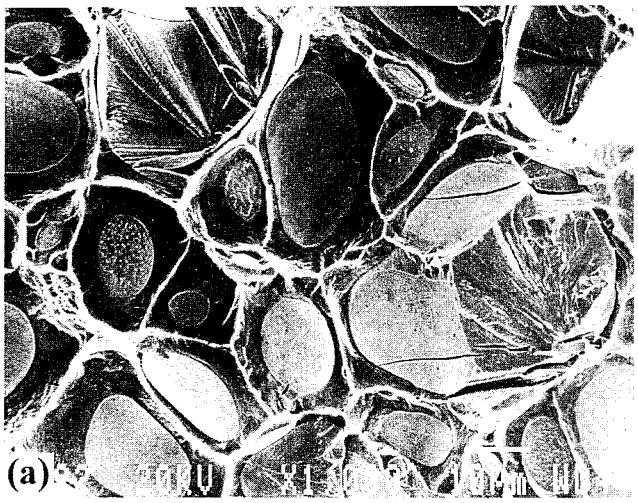


Fig. 2—Transmission electron micrographs showing dislocations and subgrain structures in the matrix of the specimens (*a*) as-sintered, (*b*) heat-treated for 5 cycles, and (*c*) heat-treated for 20 cycles.

droplets at edge regions appears smaller than that of the pre-existing ones at center regions. If the formation of the matrix phase is a result of the precipitation of supersaturated Ni and Fe in W grains,[3] the size and volume of the matrix at W/W grain boundaries must remain



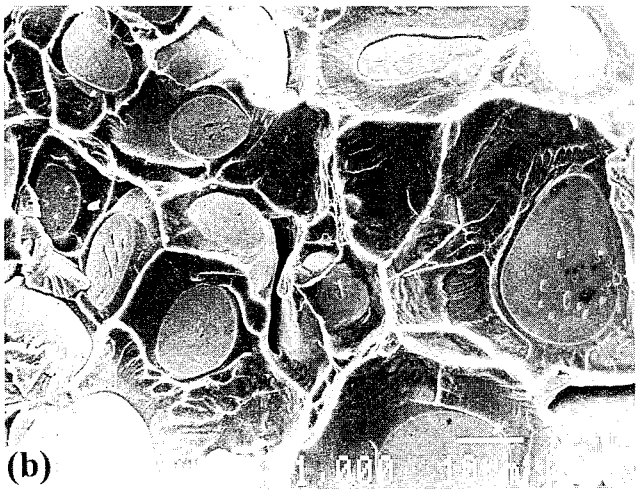




Fig. 3—The impact-fractured surfaces of the specimens heat-treated at 1150 °C for (*a*) 8 hours, (*b*) 48 hours, and (*c*) 48 hours + 1 hour.

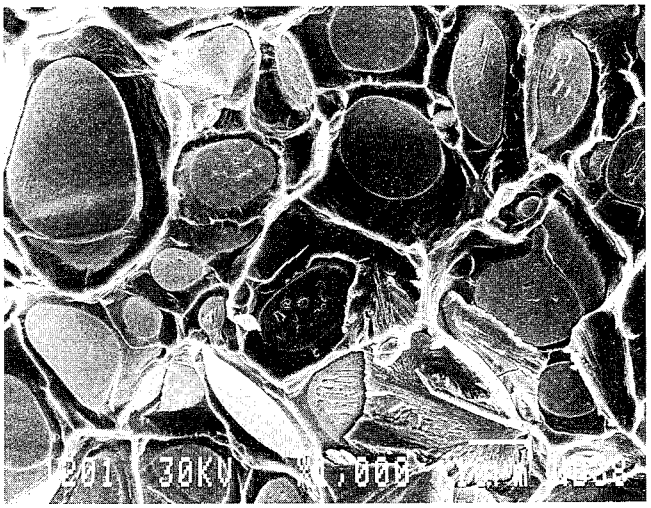


Fig. 4—The impact-fractured surface of the specimen cyclically heat-treated for 20 times and reheat-treated at 1150 °C for 48 hours.

unchanged after the additional heat treatments, in contrast to the present results.

In summary, the volume of the penetrated matrix between W/W grain boundaries increases with the number of heat-treatment cycles but appears to decrease with the heat-treatment time up to 48 hours. Almost complete elimination of the penetrated matrix is observed after reheat treating the cyclically heat-treated specimens for longer time. An additional heat treatment of specimens heat treated for longer time, however, again causes the matrix penetration. By examining the microstructures of variously heat-treated specimens, the thermal stresses introduced during the cooling of the alloy are indirectly found to be responsible for a continuous penetration of matrix into W/W grain boundaries.

REFERENCES

1. J.-W. Noh, E.-P. Kim, H.-S. Song, W.-H. Baek, K.-S. Churn, and S.-J.L. Kang: *Metall. Trans. A*, 1993, vol. 24A, pp. 2411-16.
2. B.H. Rabin, A. Bose, and R.M. German: *Int. J. Powder Metall.*, 1989, vol. 25, pp. 21-27.
3. J.B. Posthill, M.C. Hogwood, and D.V. Edmonds: *Powder Metall.*, 1986, vol. 29, pp. 45-51.
4. B.H. Rabin and R.M. German: *Metall. Trans. A*, 1985, vol. 19A, pp. 1523-32.
5. K.S. Churn, J.W. Noh, H.S. Song, E.P. Kim, S. Lee, and W.H. Baek: *'92 Intr. Conf. on Tungsten and Tungsten Alloys*, MPIF, New Jersey, 1992, pp. 397-405.
6. C.J. Smithells: *Metal Reference Book*, 4th ed., Butterworth and Co., London, 1967, vol. 3, p. 687.
7. R.M. Fulrath: *J. Am. Ceram. Soc.*, 1959, vol. 42, pp. 423-29.
8. J. Gurland: *Trans. ASM*, 1958, vol. 50, pp. 1063-71.
9. J. Gurland and N.M. Parikh: *Fracture*, H. Liebowitz, ed., Academic Press, New York, NY, and London, 1972, vol. 7, pp. 841-45.

Elastic Constants of SiC_p/Al: Measurements and Modeling

MING LEI and HASSEL LEDBETTER

Using dynamic methods, we measured Young and shear moduli of aluminum-matrix particle-reinforced composites containing up to 55 vol pct SiC particles. Using a scattered-plane-wave ensemble-average model, we calculated four elastic constants: Young, shear, and bulk moduli, and Poisson ratio. The model uses four pieces of input information: matrix elastic constants, particle elastic constants, particle volume fraction, and particle shape. Between measurement and calculation, we found good agreement. As expected, the elastic stiffnesses fall well below a rule-of-mixture prediction; the Poisson ratio falls above. Also, we report the Young-modulus-mode internal friction, which, against expectation, increases with increasing particle content.

Composite-material elastic constants, such as Young modulus, shear modulus, *etc.* provide a subject of continuing interest. The Young modulus, for example, relates directly to fundamental interatomic potentials. Also, it relates to a variety of solid-state phenomena such as the Debye temperature, diffusion, creep, and theoretical strength.[1]

Elastic properties of a composite material depend mainly on three ingredients: matrix properties, inclusion properties, and phase geometry. Phase geometry includes many variables: volume fraction, inclusion shape, inclusion orientation, inclusion size, and inclusion distribution. Many researchers gave different models to predict the macroscopic composite properties. On this subject, there are several reviews, including those by Hashin,[2] Christensen,[3] and Watt *et al.*[4]

Internal friction is an important physical property of a composite material. It relates to many physical phenomena and it is a powerful technique for studying a solid's internal structure. For a particle-reinforced composite, SiC in aluminum, the present study focuses on effects of volume fraction and inclusion geometry on elastic constants. Also, we consider internal friction. Especially, we compare model predictions with observation.

From a commercial supplier, we obtained materials with five SiC volume concentrations: 0, 20, 25, 30, and 55 pct, in the form of 1-cm plates. The supplier started with commercially available Al-6061 and SiC particles. These powders were blended, compacted, and sintered to produce billets measuring 25 × 30 × 4 cm. Billets were hot-rolled at 700 to 783 K with a reduction per pass ranging from 10 to 50 pct. Rolled plates were subjected to a standard T6 heat treatment: solution treated at 800 K for 2 hours, water quenched, and aged at 436 K for 18 hours. Figure 1 shows a typical microstructure. Quantitative metallography suggested that the particles possess an aspect ratio of approximately 3:1. Dissolving the aluminum matrix, collecting the particles, and examining them in an optical microscope gave 2.7 ± 0.9.

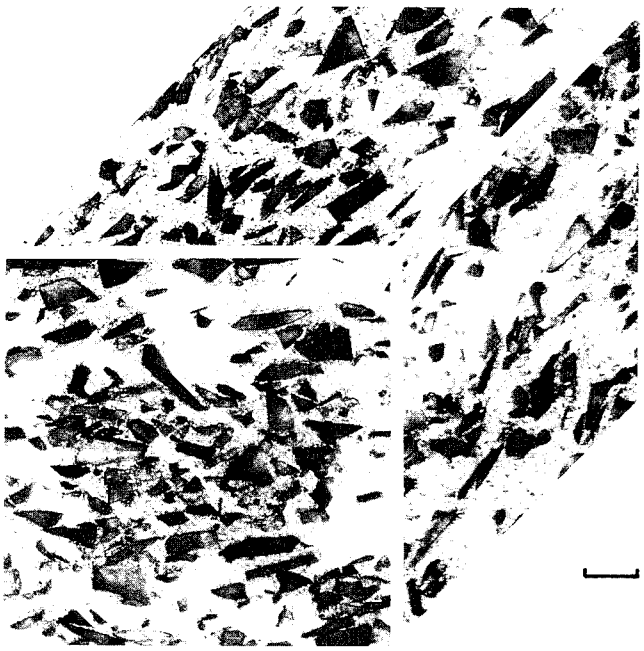


Fig. 1—Typical microstructure: 30 vol pct SiC particles in an Al-alloy matrix. Bar equals 10 μm.

Using a three-component Marx-oscillator[5,6] resonance method, we measured the Young modulus, E, the torsional modulus, T, and the associated internal friction, Q^{-1}. For the Young modulus, we used the relationship

$$E = \rho v_s^2 = 4\rho f_s^2 l_s^2 \qquad [1]$$

Here, ρ denotes mass density, v denotes sound velocity, and f and l denote resonance frequency and length, respectively. Subscript s denotes specimen. In extensional-mode vibration, we found the resonance frequency of the specimen from

$$f_s^2 = f_o^2 + (f_o^2 - f_q^2)\frac{m_q}{m_s} \qquad [2]$$

Here, m denotes mass, and subscripts o and q denote the complete oscillator and quartz crystals, respectively. For the torsional modulus, we used a similar relationship:

$$T = \rho v_s^2 = 4\rho f_s^2 l_s^2 \qquad [3]$$

But here the resonance frequency of the specimen, in a torsional mode, is given by

$$f_s^2 = f_o^2 + (f_o^2 - f_q^2)\frac{m_q}{m_s}\left(\frac{d_q}{d_s}\right)^{1/2} \qquad [4]$$

Here, d denotes diameter. From standard sources,[7] we know that for a transversely isotropic material, the torsional modulus equals the shear modulus, G.

For a sharp, Lorentzean resonance peak, we obtain the specimen's internal friction from a relationship similar to Eq. [2]:

$$Q_s^{-1} = Q_o^{-1} + (Q_o^{-1} - Q_q^{-1})\frac{m_q}{m_s} \qquad [5]$$

MING LEI, formerly Visiting Scientist, Materials Science and Engineering Laboratory, National Institute of Standards and Technology, is Staff Scientist, Quatrosonics, Albuquerque, NM 87109. HASSEL LEDBETTER, Research Metallurgist, is with the Materials Science and Engineering Laboratory, National Institute of Science and Technology, Boulder, CO 80303.

Manuscript submitted December 23, 1988.

U.S. GOVERNMENT WORK NOT PROTECTED BY U.S. COPYRIGHT

Table I. Properties of Constituent Materials.

	ρ (g/cm^3)	E (GPa)	μ (GPa)	B (GPa)	k (GPa)	λ (GPa)	ν
SiC	3.181	440.6	188.1	223.4	286.1	98	0.1712
Al	2.688	71.5	26.7	74.8	83.7	57	0.3405

Equations [2], [4], and [5] apply only near resonance when

$$f_s \cong f_q \cong f_o \qquad [6]$$

Table I shows the properties of the composite's constituent materials. Figure 2 shows the measurements of the Young and torsional moduli. Figure 3 shows the derived bulk modulus and Poisson ratio. Figure 4 shows the measurements of internal friction in an extensional (Young modulus) mode.

In the following, we consider principally the explanation for the dependence of E, T, and Q^{-1} on volume percent particle. Also, we consider particle shape.

Using a multiple-scattering plane-wave approach, Ledbetter and Datta[8] studied the elastic properties of a composite material containing randomly distributed and randomly oriented ellipsoidal particles. They calculated the effective wave speeds of plane waves, both longitudinal and shear. In the long-wavelength limit, they gave relationships for the bulk and shear moduli:

$$\frac{B - B_m}{B_p - B_m} = \frac{\frac{1}{3}\bar{c}\sum_{i,j=1}^{3} T_{iijj}}{1 - \frac{\bar{c}(B_p - B_m)}{3B_m + 4G_m}\sum_{i,j=1}^{3} T_{iijj}} \qquad [7]$$

$$\frac{G - G_m}{G_p - G_m} = \frac{\frac{1}{5}\bar{c}G_m\left(\sum_{i,j=1}^{3} T_{ijij} - \frac{1}{3}\sum_{i,j=1}^{3} T_{iijj}\right)}{G_m - \frac{2\bar{c}}{75}\frac{(G_p - G_m)(3\lambda_m + 8G_m)}{\lambda_m + 2G_m}\left(\sum_{i,j=1}^{3} T_{ijij} - \frac{1}{3}\sum_{i,j=1}^{3} T_{iijj}\right)} \qquad [8]$$

Here, B and $\bar{c}$ denote the bulk modulus and the volume fraction of particles, and λ is a Lamé constant. Subscripts m and p denote matrix and particle, respectively. Also,

$$T_{ijij} = T_{jiji} = \frac{1}{2(1 + 2US_{ijij})}, \qquad \text{for } i, j = 1, 2, 3 \qquad [9]$$

$$[T_{ijij}] = \begin{bmatrix} 1 + US_{1111} + VS_1 & US_{1122} + VS_1 & US_{1133} + VS_1 \\ US_{2211} + VS_2 & 1 + US_{2222} + VS_2 & US_{2233} + VS_2 \\ US_{3311} + VS_3 & US_{3322} + VS_3 & 1 + US_{3333} + VS_3 \end{bmatrix}^{-1} \qquad [10]$$

$$U = \frac{G_p}{G_m} - 1 \qquad [11]$$

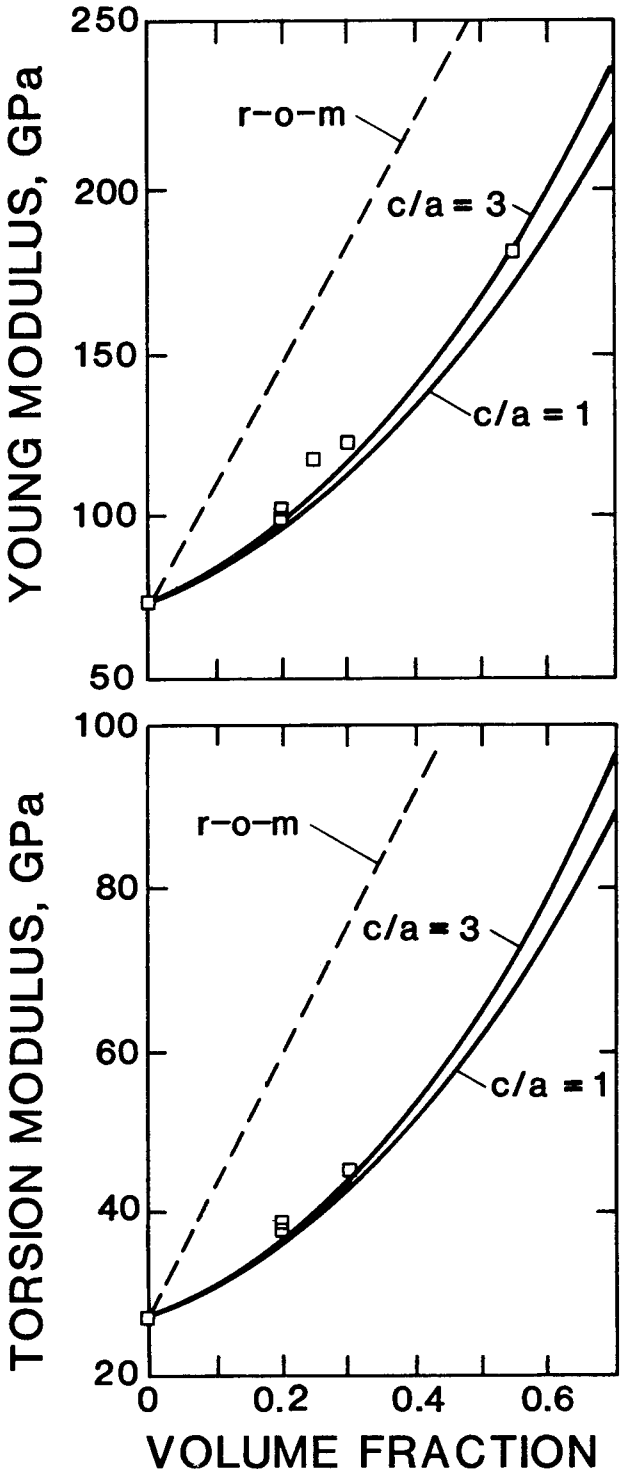


Fig. 2—Upper. The Young modulus *vs* particle volume fraction, $\bar{c}$. Points represent measurements. Dashed line indicates linear rule-of-mixture. Curves represent model predictions for two particle aspect ratios: $c/a = 1$ (spheres) and $c/a = 3$ (prolate spheroids). Lower. Shear modulus *vs* particle volume fraction.

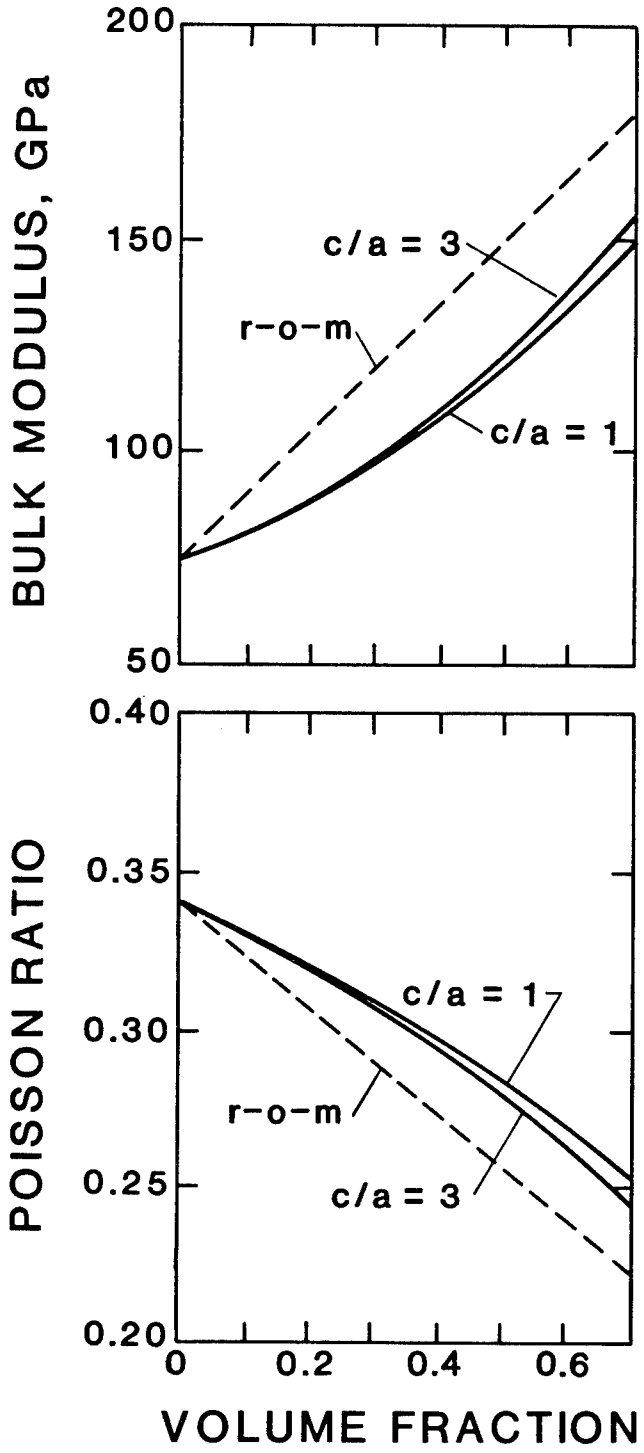


Fig. 3—Upper. Bulk modulus *vs* particle volume fraction. See figure legend 2. Lower. Poisson ratio *vs* particle volume fraction.

$$V = \frac{1}{3}\left(\frac{B_p}{B_m} - \frac{G_p}{G_m}\right) \qquad [12]$$

$$S_i = \sum_{j=1}^{3} S_{iijj} \qquad [13]$$

The S_{ijkl} were defined by Eshelby[9] and apply to a general ellipsoid and thus contain the particle-shape factor.

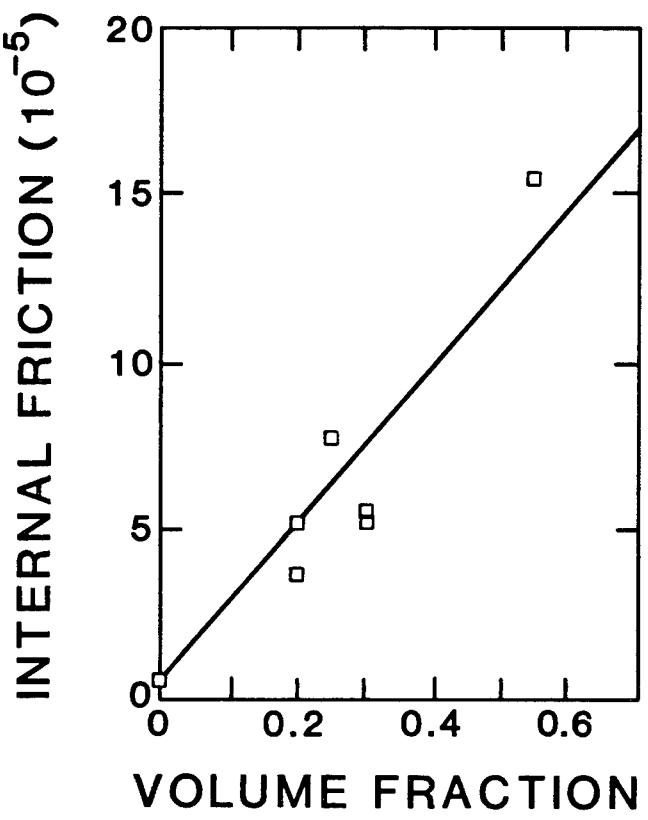


Fig. 4—Young-modulus-mode internal friction *vs* particle volume fraction. Line represents a linear-least-squares fit to measurements. At $\bar{c} = 0.2$ and 0.3, there are two measurements within the plate: rolling and transverse directions.

We invoke the well-known relationships for isotropic-material Young modulus and Poisson ratio:

$$E = \frac{9BG}{3B + G} \qquad [14]$$

$$\nu = \frac{1}{2}\frac{3B - 2G}{3B + G} \qquad [15]$$

First, we consider SiC as spherical particles distributed randomly in a homogeneous aluminum matrix. Figure 2 shows the model calculations for the Young and shear (torsional) moduli for spherical particles ($a = b = c$). These results agree, both numerically and analytically, with Hashin's[10] composite-sphere-model equations for elastic moduli. For both E and G, the theoretical calculations predict results below measurements.

Second, we consider SiC particles as spheroids ($a = b \neq c$). For both the Young and shear (torsional) moduli, we found that a prolate-spheroid model best fits observation. From metallographic results, we took an aspect ratio (c/a) of three. If the real aspect ratio is near two or four, the calculation results would change only slightly. Model calculations for E and G are shown in Figure 2. Figure 3 shows model calculations for the bulk modulus and Poisson ratio for both spherical and nonspherical particles. For all four elastic constants, we show straight lines representing a linear rule-of-mixture.

Now, we consider the internal friction associated with Young modulus measurements. Figure 4 shows that Q^{-1} increases with increasing SiC-particle volume fraction.

This result surprises us because we expected a high stiffness material such as SiC to possess a low internal friction. Thus, Q^{-1} would decrease with increasing SiC-particle volume fraction. A possible explanation for this phenomenon lies in the interfaces, either themselves, or as sources of structural defects such as dislocations arising from thermal-expansivity mismatch. Several previous studies[11] on metal-matrix composites showed that interfaces contribute negligibly to internal friction. Thus, understanding this phenomenon requires further study.

From this study on SiC particle-reinforced composite materials, we reached four conclusions.

1. Physical properties of a composite material depend strongly on the volume fraction and on the particle shape.
2. A model calculation based on randomly distributed spherical particles predicts slightly low elastic stiffnesses.
3. Theoretical calculations suggest that the studied composite materials contain prolate-spheroid-shaped SiC particles. Metallography supports this prediction.
4. Against expectation, the internal friction associated with Young modulus measurements increases with increasing inclusion content. For this, we offer a tentative explanation: higher mobile dislocation density caused by thermal-expansivity mismatch.

REFERENCES

1. G. Grimvall and S. Sjödin: *Phys. Scripta*, 1974, vol. 10, p. 340.
2. Z. Hashin: *Theory of Fiber Reinforced Materials*, NASA Contract Report No. CR 1974, 1972, pp. 67-383.
3. R.M. Christensen: *Mechanics of Composite Materials*, Wiley, New York, NY, 1979, pp. 31-151.
4. J.P. Watt, G.F. Davies, and R.J. O'Connell: *Rev. Geophys. Space Phys.*, 1976, vol. 14, pp. 541-63.
5. J. Marx: *Rev. Sci. Instrum.*, 1951, vol. 22, pp. 503-509.
6. W.H. Robbinson and A. Edgar: *IEEE Trans. Sonics Ultrason.*, 1974, vol. SU-21, pp. 98-105.
7. R.F.S. Hearmon: *Applied Anisotropic Elasticity*, Oxford University Press, Oxford, United Kingdom, 1961, p. 51.
8. H.M. Ledbetter and S.K. Datta: *J. Acoust. Soc. Am.*, 1986, vol. 79, pp. 239-48.
9. J.D. Eshelby: *Proc. R. Soc. London*, 1957, vol. A241, pp. 376-96.
10. Z. Hashin: *J. Appl. Mech.*, 1962, vol. 29, pp. 143-50.
11. N. Igata and A. Kohyama: *Trans. Jpn. Soc. Compos. Mater.*, 1976, vol. 2, pp. 30-35.

Elastic Compliance and Hill's Quadratic Yield Function for Weakly Orthotropic Sheets of Cubic Metals

CHI-SING MAN

Since the correlation of elastic and plastic anisotropy in textured sheets of cubic metals was first demonstrated by Stickels and Mould[1] on steel, many researchers have reported similar findings (well documented for steel, less so for copper and brass, and mixed results reported for aluminum alloys). This correlation suggests the possibility that the plastic anisotropic parameters of sheet metals (the average strain ratio $\bar{r}$, the planar anisotropy Δr, percent earing, *etc.*), which are usually determined by destructive tests, could be inferred from nondestructive measurements of elastic anisotropic parameters. Indeed, much work has been done lately in exploring engineering applications of this possibility, *e.g.*, the on-line determination of r value of steel sheets by ultrasonic techniques.[2–5]

Attempts (*cf.*, for instance, Davies *et al.*[6] and Tang[7]) have been made to explain the aforementioned correlation. The purpose of the present note, however, is that of (phenomenological) constitutive modeling. As a generalization of the experimental findings, we seek a simple yield function that would embody correlation of elastic and plastic anisotropy for homogeneous, weakly orthotropic sheets of cubic metals. Here, by "weakly orthotropic" is meant that the sheets are weakly textured: the material points of the sheets are orthotropic but nearly isotropic. A quantitative characterization of what we mean by "weak" is given in the paragraph containing Eq. [3] and in the sentence preceding Eq. [11].

The elastic properties of a material are defined by its elasticity tensor $\mathbf{C}$ (or, equivalently, by its compliance tensor $\mathbf{K}$, the inverse of $\mathbf{C}$); its plastic behavior is characterized by the yield function f. The correlation between elastic and plastic anisotropy indicates that for sheet metals, $\mathbf{K}$ and f are somehow related. In this note, we investigate this relationship for homogeneous sheets of cubic metals that are weakly orthotropic and whose yield function assumes Hill's classical quadratic form. Henceforth, we choose a Cartesian coordinate system whose X, Y, and Z axes lie in the rolling direction, the transverse direction in the plane of the sheet, and the direction normal to this plane, respectively. Under this coordinate system, Hill's quadratic yield criterion is[8]

$$2f(\mathbf{T}) = F(T_{22} - T_{33})^2 + G(T_{33} - T_{11})^2 + H(T_{11} - T_{22})^2 + 2LT_{23}^2 + 2MT_{13}^2 + 2NT_{12}^2 = 1 \qquad [1]$$

where T_{ij} are the components of the stress tensor $\mathbf{T}$, and $F, G, \ldots, N$ are "parameters characteristic of the current state of anisotropy." For isotropic sheets, Hill's quadratic yield criterion reduces to that of von Mises, which can be written as

$$\boldsymbol{\sigma} \cdot \mathbf{K}[\boldsymbol{\sigma}] = \frac{1}{2\mu} \operatorname{tr} \boldsymbol{\sigma}^2 = k^2 \qquad [2]$$

here tr stands for "trace"; $\boldsymbol{\sigma} \equiv \mathbf{T} - ((\operatorname{tr} \mathbf{T})/3)\mathbf{I}$, where $\mathbf{I}$ is the identity tensor, denotes the deviatoric stress; μ is the shear modulus; $k^2 > 0$ is a material parameter; the dot product of two second-order tensors $\mathbf{A}$ and $\mathbf{B}$ is defined as $\mathbf{A} \cdot \mathbf{B} = \operatorname{tr}(\mathbf{A}^T\mathbf{B})$, where $\mathbf{A}^T$ is the transpose of $\mathbf{A}$.

For orthotropic sheets of cubic metals, we can express the components of the compliance tensor $\mathbf{K}$ in terms of the single-crystal elastic constants and the texture

CHI-SING MAN, Associate Professor, is with the Department of Mathematics, University of Kentucky, Lexington, KY 40506-0027.

Manuscript submitted January 3, 1994.

coefficients W_{400}, W_{420}, and W_{440}. To first order with respect to the texture coefficients, the Voigt, Reuss, and Hill averaging procedures all lead to the same formal expressions for the components of **K**. In the reduced notation, we can write down explicit expressions for the nonzero components of **K** as follows:[9]

$$(K_{11}, K_{22}, K_{33}) = \frac{1}{E_0}(1, 1, 1) - 2\kappa(\delta_1, \delta_2, \delta_3)$$

$$(K_{23}, K_{13}, K_{12}) = \frac{-\nu_0}{E_0}(1, 1, 1) + \kappa(\delta_4, \delta_5, \delta_6)$$

$$(K_{44}, K_{55}, K_{66}) = \frac{1}{\mu_0}(1, 1, 1) + 4\kappa(\delta_4, \delta_5, \delta_6) \quad [3]$$

here μ_0, E_0, and ν_0 are the shear modulus, Young's modulus, and Poisson ratio in the isotropic limit, respectively; κ is an anisotropic factor that depends on the single-crystal elastic constants; $\delta_1 = (\delta_5 + \delta_6)/2$, $\delta_2 = (\delta_4 + \delta_6)/2$, $\delta_3 = (\delta_4 + \delta_5)/2$, and

$$\delta_4 = -(16\sqrt{2}\pi^2/35)(W_{400} + \sqrt{5/2}\, W_{420})$$

$$\delta_5 = -(16\sqrt{2}\pi^2/35)(W_{400} - \sqrt{5/2}\, W_{420})$$

$$\delta_6 = (4\sqrt{2}\pi^2/35)(W_{400} - \sqrt{70}\, W_{440}) \quad [4]$$

The Voigt, Reuss, and Hill averaging procedures result in the same isotropic bulk modulus but different values of μ_0 and κ. For our subsequent discussion, however, it is the form of the expressions in Eq. [3] that really matters; the specific values of μ_0, E_0, ν_0, and κ are of little consequence. Henceforth, we shall restrict our attention to weakly orthotropic sheets and shall use Eq. [3] in our calculations. Indeed, we shall assume that the absolute value of the products $\kappa_0 W_{400}$, $\kappa_0 W_{420}$, and $\kappa_0 W_{440}$ are much smaller than 1 for the sheets in question so that we can, in our calculations, drop all terms quadratic or higher in these products. A glance at Eq. [3] reveals that it is natural to write

$$\mathbf{K} = \mathbf{K}_0 + \mathbf{K}' \quad [5]$$

where $\mathbf{K}_0$ is the isotropic part that remains when the texture coefficients vanish, and the anisotropic part $\mathbf{K}'$ is linear in the elastic anisotropic factor κ.

We seek within the class of Hill's quadratic yield functions those that deliver linear correlation of elastic and plastic anisotropy for weakly orthotropic sheets of cubic metals. It can be proved that all such quadratic yield criteria necessarily assume the form[10]

$$\boldsymbol{\sigma} \cdot \mathbf{K}_0[\boldsymbol{\sigma}] + \gamma(\boldsymbol{\sigma} \cdot \mathbf{K}'[\boldsymbol{\sigma}]) = k^2 \quad [6]$$

or

$$\frac{3}{2}\,\mathrm{tr}\,\boldsymbol{\sigma}^2 + \beta\left(\boldsymbol{\sigma} \cdot \frac{1}{\kappa}\mathbf{K}'[\boldsymbol{\sigma}]\right) = Y_0^2 \quad [7]$$

where γ and k^2 are material parameters, $\beta \equiv 3\kappa\mu_0\gamma$, and $Y_0^2 \equiv 3\mu_0 k^2$. Because the parameters β and Y_0^2 are to be determined empirically, and because $\mathbf{K}'/\kappa$ depends only on the texture coefficients, we see that in effect the same yield criterion will result from Eq. [6], irrespective of whether we choose the Voigt, Reuss, or Hill averaging procedure for the evaluation of **K**. Since only the deviatoric part of the stress appears in Eq. [6], a superimposed hydrostatic pressure will have no effect on yielding. Equation [6] reduces to the von Mises criterion (see Eq. [2]) in the isotropic limit.

From Eqs. [1], [3], [5], and [6], we obtain the following simple expressions for the material parameters in Hill's quadratic yield criterion:

$$(F, G, H) = \frac{1}{k^2}\left(\frac{1}{6\mu_0}(1, 1, 1) - \kappa\gamma(\delta_4, \delta_5, \delta_6)\right) \quad [8]$$

$$(L, M, N) = \frac{1}{k^2}\left(\frac{1}{2\mu_0}(1, 1, 1) + 2\kappa\gamma(\delta_4, \delta_5, \delta_6)\right). \quad [9]$$

In what follows, we consider a batch of samples that have the same values of μ_0, E_0, κ, and γ but possibly have different k^2 values. Let $r(\theta)$ and $E(\theta)$ be the plastic strain ratio and the Young's modulus measured on a coupon cut at an angle θ with respect to the rolling direction, respectively. We assume that during the measurements the sheets in question are in plane stress. It follows that[8]

$$r(\theta) = \frac{H + (2N - F - G - 4H)\sin^2\theta\cos^2\theta}{F\sin^2\theta + G\cos^2\theta} \quad [10]$$

Using this expression and Eqs. [4], [8], and [9] we find, after dropping all terms quadratic or higher in the products βW_{400}, βW_{420}, and βW_{440} (where $\beta = 3\kappa\mu_0\gamma$), that

$$\bar{r} \equiv \frac{1}{4}\left(r(0) + r\left(\frac{\pi}{2}\right) + 2r\left(\frac{\pi}{4}\right)\right)$$

$$= 1 + \frac{15\mu_0\kappa\gamma}{2}\delta_3 \quad [11]$$

$$= 1 - \frac{24\sqrt{2}\pi^2\mu_0\kappa\gamma}{7}W_{400} \quad [12]$$

$$\Delta r \equiv \frac{1}{2}\left(r(0) + r\left(\frac{\pi}{2}\right) - 2r\left(\frac{\pi}{4}\right)\right)$$

$$= -3\mu_0\kappa\gamma(\delta_3 + 4\delta_6) \quad [13]$$

$$= \frac{96\pi^2\mu_0\kappa\gamma}{\sqrt{35}}W_{440} \quad [14]$$

Thus, under the present modeling, $\bar{r} - 1$ and Δr are linearly correlated to the texture coefficients W_{400} and W_{440}, respectively. As Δr is independent of W_{420}, one may question whether it is adequate to represent "planar anisotropy" by the current definition of Δr.

From the definition of Young's modulus, we deduce that

$$\bar{E} \equiv \frac{1}{4}\left(E(0) + E\left(\frac{\pi}{2}\right) + 2E\left(\frac{\pi}{4}\right)\right)$$

$$= E_0 + \frac{3\kappa E_0^2}{4}\delta_3 \quad [15]$$

$$\Delta E \equiv \frac{1}{2}\left(E(0) + E\left(\frac{\pi}{2}\right) - 2E\left(\frac{\pi}{4}\right)\right)$$

$$= \frac{\kappa E_0^2}{2}(\delta_3 + 4\delta_6) \quad [16]$$

From Eqs. [11] and [15], we observe that

$$\bar{r} = 1 + \frac{10\mu_0\gamma}{E_0^2}(\bar{E} - E_0) \qquad [17]$$

Similarly, we obtain from Eqs. [13] and [16] the relation

$$\Delta r = -\frac{6\mu_0\gamma}{E_0^2}\Delta E \qquad [18]$$

Hence, in addition to predicting the linear correlations of $\bar{r} - 1$ *vs* $\bar{E} - E_0$ and of Δr against ΔE, the present theory dictates also that the slopes of these two straight lines (dependent variables: $\bar{r} - 1$, Δr; independent variables: $\bar{E} - E_0$, ΔE) have a ratio of $-5/3$. While one would expect that Eq. [6] and the assumption of weak anisotropy would lead to various linear correlations between plastic and elastic anisotropic parameters, this slope ratio of $-5/3$, universal in the sense that it is independent of $\mathbf{K}$, γ, and k^2, is not an obvious consequence.

The article of Stickels and Mould[1] includes data by which we can determine whether this predicted slope ratio of $-5/3$ is corroborated by their steel samples. The 35 samples of Stickels and Mould have an $\bar{r}$ value that runs from 0.66 to 2.73. Since the present theory pertains to weakly anisotropic sheets, we consider only those 24 samples with $\bar{r} \leq 1.50$. Following the original work, we express $\bar{E}$ and ΔE in 10^6 psi (or 6.895 GPa). For the 24 samples, we find that $\bar{r} = 0.48\ \bar{E} - 13.96$; the uncertainty in the slope is 0.04, and the correlation coefficient is 0.93. For the Δr *vs* ΔE plot, we seek the slope m so that the equation $\Delta r = m\Delta E$ best fits the data. We obtain $m = -0.30 \pm 0.02$, and the correlation coefficient is -0.95. The predicted slope ratio of $-5/3$ compares favorably with the empirically determined value of -1.6 ± 0.2.

From Eqs. [12] and [14], we observe likewise that the two straight lines which relate $\bar{r}$ to W_{400} and Δr to W_{440}, respectively, are predicted to have a slope ratio of $-\sqrt{70}/28$. The existence of such "universal" slope ratios in the present modeling reflects purely the effect of material symmetry, namely, that which pertains to a weakly orthotropic sheet texture resulting from the preferred orientation of cubic crystallites. The predicted universal slope ratios could serve as a means for the corroboration or refutation of the present phenomenological theory, which is based on Hill's quadratic yield criterion. It will be interesting to see whether the more refined micromechanical theories in the literature (*e.g.*, that of Davies *et al.*[6]) also predict the existence of such universal slope ratios and, if they do, to compute the predicted values of these ratios.

Hill's quadratic yield function has six material parameters. If a material has a yield function that assumes the form given in Eq. [6] or [7], plasticity experiments are required for the determination of only two parameters, namely, $\beta \equiv 3\kappa\mu_0\gamma$ and $Y_0^2 \equiv 3\mu_0 k^2$. Further information required for the evaluation of Hill's parameters (*cf.* Eqs. [8] and [9]) is embodied in the texture coefficients W_{400}, W_{420}, and W_{440}, which can be ascertained by X-ray or ultrasonic techniques.

It would be interesting to see whether Eq. [6] could adequately serve as the initial yield criterion for some sheet metal. In this regard, steel clearly is the most promising candidate for further study.

The research reported here was supported in part with funds from the National Science Foundation (Grant. No. EHR-9108764) and the Commonwealth of Kentucky through the Kentucky EPSCoR Advanced Development Program.

REFERENCES

1. C.A. Stickels and P.R. Mould: *Metall. Trans.*, 1970, vol. 1, pp. 1303-12.
2. M. Hirao, H. Fukuoka, K. Fujisawa, and R. Murayama: *J. Nondest. Eval.*, 1993, vol. 12, pp. 27-32.
3. A.V. Clark, Y. Berlinsky, N. Izworski, Y. Cohen, D.V. Mitrakovic, and S.R. Schaps: *J. Nondest. Eval.*, 1993, vol. 12, pp. 33-43.
4. R.B. Thompson, E.P. Papadakis, D.D. Bluhm, G.A. Alers, K. Forouraghi, H.D. Skank, and S.J. Wormley: *J. Nondest. Eval.*, 1993, vol. 12, pp. 45-62.
5. K. Kawashima, T. Hyoguchi, and T. Akagi: *J. Nondest. Eval.*, 1993, vol. 12, pp. 71-77.
6. G.J. Davies, D.J. Goodwill, and J.S. Kallend: *Metall. Trans.*, 1972, vol. 3, pp. 1627-31.
7. W. Tang: Ph.D. Dissertation, University of Kentucky, Lexington, KY, Dec. 1993.
8. R. Hill: *The Mathematical Theory of Plasticity*, Clarendon Press, Oxford, 1950, pp. 318-23.
9. M. Hirao, K. Aoki, and H. Fukuoka: *J. Acoust. Soc. Am.*, 1987, vol. 81, pp. 1434-40.
10. C.-S. Man: in *Review of Progress in Quantitative Nondestructive Evaluation*, D.O. Thompson and D.E. Chimenti, eds., Plenum Press, New York, NY, vol. 14, in press.

Microstructural Evolution of an Overlay Coating on a Single-Crystal Nickel-Base Superalloy

T.C. TOTEMEIER, W.F. GALE, and J.E. KING

High-temperature overlay coatings of the MCrAlY type (where M is Ni, Co, or Ni + Co) formed *via* physical vapor deposition or plasma spray methods are finding increasing use in turbine blade applications because of their high-temperature oxidation and sulfidation resistance.[1,2] Their mechanical behavior and resistance to environmental degradation have been extensively characterized,[3,4] however, little attention has been paid either to the coating microstructure on a fine scale or to the evolution of the microstructure from the as-coated condition through to the substrate heat treatment and subsequent thermal exposure. This communication reports

T.C. TOTEMEIER, Graduate Student, and J.E. KING, Lecturer, are with the Department of Materials Science and Metallurgy, University of Cambridge, Cambridge CB2 3QZ, United Kingdom. W.F. GALE, Assistant Professor, is with the Materials Engineering Program, Auburn University, Auburn, AL 36849.

Manuscript submitted March 31, 1994.

on a transmission electron microscopy (TEM) and scanning electron microscopy (SEM) based microstructural study of a low-pressure plasma-sprayed (LPPS) CoNiCrAlY coating on a single-crystal nickel-base superalloy substrate. The microstructure of the coating was characterized after each of the following stages of treatment: plasma spraying, a diffusion heat treatment of 1 hour at 1100 °C, a substrate aging treatment of 16 hours at 870 °C, and 140 hour thermal exposures in laboratory air at temperatures of 850 °C and 1100 °C.

The substrate used for the study was a high γ' volume fraction nickel-base superalloy with principal alloying additions of Co, Cr, Al, and Ti. Examination of TEM specimens prepared using the "edge-on" method[5] was performed using a PHILIPS* 400T microscope operating at an accelerating voltage of 120 kV; energy dispersive X-ray analysis was also performed. Metallographic cross sections of the coating following the substrate aging treatment and thermal exposures were prepared using standard grinding and polishing procedures.

*PHILIPS is a trademark of Philips Electronic Instruments Corp., Mahwah, NJ.

The bulk of the as-sprayed coating consisted of a fine, randomly oriented, two-phase mixture of β-(Ni, Co)Al (ordered B2 structure) and γ-(Ni, Co) (disordered fcc structure). A grain size of 0.5 to 1.0 μm was observed; this observation and the random grain orientations reflect the high cooling rates involved in splat solidification. The γ phase was extensively twinned, a result of the depression of the stacking fault energy (SFE) of γ by the presence of Co. Tweed contrast, commonly observed with β phase in bulk aluminide,[6] was noted for β phase in the as-sprayed coating. A number of $M_{23}C_6$ particles were found at the centers of γ grains, the presence of which can be attributed to residual carbon in the starting powders. Oxide deposits were visible on the original splat interfaces in some areas.

A distinctly different microstructure was observed immediately adjacent to the substrate (in a band of width approximately 2 μm), which consisted of flattened, pancake-shape γ grains about 8 μm in length and the same width as the layer, separated from each other and the γ/γ' substrate by high-angle grain boundaries. These grains contained some randomly oriented β-phase precipitates (Figure 1). Again, the lack of an orientation relationship between γ and β suggests that the microstructure evolved strictly during solidification and not in the solid state. A possible mechanism for the formation of this region is that a very small layer of the substrate was liquefied by the impact of the first splat of the coating. The mixing of the substrate liquid with the splat enriched the Ni and diluted the Al content of the splat, resulting in a microstructure with less β phase than the main region of the coating. Compared to the main coating, a lower Co:Ni ratio was observed in the region of the coating adjacent to the substrate, and this observation is consistent with the dilution of the initial splats by localized liquidation of the substrate. Further evidence for melting was provided by the incorporation of small NiO precipitates, originally present just below the surface of the substrate, into the interfacial layer of the coating.



Fig. 1—Dark-field (g = $(020)_\gamma$) TEM image of pancake-shaped γ grains with β precipitates along the coating-substrate interface in an as-sprayed coating.

This could only have occurred during mixing of the substrate and coating liquids.

The coating microstructure following a 1-hour diffusion heat treatment at 1100 °C was generally similar to that of the as-sprayed coating. However, an interesting contrast event was observed in the β phase, which was not present in the as-sprayed condition. This consisted of lamellar features distributed throughout the β phase (Figure 2). These were most strongly visible in weak-beam images and did not produce distinct additional reflections. The lamellar contrast was observed with $\{110\}_\beta$ fundamental reflections; no contrast was visible with $\{111\}_\beta$ superlattice, $\{100\}_\beta$ superlattice, $\{112\}_\beta$ fundamental, or $\{200\}_\beta$ fundamental reflections (only the usual

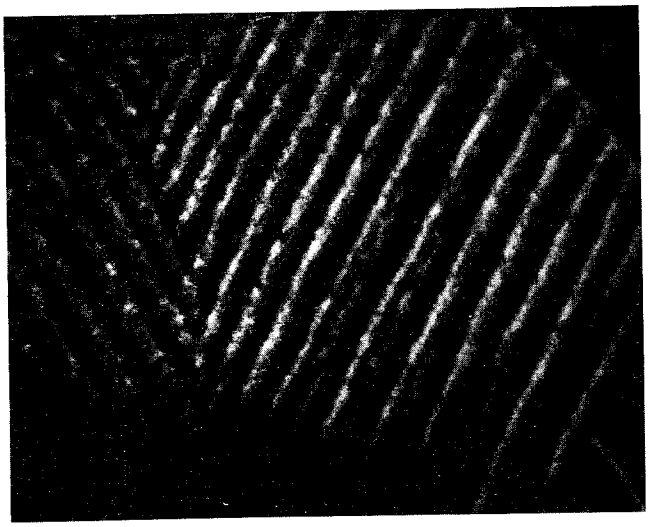


Fig. 2—Weak-beam dark-field (g = $(1\bar{1}0)_\beta$) TEM image of lamellar contrast as observed in β grains following diffusion heat treatment.

tweed contrast was observed). The origin of this contrast is not currently understood, but it is presumably related to the inherent instability of the β-NiAl phase.

The bulk of the coating was relatively unaffected by the substrate aging treatment of 16 hours at 870 °C. The microstructure still consisted of a fine two-phase β-γ microstructure, as shown in Figure 3. The lower temperature aging treatment did result in the formation of σ-phase precipitates in the β phase (with an orientation relationship $[111]_\beta \| [110]_\sigma$, $(\bar{1}10)_\beta \| (1\bar{1}0)_\sigma$) and $M_{23}C_6$ precipitates in γ (cube-cube orientation relationship). However, there were significant changes in the microstructure at the coating-substrate interface. In a region from the coating-substrate interface to 5 μm into the coating, the grain size increased to 1.5 to 3 μm. The formation of fine (100 nm in diameter) spherical γ' precipitates was observed in the γ phase in this region of the coating (Figure 4), which correlated with a reduction in the Co to Ni ratio due to interdiffusion with the Ni-rich substrate. Replacement of Co by Ni stabilizes the γ' phase at the expense of γ. Another factor contributing to the formation of γ' could be the loss of chromium to the substrate through interdiffusion. Chromium favors the formation of disordered γ over ordered γ'.

Thermal exposure for 140 hours at 850 °C produced further changes in the microstructure, although for the most part, the two-phase γ-β structure still existed. Aluminum loss at the coating surface due to the formation of Al_2O_3 resulted in the depletion of β phase at the coating surface and at surface-connected pores. Additional formation of $M_{23}C_6$ precipitates in the γ coating matrix near the substrate was also observed.

More extreme changes in the microstructure were observed following exposure for 140 hours at 1100 °C. As shown in Figure 5, the loss of aluminum at the surface resulted in a large β-depleted zone (40 μm in thickness). Only a small region in the center of the coating still retained any resemblance to the original γ-β microstructure. Extensive interdiffusion with the substrate occurred, the result being a 30-μm-thick region of γ with large, elongated precipitates believed to be β phase. These precipitates could not be conclusively identified using TEM because of their tendency to be removed during the ion-milling phase of specimen preparation, but their etching/staining characteristics are those of β phase. The coating grew considerably in thickness at the expense of the substrate. The originally 95-μm-thick coating was

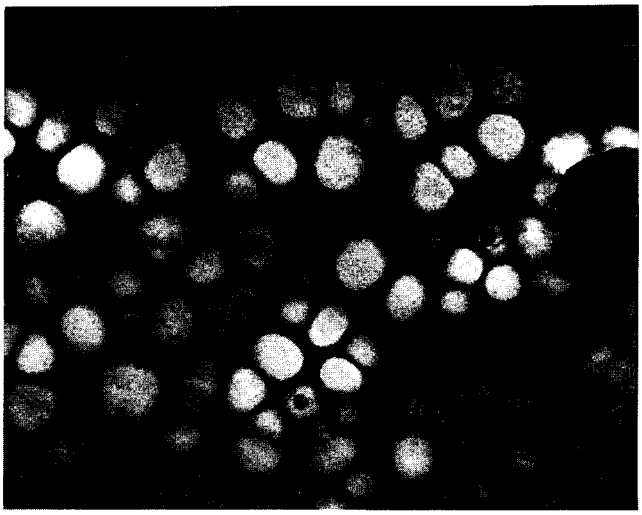


Fig. 4 — Dark-field ($g = (110)_{\gamma'}$) TEM image of fine spherical γ' precipitates in a γ matrix near the coating-substrate interface in a coating following substrate aging treatment.

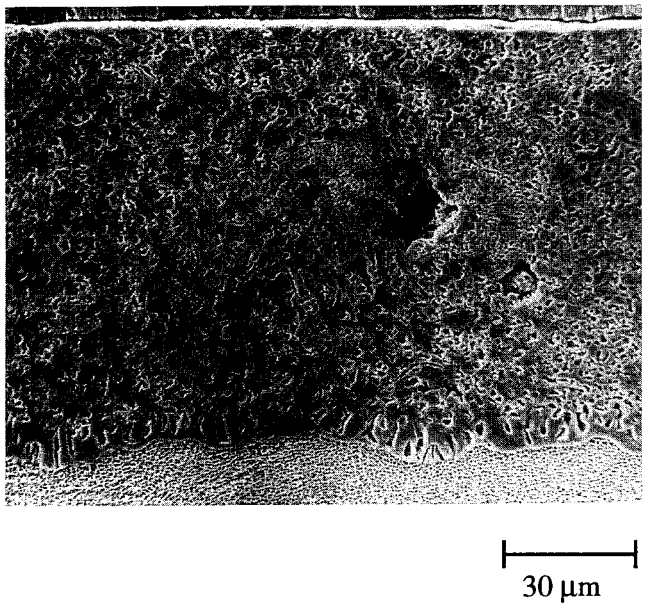


Fig. 3 — SEM microstructure of a coating following substrate aging treatment.

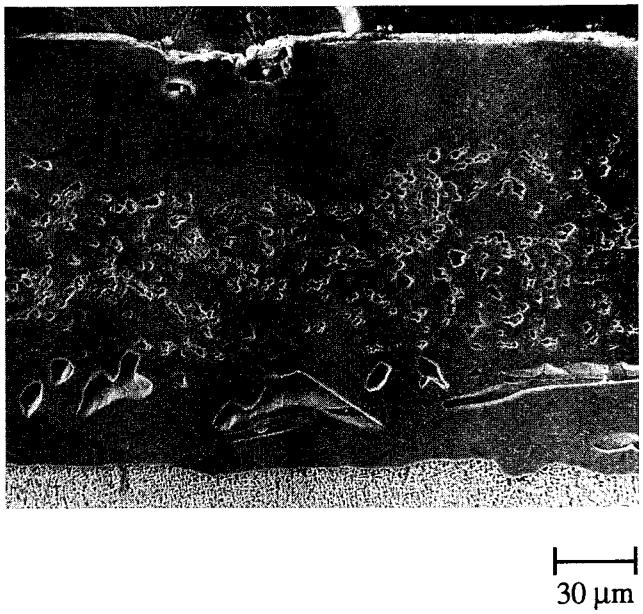


Fig. 5 — SEM microstructure of a coating following thermal exposure for 140 hours at 1100 °C.

160 μm after exposure at 1100 °C, reflecting the extent to which interdiffusion with the substrate occurred.

The authors wish to acknowledge Professor C.J. Humphreys for provision of laboratory facilities at Cambridge and Mr. S. Williams and the late Dr. T.N. Rhys-Jones of the Turbine Aerofoil R&D and Surface Technology Group of Rolls-Royce plc. for their assistance with the project. Financial support for the project and for WFG was provided by Rolls-Royce plc. and the Science and Engineering Research Council. Financial support for TCT was provided by the Marshall Aid Commemoration Commission of the Association of Commonwealth Universities.

REFERENCES

1. G.W. Meetham: in *High-Temperature Alloys for Gas Turbines and Other Applications*, W. Betz, R. Brunetaud, D. Coutsouradis, H. Fischmeister, T.B. Gibbons, I. Kvernes, Y. Lindblom, J.B. Marriott, and D.B. Meadowcroft, eds., D. Reidel Publishing Company, Dordrecht, The Netherlands, 1986, pp. 1-19.
2. F.S. Petit and G.W. Goward: in *Coatings for High-Temperature Applications*, E. Lang, ed., Applied Science Publishers, Barking, Essex, United Kingdom, 1983, pp. 341-59.
3. R.W. Smith: *Thin Solid Films*, 1981, vol. 84, pp. 59-72.
4. F.J. Pennisi and D.K. Gupta: *Thin Solid Films*, 1981, vol. 84, pp. 49-58.
5. W.F. Gale and J.E. King: *Metall. Trans. A*, 1992, vol. 23A, pp. 2657-65.
6. I.M. Robertson and C.M. Wayman: *Metall. Trans. A*, 1984, vol. 15A, pp. 1353-57.

Contents

METALLURGICAL AND MATERIALS TRANSACTIONS B—Process Metallurgy—Volume 25B, DECEMBER 1994

The 1993 Extraction and Processing Lecture
The Minerals, Metals & Materials Society

Y. Austin Chang 789 The Role of Chemical Metallurgy in the Emerging Field of Materials Science and Engineering

Hydrometallurgy

Yichang Guan and Kenneth N. Han 817 An Electrochemical Study on the Dissolution of Gold and Copper from Gold/Copper Alloys

J.S.J. Van Deventer and P.F. Van Der Merwe 829 The Mechanism of Elution of Gold Cyanide from Activated Carbon

Pyrometallurgy

M. Nagamori, W.J. Errington, P.J. Mackey, and D. Poggi 839 Thermodynamic Simulation Model of the Isasmelt Process for Copper Matte

Transport Phenomena

Zuohua Lin and R.I.L. Guthrie 855 Modeling of Metallurgical Emulsions

Amrita Verma and J.W. Evans 937 Communication: Measurements of the Electrical Conductivity of Wood's Alloy and Other Low Melting Point Alloys

Physical Chemistry

G.A. Brooks and W.J. Rankin 865 Solid-Solution Formation between Arsenic and Antimony Oxides

G.A. Brooks, W.J. Rankin, and N.B. Gray 873 Thermal Separation of Arsenic and Antimony Oxides

J. Bygdén, Du Sichen, and S. Seetharaman 885 A Thermodynamic Study of the Molybdenum-Oxygen System

Kwang Ro Lee and Hideaki Suito 893 Activities of Fe_tO in $CaO-Al_2O_3-SiO_2-Fe_tO$ (<5 Pct) Slags Saturated with Liquid Iron

Ryouji Noguchi, Kichiya Suzuki, Fumitaka Tsukihashi, and Nobuo Sano 903 Thermodynamics of Boron in a Silicon Melt

A. Sharan, T. Nagasaka, and A.W. Cramb 939 Communication: Densities of Liquid Fe-Ni and Fe-Cr Alloys

Solidification

Jyrki Miettinen and Seppo Louhenkilpi 909 Calculation of Thermophysical Properties of Carbon and Low Alloyed Steels for Modeling of Solidification Processes

Mathematical Modeling

Ney J. Luiggi and Angel E. Betancourt 917 Multiphase Precipitation of Carbides in Fe-C Systems: Part I. Model Based Upon Simple Kinetic Reactions

Ney J. Luiggi and Angel E. Betancourt 927 Multiphase Precipitation of Carbides in Fe-C System: Part II. Model Based on Kinetics of Complex Reactions

943 Contents, *Metallurgical and Materials Transactions A*, Volume 25A, November 1994

944 Contents, *Metallurgical and Materials Transactions A*, Volume 25A, December 1994

Combined Index to Volumes 25A and 25B follows page 2842

Combined Author Index

Aaronson, H.I. 1797-1819A
1923-1931A
2631-2637A
2655-2673A
Abe, T. 911-918A
Abramov, E. 949-959A
Acosta, P. 1241-1248A
Adcock, P.W. 505-518B
Advani, A.H. 1325-1331A
Agarwala, R.C. 851-856A
Agarwala, V. 851-856A
Ågren, J. 1127-1134A
Ahmady, S.M. 1097-1102A
Ai, S.H. 1713-1723A
Aikin, R.M., Jr. 2461-2468A
Akmoulin, I.A. 1655-1666A
Alarcón, O.E. 961-968A
Aldrich, C. 303-306B
Allain, E. 193-205B
Allaire, C. 221-226B
Allibert, M. 645-651B
Alman, D.E. 1033-1040A
Alpas, A.T. 969-983A
Amey, S.L. 723-732A
Anderson, J.P. 17-35A
1561-1573A
Anderson, K.R. 2235-2245A
Anderson, P.M. 415-425A
Angeliu, T.M. 1169-1183A
Antia, D.P. 2675-2681A
2827-2828A
Antolovich, S.D. 2469-2476A
Anyalebechi, P.N. 111-122B
Araki, H. 873-876A
Asai, S. 165-170B
Asthana, R. 225-230A
Aswath, P.B. 287-297A
1041-1050A
Atkinson, C. 2683-2694A
2683-2694A
Azari, H.N. 2153-2160A

Babu, S.S. 499-508A
Bai, J.B. 1185-1197A
1199-1208A
Baldwin, M.D. 2497-2506A
Barlat, F. 1209-1216A
2783-2795A
Bartholomeusz, M.F. 2161-2171A
2371-2381A
Bassler, B.T. 1301-1308A
Battaile, C.C. 865-870A
Bautista, R.G. 171-183B
Bayuzick, R.J. 1301-1308A
Bech, N.C. 2461-2468A
Beck, T.R. 661-668B
Beckermann, C. 1081-1093A
Benz, M.G. 203-212A
213-219A
Beris, A.N. 761-771B
Betancourt, A.E. 917-925B
927-935B
Bhadeshia, H.K.D.H. 705-714A
1603-1611A
Bhaduri, S.C. 435-441B
Bingert, J.F. 461-472A
Birla, N.C. 1693-1702A
Biswas, S.K. 2173-2179A
Blackburn, D. 321-331B
Blaz, L. 257-266A
Bodnar, R.L. 665-675A
763-773A
Bourell, D.L. 677-685A
Bourne, J.P. 2683-2694A
Bracconi, P. 509-520A
Brass, A.M. 1159-1167A
2117-2130A
2131-2143A
Brebrick, R.F. 2331-2340A
Briber, R.M. 2461-2468A
Brimacombe, J.K. 681-693B
Bronson, A. 1325-1331A
Brooks, G.A. 865-871B
873-884B
Buchheit, T.E. 2383-2389A
Bui, R.T. 607-618B
Bygdén, J. 519-525B
885-891B

Carro, G. 1301-1308A
Castello-Branco, M.A.S.C. 359-371B
Cesari, E. 687-695A
Chan, K.S. 299-308A
1217-1228A
Chanfreau, A. 2117-2130A
2131-2143A
Chang, C.Y. 545-555A
Chang, E. 545-555A
Chang, Y.A. 656-658A
789-816B
Chattopadhyay, K. 2631-2637A
Chaturvedi, M.C. 1733-1745A
Chaudhuri, K. 1109-1118A
Chaudhury, P.K. 2391-2401A
Chen, A.A. 473-480B
Chen, C.-C. 415-423B
Chen, G. 2073-2082A
2639-2646A
Chen, H. 17-35A
1561-1573A
Chen, J.K. 2073-2082A
2639-2646A
Chen, L.H. 557-561A
821-825A
2305-2309A
Chen, S.-L. 656-658A
Chen, S.F. 557-561A
2305-2309A
Chen, W.X. 539-544A
Chêne, J. 1159-1167A
2117-2130A
2131-2143A
Chidambaram, P.R. 2083-2090A
2497-2506A
Chin, B.A. 193-202A
Chiou, W.-C. 985-992A
Cho, S.-W. 5-13B
Choubey, R. 993-1004A
Chow, C.K. 135-145A
Christ, H.-J. 407-413A
Christ, H.J. 401-406A
Christian, J.W. 1821-1839A
Christodoulou, L. 2181-2197A
Chu, S. 637-642A
Chung, K. 1209-1216A
Cieslak, M.J. 697-704A
789-798A
Cima, M.J. 1747-1760A
Clark, R.K. 89-97A
Cohen, J.B. 2565-2568A
Compton, L.M. 2145-2152A
Comstock, R.J., Jr. 2091-2099A
Coroneos, A.C. 505-518B
Cortial, F. 241-248A
Costa E Silva, A. 5-15A
Cotton, J.D. 461-472A
2303-2305A
Courtney, T.H. 147-158A
2091-2099A
Cramb, A.W. 306-308B
626-628B
939-942B
Cross, C.E. 2705-2714A

Daehn, G.S. 415-425A
589-598A
2723-2735A
2723-2735A
Dahmen, U. 1857-1863A
Dantzig, J.A. 443-457B
1063-1079A
Davidson, P.A. 293-302B
Davis, C.L. 563-573A
Dayananda, M.A. 1649-1653A
de Lugo, M.M. 1325-1331A
Dean, N.F. 2295-2301A
DeArdo, A.J. 277-286A
Demir, O. 549-559B
Desclaux, P. 43-51B
221-226B
DeWitt, D.P. 449-462B
Dhindaw, B.K. 2525-2534A
Dhurjati, P.S. 761-771B
Diao, Q.Z. 1051-1062A
Djona, M. 481-490B
Doan, R.C. 381-388A
Dreisinger, D.B. 473-480B
Drevet, B. 599-605A
Drew, R.A.L. 2357-2370A
Drewien, C.A. 249-255A
1119-1125A
Droenen, P.-E. 521-530A
Drury, W.J. 919-928A
Duby, P. 351-358B
Duda, P.M. 623-625B
Dunn, P.S. 461-472A
Dutta, G. 1591-1602A
Dutta, I. 1591-1602A
Dutta, S.K. 15-26B

Earthman, J.C. 2477-2482A
Echeverria, A. 1579-1590A
Edwards, G.R. 697-704A
789-798A
2083-2090A
2497-2506A
2705-2714A
Ehrhard, P. 427-435A
Eliezer, D. 949-959A
Engström, A. 1127-1134A
Enomoto, M. 1947-1953A
Epperson, J.E. 17-35A
Era, H. 2542-2546A
Eric, R.H. 53-61B
549-559B
Errington, W.J. 839-853B
Espié, L. 599-605A
Espiell, F. 185-191B
Eustathopoulos, N. 599-605A
Evangelista, E. 257-266A
Evans, J.W. 333-340B
341-349B
937-939B

Fan, C.G. 1015-1023A
Fang, H.-S. 2001-2007A
2615-2619A
Fernández, M. 185-191B
Figueredo, A.M. 1747-1760A
Finot, M. 2403-2420A
Flemings, M.C. 1747-1760A
2295-2301A
Fleury, E. 99-109A
Flood, S.C. 293-302B
Foley, J.C. 230-233A
François, D. 1185-1197A
1199-1208A
Fray, D.J. 373-378B
Fredriksson, H. 123-133B
Freiburg, C. 2535-2538A
Frenk, A. 281-291B
Fruehan, R.J. 245-253B
306-308B
Fu, H. 637-642A
Fujiwara, H. 695-701B
Furukawa, T. 2647-2653A

Gaballah, I. 193-205B
481-490B
Gale, W.F. 2837-2840A
2837-2840A
Gandin, Ch.-A. 629-635A
Gangloff, R.P. 365-379A
Gangopadhyay, U. 607-615A
Garcia, C.I. 277-286A
Gasc, G. 509-520A
Gaskell, D.R. 449-462B
Gaudett, M.A. 775-787A
Gavriljuk, V.G. 889-909A
Ghosh, A. 15-26B
1095-1097A
Ghosh, A.K. 2017-2026A
2027-2038A
2039-2048A
2049-2061A
Ghosh, S. 2723-2735A
2723-2735A
Gibeling, J.C. 2235-2245A
2453-2460A
2453-2460A
Gigliotti, M.F.X. 2321-2329A
Gilbert, J.B., II 773-778B
Gilbon, D. 1199-1208A
Gillis, P.P. 961-968A
Gilmore, R.S. 2321-2329A
Gingerich, K.A. 857-864A
Glazer, J. 1249-1257A
Gnanasekaran, T. 63-72B
Goettsch, D.D. 1063-1079A
Goggins, K.M. 2101-2109A
Gokhale, A.M. 919-928A
Goldstein, J.I. 249-255A
1119-1125A
1627-1637A
1639-1648A
Goldstein, J.L.F. 2715-2722A
Golovin, I.S. 111-124A
Gonzalez, J. 1159-1167A
González-Doncel, G. 1241-1248A
Goo, E. 57-61A
715-721A
Gortais, J. 645-651B
Goto, K. 405-413B
Gowri, S. 437-448A
Gozzi, D. 561-568B
Granati, P. 561-568B
Gray, G.T., III 1025-1031A
Gray, N.B. 873-884B
Gregg, J.M. 1603-1611A
Groh, H.C., III 2507-2516A
Groza, J.R. 2235-2245A
Grugel, R.N. 865-870A
Grushko, B. 2535-2538A
Gruzleski, J.E. 1761-1773A
Guan, Y. 817-827B
Guo, Q. 73-77B
Gupta, D. 227-233B
Guthrie, R.I.L. 308-312B
855-864B

Haas, P.A. 505-518B
Hackney, S.A. 1613-1625A
Haggerty, J.S. 1747-1760A
Hall, E.L. 213-219A
Hall, M.G. 1797-1819A
1923-1931A
Hamada, Y. 2581-2599A
Han, B. 2285-2294A
Han, K.N. 817-827B
Hana, Y. 873-876A
Hansen, S.S. 665-675A
763-773A
Hariprasad, S. 1005-1014A
Harper, C.P. 1591-1602A
Hashimoto, K. 321-330A
Hashmi, F.H. 2421-2425A
Hassani, F. 125-133A
Haut, C. 2131-2143A
Hayashi, S. 405-413B
741-748B
Hayasi, K. 349-356A
Heldt, L.A. 1285-1290A
Hendrix, D.E. 505-518B
Herrmann, R.K. 89-97A
Hillert, M. 1957-1966A
Himbeault, D.D. 135-145A
Hirth, J.P. 1885-1894A
2655-2673A
2655-2673A
Hmelo, A.B. 865-870A
Ho, N.-J. 415-423B
Hochanadel, P.W. 697-704A
789-798A
Hodaj, F. 645-651B
Hodgson, P.D. 389-400A
Hoffman, P.B. 2453-2460A
2453-2460A
Hofmeister, W.H. 1301-1308A
Hogarth, J. 111-122B
Höglund, L. 1127-1134A
Hong, M.-H. 2828-2831A
Hono, K. 499-508A
Hort, W. 2695-2703A
Howard, R.L. 27-32B
Howe, J.M. 617-627A
1917-1922A
Hsu, D.K. 799-809A
811-819A
Hsu, T.-C.J. 415-423B
Hsu, T.Y. 2555-2564A
Hu, C.-T. 985-992A
Hu, X. 2723-2735A
Huang, X. 527-547B
Hugo, G.R. 1841-1856A
Hussain, K. 2421-2425A
Hyde, R.S. 1229-1240A
Hyndman, D.A. 623-625B

Ichinose, M. 531-537A
Ichise, E. 695-701B
Iguchi, Y. 405-413B
741-748B
Ihn, T.-H. 1575-1578A
Imamura, M. 637-644B
Inoue, A. 1323-1325A
Inoue, R. 235-244B
Inouye, T.K. 695-701B
Ipser, H. 63-72B
Ishida, K. 473-485A
531-537A
Ishikawa, F. 929-936A
Ito, K. 703-711B
Itoh, N. 321-330A
Iwase, M. 695-701B
Iyer, K.M. 207-219B
619-623B

Jacob, K.T. 149-151B
173-180A
Jahanshahi, S. 277-280B
Jain, V.K. 2753-2768A
Janovec, J. 267-275A
Jeong, H. 799-809A
811-819A
Jerina, K.L. 1005-1014A
Jha, S. 2017-2026A
Ji, N. 1199-1208A
Jia, C.C. 473-485A
Jiménez, J.A. 1241-1248A
Johnson, W.B. 761-771B
Johnson, W.C. 2695-2703A

Jonas, J.J. 125-133A 389-400A
Jong, S.-H. 643-650A
Joo, S.-K. 1575-1578A
Jordan, C.E. 937-947A 2101-2109A
Juneja, J.M. 876-881A
Jung, S.B. 873-876A
Jung, Y.C. 1981-1989A

Kailas, S.V. 2173-2179A
Kajiwara, S. 63-71A
Kale, G.M. 373-378B
Kamat, S.V. 2439-2452A
Kampe, S.L. 2181-2197A
Kandra, J.T. 1667-1679A
Kang, M.K. 1941-1946A 2601-2608A 2609-2614A
Kang, S.-J.L. 2828-2831A
Karbhari, V.M. 761-771B
Kasul, D.B. 1285-1290A
Kaufman, M.J. 5-15A 2111-2116A
Kaukler, W.F. 1775-1777A
Kawamura, T. 165-170B
Kaysser, W.A. 677-685A
Keiser, D.D., Jr. 1649-1653A
Khan, A.Q. 2421-2425A
Khodadadi, J.M. 669-680B
Kikuchi, M. 2639-2646A
Kim, G.-H. 2828-2831A
Kim, H.K. 2477-2482A
Kim, S.-G. 2815-2826A
Kim, T.H. 2213-2223A
Kim, Y. 2199-2205A
Kim, Y.-W. 1217-1228A
Kimura, T. 33-42B
King, J.E. 563-573A 2837-2840A 2837-2840A
Kishitake, K. 2542-2546A
Kishore, R. 653-656A
Kleppa, O.J. 73-77B
Kobayashi, T. 1655-1666A 2427-2437A
Kocaefe, D. 607-618B
Koch, J. 425-434B
Kodai, A. 2009-2016A
Konishi, Y. 165-170B
Kooi, B.J. 2797-2814A
Kordon, A.K. 761-771B
Koseki, T. 1309-1321A
Koul, A.K. 575-588A
Koymen, A.R. 1041-1050A
Kramer, P.A. 1249-1257A
Krauss, G. 1147-1158A 1229-1240A
Krishnan, P. 2111-2116A
Kumar, S. 435-441B
Kumar, S.G. 91-96B
Kuo, K.H. 47-56A
Kutumbarao, V.V. 2439-2452A
Kwon, D. 2213-2223A

Lahiri, A.K. 227-233B
Lan, X.K. 669-680B
Langberg, D.E. 653-660B
Larsen, D.E. 2181-2197A
Lavernia, E.J. 135-147B 2341-2355A
Lawson, L. 2265-2274A
Ledbetter, H. 2832-2835A 2832-2835A
Lederich, R.J. 1005-1014A
Lee, E. 2207-2212A
Lee, E.H. 193-202A
Lee, E.W. 1667-1679A
Lee, I.-G. 2017-2026A
Lee, J.K. 2073-2082A
Lee, S. 2213-2223A
Lee, S.-W. 1575-1578A
Lei, M. 2832-2835A
Lele, S. 2517-2523A
Lerch, B.A. 309-319A
Li, C.-M. 2615-2619A
Li, H. 79-89B
Li, J. 637-642A
Li, P. 2542-2546A
Li, Y.Y. 1015-1023A
Liang, X. 2341-2355A
Liaw, P.K. 799-809A 811-819A
Liddell, K.C. 171-183B
Lin, C.S. 721-730B
Lin, Y.F. 821-825A
Lin, Z. 855-864B
Lisovsky, A.F. 733-740A
Liu, C.D. 545-555A
Liu, D.H. 2601-2608A 2609-2614A
Liu, H.W. 223-225A
Liu, P. 2225-2233A
Liu, Q.Q. 539-544A
Liu, S. 2285-2294A
Liu, S.K. 1991-2000A
Liu, Y. 37-46A 81-87A 425-434B 487-497A 749-759B
Liu, Z. 637-642A
Lloyd, C.L. 773-778B
Long, Q.Y. 1015-1023A
Louhenkilpi, S. 909-916B
Lu, W.-K. 579-587B
Lui, T.S. 557-561A 821-825A 2305-2309A
Luiggi, N.J. 917-925B 927-935B
Luo, W.-Z. 569-578B

Ma, D. 579-587B
Ma, X.L. 47-56A
Maccagno, T.M. 125-133A
Machida, N. 2647-2653A
Machmeier, P.M. 827-837A
Mackey, P.J. 839-853B
Maki, T. 2009-2016A
Malakondaiah, G. 183-192A 2439-2452A
Malau, K. 193-205B
Man, C.-S. 2835-2837A
Mannan, S.L. 159-171A
Manrique, M. 713-720B
Marder, A.R. 249-255A 937-947A 1119-1125A 2101-2109A
Margolin, H. 1259-1265A 1291-1299A
Marsden, C.F. 281-291B
Martin, J.W. 651-653A
Marukawa, K. 2621-2629A
Maruyama, S. 2621-2629A
Massalski, T.B. 73-79A 1579-1590A
Masumoto, T. 1323-1325A
Matatya, M.C. 2737-2752A
Mataya, M.C. 1147-1158A
Matlock, D.K. 1229-1240A
Matousek, J.W. 463-465B
Matsumiya, T. 1309-1321A
Matuszewski, T. 827-837A
Maurice, D. 147-158A
Mazumdar, D.F. 308-312B
Mazumder, J. 37-46A 425-434B 487-497A 749-759B
McCartney, D.G. 1097-1102A
McCarty, E.D. 1613-1625A
McQueen, H.J. 827-837A
Medrano, R.E. 961-968A
Mendiratta, M.G. 2769-2781A
Meng, X.K. 1941-1946A 2601-2608A 2609-2614A
Meshii, M. 721-730B 2265-2274A
Meyer-Joly, M.-Ch. 193-205B
Michal, G.M. 723-732A
Michaud, V.J. 2145-2152A
Miettinen, J. 909-916B
Miller, M. 857-864A
Minamino, Y. 873-876A
Miracle, D.B. 2769-2781A
Mishra, B. 151-154B
Mishra, N.S. 2517-2523A
Mittenmeijer, E.J. 2797-2814A 2797-2814A
Mo, A. 597-605B
Mohamed, F.A. 2391-2401A
Mohan, S. 851-856A
Moore, J.J. 27-32B 151-154B
Morris, D.G. 449-451A
Morris, J.G. 357-364A
Morris, J.W., Jr. 1249-1257A 2715-2722A
Mortensen, A. 2145-2152A 2295-2301A
Mou, Y. 1905-1915A
Muddle, B.C. 1841-1856A
Mughrabi, H. 401-406A 407-413A
Mukhopadhyay, S. 173-180A
Mukhopadyhay, P. 653-656A
Muraleedharan, K. 1693-1702A
Murthy, A.S. 57-61A
Murty, G.S. 2153-2160A
Muscat, D. 2357-2370A

Nadutov, V.M. 889-909A
Nagamori, M. 321-331B 839-853B
Nagasaka, T. 245-253B 306-308B 626-628B 939-942B
Nakamura, M. 321-330A 331-340A
Nakamura, Y. 97-101B 385-389B
Nakanishi, N. 2647-2653A
Nakkalil, R. 1733-1745A
Narayanan, L.A. 1761-1773A
Nash, P. 871-874A
Nastasi, M. 1579-1590A
Needleman, A. 839-850A 2403-2420A
Nelson, L.S. 623-625B
Ng, K. 255-263B 265-275B 379-384B
Nicholas, T. 183-192A
Nie, J.F. 1841-1856A
Niewczas, M. 257-266A
Niikura, A. 1323-1325A
Niinomi, M. 1655-1666A
Nili Ahmadabadi, M. 911-918A
Nilmani, M. 653-660B
Nilsson, J.O. 2225-2233A
Nishizawa, T. 473-485A 531-537A
Niyama, E. 911-918A
Noebe, R.D. 309-319A 2303-2305A
Noguchi, R. 903-907B
Noh, J.-W. 2828-2831A
Nourbakhsh, S. 1259-1265A 1291-1299A
Noyan, I.C. 341-347A

Ochi, T. 929-936A
Ochiai, S. 349-356A
O'Connor, T.G. 443-457B
Ogawa, T. 1309-1321A
Ohide, T. 911-918A
Ohmore, Y. 1981-1989A
Ohtani, H. 1981-1989A
Ohtsubo, H. 1981-1989A
Ohtsuka, H. 63-71A
Ojha, S.N. 2517-2523A
Ojima, K. 2491-2496A
Okaguchi, S. 1981-1989A
Olson, D.L. 2083-2090A
Osamura, K. 349-356A
Ouellet, R. 607-618B
Outlaw, R.A. 89-97A
Overfelt, T. 154-157B
Ozok, H. 53-61B

Palmiere, E.J. 277-286A
Pandey, O.P. 2517-2523A
Park, D. 357-364A
Park, K. 2199-2205A
Park, K.-T. 2391-2401A
Paruchuri, M.R. 73-79A
Patterson, B.R. 81-87A
Patterson, R.A. 461-472A
Payer, J.H. 723-732A
Peng, Y.T. 1041-1050A
Perepezko, J.H. 230-233A 1109-1118A
Perocchi, L.C. 2321-2329A
Picasso, M. 281-291B
Picornell, C. 687-695A
Pien, S.J. 669-680B
Pirzada, S.A. 713-720B
Pitchumani, R. 761-771B
Poggi, D. 839-853B
Polonis, D.H. 1135-1146A
Porr, W.C., Jr. 365-379A
Prasad, N.E. 2439-2452A
Prasad, R.V.R.K. 1693-1702A
Prasad, Y.V.R.K. 2173-2179A 2275-2284A
Prioul, C. 1185-1197A 1199-1208A
Puls, M.P. 135-145A 993-1004A
Purdy, G.R. 1875-1883A

Raghavan, V. 2675-2681A 2827-2828A
Raihle, C.-M. 123-133B
Raizenne, M.D. 575-588A
Ramachandra, C. 2517-2523A
Ramirez, J.E. 2285-2294A
Rankin, W.J. 79-89B 865-871B 873-884B
Rao, G.R. 193-202A
Rao, K.B.S. 159-171A
Rao, K.V.S.J. 1095-1097A
Rappaz, M. 281-291B 629-635A
Rath, B.B. 2655-2673A 2655-2673A
Ratnaparkhi, P.L. 617-627A
Rawers, J.C. 381-388A
Ray, K.K. 1095-1097A
Ray, R. 2017-2026A
Reddy, R.G. 91-96B
Reed, R.C. 2683-2694A 2683-2694A
Rèmy, L. 99-109A
Reynolds, W.T., Jr. 2073-2082A 2639-2646A
Rhee, W.H. 1259-1265A
Rhodes, C.G. 1267-1283A
Richards, N.L. 1733-1745A
Richards, S.R. 27-32B
Richmond, O. 1209-1216A
Rios, P.R. 221-223A
Rizzo, H.F. 1579-1590A
Robino, C.V. 697-704A 789-798A
Robles, J. 2235-2245A
Rollett, A.D. 1025-1031A
Rosenberger, F. 1775-1777A
Ross, T.W., III 2639-2646A
Rossing, B.R. 761-771B
Roucoules, C. 389-400A
Rousar, I. 661-668B
Ruano, O.A. 1241-1248A
Rumaner, L.E. 203-212A 213-219A
Russell, K.C. 1933-1939A
Rvishankar, N. 2631-2637A
Ryum, N. 521-530A

Sabathier, V. 2705-2714A
Sackschewsky, V.E. 2737-2752A
Sade, M. 687-695A
Sadler, P. 2181-2197A
Sahin, O. 1259-1265A 1291-1299A
Saji, S. 873-876A 1102-1104A
Sakurai, T. 499-508A
Samuel, A.M. 2247-2263A
Samuel, F.H. 437-448A 1761-1773A 2247-2263A
Sankaran, S.N. 89-97A
Sano, N. 903-907B
Sasaki, M. 2265-2274A
Sastry, D.H. 159-171A
Sastry, S.M.L. 1005-1014A
Sato, S. 2621-2629A
Schadler, L.S. 341-347A
Schlesinger, M.E. 569-578B
Schmauder, S. 1725-1731A
Schüssler, A. 427-435A
Schvezov, C. 397-403B
Schwerdtfeger, K. 359-371B 497-504B
Scully, J.R. 775-787A
Seetharaman, S. 149-151B 391-396B 519-525B 589-595B 876-881A 885-891B
Seetharaman, V. 2753-2768A
Seetharman, V. 2539-2542A
Segarra, M. 185-191B
Semiatin, S.L. 1681-1692A 2539-2542A 2753-2768A
Sen, S. 2525-2534A
Sha, W. 705-714A 2538-2539A
Shannon, R.E. 799-809A 811-819A
Sharan, A. 626-628B 939-942B
Shekhar, R. 333-340B 341-349B
Shen, F. 669-680B
Shen, Y. 1147-1158A
Shen, Y.-L. 839-850A 2403-2420A
Shi, Z. 637-642A
Shibata, K. 37-46A 425-434B 487-497A 749-759B
Shiflet, G.J. 1895-1903A
Shigematsu, T. 2647-2653A
Shimizu, K. 2569-2579A 2569-2579A
Shimpo, R. 97-101B 385-389B
Shin, S.-H. 2815-2826A 2815-2826A
Shivpuri, R. 1681-1692A
Sichen, D. 391-396B 519-525B 589-595B 885-891B

Singh, V. 1693-1702A
Siviour, N.G. 255-263B
265-275B
379-384B
Smith, G.D.W. 2538-2539A
Smith, P.R. 1267-1283A
1267-1283A
Sohn, H.Y. 207-219B
619-623B
Somani, M.C. 1693-1702A
Somers, M.A.J. 2797-2814A
2797-2814A
Soper, J.C. 1681-1692A
Spanos, G. 1967-1980A
Spear, W.S. 1135-1146A
Sridhar, S. 391-396B
Srinivasan, N. 2275-2284A
Srinivasan, N.S. 876-881A
Srivastava, S.K. 851-856A
Steen, P.H. 427-435A
Stefanescu, D.M. 2525-2534A
Stigenberg, A.H. 2225-2233A
Stoloff, N.S. 1033-1040A
Subramanian, P.R. 2769-2781A
Suito, H. 5-13B
33-42B
235-244B
893-902B
Sun, S. 277-280B
Sun, X.K. 539-544A
Sundararaman, M. 653-656A
Suresh, S. 839-850A
2403-2420A
Sussman, R.C. 527-547B
Sutherland, T.J. 2453-2460A
2453-2460A
Suzuki, K. 903-907B
Suzuki, T. 321-330A
2815-2826A
2815-2826A
Svoboda, M. 267-275A
Syu, D.-G.C. 2027-2038A
2039-2048A
2049-2061A

Tadaki, T. 2569-2579A
Takahashi, J. 1102-1104A
Takahashi, T. 929-936A
Takasaki, A. 2491-2496A
Takezawa, K. 2621-2629A
Taneda, Y. 2491-2496A
Tanino, M. 911-918A
Tauqir, A. 2421-2425A
Taylor, P.R. 713-720B
Thoma, D.J. 230-233A
Thomas, B.G. 527-547B
Thompson, S.W. 1147-1158A
Thonstad, J. 661-668B
Tian, Y.W. 103-109B
Tintillier, R. 629-635A
Togashi, F. 531-537A
Toguri, J.M. 637-644B
Tokuda, M. 703-711B
Totemeier, T.C. 2837-2840A
2837-2840A
Tsai, A.P. 1323-1325A
Tsai, H.L. 1051-1062A
Tseng, C.C. 1147-1158A
Tsuji, S. 741-751A
753-761A
Tsujimoto, T. 321-330A
Tsukihashi, F. 903-907B
Tsuzaki, K. 2009-2016A

Ueda, Y.-I. 741-748B
Ullakko, K. 889-909A
Umeda, T. 2815-2826A
2815-2826A
University of Southern California
Langdon, T.G. 2309-2311A
Upadhyaya, G.S. 2153-2160A
Ur, S.C. 871-874A
Utigard, T. 491-496B
Utigard, T.A. 43-51B

Valsan, M. 159-171A
van der Merwe, J.H. 1895-1903A
Van Der Merwe, P.F. 829-838B
Van Deventer, J.S.J. 303-306B
829-838B
Varin, R.A. 1703-1711A
Varma, S.K. 1325-1331A
Verma, A. 937-939B
Vidal, R. 351-358B
Vyrostkova, A. 267-275A

Wagnière, J.-D. 281-291B
Wagoner, R.H. 2723-2735A
2723-2735A
Wallace, W. 575-588A
658-659A
Wang, C.Y. 1081-1093A
Wang, J.-J. 2001-2007A
Wang, T.G. 865-870A
Wang, Z.C. 103-109B
Wang, Z.G. 1713-1723A
Wanqi, J. 731-739B
Warczok, A. 43-51B
Was, G.S. 1169-1183A
Wayman, C.M. 1787-1795A
2581-2599A
2655-2673A
2655-2673A
Weatherly, G.C. 1865-1874A
Webb, G. 2469-2476A
Wei, Q.M. 1941-1946A
Weinberg, F. 397-403B
Weiss, T. 497-504B
Welch, B.J. 27-32B
Welter, J.-M. 645-651B
Wert, J.A. 2161-2171A
2371-2381A
2383-2389A
West, A.C. 351-358B
White, D.A. 449-462B
Williams, D.B. 1627-1637A
1639-1648A
Winnicka, M.B. 1703-1711A
Witczak, Z. 1703-1711A
Wolfenstine, J. 2477-2482A
Wright, S.I. 1025-1031A
Wu, M.H. 2581-2599A
Wu, X.J. 575-588A
658-659A
Wu, Y. 135-147B
Wynblatt, P. 607-615A

Xing, Z.S. 1015-1023A
Xu, J. 539-544A
Xu, L. 589-598A

Yamada, S. 2427-2437A
Yamada, W. 1309-1321A
Yamane, T. 873-876A
1102-1104A
Yang, L. 1991-2000A
Yang, Q.M. 1941-1946A
Yang, T.Y. 715-721A
Yang, Y.Q. 1941-1946A
2601-2608A
2609-2614A
Yapu, W. 185-191B
Yeh, H.-W. 643-650A
Yong, Z. 1725-1731A
Yoon, D.Y. 2828-2831A
Yu, H.L. 103-109B
Yu, T.-C. 2331-2340A
Yue, S. 125-133A
389-400A

Zauter, R. 401-406A
407-413A
Zeng, X.-H. 2783-2795A
Zentner, L.K. 449-462B
Zhang, D.L. 73-79A
Zhang, H. 415-425A
Zhang, J. 135-147B
969-983A
1627-1637A
1639-1648A
1991-2000A
Zhang, L. 223-225A
Zhang, W. 1875-1883A
Zhang, W.-Z. 1865-1874A
Zhang, X.H. 103-109B
Zhang, Y. 306-308B
1102-1104A
Zheng, Y.-K. 2001-2007A
Zheng, Y.S. 1713-1723A
Zhonghua, L. 1725-1731A
Zhou, J.K. 103-109B
Zhou, M. 681-693B
Zhou, X.W. 2555-2564A
Zhu, D.G. 1991-2000A
Zocco, T. 1579-1590A
Zurek, A.K. 2483-2489A

Combined Subject Index

Abatement
See Corrosion prevention

Abrasive wear, Microstructural effects
Effect of Microstructure (Particulate Size and Volume Fraction) and Counterface Material on the Sliding Wear Resistance of Particulate-Reinforced Aluminum Matrix Composites. 969-983A

Absolute viscosity
See Viscosity

Absorbance
See Absorption (material)

Absorbing
See Absorption (material)

Absorption (material), Environmental effects
Modeling Hydrogen Entry and Exit in Metals Exposed to Multiple Charging Processes. 723-732A

Acid leaching
See Hydrochloric acid leaching

Actinide metal alloys
See Uranium base alloys

Actinide metals
See Uranium

Activation energy
Investigation of the Kinetics of Reduction of Nickel Tungstate by Hydrogen. 391-396B

Activation entropy
See Activation energy
Entropy

Activity (chemical)
Equilibrium Distribution of Fe, Ni, Sb, and Sn between Liquid Cu and a CaO-Rich Slag. 645-651B
A Thermodynamic Study of BaO + $BaCl_2$ + Cr_2O_3 Fluxes Used for the Removal of Phosphorus From Chromium-Containing Iron Melts. 695-701B
Activities of Fe_tO in CaO-Al_2O_3-SiO_2-Fe_tO (5%) Slags Saturated With Liquid Iron. 893-902B
Thermodynamics of Boron in a Silicon Melt. 903-907B

Activity (chemical), Alloying effects
Thermodynamics of Oxygen and Nitrogen in Liquid Nickel Equilibrated With CaO—TiO_x and CaO—TiO_x—Al_2O_3 Melts. 5-13B

Activity coefficients
See Activity (chemical)

Acurad process
See Die casting

Adsorption
Adsorption Kinetics of Dicyanoaurate and Dicyanoargentate Ions in Activated Carbon. 185-191B
Nanocrystalline Iron Sintering Behavior and Microstructural Development. 677-685A

Adsorption, Alloying effects
Solid-State Wetting of Graphite by Lead and Pb—Ni Alloys. 607-615A

Aeration
Observations on the Effect of Medium Density and Viscosity on the Rate of Induced Aeration in Agitated Vessels. 303-306B

Aerospace
Elevated Temperature Fracture of RS/PM Alloy 8009. I. Fracture Mechanics Behavior. 365-379A

Aerospace industry
See Aerospace

Age hardening
See Aging
Aging (artificial)
Aging (natural)
Precipitation hardening

Age hardening steels
See Precipitation hardening steels

Ageing
See Aging

Agents
See Catalysts

Aging
See also Aging (artificial)
Aging (natural)
Strain aging
The Effect of Aging on Wear Characteristics of Rheocast-Leaded Aluminum Alloys. 851-856A
Multiphase Precipitation of Carbides in Fe-C Systems. I. Model Based Upon Simple Kinetic Reactions. 917-925B
Multiphase Precipitation of Carbides in Fe-C System. II. Model Based on Kinetics of Complex Reactions. 927-935B
A Discussion on the Formation of Bainite and Other Precipitates in Copper-Zinc and Silver-Zinc Alloys. (Conference Paper) 2621-2629A

Aging (artificial)
Effects of Carbon Content and Ausaging on $\gamma \rightleftarrows \alpha'$ Transformation Behavior and Reverse-Transformed Structure in Fe—Ni—Co—Al—C Alloys. 63-71A
Microstructural Study of the Titanium Alloy Ti—15Mo—2.7Nb—3Al—0.2Si (TIMETAL 21S). 1109-1118A
Interstitial Precipitation in Fe—Cr—Al Alloys. 1135-1146A
Decomposition of Iron—Nickel Martensite: Implications for the Low-Temperature ($\leq$ 500°C) Fe—NI Phase Diagram. 1627-1637A
Fracture Toughness of Quaternary Al-Li-Cu-Mg Alloy Under Mode I, Mode II, and Mode III Loading Conditions. 2439-2452A

Aging (natural)
Aging of Freshly Formed Iron-Based Martensites at Low Temperatures. (Review) 889-909A

Agitation
See Bubbling

Air, Environment
Environmental Effect on Room-Temperature Ductility of Isothermally Forged TiAl-Base Alloys. 321-330A

Air melting
See Melting

Aircomatic welding
See Gas metal arc welding

Aircraft components, Materials selection
The Influence of SiC Particulates on Fatigue Crack Propagation in a Rapidly Solidified Al-Fe-V-Si Alloy. 2453-2460A

Aircraft components, Mechanical properties
The Orientation Dependence of Fatigue-Crack Growth in 8090 Aluminum—Lithium Plate. 575-588A

Aircraft components, Metal working
Superplastic Behavior of Thermomechanically Treated P/M 7091 Aluminum Alloy. 2153-2160A

Aircraft equipment
See Aircraft components

Alkali metals
See Lithium

Alkaline earth metal alloys
See Calcium base alloys
Magnesium base alloys

Alkaline earth metals
See Barium
Calcium
Magnesium

Allotropic transformation, Temperature effects
Mg—Pb Phase Diagram and Phase Transformations in the Intermetallic Compounds Mg_2Pb and β'. 265-275B

Alloy powders, Microstructure
Surface Characterization and Reactivity of a Nitrogen Atomized 304L Stainless Steel Powder. 509-520A

Alloy steels
See Chromium steels
High strength steels
Low alloy steels
Manganese steels
Molybdenum steels
Nickel steels
Precipitation hardening steels

Alloying
See Mechanical alloying

Alpha annealing
See Annealing

Alpha iron, Alloying effects
Effect of Alloying Elements on the Solidification Characteristics and Microstructure of Al—Si—Cu—Mg—Fe 380 Alloy. 437-448A

Alphatizing
See Annealing

Alumina
See Aluminum oxide

Aluminium
See Aluminum

Aluminum, Alloying elements
Thermodynamics of Oxygen and Nitrogen in Liquid Nickel Equilibrated With CaO—TiO_x and CaO—TiO_x—Al_2O_3 Melts. 5-13B

Aluminum, Binary systems
Partition of Alloying Elements Between γ (A1), γ' ($L1_2$), and β (B2) Phases in Ni—Al Base Systems. 473-485A

Aluminum, Casting
Natural Convection in an Aluminum Ingot: a Mathematical Model. 293-302B
Mathematical and Physical Modeling Studies of Molten Aluminum Flow in a Tundish. 669-680B

Aluminum, Composite materials
A Two-Phase Flow Model of the Stirring of Al)SiC Composite Melt. 607-618B
The Morphological Stability of Lateral Growth in Solid—Solid Phase Transformation During Thin-Film Interdiffusion in Aluminum/Copper Bimetal Films. 1613-1625A
Capillarity in Isothermal Infiltration of Alumina Fiber Preforms With Aluminum. 2145-2152A

Modelling the Infiltration Kinetics of Molten Aluminum Into Porous Titanium Carbide. 2357-2370A

Aluminum, Diffusion
Anomalous Diffusion of Aluminum in β-Titanium. 873-876A

Aluminum, Extraction
Cyanide Inhibitors for the Carbon Cathode Materials in Aluminum Reduction Cells. 221-226B
Physical Modeling Studies of Electrolyte Flow Due to Gas Evolution and Some Aspects of Bubble Behavior in Advanced Hall Cells. I. Flow in Cells With a Flat Anode. 333-340B
Physical Modeling Studies of Electrolyte Flow Due to Gas Evolution and Some Aspects of Bubble Behavior in Advanced Hall Cells. II. Flow and Interpolar Resistance in Cells With a Grooved Anode. 341-349B
Energy Efficiency Considerations on Monopolar vs. Bipolar Fused Salt Electrolysis Cells. 661-668B
Measurements of the Electrical Conductivity of Wood's Alloy and Other Low Melting Point Alloys. 937-939B

Aluminum, Mechanical properties
Elastic Compliance and Hill's Quadratic Yield Function for Weakly Orthotropic Sheets of Cubic Metals. 2835-2837A

Aluminum, Powder technology
Formation of Metastable and Equilibrium Phases During Mechanical Alloying of Aluminum and Magnesium Powders. 73-79A

Aluminum base alloys, Atomic properties
The Diffuse-Scattering Method for Investigating Locally Ordered Binary Solid Solutions. 17-35A

Aluminum base alloys, Casting
Effect of Alloying Elements on the Solidification Characteristics and Microstructure of Al—Si—Cu—Mg—Fe 380 Alloy. 437-448A
The Cast Structure of a 7075 Alloy Produced by a Water-Cooling Centrifugal Casting Method. 643-650A
The Effect of Aging on Wear Characteristics of Rheocast-Leaded Aluminum Alloys. 851-856A
Fatigue Crack Growth Rates and Fracture Toughness of Rapidly Solidified Al—8.5Fe—1.2V—1.7Si Alloys. 1005-1014A
Modeling of the Formation of Under-Riser Macrosegregation During Solidification of Binary Alloys. 1051-1062A
Prediction of Columnar to Equiaxed Transition During Diffusion-Controlled Dendritic Alloy Solidification. 1081-1093A
Solidification Macrostructures and Macrosegregation in Aluminum Alloys Cooled From Above. 1097-1102A
Calorimetric Evaluation of Nonequilibrium State in As-Melt Spun Al—1.72 and Al—3.12 at.% Cu Alloys and Al—6.74, Al—8.48, and Al—11.97 at.% Si Alloys. 1102-1104A
Microsegregation in Cellular Solidification. 2295-2301A

Aluminum base alloys, Cladding
Transmission Electron Microscopy Study of Martensites in Laser-Clad Ni—Al Bronze on Aluminium Alloy AA333. 37-46A
Processing, Microstructure, and Properties of Laser-Clad Nickel Alloy FP-5 on Al Alloy AA333. 425-434B
Laser Cladding of Nickel-Aluminum Bronze on Al Alloy AA333. 749-759B

Aluminum base alloys, Composite materials
Modeling of the Incorporation of Ceramic Particulates in Metallic Droplets During Spray Atomization and Coinjection. 135-147B
Characterization of Anisotropic Elastic Constants of Silicon-Carbide Particulate Reinforced Aluminum Metal Matrix Composites. I. Experiment. 799-809A
Characterization of Anisotropic Elastic Constants of Silicon-Carbide Particulate Reinforced Aluminum Metal Matrix Composites. II. Theory. 811-819A
Effect of Microstructure (Particulate Size and Volume Fraction) and Counterface Material on the Sliding Wear Resistance of Particulate-Reinforced Aluminum Matrix Composites. 969-983A
Cubic AlNi Compound Dispersed Magnesium-Based Amorphous Matrix Composites Prepared by Rapid Solidification. 1323-1325A
Role of Al_2O_3 Particulate Reinforcements on Precipitation in 2014 Aluminum-Matrix Composites. 1591-1602A
Forging Limits for an Aluminum Matrix Composite. I. Experimental Results. (Conference Paper) 2027-2038A
Forging Limit for an Aluminum Matrix Composite. II. Analysis. (Conference Paper) 2039-2048A
Stress-State Dependence of Strain-Hardening Behavior in 2014 Al/15 vol.% Al_2O_3 Composite. (Conference Paper) 2049-2061A
Microstructural Analysis of Fracture Toughness Variation in 2XXX-Series Aluminum Alloy Composites Reinforced With SiC Whiskers. 2213-2223A
Effect of Heat Treatment on the Microstructure, Tensile Properties, and Fracture Behavior of Permanent Mold Al-10 wt.% Si-0.6 wt.% Mg/SiC/10p Composite Castings. 2247-2263A
Low-Cycle Fatigue Properties of a SiC Whisker-Reinforced 2124 Aluminum Alloy. 2265-2274A
Micromechanical Modelling of Reinforcement Fracture in Particle-Reinforced Metal-Matrix Composites. 2403-2420A
The Influence of SiC Particulates on Fatigue Crack Propagation in a Rapidly Solidified Al-Fe-V-Si Alloy. 2453-2460A
Fracture Toughness of Discontinuously Reinforced Al-4Cu-1.5Mg/TiB_2 Composites. 2461-2468A
Kinetic Study of Low-Temperature Transient Liquid Phase Joining of an Aluminum-SiC Composite. 2705-2714A
Elastic Constants of SiC_p/Al: Measurements and Modeling. 2832-2835A

Aluminum base alloys, Diffusion
A History of the Controversy Over the Roles of Shear and Diffusion in Plate Formation Above M_d and a Comparison of the Atomic Mechanisms of These Processes. (Conference Paper, Review) 1797-1819A

Aluminum base alloys, Heat treatment
Effect of Supereutectic Homogenization on Incidence of Porosity in Aluminum Alloy 2014 Ingot. 111-122B
Al_2Ti Precipitation in $Al_{64}Fe_8Ti_{28}$ Alloy. 715-721A
The Effect of Thermal Exposure on Microstructural Stability and Creep Resistance of a Two-Phase TiAl/Ti_3Al Lamellar Alloy. 2371-2381A

Aluminum base alloys, Mechanical properties
Discussion of "Grain Growth of a Superplastic 7475 Aluminum Alloy". 221-223A
The Tensile Deformation Behavior of AA 3004 Aluminum Alloy. 357-364A
Elevated Temperature Fracture of RS/PM Alloy 8009. I. Fracture Mechanics Behavior. 365-379A
The Orientation Dependence of Fatigue-Crack Growth in 8090 Aluminum—Lithium Plate. 575-588A
The Elastic Strain Energy of Growth Ledges on Coherent and Partially Coherent Precipitates. 2073-2082A
Fracture Toughness of Quaternary Al-Li-Cu-Mg Alloy Under Mode I, Mode II, and Mode III Loading Conditions. 2439-2452A

Aluminum base alloys, Melting
Local Melting in Al—Mg—Zn—Alloys. 521-530A
An Internal Variable Description of Solidification Suitable for Macrosegregation Modeling. 597-605B

Aluminum base alloys, Metal working
Anisotropic Plastic Potentials for Polycrystals and Application to the Design of Optimum Blank Shapes in Sheet Forming. 1209-1216A
Relationships of Slip Morphology, Microcracking, and Fracture Resistance in a Lamellar TiAl-Alloy. 1217-1228A
Superplastic Behavior of Thermomechanically Treated P/M 7091 Aluminum Alloy. 2153-2160A
Effects of Texture Gradients on Yield Loci and Forming Limit Diagrams in Various Aluminum-Lithium Sheet Alloys. 2783-2795A

Aluminum base alloys, Microstructure
Crystallographic Characteristics of the Al—Co Decagonal Quasicrystal and Its Monoclinic Approximant τ^2-$Al_{13}Co_4$. 47-56A

Aluminum base alloys, Phase transformations
Application of the Theory of Martensite Crystallography to Displacive Phase Transformations in Substitutional Nonferrous Alloys. (Conference Paper, Review) 1841-1856A
Atomic Site Correspondence and Surface Relief in the Formation of Plate-Shaped Transformation Products. (Conference Paper) 1917-1922A

Aluminum base alloys, Phases (state of matter)
Supersaturation of the Al_2Y Laves Phase by Rapid Solidification. 230-233A
Further Discussions on the Solute Redistribution During Dendritic Solidification of Binary Alloys. 731-739B
Crystallization Behavior of Iron-Containing Intermetallic Compounds in 319 Aluminum Alloy. 1761-1773A
X-Ray Microscopic Observations of Metal Solidification Dynamics. 1775-1777A
Effects of Precursor Matrix Events on Subsequent Nucleation. (Conference Paper) 1933-1939A

Aluminum base alloys, Powder technology
Evolution of Interaction Domain Microstructure During Spray Deposition. 2341-2355A
Numerical Analysis of the Rapid Solidification of Gas-Atomized Al-8 wt.% Iron Droplets. 2815-2826A

Aluminum base alloys, Reactions (chemical)
Solubility and Thermodynamic Properties of Y_2O_3 in LiF—YF_3 Melts. 91-96B
Interactions Between Drops of a Molten Aluminum)Lithium Alloy and Liquid Water. 623-625B
High-Temperature Oxidation of Cathodically Hydrogen-Charged Two-Phase (Ti_3Al, TiAl) Titanium Aluminides. 2491-2496A

Aluminum base alloys, Welding
Characterization of a Diffusion-Bonded Al—Mg Alloy/SiC Interface by High Resolution and Analytical Electron Microscopy. 617-627A

Aluminum bronzes, Claddings
Transmission Electron Microscopy Study of Martensites in Laser-Clad Ni—Al Bronze on Aluminium Alloy AA333. 37-46A

Aluminum compounds
See also Aluminum oxide

Aluminum compounds, Composite materials
Fiber Strength and Fiber/Matrix Bond Strength in Single Crystal Al_2O_3 Fiber Reinforced Ni_3Al Based Composites. 1259-1265A
A Structural Study of Oxidation in a Zirconia-Toughened Alumina Fiber-Reinforced NiAl Composite. 1291-1299A
Development and Characterization of Interface Coatings in Molybdenum-Reinforced NiAl Matrix Composites. 2111-2116A
Melt-Processed Ni_3Al Matrix Composites Reinforced With TiC Particles. 2525-2534A

Aluminum compounds, Extrusion
Discussion of "The Role of Microstructure on Strength and Ductility of Hot-Extruded Mechanically Alloyed NiAl" and Author's Reply. 2303-2305A

Aluminum compounds, Forging
Microstructure Development During Conventional and Isothermal Hot Forging of a Near-γ Titanium Aluminide. 2753-2768A

Aluminum compounds, Mechanical properties
Tensile Ductility of Extrinsically Toughened Intermetallics. 299-308A
Low-Cycle Fatigue Behavior of Polycrystalline NiAl at 1000K. 309-319A
Environmental Effect on Room-Temperature Ductility of Isothermally Forged TiAl-Base Alloys. 321-330A
Ordering and Mechanical Strength in $L1_2$ Cubic Titanium Trialuminides. 449-451A
The Effects of Hydrostatic Pressure on the Compressive Mechanical Behavior of $L1_2$ Al_3 Ti-Based Intermetallic. 1703-1711A
Modeling Creep Deformation of a Two-Phase TiAl/Ti_3Al Alloy With a Lamellar Microstructure. 2161-2171A

Low Cycle Fatigue Behavior of Polycrystalline Ni_3Al Alloys at Ambient and Elevated Temperatures. 2469-2476A
Creep Characteristics of Single Crystalline Ni_3Al(Ta,B). 2477-2482A
Microstructures and Mechanial Behavior of NiAl-Mo and NiAl-Mo-Ti Two-Phase Alloys. 2769-2781A

Aluminum compounds, Microstructure
Discussion of "Crystallographic Characterization of the Al-Co Decagonal Quasicrystal and Its Monoclinic Approximant τ^2-$Al_{13}Co_4$". 2535-2538A

Aluminum compounds, Powder technology
Determination of Residual Nickel in Mechanically Alloyed NiAl. 871-874A
High-Performance Ni_3Al Synthesized From Composite Powders. 985-992A
Evolution of Interaction Domain Microstructure During Spray Deposition. 2341-2355A

Aluminum compounds, Rolling
High-Temperature Deformation of B2 NiAl-Base Alloys. (Conference Paper) 2017-2026A

Aluminum killed steels, Coating
Morphology Development in Hot-Dip Galvanneal Coatings. 937-947A

Aluminum killed steels, Steel making
Thermodynamics of Oxygen, Nitrogen, and Sulfur in Liquid Iron Equilibrated With $CaO—Al_2O_3—MgO$ Slags. 235-244B

Aluminum oxide, Brazing
Spreading and Interlayer Formation at the Copper-Copper Oxide/Polycrystalline Alumina Interface. 2497-2506A

Aluminum oxide, Composite materials
Modeling of the Incorporation of Ceramic Particulates in Metallic Droplets During Spray Atomization and Coinjection. 135-147B
Effect of Microstructure (Particulate Size and Volume Fraction) and Counterface Material on the Sliding Wear Resistance of Particulate-Reinforced Aluminum Matrix Composites. 969-983A
Fiber Strength and Fiber/Matrix Bond Strength in Single Crystal Al_2O_3 Fiber Reinforced Ni_3Al Based Composites. 1259-1265A
A Structural Study of Oxidation in a Zirconia-Toughened Alumina Fiber-Reinforced NiAl Composite. 1291-1299A
Role of Al_2O_3 Particulate Reinforcements on Precipitation in 2014 Aluminum-Matrix Composites. 1591-1602A
Forging Limits for an Aluminum Matrix Composite. I. Experimental Results. (Conference Paper) 2027-2038A
Forging Limit for an Aluminum Matrix Composite. II. Analysis. (Conference Paper) 2039-2048A
Stress-State Dependence of Strain-Hardening Behavior in 2014 Al/15 vol.% Al_2O_3 Composite. (Conference Paper) 2049-2061A
Capillarity in Isothermal Infiltration of Alumina Fiber Preforms With Aluminum. 2145-2152A
Low-Cycle Fatigue of Dispersion-Strengthened Copper. 2235-2245A

Amorphous structure
Structure of As-Deposited Iron—Zinc Coatings From Chloride Bath. 249-255A

Amorphous structure, Cooling effects
Cubic AlNi Compound Dispersed Magnesium-Based Amorphous Matrix Composites Prepared by Rapid Solidification. 1323-1325A

Anisotropy
Characterization of Anisotropic Elastic Constants of Silicon-Carbide Particulate Reinforced Aluminum Metal Matrix Composites. II. Theory. 811-819A
Efficient Measurement of Microstructural Surface Area Using Trisector. 919-928A
Elastic Compliance and Hill's Quadratic Yield Function for Weakly Orthotropic Sheets of Cubic Metals. 2835-2837A

Annealing
See also Homogenizing
Spheroidizing
Mechanism of Damping Capacity of High-Chromium Steels and α-Iron and Its Dependence on Some External Factors. 111-124A
Discussion of "Grain Growth of a Superplastic 7475 Aluminum Alloy". 221-223A
Computer Algorithms for Radiometric Measurement of Temperature During the Galvanneal Process. 449-462B
The Effect of Phosphorus Segregation on the Intermediate-Temperature Embrittlement of Ferritic, Spheroidal Graphite Cast Iron. 557-561A
The Effect of Steel Chemistry on the Formation of Fe-Zn Intermetallic Compounds of Galvanneal-Coated Steel Sheets. 721-730B
Morphology Development in Hot-Dip Galvanneal Coatings. 937-947A
Auger Electron Analysis of the Initial Oxidation of Titanium Aluminides Based on Ti—48Al. 1041-1050A
Microstructural Study of the Titanium Alloy Ti—15Mo—2.7Nb—3Al—0.2Si (TIMETAL 21S). 1109-1118A
Interstitial Precipitation in Fe—Cr—Al Alloys. 1135-1146A
Formation and Stability of Metastable Structures and Amorphous Phases in Pu—V, Pu—TA, and Pu—Yb Systems With Positive Heats of Mixing. 1579-1590A
Dynamic Fracture Behavior of Ti—6Al—4V Alloy With Various Stabilities of β Phase. 1655-1666A
Interfacial Layer Development in Hot-Dip Galvanneal Coatings on Interstitial Free (IF) Steel. 2101-2109A
The Effect of Thermal Exposure on Microstructural Stability and Creep Resistance of a Two-Phase $TiAl/Ti_3Al$ Lamellar Alloy. 2371-2381A

Anodes
Physical Modeling Studies of Electrolyte Flow Due to Gas Evolution and Some Aspects of Bubble Behavior in Advanced Hall Cells. II. Flow and Interpolar Resistance in Cells With a Grooved Anode. 341-349B

Antifriction alloys
See Tin base alloys

Antimony, Ternary systems
Thermodynamic Analysis of the In-Ga-Sb System. 2331-2340A

Antiphase boundaries
Long-Range Ordering in the Early Stages of Precipitation)a Brief Review. (Conference Paper) 2565-2568A
Transformation Characteristics of α_1 Plates in Cu-Zn-Al Alloys. (Conference Paper) 2581-2599A

Arc spraying
See Plasma spraying

Arc welds
See Welded joints

Argon arc welding
See Gas tungsten arc welding

Arrhenius activation energy
See Activation energy

Artificial aging
See Aging (artificial)

Astroceram
See Ceramics

Atomic diffusion
See Diffusion

Atomic properties
See Atomic structure
Electronic structure

Atomic structure
The Diffuse-Scattering Method for Investigating Locally Ordered Binary Solid Solutions. 17-35A
Determination of the Short-Range Order Structure of Au—25 at.% Fe Using Wide-Angle Diffuse Synchrotron X-Ray Scattering. 1561-1573A
The Phenomenological Theory of Martensite Crystallography: Interrelationships. (Conference Paper) 1787-1795A
The Role of Structural Ledges as Misfit-Compensating Defects: FCC-BCC Interphase Boundaries. (Conference Paper) 1895-1903A
Intrinsic Ledges at Interphase Boundaries and the Crystallography of Precipitate Plates. (Conference Paper) 1905-1915A
Discussion of "Crystallographic Characterization of the Al-Co Decagonal Quasicrystal and Its Monoclinic Approximant τ^2-$Al_{13}Co_4$". 2535-2538A

Atomic structure, Alloying effects
Compositional and Microstructural Changes Which Attend Reheating and Grain Coarsening in Steels Containing Niobium. 277-286A
Transmission Electron Microscopy Crystal Structure Study of the Chromium-Rich Phase in a Laser-Clad Nickel Alloy. 487-497A
On the Prebainitic Phenomenon in Some Alloys. (Conference Paper) 1941-1946A
Thermodynamics and Kinetics of the Formation of Widmanstätten Ferrite Plates in Ferrous Alloys. (Conference Paper) 1947-1953A

Atomic structure, Cooling effects
Chemical Composition and Structural Identification of Eutectic Carbide in 1% Manganese Ductile Iron. 911-918A

Atomic structure, Diffusion effects
Multiphase Binary Diffusion in Infinite and Semi-Infinite Media. II. On the Numerical Calculation of the Rate Constants for Formation of Product Phases. 753-761A
Crystallographic Theories, Interface Structures, and Transformation Mechanisms. (Conference Paper) 1821-1839A
Application of the Theory of Martensite Crystallography to Displacive Phase Transformations in Substitutional Nonferrous Alloys. (Conference Paper, Review) 1841-1856A
Atomic Site Correspondence and Surface Relief in the Formation of Plate-Shaped Transformation Products. (Conference Paper) 1917-1922A
Formation of Invariant Plane-Strain and Tent-Shaped Surface Reliefs by the Diffusional Ledge Mechanism. (Conference Paper) 1923-1931A

Atomic structure, Heating effects
Atom Probe Field Ion Microscopy Study of the Partitioning of Substitutional Elements During Tempering of a Low-Alloy Steel Martensite. 499-508A
Aging of Freshly Formed Iron-Based Martensites at Low Temperatures. (Review) 889-909A
Formation and Stability of Metastable Structures and Amorphous Phases in Pu—V, Pu—TA, and Pu—Yb Systems With Positive Heats of Mixing. 1579-1590A

Atomic structure, Stress effects
A History of the Controversy Over the Roles of Shear and Diffusion in Plate Formation Above M_d and a Comparison of the Atomic Mechanisms of These Processes. (Conference Paper, Review) 1797-1819A

Atomic structure, Temperature effects
The Grand Partition Function of Dilute Biregular Solutions. 703-711B

Atomization
See Atomizing

Atomizing
Modeling of the Incorporation of Ceramic Particulates in Metallic Droplets During Spray Atomization and Coinjection. 135-147B
Surface Characterization and Reactivity of a Nitrogen Atomized 304L Stainless Steel Powder. 509-520A
Fatigue Crack Growth Rates and Fracture Toughness of Rapidly Solidified Al—8.5Fe—1.2V—1.7Si Alloys. 1005-1014A

Superplastic Behavior of Two Ultrahigh Boron Steels. 1241-1248A
Evolution of Interaction Domain Microstructure During Spray Deposition. 2341-2355A
Numerical Analysis of the Rapid Solidification of Gas-Atomized Al-8 wt.% Iron Droplets. 2815-2826A

Attaching
See Joining

Attenuation
See Damping

Attrition
See Wear

Auger electron spectroscopy
Auger Electron Analysis of the Initial Oxidation of Titanium Aluminides Based on Ti—48Al. 1041-1050A

Austenite
The Phenomenological Theory of Martensite Crystallography: Interrelationships. (Conference Paper) 1787-1795A
The Chromium Equivalents of Ferrite Stabilizers in Commercial Stainless Steels. 2827-2828A

Austenite, Alloying effects
Effects of Carbon Content and Ausaging on $\gamma \rightleftarrows \alpha'$ Transformation Behavior and Reverse-Transformed Structure in Fe—Ni—Co—Al—C Alloys. 63-71A
Compositional and Microstructural Changes Which Attend Reheating and Grain Coarsening in Steels Containing Niobium. 277-286A
Morphological Stability of γ/α Interface Formed by Carburization in Fe—C—X Alloys. 531-537A
Effects of Austenite Grain Size and Cooling Rate on Widmanstätten Ferrite Formation in Low-Alloy Steels. 665-675A
The Fine Structure and Formation Mechanism of Lower Bainite. (Conference Paper) 1967-1980A

Austenite, Cooling effects
Softening and Microstructural Change Following the Dynamic Recrystallization of Austenite. 389-400A
Intragranular Ferrite Nucleation in Medium-Carbon Vanadium Steels. 929-936A

Austenite, Deformation effects
Effects of Precursor Matrix Events on Subsequent Nucleation. (Conference Paper) 1933-1939A

Austenite, Diffusion effects
Diffusion in Growth of Bainite. (Conference Paper) 1957-1966A
Formation Mechanism of Bainitic Ferrite in an Fe)2% Si)0.6% C Alloy. (Conference Paper) 2009-2016A

Austenite, Heating effects
Heat Treatment of Investment Cast PH 13-8 Molybdenum Stainless Steel. II. Isothermal Aging Kinetics. 697-704A
Aging of Freshly Formed Iron-Based Martensites at Low Temperatures. (Review) 889-909A
Phosphorus and Carbon Segregation: Effects on Fatigue and Fracture of Gas-Carburized Modified 4320 Steel. 1229-1240A
Formation Mechanism of Bainite Ferrite and Carbide. (Conference Paper) 2001-2007A

Austenite, Temperature effects
Thermodynamics of the Iron)Carbon)Zinc System. 569-578B
Fracture and the Formation of Sigma Phase, $M_{23}C_6$, and Austenite From Delta—Ferrite in an AISI 304L Stainless Steel. 1147-1158A

Austenitic stainless steels, Corrosion
Influence of Near-Surface Microstructures on the Transient Current Response in Fe—Cr—Ni Alloys During Scratch Tests. 1325-1331A

Austenitic stainless steels, Diffusion
Interdiffusion Between Uranium—Zirconium Fuel vs. Selected Cladding Steels. 1649-1653A

Austenitic stainless steels, Heat treatment
Applicability of Bond Percolation Theory to Intergranular Stress-Corrosion Cracking of Sensitized AISI 304 Stainless Steel. 775-787A

Austenitic stainless steels, Irradiation
Helium 3 Precipitation in AISI 316L Stainless Steel Induced by Radioactive Decay of Tritium: Microstructural Study of Helium Bubble Precipitation. 2117-2130A
Helium 3 Precipitation in AISI 316L Stainless Steel Induced by Radioactive Decay of Tritium: Growth Mechanism of Helium Bubbles. 2131-2143A

Austenitic stainless steels, Mechanical properties
Some Aspects of Thermomechanical Fatigue of AISI 304L Stainless Steel. I. Creep—Fatigue Damage. 401-406A
Some Aspects of Thermomechanical Fatigue of AISI 304L Stainless Steel. II. Dislocation Arrangements. 407-413A
The Effects of Hydrogen on the Mechanical Behavior of Austenitic Stainless Steels at Room Temperature. 1015-1023A
Fracture and the Formation of Sigma Phase, $M_{23}C_6$, and Austenite From Delta—Ferrite in an AISI 304L Stainless Steel. 1147-1158A
Effect of Internal Heating During Hot Compression on the Stress-Strain Behavior of Alloy 304L. 2737-2752A

Austenitic stainless steels, Phases (state of matter)
The Chromium Equivalents of Selected Elements in Austenitic Stainless Steel. 2675-2681A
The Chromium Equivalents of Ferrite Stabilizers in Commercial Stainless Steels. 2827-2828A

Austenitic stainless steels, Powder technology
Surface Characterization and Reactivity of a Nitrogen Atomized 304L Stainless Steel Powder. 509-520A

Austenitizing
Influence of Tempering Temperature on Stability of Carbide Phases in 2.6Cr—0.7Mo—0.3V Steel With Various Carbon Content. 267-275A
The Effects of Double Austenitization on the Mechanical Properties of a 0.34C Containing Low-Alloy Ni—Cr—Mo—V Steel. 545-555A
Effects of Widmanstätten Ferrite on the Mechanical Properties of a 0.2% C—0.7% Mn Steel. 763-773A
Intragranular Ferrite Nucleation in Medium-Carbon Vanadium Steels. 929-936A

Auto oxidation
See Oxidation

Autodiffusion
See Diffusion

Automatic control
See Computer control

Automobile components
See Automotive components

Automotive bodies, Coating
Structure of As-Deposited Iron—Zinc Coatings From Chloride Bath. 249-255A
The Effect of Steel Chemistry on the Formation of Fe-Zn Intermetallic Compounds of Galvanneal-Coated Steel Sheets. 721-730B
η to G Phase Transformation in Electrodeposited Iron—Zinc Alloy Coatings. 1119-1125A

Automotive bodies, Mechanical properties
The Tensile Deformation Behavior of AA 3004 Aluminum Alloy. 357-364A

Automotive components
See also Automotive bodies

Automotive components, Welding
Resistance Spot Welding of Precoated Steel Sheet: Computational Heat-Transfer Analysis. 415-423B

Axial stress
The Effect of Triaxial Stress on Ductility and Fracture Morphology of Ferritic Spheroidal Graphite Cast Iron. 821-825A
Stress-State Dependence of Strain-Hardening Behavior in 2014 Al/15 vol.% Al_2O_3 Composite. (Conference Paper) 2049-2061A
Flow Instabilities and Fracture in Ti-6Al-4V Deformed in Compression at 298-673K. 2173-2179A
Modeling the Effects of Stress State and Crystal Orientation on the Stress-Induced Transformation of NiTi Single Crystals. 2383-2389A

Backscattering, Diffusion effects
Formation of Invariant Plane-Strain and Tent-Shaped Surface Reliefs by the Diffusional Ledge Mechanism. (Conference Paper) 1923-1931A

Bacterial leaching
Observations on the Effect of Medium Density and Viscosity on the Rate of Induced Aeration in Agitated Vessels. 303-306B

Bainite
Growth Kinetics and High-Temperature TEM In Situ Observation of Bainite in a Cu-Zn Alloy. (Conference Paper) 2609-2614A
A Discussion on the Formation of Bainite and Other Precipitates in Copper-Zinc and Silver-Zinc Alloys. (Conference Paper) 2621-2629A
Bainitelike Transformations in Some Oxide Ceramics. (Conference Paper) 2647-2653A

Bainite, Alloying effects
On the Prebainitic Phenomenon in Some Alloys. (Conference Paper) 1941-1946A
The Fine Structure and Formation Mechanism of Lower Bainite. (Conference Paper) 1967-1980A

Bainite, Diffusion effects
Diffusion in Growth of Bainite. (Conference Paper) 1957-1966A
Formation Mechanism of Bainitic Ferrite in an Fe)2% Si)0.6% C Alloy. (Conference Paper) 2009-2016A

Bainite, Heating effects
Titanium-Rich Mineral Phases and the Nucleation of Bainite. 1603-1611A
Formation Mechanism of Bainite Ferrite and Carbide. (Conference Paper) 2001-2007A

Bainite, Stress effects
Short Fatigue Crack Growth Behavior in a Ferritic-Bainitic Steel. 2421-2425A

Bainite, Temperature effects
Morphology of Bainite and Widmanstätten Ferrite. (Conference Paper) 1981-1989A

Ball milling
Formation of Metastable and Equilibrium Phases During Mechanical Alloying of Aluminum and Magnesium Powders. 73-79A
Mechanical Processing of Iron Powders in Reactive and Nonreactive Gas Atmospheres. 381-388A

Barium, Quaternary systems
Thermodynamic Study of $BaCuO_2$ and $BaCu_2O_2$. 385-389B

Batch annealing
See Vacuum annealing

Bearing alloys
See Bearing steels

Bearing steels, Mechanical properties
Effect of Microstructure (Particulate Size and Volume Fraction) and Counterface Material on the Sliding Wear Resistance of Particulate-Reinforced Aluminum Matrix Composites. 969-983A

Bend properties
See Bend strength
Bending fatigue

Bend strength, Alloying effects
Microstructures and Mechanial Behavior of NiAl-Mo and NiAl-Mo-Ti Two-Phase Alloys. 2769-2781A

Bend tests
Fracture of Glass in Tensile and Bending Tests. 961-968A
Evaluation of Static and Dynamic Fracture Toughness in Ductile Cast Iron. 2427-2437A

Bendability
See Formability

Bending fatigue, Heating effects
Phosphorus and Carbon Segregation: Effects on Fatigue and Fracture of Gas-Carburized Modified 4320 Steel. 1229-1240A
The Role of Magnesium-Containing Spheroidizer and Counteraction of Misch Metal in the Intermediate Temperature Intergranular Embrittlement of Ferritic Nodular Iron. 2305-2309A

Bending strength
See Bend strength

Bending tests
See Bend tests

Beneficiation
See Flotation

Bi-polar cells
Energy Efficiency Considerations on Monopolar vs. Bipolar Fused Salt Electrolysis Cells. 661-668B

Biaxial stress
See Axial stress

Billet casting
On the Formation of Pipes and Centerline Segregates in Continuously Cast Billets. 123-133B

Bimetals, Phases (state of matter)
The Morphological Stability of Lateral Growth in Solid—Solid Phase Transformation During Thin-Film Interdiffusion in Aluminum/Copper Bimetal Films. 1613-1625A

Binary systems, Phase transformations
Mg—Pb Phase Diagram and Phase Transformations in the Intermetallic Compounds Mg_2Pb and β'. 265-275B
The Invariant Line and Precipitate Morphology in FCC-BCC Systems. (Conference Paper) 1865-1874A

Binary systems, Phases (state of matter)
Partition of Alloying Elements Between γ (A1), γ' ($L1_2$), and β (B2) Phases in Ni—Al Base Systems. 473-485A
Multiphase Binary Diffusion in Infinite and Semi-Infinite Media. II. On the Numerical Calculation of the Rate Constants for Formation of Product Phases. 753-761A
Formation and Stability of Metastable Structures and Amorphous Phases in Pu—V, Pu—TA, and Pu—Yb Systems With Positive Heats of Mixing. 1579-1590A

Bioleaching
See Bacterial leaching

Bismuth, Alloying elements
A Process for Debismuthizing Lead With Magnesium. 379-384B

Bismuth, Ternary systems
Thermodynamic Study of the Bi—Ca—O System. 97-101B
Crystallization Studies of the β^* (Mg_2Pb) Phase and Its Phase Boundaries in the Pb—Mg—Bi System. 255-263B

Blast furnace chemistry
High-Temperature Isopiestic Studies on the Ternary Slag PbO—SiO_2—B_2O_3 at 1273K. 103-109B
Thermodynamics of Oxygen, Nitrogen, and Sulfur in Liquid Iron Equilibrated With CaO—Al_2O_3—MgO Slags. 235-244B
An Alternative Gibbs—Duhem Method for the Calculation of Activities From the Redox Data for Iron Oxide in Ternary Oxide Systems. 277-280B
Chemical Equilibria Between Silicon and Slag Melts. 497-504B
Kinetics in Muliticomponent Metallic)Ionic Systems. 579-587B
A Thermodynamic Study of BaO + $BaCl_2$ + Cr_2O_3 Fluxes Used for the Removal of Phosphorus From Chromium-Containing Iron Melts. 695-701B
Improvement in the Reducibility of Wustite Assisted by the Intensified Surface Segregation of Calcium Ions by the Double Addition of CaO and SiO_2. 741-748B

Blast furnace practice
The Measurement of the Heat-Transfer Coefficient Between High-Temperature Liquids and Solid Surfaces. 43-51B

Blast furnace slags
The Measurement of the Heat-Transfer Coefficient Between High-Temperature Liquids and Solid Surfaces. 43-51B
Thermodynamics and Phase Relations of the Fe—O—S—SiO_2(sat) System at 1200°C and the Effect of Copper. 79-89B
High-Temperature Isopiestic Studies on the Ternary Slag PbO—SiO_2—B_2O_3 at 1273K. 103-109B
Thermodynamics of Oxygen, Nitrogen, and Sulfur in Liquid Iron Equilibrated With CaO—Al_2O_3—MgO Slags. 235-244B
An Alternative Gibbs—Duhem Method for the Calculation of Activities From the Redox Data for Iron Oxide in Ternary Oxide Systems. 277-280B
Equilibrium Oxygen Pressures of Iron Silicate Slags. 463-465B
Chemical Equilibria Between Silicon and Slag Melts. 497-504B
A Model for Estimation of Viscosities of Complex Metallic and Ionic Melts. 519-525B
Improvement in the Reducibility of Wustite Assisted by the Intensified Surface Segregation of Calcium Ions by the Double Addition of CaO and SiO_2. 741-748B
Measurements of High-Temperature Viscosities of Liquid Boron Trioxide. 876-881A

Blast furnace slags, Phases (state of matter)
A Thermodynamic Study of BaO + $BaCl_2$ + Cr_2O_3 Fluxes Used for the Removal of Phosphorus From Chromium-Containing Iron Melts. 695-701B

Blast furnace slags, Reactions (chemical)
Kinetics in Muliticomponent Metallic)Ionic Systems. 579-587B

Blast furnace slags, Recovering
Vanadium Distribution in Melts Intermediate to Ferroalloy Production From Vanadiferous Slag. 27-32B

Blast furnace slags, Reduction (chemical)
An Analysis of Slag Stratification in Nickel Laterite Smelting Furnaces Due to Composition and Temperature Gradients. 491-496B

Blast furnaces
Calcium Deoxidation Equilibrium in Liquid Iron. 33-42B

Blasts (explosions)
See Explosions

Blending
See Powder blending

Blunging
See Mixing

Bohr model
See Atomic structure

Bomb reduction
See Reduction (chemical)

Bombs (pressure vessels)
See Pressure vessels

Bonding strength, Stress effects
Fiber Strength and Fiber/Matrix Bond Strength in Single Crystal Al_2O_3 Fiber Reinforced Ni_3Al Based Composites. 1259-1265A

Borides, Composite materials
Modeling of the Incorporation of Ceramic Particulates in Metallic Droplets During Spray Atomization and Coinjection. 135-147B
Room-Temperature Strength and Deformation of TiB_2-Reinforced Near-γ Titanium Aluminides. 2181-2197A
Thermal-Mechanical Fatigue of Ti-48Al-2V Alloy and Its Composite. 2207-2212A
Fracture Toughness of Discontinuously Reinforced Al-4Cu-1.5Mg/TiB_2 Composites. 2461-2468A

Boron, Dopants
Effects of Simultaneous Boron and Nitrogen Implantation on Microhardness and Fatigue Properties of Fe—13Cr—15Ni Alloys. 193-202A

Boron, Impurities
Thermodynamics of Boron in a Silicon Melt. 903-907B

Boron compounds
See Borides

Boron intensified steels
See Boron steels

Boron steels, Powder technology
Superplastic Behavior of Two Ultrahigh Boron Steels. 1241-1248A

Boundaries
See Antiphase boundaries
Grain boundaries
Phase boundary

Brasses, Mechanical properties
Elastic Compliance and Hill's Quadratic Yield Function for Weakly Orthotropic Sheets of Cubic Metals. 2835-2837A

Brasses, Microstructure
Characterization of Inhomogeneous Elastic Deformation With X-Ray Diffraction. 341-347A
High-Resolution Analytical Electron Microscopy Study of Isothermal Plate-Shaped Products in Some β-Phase Alloys. (Conference Paper) 2569-2579A

Brasses, Phase transformations
On the Prebainitic Phenomenon in Some Alloys. (Conference Paper) 1941-1946A
Thermodynamic Consideration of Formation Mechanism of α_1 Plate in βCu-Base Alloys. (Conference Paper) 2555-2564A
Transformation Characteristics of α_1 Plates in Cu-Zn-Al Alloys. (Conference Paper) 2581-2599A
The Formation Mechanism of Plate in β Cu-Zn and Cu-Zn-Al Alloys. (Conference Paper) 2601-2608A
Growth Kinetics and High-Temperature TEM In Situ Observation of Bainite in a Cu-Zn Alloy. (Conference Paper) 2609-2614A
Study on the Transformation Mechanism of α_1 Plates in a Copper-Zinc-Aluminum Alloy. (Conference Paper) 2615-2619A
A Discussion on the Formation of Bainite and Other Precipitates in Copper-Zinc and Silver-Zinc Alloys. (Conference Paper) 2621-2629A
Mechanism of the Early Stages of α_1 Plate Formation in a Cu-39% Zinc Alloy. (Conference Paper) 2631-2637A

Braze
See Brazing

Braze bonding
See Brazing

Brazing
Spreading and Interlayer Formation at the Copper-Copper Oxide/Polycrystalline Alumina Interface. 2497-2506A

Brittle fracture, Microstructural effects
Fracture and the Formation of Sigma Phase, $M_{23}C_6$, and Austenite From Delta—Ferrite in an AISI 304L Stainless Steel. 1147-1158A

Brittle fracture, Stress effects
Coefficients of Thermal Expansion of Metal-Matrix Composites for Electronic Packaging. 839-850A

Brittleness, Coating effects
Processing, Microstructure, and Properties of Laser-Clad Nickel Alloy FP-5 on Al Alloy AA333. 425-434B

Brittleness, Environmental effects
Hydride Embrittlement in Zircaloy-4 Plate. I. Influence of Microstructure on the Hydride Embrittlement in Zircaloy-4 at 20 and 350°C. 1185-1197A

Brittleness, Heating effects
Al_2Ti Precipitation in $Al_{64}Fe_8Ti_{28}$ Alloy. 715-721A

Brittleness, Stress effects
Fracture of Glass in Tensile and Bending Tests. 961-968A

Brittleness, Temperature effects
Comparison of Orthorhombic and Alpha-Two Titanium Aluminides as Matrices for Continuous SiC-Reinforced Composites. 1267-1283A

Bronzes
See also Aluminum bronzes

Bronzes, Claddings
Laser Cladding of Nickel-Aluminum Bronze on Al Alloy AA333. 749-759B

Bubbles
Helium 3 Precipitation in AISI 316L Stainless Steel Induced by Radioactive Decay of Tritium: Growth Mechanism of Helium Bubbles. 2131-2143A

Bubbles, Radiation effects
Helium 3 Precipitation in AISI 316L Stainless Steel Induced by Radioactive Decay of Tritium: Microstructural Study of Helium Bubble Precipitation. 2117-2130A

Bubbling
Large-Scale Measurements of the Physical Characteristics of Round Vertical Bubble Plumes in Liquids. 359-371B
Modeling of Metallurgical Emulsions. 855-864B

Bulk modulus
Elastic Constants of SiC_p/Al: Measurements and Modeling. 2832-2835A

Buoyancy
Sticking of Solids in Liquids. 397-403B

Burdening
See Blast furnace practice

Burning
See Combustion

Cakes (metal)
See Ingots

Calcining
See Roasting

Calcium, Alloying elements
Calcium Deoxidation Equilibrium in Liquid Iron. 33-42B

Calcium, Steel making
Thermodynamics of Oxygen, Nitrogen, and Sulfur in Liquid Iron Equilibrated With $CaO—Al_2O_3—MgO$ Slags. 235-244B

Calcium, Ternary systems
Thermodynamic Study of the Bi—Ca—O System. 97-101B

Calcium base alloys, Reactions (chemical)
Thermodynamic Estimation of $\Delta H_f^?$ for $CaGa_2$ Intermetallic. 151-154B

Calculating
See Computation
Computer programs
Numerical analysis

Calculation
See Computation
Computer programs
Numerical analysis

Calorimetry
Standard Enthalpies of Formation of Some Praseodymium Alloys of High-Temperature Direct Synthesis Calorimetry. 73-77B
Oxygen Potentials in Nickel + NiO and Nickel + Cr_2O_3 + $NiCr_2O_4$ Systems. 373-378B

Capillarity
Capillarity in Isothermal Infiltration of Alumina Fiber Preforms With Aluminum. 2145-2152A

Carbides
See also Cemented carbides
Silicon carbide

Carbides, Composite materials
Development and Characterization of Interface Coatings in Molybdenum-Reinforced NiAl Matrix Composites. 2111-2116A

Carbon
See also Graphite

Carbon, Alloying elements
Effects of Carbon Content and Ausaging on $\gamma \rightleftarrows \alpha'$ Transformation Behavior and Reverse-Transformed Structure in Fe—Ni—Co—Al—C Alloys. 63-71A
Influence of Tempering Temperature on Stability of Carbide Phases in 2.6Cr—0.7Mo—0.3V Steel With Various Carbon Content. 267-275A
Compositional and Microstructural Changes Which Attend Reheating and Grain Coarsening in Steels Containing Niobium. 277-286A
On the Prebainitic Phenomenon in Some Alloys. (Conference Paper) 1941-1946A
Thermodynamics and Kinetics of the Formation of Widmanstätten Ferrite Plates in Ferrous Alloys. (Conference Paper) 1947-1953A
The Fine Structure and Formation Mechanism of Lower Bainite. (Conference Paper) 1967-1980A

Carbon, Diffusion
Diffusion in Growth of Bainite. (Conference Paper) 1957-1966A

Carbon, Dopants
Effects of Simultaneous Boron and Nitrogen Implantation on Microhardness and Fatigue Properties of Fe—13Cr—15Ni Alloys. 193-202A

Carbon, Ternary systems
Thermodynamics of the Iron)Carbon)Zinc System. 569-578B

Carbon compounds
See Carbides

Carbon in pulp process
Adsorption Kinetics of Dicyanoaurate and Dicyanoargentate Ions in Activated Carbon. 185-191B
The Mechanism of Elution of Gold Cyanide From Activated Carbon. 829-838B

Carbon manganese steels, Heat treatment
Effects of Widmanstätten Ferrite on the Mechanical Properties of a 0.2% C—0.7% Mn Steel. 763-773A

Carbon manganese steels, Mechanical properties
Short Fatigue Crack Growth Behavior in a Ferritic-Bainitic Steel. 2421-2425A

Carbon manganese steels, Phases (state of matter)
Effects of Austenite Grain Size and Cooling Rate on Widmanstätten Ferrite Formation in Low-Alloy Steels. 665-675A

Carbon steels
See also Carbon manganese steels
High carbon steels
Low carbon steels
Medium carbon steels

Carbon steels, Casting
Calculation of Thermophysical Properties of Carbon and Low Alloyed Steels for Modeling of Solidification Processes. 909-916B

Carbon steels, Phases (state of matter)
Formation Mechanism of Bainite Ferrite and Carbide. (Conference Paper) 2001-2007A

Carbonizing (combustion)
See Coking

Carburization
See Carburizing

Carburizing
Morphological Stability of γ/α Interface Formed by Carburization in Fe—C—X Alloys. 531-537A
Computer Simulation of Diffusion in Multiphase Systems. 1127-1134A
Phosphorus and Carbon Segregation: Effects on Fatigue and Fracture of Gas-Carburized Modified 4320 Steel. 1229-1240A
Development and Characterization of Interface Coatings in Molybdenum-Reinforced NiAl Matrix Composites. 2111-2116A

Case carburizing
See Carburizing

Case hardening
See Carburizing

Case hardness
See Surface hardness

Cast iron
See also Gray iron

Cast iron, Heat treatment
The Effect of Phosphorus Segregation on the Intermediate-Temperature Embrittlement of Ferritic, Spheroidal Graphite Cast Iron. 557-561A

Cast iron, Mechanical properties
The Effect of Triaxial Stress on Ductility and Fracture Morphology of Ferritic Spheroidal Graphite Cast Iron. 821-825A

Castaing microprobes
See Electron probes

Casting
See Billet casting
Centrifugal casting
Chill casting
Continuous casting
Ingot casting
Melt spinning
Pressure casting
Rheocasting
Slab casting

Casting defects
Water-Modeling Study of the Surface Disturbances in Continuous Slab Caster. 227-233B

Casting defects, Cooling effects
A Note on the Sensitivity of Solidification Models to Thermophysical Properties. 154-157B
Modeling of the Formation of Under-Riser Macrosegregation During Solidification of Binary Alloys. 1051-1062A
Modeling Microstructure Development in Gray Cast Irons. 1063-1079A
Microsegregation in Cellular Solidification. 2295-2301A

Castings
See also Centrifugal castings
Chill castings
Ingots
Pressure castings

Castings, Heat treatment
The Effect of Aging on Wear Characteristics of Rheocast-Leaded Aluminum Alloys. 851-856A
Effect of Heat Treatment on the Microstructure, Tensile Properties, and Fracture Behavior of Permanent Mold Al-10 wt.% Si-0.6 wt.% Mg/SiC/10p Composite Castings. 2247-2263A

Castings, Mechanical properties
Modeling the Thin-Slab Continuous-Casting Mold. 443-457B

Castings, Phases (state of matter)
Crystallization Behavior of Iron-Containing Intermetallic Compounds in 319 Aluminum Alloy. 1761-1773A

Catalysts, Recovering
Processing of Spent Hydrorefining Catalysts by Selective Chlorination. 481-490B

Catalytic converters
See Automotive components

CCT curves
See TTT curves

Cells
See Electrolytic cells

Cemented carbides, Powder technology
Thermodynamics of Isolated Pores Filling With Liquid in Sintered Composite Materials. 733-740A

Cementite, Heating effects
Atom Probe Field Ion Microscopy Study of the Partitioning of Substitutional Elements During Tempering of a Low-Alloy Steel Martensite. 499-508A
Phosphorus and Carbon Segregation: Effects on Fatigue and Fracture of Gas-Carburized Modified 4320 Steel. 1229-1240A

Cementite, Temperature effects
Morphology of Bainite and Widmanstätten Ferrite. (Conference Paper) 1981-1989A

Centrifugal casting
The Cast Structure of a 7075 Alloy Produced by a Water-Cooling Centrifugal Casting Method. 643-650A

Centrifugal castings, Microstructure
The Cast Structure of a 7075 Alloy Produced by a Water-Cooling Centrifugal Casting Method. 643-650A

Centrifuging
The Effect of Enhanced Gravity Levels on Microstructural Development in Pb—50 wt.% Sn Alloys During Controlled Directional Solidification. 865-870A

Ceramic mold casting
See Investment casting

Ceramic mold castings
See Investment castings

Ceramics
See also Aluminum oxide
Silicon carbide
Titanium carbide
Tungsten carbide

Ceramics, Powder technology
Preparation and Properties of Fine Hematite Powders by Hydrolysis of Iron Carboxylate Solutions. 165-170B

Cermets
See Cemented carbides

Charging
High-Temperature Oxidation of Cathodically Hydrogen-Charged Two-Phase (Ti_3Al, TiAl) Titanium Aluminides. 2491-2496A

Charging, Environmental effects
Modeling Hydrogen Entry and Exit in Metals Exposed to Multiple Charging Processes. 723-732A

Charpy impact tests
See Impact tests

Charring
See Combustion

Chemical analysis
See Qualitative analysis

Chemical equilibrium
Calcium Deoxidation Equilibrium in Liquid Iron. 33-42B
Thermodynamics of Oxygen, Nitrogen, and Sulfur in Liquid Iron Equilibrated With CaO—Al_2O_3—MgO Slags. 235-244B
Chemical Equilibria Between Silicon and Slag Melts. 497-504B
Equilibrium Distribution of Fe, Ni, Sb, and Sn between Liquid Cu and a CaO-Rich Slag. 645-651B
The Shapes of the Phase Boundaries of Two Ideal Solution Phases in Ternary and Higher Order Systems. 656-658A
Spreading and Interlayer Formation at the Copper-Copper Oxide/Polycrystalline Alumina Interface. 2497-2506A

Chemical equilibrium, Alloying effects
Thermodynamics of Oxygen and Nitrogen in Liquid Nickel Equilibrated With CaO—TiO_x and CaO—TiO_x—Al_2O_3 Melts. 5-13B
Morphological Stability of γ/α Interface Formed by Carburization in Fe—C—X Alloys. 531-537A

Chemical equilibrium, Cooling effects
Crystallization Studies of the β' (Mg_2Pb) Phase and Its Phase Boundaries in the Pb—Mg—Bi System. 255-263B
Further Discussions on the Solute Redistribution During Dendritic Solidification of Binary Alloys. 731-739B
Calorimetric Evaluation of Nonequilibrium State in As-Melt Spun Al—1.72 and Al—3.12 at.% Cu Alloys and Al—6.74, Al—8.48, and Al—11.97 at.% Si Alloys. 1102-1104A

Chemical equilibrium, Deformation effects
Formation of Metastable and Equilibrium Phases During Mechanical Alloying of Aluminum and Magnesium Powders. 73-79A

Chemical equilibrium, Diffusion effects
Multiphase Binary Diffusion in Infinite and Semi-Infinite Media. II. On the Numerical Calculation of the Rate Constants for Formation of Product Phases. 753-761A

Chemical equilibrium, pH effects
Simulation of In Situ Uraninite Leaching. I. A Partial Equilibrium Model of the NH_4HCO_3—$(NH_4)_2CO_3$—H_2O_2 Leaching System. 171-183B

Chemical equilibrium, Pressure effects
Thermodynamic Study of $BaCuO_2$ and $BaCu_2O_2$. 385-389B

Chemical equilibrium, Temperature effects
Phase Relations in the Mo—Si—C System Relevant to the Processing of $MoSi_2$—SiC Composites. 5-15A
High-Temperature Phase Relations and Thermodynamics in the Iron—Lead—Sulfur System. 53-61B
Oxygen Potentials in Nickel + NiO and Nickel + Cr_2O_3 + $NiCr_2O_4$ Systems. 373-378B
Partition of Alloying Elements Between γ (A1), γ' ($L1_2$), and β (B2) Phases in Ni—Al Base Systems. 473-485A
Local Melting in Al—Mg—Zn—Alloys. 521-530A
Thermodynamics of the Iron)Carbon)Zinc System. 569-578B
Thermodynamics of the Liquid }xCu + yAu + (1—x—y)Ge}, ($0.75 \leq x \leq 1$, $0 \leq y \leq 0.125$) Alloys at 1550K by Knudsen Effusion Mass Spectrometry. 857-864A

Chemical kinetics
See Reaction kinetics

Chemical metallurgy
See Process metallurgy

Chemical processes
See Reactions (chemical)

Chemical properties
See Activity (chemical)
Reactivity

Chemical reactions
See Reactions (chemical)

Chemical reduction
See Reduction (chemical)

Chemistry
See Electrochemistry
Physical chemistry
Surface chemistry
Thermochemistry

Chill casting
See also Direct chill casting
Modeling of the Formation of Under-Riser Macrosegregation During Solidification of Binary Alloys. 1051-1062A
Prediction of Columnar to Equiaxed Transition During Diffusion-Controlled Dendritic Alloy Solidification. 1081-1093A

Chill castings, Microstructure
Prediction of Columnar to Equiaxed Transition During Diffusion-Controlled Dendritic Alloy Solidification. 1081-1093A

Chlorination
See Hydrochlorination

Chromium, Alloying elements
Influence of Tempering Temperature on Stability of Carbide Phases in 2.6Cr—0.7Mo—0.3V Steel With Various Carbon Content. 267-275A
Transmission Electron Microscopy Crystal Structure Study of the Chromium-Rich Phase in a Laser-Clad Nickel Alloy. 487-497A
The Influence of the Alloying Elements Upon the Transformation Kinetics and Morphologies of Ferrite Plates in Alloy Steels. (Conference Paper) 1991-2000A

Chromium, Extraction
A Mathematical Model of Ionic Transport in a Porous Diaphragm of a Chrome—Alum Cell. 351-358B

Chromium, Ternary systems
Numerical Modeling of Solidification and Subsequent Transformation of Fe—Cr—Ni Alloys. 1309-1321A

Chromium base alloys, Phase transformations
The Selection of Precipitate Habit Planes in Cr-32 wt.% Ni. (Conference Paper) 2639-2646A

Chromium carbide, Composite materials
Thermodynamics of Isolated Pores Filling With Liquid in Sintered Composite Materials. 733-740A

Chromium compounds
See also Chromium carbide

Chromium compounds, Mechanical properties
Elastic Constants of Some Transition-Metal-Disilicide Single Crystals. 331-340A

Chromium molybdenum nickel steels
See Nickel chromium molybdenum steels

Chromium molybdenum steels
See also Chromium molybdenum vanadium steels
Nickel chromium molybdenum steels

Chromium molybdenum steels, Phases (state of matter)
Precipitation of BCC Phase from Nonequilibrium A13-Type Phase in Rapidly Solidified High-Carbon Fe-Cr-Mo Alloy. 2542-2546A

Chromium molybdenum vanadium steels, Heat treatment
Influence of Tempering Temperature on Stability of Carbide Phases in 2.6Cr—0.7Mo—0.3V Steel With Various Carbon Content. 267-275A

Chromium nickel molybdenum steels
See Nickel chromium molybdenum steels

Chromium steels
See also Chromium molybdenum steels

Chromium steels, Heat treatment
Mechanism of Damping Capacity of High-Chromium Steels and α-Iron and Its Dependence on Some External Factors. 111-124A

Chromium vanadium steels
See Chromium molybdenum vanadium steels

Cladding
Multiphase Binary Diffusion in Infinite and Semi-Infinite Media. I. On the Determination of Interdiffusion Coefficients. 741-751A

Claddings, Diffusion
Interdiffusion Between Uranium—Zirconium Fuel vs. Selected Cladding Steels. 1649-1653A

Claddings, Microstructure
Transmission Electron Microscopy Crystal Structure Study of the Chromium-Rich Phase in a Laser-Clad Nickel Alloy. 487-497A

Cleaning
See Washing

Cleavage, Heating effects
Al_2Ti Precipitation in $Al_{64}Fe_8Ti_{28}$ Alloy. 715-721A

Close packed hexagon
See Hexagonal lattice

Clustering
The Diffuse-Scattering Method for Investigating Locally Ordered Binary Solid Solutions. 17-35A

Clustering, Heating effects
Aging of Freshly Formed Iron-Based Martensites at Low Temperatures. (Review) 889-909A

Coating
See Diffusion coating
Glazing

Coatings
See Protective coatings
Sprayed coatings

Cobalt, Composite materials
Thermodynamics of Isolated Pores Filling With Liquid in Sintered Composite Materials. 733-740A

Cobalt, Recovering
Processing of Spent Hydrorefining Catalysts by Selective Chlorination. 481-490B

Cobalt base alloys, Cladding
A Simple but Realistic Model for Laser Cladding. 281-291B

Cobalt base alloys, Mechanical properties
On Morphologies, Microsegregation, and Mechanical Behavior of Directionally Solidified Cobalt-Base Superalloy at Medium Cooling Rate. 637-642A

Cobalt base alloys, Phase transformations
Atomic Site Correspondence and Surface Relief in the Formation of Plate-Shaped Transformation Products. (Conference Paper) 1917-1922A

Cobalt compounds, Mechanical properties
Elastic Constants of Some Transition-Metal-Disilicide Single Crystals. 331-340A

Cobalt compounds, Microstructure
Discussion of "Crystallographic Characterization of the Al-Co Decagonal Quasicrystal and Its Monoclinic Approximant τ^2-$Al_{13}Co_4$". 2535-2538A

COD
See Crack opening displacement

Coefficient of expansion
See Thermal expansion

Coefficient of thermal expansion
See Thermal expansion

Coking
Study of Nonisothermal Reduction of Iron Ore—Coal/Char Composite Pellet. 15-26B
Thermodynamic Stability of Metallurgical Coke Relative to Graphite. 149-151B

Cold aging
See Aging (natural)

Cold cracking (welds)
See Weld defects

Cold deformation
See Deformation

Cold ductility
See Ductility

Cold formability
See Formability

Cold rolling
Alligatoring and Damage in the Cold Rolling of Spheroidized Steels. 589-598A

Cold shortness
See Brittleness

Cold stretching
See Stretching

Cold working
See Cold rolling

Columbium
See Niobium

Columbium compounds
See Niobium compounds

Columnar structure, Cooling effects
Prediction of Columnar to Equiaxed Transition During Diffusion-Controlled Dendritic Alloy Solidification. 1081-1093A
Solidification Macrostructures and Macrosegregation in Aluminum Alloys Cooled From Above. 1097-1102A

Combustion
Interactions Between Drops of a Molten Aluminum)Lithium Alloy and Liquid Water. 623-625B

Combustion, Temperature effects
Thermodynamic Estimation of ΔH_f° for $CaGa_2$ Intermetallic. 151-154B

Compliance (elasticity)
See Modulus of elasticity

Components
See Aircraft components
Automotive components
Engine components
Nuclear reactor components

Composite materials
See Fiber composites
Particulate composites
Whisker composites

Compounds
See Aluminum compounds
Intermetallics
Tin compounds

Compression casting
See Pressure casting

Compression strength
See Compressive strength

Compression tests
Precipitation Effects During Hot Deformation of a Copper Alloy. 257-266A
Effect of Orientation on Crystallographic Cracking in Notched Nickel-Base Superalloy Single Crystal Subjected to Far-Field Cyclic Compression. 287-297A
Textural and Microstructural Gradient Effects on the Mechanical Behavior of a Tantalum Plate. 1025-1031A
Evaluation of Homogeneous Compression Flow Curves Using Square Cross-Sectioned Specimens. 1095-1097A
Effect of Internal Heating During Hot Compression on the Stress-Strain Behavior of Alloy 304L. 2737-2752A

Compressive modulus
See Modulus of elasticity

Compressive properties
See also Compressive strength

Compressive properties, Microstructural effects
Temperature and Microstructural Dependence of the Deformation of a High Niobium, Titanium—Aluminum Alloy. 1667-1679A

Compressive properties, Pressure effects
The Effects of Hydrostatic Pressure on the Compressive Mechanical Behavior of $L1_2$ Al_3 Ti-Based Intermetallic. 1703-1711A

Compressive properties, Stress effects
Characteristics of the Martensitic Transformation and the Induced Two-Way Shape Memory Effect After Training by Compressive Pseudoelastic Cycling in Cu—Zn—Al Single Crystals. 687-695A
Flow Instabilities and Fracture in Ti-6Al-4V Deformed in Compression at 298-673K. 2173-2179A

Compressive strength
Study of Nonisothermal Reduction of Iron Ore—Coal/Char Composite Pellet. 15-26B

Compressive strength, Deformation effects
Alligatoring and Damage in the Cold Rolling of Spheroidized Steels. 589-598A

Compressive yield strength
See Compressive strength

Computation
The Chromium Equivalents of Selected Elements in Austenitic Stainless Steel. 2675-2681A
The Chromium Equivalents of Ferrite Stabilizers in Commercial Stainless Steels. 2827-2828A

Computer control
A Simple but Realistic Model for Laser Cladding. 281-291B

Computer programs
Calculation of Thermophysical Properties of Carbon and Low Alloyed Steels for Modeling of Solidification Processes. 909-916B

Computer simulation
A Comparison of Three Mathematical Modeling Procedures for Simulating Fluid Flow Phenomena in Bubble-Stirred Ladles. 308-312B
Computer Algorithms for Radiometric Measurement of Temperature During the Galvanneal Process. 449-462B
Thermodynamic Simulation Model of the Isasmelt Process for Copper Matte. 839-853B
Gas Trapping and Release in Polycrystalline Nickel Preimplanted With Helium. 949-959A
Computer Simulation of Diffusion in Multiphase Systems. 1127-1134A

Numerical Modeling of Solidification and Subsequent Transformation of Fe—Cr—Ni Alloys. 1309-1321A
Numerical Modeling of γ Precipitate Growth During Fe—Ni Martensite Decomposition at Low Temperatures (≤ 400°C). 1639-1648A
Transformation, Microcrack, and Thermal Residual Stress as Interactive Processes in ZrO_2-Toughened Al_2O_3, Simulated by the Finite Element Method. 1725-1731A
Diffusional Boundary Conditions During Coarsening of Elastically Interacting Precipitates. 2695-2703A

Computing
See Computation

Concast
See Continuous casting

Concentration (stress)
See Stress concentration

Conducting sheet analog
See Heat transmission

Conductivity
See Resistivity
Thermal conductivity

Conductivity (electrical)
See Resistivity

Connecting
See Joining

Contact testing
See Ultrasonic testing

Continuous casting
See also Direct chill casting
On the Formation of Pipes and Centerline Segregates in Continuously Cast Billets. 123-133B
Water-Modeling Study of the Surface Disturbances in Continuous Slab Caster. 227-233B
Modeling the Thin-Slab Continuous-Casting Mold. 443-457B
Simulation of Argon Gas Flow Effects in a Continuous Slab Caster. 527-547B
Mathematical and Physical Modeling Studies of Molten Aluminum Flow in a Tundish. 669-680B

Contraction
See Shrinkage

Control
See Process control

Convection
Natural Convection in an Aluminum Ingot: a Mathematical Model. 293-302B
Three-Dimensional Finite Element Modeling of Gas Metal-Arc Welding. 435-441B

Cooling
See Supercooling

Cooling rate
A Note on the Sensitivity of Solidification Models to Thermophysical Properties. 154-157B
Effect of Alloying Elements on the Solidification Characteristics and Microstructure of Al—Si—Cu—Mg—Fe 380 Alloy. 437-448A
Local Melting in Al—Mg—Zn—Alloys. 521-530A
On Morphologies, Microsegregation, and Mechanical Behavior of Directionally Solidified Cobalt-Base Superalloy at Medium Cooling Rate. 637-642A
The Cast Structure of a 7075 Alloy Produced by a Water-Cooling Centrifugal Casting Method. 643-650A
Effects of Austenite Grain Size and Cooling Rate on Widmanstätten Ferrite Formation in Low-Alloy Steels. 665-675A
Effects of Widmanstätten Ferrite on the Mechanical Properties of a 0.2% C—0.7% Mn Steel. 763-773A
Chemical Composition and Structural Identification of Eutectic Carbide in 1% Manganese Ductile Iron. 911-918A
Modeling of the Formation of Under-Riser Macrosegregation During Solidification of Binary Alloys. 1051-1062A
The Velocity of Solidification of Highly Undercooled Nickel. 1301-1308A
Crystallization Behavior of Iron-Containing Intermetallic Compounds in 319 Aluminum Alloy. 1761-1773A
Evolution of Interaction Domain Microstructure During Spray Deposition. 2341-2355A
Undercooling-Induced Macrosegregation in Directional Solidification. 2507-2516A

Copper, Alloying elements
Effect of Alloying Elements on the Solidification Characteristics and Microstructure of Al—Si—Cu—Mg—Fe 380 Alloy. 437-448A

Copper, Binary systems
Multiphase Binary Diffusion in Infinite and Semi-Infinite Media. II. On the Numerical Calculation of the Rate Constants for Formation of Product Phases. 753-761A

Copper, Brazing
Spreading and Interlayer Formation at the Copper-Copper Oxide/Polycrystalline Alumina Interface. 2497-2506A

Copper, Composite materials
Thermodynamics of Isolated Pores Filling With Liquid in Sintered Composite Materials. 733-740A
The Morphological Stability of Lateral Growth in Solid—Solid Phase Transformation During Thin-Film Interdiffusion in Aluminum/Copper Bimetal Films. 1613-1625A

Copper, Extraction
Thermodynamics and Phase Relations of the Fe—O—S—SiO_2(sat) System at 1200°C and the Effect of Copper. 79-89B
Thermal Treatment of Complex Sulfide Ores in N_2 and H_2 Atmospheres: a New Approach for the Extraction of Their Valuable Elements. (Review) 193-205B
Physical and Mathematical Modeling of Pyrometallurgical Channel Reactors With Bottom Gas Injection. Residence Time Distribution Analysis and Ideal-Reactor-Network Model. 207-219B
An Electrochemical Study on the Dissolution of Gold and Copper from Gold/Copper Alloys. 817-827B
Thermodynamic Simulation Model of the Isasmelt Process for Copper Matte. 839-853B

Copper, Mechanical properties
Elastic Compliance and Hill's Quadratic Yield Function for Weakly Orthotropic Sheets of Cubic Metals. 2835-2837A

Copper, Metallography
Efficient Measurement of Microstructural Surface Area Using Trisector. 919-928A

Copper, Physical properties
Sticking of Solids in Liquids. 397-403B

Copper, Powder technology
Determination of Pore Mobility During Sintering. 81-87A

Copper, Quaternary systems
Thermodynamic Study of $BaCuO_2$ and $BaCu_2O_2$. 385-389B

Copper, Recovering
Equilibrium Values for the Dissolution of Solid Copper Into FeS—Na_2S Mattes. 306-308B

Copper, Reduction (chemical)
Equilibrium Oxygen Pressures of Iron Silicate Slags. 463-465B

Copper, Refining
Equilibrium Distribution of Fe, Ni, Sb, and Sn between Liquid Cu and a CaO-Rich Slag. 645-651B

Copper, Soldering
The Effect of Substrate on the Microstructure and Creep of Eutectic Indium-Tin. 2715-2722A

Copper, Ternary systems
Thermodynamic Properties of Ternary Liquid Cu—Mg—Ni Alloys. 63-72B
The Grand Partition Function of Dilute Biregular Solutions. 703-711B
Thermodynamics of the Liquid {xCu + yAu + (1—x—y)Ge}, ($0.75 \leq x \leq 1$, $0 \leq y \leq 0.125$) Alloys at 1550K by Knudsen Effusion Mass Spectrometry. 857-864A

Copper base alloys
See also Brasses
Bronzes

Copper base alloys, Atomic properties
The Diffuse-Scattering Method for Investigating Locally Ordered Binary Solid Solutions. 17-35A

Copper base alloys, Casting
Nonequilibrium Solidification of Undercooled Melt of Ag-Cu Alloy Entrained in the Primary Phase. 2517-2523A

Copper base alloys, Composite materials
Low-Cycle Fatigue of Dispersion-Strengthened Copper. 2235-2245A

Copper base alloys, Diffusion
A History of the Controversy Over the Roles of Shear and Diffusion in Plate Formation Above M_d and a Comparison of the Atomic Mechanisms of These Processes. (Conference Paper, Review) 1797-1819A

Copper base alloys, Mechanical properties
Precipitation Effects During Hot Deformation of a Copper Alloy. 257-266A
Characteristics of the Martensitic Transformation and the Induced Two-Way Shape Memory Effect After Training by Compressive Pseudoelastic Cycling in Cu—Zn—Al Single Crystals. 687-695A

Copper base alloys, Phase transformations
Application of the Theory of Martensite Crystallography to Displacive Phase Transformations in Substitutional Nonferrous Alloys. (Conference Paper, Review) 1841-1856A
A Comparison Between Three Simple Crystallographic Principles of Precipitate Morphology. (Conference Paper) 1857-1863A
Thermodynamic Consideration of Formation Mechanism of α_1 Plate in βCu-Base Alloys. (Conference Paper) 2555-2564A

Copper base alloys, Powder technology
Elevated-Temperature Stability of Mechanically Alloyed Copper-Niobium Powders. 2091-2099A

Copper base alloys, Reactions (chemical)
Experimental Study of the Influence of Interfacial Energies and Reactivity on Wetting in Metal/Oxide Systems. 599-605A
Kinetics of Interlayer Formation on Polycrystalline α-Al_2O_3/Copper-Titanium Alloy Interface. 2083-2090A

Copper base alloys, Welding
Effect of Welding Variables and Solidification Substructure on Weld Metal Porosity. 2285-2294A

Copper mattes, Synthesis
Thermodynamic Simulation Model of the Isasmelt Process for Copper Matte. 839-853B

Core hardness
See Hardness

Corex process
See Ironmaking

Corrodents
See Corrosion environments

Corrosion
See also Stress corrosion cracking

Corrosion, Environmental effects
On Low-Temperature Environment-Assisted Fatigue Crack Propagation. 658-659A

Corrosion, Microstructural effects
Influence of Near-Surface Microstructures on the Transient Current Response in Fe—Cr—Ni Alloys During Scratch Tests. 1325-1331A

Corrosion cracking
See Stress corrosion cracking

Corrosion environments
On Low-Temperature Environment-Assisted Fatigue Crack Propagation. 658-659A

Corrosion potential, Diffusion effects
Tritium Distribution at the Crack Tip of High-Strength Steels Submitted to Stress Corrosion Cracking. 1159-1167A

Corrosion prevention
See also Passivation

Corrosion prevention, Coating effects
Structure of As-Deposited Iron—Zinc Coatings From Chloride Bath. 249-255A

Corrosion resistance, Coating effects
Morphology Development in Hot-Dip Galvanneal Coatings. 937-947A

Corrosion resistance, Heating effects
Interstitial Precipitation in Fe—Cr—Al Alloys. 1135-1146A

Corrosion resistant steels
See Stainless steels

Coupling (process)
See Joining

CO2 arc welding
See Gas metal arc welding

Crack growth
See Crack propagation

Crack initiation
Efficient Measurement of Microstructural Surface Area Using Trisector. 919-928A

Crack initiation, Coating effects
The Influence of Laser Glazing on Fatigue Crack Growth in Ti—24Al—11Nb. 183-192A
Processing, Microstructure, and Properties of Laser-Clad Nickel Alloy FP-5 on Al Alloy AA333. 425-434B

Crack initiation, Composition effects
The Effect of Niobium Morphology on the Cyclic Oxidation Resistance of $MoSi_2$/20 vol.% Niobium Composites. 1033-1040A

Crack initiation, Cooling effects
On Morphologies, Microsegregation, and Mechanical Behavior of Directionally Solidified Cobalt-Base Superalloy at Medium Cooling Rate. 637-642A
Fatigue Crack Growth Rates and Fracture Toughness of Rapidly Solidified Al—8.5Fe—1.2V—1.7Si Alloys. 1005-1014A

Crack initiation, Deformation effects
Modeling the Thin-Slab Continuous-Casting Mold. 443-457B
Alligatoring and Damage in the Cold Rolling of Spheroidized Steels. 589-598A
Relationships of Slip Morphology, Microcracking, and Fracture Resistance in a Lamellar TiAl-Alloy. 1217-1228A
Hot Deformation Characteristics of INCONEL Alloy MA 754 and Development of a Processing Map. 1693-1702A
High-Temperature Deformation of B2 NiAl-Base Alloys. (Conference Paper) 2017-2026A
Microstructural Control in Hot Working of IN-718 Superalloy Using Processing Map. 2275-2284A

Crack initiation, Diffusion effects
Tritium Distribution at the Crack Tip of High-Strength Steels Submitted to Stress Corrosion Cracking. 1159-1167A

Crack initiation, Environmental effects
Hydride Embrittlement in Zircaloy-4 Plate. I. Influence of Microstructure on the Hydride Embrittlement in Zircaloy-4 at 20 and 350°C. 1185-1197A

Crack initiation, Heating effects
Al_2Ti Precipitation in $Al_{64}Fe_8Ti_{28}$ Alloy. 715-721A
Effect of Heat Treatment on the Microstructure, Tensile Properties, and Fracture Behavior of Permanent Mold Al-10 wt.% Si-0.6 wt.% Mg/SiC/10p Composite Castings. 2247-2263A

Crack initiation, High temperature effects
Effect of Strain Rate on the High-Temperature Low-Cycle Fatigue Properties of a Nimonic PE-16 Superalloy. 159-171A
Elevated Temperature Fracture of RS/PM Alloy 8009. I. Fracture Mechanics Behavior. 365-379A
The Workability of Commercial and Experimental 0.6% Carbon Low Alloy Steels in the Temperature Range of 650-870°C. 827-837A

Crack initiation, Microstructural effects
Effect of Microstructure (Particulate Size and Volume Fraction) and Counterface Material on the Sliding Wear Resistance of Particulate-Reinforced Aluminum Matrix Composites. 969-983A
The Study of Adiabatic Shear Band Instability in a Pearlitic 4340 Steel Using a Dynamic Punch Test. 2483-2489A

Crack initiation, Pressure effects
The Effects of Hydrostatic Pressure on the Compressive Mechanical Behavior of $L1_2$ Al_3 Ti-Based Intermetallic. 1703-1711A

Crack initiation, Radiation effects
Effects of Simultaneous Boron and Nitrogen Implantation on Microhardness and Fatigue Properties of Fe—13Cr—15Ni Alloys. 193-202A

Crack initiation, Stress effects
Behavior of Nickel-Base Superalloy Single Crystals Under Thermal—Mechanical Fatigue. 99-109A
Effect of Orientation on Crystallographic Cracking in Notched Nickel-Base Superalloy Single Crystal Subjected to Far-Field Cyclic Compression. 287-297A
Tensile Ductility of Extrinsically Toughened Intermetallics. 299-308A
Some Aspects of Thermomechanical Fatigue of AISI 304L Stainless Steel. I. Creep—Fatigue Damage. 401-406A
Cleavage Initiation in the Intercritically Reheated Coarse-Grained Heat-Affected Zone: I. Fractographic Evidence. 563-573A
Crack Initiation at Long Radial Hydrides in Zr—2.5Nb Pressure Tube Material at Elevated Temperatures. 993-1004A
Mixed-Mode I and II Fatigue Threshold and Crack Closure in Dual-Phase Steels. 1713-1723A
Transformation, Microcrack, and Thermal Residual Stress as Interactive Processes in ZrO_2-Toughened Al_2O_3, Simulated by the Finite Element Method. 1725-1731A
Forging Limits for an Aluminum Matrix Composite. I. Experimental Results. (Conference Paper) 2027-2038A
Low-Cycle Fatigue of Dispersion-Strengthened Copper. 2235-2245A
Low-Cycle Fatigue Properties of a SiC Whisker-Reinforced 2124 Aluminum Alloy. 2265-2274A
Micromechanical Modelling of Reinforcement Fracture in Particle-Reinforced Metal-Matrix Composites. 2403-2420A
Short Fatigue Crack Growth Behavior in a Ferritic-Bainitic Steel. 2421-2425A
Evaluation of Static and Dynamic Fracture Toughness in Ductile Cast Iron. 2427-2437A
Low Cycle Fatigue Behavior of Polycrystalline Ni_3Al Alloys at Ambient and Elevated Temperatures. 2469-2476A

Crack opening displacement, Stress effects
Cleavage Initiation in the Intercritically Reheated Coarse-Grained Heat-Affected Zone: I. Fractographic Evidence. 563-573A

Crack propagation, Coating effects
The Influence of Laser Glazing on Fatigue Crack Growth in Ti—24Al—11Nb. 183-192A
The Effect of Low Gold Concentrations on the Creep of Eutectic Tin—Lead Joints. 1249-1257A

Crack propagation, Composition effects
The Effect of Niobium Morphology on the Cyclic Oxidation Resistance of $MoSi_2$/20 vol.% Niobium Composites. 1033-1040A

Crack propagation, Cooling effects
On Morphologies, Microsegregation, and Mechanical Behavior of Directionally Solidified Cobalt-Base Superalloy at Medium Cooling Rate. 637-642A
Fatigue Crack Growth Rates and Fracture Toughness of Rapidly Solidified Al—8.5Fe—1.2V—1.7Si Alloys. 1005-1014A

Crack propagation, Environmental effects
On Low-Temperature Environment-Assisted Fatigue Crack Propagation. 658-659A
Embrittlement of B2 Iron Aluminide by Water Vapor and by Hydrogen. 1285-1290A

Crack propagation, Heating effects
The Effect of Phosphorus Segregation on the Intermediate-Temperature Embrittlement of Ferritic, Spheroidal Graphite Cast Iron. 557-561A
Applicability of Bond Percolation Theory to Intergranular Stress-Corrosion Cracking of Sensitized AISI 304 Stainless Steel. 775-787A
Dynamic Fracture Behavior of Ti—6Al—4V Alloy With Various Stabilities of β Phase. 1655-1666A
Fracture Toughness of Quaternary Al-Li-Cu-Mg Alloy Under Mode I, Mode II, and Mode III Loading Conditions. 2439-2452A

Crack propagation, High temperature effects
Low-Cycle Fatigue Behavior of Polycrystalline NiAl at 1000K. 309-319A

Crack propagation, Microstructural effects
The Orientation Dependence of Fatigue-Crack Growth in 8090 Aluminum—Lithium Plate. 575-588A

Crack propagation, Radiation effects
Effects of Simultaneous Boron and Nitrogen Implantation on Microhardness and Fatigue Properties of Fe—13Cr—15Ni Alloys. 193-202A

Crack propagation, Stress effects
Effect of Orientation on Crystallographic Cracking in Notched Nickel-Base Superalloy Single Crystal Subjected to Far-Field Cyclic Compression. 287-297A
Mixed-Mode I and II Fatigue Threshold and Crack Closure in Dual-Phase Steels. 1713-1723A
Forging Limits for an Aluminum Matrix Composite. I. Experimental Results. (Conference Paper) 2027-2038A
Low-Cycle Fatigue Properties of a SiC Whisker-Reinforced 2124 Aluminum Alloy. 2265-2274A
Micromechanical Modelling of Reinforcement Fracture in Particle-Reinforced Metal-Matrix Composites. 2403-2420A
Short Fatigue Crack Growth Behavior in a Ferritic-Bainitic Steel. 2421-2425A
The Influence of SiC Particulates on Fatigue Crack Propagation in a Rapidly Solidified Al-Fe-V-Si Alloy. 2453-2460A

Crack resistance
See Crack propagation

Cracking (fracturing)
See Crack initiation
Crack propagation
Stress corrosion cracking

Cratering (wear)
See Wear

Cratering (welding)
See Weld defects

Creep (materials)
See also Creep rate
Creep rupture strength
The Effect of Substrate on the Microstructure and Creep of Eutectic Indium-Tin. 2715-2722A

Creep (materials), Composition effects
The Effects of Hydrogen on the Mechanical Behavior of Austenitic Stainless Steels at Room Temperature. 1015-1023A

Creep (materials), Deformation effects
Superplastic Behavior of Two Ultrahigh Boron Steels. 1241-1248A

Creep (materials), High temperature effects
Low-Cycle Fatigue Behavior of Polycrystalline NiAl at 1000K. 309-319A

Creep (materials), Microstructural effects
Some Aspects of Thermomechanical Fatigue of AISI 304L Stainless Steel. II. Dislocation Arrangements. 407-413A

Creep (materials), Stress effects
Some Aspects of Thermomechanical Fatigue of AISI 304L Stainless Steel. I. Creep—Fatigue Damage. 401-406A

Creep (materials), Temperature effects
Comparison of Orthorhombic and Alpha-Two Titanium Aluminides as Matrices for Continuous SiC-Reinforced Composites. 1267-1283A

Creep limit
See Creep (materials)

Creep properties
See Creep (materials)

Creep rate, Heating effects
The Effect of Thermal Exposure on Microstructural Stability and Creep Resistance of a Two-Phase TiAl/Ti_3Al Lamellar Alloy. 2371-2381A

Creep rate, Microstructural effects
Modeling Creep Deformation of a Two-Phase TiAl/Ti_3Al Alloy With a Lamellar Microstructure. 2161-2171A

Creep rate, Stress effects
Creep and Intergranular Cracking of Ni—Cr—Fe—C in 360°C Argon. 1169-1183A
Effect of Iron on the Superplastic Deformation of Zn-22%Al. 2391-2401A
Creep Characteristics of Single Crystalline $Ni_3Al(Ta,B)$. 2477-2482A

Creep rupture strength, Cooling effects
On Morphologies, Microsegregation, and Mechanical Behavior of Directionally Solidified Cobalt-Base Superalloy at Medium Cooling Rate. 637-642A

Creeping
See Creep (materials)

Critical current (superconductivity), Alloying effects
Effect of Oxygen and Zirconium on the Growth and Superconducting Properties of Nb_3Sn. 203-212A
The Role of Oxygen and Zirconium in the Formation and Growth of Nb_3Sn Grains. 213-219A

Critical current (superconductivity), Microstructural effects
Directional Phase Formation on Melting via Peritectic Reaction. 1747-1760A

Cross tension test
See Tension tests

Crushing strength
See Compressive strength

Crystal defects
See also Dislocations
Displacements (lattice)
Stacking faults
The Role of Structural Ledges as Misfit-Compensating Defects: FCC-BCC Interphase Boundaries. (Conference Paper) 1895-1903A

Crystal lattices
See also Hexagonal lattice
Thermodynamics and Long-Range Order of Interstitials in a Hexagonal Close-Packed Lattice. 2797-2814A

Crystal orientation
See Crystal structure

Crystal structure
See also Quasicrystalline structure
Transmission Electron Microscopy Study of Martensites in Laser-Clad Ni—Al Bronze on Aluminium Alloy AA333. 37-46A
Triclinic Ni_2Al Phase in 63.1 at.% NiAl. 57-61A
Structure of As-Deposited Iron—Zinc Coatings From Chloride Bath. 249-255A
Ordering and Mechanical Strength in $L1_2$ Cubic Titanium Trialuminides. 449-451A
Surface Characterization and Reactivity of a Nitrogen Atomized 304L Stainless Steel Powder. 509-520A
Nanocrystalline Iron Sintering Behavior and Microstructural Development. 677-685A
The Effect of Steel Chemistry on the Formation of Fe-Zn Intermetallic Compounds of Galvanneal-Coated Steel Sheets. 721-730B
The Phenomenological Theory of Martensite Crystallography: Interrelationships. (Conference Paper) 1787-1795A
Ledges and Dislocations in Phase Transformations. (Conference Paper) 1885-1894A
Intrinsic Ledges at Interphase Boundaries and the Crystallography of Precipitate Plates. (Conference Paper) 1905-1915A
The Elastic Strain Energy of Growth Ledges on Coherent and Partially Coherent Precipitates. 2073-2082A
High-Resolution Analytical Electron Microscopy Study of Isothermal Plate-Shaped Products in Some β-Phase Alloys. (Conference Paper) 2569-2579A
Transformation Characteristics of α_1 Plates in Cu-Zn-Al Alloys. (Conference Paper) 2581-2599A
The Selection of Precipitate Habit Planes in Cr-32 wt.% Ni. (Conference Paper) 2639-2646A

Crystal structure, Alloying effects
Effect of Alloying Elements on the Solidification Characteristics and Microstructure of Al—Si—Cu—Mg—Fe 380 Alloy. 437-448A
Transmission Electron Microscopy Crystal Structure Study of the Chromium-Rich Phase in a Laser-Clad Nickel Alloy. 487-497A
The Fine Structure and Formation Mechanism of Lower Bainite. (Conference Paper) 1967-1980A

Crystal structure, Coating effects
Processing, Microstructure, and Properties of Laser-Clad Nickel Alloy FP-5 on Al Alloy AA333. 425-434B

Crystal structure, Cooling effects
Microstructure and Mechanical Properties of Ti—40 wt.% Ta (Ti—15 at.% Ta). 461-472A
Chemical Composition and Structural Identification of Eutectic Carbide in 1% Manganese Ductile Iron. 911-918A

Crystal structure, Deformation effects
Discussion of "The Role of Microstructure on Strength and Ductility of Hot-Extruded Mechanically Alloyed NiAl" and Author's Reply. 2303-2305A
Microstructure Development During Conventional and Isothermal Hot Forging of a Near-γ Titanium Aluminide. 2753-2768A

Crystal structure, Diffusion effects
Crystallographic Theories, Interface Structures, and Transformation Mechanisms. (Conference Paper) 1821-1839A
Application of the Theory of Martensite Crystallography to Displacive Phase Transformations in Substitutional Nonferrous Alloys. (Conference Paper, Review) 1841-1856A
A Comparison Between Three Simple Crystallographic Principles of Precipitate Morphology. (Conference Paper) 1857-1863A
Formation of Invariant Plane-Strain and Tent-Shaped Surface Reliefs by the Diffusional Ledge Mechanism. (Conference Paper) 1923-1931A

Crystal structure, Heating effects
Formation and Stability of Metastable Structures and Amorphous Phases in Pu—V, Pu—TA, and Pu—Yb Systems With Positive Heats of Mixing. 1579-1590A
Titanium-Rich Mineral Phases and the Nucleation of Bainite. 1603-1611A

Crystal structure, Stress effects
Behavior of Nickel-Base Superalloy Single Crystals Under Thermal—Mechanical Fatigue. 99-109A
Characterization of Inhomogeneous Elastic Deformation With X-Ray Diffraction. 341-347A
Transformation, Microcrack, and Thermal Residual Stress as Interactive Processes in ZrO_2-Toughened Al_2O_3, Simulated by the Finite Element Method. 1725-1731A
A History of the Controversy Over the Roles of Shear and Diffusion in Plate Formation Above M_d and a Comparison of the Atomic Mechanisms of These Processes. (Conference Paper, Review) 1797-1819A
Low-Cycle Fatigue of Dispersion-Strengthened Copper. 2235-2245A
Modeling the Effects of Stress State and Crystal Orientation on the Stress-Induced Transformation of NiTi Single Crystals. 2383-2389A
Creep Characteristics of Single Crystalline $Ni_3Al(Ta,B)$. 2477-2482A

Crystal structure, Temperature effects
Gradient Solid Electrolytes for Thermodynamic Measurements: System Na_2CO_3—Na_2SO_4. 173-180A
Temperature and Microstructural Dependence of the Deformation of a High Niobium, Titanium—Aluminum Alloy. 1667-1679A

Crystal structure, Welding effects
The α/β Interface Phase in Titanium Alloys: Artifact or Real Phase Contribution to Problem Resolution. 241-248A

Crystallinity
See Crystal structure

Crystallization
See also Recrystallization

Crystallization, Alloying effects
A Process for Debismuthizing Lead With Magnesium. 379-384B

Crystallization, Cooling effects
Crystallization Studies of the β' (Mg_2Pb) Phase and Its Phase Boundaries in the Pb—Mg—Bi System. 255-263B
Cubic AlNi Compound Dispersed Magnesium-Based Amorphous Matrix Composites Prepared by Rapid Solidification. 1323-1325A
Crystallization Behavior of Iron-Containing Intermetallic Compounds in 319 Aluminum Alloy. 1761-1773A

Crystallography
High-Resolution Analytical Electron Microscopy Study of Isothermal Plate-Shaped Products in Some β-Phase Alloys. (Conference Paper) 2569-2579A

Crystals
See Single crystals

CTT curves
See TTT curves

Curie point
See Curie temperature

Curie temperature, Alloying effects
Determination of Residual Nickel in Mechanically Alloyed NiAl. 871-874A

Current density
Physical Modeling Studies of Electrolyte Flow Due to Gas Evolution and Some Aspects of Bubble Behavior in Advanced Hall Cells. II. Flow and Interpolar Resistance in Cells With a Grooved Anode. 341-349B
A Mathematical Model of Ionic Transport in a Porous Diaphragm of a Chrome—Alum Cell. 351-358B

Current density, Microstructural effects
Influence of Near-Surface Microstructures on the Transient Current Response in Fe—Cr—Ni Alloys During Scratch Tests. 1325-1331A
Directional Phase Formation on Melting via Peritectic Reaction. 1747-1760A

Curves
See Stress strain curves
TTT curves

Cyanidation
Adsorption Kinetics of Dicyanoaurate and Dicyanoargentate Ions in Activated Carbon. 185-191B
Cyanide Inhibitors for the Carbon Cathode Materials in Aluminum Reduction Cells. 221-226B
An Electrochemical Study on the Dissolution of Gold and Copper from Gold/Copper Alloys. 817-827B
The Mechanism of Elution of Gold Cyanide From Activated Carbon. 829-838B

Cyanide process
See Cyanidation

Cycles
See Stress cycle

Cyclic loads
Effect of Orientation on Crystallographic Cracking in Notched Nickel-Base Superalloy Single Crystal Subjected to Far-Field Cyclic Compression. 287-297A
The Role of Magnesium-Containing Spheroidizer and Counteraction of Misch Metal in the Intermediate Temperature Intergranular Embrittlement of Ferritic Nodular Iron. 2305-2309A
Micromechanical Modelling of Reinforcement Fracture in Particle-Reinforced Metal-Matrix Composites. 2403-2420A
Low Cycle Fatigue Behavior of Polycrystalline Ni_3Al Alloys at Ambient and Elevated Temperatures. 2469-2476A

Damage
See Radiation damage

Damage tolerance, Heating effects
Heat Treatment of Investment Cast PH 13-8Mo Stainless Steel. I. Mechanical Properties and Microstructure. 789-798A

Damping, Heating effects
Mechanism of Damping Capacity of High-Chromium Steels and α-Iron and Its Dependence on Some External Factors. 111-124A

Decarbonizing
See Decarburizing

Decarburizing
Reduction of Chromite in Liquid Fe)Cr)C)Si Alloys. 549-559B

Decarburizing, Pressure effects
Kinetics of the Reaction of H_2O Gas With Liquid Iron. 245-253B

Decay
See Radioactive decay

Decomposition
See Phase decomposition

Decomposition reactions
See also Hydrolysis

Decomposition reactions, Temperature effects
Thermal Treatment of Complex Sulfide Ores in N_2 and H_2 Atmospheres: a New Approach for the Extraction of Their Valuable Elements. (Review) 193-205B

Deep carburizing
See Carburizing

Deep hardening
See Hardening

Defects
See Casting defects
Crystal defects
Inclusions
Surface defects
Weld defects

Deflagration
See Combustion

Deformability
See Formability

Deformation
See also Plastic deformation
A Plane Strain Punch Stretching Test for Evaluating Stamping Formability of Steel Sheets. 2199-2205A

Deformation, Radiation effects
Deformation Behavior of Irradiated Zr—2.5Nb Pressure Tube Material. 135-145A

Deforming
See Deformation

Degradation
See Corrosion

Delaminating
Efficient Measurement of Microstructural Surface Area Using Trisector. 919-928A

Delaminating, High temperature effects
Elevated Temperature Fracture of RS/PM Alloy 8009. I. Fracture Mechanics Behavior. 365-379A

Delta iron, Temperature effects
Fracture and the Formation of Sigma Phase, $M_{23}C_6$, and Austenite From Delta—Ferrite in an AISI 304L Stainless Steel. 1147-1158A

Dendrite
See Dendritic structure

Dendritic structure
Surface Characterization and Reactivity of a Nitrogen Atomized 304L Stainless Steel Powder. 509-520A

Dendritic structure, Cooling effects
Natural Convection in an Aluminum Ingot: a Mathematical Model. 293-302B
Three-Dimensional Simulation of the Grain Formation in Investment Castings. 629-635A
On Morphologies, Microsegregation, and Mechanical Behavior of Directionally Solidified Cobalt-Base Superalloy at Medium Cooling Rate. 637-642A
Further Discussions on the Solute Redistribution During Dendritic Solidification of Binary Alloys. 731-739B
Prediction of Columnar to Equiaxed Transition During Diffusion-Controlled Dendritic Alloy Solidification. 1081-1093A
Solidification Macrostructures and Macrosegregation in Aluminum Alloys Cooled From Above. 1097-1102A
Evolution of Interaction Domain Microstructure During Spray Deposition. 2341-2355A
Undercooling-Induced Macrosegregation in Directional Solidification. 2507-2516A

Dendritic structure, Field effects
The Effect of Enhanced Gravity Levels on Microstructural Development in Pb—50 wt.% Sn Alloys During Controlled Directional Solidification. 865-870A

Dendritic structure, Temperature effects
An Internal Variable Description of Solidification Suitable for Macrosegregation Modeling. 597-605B

Dendritic structure, Welding effects
Effect of Welding Variables and Solidification Substructure on Weld Metal Porosity. 2285-2294A

Densification
Determination of Pore Mobility During Sintering. 81-87A
Effect of Cobalt Addition on the Liquid-Phase Sintering of Tungsten—Copper Prepared by the Fluidized Bed Reduction Method. 1575-1578A

Density
Observations on the Effect of Medium Density and Viscosity on the Rate of Induced Aeration in Agitated Vessels. 303-306B
Physicochemical Properties of Nickel Electrolytes. 637-644B
Densities of Liquid Fe-Ni and Fe-Cr Alloys. 939-942B
High-Performance Ni_3Al Synthesized From Composite Powders. 985-992A

Density, High temperature effects
Density Measurements of the Lithium Fluoride/Lithium Sulfide Eutectic at High Temperature. 773-778B

Deoxidation
See Deoxidizing

Deoxidizing
Calcium Deoxidation Equilibrium in Liquid Iron. 33-42B

Deoxidizing, Alloying effects
Thermodynamics of Oxygen and Nitrogen in Liquid Nickel Equilibrated With $CaO—TiO_x$ and $CaO—TiO_x—Al_2O_3$ Melts. 5-13B

Dephosphorizing
A Thermodynamic Study of $BaO + BaCl_2 + Cr_2O_3$ Fluxes Used for the Removal of Phosphorus From Chromium-Containing Iron Melts. 695-701B

Deposition
See Electrodeposition
Sedimentation

Depth profiling
Surface Segregation of Calcium Oxide in Wustite and Its Effects on the Reduction. 405-413B
Gas Trapping and Release in Polycrystalline Nickel Preimplanted With Helium. 949-959A
Auger Electron Analysis of the Initial Oxidation of Titanium Aluminides Based on Ti—48Al. 1041-1050A

Desorption
Adsorption Kinetics of Dicyanoaurate and Dicyanoargentate Ions in Activated Carbon. 185-191B

Desorption, Radiation effects
Gas Trapping and Release in Polycrystalline Nickel Preimplanted With Helium. 949-959A

Desorption, Temperature effects
Barrier-Layer Formation and Its Control During Hydrogen Permeation Through Ti—24Al—11Nb Alloy. 89-97A

Detectors
See Sensors

Deuterium, Sorption
Gas Trapping and Release in Polycrystalline Nickel Preimplanted With Helium. 949-959A

Diagrams
See Stress strain curves

Diamond pyramid hardness, Coating effects
Processing, Microstructure, and Properties of Laser-Clad Nickel Alloy FP-5 on Al Alloy AA333. 425-434B

Diamond pyramid hardness, Pressure effects
The Effects of Hydrostatic Pressure on the Compressive Mechanical Behavior of $L1_2$ Al_3 Ti-Based Intermetallic. 1703-1711A

Die casting
Effect of Alloying Elements on the Solidification Characteristics and Microstructure of Al—Si—Cu—Mg—Fe 380 Alloy. 437-448A

Diffraction
See Electron diffraction
X ray diffraction

Diffusion
Determination of Pore Mobility During Sintering. 81-87A
Adsorption Kinetics of Dicyanoaurate and Dicyanoargentate Ions in Activated Carbon. 185-191B
Cyanide Inhibitors for the Carbon Cathode Materials in Aluminum Reduction Cells. 221-226B
Interactions Between Drops of a Molten Aluminum)Lithium Alloy and Liquid Water. 623-625B
Multiphase Binary Diffusion in Infinite and Semi-Infinite Media. I. On the Determination of Interdiffusion Coefficients. 741-751A
Multiphase Binary Diffusion in Infinite and Semi-Infinite Media. II. On the Numerical Calculation of the Rate Constants for Formation of Product Phases. 753-761A
η to G Phase Transformation in Electrodeposited Iron—Zinc Alloy Coatings. 1119-1125A
Intrinsic Ledges at Interphase Boundaries and the Crystallography of Precipitate Plates. (Conference Paper) 1905-1915A
High-Resolution Analytical Electron Microscopy Study of Isothermal Plate-Shaped Products in Some β-Phase Alloys. (Conference Paper) 2569-2579A
Growth Kinetics and High-Temperature TEM In Situ Observation of Bainite in a Cu-Zn Alloy. (Conference Paper) 2609-2614A
Study on the Transformation Mechanism of α_1 Plates in a Copper-Zinc-Aluminum Alloy. (Conference Paper) 2615-2619A
Mechanism of the Early Stages of α_1 Plate Formation in a Cu-39% Zinc Alloy. (Conference Paper) 2631-2637A
Diffusion-Controlled Growth in Ternary Systems. 2683-2694A
Diffusional Boundary Conditions During Coarsening of Elastically Interacting Precipitates. 2695-2703A

Diffusion, Alloying effects
Effect of Oxygen and Zirconium on the Growth and Superconducting Properties of Nb_3Sn. 203-212A
On the Prebainitic Phenomenon in Some Alloys. (Conference Paper) 1941-1946A
Thermodynamics and Kinetics of the Formation of Widmanstätten Ferrite Plates in Ferrous Alloys. (Conference Paper) 1947-1953A
Elevated-Temperature Stability of Mechanically Alloyed Copper-Niobium Powders. 2091-2099A

Diffusion, Cooling effects
Further Discussions on the Solute Redistribution During Dendritic Solidification of Binary Alloys. 731-739B
Prediction of Columnar to Equiaxed Transition During Diffusion-Controlled Dendritic Alloy Solidification. 1081-1093A
Microsegregation in Cellular Solidification. 2295-2301A

Diffusion, Diffusion effects
Decomposition of Iron—Nickel Martensite: Implications for the Low-Temperature (≤ 500°C) Fe—NI Phase Diagram. 1627-1637A

Diffusion, Heating effects
Hydrogen Permeation Behavior in IN718 and GH761 Superalloys. 539-544A
Heat Treatment of Investment Cast PH 13-8 Molybdenum Stainless Steel. II. Isothermal Aging Kinetics. 697-704A
Computer Simulation of Diffusion in Multiphase Systems. 1127-1134A
Interstitial Precipitation in Fe—Cr—Al Alloys. 1135-1146A
A Structural Study of Oxidation in a Zirconia-Toughened Alumina Fiber-Reinforced NiAl Composite. 1291-1299A

Diffusion, Low temperature effects
Numerical Modeling of γ Precipitate Growth During Fe—Ni Martensite Decomposition at Low Temperatures (≤ 400°C). 1639-1648A

Diffusion, Radiation effects
Helium 3 Precipitation in AISI 316L Stainless Steel Induced by Radioactive Decay of Tritium: Growth Mechanism of Helium Bubbles. 2131-2143A

Diffusion, Stress effects
A History of the Controversy Over the Roles of Shear and Diffusion in Plate Formation Above M_d and a Comparison of the Atomic Mechanisms of These Processes. (Conference Paper, Review) 1797-1819A
Effect of Iron on the Superplastic Deformation of Zn-22%Al. 2391-2401A

Diffusion, Temperature effects
Barrier-Layer Formation and Its Control During Hydrogen Permeation Through Ti—24Al—11Nb Alloy. 89-97A
An Internal Variable Description of Solidification Suitable for Macrosegregation Modeling. 597-605B
Anomalous Diffusion of Aluminum in β-Titanium. 873-876A
Numerical Modeling of Solidification and Subsequent Transformation of Fe—Cr—Ni Alloys. 1309-1321A
Kinetics of Interlayer Formation on Polycrystalline α-Al_2O_3/Copper-Titanium Alloy Interface. 2083-2090A

Diffusion bonding
See Diffusion welding

Diffusion coating
Multiphase Binary Diffusion in Infinite and Semi-Infinite Media. I. On the Determination of Interdiffusion Coefficients. 741-751A

Diffusion coating (process)
See Diffusion coating

Diffusion coefficient
See Diffusion

Diffusion couples
See Diffusion

Diffusion welding
Characterization of a Diffusion-Bonded Al—Mg Alloy/SiC Interface by High Resolution and Analytical Electron Microscopy. 617-627A

Diffusivity, Environmental effects
Modeling Hydrogen Entry and Exit in Metals Exposed to Multiple Charging Processes. 723-732A

Diffusivity, Heating effects
Role of Al_2O_3 Particulate Reinforcements on Precipitation in 2014 Aluminum-Matrix Composites. 1591-1602A

Direct chill casting
Solidification Macrostructures and Macrosegregation in Aluminum Alloys Cooled From Above. 1097-1102A

Directional solidification
On Morphologies, Microsegregation, and Mechanical Behavior of Directionally Solidified Cobalt-Base Superalloy at Medium Cooling Rate. 637-642A
Further Discussions on the Solute Redistribution During Dendritic Solidification of Binary Alloys. 731-739B
The Effect of Enhanced Gravity Levels on Microstructural Development in Pb—50 wt.% Sn Alloys During Controlled Directional Solidification. 865-870A
Directional Phase Formation on Melting via Peritectic Reaction. 1747-1760A
Undercooling-Induced Macrosegregation in Directional Solidification. 2507-2516A

Dislocation climb
See Dislocation mobility

Dislocation density
Some Aspects of Thermomechanical Fatigue of AISI 304L Stainless Steel. II. Dislocation Arrangements. 407-413A
Strain Hardening in Underaged Inconel 718. 653-656A
Heat Treatment of Investment Cast PH 13-8Mo Stainless Steel. I. Mechanical Properties and Microstructure. 789-798A
Influence of Near-Surface Microstructures on the Transient Current Response in Fe—Cr—Ni Alloys During Scratch Tests. 1325-1331A

Dislocation density, Composition effects
The Effects of Hydrogen on the Mechanical Behavior of Austenitic Stainless Steels at Room Temperature. 1015-1023A

Dislocation density, Deformation effects
Microstructural Control in Hot Working of IN-718 Superalloy Using Processing Map. 2275-2284A
Discussion of "The Role of Microstructure on Strength and Ductility of Hot-Extruded Mechanically Alloyed NiAl" and Author's Reply. 2303-2305A

Dislocation density, Heating effects
Heat Treatment of Investment Cast PH 13-8 Molybdenum Stainless Steel. II. Isothermal Aging Kinetics. 697-704A
Role of Al_2O_3 Particulate Reinforcements on Precipitation in 2014 Aluminum-Matrix Composites. 1591-1602A

Dislocation density, Low temperature effects
Numerical Modeling of γ Precipitate Growth During Fe—Ni Martensite Decomposition at Low Temperatures (≤ 400°C). 1639-1648A

Dislocation density, Radiation effects
Helium 3 Precipitation in AISI 316L Stainless Steel Induced by Radioactive Decay of Tritium: Microstructural Study of Helium Bubble Precipitation. 2117-2130A

Dislocation density, Stress effects
A Simplified Method of Calculating the Stress Field at the Tip of a Discrete Dislocation Pileup in a Finite Crystal. 223-225A
Low-Cycle Fatigue of Dispersion-Strengthened Copper. 2235-2245A
Low Cycle Fatigue Behavior of Polycrystalline Ni_3Al Alloys at Ambient and Elevated Temperatures. 2469-2476A

Dislocation loops, Diffusion effects
A Comparison Between Three Simple Crystallographic Principles of Precipitate Morphology. (Conference Paper) 1857-1863A
On the Role of Interphase-Boundary Structure in Plate Growth by Diffusional Mechanisms. (Conference Paper) 1875-1883A

Dislocation mobility, Composition effects
The Effects of Hydrogen on the Mechanical Behavior of Austenitic Stainless Steels at Room Temperature. 1015-1023A

Dislocation mobility, Deformation effects
The Tensile Deformation Behavior of AA 3004 Aluminum Alloy. 357-364A

Dislocation mobility, Diffusion effects
Crystallographic Theories, Interface Structures, and Transformation Mechanisms. (Conference Paper) 1821-1839A
On the Role of Interphase-Boundary Structure in Plate Growth by Diffusional Mechanisms. (Conference Paper) 1875-1883A

Dislocation mobility, Stress effects
A History of the Controversy Over the Roles of Shear and Diffusion in Plate Formation Above M_d and a Comparison of the Atomic Mechanisms of These Processes. (Conference Paper, Review) 1797-1819A
Effect of Iron on the Superplastic Deformation of Zn-22%Al. 2391-2401A
Creep Characteristics of Single Crystalline Ni_3Al(Ta,B). 2477-2482A

Dislocations
See also Dislocation loops
Edge dislocations
Screw dislocations

Ledges and Dislocations in Phase Transformations. (Conference Paper) 1885-1894A
The Role of Structural Ledges as Misfit-Compensating Defects: FCC-BCC Interphase Boundaries. (Conference Paper) 1895-1903A
Intrinsic Ledges at Interphase Boundaries and the Crystallography of Precipitate Plates. (Conference Paper) 1905-1915A

Dislocations, Alloying effects
Effects of Carbon Content and Ausaging on $\gamma \rightleftarrows \alpha'$ Transformation Behavior and Reverse-Transformed Structure in Fe—Ni—Co—Al—C Alloys. 63-71A

Dislocations, Deformation effects
Effects of Precursor Matrix Events on Subsequent Nucleation. (Conference Paper) 1933-1939A

Dislocations, Diffusion effects
Application of the Theory of Martensite Crystallography to Displacive Phase Transformations in Substitutional Nonferrous Alloys. (Conference Paper, Review) 1841-1856A
The Invariant Line and Precipitate Morphology in FCC-BCC Systems. (Conference Paper) 1865-1874A

Dislocations, Heating effects
Mechanism of Damping Capacity of High-Chromium Steels and α-Iron and Its Dependence on Some External Factors. 111-124A
Aging of Freshly Formed Iron-Based Martensites at Low Temperatures. (Review) 889-909A
Interstitial Precipitation in Fe—Cr—Al Alloys. 1135-1146A

Dislocations, Radiation effects
Deformation Behavior of Irradiated Zr—2.5Nb Pressure Tube Material. 135-145A
Helium 3 Precipitation in AISI 316L Stainless Steel Induced by Radioactive Decay of Tritium: Growth Mechanism of Helium Bubbles. 2131-2143A

Dispersing
See Emulsification

Dispersion hardening, Cooling effects
Characterization of Mechanically Alloyed Oxide Dispersion-Strengthened Nickel-Base Superalloy MA760. 705-714A

Displacement spikes
See Displacements (lattice)

Displacements (lattice)
Intrinsic Ledges at Interphase Boundaries and the Crystallography of Precipitate Plates. (Conference Paper) 1905-1915A

Displacements (lattice), Diffusion effects
Crystallographic Theories, Interface Structures, and Transformation Mechanisms. (Conference Paper) 1821-1839A

Dissimilar materials, Brazing
Spreading and Interlayer Formation at the Copper-Copper Oxide/Polycrystalline Alumina Interface. 2497-2506A

Dissimilar materials, Welding
Characterization of a Diffusion-Bonded Al—Mg Alloy/SiC Interface by High Resolution and Analytical Electron Microscopy. 617-627A

Dissimilar metals, Soldering
The Effect of Low Gold Concentrations on the Creep of Eutectic Tin—Lead Joints. 1249-1257A

Dissimilar metals, Welding
Effect of Welding Variables and Solidification Substructure on Weld Metal Porosity. 2285-2294A

Dissociated ammonia brazing
See Brazing

Dissociation energy
See Free energy
Heat of formation

Dissolution
Equilibrium Values for the Dissolution of Solid Copper Into FeS—Na_2S Mattes. 306-308B
Small Cell Experiments for Electrolytic Reduction of Uranium Oxides to Uranium Metal Using Fluoride Salts. 505-518B
Local Melting in Al—Mg—Zn—Alloys. 521-530A
An Electrochemical Study on the Dissolution of Gold and Copper from Gold/Copper Alloys. 817-827B

Dissolution, Alloying effects
The Role of Oxygen and Zirconium in the Formation and Growth of Nb_3Sn Grains. 213-219A

Dissolution, Cooling effects
Characterization of Mechanically Alloyed Oxide Dispersion-Strengthened Nickel-Base Superalloy MA760. 705-714A

Dissolution, Environmental effects
On Low-Temperature Environment-Assisted Fatigue Crack Propagation. 658-659A

Dissolution, Heating effects
Computer Simulation of Diffusion in Multiphase Systems. 1127-1134A
Interstitial Precipitation in Fe—Cr—Al Alloys. 1135-1146A

Dissolution, pH effects
Simulation of In Situ Uraninite Leaching. I. A Partial Equilibrium Model of the NH_4HCO_3—$(NH_4)_2CO_3$—H_2O_2 Leaching System. 171-183B

Dissolution, Stress effects
Fiber Strength and Fiber/Matrix Bond Strength in Single Crystal Al_2O_3 Fiber Reinforced Ni_3Al Based Composites. 1259-1265A

Dissolution, Temperature effects
Solubility and Thermodynamic Properties of Y_2O_3 in LiF—YF_3 Melts. 91-96B
Thermal Treatment of Complex Sulfide Ores in N_2 and H_2 Atmospheres: a New Approach for the Extraction of Their Valuable Elements. (Review) 193-205B

Dissolving
See Dissolution

Drawing (heat treatment)
See Tempering

Drop tests
See Impact tests

Dual phase steels, Mechanical properties
Mixed-Mode I and II Fatigue Threshold and Crack Closure in Dual-Phase Steels. 1713-1723A

Ductile brittle transition, Heating effects
Dynamic Fracture Behavior of Ti—6Al—4V Alloy With Various Stabilities of β Phase. 1655-1666A

Ductile fracture, Heating effects
Fracture Toughness of Quaternary Al-Li-Cu-Mg Alloy Under Mode I, Mode II, and Mode III Loading Conditions. 2439-2452A

Ductile fracture, Microstructural effects
The Study of Adiabatic Shear Band Instability in a Pearlitic 4340 Steel Using a Dynamic Punch Test. 2483-2489A

Ductile fracture, Stress effects
Evaluation of Static and Dynamic Fracture Toughness in Ductile Cast Iron. 2427-2437A

Ductile iron
See Nodular iron

Ductility
Factors Influencing the Exceptional Ductility of a Superplastic Pb-62% Sn Alloy. 2309-2311A
The Effect of Inertia on Tensile Ductility. 2723-2735A

Ductility, Alloying effects
Elevated-Temperature Stability of Mechanically Alloyed Copper-Niobium Powders. 2091-2099A

Ductility, Composition effects
The Effect of Niobium Morphology on the Cyclic Oxidation Resistance of $MoSi_2$/20 vol.% Niobium Composites. 1033-1040A
Room-Temperature Strength and Deformation of TiB_2-Reinforced Near-γ Titanium Aluminides. 2181-2197A

Ductility, Deformation effects
High-Temperature Deformation of B2 NiAl-Base Alloys. (Conference Paper) 2017-2026A
Superplastic Behavior of Thermomechanically Treated P/M 7091 Aluminum Alloy. 2153-2160A
Discussion of "The Role of Microstructure on Strength and Ductility of Hot-Extruded Mechanically Alloyed NiAl" and Author's Reply. 2303-2305A

Ductility, Environmental effects
Environmental Effect on Room-Temperature Ductility of Isothermally Forged TiAl-Base Alloys. 321-330A
Embrittlement of B2 Iron Aluminide by Water Vapor and by Hydrogen. 1285-1290A

Ductility, Heating effects
The Effects of Double Austenitization on the Mechanical Properties of a 0.34C Containing Low-Alloy Ni—Cr—Mo—V Steel. 545-555A
Heat Treatment of Investment Cast PH 13-8Mo Stainless Steel. I. Mechanical Properties and Microstructure. 789-798A
Effect of Heat Treatment on the Microstructure, Tensile Properties, and Fracture Behavior of Permanent Mold Al-10 wt.% Si-0.6 wt.% Mg/SiC/10p Composite Castings. 2247-2263A
The Role of Magnesium-Containing Spheroidizer and Counteraction of Misch Metal in the Intermediate Temperature Intergranular Embrittlement of Ferritic Nodular Iron. 2305-2309A

Ductility, High temperature effects
The Workability of Commercial and Experimental 0.6% Carbon Low Alloy Steels in the Temperature Range of 650-870°C. 827-837A

Ductility, Microstructural effects
Microstructure and Mechanical Properties of Ti—40 wt.% Ta (Ti—15 at.% Ta). 461-472A
Microstructural Analysis of Fracture Toughness Variation in 2XXX-Series Aluminum Alloy Composites Reinforced With SiC Whiskers. 2213-2223A

Ductility, Stress effects
Tensile Ductility of Extrinsically Toughened Intermetallics. 299-308A
The Effect of Triaxial Stress on Ductility and Fracture Morphology of Ferritic Spheroidal Graphite Cast Iron. 821-825A
Coefficients of Thermal Expansion of Metal-Matrix Composites for Electronic Packaging. 839-850A
Creep and Intergranular Cracking of Ni—Cr—Fe—C in 360°C Argon. 1169-1183A
Fiber Strength and Fiber/Matrix Bond Strength in Single Crystal Al_2O_3 Fiber Reinforced Ni_3Al Based Composites. 1259-1265A
Evaluation of Static and Dynamic Fracture Toughness in Ductile Cast Iron. 2427-2437A
Fracture Toughness of Discontinuously Reinforced Al-4Cu-1.5Mg/TiB_2 Composites. 2461-2468A

Ductility, Temperature effects
Behavior of Steels Near the Incipient Melting Temperature. 125-133A

Dynamic loads
See Loads (forces)

Dynamic tests
See Impact tests

Dynamics
See Kinetics

Edge dislocations, Diffusion effects
On the Role of Interphase-Boundary Structure in Plate Growth by Diffusional Mechanisms. (Conference Paper) 1875-1883A

Edge dislocations, Stress effects
A Simplified Method of Calculating the Stress Field at the Tip of a Discrete Dislocation Pileup in a Finite Crystal. 223-225A

Elastic constants
See also Magnetoelastic effect
Modulus of elasticity
Poissons ratio
The Role of Structural Ledges as Misfit-Compensating Defects: FCC-BCC Interphase Boundaries. (Conference Paper) 1895-1903A
Elastic Constants of SiC_p/Al: Measurements and Modeling. 2832-2835A

Elastic modulus
See Modulus of elasticity

Elastic properties
See Elastic constants

Elasticity
See also Pseudoelasticity

Elasticity, Composition effects
The Effects of Hydrogen on the Mechanical Behavior of Austenitic Stainless Steels at Room Temperature. 1015-1023A

Elasticity, Deformation effects
Modeling of Mechanical Alloying. I. Deformation, Coalescence, and Fragmentation Mechanisms. 147-158A
Modeling the Thin-Slab Continuous-Casting Mold. 443-457B

Elasticity, Diffusion effects
The Invariant Line and Precipitate Morphology in FCC-BCC Systems. (Conference Paper) 1865-1874A

Elasticity, Microstructure
The Elastic Strain Energy of Growth Ledges on Coherent and Partially Coherent Precipitates. 2073-2082A

Elasticity, Stress effects
Characterization of Inhomogeneous Elastic Deformation With X-Ray Diffraction. 341-347A
Analysis of Thermally Induced Stress and Strain in Continuous Fiber-Reinforced Composites. 415-425A

Electric conductors (materials)
See Electrolytes
Superconductors

Electric generators
See Solar generators

Electric potential, Temperature effects
Oxygen Potentials in Nickel + NiO and Nickel + Cr_2O_3 + $NiCr_2O_4$ Systems. 373-378B

Electrical conductivity
See Resistivity

Electrical phenomena
See Electric potential

Electrical properties
See Critical current (superconductivity)
Current density
Resistivity

Electrical resistivity
See Resistivity

Electroceramics
See Ceramics

Electrochemistry
Sulfur Determination in Carbon-Saturated Iron by Solid-State Electrochemical Sensor. 561-568B
Kinetics in Muliticomponent Metallic)Ionic Systems. 579-587B
An Electrochemical Study on the Dissolution of Gold and Copper from Gold/Copper Alloys. 817-827B

Electrochemistry, Diffusion effects
Tritium Distribution at the Crack Tip of High-Strength Steels Submitted to Stress Corrosion Cracking. 1159-1167A

Electrochemistry, Environmental effects
Modeling Hydrogen Entry and Exit in Metals Exposed to Multiple Charging Processes. 723-732A

Electrode potentials
See Corrosion potential

Electrodeposition
Structure of As-Deposited Iron—Zinc Coatings From Chloride Bath. 249-255A
η to G Phase Transformation in Electrodeposited Iron—Zinc Alloy Coatings. 1119-1125A

Electrodes
See Anodes

Electrogas welding
See Gas metal arc welding

Electrolysis
See also Reduction (electrolytic)
Thermodynamic Stability of Metallurgical Coke Relative to Graphite. 149-151B
Physical Modeling Studies of Electrolyte Flow Due to Gas Evolution and Some Aspects of Bubble Behavior in Advanced Hall Cells. I. Flow in Cells With a Flat Anode. 333-340B
Physical Modeling Studies of Electrolyte Flow Due to Gas Evolution and Some Aspects of Bubble Behavior in Advanced Hall Cells. II. Flow and Interpolar Resistance in Cells With a Grooved Anode. 341-349B

Electrolytes, Phases (state of matter)
Gradient Solid Electrolytes for Thermodynamic Measurements: System Na_2CO_3—Na_2SO_4. 173-180A

Electrolytic cells
See also Bi-polar cells
Oxygen Potentials in Nickel + NiO and Nickel + Cr_2O_3 + $NiCr_2O_4$ Systems. 373-378B
Small Cell Experiments for Electrolytic Reduction of Uranium Oxides to Uranium Metal Using Fluoride Salts. 505-518B

Electrolytic deposition
See Electrodeposition

Electrolytic reduction
See Reduction (electrolytic)

Electromagnetic stirring
Measurements of the Electrical Conductivity of Wood's Alloy and Other Low Melting Point Alloys. 937-939B

Electrometallurgy
Physical Modeling Studies of Electrolyte Flow Due to Gas Evolution and Some Aspects of Bubble Behavior in Advanced Hall Cells. I. Flow in Cells With a Flat Anode. 333-340B
Physical Modeling Studies of Electrolyte Flow Due to Gas Evolution and Some Aspects of Bubble Behavior in Advanced Hall Cells. II. Flow and Interpolar Resistance in Cells With a Grooved Anode. 341-349B
A Mathematical Model of Ionic Transport in a Porous Diaphragm of a Chrome—Alum Cell. 351-358B
Energy Efficiency Considerations on Monopolar vs. Bipolar Fused Salt Electrolysis Cells. 661-668B

Electromotive force
See Electric potential

Electron beam processing
See Electron beam welding

Electron beam welding
The Influence of Electron-Beam Welding Parameters on Heat-Affected-Zone Microfissuring in Incoloy 903. 1733-1745A

Electron diffraction
Crystallographic Characteristics of the Al—Co Decagonal Quasicrystal and Its Monoclinic Approximant τ^2-$Al_{13}Co_4$. 47-56A
Triclinic Ni_2Al Phase in 63.1 at.% NiAl. 57-61A

Electron microprobes
See Electron probes

Electron microscopy
See also Transmission electron microscopy
Characterization of a Diffusion-Bonded Al—Mg Alloy/SiC Interface by High Resolution and Analytical Electron Microscopy. 617-627A

Electron probes
Kinetics in Muliticomponent Metallic)Ionic Systems. 579-587B

Electron spectroscopy
See Auger electron spectroscopy
Photoelectron spectroscopy

Electron structure
See Electronic structure

Electronic structure
Triclinic Ni_2Al Phase in 63.1 at.% NiAl. 57-61A
The Effect of Steel Chemistry on the Formation of Fe-Zn Intermetallic Compounds of Galvanneal-Coated Steel Sheets. 721-730B
Discussion of "Crystallographic Characterization of the Al-Co Decagonal Quasicrystal and Its Monoclinic Approximant τ^2-$Al_{13}Co_4$". 2535-2538A

Electronic structure, Diffusion effects
Formation of Invariant Plane-Strain and Tent-Shaped Surface Reliefs by the Diffusional Ledge Mechanism. (Conference Paper) 1923-1931A

Electropotential
See Electric potential

Electroreduction
See Electrowinning

Electrorefining
Physicochemical Properties of Nickel Electrolytes. 637-644B

Electrowinning
See also Hall Heroult process
Thermodynamic Stability of Metallurgical Coke Relative to Graphite. 149-151B
A Mathematical Model of Ionic Transport in a Porous Diaphragm of a Chrome—Alum Cell. 351-358B
Physicochemical Properties of Nickel Electrolytes. 637-644B

Elevated temperature
See High temperature

Elongation
High-Performance Ni_3Al Synthesized From Composite Powders. 985-992A
Factors Influencing the Exceptional Ductility of a Superplastic Pb-62% Sn Alloy. 2309-2311A

Elongation, Composition effects
Melt-Processed Ni_3Al Matrix Composites Reinforced With TiC Particles. 2525-2534A

Elongation, Cooling effects
On Morphologies, Microsegregation, and Mechanical Behavior of Directionally Solidified Cobalt-Base Superalloy at Medium Cooling Rate. 637-642A

Elongation, Deformation effects
Superplastic Behavior of Two Ultrahigh Boron Steels. 1241-1248A

Superplastic Behavior of Thermomechanically Treated P/M 7091 Aluminum Alloy. 2153-2160A

Elongation, Environmental effects
Environmental Effect on Room-Temperature Ductility of Isothermally Forged TiAl-Base Alloys. 321-330A
Hydride Embrittlement in Zircaloy-4 Plate. I. Influence of Microstructure on the Hydride Embrittlement in Zircaloy-4 at 20 and 350°C. 1185-1197A

Elongation, Heating effects
Effect of Heat Treatment on the Microstructure, Tensile Properties, and Fracture Behavior of Permanent Mold Al-10 wt.% Si-0.6 wt.% Mg/SiC/10p Composite Castings. 2247-2263A

Elongation, Microstructural effects
Precipitation Effects During Hot Deformation of a Copper Alloy. 257-266A

Embrittlement
See also Hydrogen embrittlement

Embrittlement, Heating effects
The Effect of Phosphorus Segregation on the Intermediate-Temperature Embrittlement of Ferritic, Spheroidal Graphite Cast Iron. 557-561A
The Role of Magnesium-Containing Spheroidizer and Counteraction of Misch Metal in the Intermediate Temperature Intergranular Embrittlement of Ferritic Nodular Iron. 2305-2309A

Embrittlement, Stress effects
Low Cycle Fatigue Behavior of Polycrystalline Ni_3Al Alloys at Ambient and Elevated Temperatures. 2469-2476A

Emissivity, Heating effects
Computer Algorithms for Radiometric Measurement of Temperature During the Galvanneal Process. 449-462B

Emulsification
Modeling of Metallurgical Emulsions. 855-864B
Densities of Liquid Fe-Ni and Fe-Cr Alloys. 939-942B

Energy
See Free energy
Surface energy

Energy of activation
See Activation energy

Energy of dissociation
See Free energy
Heat of formation

Energy of formation
See Free energy
Heat of formation

Energy of fracture
See Toughness

Energy of solution
See Free energy
Heat of solution

Engine components
See also Turbine blades

Engine components, Fabrication
Microstructural Control in Hot Working of IN-718 Superalloy Using Processing Map. 2275-2284A

Engines
See Gas turbine engines
Turbojet engines

Enthalpy
Standard Enthalpies of Formation of Some Praseodymium Alloys of High-Temperature Direct Synthesis Calorimetry. 73-77B
Solubility and Thermodynamic Properties of Y_2O_3 in LiF—YF_3 Melts. 91-96B
Surface Segregation of Calcium Oxide in Wustite and Its Effects on the Reduction. 405-413B

Entropy
Solubility and Thermodynamic Properties of Y_2O_3 in LiF—YF_3 Melts. 91-96B

Entropy of activation
See Activation energy
Entropy

Entropy of formation
See Entropy
Heat of formation

Entropy of reaction
See Entropy

Entropy of solution
See Entropy
Heat of solution

Entropy of transformation
See Entropy

Environment
See Corrosion environments

Equilibrium
See Chemical equilibrium

Equilibrium constants
See Chemical equilibrium

Esso Little process
See Fluidized bed reduction

Eutectic reactions, Temperature effects
Mg—Pb Phase Diagram and Phase Transformations in the Intermetallic Compounds Mg_2Pb and β'. 265-275B

Eutectic reactions, Welding effects
The Influence of Electron-Beam Welding Parameters on Heat-Affected-Zone Microfissuring in Incoloy 903. 1733-1745A

Eutectics, High temperature effects
Density Measurements of the Lithium Fluoride/Lithium Sulfide Eutectic at High Temperature. 773-778B

Eutectoid reactions, Diffusion effects
Decomposition of Iron—Nickel Martensite: Implications for the Low-Temperature (≤ 500°C) Fe—NI Phase Diagram. 1627-1637A

Expansion
See Thermal expansion

Explosions
Interactions Between Drops of a Molten Aluminum)Lithium Alloy and Liquid Water. 623-625B

Extraction
See Carbon in pulp process
Cyanidation

Extractive metallurgy
See also Electrometallurgy
Hydrometallurgy
Pyrometallurgy
Solid-Solution Formation Between Arsenic and Antimony Oxides. 865-871B
Thermal Separation of Arsenic and Antimony Oxides. 873-884B
A Thermodynamic Study of the Molybdenum-Oxygen System. 885-891B

Extrusion
See Hot extrusion

Extrusion casting
See Pressure casting

Extrusions, Microstructure
Discussion of "The Distribution of Dispersoid Phases in the Extruded ODS Superalloy MA-957 and Reply. 651-653A

Failure
See Delaminating
Fatigue failure

Fatigue (materials)
See also Bending fatigue
Fatigue life
Fatigue strength
Low cycle fatigue
Thermal fatigue

Fatigue (materials), Coating effects
The Influence of Laser Glazing on Fatigue Crack Growth in Ti—24Al—11Nb. 183-192A

Fatigue (materials), Cooling effects
Fatigue Crack Growth Rates and Fracture Toughness of Rapidly Solidified Al—8.5Fe—1.2V—1.7Si Alloys. 1005-1014A

Fatigue (materials), Environmental effects
On Low-Temperature Environment-Assisted Fatigue Crack Propagation. 658-659A

Fatigue (materials), Microstructural effects
Some Aspects of Thermomechanical Fatigue of AISI 304L Stainless Steel. II. Dislocation Arrangements. 407-413A

Fatigue (materials), Stress effects
Behavior of Nickel-Base Superalloy Single Crystals Under Thermal—Mechanical Fatigue. 99-109A
Effect of Orientation on Crystallographic Cracking in Notched Nickel-Base Superalloy Single Crystal Subjected to Far-Field Cyclic Compression. 287-297A
Some Aspects of Thermomechanical Fatigue of AISI 304L Stainless Steel. I. Creep—Fatigue Damage. 401-406A
Mixed-Mode I and II Fatigue Threshold and Crack Closure in Dual-Phase Steels. 1713-1723A
Short Fatigue Crack Growth Behavior in a Ferritic-Bainitic Steel. 2421-2425A
The Influence of SiC Particulates on Fatigue Crack Propagation in a Rapidly Solidified Al-Fe-V-Si Alloy. 2453-2460A

Fatigue cracking
See Fatigue (materials)
Fatigue failure

Fatigue failure, Microstructural effects
The Orientation Dependence of Fatigue-Crack Growth in 8090 Aluminum—Lithium Plate. 575-588A

Fatigue fracture
See Fatigue failure

Fatigue life, High temperature effects
Effect of Strain Rate on the High-Temperature Low-Cycle Fatigue Properties of a Nimonic PE-16 Superalloy. 159-171A
Low-Cycle Fatigue Behavior of Polycrystalline NiAl at 1000K. 309-319A

Fatigue life, Radiation effects
Effects of Simultaneous Boron and Nitrogen Implantation on Microhardness and Fatigue Properties of Fe—13Cr—15Ni Alloys. 193-202A

Fatigue life, Stress effects
Low-Cycle Fatigue of Dispersion-Strengthened Copper. 2235-2245A

Fatigue properties
See Fatigue (materials)

Fatigue strength, Cooling effects
Modeling Microstructure Development in Gray Cast Irons. 1063-1079A

Fatigue strength, Stress effects
Low Cycle Fatigue Behavior of Polycrystalline Ni_3Al Alloys at Ambient and Elevated Temperatures. 2469-2476A

Ferric compounds
See Iron compounds

Ferrite
The Chromium Equivalents of Ferrite Stabilizers in Commercial Stainless Steels. 2827-2828A

Ferrite, Alloying effects
Morphological Stability of γ/α Interface Formed by Carburization in Fe—C—X Alloys. 531-537A
Effects of Austenite Grain Size and Cooling Rate on Widmanstätten Ferrite Formation in Low-Alloy Steels. 665-675A
Thermodynamics and Kinetics of the Formation of Widmanstätten Ferrite Plates in Ferrous Alloys. (Conference Paper) 1947-1953A
The Fine Structure and Formation Mechanism of Lower Bainite. (Conference Paper) 1967-1980A
The Influence of the Alloying Elements Upon the Transformation Kinetics and Morphologies of Ferrite Plates in Alloy Steels. (Conference Paper) 1991-2000A

Ferrite, Cooling effects
Effects of Widmanstätten Ferrite on the Mechanical Properties of a 0.2% C—0.7% Mn Steel. 763-773A
Intragranular Ferrite Nucleation in Medium-Carbon Vanadium Steels. 929-936A
Modeling Microstructure Development in Gray Cast Irons. 1063-1079A
Precipitation of BCC Phase from Nonequilibrium A13-Type Phase in Rapidly Solidified High-Carbon Fe-Cr-Mo Alloy. 2542-2546A

Ferrite, Deformation effects
Effects of Precursor Matrix Events on Subsequent Nucleation. (Conference Paper) 1933-1939A

Ferrite, Diffusion effects
Diffusion in Growth of Bainite. (Conference Paper) 1957-1966A
Formation Mechanism of Bainitic Ferrite in an Fe)2% Si)0.6% C Alloy. (Conference Paper) 2009-2016A

Ferrite, Heating effects
Formation Mechanism of Bainite Ferrite and Carbide. (Conference Paper) 2001-2007A

Ferrite, Stress effects
Short Fatigue Crack Growth Behavior in a Ferritic-Bainitic Steel. 2421-2425A

Ferrite, Temperature effects
Thermodynamics of the Iron)Carbon)Zinc System. 569-578B
Fracture and the Formation of Sigma Phase, $M_{23}C_6$, and Austenite From Delta—Ferrite in an AISI 304L Stainless Steel. 1147-1158A
Morphology of Bainite and Widmanstätten Ferrite. (Conference Paper) 1981-1989A

Ferritic stainless steels, Heat treatment
Interstitial Precipitation in Fe—Cr—Al Alloys. 1135-1146A

Ferroalloys
See Ferronickel

Ferromagnetism, Alloying effects
Determination of Residual Nickel in Mechanically Alloyed NiAl. 871-874A

Ferronickel, Reduction (chemical)
An Analysis of Slag Stratification in Nickel Laterite Smelting Furnaces Due to Composition and Temperature Gradients. 491-496B

Ferrous alloys
See also Cast iron
Steels

Ferrous alloys, Coatings
Structure of As-Deposited Iron—Zinc Coatings From Chloride Bath. 249-255A
η to G Phase Transformation in Electrodeposited Iron—Zinc Alloy Coatings. 1119-1125A

Ferrous alloys, Diffusion
A History of the Controversy Over the Roles of Shear and Diffusion in Plate Formation Above M_d and a Comparison of the Atomic Mechanisms of These Processes. (Conference Paper, Review) 1797-1819A

Ferrous alloys, Heat treatment
Effects of Simultaneous Boron and Nitrogen Implantation on Microhardness and Fatigue Properties of Fe—13Cr—15Ni Alloys. 193-202A
Multiphase Precipitation of Carbides in Fe-C Systems. I. Model Based Upon Simple Kinetic Reactions. 917-925B
Multiphase Precipitation of Carbides in Fe-C System. II. Model Based on Kinetics of Complex Reactions. 927-935B

Ferrous alloys, Mechanical properties
Effects of Carbon Content and Ausaging on $\gamma \rightleftarrows \alpha'$ Transformation Behavior and Reverse-Transformed Structure in Fe—Ni—Co—Al—C Alloys. 63-71A
Effect of Strain Rate on the High-Temperature Low-Cycle Fatigue Properties of a Nimonic PE-16 Superalloy. 159-171A
Embrittlement of B2 Iron Aluminide by Water Vapor and by Hydrogen. 1285-1290A
The Elastic Strain Energy of Growth Ledges on Coherent and Partially Coherent Precipitates. 2073-2082A

Ferrous alloys, Phase transformations
On the Prebainitic Phenomenon in Some Alloys. (Conference Paper) 1941-1946A
Thermodynamics and Kinetics of the Formation of Widmanstätten Ferrite Plates in Ferrous Alloys. (Conference Paper) 1947-1953A
The Influence of the Alloying Elements Upon the Transformation Kinetics and Morphologies of Ferrite Plates in Alloy Steels. (Conference Paper) 1991-2000A

Ferrous alloys, Phases (state of matter)
Effects of Precursor Matrix Events on Subsequent Nucleation. (Conference Paper) 1933-1939A
The Fine Structure and Formation Mechanism of Lower Bainite. (Conference Paper) 1967-1980A
Formation Mechanism of Bainitic Ferrite in an Fe)2% Si)0.6% C Alloy. (Conference Paper) 2009-2016A

Ferrous alloys, Powder technology
Mechanical Processing of Iron Powders in Reactive and Nonreactive Gas Atmospheres. 381-388A

Ferrous compounds
See Iron compounds

Ferrous metals
See Ferrous alloys

Fiber composites, Heat treatment
Microstructural Study of the Titanium Alloy Ti—15Mo—2.7Nb—3Al—0.2Si (TIMETAL 21S). 1109-1118A
Development and Characterization of Interface Coatings in Molybdenum-Reinforced NiAl Matrix Composites. 2111-2116A

Fiber composites, Mechanical properties
Analysis of Thermally Induced Stress and Strain in Continuous Fiber-Reinforced Composites. 415-425A
Fiber Strength and Fiber/Matrix Bond Strength in Single Crystal Al_2O_3 Fiber Reinforced Ni_3Al Based Composites. 1259-1265A
Comparison of Orthorhombic and Alpha-Two Titanium Aluminides as Matrices for Continuous SiC-Reinforced Composites. 1267-1283A

Fiber composites, Oxidation
The Effect of Niobium Morphology on the Cyclic Oxidation Resistance of $MoSi_2$/20 vol.% Niobium Composites. 1033-1040A
A Structural Study of Oxidation in a Zirconia-Toughened Alumina Fiber-Reinforced NiAl Composite. 1291-1299A

Fiber composites, Phases (state of matter)
Phase Relations in the Mo—Si—C System Relevant to the Processing of $MoSi_2$—SiC Composites. 5-15A

Fiber composites, Physical properties
Capillarity in Isothermal Infiltration of Alumina Fiber Preforms With Aluminum. 2145-2152A

Fiber composites, Synthesis
Investigation of the Kinetics of Reduction of Nickel Tungstate by Hydrogen. 391-396B
Thermofluid Analysis and Design of a Low-Temperature Preforming Process. 761-771B

Fiber metal brazing
See Brazing

Fields (physics)
See Magnetic fields

Filler metal
See also Solders
Kinetic Study of Low-Temperature Transient Liquid Phase Joining of an Aluminum-SiC Composite. 2705-2714A

Films
See Thin films

Finite element method
Resistance Spot Welding of Precoated Steel Sheet: Computational Heat-Transfer Analysis. 415-423B
Depth of Melt-Pool and Heat-Affected Zone in Laser Surface Treatments. 427-435A
Three-Dimensional Finite Element Modeling of Gas Metal-Arc Welding. 435-441B
Modeling the Thin-Slab Continuous-Casting Mold. 443-457B
Simulation of Argon Gas Flow Effects in a Continuous Slab Caster. 527-547B
Mathematical and Physical Modeling Studies of Molten Aluminum Flow in a Tundish. 669-680B
Coefficients of Thermal Expansion of Metal-Matrix Composites for Electronic Packaging. 839-850A
Modeling Microstructure Development in Gray Cast Irons. 1063-1079A
Anisotropic Plastic Potentials for Polycrystals and Application to the Design of Optimum Blank Shapes in Sheet Forming. 1209-1216A
Transformation, Microcrack, and Thermal Residual Stress as Interactive Processes in ZrO_2-Toughened Al_2O_3, Simulated by the Finite Element Method. 1725-1731A

Fissile materials
See Nuclear fuels

Flexural vibration
See Fatigue (materials)

Flotation
Observations on the Effect of Medium Density and Viscosity on the Rate of Induced Aeration in Agitated Vessels. 303-306B

Flow
See Fluid flow

Flow stress
See Yield strength

Fluid bed reduction
See Fluidized bed reduction

Fluid flow
See also Gas flow
The Measurement of the Heat-Transfer Coefficient Between High-Temperature Liquids and Solid Surfaces. 43-51B
Mathematical and Physical Modeling Studies of Molten Aluminum Flow in a Tundish. 669-680B
Critical Fluid-Flow Phenomenon in a Gas-Stirred Ladle. 681-693B
Modeling of the Formation of Under-Riser Macrosegregation During Solidification of Binary Alloys. 1051-1062A

Fluid mechanics
Sticking of Solids in Liquids. 397-403B

Fluid mold casting
See Centrifugal casting

Fluidity
See Viscosity

Fluidized bed reduction
Effect of Cobalt Addition on the Liquid-Phase Sintering of Tungsten—Copper Prepared by the Fluidized Bed Reduction Method. 1575-1578A

Focussons
See Displacements (lattice)

Foil, Welding
The α/β Interface Phase in Titanium Alloys: Artifact or Real Phase Contribution to Problem Resolution. 241-248A

Foil (metal)
See Foil

Foil brazing
See Brazing

Foils (structural shapes)
See Foil

Force
See Loads (forces)

Forging
See Hot forging

Forgings, Mechanical properties
Environmental Effect on Room-Temperature Ductility of Isothermally Forged TiAl-Base Alloys. 321-330A

Formability
A Plane Strain Punch Stretching Test for Evaluating Stamping Formability of Steel Sheets. 2199-2205A

Formability, Deformation effects
The Tensile Deformation Behavior of AA 3004 Aluminum Alloy. 357-364A

Formability, Microstructural effects
Effects of Texture Gradients on Yield Loci and Forming Limit Diagrams in Various Aluminum-Lithium Sheet Alloys. 2783-2795A

Formation entropy
See Entropy
Heat of formation

Forming
See Punching
Stamping
Stretching
Superplastic forming

Forming limit
See Formability

Fracture mechanics
See Crack opening displacement

Fracture strength, Alloying effects
Microstructures and Mechanial Behavior of NiAl-Mo and NiAl-Mo-Ti Two-Phase Alloys. 2769-2781A

Fracture strength, Heating effects
Effect of Heat Treatment on the Microstructure, Tensile Properties, and Fracture Behavior of Permanent Mold Al-10 wt.% Si-0.6 wt.% Mg/SiC/10p Composite Castings. 2247-2263A

Fracture strength, Stress effects
The Effect of Triaxial Stress on Ductility and Fracture Morphology of Ferritic Spheroidal Graphite Cast Iron. 821-825A
Flow Instabilities and Fracture in Ti-6Al-4V Deformed in Compression at 298-673K. 2173-2179A

Fracture toughness, Cooling effects
Fatigue Crack Growth Rates and Fracture Toughness of Rapidly Solidified Al—8.5Fe—1.2V—1.7Si Alloys. 1005-1014A

Fracture toughness, Deformation effects
Relationships of Slip Morphology, Microcracking, and Fracture Resistance in a Lamellar TiAl-Alloy. 1217-1228A

Fracture toughness, Heating effects
Phosphorus and Carbon Segregation: Effects on Fatigue and Fracture of Gas-Carburized Modified 4320 Steel. 1229-1240A
Dynamic Fracture Behavior of Ti—6Al—4V Alloy With Various Stabilities of β Phase. 1655-1666A
Isothermal Formation of Quasicrystalline Precipitates and Their Effect on Strength in a 12Cr-9Ni-4Mo Maraging Stainless Steel. 2225-2233A
Fracture Toughness of Quaternary Al-Li-Cu-Mg Alloy Under Mode I, Mode II, and Mode III Loading Conditions. 2439-2452A

Fracture toughness, High temperature effects
Elevated Temperature Fracture of RS/PM Alloy 8009. I. Fracture Mechanics Behavior. 365-379A

Fracture toughness, Microstructural effects
Microstructural Analysis of Fracture Toughness Variation in 2XXX-Series Aluminum Alloy Composites Reinforced With SiC Whiskers. 2213-2223A

Fracture toughness, Radiation effects
Deformation Behavior of Irradiated Zr—2.5Nb Pressure Tube Material. 135-145A

Fracture toughness, Stress effects
Tensile Ductility of Extrinsically Toughened Intermetallics. 299-308A
Transformation, Microcrack, and Thermal Residual Stress as Interactive Processes in ZrO_2-Toughened Al_2O_3, Simulated by the Finite Element Method. 1725-1731A
Evaluation of Static and Dynamic Fracture Toughness in Ductile Cast Iron. 2427-2437A
The Influence of SiC Particulates on Fatigue Crack Propagation in a Rapidly Solidified Al-Fe-V-Si Alloy. 2453-2460A
Fracture Toughness of Discontinuously Reinforced Al-4Cu-1.5Mg/TiB_2 Composites. 2461-2468A

Fracturing
See Brittle fracture
Ductile fracture
Intergranular fracture
Transgranular fracture

Free energy
See also Activation energy
Thermodynamics of Oxygen and Nitrogen in Liquid Nickel Equilibrated With CaO—TiO_x and CaO—TiO_x—Al_2O_3 Melts. 5-13B
Phase Relations in the Mo—Si—C System Relevant to the Processing of $MoSi_2$—SiC Composites. 5-15A
Thermodynamic Properties of Ternary Liquid Cu—Mg—Ni Alloys. 63-72B
Solubility and Thermodynamic Properties of Y_2O_3 in LiF—YF_3 Melts. 91-96B
Thermodynamic Study of the Bi—Ca—O System. 97-101B
Thermodynamic Stability of Metallurgical Coke Relative to Graphite. 149-151B
Gradient Solid Electrolytes for Thermodynamic Measurements: System Na_2CO_3—Na_2SO_4. 173-180A
An Alternative Gibbs—Duhem Method for the Calculation of Activities From the Redox Data for Iron Oxide in Ternary Oxide Systems. 277-280B
Oxygen Potentials in Nickel + NiO and Nickel + Cr_2O_3 + $NiCr_2O_4$ Systems. 373-378B
Thermodynamic Study of $BaCuO_2$ and $BaCu_2O_2$. 385-389B
Estimation of the Viscosities of Binary Metallic Melts Using Gibbs Energies of Mixing. 589-595B
Solid-State Wetting of Graphite by Lead and Pb—Ni Alloys. 607-615A
The Shapes of the Phase Boundaries of Two Ideal Solution Phases in Ternary and Higher Order Systems. 656-658A
The Grand Partition Function of Dilute Biregular Solutions. 703-711B
Thermodynamics of the Liquid $\{xCu + yAu + (1-x-y)Ge\}$, $(0.75 \leq x \leq 1, 0 \leq y \leq 0.125)$ Alloys at 1550K by Knudsen Effusion Mass Spectrometry. 857-864A
Thermodynamic Analysis of the In-Ga-Sb System. 2331-2340A

Free energy of activation
See Activation energy

Free energy of dissociation
See Free energy
Heat of formation

Free energy of formation
See Free energy
Heat of formation

Free energy of reaction
See Free energy

Free energy of solution
See Free energy
Heat of solution

Free energy of transformation
See Free energy

Freezing points
See Melting points

Friction
See Sliding friction

Frictional wear, Microstructural effects
Effect of Microstructure (Particulate Size and Volume Fraction) and Counterface Material on the Sliding Wear Resistance of Particulate-Reinforced Aluminum Matrix Composites. 969-983A

Fuels
See Nuclear fuels

Furnaces
See Blast furnaces

Fused salt electrolysis
See Hall Heroult process

Fusion (melting)
See Melting

Fusion welding
See Electron beam welding

Gallium, Ternary systems
Thermodynamic Analysis of the In-Ga-Sb System. 2331-2340A

Gallium base alloys, Reactions (chemical)
Thermodynamic Estimation of ΔH_f° for $CaGa_2$ Intermetallic. 151-154B

Galvanic cells
See Electrolytic cells

Galvanized steels, Heat treatment
Interfacial Layer Development in Hot-Dip Galvanneal Coatings on Interstitial Free (IF) Steel. 2101-2109A

Galvanizing
See also Hot dip galvanizing
The Effect of Steel Chemistry on the Formation of Fe-Zn Intermetallic Compounds of Galvanneal-Coated Steel Sheets. 721-730B

Galvannealing
See Annealing

Gamma ray photoelectron spectroscopy
See Photoelectron spectroscopy

Gas flow
Critical Fluid-Flow Phenomenon in a Gas-Stirred Ladle. 681-693B

Gas metal arc welding
Three-Dimensional Finite Element Modeling of Gas Metal-Arc Welding. 435-441B

Gas permeability
See Permeability

Gas tungsten arc welding
The α/β Interface Phase in Titanium Alloys: Artifact or Real Phase Contribution to Problem Resolution. 241-248A
Effect of Welding Variables and Solidification Substructure on Weld Metal Porosity. 2285-2294A

Gas turbine engines, Fabrication
Microstructural Control in Hot Working of IN-718 Superalloy Using Processing Map. 2275-2284A

Gas turbines
See Gas turbine engines

Gases
See Air

Germanium, Ternary systems
Thermodynamics of the Liquid (xCu + yAu + (1—x—y)Ge), ($0.75 \leq x \leq 1$, $0 \leq y \leq 0.125$) Alloys at 1550K by Knudsen Effusion Mass Spectrometry. 857-864A

Gibbs free energy
See Free energy

Glazing
The Influence of Laser Glazing on Fatigue Crack Growth in Ti—24Al—11Nb. 183-192A

GMAW
See Gas metal arc welding

Gold, Coatings
The Effect of Low Gold Concentrations on the Creep of Eutectic Tin—Lead Joints. 1249-1257A

Gold, Extraction
Adsorption Kinetics of Dicyanoaurate and Dicyanoargentate Ions in Activated Carbon. 185-191B
An Electrochemical Study on the Dissolution of Gold and Copper from Gold/Copper Alloys. 817-827B
The Mechanism of Elution of Gold Cyanide From Activated Carbon. 829-838B

Gold, Ternary systems
Thermodynamics of the Liquid (xCu + yAu + (1—x—y)Ge), ($0.75 \leq x \leq 1$, $0 \leq y \leq 0.125$) Alloys at 1550K by Knudsen Effusion Mass Spectrometry. 857-864A

Gold base alloys, Atomic properties
Determination of the Short-Range Order Structure of Au—25 at.% Fe Using Wide-Angle Diffuse Synchrotron X-Ray Scattering. 1561-1573A

Gold base alloys, Phase transformations
Application of the Theory of Martensite Crystallography to Displacive Phase Transformations in Substitutional Nonferrous Alloys. (Conference Paper, Review) 1841-1856A

Grain boundaries
Precipitation Effects During Hot Deformation of a Copper Alloy. 257-266A
Efficient Measurement of Microstructural Surface Area Using Trisector. 919-928A
Ledges and Dislocations in Phase Transformations. (Conference Paper) 1885-1894A

Grain boundaries, Coating effects
The Effect of Low Gold Concentrations on the Creep of Eutectic Tin—Lead Joints. 1249-1257A

Grain boundaries, Deformation effects
Microstructure and Sound Velocity of Ti-N-O Synthetic Inclusions in Ti-6Al-4V. 2321-2329A

Grain boundaries, Diffusion effects
Determination of Pore Mobility During Sintering. 81-87A

Grain boundaries, Heating effects
The Effect of Phosphorus Segregation on the Intermediate-Temperature Embrittlement of Ferritic, Spheroidal Graphite Cast Iron. 557-561A
Applicability of Bond Percolation Theory to Intergranular Stress-Corrosion Cracking of Sensitized AISI 304 Stainless Steel. 775-787A
The Cause of Matrix Penetration of W/W Grain Boundaries During Heat Treatment of W-Ni-Fe Heavy Alloy. 2828-2831A

Grain boundaries, Radiation effects
Effects of Simultaneous Boron and Nitrogen Implantation on Microhardness and Fatigue Properties of Fe—13Cr—15Ni Alloys. 193-202A

Grain boundaries, Stress effects
Creep and Intergranular Cracking of Ni—Cr—Fe—C in 360°C Argon. 1169-1183A

Grain boundaries, Temperature effects
Morphology of Bainite and Widmanstätten Ferrite. (Conference Paper) 1981-1989A

Grain boundaries, Welding effects
The Influence of Electron-Beam Welding Parameters on Heat-Affected-Zone Microfissuring in Incoloy 903. 1733-1745A

Grain boundary migration, Stress effects
Effect of Iron on the Superplastic Deformation of Zn-22%Al. 2391-2401A

Grain boundary sliding, Deformation effects
Superplastic Behavior of Two Ultrahigh Boron Steels. 1241-1248A

Grain growth
Mechanical Processing of Iron Powders in Reactive and Nonreactive Gas Atmospheres. 381-388A

Grain growth, Alloying effects
Effect of Oxygen and Zirconium on the Growth and Superconducting Properties of Nb_3Sn. 203-212A
The Role of Oxygen and Zirconium in the Formation and Growth of Nb_3Sn Grains. 213-219A

Grain growth, Cooling effects
Three-Dimensional Simulation of the Grain Formation in Investment Castings. 629-635A
Prediction of Columnar to Equiaxed Transition During Diffusion-Controlled Dendritic Alloy Solidification. 1081-1093A

Grain growth, Heating effects
Discussion of "Grain Growth of a Superplastic 7475 Aluminum Alloy". 221-223A

Grain growth, Radiation effects
Helium 3 Precipitation in AISI 316L Stainless Steel Induced by Radioactive Decay of Tritium: Microstructural Study of Helium Bubble Precipitation. 2117-2130A

Grain refinement, Composition effects
Room-Temperature Strength and Deformation of TiB_2-Reinforced Near-γ Titanium Aluminides. 2181-2197A

Grain size
Structure of As-Deposited Iron—Zinc Coatings From Chloride Bath. 249-255A
Mechanical Processing of Iron Powders in Reactive and Nonreactive Gas Atmospheres. 381-388A
Nanocrystalline Iron Sintering Behavior and Microstructural Development. 677-685A
Textural and Microstructural Gradient Effects on the Mechanical Behavior of a Tantalum Plate. 1025-1031A
Influence of Near-Surface Microstructures on the Transient Current Response in Fe—Cr—Ni Alloys During Scratch Tests. 1325-1331A

Grain size, Alloying effects
Effect of Oxygen and Zirconium on the Growth and Superconducting Properties of Nb_3Sn. 203-212A
The Role of Oxygen and Zirconium in the Formation and Growth of Nb_3Sn Grains. 213-219A
Compositional and Microstructural Changes Which Attend Reheating and Grain Coarsening in Steels Containing Niobium. 277-286A
Effects of Austenite Grain Size and Cooling Rate on Widmanstätten Ferrite Formation in Low-Alloy Steels. 665-675A

Grain size, Coating effects
The Effect of Low Gold Concentrations on the Creep of Eutectic Tin—Lead Joints. 1249-1257A

Grain size, Cooling effects
Softening and Microstructural Change Following the Dynamic Recrystallization of Austenite. 389-400A
The Cast Structure of a 7075 Alloy Produced by a Water-Cooling Centrifugal Casting Method. 643-650A
Effects of Widmanstätten Ferrite on the Mechanical Properties of a 0.2% C—0.7% Mn Steel. 763-773A
Modeling Microstructure Development in Gray Cast Irons. 1063-1079A

Grain size, Deformation effects
Hot Deformation Characteristics of INCONEL Alloy MA 754 and Development of a Processing Map. 1693-1702A
Superplastic Behavior of Thermomechanically Treated P/M 7091 Aluminum Alloy. 2153-2160A

Grain size, Diffusion effects
Crystallographic Theories, Interface Structures, and Transformation Mechanisms. (Conference Paper) 1821-1839A

Grain size, Heating effects
Discussion of "Grain Growth of a Superplastic 7475 Aluminum Alloy". 221-223A
Influence of Tempering Temperature on Stability of Carbide Phases in 2.6Cr—0.7Mo—0.3V Steel With Various Carbon Content. 267-275A
The Effects of Double Austenitization on the Mechanical Properties of a 0.34C Containing Low-Alloy Ni—Cr—Mo—V Steel. 545-555A

Grain size, Stress effects
Cleavage Initiation in the Intercritically Reheated Coarse-Grained Heat-Affected Zone: I. Fractographic Evidence. 563-573A
Low-Cycle Fatigue of Dispersion-Strengthened Copper. 2235-2245A
Effect of Iron on the Superplastic Deformation of Zn-22%Al. 2391-2401A

Grain size stress effects
Forging Limit for an Aluminum Matrix Composite. II. Analysis. (Conference Paper) 2039-2048A

Grain structure
See also Dendritic structure
Some Aspects of Thermomechanical Fatigue of AISI 304L Stainless Steel. II. Dislocation Arrangements. 407-413A
The Effect of Steel Chemistry on the Formation of Fe-Zn Intermetallic Compounds of Galvanneal-Coated Steel Sheets. 721-730B
η to G Phase Transformation in Electrodeposited Iron—Zinc Alloy Coatings. 1119-1125A
Factors Influencing the Exceptional Ductility of a Superplastic Pb-62% Sn Alloy. 2309-2311A

Grain structure, Alloying effects
Compositional and Microstructural Changes Which Attend Reheating and Grain Coarsening in Steels Containing Niobium. 277-286A

Grain structure, Cooling effects
Three-Dimensional Simulation of the Grain Formation in Investment Castings. 629-635A

The Cast Structure of a 7075 Alloy Produced by a Water-Cooling Centrifugal Casting Method. 643-650A
Characterization of Mechanically Alloyed Oxide Dispersion-Strengthened Nickel-Base Superalloy MA760. 705-714A
Intragranular Ferrite Nucleation in Medium-Carbon Vanadium Steels. 929-936A
Solidification Macrostructures and Macrosegregation in Aluminum Alloys Cooled From Above. 1097-1102A
Evolution of Interaction Domain Microstructure During Spray Deposition. 2341-2355A

Grain structure, Deformation effects
Superplastic Behavior of Two Ultrahigh Boron Steels. 1241-1248A
Microstructural Control in Hot Working of IN-718 Superalloy Using Processing Map. 2275-2284A
Discussion of "The Role of Microstructure on Strength and Ductility of Hot-Extruded Mechanically Alloyed NiAl" and Author's Reply. 2303-2305A
Microstructure and Sound Velocity of Ti-N-O Synthetic Inclusions in Ti-6Al-4V. 2321-2329A

Grain structure, Diffusion effects
Formation of Invariant Plane-Strain and Tent-Shaped Surface Reliefs by the Diffusional Ledge Mechanism. (Conference Paper) 1923-1931A

Grain structure, Environmental effects
Environmental Effect on Room-Temperature Ductility of Isothermally Forged TiAl-Base Alloys. 321-330A

Grain structure, Heating effects
Auger Electron Analysis of the Initial Oxidation of Titanium Aluminides Based on Ti—48Al. 1041-1050A
Development and Characterization of Interface Coatings in Molybdenum-Reinforced NiAl Matrix Composites. 2111-2116A

Grain structure, High temperature effects
Effect of Strain Rate on the High-Temperature Low-Cycle Fatigue Properties of a Nimonic PE-16 Superalloy. 159-171A

Grain structure, Radiation effects
Deformation Behavior of Irradiated Zr—2.5Nb Pressure Tube Material. 135-145A

Grain structure, Stress effects
Characterization of Inhomogeneous Elastic Deformation With X-Ray Diffraction. 341-347A
Thermal-Mechanical Fatigue of Ti-48Al-2V Alloy and Its Composite. 2207-2212A
Low-Cycle Fatigue of Dispersion-Strengthened Copper. 2235-2245A

Grain structure, Temperature effects
Temperature and Microstructural Dependence of the Deformation of a High Niobium, Titanium—Aluminum Alloy. 1667-1679A

Graphite, Reactions (chemical)
Solid-State Wetting of Graphite by Lead and Pb—Ni Alloys. 607-615A

Graphitic structure
See also Nodular graphitic structure

Graphitic structure, Heating effects
The Effect of Phosphorus Segregation on the Intermediate-Temperature Embrittlement of Ferritic, Spheroidal Graphite Cast Iron. 557-561A

Gravitation
The Effect of Enhanced Gravity Levels on Microstructural Development in Pb—50 wt.% Sn Alloys During Controlled Directional Solidification. 865-870A

Gravity
See Gravitation

Gray cast iron
See Gray iron

Gray iron
See also Nodular iron

Gray iron, Casting
Modeling Microstructure Development in Gray Cast Irons. 1063-1079A

Green sand casting
A Note on the Sensitivity of Solidification Models to Thermophysical Properties. 154-157B

Grey iron
See Gray iron

Growth
See Grain growth

GTAW
See Gas tungsten arc welding

Hall Heroult process
Physical Modeling Studies of Electrolyte Flow Due to Gas Evolution and Some Aspects of Bubble Behavior in Advanced Hall Cells. I. Flow in Cells With a Flat Anode. 333-340B
Physical Modeling Studies of Electrolyte Flow Due to Gas Evolution and Some Aspects of Bubble Behavior in Advanced Hall Cells. II. Flow and Interpolar Resistance in Cells With a Grooved Anode. 341-349B
Energy Efficiency Considerations on Monopolar vs. Bipolar Fused Salt Electrolysis Cells. 661-668B
Measurements of the Electrical Conductivity of Wood's Alloy and Other Low Melting Point Alloys. 937-939B

Hard metals
See Cemented carbides

Hard soldering
See Brazing

Hardening
See also Surface hardening

Hardening, Heating effects
Heat Treatment of Investment Cast PH 13-8 Molybdenum Stainless Steel. II. Isothermal Aging Kinetics. 697-704A

Hardmetals
See Cemented carbides

Hardness
See also Diamond pyramid hardness
Microhardness
Surface hardness

Hardness, Coating effects
The Influence of Laser Glazing on Fatigue Crack Growth in Ti—24Al—11Nb. 183-192A

Hardness, Deformation effects
Modeling of Mechanical Alloying. I. Deformation, Coalescence, and Fragmentation Mechanisms. 147-158A

Hardness, Heating effects
Heat Treatment of Investment Cast PH 13-8 Molybdenum Stainless Steel. II. Isothermal Aging Kinetics. 697-704A
Heat Treatment of Investment Cast PH 13-8Mo Stainless Steel. I. Mechanical Properties and Microstructure. 789-798A
The Effect of Aging on Wear Characteristics of Rheocast-Leaded Aluminum Alloys. 851-856A
Isothermal Formation of Quasicrystalline Precipitates and Their Effect on Strength in a 12Cr-9Ni-4Mo Maraging Stainless Steel. 2225-2233A

HAZ
See Heat affected zone

Hazelett process
See Continuous casting

Heat affected zone
Depth of Melt-Pool and Heat-Affected Zone in Laser Surface Treatments. 427-435A
Cleavage Initiation in the Intercritically Reheated Coarse-Grained Heat-Affected Zone: I. Fractographic Evidence. 563-573A
The Influence of Electron-Beam Welding Parameters on Heat-Affected-Zone Microfissuring in Incoloy 903. 1733-1745A

Heat capacity
See Specific heat

Heat checking
See Thermal fatigue

Heat conductivity
See Thermal conductivity

Heat content
See Enthalpy

Heat flow
See Heat transmission

Heat flux
See Heat transmission

Heat measurement
See Calorimetry

Heat of activation
See Activation energy

Heat of condensation
See Heat of vaporization

Heat of decomposition
See Heat of formation

Heat of dissociation
See Heat of formation

Heat of dissolution
See Heat of solution

Heat of formation
Oxygen Potentials in Nickel + NiO and Nickel + Cr_2O_3 + $NiCr_2O_4$ Systems. 373-378B
Thermodynamic Analysis of the In-Ga-Sb System. 2331-2340A

Heat of mixing
See also Heat of solution
Estimation of the Viscosities of Binary Metallic Melts Using Gibbs Energies of Mixing. 589-595B
Formation and Stability of Metastable Structures and Amorphous Phases in Pu—V, Pu—TA, and Pu—Yb Systems With Positive Heats of Mixing. 1579-1590A
Thermodynamic Analysis of the In-Ga-Sb System. 2331-2340A

Heat of reaction
See Heat of formation

Heat of solution
The Grand Partition Function of Dilute Biregular Solutions. 703-711B

Heat of transformation
See Heat of vaporization

Heat of vaporization
Thermodynamic Predictions for Material Processing in a Plasma Reactor Using Solid Oxide Feed Materials. 713-720B

Heat resistant alloys
See Superalloys

Heat transfer
The Measurement of the Heat-Transfer Coefficient Between High-Temperature Liquids and Solid Surfaces. 43-51B
Thermodynamic Predictions for Material Processing in a Plasma Reactor Using Solid Oxide Feed Materials. 713-720B
Calculation of Thermophysical Properties of Carbon and Low Alloyed Steels for Modeling of Solidification Processes. 909-916B

Heat transmission
Modeling Microstructure Development in Gray Cast Irons. 1063-1079A

Heat treatment
See also Annealing
Austenitizing
Isothermal treatment
Quenching (cooling)
Solution heat treatment
Tempering
The Cause of Matrix Penetration of W/W Grain Boundaries During Heat Treatment of W-Ni-Fe Heavy Alloy. 2828-2831A

Heating
See Roasting

Heats (energies)
See Heat of mixing

Heavy metal alloys
See Lead base alloys
Tin base alloys

Heavy metals
See Antimony
Bismuth
Lead (metal)
Tin

Heliarc welding
See Gas tungsten arc welding

Helium, Dopants
Gas Trapping and Release in Polycrystalline Nickel Preimplanted With Helium. 949-959A
Helium 3 Precipitation in AISI 316L Stainless Steel Induced by Radioactive Decay of Tritium: Microstructural Study of Helium Bubble Precipitation. 2117-2130A

Helmholtz free energy
See Free energy

Heterogeneous structure
Textural and Microstructural Gradient Effects on the Mechanical Behavior of a Tantalum Plate. 1025-1031A

Heterogeneous structure, Alloying effects
Effect of Oxygen and Zirconium on the Growth and Superconducting Properties of Nb_3Sn. 203-212A

Heterogeneous structure, Cooling effects
Characterization of Mechanically Alloyed Oxide Dispersion-Strengthened Nickel-Base Superalloy MA760. 705-714A

Heterogeneous structure, Deformation effects
Discussion of "The Distribution of Dispersoid Phases in the Extruded ODS Superalloy MA-957 and Reply. 651-653A

Heterogeneous structure, Heating effects
Mechanism of Damping Capacity of High-Chromium Steels and α-Iron and Its Dependence on Some External Factors. 111-124A

Heterogeneous structure, Stress effects
Characterization of Inhomogeneous Elastic Deformation With X-Ray Diffraction. 341-347A
Short Fatigue Crack Growth Behavior in a Ferritic-Bainitic Steel. 2421-2425A

Heterogeneous structure stress effects
Forging Limit for an Aluminum Matrix Composite. II. Analysis. (Conference Paper) 2039-2048A

Hexagonal close packed lattice
See Hexagonal lattice

Hexagonal lattice
Thermodynamics and Long-Range Order of Interstitials in a Hexagonal Close-Packed Lattice. 2797-2814A

High alloy steels
See Maraging steels
Stainless steels

High carbon steels, Mechanical properties
The Workability of Commercial and Experimental 0.6% Carbon Low Alloy Steels in the Temperature Range of 650-870°C. 827-837A

High carbon steels, Rolling
Alligatoring and Damage in the Cold Rolling of Spheroidized Steels. 589-598A

High energy electron diffraction
See Electron diffraction

High energy milling
See Mechanical alloying

High strength steels, Corrosion
Tritium Distribution at the Crack Tip of High-Strength Steels Submitted to Stress Corrosion Cracking. 1159-1167A

High strength steels, Mechanical properties
The Study of Adiabatic Shear Band Instability in a Pearlitic 4340 Steel Using a Dynamic Punch Test. 2483-2489A

High temperature
Effect of Internal Heating During Hot Compression on the Stress-Strain Behavior of Alloy 304L. 2737-2752A

HIP
See Hot isostatic pressing

Homogeneous structure
Thermodynamics of Isolated Pores Filling With Liquid in Sintered Composite Materials. 733-740A
Efficient Measurement of Microstructural Surface Area Using Trisector. 919-928A

Homogenizing
Effect of Supereutectic Homogenization on Incidence of Porosity in Aluminum Alloy 2014 Ingot. 111-122B
Al_2Ti Precipitation in $Al_{64}Fe_8Ti_{28}$ Alloy. 715-721A
Heat Treatment of Investment Cast PH 13-8Mo Stainless Steel. I. Mechanical Properties and Microstructure. 789-798A
The Effect of Aging on Wear Characteristics of Rheocast-Leaded Aluminum Alloys. 851-856A
Aging of Freshly Formed Iron-Based Martensites at Low Temperatures. (Review) 889-909A
Effect of Heat Treatment on the Microstructure, Tensile Properties, and Fracture Behavior of Permanent Mold Al-10 wt.% Si-0.6 wt.% Mg/SiC/10p Composite Castings. 2247-2263A

Hot brittleness
See Brittleness

Hot cracking (welds)
See Weld defects

Hot deformation
See Deformation

Hot dip coating
See Hot dip galvanizing

Hot dip galvanizing
Morphology Development in Hot-Dip Galvanneal Coatings. 937-947A
Interfacial Layer Development in Hot-Dip Galvanneal Coatings on Interstitial Free (IF) Steel. 2101-2109A

Hot ductility
See Ductility

Hot extrusion
Discussion of "The Role of Microstructure on Strength and Ductility of Hot-Extruded Mechanically Alloyed NiAl" and Author's Reply. 2303-2305A

Hot forging
Microstructural Control in Hot Working of IN-718 Superalloy Using Processing Map. 2275-2284A
Microstructure Development During Conventional and Isothermal Hot Forging of a Near-γ Titanium Aluminide. 2753-2768A

Hot forming
See Hot forging

Hot hardness
See Hardness

Hot isostatic pressing
Modeling of Mechanical Alloying. I. Deformation, Coalescence, and Fragmentation Mechanisms. 147-158A
Mechanical Processing of Iron Powders in Reactive and Non-reactive Gas Atmospheres. 381-388A
High-Performance Ni_3Al Synthesized From Composite Powders. 985-992A
Superplastic Behavior of Two Ultrahigh Boron Steels. 1241-1248A
Microstructure and Sound Velocity of Ti-N-O Synthetic Inclusions in Ti-6Al-4V. 2321-2329A

Hot pressing
See Hot isostatic pressing

Hot reduction
See Hot working

Hot rolling
See also Pack rolling
Effects of Austenite Grain Size and Cooling Rate on Widmanstätten Ferrite Formation in Low-Alloy Steels. 665-675A
A Simple Model for Conventional Hot Rolling of Sheet Materials. 1681-1692A
High-Temperature Deformation of B2 NiAl-Base Alloys. (Conference Paper) 2017-2026A

Hot roughing
See Hot rolling

Hot shortness
See Brittleness

Hot strength
See Tensile strength

Hot tensile strength
See Tensile strength

Hot torsion tests
See Torsion tests

Hot working
See also Hot extrusion
Hot rolling
Microstructural Control in Hot Working of IN-718 Superalloy Using Processing Map. 2275-2284A

Hydrides, Environment
Hydride Embrittlement in Zircaloy-4 Plate. I. Influence of Microstructure on the Hydride Embrittlement in Zircaloy-4 at 20 and 350°C. 1185-1197A

Hydrochloric acid leaching
Slurry Filtration and Cake Washing After the HCl-Leach of Magnesite and Serpentine—Continuous Washing Model. 321-331B

Hydrochlorination
Processing of Spent Hydrorefining Catalysts by Selective Chlorination. 481-490B

Hydrogen
See also Deuterium
Tritium

Hydrogen, Alloying elements
High-Temperature Oxidation of Cathodically Hydrogen-Charged Two-Phase (Ti_3Al, TiAl) Titanium Aluminides. 2491-2496A

Hydrogen, Dopants
The Effects of Hydrogen on the Mechanical Behavior of Austenitic Stainless Steels at Room Temperature. 1015-1023A

Hydrogen, Environment
Embrittlement of B2 Iron Aluminide by Water Vapor and by Hydrogen. 1285-1290A

Hydrogen, Sorption
Barrier-Layer Formation and Its Control During Hydrogen Permeation Through Ti—24Al—11Nb Alloy. 89-97A

Hydrogen compounds
See Hydrides

Hydrogen embrittlement, Diffusion effects
Tritium Distribution at the Crack Tip of High-Strength Steels Submitted to Stress Corrosion Cracking. 1159-1167A

Hydrogen embrittlement, Environmental effects
Hydride Embrittlement in Zircaloy-4 Plate. I. Influence of Microstructure on the Hydride Embrittlement in Zircaloy-4 at 20 and 350°C. 1185-1197A
Embrittlement of B2 Iron Aluminide by Water Vapor and by Hydrogen. 1285-1290A

Hydrogen embrittlement, Heating effects
Hydrogen Permeation Behavior in IN718 and GH761 Superalloys. 539-544A

Hydrogenation
Investigation of the Kinetics of Reduction of Nickel Tungstate by Hydrogen. 391-396B

Hydrogenation, Environmental effects
Modeling Hydrogen Entry and Exit in Metals Exposed to Multiple Charging Processes. 723-732A

Hydrogenation, Heating effects
Hydrogen Permeation Behavior in IN718 and GH761 Superalloys. 539-544A

Hydrolysis
Preparation and Properties of Fine Hematite Powders by Hydrolysis of Iron Carboxylate Solutions. 165-170B

Hydrolytic resistance
See Corrosion resistance

Hydrometallurgy
Thermal Treatment of Complex Sulfide Ores in N_2 and H_2 Atmospheres: a New Approach for the Extraction of Their Valuable Elements. (Review) 193-205B
Slurry Filtration and Cake Washing After the HCl-Leach of Magnesite and Serpentine—Continuous Washing Model. 321-331B
The Ferric Fluosilicate Leaching of Lead Concentrates. I. Kinetic Studies. 473-480B
An Electrochemical Study on the Dissolution of Gold and Copper from Gold/Copper Alloys. 817-827B
The Mechanism of Elution of Gold Cyanide From Activated Carbon. 829-838B

Hydrostatic pressure
The Effect of Triaxial Stress on Ductility and Fracture Morphology of Ferritic Spheroidal Graphite Cast Iron. 821-825A
The Effects of Hydrostatic Pressure on the Compressive Mechanical Behavior of $L1_2$ Al_3 Ti-Based Intermetallic. 1703-1711A

I R drop
See Electric potential

Immersion testing (ultrasonic)
See Ultrasonic testing

Impact strength, Heating effects
The Effects of Double Austenitization on the Mechanical Properties of a 0.34C Containing Low-Alloy Ni—Cr—Mo—V Steel. 545-555A

Impact strength, Stress effects
Cleavage Initiation in the Intercritically Reheated Coarse-Grained Heat-Affected Zone: I. Fractographic Evidence. 563-573A

Impact tests
The Study of Adiabatic Shear Band Instability in a Pearlitic 4340 Steel Using a Dynamic Punch Test. 2483-2489A

Impact toughness
See Impact strength

Impermeability
See Permeability

Impurities
See also Interstitial impurities

Impurities, Diffusion
Anomalous Diffusion of Aluminum in β-Titanium. 873-876A

In situ leaching, pH effects
Simulation of In Situ Uraninite Leaching. I. A Partial Equilibrium Model of the NH_4HCO_3—$(NH_4)_2CO_3$—H_2O_2 Leaching System. 171-183B

Incineration
See Combustion

Inclusions, Deformation effects
Microstructure and Sound Velocity of Ti-N-O Synthetic Inclusions in Ti-6Al-4V. 2321-2329A

Indium, Ternary systems
Thermodynamic Analysis of the In-Ga-Sb System. 2331-2340A

Inelasticity
See Elasticity

Inert gas welding
See Gas tungsten arc welding

Ingot casting
See also Direct chill casting
Natural Convection in an Aluminum Ingot: a Mathematical Model. 293-302B
The Cast Structure of a 7075 Alloy Produced by a Water-Cooling Centrifugal Casting Method. 643-650A
Modeling of the Formation of Under-Riser Macrosegregation During Solidification of Binary Alloys. 1051-1062A

Ingots, Microstructure
The Cast Structure of a 7075 Alloy Produced by a Water-Cooling Centrifugal Casting Method. 643-650A
Solidification Macrostructures and Macrosegregation in Aluminum Alloys Cooled From Above. 1097-1102A

Initiation
See Crack initiation

Injection casting
See Die casting

Injection molding
Thermofluid Analysis and Design of a Low-Temperature Preforming Process. 761-771B

Inorganic compounds
See Ceramics

Intensity
See Stress intensity

Interface reactions
Kinetics in Multicomponent Metallic Ionic Systems. 579-587B
Experimental Study of the Influence of Interfacial Energies and Reactivity on Wetting in Metal/Oxide Systems. 599-605A
Spreading and Interlayer Formation at the Copper-Copper Oxide/Polycrystalline Alumina Interface. 2497-2506A

Interface reactions, Alloying effects
The Role of Oxygen and Zirconium in the Formation and Growth of Nb_3Sn Grains. 213-219A
Solid-State Wetting of Graphite by Lead and Pb—Ni Alloys. 607-615A

Interface reactions, Diffusion effects
Decomposition of Iron—Nickel Martensite: Implications for the Low-Temperature ($\leq$ 500°C) Fe—NI Phase Diagram. 1627-1637A

Interface reactions, Heating effects
Interfacial Layer Development in Hot-Dip Galvanneal Coatings on Interstitial Free (IF) Steel. 2101-2109A
Development and Characterization of Interface Coatings in Molybdenum-Reinforced NiAl Matrix Composites. 2111-2116A

Interface reactions, Low temperature effects
Numerical Modeling of γ Precipitate Growth During Fe—Ni Martensite Decomposition at Low Temperatures ($\leq$ 400°C). 1639-1648A

Interface reactions, Temperature effects
Kinetics of Interlayer Formation on Polycrystalline α-Al_2O_3/Copper-Titanium Alloy Interface. 2083-2090A

Interfaces
Diffusional Boundary Conditions During Coarsening of Elastically Interacting Precipitates. 2695-2703A
Numerical Analysis of the Rapid Solidification of Gas-Atomized Al-8 wt.% Iron Droplets. 2815-2826A

Interfacial energy
See Surface energy

Interfacial surface tension
See Surface tension

Intergranular corrosion, Heating effects
Applicability of Bond Percolation Theory to Intergranular Stress-Corrosion Cracking of Sensitized AISI 304 Stainless Steel. 775-787A

Intergranular corrosion, Stress effects
Creep and Intergranular Cracking of Ni—Cr—Fe—C in 360°C Argon. 1169-1183A

Intergranular fracture, Heating effects
The Role of Magnesium-Containing Spheroidizer and Counteraction of Misch Metal in the Intermediate Temperature Intergranular Embrittlement of Ferritic Nodular Iron. 2305-2309A
Fracture Toughness of Quaternary Al-Li-Cu-Mg Alloy Under Mode I, Mode II, and Mode III Loading Conditions. 2439-2452A

Intergranular fracture, Stress effects
Thermal-Mechanical Fatigue of Ti-48Al-2V Alloy and Its Composite. 2207-2212A

Intergranular precipitation, Diffusion effects
Decomposition of Iron—Nickel Martensite: Implications for the Low-Temperature ($\leq$ 500°C) Fe—NI Phase Diagram. 1627-1637A

Interlayers
The Effect of Substrate on the Microstructure and Creep of Eutectic Indium-Tin. 2715-2722A

Intermetallic compounds
See Intermetallics

Intermetallic phases
The Diffuse-Scattering Method for Investigating Locally Ordered Binary Solid Solutions. 17-35A
Crystallographic Characteristics of the Al—Co Decagonal Quasicrystal and Its Monoclinic Approximant τ^2-$Al_{13}Co_4$. 47-56A
Triclinic Ni_2Al Phase in 63.1 at.% NiAl. 57-61A
Precipitation Effects During Hot Deformation of a Copper Alloy. 257-266A
Effect of Cobalt Addition on the Liquid-Phase Sintering of Tungsten—Copper Prepared by the Fluidized Bed Reduction Method. 1575-1578A
Microstructural Analysis of Fracture Toughness Variation in 2XXX-Series Aluminum Alloy Composites Reinforced With SiC Whiskers. 2213-2223A

Intermetallic phases, Alloying effects
A Process for Debismuthizing Lead With Magnesium. 379-384B

Intermetallic phases, Composition effects
Supersaturation of the Al_2Y Laves Phase by Rapid Solidification. 230-233A
High-Temperature Oxidation of Cathodically Hydrogen-Charged Two-Phase (Ti_3Al, TiAl) Titanium Aluminides. 2491-2496A

Intermetallic phases, Cooling effects
Crystallization Studies of the β' (Mg_2Pb) Phase and Its Phase Boundaries in the Pb—Mg—Bi System. 255-263B
Cubic AlNi Compound Dispersed Magnesium-Based Amorphous Matrix Composites Prepared by Rapid Solidification. 1323-1325A
Crystallization Behavior of Iron-Containing Intermetallic Compounds in 319 Aluminum Alloy. 1761-1773A

Intermetallic phases, Deformation effects
Relationships of Slip Morphology, Microcracking, and Fracture Resistance in a Lamellar TiAl-Alloy. 1217-1228A

Intermetallic phases, Diffusion effects
Interdiffusion Between Uranium—Zirconium Fuel vs. Selected Cladding Steels. 1649-1653A
Application of the Theory of Martensite Crystallography to Displacive Phase Transformations in Substitutional Nonferrous Alloys. (Conference Paper, Review) 1841-1856A
Formation of Invariant Plane-Strain and Tent-Shaped Surface Reliefs by the Diffusional Ledge Mechanism. (Conference Paper) 1923-1931A

Intermetallic phases, Environmental effects
Embrittlement of B2 Iron Aluminide by Water Vapor and by Hydrogen. 1285-1290A

Intermetallic phases, Heating effects
Influence of Tempering Temperature on Stability of Carbide Phases in 2.6Cr—0.7Mo—0.3V Steel With Various Carbon Content. 267-275A
Heat Treatment of Investment Cast PH 13-8 Molybdenum Stainless Steel. II. Isothermal Aging Kinetics. 697-704A
Al_2Ti Precipitation in $Al_{64}Fe_8Ti_{28}$ Alloy. 715-721A
Heat Treatment of Investment Cast PH 13-8Mo Stainless Steel. I. Mechanical Properties and Microstructure. 789-798A
Auger Electron Analysis of the Initial Oxidation of Titanium Aluminides Based on Ti—48Al. 1041-1050A
A Structural Study of Oxidation in a Zirconia-Toughened Alumina Fiber-Reinforced NiAl Composite. 1291-1299A
The Effect of Thermal Exposure on Microstructural Stability and Creep Resistance of a Two-Phase TiAl/Ti_3Al Lamellar Alloy. 2371-2381A

Intermetallic phases, Stress effects
A History of the Controversy Over the Roles of Shear and Diffusion in Plate Formation Above M_d and a Comparison of the Atomic Mechanisms of These Processes. (Conference Paper, Review) 1797-1819A

Intermetallic phases, Temperature effects
Phase Relations in the Mo—Si—C System Relevant to the Processing of $MoSi_2$—SiC Composites. 5-15A
Standard Enthalpies of Formation of Some Praseodymium Alloys of High-Temperature Direct Synthesis Calorimetry. 73-77B
Thermodynamic Estimation of ΔH_f° for $CaGa_2$ Intermetallic. 151-154B
Mg—Pb Phase Diagram and Phase Transformations in the Intermetallic Compounds Mg_2Pb and β'. 265-275B
Comparison of Orthorhombic and Alpha-Two Titanium Aluminides as Matrices for Continuous SiC-Reinforced Composites. 1267-1283A
Improved Thermochemical Calculations for Maraging Steels and Comparison With Atom Probe Measurement of Phase Composition. 2538-2539A

Intermetallic phases, Welding effects
Characterization of a Diffusion-Bonded Al—Mg Alloy/SiC Interface by High Resolution and Analytical Electron Microscopy. 617-627A

Intermetallics, Coatings
The Effect of Steel Chemistry on the Formation of Fe-Zn Intermetallic Compounds of Galvanneal-Coated Steel Sheets. 721-730B

Intermetallics, Composite materials
Phase Relations in the Mo—Si—C System Relevant to the Processing of $MoSi_2$—SiC Composites. 5-15A
Fiber Strength and Fiber/Matrix Bond Strength in Single Crystal Al_2O_3 Fiber Reinforced Ni_3Al Based Composites. 1259-1265A
A Structural Study of Oxidation in a Zirconia-Toughened Alumina Fiber-Reinforced NiAl Composite. 1291-1299A
Development and Characterization of Interface Coatings in Molybdenum-Reinforced NiAl Matrix Composites. 2111-2116A
Melt-Processed Ni_3Al Matrix Composites Reinforced With TiC Particles. 2525-2534A

Intermetallics, Extrusion
Discussion of "The Role of Microstructure on Strength and Ductility of Hot-Extruded Mechanically Alloyed NiAl" and Author's Reply. 2303-2305A

Intermetallics, Forging
Microstructure Development During Conventional and Isothermal Hot Forging of a Near-γ Titanium Aluminide. 2753-2768A

Intermetallics, Mechanical properties
Tensile Ductility of Extrinsically Toughened Intermetallics. 299-308A
Low-Cycle Fatigue Behavior of Polycrystalline NiAl at 1000K. 309-319A
Environmental Effect on Room-Temperature Ductility of Isothermally Forged TiAl-Base Alloys. 321-330A
Elastic Constants of Some Transition-Metal-Disilicide Single Crystals. 331-340A
Ordering and Mechanical Strength in $L1_2$ Cubic Titanium Trialuminides. 449-451A
The Effects of Hydrostatic Pressure on the Compressive Mechanical Behavior of $L1_2$ Al_3 Ti-Based Intermetallic. 1703-1711A
Modeling Creep Deformation of a Two-Phase TiAl/Ti_3Al Alloy With a Lamellar Microstructure. 2161-2171A
Low Cycle Fatigue Behavior of Polycrystalline Ni_3Al Alloys at Ambient and Elevated Temperatures. 2469-2476A
Creep Characteristics of Single Crystalline Ni_3Al(Ta,B). 2477-2482A
Microstructures and Mechanial Behavior of NiAl-Mo and NiAl-Mo-Ti Two-Phase Alloys. 2769-2781A

Intermetallics, Microstructure
Discussion of "Crystallographic Characterization of the Al-Co Decagonal Quasicrystal and Its Monoclinic Approximant τ^2-$Al_{13}Co_4$". 2535-2538A

Intermetallics, Powder technology
Determination of Residual Nickel in Mechanically Alloyed NiAl. 871-874A
High-Performance Ni_3Al Synthesized From Composite Powders. 985-992A
Evolution of Interaction Domain Microstructure During Spray Deposition. 2341-2355A

Intermetallics, Rolling
High-Temperature Deformation of B2 NiAl-Base Alloys. (Conference Paper) 2017-2026A

Intermetallics, Superconductivity
Effect of Oxygen and Zirconium on the Growth and Superconducting Properties of Nb_3Sn. 203-212A
The Role of Oxygen and Zirconium in the Formation and Growth of Nb_3Sn Grains. 213-219A

Internal combustion engines
See Gas turbine engines

Internal stress
See Residual stress

Interstitial impurities
Thermodynamics and Long-Range Order of Interstitials in a Hexagonal Close-Packed Lattice. 2797-2814A

Investment casting
Three-Dimensional Simulation of the Grain Formation in Investment Castings. 629-635A

Investment casting, Microstructure
Three-Dimensional Simulation of the Grain Formation in Investment Castings. 629-635A

Investment castings, Heat treatment
Heat Treatment of Investment Cast PH 13-8 Molybdenum Stainless Steel. II. Isothermal Aging Kinetics. 697-704A
Heat Treatment of Investment Cast PH 13-8Mo Stainless Steel. I. Mechanical Properties and Microstructure. 789-798A

Investment castings, Mechanical properties
Room-Temperature Strength and Deformation of TiB_2-Reinforced Near-γ Titanium Aluminides. 2181-2197A

Investment molding
See Investment casting

Ion implantation
Effects of Simultaneous Boron and Nitrogen Implantation on Microhardness and Fatigue Properties of Fe—13Cr—15Ni Alloys. 193-202A
Gas Trapping and Release in Polycrystalline Nickel Preimplanted With Helium. 949-959A

IR drop
See Electric potential

Iron, Alloying elements
Effect of Alloying Elements on the Solidification Characteristics and Microstructure of Al—Si—Cu—Mg—Fe 380 Alloy. 437-448A
Effect of Iron on the Superplastic Deformation of Zn-22%Al. 2391-2401A

Iron, Extraction
Thermal Treatment of Complex Sulfide Ores in N_2 and H_2 Atmospheres: a New Approach for the Extraction of Their Valuable Elements. (Review) 193-205B
Surface Segregation of Calcium Oxide in Wustite and Its Effects on the Reduction. 405-413B

Iron, Powder technology
Nanocrystalline Iron Sintering Behavior and Microstructural Development. 677-685A

Iron, Reduction (chemical)
Kinetics of the Reaction of H_2O Gas With Liquid Iron. 245-253B

Iron, Steel making
Sulfur Determination in Carbon-Saturated Iron by Solid-State Electrochemical Sensor. 561-568B

Iron, Ternary systems
High-Temperature Phase Relations and Thermodynamics in the Iron—Lead—Sulfur System. 53-61B
Thermodynamics of the Iron)Carbon)Zinc System. 569-578B
Numerical Modeling of Solidification and Subsequent Transformation of Fe—Cr—Ni Alloys. 1309-1321A

Iron and steel making
See Ironmaking
Steel making

Iron base alloys
See Ferrous alloys

Iron compounds, Coatings
The Effect of Steel Chemistry on the Formation of Fe-Zn Intermetallic Compounds of Galvanneal-Coated Steel Sheets. 721-730B

Iron constituents
See Alpha iron
Delta iron

Iron ores, Reduction (chemical)
Study of Nonisothermal Reduction of Iron Ore—Coal/Char Composite Pellet. 15-26B

Iron oxides
See Wustite

Iron powder
See Iron

Ironmaking
Study of Nonisothermal Reduction of Iron Ore—Coal/Char Composite Pellet. 15-26B
Vanadium Distribution in Melts Intermediate to Ferroalloy Production From Vanadiferous Slag. 27-32B
An Alternative Gibbs—Duhem Method for the Calculation of Activities From the Redox Data for Iron Oxide in Ternary Oxide Systems. 277-280B
Improvement in the Reducibility of Wustite Assisted by the Intensified Surface Segregation of Calcium Ions by the Double Addition of CaO and SiO_2. 741-748B
Measurements of High-Temperature Viscosities of Liquid Boron Trioxide. 876-881A
A Thermodynamic Study of the Molybdenum-Oxygen System. 885-891B

Irradiation damage
See Radiation damage

Isostatic pressing
See Hot isostatic pressing

Isothermal treatment
Heat Treatment of Investment Cast PH 13-8 Molybdenum Stainless Steel. II. Isothermal Aging Kinetics. 697-704A
Applicability of Bond Percolation Theory to Intergranular Stress-Corrosion Cracking of Sensitized AISI 304 Stainless Steel. 775-787A

Izod impact tests
See Impact tests

Jet engines
See Gas turbine engines

Joining
See also Brazing
Kinetic Study of Low-Temperature Transient Liquid Phase Joining of an Aluminum-SiC Composite. 2705-2714A

Joints
See Soldered joints
Welded joints

Junghans Rossi casting
See Continuous casting

Killed steels
See Aluminum killed steels

Kinetics
See also Reaction kinetics
Multiphase Precipitation of Carbides in Fe-C Systems. I. Model Based Upon Simple Kinetic Reactions. 917-925B
Multiphase Precipitation of Carbides in Fe-C System. II. Model Based on Kinetics of Complex Reactions. 927-935B
Growth Kinetics and High-Temperature TEM In Situ Observation of Bainite in a Cu-Zn Alloy. (Conference Paper) 2609-2614A

Kold casting
See Investment casting

Ladle metallurgy
A Comparison of Three Mathematical Modeling Procedures for Simulating Fluid Flow Phenomena in Bubble-Stirred Ladles. 308-312B
Critical Fluid-Flow Phenomenon in a Gas-Stirred Ladle. 681-693B

Lamellar structure, Alloying effects
Elevated-Temperature Stability of Mechanically Alloyed Copper-Niobium Powders. 2091-2099A

Lamellar structure, Deformation effects
Relationships of Slip Morphology, Microcracking, and Fracture Resistance in a Lamellar TiAl-Alloy. 1217-1228A

Lamellar structure, Heating effects
The Effect of Thermal Exposure on Microstructural Stability and Creep Resistance of a Two-Phase TiAl/Ti_3Al Lamellar Alloy. 2371-2381A

Lamellar structure, High temperature effects
The Workability of Commercial and Experimental 0.6% Carbon Low Alloy Steels in the Temperature Range of 650-870°C. 827-837A

Lamellar structure, Stress effects
Thermal-Mechanical Fatigue of Ti-48Al-2V Alloy and Its Composite. 2207-2212A

Lamellar structure, Temperature effects
Temperature and Microstructural Dependence of the Deformation of a High Niobium, Titanium—Aluminum Alloy. 1667-1679A
Modeling Creep Deformation of a Two-Phase TiAl/Ti_3Al Alloy With a Lamellar Microstructure. 2161-2171A

Laminates
See Bimetals

Laser beam hardening
Depth of Melt-Pool and Heat-Affected Zone in Laser Surface Treatments. 427-435A

Laser beam melting
A Simple but Realistic Model for Laser Cladding. 281-291B
Depth of Melt-Pool and Heat-Affected Zone in Laser Surface Treatments. 427-435A

Laser processing
See also Laser beam hardening
Laser beam melting
Transmission Electron Microscopy Study of Martensites in Laser-Clad Ni—Al Bronze on Aluminium Alloy AA333. 37-46A
The Influence of Laser Glazing on Fatigue Crack Growth in Ti—24Al—11Nb. 183-192A
Processing, Microstructure, and Properties of Laser-Clad Nickel Alloy FP-5 on Al Alloy AA333. 425-434B
Laser Cladding of Nickel-Aluminum Bronze on Al Alloy AA333. 749-759B

Lattice constant
See Lattice parameters

Lattice defects
See Crystal defects

Lattice displacements
See Displacements (lattice)

Lattice parameters
Surface Segregation of Calcium Oxide in Wustite and Its Effects on the Reduction. 405-413B
The Shapes of the Phase Boundaries of Two Ideal Solution Phases in Ternary and Higher Order Systems. 656-658A
Improvement in the Reducibility of Wustite Assisted by the Intensified Surface Segregation of Calcium Ions by the Double Addition of CaO and SiO_2. 741-748B
Textural and Microstructural Gradient Effects on the Mechanical Behavior of a Tantalum Plate. 1025-1031A
The Phenomenological Theory of Martensite Crystallography: Interrelationships. (Conference Paper) 1787-1795A
Ledges and Dislocations in Phase Transformations. (Conference Paper) 1885-1894A
The Role of Structural Ledges as Misfit-Compensating Defects: FCC-BCC Interphase Boundaries. (Conference Paper) 1895-1903A
The Elastic Strain Energy of Growth Ledges on Coherent and Partially Coherent Precipitates. 2073-2082A
Mechanism of the Early Stages of α_1 Plate Formation in a Cu-39% Zinc Alloy. (Conference Paper) 2631-2637A

Lattice parameters, Alloying effects
Transmission Electron Microscopy Crystal Structure Study of the Chromium-Rich Phase in a Laser-Clad Nickel Alloy. 487-497A

Lattice parameters, Composition effects
Supersaturation of the Al_2Y Laves Phase by Rapid Solidification. 230-233A

Lattice parameters, Cooling effects
Chemical Composition and Structural Identification of Eutectic Carbide in 1% Manganese Ductile Iron. 911-918A

Lattice parameters, Diffusion effects
Determination of Pore Mobility During Sintering. 81-87A
Crystallographic Theories, Interface Structures, and Transformation Mechanisms. (Conference Paper) 1821-1839A
The Invariant Line and Precipitate Morphology in FCC-BCC Systems. (Conference Paper) 1865-1874A
On the Role of Interphase-Boundary Structure in Plate Growth by Diffusional Mechanisms. (Conference Paper) 1875-1883A

Lattice parameters, Heating effects
Formation and Stability of Metastable Structures and Amorphous Phases in Pu—V, Pu—TA, and Pu—Yb Systems With Positive Heats of Mixing. 1579-1590A
Dynamic Fracture Behavior of Ti—6Al—4V Alloy With Various Stabilities of β Phase. 1655-1666A

Lattice parameters, Radiation effects
Gas Trapping and Release in Polycrystalline Nickel Preimplanted With Helium. 949-959A

Lattice parameters, Welding effects
The α/β Interface Phase in Titanium Alloys: Artifact or Real Phase Contribution to Problem Resolution. 241-248A

Lattice vacancies
Role of Al_2O_3 Particulate Reinforcements on Precipitation in 2014 Aluminum-Matrix Composites. 1591-1602A

Lattice vacancies, Radiation effects
Helium 3 Precipitation in AISI 316L Stainless Steel Induced by Radioactive Decay of Tritium: Growth Mechanism of Helium Bubbles. 2131-2143A

Lattices
See Crystal lattices

Laundering
See Washing

Laves phase, Composition effects
Supersaturation of the Al_2Y Laves Phase by Rapid Solidification. 230-233A

Laves phase, Temperature effects
Improved Thermochemical Calculations for Maraging Steels and Comparison With Atom Probe Measurement of Phase Composition. 2538-2539A

Layers
See Interlayers

Leaching
See also Bacterial leaching
In situ leaching
The Ferric Fluosilicate Leaching of Lead Concentrates. I. Kinetic Studies. 473-480B

Lead (metal), Alloying elements
A Process for Debismuthizing Lead With Magnesium. 379-384B

Lead (metal), Binary systems
Mg—Pb Phase Diagram and Phase Transformations in the Intermetallic Compounds Mg_2Pb and β'. 265-275B

Lead (metal), Extraction
Physical and Mathematical Modeling of Pyrometallurgical Channel Reactors With Bottom Gas Injection. Residence Time Distribution Analysis and Ideal-Reactor-Network Model. 207-219B
The Ferric Fluosilicate Leaching of Lead Concentrates. I. Kinetic Studies. 473-480B

Lead (metal), Microstructure
Characterization of Inhomogeneous Elastic Deformation With X-Ray Diffraction. 341-347A

Lead (metal), Physical properties
Sticking of Solids in Liquids. 397-403B

Lead (metal), Soldering
The Effect of Low Gold Concentrations on the Creep of Eutectic Tin—Lead Joints. 1249-1257A

Lead (metal), Ternary systems
High-Temperature Phase Relations and Thermodynamics in the Iron—Lead—Sulfur System. 53-61B
Crystallization Studies of the β' (Mg_2Pb) Phase and Its Phase Boundaries in the Pb—Mg—Bi System. 255-263B
The Grand Partition Function of Dilute Biregular Solutions. 703-711B

Lead base alloys, Casting
Undercooling-Induced Macrosegregation in Directional Solidification. 2507-2516A

Lead base alloys, Microstructure
The Effect of Enhanced Gravity Levels on Microstructural Development in Pb—50 wt.% Sn Alloys During Controlled Directional Solidification. 865-870A

Lead base alloys, Reactions (chemical)
Solid-State Wetting of Graphite by Lead and Pb—Ni Alloys. 607-615A

Life
See Fatigue life

Light metal alloys
See Aluminum base alloys
Magnesium base alloys
Titanium base alloys

Light metals
See Aluminum
Magnesium
Titanium

Line defects
See Dislocations

Linking
See Joining

Liquefaction
See Melting

Liquid metals, Physical properties
Densities of Liquid Fe-Ni and Fe-Cr Alloys. 939-942B

Liquid phase diffusion
See Diffusion

Liquid phase sintering
Preparation and Properties of Fine Hematite Powders by Hydrolysis of Iron Carboxylate Solutions. 165-170B
Effect of Cobalt Addition on the Liquid-Phase Sintering of Tungsten—Copper Prepared by the Fluidized Bed Reduction Method. 1575-1578A

Liquid phases
The Measurement of the Heat-Transfer Coefficient Between High-Temperature Liquids and Solid Surfaces. 43-51B
An Empirical Correlation Between Contact Angles and Surface Tension in Some Ceramic—Metal Systems. 225-230A
Large-Scale Measurements of the Physical Characteristics of Round Vertical Bubble Plumes in Liquids. 359-371B
Sticking of Solids in Liquids. 397-403B
Experimental Study of the Influence of Interfacial Energies and Reactivity on Wetting in Metal/Oxide Systems. 599-605A
A Two-Phase Flow Model of the Stirring of Al)SiC Composite Melt. 607-618B
Backmixing in Channel Reactors With High-Strength Bottom Gas Injection. 619-623B
Surface Tensions of Liquid Fe-Cr and Fe-Cr-N Alloys. 626-628B
The Shapes of the Phase Boundaries of Two Ideal Solution Phases in Ternary and Higher Order Systems. 656-658A
Thermodynamics of Isolated Pores Filling With Liquid in Sintered Composite Materials. 733-740A
X-Ray Microscopic Observations of Metal Solidification Dynamics. 1775-1777A
Kinetic Study of Low-Temperature Transient Liquid Phase Joining of an Aluminum-SiC Composite. 2705-2714A

Liquid phases, Alloying effects
Thermodynamics of Oxygen and Nitrogen in Liquid Nickel Equilibrated With $CaO—TiO_x$ and $CaO—TiO_x—Al_2O_3$ Melts. 5-13B
The Role of Oxygen and Zirconium in the Formation and Growth of Nb_3Sn Grains. 213-219A

Liquid phases, Cooling effects
Crystallization Studies of the β' (Mg_2Pb) Phase and Its Phase Boundaries in the Pb—Mg—Bi System. 255-263B
Further Discussions on the Solute Redistribution During Dendritic Solidification of Binary Alloys. 731-739B
The Velocity of Solidification of Highly Undercooled Nickel. 1301-1308A
Crystallization Behavior of Iron-Containing Intermetallic Compounds in 319 Aluminum Alloy. 1761-1773A
Microsegregation in Cellular Solidification. 2295-2301A
Undercooling-Induced Macrosegregation in Directional Solidification. 2507-2516A
Nonequilibrium Solidification of Undercooled Melt of Ag-Cu Alloy Entrained in the Primary Phase. 2517-2523A

Liquid phases, Diffusion effects
The Morphological Stability of Lateral Growth in Solid—Solid Phase Transformation During Thin-Film Interdiffusion in Aluminum/Copper Bimetal Films. 1613-1625A

Liquid phases, High temperature effects
Density Measurements of the Lithium Fluoride/Lithium Sulfide Eutectic at High Temperature. 773-778B

Liquid phases, Temperature effects
High-Temperature Phase Relations and Thermodynamics in the Iron—Lead—Sulfur System. 53-61B
Thermodynamic Properties of Ternary Liquid Cu—Mg—Ni Alloys. 63-72B
Gradient Solid Electrolytes for Thermodynamic Measurements: System $Na_2CO_3—Na_2SO_4$. 173-180A
Mg—Pb Phase Diagram and Phase Transformations in the Intermetallic Compounds Mg_2Pb and β'. 265-275B
Thermodynamics of the Iron)Carbon)Zinc System. 569-578B
An Internal Variable Description of Solidification Suitable for Macrosegregation Modeling. 597-605B
Thermodynamics of the Liquid {xCu + yAu + (1—x—y)Ge}, ($0.75 \leq x \leq 1, 0 \leq y \leq 0.125$) Alloys at 1550K by Knudsen Effusion Mass Spectrometry. 857-864A
Thermodynamic Analysis of the In-Ga-Sb System. 2331-2340A

Liquid phases, Welding effects
The Influence of Electron-Beam Welding Parameters on Heat-Affected-Zone Microfissuring in Incoloy 903. 1733-1745A

Liquids
See Liquid metals
Melts

Liquidus, Temperature effects
Thermodynamic Analysis of the In-Ga-Sb System. 2331-2340A

Lithium, Physical properties
Density Measurements of the Lithium Fluoride/Lithium Sulfide Eutectic at High Temperature. 773-778B

Live loads
See Cyclic loads

Lixiviation
See Leaching

Load distribution
See Loads (forces)

Loads (forces)
Tensile Ductility of Extrinsically Toughened Intermetallics. 299-308A
Elevated Temperature Fracture of RS/PM Alloy 8009. I. Fracture Mechanics Behavior. 365-379A
Some Aspects of Thermomechanical Fatigue of AISI 304L Stainless Steel. I. Creep—Fatigue Damage. 401-406A
Effect of Microstructure (Particulate Size and Volume Fraction) and Counterface Material on the Sliding Wear Resistance of Particulate-Reinforced Aluminum Matrix Composites. 969-983A
Creep and Intergranular Cracking of Ni—Cr—Fe—C in 360°C Argon. 1169-1183A
Embrittlement of B2 Iron Aluminide by Water Vapor and by Hydrogen. 1285-1290A
Mixed-Mode I and II Fatigue Threshold and Crack Closure in Dual-Phase Steels. 1713-1723A
Evaluation of Static and Dynamic Fracture Toughness in Ductile Cast Iron. 2427-2437A
Load-Signature Analysis for Pack Rolling of Near-Gamma Titanium Aluminide Alloys. 2539-2542A

Long range order
Ordering and Mechanical Strength in $L1_2$ Cubic Titanium Trialuminides. 449-451A
Long-Range Ordering in the Early Stages of Precipitation)a Brief Review. (Conference Paper) 2565-2568A
Thermodynamics and Long-Range Order of Interstitials in a Hexagonal Close-Packed Lattice. 2797-2814A

Long range order, Diffusion effects
Formation of Invariant Plane-Strain and Tent-Shaped Surface Reliefs by the Diffusional Ledge Mechanism. (Conference Paper) 1923-1931A

Long range order, Stress effects
A History of the Controversy Over the Roles of Shear and Diffusion in Plate Formation Above M_d and a Comparison of the Atomic Mechanisms of These Processes. (Conference Paper, Review) 1797-1819A

Loops (dislocation)
See Dislocation loops

Lost wax investment casting
See Investment casting

Lost wax process
See Investment casting

Low alloy steels
See also Boron steels

Low alloy steels, Casting
Calculation of Thermophysical Properties of Carbon and Low Alloyed Steels for Modeling of Solidification Processes. 909-916B

Low alloy steels, Heat treatment
Atom Probe Field Ion Microscopy Study of the Partitioning of Substitutional Elements During Tempering of a Low-Alloy Steel Martensite. 499-508A

Low alloy steels, Mechanical properties
The Workability of Commercial and Experimental 0.6% Carbon Low Alloy Steels in the Temperature Range of 650-870°C. 827-837A

Low alloy steels, Microstructure
Compositional and Microstructural Changes Which Attend Reheating and Grain Coarsening in Steels Containing Niobium. 277-286A
Formation of Invariant Plane-Strain and Tent-Shaped Surface Reliefs by the Diffusional Ledge Mechanism. (Conference Paper) 1923-1931A

Low alloy steels, Phases (state of matter)
Effects of Austenite Grain Size and Cooling Rate on Widmanstätten Ferrite Formation in Low-Alloy Steels. 665-675A
Titanium-Rich Mineral Phases and the Nucleation of Bainite. 1603-1611A
Diffusion in Growth of Bainite. (Conference Paper) 1957-1966A

Low carbon steels, Coating
The Effect of Steel Chemistry on the Formation of Fe-Zn Intermetallic Compounds of Galvanneal-Coated Steel Sheets. 721-730B

Low carbon steels, Mechanical properties
Behavior of Steels Near the Incipient Melting Temperature. 125-133A

Low carbon steels, Reactions (chemical)
Modeling Hydrogen Entry and Exit in Metals Exposed to Multiple Charging Processes. 723-732A

Low carbon steels, Rolling
Alligatoring and Damage in the Cold Rolling of Spheroidized Steels. 589-598A

Low cycle fatigue, Heating effects
The Role of Magnesium-Containing Spheroidizer and Counteraction of Misch Metal in the Intermediate Temperature Intergranular Embrittlement of Ferritic Nodular Iron. 2305-2309A

Low cycle fatigue, High temperature effects
Effect of Strain Rate on the High-Temperature Low-Cycle Fatigue Properties of a Nimonic PE-16 Superalloy. 159-171A
Low-Cycle Fatigue Behavior of Polycrystalline NiAl at 1000K. 309-319A

Low cycle fatigue, Stress effects
Low-Cycle Fatigue of Dispersion-Strengthened Copper. 2235-2245A
Low-Cycle Fatigue Properties of a SiC Whisker-Reinforced 2124 Aluminum Alloy. 2265-2274A
Low Cycle Fatigue Behavior of Polycrystalline Ni_3Al Alloys at Ambient and Elevated Temperatures. 2469-2476A

Macrostructure, Temperature effects
An Internal Variable Description of Solidification Suitable for Macrosegregation Modeling. 597-605B

Magnesium, Alloying elements
Effect of Alloying Elements on the Solidification Characteristics and Microstructure of Al—Si—Cu—Mg—Fe 380 Alloy. 437-448A

Magnesium, Binary systems
Mg—Pb Phase Diagram and Phase Transformations in the Intermetallic Compounds Mg_2Pb and β'. 265-275B

Magnesium, Powder technology
Formation of Metastable and Equilibrium Phases During Mechanical Alloying of Aluminum and Magnesium Powders. 73-79A

Magnesium, Steel making
Thermodynamics of Oxygen, Nitrogen, and Sulfur in Liquid Iron Equilibrated With $CaO—Al_2O_3—MgO$ Slags. 235-244B

Magnesium, Ternary systems
Thermodynamic Properties of Ternary Liquid Cu—Mg—Ni Alloys. 63-72B
Crystallization Studies of the β^* (Mg_2Pb) Phase and Its Phase Boundaries in the Pb—Mg—Bi System. 255-263B

Magnesium base alloys, Composite materials
Cubic AlNi Compound Dispersed Magnesium-Based Amorphous Matrix Composites Prepared by Rapid Solidification. 1323-1325A

Magnesium base alloys, Phases (state of matter)
A Process for Debismuthizing Lead With Magnesium. 379-384B

Magnetic fields
Mechanism of Damping Capacity of High-Chromium Steels and α-Iron and Its Dependence on Some External Factors. 111-124A
Determination of Residual Nickel in Mechanically Alloyed NiAl. 871-874A

Magnetic flux welding
See Gas metal arc welding

Magnetic force
See Magnetic fields

Magnetic permeability, Heating effects
Aging of Freshly Formed Iron-Based Martensites at Low Temperatures. (Review) 889-909A

Magnetic properties
See Curie temperature
Magnetic permeability
Magnetoelastic effect

Magnetic susceptibility
See Magnetic permeability

Magnetism
See Ferromagnetism

Magnetoacoustic effect
See Magnetoelastic effect

Magnetoelastic effect
Mechanism of Damping Capacity of High-Chromium Steels and α-Iron and Its Dependence on Some External Factors. 111-124A

Magnetomechanical properties
See Magnetoelastic effect

Manganese, Alloying elements
Behavior of Steels Near the Incipient Melting Temperature. 125-133A
Effect of Alloying Elements on the Solidification Characteristics and Microstructure of Al—Si—Cu—Mg—Fe 380 Alloy. 437-448A
Thermodynamics and Kinetics of the Formation of Widmanstätten Ferrite Plates in Ferrous Alloys. (Conference Paper) 1947-1953A
The Influence of the Alloying Elements Upon the Transformation Kinetics and Morphologies of Ferrite Plates in Alloy Steels. (Conference Paper) 1991-2000A

Manganese steels, Mechanical properties
Cleavage Initiation in the Intercritically Reheated Coarse-Grained Heat-Affected Zone: I. Fractographic Evidence. 563-573A

Maraging steels, Heat treatment
Isothermal Formation of Quasicrystalline Precipitates and Their Effect on Strength in a 12Cr-9Ni-4Mo Maraging Stainless Steel. 2225-2233A

Maraging steels, Phases (state of matter)
Improved Thermochemical Calculations for Maraging Steels and Comparison With Atom Probe Measurement of Phase Composition. 2538-2539A

Martensite
Transmission Electron Microscopy Study of Martensites in Laser-Clad Ni—Al Bronze on Aluminium Alloy AA333. 37-46A
The Phenomenological Theory of Martensite Crystallography: Interrelationships. (Conference Paper) 1787-1795A
Intrinsic Ledges at Interphase Boundaries and the Crystallography of Precipitate Plates. (Conference Paper) 1905-1915A

Martensite, Deformation effects
Effects of Precursor Matrix Events on Subsequent Nucleation. (Conference Paper) 1933-1939A

Martensite, Diffusion effects
Decomposition of Iron—Nickel Martensite: Implications for the Low-Temperature ($\leq$ 500°C) Fe—NI Phase Diagram. 1627-1637A

Martensite, Heating effects
Mechanism of Damping Capacity of High-Chromium Steels and α-Iron and Its Dependence on Some External Factors. 111-124A
Atom Probe Field Ion Microscopy Study of the Partitioning of Substitutional Elements During Tempering of a Low-Alloy Steel Martensite. 499-508A
Aging of Freshly Formed Iron-Based Martensites at Low Temperatures. (Review) 889-909A

Martensite, Low temperature effects
Numerical Modeling of γ Precipitate Growth During Fe—Ni Martensite Decomposition at Low Temperatures ($\leq$ 400°C). 1639-1648A

Martensitic stainless steels, Diffusion
Interdiffusion Between Uranium—Zirconium Fuel vs. Selected Cladding Steels. 1649-1653A

Martensitic stainless steels, Heat treatment
Aging of Freshly Formed Iron-Based Martensites at Low Temperatures. (Review) 889-909A

Martensitic transformations
High-Resolution Analytical Electron Microscopy Study of Isothermal Plate-Shaped Products in Some β-Phase Alloys. (Conference Paper) 2569-2579A

Martensitic transformations, Alloying effects
Effects of Carbon Content and Ausaging on $\gamma \rightleftarrows \alpha'$ Transformation Behavior and Reverse-Transformed Structure in Fe—Ni—Co—Al—C Alloys. 63-71A

Martensitic transformations, Cooling effects
Microstructure and Mechanical Properties of Ti—40 wt.% Ta (Ti—15 at.% Ta). 461-472A

Martensitic transformations, Diffusion effects
The Invariant Line and Precipitate Morphology in FCC-BCC Systems. (Conference Paper) 1865-1874A
Atomic Site Correspondence and Surface Relief in the Formation of Plate-Shaped Transformation Products. (Conference Paper) 1917-1922A

Martensitic transformations, Stress effects
Characteristics of the Martensitic Transformation and the Induced Two-Way Shape Memory Effect After Training by Compressive Pseudoelastic Cycling in Cu—Zn—Al Single Crystals. 687-695A
Modeling the Effects of Stress State and Crystal Orientation on the Stress-Induced Transformation of NiTi Single Crystals. 2383-2389A

Materials
See Ceramics
Dissimilar materials

Mathematical analysis
See Numerical analysis

Mathematical models
Thermodynamics of Oxygen and Nitrogen in Liquid Nickel Equilibrated With $CaO—TiO_x$ and $CaO—TiO_x—Al_2O_3$ Melts. 5-13B
The Diffuse-Scattering Method for Investigating Locally Ordered Binary Solid Solutions. 17-35A
The Measurement of the Heat-Transfer Coefficient Between High-Temperature Liquids and Solid Surfaces. 43-51B
High-Temperature Phase Relations and Thermodynamics in the Iron—Lead—Sulfur System. 53-61B
Standard Enthalpies of Formation of Some Praseodymium Alloys of High-Temperature Direct Synthesis Calorimetry. 73-77B
Determination of Pore Mobility During Sintering. 81-87A

Barrier-Layer Formation and Its Control During Hydrogen Permeation Through Ti—24Al—11Nb Alloy. 89-97A
Solubility and Thermodynamic Properties of Y_2O_3 in LiF—YF_3 Melts. 91-96B
High-Temperature Isopiestic Studies on the Ternary Slag PbO—SiO_2—B_2O_3 at 1273K. 103-109B
Modeling of the Incorporation of Ceramic Particulates in Metallic Droplets During Spray Atomization and Coinjection. 135-147B
Modeling of Mechanical Alloying. I. Deformation, Coalescence, and Fragmentation Mechanisms. 147-158A
A Note on the Sensitivity of Solidification Models to Thermophysical Properties. 154-157B
Simulation of In Situ Uraninite Leaching. I. A Partial Equilibrium Model of the NH_4HCO_3—$(NH_4)_2CO_3$—H_2O_2 Leaching System. 171-183B
Adsorption Kinetics of Dicyanoaurate and Dicyanoargentate Ions in Activated Carbon. 185-191B
Physical and Mathematical Modeling of Pyrometallurgical Channel Reactors With Bottom Gas Injection. Residence Time Distribution Analysis and Ideal-Reactor-Network Model. 207-219B
Discussion of "Grain Growth of a Superplastic 7475 Aluminum Alloy". 221-223A
A Simplified Method of Calculating the Stress Field at the Tip of a Discrete Dislocation Pileup in a Finite Crystal. 223-225A
Thermodynamics of Oxygen, Nitrogen, and Sulfur in Liquid Iron Equilibrated With CaO—Al_2O_3—MgO Slags. 235-244B
Kinetics of the Reaction of H_2O Gas With Liquid Iron. 245-253B
An Alternative Gibbs—Duhem Method for the Calculation of Activities From the Redox Data for Iron Oxide in Ternary Oxide Systems. 277-280B
A Simple but Realistic Model for Laser Cladding. 281-291B
Effect of Orientation on Crystallographic Cracking in Notched Nickel-Base Superalloy Single Crystal Subjected to Far-Field Cyclic Compression. 287-297A
Natural Convection in an Aluminum Ingot: a Mathematical Model. 293-302B
Tensile Ductility of Extrinsically Toughened Intermetallics. 299-308A
Equilibrium Values for the Dissolution of Solid Copper Into FeS—Na_2S Mattes. 306-308B
A Comparison of Three Mathematical Modeling Procedures for Simulating Fluid Flow Phenomena in Bubble-Stirred Ladles. 308-312B
Slurry Filtration and Cake Washing After the HCl-Leach of Magnesite and Serpentine—Continuous Washing Model. 321-331B
Characterization of Inhomogeneous Elastic Deformation With X-Ray Diffraction. 341-347A
Estimation of Interfacial Shear Strength Between Superconducting Oxides and Silver Sheath From Multiple-Fracture Phenomenon of the Oxide. 349-356A
A Mathematical Model of Ionic Transport in a Porous Diaphragm of a Chrome—Alum Cell. 351-358B
The Tensile Deformation Behavior of AA 3004 Aluminum Alloy. 357-364A
Large-Scale Measurements of the Physical Characteristics of Round Vertical Bubble Plumes in Liquids. 359-371B
Oxygen Potentials in Nickel + NiO and Nickel + Cr_2O_3 + $NiCr_2O_4$ Systems. 373-378B
Softening and Microstructural Change Following the Dynamic Recrystallization of Austenite. 389-400A
Sticking of Solids in Liquids. 397-403B
Analysis of Thermally Induced Stress and Strain in Continuous Fiber-Reinforced Composites. 415-425A
Modeling the Thin-Slab Continuous-Casting Mold. 443-457B
Equilibrium Oxygen Pressures of Iron Silicate Slags. 463-465B
An Analysis of Slag Stratification in Nickel Laterite Smelting Furnaces Due to Composition and Temperature Gradients. 491-496B
Small Cell Experiments for Electrolytic Reduction of Uranium Oxides to Uranium Metal Using Fluoride Salts. 505-518B
Surface Characterization and Reactivity of a Nitrogen Atomized 304L Stainless Steel Powder. 509-520A
A Model for Estimation of Viscosities of Complex Metallic and Ionic Melts. 519-525B
Local Melting in Al—Mg—Zn—Alloys. 521-530A
Morphological Stability of γ/α Interface Formed by Carburization in Fe—C—X Alloys. 531-537A
Hydrogen Permeation Behavior in IN718 and GH761 Superalloys. 539-544A
Sulfur Determination in Carbon-Saturated Iron by Solid-State Electrochemical Sensor. 561-568B
Thermodynamics of the Iron)Carbon)Zinc System. 569-578B
The Orientation Dependence of Fatigue-Crack Growth in 8090 Aluminum—Lithium Plate. 575-588A
Kinetics in Multicomponent Metallic)Ionic Systems. 579-587B
Estimation of the Viscosities of Binary Metallic Melts Using Gibbs Energies of Mixing. 589-595B
Alligatoring and Damage in the Cold Rolling of Spheroidized Steels. 589-598A
An Internal Variable Description of Solidification Suitable for Macrosegregation Modeling. 597-605B
Experimental Study of the Influence of Interfacial Energies and Reactivity on Wetting in Metal/Oxide Systems. 599-605A
Solid-State Wetting of Graphite by Lead and Pb—Ni Alloys. 607-615A
A Two-Phase Flow Model of the Stirring of Al)SiC Composite Melt. 607-618B
Three-Dimensional Simulation of the Grain Formation in Investment Castings. 629-635A
Equilibrium Distribution of Fe, Ni, Sb, and Sn between Liquid Cu and a CaO-Rich Slag. 645-651B
Discussion of "The Distribution of Dispersoid Phases in the Extruded ODS Superalloy MA-957 and Reply. 651-653A
The Shapes of the Phase Boundaries of Two Ideal Solution Phases in Ternary and Higher Order Systems. 656-658A
Energy Efficiency Considerations on Monopolar vs. Bipolar Fused Salt Electrolysis Cells. 661-668B
Critical Fluid-Flow Phenomenon in a Gas-Stirred Ladle. 681-693B
Heat Treatment of Investment Cast PH 13-8 Molybdenum Stainless Steel. II. Isothermal Aging Kinetics. 697-704A
The Grand Partition Function of Dilute Biregular Solutions. 703-711B
Modeling Hydrogen Entry and Exit in Metals Exposed to Multiple Charging Processes. 723-732A
Further Discussions on the Solute Redistribution During Dendritic Solidification of Binary Alloys. 731-739B
Thermodynamics of Isolated Pores Filling With Liquid in Sintered Composite Materials. 733-740A
Multiphase Binary Diffusion in Infinite and Semi-Infinite Media. I. On the Determination of Interdiffusion Coefficients. 741-751A
Multiphase Binary Diffusion in Infinite and Semi-Infinite Media. II. On the Numerical Calculation of the Rate Constants for Formation of Product Phases. 753-761A
Thermofluid Analysis and Design of a Low-Temperature Preforming Process. 761-771B
Density Measurements of the Lithium Fluoride/Lithium Sulfide Eutectic at High Temperature. 773-778B
Characterization of Anisotropic Elastic Constants of Silicon-Carbide Particulate Reinforced Aluminum Metal Matrix Composites. I. Experiment. 799-809A
Characterization of Anisotropic Elastic Constants of Silicon-Carbide Particulate Reinforced Aluminum Metal Matrix Composites. II. Theory. 811-819A
The Workability of Commercial and Experimental 0.6% Carbon Low Alloy Steels in the Temperature Range of 650-870°C. 827-837A
Modeling of Metallurgical Emulsions. 855-864B
Thermodynamics of the Liquid {xCu + yAu + (1—x—y)Ge}, ($0.75 \leq x \leq 1$, $0 \leq y \leq 0.125$) Alloys at 1550K by Knudsen Effusion Mass Spectrometry. 857-864A
The Effect of Enhanced Gravity Levels on Microstructural Development in Pb—50 wt.% Sn Alloys During Controlled Directional Solidification. 865-870A
Anomalous Diffusion of Aluminum in β-Titanium. 873-876A
Calculation of Thermophysical Properties of Carbon and Low Alloyed Steels for Modeling of Solidification Processes. 909-916B
Intragranular Ferrite Nucleation in Medium-Carbon Vanadium Steels. 929-936A
Fracture of Glass in Tensile and Bending Tests. 961-968A
Modeling of the Formation of Under-Riser Macrosegregation During Solidification of Binary Alloys. 1051-1062A
Modeling Microstructure Development in Gray Cast Irons. 1063-1079A
Prediction of Columnar to Equiaxed Transition During Diffusion-Controlled Dendritic Alloy Solidification. 1081-1093A
Calorimetric Evaluation of Nonequilibrium State in As-Melt Spun Al—1.72 and Al—3.12 at.% Cu Alloys and Al—6.74, Al—8.48, and Al—11.97 at.% Si Alloys. 1102-1104A
Computer Simulation of Diffusion in Multiphase Systems. 1127-1134A
Anisotropic Plastic Potentials for Polycrystals and Application to the Design of Optimum Blank Shapes in Sheet Forming. 1209-1216A
Numerical Modeling of Solidification and Subsequent Transformation of Fe—Cr—Ni Alloys. 1309-1321A
The Morphological Stability of Lateral Growth in Solid—Solid Phase Transformation During Thin-Film Interdiffusion in Aluminum/Copper Bimetal Films. 1613-1625A
Numerical Modeling of γ Precipitate Growth During Fe—Ni Martensite Decomposition at Low Temperatures ($\leq$ 400°C). 1639-1648A
A Simple Model for Conventional Hot Rolling of Sheet Materials. 1681-1692A
Directional Phase Formation on Melting via Peritectic Reaction. 1747-1760A
The Phenomenological Theory of Martensite Crystallography: Interrelationships. (Conference Paper) 1787-1795A
The Invariant Line and Precipitate Morphology in FCC-BCC Systems. (Conference Paper) 1865-1874A
Ledges and Dislocations in Phase Transformations. (Conference Paper) 1885-1894A
The Role of Structural Ledges as Misfit-Compensating Defects: FCC-BCC Interphase Boundaries. (Conference Paper) 1895-1903A
The Influence of the Alloying Elements Upon the Transformation Kinetics and Morphologies of Ferrite Plates in Alloy Steels. (Conference Paper) 1991-2000A
The Elastic Strain Energy of Growth Ledges on Coherent and Partially Coherent Precipitates. 2073-2082A
Elevated-Temperature Stability of Mechanically Alloyed Copper-Niobium Powders. 2091-2099A
Helium 3 Precipitation in AISI 316L Stainless Steel Induced by Radioactive Decay of Tritium: Growth Mechanism of Helium Bubbles. 2131-2143A
Capillarity in Isothermal Infiltration of Alumina Fiber Preforms With Aluminum. 2145-2152A
Modeling Creep Deformation of a Two-Phase TiAl/Ti_3Al Alloy With a Lamellar Microstructure. 2161-2171A
Microstructural Control in Hot Working of IN-718 Superalloy Using Processing Map. 2275-2284A
Microsegregation in Cellular Solidification. 2295-2301A
Thermodynamic Analysis of the In-Ga-Sb System. 2331-2340A
Modelling the Infiltration Kinetics of Molten Aluminum Into Porous Titanium Carbide. 2357-2370A
Modeling the Effects of Stress State and Crystal Orientation on the Stress-Induced Transformation of NiTi Single Crystals. 2383-2389A
Effect of Iron on the Superplastic Deformation of Zn-22%Al. 2391-2401A
Micromechanical Modelling of Reinforcement Fracture in Particle-Reinforced Metal-Matrix Composites. 2403-2420A
Short Fatigue Crack Growth Behavior in a Ferritic-Bainitic Steel. 2421-2425A
Evaluation of Static and Dynamic Fracture Toughness in Ductile Cast Iron. 2427-2437A
Undercooling-Induced Macrosegregation in Directional Solidification. 2507-2516A
Elastic Constants of SiC_p/Al: Measurements and Modeling. 2832-2835A

Mathematical models, Cooling effects

On Morphologies, Microsegregation, and Mechanical Behavior of Directionally Solidified Cobalt-Base Superalloy at Medium Cooling Rate. 637-642A

Mathematical models, Deformation effects
Hot Deformation Characteristics of INCONEL Alloy MA 754 and Development of a Processing Map. 1693-1702A

Mathematics
See Finite element method
Mathematical models

Mattes
See Copper mattes

Measurement
See Mechanical measurements

Mechanical alloying
Formation of Metastable and Equilibrium Phases During Mechanical Alloying of Aluminum and Magnesium Powders. 73-79A
Modeling of Mechanical Alloying. I. Deformation, Coalescence, and Fragmentation Mechanisms. 147-158A
Mechanical Processing of Iron Powders in Reactive and Nonreactive Gas Atmospheres. 381-388A
Characterization of Mechanically Alloyed Oxide Dispersion-Strengthened Nickel-Base Superalloy MA760. 705-714A
Determination of Residual Nickel in Mechanically Alloyed NiAl. 871-874A
Elevated-Temperature Stability of Mechanically Alloyed Copper-Niobium Powders. 2091-2099A

Mechanical measurements
Elastic Constants of SiC_p/Al: Measurements and Modeling. 2832-2835A

Mechanical properties
See Bonding strength
Brittleness
Compressive properties
Creep (materials)
Ductile brittle transition
Ductility
Elastic constants
Elasticity
Fatigue (materials)
Fracture strength
Hardness
Impact strength
Plasticity
Shear properties
Stiffness
Strain
Tear strength
Thermoelastic properties
Toughness
Wear
Wear resistance

Mechanical tests
See Bend tests
Compression tests
Scratch tests
Tension tests
Torsion tests

Mechanical wear
See Wear

Mechanics
See Fluid mechanics

Mechanisms
Thermodynamic Consideration of Formation Mechanism of α_1 Plate in βCu-Base Alloys. (Conference Paper) 2555-2564A
Transformation Characteristics of α_1 Plates in Cu-Zn-Al Alloys. (Conference Paper) 2581-2599A
The Formation Mechanism of Plate in β Cu-Zn and Cu-Zn-Al Alloys. (Conference Paper) 2601-2608A
Growth Kinetics and High-Temperature TEM In Situ Observation of Bainite in a Cu-Zn Alloy. (Conference Paper) 2609-2614A
Study on the Transformation Mechanism of α_1 Plates in a Copper-Zinc-Aluminum Alloy. (Conference Paper) 2615-2619A
Mechanism of the Early Stages of α_1 Plate Formation in a Cu-39% Zinc Alloy. (Conference Paper) 2631-2637A
The Selection of Precipitate Habit Planes in Cr-32 wt.% Ni. (Conference Paper) 2639-2646A

Medium carbon steels, Heat treatment
Intragranular Ferrite Nucleation in Medium-Carbon Vanadium Steels. 929-936A

Medium carbon steels, Mechanical properties
Behavior of Steels Near the Incipient Melting Temperature. 125-133A

Medium carbon steels, Rolling
Alligatoring and Damage in the Cold Rolling of Spheroidized Steels. 589-598A

Melt spinning
Calorimetric Evaluation of Nonequilibrium State in As-Melt Spun Al—1.72 and Al—3.12 at.% Cu Alloys and Al—6.74, Al—8.48, and Al—11.97 at.% Si Alloys. 1102-1104A
Cubic AlNi Compound Dispersed Magnesium-Based Amorphous Matrix Composites Prepared by Rapid Solidification. 1323-1325A
Modelling the Infiltration Kinetics of Molten Aluminum Into Porous Titanium Carbide. 2357-2370A
Melt-Processed Ni_3Al Matrix Composites Reinforced With TiC Particles. 2525-2534A

Melting
See also Laser beam melting
Surface Tensions of Liquid Fe-Cr and Fe-Cr-N Alloys. 626-628B

Melting, Welding effects
The Influence of Electron-Beam Welding Parameters on Heat-Affected-Zone Microfissuring in Incoloy 903. 1733-1745A

Melting points
Solubility and Thermodynamic Properties of Y_2O_3 in LiF—YF_3 Melts. 91-96B
Gradient Solid Electrolytes for Thermodynamic Measurements: System Na_2CO_3—Na_2SO_4. 173-180A

Melting points, Alloying effects
Behavior of Steels Near the Incipient Melting Temperature. 125-133A

Melting points, Temperature effects
Thermodynamic Analysis of the In-Ga-Sb System. 2331-2340A

Melts
See also Liquid metals

Melts, Physical properties
Estimation of the Viscosities of Binary Metallic Melts Using Gibbs Energies of Mixing. 589-595B
A Two-Phase Flow Model of the Stirring of Al)SiC Composite Melt. 607-618B

Memory (shape)
See Shape memory

Metal carbides
See Chromium carbide
Titanium carbide
Tungsten carbide

Metal inert gas welding
See Gas metal arc welding

Metal powders
See Alloy powders

Metal scrap, Recovering
Equilibrium Values for the Dissolution of Solid Copper Into FeS—Na_2S Mattes. 306-308B

Metal working
See Hot working
Thermomechanical treatment

Metallic compounds
See Intermetallics

Metallographic structures
See Microstructure

Metallography
See Crystallography

Metalloids
See Boron
Carbon
Germanium
Silicon

Metallurgical analysis
See Qualitative analysis
Sampling

Metallurgical constituents
See Ferrite
Laves phase

Metallurgy
See Powder metallurgy
Process metallurgy

Metals
See Dissimilar metals
Filler metal
Liquid metals

Metastable phases
The Selection of Precipitate Habit Planes in Cr-32 wt.% Ni. (Conference Paper) 2639-2646A

Metastable phases, Composition effects
Supersaturation of the Al_2Y Laves Phase by Rapid Solidification. 230-233A

Metastable phases, Cooling effects
Microstructure and Mechanical Properties of Ti—40 wt.% Ta (Ti—15 at.% Ta). 461-472A
Nonequilibrium Solidification of Undercooled Melt of Ag-Cu Alloy Entrained in the Primary Phase. 2517-2523A
Precipitation of BCC Phase from Nonequilibrium A13-Type Phase in Rapidly Solidified High-Carbon Fe-Cr-Mo Alloy. 2542-2546A

Metastable phases, Deformation effects
Formation of Metastable and Equilibrium Phases During Mechanical Alloying of Aluminum and Magnesium Powders. 73-79A
A Simple Model for Conventional Hot Rolling of Sheet Materials. 1681-1692A

Metastable phases, Diffusion effects
Application of the Theory of Martensite Crystallography to Displacive Phase Transformations in Substitutional Nonferrous Alloys. (Conference Paper, Review) 1841-1856A

Metastable phases, Heating effects
Microstructural Study of the Titanium Alloy Ti—15Mo—2.7Nb—3Al—0.2Si (TIMETAL 21S). 1109-1118A
Formation and Stability of Metastable Structures and Amorphous Phases in Pu—V, Pu—TA, and Pu—Yb Systems With Positive Heats of Mixing. 1579-1590A

Metastable phases, Temperature effects
Partition of Alloying Elements Between γ (A1), γ' ($L1_2$), and β (B2) Phases in Ni—Al Base Systems. 473-485A

Metathesis
See Decomposition reactions

Microbial leaching
See Bacterial leaching

Microcracking
See Crack initiation

Microhardness, Cooling effects
Characterization of Mechanically Alloyed Oxide Dispersion-Strengthened Nickel-Base Superalloy MA760. 705-714A

Microhardness, Microstructural effects
Precipitation Effects During Hot Deformation of a Copper Alloy. 257-266A
Role of Al_2O_3 Particulate Reinforcements on Precipitation in 2014 Aluminum-Matrix Composites. 1591-1602A

Microhardness, Pressure effects
The Effects of Hydrostatic Pressure on the Compressive Mechanical Behavior of $L1_2$ Al_3 Ti-Based Intermetallic. 1703-1711A

Microhardness, Radiation effects
Effects of Simultaneous Boron and Nitrogen Implantation on Microhardness and Fatigue Properties of Fe—13Cr—15Ni Alloys. 193-202A

Microprobes
See Electron probes

Microscopy
See Electron microscopy

Microshrinkage
See Shrinkage

Microstructure
See also Amorphous structure
Crystal structure
Dislocation density
Grain size
Grain structure
Graphitic structure
Heterogeneous structure
Homogeneous structure
Lamellar structure
Spheroidal structure
Texture

Microstructure, Alloying effects
Microstructures and Mechanial Behavior of NiAl-Mo and NiAl-Mo-Ti Two-Phase Alloys. 2769-2781A

Microstructure, Composition effects
High-Temperature Oxidation of Cathodically Hydrogen-Charged Two-Phase (Ti_3Al, TiAl) Titanium Aluminides. 2491-2496A

Microstructure, Cooling effects
Fatigue Crack Growth Rates and Fracture Toughness of Rapidly Solidified Al—8.5Fe—1.2V—1.7Si Alloys. 1005-1014A

Microstructure, Deformation effects
A Simple Model for Conventional Hot Rolling of Sheet Materials. 1681-1692A

Microstructure, Heating effects
Morphology Development in Hot-Dip Galvanneal Coatings. 937-947A

Mig arc welding
See Gas metal arc welding

MIG welding
See Gas metal arc welding

Migration
See Diffusion

Mild carbon steels
See Low carbon steels

Mild steels
See Carbon steels

Mixing
See also Mechanical alloying
Backmixing in Channel Reactors With High-Strength Bottom Gas Injection. 619-623B

Mobility
See Dislocation mobility

Modulus of elasticity
Elastic Constants of SiC_p/Al: Measurements and Modeling. 2832-2835A

Modulus of elasticity, Composition effects
Room-Temperature Strength and Deformation of TiB_2-Reinforced Near-γ Titanium Aluminides. 2181-2197A
Melt-Processed Ni_3Al Matrix Composites Reinforced With TiC Particles. 2525-2534A

Modulus of elasticity, Microstructural effects
Characterization of Anisotropic Elastic Constants of Silicon-Carbide Particulate Reinforced Aluminum Metal Matrix Composites. I. Experiment. 799-809A

Modulus of elasticity, Stress effects
Behavior of Nickel-Base Superalloy Single Crystals Under Thermal—Mechanical Fatigue. 99-109A
Characterization of Anisotropic Elastic Constants of Silicon-Carbide Particulate Reinforced Aluminum Metal Matrix Composites. II. Theory. 811-819A

Modulus of elasticity, Temperature effects
Elastic Constants of Some Transition-Metal-Disilicide Single Crystals. 331-340A

Modulus of rigidity
See Shear modulus

Modulus of shear
See Shear modulus

Modulus of torsion
See Shear modulus

Moistening
See Wetting

Moisture
See Water

Molten metals
See Liquid metals

Molybdenum, Alloying elements
Influence of Tempering Temperature on Stability of Carbide Phases in 2.6Cr—0.7Mo—0.3V Steel With Various Carbon Content. 267-275A
The Influence of the Alloying Elements Upon the Transformation Kinetics and Morphologies of Ferrite Plates in Alloy Steels. (Conference Paper) 1991-2000A
Microstructures and Mechanial Behavior of NiAl-Mo and NiAl-Mo-Ti Two-Phase Alloys. 2769-2781A

Molybdenum, Composite materials
Development and Characterization of Interface Coatings in Molybdenum-Reinforced NiAl Matrix Composites. 2111-2116A

Molybdenum, Recovering
Processing of Spent Hydrorefining Catalysts by Selective Chlorination. 481-490B

Molybdenum chromium nickel steels
See Nickel chromium molybdenum steels

Molybdenum chromium steels
See Chromium molybdenum steels

Molybdenum compounds, Composite materials
Phase Relations in the Mo—Si—C System Relevant to the Processing of $MoSi_2$—SiC Composites. 5-15A
The Effect of Niobium Morphology on the Cyclic Oxidation Resistance of $MoSi_2$/20 vol.% Niobium Composites. 1033-1040A

Molybdenum nickel chromium steels
See Nickel chromium molybdenum steels

Molybdenum steels
See also Chromium molybdenum steels

Molybdenum steels, Heat treatment
Softening and Microstructural Change Following the Dynamic Recrystallization of Austenite. 389-400A

Monel
See Nickel base alloys

Monocrystals
See Single crystals

Multiaxial stress
See Axial stress

Natural aging
See Aging (natural)

Near net shaping
Modeling the Thin-Slab Continuous-Casting Mold. 443-457B
Modelling the Infiltration Kinetics of Molten Aluminum Into Porous Titanium Carbide. 2357-2370A

Necking, Stress effects
Crack Initiation at Long Radial Hydrides in Zr—2.5Nb Pressure Tube Material at Elevated Temperatures. 993-1004A

Nickel, Alloying elements
Solid-State Wetting of Graphite by Lead and Pb—Ni Alloys. 607-615A
Thermodynamics and Kinetics of the Formation of Widmanstatten Ferrite Plates in Ferrous Alloys. (Conference Paper) 1947-1953A

Nickel, Binary systems
Partition of Alloying Elements Between γ (A1), γ' ($L1_2$), and β (B2) Phases in Ni—Al Base Systems. 473-485A

Nickel, Composite materials
Thermodynamics of Isolated Pores Filling With Liquid in Sintered Composite Materials. 733-740A

Nickel, Microstructure
Characterization of Inhomogeneous Elastic Deformation With X-Ray Diffraction. 341-347A

Nickel, Phases (state of matter)
The Velocity of Solidification of Highly Undercooled Nickel. 1301-1308A

Nickel, Physical properties
Sticking of Solids in Liquids. 397-403B

Nickel, Recovering
Processing of Spent Hydrorefining Catalysts by Selective Chlorination. 481-490B

Nickel, Refining
Physicochemical Properties of Nickel Electrolytes. 637-644B

Nickel, Sorption
Gas Trapping and Release in Polycrystalline Nickel Preimplanted With Helium. 949-959A

Nickel, Structural hardening
Diffusional Boundary Conditions During Coarsening of Elastically Interacting Precipitates. 2695-2703A

Nickel, Ternary systems
Thermodynamic Properties of Ternary Liquid Cu—Mg—Ni Alloys. 63-72B
Numerical Modeling of Solidification and Subsequent Transformation of Fe—Cr—Ni Alloys. 1309-1321A

Nickel base alloys, Atomic properties
The Diffuse-Scattering Method for Investigating Locally Ordered Binary Solid Solutions. 17-35A

Nickel base alloys, Casting
Three-Dimensional Simulation of the Grain Formation in Investment Castings. 629-635A

Nickel base alloys, Claddings
Processing, Microstructure, and Properties of Laser-Clad Nickel Alloy FP-5 on Al Alloy AA333. 425-434B

Nickel base alloys, Coating
Microstructural Evolution of an Overlay Coating on a Single-Crystal Nickel-Base Superalloy. 2837-2840A

Nickel base alloys, Composite materials
Investigation of the Kinetics of Reduction of Nickel Tungstate by Hydrogen. 391-396B

Nickel base alloys, Corrosion
Creep and Intergranular Cracking of Ni—Cr—Fe—C in 360°C Argon. 1169-1183A

Nickel base alloys, Extrusion
Discussion of "The Distribution of Dispersoid Phases in the Extruded ODS Superalloy MA-957 and Reply. 651-653A

Nickel base alloys, Heat treatment
Hydrogen Permeation Behavior in IN718 and GH761 Superalloys. 539-544A
Computer Simulation of Diffusion in Multiphase Systems. 1127-1134A

Nickel base alloys, Mechanical properties
Behavior of Nickel-Base Superalloy Single Crystals Under Thermal—Mechanical Fatigue. 99-109A
Effect of Orientation on Crystallographic Cracking in Notched Nickel-Base Superalloy Single Crystal Subjected to Far-Field Cyclic Compression. 287-297A
Characterization of Mechanically Alloyed Oxide Dispersion-Strengthened Nickel-Base Superalloy MA760. 705-714A
Hot Deformation Characteristics of INCONEL Alloy MA 754 and Development of a Processing Map. 1693-1702A
Modeling the Effects of Stress State and Crystal Orientation on the Stress-Induced Transformation of NiTi Single Crystals. 2383-2389A

Nickel base alloys, Metal working
Microstructural Control in Hot Working of IN-718 Superalloy Using Processing Map. 2275-2284A

Nickel base alloys, Microstructure
Transmission Electron Microscopy Crystal Structure Study of the Chromium-Rich Phase in a Laser-Clad Nickel Alloy. 487-497A

Nickel base alloys, Oxidation
Oxygen Potentials in Nickel + NiO and Nickel + Cr_2O_3 + $NiCr_2O_4$ Systems. 373-378B

Nickel base alloys, Phases (state of matter)
Triclinic Ni_2Al Phase in 63.1 at.% NiAl. 57-61A

Nickel base alloys, Reactions (chemical)
Thermodynamics of Oxygen and Nitrogen in Liquid Nickel Equilibrated With CaO—TiO_x and CaO—TiO_x—Al_2O_3 Melts. 5-13B

Nickel base alloys, Structural hardening
Strain Hardening in Underaged Inconel 718. 653-656A

Nickel base alloys, Welding
The Influence of Electron-Beam Welding Parameters on Heat-Affected-Zone Microfissuring in Incoloy 903. 1733-1745A
Effect of Welding Variables and Solidification Substructure on Weld Metal Porosity. 2285-2294A

Nickel chromium molybdenum steels, Heat treatment
The Effects of Double Austenitization on the Mechanical Properties of a 0.34C Containing Low-Alloy Ni—Cr—Mo—V Steel. 545-555A
Phosphorus and Carbon Segregation: Effects on Fatigue and Fracture of Gas-Carburized Modified 4320 Steel. 1229-1240A

Nickel chromium steels
See Nickel chromium molybdenum steels

Nickel compounds, Composite materials
Fiber Strength and Fiber/Matrix Bond Strength in Single Crystal Al_2O_3 Fiber Reinforced Ni_3Al Based Composites. 1259-1265A
A Structural Study of Oxidation in a Zirconia-Toughened Alumina Fiber-Reinforced NiAl Composite. 1291-1299A
Development and Characterization of Interface Coatings in Molybdenum-Reinforced NiAl Matrix Composites. 2111-2116A
Melt-Processed Ni_3Al Matrix Composites Reinforced With TiC Particles. 2525-2534A

Nickel compounds, Extrusion
Discussion of "The Role of Microstructure on Strength and Ductility of Hot-Extruded Mechanically Alloyed NiAl" and Author's Reply. 2303-2305A

Nickel compounds, Mechanical properties
Low-Cycle Fatigue Behavior of Polycrystalline NiAl at 1000K. 309-319A
Low Cycle Fatigue Behavior of Polycrystalline Ni_3Al Alloys at Ambient and Elevated Temperatures. 2469-2476A
Creep Characteristics of Single Crystalline Ni_3Al(Ta,B). 2477-2482A
Microstructures and Mechanial Behavior of NiAl-Mo and NiAl-Mo-Ti Two-Phase Alloys. 2769-2781A

Nickel compounds, Powder technology
Determination of Residual Nickel in Mechanically Alloyed NiAl. 871-874A
High-Performance Ni_3Al Synthesized From Composite Powders. 985-992A

Nickel compounds, Rolling
High-Temperature Deformation of B2 NiAl-Base Alloys. (Conference Paper) 2017-2026A

Nickel molybdenum chromium steels
See Nickel chromium molybdenum steels

Nickel molybdenum steels
See Nickel chromium molybdenum steels

Nickel steels, Phases (state of matter)
Decomposition of Iron—Nickel Martensite: Implications for the Low-Temperature (≤ 500°C) Fe—NI Phase Diagram. 1627-1637A
Numerical Modeling of γ Precipitate Growth During Fe—Ni Martensite Decomposition at Low Temperatures (≤ 400°C). 1639-1648A

Niobium, Alloying elements
Compositional and Microstructural Changes Which Attend Reheating and Grain Coarsening in Steels Containing Niobium. 277-286A
Effects of Austenite Grain Size and Cooling Rate on Widmanstätten Ferrite Formation in Low-Alloy Steels. 665-675A

Niobium, Composite materials
The Effect of Niobium Morphology on the Cyclic Oxidation Resistance of $MoSi_2$/20 vol.% Niobium Composites. 1033-1040A

Niobium compounds, Superconductivity
Effect of Oxygen and Zirconium on the Growth and Superconducting Properties of Nb_3Sn. 203-212A
The Role of Oxygen and Zirconium in the Formation and Growth of Nb_3Sn Grains. 213-219A

Nitrogen, Alloying elements
Compositional and Microstructural Changes Which Attend Reheating and Grain Coarsening in Steels Containing Niobium. 277-286A

Nitrogen, Dopants
Effects of Simultaneous Boron and Nitrogen Implantation on Microhardness and Fatigue Properties of Fe—13Cr—15Ni Alloys. 193-202A

Nodular graphitic structure, Stress effects
The Effect of Triaxial Stress on Ductility and Fracture Morphology of Ferritic Spheroidal Graphite Cast Iron. 821-825A

Nodular iron, Heat treatment
The Role of Magnesium-Containing Spheroidizer and Counteraction of Misch Metal in the Intermediate Temperature Intergranular Embrittlement of Ferritic Nodular Iron. 2305-2309A

Nodular iron, Mechanical properties
Evaluation of Static and Dynamic Fracture Toughness in Ductile Cast Iron. 2427-2437A

Nodular iron, Microstructure
Chemical Composition and Structural Identification of Eutectic Carbide in 1% Manganese Ductile Iron. 911-918A

Nodules (graphite)
See Nodular graphitic structure

Nondestructive testing
See Ultrasonic testing

Nonferrous alloys
See Cobalt base alloys
Nickel base alloys
Zinc base alloys
Zirconium base alloys

Nonferrous metals
See Cobalt
Copper
Gallium
Indium
Manganese
Nickel
Yttrium
Zinc
Zirconium

Nonferrous smelting
See Smelting

Notch brittleness
See Brittleness

Notch ductility
See Ductility

Notch impact strength
See Impact strength

Notch impact tests
See Impact tests

Notched bar tensile test
See Tension tests

Notched bend test
See Bend tests

Nuclear fuels, Diffusion
Interdiffusion Between Uranium—Zirconium Fuel vs. Selected Cladding Steels. 1649-1653A

Nuclear reactor components, Irradiation
Deformation Behavior of Irradiated Zr—2.5Nb Pressure Tube Material. 135-145A

Nuclear reactor components, Materials selection
Hydride Embrittlement in Zircaloy-4 Plate. II. Interaction Between the Tensile Stress and the Hydride Morphology. 1199-1208A

Nuclear reactor components, Mechanical properties
Hydride Embrittlement in Zircaloy-4 Plate. I. Influence of Microstructure on the Hydride Embrittlement in Zircaloy-4 at 20 and 350°C. 1185-1197A

Nucleation
High-Resolution Analytical Electron Microscopy Study of Isothermal Plate-Shaped Products in Some β-Phase Alloys. (Conference Paper) 2569-2579A
The Formation Mechanism of Plate in β Cu-Zn and Cu-Zn-Al Alloys. (Conference Paper) 2601-2608A

Nucleation, Alloying effects
Effects of Carbon Content and Ausaging on $\gamma \rightleftarrows \alpha'$ Transformation Behavior and Reverse-Transformed Structure in Fe—Ni—Co—Al—C Alloys. 63-71A
Effects of Austenite Grain Size and Cooling Rate on Widmanstätten Ferrite Formation in Low-Alloy Steels. 665-675A
On the Prebainitic Phenomenon in Some Alloys. (Conference Paper) 1941-1946A

Nucleation, Cooling effects
Intragranular Ferrite Nucleation in Medium-Carbon Vanadium Steels. 929-936A
Modeling Microstructure Development in Gray Cast Irons. 1063-1079A
The Velocity of Solidification of Highly Undercooled Nickel. 1301-1308A
Undercooling-Induced Macrosegregation in Directional Solidification. 2507-2516A

Nucleation, Deformation effects
Effects of Precursor Matrix Events on Subsequent Nucleation. (Conference Paper) 1933-1939A

Nucleation, Heating effects
Titanium-Rich Mineral Phases and the Nucleation of Bainite. 1603-1611A
Formation Mechanism of Bainite Ferrite and Carbide. (Conference Paper) 2001-2007A

Nucleation, Radiation effects
Helium 3 Precipitation in AISI 316L Stainless Steel Induced by Radioactive Decay of Tritium: Growth Mechanism of Helium Bubbles. 2131-2143A

Nucleation, Temperature effects
Morphology of Bainite and Widmanstätten Ferrite. (Conference Paper) 1981-1989A

Nuclei (transformation)
See Nucleation

Numerical analysis
Diffusion-Controlled Growth in Ternary Systems. 2683-2694A
Numerical Analysis of the Rapid Solidification of Gas-Atomized Al-8 wt.% Iron Droplets. 2815-2826A

Order disorder
See also Long range order
Short range order
The Diffuse-Scattering Method for Investigating Locally Ordered Binary Solid Solutions. 17-35A
Transmission Electron Microscopy Study of Martensites in Laser-Clad Ni—Al Bronze on Aluminium Alloy AA333. 37-46A
Transformation Characteristics of α_1 Plates in Cu-Zn-Al Alloys. (Conference Paper) 2581-2599A

Order disorder, Composition effects
Supersaturation of the Al_2Y Laves Phase by Rapid Solidification. 230-233A

Order disorder, Deformation effects
Relationships of Slip Morphology, Microcracking, and Fracture Resistance in a Lamellar TiAl-Alloy. 1217-1228A

Order disorder, Heating effects
Al_2Ti Precipitation in $Al_{64}Fe_8Ti_{28}$ Alloy. 715-721A

Order disorder, Temperature effects
Comparison of Orthorhombic and Alpha-Two Titanium Aluminides as Matrices for Continuous SiC-Reinforced Composites. 1267-1283A

Ordered alloys
See Intermetallics

Ordering
See Order disorder

Ores
See Iron ores

Orientation
See Orientation relationships

Orientation relationships
The Orientation Dependence of Fatigue-Crack Growth in 8090 Aluminum—Lithium Plate. 575-588A
Mechanism of the Early Stages of α_1 Plate Formation in a Cu-39% Zinc Alloy. (Conference Paper) 2631-2637A
The Selection of Precipitate Habit Planes in Cr-32 wt.% Ni. (Conference Paper) 2639-2646A

Oxidation
Physical Modeling Studies of Electrolyte Flow Due to Gas Evolution and Some Aspects of Bubble Behavior in Advanced Hall Cells. II. Flow and Interpolar Resistance in Cells With a Grooved Anode. 341-349B
A Mathematical Model of Ionic Transport in a Porous Diaphragm of a Chrome—Alum Cell. 351-358B
Surface Characterization and Reactivity of a Nitrogen Atomized 304L Stainless Steel Powder. 509-520A
Interactions Between Drops of a Molten Aluminum)Lithium Alloy and Liquid Water. 623-625B
High-Performance Ni_3Al Synthesized From Composite Powders. 985-992A

Oxidation, Composition effects
High-Temperature Oxidation of Cathodically Hydrogen-Charged Two-Phase (Ti_3Al, TiAl) Titanium Aluminides. 2491-2496A

Oxidation, Heating effects
Auger Electron Analysis of the Initial Oxidation of Titanium Aluminides Based on Ti—48Al. 1041-1050A
A Structural Study of Oxidation in a Zirconia-Toughened Alumina Fiber-Reinforced NiAl Composite. 1291-1299A

Oxidation, Pressure effects
Kinetics of the Reaction of H_2O Gas With Liquid Iron. 245-253B

Oxidation, Stress effects
Behavior of Nickel-Base Superalloy Single Crystals Under Thermal—Mechanical Fatigue. 99-109A

Oxidation, Temperature effects
Kinetics of Interlayer Formation on Polycrystalline α-Al_2O_3/Copper-Titanium Alloy Interface. 2083-2090A

Oxidation resistance, Composition effects
The Effect of Niobium Morphology on the Cyclic Oxidation Resistance of $MoSi_2$/20 vol.% Niobium Composites. 1033-1040A
Melt-Processed Ni_3Al Matrix Composites Reinforced With TiC Particles. 2525-2534A

Oxidation resistance, Temperature effects
Oxygen Potentials in Nickel + NiO and Nickel + Cr_2O_3 + $NiCr_2O_4$ Systems. 373-378B

Oxides
See also Aluminum oxide

Oxides, Phase transformations
Bainitelike Transformations in Some Oxide Ceramics. (Conference Paper) 2647-2653A

Oxidizing
See Oxidation

Oxygen, Alloying elements
Effect of Oxygen and Zirconium on the Growth and Superconducting Properties of Nb_3Sn. 203-212A
The Role of Oxygen and Zirconium in the Formation and Growth of Nb_3Sn Grains. 213-219A

Oxygen, Quaternary systems
Thermodynamic Study of $BaCuO_2$ and $BaCu_2O_2$. 385-389B

Oxygen, Ternary systems
Thermodynamic Study of the Bi—Ca—O System. 97-101B

Oxygen compounds
See Oxides

Pack rolling, Pressure effects
Load-Signature Analysis for Pack Rolling of Near-Gamma Titanium Aluminide Alloys. 2539-2542A

Packet rolling
See Pack rolling

Packing (amorphous structure)
See Amorphous structure

Packing (crystal density)
See Crystal structure

Packing (liquid structure)
See Atomic structure

Parameters
See Lattice parameters
Welding parameters

Partial pressure
Thermodynamic Study of $BaCuO_2$ and $BaCu_2O_2$. 385-389B
Thermodynamics of the Liquid {xCu + yAu + (1—x—y)Ge}, ($0.75 \leq x \leq 1$, $0 \leq y \leq 0.125$) Alloys at 1550K by Knudsen Effusion Mass Spectrometry. 857-864A

Particulate composites, Casting
Cubic AlNi Compound Dispersed Magnesium-Based Amorphous Matrix Composites Prepared by Rapid Solidification. 1323-1325A

Particulate composites, Fabrication
Modelling the Infiltration Kinetics of Molten Aluminum Into Porous Titanium Carbide. 2357-2370A
Melt-Processed Ni_3Al Matrix Composites Reinforced With TiC Particles. 2525-2534A

Particulate composites, Forging
Forging Limits for an Aluminum Matrix Composite. I. Experimental Results. (Conference Paper) 2027-2038A
Forging Limit for an Aluminum Matrix Composite. II. Analysis. (Conference Paper) 2039-2048A

Particulate composites, Heat treatment
Effect of Heat Treatment on the Microstructure, Tensile Properties, and Fracture Behavior of Permanent Mold Al-10 wt.% Si-0.6 wt.% Mg/SiC/10p Composite Castings. 2247-2263A

Particulate composites, Joining
Kinetic Study of Low-Temperature Transient Liquid Phase Joining of an Aluminum-SiC Composite. 2705-2714A

Particulate composites, Mechanical properties
Characterization of Anisotropic Elastic Constants of Silicon-Carbide Particulate Reinforced Aluminum Metal Matrix Composites. II. Theory. 811-819A
Coefficients of Thermal Expansion of Metal-Matrix Composites for Electronic Packaging. 839-850A
Effect of Microstructure (Particulate Size and Volume Fraction) and Counterface Material on the Sliding Wear Resistance of Particulate-Reinforced Aluminum Matrix Composites. 969-983A
Transformation, Microcrack, and Thermal Residual Stress as Interactive Processes in ZrO_2-Toughened Al_2O_3, Simulated by the Finite Element Method. 1725-1731A
Room-Temperature Strength and Deformation of TiB_2-Reinforced Near-γ Titanium Aluminides. 2181-2197A
Thermal-Mechanical Fatigue of Ti-48Al-2V Alloy and Its Composite. 2207-2212A
Low-Cycle Fatigue of Dispersion-Strengthened Copper. 2235-2245A
Micromechanical Modelling of Reinforcement Fracture in Particle-Reinforced Metal-Matrix Composites. 2403-2420A
The Influence of SiC Particulates on Fatigue Crack Propagation in a Rapidly Solidified Al-Fe-V-Si Alloy. 2453-2460A

Fracture Toughness of Discontinuously Reinforced Al-4Cu-1.5Mg/TiB_2 Composites. 2461-2468A
Elastic Constants of SiC_p/Al: Measurements and Modeling. 2832-2835A

Particulate composites, Oxidation
The Effect of Niobium Morphology on the Cyclic Oxidation Resistance of $MoSi_2$/20 vol.% Niobium Composites. 1033-1040A

Particulate composites, Phases (state of matter)
A Two-Phase Flow Model of the Stirring of Al)SiC Composite Melt. 607-618B

Particulate composites, Powder technology
Modeling of the Incorporation of Ceramic Particulates in Metallic Droplets During Spray Atomization and Coinjection. 135-147B
Characterization of Anisotropic Elastic Constants of Silicon-Carbide Particulate Reinforced Aluminum Metal Matrix Composites. I. Experiment. 799-809A
Microstructural Analysis of Fracture Toughness Variation in 2XXX-Series Aluminum Alloy Composites Reinforced With SiC Whiskers. 2213-2223A

Particulate composites, Structural hardening
Stress-State Dependence of Strain-Hardening Behavior in 2014 Al/15 vol.% Al_2O_3 Composite. (Conference Paper) 2049-2061A

Particulate composites Structural hardening
Role of Al_2O_3 Particulate Reinforcements on Precipitation in 2014 Aluminum-Matrix Composites. 1591-1602A

Passivation, Microstructural effects
Influence of Near-Surface Microstructures on the Transient Current Response in Fe—Cr—Ni Alloys During Scratch Tests. 1325-1331A

Pearlite
The Study of Adiabatic Shear Band Instability in a Pearlitic 4340 Steel Using a Dynamic Punch Test. 2483-2489A

Pearlite, Cooling effects
Effects of Widmanstätten Ferrite on the Mechanical Properties of a 0.2% C—0.7% Mn Steel. 763-773A
Modeling Microstructure Development in Gray Cast Irons. 1063-1079A

Pearlite, Stress effects
Evaluation of Static and Dynamic Fracture Toughness in Ductile Cast Iron. 2427-2437A

Penetration, Temperature effects
Barrier-Layer Formation and Its Control During Hydrogen Permeation Through Ti—24Al—11Nb Alloy. 89-97A

Penrose tiling
See Quasicrystalline structure

Percolation
Applicability of Bond Percolation Theory to Intergranular Stress-Corrosion Cracking of Sensitized AISI 304 Stainless Steel. 775-787A

Peritectic reactions
Directional Phase Formation on Melting via Peritectic Reaction. 1747-1760A

Peritectic reactions, Cooling effects
Crystallization Studies of the β' (Mg_2Pb) Phase and Its Phase Boundaries in the Pb—Mg—Bi System. 255-263B

Permanent mold casting
See Die casting

Permeability, Heating effects
Hydrogen Permeation Behavior in IN718 and GH761 Superalloys. 539-544A

Permeability, Temperature effects
Barrier-Layer Formation and Its Control During Hydrogen Permeation Through Ti—24Al—11Nb Alloy. 89-97A

Permeability (magnetic)
See Magnetic permeability

Permeation
See Penetration

Phase boundary
The Shapes of the Phase Boundaries of Two Ideal Solution Phases in Ternary and Higher Order Systems. 656-658A
The Role of Structural Ledges as Misfit-Compensating Defects: FCC-BCC Interphase Boundaries. (Conference Paper) 1895-1903A
Intrinsic Ledges at Interphase Boundaries and the Crystallography of Precipitate Plates. (Conference Paper) 1905-1915A

Phase boundary, Alloying effects
The Fine Structure and Formation Mechanism of Lower Bainite. (Conference Paper) 1967-1980A
The Influence of the Alloying Elements Upon the Transformation Kinetics and Morphologies of Ferrite Plates in Alloy Steels. (Conference Paper) 1991-2000A

Phase boundary, Diffusion effects
Multiphase Binary Diffusion in Infinite and Semi-Infinite Media. II. On the Numerical Calculation of the Rate Constants for Formation of Product Phases. 753-761A
On the Role of Interphase-Boundary Structure in Plate Growth by Diffusional Mechanisms. (Conference Paper) 1875-1883A

Phase boundary, Heating effects
Formation Mechanism of Bainite Ferrite and Carbide. (Conference Paper) 2001-2007A

Phase boundary, Temperature effects
High-Temperature Phase Relations and Thermodynamics in the Iron—Lead—Sulfur System. 53-61B

Phase decomposition
See also Spinodal decomposition
Multiphase Precipitation of Carbides in Fe-C Systems. I. Model Based Upon Simple Kinetic Reactions. 917-925B
Multiphase Precipitation of Carbides in Fe-C System. II. Model Based on Kinetics of Complex Reactions. 927-935B

Phase decomposition, Alloying effects
The Influence of the Alloying Elements Upon the Transformation Kinetics and Morphologies of Ferrite Plates in Alloy Steels. (Conference Paper) 1991-2000A

Phase decomposition, Diffusion effects
Decomposition of Iron—Nickel Martensite: Implications for the Low-Temperature ($\leq$ 500°C) Fe—NI Phase Diagram. 1627-1637A

Phase decomposition, Low temperature effects
Numerical Modeling of γ Precipitate Growth During Fe—Ni Martensite Decomposition at Low Temperatures ($\leq$ 400°C). 1639-1648A

Phase diagram reactions
See also Eutectic reactions
Eutectoid reactions
Martensitic transformations
Peritectic reactions
Phase decomposition

Phase diagram reactions, Deformation effects
Microstructure and Sound Velocity of Ti-N-O Synthetic Inclusions in Ti-6Al-4V. 2321-2329A

Phase diagram reactions, Heating effects
Interfacial Layer Development in Hot-Dip Galvanneal Coatings on Interstitial Free (IF) Steel. 2101-2109A

Phase stability
Experimental Study of the Influence of Interfacial Energies and Reactivity on Wetting in Metal/Oxide Systems. 599-605A
Spreading and Interlayer Formation at the Copper-Copper Oxide/Polycrystalline Alumina Interface. 2497-2506A

Phase stability, Alloying effects
Morphological Stability of γ/α Interface Formed by Carburization in Fe—C—X Alloys. 531-537A

Phase stability, Deformation effects
Microstructure and Sound Velocity of Ti-N-O Synthetic Inclusions in Ti-6Al-4V. 2321-2329A

Phase stability, Diffusion effects
The Morphological Stability of Lateral Growth in Solid—Solid Phase Transformation During Thin-Film Interdiffusion in Aluminum/Copper Bimetal Films. 1613-1625A

Phase stability, Heating effects
Influence of Tempering Temperature on Stability of Carbide Phases in 2.6Cr—0.7Mo—0.3V Steel With Various Carbon Content. 267-275A
The Effect of Phosphorus Segregation on the Intermediate-Temperature Embrittlement of Ferritic, Spheroidal Graphite Cast Iron. 557-561A
Microstructural Study of the Titanium Alloy Ti—15Mo—2.7Nb—3Al—0.2Si (TIMETAL 21S). 1109-1118A
Dynamic Fracture Behavior of Ti—6Al—4V Alloy With Various Stabilities of β Phase. 1655-1666A
The Effect of Thermal Exposure on Microstructural Stability and Creep Resistance of a Two-Phase TiAl/Ti_3Al Lamellar Alloy. 2371-2381A

Phase stability, Temperature effects
Partition of Alloying Elements Between γ (A1), γ' ($L1_2$), and β (B2) Phases in Ni—Al Base Systems. 473-485A
Improved Thermochemical Calculations for Maraging Steels and Comparison With Atom Probe Measurement of Phase Composition. 2538-2539A

Phase structure
See Solid phases

Phase transformations
See also Allotropic transformation
Martensitic transformations
Crystallographic Characteristics of the Al—Co Decagonal Quasicrystal and Its Monoclinic Approximant τ^2-$Al_{13}Co_4$. 47-56A
η to G Phase Transformation in Electrodeposited Iron—Zinc Alloy Coatings. 1119-1125A
Titanium-Rich Mineral Phases and the Nucleation of Bainite. 1603-1611A
Ledges and Dislocations in Phase Transformations. (Conference Paper) 1885-1894A
Thermodynamic Consideration of Formation Mechanism of α_1 Plate in βCu-Base Alloys. (Conference Paper) 2555-2564A
Transformation Characteristics of α_1 Plates in Cu-Zn-Al Alloys. (Conference Paper) 2581-2599A
The Formation Mechanism of Plate in β Cu-Zn and Cu-Zn-Al Alloys. (Conference Paper) 2601-2608A
Growth Kinetics and High-Temperature TEM In Situ Observation of Bainite in a Cu-Zn Alloy. (Conference Paper) 2609-2614A
Study on the Transformation Mechanism of α_1 Plates in a Copper-Zinc-Aluminum Alloy. (Conference Paper) 2615-2619A
A Discussion on the Formation of Bainite and Other Precipitates in Copper-Zinc and Silver-Zinc Alloys. (Conference Paper) 2621-2629A
Mechanism of the Early Stages of α_1 Plate Formation in a Cu-39% Zinc Alloy. (Conference Paper) 2631-2637A
The Selection of Precipitate Habit Planes in Cr-32 wt.% Ni. (Conference Paper) 2639-2646A
Bainitelike Transformations in Some Oxide Ceramics. (Conference Paper) 2647-2653A
General Discussion Session of the Pacific Rim Conference on the Roles of Shear and Diffusion in the Formation of Plate-Shaped Transformation Products. (Conference Paper) 2655-2673A
Diffusion-Controlled Growth in Ternary Systems. 2683-2694A

Phase transformations, Alloying effects
Effects of Austenite Grain Size and Cooling Rate on Widmanstätten Ferrite Formation in Low-Alloy Steels. 665-675A

On the Prebainitic Phenomenon in Some Alloys. (Conference Paper) 1941-1946A
Thermodynamics and Kinetics of the Formation of Widmanstätten Ferrite Plates in Ferrous Alloys. (Conference Paper) 1947-1953A
The Fine Structure and Formation Mechanism of Lower Bainite. (Conference Paper) 1967-1980A
The Influence of the Alloying Elements Upon the Transformation Kinetics and Morphologies of Ferrite Plates in Alloy Steels. (Conference Paper) 1991-2000A

Phase transformations, Cooling effects
Intragranular Ferrite Nucleation in Medium-Carbon Vanadium Steels. 929-936A
Calorimetric Evaluation of Nonequilibrium State in As-Melt Spun Al—1.72 and Al—3.12 at.% Cu Alloys and Al—6.74, Al—8.48, and Al—11.97 at.% Si Alloys. 1102-1104A
Microsegregation in Cellular Solidification. 2295-2301A

Phase transformations, Deformation effects
A Simple Model for Conventional Hot Rolling of Sheet Materials. 1681-1692A
Effects of Precursor Matrix Events on Subsequent Nucleation. (Conference Paper) 1933-1939A

Phase transformations, Diffusion effects
The Morphological Stability of Lateral Growth in Solid—Solid Phase Transformation During Thin-Film Interdiffusion in Aluminum/Copper Bimetal Films. 1613-1625A
Crystallographic Theories, Interface Structures, and Transformation Mechanisms. (Conference Paper) 1821-1839A
Application of the Theory of Martensite Crystallography to Displacive Phase Transformations in Substitutional Nonferrous Alloys. (Conference Paper, Review) 1841-1856A
A Comparison Between Three Simple Crystallographic Principles of Precipitate Morphology. (Conference Paper) 1857-1863A
On the Role of Interphase-Boundary Structure in Plate Growth by Diffusional Mechanisms. (Conference Paper) 1875-1883A
Diffusion in Growth of Bainite. (Conference Paper) 1957-1966A
Formation Mechanism of Bainitic Ferrite in an Fe)2% Si)0.6% C Alloy. (Conference Paper) 2009-2016A

Phase transformations, Stress effects
Transformation, Microcrack, and Thermal Residual Stress as Interactive Processes in ZrO_2-Toughened Al_2O_3, Simulated by the Finite Element Method. 1725-1731A
A History of the Controversy Over the Roles of Shear and Diffusion in Plate Formation Above M_d and a Comparison of the Atomic Mechanisms of These Processes. (Conference Paper, Review) 1797-1819A

Phase transformations, Temperature effects
Behavior of Steels Near the Incipient Melting Temperature. 125-133A
Thermodynamic Predictions for Material Processing in a Plasma Reactor Using Solid Oxide Feed Materials. 713-720B
Fracture and the Formation of Sigma Phase, $M_{23}C_6$, and Austenite From Delta—Ferrite in an AISI 304L Stainless Steel. 1147-1158A
Numerical Modeling of Solidification and Subsequent Transformation of Fe—Cr—Ni Alloys. 1309-1321A

Phases (state of matter)
See also Intermetallic phases
Liquid phases
Metastable phases
Solid phases
Vapor phases
Structure of As-Deposited Iron—Zinc Coatings From Chloride Bath. 249-255A
Kinetics in Muliticomponent Metallic)Ionic Systems. 579-587B
Multiphase Binary Diffusion in Infinite and Semi-Infinite Media. I. On the Determination of Interdiffusion Coefficients. 741-751A
Directional Phase Formation on Melting via Peritectic Reaction. 1747-1760A
The Chromium Equivalents of Selected Elements in Austenitic Stainless Steel. 2675-2681A

Phases (state of matter), Alloying effects
Transmission Electron Microscopy Crystal Structure Study of the Chromium-Rich Phase in a Laser-Clad Nickel Alloy. 487-497A

Phases (state of matter), Heating effects
Computer Simulation of Diffusion in Multiphase Systems. 1127-1134A

Phases (state of matter), Pressure effects
Thermodynamic Study of $BaCuO_2$ and $BaCu_2O_2$. 385-389B

Phases (state of matter), Temperature effects
Thermodynamic Study of the Bi—Ca—O System. 97-101B
Local Melting in Al—Mg—Zn—Alloys. 521-530A
The Grand Partition Function of Dilute Biregular Solutions. 703-711B
Kinetics of Interlayer Formation on Polycrystalline α-Al_2O_3/Copper-Titanium Alloy Interface. 2083-2090A
Modeling Creep Deformation of a Two-Phase TiAl/Ti_3Al Alloy With a Lamellar Microstructure. 2161-2171A

Phases (state of matter), Welding effects
The α/β Interface Phase in Titanium Alloys: Artifact or Real Phase Contribution to Problem Resolution. 241-248A

Photo oxidation
See Oxidation

Photodecomposition
See Decomposition reactions

Photoelectron spectroscopy
Surface Characterization and Reactivity of a Nitrogen Atomized 304L Stainless Steel Powder. 509-520A

Photoemission spectroscopy
See Photoelectron spectroscopy

Physical chemistry
Solid-Solution Formation Between Arsenic and Antimony Oxides. 865-871B
Thermal Separation of Arsenic and Antimony Oxides. 873-884B

Physical properties
See Anisotropy
Buoyancy
Capillarity
Density
Diffusivity
Permeability
Porosity
Solubility
Surface tension

Pipe, Casting
On the Formation of Pipes and Centerline Segregates in Continuously Cast Billets. 123-133B

Pitting potential
See Corrosion potential

Plasma arc plating
See Plasma spraying

Plasma arc spraying
See Plasma spraying

Plasma jet spraying
See Plasma spraying

Plasma processing
See also Plasma spraying
Thermodynamic Predictions for Material Processing in a Plasma Reactor Using Solid Oxide Feed Materials. 713-720B

Plasma spraying
Microstructural Evolution of an Overlay Coating on a Single-Crystal Nickel-Base Superalloy. 2837-2840A

Plastic deformation
Alligatoring and Damage in the Cold Rolling of Spheroidized Steels. 589-598A
Relationships of Slip Morphology, Microcracking, and Fracture Resistance in a Lamellar TiAl-Alloy. 1217-1228A
Effects of Precursor Matrix Events on Subsequent Nucleation. (Conference Paper) 1933-1939A

Plastic deformation, Environmental effects
On Low-Temperature Environment-Assisted Fatigue Crack Propagation. 658-659A

Plastic deformation, Pressure effects
The Effects of Hydrostatic Pressure on the Compressive Mechanical Behavior of $L1_2$ Al_3 Ti-Based Intermetallic. 1703-1711A

Plastic deformation, Stress effects
Analysis of Thermally Induced Stress and Strain in Continuous Fiber-Reinforced Composites. 415-425A
Coefficients of Thermal Expansion of Metal-Matrix Composites for Electronic Packaging. 839-850A
Crack Initiation at Long Radial Hydrides in Zr—2.5Nb Pressure Tube Material at Elevated Temperatures. 993-1004A
Flow Instabilities and Fracture in Ti-6Al-4V Deformed in Compression at 298-673K. 2173-2179A
Low-Cycle Fatigue of Dispersion-Strengthened Copper. 2235-2245A
Effect of Iron on the Superplastic Deformation of Zn-22%Al. 2391-2401A

Plastic strain
See Plastic deformation

Plasticity
See also Superplasticity

Plasticity, Composition effects
Room-Temperature Strength and Deformation of TiB_2-Reinforced Near-γ Titanium Aluminides. 2181-2197A

Plasticity, Deformation effects
Anisotropic Plastic Potentials for Polycrystals and Application to the Design of Optimum Blank Shapes in Sheet Forming. 1209-1216A

Plasticity, High temperature effects
Low-Cycle Fatigue Behavior of Polycrystalline NiAl at 1000K. 309-319A

Plasticity, Microstructural effects
Microstructure and Mechanical Properties of Ti—40 wt.% Ta (Ti—15 at.% Ta). 461-472A
Textural and Microstructural Gradient Effects on the Mechanical Behavior of a Tantalum Plate. 1025-1031A

Plasticity, Stress effects
Crack Initiation at Long Radial Hydrides in Zr—2.5Nb Pressure Tube Material at Elevated Temperatures. 993-1004A
Hydride Embrittlement in Zircaloy-4 Plate. II. Interaction Between the Tensile Stress and the Hydride Morphology. 1199-1208A
Modeling the Effects of Stress State and Crystal Orientation on the Stress-Induced Transformation of NiTi Single Crystals. 2383-2389A

Plasticity stress effects
Forging Limit for an Aluminum Matrix Composite. II. Analysis. (Conference Paper) 2039-2048A

Plate metal, Casting
A Note on the Sensitivity of Solidification Models to Thermophysical Properties. 154-157B

Plate metal, Heat treatment
Effects of Widmanstätten Ferrite on the Mechanical Properties of a 0.2% C—0.7% Mn Steel. 763-773A

Plate metal, Mechanical properties
Textural and Microstructural Gradient Effects on the Mechanical Behavior of a Tantalum Plate. 1025-1031A

Fracture and the Formation of Sigma Phase, $M_{23}C_6$, and Austenite From Delta—Ferrite in an AISI 304L Stainless Steel. 1147-1158A

Platinum
Thermodynamic Stability of Metallurgical Coke Relative to Graphite. 149-151B

Platinum metals
See Platinum

Plutonium, Binary systems
Formation and Stability of Metastable Structures and Amorphous Phases in Pu—V, Pu—TA, and Pu—Yb Systems With Positive Heats of Mixing. 1579-1590A

Point defects
See Lattice vacancies

Poissons ratio
Elastic Constants of SiC_p/Al: Measurements and Modeling. 2832-2835A

Poissons ratio, Temperature effects
Elastic Constants of Some Transition-Metal-Disilicide Single Crystals. 331-340A

Poling
See Deoxidizing

Polygonization
η to G Phase Transformation in Electrodeposited Iron—Zinc Alloy Coatings. 1119-1125A

Pores
See Porosity

Porosity
Nanocrystalline Iron Sintering Behavior and Microstructural Development. 677-685A
Characterization of Anisotropic Elastic Constants of Silicon-Carbide Particulate Reinforced Aluminum Metal Matrix Composites. I. Experiment. 799-809A
Capillarity in Isothermal Infiltration of Alumina Fiber Preforms With Aluminum. 2145-2152A

Porosity, Coating effects
The Effect of Low Gold Concentrations on the Creep of Eutectic Tin—Lead Joints. 1249-1257A

Porosity, Cooling effects
On the Formation of Pipes and Centerline Segregates in Continuously Cast Billets. 123-133B

Porosity, Diffusion effects
Determination of Pore Mobility During Sintering. 81-87A

Porosity, Heating effects
Effect of Supereutectic Homogenization on Incidence of Porosity in Aluminum Alloy 2014 Ingot. 111-122B

Porosity, Welding effects
Effect of Welding Variables and Solidification Substructure on Weld Metal Porosity. 2285-2294A

Porosity stress effects
Forging Limit for an Aluminum Matrix Composite. II. Analysis. (Conference Paper) 2039-2048A

Potential (electric)
See Electric potential

Pots (electrolytic)
See Electrolytic cells

Powder blending
Mechanical Processing of Iron Powders in Reactive and Nonreactive Gas Atmospheres. 381-388A

Powder metallurgy
See also Sintering (powder metallurgy)
Characterization of Anisotropic Elastic Constants of Silicon-Carbide Particulate Reinforced Aluminum Metal Matrix Composites. I. Experiment. 799-809A
Superplastic Behavior of Two Ultrahigh Boron Steels. 1241-1248A
Microstructural Analysis of Fracture Toughness Variation in 2XXX-Series Aluminum Alloy Composites Reinforced With SiC Whiskers. 2213-2223A
Low-Cycle Fatigue Properties of a SiC Whisker-Reinforced 2124 Aluminum Alloy. 2265-2274A
Microstructure and Sound Velocity of Ti-N-O Synthetic Inclusions in Ti-6Al-4V. 2321-2329A

Powder metallurgy parts, Metal working
Superplastic Behavior of Thermomechanically Treated P/M 7091 Aluminum Alloy. 2153-2160A

Powder technology
See also Atomizing
Powder metallurgy
The Injection of Solids Using a Reactive Carrier Gas. 653-660B

Praseodymium base alloys, Phases (state of matter)
Standard Enthalpies of Formation of Some Praseodymium Alloys of High-Temperature Direct Synthesis Calorimetry. 73-77B

Precious metal alloys
See Gold base alloys
Silver base alloys

Precious metals
See Gold
Silver

Precipitates, Diffusion effects
A Comparison Between Three Simple Crystallographic Principles of Precipitate Morphology. (Conference Paper) 1857-1863A

Precipitation
See also Intergranular precipitation
Sedimentation
Triclinic Ni_2Al Phase in 63.1 at.% NiAl. 57-61A
The Role of Oxygen and Zirconium in the Formation and Growth of Nb_3Sn Grains. 213-219A
Precipitation Effects During Hot Deformation of a Copper Alloy. 257-266A
Multiphase Precipitation of Carbides in Fe-C Systems. I. Model Based Upon Simple Kinetic Reactions. 917-925B
Multiphase Precipitation of Carbides in Fe-C System. II. Model Based on Kinetics of Complex Reactions. 927-935B
Intrinsic Ledges at Interphase Boundaries and the Crystallography of Precipitate Plates. (Conference Paper) 1905-1915A
The Elastic Strain Energy of Growth Ledges on Coherent and Partially Coherent Precipitates. 2073-2082A
Microstructural Analysis of Fracture Toughness Variation in 2XXX-Series Aluminum Alloy Composites Reinforced With SiC Whiskers. 2213-2223A
Melt-Processed Ni_3Al Matrix Composites Reinforced With TiC Particles. 2525-2534A
Long-Range Ordering in the Early Stages of Precipitation)a Brief Review. (Conference Paper) 2565-2568A
A Discussion on the Formation of Bainite and Other Precipitates in Copper-Zinc and Silver-Zinc Alloys. (Conference Paper) 2621-2629A
The Selection of Precipitate Habit Planes in Cr-32 wt.% Ni. (Conference Paper) 2639-2646A

Precipitation, Alloying effects
Compositional and Microstructural Changes Which Attend Reheating and Grain Coarsening in Steels Containing Niobium. 277-286A
Thermodynamics and Kinetics of the Formation of Widmanstätten Ferrite Plates in Ferrous Alloys. (Conference Paper) 1947-1953A
The Fine Structure and Formation Mechanism of Lower Bainite. (Conference Paper) 1967-1980A

Precipitation, Cooling effects
Characterization of Mechanically Alloyed Oxide Dispersion-Strengthened Nickel-Base Superalloy MA760. 705-714A
Intragranular Ferrite Nucleation in Medium-Carbon Vanadium Steels. 929-936A
Precipitation of BCC Phase from Nonequilibrium A13-Type Phase in Rapidly Solidified High-Carbon Fe-Cr-Mo Alloy. 2542-2546A

Precipitation, Diffusion effects
The Invariant Line and Precipitate Morphology in FCC-BCC Systems. (Conference Paper) 1865-1874A
Atomic Site Correspondence and Surface Relief in the Formation of Plate-Shaped Transformation Products. (Conference Paper) 1917-1922A

Precipitation, Heating effects
Hydrogen Permeation Behavior in IN718 and GH761 Superalloys. 539-544A
The Effects of Double Austenitization on the Mechanical Properties of a 0.34C Containing Low-Alloy Ni—Cr—Mo—V Steel. 545-555A
Heat Treatment of Investment Cast PH 13-8 Molybdenum Stainless Steel. II. Isothermal Aging Kinetics. 697-704A
Al_2Ti Precipitation in $Al_{64}Fe_8Ti_{28}$ Alloy. 715-721A
Heat Treatment of Investment Cast PH 13-8Mo Stainless Steel. I. Mechanical Properties and Microstructure. 789-798A
Microstructural Study of the Titanium Alloy Ti—15Mo—2.7Nb—3Al—0.2Si (TIMETAL 21S). 1109-1118A
Interstitial Precipitation in Fe—Cr—Al Alloys. 1135-1146A
Role of Al_2O_3 Particulate Reinforcements on Precipitation in 2014 Aluminum-Matrix Composites. 1591-1602A
Formation Mechanism of Bainite Ferrite and Carbide. (Conference Paper) 2001-2007A
Isothermal Formation of Quasicrystalline Precipitates and Their Effect on Strength in a 12Cr-9Ni-4Mo Maraging Stainless Steel. 2225-2233A

Precipitation, Low temperature effects
Numerical Modeling of γ Precipitate Growth During Fe—Ni Martensite Decomposition at Low Temperatures ($\leq$ 400°C). 1639-1648A

Precipitation, Radiation effects
Helium 3 Precipitation in AISI 316L Stainless Steel Induced by Radioactive Decay of Tritium: Microstructural Study of Helium Bubble Precipitation. 2117-2130A
Helium 3 Precipitation in AISI 316L Stainless Steel Induced by Radioactive Decay of Tritium: Growth Mechanism of Helium Bubbles. 2131-2143A

Precipitation, Stress effects
Stress-State Dependence of Strain-Hardening Behavior in 2014 Al/15 vol.% Al_2O_3 Composite. (Conference Paper) 2049-2061A

Precipitation, Temperature effects
Morphology of Bainite and Widmanstätten Ferrite. (Conference Paper) 1981-1989A
Improved Thermochemical Calculations for Maraging Steels and Comparison With Atom Probe Measurement of Phase Composition. 2538-2539A

Precipitation, Welding effects
Characterization of a Diffusion-Bonded Al—Mg Alloy/SiC Interface by High Resolution and Analytical Electron Microscopy. 617-627A

Precipitation hardening
Diffusional Boundary Conditions During Coarsening of Elastically Interacting Precipitates. 2695-2703A

Precipitation hardening alloys
See Precipitation hardening steels

Precipitation hardening steels
See also Maraging steels

Precipitation hardening steels, Heat treatment
Heat Treatment of Investment Cast PH 13-8 Molybdenum Stainless Steel. II. Isothermal Aging Kinetics. 697-704A

Heat Treatment of Investment Cast PH 13-8Mo Stainless Steel. I. Mechanical Properties and Microstructure. 789-798A

Precision casting
See Investment casting

Preferential attack (corrosion)
See Intergranular corrosion

Preforming
Thermofluid Analysis and Design of a Low-Temperature Preforming Process. 761-771B

Pressure
See Partial pressure
Vacuum

Pressure casting
Fiber Strength and Fiber/Matrix Bond Strength in Single Crystal Al_2O_3 Fiber Reinforced Ni_3Al Based Composites. 1259-1265A

Pressure castings, Oxidation
A Structural Study of Oxidation in a Zirconia-Toughened Alumina Fiber-Reinforced NiAl Composite. 1291-1299A

Pressure die casting
See Die casting

Pressure molding
See Injection molding

Pressure vessels, Irradiation
Deformation Behavior of Irradiated Zr—2.5Nb Pressure Tube Material. 135-145A

Pressure welding
See Diffusion welding

Primary displacements
See Displacements (lattice)

Process control
A Simple but Realistic Model for Laser Cladding. 281-291B
Slurry Filtration and Cake Washing After the HCl-Leach of Magnesite and Serpentine—Continuous Washing Model. 321-331B
Three-Dimensional Finite Element Modeling of Gas Metal-Arc Welding. 435-441B
Modeling the Thin-Slab Continuous-Casting Mold. 443-457B
Computer Algorithms for Radiometric Measurement of Temperature During the Galvanneal Process. 449-462B

Process metallurgy
See also Extractive metallurgy
The Role of Chemical Metallurgy in the Emerging Field of Materials Science and Engineering. (Review) 789-816B

Propagation
See Crack propagation

Properzi process
See Continuous casting

Protective coatings, Heat treatment
Morphology Development in Hot-Dip Galvanneal Coatings. 937-947A

Protective coatings, Microstructure
Structure of As-Deposited Iron—Zinc Coatings From Chloride Bath. 249-255A
The Effect of Steel Chemistry on the Formation of Fe-Zn Intermetallic Compounds of Galvanneal-Coated Steel Sheets. 721-730B

Pseudoelasticity, Stress effects
Characteristics of the Martensitic Transformation and the Induced Two-Way Shape Memory Effect After Training by Compressive Pseudoelastic Cycling in Cu—Zn—Al Single Crystals. 687-695A

Puddling
See Ironmaking

Pulse echo technique
See Ultrasonic testing

Punching
Effects of Texture Gradients on Yield Loci and Forming Limit Diagrams in Various Aluminum-Lithium Sheet Alloys. 2783-2795A

Purification
Thermal Separation of Arsenic and Antimony Oxides. 873-884B
Thermodynamics of Boron in a Silicon Melt. 903-907B

Pyroceram
See Ceramics

Pyrometallurgy
Vanadium Distribution in Melts Intermediate to Ferroalloy Production From Vanadiferous Slag. 27-32B
Thermodynamics and Phase Relations of the Fe—O—S—SiO_2(sat) System at 1200°C and the Effect of Copper. 79-89B
Thermodynamic Stability of Metallurgical Coke Relative to Graphite. 149-151B
Thermal Treatment of Complex Sulfide Ores in N_2 and H_2 Atmospheres: a New Approach for the Extraction of Their Valuable Elements. (Review) 193-205B
Physical and Mathematical Modeling of Pyrometallurgical Channel Reactors With Bottom Gas Injection. Residence Time Distribution Analysis and Ideal-Reactor-Network Model. 207-219B
A Process for Debismuthizing Lead With Magnesium. 379-384B
Equilibrium Oxygen Pressures of Iron Silicate Slags. 463-465B
The Ferric Fluosilicate Leaching of Lead Concentrates. I. Kinetic Studies. 473-480B
Thermodynamic Simulation Model of the Isasmelt Process for Copper Matte. 839-853B

Qualitative analysis
Sulfur Determination in Carbon-Saturated Iron by Solid-State Electrochemical Sensor. 561-568B

Quasicrystalline structure
Crystallographic Characteristics of the Al—Co Decagonal Quasicrystal and Its Monoclinic Approximant τ^2-$Al_{13}Co_4$. 47-56A
Discussion of "Crystallographic Characterization of the Al-Co Decagonal Quasicrystal and Its Monoclinic Approximant τ^2-$Al_{13}Co_4$". 2535-2538A

Quasicrystalline structure, Heating effects
Isothermal Formation of Quasicrystalline Precipitates and Their Effect on Strength in a 12Cr-9Ni-4Mo Maraging Stainless Steel. 2225-2233A

Quaternary systems, Phases (state of matter)
Thermodynamic Study of $BaCuO_2$ and $BaCu_2O_2$. 385-389B

Quench bend tests
See Bend tests

Quenching (cooling)
See also Quenching and tempering
Water quenching
Mechanism of Damping Capacity of High-Chromium Steels and α-Iron and Its Dependence on Some External Factors. 111-124A
Softening and Microstructural Change Following the Dynamic Recrystallization of Austenite. 389-400A
The Effect of Phosphorus Segregation on the Intermediate-Temperature Embrittlement of Ferritic, Spheroidal Graphite Cast Iron. 557-561A
Multiphase Precipitation of Carbides in Fe-C Systems. I. Model Based Upon Simple Kinetic Reactions. 917-925B
Multiphase Precipitation of Carbides in Fe-C System. II. Model Based on Kinetics of Complex Reactions. 927-935B
Microstructural Study of the Titanium Alloy Ti—15Mo—2.7Nb—3Al—0.2Si (TiMETAL 21S). 1109-1118A
Dynamic Fracture Behavior of Ti—6Al—4V Alloy With Various Stabilities of β Phase. 1655-1666A
Nonequilibrium Solidification of Undercooled Melt of Ag-Cu Alloy Entrained in the Primary Phase. 2517-2523A

Quenching and tempering
Influence of Tempering Temperature on Stability of Carbide Phases in 2.6Cr—0.7Mo—0.3V Steel With Various Carbon Content. 267-275A

Quenching stresses
See Residual stress

Radiation damage
Helium 3 Precipitation in AISI 316L Stainless Steel Induced by Radioactive Decay of Tritium: Microstructural Study of Helium Bubble Precipitation. 2117-2130A
Helium 3 Precipitation in AISI 316L Stainless Steel Induced by Radioactive Decay of Tritium: Growth Mechanism of Helium Bubbles. 2131-2143A

Radioactive decay, Radiation effects
Helium 3 Precipitation in AISI 316L Stainless Steel Induced by Radioactive Decay of Tritium: Microstructural Study of Helium Bubble Precipitation. 2117-2130A

Radioactive disintegration
See Radioactive decay

Radiocrystallography
See Crystallography

Raney nickel
See Catalysts

Rapid solidification
Formation of Metastable and Equilibrium Phases During Mechanical Alloying of Aluminum and Magnesium Powders. 73-79A
Supersaturation of the Al_2Y Laves Phase by Rapid Solidification. 230-233A
The Cast Structure of a 7075 Alloy Produced by a Water-Cooling Centrifugal Casting Method. 643-650A
Fatigue Crack Growth Rates and Fracture Toughness of Rapidly Solidified Al—8.5Fe—1.2V—1.7Si Alloys. 1005-1014A
Calorimetric Evaluation of Nonequilibrium State in As-Melt Spun Al—1.72 and Al—3.12 at.% Cu Alloys and Al—6.74, Al—8.48, and Al—11.97 at.% Si Alloys. 1102-1104A
Cubic AlNi Compound Dispersed Magnesium-Based Amorphous Matrix Composites Prepared by Rapid Solidification. 1323-1325A
High-Temperature Deformation of B2 NiAl-Base Alloys. (Conference Paper) 2017-2026A
Nonequilibrium Solidification of Undercooled Melt of Ag-Cu Alloy Entrained in the Primary Phase. 2517-2523A
Precipitation of BCC Phase from Nonequilibrium A13-Type Phase in Rapidly Solidified High-Carbon Fe-Cr-Mo Alloy. 2542-2546A
Numerical Analysis of the Rapid Solidification of Gas-Atomized Al-8 wt.% Iron Droplets. 2815-2826A

Rare earth alloys
See Praseodymium base alloys

Rare earth metals
See Ytterbium

Rare gases
See Helium

Rates
See Cooling rate
Strain rate
Wear rate

Ratios
See Poissons ratio

Reaction entropy
See Entropy

Reaction kinetics
Adsorption Kinetics of Dicyanoaurate and Dicyanoargentate Ions in Activated Carbon. 185-191B

Investigation of the Kinetics of Reduction of Nickel Tungstate by Hydrogen. 391-396B
Kinetics in Muliticomponent Metallic)Ionic Systems. 579-587B

Reaction kinetics, Pressure effects
Kinetics of the Reaction of H_2O Gas With Liquid Iron. 245-253B

Reactions (chemical)
See also Blast furnace chemistry
Combustion
Decomposition reactions
Deoxidizing
Dephosphorizing
Dissolution
Electrolysis
Hydrogenation
Interface reactions
Oxidation
Interactions Between Drops of a Molten Aluminum)Lithium Alloy and Liquid Water. 623-625B

Reactions (nuclear)
See Radioactive decay
Thermonuclear reactions

Reactivity
Experimental Study of the Influence of Interfacial Energies and Reactivity on Wetting in Metal/Oxide Systems. 599-605A

Reactivity (chemical)
See Activity (chemical)

Reactor fuels
See Nuclear fuels

Reclamation
See Recycling

Recrystallization
See also Grain refinement
Effect of Internal Heating During Hot Compression on the Stress-Strain Behavior of Alloy 304L. 2737-2752A

Recrystallization, Cooling effects
Softening and Microstructural Change Following the Dynamic Recrystallization of Austenite. 389-400A
Characterization of Mechanically Alloyed Oxide Dispersion-Strengthened Nickel-Base Superalloy MA760. 705-714A

Recrystallization, Deformation effects
Discussion of "The Distribution of Dispersoid Phases in the Extruded ODS Superalloy MA-957 and Reply. 651-653A
Hot Deformation Characteristics of INCONEL Alloy MA 754 and Development of a Processing Map. 1693-1702A
Superplastic Behavior of Thermomechanically Treated P/M 7091 Aluminum Alloy. 2153-2160A
Microstructural Control in Hot Working of IN-718 Superalloy Using Processing Map. 2275-2284A
Microstructure Development During Conventional and Isothermal Hot Forging of a Near-γ Titanium Aluminide. 2753-2768A

Recrystallization, Heating effects
Microstructural Study of the Titanium Alloy Ti—15Mo—2.7Nb—3Al—0.2Si (TIMETAL 21S). 1109-1118A

Recrystallization, Radiation effects
Helium 3 Precipitation in AISI 316L Stainless Steel Induced by Radioactive Decay of Tritium: Microstructural Study of Helium Bubble Precipitation. 2117-2130A

Recrystallization, Temperature effects
Behavior of Steels Near the Incipient Melting Temperature. 125-133A

Recrystallization, Welding effects
The Influence of Electron-Beam Welding Parameters on Heat-Affected-Zone Microfissuring in Incoloy 903. 1733-1745A

Recycling
Equilibrium Values for the Dissolution of Solid Copper Into FeS—Na_2S Mattes. 306-308B
Processing of Spent Hydrorefining Catalysts by Selective Chlorination. 481-490B

Red hardness
See Hardness

Red shortness
See Brittleness

Reduction
See Reduction (chemical)
Reduction (electrolytic)

Reduction (chemical)
See also Deoxidizing
Cyanide Inhibitors for the Carbon Cathode Materials in Aluminum Reduction Cells. 221-226B
Investigation of the Kinetics of Reduction of Nickel Tungstate by Hydrogen. 391-396B
Surface Characterization and Reactivity of a Nitrogen Atomized 304L Stainless Steel Powder. 509-520A
Reduction of Chromite in Liquid Fe)Cr)C)Si Alloys. 549-559B

Reduction (electrolytic)
See also Electrowinning
Small Cell Experiments for Electrolytic Reduction of Uranium Oxides to Uranium Metal Using Fluoride Salts. 505-518B

Reduction of area, Environmental effects
Hydride Embrittlement in Zircaloy-4 Plate. I. Influence of Microstructure on the Hydride Embrittlement in Zircaloy-4 at 20 and 350°C. 1185-1197A

Reduction of area, Microstructural effects
Fracture and the Formation of Sigma Phase, $M_{23}C_6$, and Austenite From Delta—Ferrite in an AISI 304L Stainless Steel. 1147-1158A

Reduction of area, Stress effects
Creep and Intergranular Cracking of Ni—Cr—Fe—C in 360°C Argon. 1169-1183A

Refining
See Electrorefining

Refractory alloys
See Chromium base alloys
Tungsten base alloys

Refractory metal compounds
See Chromium compounds
Molybdenum compounds
Niobium compounds
Vanadium compounds

Refractory metals
See Chromium
Molybdenum
Niobium
Tantalum
Tungsten
Vanadium

Relaxation
See Stress relaxation

Remelting
See Melting

Replicast process
See Investment casting

Residual stress
The Influence of Laser Glazing on Fatigue Crack Growth in Ti—24Al—11Nb. 183-192A
Estimation of Interfacial Shear Strength Between Superconducting Oxides and Silver Sheath From Multiple-Fracture Phenomenon of the Oxide. 349-356A
Coefficients of Thermal Expansion of Metal-Matrix Composites for Electronic Packaging. 839-850A
Hydride Embrittlement in Zircaloy-4 Plate. II. Interaction Between the Tensile Stress and the Hydride Morphology. 1199-1208A
Phosphorus and Carbon Segregation: Effects on Fatigue and Fracture of Gas-Carburized Modified 4320 Steel. 1229-1240A
Transformation, Microcrack, and Thermal Residual Stress as Interactive Processes in ZrO_2-Toughened Al_2O_3, Simulated by the Finite Element Method. 1725-1731A

Resistance
See Corrosion resistance

Resistance spot welding
Resistance Spot Welding of Precoated Steel Sheet: Computational Heat-Transfer Analysis. 415-423B

Resistance welding
See Resistance spot welding

Resistance welds
See Welded joints

Resistivity
Physicochemical Properties of Nickel Electrolytes. 637-644B

Resistivity, Heating effects
Aging of Freshly Formed Iron-Based Martensites at Low Temperatures. (Review) 889-909A
Isothermal Formation of Quasicrystalline Precipitates and Their Effect on Strength in a 12Cr-9Ni-4Mo Maraging Stainless Steel. 2225-2233A

Resistivity, Microstructural effects
Role of Al_2O_3 Particulate Reinforcements on Precipitation in 2014 Aluminum-Matrix Composites. 1591-1602A

Resistivity, Temperature effects
Gradient Solid Electrolytes for Thermodynamic Measurements: System Na_2CO_3—Na_2SO_4. 173-180A

Resonance testing
See Ultrasonic testing

Rheocasting
The Effect of Aging on Wear Characteristics of Rheocast-Leaded Aluminum Alloys. 851-856A

Rheological properties
See Viscoplasticity
Viscosity

Risers
Modeling of the Formation of Under-Riser Macrosegregation During Solidification of Binary Alloys. 1051-1062A

Roasting
Processing of Spent Hydrorefining Catalysts by Selective Chlorination. 481-490B
An Analysis of Slag Stratification in Nickel Laterite Smelting Furnaces Due to Composition and Temperature Gradients. 491-496B

Roll spot welding
See Resistance spot welding

Rolling
See Cold rolling
Hot rolling

Roughing (rolling)
See Hot rolling

Roughness, Heating effects
Computer Algorithms for Radiometric Measurement of Temperature During the Galvanneal Process. 449-462B

Rupture strength
See Creep rupture strength

Sampling
Efficient Measurement of Microstructural Surface Area Using Trisector. 919-928A

Sand casting
See Green sand casting

Sap process
See Dispersion hardening

Scattering
See also Backscattering
X ray scattering
The Diffuse-Scattering Method for Investigating Locally Ordered Binary Solid Solutions. 17-35A

Schottky defect
See Lattice vacancies

Scrap
See Metal scrap

Scrap metal
See Metal scrap

Scratch tests
Influence of Near-Surface Microstructures on the Transient Current Response in Fe—Cr—Ni Alloys During Scratch Tests. 1325-1331A

Screw dislocations, Stress effects
A Simplified Method of Calculating the Stress Field at the Tip of a Discrete Dislocation Pileup in a Finite Crystal. 223-225A

Season cracking
See Stress corrosion cracking

Secondary displacements
See Displacements (lattice)

Sedimentation
A Two-Phase Flow Model of the Stirring of Al)SiC Composite Melt. 607-618B

Seeding
See Nucleation

Segregation process
Surface Segregation of Calcium Oxide in Wustite and Its Effects on the Reduction. 405-413B

Segregations
Improvement in the Reducibility of Wustite Assisted by the Intensified Surface Segregation of Calcium Ions by the Double Addition of CaO and SiO_2. 741-748B

Segregations, Alloying effects
Solid-State Wetting of Graphite by Lead and Pb—Ni Alloys. 607-615A

Segregations, Cooling effects
On the Formation of Pipes and Centerline Segregates in Continuously Cast Billets. 123-133B
On Morphologies, Microsegregation, and Mechanical Behavior of Directionally Solidified Cobalt-Base Superalloy at Medium Cooling Rate. 637-642A
Chemical Composition and Structural Identification of Eutectic Carbide in 1% Manganese Ductile Iron. 911-918A
Modeling of the Formation of Under-Riser Macrosegregation During Solidification of Binary Alloys. 1051-1062A
Solidification Macrostructures and Macrosegregation in Aluminum Alloys Cooled From Above. 1097-1102A
Microsegregation in Cellular Solidification. 2295-2301A
Undercooling-Induced Macrosegregation in Directional Solidification. 2507-2516A

Segregations, Heating effects
The Effects of Double Austenitization on the Mechanical Properties of a 0.34C Containing Low-Alloy Ni—Cr—Mo—V Steel. 545-555A
The Effect of Phosphorus Segregation on the Intermediate-Temperature Embrittlement of Ferritic, Spheroidal Graphite Cast Iron. 557-561A
Phosphorus and Carbon Segregation: Effects on Fatigue and Fracture of Gas-Carburized Modified 4320 Steel. 1229-1240A

Segregations, Stress effects
Effect of Iron on the Superplastic Deformation of Zn-22%Al. 2391-2401A

Segregations, Temperature effects
An Internal Variable Description of Solidification Suitable for Macrosegregation Modeling. 597-605B

Self diffusion
See Diffusion

Semiconductors
See Germanium
Silicon

Semicontinuous casting
See Continuous casting

Semikilling
See Deoxidizing

Sensible heat
See Enthalpy

Sensitizing
Applicability of Bond Percolation Theory to Intergranular Stress-Corrosion Cracking of Sensitized AISI 304 Stainless Steel. 775-787A

Sensors, Phases (state of matter)
Gradient Solid Electrolytes for Thermodynamic Measurements: System Na_2CO_3—Na_2SO_4. 173-180A

Separation
See Segregation process

Shape memory, Alloying effects
Effects of Carbon Content and Ausaging on $\gamma \rightleftarrows \alpha'$ Transformation Behavior and Reverse-Transformed Structure in Fe—Ni—Co—Al—C Alloys. 63-71A

Shape memory, Stress effects
Characteristics of the Martensitic Transformation and the Induced Two-Way Shape Memory Effect After Training by Compressive Pseudoelastic Cycling in Cu—Zn—Al Single Crystals. 687-695A
Modeling the Effects of Stress State and Crystal Orientation on the Stress-Induced Transformation of NiTi Single Crystals. 2383-2389A

Shaping
See Near net shaping

Shear bands
See Slip planes

Shear modulus
Elastic Constants of SiC_p/Al: Measurements and Modeling. 2832-2835A

Shear modulus, Temperature effects
Elastic Constants of Some Transition-Metal-Disilicide Single Crystals. 331-340A

Shear properties
See also Shear modulus
Shear strength
Shear stress

Shear properties, Deformation effects
Modeling of Mechanical Alloying. I. Deformation, Coalescence, and Fragmentation Mechanisms. 147-158A

Shear strength, High temperature effects
The Workability of Commercial and Experimental 0.6% Carbon Low Alloy Steels in the Temperature Range of 650-870°C. 827-837A

Shear strength, Stress effects
Estimation of Interfacial Shear Strength Between Superconducting Oxides and Silver Sheath From Multiple-Fracture Phenomenon of the Oxide. 349-356A

Shear stress
Evaluation of Homogeneous Compression Flow Curves Using Square Cross-Sectioned Specimens. 1095-1097A
Fiber Strength and Fiber/Matrix Bond Strength in Single Crystal Al_2O_3 Fiber Reinforced Ni_3Al Based Composites. 1259-1265A
A History of the Controversy Over the Roles of Shear and Diffusion in Plate Formation Above M_d and a Comparison of the Atomic Mechanisms of These Processes. (Conference Paper, Review) 1797-1819A
Effect of Iron on the Superplastic Deformation of Zn-22%Al. 2391-2401A

Shear stress, Microstructural effects
The Study of Adiabatic Shear Band Instability in a Pearlitic 4340 Steel Using a Dynamic Punch Test. 2483-2489A

Sheaths, Mechanical properties
Estimation of Interfacial Shear Strength Between Superconducting Oxides and Silver Sheath From Multiple-Fracture Phenomenon of the Oxide. 349-356A

Sheet metal
See also Foil

Sheet metal, Coating
Morphology Development in Hot-Dip Galvanneal Coatings. 937-947A
η to G Phase Transformation in Electrodeposited Iron—Zinc Alloy Coatings. 1119-1125A

Sheet metal, Metal working
Anisotropic Plastic Potentials for Polycrystals and Application to the Design of Optimum Blank Shapes in Sheet Forming. 1209-1216A
A Plane Strain Punch Stretching Test for Evaluating Stamping Formability of Steel Sheets. 2199-2205A

Sheet metal, Reactions (chemical)
Modeling Hydrogen Entry and Exit in Metals Exposed to Multiple Charging Processes. 723-732A

Sheet metal, Rolling
A Simple Model for Conventional Hot Rolling of Sheet Materials. 1681-1692A

Sheet metal, Welding
Resistance Spot Welding of Precoated Steel Sheet: Computational Heat-Transfer Analysis. 415-423B

Sheet steel
See Strip steel

Sherritt Gordon process
See Hydrometallurgy
Powder technology

Shielded arc welding
See Gas metal arc welding

Short arc welding
See Gas metal arc welding

Short range order
Determination of the Short-Range Order Structure of Au—25 at.% Fe Using Wide-Angle Diffuse Synchrotron X-Ray Scattering. 1561-1573A

Short range order, Heating effects
Aging of Freshly Formed Iron-Based Martensites at Low Temperatures. (Review) 889-909A

Shrinkage, Cooling effects
A Note on the Sensitivity of Solidification Models to Thermophysical Properties. 154-157B

Further Discussions on the Solute Redistribution During Dendritic Solidification of Binary Alloys. 731-739B
Modeling of the Formation of Under-Riser Macrosegregation During Solidification of Binary Alloys. 1051-1062A

Shrinkage, Heating effects
Effect of Supereutectic Homogenization on Incidence of Porosity in Aluminum Alloy 2014 Ingot. 111-122B

Sigma hard facing
See Gas metal arc welding

Sigma phase, Temperature effects
Fracture and the Formation of Sigma Phase, $M_{23}C_6$, and Austenite From Delta—Ferrite in an AISI 304L Stainless Steel. 1147-1158A

Sigma welding
See Gas metal arc welding

Silicides, Composite materials
Phase Relations in the Mo—Si—C System Relevant to the Processing of $MoSi_2$—SiC Composites. 5-15A
The Effect of Niobium Morphology on the Cyclic Oxidation Resistance of $MoSi_2$/20 vol.% Niobium Composites. 1033-1040A

Silicides, Mechanical properties
Elastic Constants of Some Transition-Metal-Disilicide Single Crystals. 331-340A

Silicon, Extraction
Chemical Equilibria Between Silicon and Slag Melts. 497-504B

Silicon, Refining
Thermodynamics of Boron in a Silicon Melt. 903-907B

Silicon carbide, Composite materials
Phase Relations in the Mo—Si—C System Relevant to the Processing of $MoSi_2$—SiC Composites. 5-15A
Modeling of the Incorporation of Ceramic Particulates in Metallic Droplets During Spray Atomization and Coinjection. 135-147B
A Two-Phase Flow Model of the Stirring of Al)SiC Composite Melt. 607-618B
Characterization of Anisotropic Elastic Constants of Silicon-Carbide Particulate Reinforced Aluminum Metal Matrix Composites. I. Experiment. 799-809A
Characterization of Anisotropic Elastic Constants of Silicon-Carbide Particulate Reinforced Aluminum Metal Matrix Composites. II. Theory. 811-819A
Effect of Microstructure (Particulate Size and Volume Fraction) and Counterface Material on the Sliding Wear Resistance of Particulate-Reinforced Aluminum Matrix Composites. 969-983A
Comparison of Orthorhombic and Alpha-Two Titanium Aluminides as Matrices for Continuous SiC-Reinforced Composites. 1267-1283A
Microstructural Analysis of Fracture Toughness Variation in 2XXX-Series Aluminum Alloy Composites Reinforced With SiC Whiskers. 2213-2223A
Effect of Heat Treatment on the Microstructure, Tensile Properties, and Fracture Behavior of Permanent Mold Al-10 wt.% Si-0.6 wt.% Mg/SiC/10p Composite Castings. 2247-2263A
Low-Cycle Fatigue Properties of a SiC Whisker-Reinforced 2124 Aluminum Alloy. 2265-2274A
Micromechanical Modelling of Reinforcement Fracture in Particle-Reinforced Metal-Matrix Composites. 2403-2420A
The Influence of SiC Particulates on Fatigue Crack Propagation in a Rapidly Solidified Al-Fe-V-Si Alloy. 2453-2460A
Kinetic Study of Low-Temperature Transient Liquid Phase Joining of an Aluminum-SiC Composite. 2705-2714A
Elastic Constants of SiC_p/Al: Measurements and Modeling. 2832-2835A

Silicon carbide, Welding
Characterization of a Diffusion-Bonded Al—Mg Alloy/SiC Interface by High Resolution and Analytical Electron Microscopy. 617-627A

Silicon compounds
See Silicides
Silicon carbide

Silver, Extraction
Adsorption Kinetics of Dicyanoaurate and Dicyanoargentate Ions in Activated Carbon. 185-191B

Silver, Mechanical properties
Estimation of Interfacial Shear Strength Between Superconducting Oxides and Silver Sheath From Multiple-Fracture Phenomenon of the Oxide. 349-356A

Silver, Ternary systems
The Grand Partition Function of Dilute Biregular Solutions. 703-711B

Silver base alloys, Microstructure
High-Resolution Analytical Electron Microscopy Study of Isothermal Plate-Shaped Products in Some β-Phase Alloys. (Conference Paper) 2569-2579A

Silver base alloys, Phase transformations
Application of the Theory of Martensite Crystallography to Displacive Phase Transformations in Substitutional Nonferrous Alloys. (Conference Paper, Review) 1841-1856A
A Discussion on the Formation of Bainite and Other Precipitates in Copper-Zinc and Silver-Zinc Alloys. (Conference Paper) 2621-2629A

Simulation
See Computer simulation

Single crystals, Coating
Microstructural Evolution of an Overlay Coating on a Single-Crystal Nickel-Base Superalloy. 2837-2840A

Sintering
See Sintering (powder metallurgy)

Sintering (powder metallurgy)
See also Liquid phase sintering
Determination of Pore Mobility During Sintering. 81-87A
Modeling of Mechanical Alloying. I. Deformation, Coalescence, and Fragmentation Mechanisms. 147-158A
Nanocrystalline Iron Sintering Behavior and Microstructural Development. 677-685A
Thermodynamics of Isolated Pores Filling With Liquid in Sintered Composite Materials. 733-740A
High-Performance Ni_3Al Synthesized From Composite Powders. 985-992A

Slab casting
On the Formation of Pipes and Centerline Segregates in Continuously Cast Billets. 123-133B
Water-Modeling Study of the Surface Disturbances in Continuous Slab Caster. 227-233B
Modeling the Thin-Slab Continuous-Casting Mold. 443-457B
Simulation of Argon Gas Flow Effects in a Continuous Slab Caster. 527-547B

Slags
See also Blast furnace slags
Equilibrium Distribution of Fe, Ni, Sb, and Sn between Liquid Cu and a CaO-Rich Slag. 645-651B
Modeling of Metallurgical Emulsions. 855-864B
Activities of Fe_tO in CaO-Al_2O_3-SiO_2-Fe_tO (5%) Slags Saturated With Liquid Iron. 893-902B
Densities of Liquid Fe-Ni and Fe-Cr Alloys. 939-942B

Slags, Reactions (chemical)
Thermodynamics of Oxygen and Nitrogen in Liquid Nickel Equilibrated With CaO—TiO_x and CaO—TiO_x—Al_2O_3 Melts. 5-13B

Sliding friction, Microstructural effects
Effect of Microstructure (Particulate Size and Volume Fraction) and Counterface Material on the Sliding Wear Resistance of Particulate-Reinforced Aluminum Matrix Composites. 969-983A

Sling casting
See Centrifugal casting

Slip
See also Slip planes

Slip, Deformation effects
Relationships of Slip Morphology, Microcracking, and Fracture Resistance in a Lamellar TiAl-Alloy. 1217-1228A
Discussion of "The Role of Microstructure on Strength and Ductility of Hot-Extruded Mechanically Alloyed NiAl" and Author's Reply. 2303-2305A

Slip, Radiation effects
Effects of Simultaneous Boron and Nitrogen Implantation on Microhardness and Fatigue Properties of Fe—13Cr—15Ni Alloys. 193-202A

Slip bands
See Slip planes

Slip planes
The Study of Adiabatic Shear Band Instability in a Pearlitic 4340 Steel Using a Dynamic Punch Test. 2483-2489A

Smelting
Vanadium Distribution in Melts Intermediate to Ferroalloy Production From Vanadiferous Slag. 27-32B
The Measurement of the Heat-Transfer Coefficient Between High-Temperature Liquids and Solid Surfaces. 43-51B
Physical and Mathematical Modeling of Pyrometallurgical Channel Reactors With Bottom Gas Injection. Residence Time Distribution Analysis and Ideal-Reactor-Network Model. 207-219B
Equilibrium Oxygen Pressures of Iron Silicate Slags. 463-465B
The Ferric Fluosilicate Leaching of Lead Concentrates. I. Kinetic Studies. 473-480B
An Analysis of Slag Stratification in Nickel Laterite Smelting Furnaces Due to Composition and Temperature Gradients. 491-496B
Modeling of Metallurgical Emulsions. 855-864B

Smelting, Pressure effects
Kinetics of the Reaction of H_2O Gas With Liquid Iron. 245-253B

Soft annealing
See Annealing

Soft solders
See Solders

Solar cells
See Solar generators

Solar generators
Thermodynamics of Boron in a Silicon Melt. 903-907B

Soldered joints, Coating
The Effect of Low Gold Concentrations on the Creep of Eutectic Tin—Lead Joints. 1249-1257A

Soldered joints, Mechanical properties
The Effect of Substrate on the Microstructure and Creep of Eutectic Indium-Tin. 2715-2722A

Solders
The Effect of Substrate on the Microstructure and Creep of Eutectic Indium-Tin. 2715-2722A

Solid phases
The Measurement of the Heat-Transfer Coefficient Between High-Temperature Liquids and Solid Surfaces. 43-51B
An Empirical Correlation Between Contact Angles and Surface Tension in Some Ceramic—Metal Systems. 225-230A
Sticking of Solids in Liquids. 397-403B

X-Ray Microscopic Observations of Metal Solidification Dynamics. 1775-1777A

Solid phases, Alloying effects
The Role of Oxygen and Zirconium in the Formation and Growth of Nb_3Sn Grains. 213-219A

Solid phases, Cooling effects
Further Discussions on the Solute Redistribution During Dendritic Solidification of Binary Alloys. 731-739B
The Velocity of Solidification of Highly Undercooled Nickel. 1301-1308A
Microsegregation in Cellular Solidification. 2295-2301A
Nonequilibrium Solidification of Undercooled Melt of Ag-Cu Alloy Entrained in the Primary Phase. 2517-2523A

Solid phases, Diffusion effects
The Morphological Stability of Lateral Growth in Solid—Solid Phase Transformation During Thin-Film Interdiffusion in Aluminum/Copper Bimetal Films. 1613-1625A
Application of the Theory of Martensite Crystallography to Displacive Phase Transformations in Substitutional Nonferrous Alloys. (Conference Paper, Review) 1841-1856A

Solid phases, Heating effects
Mechanism of Damping Capacity of High-Chromium Steels and α-Iron and Its Dependence on Some External Factors. 111-124A
Formation and Stability of Metastable Structures and Amorphous Phases in Pu—V, Pu—TA, and Pu—Yb Systems With Positive Heats of Mixing. 1579-1590A

Solid phases, Temperature effects
High-Temperature Phase Relations and Thermodynamics in the Iron—Lead—Sulfur System. 53-61B
Gradient Solid Electrolytes for Thermodynamic Measurements: System Na_2CO_3—Na_2SO_4. 173-180A
Thermodynamics of the Iron)Carbon)Zinc System. 569-578B
Numerical Modeling of Solidification and Subsequent Transformation of Fe—Cr—Ni Alloys. 1309-1321A
Thermodynamic Analysis of the In-Ga-Sb System. 2331-2340A

Solid solutions
Solid-Solution Formation Between Arsenic and Antimony Oxides. 865-871B

Solidification
See also Directional solidification
Rapid solidification
Effect of Supereutectic Homogenization on Incidence of Porosity in Aluminum Alloy 2014 Ingot. 111-122B
A Note on the Sensitivity of Solidification Models to Thermophysical Properties. 154-157B
Effect of Alloying Elements on the Solidification Characteristics and Microstructure of Al—Si—Cu—Mg—Fe 380 Alloy. 437-448A
Three-Dimensional Simulation of the Grain Formation in Investment Castings. 629-635A
Calculation of Thermophysical Properties of Carbon and Low Alloyed Steels for Modeling of Solidification Processes. 909-916B
Modeling Microstructure Development in Gray Cast Irons. 1063-1079A
Prediction of Columnar to Equiaxed Transition During Diffusion-Controlled Dendritic Alloy Solidification. 1081-1093A
Solidification Macrostructures and Macrosegregation in Aluminum Alloys Cooled From Above. 1097-1102A
The Velocity of Solidification of Highly Undercooled Nickel. 1301-1308A
X-Ray Microscopic Observations of Metal Solidification Dynamics. 1775-1777A
Effect of Welding Variables and Solidification Substructure on Weld Metal Porosity. 2285-2294A

Solidification, Cooling effects
Crystallization Behavior of Iron-Containing Intermetallic Compounds in 319 Aluminum Alloy. 1761-1773A
Microsegregation in Cellular Solidification. 2295-2301A
Evolution of Interaction Domain Microstructure During Spray Deposition. 2341-2355A

Solidification, Temperature effects
An Internal Variable Description of Solidification Suitable for Macrosegregation Modeling. 597-605B
Numerical Modeling of Solidification and Subsequent Transformation of Fe—Cr—Ni Alloys. 1309-1321A

Solidification, Welding effects
The Influence of Electron-Beam Welding Parameters on Heat-Affected-Zone Microfissuring in Incoloy 903. 1733-1745A

Solubility
Thermodynamics and Phase Relations of the Fe—O—S—SiO_2(sat) System at 1200°C and the Effect of Copper. 79-89B
Interactions Between Drops of a Molten Aluminum)Lithium Alloy and Liquid Water. 623-625B

Solubility, Alloying effects
Thermodynamics of Oxygen and Nitrogen in Liquid Nickel Equilibrated With CaO—TiO_x and CaO—TiO_x—Al_2O_3 Melts. 5-13B
Compositional and Microstructural Changes Which Attend Reheating and Grain Coarsening in Steels Containing Niobium. 277-286A

Solubility, Temperature effects
Solubility and Thermodynamic Properties of Y_2O_3 in LiF—YF_3 Melts. 91-96B

Solubility, Welding effects
Effect of Welding Variables and Solidification Substructure on Weld Metal Porosity. 2285-2294A

Solution entropy
See Entropy
Heat of solution

Solution heat treatment
Hydrogen Permeation Behavior in IN718 and GH761 Superalloys. 539-544A
Heat Treatment of Investment Cast PH 13-8Mo Stainless Steel. I. Mechanical Properties and Microstructure. 789-798A
Microstructural Study of the Titanium Alloy Ti—15Mo—2.7Nb—3Al—0.2Si (TIMETAL 21S). 1109-1118A
Effect of Heat Treatment on the Microstructure, Tensile Properties, and Fracture Behavior of Permanent Mold Al-10 wt.% Si-0.6 wt.% Mg/SiC/10p Composite Castings. 2247-2263A

Solution potential
See Corrosion potential

Solutions
See Solid solutions

Sorption
See Absorption (material)
Adsorption
Desorption

Space lattices
See Crystal lattices

Specific density
See Density

Specific gravity
See Density

Specific heat, Cooling effects
A Note on the Sensitivity of Solidification Models to Thermophysical Properties. 154-157B

Specific heat, Temperature effects
Three-Dimensional Finite Element Modeling of Gas Metal-Arc Welding. 435-441B

Specific resistance
See Resistivity

Specific volume
See Density

Specific weight
See Density

Spelter
See Zinc

Spheroidal graphite
See Nodular graphitic structure

Spheroidal iron
See Nodular iron

Spheroidal structure
See also Nodular graphitic structure

Spheroidal structure, Cooling effects
Evolution of Interaction Domain Microstructure During Spray Deposition. 2341-2355A

Spheroidal structure, Heating effects
The Effect of Phosphorus Segregation on the Intermediate-Temperature Embrittlement of Ferritic, Spheroidal Graphite Cast Iron. 557-561A

Spheroidal structure, High temperature effects
The Workability of Commercial and Experimental 0.6% Carbon Low Alloy Steels in the Temperature Range of 650-870°C. 827-837A

Spheroidizing
Alligatoring and Damage in the Cold Rolling of Spheroidized Steels. 589-598A
The Role of Magnesium-Containing Spheroidizer and Counteraction of Misch Metal in the Intermediate Temperature Intergranular Embrittlement of Ferritic Nodular Iron. 2305-2309A
The Effect of Thermal Exposure on Microstructural Stability and Creep Resistance of a Two-Phase TiAl/Ti_3Al Lamellar Alloy. 2371-2381A

Spheroids
See Spheroidal structure

Spin casting
See Centrifugal casting

Spinodal decomposition, Cooling effects
Nonequilibrium Solidification of Undercooled Melt of Ag-Cu Alloy Entrained in the Primary Phase. 2517-2523A

Spinodal decomposition, Deformation effects
Effects of Precursor Matrix Events on Subsequent Nucleation. (Conference Paper) 1933-1939A

Splicing
See Joining

Sponginess
See Porosity

Spot welding
See Resistance spot welding

Sprayed coatings, Microstructure
Microstructural Evolution of an Overlay Coating on a Single-Crystal Nickel-Base Superalloy. 2837-2840A

Stability
See Phase stability
Thermal stability

Stacking faults
The Formation Mechanism of Plate in β Cu-Zn and Cu-Zn-Al Alloys. (Conference Paper) 2601-2608A
Study on the Transformation Mechanism of α_1 Plates in a Copper-Zinc-Aluminum Alloy. (Conference Paper) 2615-2619A

Stacking faults, Diffusion effects
Application of the Theory of Martensite Crystallography to Displacive Phase Transformations in Substitutional Nonferrous Alloys. (Conference Paper, Review) 1841-1856A

Stacking faults, Heating effects
Interstitial Precipitation in Fe—Cr—Al Alloys. 1135-1146A

Stainless steels
See also Austenitic stainless steels
Ferritic stainless steels
Martensitic stainless steels

Stainless steels, Phase transformations
The Invariant Line and Precipitate Morphology in FCC-BCC Systems. (Conference Paper) 1865-1874A

Stainless steels, Physical properties
Surface Tensions of Liquid Fe-Cr and Fe-Cr-N Alloys. 626-628B

Stainless steels, Steel making
Reduction of Chromite in Liquid Fe)Cr)C)Si Alloys. 549-559B
A Thermodynamic Study of BaO + $BaCl_2$ + Cr_2O_3 Fluxes Used for the Removal of Phosphorus From Chromium-Containing Iron Melts. 695-701B

Stamping
A Plane Strain Punch Stretching Test for Evaluating Stamping Formability of Steel Sheets. 2199-2205A

Static fatigue
See Creep rupture strength

Static loads
See Loads (forces)

Static pressure
See Hydrostatic pressure

Steel constituents
See Austenite
Bainite
Cementite
Martensite
Pearlite
Sigma phase

Steel converters
See Top blown converters

Steel making
Calcium Deoxidation Equilibrium in Liquid Iron. 33-42B
High-Temperature Isopiestic Studies on the Ternary Slag PbO—SiO_2—B_2O_3 at 1273K. 103-109B
Physical and Mathematical Modeling of Pyrometallurgical Channel Reactors With Bottom Gas Injection. Residence Time Distribution Analysis and Ideal-Reactor-Network Model. 207-219B
Kinetics of the Reaction of H_2O Gas With Liquid Iron. 245-253B
A Comparison of Three Mathematical Modeling Procedures for Simulating Fluid Flow Phenomena in Bubble-Stirred Ladles. 308-312B
Large-Scale Measurements of the Physical Characteristics of Round Vertical Bubble Plumes in Liquids. 359-371B
Backmixing in Channel Reactors With High-Strength Bottom Gas Injection. 619-623B
The Injection of Solids Using a Reactive Carrier Gas. 653-660B
Critical Fluid-Flow Phenomenon in a Gas-Stirred Ladle. 681-693B
Measurements of High-Temperature Viscosities of Liquid Boron Trioxide. 876-881A
Activities of Fe_tO in CaO-Al_2O_3-SiO_2-Fe_tO (5%) Slags Saturated With Liquid Iron. 893-902B
Densities of Liquid Fe-Ni and Fe-Cr Alloys. 939-942B

Steels
See also Carbon steels
Dual phase steels
Galvanized steels
Structural steels

Steels, Casting
On the Formation of Pipes and Centerline Segregates in Continuously Cast Billets. 123-133B
A Note on the Sensitivity of Solidification Models to Thermophysical Properties. 154-157B
Water-Modeling Study of the Surface Disturbances in Continuous Slab Caster. 227-233B
Modeling the Thin-Slab Continuous-Casting Mold. 443-457B
Simulation of Argon Gas Flow Effects in a Continuous Slab Caster. 527-547B

Steels, Coating
η to G Phase Transformation in Electrodeposited Iron—Zinc Alloy Coatings. 1119-1125A

Steels, Heat treatment
Morphological Stability of γ/α Interface Formed by Carburization in Fe—C—X Alloys. 531-537A

Steels, Mechanical properties
Elastic Compliance and Hill's Quadratic Yield Function for Weakly Orthotropic Sheets of Cubic Metals. 2835-2837A

Steels, Metal working
A Plane Strain Punch Stretching Test for Evaluating Stamping Formability of Steel Sheets. 2199-2205A

Steels, Metallography
Efficient Measurement of Microstructural Surface Area Using Trisector. 919-928A

Steels, Phase transformations
Diffusion-Controlled Growth in Ternary Systems. 2683-2694A

Steels, Phases (state of matter)
The Phenomenological Theory of Martensite Crystallography: Interrelationships. (Conference Paper) 1787-1795A
Morphology of Bainite and Widmanstätten Ferrite. (Conference Paper) 1981-1989A

Steels, Recovering
Equilibrium Values for the Dissolution of Solid Copper Into FeS—Na_2S Mattes. 306-308B

Steels, Welding
Resistance Spot Welding of Precoated Steel Sheet: Computational Heat-Transfer Analysis. 415-423B

Stibium
See Antimony

Stiffness, Heating effects
Development and Characterization of Interface Coatings in Molybdenum-Reinforced NiAl Matrix Composites. 2111-2116A

Stiffness, Microstructural effects
The Orientation Dependence of Fatigue-Crack Growth in 8090 Aluminum—Lithium Plate. 575-588A
Characterization of Anisotropic Elastic Constants of Silicon-Carbide Particulate Reinforced Aluminum Metal Matrix Composites. I. Experiment. 799-809A

Stiffness, Stress effects
Characterization of Anisotropic Elastic Constants of Silicon-Carbide Particulate Reinforced Aluminum Metal Matrix Composites. II. Theory. 811-819A
Coefficients of Thermal Expansion of Metal-Matrix Composites for Electronic Packaging. 839-850A
Low-Cycle Fatigue Properties of a SiC Whisker-Reinforced 2124 Aluminum Alloy. 2265-2274A

Stirring
See also Electromagnetic stirring
A Two-Phase Flow Model of the Stirring of Al)SiC Composite Melt. 607-618B

Strain
Characterization of Inhomogeneous Elastic Deformation With X-Ray Diffraction. 341-347A
Characterization of Anisotropic Elastic Constants of Silicon-Carbide Particulate Reinforced Aluminum Metal Matrix Composites. II. Theory. 811-819A
η to G Phase Transformation in Electrodeposited Iron—Zinc Alloy Coatings. 1119-1125A
The Phenomenological Theory of Martensite Crystallography: Interrelationships. (Conference Paper) 1787-1795A
A Plane Strain Punch Stretching Test for Evaluating Stamping Formability of Steel Sheets. 2199-2205A

Strain, Diffusion effects
A Comparison Between Three Simple Crystallographic Principles of Precipitate Morphology. (Conference Paper) 1857-1863A

Strain, Heating effects
Interstitial Precipitation in Fe—Cr—Al Alloys. 1135-1146A
The Effect of Thermal Exposure on Microstructural Stability and Creep Resistance of a Two-Phase TiAl/Ti_3Al Lamellar Alloy. 2371-2381A

Strain, High temperature effects
Low-Cycle Fatigue Behavior of Polycrystalline NiAl at 1000K. 309-319A
Elevated Temperature Fracture of RS/PM Alloy 8009. I. Fracture Mechanics Behavior. 365-379A

Strain, Microstructural effects
Precipitation Effects During Hot Deformation of a Copper Alloy. 257-266A
Microstructure and Mechanical Properties of Ti—40 wt.% Ta (Ti—15 at.% Ta). 461-472A
Textural and Microstructural Gradient Effects on the Mechanical Behavior of a Tantalum Plate. 1025-1031A
Temperature and Microstructural Dependence of the Deformation of a High Niobium, Titanium—Aluminum Alloy. 1667-1679A
Microstructural Analysis of Fracture Toughness Variation in 2XXX-Series Aluminum Alloy Composites Reinforced With SiC Whiskers. 2213-2223A
The Study of Adiabatic Shear Band Instability in a Pearlitic 4340 Steel Using a Dynamic Punch Test. 2483-2489A

Strain, Microstructure
The Elastic Strain Energy of Growth Ledges on Coherent and Partially Coherent Precipitates. 2073-2082A

Strain, Stress effects
Micromechanical Modelling of Reinforcement Fracture in Particle-Reinforced Metal-Matrix Composites. 2403-2420A
Fracture Toughness of Discontinuously Reinforced Al-4Cu-1.5Mg/TiB_2 Composites. 2461-2468A

Strain aging, High temperature effects
Effect of Strain Rate on the High-Temperature Low-Cycle Fatigue Properties of a Nimonic PE-16 Superalloy. 159-171A

Strain aging, Radiation effects
Deformation Behavior of Irradiated Zr—2.5Nb Pressure Tube Material. 135-145A

Strain hardening
Strain Hardening in Underaged Inconel 718. 653-656A
The Effect of Inertia on Tensile Ductility. 2723-2735A

Strain hardening, Heating effects
The Effect of Thermal Exposure on Microstructural Stability and Creep Resistance of a Two-Phase TiAl/Ti_3Al Lamellar Alloy. 2371-2381A

Strain hardening, Microstructural effects
The Study of Adiabatic Shear Band Instability in a Pearlitic 4340 Steel Using a Dynamic Punch Test. 2483-2489A

Strain hardening, Stress effects
Stress-State Dependence of Strain-Hardening Behavior in 2014 Al/15 vol.% Al_2O_3 Composite. (Conference Paper) 2049-2061A

Strain rate
Discussion of "The Distribution of Dispersoid Phases in the Extruded ODS Superalloy MA-957 and Reply. 651-653A

Factors Influencing the Exceptional Ductility of a Superplastic Pb-62% Sn Alloy. 2309-2311A
The Effect of Inertia on Tensile Ductility. 2723-2735A
Effect of Internal Heating During Hot Compression on the Stress-Strain Behavior of Alloy 304L. 2737-2752A

Strain rate, Composition effects
The Effects of Hydrogen on the Mechanical Behavior of Austenitic Stainless Steels at Room Temperature. 1015-1023A

Strain rate, Cooling effects
Softening and Microstructural Change Following the Dynamic Recrystallization of Austenite. 389-400A
Evolution of Interaction Domain Microstructure During Spray Deposition. 2341-2355A

Strain rate, Deformation effects
The Tensile Deformation Behavior of AA 3004 Aluminum Alloy. 357-364A
Anisotropic Plastic Potentials for Polycrystals and Application to the Design of Optimum Blank Shapes in Sheet Forming. 1209-1216A
Hot Deformation Characteristics of INCONEL Alloy MA 754 and Development of a Processing Map. 1693-1702A
High-Temperature Deformation of B2 NiAl-Base Alloys. (Conference Paper) 2017-2026A
Superplastic Behavior of Thermomechanically Treated P/M 7091 Aluminum Alloy. 2153-2160A
Microstructural Control in Hot Working of IN-718 Superalloy Using Processing Map. 2275-2284A

Strain rate, Environmental effects
Embrittlement of B2 Iron Aluminide by Water Vapor and by Hydrogen. 1285-1290A

Strain rate, High temperature effects
Effect of Strain Rate on the High-Temperature Low-Cycle Fatigue Properties of a Nimonic PE-16 Superalloy. 159-171A

Strain rate, Microstructural effects
Some Aspects of Thermomechanical Fatigue of AISI 304L Stainless Steel. II. Dislocation Arrangements. 407-413A
The Study of Adiabatic Shear Band Instability in a Pearlitic 4340 Steel Using a Dynamic Punch Test. 2483-2489A

Strain rate, Stress effects
Forging Limits for an Aluminum Matrix Composite. I. Experimental Results. (Conference Paper) 2027-2038A
Flow Instabilities and Fracture in Ti-6Al-4V Deformed in Compression at 298-673K. 2173-2179A
Low Cycle Fatigue Behavior of Polycrystalline Ni_3Al Alloys at Ambient and Elevated Temperatures. 2469-2476A

Strain rate, Temperature effects
Behavior of Steels Near the Incipient Melting Temperature. 125-133A

Strain rate stress effects
Forging Limit for an Aluminum Matrix Composite. II. Analysis. (Conference Paper) 2039-2048A

Stress aging
See Strain aging

Stress concentration
Cleavage Initiation in the Intercritically Reheated Coarse-Grained Heat-Affected Zone: I. Fractographic Evidence. 563-573A
Characterization of Anisotropic Elastic Constants of Silicon-Carbide Particulate Reinforced Aluminum Metal Matrix Composites. II. Theory. 811-819A

Stress corrosion cracking
Creep and Intergranular Cracking of Ni—Cr—Fe—C in 360°C Argon. 1169-1183A

Stress corrosion cracking, Diffusion effects
Tritium Distribution at the Crack Tip of High-Strength Steels Submitted to Stress Corrosion Cracking. 1159-1167A

Stress corrosion cracking, Heating effects
Applicability of Bond Percolation Theory to Intergranular Stress-Corrosion Cracking of Sensitized AISI 304 Stainless Steel. 775-787A

Stress corrosion resistance
See Corrosion resistance

Stress cycle
Behavior of Nickel-Base Superalloy Single Crystals Under Thermal—Mechanical Fatigue. 99-109A
Effect of Strain Rate on the High-Temperature Low-Cycle Fatigue Properties of a Nimonic PE-16 Superalloy. 159-171A
Characteristics of the Martensitic Transformation and the Induced Two-Way Shape Memory Effect After Training by Compressive Pseudoelastic Cycling in Cu—Zn—Al Single Crystals. 687-695A
Thermal-Mechanical Fatigue of Ti-48Al-2V Alloy and Its Composite. 2207-2212A
Low-Cycle Fatigue of Dispersion-Strengthened Copper. 2235-2245A

Stress distribution
See Stress concentration

Stress intensity
Effect of Orientation on Crystallographic Cracking in Notched Nickel-Base Superalloy Single Crystal Subjected to Far-Field Cyclic Compression. 287-297A
Tensile Ductility of Extrinsically Toughened Intermetallics. 299-308A
Characterization of Inhomogeneous Elastic Deformation With X-Ray Diffraction. 341-347A
Characteristics of the Martensitic Transformation and the Induced Two-Way Shape Memory Effect After Training by Compressive Pseudoelastic Cycling in Cu—Zn—Al Single Crystals. 687-695A
Fracture of Glass in Tensile and Bending Tests. 961-968A
Crack Initiation at Long Radial Hydrides in Zr—2.5Nb Pressure Tube Material at Elevated Temperatures. 993-1004A
Evaluation of Homogeneous Compression Flow Curves Using Square Cross-Sectioned Specimens. 1095-1097A
Creep and Intergranular Cracking of Ni—Cr—Fe—C in 360°C Argon. 1169-1183A
Mixed-Mode I and II Fatigue Threshold and Crack Closure in Dual-Phase Steels. 1713-1723A
Transformation, Microcrack, and Thermal Residual Stress as Interactive Processes in ZrO_2-Toughened Al_2O_3, Simulated by the Finite Element Method. 1725-1731A
Modeling Creep Deformation of a Two-Phase TiAl/Ti_3Al Alloy With a Lamellar Microstructure. 2161-2171A
Thermal-Mechanical Fatigue of Ti-48Al-2V Alloy and Its Composite. 2207-2212A
Low-Cycle Fatigue Properties of a SiC Whisker-Reinforced 2124 Aluminum Alloy. 2265-2274A
Modeling the Effects of Stress State and Crystal Orientation on the Stress-Induced Transformation of NiTi Single Crystals. 2383-2389A
Effect of Iron on the Superplastic Deformation of Zn-22%Al. 2391-2401A
Short Fatigue Crack Growth Behavior in a Ferritic-Bainitic Steel. 2421-2425A
The Influence of SiC Particulates on Fatigue Crack Propagation in a Rapidly Solidified Al-Fe-V-Si Alloy. 2453-2460A
Fracture Toughness of Discontinuously Reinforced Al-4Cu-1.5Mg/TiB_2 Composites. 2461-2468A
Creep Characteristics of Single Crystalline Ni_3Al(Ta,B). 2477-2482A

Stress relaxation, Composition effects
The Effects of Hydrogen on the Mechanical Behavior of Austenitic Stainless Steels at Room Temperature. 1015-1023A

Stress rupture strength
See Creep rupture strength

Stress strain curves
Behavior of Nickel-Base Superalloy Single Crystals Under Thermal—Mechanical Fatigue. 99-109A
Effect of Strain Rate on the High-Temperature Low-Cycle Fatigue Properties of a Nimonic PE-16 Superalloy. 159-171A
Estimation of Interfacial Shear Strength Between Superconducting Oxides and Silver Sheath From Multiple-Fracture Phenomenon of the Oxide. 349-356A
Textural and Microstructural Gradient Effects on the Mechanical Behavior of a Tantalum Plate. 1025-1031A
The Effects of Hydrostatic Pressure on the Compressive Mechanical Behavior of $L1_2$ Al_3 Ti-Based Intermetallic. 1703-1711A
Flow Instabilities and Fracture in Ti-6Al-4V Deformed in Compression at 298-673K. 2173-2179A
Low-Cycle Fatigue of Dispersion-Strengthened Copper. 2235-2245A
Effect of Internal Heating During Hot Compression on the Stress-Strain Behavior of Alloy 304L. 2737-2752A

Stresses
See Axial stress
Residual stress
Stress intensity
Tensile stress
Thermal stresses

Stretching
Effects of Texture Gradients on Yield Loci and Forming Limit Diagrams in Various Aluminum-Lithium Sheet Alloys. 2783-2795A

Strip
See Strip steel

Strip steel, Heat treatment
Computer Algorithms for Radiometric Measurement of Temperature During the Galvanneal Process. 449-462B

Structural hardening
See Dispersion hardening
Precipitation hardening
Strain hardening

Structural materials
See Structural steels

Structural steels, Mechanical properties
Evaluation of Homogeneous Compression Flow Curves Using Square Cross-Sectioned Specimens. 1095-1097A

Structure (atomic)
See Atomic structure

Structures (crystalline)
See Crystal structure
Grain structure
Macrostructure
Microstructure

Submerged arc welds
See Welded joints

Suction
See Vacuum

Sulfur, Chemical analysis
Sulfur Determination in Carbon-Saturated Iron by Solid-State Electrochemical Sensor. 561-568B

Sulfur, Ternary systems
High-Temperature Phase Relations and Thermodynamics in the Iron—Lead—Sulfur System. 53-61B

Sulphur
See Sulfur

Superalloys, Casting
Three-Dimensional Simulation of the Grain Formation in Investment Castings. 629-635A

Superalloys, Cladding
A Simple but Realistic Model for Laser Cladding. 281-291B

Superalloys, Coating
Microstructural Evolution of an Overlay Coating on a Single-Crystal Nickel-Base Superalloy. 2837-2840A

Superalloys, Extrusion
Discussion of "The Distribution of Dispersoid Phases in the Extruded ODS Superalloy MA-957 and Reply. 651-653A

Superalloys, Heat treatment
Hydrogen Permeation Behavior in IN718 and GH761 Superalloys. 539-544A

Superalloys, Mechanical properties
Behavior of Nickel-Base Superalloy Single Crystals Under Thermal—Mechanical Fatigue. 99-109A
Effect of Strain Rate on the High-Temperature Low-Cycle Fatigue Properties of a Nimonic PE-16 Superalloy. 159-171A
Effect of Orientation on Crystallographic Cracking in Notched Nickel-Base Superalloy Single Crystal Subjected to Far-Field Cyclic Compression. 287-297A
On Morphologies, Microsegregation, and Mechanical Behavior of Directionally Solidified Cobalt-Base Superalloy at Medium Cooling Rate. 637-642A
Characterization of Mechanically Alloyed Oxide Dispersion-Strengthened Nickel-Base Superalloy MA760. 705-714A
Hot Deformation Characteristics of INCONEL Alloy MA 754 and Development of a Processing Map. 1693-1702A

Superalloys, Metal working
Microstructural Control in Hot Working of IN-718 Superalloy Using Processing Map. 2275-2284A

Superalloys, Structural hardening
Strain Hardening in Underaged Inconel 718. 653-656A
Diffusional Boundary Conditions During Coarsening of Elastically Interacting Precipitates. 2695-2703A

Superalloys, Welding
The Influence of Electron-Beam Welding Parameters on Heat-Affected-Zone Microfissuring in Incoloy 903. 1733-1745A

Superconductors
Directional Phase Formation on Melting via Peritectic Reaction. 1747-1760A

Superconductors, Microstructure
The Role of Oxygen and Zirconium in the Formation and Growth of Nb_3Sn Grains. 213-219A

Superconductors, Phases (state of matter)
Thermodynamic Study of $BaCuO_2$ and $BaCu_2O_2$. 385-389B

Supercooling
Crystallization Studies of the β' (Mg_2Pb) Phase and Its Phase Boundaries in the Pb—Mg—Bi System. 255-263B
The Velocity of Solidification of Highly Undercooled Nickel. 1301-1308A
Nonequilibrium Solidification of Undercooled Melt of Ag-Cu Alloy Entrained in the Primary Phase. 2517-2523A
Numerical Analysis of the Rapid Solidification of Gas-Atomized Al-8 wt.% Iron Droplets. 2815-2826A

Superplastic forming
Superplastic Behavior of Thermomechanically Treated P/M 7091 Aluminum Alloy. 2153-2160A

Superplasticity
Factors Influencing the Exceptional Ductility of a Superplastic Pb-62% Sn Alloy. 2309-2311A

Superplasticity, Deformation effects
Superplastic Behavior of Two Ultrahigh Boron Steels. 1241-1248A
Superplastic Behavior of Thermomechanically Treated P/M 7091 Aluminum Alloy. 2153-2160A

Superplasticity, Microstructural effects
Discussion of "Grain Growth of a Superplastic 7475 Aluminum Alloy". 221-223A

Superplasticity, Stress effects
Effect of Iron on the Superplastic Deformation of Zn-22%Al. 2391-2401A

Surface analysis (chemical)
See Depth profiling

Surface chemistry
Adsorption Kinetics of Dicyanoaurate and Dicyanoargentate Ions in Activated Carbon. 185-191B
Surface Segregation of Calcium Oxide in Wustite and Its Effects on the Reduction. 405-413B
Surface Characterization and Reactivity of a Nitrogen Atomized 304L Stainless Steel Powder. 509-520A
Nanocrystalline Iron Sintering Behavior and Microstructural Development. 677-685A
Improvement in the Reducibility of Wustite Assisted by the Intensified Surface Segregation of Calcium Ions by the Double Addition of CaO and SiO_2. 741-748B

Surface chemistry, Alloying effects
Solid-State Wetting of Graphite by Lead and Pb—Ni Alloys. 607-615A

Surface chemistry, Composition effects
High-Temperature Oxidation of Cathodically Hydrogen-Charged Two-Phase (Ti_3Al, TiAl) Titanium Aluminides. 2491-2496A

Surface chemistry, Diffusion effects
Multiphase Binary Diffusion in Infinite and Semi-Infinite Media. II. On the Numerical Calculation of the Rate Constants for Formation of Product Phases. 753-761A

Surface chemistry, Environmental effects
Modeling Hydrogen Entry and Exit in Metals Exposed to Multiple Charging Processes. 723-732A

Surface chemistry, Heating effects
Computer Algorithms for Radiometric Measurement of Temperature During the Galvanneal Process. 449-462B
Auger Electron Analysis of the Initial Oxidation of Titanium Aluminides Based on Ti—48Al. 1041-1050A

Surface chemistry, Microstructural effects
Influence of Near-Surface Microstructures on the Transient Current Response in Fe—Cr—Ni Alloys During Scratch Tests. 1325-1331A

Surface chemistry, Pressure effects
Kinetics of the Reaction of H_2O Gas With Liquid Iron. 245-253B

Surface chemistry, Radiation effects
Gas Trapping and Release in Polycrystalline Nickel Preimplanted With Helium. 949-959A

Surface defects
Water-Modeling Study of the Surface Disturbances in Continuous Slab Caster. 227-233B

Surface defects, Stress effects
Fracture of Glass in Tensile and Bending Tests. 961-968A

Surface diffusion
See Diffusion

Surface energy
An Empirical Correlation Between Contact Angles and Surface Tension in Some Ceramic—Metal Systems. 225-230A

Surface hardening
See also Laser beam hardening
Depth of Melt-Pool and Heat-Affected Zone in Laser Surface Treatments. 427-435A

Surface hardness, Radiation effects
Effects of Simultaneous Boron and Nitrogen Implantation on Microhardness and Fatigue Properties of Fe—13Cr—15Ni Alloys. 193-202A

Surface properties
See Emissivity
Roughness
Surface structure
Surface tension
Wetting

Surface roughness
See Roughness

Surface structure
The Diffuse-Scattering Method for Investigating Locally Ordered Binary Solid Solutions. 17-35A
Structure of As-Deposited Iron—Zinc Coatings From Chloride Bath. 249-255A
A Simple but Realistic Model for Laser Cladding. 281-291B
Surface Characterization and Reactivity of a Nitrogen Atomized 304L Stainless Steel Powder. 509-520A
The Orientation Dependence of Fatigue-Crack Growth in 8090 Aluminum—Lithium Plate. 575-588A
Nanocrystalline Iron Sintering Behavior and Microstructural Development. 677-685A
Thermodynamics of Isolated Pores Filling With Liquid in Sintered Composite Materials. 733-740A
Improvement in the Reducibility of Wustite Assisted by the Intensified Surface Segregation of Calcium Ions by the Double Addition of CaO and SiO_2. 741-748B
Efficient Measurement of Microstructural Surface Area Using Trisector. 919-928A
Effect of Microstructure (Particulate Size and Volume Fraction) and Counterface Material on the Sliding Wear Resistance of Particulate-Reinforced Aluminum Matrix Composites. 969-983A
Influence of Near-Surface Microstructures on the Transient Current Response in Fe—Cr—Ni Alloys During Scratch Tests. 1325-1331A
X-Ray Microscopic Observations of Metal Solidification Dynamics. 1775-1777A
The Phenomenological Theory of Martensite Crystallography: Interrelationships. (Conference Paper) 1787-1795A
Ledges and Dislocations in Phase Transformations. (Conference Paper) 1885-1894A
The Role of Structural Ledges as Misfit-Compensating Defects: FCC-BCC Interphase Boundaries. (Conference Paper) 1895-1903A
Spreading and Interlayer Formation at the Copper-Copper Oxide/Polycrystalline Alumina Interface. 2497-2506A

Surface structure, Alloying effects
Morphological Stability of γ/α Interface Formed by Carburization in Fe—C—X Alloys. 531-537A

Surface structure, Coating effects
The Influence of Laser Glazing on Fatigue Crack Growth in Ti—24Al—11Nb. 183-192A
Processing, Microstructure, and Properties of Laser-Clad Nickel Alloy FP-5 on Al Alloy AA333. 425-434B

Surface structure, Composition effects
High-Temperature Oxidation of Cathodically Hydrogen-Charged Two-Phase (Ti_3Al, TiAl) Titanium Aluminides. 2491-2496A

Surface structure, Cooling effects
Natural Convection in an Aluminum Ingot: a Mathematical Model. 293-302B
Three-Dimensional Simulation of the Grain Formation in Investment Castings. 629-635A
Fatigue Crack Growth Rates and Fracture Toughness of Rapidly Solidified Al—8.5Fe—1.2V—1.7Si Alloys. 1005-1014A

Surface structure, Diffusion effects
Crystallographic Theories, Interface Structures, and Transformation Mechanisms. (Conference Paper) 1821-1839A
On the Role of Interphase-Boundary Structure in Plate Growth by Diffusional Mechanisms. (Conference Paper) 1875-1883A

Formation of Invariant Plane-Strain and Tent-Shaped Surface Reliefs by the Diffusional Ledge Mechanism. (Conference Paper) 1923-1931A

Surface structure, Heating effects
Atom Probe Field Ion Microscopy Study of the Partitioning of Substitutional Elements During Tempering of a Low-Alloy Steel Martensite. 499-508A
The Effect of Phosphorus Segregation on the Intermediate-Temperature Embrittlement of Ferritic, Spheroidal Graphite Cast Iron. 557-561A
Morphology Development in Hot-Dip Galvanneal Coatings. 937-947A
Auger Electron Analysis of the Initial Oxidation of Titanium Aluminides Based on Ti—48Al. 1041-1050A
Development and Characterization of Interface Coatings in Molybdenum-Reinforced NiAl Matrix Composites. 2111-2116A

Surface structure, Welding effects
Characterization of a Diffusion-Bonded Al—Mg Alloy/SiC Interface by High Resolution and Analytical Electron Microscopy. 617-627A

Surface tension
An Empirical Correlation Between Contact Angles and Surface Tension in Some Ceramic—Metal Systems. 225-230A
Sticking of Solids in Liquids. 397-403B
Surface Tensions of Liquid Fe-Cr and Fe-Cr-N Alloys. 626-628B
Physicochemical Properties of Nickel Electrolytes. 637-644B

Susceptibility (magnetic)
See Magnetic permeability

Synthesis, Temperature effects
Thermodynamic Estimation of ΔH_f^0 for $CaGa_2$ Intermetallic. 151-154B

Systems (metallurgical)
See Binary systems
Quaternary systems
Ternary systems

Tanks (electrolytic)
See Electrolytic cells

Tantalum, Binary systems
Formation and Stability of Metastable Structures and Amorphous Phases in Pu—V, Pu—TA, and Pu—Yb Systems With Positive Heats of Mixing. 1579-1590A

Tantalum, Mechanical properties
Textural and Microstructural Gradient Effects on the Mechanical Behavior of a Tantalum Plate. 1025-1031A

Tear strength, High temperature effects
Elevated Temperature Fracture of RS/PM Alloy 8009. I. Fracture Mechanics Behavior. 365-379A

Temperature
See Curie temperature
High temperature

Tempering
See also Quenching and tempering
Atom Probe Field Ion Microscopy Study of the Partitioning of Substitutional Elements During Tempering of a Low-Alloy Steel Martensite. 499-508A
The Effects of Double Austenitization on the Mechanical Properties of a 0.34C Containing Low-Alloy Ni—Cr—Mo—V Steel. 545-555A
Isothermal Formation of Quasicrystalline Precipitates and Their Effect on Strength in a 12Cr-9Ni-4Mo Maraging Stainless Steel. 2225-2233A

Tenacity
See Tensile strength

Tensile modulus
See Modulus of elasticity

Tensile properties
See Elongation
Necking
Reduction of area
Tensile strength
Yield strength

Tensile shear strength
See Shear strength

Tensile strength, Composition effects
Room-Temperature Strength and Deformation of TiB_2-Reinforced Near-γ Titanium Aluminides. 2181-2197A
Melt-Processed Ni_3Al Matrix Composites Reinforced With TiC Particles. 2525-2534A

Tensile strength, Cooling effects
Effects of Widmanstätten Ferrite on the Mechanical Properties of a 0.2% C—0.7% Mn Steel. 763-773A

Tensile strength, Environmental effects
Hydride Embrittlement in Zircaloy-4 Plate. I. Influence of Microstructure on the Hydride Embrittlement in Zircaloy-4 at 20 and 350°C. 1185-1197A

Tensile strength, Heating effects
The Effects of Double Austenitization on the Mechanical Properties of a 0.34C Containing Low-Alloy Ni—Cr—Mo—V Steel. 545-555A
Heat Treatment of Investment Cast PH 13-8Mo Stainless Steel. I. Mechanical Properties and Microstructure. 789-798A
Effect of Heat Treatment on the Microstructure, Tensile Properties, and Fracture Behavior of Permanent Mold Al-10 wt.% Si-0.6 wt.% Mg/SiC/10p Composite Castings. 2247-2263A

Tensile strength, Microstructural effects
Fracture and the Formation of Sigma Phase, $M_{23}C_6$, and Austenite From Delta—Ferrite in an AISI 304L Stainless Steel. 1147-1158A
Microstructural Analysis of Fracture Toughness Variation in 2XXX-Series Aluminum Alloy Composites Reinforced With SiC Whiskers. 2213-2223A

Tensile strength, Stress effects
Cleavage Initiation in the Intercritically Reheated Coarse-Grained Heat-Affected Zone: I. Fractographic Evidence. 563-573A
Crack Initiation at Long Radial Hydrides in Zr—2.5Nb Pressure Tube Material at Elevated Temperatures. 993-1004A

Tensile stress
Behavior of Steels Near the Incipient Melting Temperature. 125-133A
The Influence of Laser Glazing on Fatigue Crack Growth in Ti—24Al—11Nb. 183-192A
A Simplified Method of Calculating the Stress Field at the Tip of a Discrete Dislocation Pileup in a Finite Crystal. 223-225A
Characteristics of the Martensitic Transformation and the Induced Two-Way Shape Memory Effect After Training by Compressive Pseudoelastic Cycling in Cu—Zn—Al Single Crystals. 687-695A
Fracture of Glass in Tensile and Bending Tests. 961-968A
Hydride Embrittlement in Zircaloy-4 Plate. II. Interaction Between the Tensile Stress and the Hydride Morphology. 1199-1208A
Transformation, Microcrack, and Thermal Residual Stress as Interactive Processes in ZrO_2-Toughened Al_2O_3, Simulated by the Finite Element Method. 1725-1731A
Forging Limits for an Aluminum Matrix Composite. I. Experimental Results. (Conference Paper) 2027-2038A
Forging Limit for an Aluminum Matrix Composite. II. Analysis. (Conference Paper) 2039-2048A
Modeling the Effects of Stress State and Crystal Orientation on the Stress-Induced Transformation of NiTi Single Crystals. 2383-2389A
Micromechanical Modelling of Reinforcement Fracture in Particle-Reinforced Metal-Matrix Composites. 2403-2420A

Tensile tests
See Tension tests

Tensile yield strength
See Yield strength

Tension impact tests
See Impact tests

Tension tests
Environmental Effect on Room-Temperature Ductility of Isothermally Forged TiAl-Base Alloys. 321-330A
Fracture of Glass in Tensile and Bending Tests. 961-968A
The Effect of Inertia on Tensile Ductility. 2723-2735A

Ternary systems
Thermodynamic Properties of Ternary Liquid Cu—Mg—Ni Alloys. 63-72B

Ternary systems, Phase transformations
Numerical Modeling of Solidification and Subsequent Transformation of Fe—Cr—Ni Alloys. 1309-1321A
Diffusion-Controlled Growth in Ternary Systems. 2683-2694A

Ternary systems, Phases (state of matter)
High-Temperature Phase Relations and Thermodynamics in the Iron—Lead—Sulfur System. 53-61B
Thermodynamic Study of the Bi—Ca—O System. 97-101B
Crystallization Studies of the β' (Mg_2Pb) Phase and Its Phase Boundaries in the Pb—Mg—Bi System. 255-263B
Thermodynamics of the Iron)Carbon)Zinc System. 569-578B
The Grand Partition Function of Dilute Biregular Solutions. 703-711B
Thermodynamics of the Liquid {xCu + yAu + (1—x—y)Ge}, ($0.75 \leq x \leq 1$, $0 \leq y \leq 0.125$) Alloys at 1550K by Knudsen Effusion Mass Spectrometry. 857-864A
Thermodynamic Analysis of the In-Ga-Sb System. 2331-2340A

Tertiary displacements
See Displacements (lattice)

Texture
The Orientation Dependence of Fatigue-Crack Growth in 8090 Aluminum—Lithium Plate. 575-588A
Textural and Microstructural Gradient Effects on the Mechanical Behavior of a Tantalum Plate. 1025-1031A
Effects of Texture Gradients on Yield Loci and Forming Limit Diagrams in Various Aluminum-Lithium Sheet Alloys. 2783-2795A

Texture, Deformation effects
Anisotropic Plastic Potentials for Polycrystals and Application to the Design of Optimum Blank Shapes in Sheet Forming. 1209-1216A
High-Temperature Deformation of B2 NiAl-Base Alloys. (Conference Paper) 2017-2026A
Discussion of "The Role of Microstructure on Strength and Ductility of Hot-Extruded Mechanically Alloyed NiAl" and Author's Reply. 2303-2305A

Texture, Radiation effects
Deformation Behavior of Irradiated Zr—2.5Nb Pressure Tube Material. 135-145A

Texture, Stress effects
Characterization of Inhomogeneous Elastic Deformation With X-Ray Diffraction. 341-347A

Thawing
See Melting

Thermal capacity
See Specific heat

Thermal conductivity
Resistance Spot Welding of Precoated Steel Sheet: Computational Heat-Transfer Analysis. 415-423B

Thermal conductivity, Cooling effects
A Note on the Sensitivity of Solidification Models to Thermophysical Properties. 154-157B

Thermal conductivity, Temperature effects
Three-Dimensional Finite Element Modeling of Gas Metal-Arc Welding. 435-441B

Thermal expansion, Stress effects
Coefficients of Thermal Expansion of Metal-Matrix Composites for Electronic Packaging. 839-850A

Thermal fatigue, Deformation effects
Modeling the Thin-Slab Continuous-Casting Mold. 443-457B

Thermal fatigue, Stress effects
Thermal-Mechanical Fatigue of Ti-48Al-2V Alloy and Its Composite. 2207-2212A

Thermal fatigue, Temperature effects
Comparison of Orthorhombic and Alpha-Two Titanium Aluminides as Matrices for Continuous SiC-Reinforced Composites. 1267-1283A

Thermal flux
See Heat transmission

Thermal properties
See Emissivity
Melting points
Specific heat
Thermal conductivity
Thermal expansion
Thermal stability
Vapor pressure

Thermal reduction
See Fluidized bed reduction
Smelting

Thermal resistivity
See Thermal conductivity

Thermal spraying
See Plasma spraying

Thermal stability, Alloying effects
Elevated-Temperature Stability of Mechanically Alloyed Copper-Niobium Powders. 2091-2099A

Thermal stability, Composition effects
Melt-Processed Ni_3Al Matrix Composites Reinforced With TiC Particles. 2525-2534A

Thermal stability, Microstructural effects
Characterization of Anisotropic Elastic Constants of Silicon-Carbide Particulate Reinforced Aluminum Metal Matrix Composites. I. Experiment. 799-809A

Thermal stability, Temperature effects
Comparison of Orthorhombic and Alpha-Two Titanium Aluminides as Matrices for Continuous SiC-Reinforced Composites. 1267-1283A

Thermal stresses
Effect of Strain Rate on the High-Temperature Low-Cycle Fatigue Properties of a Nimonic PE-16 Superalloy. 159-171A
Analysis of Thermally Induced Stress and Strain in Continuous Fiber-Reinforced Composites. 415-425A
Cleavage Initiation in the Intercritically Reheated Coarse-Grained Heat-Affected Zone: I. Fractographic Evidence. 563-573A
On Low-Temperature Environment-Assisted Fatigue Crack Propagation. 658-659A
Transformation, Microcrack, and Thermal Residual Stress as Interactive Processes in ZrO_2-Toughened Al_2O_3, Simulated by the Finite Element Method. 1725-1731A
Modeling Creep Deformation of a Two-Phase TiAl/Ti_3Al Alloy With a Lamellar Microstructure. 2161-2171A

Thermochemistry
Improved Thermochemical Calculations for Maraging Steels and Comparison With Atom Probe Measurement of Phase Composition. 2538-2539A

Thermodynamics
See also Enthalpy
Entropy
Free energy
Calcium Deoxidation Equilibrium in Liquid Iron. 33-42B
High-Temperature Phase Relations and Thermodynamics in the Iron—Lead—Sulfur System. 53-61B
Thermodynamics and Phase Relations of the Fe—O—S—SiO_2(sat) System at 1200°C and the Effect of Copper. 79-89B
Gradient Solid Electrolytes for Thermodynamic Measurements: System Na_2CO_3—Na_2SO_4. 173-180A
Thermodynamics of Oxygen, Nitrogen, and Sulfur in Liquid Iron Equilibrated With CaO—Al_2O_3—MgO Slags. 235-244B
Thermodynamics of the Iron)Carbon)Zinc System. 569-578B
Experimental Study of the Influence of Interfacial Energies and Reactivity on Wetting in Metal/Oxide Systems. 599-605A
Thermodynamics of Isolated Pores Filling With Liquid in Sintered Composite Materials. 733-740A
Thermodynamic Simulation Model of the Isasmelt Process for Copper Matte. 839-853B
Thermodynamics of the Liquid |xCu + yAu + (1—x—y)Ge|, ($0.75 \leq x \leq 1$, $0 \leq y \leq 0.125$) Alloys at 1550K by Knudsen Effusion Mass Spectrometry. 857-864A
Thermal Separation of Arsenic and Antimony Oxides. 873-884B
A Thermodynamic Study of the Molybdenum-Oxygen System. 885-891B
Thermodynamics of Boron in a Silicon Melt. 903-907B
Calculation of Thermophysical Properties of Carbon and Low Alloyed Steels for Modeling of Solidification Processes. 909-916B
Intragranular Ferrite Nucleation in Medium-Carbon Vanadium Steels. 929-936A
Computer Simulation of Diffusion in Multiphase Systems. 1127-1134A
Numerical Modeling of Solidification and Subsequent Transformation of Fe—Cr—Ni Alloys. 1309-1321A
Thermodynamics and Kinetics of the Formation of Widmanstätten Ferrite Plates in Ferrous Alloys. (Conference Paper) 1947-1953A
Thermodynamic Consideration of Formation Mechanism of α_1 Plate in βCu-Base Alloys. (Conference Paper) 2555-2564A
The Chromium Equivalents of Selected Elements in Austenitic Stainless Steel. 2675-2681A
Diffusion-Controlled Growth in Ternary Systems. 2683-2694A
Thermodynamics and Long-Range Order of Interstitials in a Hexagonal Close-Packed Lattice. 2797-2814A

Thermoelastic properties
See also Shape memory

Thermoelastic properties, Microstructural effects
Some Aspects of Thermomechanical Fatigue of AISI 304L Stainless Steel. II. Dislocation Arrangements. 407-413A

Thermoelastic properties, Stress effects
Behavior of Nickel-Base Superalloy Single Crystals Under Thermal—Mechanical Fatigue. 99-109A
Some Aspects of Thermomechanical Fatigue of AISI 304L Stainless Steel. I. Creep—Fatigue Damage. 401-406A
Modeling the Effects of Stress State and Crystal Orientation on the Stress-Induced Transformation of NiTi Single Crystals. 2383-2389A

Thermomechanical properties
See Thermoelastic properties

Thermomechanical treatment
Compositional and Microstructural Changes Which Attend Reheating and Grain Coarsening in Steels Containing Niobium. 277-286A
Superplastic Behavior of Thermomechanically Treated P/M 7091 Aluminum Alloy. 2153-2160A

Thermonuclear reactions, Radiation effects
Helium 3 Precipitation in AISI 316L Stainless Steel Induced by Radioactive Decay of Tritium: Microstructural Study of Helium Bubble Precipitation. 2117-2130A

Thermostability
See Thermal stability

Thin films, Phases (state of matter)
The Morphological Stability of Lateral Growth in Solid—Solid Phase Transformation During Thin-Film Interdiffusion in Aluminum/Copper Bimetal Films. 1613-1625A

Tig arc welding
See Gas tungsten arc welding

TIG welding
See Gas tungsten arc welding

Time temperature transformation curves
See TTT curves

Tin, Microstructure
Characterization of Inhomogeneous Elastic Deformation With X-Ray Diffraction. 341-347A

Tin, Physical properties
Sticking of Solids in Liquids. 397-403B

Tin, Soldering
The Effect of Low Gold Concentrations on the Creep of Eutectic Tin—Lead Joints. 1249-1257A

Tin base alloys, Casting
Prediction of Columnar to Equiaxed Transition During Diffusion-Controlled Dendritic Alloy Solidification. 1081-1093A

Tin base alloys, Mechanical properties
Factors Influencing the Exceptional Ductility of a Superplastic Pb-62% Sn Alloy. 2309-2311A

Tin compounds, Superconductivity
Effect of Oxygen and Zirconium on the Growth and Superconducting Properties of Nb_3Sn. 203-212A
The Role of Oxygen and Zirconium in the Formation and Growth of Nb_3Sn Grains. 213-219A

Titanium, Alloying elements
Thermodynamics of Oxygen and Nitrogen in Liquid Nickel Equilibrated With CaO—TiO_x and CaO—TiO_x—Al_2O_3 Melts. 5-13B
Effects of Austenite Grain Size and Cooling Rate on Widmanstätten Ferrite Formation in Low-Alloy Steels. 665-675A
Microstructures and Mechanial Behavior of NiAl-Mo and NiAl-Mo-Ti Two-Phase Alloys. 2769-2781A

Titanium, Diffusion
Anomalous Diffusion of Aluminum in β-Titanium. 873-876A

Titanium base alloys
Microstructure and Sound Velocity of Ti-N-O Synthetic Inclusions in Ti-6Al-4V. 2321-2329A

Titanium base alloys, Coating
The Influence of Laser Glazing on Fatigue Crack Growth in Ti—24Al—11Nb. 183-192A

Titanium base alloys, Composite materials
Microstructural Study of the Titanium Alloy Ti—15Mo—2.7Nb—3Al—0.2Si (TIMETAL 21S). 1109-1118A
Comparison of Orthorhombic and Alpha-Two Titanium Aluminides as Matrices for Continuous SiC-Reinforced Composites. 1267-1283A
Room-Temperature Strength and Deformation of TiB_2-Reinforced Near-γ Titanium Aluminides. 2181-2197A
Thermal-Mechanical Fatigue of Ti-48Al-2V Alloy and Its Composite. 2207-2212A

Titanium base alloys, Diffusion
A History of the Controversy Over the Roles of Shear and Diffusion in Plate Formation Above M_d and a Comparison of the Atomic Mechanisms of These Processes. (Conference Paper, Review) 1797-1819A

Titanium base alloys, Heat treatment
The Effect of Thermal Exposure on Microstructural Stability and Creep Resistance of a Two-Phase TiAl/Ti_3Al Lamellar Alloy. 2371-2381A

Titanium base alloys, Mechanical properties
Microstructure and Mechanical Properties of Ti—40 wt.% Ta (Ti—15 at.% Ta). 461-472A
Dynamic Fracture Behavior of Ti—6Al—4V Alloy With Various Stabilities of β Phase. 1655-1666A
Temperature and Microstructural Dependence of the Deformation of a High Niobium, Titanium—Aluminum Alloy. 1667-1679A
The Elastic Strain Energy of Growth Ledges on Coherent and Partially Coherent Precipitates. 2073-2082A
Flow Instabilities and Fracture in Ti-6Al-4V Deformed in Compression at 298-673K. 2173-2179A
Modeling the Effects of Stress State and Crystal Orientation on the Stress-Induced Transformation of NiTi Single Crystals. 2383-2389A

Titanium base alloys, Metal working
Relationships of Slip Morphology, Microcracking, and Fracture Resistance in a Lamellar TiAl-Alloy. 1217-1228A

Titanium base alloys, Oxidation
Auger Electron Analysis of the Initial Oxidation of Titanium Aluminides Based on Ti—48Al. 1041-1050A

Titanium base alloys, Powder technology
Microstructure and Sound Velocity of Ti-N-O Synthetic Inclusions in Ti-6Al-4V. 2321-2329A

Titanium base alloys, Reactions (chemical)
High-Temperature Oxidation of Cathodically Hydrogen-Charged Two-Phase (Ti_3Al, TiAl) Titanium Aluminides. 2491-2496A

Titanium base alloys, Rolling
A Simple Model for Conventional Hot Rolling of Sheet Materials. 1681-1692A
Load-Signature Analysis for Pack Rolling of Near-Gamma Titanium Aluminide Alloys. 2539-2542A

Titanium base alloys, Sorption
Barrier-Layer Formation and Its Control During Hydrogen Permeation Through Ti—24Al—11Nb Alloy. 89-97A

Titanium base alloys, Welding
The α/β Interface Phase in Titanium Alloys: Artifact or Real Phase Contribution to Problem Resolution. 241-248A

Titanium carbide, Composite materials
Modelling the Infiltration Kinetics of Molten Aluminum Into Porous Titanium Carbide. 2357-2370A
Melt-Processed Ni_3Al Matrix Composites Reinforced With TiC Particles. 2525-2534A

Titanium compounds
See also Titanium carbide

Titanium compounds, Forging
Microstructure Development During Conventional and Isothermal Hot Forging of a Near-γ Titanium Aluminide. 2753-2768A

Titanium compounds, Mechanical properties
Tensile Ductility of Extrinsically Toughened Intermetallics. 299-308A
Environmental Effect on Room-Temperature Ductility of Isothermally Forged TiAl-Base Alloys. 321-330A
Elastic Constants of Some Transition-Metal-Disilicide Single Crystals. 331-340A
Ordering and Mechanical Strength in $L1_2$ Cubic Titanium Trialuminides. 449-451A
The Effects of Hydrostatic Pressure on the Compressive Mechanical Behavior of $L1_2$ Al_3 Ti-Based Intermetallic. 1703-1711A
Modeling Creep Deformation of a Two-Phase TiAl/Ti_3Al Alloy With a Lamellar Microstructure. 2161-2171A

Top blown converters
Backmixing in Channel Reactors With High-Strength Bottom Gas Injection. 619-623B

Torsion tests
Softening and Microstructural Change Following the Dynamic Recrystallization of Austenite. 389-400A

Torsional modulus
See Shear modulus

Torsional strength
See Shear strength

Total heat
See Enthalpy

Toughness
See also Fracture toughness

Toughness, Alloying effects
Microstructures and Mechanial Behavior of NiAl-Mo and NiAl-Mo-Ti Two-Phase Alloys. 2769-2781A

Toughness, Cooling effects
Effects of Widmanstätten Ferrite on the Mechanical Properties of a 0.2% C—0.7% Mn Steel. 763-773A

Toughness, Heating effects
Development and Characterization of Interface Coatings in Molybdenum-Reinforced NiAl Matrix Composites. 2111-2116A

Toughness, Microstructure
The Elastic Strain Energy of Growth Ledges on Coherent and Partially Coherent Precipitates. 2073-2082A

Transformation entropy
See Entropy

Transformations (materials)
See Phase transformations

Transgranular fracture, Heating effects
Fracture Toughness of Quaternary Al-Li-Cu-Mg Alloy Under Mode I, Mode II, and Mode III Loading Conditions. 2439-2452A

Transition metal alloys
See Cobalt base alloys
Copper base alloys
Ferrous alloys
Nickel base alloys
Titanium base alloys
Zinc base alloys
Zirconium base alloys

Transition metal compounds
See Cobalt compounds
Iron compounds
Nickel compounds
Titanium compounds
Zinc compounds

Transition metals
See Cobalt
Copper
Iron
Manganese
Nickel
Titanium
Yttrium
Zinc
Zirconium

Transmission
See Heat transmission

Transmission electron microscopy
Transmission Electron Microscopy Study of Martensites in Laser-Clad Ni—Al Bronze on Aluminium Alloy AA333. 37-46A
Transmission Electron Microscopy Crystal Structure Study of the Chromium-Rich Phase in a Laser-Clad Nickel Alloy. 487-497A
Al_2Ti Precipitation in $Al_{64}Fe_8Ti_{28}$ Alloy. 715-721A
Interstitial Precipitation in Fe—Cr—Al Alloys. 1135-1146A

Transuranium metals
See Plutonium

Triaxial stress
See Axial stress

Tritium, Diffusion
Tritium Distribution at the Crack Tip of High-Strength Steels Submitted to Stress Corrosion Cracking. 1159-1167A

Tritium, Dopants
Helium 3 Precipitation in AISI 316L Stainless Steel Induced by Radioactive Decay of Tritium: Microstructural Study of Helium Bubble Precipitation. 2117-2130A
Helium 3 Precipitation in AISI 316L Stainless Steel Induced by Radioactive Decay of Tritium: Growth Mechanism of Helium Bubbles. 2131-2143A

TTT curves
Bainitelike Transformations in Some Oxide Ceramics. (Conference Paper) 2647-2653A

Tubular goods
See Pipe

Tundishes
Mathematical and Physical Modeling Studies of Molten Aluminum Flow in a Tundish. 669-680B

Tungsten, Composite materials
Investigation of the Kinetics of Reduction of Nickel Tungstate by Hydrogen. 391-396B

Tungsten, Powder technology
Determination of Pore Mobility During Sintering. 81-87A

Tungsten arc welding
See Gas tungsten arc welding

Tungsten base alloys, Heat treatment
The Cause of Matrix Penetration of W/W Grain Boundaries During Heat Treatment of W-Ni-Fe Heavy Alloy. 2828-2831A

Tungsten base alloys, Powder technology
Effect of Cobalt Addition on the Liquid-Phase Sintering of Tungsten—Copper Prepared by the Fluidized Bed Reduction Method. 1575-1578A

Tungsten carbide, Composite materials
Thermodynamics of Isolated Pores Filling With Liquid in Sintered Composite Materials. 733-740A

Tungsten compounds
See Tungsten carbide

Tungsten inert gas welding
See Gas tungsten arc welding

Turbine blades, Microstructure
The Effect of Enhanced Gravity Levels on Microstructural Development in Pb—50 wt.% Sn Alloys During Controlled Directional Solidification. 865-870A

Turbines
See Gas turbine engines

Turbojet engines, Materials selection
Investigation of the Kinetics of Reduction of Nickel Tungstate by Hydrogen. 391-396B

Twinning
Crystallographic Characteristics of the Al—Co Decagonal Quasicrystal and Its Monoclinic Approximant τ^2-$Al_{13}Co_4$. 47-56A
Triclinic Ni_2Al Phase in 63.1 at.% NiAl. 57-61A
Strain Hardening in Underaged Inconel 718. 653-656A

Ultimate shear strength
See Shear strength

Ultimate tensile strength
See Tensile strength

Ultrasonic testing
Characterization of Anisotropic Elastic Constants of Silicon-Carbide Particulate Reinforced Aluminum Metal Matrix Composites. I. Experiment. 799-809A

Ultraviolet photoelectron spectroscopy
See Photoelectron spectroscopy

Undercooling
See Supercooling

Uranium, Extraction
Small Cell Experiments for Electrolytic Reduction of Uranium Oxides to Uranium Metal Using Fluoride Salts. 505-518B

Uranium, Reactions (chemical)
Simulation of In Situ Uraninite Leaching. I. A Partial Equilibrium Model of the NH_4HCO_3—$(NH_4)_2CO_3$—H_2O_2 Leaching System. 171-183B

Uranium base alloys, Diffusion
Interdiffusion Between Uranium—Zirconium Fuel vs. Selected Cladding Steels. 1649-1653A

V notch Charpy impact tests
See Impact tests

V notch Charpy tests
See Impact tests

Vacancies (crystal defects)
See Lattice vacancies

Vacancies (lattice)
See Lattice vacancies

Vacuum, Environment
Environmental Effect on Room-Temperature Ductility of Isothermally Forged TiAl-Base Alloys. 321-330A

Vacuum annealing
A Structural Study of Oxidation in a Zirconia-Toughened Alumina Fiber-Reinforced NiAl Composite. 1291-1299A

Vanadium, Alloying elements
Influence of Tempering Temperature on Stability of Carbide Phases in 2.6Cr—0.7Mo—0.3V Steel With Various Carbon Content. 267-275A

Vanadium, Binary systems
Formation and Stability of Metastable Structures and Amorphous Phases in Pu—V, Pu—TA, and Pu—Yb Systems With Positive Heats of Mixing. 1579-1590A

Vanadium, Recovering
Vanadium Distribution in Melts Intermediate to Ferroalloy Production From Vanadiferous Slag. 27-32B
Processing of Spent Hydrorefining Catalysts by Selective Chlorination. 481-490B

Vanadium compounds, Mechanical properties
Elastic Constants of Some Transition-Metal-Disilicide Single Crystals. 331-340A

Vapor phases
An Empirical Correlation Between Contact Angles and Surface Tension in Some Ceramic—Metal Systems. 225-230A

Vapor pressure
Kinetics of the Reaction of H_2O Gas With Liquid Iron. 245-253B

Vapors
See Water vapor

Vessels
See Pressure vessels

Vickers hardness
See Diamond pyramid hardness

Viscoplasticity, Deformation effects
Modeling the Thin-Slab Continuous-Casting Mold. 443-457B

Viscoplasticity, Stress effects
Micromechanical Modelling of Reinforcement Fracture in Particle-Reinforced Metal-Matrix Composites. 2403-2420A

Viscosity
Observations on the Effect of Medium Density and Viscosity on the Rate of Induced Aeration in Agitated Vessels. 303-306B
Sticking of Solids in Liquids. 397-403B
A Model for Estimation of Viscosities of Complex Metallic and Ionic Melts. 519-525B
A Two-Phase Flow Model of the Stirring of Al)SiC Composite Melt. 607-618B
Physicochemical Properties of Nickel Electrolytes. 637-644B
Measurements of High-Temperature Viscosities of Liquid Boron Trioxide. 876-881A

Viscosity, Composition effects
The Effects of Hydrogen on the Mechanical Behavior of Austenitic Stainless Steels at Room Temperature. 1015-1023A

Viscosity, Temperature effects
Estimation of the Viscosities of Binary Metallic Melts Using Gibbs Energies of Mixing. 589-595B

Voids, Deformation effects
Alligatoring and Damage in the Cold Rolling of Spheroidized Steels. 589-598A

Voids, Heating effects
Effect of Heat Treatment on the Microstructure, Tensile Properties, and Fracture Behavior of Permanent Mold Al-10 wt.% Si-0.6 wt.% Mg/SiC/10p Composite Castings. 2247-2263A

Voids, Stress effects
Creep and Intergranular Cracking of Ni—Cr—Fe—C in 360°C Argon. 1169-1183A
Thermal-Mechanical Fatigue of Ti-48Al-2V Alloy and Its Composite. 2207-2212A
Fracture Toughness of Discontinuously Reinforced Al-4Cu-1.5Mg/TiB_2 Composites. 2461-2468A

Voltage
See Electric potential

Voltage drop
See Electric potential

Washing
Slurry Filtration and Cake Washing After the HCl-Leach of Magnesite and Serpentine—Continuous Washing Model. 321-331B

Water, Reactions (chemical)
Interactions Between Drops of a Molten Aluminum)Lithium Alloy and Liquid Water. 623-625B

Water quenching
Microstructure and Mechanical Properties of Ti—40 wt.% Ta (Ti—15 at.% Ta). 461-472A
Local Melting in Al—Mg—Zn—Alloys. 521-530A
Interstitial Precipitation in Fe—Cr—Al Alloys. 1135-1146A
The Cause of Matrix Penetration of W/W Grain Boundaries During Heat Treatment of W-Ni-Fe Heavy Alloy. 2828-2831A

Water vapor, Environment
Embrittlement of B2 Iron Aluminide by Water Vapor and by Hydrogen. 1285-1290A

Wear
See also Abrasive wear
Frictional wear

Wear, Stress effects
Fracture Toughness of Discontinuously Reinforced Al-4Cu-1.5Mg/TiB_2 Composites. 2461-2468A

Wear rate, Microstructural effects
Effect of Microstructure (Particulate Size and Volume Fraction) and Counterface Material on the Sliding Wear Resistance of Particulate-Reinforced Aluminum Matrix Composites. 969-983A

Wear resistance, Coating effects
Processing, Microstructure, and Properties of Laser-Clad Nickel Alloy FP-5 on Al Alloy AA333. 425-434B

Wear resistance, Heating effects
The Effect of Aging on Wear Characteristics of Rheocast-Leaded Aluminum Alloys. 851-856A

Wear resistance, Microstructural effects
Effect of Microstructure (Particulate Size and Volume Fraction) and Counterface Material on the Sliding Wear Resistance of Particulate-Reinforced Aluminum Matrix Composites. 969-983A

Weathering steels
See Structural steels

Weld defects
The α/β Interface Phase in Titanium Alloys: Artifact or Real Phase Contribution to Problem Resolution. 241-248A
Effect of Welding Variables and Solidification Substructure on Weld Metal Porosity. 2285-2294A

Weldability
Resistance Spot Welding of Precoated Steel Sheet: Computational Heat-Transfer Analysis. 415-423B

Welded joints, Heat treatment
Computer Simulation of Diffusion in Multiphase Systems. 1127-1134A

Welded joints, Microstructure
The α/β Interface Phase in Titanium Alloys: Artifact or Real Phase Contribution to Problem Resolution. 241-248A

Welded joints, Phases (state of matter)
Characterization of a Diffusion-Bonded Al—Mg Alloy/SiC Interface by High Resolution and Analytical Electron Microscopy. 617-627A
The Influence of Electron-Beam Welding Parameters on Heat-Affected-Zone Microfissuring in Incoloy 903. 1733-1745A

Welded joints, Physical properties
Effect of Welding Variables and Solidification Substructure on Weld Metal Porosity. 2285-2294A

Welded joints, Thermal properties
Three-Dimensional Finite Element Modeling of Gas Metal-Arc Welding. 435-441B

Welding parameters
Resistance Spot Welding of Precoated Steel Sheet: Computational Heat-Transfer Analysis. 415-423B
The Influence of Electron-Beam Welding Parameters on Heat-Affected-Zone Microfissuring in Incoloy 903. 1733-1745A

Welds
See Welded joints

Wetting
An Empirical Correlation Between Contact Angles and Surface Tension in Some Ceramic—Metal Systems. 225-230A

Experimental Study of the Influence of Interfacial Energies and Reactivity on Wetting in Metal/Oxide Systems. 599-605A
Capillarity in Isothermal Infiltration of Alumina Fiber Preforms With Aluminum. 2145-2152A
Modelling the Infiltration Kinetics of Molten Aluminum Into Porous Titanium Carbide. 2357-2370A

Wetting, Alloying effects
Solid-State Wetting of Graphite by Lead and Pb—Ni Alloys. 607-615A

Wetting, Temperature effects
Kinetics of Interlayer Formation on Polycrystalline α-Al_2O_3/Copper-Titanium Alloy Interface. 2083-2090A

Whisker composites, Powder technology
Microstructural Analysis of Fracture Toughness Variation in 2XXX-Series Aluminum Alloy Composites Reinforced With SiC Whiskers. 2213-2223A
Low-Cycle Fatigue Properties of a SiC Whisker-Reinforced 2124 Aluminum Alloy. 2265-2274A

White metal (copper matte)
See Copper mattes

Wolfram
See Tungsten

Work hardening
See Strain hardening

Work strengthening
See Strain hardening

Workability
See also Formability

Workability, High temperature effects
The Workability of Commercial and Experimental 0.6% Carbon Low Alloy Steels in the Temperature Range of 650-870°C. 827-837A

Wustite, Reduction (chemical)
Surface Segregation of Calcium Oxide in Wustite and Its Effects on the Reduction. 405-413B
Improvement in the Reducibility of Wustite Assisted by the Intensified Surface Segregation of Calcium Ions by the Double Addition of CaO and SiO_2. 741-748B

X ray analysis
See X ray diffraction

X ray diffraction
Crystallographic Characteristics of the Al—Co Decagonal Quasicrystal and Its Monoclinic Approximant τ^2-$Al_{13}Co_4$. 47-56A

X ray diffractometer
See X ray diffraction

X ray photoelectron spectroscopy
See Photoelectron spectroscopy

X ray scattering
Determination of the Short-Range Order Structure of Au—25 at.% Fe Using Wide-Angle Diffuse Synchrotron X-Ray Scattering. 1561-1573A

Yield strain
See Strain

Yield strength, Composition effects
The Effects of Hydrogen on the Mechanical Behavior of Austenitic Stainless Steels at Room Temperature. 1015-1023A
Room-Temperature Strength and Deformation of TiB_2-Reinforced Near-γ Titanium Aluminides. 2181-2197A
Melt-Processed Ni_3Al Matrix Composites Reinforced With TiC Particles. 2525-2534A

Yield strength, Cooling effects
Effects of Widmanstätten Ferrite on the Mechanical Properties of a 0.2% C—0.7% Mn Steel. 763-773A

Yield strength, Deformation effects
The Tensile Deformation Behavior of AA 3004 Aluminum Alloy. 357-364A
Hot Deformation Characteristics of INCONEL Alloy MA 754 and Development of a Processing Map. 1693-1702A
High-Temperature Deformation of B2 NiAl-Base Alloys. (Conference Paper) 2017-2026A

Yield strength, Environmental effects
Hydride Embrittlement in Zircaloy-4 Plate. I. Influence of Microstructure on the Hydride Embrittlement in Zircaloy-4 at 20 and 350°C. 1185-1197A

Yield strength, Heating effects
The Effects of Double Austenitization on the Mechanical Properties of a 0.34C Containing Low-Alloy Ni—Cr—Mo—V Steel. 545-555A
Effect of Heat Treatment on the Microstructure, Tensile Properties, and Fracture Behavior of Permanent Mold Al-10 wt.% Si-0.6 wt.% Mg/SiC/10p Composite Castings. 2247-2263A

Yield strength, High temperature effects
Elevated Temperature Fracture of RS/PM Alloy 8009. I. Fracture Mechanics Behavior. 365-379A
The Workability of Commercial and Experimental 0.6% Carbon Low Alloy Steels in the Temperature Range of 650-870°C. 827-837A

Yield strength, Microstructural effects
Precipitation Effects During Hot Deformation of a Copper Alloy. 257-266A
Ordering and Mechanical Strength in $L1_2$ Cubic Titanium Trialuminides. 449-451A
Textural and Microstructural Gradient Effects on the Mechanical Behavior of a Tantalum Plate. 1025-1031A
Temperature and Microstructural Dependence of the Deformation of a High Niobium, Titanium—Aluminum Alloy. 1667-1679A
Microstructural Analysis of Fracture Toughness Variation in 2XXX-Series Aluminum Alloy Composites Reinforced With SiC Whiskers. 2213-2223A

Yield strength, Pressure effects
The Effects of Hydrostatic Pressure on the Compressive Mechanical Behavior of $L1_2$ Al_3 Ti-Based Intermetallic. 1703-1711A

Yield strength, Radiation effects
Deformation Behavior of Irradiated Zr—2.5Nb Pressure Tube Material. 135-145A

Yield strength, Stress effects
Behavior of Nickel-Base Superalloy Single Crystals Under Thermal—Mechanical Fatigue. 99-109A
Analysis of Thermally Induced Stress and Strain in Continuous Fiber-Reinforced Composites. 415-425A
Crack Initiation at Long Radial Hydrides in Zr—2.5Nb Pressure Tube Material at Elevated Temperatures. 993-1004A
Evaluation of Homogeneous Compression Flow Curves Using Square Cross-Sectioned Specimens. 1095-1097A
Hydride Embrittlement in Zircaloy-4 Plate. II. Interaction Between the Tensile Stress and the Hydride Morphology. 1199-1208A
Stress-State Dependence of Strain-Hardening Behavior in 2014 Al/15 vol.% Al_2O_3 Composite. (Conference Paper) 2049-2061A
Flow Instabilities and Fracture in Ti-6Al-4V Deformed in Compression at 298-673K. 2173-2179A

Yield strength, Temperature effects
Behavior of Steels Near the Incipient Melting Temperature. 125-133A

Yield stress
See Yield strength

Youngs modulus
See Modulus of elasticity

Ytterbium, Binary systems
Formation and Stability of Metastable Structures and Amorphous Phases in Pu—V, Pu—TA, and Pu—Yb Systems With Positive Heats of Mixing. 1579-1590A

Yttrium, Alloying elements
Supersaturation of the Al_2Y Laves Phase by Rapid Solidification. 230-233A

Yttrium, Quaternary systems
Thermodynamic Study of $BaCuO_2$ and $BaCu_2O_2$. 385-389B

Yttrium, Reactions (chemical)
Solubility and Thermodynamic Properties of Y_2O_3 in LiF—YF_3 Melts. 91-96B

Zinc, Alloying elements
Effect of Alloying Elements on the Solidification Characteristics and Microstructure of Al—Si—Cu—Mg—Fe 380 Alloy. 437-448A
On the Prebainitic Phenomenon in Some Alloys. (Conference Paper) 1941-1946A

Zinc, Binary systems
Multiphase Binary Diffusion in Infinite and Semi-Infinite Media. II. On the Numerical Calculation of the Rate Constants for Formation of Product Phases. 753-761A

Zinc, Coatings
Computer Algorithms for Radiometric Measurement of Temperature During the Galvanneal Process. 449-462B

Zinc, Extraction
Thermal Treatment of Complex Sulfide Ores in N_2 and H_2 Atmospheres: a New Approach for the Extraction of Their Valuable Elements. (Review) 193-205B
The Ferric Fluosilicate Leaching of Lead Concentrates. I. Kinetic Studies. 473-480B

Zinc, Ternary systems
Thermodynamics of the Iron)Carbon)Zinc System. 569-578B

Zinc base alloys, Mechanical properties
Effect of Iron on the Superplastic Deformation of Zn-22%Al. 2391-2401A

Zinc compounds, Coatings
The Effect of Steel Chemistry on the Formation of Fe-Zn Intermetallic Compounds of Galvanneal-Coated Steel Sheets. 721-730B

Zinc plating
See Galvanizing

Zirconium, Alloying elements
Effect of Oxygen and Zirconium on the Growth and Superconducting Properties of Nb_3Sn. 203-212A
The Role of Oxygen and Zirconium in the Formation and Growth of Nb_3Sn Grains. 213-219A

Zirconium base alloys, Mechanical properties
Deformation Behavior of Irradiated Zr—2.5Nb Pressure Tube Material. 135-145A
Crack Initiation at Long Radial Hydrides in Zr—2.5Nb Pressure Tube Material at Elevated Temperatures. 993-1004A
Hydride Embrittlement in Zircaloy-4 Plate. I. Influence of Microstructure on the Hydride Embrittlement in Zircaloy-4 at 20 and 350°C. 1185-1197A
Hydride Embrittlement in Zircaloy-4 Plate. II. Interaction Between the Tensile Stress and the Hydride Morphology. 1199-1208A

STYLING OF REFERENCES

1. A *journal* reference should be readily available on subscription and included in most library collections. Use journal abbreviations as given in the current listing of *Chemical Abstracts Service Source Index*. Article titles are not to be included.
   Example: Author: *Journal*, year, ser., vol., pp.
   R.M. Horn and Robert O. Ritchie: *Metall. Trans. A*, 1978, vol. 9A, pp. 1039-53.
2. References to *books* should include the title and pages within the book.
   Example: Author: *Book*, edition, publisher, place, date, pages.
   George E. Dieter: *Mechanical Metallurgy*, 2nd ed., McGraw-Hill Book Co., New York, NY, 1976, pp. 160-65.
3. A "*private communication*" or "*unpublished research*" may be referenced when required to give proper credit. The citation must include the affiliation and address of the person involved, as well as the year. *Papers Presented at Meetings but not Published* fall under this category.
   Example: J.J. Doe: AAA Company, Washington, DC, unpublished research, 1988.
4. References to *Internal Reports* and other publications of limited availability* are not desirable. However, they will be permitted when the use results in a saving of page space or is required for proper recognition. In these matters, the author's judgment must be supported by the review committee and editor. The report should be available on request and include the source from which a copy may be obtained.
   Example: J.J. Doe: Report No. 738, AAA Company, Washington, DC, January 1988.
5. *In Press* references must include the name of the journal. Balance of reference should be supplied when available. This may be done on the proofs.
6. References such as *submitted for publication* and *to be published* are not acceptable. If the item is still undergoing review, use same format as in 3 above.
7. References must be numbered throughout the manuscript and presented in consecutive numerical order on Reference page.
8. No other references will be published.

*Not available by subscription.

INFORMATION ON PAGE CHARGES AND REPRINTS

METALLURGICAL AND MATERIALS TRANSACTIONS, like many other scientific and technical journals, depends on author page charges for a significant part of its support. Therefore a charge of $75.00 per printed page is levied for all papers published. This charge is $70.00 per printed page for manuscripts submitted on computer diskette (see *Metall. Trans. A*, 1985, vol. 16A, p. 2082). One hundred reprints will be supplied without additional charge for every paper on which the payment of these charges is authorized. It is expected that each author or sponsoring institution will contribute fairly to the support of METALLURGICAL AND MATERIALS TRANSACTIONS through payment of the page charges.

However, in special cases in which the author would have to pay the charges personally, such charges may be waived upon written request. Instructions and forms regarding page charges, waivers, and reprints will be forwarded from the editorial office and appropriate action should be taken at that time. These and any other special matters related to page charges should be referred to METALLURGICAL AND MATERIALS TRANSACTIONS, Carnegie Mellon University, Schenley Park, Pittsburgh, PA 15213.

PUBLICATION OF SYMPOSIUM PAPERS IN METALLURGICAL AND MATERIALS TRANSACTIONS

There are special situations when it is desirable to publish a group of papers concurrently in METALLURGICAL AND MATERIALS TRANSACTIONS. Typically, these arise when a technical committee has organized a limited meeting program of two or three half-day sessions on a particular theme. The material must be original, of high quality, and closely correlated but not sufficient to justify an independent monograph or proceedings-type publication. A high percentage of these would normally be published as METALLURGICAL AND MATERIALS TRANSACTIONS papers, but the authors and committees feel there is an additional benefit from concurrent publication.

To obtain approval, the chairman of the symposium program should write to the editor outlining the symposium scope, the papers to be considered, with abstracts if available, and the plans for payment of page charges. On receipt of this information, the editor will submit a request to the Joint Commission for approval. All manuscripts in the symposium will be reviewed according to METALLURGICAL AND MATERIALS TRANSACTIONS standard review procedure.

An example of a symposium published by METALLURGICAL AND MATERIALS TRANSACTIONS: "Symposium on the Mechanical, Microstructural and Fracture Processes in Superplasticity," *Metall. Trans. A*, 1982, vol. 13A, pp. 688-743.

COPYRIGHT POLICY

METALLURGICAL AND MATERIALS TRANSACTIONS is subject to the U.S. Copyright Law which became effective on January 1, 1978. Accordingly, the signed copyright transfer form must be received in the Editor's Office before the article can be processed for publication. This form, published in the February issue of METALLURGICAL AND MATERIALS TRANSACTIONS A and METALLURGICAL AND MATERIALS TRANSACTIONS B, must be *signed by each author* unless excepted as noted under Part A, "work made for hire" or Part B which pertains to U.S. Government employees. Other copyright transfer forms may not be substituted for this form.

This copyright transfer formalizes the author-publisher relations of professional societies and becomes effective when the manuscript is accepted for publication. If the article is not published in METALLURGICAL AND MATERIALS TRANSACTIONS, the copyright transfer will not take effect. As the copyright owners for articles in METALLURGICAL AND MATERIALS TRANSACTIONS, ASM and TMS-AIME will continue to promote the widest dissemination of the technical information printed in these journals.

ANNUAL AWARDS

TMS—**Champion H. Mathewson Award**: Established to honor Dr. Champion H. Mathewson, President of the Institute in 1943, award is made for a paper which represents a notable contribution to metallurgical or materials science. Paper must have been published in *Metallurgical and Materials Transactions A* or *B* or any other TMS publication within the three-year period preceding the award.

ASM—**Marcus A. Grossmann Young Author Award**: Established to honor Dr. Marcus A. Grossmann, President of ASM in 1944, award is made to suitable author whose age is less than 40 years of age on 1 January of year in which paper was published in *Metallurgical and Materials Transactions*. Paper must have been published in the calendar year preceding that in which award is to be made.

ASM—**Henry Marion Howe Award**: Established to honor Dr. Henry Marion Howe, this is the oldest of the ASM awards and metals. Paper must have been published in the calendar year preceding that in which award is to be made.

Statement of Ownership, Management and Circulation

(Required by 39 U.S.C. 3685)

1A. Title of Publication	1B. PUBLICATION NO.	2. Date of Filing
Metallurgical & Materials Transactions A	0 3 6 0 2 1 3 3	September 30, 1994
3. Frequency of Issue	3A. No. of Issues Published Annually	3B. Annual Subscription Price
Monthly (1994)	12	$696.00

4. Complete Mailing Address of Known Office of Publication *(Street, City, County, State and ZIP+4 Code) (Not printers)*

420 Commonwealth Drive, Warrendale, PA 15086 (Allegheny County)

5. Complete Mailing Address of the Headquarters of General Business Offices of the Publisher *(Not printer)*

420 Commonwealth Drive, Warrendale, PA 15086

6. Full Names and Complete Mailing Address of Publisher, Editor, and Managing Editor ***(This item MUST NOT be blank)***

Publisher *(Name and Complete Mailing Address)*

Alexander R. Scott, TMS, 420 Commonwealth Drive, Warrendale, PA 15086

Editor *(Name and Complete Mailing Address)*

David Laughlin, Carnegie Mellon University, Pittsburgh, PA 15213

Managing Editor *(Name and Complete Mailing Address)*

7. Owner *(If owned by a corporation, its name and address must be stated and also immediately thereunder the names and addresses of stockholders owning or holding I percent or more of total amount of stock. If not owned by a corporation, the names and addresses of the individual owners must be given. If owned by a partnership or other unincorporated firm, its name and address, as well as that of each individual must be given. If the publication is published by a nonprofit organization, its name and address must be stated.) (Item must be completed.)*

Full Name	Complete Mailing Address
Owned jointly by The Minerals, Metals & Materials Society and ASM International	420 Commonwealth Drive Warrendale, PA 15086 Materials Park, OH 44073

8. Known Bondholders, Mortgagees, and Other Security Holders Owning or Holding 1 Percent or More of Total Amount of Bonds, Mortgages or Other Securities *(If there are none, so state)*

Full Name	Complete Mailing Address

9. For Completion by Nonprofit Organizations Authorized To Mail at Special Rates *(DMM Section 424.12 only)*
The purpose, function, and nonprofit status of this organization and the exempt status for Federal income tax purposes *(Check one)*

☐ (1) Has Not Changed During Preceding 12 Months
☐ (2) Has Changed During Preceding 12 Months
(If changed, publisher must submit explanation of change with this statement.)

10. Extent and Nature of Circulation *(See instructions on reverse side)*	Average No. Copies Each Issue During Preceding 12 Months	Actual No. Copies of Single Issue Published Nearest to Filing Date
A. Total No. Copies *(Net Press Run)*	3,420	3,263
B. Paid and/or Requested Circulation 1. Sales through dealers and carriers, street vendors and counter sales	-	-
2. Mail Subscription *(Paid and/or requested)*	2,528	2,552
C. Total Paid and/or Requested Circulation *(Sum of 10B1 and 10B2)*	2,528	2,552
D. Free Distribution by Mail, Carrier or Other Means Samples, Complimentary, and Other Free Copies	764	648
E. Total Distribution *(Sum of C and D)*	3,292	3,200
F. Copies Not Distributed 1. Office use, left over, unaccounted, spoiled after printing	128	63
2. Return from News Agents	-	-
G. TOTAL *(Sum of E, F1 and 2—should equal net press run shown in A)*	3,420	3,263

11. **I certify that the statements made by me above are correct and complete**

Signature and Title of Editor, Publisher, Business Manager, or Owner

Alexander R. Scott, Publisher